INFORMATION TO USERS

This manuscript has been reproduced from the microfilm master. UMI films the text directly from the original or copy submitted. Thus, some thesis and dissertation copies are in typewriter face, while others may be from any type of computer printer.

The quality of this reproduction is dependent upon the quality of the copy submitted. Broken or indistinct print, colored or poor quality illustrations and photographs, print bleedthrough, substandard margins, and improper alignment can adversely affect reproduction.

In the unlikely event that the author did not send UMI a complete manuscript and there are missing pages, these will be noted. Also, if unauthorized copyright material had to be removed, a note will indicate the deletion.

Oversize materials (e.g., maps, drawings, charts) are reproduced by sectioning the original, beginning at the upper left-hand corner and continuing from left to right in equal sections with small overlaps.

Photographs included in the original manuscript have been reproduced xerographically in this copy. Higher quality 6" x 9" black and white photographic prints are available for any photographs or illustrations appearing in this copy for an additional charge. Contact UMI directly to order.

ProQuest Information and Learning
300 North Zeeb Road, Ann Arbor, MI 48106-1346 USA
800-521-0600

University of Alberta

M11 Channel at TRIUMF, Another Surface Muon Source

by

Farhana Sobratee 

A thesis submitted to the Faculty of Graduate Studies and Research in partial fulfillment of the requirements for the degree of Master of Science

Department of Physics

Edmonton, Alberta

Spring 2000

University of Alberta

Library Release Form

NAME OF AUTHOR:	Farhana Sobratee
TITLE OF THESIS:	M11 Channel at TRIUMF, Another Surface Muon Source
DEGREE:	Master of Science
YEAR THIS DEGREE GRANTED:	2000

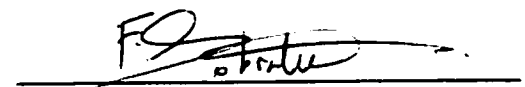

Farhana Sobratee
Apartment 1007
11147 82 Avenue
Edmonton Alberta T6G 0T5
CANADA

December 23, 1999

University of Alberta

Faculty of Graduate Studies and Research

The undersigned certify that they have read, and recommend to the Faculty of Graduate Studies and Research for acceptance, a thesis entitled **M11 Channel at TRIUMF, Another Surface Muon Source** submitted by **Farhana Sobratee** in partial fulfillment of the requirements for the degree of Master of Science.

Nathan L. Rodning (Supervisor)

Michael Brett (External)

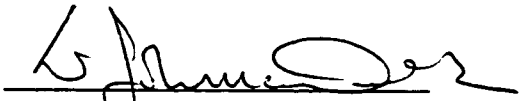

W. John McDonald

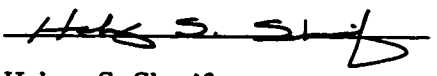

Helmy S. Sherif

DATE: December 1st, 1999.

Abstract

This thesis presents the results of a beam test on the M11 channel at TRIUMF using data collected with a Muon Spin Rotation (μSR) detector setup. The beam test was performed at a momentum range of few percent above and below the $\mu - \pi$ edge (at 29.79 Mev/c) to search for polarized muons. The polarized muons (a.k.a. surface muons) are produced from a π^+ decay at rest near the surface of the production target. Some interesting features of the surface and unpolarized cloud muons in the beam are presented at this momentum range. The background and its depolarization effect on the surface muons across the cyclotron RF period of 43.6 ns are investigated. It was found that this beamline can be used as a surface μ^+ source.

You will never be happy if you continue to search for what happiness consists of.
You will never live if you are looking for the meaning of life.

Albert Camus

To

Missrah, my mother.

Acknowledgements

I would like to thank Professor Nathan L. Rodning of the University of Alberta for his guidance, support and time, and for being my supervisor since April 1998. The funding from the Research Corporation for one semester is gratefully acknowleged. I appreciate the contribution of all the people of the E614 collaboration and the people of the μSR facility at TRIUMF for making this beam test possible. Also my sincere acknowledgement goes to Dr Peter W Green for his patience in helping me out with using his NOVA data analysis system.

The members of the supervisory and examining committee and specially the E614 collaborators, Dr David Gill, Dr Pierre Depommier, Dr Carl Gigliardi and Dr Peter Gumplinger have my gratitude for their many useful comments.

Finally, I would like to thank all of my friends and colleagues for their support.

Table of Contents

List of Tables

List of Figures

Chapter 1

INTRODUCTION

1.1 Motivation and Objectives

It was suggested that the M11 channel can be an alternative source of polarized muons at TRIUMF for various muon stopping experiments and that it can be used to perform preliminary diagnostic tests for experiment E614. E614 is a high precision muon decay experiment under preparation at TRIUMF and will be performed on the M13 beamline.

The objective of the beam test on M11 is to search for polarized muons. M11 is a secondary beamline optimized for the transport of high momentum pions and muons, and had not been used previously at low momentum. The polarized muons on the M11 beamline are "surface" muons which are produced from pions decaying at rest at the surface of the production target. The physics behind the production of the ideal monoenergetic polarized muons is given in Chapter 2.

On seeing the signature time of flight spectra of polarized muons during a preliminary test with a simple set-up of three scintillators, arrangement was made for an experimental set-up whereby a technique called muon spin rotation (μSR)

is used. From this the following quantities are determined for M11:

- the flux of the different particles in the beamline (polarized and unpolarized muons, positrons and pions),
- the polarization of the muons,
- and a time window to discriminate between polarized muons and contaminant particles.

An overview of the μSR technique which involves the stopping and decay of a polarized muon will be provided in Chapter 2. Chapter 3 will elaborate on the experimental set-up. The analysis of the data and results will be discussed in Chapter 4, and finally the conclusion will be given Chapter 5.

Chapter 2

THEORY

2.1 The ideal monoenergetic polarized μ beam

The collision of an accelerated primary proton beam ($\sim$ 500 MeV) with the nuclei of the production target, e.g. carbon ^{12}C, produces positive pions (π^+) via the possible reaction

$$p + ^{12}C \rightarrow \pi^+ + X.$$

From the subsequent decay of the pions (τ_{π^+}=26.03 ns), positive muons (μ^+) are formed via the two-body decay

$$\pi^+ \rightarrow \mu^+ + \nu_\mu.$$

In the pion's rest frame, linear momentum conservation requires that the decay products, μ^+ and ν_μ are emitted in opposite directions with equal momenta. Also because the pion is a spinless particle (i.e. it has no intrinsic angular momentum), conservation of angular momentum requires that μ^+ and ν_μ have equal and opposite spin. This decay process is governed by the weak interaction which - as defined in the Standard Model - has the remarkable property that it creates only left-handed or negative helicity neutrinos, i.e. the neutrinos have their

	positive muon μ^+	**positive pion** π^+	**positron** e^+
Lifetime	2.19703(4) μs	26.033(5) ns	$>4.3\times10^{23}$ y
Type	lepton	meson	lepton
Mass (MeV/c^2)	105.658389(34)	139.56995(35)	0.51099907(15)
Mass (m_e)	207	273	1
Charge (e)	+1	+1	+1
Spin ($\hbar$)	$\frac{1}{2}$	0	$\frac{1}{2}$

Table 2.1: Selected properties of the positive muon and other particles [1].

	electron neutrino ν_e	**muon neutrino** ν_μ
Type	lepton	lepton
Mass	$<$ 15 eV	$<$ 0.17 MeV
Mean life/mass	$>$ 7 $\times10^9$ s/eV	$>$ 15.4 s/eV
Charge (e)	0	0
Spin ($\hbar$)	$\frac{1}{2}$	$\frac{1}{2}$

Table 2.2: Selected properties of the electron and muon neutrinos [1].

spin angular momentum and linear momentum in opposite direction; and right-handed or positive helicity antineutrinos. The mirror-image reaction does not occur in nature, because the parity inversion performed by the mirror changes a left-handed neutrino to a right-handed one, which the weak interaction has not been seen to produce. Hence, the μ^+ must also have its spin antiparallel to its momentum. This gives a monoenergetic beam of perfectly spin-polarized muons from pion decay. Some properties of the positive muon and other particles referred to in this thesis are given in Table 2.1 and Table 2.2.

2.2 The Surface Muon Beam

The surface muon beam also known as "Arizona" beam was first realized after the pioneering work of Pifer *et al.* in 1976 from University of Arizona [2]. The concept of surface muon beams was motivated by the search for muonium-to-antimuonium conversion $\mu^+e^- \rightarrow \mu^-e^+$ [3]. It arose because of the need for high intensities of low energy μ^+'s that can be stopped in samples of convenient thickness (less than 1 cm). These are available in the required intensities only from the two-body pion decay

$$\pi^+ \rightarrow \mu^+ + \nu_\mu, \tag{2.1}$$

from which the muon emerges with a momentum of 29.79 MeV/c and a kinetic energy of 4.119 MeV in the pion rest frame. The lifetime of the free charged pion is 26.03 ns.

Commonly, μ^+ beams today are emitted from pion decay at rest in the surface layer of the primary target where the pions themselves are produced by collisions of high energy protons with the target nuclei, as illustrated in Figure 2.1 - hence the common name, *surface muons* [3]. This mode is not available for negative muons because a negative pion (π^-) stopping in the target behaves like a heavy electron and rapidly cascades down to tightly bound orbitals where the π^- wavefunction overlaps with the nuclear wave function resulting in a very high probability for strong interactions. Positive pions that have come to rest in solids take up interstitial positions between atoms so they are too far from nuclei to be captured. Their lifetime is unaffected by any properties of the target material.

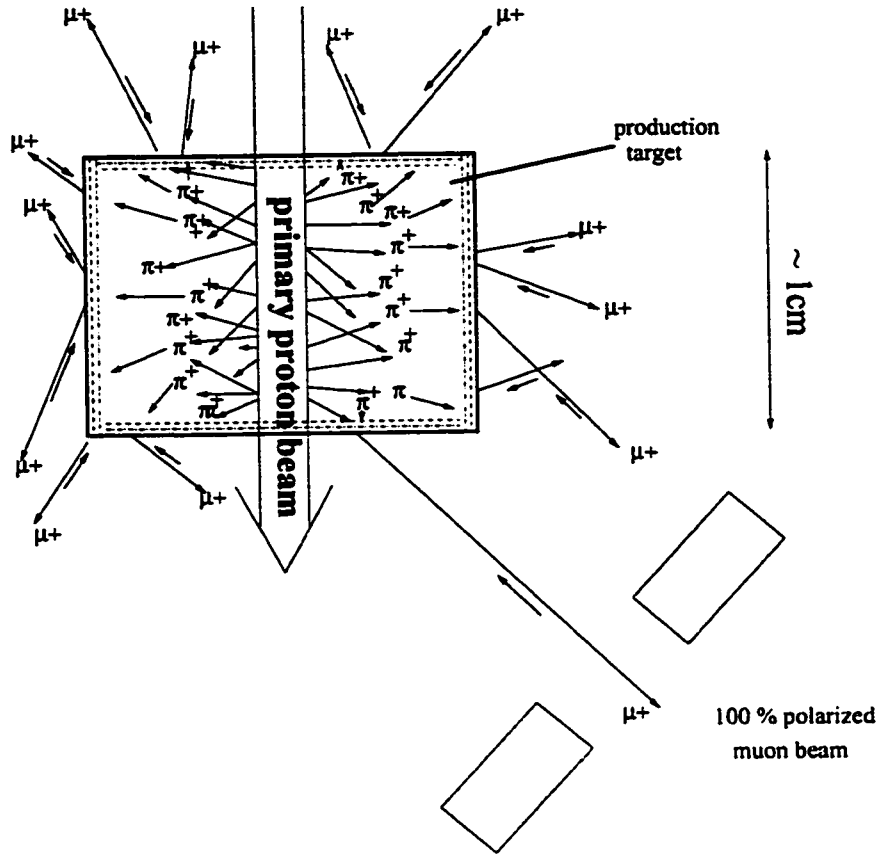

Figure 2.1: "Arizona" or "surface muon" beam produced from pion decaying at rest near the surface of the production target.

2.2.1 Surface Muon As A Probe

An ever-increasing number of stopping muon (μ^+) experiments involve subatomic, atomic, molecular and condensed-matter physics and chemistry. The most rapidly expanding application of surface muon beams is the muon spin rotation and/or relaxation (μSR), where muons probe a variety of states of matter. In these applications, the surface muon beam offers the advantages of high stopping rates in very small samples, a high degree of polarization and low cost of construction and operation [3].

In the chemical application, simple calculations of chemical reaction processes and molecular structure are allowed due to the fact that the muonium atom (Mu=μ^+e^-) and the hydrogen atom have the same size, almost the same reduced mass and ionizing potential.

The application in condensed matter physics might be titled: "The Muon as a Magnetic Probe." Here μ^+SR is used to learn the location, electronic structure and dynamical behaviour of muonium atoms in semiconductors. The study of quantum diffusion of μ^+ and Mu in solids is another very important field, having implications for the electronic and diffusive transport properties of the material. Because muon decay provides a non-electromagnetic "signal," μSR is a unique probe for the magnetic behaviour of superconductors without causing distortion.

In particle physics the surface muon makes possible the study of the main muon decay mode $\mu \rightarrow e\nu\bar{\nu}$ which serves as an ideal probe of the space-time structure of the weak interaction. This comes about because the purely leptonic nature of this decay eliminates any uncertainties due to the internal structure of the particles.

2.3 Parity Violation

It was proposed by Lee and Yang in 1956 [4] that space-time principles of invariance under charge conjugation, time reversal, and parity transformation are violated by the weak interactions responsible for the decay of nuclei, mesons, and strange particles. Their hypothesis was accompanied by the suggestion that confirmation should be sought (among other places) in the study of the successive decay reactions

$$\pi^+ \rightarrow \mu^+ \nu_\mu \tag{2.2}$$

$$\mu^+ \rightarrow e^+ \bar{\nu_\mu} \nu_e \,. \tag{2.3}$$

They pointed out that parity nonconservation implies a polarization of the spin of the antimuons (μ^+'s) emitted from stopped pions (π^+'s) in Equation (2.2) opposite the direction of motion and that furthermore, the angular distribution of the positrons e^+ in Equation (2.3) should serve as an analyzer for the muon polarization. The first confirmation of parity violation in weak interactions immediately followed from the results of

- the famous experiment on β decay of oriented nuclei by Wu *et al.* [5],
- and the above suggested meson experiment performed by Garwin *et al.*, by stopping, in carbon, the μ^+ beam formed by forward decay in flight of π^+ mesons [6].

The most remarkable feature of the positive pion decay is that it maximally violates parity symmetry, causing the μ^+ to be emitted with perfect spin polarization (Figure 2.2). The propensity of the muon decay positron in (2.3) to be emitted in the direction of the spin of the μ^+ is another consequence of parity violation which allows us to infer the muon spin distribution. The information is delivered to the experimenter in the form of rather high energy (up to 52.83 MeV) positrons which readily penetrate sample holders, cryostat and the detectors used to establish the time and direction of the muon decay.

2.4 Michel Spectrum- the Standard Model explanation for muon decay

Soon after the discovery of parity violation it was established that to the first approximation the weak charged currents have "$V - A$" (vector minus axial vector) structure. All measurements in direct muon decay $\mu^- \rightarrow e^- + \nu_\mu + \overline{\nu}_e$, and its inverse, $\nu_\mu + e^- \rightarrow \mu^- + \nu_e$ are successfully described by the "V-A"

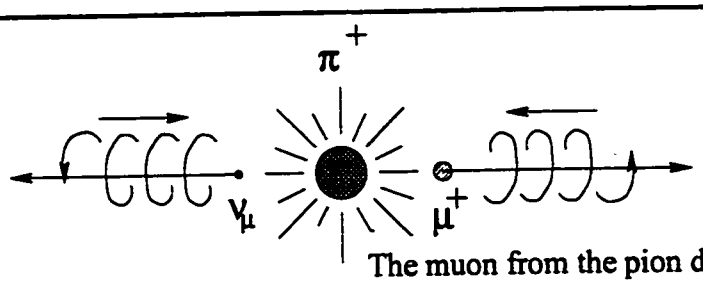

Figure 2.2: A pion π^+ decay at rest (the mirror image of which can not occur in nature) producing a perfectly polarized antimuon μ^+ and neutrino ν_μ.

interaction, which is a particular case of a local, derivative-free, lepton-number conserving, four fermion interaction [7]. At energies well below $m_W c^2$, where m_W ($= 80.41 \pm 0.10$ GeV) is the mass of W, the intermediate vector boson mediating the weak interaction, the matrix element of muon decay is

$$\sum_{\substack{\gamma=S,V,T \\ \epsilon,\mu=R,L}} g^{\gamma}_{\epsilon\mu} \langle \bar{e}_\epsilon | \Gamma^\gamma | \nu_e \rangle \langle \bar{\nu}_\mu | \Gamma_\gamma | \mu_\mu \rangle. \tag{2.4}$$

γ labels the type of interaction: Γ^S, Γ^V, Γ^T represent a scalar, vector, or tensor interaction. The indices $\epsilon, \mu = R, L$ indicate the right- or left-handed chirality of the electron or muon. The chiralities of the states ν_e and $\bar{\nu}_\mu$ are then determined by the values of γ, ϵ and μ. Existing information on the weak coupling constants, $g^{\gamma}_{\epsilon\mu}$ are given in Table 2.3.

The muon decay mode $\mu \to e\nu\bar{\nu}$ has a branching ratio of $\approx 100\%$ [1]. Table 2.4 below shows the information on the μ^+ decay modes.

$\mid g^S_{RR} \mid < 0.066$	$\mid g^V_{RR} \mid < 0.033$	$\mid g^T_{RR} \mid \equiv 0$
$\mid g^S_{LR} \mid < 0.125$	$\mid g^V_{LR} \mid < 0.060$	$\mid g^T_{LR} \mid < 0.036$
$\mid g^S_{RL} \mid < 0.424$	$\mid g^V_{RL} \mid < 0.110$	$\mid g^T_{RL} \mid < 0.122$
$\mid g^S_{LL} \mid < 0.550$	$\mid g^V_{LL} \mid > 0.960$	$\mid g^T_{LL} \mid \equiv 0$

Table 2.3: Coupling constants $g^\gamma_{\epsilon\mu}$. 90% confidence level experimental limits [[1]]. The experimental uncertainty on the muon polarization in pion decay is included

.

Neglecting radiative corrections and masses of the neutrinos and $e^\pm$, the differential decay probability to obtain an $e^\pm$ with (reduced) energy between x and $x + dx$, emitted at an angle between θ and $\theta + d\theta$ with respect to the muon spin $\vec{P}_\mu$ in the rest frame of a muon ($\mu^\pm$) measured by a polarization insensitive detector, is given by

$$\frac{d^2\Gamma}{x^2 dx\, d\cos\theta} \sim 3(1-x) + \frac{2\rho}{3}(4x-3) \pm P_\mu \xi \cos\theta \left[1 - x + \frac{2\delta}{3}(4x-3)\right]. \qquad (2.5)$$

$P_\mu = |\vec{P}_\mu|$ is the degree of muon polarization and $x \equiv E_e/\max(E_e)$ is the reduced energy, where the maximum $e^\pm$ energy, $\max(E_e) = m_\mu/2 = 52.83$ MeV. ρ, ξ, and δ and another parameter η, that appears if m_e is not neglected, are the Michel parameters which are bilinear combinations of the weak interaction coupling constants $g^\gamma_{\epsilon\mu}$. The Standard Model interaction corresponds to one single amplitude g^V_{LL} being unity and all the others being zero, which gives $\rho = \xi\delta = 3/4$, $\xi = 1$ and $\eta = 0$.

μ^+ Decay Modes		
Mode	**fraction ($\Gamma_i\Gamma$)**	**Confidence level**
Γ_1 $e^+\bar{\nu}_\mu\nu_e$	$\approx 100\%$	
Γ_2 $e^+\bar{\nu}_\mu\nu_e\gamma$	$(1.4\pm0.4)\%$	
Γ_3 $e^+\bar{\nu}_\mu\nu_e e^+e^-$	$(3.4 \pm 0.4) \times 10^{-5}$	
Γ_4 $e^+\nu_\mu\bar{\nu}_e$	$< 1.2\%$	90%
Γ_5 $e^+\gamma$	$< 1.2 \times 10^{-11}$	90%
Γ_6 $e^+e^-e^+$	$< 1.0 \times 10^{-12}$	90%
Γ_7 $e^+2\gamma$	$< 7.2 \times 10^{-11}$	90%

Table 2.4: Experimental data on muon decay modes [1]. The limit on Γ_5 was updated in 1999 [8].

2.4.1 The asymmetry, α

The energy and angular distribution of $e^\pm$ from $\mu^\pm$ decay, Equation (2.5), can be rewritten as

$$\frac{d^2\Gamma}{dx\, d\cos\theta} \sim F(x)\ [1 + \alpha(x)\cos\theta]\,, \tag{2.6}$$

where $\alpha(x)$ is the anisotropic part of the spectrum, traditionally called the asymmetry and also connotes the *polarization of the muon spin ensemble* since it incorporates P_μ; and $F(x)$ is the isotropic energy dependent term. Using the Standard Model value of the Michel parameters, the asymmetry factor α depends on the $e^\pm$ energy as

$$\alpha(x) = \pm P_\mu \frac{2x-1}{3-2x}$$

and the normalized isotropic part of $e^\pm$ energy spectrum has the form

$$F(x) = 2x^2(3-2x)$$

The decay distribution (Equation 2.6), $F(x)$ and $\alpha(x)$ are shown graphically in Figure 2.3.

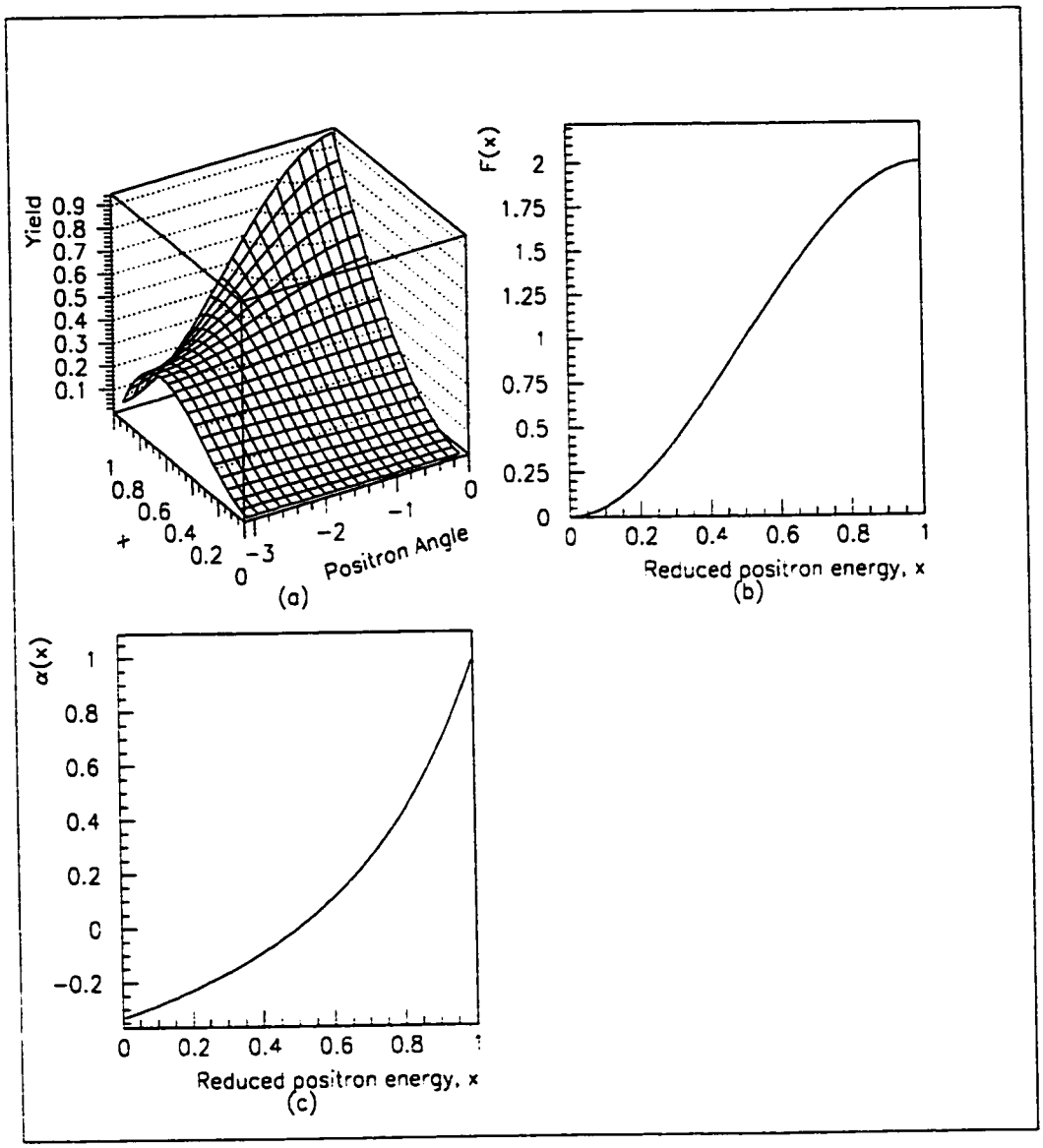

Figure 2.3: Reduced e^+ energy dependence of:(a) the energy and angular distribution of e^+ from μ^+ decay, (b) the isotropic energy term, $F(x)$ in the Michel spectrum, and (c) μ^+ decay asymmetry $\alpha(x)$.

For a 100% polarized $\mu^{\pm}$ beam, the theoretical asymmetry averaged over all the possible $e^{\pm}$ energies from $x = 0$ to $x = 1$ is

$$\langle \alpha \rangle = \int_0^1 \alpha(x)\ F(x)\ dx = \pm\frac{1}{3},$$

which is very difficult to realize in practice. The empirical asymmetry α in a given detector is dependent on the thickness, geometry and material of detectors and target and the magnetic field.

2.5 Muon Spin Rotation, μSR

The beam test makes use of the μSR techniques whereby interesting properties of the M11 channel are found. An overview of the physics taking place in μSR is given here. The success of the μSR technique relies on two circumstances. These are: the intrinsic polarization of the muons during their production from pions $\pi^+ \rightarrow \mu^+\nu$; and the anisotropy (preferred direction along the muon spin) of the positron emission in their subsequent decay $\mu^+ \rightarrow e^+\bar{\nu}_\mu\nu_e$ [10].

In this beam test the μSR technique is used to measure the polarization of the surface muon beam. The muons are actually stopped in the sample in an external magnetic field and decay at rest into a positron, a neutrino and antineutrino (Figure 2.4). Muon spin rotation is illustrated in schematic form in Figure 2.5. It is worthwhile to mention that it is not a scattering process. The essence of muon spin rotation lies in the fact that the magnetic field applied transverse (perpendicular) to the initial direction of the muon spin polarization vector causes the the muon spin to precess around it at its Larmor frequency (Figure 2.5(b)), given by the muon gyromagnetic ratio

$$\gamma_\mu/2\pi = \frac{1}{2\pi}\frac{e[C]}{m_\mu[kg]} = 1.3553879(9) \times 10^8 \text{ Hz T}^{-1}.$$

The incident surface muon beam produced in the pion decay process is essentially

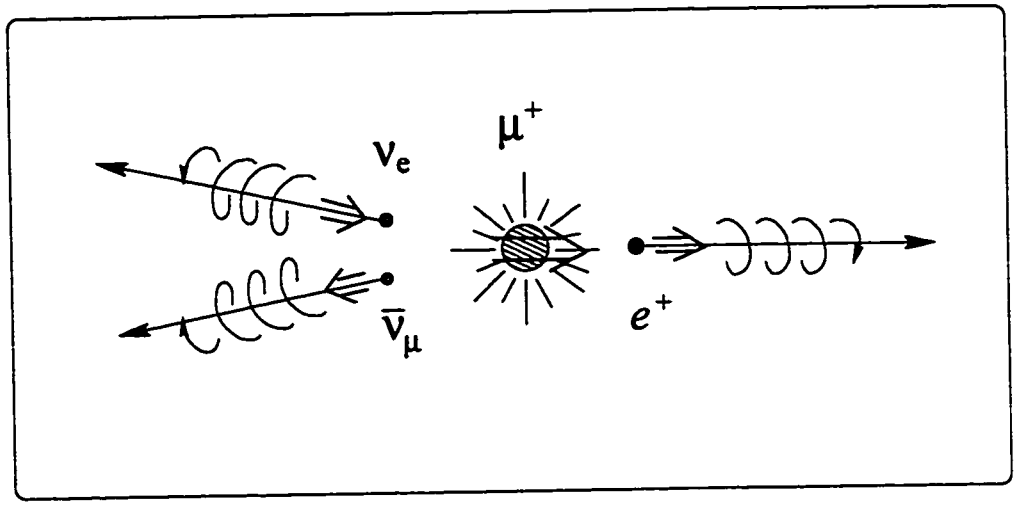

Figure 2.4: Schematic form of positive muon decay in the maximum probability case when the neutrino and antineutrino go off in the same direction together, and the positron exits along the antimuon's spin with maximum energy of 53 MeV.

100% polarized. The initial polarization of the muon can be substantially preserved throughout the transport of the beam (in part because $g_\mu - 2$ is small) and in the actual process of implantation and thermalization. On implantation into matter all muon spins point in the same direction and in the absence of other interactions will decay with a characteristic angular distribution $P(\theta) = 1 + \alpha \cos(\theta)$ (Figure 2.6), favouring the direction of the polarization vector.

Information on the muon polarization is carried by the decay positrons which are sufficiently energetic to escape from the sample and are readily detected in simple scintillation counters placed in the plane which is along the beam direction, perpendicular to the magnetic field. One can imagine a somewhat diffuse 'lighthouse beam' of positrons sweeping around, periodically illuminating the detector.

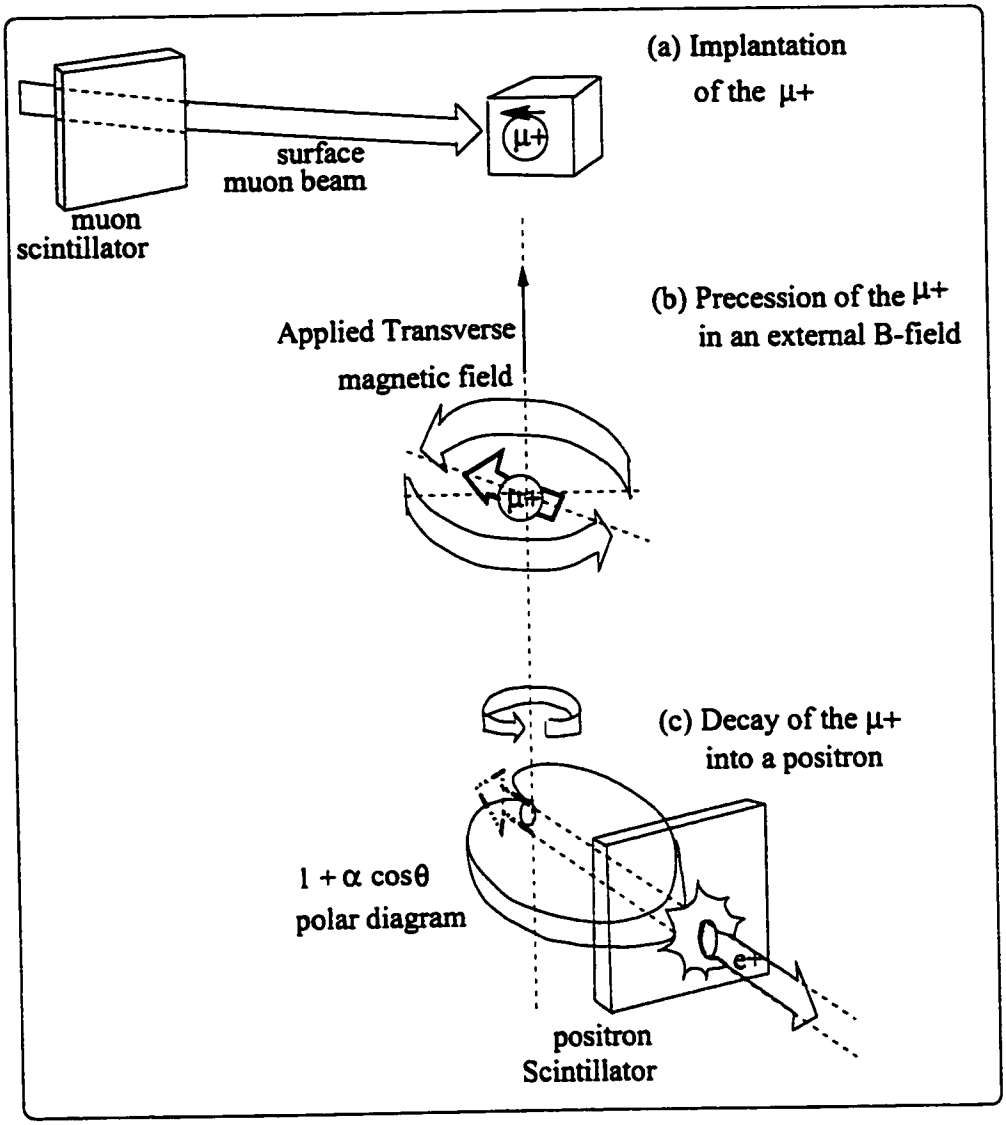

Figure 2.5: Representation of (a) muon implantation (b) muon spin rotation (i.e. Larmor precession in a transverse magnetic field) and (c) disintegration of the muons and detection of the emitted positrons. The polar diagram in (c) rotates with the muon spin.

Decay event data from the positron scintillation counters are fed into an electronic data acquisition system leading to the gradual accumulation of a muon spin rotation spectrum of decay event counts against time, an example of which is shown in Figure 2.7. The horizontal axis represents the time elapsed from the detection of a muon in the muon counter to its decay into a positron in the sample. The overall exponential decay reflects the muon lifetime (2.2 microseconds) and the precession of the muon spins is manifest in the superimposed oscillations as the muon polarization sweeps past the positron detector.

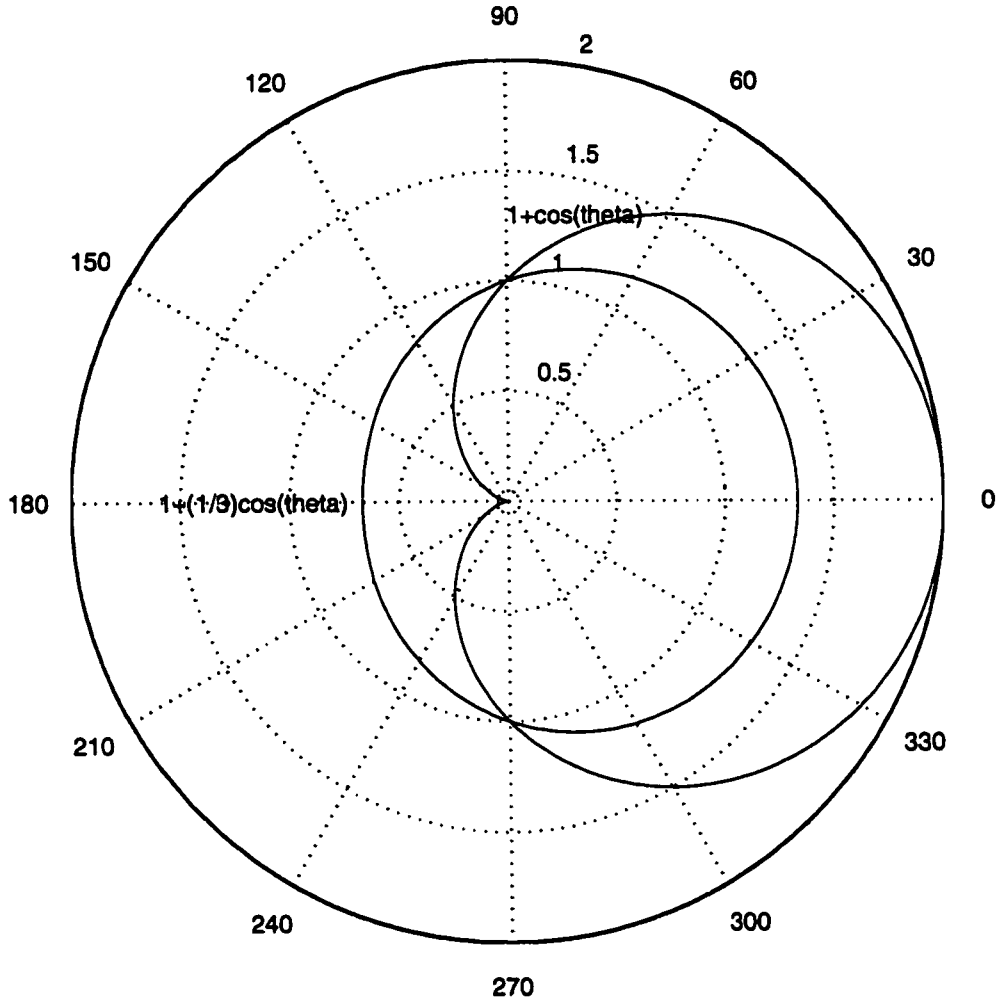

Figure 2.6: Angular distribution $P(\theta) = 1 + \alpha\cos(\theta)$ of the e^+ from μ^+ decay. The asymmetry (anisotropy) α is 100% for the highest e^+ energy (52.83 MeV) and $\frac{1}{3}$ when averaged over all possible e^+ energies.

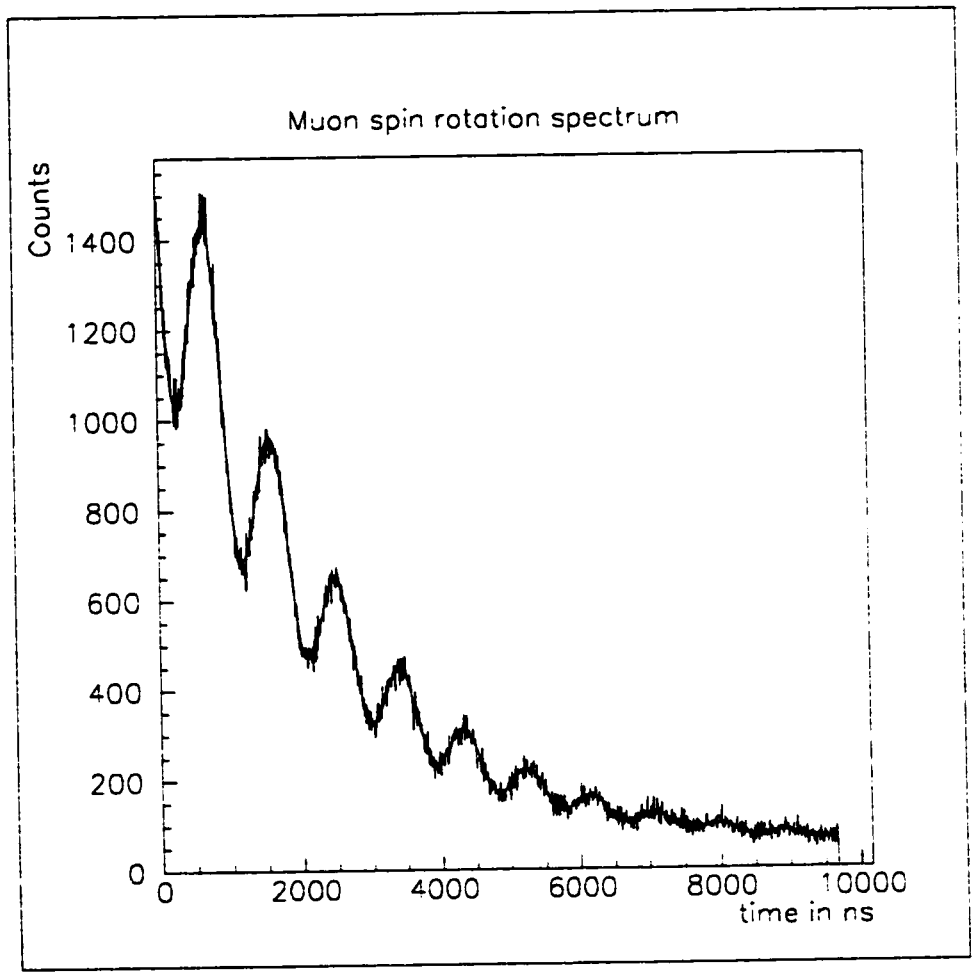

Figure 2.7: Time spectrum for a simple μSR experiment with a transverse field.

Chapter 3

EXPERIMENTAL SET-UP

3.1 M11 Secondary Beamline

The experiment was performed on one of the secondary beamlines, M11, of the 500-MeV cyclotron at TRIUMF, Vancouver (Figure 3.1). The cyclotron has a beam burst period of 43.6 ns so that a brief pulse ($\sim$ 4 ns) of protons is delivered every 43.6 ns (at high currents it is necessary to spread the proton beam pulse out in time to reduce space charge effects). M11 views the production target 1AT1 which is 1 cm graphite at $\approx 3^{\circ}$ with respect to the primary proton beam, and can be tuned to select surface muons obtained from the decay of positive pions (π^+). The pions are first produced by the collision of the primary proton beam with the nuclei of the 1AT1 target. Positive pions then decay with a lifetime of 26.03 ns to produce one muon neutrino (ν_μ) and one positive muon (μ^+).

Perhaps the most important development in muon beam technology was the realization that by removing the windows that isolated the primary and secondary particle beamlines, and turning down the momentum tuning of the secondary channel, the low momentum positively charged surface muons could be brought out to an experiment [2]. Those positive pions that happen to come to

Figure 3.1: TRIUMF beamlines

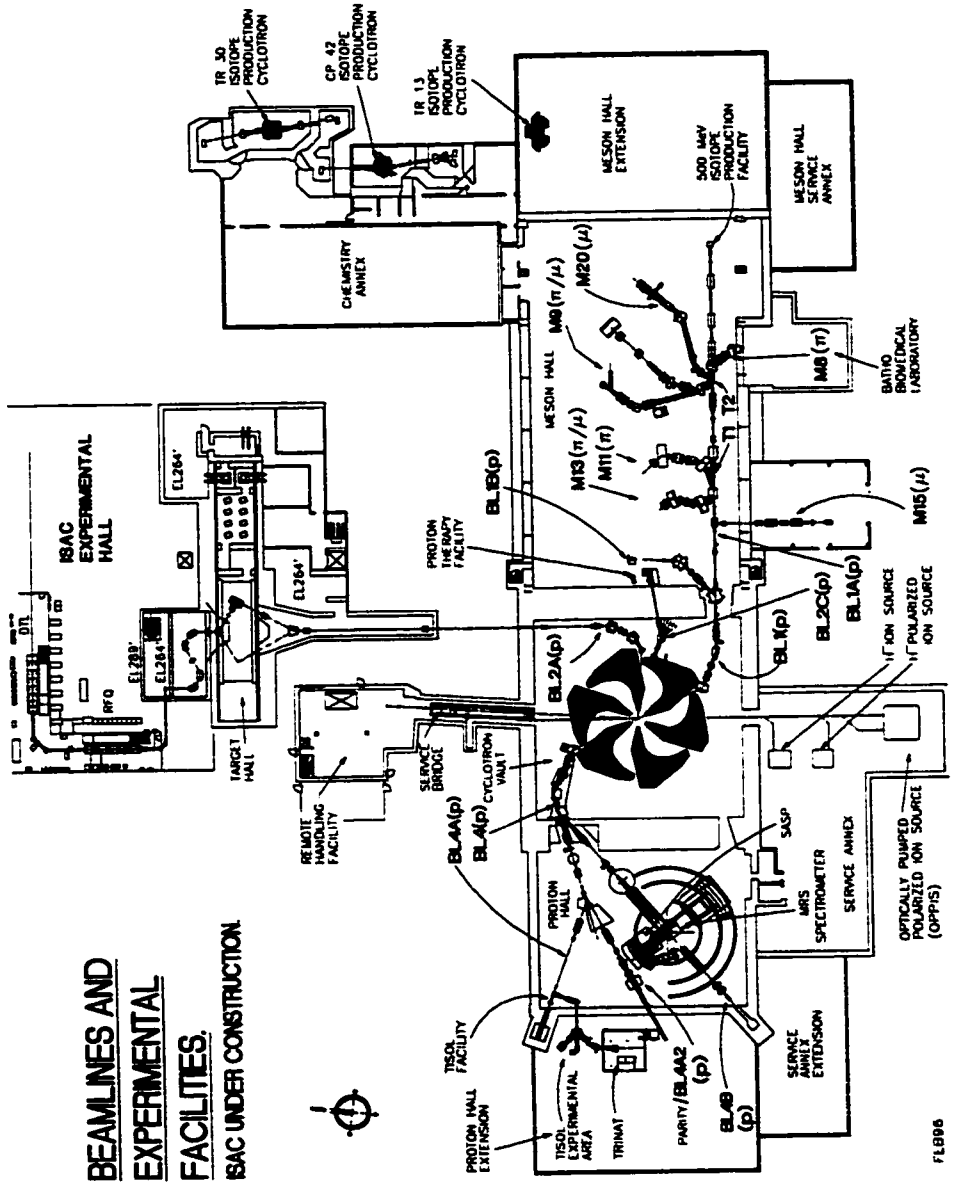

rest just within the surface of the pion production target decay to muons that need penetrate only a short distance (a fraction of a millimeter at most) to escape from the target into the beamline vacuum, with momenta up to the maximum of $p_{max} = 29.79$ MeV/c. The distribution of the muons from the pion decay is isotropic.

These muons have a range of about of 0.8 mm in graphite so they conveniently penetrate several thin windows but still stop in small samples, while the spin of the muons remains almost completely polarized. Surface muon beams are not mono-energetic since muons will come from pions decaying at various depths in the pion production target; those that start out deeper will lose more energy on their way out. The resulting muon flux rises with momentum, then drops sharply at the "surface muon edge" at p_{max}. The secondary beamline, with magnetic steering elements and positron separators (velocity selectors which remove positron contamination from the muon beam) are tuned to transport muons in a narrow momentum range $\Delta P/P$ of a few percent, with P chosen to be $\sim$1/2% below the surface muon edge, in order to achieve the greatest beam intensity.

The M11 beam line has two 60° left bends and is 11 m long. Figure 3.2 shows the layout of the beam line and the location of the two foci and the slits. M11 may be considered to be composed of the following three sections:

- The front-end which separates the secondary pion beam from the primary proton beam.
- The middle section which defines the beam momentum, produces a dispersed double-focus at the mid-plane.
- The rear section which produces a doubly achromatic beam spot at the experimental target position.

Figure 3.2: Layout of M11 channel. The angle particles are emitted into M11 from the target relative to the incident proton beam is shown larger for clarity, in reality it is $\approx 3°$.

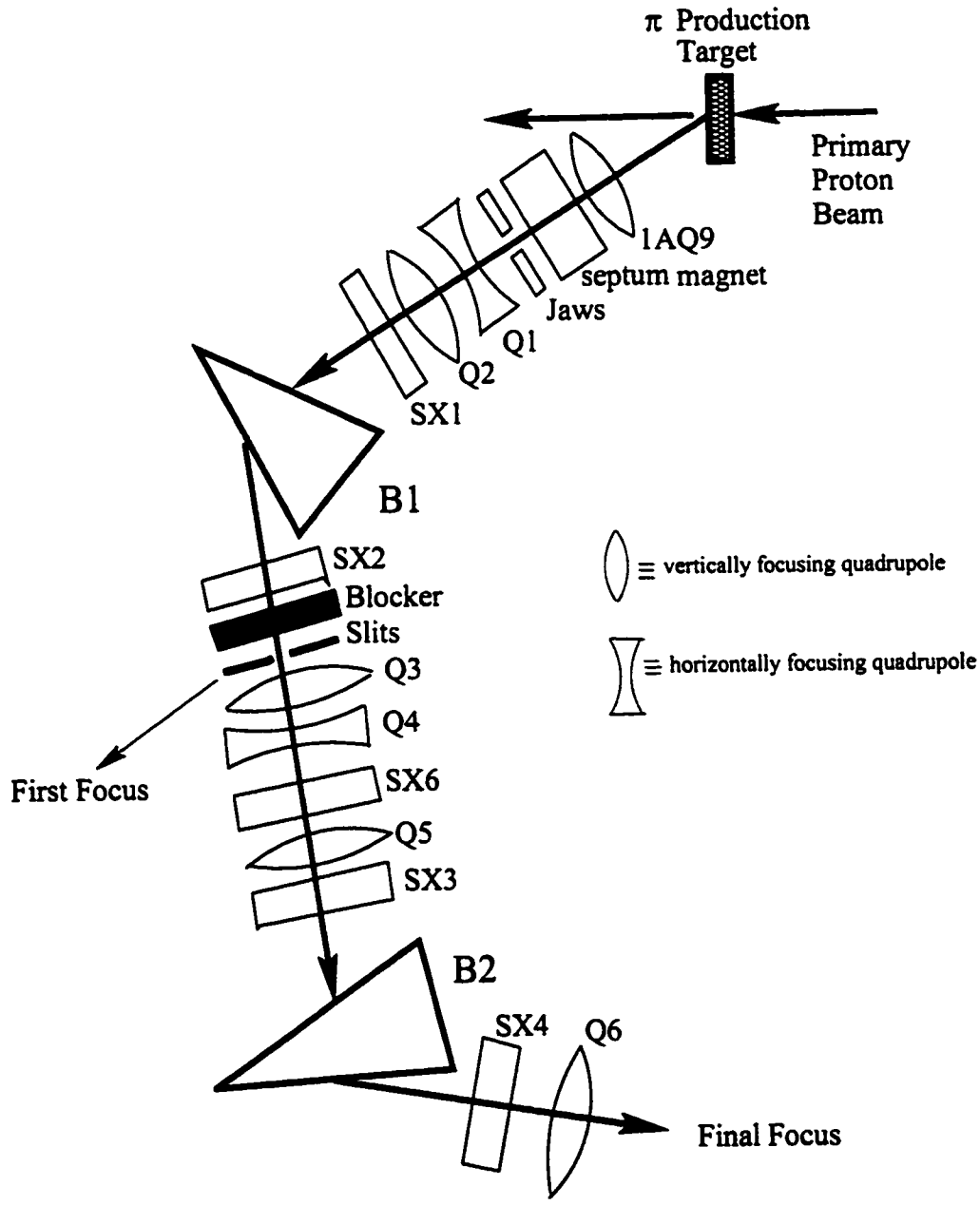

M11 has slits for selecting the desired particles at the momentum dispersed focus and the beam momentum acceptance. The momentum dispersion at the mid-plane is 18 mm per % $\frac{\Delta P}{P}$. One may choose the momentum bite by setting this midplane slit accordingly. In the experiment Δ P/P is chosen to be $\frac{1}{2}$%, i.e. M11 is tuned to transport muons in a momentum range ΔP/P of $\frac{1}{2}$%.

The momentum of M11 is chosen by altering the current in the first dipole bending magnet via computer control to select various percentages of the initial reference momentum. The current in the other components in the beamline are set by tuning to optimize flux. From reference [9] the momentum of the pion beam in M11 is given by

$$P = [\{(\text{ B1 Magnetic field in gauss }) \times 0.03255\} - 0.26] \pm 0.25\% \text{ MeV}/c\,, \qquad (3.1)$$

with no absorber in the mid-plane. No correction for absorber energy loss is needed since no absorber is included. However this calibration is low by 2%.

The maximum momentum available on M11 is 416 MeV/c limited by the septum magnet power supply. There is no minimum energy, although below 130 MeV/c it may be better to use M13 because of its larger solid angular acceptance [9].

Most runs were taken with a 100 μA proton beam.

3.2 Detector Set-up

Figure 3.3 illustrates the basic experimental arrangement. Muons were detected at the end of the secondary beam channel and in front of the stopping aluminum target with external and internal 0.25 mm thick plastic scintillator counters, C_{in} and C_{out} respectively. Range of 4.1 MeV muons in the counters is $\sim$ 1.3 mm.

The positron detector array consists of six scintillation counters, 6.4 mm thick, labelled:

1. F_{in} (inner forward),
2. B_{in} (inner backward),
3. F_{out} (outer forward),
4. B_{out} (outer backward),
5. U (upward), and
6. D (downward)

according to a "beam's eye view" naming convention.

The external magnetic field, provided by Helmholtz coils, is 70 gauss and is applied perpendicular to the muon polarization, causing the muon spins to undergo Larmor precession about the field. Since the decay e^+ will follow a helical path in the external field the dimensions of the positron detector array is such as to optimize its efficiency. For instance, at $p_e = 30$ MeV/c the radius of curvature ρ_e of an orbit perpendicular to $B = 70$ gauss (0.007 tesla) is 14.3 m , as given by the formula

$$\rho\,[\mathrm{m}] = \frac{p\,[\mathrm{MeV}/c]}{300 \times B\,[\mathrm{tesla}]}.$$

3.3 Stopping of the Polarized Muons in Aluminum

The muon stopping material is an aluminum sample of purity 99.999% and thickness 1.0 mm, contained in an evacuated cryostat at room temperature. With the

Figure 3.3: Side view of the detector setup

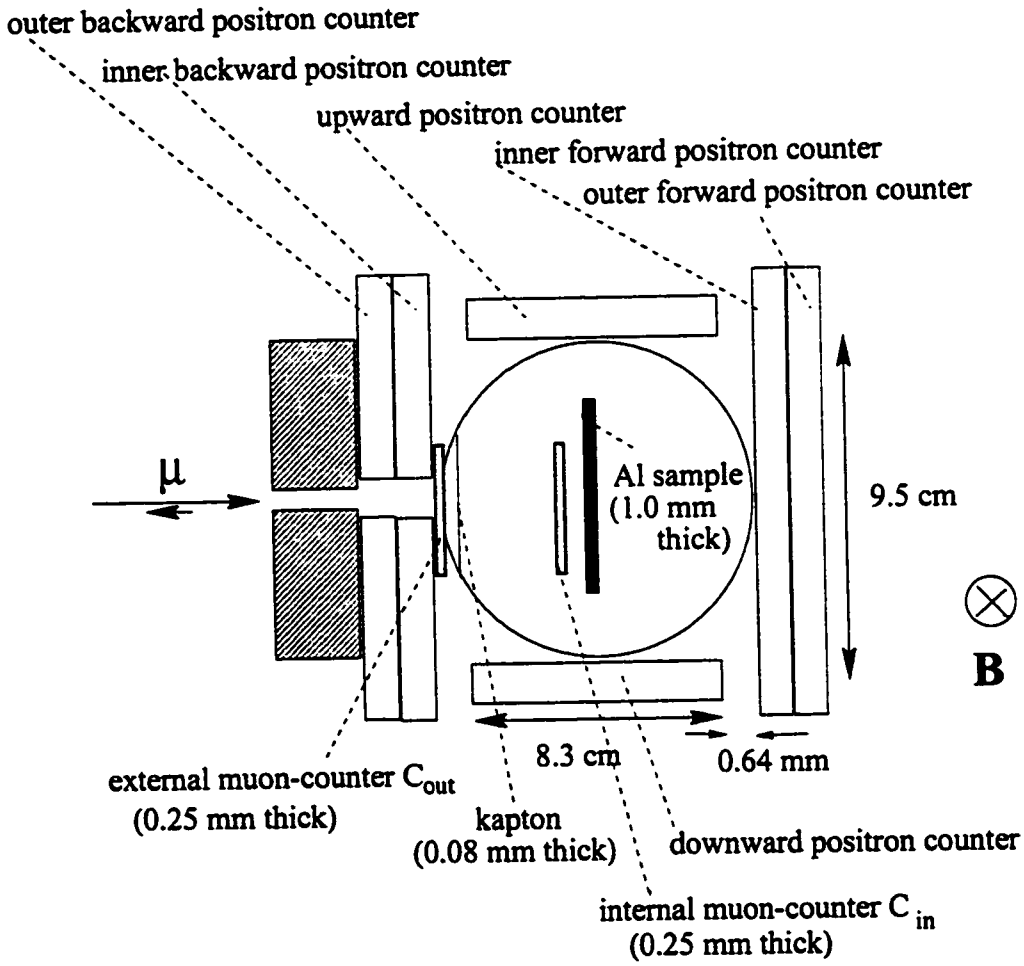

beamline tuned to 29.79 MeV/c selection is made for the muons coming only from the decay of pions that are at rest near the surface of the production target. This is because muons produced within the target lose momentum in making their way to the surface. The range of these 'surface muons' is small - approximately 0.6 mm in aluminum. Therefore, thin windows in the beamline and the cryostat are required to allow the muons to reach their destination. All of the surface muons are stopped in a thin target.

Stopping the polarized muons involves their implantation and thermalization in a medium. The slowing down and stopping of the muons in metals is a complex process. The time scales for the various processes by which the μ^+'s lose their kinetic energy are short. The μ^+'s are decelerated within 100 picoseconds, which is too rapid to allow any significant loss of polarization [11]. Also the primary processes bring into play only electrostatic interactions or electron scattering which are *not* spin-dependent [10].So there is rarely any loss of polarization during thermalization, especially in metallic samples [10].

Any variation of the local field between different occupation sites in the stopping sample will result in the muons dephasing as they precess, with a corresponding gradual loss of polarization described by a relaxation function. These characteristic frequencies and relaxation functions constitute the spectroscopy of the system. For aluminum the relaxation is negligible.

Furthermore it is now known that μ^+ depolarization is intimately related to the formation of muonium through electron capture (Mu = μ^+e^-) [12]. Whatever excitations of the medium that the muon passage may produce are quickly dissipated and the electronic structure "heals" by the time the muon reaches thermal energies. Polarized muons "see" an isotropic environment in aluminum. In fact, pure aluminum gives rise to practically no depolarization of μ^+ in the

temperature range 1-300 K [13].

3.4 Electronics

An anticoincidence between the external muon counter and the internal decay positron counter is used as trigger, i.e. $C_{out}.\overline{F_{in}}$. Pulse-height and timing information were measured with analogue to digital converters (ADC's) (LeCroy 2249A and 2249W) and TDC's (LeCroy 4208 and 2228A). The TDC (LeCroy 4208) used for the muon decay time has a time resolution of 1 ns and the other which is used for the time of flight of the beam particles has a time resolution of $\frac{1}{4}$ ns. Events were recorded on tapes at a rate of $\sim 10^3\ s^{-1}$. Data aquisition was done using the VDACS acquisition system [14].

Raw counter pulses are fed to fast discriminators which generate logic pulses if the raw pulse height is above a set threshold. The logic pulses are then processed by the electronic circuit shown schematically in Figure 3.4. An incident muon generates a pulse in the muon counters, C_{out} and C_{in} . A trigger in C_{out} but not in the inner positron counter sends a start pulse to a fast digitizer (high-frequency "clock") of the 4208 TDC. Later the muon decays in the aluminum sample, triggering a stop pulse in the positron counters, which stops the clock. The time interval is digitized and the corresponding bin in a time histogram is incremented.

The method used to acumulate μSR histograms requires that only one muon be present in the sample at a time. This imposes a limit on the rate at which muons would be implanted in the sample (and therefore on the rate at which data can be accumulated). The probability of getting two muons is

$$P = R\tau,$$

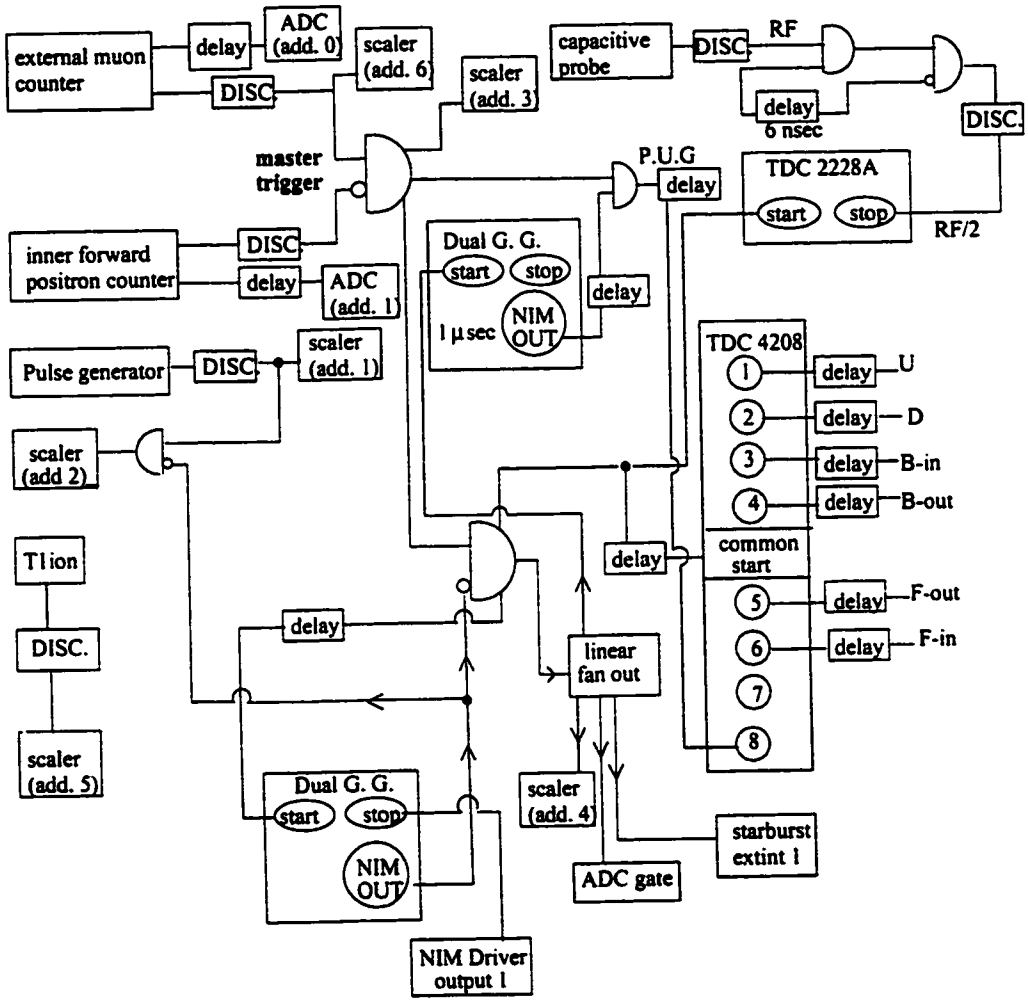

Figure 3.4: Electronics for data aquisition

where

$$R = \text{muon flux rate (Hz), and}$$
$$\tau = \text{"gate" time, i.e. maximum of } (t_{stop}\text{-}t_{start})$$

For $P \ll 1$, it is necessary to have $R \ll 1/\tau$. Muons are being delivered on M11 at a rate up to $\sim 10^3 s^{-1}$ and the time interval τ between a start pulse and a stop pulse is ≤ 9.7 microseconds. So the probability of a second muon entering the system while the decay time of the first muon is being measured is $\sim 1\%$. The histogram incremented by the pile-up-gate is for counting events with pile-up muons throughout the gate τ.

The TDC (LeCroy 2228A) is started by the event trigger and stopped by the cyclotron capacitive probe pulse prescaled by 1/2. The division by 2 gives a stop as much as twice the cyclotron period after the start. This allows a complete RF cycle to be observed without distortion from the edges of the coincidence overlap in the event trigger hardware.

Chapter 4

DATA ANALYSIS AND RESULTS

4.1 Choosing the momentum of M11

The beam test was done only for positive particles at several momenta in the range a few percent below and above 30 MeV/c. The reference tune used for the M11 beam line is shown in Table 4.1 below. Since the momentum calibration given by equation 3.1 is not quite right, the momenta were calculated by simple scaling based on the fact that this particular setting is found to be at a momentum 1/4 % below the $\mu - \pi$ edge, i.e. the reference momentum chosen is 29.72 MeV/c. The $\mu - \pi$ edge occurs at 29.79 MeV/c, the momentum at which a muon is produced from a pion decaying at rest. To pick a momentum at, e.g. 1% above the reference momentum of 29.72 MeV/c, the following procedures are taken:

- the beam line is adjusted via computer control through the command "m11 scale by 1 %"
- some time is allowed for the the current in the elements to stabilize to their new values

- the current in B2 is adjusted so that the ratio of the fluxes, B1 and B2 (from NMR read-outs) is 1.025
- the current in the septum magnet is adjusted so that the ratio of the flux in B1 (from NMR read-out) to the current in the septum = 3.012.

Reference Tune Chosen for M11		
Element	**DAC**	**Current (A)**
B1	34128	49.32
B2	28798	31.86
Q1	510	22.95
Q2	482	20.26
Q3	559	25.39
Q4	29802	44.68
Q5	480	22.71
Q6	878	42.97
SX1	113	13.96
SX2	222	2.25
SX3	957	7.62
SX4	599	5.96
SX2.5	204	2.15
Septum	2312	301.18
1AQ9	35154	40.28

Table 4.1: Setting of the M11 components at the reference momentum.

As the momentum of the beamline was changed in steps of 1/4% from the reference momentum chosen at 29.72 MeV/c it was found that the hysteresis

level is 0.03 %, i.e. the magnetic field intensity, measured using an NMR probe, in the benders B1 and B2 (see Figure 3.2) is reproducible up to within 0.03%.

Data was analyzed on line and off line using the NOVA data analysis system [15]. Electrons, muons, and pions were distinguished when possible in the thin counters C_{in} and C_{out} by pulse height and by timing against the machine RF signal.

4.2 Transition at the $\mu - \pi$ edge

An interesting feature of the surface muons produced in the target is that they occur up to beamline momentum of 29.79 MeV/c, (the $\mu - \pi$ edge), whereas positrons, cloud muons and pions are transported at a wide range of momentum. Muon clouds originate from pion decays outside, but in the vicinity of the target with the right momentum and direction necessary to make it through the beam transport system.

Figure 4.1 shows the time of flight of the M11 beam relative to the cyclotron RF at p = 29.8 MeV/c, 30.4 MeV/c (2% above the $\mu - \pi$ edge) and 33.1 MeV/c (11% above the edge). The raw TOF spectra are obtained without any cut and the spectra with ADC cut are obtained by selecting events with ADC channel greater than 130 for the external C_{out} counter. This cut is made to partially suppress the e^+'s. Note that the horizontal axis runs backward in time since the 2228A TDC is started by the event trigger and stopped by the cyclotron RF. The following six properties are observed from Figure 4.1:

- The characteristic exponential decrease in the surface μ^+ flux with time due to pion at rest with a mean life of 26 ns, in Figure 4.1(b). Figure 4.1(b) is the time of flight spectrum at 29.8 MeV/c with partial positron suppression.

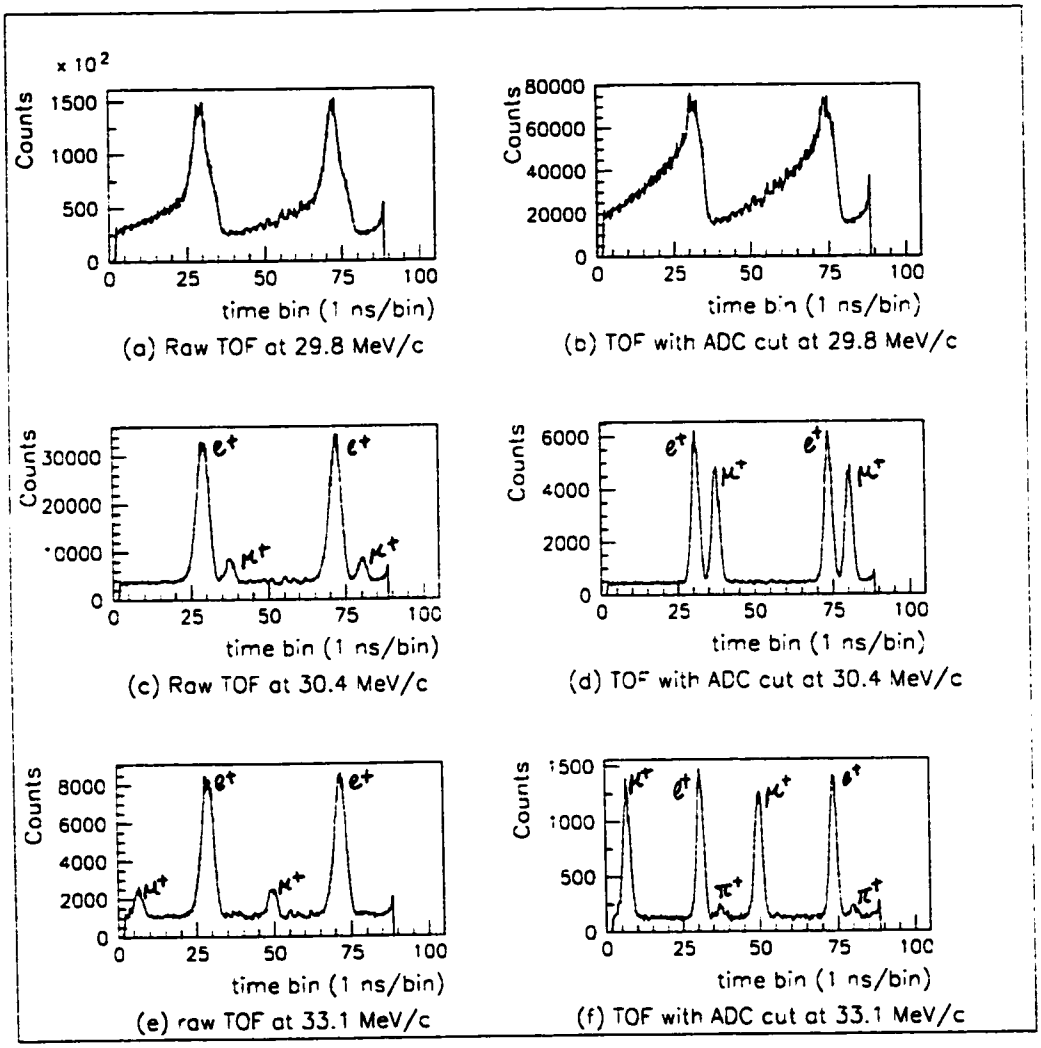

Figure 4.1: Transition at the $\mu - \pi$ edge. The ADC cut (ADC1 > 130, see Figure 4.2) on the pulse height distribution for the C_{out} is to partially suppress the positrons in the time of flight spectra. The horizontal axis runs backward in time.

- The negligible existence of surface μ^+ at momenta above the $\mu - \pi$ edge as seen from the absence of the exponential decrease in flux with time.

- The cloud μ^+ which has the property of being time correlated becomes noticeable above the $\mu - \pi$ edge. The cloud μ^+ peak walks across the TOF spectrum with change in momentum. The difference in flight time for μ^+ relative to e^+ is determined by the length of the flight path and the particle masses.

- The flat background of e^+'s from $\mu^+ \rightarrow e^+\nu\bar{\nu}$ decay following $\pi^+ \rightarrow \mu^+\nu$ decay.

- The e^+ peak which are time correlated with the cyclotron RF signal from $\pi^0 \rightarrow \gamma\gamma$ decays in the production target whereby a photon is converted to an e^+e^- pair [16, 17].

- The π^+ peak becomes noticeable above the $\mu - \pi$ edge in Figure 4.1(f), the time of flight with partial positron suppression at 33.1 MeV/c.

4.3 Event selection (background positrons)

The raw pulse height distribution in C_{in} and C_{out} (Figure 4.2) at 29.79 MeV/c shows that the amount of positrons is not negligible but not overwhelming. In fact, as will be seen later, the ratio of positron to muon is ~1:1. The positrons appear to have a higher energy loss in the C_{out} counter than in the C_{in} counter. There is a definite pulse shape difference between muons and positrons in the pulse height distribution in C_{in} and C_{out} (Figure 4.2). It is not possible to have a cut in the energy loss in C_{out} which would be good enough to suppress the positrons with negligible loss in muons (μ^+'s). To suppress the positron background to a trivial level, the off-line selection on ADC channel higher than

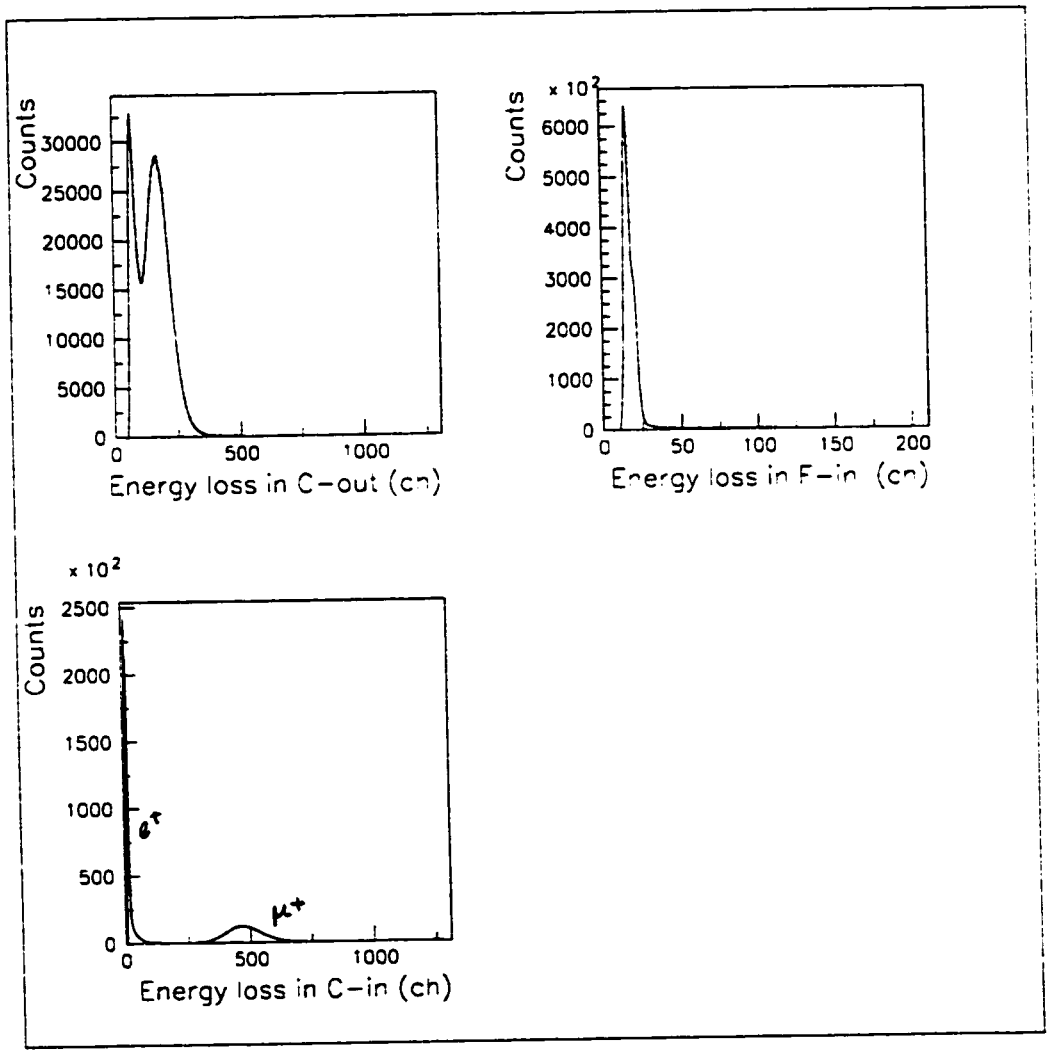

Figure 4.2: Pulse height spectra without cuts at a momentum when the surface μ^+ flux is high at the $\mu - \pi$ edge.

200 for the C_{in} counter was applied. The cut reduced the positron background to ~1% of the total μ^+ flux, without any cut applied to the C_{out} counter.

4.4 Particle Fluxes

The fluxes for (surface and cloud) muons and the positrons are plotted in Figure 4.3. The slits are 9 mm open giving a $\Delta P/P$ of $\frac{1}{2}\%$ (the channel transmission reaches its maximum at $\sim$ 100 mm with $\Delta P/P = 5\%$). Only the pulse height distribution of the C_{in} counter was used to calculate the flux because of the clean cut available on it to separate the μ^+'s from the e^+'s. The flux at other momenta using this method is not available because of lack of data. The variation in e^+ flux with momentum follows the same trend as that of the μ^+'s which indicates that a large portion of the e^+'s comes from muon decay in the detector setup. It must be noted that there are many positrons that could pass uncounted because they are below the threshold of the C_{in} counter.

The appearance of pions (π^+'s) is seen from the time of flight spectrum (see Figure 4.1(f)) only at 33.1 MeV/c which is the highest momentum M11 was run at in the beam test. On applying cuts, summing over the π^+ peak and making correction for the flat background positrons in the TOF spectrum , the π^+ flux is 0.018 $\pm$ 0.001 counts/(μA sec) which is $\approx$ 7 % of the cloud μ^+ flux. Note that 33.1 MeV/c muons (with a kinetic energy of 5.1 MeV) have a range of 1.0 mm in aluminum. Thus muons beyond that momentum will pass uncounted because they will go through the 1.0 mm thick aluminum target and then vetoed in the trigger by hitting the F_{in} counter.

Particle fluxes with computer live time corrections were calculated as follows:

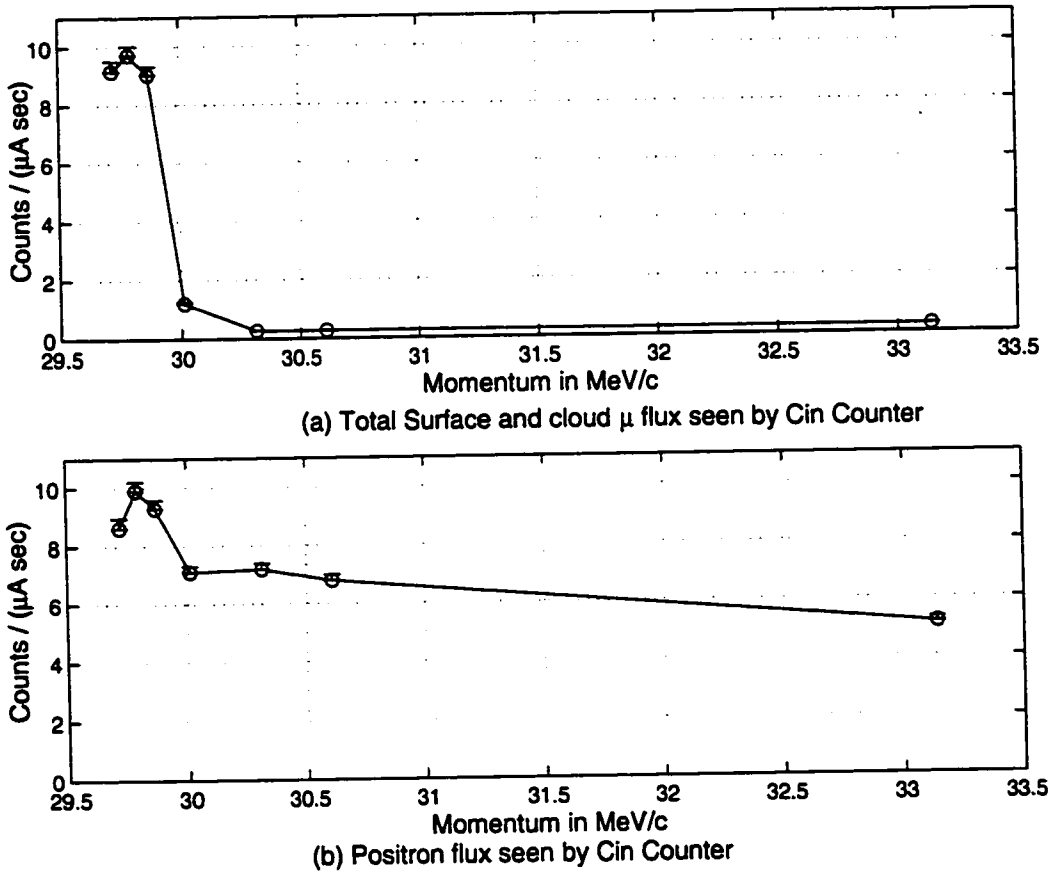

Figure 4.3: Change in flux of (cloud and surface) μ^+ and e^+ with momentum at $\Delta P/P = \frac{1}{2}\%$. The μ^+ flux is highest at the $\mu - \pi$ edge ($p = 29.79$ MeV/c). Note that there are many positrons that could pass "unseen" by the C_{in} counter.

$$\mu \text{ flux in counts per } (\mu\text{A second})$$

$$= \frac{\text{sum of counts in the } \mu \text{ peak of the } C_{in} \text{ pulse height spectrum}}{\text{total T1-ion counts}}$$

$$\times \frac{\text{T1-ion count rate per } \mu\text{A current of the primary proton beam}}{\text{computer live time fraction}}.$$

The total T1-ion count rate per μA current of the primary proton beam is obtained by calculating the average

$$\left\langle \frac{\text{T1-ion flux rate from the visual scalers}}{\text{instantaneous proton beam current}} \right\rangle = 267.4 \pm 7.0 \text{counts}/(\mu\text{A sec}).$$

The primary proton beam current was usually not constant and varied from 98 μA to 133 μA and was sometimes off for a while during which the analysis is stopped. The computer live time fraction is given by:

$$\text{live time fraction} = \frac{\text{total triggers when the computer is not busy}}{\text{total triggers}},$$

where the trigger is the anticoincidence $C_{out}.\overline{F_{in}}$. The live time fraction varied from 56 % to 86 % at momenta when the surface muon flux is high and zero respectively.

4.5 Fit For The Determination Of The Asymmetry

The transverse-field muon-precession data are normally analyzed with the expression

$$N(t) = N_o \exp(-t/t_\mu)[1 + \alpha P(t) \cos \omega t + \phi] + Bkg, \tag{4.1}$$

where t_μ=2.20 μs is the mean lifetime of the muon, ω is the precession frequency, α is the the muon decay asymmetry, and *Bkg* is the accidental flat background. Relaxation of the polarization *P(t)* is typically taken as either Gaussian $\exp(-\sigma^2 t^2)$ or exponential $\exp(-\lambda t)$ [13]. The impurities in the aluminum sample are low enough to neglect the effect of depolarization of the μ^+ as it is implanted and stopped in the sample (i.e., $P(t) = 1$, in the analysis). The free parameters are N_o, α, ω, ϕ and *Bkg*. These are referred to as P_1, P_2, P_3, P_4, and P_5 by the fitting software.

Each of the six positron counters in Figure 3.3 behaves as a single detector. However only the upward and downward counters are used to determine the asymmetry and polarization because the data has a smaller background. Figure 4.4 shows the time spectrum of the six counters without cuts; the positron background contamination is worse in forward-decay beams.

Figure 4.5 shows the variation in the asymmetry of the raw signal (with no cuts applied) from the upward and downward e^+ counters with momentum in the range ~2% above and below the $\mu - \pi$ edge (29.8 MeV/c). The data includes background e^+'s and cloud μ^+'s. It is expected that the asymmetry of the surface muons is nearest to 1/3 at 29.8 MeV/c, see Table 4.2. From Table 4.2, it is seen that there is an uncertainty of 1/4% in the value of the momentum at the $\mu-\pi$ edge. The pulse height distribution in C_{in} is not available to suppress the background e^+'s at all the momenta in Figure 4.5, since the threshold level of the discriminator from the C_{in} counter was too high. From here onwards, only the downward positron counter is used to analyze the beam polarization.

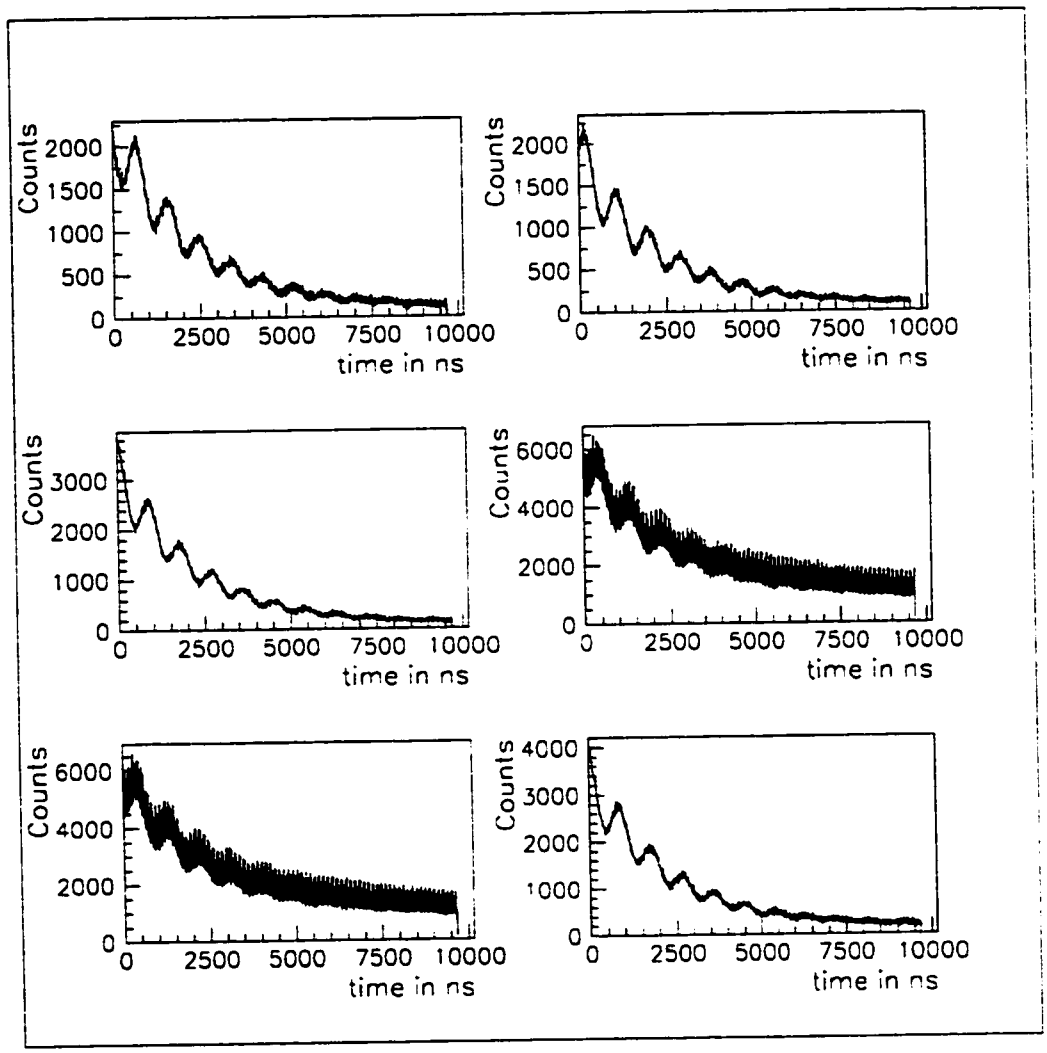

Figure 4.4: Time spectra of the positron counters U, D, B_{in}, F_{in}, F_{out}, B_{out} without cuts (row by row from left to right).

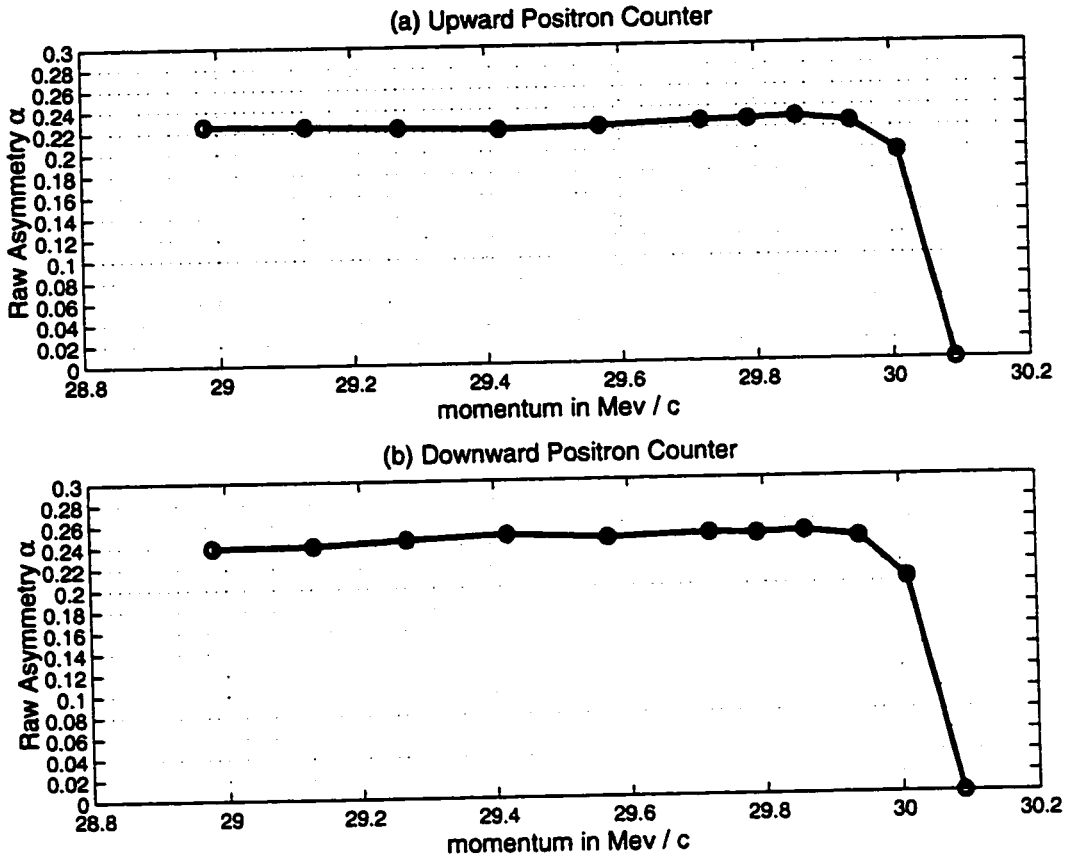

Figure 4.5: Raw asymmetry, α, of signal from (a) the upward e^+ counter and (b) downward positron counter. Statistical error in α is negligible and the background includes cloud μ^+'s, beam e^+'s and e^+'s from μ^+ decay in the detector setup.

Momentum in MeV/c	upward e^+ counter		downward e^+ counter	
	raw α	α with ADC cut	raw α	α with ADC cut
29.72	0.227	0.265	0.248	0.277
29.79	0.228	0.268	0.247	0.275
29.87	0.230	0.263	0.249	0.279
30.01	0.197	0.222	0.205	0.227

Table 4.2: Asymmetry of the surface muons at different momenta about the $\mu-\pi$ edge from the upward and downward positron counters. The statistical error is negligible.

4.6 Pile-up gate

The logic for the pile-up gate trigger is

$$\text{P.U.G.} = \text{trigger.(delayed trigger.}\overline{BUSY}\text{)}.$$

Here, only the case at $p = 29.79$ MeV/c is considered. The flat pile-up time spectrum in Figure 4.6(a), apart from the sharp peak shows that pile-up particles are arriving at random in time in the time gate. Pile-up muons are the muons arriving in the "μSR" time gate τ of ~ 9.7 μs followed by another particle. The latter can be a positron, a pion or another muon. If the second particle is a muon, the determination of the decay time will be uncertain, invalidating the determination of the decay asymmetry. On summing for the pile-up muons in the pulse height distribution for pile-up particles in the C_{in} scintillation counter (see Figure 4.6(e)) , their contribution is 2.7% of the total μ^+ flux. This value agrees with the estimation made in section 3.4. The pile-up muons in the sharp peak amount to 0.26 % of the total μ^+ flux.

The time of flight distributions for the pile-up gate in Figures 4.6(c) and (d) show that the pile-up particles are surface muons and positrons. The pile-up

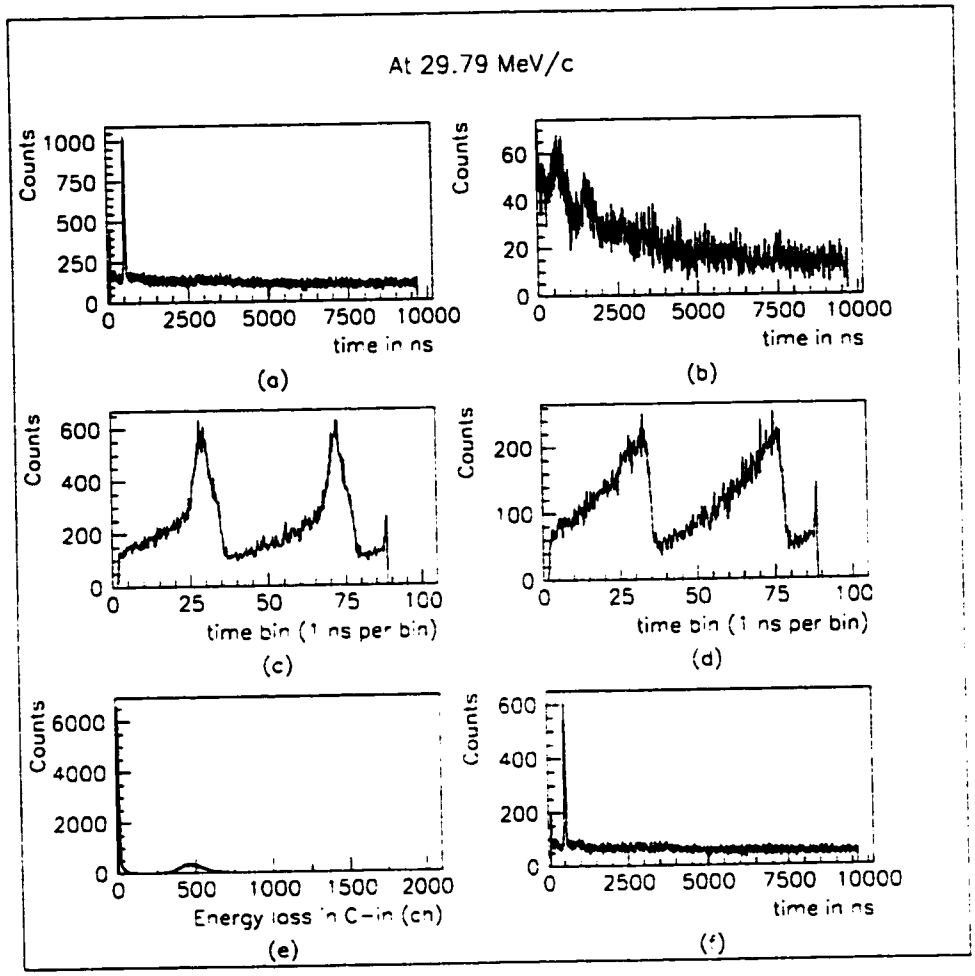

Figure 4.6: (a) Pile-up gate time spectrum with no cuts, (b) time spectrum for pile-up particles in upward e^+-counter, (c) TOF of pile-up particles, (d) TOF of pile-up particles with positron suppression , (e) pulse height distribution for pile-up particles in the C_{in} scintillation counter, (e) Pile-up gate time spectrum with positron suppression.

particles going in the U counter have a polarization of 75.5 $\pm$ 0.9 % (see the asymmetry fit in Figure 4.7). On the other hand polarization of the pile-up muons arriving after the sharp peak in the positron counter U in the time gate has a polarization of 99.9 $\pm$ 1.5 % .

There was no provision in the electronics to reject these pile-up muons. The rejection was done in the analysis. It will be seen in the last section of this chapter that the distortion in the μSR spectra due to the pile-up particles is negligible. Hence the probability that a second surface muon enters the time gate τ is negligible. The pile-up gate more likely is set by a positron following a muon into the system. This would imply that the positron flux is a few times greater than the muon flux.

4.7 Cloud μ^+, its flux and polarization

Whether the cloud μ^+'s at the selected momenta are polarized or have a polarization opposite to that of surface μ^+'s is questionable. Four runs above the $\mu-\pi$ edge, where there are no apparent surface μ^+'s, are chosen to deal with this issue. Time of flight cuts were applied to the latter to select cloud μ^+'s. Also pulse height cuts are applied to suppress the flat background of decay positrons.

There is no convergence when the fitting Equation 4.1 is applied to the cloud muon data sample. Figure 4.8 shows the time spectra for positron decay from cloud muons at 30.1, 30.5, 30.6 and 33.1 MeV/c. They are fitted with the exponential fit

$$N(\mathrm{t}) = N_o \exp(\mathrm{t}/\mathrm{t}_\mu) + Bkg, \tag{4.2}$$

where $\mathrm{t}_\mu = 2.20$ μs is the mean lifetime of the muon, and Bkg is the accidental flat background. The free parameters are N_o, t_μ and Bkg referred to as P_1, P_2

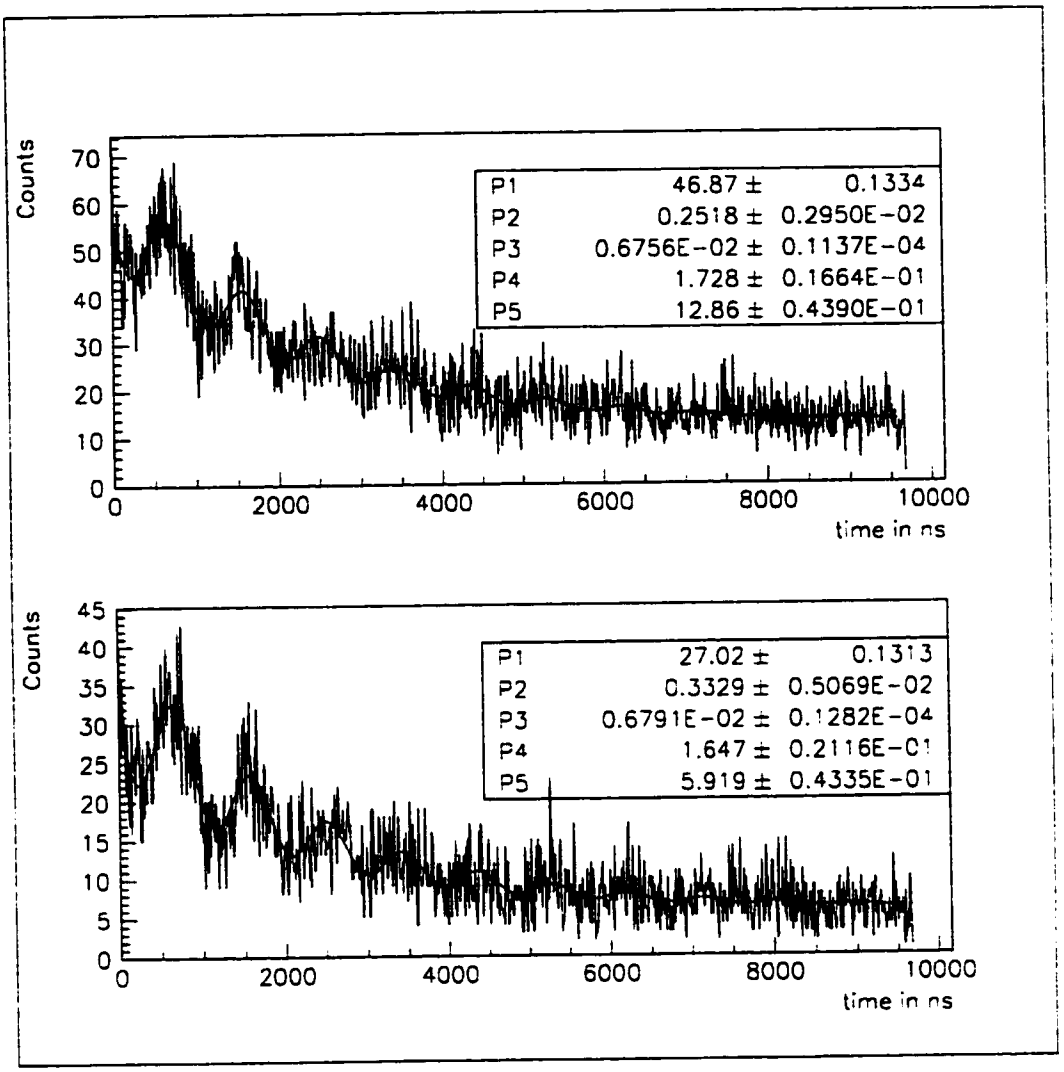

Figure 4.7: Above: the asymmetry for the decay of the pile-up muons, with no cuts, in counter U is 0.252 ± 0.003. Below: the fit for asymmetry for the decay of the pile-up muons, with positron suppression, arriving in counter U after the sharp peak in the time gate (see Figure 4.6(a)); it is 0.333 ± 0.005.

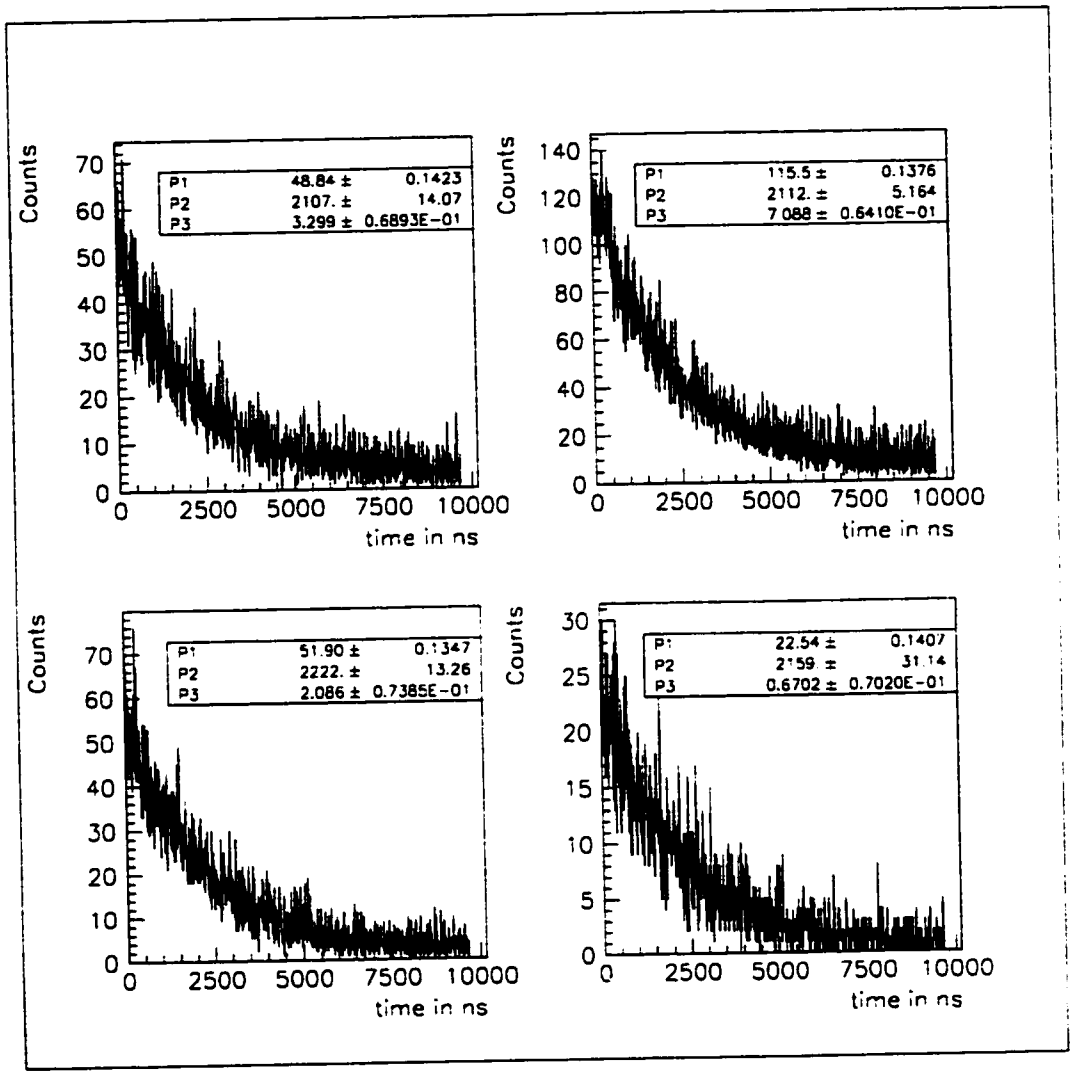

Figure 4.8: Spectra of e^+ decay from cloud μ^+'s at 30.1, 30.5, 30.6 and 33.1 MeV/c; the absence of sinusoidal variation verifies the fact that the cloud μ^+'s are not polarized.

and P_3 by the fitting software. The absence of sinusoidal variation verifies the fact that the cloud μ^+'s are not polarized. The fitting value for t_μ is best for the bottom left spectrum at 30.6 MeV/c because for this particular run there is more data and the pulse height distribution for the C_{in} counter is available for a better suppression of background decay positrons.

The highest momentum at which the beamline M11 was run is 33.1 MeV/c. From 30.3 to 33.1 MeV/c, where there is cloud μ^+ and no apparent surface μ^+, the total μ^+ flux, is calculated using the method in the section on "Particle Fluxes". It is almost constant at 0.25 $\pm$ 0.02 counts/(μA second) (see Figure 4.3). It is extrapolated that at the $\mu - \pi$ edge, at 29.8 MeV/c, the cloud μ^+ flux has the same value.

The following is an argument to explain why the cloud muon does not have a polarization opposite to that of the surface muon. When the beamline is tuned for a momentum above the $\mu-\pi$ edge that momentum can be the sum of momenta of a pion with a few MeV/c directed into the beamline and a muon decaying in the same direction, as exemplified in Figure 4.9(a). There is also the case where the pion has a momentum larger than the beamline tune momentum and the muon decaying in the backward direction, as illustrated in Figure 4.9(b). The muon in the the first case will have a polarization opposite of that in the second case. The absence of the sinusoidal variation in the spectra in Figure 4.8, implying zero polarization, shows that the two possibilities occur with equal probability at the angle of 2.5° at which M11 views the π production target. Cloud muons decrease the apparent polarization of the surface beam by the same percentage of cloud muons in the beamline .

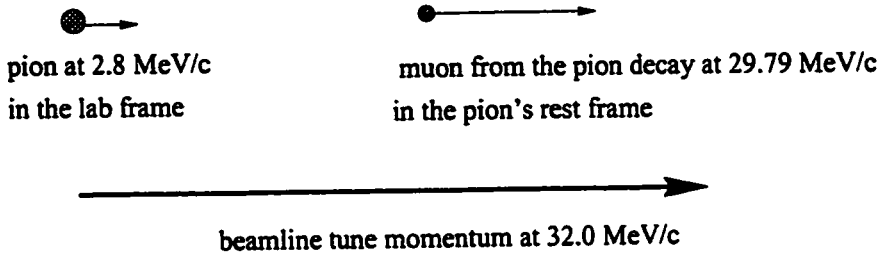

(a) The muon coming off in the forward direction.

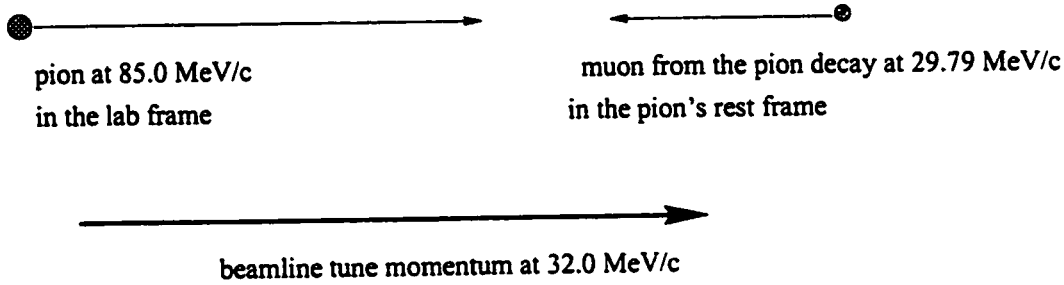

(b) The muon coming off in the backward direction.

Figure 4.9: Momentum of muon from pion decay in flight above the $\mu - \pi$ edge, at a beamline tune momentum $p = 32.0$ MeVc.

4.8 Some features across the RF cycle at the $\mu - \pi$ edge

At the $\mu - \pi$ edge ($p = 29.79$ MeV/c), the flux of surface muons is at a maximum. In order to obtain a surface muon flux with minimum background contamination and hence optimizing the beam polarization, a detailed analysis of some important features is done across the RF cyclotron period. The latter is of a duration of 43.5 nanoseconds; it is divided into six bins of 7.25 nanoseconds. The RF period is chosen between two maxima in the surface muon flux in the TOF spectrum in Figure 4.14(a). Figure 4.14(a) shows the time of flight spectrum at the $\mu - \pi$ edge with pulse height cut for positron suppression. The TOF spectrum is for one RF cycle from 32.5 ns to 76.0 ns. The flux of the different particles and the asymmetry of the muon decay are investigated in these bins and a time window in the TOF spectrum is then selected in which there are essentially no contaminant particles.

4.8.1 μ^+, e^+ and π^+, Their Flux and Time of Arrival

Figure 4.10 shows the variation in total (surface and cloud) muon flux and the positron flux at the $\mu - \pi$ edge ($p = 29.79$ MeV/c). By referring to Figure 4.1 it can be deduced that the beam positrons arrive in the 1st and 6th bins.

Based on the fact that the beam e^+ peak does not move with a change in momentum of the beam; because due to small positron mass it travels with a velocity very close to the speed of light from the 1AT1 production target; and from the TOF spectra at 29.9 MeV/c, 30.0 MeV/c and 30.1 MeV/c in Figure 4.11, the following observations are made (a more detailed analysis is made in the following sections):

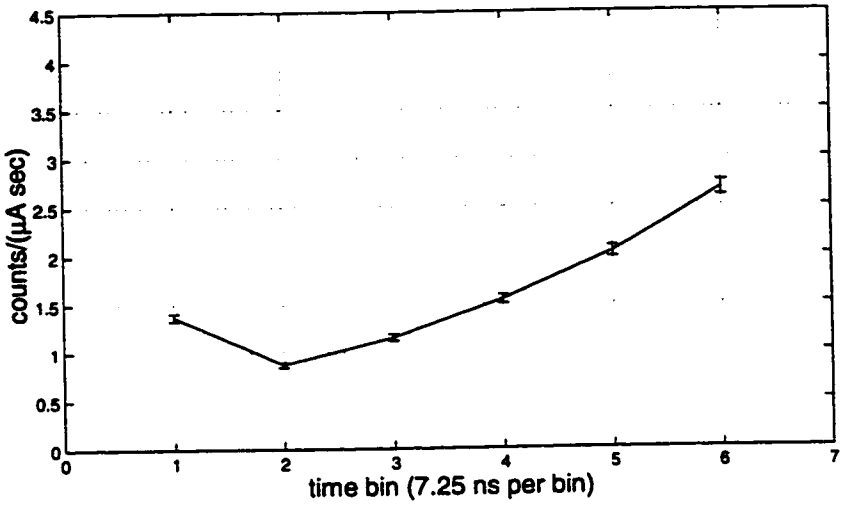

(a) Total Surface and cloud muon flux

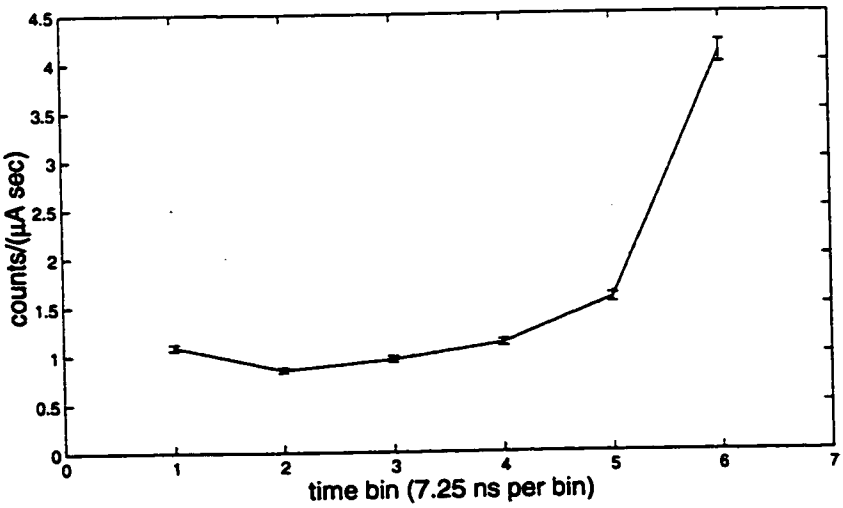

(b) Positron flux

Figure 4.10: (a) Total muon flux and, (b) total positron flux, across one RF cycle divided into six bins at the $\mu - \pi$ edge. The horizontal axis goes backward in time.

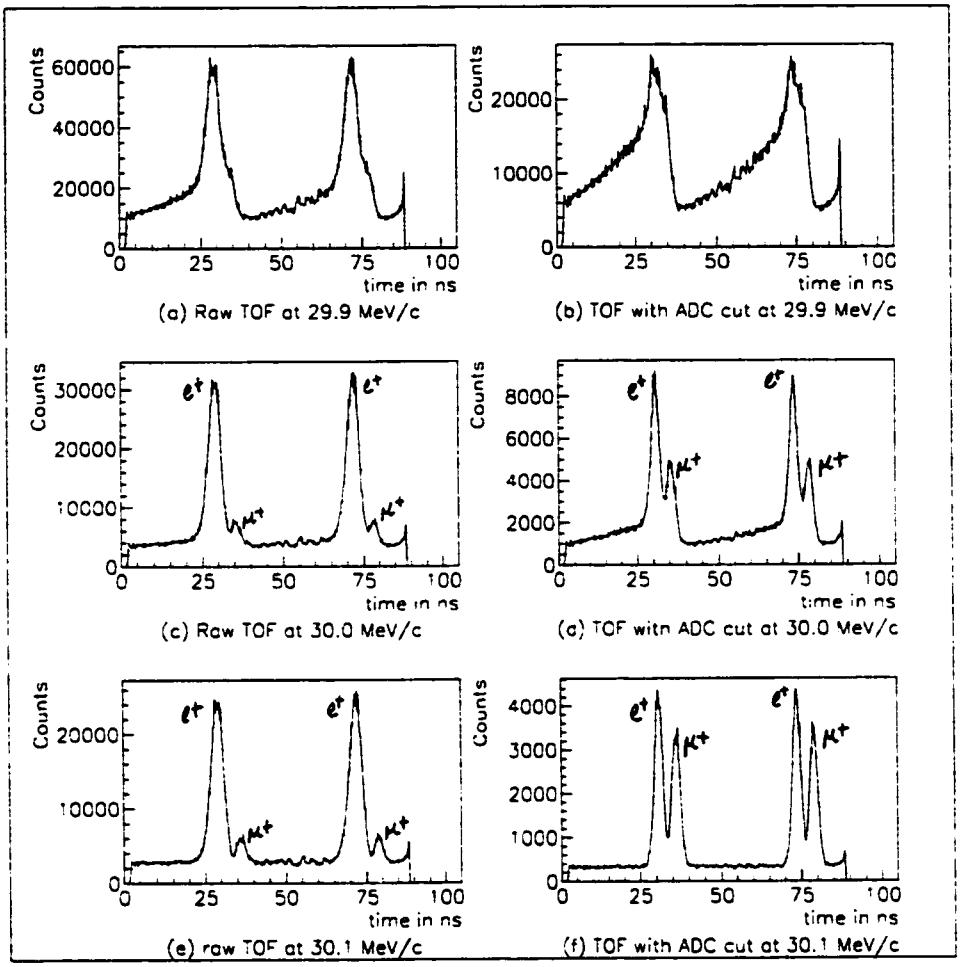

Figure 4.11: From these TOF spectra it is concluded that the beam e^+ and the cloud μ^+ peaks arrive almost in time at the $\mu - \pi$ edge at 29.8 MeV/c. Note: the horizontal axis goes backward in time.

- At the $\mu - \pi$ edge (29.8 MeV/c), the cloud muon peak arrives almost in time with the beam e^+'s which are time correlated with the cyclotron RF.
- At 29.8 MeV/c both the beam e^+'s and the cloud μ^+ peaks arrive almost in time with the sharp rise in surface μ^+ flux in the TOF spectrum.

Hence, unwanted beam positrons and cloud muons appear in the first and sixth bins.

Pions are time correlated to the RF cycle since they originate from the production target. Because the pion is more massive than muon or positron, the pion peak is expected to arrive later than the beam positron and cloud muon peaks (see Table 4.3 below). Thus, at the $\mu - \pi$ edge, pions arriving at a negligibly small rate of ~0.02 counts/(μA second) are also overlapping with the cloud muon and beam positrons peaks too.

Particle	mass in MeV/c^2	mean life	flight time
e^+	0.51099907(15)	stable	37 ns
μ^+	105.658389(34)	2.19703(4) μs	135 ns
π^+	139.56995(35)	26.033(5) ns	176 ns

Table 4.3: Particle mass, mean life and flight time. The flight time is for 29.8 MeV/c, the nominal length of M11 channel is 11 m and the cyclotron period is 43.6 ns.

4.8.2 Cloud Muon Movement in TOF Spectrum

The movement of the cloud muon peak from $p = 30.3$ MeV/c in Figure 4.12(b) to $p = 29.8$ MeV/c in Figure 4.12(a) can be calculated kinematically. The velocity(v) and momentum (p) of a muon are related by

$$p_\mu = \gamma_\mu m_\mu v_\mu,$$

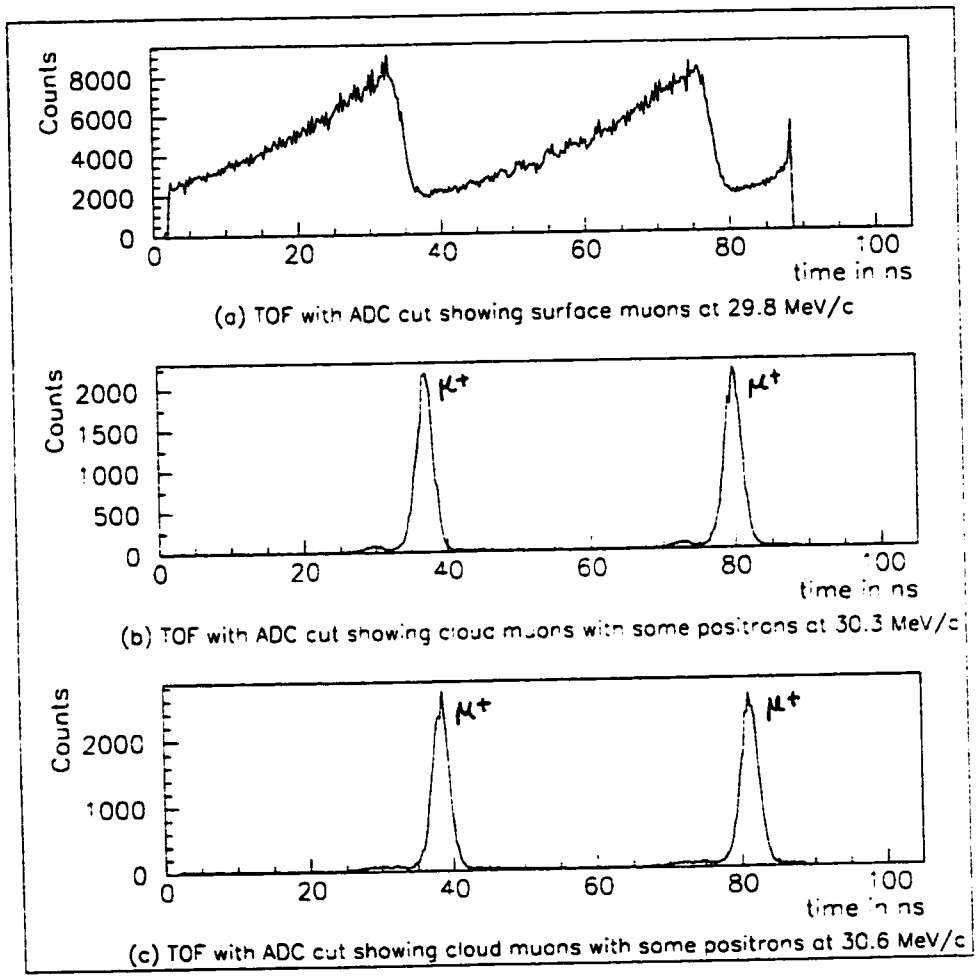

Figure 4.12: At 29.8 MeV/c, the cloud muon peaks arrive in the TOF spectrum earlier than at 30.3 MeV/c, they will sit about the sharp fall in the surface μ^+ flux near to the unsuppressed beam e^+. Note: the horizontal axis goes backward in time.

where m_μ is the rest mass of the muon and γ_μ is the relativistic factor given by

$$\gamma_\mu = \frac{1}{\sqrt{1-\left(\frac{v_\mu}{c}\right)^2}}.$$

The above equations can be rearranged to give

$$\frac{v_\mu}{c} = \sqrt{\frac{{p_\mu}^2}{{p_\mu}^2 + {m_\mu}^2}}.$$

Assuming that the cloud muons originate near the 1AT1 pion production target, the time of flight of the muons through the M11 channel is

$$t_\mu = \frac{d}{v_\mu},$$

where $d = 11$ m is the length of the M11 channel in the lab frame. For a small change $\Delta p/p$ = -1.7 % from p = 30.3 MeV/c to p = 29.8 MeV/c, Δt_μ = 2.0 nanoseconds. The formula used is

$$\Delta t_\mu = -\frac{d}{c}\frac{{m_\mu}^2}{{p_\mu}^2}\sqrt{\frac{{p_\mu}^2}{{p_\mu}^2 + {m_\mu}^2}}\frac{\Delta p_\mu}{p_\mu}.$$

The calculation is verified for the movement of the muon clouds in the TOF when p changes from 30.3 MeV/c (Figure 4.12(b)) to 30.6 MeV/c (Figure 4.12(c)); the calculated Δt_μ = 1.2 nanoseconds whereas the measured Δt_μ = 1.4 nanoseconds. There is agreement to the nearest tdc bin (0.25 nanosecond per bin).

The cloud muon peak (Gaussian in shape) has a FWHM $\sim$ 10 nanoseconds and at 29.8 MeV/c it is estimated to be centered at 35.0 ns in the TOF spectrum for one RF cycle in Figure 4.14(a). Thus most of the cloud muons ($\sim$96 %) are in the first bin and the remaining appear in the 6th bin.

4.8.3 Positron Suppression

The pulse height cut applied on the C_{in} counter suppresses the positron background from $\sim$1 positron per surface muon to $\sim$ 0.004 positron per surface muon

at 29.8 MeV/c. Figure 4.13(b) indicates the remnant positrons in the time of flight spectrum at 33.1 MeV/c when the pulse height cut is applied. This momentum is chosen as an illustration because the cloud muon peaks are arriving far behind the beam positrons. About 55 % of the remnant positrons are beam positrons and they do not move across the TOF spectrum when the beam momentum changes.

It is important to calculate this unwanted background in the six bins of the RF period in order to understand the variation in the polarization of the muon beam across the RF cycle.

4.8.4 Asymmetry Variation

It was found that the polarization of the beam is maximum at the $\mu - \pi$ edge. Since the contaminant π^+'s, cloud μ^+'s and beam e^+'s are strongly time correlated with respect to the RF it would be worthwhile to investigate how the polarization of the beam varies across one cyclotron period.

The mechanism described in Chapter two produces muons that are intrinsically close to being 100% polarized. However in a real experiment there are depolarization effects; and in this beam test there are three contributions:

- The muon beam divergence is not zero and thus the polarization is decreased by a factor given by the average of cos θ, where θ is the angle of the muon's momentum vector with respect to the beam axis.

- A typical positron detector intercepts a rather large solid angle and thus averages appreciably over positron decay angles. For the upward and downward positron detectors in the detector setup shown in Figure 3.3,

$$\langle \cos\theta \rangle = \frac{\int_{-\theta'}^{\theta'} \cos\theta \, d\theta}{2\theta'} = 0.91,$$

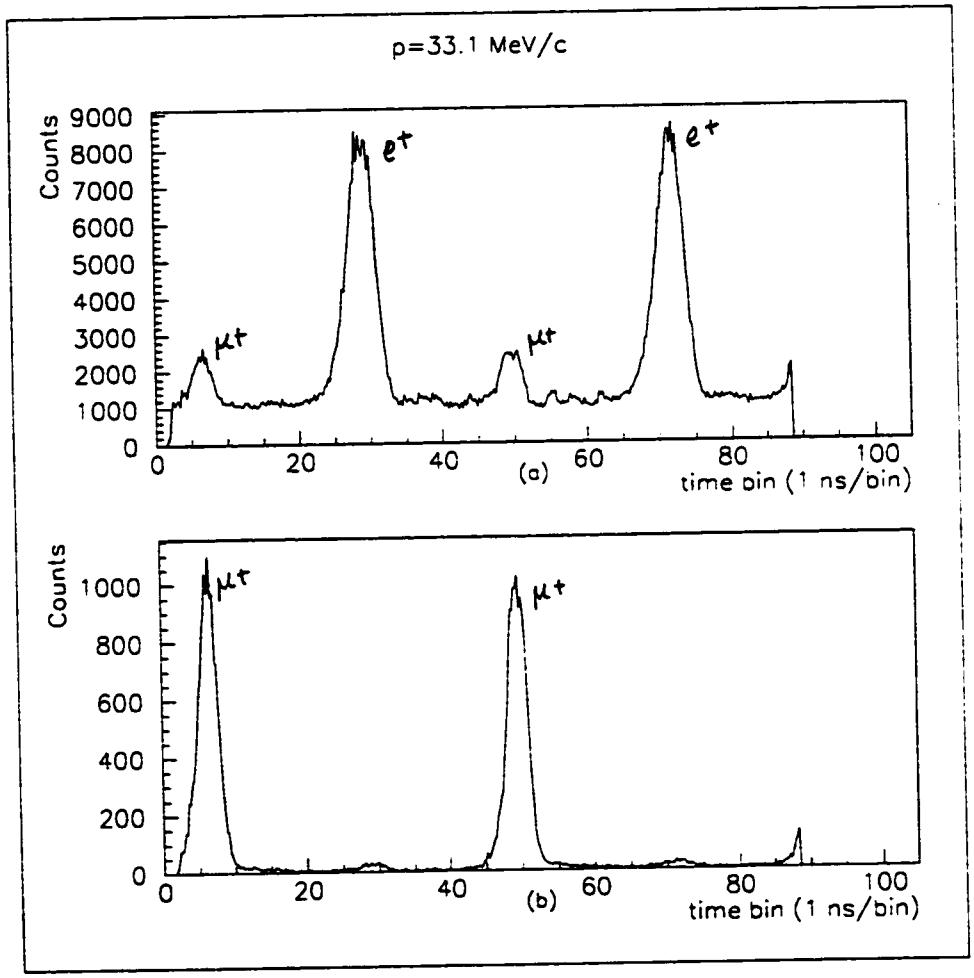

Figure 4.13: (a) Raw TOF, (b) TOF with pulse height cut, showing only cloud muons and remnant positrons.

where $2\theta'$ is the angle subtended at the aluminum target by the two positron detectors and $\theta' = \tan^{-1}\frac{3.25}{3.75}$, assuming the target position is centered with respect to the detectors. This smears the decay distribution, resulting in an apparent depolarization of 9±2% . The error of ±2% is due the uncertainty in the position and geometry of the counters.

- The depolarization effect of multiple scattering of muon passing through matter is negligible. At $\Delta p/p = \frac{1}{2}$ %, $\langle\cos\theta\rangle$=0.9999 for carbon target. Multiple scattering of the nonrelativistic muons from pion decay at rest changes the muon's direction of motion without changing its spin direction.

The asymmetry for the muon decay in the six different bins of the cyclotron period is calculated by applying the fitting equation (4.1) to the positron spectra of the upward counter corresponding to the different time bins. Two cuts are applied to the these spectra:

- A dE/dx cut on the pulse height distribution in the C_{in} counter (ADC3 > 250).
- No pile-up muon present (TDC8 < 100).

The asymmetry fits are shown in Figure 4.15 and the polarization versus bin number is plotted in Figure 4.14(b). The polarization incorporates the correction for the the finite angle effect of the positron counter, and the error bars are mostly due to the systematic uncertainty in the geometry of the counter. The following four points are noted from Figure 4.14(b):

- As explained in the previous section, the unwanted particles have a higher flux in the first and last bins; the cloud μ^+'s in the first and the e^+'s in the sixth bin.

Results at 29.8 MeV/c (flux in counts/(μA sec))			
time bin #	**backgr flux**	**(surface μ^++backgr) flux**	f_μ
1	0.258 ± 0.001	1.31 ± 0.04	0.80 ± 0.04
2	0.007 ± 0.001	0.87 ± 0.02	0.99 ± 0.04
3	0.0030 ± 0.0002	1.10 ± 0.03	1.00 ± 0.04
4	0.0019 ± 0.0001	1.49 ± 0.04	1.00 ± 0.05
5	0.0030 ± 0.0002	1.95 ± 0.06	1.00 ± 0.06
6	0.018 ± 0.001	2.57 ± 0.07	0.99 ± 0.06

Table 4.4: The background comprises remnant positrons and cloud muons, f_μ = surface μ^+/(surface μ^+ + background). The cyclotron period is divided into six bins of 7.25 nanoseconds.

- The polarization is lowest in the first bin because of the lowest surface muon to background ratio.
- The polarization rises from the first to the fifth bin because of the exponential fall with time in the surface muon flux from pion decay at rest (the horizontal axis goes backward in time) and the consequent relative decrease in the background contribution.
- The polarization drops in the sixth bin due to the fall in the surface muon to background ratio, the remnant beam positrons is highest in this bin.

The background flux, the surface muon flux and the ratio f_μ of surface muon flux to sum of surface muon and background flux are calculated in the six bins of the time of flight spectrum at 29.8 MeV/c (Figure 4.14 (a)) in the Table 4.4.

Since the background comprises cloud muons and accidental positron coincidences which are randomly polarized and have no asymmetry, it is expected that f_μ should agree with the ratio of asymmetry of the clean surface muon beam to

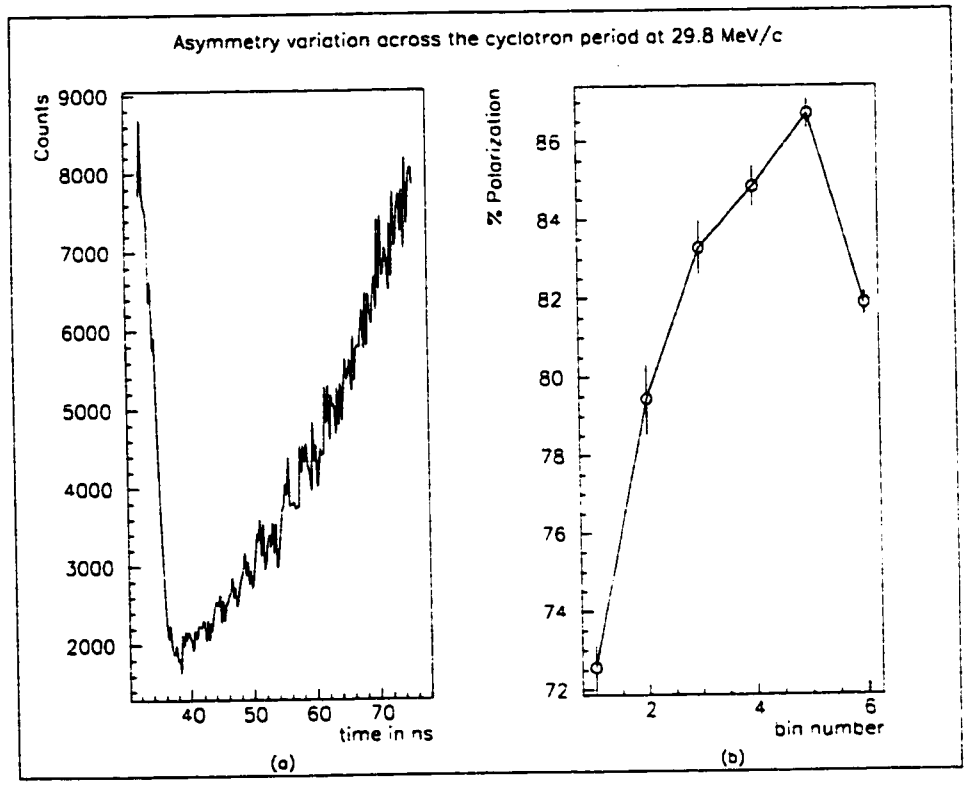

Figure 4.14: (a) The TOF spectrum for one RF cycle from 32.5 ns to 76.0 ns with ADC cut (to suppress the e^+), and (b) The polarization of the surface μ^+'s in the six bins (7.25 ns per bin) into which the TOF spectrum in (a) was divided.

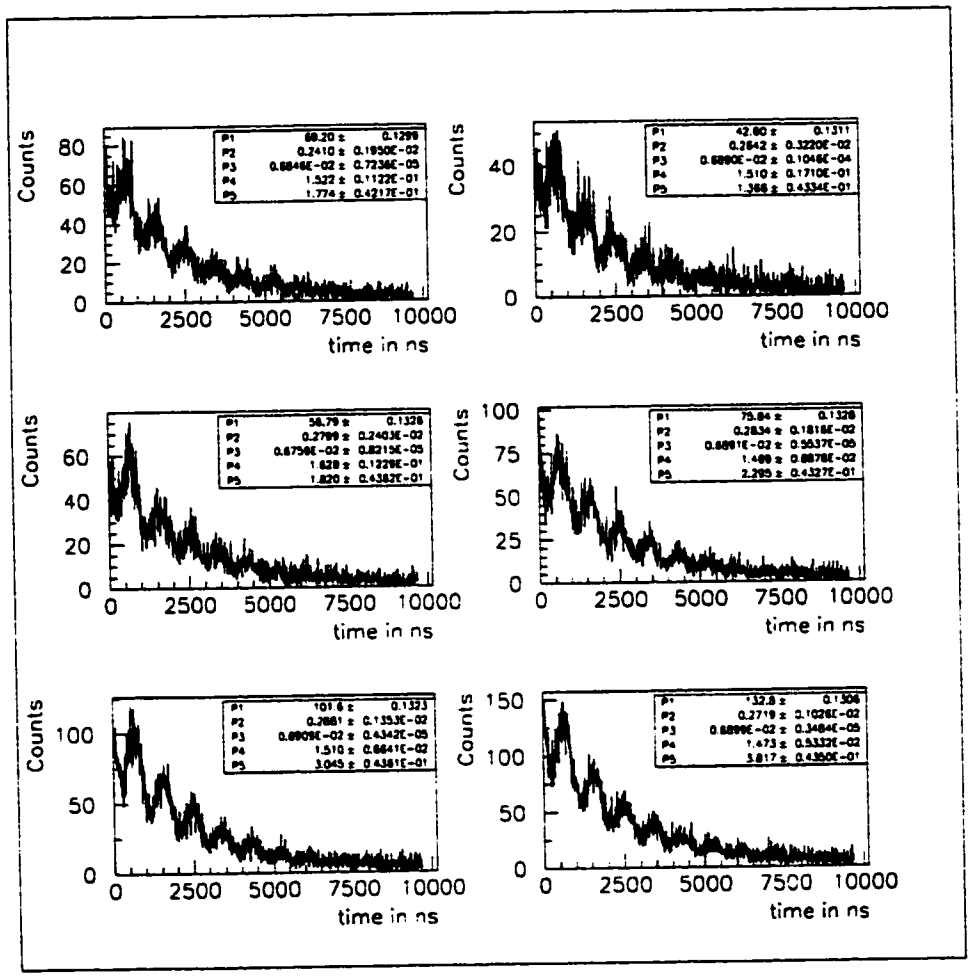

Figure 4.15: Fitting parameters at 29.79 MeV/c for muon decay in the six time bins. Cuts were applied on e^+'s, and pile-up μ^+'s. P1≡ N_0, P2≡ α, P3≡ ω, P4≡ ϕ, P5≡ Bkg.

Asymmetry results at 29.8 MeV/c		
Bin number	**measured α**	α/f_μ
1	0.2410 ± 0.0020	0.30 ± 0.02
2	0.2642 ± 0.0032	0.27 ± 0.01
3	0.2799 ± 0.0024	0.28 ± 0.01
4	0.2834 ± 0.0018	0.28 ± 0.02
5	0.2881 ± 0.0014	0.29 ± 0.02
6	0.2719 ± 0.0010	0.27 ± 0.02

Table 4.5: α/f_μ = calculated asymmetry of clean surface μ^+ beam in M11.

that of the surface muon beam with the remnant background. From the discussion above on depolarization effects the asymmetry of the clean surface muon beam in M11 is estimated to be ~ 0.28. This value can be tested by measuring the ratio α/f_μ, where α is the measured asymmetry in the different bins. If the background is understood correctly, the quantity $\alpha/f_\mu \simeq 0.28$, independent of the tdc bin. This is approximately the case, as shown in Table 4.5.

4.9 Time Window Selection

For positrons suppression pulse height selection was used. As for cloud muons and pions, one way to avoid them is to select a time window in the TOF spectrum in which cloud μ^+ peak is excluded. Moreover the time window can be selected to exclude the remanant beam positrons so that the overall positron contamination is ~ 0.3 % of the total surface muon beam flux.

An acceptance region from 45.0 ns to 71.3 ns was chosen from the time of flight at a momentum of 29.8 MeV/c. A combination of the cut based on this and the one from pulse height shape of C_{in} (i.e. ADC3 greater than 250) increases the

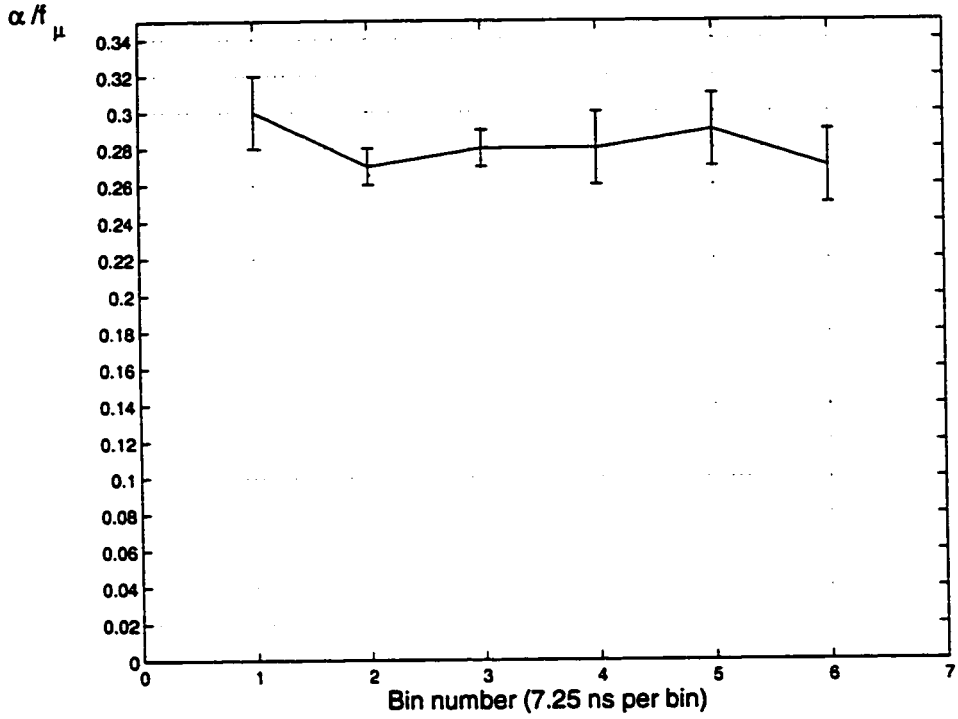

Figure 4.16: Graph of α/f_μ versus Bin number

Asymmetry at the $\mu - \pi$ edge (29.8 MeV/c)		
Selection	**asymmetry**	**Polarization**
No cuts	0.2278±0.0001	
pulse height cut	0.2682±0.0001	(88.4±2.0)%
pulse height and TOF cuts	0.2852±0.0005	(94.0±2.2)%
pulse height, TOF and pile-up-gate cuts	0.2849±0.0005	(93.9±2.2)%

Table 4.6: Selections to optimize the asymmetry at 29.8 MeV/c. The polarization incorporates the correction for the finite angle effect of the positron counter.

asymmetry from 0.228 to 0.285, see Table 4.6. Figure 4.17 shows the fit for the asymmetry. A further cut on the pile-up-gate to suppress pile-up muons leaves the asymmetry almost unchanged (Figure 4.18).

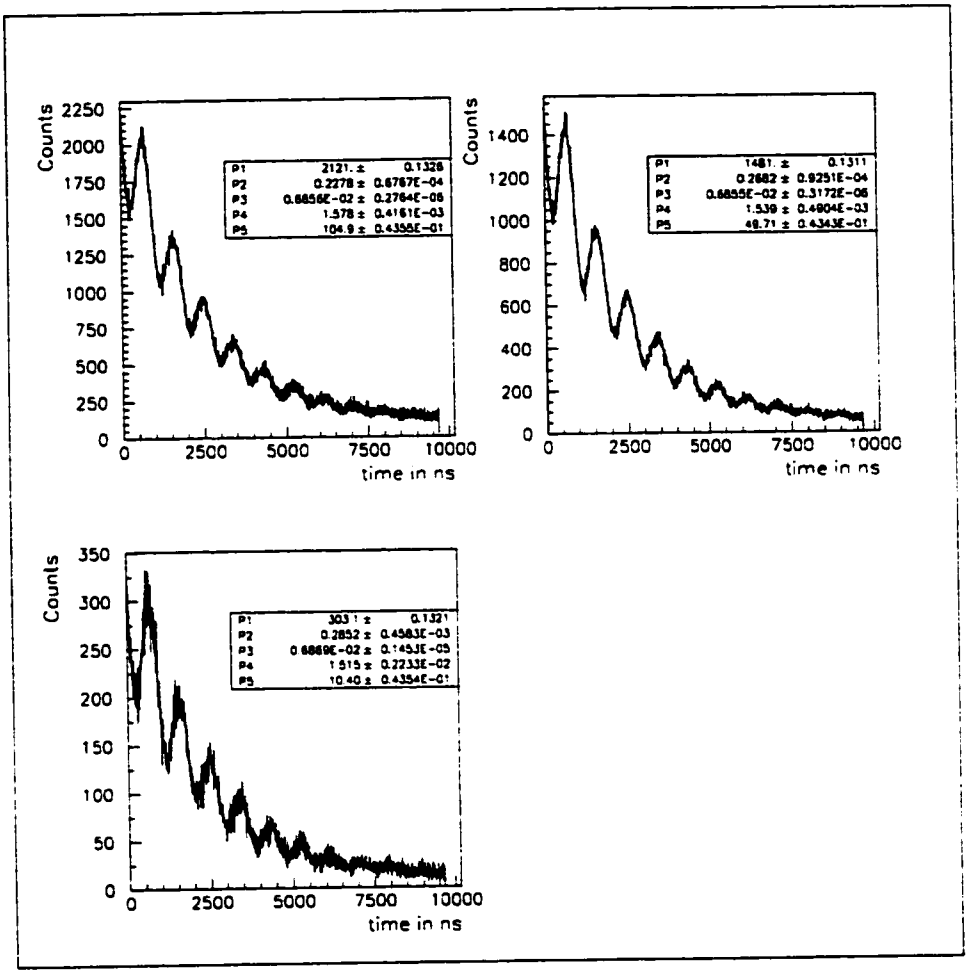

Figure 4.17: Asymmetry fits with no cuts (α=0.228), with adc cut only (α=0.268), with both time and adc cuts (α=0.285) at the $\mu - \pi$ edge. Only the upward positron counter is considered.

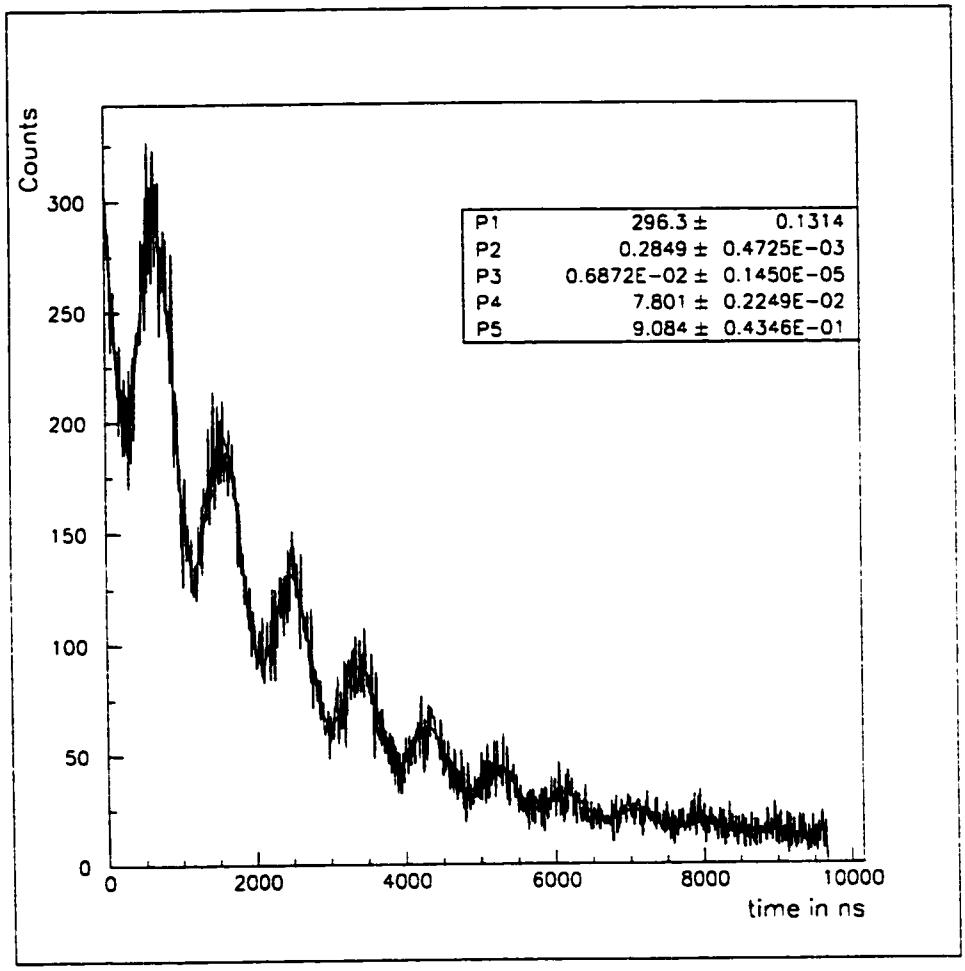

Figure 4.18: Asymmetry fits with pile-up-gate cut, time and adc cuts (α=0.285) at the $\mu - \pi$ edge. Only the upward positron counter is considered.

Chapter 5

CONCLUSION

The secondary beamline M11, known as a fast pion channel, of the 500 MeV cyclotron at TRIUMF was tested to investigate its use as a surface muon source. It was run at momenta ranging from a few % above and a few % below 30 MeV/c. The correspondig low velocity of ~4 MeV muons from pion decays at rest makes it possible to achieve excellent identification of muons with thin scintillation counters and electronic logic. Leaving the production target the beam consists of pions, muons and positrons.

A detailed analysis was done at 29.79 MeV/c (the $\mu-\pi$ edge), the momentum of surface muon from pion decay at rest in the 1AT1 production target. At this momentum the maximum surface μ^+'s flux measured on M11 is 9.5 $\pm$ 0.3 counts/μA sec, after suppression of positrons and pile-up muons. These surface μ^+'s have a polarization of 88.4$\pm$2.0%. The depolarization of ~12% is mainly due to

- the non-zero μ^+ beam divergence,
- pions and cloud muons (which is 2.7% of the surface μ^+ flux) and
- remnant positrons (which is 0.4% of the surface μ^+ flux) .

At the $\mu - \pi$ edge (29.8 MeV/c)	
Particle	**Flux in counts/μA sec**
surface μ^+	9.46±0.33
cloud μ^+	0.26±0.02
beam e^+	>6.0±0.2
decay e^+	>3.7± 0.3
π^+	$\sim$ 0.018±0.001

Table 5.1: The flux of the different particles at 29.8 MeV/c. No time cut is applied for these data.

A time window was selected from the 43.5 nanosecond RF period to suppress the beam positrons, the cloud muons and pions. It is found that the three unwanted particles are time correlated with the RF and arrive close together in time in an interval of 21 nanoseconds. Since there are surface muons at all times during the cycle, a time window selection of 26.3 ns reduces the surface μ^+ flux to 1.94 ± 0.07 counts/μA sec. The polarization increases to 93.9±2.2%. This time cut together with the ADC cut and the pile-up-gate cut reduced the background (positron contamination) to $\leq$ 0.7% of the surface muon flux. It was verified that the cloud μ^+'s do not have any asymmetry, i.e. they are not polarized. The pion flux is very small and is excluded in the time window selected.

The flux result at the $\mu - \pi$ edge (29.8 MeV/c) is shown above in Table 5.1. The decay positrons has a flat distribution in time. The value given for the pion flux is an approximation since it is actually the pion flux at 33.1 MeV/c.

To conclude, this beam test has increased our understanding of the M11 at the transition momentum 29.8 MeV/c where the surface muon flux is at its maximum and then drops to zero.

Bibliography

[1] C.Caso *et al.*, The European Physical Journal **C3** (1998) 1.

[2] A. E. Pifer, T. Bowen, and K. R. Kendall, Nucl. Instrum. Methods **135**, 39, (1976).

[3] T. Bowen, Physics Today **38**, 22 (July 1985).

[4] T. D. Lee and C. N. Yang, Phys. Rev. **104**, 254 (1956)

[5] C. S. Wu *et al.*, Phys. Rev. **105**, 1413 (1957).

[6] R. L. Garwin, L. M. Lederman and M Weinrich, Phys. Rev. **105**, 1415 (1957).

[7] L. Michel, Proc. Phys. Soc. **A63**, 514 (1950).

[8] M. L. Brooks *et al.*, Phys. Rev. Lett. **83**, 1521 (1999).

[9] TRIUMF Users Handbook, 1987.

[10] S. F. G. Cox, J. Phys. C **20**, 3187 (1987).

[11] A. Amato, Rev. Mod. Phys. **69**(4), 1124 (1997).

[12] D.Fleming and M Senba in: Prespective of Meson Science, Chapter 8, eds. T. Yamazaki, K. Nakai and K. Nagamine (Elsevier Science Publishers B.V. 1992).

[13] K. W. Kehr,D. Richter, and J. -M. Welter, Phys. Rev. B **26**(2), 567 (1982).

[14] TRIUMF Data Aquisition Systems Group web repository, VDACS Data Aquisition System.

[15] P. W. Green, NOVA Data Analysis System, Version 2.0, 1995.

[16] T.Numao *et al.*, Phys. Rev. D **52**, 4855 (1995).

[17] C. J. Oram *et al.*, Nucl. Instrum. Methods **179** , 95 (1981) .

INFORMATION TO USERS

This manuscript has been reproduced from the microfilm master. UMI films the text directly from the original or copy submitted. Thus, some thesis and dissertation copies are in typewriter face, while others may be from any type of computer printer.

The quality of this reproduction is dependent upon the quality of the copy submitted. Broken or indistinct print, colored or poor quality illustrations and photographs, print bleedthrough, substandard margins, and improper alignment can adversely affect reproduction.

In the unlikely event that the author did not send UMI a complete manuscript and there are missing pages, these will be noted. Also, if unauthorized copyright material had to be removed, a note will indicate the deletion.

Oversize materials (e.g., maps, drawings, charts) are reproduced by sectioning the original, beginning at the upper left-hand corner and continuing from left to right in equal sections with small overlaps.

Photographs included in the original manuscript have been reproduced xerographically in this copy. Higher quality 6" x 9" black and white photographic prints are available for any photographs or illustrations appearing in this copy for an additional charge. Contact UMI directly to order.

ProQuest Information and Learning
300 North Zeeb Road, Ann Arbor, MI 48106-1346 USA
800-521-0600

University of Alberta

Resistive Hybrid Tactile Sensor

by

Kam Chau So ©

A thesis submitted to the Faculty of Graduate Studies and Research in partial fulfillment of the requirements for the degree of **Master of Science.**

Department of Computing Science

Edmonton, Alberta
Spring 2000

University of Alberta

Library Release Form

Name of Author: Kam Chau So

Title of Thesis: Resistive Hybrid Tactile Sensor

Degree: Master of Science

Year this Degree Granted: 2000

Kam Chau So
18839-51 Ave
Edmonton, Alberta
Canada, T6M 2L1

Date: March 20, 2000

University of Alberta

Faculty of Graduate Studies and Research

The undersigned certify that they have read, and recommend to the Faculty of Graduate Studies and Research for acceptance, a thesis entitled **Resistive Hybrid Tactile Sensor** submitted by Kam Chau So in partial fulfillment of the requirements for the degree of **Master of Science.**

. . . . . .

Dr Hong Zhang

. . . . . .

Dr Duncan Elliott

. . . . . .

Dr Jim Hoover

Date: March 20, 2000

Abstract

This thesis introduces a new touch sensor design, called a hybrid tactile sensor. It is a combination of analog and digital touch sensing technologies. In practice, analog touch sensing technology is simple and widely used in electronic touch screens and touchpads. However, it is limited to detecting point contacts. A Digital touch sensing array, on the other hand, provides shape discrimination, but it requires more complex circuit design and generates larger amount of raw data for processing. This research focuses on the development of a new sensor design that is simple and capable of shape recognition. Different models of hybrid tactile sensors are studied and simulations are done to verify their characteristics. Physical prototypes are constructed using inexpensive materials, such as conductive silicone rubber and fabric mesh. Experiments are done and their results are analyzed.

To my wife, Mimi

Acknowledgements

Thanks to my supervisor, Dr Hong Zhang for all the support throughout the research. His guidance and numerous ideas are invaluable.

Thanks to the support from the people in the Computer Vision and Robotics Research Group. I am grateful to Johnathan who provides the skeleton of the communication program used to interface the cylindrical hybrid sensor to the terminal. Thanks also go to Dr Duncan Elliott and Dr Jim Hoover for their constructive suggestions.

Last but not least, thanks to my wife, Mimi for spending so much time proof-reading the manuscript of this thesis.

Contents

List of Figures

List of Tables

Chapter 1

Introduction

The sense of touch is an important sensing modality in robotic applications. Various tactile information such as location, orientation, size, shape, weight, pressure, temperature and surface texture are important for a robot to navigate and perform its task efficiently and safely [1] [2]. To collect tactile information, a tactile sensor is used. It measures the parameters of contact interaction between the device and a physical stimulus. In general, the interaction takes place within a touch-sensitive region of the device's surface. Although limited by the structure, materials and applications of a tactile sensor, it is possible for its sensing surface to conform to virtually any shape or contour [3]. An overview of tactile sensing technologies and sensors is presented in the next section. It is followed by an introduction on the motivation of the research. An outline of the thesis will be given in the last section.

1.1 Overview of Tactile Sensing Technologies and Sensors

Tactile sensors can be categorized in a number of ways. For instance, they are commonly categorized by the way they transduce tactile parameters into a form suitable for computer analysis [4]. The following is a summary of tactile sensors commonly used in robotic applications:

(a) Resistive and conductive tactile sensors measure the change in resistance or conductance of a resistive or conductive material when an external force is applied. The material commonly used is elastomer (elastic polymer). Its deformation by an external pressure causes a change in local particle density, which in turns alters its resistivity or conductivity. This type of tactile sensors are among the earliest being developed and widely used in industry. These sensors have a large dynamic range, good overload tolerance and are very robust. However, they also have problems such

as hysteresis, limited spatial resolution, non-linear response characteristics. Typical designs are those developed by Robertson and Walkden [5] and M. Inaba *et al.* [6].

(b) Piezoelectric tactile sensors generate voltage across the sensing element when pressure is exerted on them, whereas pyroelectric tactile sensors generate a voltage when there is a change of temperature to the sensing element. The generated voltage is proportional to the applied pressure for the former and temperature for the latter. In both types of sensors, no external voltage is required and continuous analog output is available. They are inherently dynamic. If pressure or temperature is applied and kept unchanged, the corresponding sensor output decays to zero. In other words, these sensors are most suitable for registering the change in pressure or temperature. The materials commonly used are polymers with piezoelectric or pyroelectric properties. These sensors usually have a wide dynamic range. They are quite durable and capable of either force or temperature measurement. However, they have drawbacks such as complexity in sensor designs. Moreover, the piezoelectric and pyroelectric effects generally co-exist in the sensor materials, and hinder the applications when only either one of the parameters is required. Typical examples of these types of sensors are designed by Dario and De Rossi [7], J. S. Son *et al.* [8] and Dargahi *et al.* [9].

(c) Capacitive tactile sensors measure capacitance that varies with applied loads. The sensor element consists of an dielectric elastomer sandwiched between the electrode plates of a capacitor. External force is applied and causes physical deformation or displacement of the elastomer that changes the effective capacitance of the sensing element. Such a change in capacitance is proportional to the external pressure. These sensors are fairly robust, have a wide dynamic range and a reasonably linear response. However, they are prone to noise, sensitive to temperature change and have limited spatial resolution. A typical example of this kind of sensors is described by Siegel *et al.* [10].

(d) Magnetic tactile sensors detect a change in magnetic field by either of the following ways. First, magnetoelastic materials are used, which exhibit a change in the magnetic field when subjected to mechanical stress. Second, it is possible to detect the change of magnetic flux from relative mechanical displacement between the core and the surrounding coil of a solenoid-like structure. Those sensors based on mechanical displacement are simple in design and exhibit a wide dynamic range. Yet their spatial resolution is limited, whereas sensors that use magnetoelastic materials are relatively

superior in detecting normal force, torque and shear force. However, they are prone to noise, and additional AC noise shielding circuitry is required to protect the materials.

(e) Mechanical tactile sensors measure the mechanical displacement caused by an applied force. A typical example is a linear potentiometer with its sliding arm (output electrode) moved by an external force to produce an output proportional to the displacement (or the applied force). Even a spring-loaded switch that indicates an open or close contact is a common sensing element. In general, mechanical sensors are simple and robust. They can be used to sense the magnitude of applied force, linear and angular displacements. However, they are usually bulky and provide very limited spatial resolution.

(f) Electrochemical tactile sensors are based on the phenomenon of streaming potentials. In the example proposed by De Rossi *et al.* [11], an ionized gel containing an immobile negative charge with balanced amount of mobile positive charge is used. The gel is contained in a compliant structure. When external force is applied to the gel, positively charged liquid is forced out of the gel into a reservoir. Thus, an imbalanced amount of ions in the gel constitutes a streaming potential which can be used to indicate the magnitude of pressure applied.

(g) Optical tactile sensors use optomechanical transduction coupled with mechanical displacement. A typical sensor is made up of an array of sensing elements covered by a compliant surface. Each sensing element has an elongated pin aligned with a photoemitter/detector pair. When an external force is applied on the compliant surface, affected pins will be displaced inward and block the corresponding light paths of its photoemitter/detector pair. The amount of displacement indicates the amount of light reaching the photodetector that, when digitized, represents the amount of pressure applied on the sensor surface. In practice, optical sensors offer very high spatial resolution. They are also inherently immune from electrical interference and can be easily integrated with other vision-based sensing modalities. However, their designs are relatively complex and costly.

(h) Acoustic tactile sensors are based on the resonant frequency of ultra-sound. In the setup used by H. Shinoda *et al.* [12], a sensing element is made up of a cavity in an elastic body from which two paths are extended to an ultrasonic transmitter/receiver pair. With no external force applied, the acoustic impedance of the cavity is high enough to block the transmission path between the transmitter/receiver pair. When

external force is exerted on the elastic body and distorted the shape of the cavity, resonant frequencies can be picked up by the receiver. Thus, the type of deformation made by a point, a line or a plane can be determined by its relationship corresponding to the resonant frequencies. Another design using a PVDF ultrasonic array is described by B. L. Hutchings *et al.* [13].

Alternatively, tactile sensors can also be classified by their dimensionalities as follows:

(a) A *zero-dimensional sensor* is the basic sensor that detects point contacts.

(b) A *one-dimensional sensor* is a collinear arrangement of zero-dimensional sensors.

(c) In a *two-dimensional sensor* , the sensing elements are arranged as a grid of dimensions $m \times n$, where m and n are the number of sensing elements in the horizontal and vertical dimensions respectively.

1.2 Motivation

Though tremendous progress is found in tactile sensing research, there are still considerable problems in existing tactile sensor designs. First, most of the tactile sensors are small in size as they are designed to fit in a dexterous robot hand. Hence they are not suitable for use on large surfaces such as the links of a robot arm or the body of a humanoid robot. Second, all existing tactile sensors are expensive to fabricate. Their costs range from $500 to $1000 per square inch. It would be extremely expensive for applications requiring large sensing areas. Third, analog tactile sensor is the simplest in design and easiest to fabricate; however, it is only capable of detecting point-contacts. No matter what the shape of the object is, only the "*geometric average* " of the area of contact can be detected and such information is represented by a pair of co-ordinates relative to the sensor's reference frame. Fourth, although digital sensing is very common and provides more precise information, such as the profile, location, and orientation of the shape in contact, the amount of raw data is on the order of n^2 for an $n \times n$ digital sensing array. It could impose considerable software processing overhead when n is large. For instance, if $n = 1000$ and each sensing element provides a single byte of data, a million bytes of data are generated in each sampling for further processing. Fifth, there is a "*parallel path*" problem [14] associated with certain designs of digital sensing array. Special circuitry is required to eliminate any phantom footprint of the original shape, which means additional cost in the manufacturing process. Finally, the existing tactile sensors tend to have fixed geometries (planar, spherical, and cylindrical) and are difficult for adaptation into arbitrary shapes.

This thesis focuses on improvements of the above-mentioned inadequacies by compromising between the analog and the digital[1] extremes of sensing techniques. Resistive material is one of the most inexpensive and commonly used elements in constructing a tactile sensor. In this study, the classical analog resistive sensor architecture is used as the basic sensing element. A hybrid sensor prototype by integrating a number of these sensing elements is introduced. This prototype shows that it is possible to put together low cost materials and relatively simple technology to improve over the inadequacies of either the analog or the digital sensors.

1.3 Thesis Outline

The rest of the thesis consists of six chapters. Chapter two provides background information in analog tactile sensing and resistive tactile sensors. Chapter three presents four models of hybrid tactile sensors. Chapter four explains two shape interpretation algorithms that work with the hybrid tactile sensors. Chapter five presents the simulation and its results of a hypothetical sensor and the shape interpretation algorithms. Chapter six discusses the experimental results of three hybrid tactile sensor prototypes. Chapter seven concludes the thesis and suggests directions for future research.

[1]It would be more proper to use the terms "continuous" and "discrete" instead of "analog" and "digital" respectively. However, the latters are widely used in the robotics industry. In this thesis, the terms "analog" and "digital" are adapted as synonyms for "continuous" and "discrete" respectively.

Chapter 2

Background and Related Information

In this chapter, an overview will be given on both analog tactile sensing and digital tactile sensing technologies. Representative models for each of them will be explained and their associated merits and inadequacies will be discussed. Finally, the last section of this chapter presents the desirable characteristics of a tactile sensor.

2.1 Analog Tactile Sensing

Analog touch sensing has been widely used in the computer industry [15]. For instance, touchpads are standard pointing devices in notebook or palm-top computers, whereas electronic whiteboards can be found in many classrooms and conference centers. Common to all these applications is a touch-based input device. Various transduction technologies have been used in achieving this capability, including capacitive, force/strain gauge, acoustic, scanning infrared, and analog resistive. In theory, most of them are zero-dimensional and categorized as analog tactile sensors. For these devices to work, one critical assumption is that the contact with the touch-sensitive surface occurs only at a point, so that the associated analog technologies can resolve the position of the contact.

Of particular interest to this research is the analog resistive technology. One common configuration of an analog resistive touch screen is the so-called *4-wire* technology, as shown in Figure 2.1. It consists of two conductive sheets with a finite resistance, typically on the order of 100 ohms per square inch, placed on top of each other. These conductive sheets are normally separated from each other when there is no contact. The top sheet carries a voltage gradient generated by applying a reference voltage on one end of the sheet and ground at the other end. The second sheet serves as the slider in a linear potentiometer. When contact

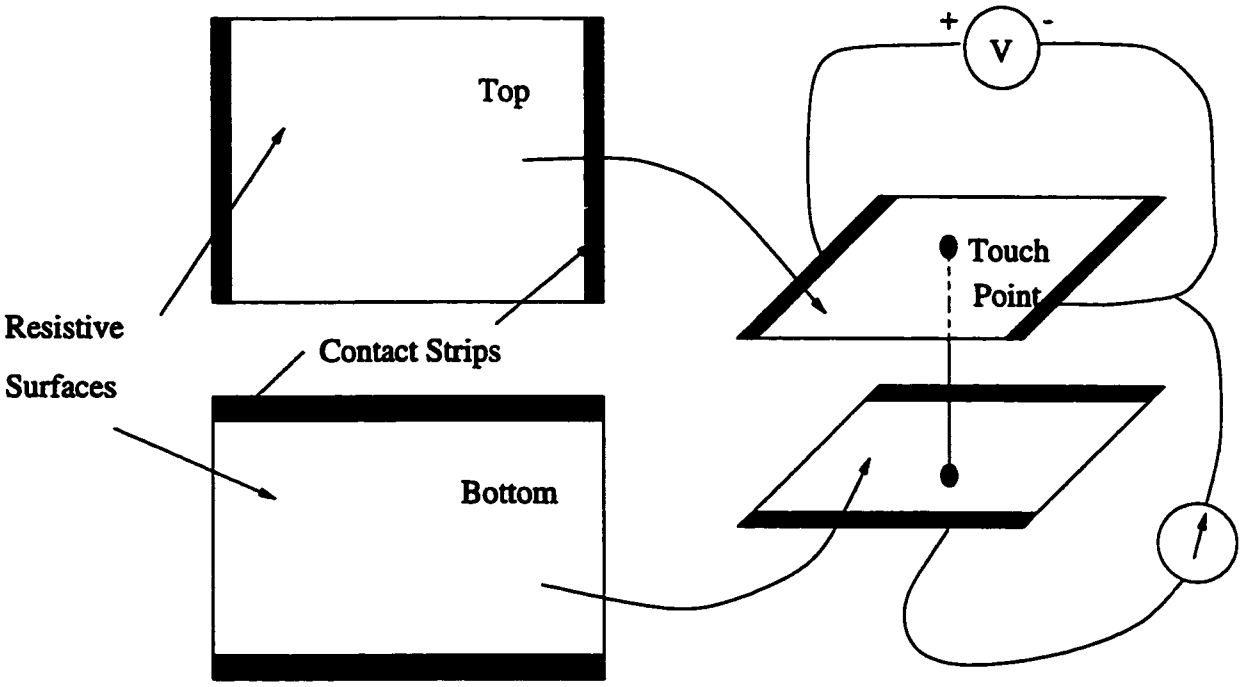

Figure 2.1: A Typical Four-Wire Analog Resistive Tactile Sensor

is made, the sheets touch at a point, creating a voltage divider. The position of the contact can be determined from the voltage measured by the bottom sheet. By reversing the roles of the sheets and repeating the above process, one can obtain a second measurement. These measurements can be used to resolve the x-y coordinates of the contact point. The sampling of the two voltages and the subsequent calculation in this analog resistive sensor are both extremely simple. The complexity of the solution does not increase with the size of the sensor surface. The sensor itself can be produced with inexpensive materials.

A number of techniques can be used to produce the spacing between the two conductive sheets. One solution is to use an air gap between the two sheets. This is a particularly simple solution for the case of a planar sensor surface such as an electronic whiteboard. Another solution is to use microspheres, which are small pressure-sensitive dots whose diameters can be on the order of one tenth of a millimeter. Yet another solution is to use an insulating fabric mesh between the two sheets. The critical pressure causing the contact can be controlled by the thickness of the fabric and the size of the holes of the mesh.

Analog resistive technology, and analog technologies in general, are an effective approach to solving the electronic touch screen problem. However, this approach is not directly applicable to robot tactile sensing because of its inability to detect multiple points of contact or determine the shape of contact. For instance, if the contact occurs at two points, the volt-

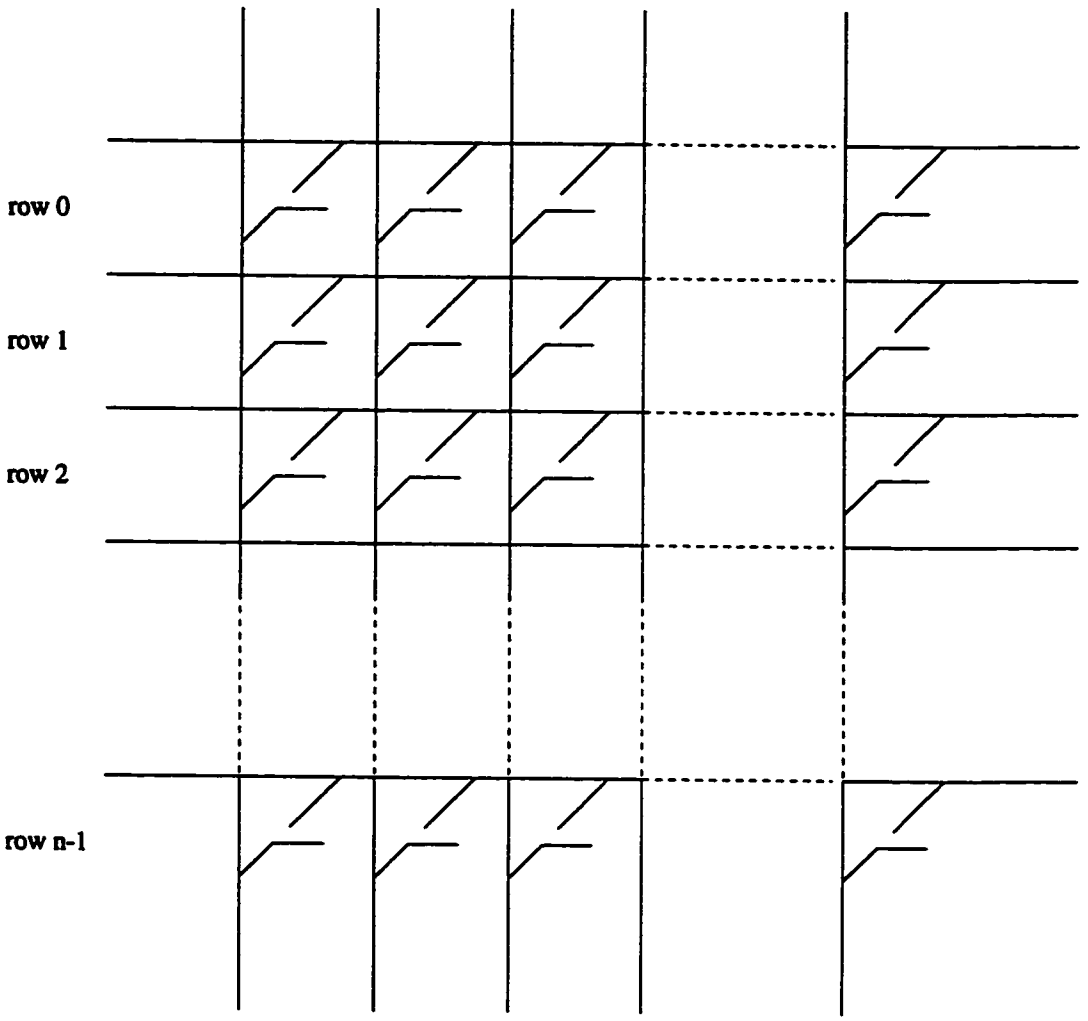

Figure 2.2: A Typical Digital Tactile Sensor with $n \times n$ cross-switches

age measurements will indicate the a point somewhere between the two contact positions. Therefore, design changes must be introduced in order to take advantage of the simplicity of the analog touch technologies.

2.2 Digital Tactile Sensing

Digital tactile sensing uses a two-dimensional array of sensing elements, called *tactels* (analogous to pixels for picture elements). Common applications of digital tactile sensors can be found on touch screens of cash registers in supermarkets, on vending machines at street corners, and on control panels of advanced equipment. Assuming there are n tactels in each row and column, the sensors area is digitized into $n \times n$ sensing sites. The simplest arrange-

ment can be a matrix of on/off switches, which indicates contact or no contact condition at the corresponding site. Figure 2.2 illustrates a typical digital tactile sensor made up of $n \times n$ cross-switches. The status of each cross-switch is obtained by the following operations:

Step 1: Apply reference signal to one and only one row, starting from row 0.

Step 2: Scan all columns, starting from column 0 to $n-1$ and record the presence of any reference signal in each column. Presence of a reference signal at any column x indicates a closure of cross-switch at row 0 and column x.

Step 3: Repeat step one and two with reference signal applied to row 1 and so on, up to row $n-1$.

With the same sensing surface area, a digital sensor offers n^2 as many sensing elements as its analog counterpart. As a result, a digital sensor provides a much higher spatial resolution. The states of the tactels constitute a tactile image of the object in contact. Such an image is far superior than just the single-point contact information provided by an analog sensor. Figure 2.3 illustrates the advantage of a digital sensor output over an analog sensor. Information of a contact object, such as its location, area, shape and orientation can be readily captured by a digital tactile sensor.

Though a digital tactile sensor is superior to its analog counterpart, the grid-like arrangement of tactels in a digital sensor causes a "parallel path" problem, as illustrated in Figure 2.4. Assume that only cross-switches $(i+1, j)$, $(i+1, j+1)$ and $(i, j+1)$ are closed. When a reference signal is applied to row i, it will also appear at the output of column j due to the existence of a parallel path made up of cross-switches $(i+1, j)$, $(i+1, j+1)$ and $(i, j+1)$. Hence, cross-switch (i, j) will be mistakenly recorded as "closed".

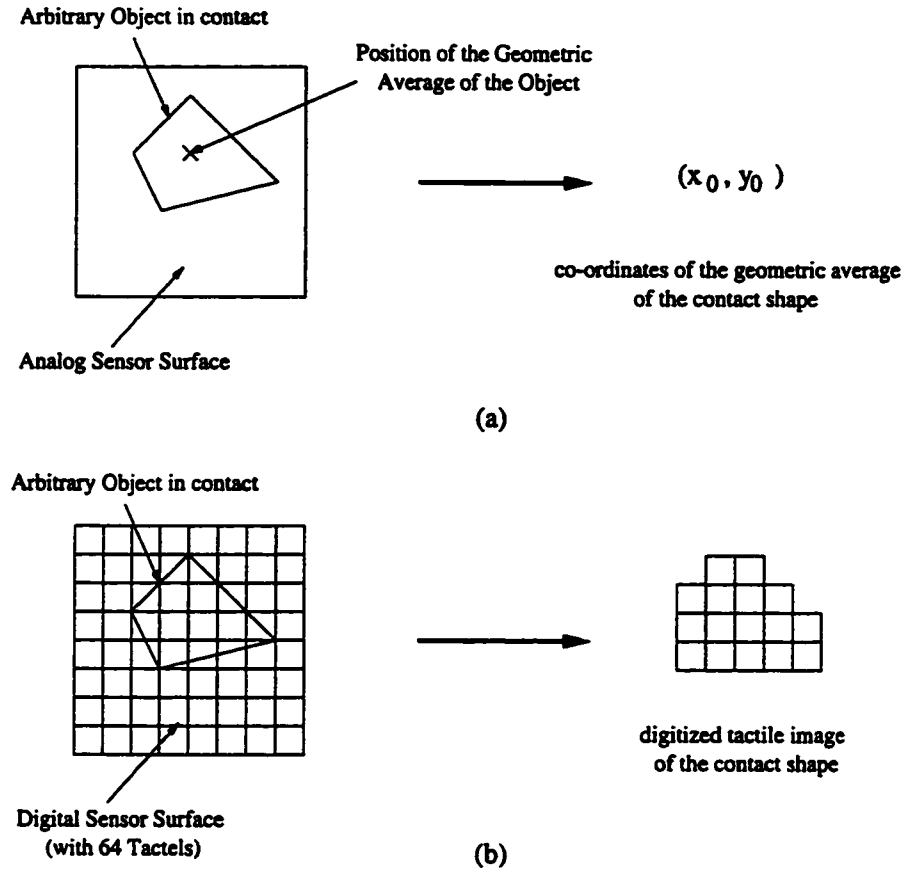

Figure 2.3: (a) Sensor Output of an Arbitrary Object from an Analog Tactile Sensor. (b) Sensor Output of the Same Object from an Digital Tactile Sensor.

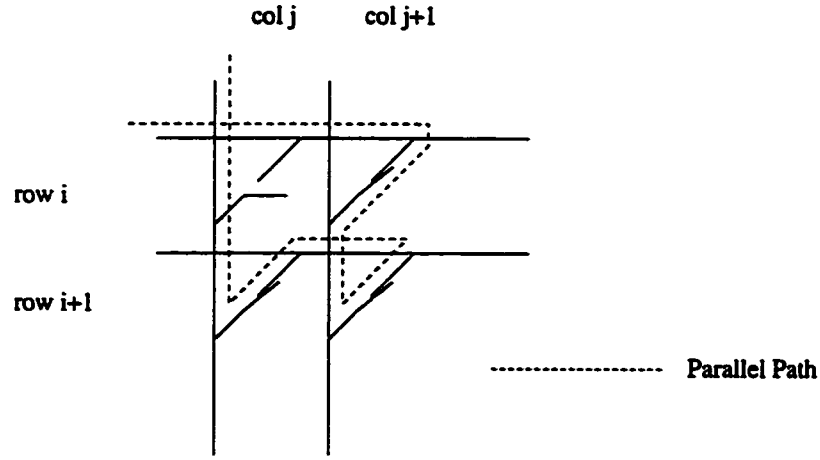

Figure 2.4: Possible Parallel Path in a Digital Tactile Sensor

Sensor Quality	Requirement
Sensor Surface	Should be both compliant and durable.
Spatial Resolution	Should be $1 - 2mm$.
Number of Sensing Elements	Should be $50 - 200$.
Minimum Sensitivity	Should be able to detect as little as $5g$, or ideally $1g$.
Sensor Output	Must be stable, repeatable and without hysteresis.
Output Response	Must be monotonic but not necessarily linear.
Sampling Frequency	Should be higher than $100Hz$.
Dynamic Range	Should be $1000 : 1$.

Table 2.1: Suggested Tactile Sensor Requirements

2.3 Typical Characteristics of Tactile Sensors

A survey done by L. D. Harmon [16] suggests that no matter what form of transduction is used, a set of tactile sensor requirements is desirable. Table 2.1 gives a summary of these requirements. Though the survey was done in the 1980's, it is still widely adopted for new tactile sensor designs.

Chapter 3

Design of The Hybrid Tactile Sensors and Their Modeling

Strictly speaking, this research exploits the capability of a one-dimensional sensor. The prototypes are called hybrid touch sensors that resulted from the combination of the analog resistive and the array touch sensing technologies. Based on various materials as well as structural and geometrical arrangements, four different sensor designs and their analytical models are presented in this chapter.

3.1 Model One: Pairs of Conductive Rubber Strips (CRS-CRS)

The first model is shown in Figure 3.1. Similar to a typical analog resistive sensor, there are two conductive sheets, one on top of the other. These sheets are made of conductive rubber, a form of elastomer doped with a conductive material. By using materials of different conductivity and/or controlling the amount of conductive materials in the manufacturing process, one can produce conductive rubbers with different conductivities. In the model, each conductive rubber sheet is divided into multiple columns or strips which are parallel to each other. Each strip on the top sheet is aligned to a corresponding strip on the bottom sheet. Effectively, there is a one dimensional array of analog resistive sensing elements, each behaving in a similar fashion to the analog touch sensor described in Section 2.1. During operation, a reference voltage is applied at one end of a strip on the top sheet and output is measured at the end of the corresponding strip on the bottom sheet. This process is done on each pair of strips in turn to complete a sampling cycle. As a result, the sensor measures the "average" position of contact along each strip and is able to detect contacts that occur along different columns. Since the sensor has a *Conductive Rubber Strip* on *Conductive*

Rubber Strip structure, it is called a *CRS-CRS* sensor.

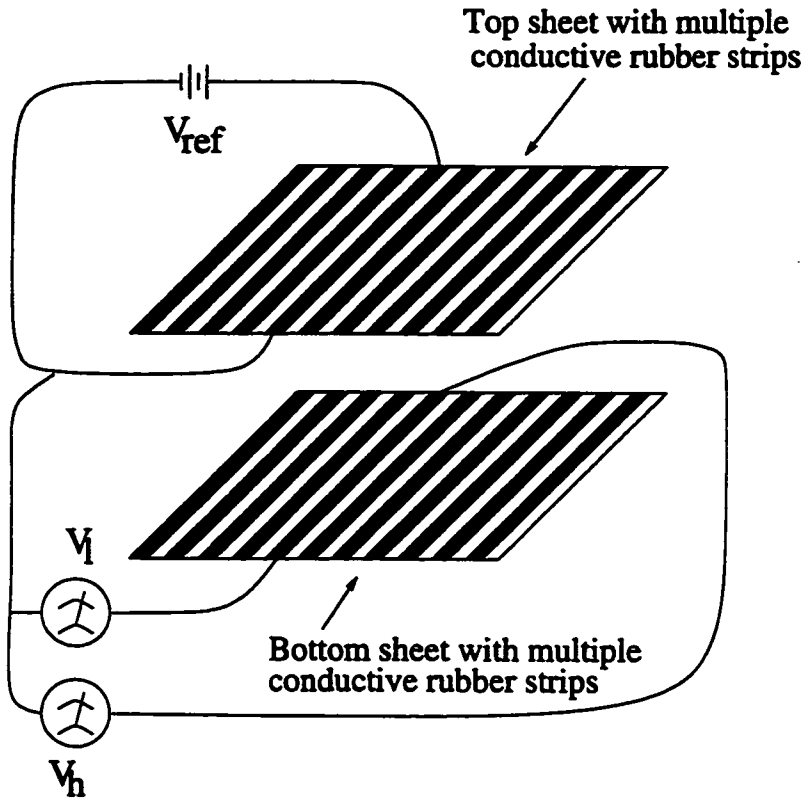

Figure 3.1: A CRS-CRS Hybrid Tactile Sensor Model

The equivalent of one pair of the sensor strips in Figure 3.1 is shown in Figure 3.2, together with its circuit diagram. The two sheets are assumed to have an identical conductivity. It is also assumed that the object contacts the sensor strip continuously so that only two parameters are required to describe the contact: the lower coordinate of the contact area (l) and the width of the contact area (w). Let L be the total length of a rubber strip in a sensing element, ρ be its linear resistivity and V_{ref} be the reference voltage. The measured voltages, V_h (output voltage at upper measuring point) and V_l (output voltage at lower measuring point) are given by:

$$\begin{aligned} V_h &= \frac{l\rho + \frac{w\rho}{2}}{L\rho - w\rho - l\rho + \frac{w\rho}{2} + l\rho} V_{ref} \\ &= \frac{l + w/2}{L - w/2} V_{ref} \end{aligned} \tag{3.1}$$

$$V_l = \frac{l\rho}{L\rho - w\rho - l\rho + \frac{w\rho}{2} + l\rho} V_{ref}$$

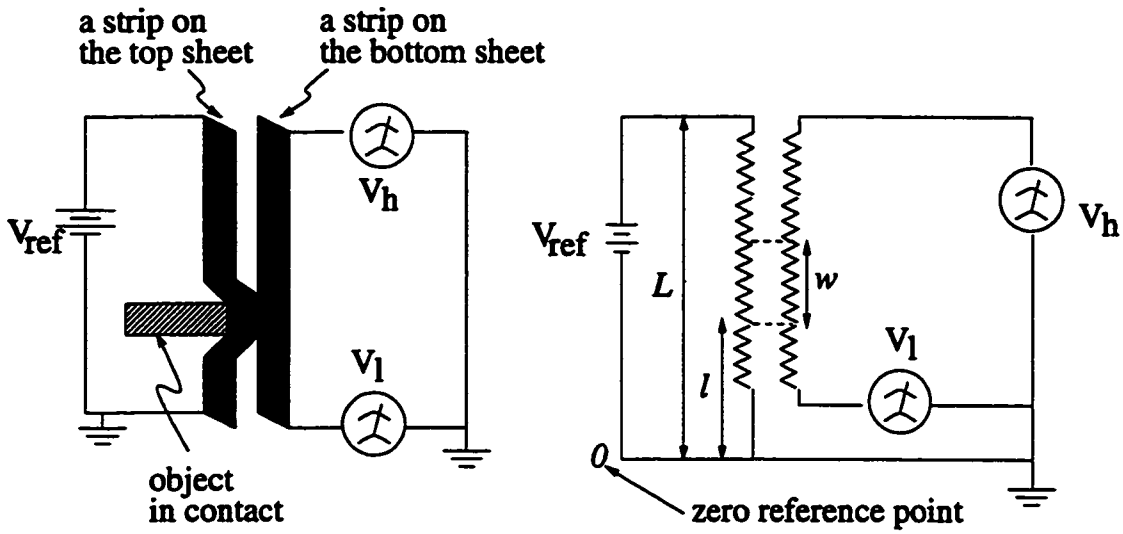

Figure 3.2: Equivalent Circuit of a Pair of Rubber Strips in Contact with an Object at Position l with a Width w

$$= \frac{l}{L - w/2} V_{ref} \tag{3.2}$$

Two quantities, k_h and k_l are further defined as follows:

$$k_h = \frac{V_h}{V_{ref}} = \frac{l + w/2}{L - w/2} \tag{3.3}$$

$$k_l = \frac{V_l}{V_{ref}} = \frac{l}{L - w/2} \tag{3.4}$$

Figure 3.3 and Figure 3.4 show the graphs of k_h and k_l (as functions of l and w) respectively. Since the quantities, L, l and w are bound by the physical dimensions of the hybrid sensor, the following constraints hold:

$$l \leq L, \qquad w \leq L \qquad \text{and} \qquad l + w \leq L$$

Since the sensor is discretized in the horizontal direction, it is a hybrid between a purely digital and a purely analog sensor. With n pairs of strips, if both V_h and V_l are measured,

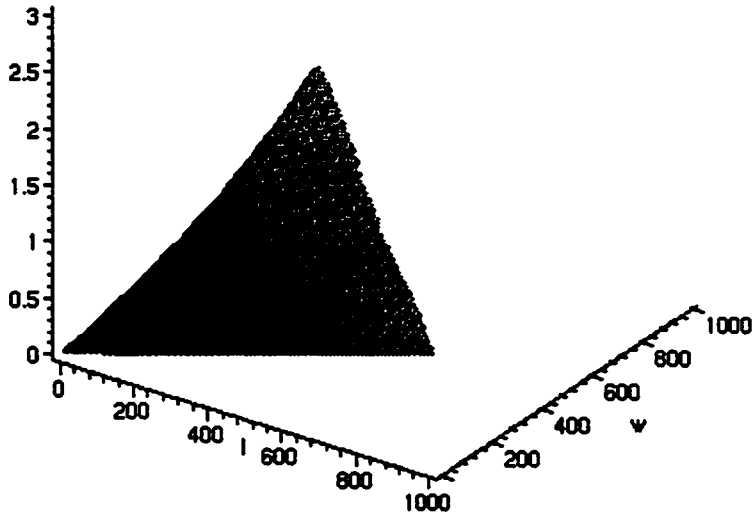

Figure 3.3: k_h as a function of l and w.

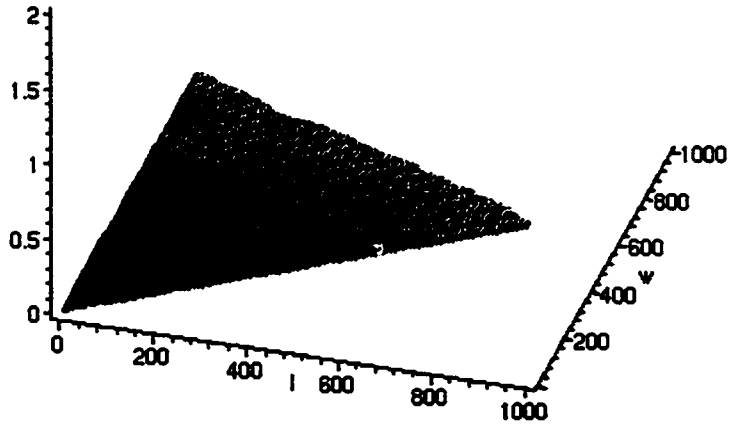

Figure 3.4: k_l as a function of l and w.

each sampling produces $2n$ data. It is defined as *double-measurement*. If only V_h or V_l is measured during a sampling cycle, only n data are available. It is defined as *single-measurement*. Two algorithms are derived to reconstruct the contact shape according to the output data set.

Each sensor required two connectors for V_{ref} and common ground. Each sensing element requires contacts for V_h and V_l. If there are n sensing elements in this type of sensor and if double-measurement is done, n connectors will be required for each V_h and V_l. Hence $2n+2$ connectors are required. If single-measurement is used, n connectors are needed for either V_h or V_l. So only $n+2$ connectors will be sufficient.

According to the definitions of k_h and k_l, the resistivities of the two rubber strips of a basic sensing element must be identical. In practice, such requirement can be relaxed. As long as their resistivities are known and linear along the length of each strip, then calibration can always be done. It should be noted that the definitions of k_h and k_l become:

$$k'_h = \frac{V'_h}{V_{ref}} = \frac{\rho_0 l + \alpha w}{\rho_0(L-l-w) + \alpha w + \rho_0 l} \tag{3.5}$$

$$k'_l = \frac{V'_l}{V_{ref}} = \frac{\rho_0 l}{\rho_0(L-l-w) + \alpha w + \rho_0 l} \tag{3.6}$$

where ρ_0 = resistivity of the energized rubber strip

ρ_1 = resistivity of the voltage measurement strip

$\alpha = \frac{\rho_0 \rho_1}{\rho_0 + \rho_1}$

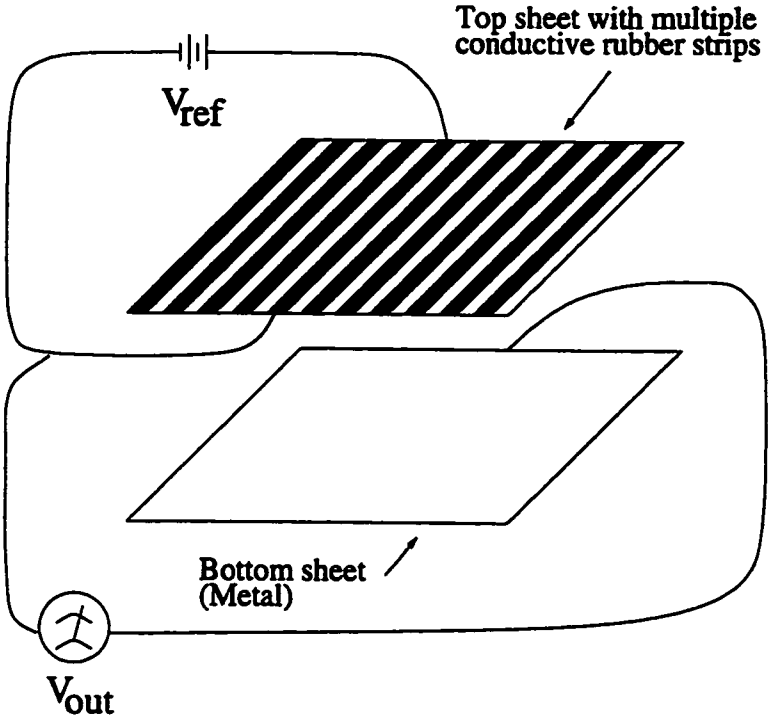

Figure 3.5: A CRS-M Hybrid Tactile Sensor Model

3.2 Model Two: Conductive Rubber Strips on Top of Metal Sheet (CRS-M)

The second model (see Figure 3.5) is a variation of the first configuration described in Section 3.1. There are also two sheets of conductive materials, one on top of the other. However, the bottom sheet is made of metal instead of conductive rubber. Similar energizing and measuring sequence is used. The parameters l and w are as defined in Section 3.1. As the bottom sheet is assumed to be a perfect conductor, the length of contact w of the sensor strip is practically a short circuit. V_h and V_l are virtually the same. Therefore only single-measurement (a set of n measurements on V_{out}) can be obtained in a sampling cycle. Since the sensor has a *Conductive Rubber Strip* on *Metal Sheet* structure, it is called a *CRS-M* sensor.

The equivalent circuit of one of the sensor strips against the metal sheet of Figure 3.5 is shown in Figure 3.6. As the length of contact w of the sensor strip is practically a short circuit, the measured voltage is given by:

$$V_{out} = \frac{l\rho}{(L-w-l)\rho + l\rho} V_{ref}$$

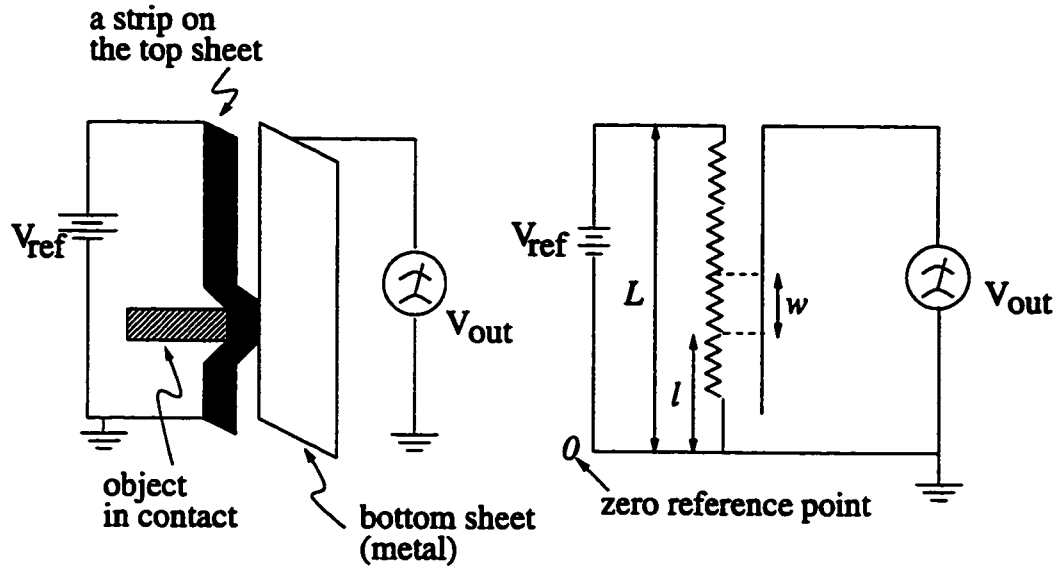

Figure 3.6: Equivalent Circuit of a Rubber Strip in Contact with an Object at Position l with a Width w against a Metal Bottom Sheet

$$= \frac{l}{L-w} V_{ref} \tag{3.7}$$

where L is the total length and ρ is the resistivity of the sensor strip respectively. The quantity, k is further defined as follows:

$$k = \frac{V_{out}}{V_{ref}} = \frac{l}{L-w} \tag{3.8}$$

Figure 3.7 shows the graph of k as functions of l and w. This sensor requires $2n+2$ connectors for n sensing elements. The resistivity of individual elastomer strip is not critical. However, it must be linear along the length of strip.

3.3 Model Three: Conductive Rubber Strips on Top of a Conductive Rubber Plane (CRS-CRP)

The third model (see Figure 3.8) is similar to the second model described in Section 3.2. The only difference is that the metal sheet at the bottom is replaced by a uniform conductive rubber sheet. In addition, it is assumed that the resistivity of the uniform conductive rubber

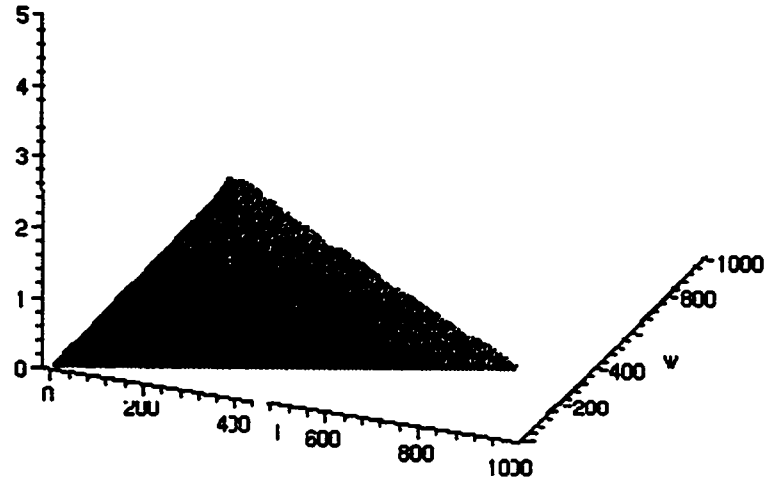

Figure 3.7: k as a function of l and w.

(ρ_{sheet}) is much higher tl an that of the top sheet (ρ_{strip}). Since the sensor has a *Conductive Rubber Strip* on *Uniform Conductive Rubber Sheet* structure, it is called a *CRS-CRP* sensor.

In each sampling cycle, reference voltage is applied to each strip of the top sheet in turn. Output voltages V_h and/or V_l are measured from the bottom sheet. In general, either single- or double-measurement can be taken from the sensor.

The equivalent circuit of one of the sensor strips against the uniform conductive rubber sheet of Figure 3.8 is shown in Figure 3.9. Unfortunately, the coupling resistance varies with different l and w. Hence V_l and V_h cannot be precisely expressed as simple mathematical functions of l and w. Only empirical data can be collected from different inputs of l and w. As a result, this setup is not suitable for practical use.

3.4 Model Four: Cylindrical Variant CRS-M (Cyl-CRS-M)

The fourth model is a geometrical variant of model two described in Section 3.2, so it is called a *Cyl-CRS-M* sensor. Instead of a planar geometry, the sensor is built into a cylindrical shape and resembles a robotic finger. The parameters and equations derived in Section 3.2 are also applicable to this sensor. Due to its relatively small curvature in

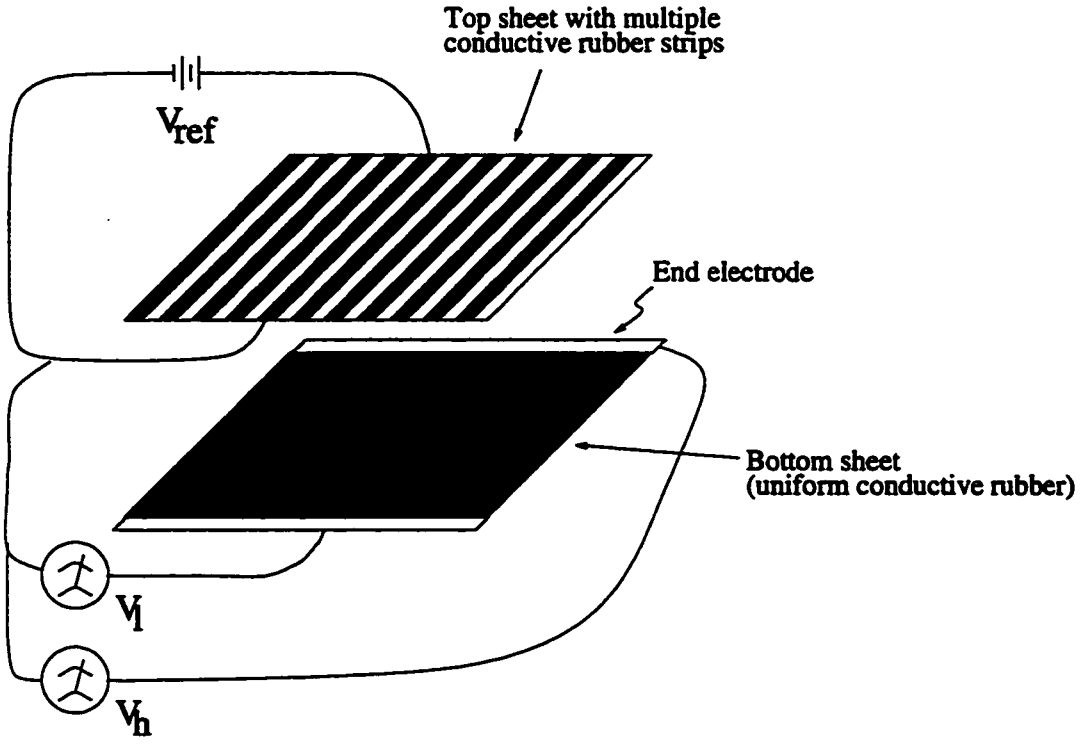

Figure 3.8: A CRS-CRP Hybrid Tactile Sensor Model

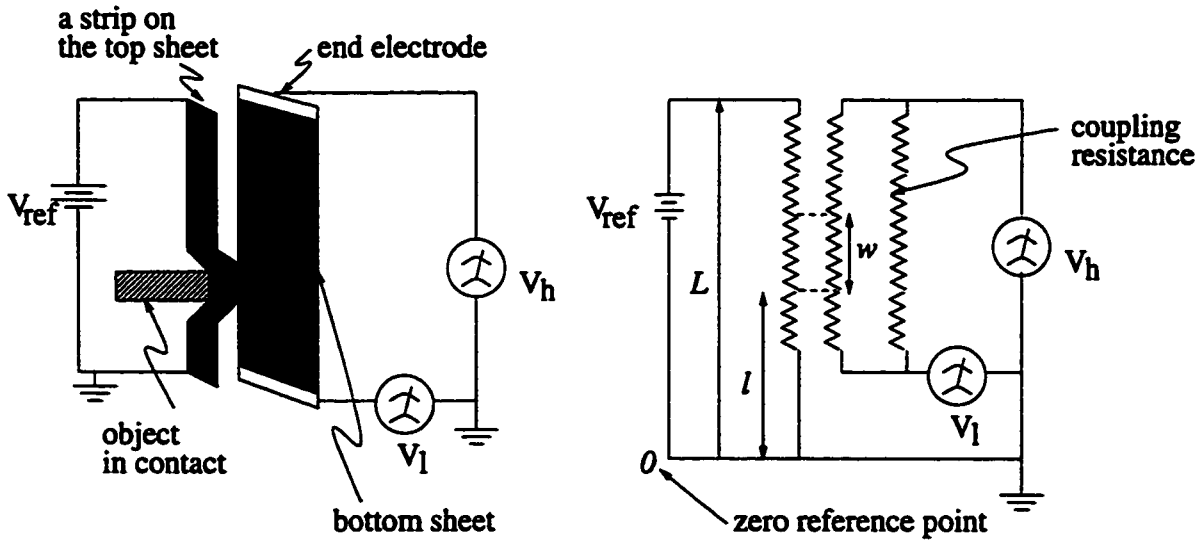

Figure 3.9: Equivalent Circuit of a Rubber Strip in Contact with an Object at Position l with a Width w against a Uniform Conductive Rubber Sheet

sensing surface, only point and limited linear contacts can be practically detected. Figure 3.10 illustrates such limitation. It can be seen from the cross-section view that only a few sensing strips can be in touch with the object. The output provided by the sensor is sufficient to determine the contact points and hence the portion of the object's edge in contact. However, no meaningful planar information about the object can be reconstructed.

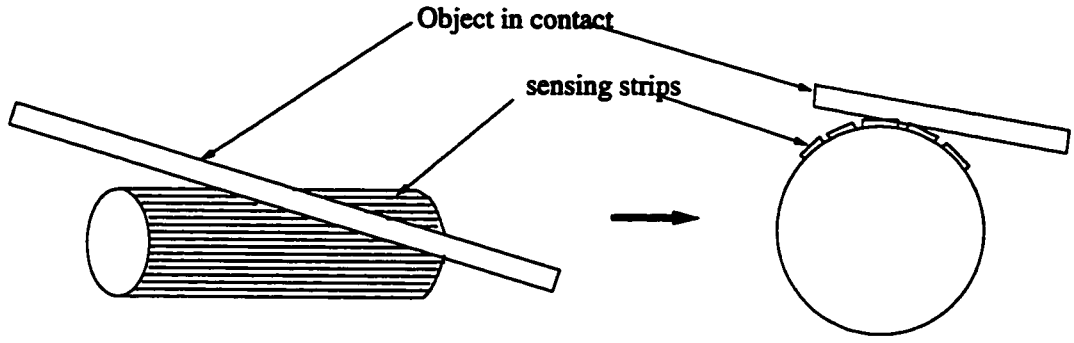

Figure 3.10: Using a Cyl-CRS-M Hybrid Tactile Sensor to Detect Point and Line Contacts

Chapter 4

Shape Interpretation

The outputs from the sensor models discussed in Chapter 3 provide abstracted geometric information about the contact shape. In order to recover geometric information, two shape interpretation algorithms, *Vertex Reconstruction* and *Profile Reconstruction* are derived according to the approach of output measurement. When applying either of these shape interpretation algorithms, some assumptions and limitations have to be considered.

4.1 Pseudo-Centers of Contact Shape

Figure 4.1 shows an arbitrary object on a hybrid tactile sensor. The quantity, $l + w/2$ from each strip is defined as the *geometric center* of contact. By joining all the geometric centers of contact, a *geometric signature* of the shape is obtained. Based on the values of k_h, k_l and k, three types of *pseudo-centers* of contact are defined.

4.1.1 k_h-Pseudo-Center

The quantity, $k_h L$ is defined as the *k_h-pseudo-center* of contact. Based on Equation (3.3), the k_h-pseudo-center differs from the geometric center by a factor of $\frac{L}{L - w/2}$, as shown in Equation (4.1). A *k_h-pseudo-signature* is obtained by joining all the k_h-pseudo-centers of contact.

$$k_h L = (l + \frac{w}{2}) \times \frac{L}{L - \frac{w}{2}} \tag{4.1}$$

It is noted that $\frac{L}{L - w/2} \geq 1$. Hence $k_h L$ is always above the geometric center in the reference frame of the sensor. In terms of transitional points, the profile of the pseudo

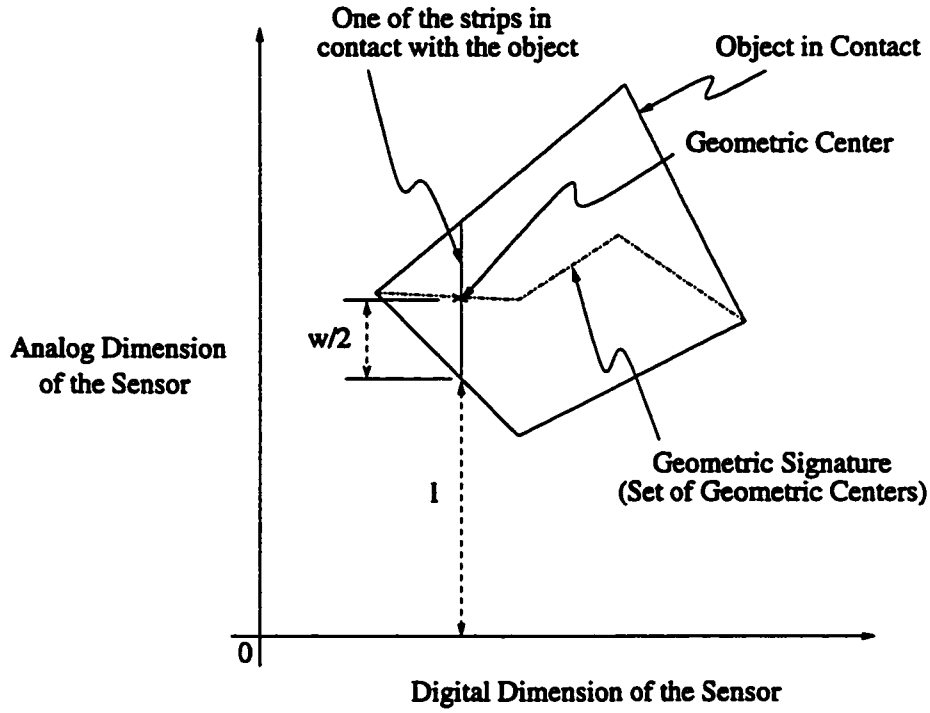

Figure 4.1: An Arbitrary Object on a Hybrid Tactile Sensor

signature follows that of the geometric signature closely. Figure 4.2 shows how the profile of a k_h-pseudo-signature changes as the contact shape moves across the sensor surface.

4.1.2 k_l-Pseudo-Center

The quantity, $k_l L$ is defined as the *k_l-pseudo-center* of contact. A *k_l-pseudo-signature* is obtained by joining all the k_l-pseudo-centers of contact. Equation (4.2) is readily obtained from the definition of k_l in Equation (3.4). Since $0 \leq k_l \leq 1$, the k_l-pseudo-center is always below the geometric center. It can be noted that as k_l approaches 0, $k_l L$ approaches l. For a practical range of w, the value of k_l is small when the contact shape is in the lower region of the sensor reference frame. Hence the profile of the k_l-pseudo-signature approaches that of the lower half of the contact shape. On the other hand, larger values of k_l occurs when the contact shape is in the upper region of the sensor. In terms of transitional points, the profile of the k_l-pseudo-signature closely resembles that of the geometric signature. Figure 4.3 illustrates how the profile of a k_l-pseudo-signature changes with the location of the contact shape on the sensor surface.

$$k_l L = l + k_l \frac{w}{2} \tag{4.2}$$

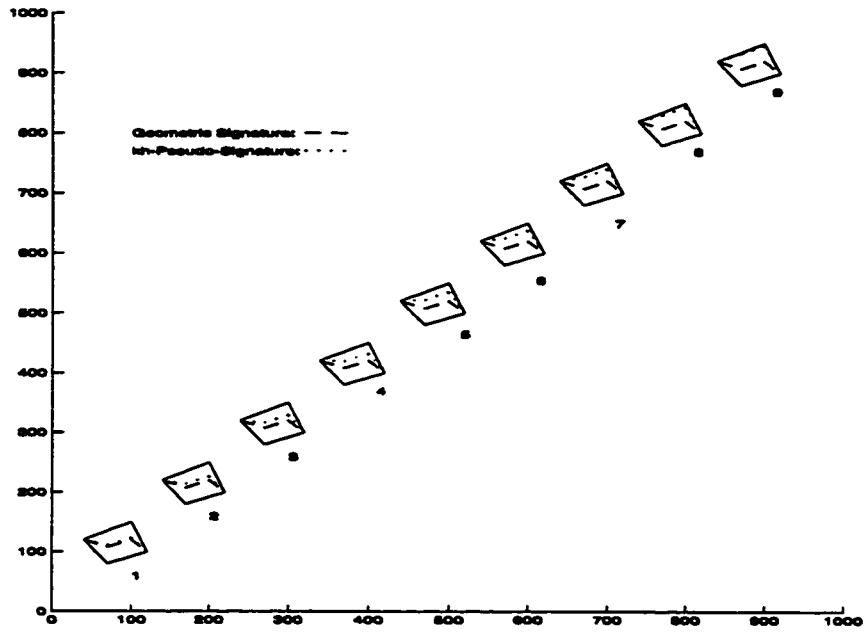

Figure 4.2: The k_h-Pseudo-Signatures of An Arbitrary Four-sided Polygon at Different Location on a Hybrid Tactile Sensor.

4.1.3 k-Pseudo-Center

The quantity, kL is defined as the *k-pseudo-center* of contact in the case of CRS-M model. A *k-pseudo-signature* is obtained by joining all the k-pseudo-centers of contact. Based on Equation (3.8), Equation (4.3) expresses kL in terms of l and w. It can be noted that the k-pseudo-center is above the geometric center when $k > \frac{1}{2}$, and vice versa when $k < \frac{1}{2}$. Since $0 \leq k \leq 1$, as k approaches 0, k_L approaches l. For a practical range of w, the values of k are small when the contact shape is in the lower region of the sensor reference frame. Hence the profile of the k-pseudo-signature approaches that of the lower half of the contact shape. On the contrary, when the contact shape is in the upper region of the sensor, larger values of k occur. The profile of the k-pseudo-signature tends to follow that of the upper half of the contact shape. When the contact shape is in the middle region of the sensor, the values of k are closer to $\frac{1}{2}$. In terms of transitional points, the profile of the k-pseudo-signature closely resembles that of the geometric signature. The changes in the profile of a k-pseudo-signature with respect to its location on the sensor is shown in Figure 4.4.

$$kL = l + kw \tag{4.3}$$

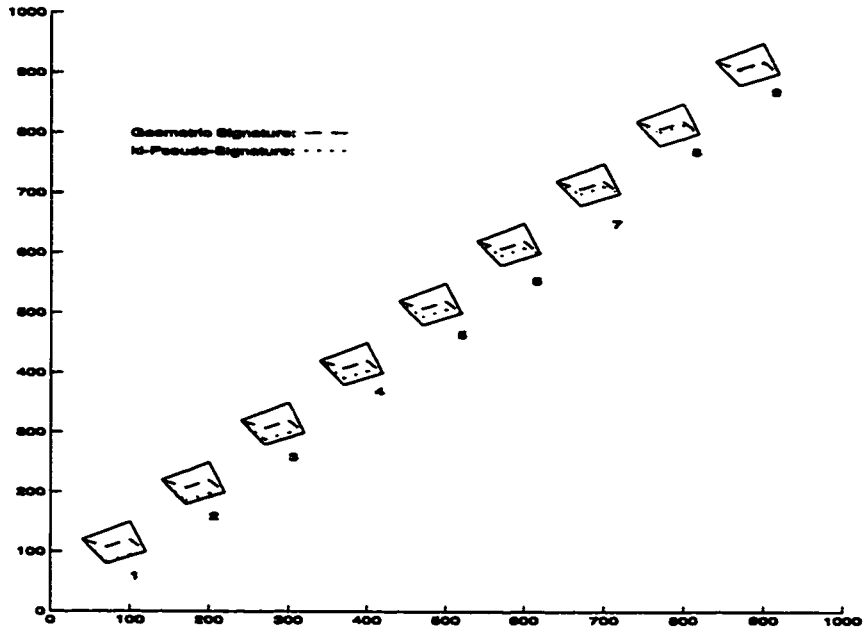

Figure 4.3: The k_l-Pseudo-Signatures of An Arbitrary Four-sided Polygon at Different Location on a Hybrid Tactile Sensor.

4.2 Vertex Reconstruction

Vertex Reconstruction is used when single-measurement is taken. It accepts an array of either k_h, k_l or k to recover the vertices of the corresponding contact shape. Before discussing how the algorithm works, a number of assumptions and limitations must be considered.

4.2.1 Assumptions on Shapes

First, it is assumed that the shape in contact must be polygonal so that it can be described by a set of vertices. Second, the polygonal shape must be strictly convex. Without such assumptions, a number of ambiguities arise. Figure 4.5 illustrates three possible cases. It can be noted that both shape X and Y in Figure 4.5(a) produce the same pseudo-signature. Whereas in Figure 4.5(b), the concavity of the shape Z makes it impossible to use just variables l and w to abstract the geometric information on the shaded portion of the shape. It is impossible to regenerate the contact shape uniquely from a given pseudo signature unless the convexity constraint is satisfied.

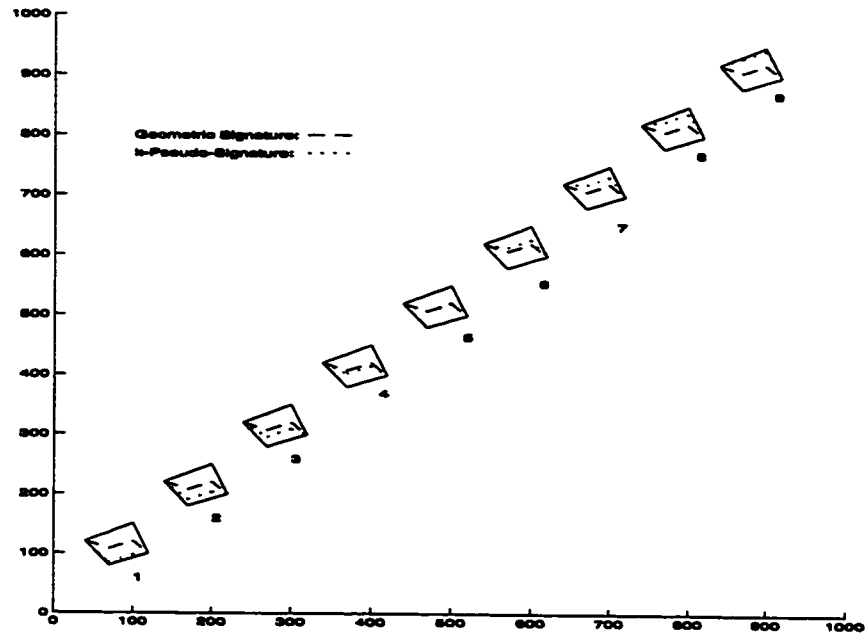

Figure 4.4: The k-Pseudo-Signatures of An Arbitrary Four-sided Polygon at Different Location on a Hybrid Tactile Sensor.

4.2.2 Characteristics of a Pseudo Signature

For simplicity, all different types of pseudo-signatures discussed in the Section 4.1 are called "pseudo-signature". Moreover, the terms "signature" and "pseudo-signature" are used interchangeably. It is important to make several observations on the characteristics of a pseudo-signature. First, the pseudo-centers of contact form a set of $N-1$ piece-wise continuous segments for an N-sided polygon if no two vertices share the same x coordinate. Figure 4.6 shows an example of a four-sided polygon. Excluding the two end vertices, there are two interior vertices. The whole polygon can be divided into three vertical sections by drawing a vertical line at each interior vertex. Since a pseudo-signature is a function of l and w, and it is piece-wise continuous in each section. At each interior vertex, either l or w changes to another linear function and discontinuity occurs. This discontinuity is reflected as transitional point on the pseudo-signature. In general, this is true in the case of a N-sided polygon. Excluding the two end vertices, there are $N-2$ interior vertices. The polygon can be divided into $N-1$ vertical sections by drawing a vertical line at each interior vertex. Hence there are $N-1$ piece-wise continuous segments in the corresponding pseudo-signature. However, when two vertices share the same x coordinate, a N-sided

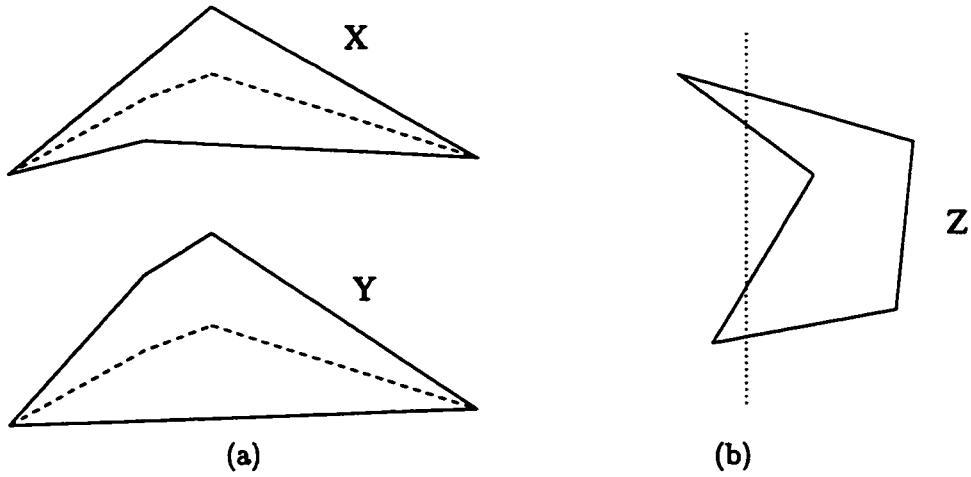

Figure 4.5: Ambiguity due to concavity (a) multiple interpretations (two polygons satisfying the same set of k_h (dashed lines are $k_h \times L$)) (b) under-determinedness (four variables required to define the two contact regions)

polygon produces a pseudo-signature with $N-2$ segments. This situation is considered as singular and one cannot apply the algorithm for shape recovery.

Second, the x coordinates of the vertices are found by detecting where line segments intersect. Along the pseudo-signature from left to right, at the intersection of two signature segments, there is a vertex above the intersection if the slope of the right line segment decreases. Otherwise, the vertex is below the intersection.

Finally, the end vertices can be determined directly from the pseudo-signature by setting $w = 0$ for these two vertices. The only unknowns of the system are the y coordinates of the interior vertices. Since equations (3.3), (3.4) and (3.8) hold for the corresponding sensor columns of these interior vertices, the polygonal shape can be solved exactly by setting up a linear system of $N-2$ equations with $N-2$ unknowns.

4.2.3 Reliability of a Pseudo-Signature.

As mentioned in Section 4.1, there are three types of pseudo-signatures based on k_h, k_l and k respectively. Though they have transitional points corresponding to the vertices of the polygonal shape, the accuracy in detecting them from the pseudo-signature determines how accurate the vertices can be recovered. In general, there is a discontinuity in the first-derivatives when two signature segments meet, except for a few configurations. With discontinuity in the first-derivatives at the intersection of two signature segments, it is relatively easy to locate the transitional point by detecting a prominent change in the gradient from one signature segment to another. Though there are a few configurations

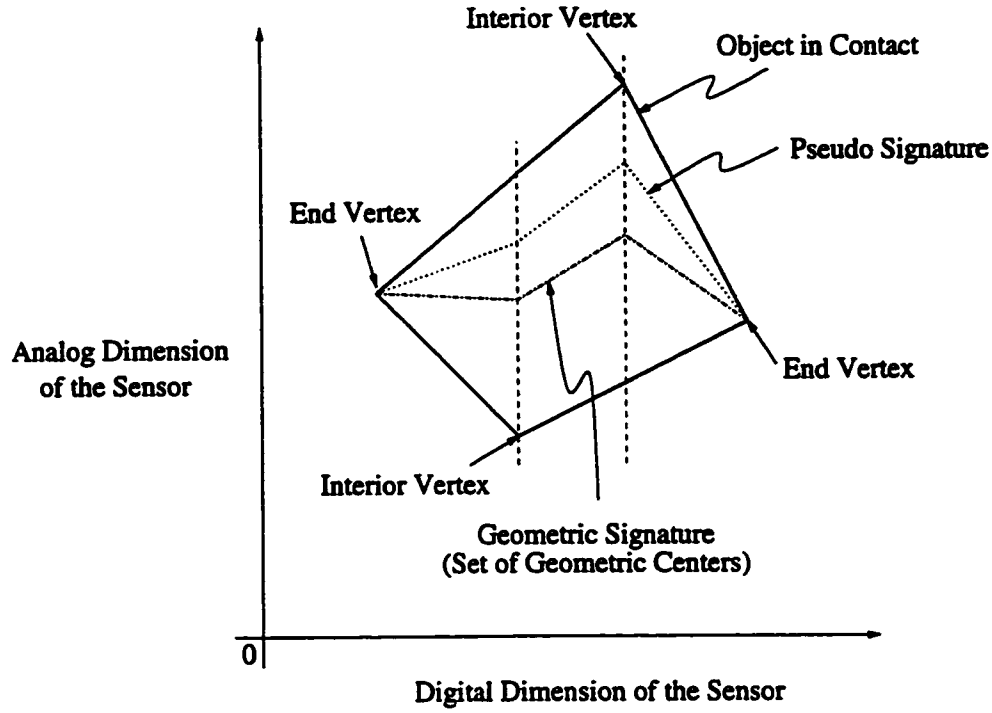

Figure 4.6: Geometric Signature and Pseudo-Signature of an Arbitrary Four-sided Polygon

that such discontinuity vanishes, they exist only when precise conditions are met. These conditions are illustrated with reference to Figure 4.7 and Figure 4.8, which depict all the possible circumstances.

In general, the following equations hold:

$$l_i = m_i x + c_i \qquad \text{for } i = 1, 2, \ldots, 6$$

where m_i and c_i are the slope and intercept of the corresponding linear equation for l_i $(i = 1, 2, \ldots, 6)$. Then the following equations also hold:

$$w_1 = l_2 - l_1 = (m_2 - m_1)x + c_2 - c_1 \tag{4.4}$$

$$w_2 = l_3 - l_1 = (m_3 - m_1)x + c_3 - c_1 \tag{4.5}$$

$$w_3 = l_6 - l_4 = (m_6 - m_4)x + c_6 - c_4 \tag{4.6}$$

$$w_4 = l_6 - l_5 = (m_6 - m_5)x + c_6 - c_5 \tag{4.7}$$

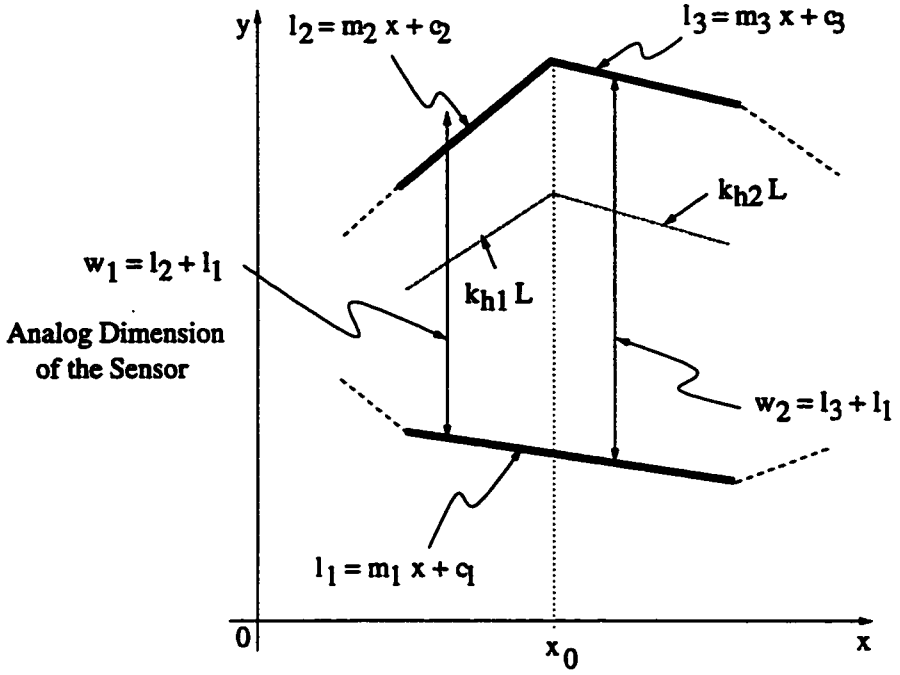

Figure 4.7: Signature Transition from One Section to Another with a Vertex at the Top

1. In case of k_h, the signature segments are given by

$$k_{h1}L = \frac{l_1 + \frac{w_1}{2}}{L - \frac{w_1}{2}} \times L = \frac{L\,(m_1 x + c_1 + m_4 x + c_4)}{2L - m_2 x - c_2 + m_1 x + c_1} \tag{4.8}$$

$$k_{h2}L = \frac{l_1 + \frac{w_2}{2}}{L - \frac{w_2}{2}} \times L = \frac{L\,(m_1 x + c_1 + m_3 x + c_3)}{2L - m_3 x - c_3 + m_1 x + c_1} \tag{4.9}$$

$$k_{h3}L = \frac{l_4 + \frac{w_3}{2}}{L - \frac{w_3}{2}} \times L = \frac{L\,(m_4 x + c_4 + m_6 x + c_6)}{2L - m_6 x - c_6 + m_4 x + c_4} \tag{4.10}$$

$$k_{h4}L = \frac{l_5 + \frac{w_4}{2}}{L - \frac{w_4}{2}} \times L = \frac{L\,(m_5 x + c_5 + m_6 x + c_6)}{2L - m_6 x - c_6 + m_5 x + c_5} \tag{4.11}$$

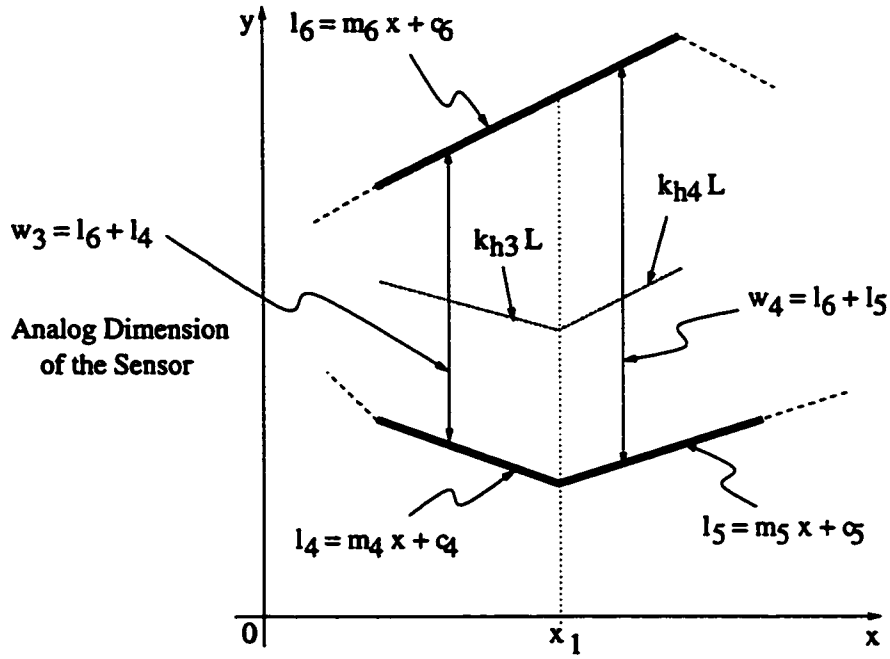

Figure 4.8: Signature Transition from One Section to Another with a Vertex at the Bottom

The gradients of the equations (4.8) to (4.11) are given by

$$\frac{d(k_{h1}L)}{dx} = \frac{L(m_1+m_2)}{2L - m_2x - c_2 + m_1x + c_1} - \frac{L(m_1x + c_1 + m_2x + c_2)(m_1 - m_2)}{(2L - m_2x - c_2 + m_1x + c_1)^2} \quad (4.12)$$

$$\frac{d(k_{h2}L)}{dx} = \frac{L(m_1+m_3)}{2L - m_3x - c_3 + m_1x + c_1} - \frac{L(m_1x + c_1 + m_3x + c_3)(m_1 - m_3)}{(2L - m_3x - c_3 + m_1x + c_1)^2} \quad (4.13)$$

$$\frac{d(k_{h3}L)}{dx} = \frac{L(m_4+m_6)}{2L - m_6x - c_6 + m_4x + c_4} - \frac{L(m_4x + c_4 + m_6x + c_6)(m_4 - m_6)}{(2L - m_6x - c_6 + m_4x + c_4)^2} \quad (4.14)$$

$$\frac{d(k_{h4}L)}{dx} = \frac{L(m_5+m_6)}{2L - m_6x - c_6 + m_5x + c_5} - \frac{L(m_5x + c_5 + m_6x + c_6)(m_5 - m_6)}{(2L - m_6x - c_6 + m_5x + c_5)^2} \quad (4.15)$$

Assume that x_0 and x_1 are the x-coordinates of the transitional points in Figure 4.7 and Figure 4.8 respectively. The best scenarios are $k_{h1}L$ and $k_{h2}L$ having their first-order derivatives discontinuous at $x = x_0$, or those of $k_{h3}L$ and $k_{h4}L$ being discontinuous at $x = x_1$. With these characteristic discontinuities, relatively simple gradient change detection techniques can be applied to obtained the transitional points from a signature. Unfortunately, there exist some combinations of m_1, m_2, m_3, c_1, c_2, c_3 and L that such discontinuities vanish. These combinations are

(a) $c2 = \frac{m_1L + m_2c_1 + m_2L}{m_1}$ and $c3 = \frac{m_1L + m_3L + m_3c_1}{m_1}$.
(b) $c4 = \frac{m_4c_6 - m_4L - m_6L}{m_6}$ and $c5 = \frac{m_5c_6 - m_5L - m_6L}{m_6}$.

2. In case of k_l, the signature segments are given by

$$k_{l1}L = \frac{l_1}{L - \frac{w_1}{2}} \times L = \frac{2L\,(m_1x + c_1)}{2L - m_2x - c_2 + m_1x + c_1} \tag{4.16}$$

$$k_{l2}L = \frac{l_1}{L - \frac{w_2}{2}} \times L = \frac{2L\,(m_1x + c_1)}{2L - m_3x - c_3 + m_1x + c_1} \tag{4.17}$$

$$k_{l3}L = \frac{l_4}{L - \frac{w_3}{2}} \times L = \frac{2L\,(m_4x + c_4)}{2L - m_6x - c_6 + m_4x + c_4} \tag{4.18}$$

$$k_{l4}L = \frac{l_5}{L - \frac{w_4}{2}} \times L = \frac{2L\,(m_5x + c_5)}{2L - m_6x - c_6 + m_5x + c_5} \tag{4.19}$$

The derivatives of the equations (4.16) to (4.19) are given by

$$\frac{d(k_{l1}L)}{dx} = \frac{2Lm_1}{2L - m_2x - c_2 + m_1x + c_1} - \frac{2L\,(m_1x + c_1)\,(m_1x - m_2)}{(2L - m_2x - c_2 + m_1x + c_1)^2} \tag{4.20}$$

$$\frac{d(k_{l2}L)}{dx} = \frac{2Lm_1}{2L - m_3x - c_3 + m_1x + c_1} - \frac{2L\,(m_1x + c_1)\,(m_1 - m_3)}{(2L - m_3x - c_3 + m_1x + c_1)^2} \tag{4.21}$$

$$\frac{d(k_{l3}L)}{dx} = \frac{2Lm_4}{2L - m_6x - c_6 + m_4x + c_4} - \frac{2L\,(m_4x + c_4)\,(m_4 - m_6)}{(2L - m_6x - c_6 + m_4x + c_4)^2} \tag{4.22}$$

$$\frac{d(k_{l4}L)}{dx} = \frac{2Lm_5}{2L - m_6x - c_6 + m_5x + c_5} - \frac{2L\,(m_5x + c_5)\,(m_5 - m_6)}{(2L - m_6x - c_6 + m_5x + c_5)^2} \tag{4.23}$$

Assume that x_0 and x_1 are the x-coordinates of the transitional points in Figure 4.7 and Figure 4.8 respectively. Similar to the case in k_h, the best scenarios are $k_{l1}L$ and $k_{l2}L$ having their first-order derivatives discontinuous at $x = x_0$, or those of $k_{l3}L$ and $k_{l4}L$ being discontinuous at $x = x_1$, which facilitate transitional points detection. However, such discontinuities do not always exist. The following combinations of m_1, m_2, m_3, c_1, c_2, c_3 and L defeat the discontinuities:

(a) $m_1 = 0$ and $c_1 = 0$ simultaneously. Fortunately, this condition is practically impossible since it implies that an entire edge of the polygon is touching the true zero reference.

(b) $c2 = \frac{m_1c_3 - m_3c_1 + m_2c_1}{m_1}$ and $c3 = \frac{2m_1L + m_3c_1}{m_1}$.

(c) $c4 = \frac{m_4(c_6 - 2L)}{m_6}$ and $c5 = \frac{m_5(c_6 - 2L)}{m_6}$.

3. In case of k, the signature segments are given by

$$k_1L = \frac{l_1}{L - w_1} \times L = \frac{L\,(m_1x + c_1)}{L - m_2x - c_2 + m_1x + c_1} \tag{4.24}$$

$$k_2L = \frac{l_1}{L - w_2} \times L = \frac{L\,(m_1x + c_1)}{L - m_3x - c_3 + m_1x + c_1} \tag{4.25}$$

$$k_3L = \frac{l_4}{L - w_3} \times L = \frac{L\,(m_4x + c_4)}{L - m_6x - c_6 + m_4x + c_4} \tag{4.26}$$

$$k_4L = \frac{l_5}{L - w_4} \times L = \frac{L\,(m_5x + c_5)}{L - m_6x - c_6 + m_5x + c_5} \tag{4.27}$$

The derivatives of the equations (4.24) to (4.27) are given by

$$\frac{d(k_1L)}{dx} = \frac{Lm_1}{L - m_2x - c_2 + m_1x + c_1} - \frac{L(m_1x + c_1)(m_1x - m_2)}{(L - m_2x - c_2 + m_1x + c_1)^2} \tag{4.28}$$

$$\frac{d(k_2L)}{dx} = \frac{Lm_1}{L - m_3x - c_3 + m_1x + c_1} - \frac{L(m_1x + c_1)(m_1 - m_3)}{(L - m_3x - c_3 + m_1x + c_1)^2} \tag{4.29}$$

$$\frac{d(k_3L)}{dx} = \frac{Lm_4}{L - m_6x - c_6 + m_4x + c_4} - \frac{L(m_4x + c_4)(m_4 - m_6)}{(L - m_6x - c_6 + m_4x + c_4)^2} \tag{4.30}$$

$$\frac{d(k_4L)}{dx} = \frac{Lm_5}{L - m_6x - c_6 + m_5x + c_5} - \frac{L(m_5x + c_5)(m_5 - m_6)}{(L - m_6x - c_6 + m_5x + c_5)^2} \tag{4.31}$$

Assume that x_0 and x_1 are the x-coordinates of the transitional points in Figure 4.7 and Figure 4.8 respectively. Similar to the cases of k_h and k_l, the best scenarios are k_1L and k_2L having their first-order derivatives discontinuous at $x = x_0$, or those of k_3L and k_4L being discontinuous at $x = x_1$, which facilitate transitional points detection. However, such discontinuities vanish with the following combinations of m_1, m_2, m_3, c_1, c_2, c_3 and L:

(a) $m_1 = 0$ and $c_1 = 0$ simultaneously. Fortunately, this condition is practically impossible as explained in the case of k_l.

(b) $c2 = \frac{m_1c_3 - m_3c_1 + m_2c_1}{m_1}$ and $c3 = \frac{m_1L + m_3c_1}{m_1}$.

(c) $m_6 = 0$ and $c_6 = L$ simultaneously. This condition is practically impossible since it implies that an entire edge of a polygon is touching the upper edge of the sensor.

(d) $c4 = \frac{m_4(c_6 - L)}{m_6}$ and $c5 = \frac{m_5(c_6 - L)}{m_6}$.

In conclusion, no matter what kind of pseudo-signature is used, there are only a few locations and orientations of a polygonal contact shape that produce pseudo-signature whose transitional points are difficult to detect.

4.2.4 Recovering the Vertices

The Vertex Reconstruction algorithm is based on the linearity of the edges of the polygonal shape. Figure 4.9(a) to (c) illustrate how a system of linear equations can be set up to recover the interior vertices. Though an arbitrary hexagon and its k_h-pseudo-signature is used in the illustration, the basic principle is applicable to any polygonal shape and pseudo-signature discussed before. As shown in Figure 4.9(a), the highlighted portion of

the polygon enables the formulation of the following equations:

$$\begin{cases} k_{h2} = \dfrac{y_{l2} + \dfrac{y_2 - y_{l2}}{2}}{L - \dfrac{y_2 - y_{l2}}{2}} \\ \dfrac{y_{l2} - y_1}{x_2 - x_1} = \dfrac{y_3 - y_1}{x_3 - x_1} \end{cases}$$

$$\Rightarrow \quad \frac{1 + k_{h2}}{1 - k_{h2}} y_2 + \frac{x_2 - x_1}{x_3 - x_1} y_3 = \frac{2k_{h2}L}{1 - k_{h2}} - \frac{x_3 - x_2}{x_3 - x_1} y_1 \tag{4.32}$$

For the next portion of the shape as shown in Figure 4.9(b), another set of linear equations is formed by the current pairs of interior vertices:

$$\begin{cases} k_{h3} = \dfrac{y_3 + \dfrac{y_{h3} - y_3}{2}}{L - \dfrac{y_{h3} - y_3}{2}} \\ \dfrac{y_{h3} - y_2}{x_3 - x_2} = \dfrac{y_4 - y_2}{x_4 - x_2} \end{cases}$$

$$\Rightarrow \quad \frac{x_4 - x_3}{x_4 - x_2} y_2 + \frac{1 - k_{h3}}{1 + k_{h3}} y_3 + \frac{x_3 - x_2}{x_4 - x_2} y_4 = \frac{2k_{h3}L}{1 + k_{h3}} \tag{4.33}$$

Similar process continues until all portions of the shape are considered (see Figure 4.9(c)). As a result, the corresponding system of linear equations is obtained as follows:

$$\begin{bmatrix} \frac{1 + k_{h2}}{1 - k_{h2}} & \frac{x_2 - x_1}{x_3 - x_1} & 0 & 0 \\ \frac{x_4 - x_3}{x_4 - x_2} & \frac{1 - k_{h3}}{1 + k_{h3}} & \frac{x_3 - x_2}{x_4 - x_2} & 0 \\ 0 & \frac{x_5 - x_4}{x_5 - x_3} & \frac{1 + k_{h4}}{1 - k_{h4}} & \frac{x_4 - x_3}{x_5 - x_3} \\ 0 & 0 & \frac{x_6 - x_5}{x_6 - x_4} & \frac{1 - k_{h5}}{1 + k_{h5}} \end{bmatrix} \begin{bmatrix} y_2 \\ y_3 \\ y_4 \\ y_5 \end{bmatrix} = \begin{bmatrix} \frac{2k_{h2}L}{1 - k_{h2}} - \frac{x_3 - x_2}{x_3 - x_1} y_1 \\ \frac{2k_{h3}L}{1 + k_{h3}} \\ \frac{2k_{h4}L}{1 - k_{h4}} \\ \frac{2k_{h5}L}{1 + k_{h5}} - \frac{x_5 - x_4}{x_6 - x_4} y_6 \end{bmatrix} \tag{4.34}$$

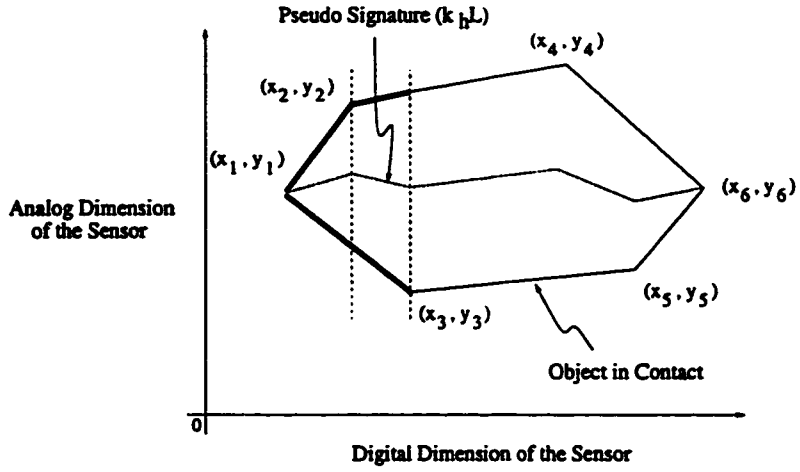

(a)

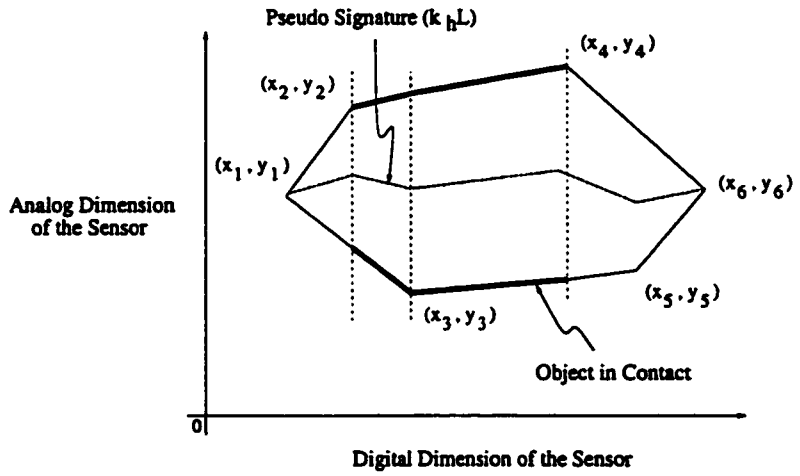

(b)

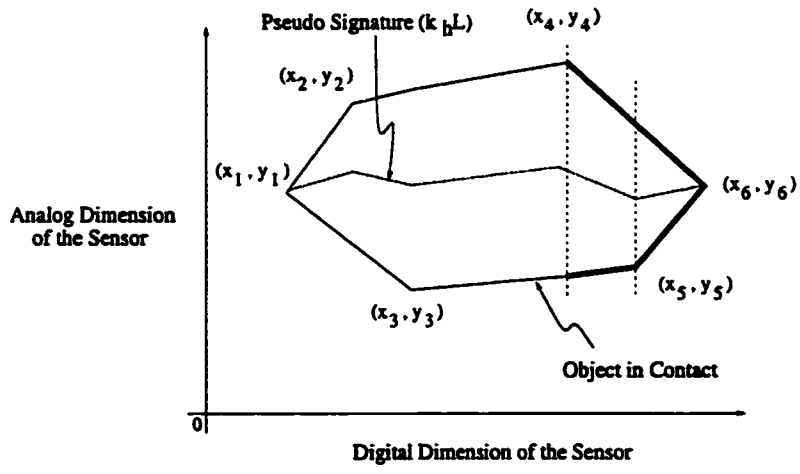

(c)

Figure 4.9: Geometric Signature and Pseudo-Signatures of an Arbitrary Tetragon

As mentioned in Section 4.2.2, the two end vertices of a polygon shape are readily found by setting $w = 0$ in corresponding equation of either k_h, k_l or k, and a system of linear equations is required to solve for the interior vertices of the polygonal shape. In general, a N-sided polygon has a system of $N-2$ linear equations in the following form:

$$\begin{bmatrix} a_{11} & a_{12} & \cdots & a_{1(N-2)} \\ a_{21} & a_{22} & \cdots & a_{2(N-2)} \\ \cdots & \cdots & \cdots & \cdots \\ a_{(N-2)1} & a_{(N-2)2} & \cdots & a_{(N-2)(N-2)} \end{bmatrix} \begin{bmatrix} y_2 \\ y_3 \\ \cdots \\ y_{N-1} \end{bmatrix} = \begin{bmatrix} b_1 \\ b_2 \\ \cdots \\ b_{N-2} \end{bmatrix} \tag{4.35}$$

The Vertex Reconstruction algorithm is used to set up the coefficients of the above matrix A (i.e. a_{11}, a_{12}, ..., $a_{(N-2)(N-2)}$) and matrix B (i.e. b_1, b_2, ..., b_{N-2}) with the following steps:

1. The algorithm starts by identifying any signature on the sensor. Consecutive non-zero values of k_h, k_l or k constitute a signature. As discussed in previous sections, the signature is a set of piece-wise continuous line segments with transitional points corresponding to vertices of the contact shape. The polygonal shape is virtually chopped into $N-1$ vertical sections.
2. The orientation of the signature segment in a section is approximated by a linear line segment joining its two end-points. The algorithm works from the left-most vertical section and takes it as the current section. It compares the orientation of the signature in the current section to that in the next section to the right. If they are both clockwise (or anti-clockwise), this next section will be the new current section and the comparison goes on. It keeps track of the number of consecutive sections with the same signature orientation until a different orientation occurs in the next section. Such comparison continues until the right-most vertical section is checked. Figure 4.10 illustrates how the orientations of the pseudo-signature segments are compared. The consecutive sections with the same signature orientations are called blocks.

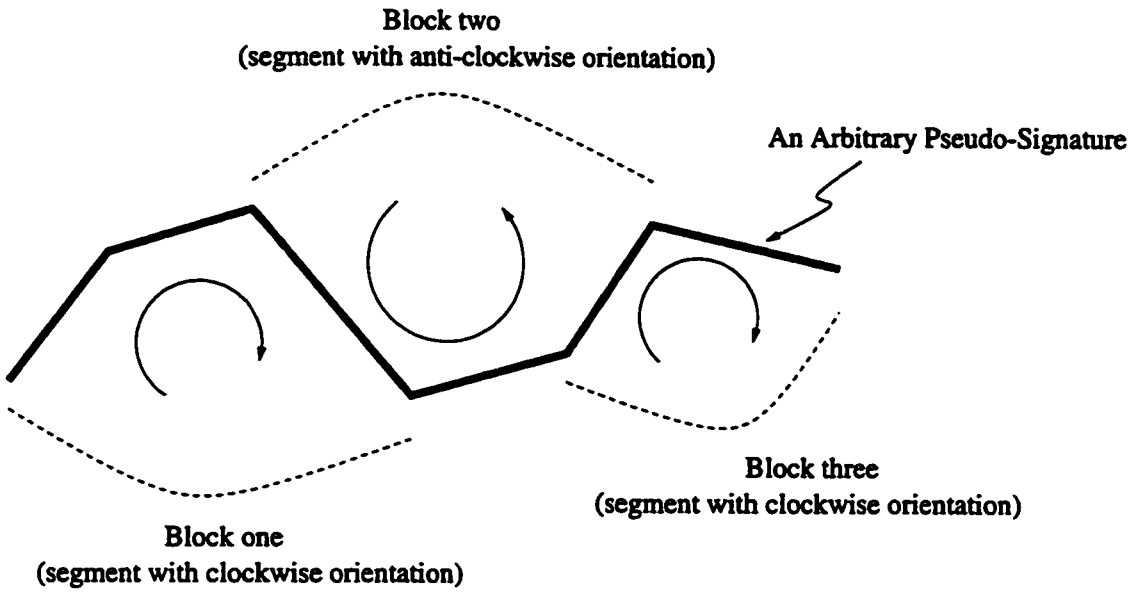

Figure 4.10: An Arbitrary Pseudo-Signature with Three Blocks of Sections

3. Initialize all coefficients in matrix A to zeros. Then assign the diagonal coefficients of matrix A and initialize matrix B as below:

   (a) In case of k_h (i.e. k_{h1}, k_{h2}, ..., k_{hN} obtained at the sensing elements corresponding to the transitional points):

   for $i = 2$ to $N - 1$

   if vertex i is above the transition

$$a_{(i-1)(i-1)} = \frac{1 + k_{hi}}{1 - k_{hi}}$$

$$b_{i-1} = \frac{2k_{hi}L}{1 - k_{hi}}$$

   else

$$a_{(i-1)(i-1)} = \frac{1 - k_{hi}}{1 + k_{hi}}$$

$$b_{i-1} = \frac{2k_{hi}L}{1 + k_{hi}}$$

(b) In case of k_l,

for $i = 2$ to $N - 1$

if vertex i is above the transition

$$a_{(i-1)(i-1)} = \frac{k_{li}}{2 - k_{li}}$$

$$b_{i-1} = \frac{2k_{li}L}{2 - k_{li}}$$

else

$$a_{(i-1)(i-1)} = \frac{2 - k_{li}}{k_{li}}$$

$$b_{i-1} = 2L$$

(c) In case of k,

for $i = 2$ to $N - 1$

if vertex i is above the transition

$$a_{(i-1)(i-1)} = \frac{k_i}{1 - k_i}$$

$$b_{i-1} = \frac{k_i L}{1 - k_i}$$

else

$$a_{(i-1)(i-1)} = \frac{1 - k_i}{k_i}$$

$$b_{i-1} = L$$

4. For the blocks obtained in step 2, there are four possible combinations of their corresponding vertex types (see Table 4.1). The coefficients of matrices A and B are then assigned according to the following rules with respect to these combinations:

Legend: *start* is the index to the first vertex of a block

end is the index to the last vertex of a block

(a) If a block is of type (I) in Table 4.1,

for $row = start$ to $end - 2$

$$a_{(row)(end-1)} = \frac{x_{row+1} - x_{start}}{x_{end} - x_{start}}$$

$$b_{row} = b_{row} - \frac{x_{end} - x_{row+1}}{x_{end} - x_{start}} y_{start}$$

(b) If a block is of type (II) in Table 4.1,

for $row = start$ to $end - 2$

$$b_{row} = b_{row} - \frac{x_{end} - x_{row+1}}{x_{end} - x_{start}} y_{start} - \frac{x_{row+1} - x_{start}}{x_{end} - x_{start}} y_{end}$$

(c) If a block is of type (III) in Table 4.1,

for $row = start$ to $end - 2$

$$a_{(row)(start-1)} = \frac{x_{end} - x_{row+1}}{x_{end} - x_{start}}$$
$$b_{row} = b_{row} - \frac{x_{row+1} - x_{start}}{x_{end} - x_{start}} y_{end}$$

(d) If a block is of type (IV) in Table 4.1,

for $row = start$ to $end - 2$

$$a_{(row)(start-1)} = \frac{x_{end} - x_{row+1}}{x_{end} - x_{start}}$$
$$a_{(row)(end-1)} = \frac{x_{row+1} - x_{start}}{x_{end} - x_{start}}$$

Block Type	Start Vertex	End Vertex	Action on
I	Left-most Vertex	Any Interior Vertex	Both Matrix A & B
II	Left-most Vertex	Right-most Vertex	Matrix B Only
III	Any Interior Vertex	Right-most Vertex	Both Matrix A & B
IV	Any Interior Vertex	Any Interior Vertex	Matrix A Only

Table 4.1: Block Types

4.3 Profile Reconstruction

Profile Reconstruction is applied if double-measurement is available. It takes both the arrays of k_l and k_h and generates the profile of the contact shape. There are also some assumptions and limitations that need to be addressed before applying this algorithm.

4.3.1 Assumptions on Shapes

In general, there is no need to assume that the contact shape is polygonal and limited concavity is allowed. However, the shape must not have concavity of the form illustrated in Figure 4.5(b).

4.3.2 Recovering the Profile

With both sets of k_l and k_h, it is possible to recover both values of l and w of each column of the sensor. By solving the equations 3.3 and 3.4 simultaneously, the values of the corresponding l and w are readily found as follows:

$$\begin{bmatrix} 1 & \frac{1+k_h}{2} \\ 1 & \frac{k_l}{2} \end{bmatrix} \begin{bmatrix} l \\ w \end{bmatrix} = \begin{bmatrix} k_h L \\ k_l L \end{bmatrix} \tag{4.36}$$

Hence, l and w are solved for each sensor column as below:

$$l = \frac{k_l L}{1 + k_h - k_l}$$

$$w = \frac{2(k_h - k_l)L}{1 + k_h - k_l}$$

In general, the profile of an object can be obtained by solving all l and w for each sensor column in contact with the object. It is noticed that both l and w of a column can be solved independent of other columns. There is no reference to the trace of the pseudo-centers. Therefore, the ambiguity due to concavity shown in Figure 4.5(a) is not a concern in this algorithm.

	Vertex Reconstruction	Profile Reconstruction
Applicable Sensor	CRS-CRS & CRS-M	CRS-CRS
Transition Point Detection	Required	Not Required
Limitation on Shapes	Convex Polygons Only	Any Convex Shapes & Certain Concave Shapes
Data Size (With n Sensing Elements)	n	$2n$

Table 4.2: Comparison Between Vertex Reconstruction and Profile Reconstruction

4.3.3 Comparison Between Vertex Reconstruction and Profile Reconstruction

Table 4.2 gives a comparison between Vertex Reconstruction and Profile Reconstruction. Vertex Reconstruction requires only k_h, k_l or k from the sensor. It can be used with both the CRS-CRS and CRS-M sensors. However, it is only capable of recovering convex polygonal

shapes and transition points detection must be done on the raw data (pseudo-signature) to determine the x-coordinates of the vertices being recovered. Profile Reconstruction, on the other hand, makes use of both k_h and k_l. Hence, it requires twice as many data as that in Vertex Reconstruction. Since only CRS-CRS sensor provides both k_h and k_l, Profile Reconstruction cannot be used with a CRS-M sensor. As Profile Reconstruction estimates l and w for each sensing element, it is capable of recovering any convex shapes and certain concave shapes.

Chapter 5

Simulations

To verify the shape recovery algorithms with different types of hybrid sensors, a number of simulations have been done using Matlab. Various parameters, such as errors in sensor outputs, geometric shape of the object in contact, its position and orientation relative to the sensor were used.

5.1 Sources of Errors

In practice, a number of sources contribute to errors in the sensor output, which in turns affect the performance of a shape recovery algorithm. To facilitate simulations and analysis, the possible error sources are grouped into two major categories, namely, quantization noise and positional uncertainty.

5.1.1 Combined Quantization Noise

As mentioned in previous Chapters, an analog-to-digital (A/D) conversion is required to turn the analog voltage into a digital form for computer processing. The maximum uncertainty in this conversion is half the resolution used. If the output voltage is digitized into a 12-bit number, the A/D quantization error will be $\pm 1/8192$ of the full scale output voltage. Besides this A/D quantization error, another kind of quantization takes place on the length of contact between an object and the sensor. Figure 5.1 illustrates how the edges of a polygon are quantized. Since each sensor column has a finite width, the measured output voltage corresponds to the average position of contact. Each of the upper and lower contact ends can have a maximum error of half the resolution. If the analog dimension is geometrically divided into 1000 units, maximum error at each contact end will be $\pm 1/2000$. Hence in the worst case, the maximum quantization error in a length of contact adds up to $\pm 1/1000$. As both of the above quantization errors are inherent in any hybrid sensor

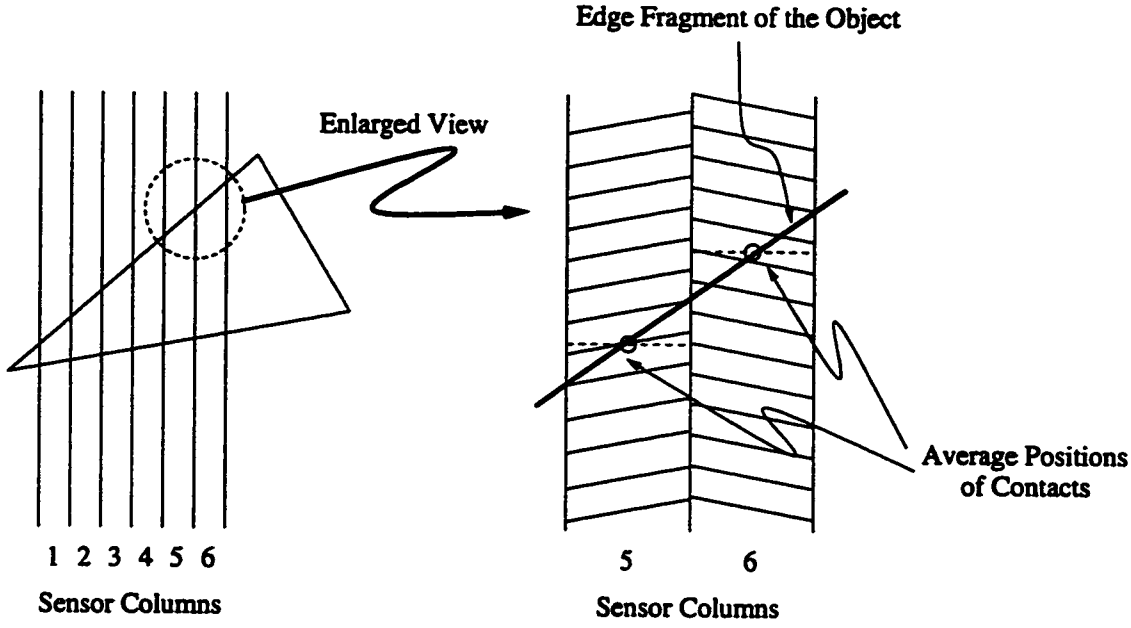

Figure 5.1: Quantization at the Edge of Contact between an Object and the Hybrid Sensor.

discussed in this thesis, they are grouped together and defined as *Combined Quantization Errors* (C.Q.E.).

5.1.2 Error in Detecting Transitions of a Pseudo-signature

As discussed in Chapter 4, a pseudo-signature is required for the Vertex Reconstruction algorithm to work. The detection of any transition in such a signature is particularly important. Even with ideal sensor output, tolerance needs to be allowed in any transition detecting algorithm. To maintain simplicity in simulations, a uniformly distributed uncertainty with a range of ± 5 units was randomly added to the horizontal coordinates of each transitions. This error is defined as *Transition Error* (T.E.).

5.1.3 Positional Uncertainty

Ideally, the contact between an object and the sensor is assumed to be perfect. However, in practical situations, it is unlikely to have perfect contact all the time. Figure 5.2 gives a typical example of imperfect contacts when an object touches a sensor surface. Factors such as the non-uniformity in CRS strips and slight mis-alignment between two CRS strips can lead to errors in the sensor output. These errors were categorized as *Positional Uncertainty* (P.U.). As there may be many combinations of these error sources, it is impossible to model the positional uncertainties precisely. In practice, P.U. are reflected as error in the measured output voltage. For instance, if δV_h is the error in the measured voltage V_h, then

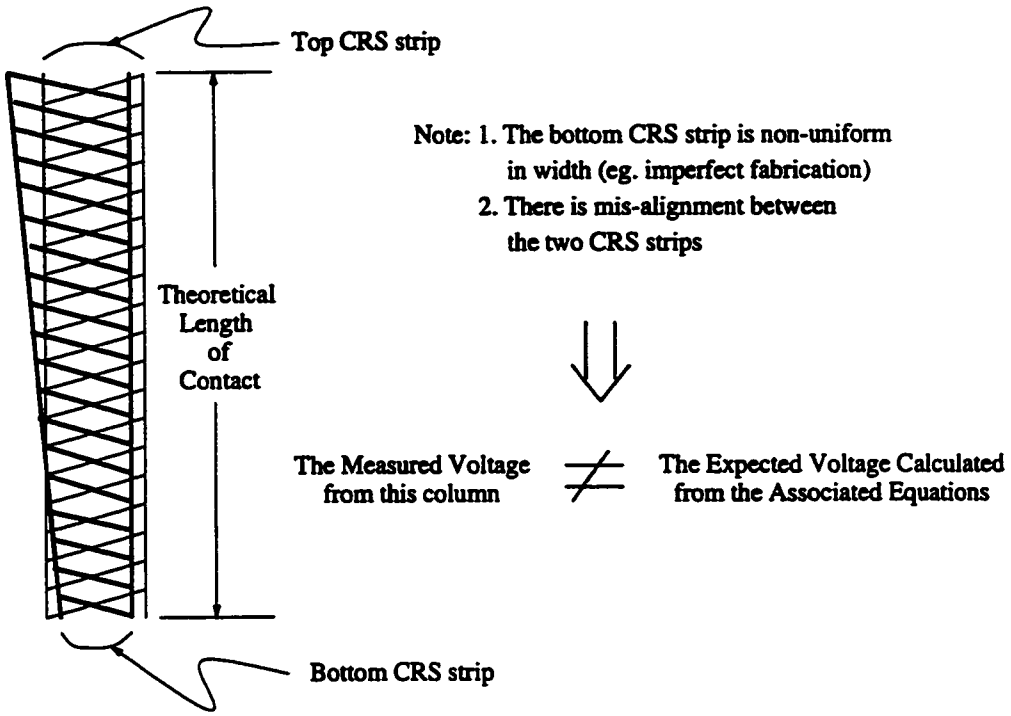

Figure 5.2: Typical Examples that Constitute Positional Uncertainty

the corresponding value of k_h will be given by:

$$\hat{k}_h = \frac{V_h + \delta V_h}{V_{ref}} = k_h + \frac{\delta V_h}{V_{ref}} = k_h + \delta k_h \tag{5.1}$$

In case of k_l and k, their values are given by:

$$\hat{k}_l = k_l + \frac{\delta V_l}{V_{ref}} = k_l + \delta k_l \tag{5.2}$$

$$\hat{k} = k + \frac{\delta V_{out}}{V_{ref}} = k + \delta k \tag{5.3}$$

where δV_l and δV_{out} are the errors in measured voltage V_l and V_{out} respectively.

As observed from equations 5.1 to 5.3, the errors due to P.U. can be represented by a percentage with respect to the reference voltage V_{ref}.

5.2 Simulated Scenarios

The simulations focus on the CRS-CRS and the CRS-M sensor structures. In the case of a CRS-CRS sensor, both the Vertex Reconstruction and the Profile Reconstruction algorithms

can be applied for shape recovery. However, only Vertex Reconstruction can be used with a CRS-M sensor. Three types of polygons, namely a triangle, a tetragon and a hexagon were used in the simulations. In each combination of the above sensor structures, shape recovery algorithms and polygonal shapes, five scenarios of shape recovery with different sensor output noise levels were simulated. These noise levels were:

1. Ideal Sensor Output (Noise-free Sensor).
2. Sensor Output with C.Q.E. (and T.E., if applicable) Only.
3. Sensor Output with C.Q.E. (and T.E., if applicable) and P.U. profile I.
4. Sensor Output with C.Q.E. (and T.E., if applicable) and P.U. profile II.

The scenarios of ideal sensors serve as control cases to verify the equations and their solutions as discussed in Chapter 4. In case of the Vertices Reconstruction Algorithm with any sensor structure, quantization noise was simulated in both the digital and the analog dimensions. The noise in the analog dimension was assumed to be the result of any analog-to-digital conversion, whereas the noise from the digital dimension was assumed to be the uncertainty in determining the horizontal coordinates of the transition of a pseudo-signature. On top of these quantization errors, two profiles (see Table 5.1) of positional uncertainties in the analog dimension were added in turns.

Profile	Percentage Error of Sensor Output With Respect To V_{ref}
I	±0 to 0.5%
II	±0 to 1%

Table 5.1: Simulated Error Profiles for Positional Uncertainty

In each simulated case, the hybrid sensor assumed a planar square geometry and its size was 1000 units in both the digital (horizontal) and the analog (vertical) dimensions. The simulated shapes were dragged across the sensor from the lower left corner to the upper right corner in 5 steps. They were also rotated by 36° counter-clockwise at each step along their trajectories. To facilitate discussion on the results, a number of metrics are required to measure how well the recovered shape matches the original.

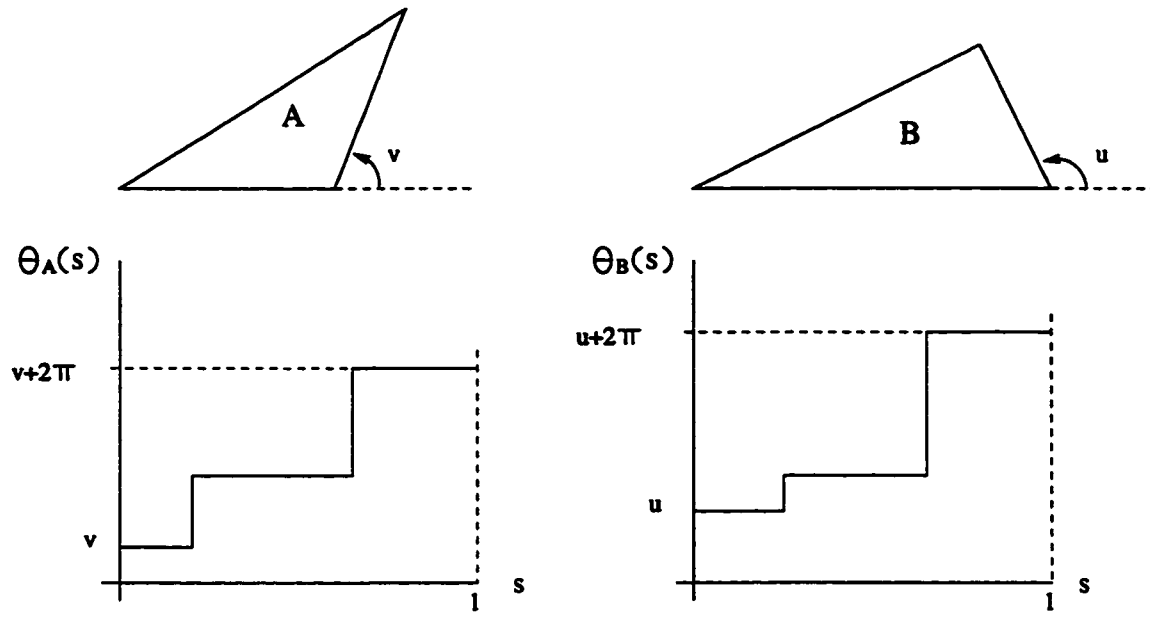

Figure 5.3: Turn Functions of Polygons A and B.

5.3 Metrics to Measure Shape Recovery Performance

This thesis focuses on the following characteristics when measuring how well the recovered shape matches the original:

(a) Shape: The similarity in profile between the original and the recovered shape.

(b) Position: The distance between the geometric centroids of the original and the recovered shape.

(c) Orientation: The deviation in orientation between the the original and the recovered shape.

In comparing similarity (or difference) in profile, the *Polygon Distance Function*, which is commonly used by researchers in computational geometry [17], has been adopted. Each polygonal shape is represented by its normalized turn function $\theta(s)$. Figure 5.3 shows the corresponding normalized turn functions for polygons A and B. The quantity, Mismatch Coefficient (M.C.), is defined as the sum of absolute difference between $\theta_A(s)$ and $\theta_B(s)$, as illustrated in Figure 5.4. In general, a perfect match corresponds to a 0 radians in M.C. and larger dis-similarity corresponds to higher values in M.C.

To measure how close the position of the recovered polygon to the original, the geometric centroids of the polygons are used as reference. The quantity, Absolute Position Error (A.P.E.), is defined as the distance between the geometric centroids of two polygons. The

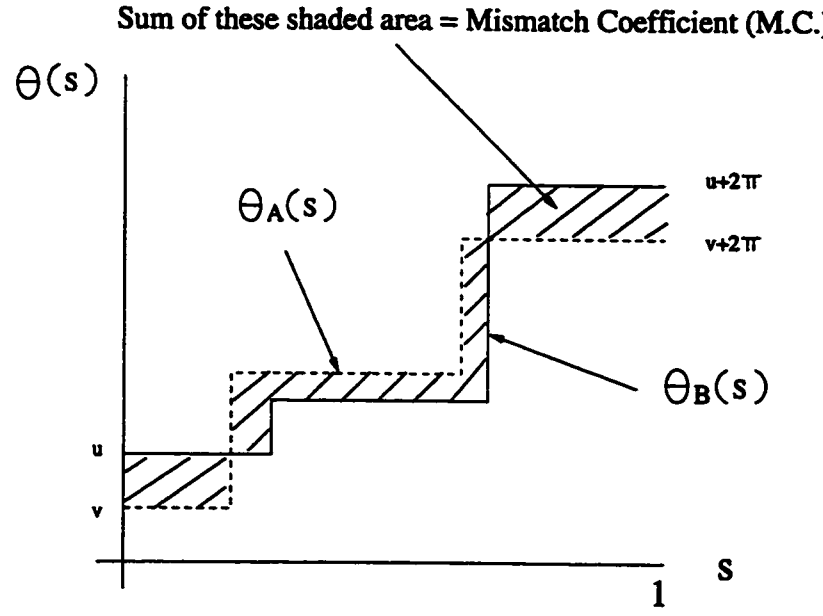

Figure 5.4: Mismatch Coefficient (M.C.) Between Polygons A and B shown in Figure 5.3.

two polygons are considered perfectly at the same position if the A.P.E. between them is 0. On the other hand, increasing A.P.E. means increasing discrepancy in positions between the two polygons.

The orientation of a polygon is defined as the angle between its reference line to the horizontal axis. The reference line is a line joining an arbitrary vertex to the geometric centroid. When comparing the orientations of the original and recovered polygons, their corresponding reference lines must be used. The quantity, Absolute Orientation Error (A.O.E.), is then defined as the difference between the orientations of the two polygons concerned. A perfect match results in a zero A.O.E., whereas increasing A.O.E. means larger deviation.

5.4 Simulation Results with a CRS-CRS Hybrid Sensor

With a CRS-CRS hybrid sensor, there is a choice of using either the Vertex Reconstruction or the Profile Reconstruction algorithm for shape recovery. The next two sections cover the simulation results of using these algorithms.

5.4.1 Vertex Reconstruction with a CRS-CRS Hybrid Sensor using k_h-Pseudo-Signature

The first set of simulations was done with a triangle on a CRS-CRS hybrid sensor using Vertex Reconstruction. In the first scenario, ideal conditions were assumed. With perfect

sensor output and transition detection in the pseudo-signatures, the values of k_h were used to recover the original shape perfectly (see Figure 5.5). In the second scenario, only C.Q.E. was introduced. The maximum quantization error was $\pm 1/1000$ (the geometric resolution in the analog dimension) in each of the concerned columns. These quantization noises were directly reflected in the sensor output. In addition, T.E. was assumed to be ranged from -5 to $+5$ units with a uniform distribution. Figure 5.6 shows the corresponding shape recovery. Graphically, the recovered shapes almost coincide with the original. In the next two scenarios, P.U. profiles I and II were added on top of the C.Q.E. and T.E. to the sensor output. Their simulation results are depicted in Figure 5.7 and Figure 5.8 respectively. Table 5.2 shows the corresponding quantitative errors in each scenario. The performance was satisfactory with P.U. profile I and the accuracy in shape recovery deteriorated with P.U. profile II. As shown in Figure 5.8, the algorithm failed to recover shape 5 and larger discrepancy was found in recovering the other shapes, especially in shape 1. This phenomenon was contributed by the following reasons:

1. Near the lower region, the relative error in k_h is large for given profile of P.U. For example, the dynamic range of the noise-free k_h is usually small for a typical polygonal shape, from 0.05 to 0.12 in shape 1 for instance. If P.U. causes a 1% error in V_h, the corresponding error in k_h will be 10%. As the recovery algorithm based heavily on the accuracy of k_h, larger error in k_h causes larger discrepancies between the recovered shapes and their originals.

2. Near the upper region, a given P.U. causes a smaller relative error in k_h. For example, the values of k_h is relatively large (from 0.86 to 0.87 in shape 5). If P.U. causes a 1% error in V_h, the corresponding error in k_h will be only around 1%. However the dynamic range of k_h in this region is relatively narrow, the effect of 1% error in k_h can cause large distortion in the signature. Figure 5.9 shows the noisy signature of shape 5 compared to its noise-free counterpart. By using the simple detection method in the simulation, too many erroneous transitional points were detected from this noisy signature and shape recovery was failed.

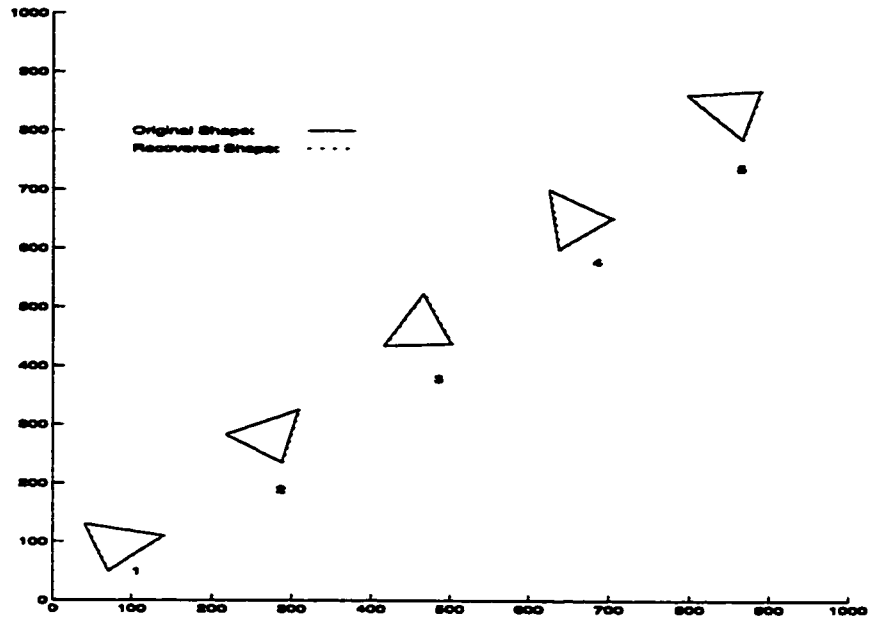

Figure 5.5: Recovering a Triangle on an ideal CRS-CRS Sensor by V.R. with k_h-Pseudo-Signature

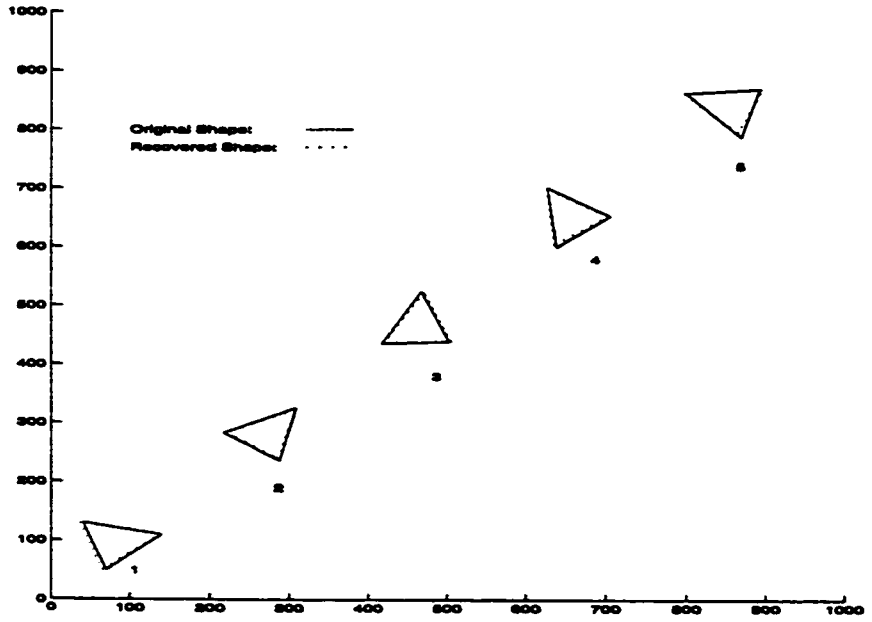

Figure 5.6: Recovering a Triangle on a CRS-CRS Sensor (C.Q.E. & T.E.) by V.R. with k_h-Pseudo-Signature

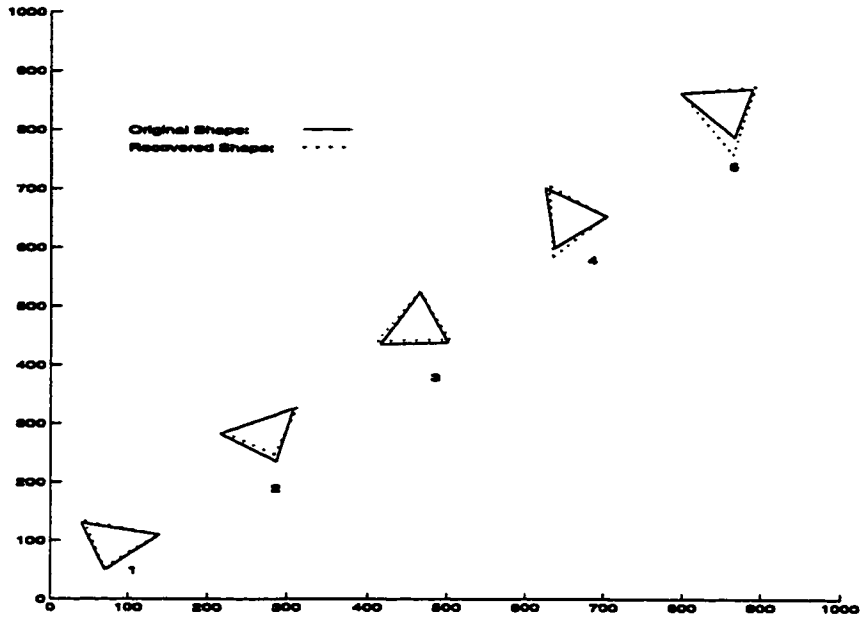

Figure 5.7: Recovering a Triangle on a CRS-CRS Sensor (C.Q.E., T.E. & P.U. Profile I) by V.R. with k_h-Pseudo-Signature

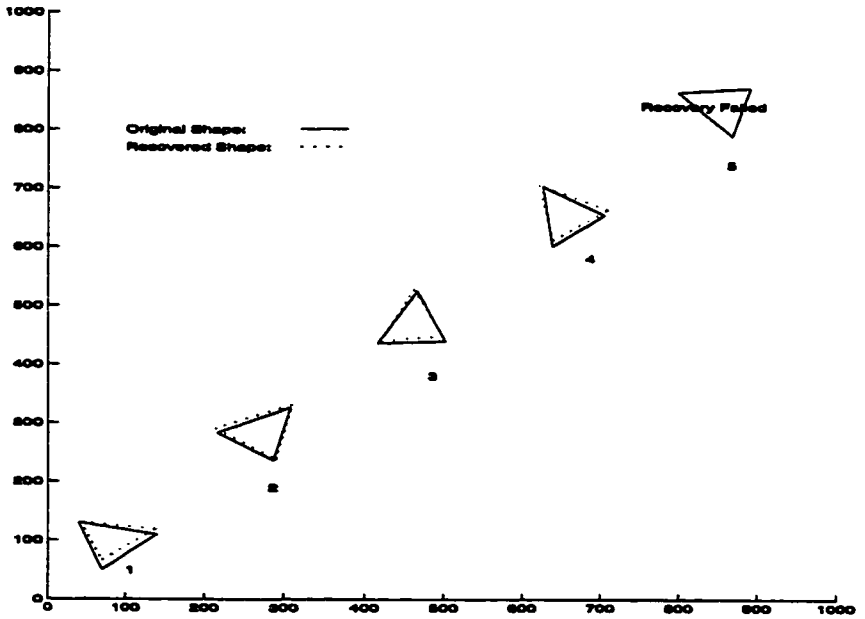

Figure 5.8: Recovering a Triangle on a CRS-CRS Sensor (C.Q.E., T.E. & P.U. P.U. Profile II) by V.R. with k_h-Pseudo-Signature

Hybrid Sensor Type: CRS-CRS Recovery Algorithm: Vertex Reconstruction Signature Type: k_h Simulated Shape: Triangle						
Reference		**Pos. 1**	**Pos. 2**	**Pos. 3**	**Pos. 4**	**Pos. 5**
Figure 5.5	M.C.	0.000	0.000	0.000	0.000	0.000
	A.O.E.	0.000	0.000	0.000	0.000	0.000
	A.P.E.	0.000	0.000	0.000	0.000	0.000
Figure 5.6	M.C.	0.031	0.048	0.020	0.039	0.059
	A.O.E.	0.007	0.019	0.023	0.001	0.049
	A.P.E.	3.670	1.167	2.333	2.580	2.775
Figure 5.7	M.C.	0.060	0.068	0.072	0.164	0.203
	A.O.E.	0.010	0.018	0.035	0.076	0.080
	A.P.E.	3.064	3.771	3.156	8.340	14.122
Figure 5.8	M.C.	0.194	0.077	0.080	0.135	-
	A.O.E.	0.015	0.029	0.025	0.080	-
	A.P.E.	6.544	3.153	3.614	7.653	-

Table 5.2: Quantitative Mismatch between the Original and the Recovered Triangle in Each Simulated Position (CRS-CRS Sensor and V.R. Algorithm with k_h-Pseudo-Signature).

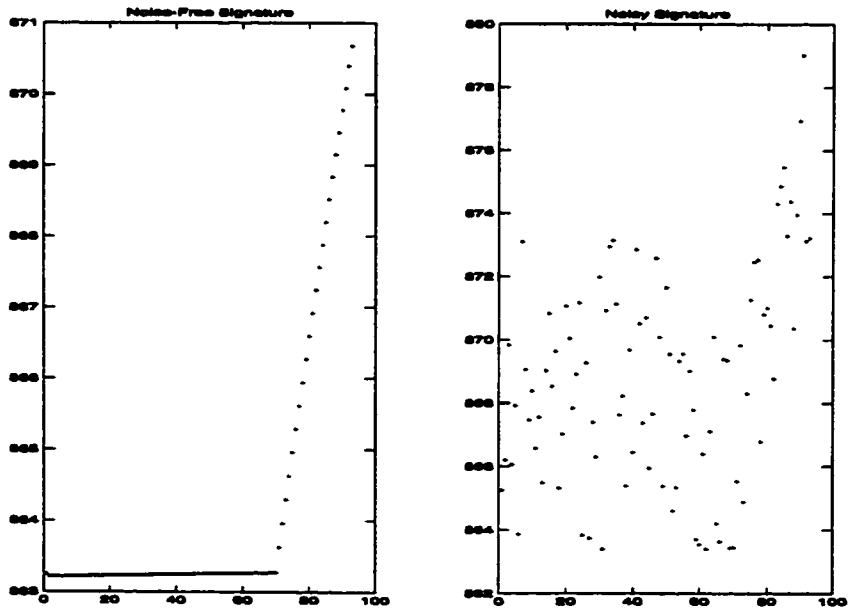

Figure 5.9: Noise-free and Noisy k_h-Pseudo-Signature of Triangular Shape 5 with P.U. Profile II

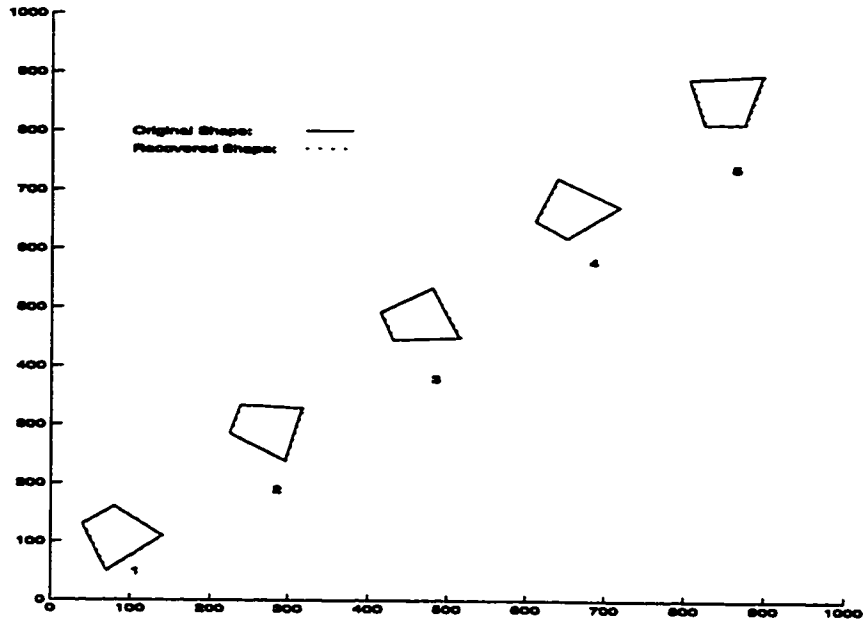

Figure 5.10: Recovering a Tetragon on an ideal CRS-CRS Sensor by V.R. with k_h-Pseudo-Signature

The second set of simulations were done with a tetragon. Figure 5.10 to Figure 5.13 show the corresponding simulation results and Table 5.3 gives their quantitative errors. With ideal sensor output, Vertex Reconstruction recovered the original tetragon perfectly. When only C.Q.E. and T.E. were added, only minor errors were found in shape recovery. Even with P.U. profile I, the tetragons could still be reconstructed. When P.U. profile II was used, the algorithm failed in recovering the shapes 1 and 5 as their signature were too noisy for transitional points detection. As seen in Figure 5.13, even shape recovery was possible, large discrepancy exist in recovering shape 4. The signature was so seriously distorted that one of the transitional points was not detected (see Figure 5.14). As a result, one interior vertex was missing and the recovered shape was more like a triangle rather than a tetragon.

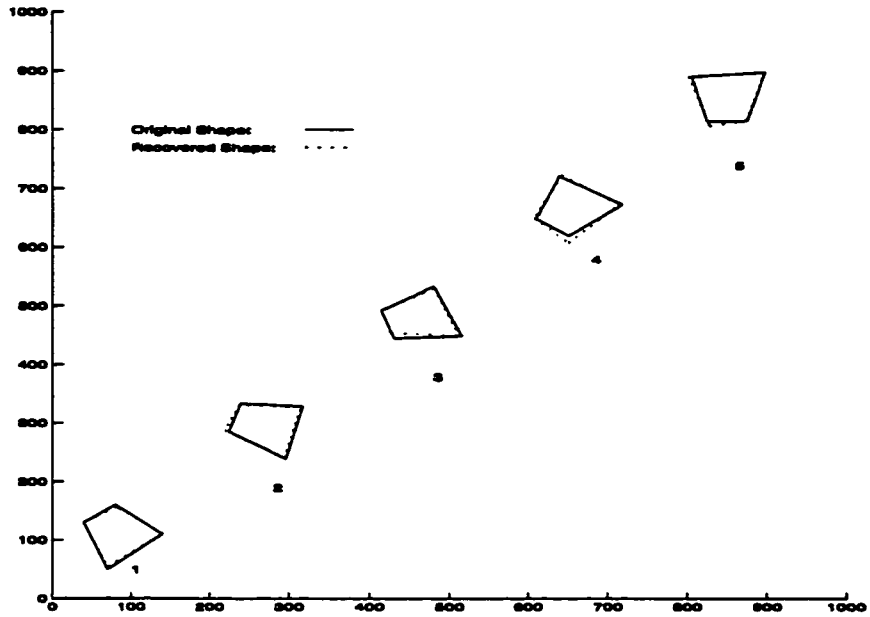

Figure 5.11: Recovering a Tetragon on a CRS-CRS Sensor (C.Q.E. & T.E.) by V.R. with k_h-Pseudo-Signature

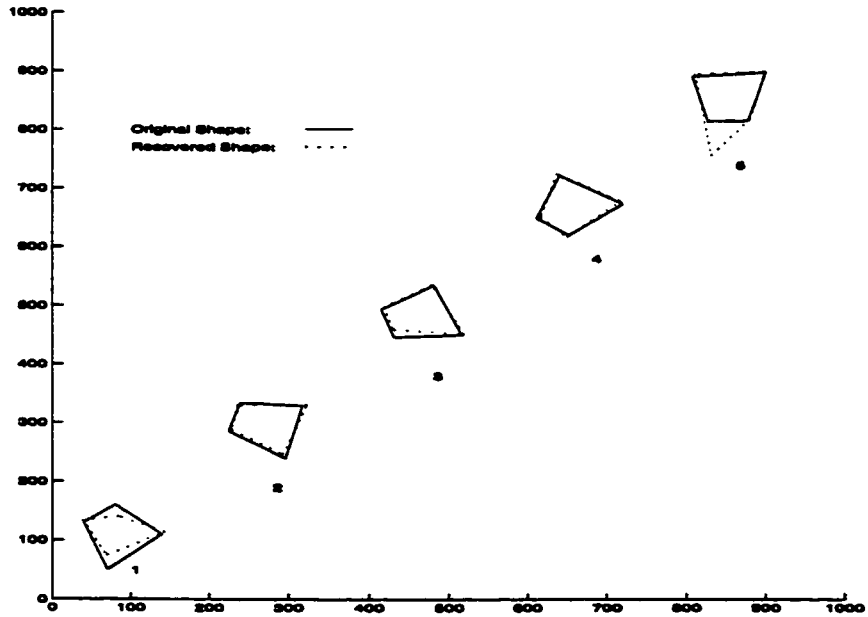

Figure 5.12: Recovering a Tetragon on a CRS-CRS Sensor (C.Q.E., T.E. & P.U. Profile I) by V.R. with k_h-Pseudo-Signature

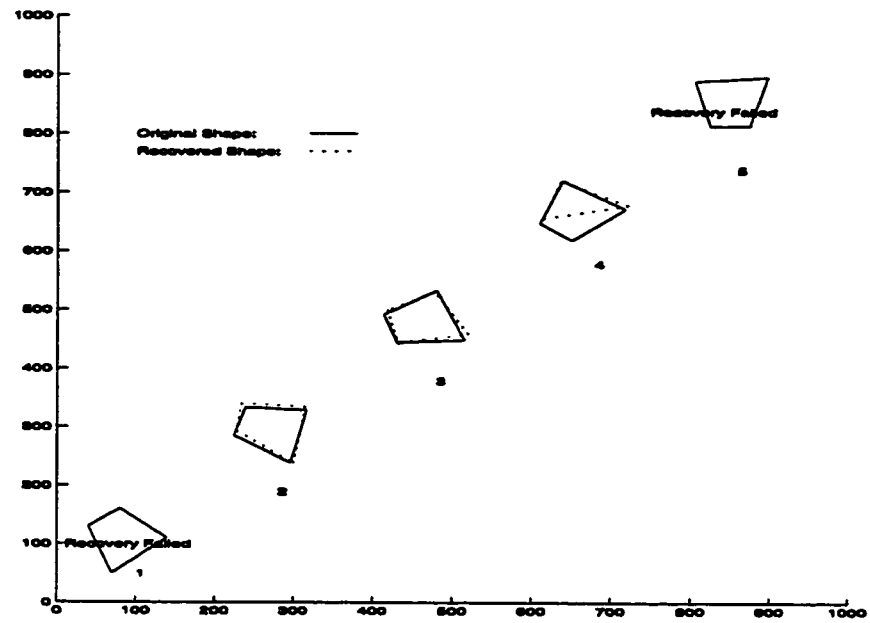

Figure 5.13: Recovering a Tetragon on a CRS-CRS Sensor (C.Q.E., T.E. & P.U. Profile II) by V.R. with k_h-Pseudo-Signature

Hybrid Sensor Type: CRS-CRS Recovery Algorithm: Vertex Reconstruction Signature Type: k_h Simulated Shape: Tetragon						
Reference		Pos. 1	Pos. 2	Pos. 3	Pos. 4	Pos. 5
Figure 5.10	M.C.	0.000	0.000	0.000	0.000	0.000
	A.O.E.	0.000	0.000	0.000	0.000	0.000
	A.P.E.	0.000	0.000	0.000	0.000	0.000
Figure 5.11	M.C.	0.059	0.056	0.172	0.267	0.290
	A.O.E.	0.011	0.038	0.020	0.089	0.011
	A.P.E.	2.549	3.018	2.321	2.371	1.881
Figure 5.12	M.C.	0.326	0.105	0.128	0.075	0.413
	A.O.E.	0.082	0.025	0.018	0.015	0.132
	A.P.E.	6.517	1.482	2.335	2.214	19.679
Figure 5.13	M.C.	-	0.197	0.211	-	-
	A.O.E.	-	0.035	0.085	-	-
	A.P.E.	-	3.745	3.822	-	-

Table 5.3: Quantitative Mismatch between the Original and the Recovered Tetragon in Each Simulated Position (CRS-CRS Sensor and V.R. Algorithm with k_h-Pseudo-Signature).

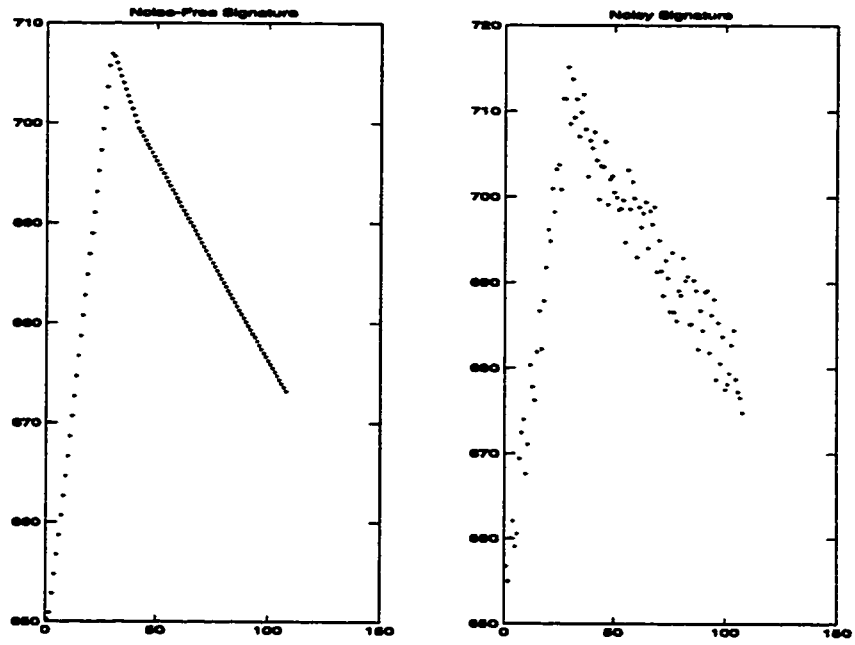

Figure 5.14: Noise-free and Noisy k_h-Pseudo-Signature of Tetragonal Shape 4 with P.U. Profile II

The third set of simulations was done with a hexagon. Figure 5.15 to Figure 5.18 show their corresponding simulation results under various error conditions. Table 5.4 summarizes their quantitative errors in each case. Similar to the results using a triangle and a tetragon, the algorithm reconstructed the original hexagon perfectly when an ideal sensor was simulated. Errors in shape recovery were still acceptable when C.Q.E. and T.E., and P.U. profile I were assumed. However, the algorithm started to perform poorly when P.U. profile II was used (see Figure 5.18). Since the dynamic range of k_h for a particular shape is usually small (from 0.1 to 0.2), it is difficult to extract transitional point from a seriously distorted signature. As the number of vertices increases, the chance of missing transitional points from the signature increases.

As mentioned in Section 4.2.1, Vertex Reconstruction algorithm is only applicable on convex polygon. Figure 5.19 shows the possible ambiguity it caused when the algorithm is used on a concave shape.

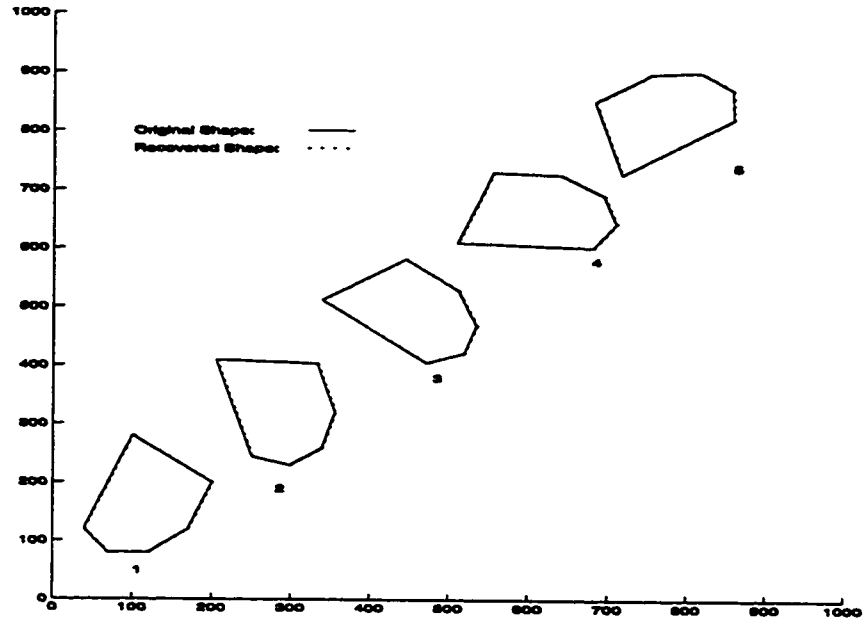

Figure 5.15: Recovering a Hexagon on an ideal CRS-CRS Sensor by V.R. with k_h-Pseudo-Signature

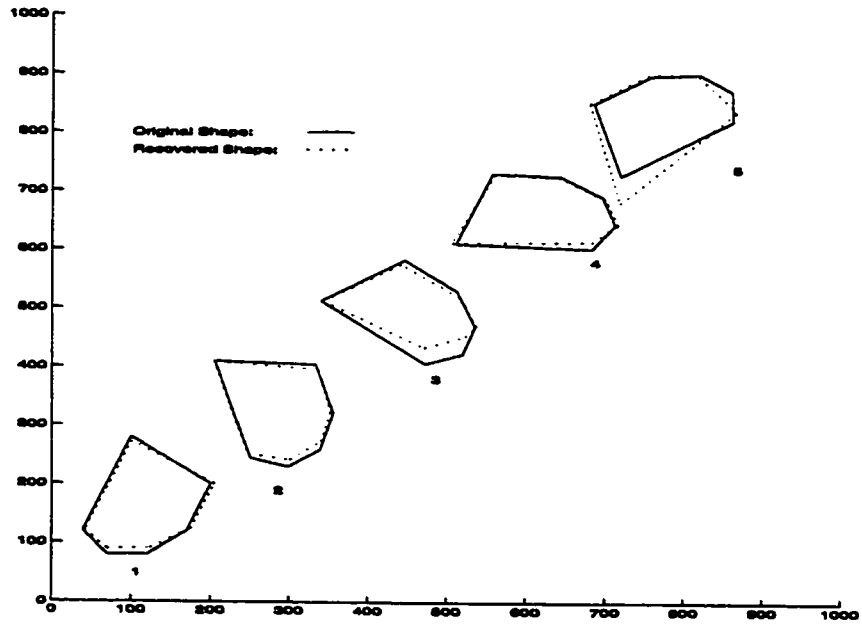

Figure 5.16: Recovering a Hexagon on a CRS-CRS Sensor (C.Q.E. & T.E.) by V.R. with k_h-Pseudo-Signature

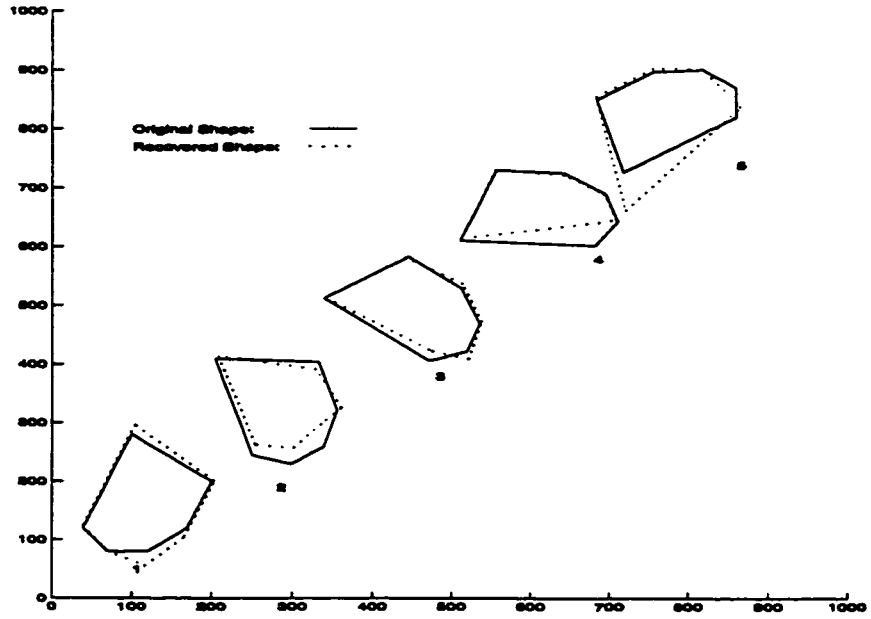

Figure 5.17: Recovering a Hexagon on a CRS-CRS Sensor (C.Q.E., T.E. & P.U. Profile I) by V.R. with k_h-Pseudo-Signature

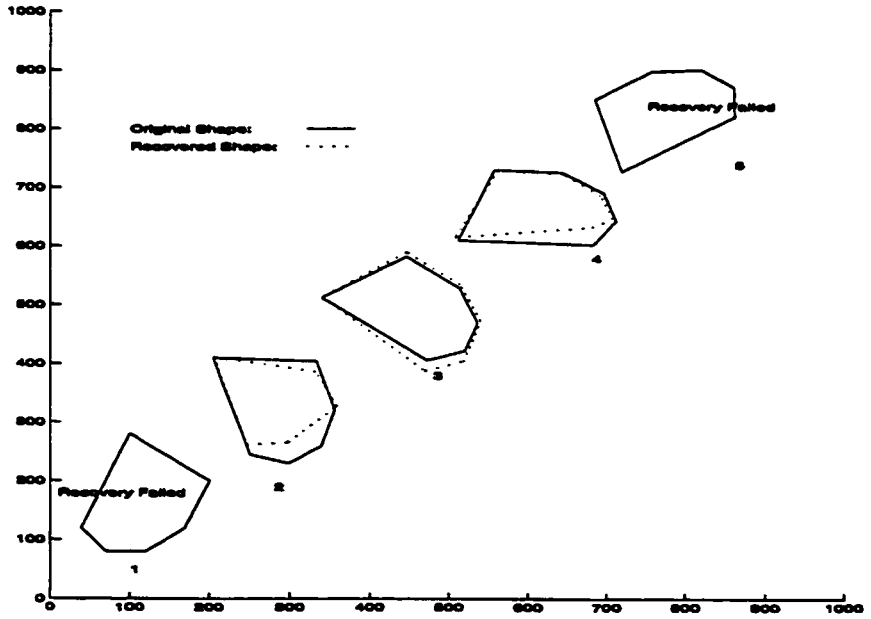

Figure 5.18: Recovering a Hexagon on a CRS-CRS Sensor (C.Q.E., T.E. & P.U. Profile II) by V.R. with k_h-Pseudo-Signature

Hybrid Sensor Type: CRS-CRS Recovery Algorithm: Vertex Reconstruction Signature Type: k_h Simulated Shape: Hexagon						
Reference		Pos. 1	Pos. 2	Pos. 3	Pos. 4	Pos. 5
Figure 5.15	M.C.	0.000	0.000	0.000	0.000	0.000
	A.O.E.	0.000	0.000	0.000	0.000	0.000
	A.P.E.	0.000	0.000	0.000	0.000	0.000
Figure 5.16	M.C.	0.119	0.175	0.185	0.285	0.436
	A.O.E.	0.022	0.029	0.048	0.018	0.091
	A.P.E.	4.212	4.486	7.071	1.644	9.206
Figure 5.17	M.C.	0.217	0.403	0.477	0.489	0.651
	A.O.E.	0.075	0.050	0.058	0.035	0.125
	A.P.E.	3.872	7.513	6.874	6.115	14.638
Figure 5.18	M.C.	-	0.401	0.474	0.492	-
	A.O.E.	-	0.062	0.026	0.038	-
	A.P.E.	-	8.766	7.886	6.872	-

Table 5.4: Quantitative Mismatch between the Original and the Recovered Hexagon in Each Simulated Position (CRS-CRS Sensor and V.R. Algorithm with k_h-Pseudo-Signature).

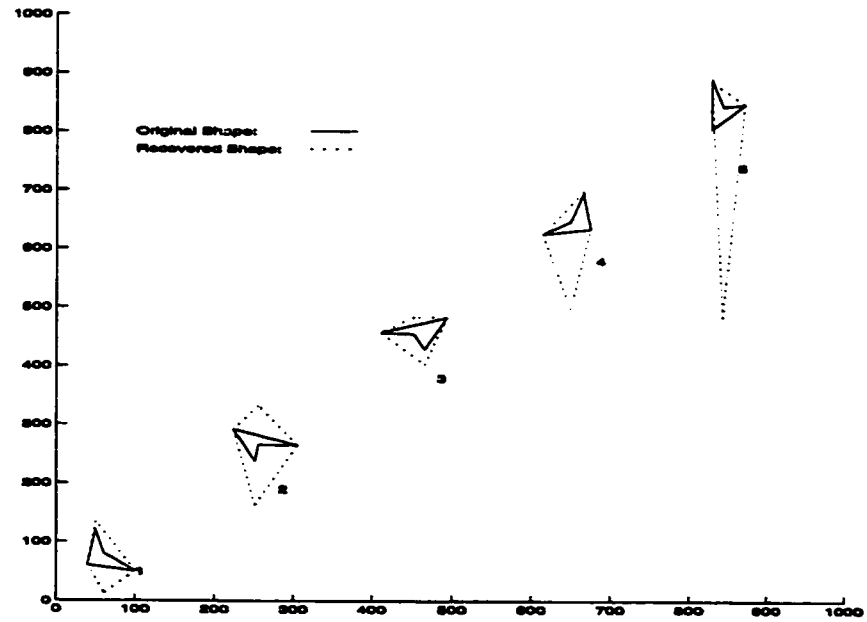

Figure 5.19: Recovering a Concave Polygon on an ideal CRS-CRS Sensor Using V.R. with k_h-Pseudo-Signature

5.4.2 Vertex Reconstruction with a CRS-CRS Hybrid Sensor using k_t-Pseudo-Signature

The fourth set of simulations was similar to the first, but based on the k_t-signature instead. In the first scenario, ideal condition was assumed. With perfect sensor output and transition detection in the pseudo-signatures, the values of k_t were used to recover the original shape perfectly (see Figure 5.20). In the second scenario, only C.Q.E. and T.E. was introduced. The maximum quantization error was $\pm 1/1000$ (the geometric resolution in the analog dimension) in each of the concerned columns. These quantization noises were directly reflected in the sensor output. In addition, T.E. was assumed to be ranged from -5 to $+5$ units with a uniform distribution. Figure 5.21 shows the corresponding shape recovery. Graphically, the recovered shapes were only slightly off from the original. In the next two scenarios, P.U. profile I and II were added on top of the C.Q.E. and T.E. to the sensor output. Their simulation results are depicted in Figure 5.22 and Figure 5.23 respectively. Table 5.5 shows the corresponding quantitative errors in each scenario. In general, the performance was still satisfactory with P.U. profiles I and II.

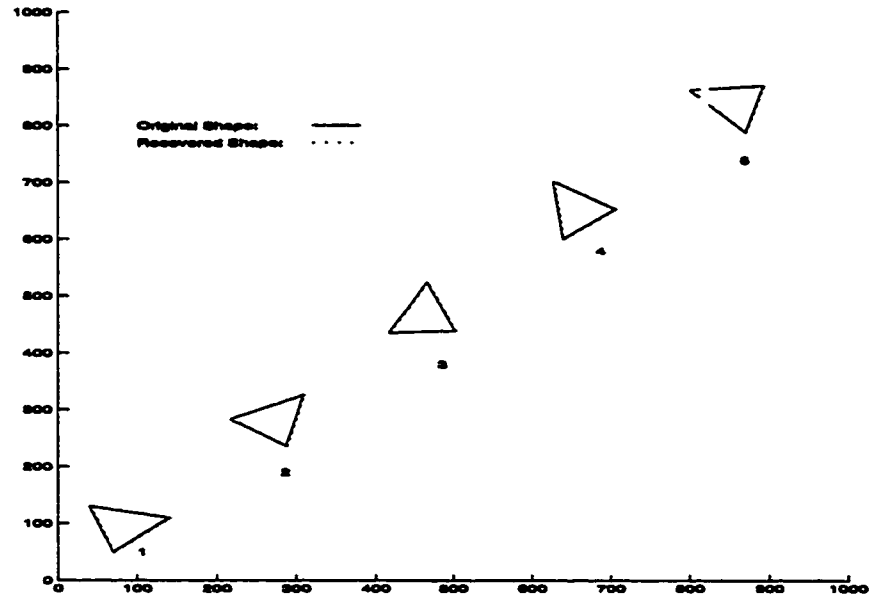

Figure 5.20: Recovering a Triangle on an ideal CRS-CRS Sensor by V.R. with k_t-Pseudo-Signature

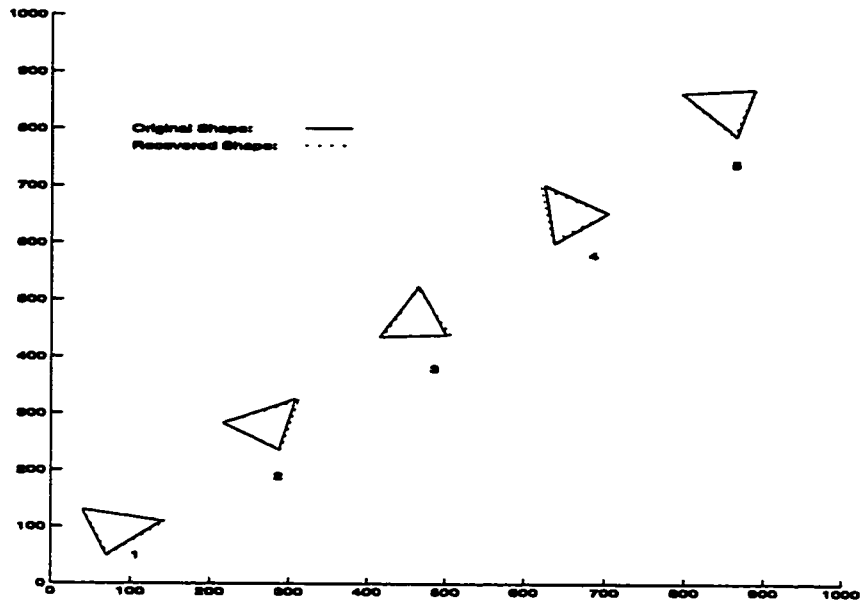

Figure 5.21: Recovering a Triangle on a CRS-CRS Sensor (C.Q.E. & T.E.) by V.R. with k_l-Pseudo-Signature

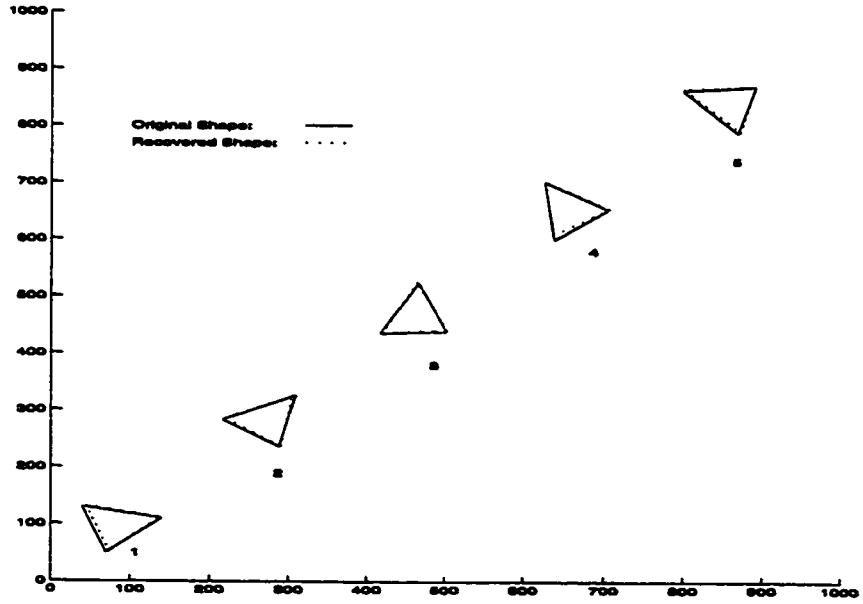

Figure 5.22: Recovering a Triangle on a CRS-CRS Sensor (C.Q.E., T.E. & P.U. Profile I) by V.R. with k_l-Pseudo-Signature

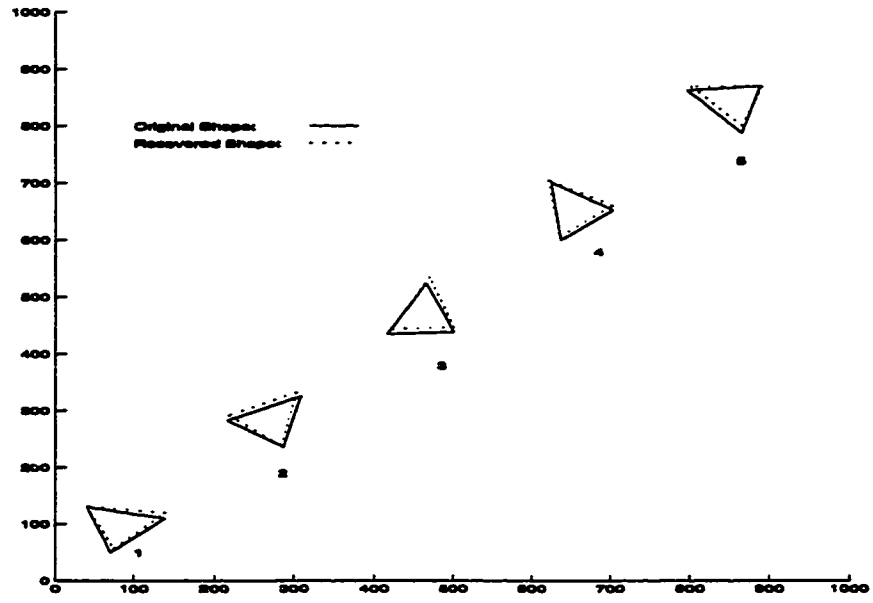

Figure 5.23: Recovering a Triangle on a CRS-CRS Sensor (C.Q.E., T.E. & P.U. Profile II) by V.R. with k_l-Pseudo-Signature

Hybrid Sensor Type: CRS-CRS Recovery Algorithm: Vertex Reconstruction Signature Type: k_l Simulated Shape: Triangle						
Reference		Pos. 1	Pos. 2	Pos. 3	Pos. 4	Pos. 5
Figure 5.20	M.C.	0.000	0.000	0.000	0.000	0.000
	A.O.E.	0.000	0.000	0.000	0.000	0.000
	A.P.E.	0.000	0.000	0.000	0.000	0.000
Figure 5.21	M.C.	0.024	0.062	0.093	0.089	0.021
	A.O.E.	0.020	0.010	0.008	0.064	0.006
	A.P.E.	2.342	2.119	2.345	2.130	1.688
Figure 5.22	M.C.	0.052	0.059	0.080	0.086	0.055
	A.O.E.	0.007	0.008	0.011	0.014	0.009
	A.P.E.	2.167	1.032	1.240	2.024	1.935
Figure 5.23	M.C.	0.098	0.083	0.105	0.090	0.125
	A.O.E.	0.026	0.029	0.015	0.024	0.035
	A.P.E.	2.431	2.645	3.234	2.115	4.254

Table 5.5: Quantitative Mismatch between the Original and the Recovered Triangle in Each Simulated Position (CRS-CRS Sensor and V.R. Algorithm with k_l-Pseudo-Signature).

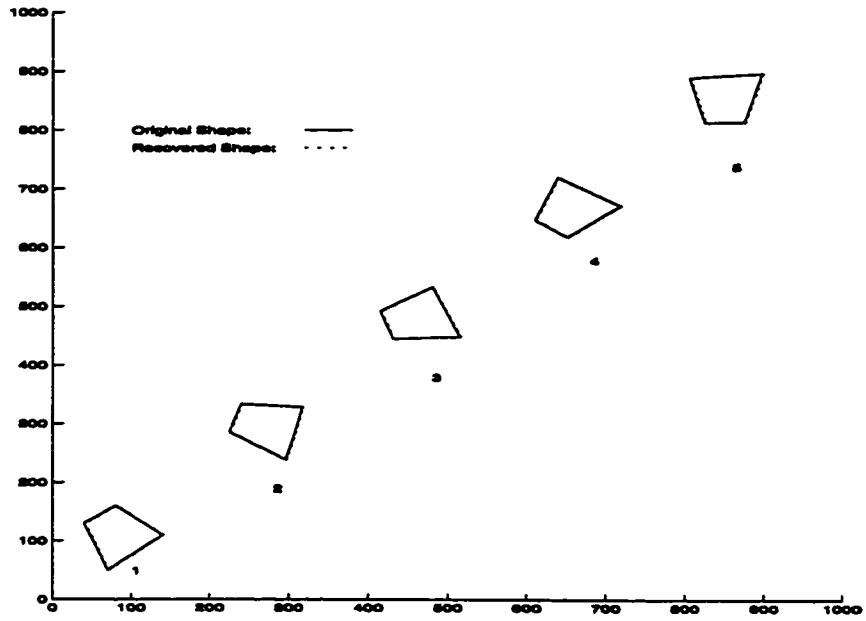

Figure 5.24: Recovering a Tetragon on an ideal CRS-CRS Sensor by V.R. with k_l-Pseudo-Signature

The fifth set of simulations were done with a tetragon. Except using k_l-signature, all other conditions are the same as the second set. Figure 5.24 to Figure 5.27 show the corresponding simulation results and Table 5.6 gives their quantitative errors. With ideal sensor output, Vertex Reconstruction recovered the original tetragon perfectly. When only C.Q.E. and T.E. were added, only insignificant errors were found in shape recovery. Even with P.U. profiles I and II, the tetragons could still be reconstructed with minor discrepancies.

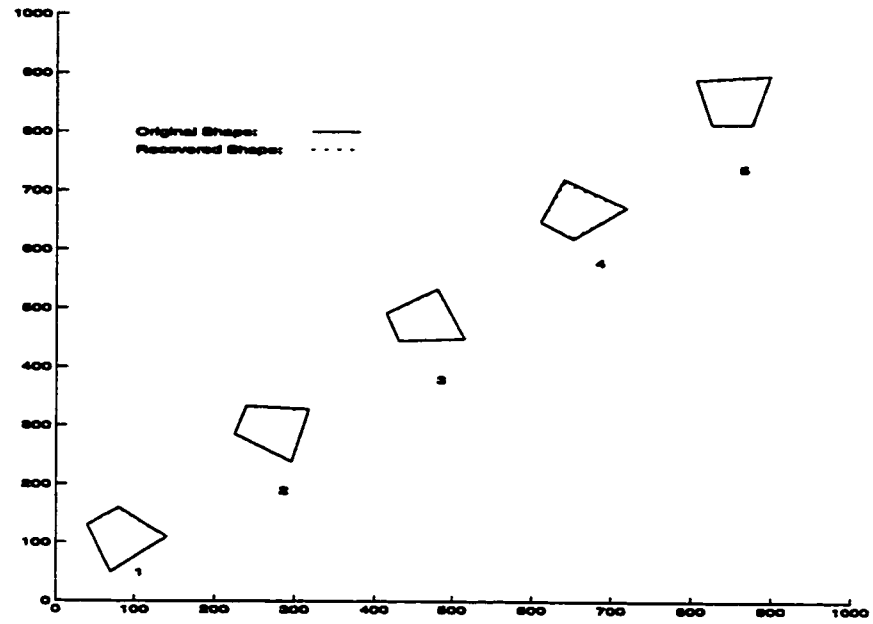

Figure 5.25: Recovering a Tetragon on a CRS-CRS Sensor (C.Q.E. & T.E.) by V.R. with k_l-Pseudo-Signature

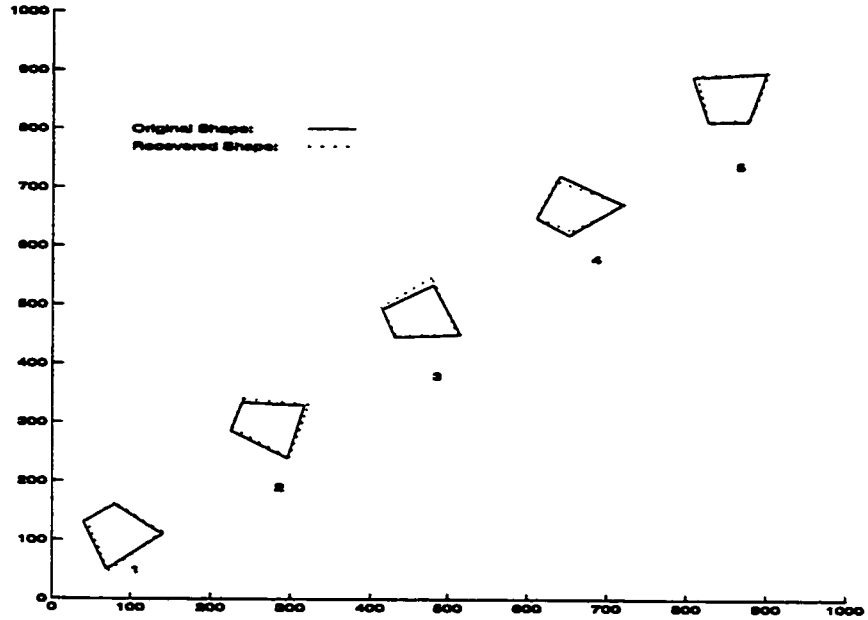

Figure 5.26: Recovering a Tetragon on a CRS-CRS Sensor (C.Q.E., T.E. & P.U. Profile I) by V.R. with k_l-Pseudo-Signature

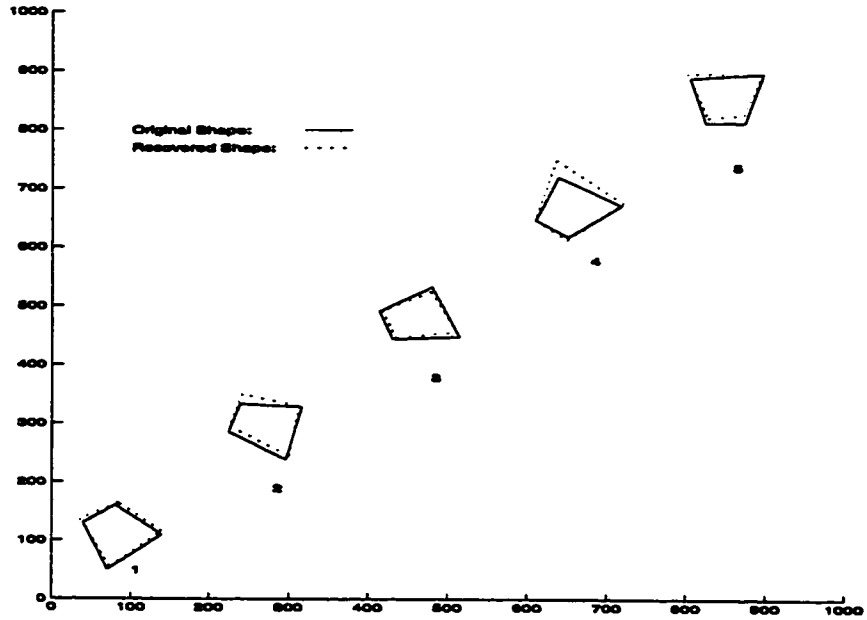

Figure 5.27: Recovering a Tetragon on a CRS-CRS Sensor (C.Q.E., T.E. & P.U. Profile II) by V.R. with k_l-Pseudo-Signature

Hybrid Sensor Type: CRS-CRS Recovery Algorithm: Vertex Reconstruction Signature Type: k_l Simulated Shape: Tetragon						
Reference		Pos. 1	Pos. 2	Pos. 3	Pos. 4	Pos. 5
Figure 5.24	M.C.	0.000	0.000	0.000	0.000	0.000
	A.O.E.	0.000	0.000	0.000	0.000	0.000
	A.P.E.	0.000	0.000	0.000	0.000	0.000
Figure 5.25	M.C.	0.013	0.015	0.020	0.057	0.025
	A.O.E.	0.001	0.015	0.002	0.020	0.008
	A.P.E.	0.550	0.525	0.800	0.525	0.325
Figure 5.26	M.C.	0.080	0.109	0.137	0.125	0.117
	A.O.E.	0.067	0.060	0.035	0.032	0.010
	A.P.E.	1.578	2.091	3.687	1.897	1.923
Figure 5.27	M.C.	0.085	0.129	0.067	0.231	0.195
	A.O.E.	0.078	0.177	0.036	0.087	0.044
	A.P.E.	1.705	3.016	1.467	5.408	3.633

Table 5.6: Quantitative Mismatch between the Original and the Recovered Tetragon in Each Simulated Position (CRS-CRS Sensor and V.R. Algorithm with k_l-Pseudo-Signature).

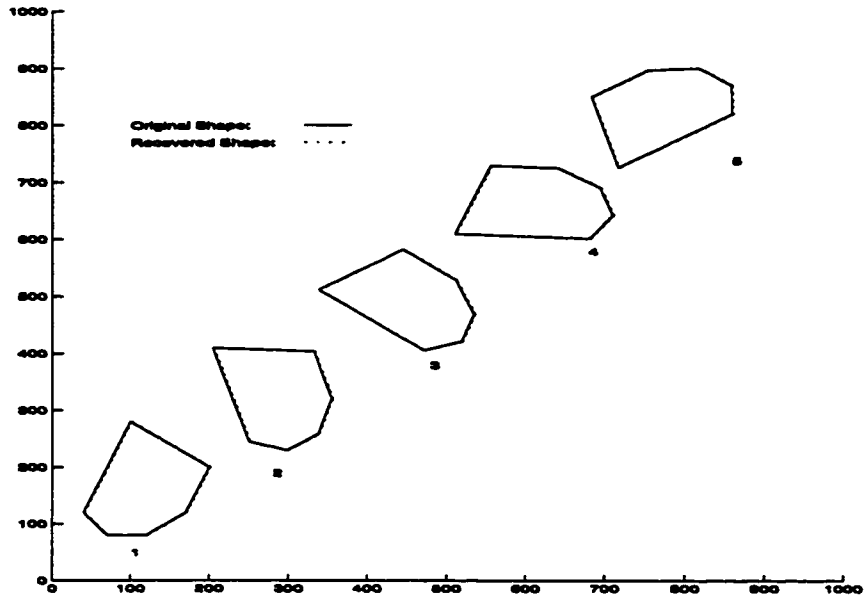

Figure 5.28: Recovering a Hexagon on an ideal CRS-CRS Sensor by V.R. with k_l-Pseudo-Signature

The sixth set of simulations was done with a hexagon. It was similar to the third set, except k_l-pseudo-signature was used instead. Figure 5.28 to Figure 5.31 show their corresponding simulation results under various error conditions. Table 5.7 summarizes their quantitative errors in each case. Similar to the results using a triangle and a tetragon, the algorithm reconstructed the original hexagon perfectly when an ideal sensor was simulated. Errors in shape recovery were still acceptable when C.Q.E. and T.E., and P.U. profile I were assumed. However, larger discrepancies in shape recovery were observed with P.U. profile II was used (see Figure 5.31). Since the dynamic range of k_h for a particular shape is usually small (from 0.1 to 0.2), it is difficult to extract transitional point from a seriously distorted signature. As the number of vertex increases, the chance of missing transitional points from the signature increases.

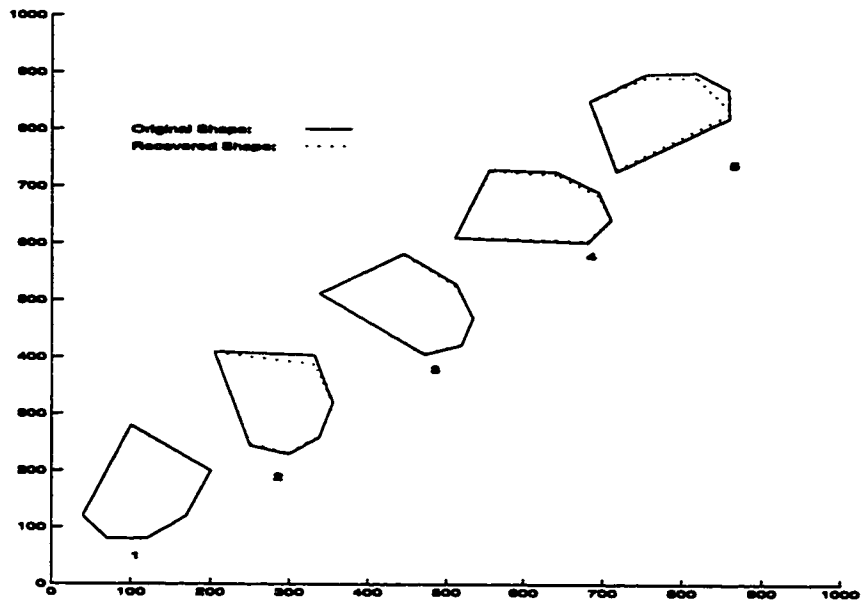

Figure 5.29: Recovering a Hexagon on a CRS-CRS Sensor (C.Q.E. & T.E.) by V.R. with k_l-Pseudo-Signature

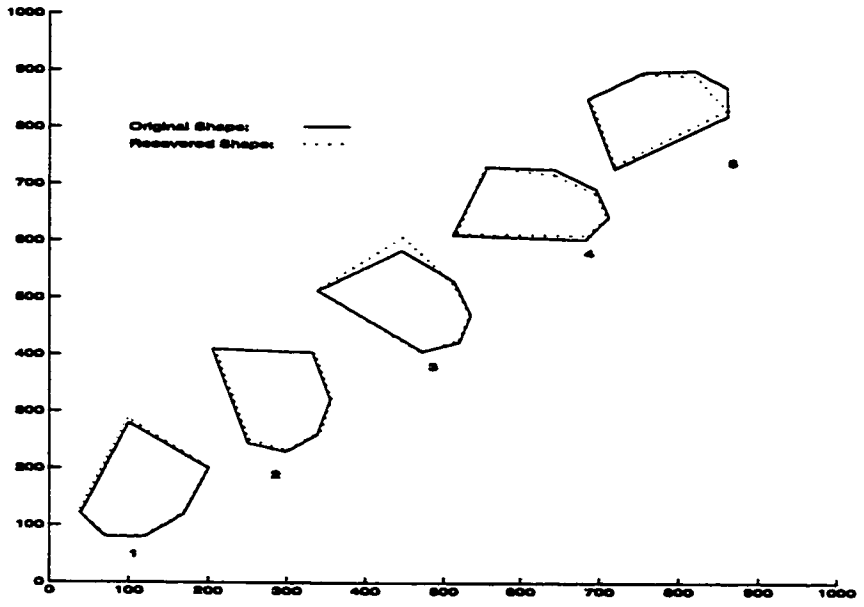

Figure 5.30: Recovering a Hexagon on a CRS-CRS Sensor (C.Q.E., T.E. & P.U. Profile I) by V.R. with k_l-Pseudo-Signature

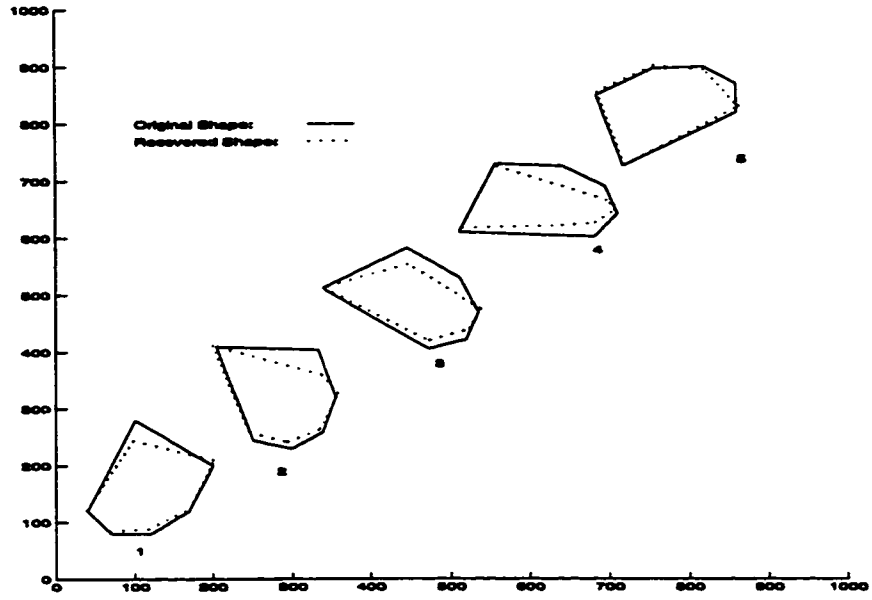

Figure 5.31: Recovering a Hexagon on a CRS-CRS Sensor (C.Q.E., T.E. & P.U. Profile II) by V.R. with k_l-Pseudo-Signature

As mentioned in Section 4.2.1, Vertex Reconstruction algorithm is only applicable on convex polygon. Figure 5.32 show the possible ambiguity it caused when the algorithm and k_l-signature is used on a concave shape.

Hybrid Sensor Type: CRS-CRS Recovery Algorithm: Vertex Reconstruction Signature Type: k_l Simulated Shape: Hexagon						
Reference		Pos. 1	Pos. 2	Pos. 3	Pos. 4	Pos. 5
Figure 5.28	M.C.	0.000	0.000	0.000	0.000	0.000
	A.O.E.	0.000	0.000	0.000	0.000	0.000
	A.P.E.	0.000	0.000	0.000	0.000	0.000
Figure 5.29	M.C.	0.010	0.093	0.034	0.060	0.169
	A.O.E.	0.002	0.007	0.003	0.014	0.059
	A.P.E.	0.333	1.950	0.483	1.567	6.567
Figure 5.30	M.C.	0.030	0.028	0.195	0.079	0.172
	A.O.E.	0.012	0.008	0.068	0.020	0.060
	A.P.E.	1.983	2.307	6.304	2.451	5.607
Figure 5.31	M.C.	0.312	0.397	0.487	0.502	0.188
	A.O.E.	0.079	0.105	0.096	0.065	0.064
	A.P.E.	6.231	7.544	8.354	8.905	5.233

Table 5.7: Quantitative Mismatch between the Original and the Recovered Hexagon in Each Simulated Position (CRS-CRS Sensor and V.R. Algorithm with k_l-Pseudo-Signature).

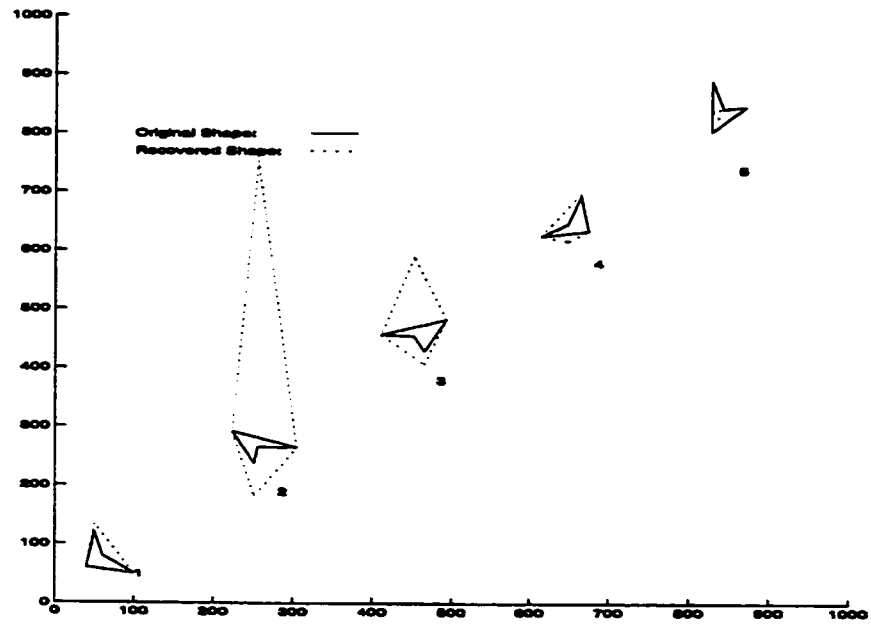

Figure 5.32: Recovering a Concave Polygon on an ideal CRS-CRS Sensor Using V.R. with k_l-Pseudo-Signature

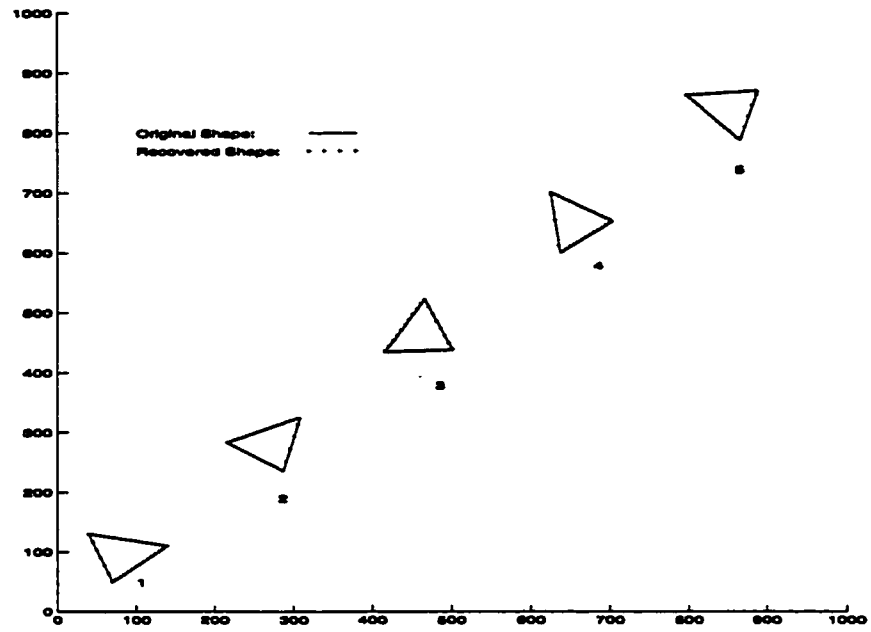

Figure 5.33: Recovering a Triangle on an ideal CRS-CRS Sensor by P.R.

5.4.3 Profile Reconstruction with a CRS-CRS Hybrid Sensor

With the choice of using both sets of k_h and k_l from a CRS-CRS hybrid sensor, Profile Reconstruction can be used for shape recovery. So the seventh set of simulations was done with a triangle on a CRS-CRS hybrid sensor using Profile Reconstruction. Figure 5.33 to Figure 5.36 show the simulation results under different error conditions. An ideal sensor was assumed in the first scenario which produced perfect result as expected. When only C.Q.E. was introduced in the second scenario, no significant error in shape recovery could be observed graphically (see Figure 5.34). Since Profile Reconstruction does not depend on the form of the pseudo-signature, T.E. was irrelevant in the simulations. As shown in Figure 5.35 and Figure 5.36, reasonably good shape recovery could be achieved. Table 5.8 summarizes the quantitative errors in shape recovery.

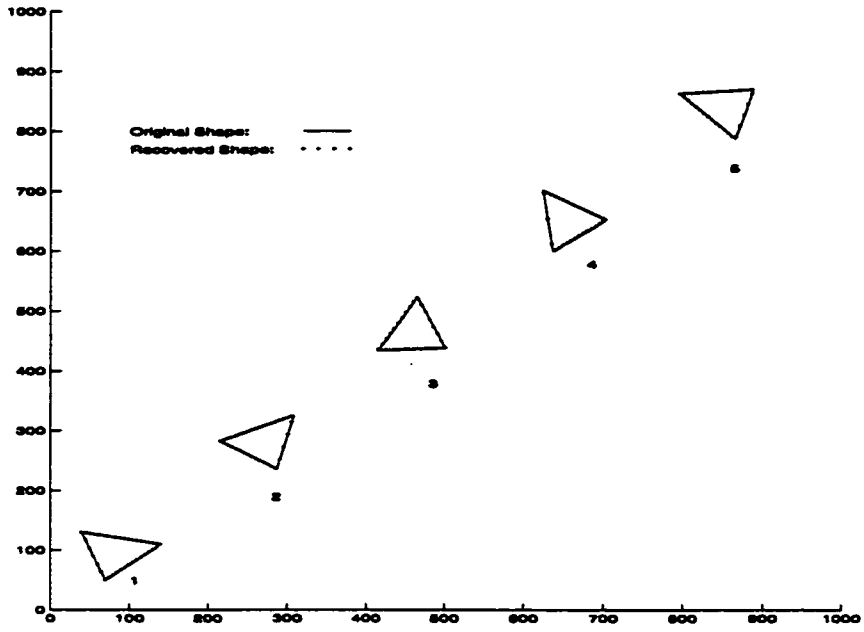

Figure 5.34: Recovering a Triangle on a CRS-CRS Sensor (C.Q.E.) by P.R.

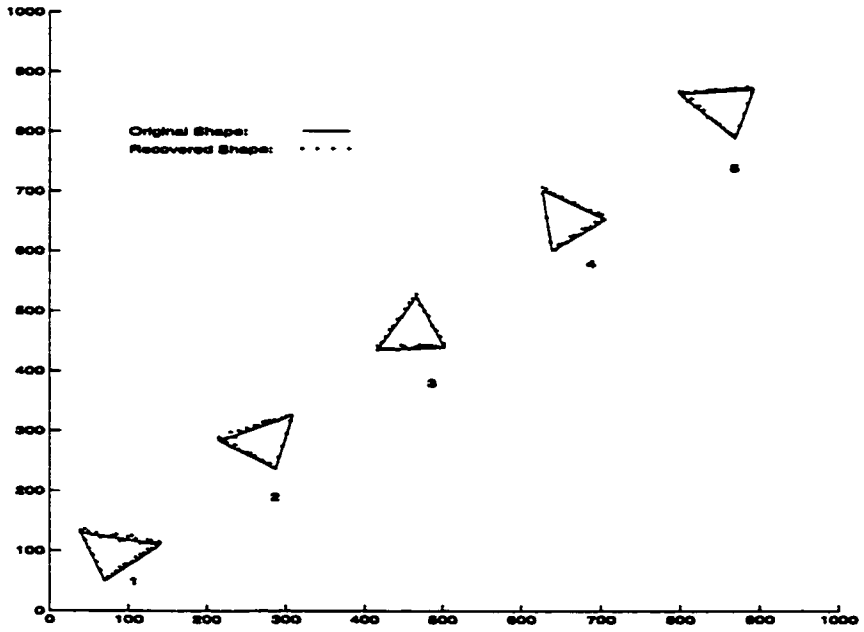

Figure 5.35: Recovering a Triangle on a CRS-CRS Sensor (C.Q.E. & P.U. Profile I) by P.R.

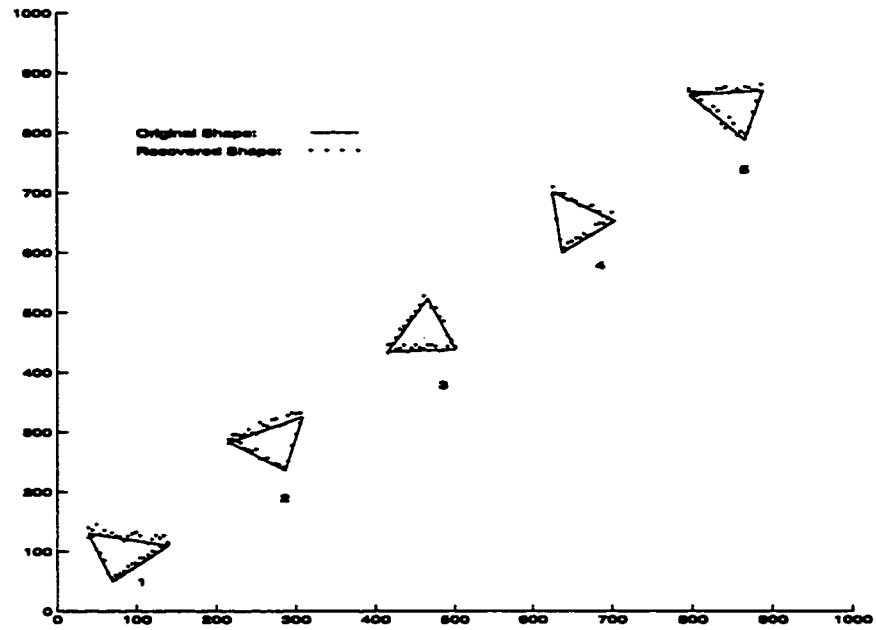

Figure 5.36: Recovering a Triangle on a CRS-CRS Sensor (C.Q.E. & P.U. Profile II) by P.R.

Hybrid Sensor Type: CRS-CRS Recovery Algorithm: Profile Reconstruction Simulated Shape: Triangle						
Reference		Pos. 1	Pos. 2	Pos. 3	Pos. 4	Pos. 5
Figure 5.33	M.C.	0.000	0.000	0.000	0.000	0.000
	A.O.E.	0.000	0.000	0.000	0.000	0.000
	A.P.E.	0.000	0.000	0.000	0.000	0.000
Figure 5.34	M.C.	0.011	0.013	0.004	0.080	0.012
	A.O.E.	0.006	0.011	0.003	0.031	0.004
	A.P.E.	0.340	0.412	0.167	0.203	0.211
Figure 5.35	M.C.	0.024	0.035	0.064	0.051	0.029
	A.O.E.	0.014	0.021	0.020	0.015	0.022
	A.P.E.	4.318	2.517	3.084	2.341	2.305
Figure 5.36	M.C.	0.104	0.086	0.072	0.062	0.069
	A.O.E.	0.094	0.027	0.042	0.015	0.032
	A.P.E.	9.866	5.012	4.368	4.667	5.328

Table 5.8: Quantitative Mismatch between the Original and the Recovered Triangle in Each Simulated Position (CRS-CRS Sensor and P.R. Algorithm).

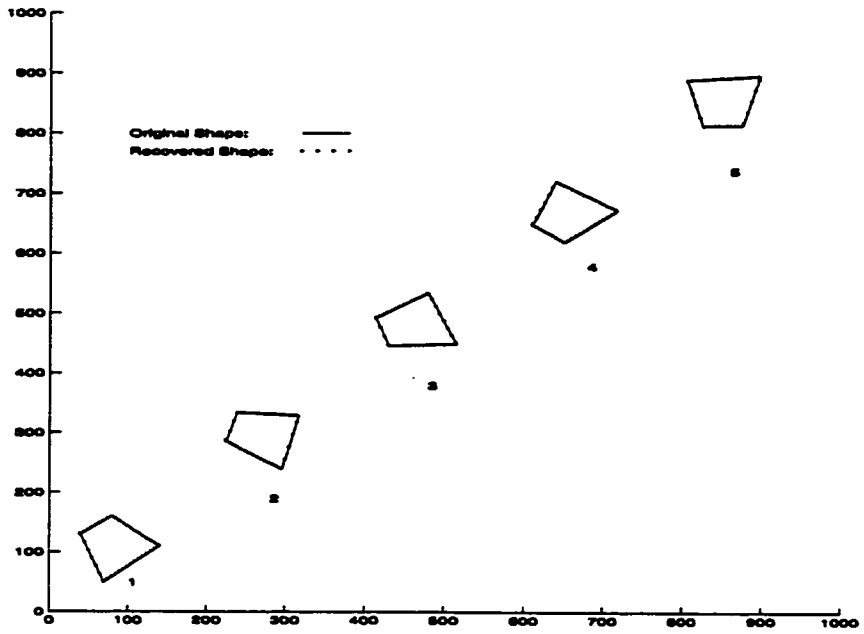

Figure 5.37: Recovering a Tetragon on an ideal CRS-CRS Sensor by P.R.

The eighth set of simulations was done with a tetragon on a CRS-CRS hybrid sensor using Profile Reconstruction. Figure 5.37 to Figure 5.40 show the simulation results under different error conditions. In the first scenario, the algorithm recovered the profile of the original tetragon perfectly when an ideal sensor was simulated. In the second scenario, there was no significant degradation in the accuracy of the algorithm in producing the original shape with the existence of C.Q.E. (see Figure 5.38). Shape recovery was acceptable with P.U. profiles I and II. Table 5.9 gives the quantitative errors in recovering a tetragon.

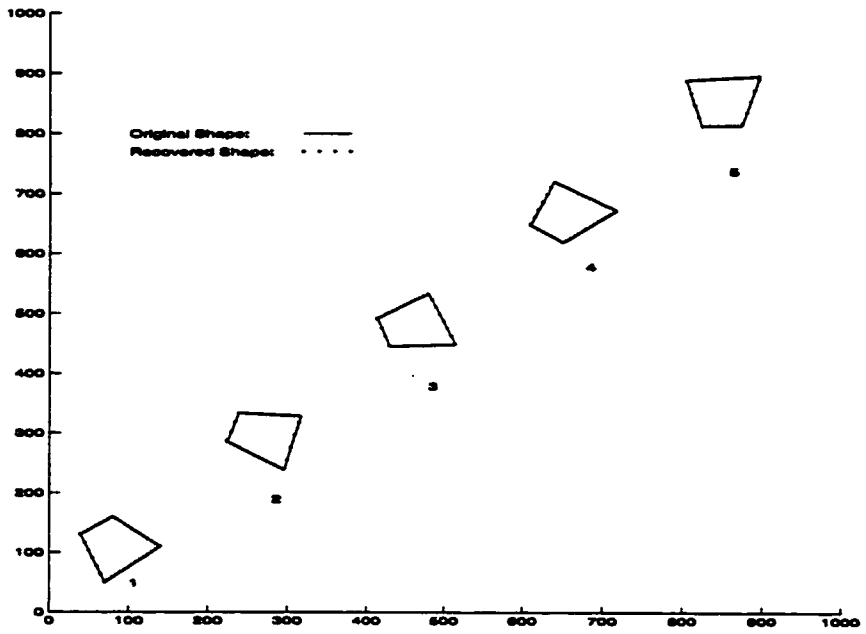

Figure 5.38: Recovering a Tetragon on a CRS-CRS Sensor (C.Q.E.) by P.R.

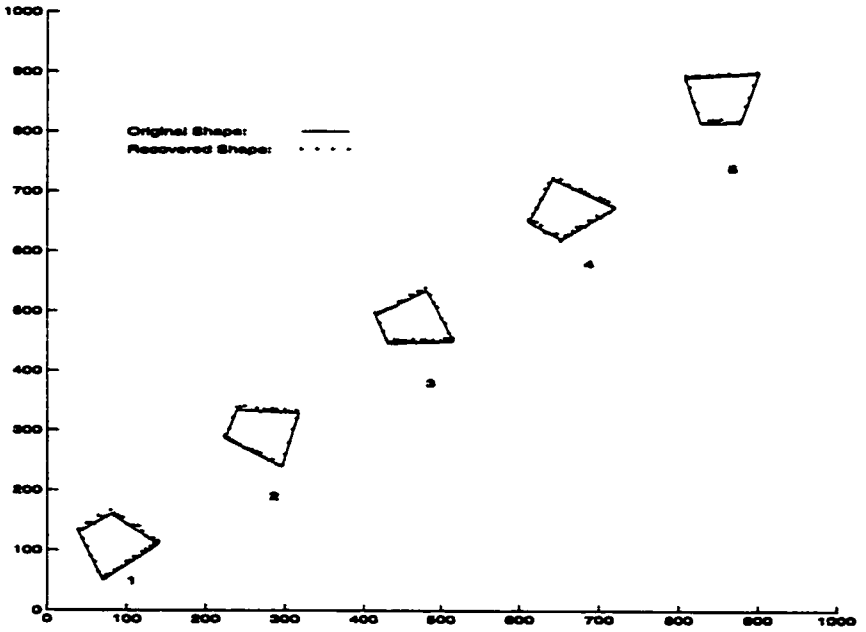

Figure 5.39: Recovering a Tetragon on a CRS-CRS Sensor (C.Q.E. & P.U. Profile I) by P.R.

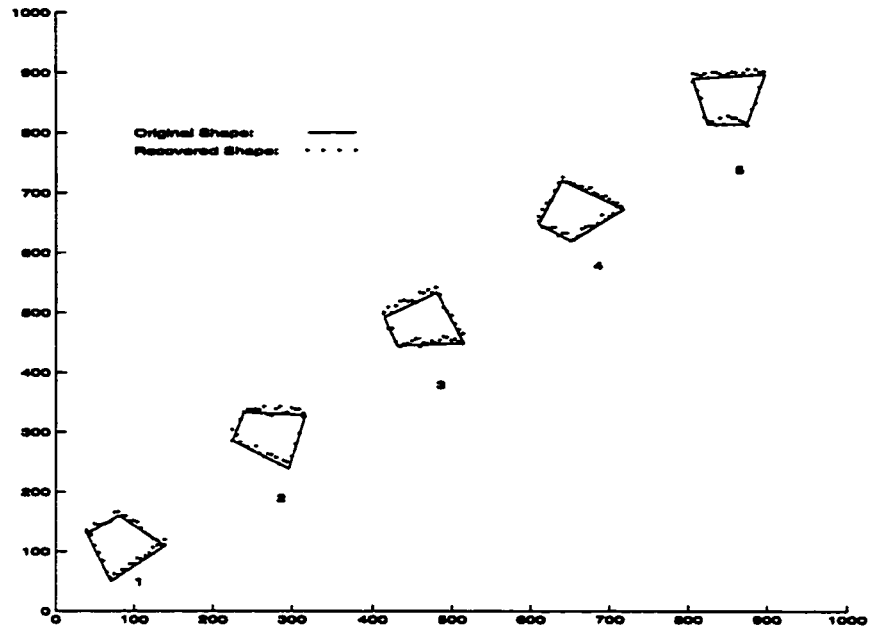

Figure 5.40: Recovering a Tetragon on a CRS-CRS Sensor (C.Q.E. & P.U. Profile II) by P.R.

Hybrid Sensor Type: CRS-CRS Recovery Algorithm: Profile Reconstruction Simulated Shape: Tetragon						
Reference		Pos. 1	Pos. 2	Pos. 3	Pos. 4	Pos. 5
Figure 5.37	M.C.	0.000	0.000	0.000	0.000	0.000
	A.O.E.	0.000	0.000	0.000	0.000	0.000
	A.P.E.	0.000	0.000	0.000	0.000	0.000
Figure 5.38	M.C.	0.005	0.019	0.031	0.016	0.015
	A.O.E.	0.001	0.015	0.008	0.016	0.003
	A.P.E.	0.175	0.641	0.776	0.056	0.340
Figure 5.39	M.C.	0.064	0.045	0.048	0.052	0.040
	A.O.E.	0.009	0.022	0.010	0.019	0.008
	A.P.E.	4.238	2.515	2.614	2.331	2.508
Figure 5.40	M.C.	0.078	0.072	0.085	0.080	0.078
	A.O.E.	0.045	0.032	0.041	0.035	0.022
	A.P.E.	4.601	5.381	6.221	5.617	5.518

Table 5.9: Quantitative Mismatch between the Original and the Recovered Tetragon in Each Simulated Position (CRS-CRS Sensor and P.R. Algorithm).

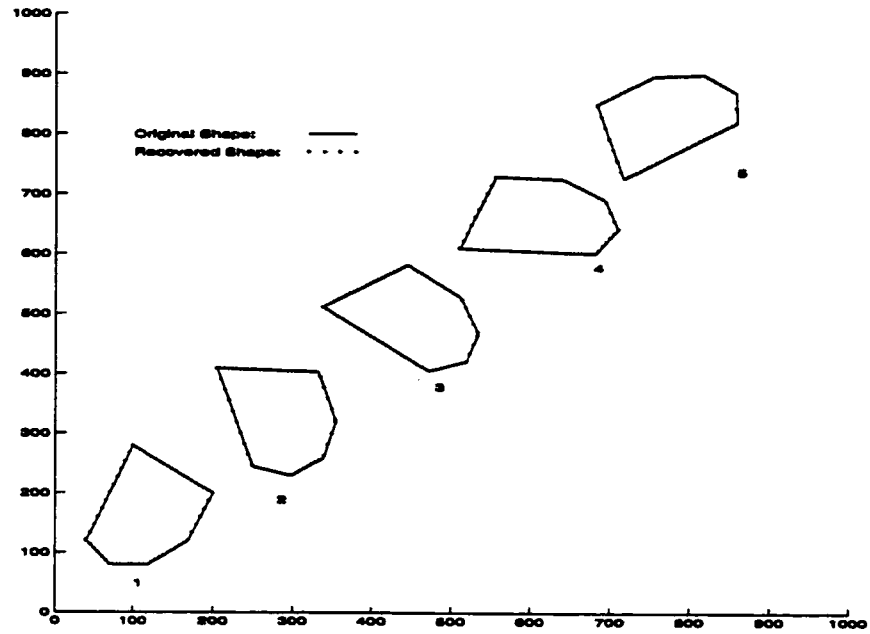

Figure 5.41: Recovering a Hexagon on an ideal CRS-CRS Sensor by P.R.

The ninth set of simulations was done with a hexagon on a CRS-CRS hybrid sensor using Profile Reconstruction. Figure 5.41 to Figure 5.44 show the simulation results with various noise levels. With an ideal sensor in the first scenario, the algorithm reproduced the profile of the original hexagon perfectly. In the second scenario, the algorithm still gave satisfactory results when only C.Q.E. was introduced (see Figure 5.42). The recovered profiles were acceptable with P.U. profiles I and II. Table 5.10 shows the quantitative errors in recovering a hexagon.

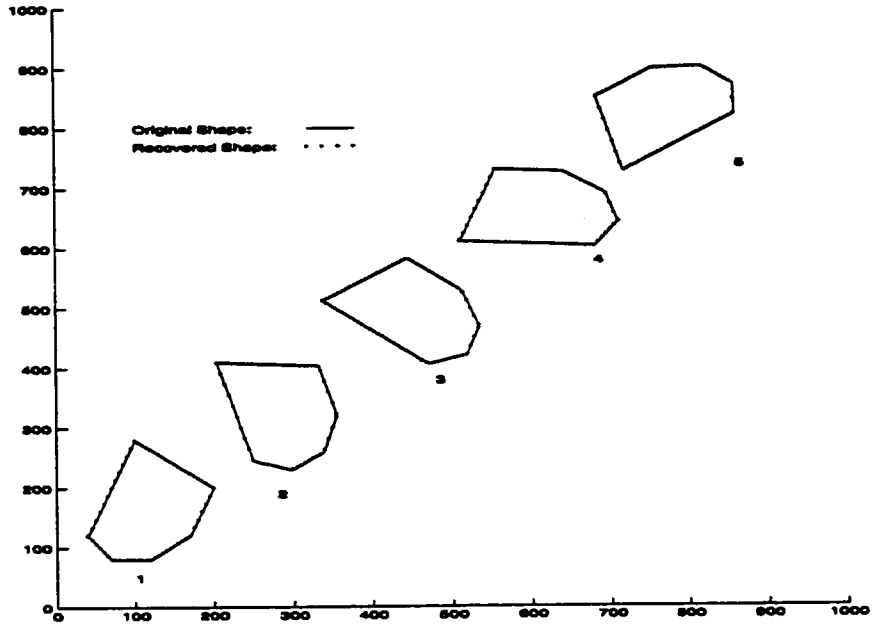

Figure 5.42: Recovering a Hexagon on a CRS-CRS Sensor (C.Q.E.) by P.R.

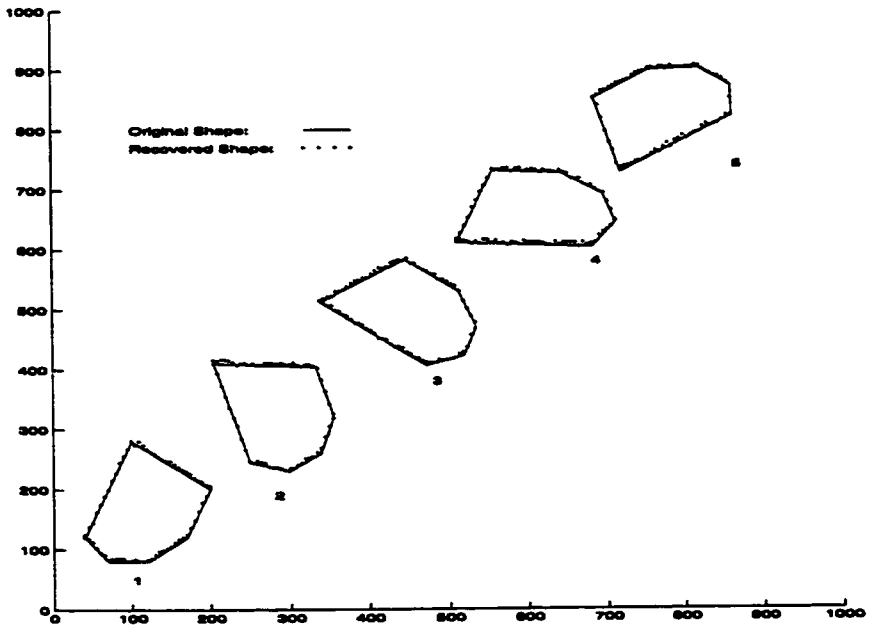

Figure 5.43: Recovering a Hexagon on a CRS-CRS Sensor (C.Q.E. & P.U. Profile I) by P.R.

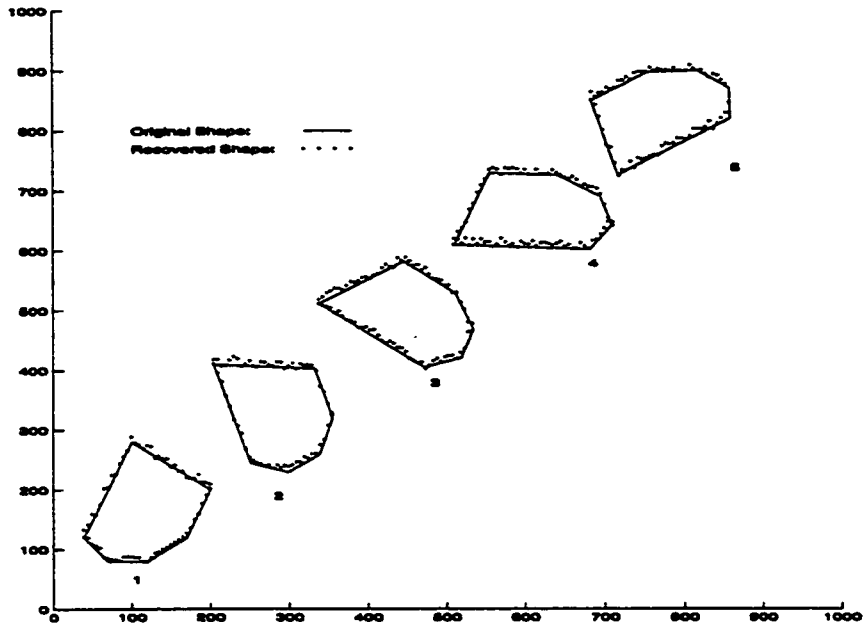

Figure 5.44: Recovering a Hexagon on a CRS-CRS Sensor (C.Q.E. & P.U. Profile II) by P.R.

Hybrid Sensor Type: CRS-CRS Recovery Algorithm: Profile Reconstruction Simulated Shape: Hexagon						
Reference		Pos. 1	Pos. 2	Pos. 3	Pos. 4	Pos. 5
Figure 5.41	M.C.	0.000	0.000	0.000	0.000	0.000
	A.O.E.	0.000	0.000	0.000	0.000	0.000
	A.P.E.	0.000	0.000	0.000	0.000	0.000
Figure 5.42	M.C.	0.006	0.023	0.015	0.032	0.034
	A.O.E.	0.009	0.001	0.004	0.008	0.022
	A.P.E.	0.050	0.644	0.480	0.264	2.750
Figure 5.43	M.C.	0.034	0.035	0.025	0.036	0.031
	A.O.E.	0.019	0.017	0.008	0.014	0.020
	A.P.E.	2.512	1.975	2.031	2.612	1.877
Figure 5.44	M.C.	0.062	0.073	0.075	0.070	0.085
	A.O.E.	0.025	0.030	0.021	0.022	0.018
	A.P.E.	3.624	2.931	3.678	4.213	3.031

Table 5.10: Quantitative Mismatch between the Original and the Recovered Hexagon in Each Simulated Position (CRS-CRS Sensor and P.R. Algorithm).

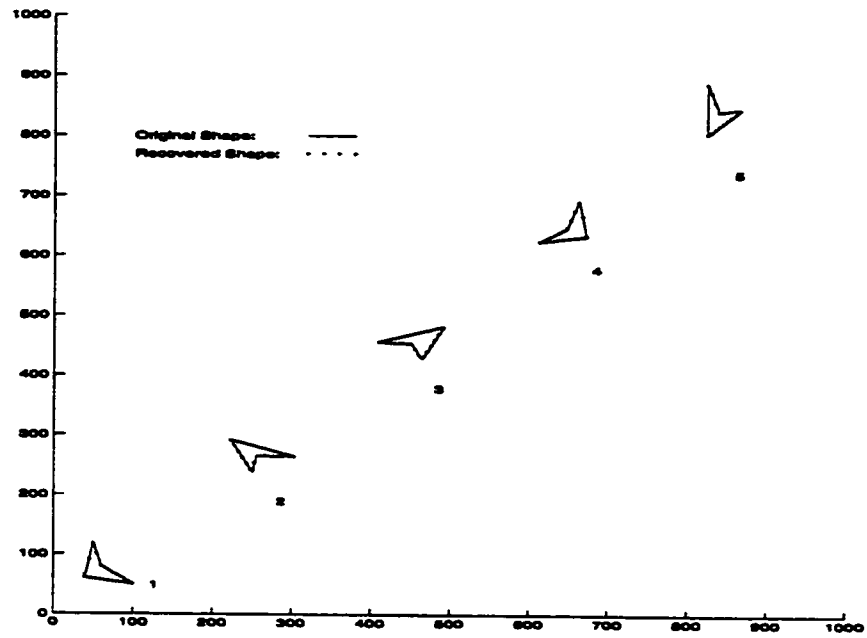

Figure 5.45: Recovering a Concave Tetragon on an ideal CRS-CRS Sensor by P.R.

As discussed in Chapter 4, the assumption of a straightly convex original shape is not necessary when the Profile Reconstruction Algorithm is used. As far as the convexity of the original shape is maintained in the digital dimension, the sets of k_h and k_l can still be used to estimate the original l and w in each sensor column. To verify this advantage of the Profile Reconstruction Algorithm, the tenth set of simulations used a concave tetragon. Figure 5.45 to Figure 5.48 show their graphical results. In the first scenario, an ideal sensor was assumed and the resulted profile matched the original perfectly (see Figure 5.45). Even when C.Q.E. was added in the second scenario, no significant mismatch between the recovered profile and the original could be observed in Figure 5.46. Satisfactory shape recovery could be achieved even under P.U. profiles I and II. Table 5.11 summarizes the quantitative error in shape recovery for the first three scenarios.

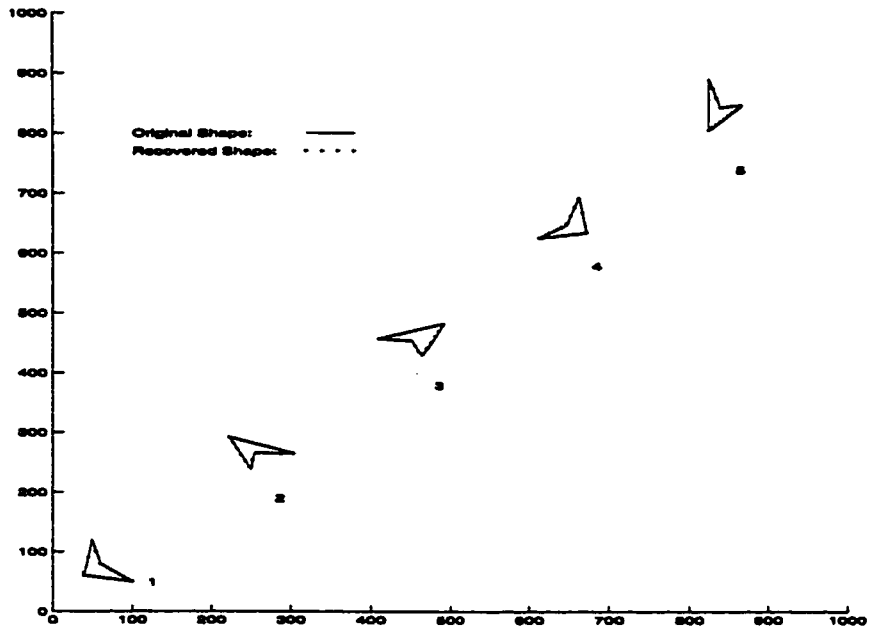

Figure 5.46: Recovering a Concave on a CRS-CRS Sensor (C.Q.E.) by P.R.

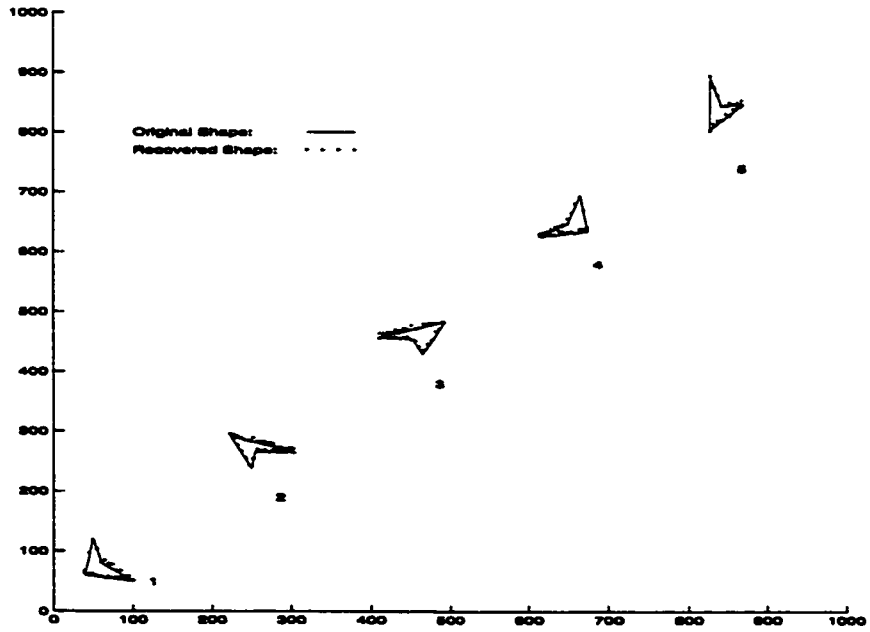

Figure 5.47: Recovering a Concave Tetragon on a CRS-CRS Sensor (C.Q.E & P.U. Profile I) by P.R.

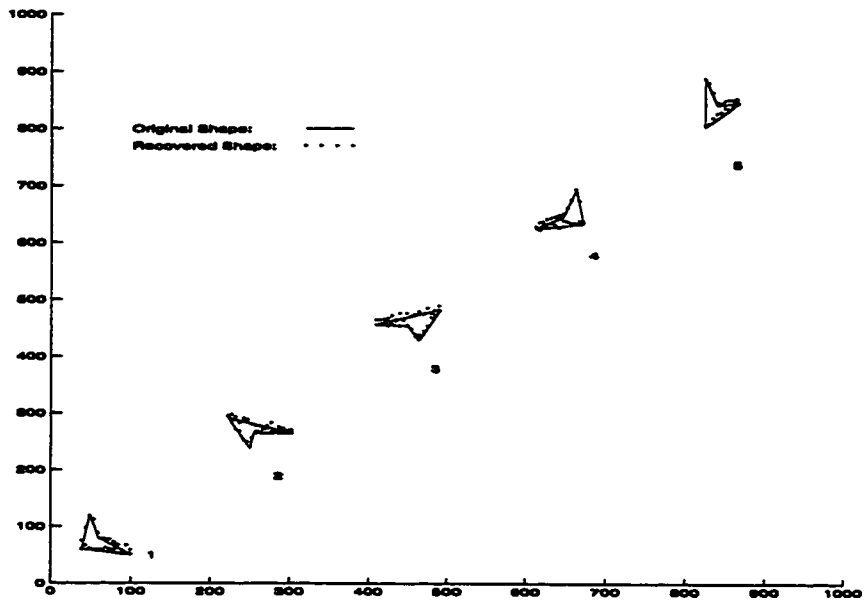

Figure 5.48: Recovering a Concave Tetragon on a CRS-CRS Sensor (C.Q.E & P.U. Profile II) by P.R.

Hybrid Sensor Type: CRS-CRS Recovery Algorithm: Profile Reconstruction Simulated Shape: Concave Tetragon						
Reference		Pos. 1	Pos. 2	Pos. 3	Pos. 4	Pos. 5
Figure 5.45	M.C.	0.000	0.000	0.000	0.000	0.000
	A.O.E.	0.000	0.000	0.000	0.000	0.000
	A.P.E.	0.000	0.000	0.000	0.000	0.000
Figure 5.46	M.C.	0.037	0.035	0.021	0.042	0.036
	A.O.E.	0.033	0.014	0.005	0.010	0.014
	A.P.E.	1.575	0.378	0.437	0.382	0.395
Figure 5.47	M.C.	0.053	0.039	0.058	0.055	0.062
	A.O.E.	0.072	0.045	0.036	0.040	0.047
	A.P.E.	3.680	3.471	3.372	2.982	3.114
Figure 5.48	M.C.	0.072	0.080	0.077	0.098	0.095
	A.O.E.	0.080	0.067	0.058	0.069	0.072
	A.P.E.	4.831	3.902	5.011	4.367	3.584

Table 5.11: Quantitative Mismatch between the Original and the Recovered Concave Tetragon in Each Simulated Position (CRS-CRS Sensor and P.R. Algorithm).

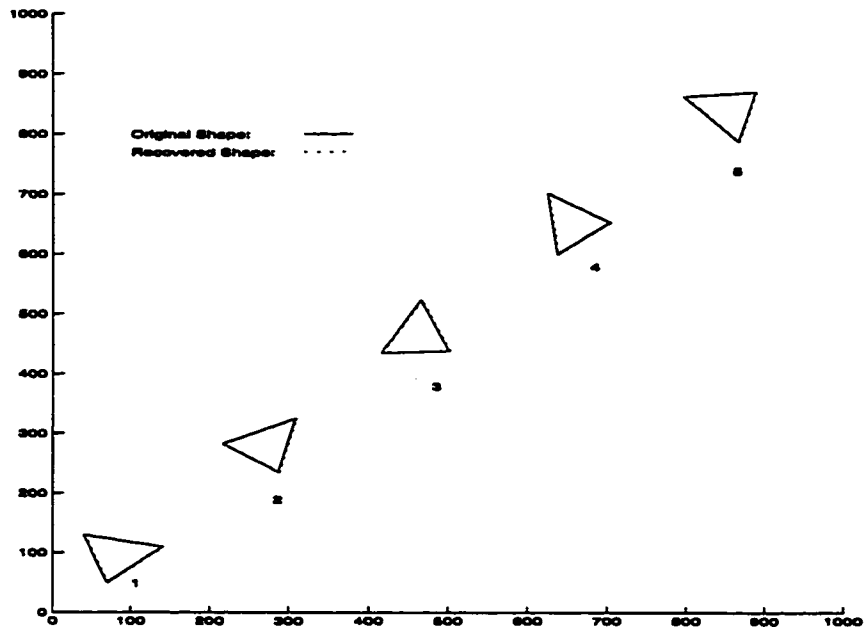

Figure 5.49: Recovering a Triangle on a ideal CRS-M Sensor by V.R.

5.5 Simulation Results with a CRS-M Hybrid Sensor

As only a set of k is provided by this type of sensor, we can only apply the Vertex Reconstruction algorithm for shape recovery. The eleventh set of simulations was done with a triangle on a CRS-M sensor using Vertex Reconstruction. Figure 5.49 to Figure 5.52 show the results of shape recovery under different error conditions and Table 5.12 summarizes the quantitative errors. In the first scenario, ideal condition was simulated and the resulting shape matched the original perfectly (see Figure 5.49). When only C.Q.E. and T.E. were included in the second scenario, the algorithm produced accurate estimates on the vertices as illustrated in Figure 5.50. In the third scenario, P.U. profiles I was added, yet only minor discrepancies were noted in the recovered shapes (see Figure 5.51). However, the performance of the algorithm got worse with increasing noise level. As shown in Figure 5.52, the recovered shapes were noisier with P.U. profile II.

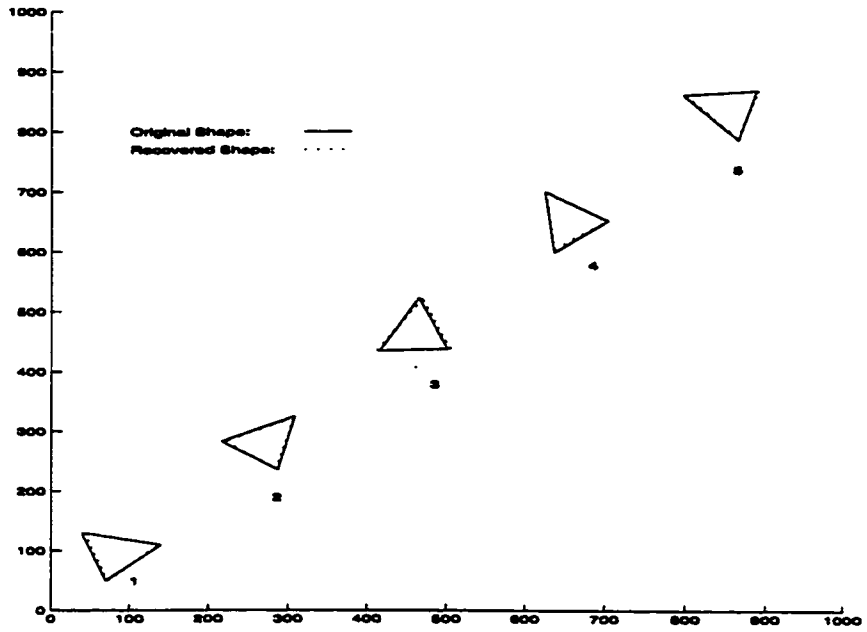

Figure 5.50: Recovering a Triangle on a CRS-M Sensor (C.Q.E. & T.E.) by V.R.

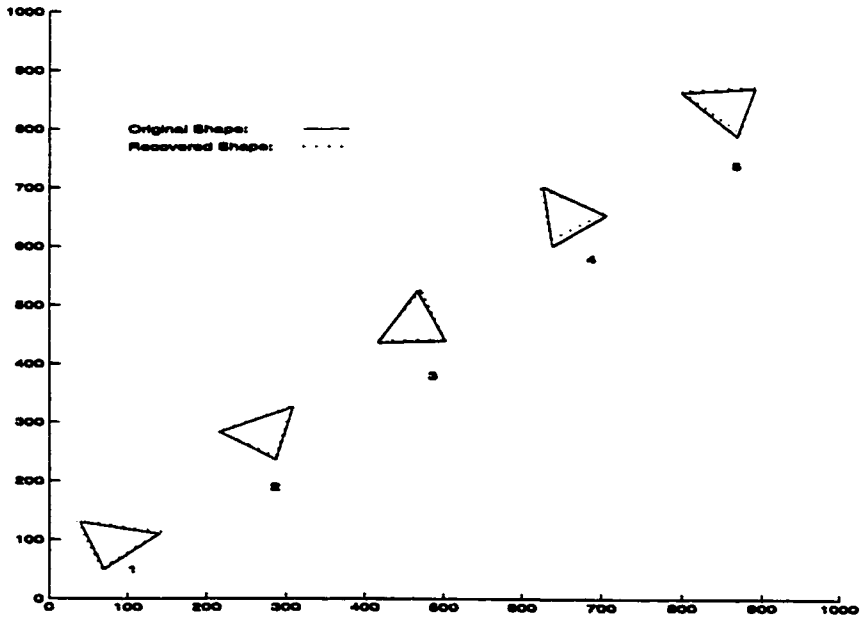

Figure 5.51: Recovering a Triangle on a CRS-M Sensor (C.Q.E., T.E. & P.U. Profile I) by V.R.

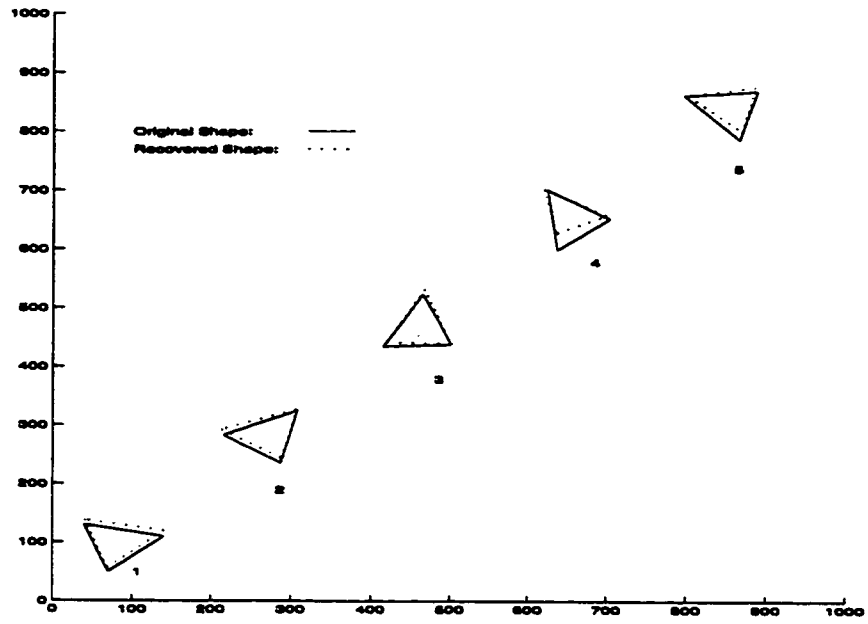

Figure 5.52: Recovering a Triangle on a CRS-M Sensor (C.Q.E., T.E. & P.U. Profile II) by V.R.

Hybrid Sensor Type: CRS-M Recovery Algorithm: Vertex Reconstruction Simulated Shape: Triangle						
Reference		Pos. 1	Pos. 2	Pos. 3	Pos. 4	Pos. 5
Figure 5.49	M.C.	0.000	0.000	0.000	0.000	0.000
	A.O.E.	0.000	0.000	0.000	0.000	0.000
	A.P.E.	0.000	0.000	0.000	0.000	0.000
Figure 5.50	M.C.	0.046	0.060	0.074	0.051	0.030
	A.O.E.	0.029	0.009	0.064	0.018	0.003
	A.P.E.	1.020	0.448	1.044	1.407	1.609
Figure 5.51	M.C.	0.055	0.072	0.063	0.088	0.076
	A.O.E.	0.011	0.023	0.030	0.056	0.043
	A.P.E.	2.315	2.612	1.981	3.207	3.650
Figure 5.52	M.C.	0.082	0.098	0.075	0.198	0.093
	A.O.E.	0.045	0.036	0.035	0.117	0.053
	A.P.E.	5.373	4.602	3.681	10.237	5.314

Table 5.12: Quantitative Mismatch between the Original and the Recovered Triangle in Each Simulated Position (CRS-M Sensor and V.R. Algorithm).

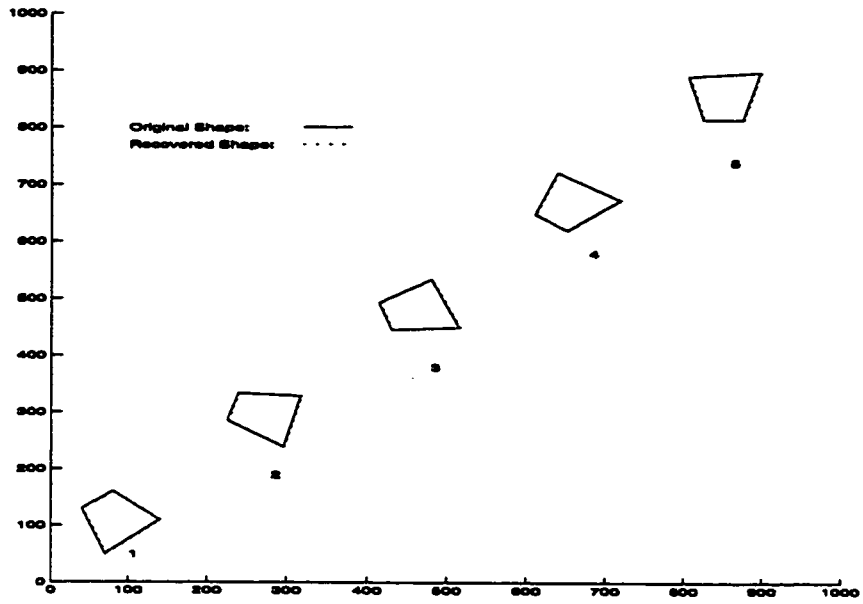

Figure 5.53: Recovering a Tetragon on a ideal CRS-M Sensor by V.R.

The twelfth set of simulations was done on a tetragon. Figure 5.53 to Figure 5.56 show graphically the results with various error conditions and Table 5.13 summarizes their quantitative errors. With an ideal CRS-M sensor, Vertex Reconstruction recovered the original tetragon perfectly. When C.Q.E. and T.E. were introduced, only insignificant errors were found in shape recovery. With P.U. profile I, the recovered shapes were only slight off from the original. The error in shape recovery increased as P.U. profile II is used.

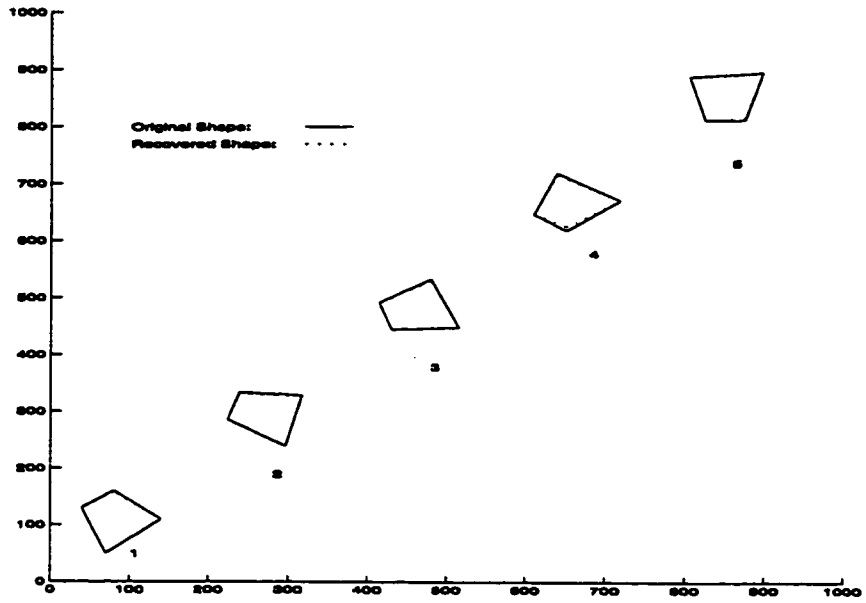

Figure 5.54: Recovering a Tetragon on a CRS-M Sensor (C.Q.E. & T.E.) by V.R.

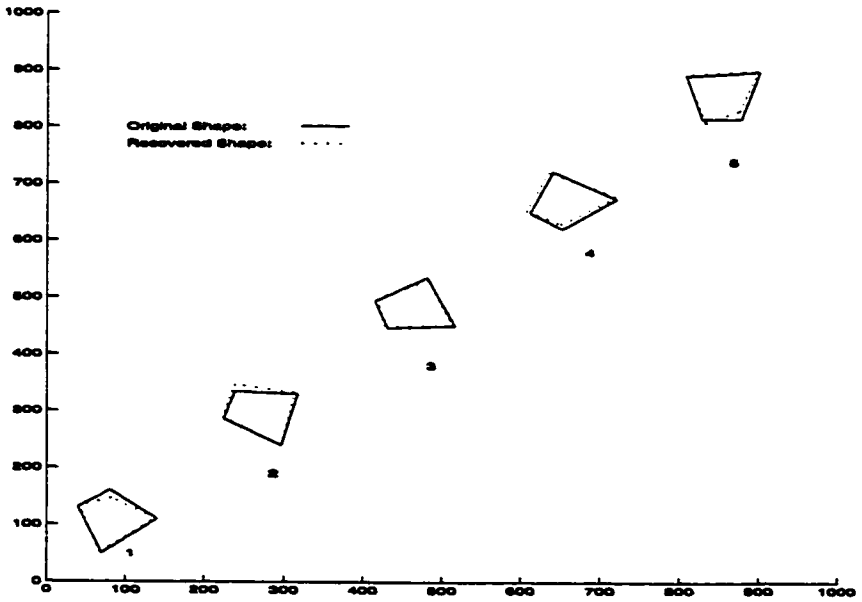

Figure 5.55: Recovering a Tetragon on a CRS-M Sensor (C.Q.E., T.E. & P.U. Profile I) by V.R.

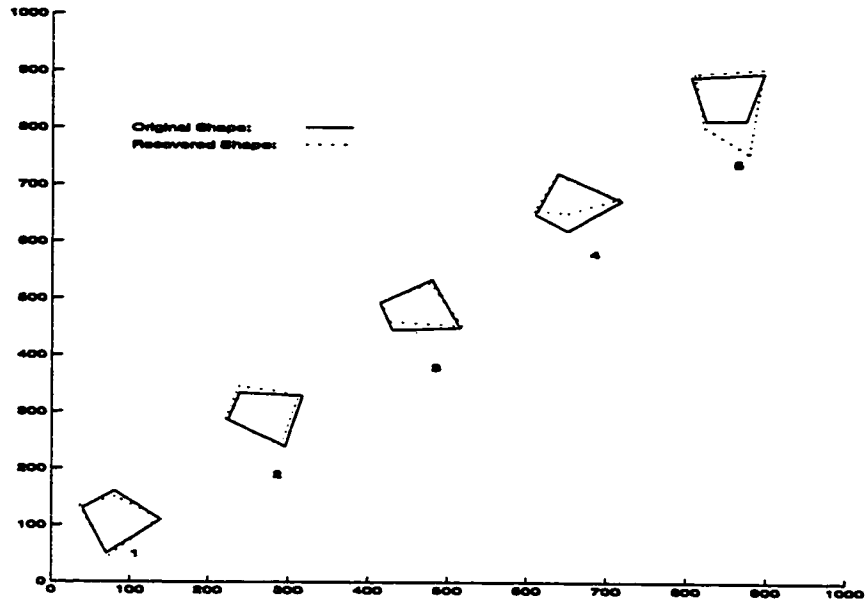

Figure 5.56: Recovering a Tetragon on a CRS-M Sensor (C.Q.E., T.E. & P.U. Profile II) by V.R.

Hybrid Sensor Type: CRS-M Recovery Algorithm: Vertex Reconstruction Simulated Shape: Tetragon						
Reference		Pos. 1	Pos. 2	Pos. 3	Pos. 4	Pos. 5
Figure 5.53	M.C.	0.000	0.000	0.000	0.000	0.000
	A.O.E.	0.000	0.000	0.000	0.000	0.000
	A.P.E.	0.000	0.000	0.000	0.000	0.000
Figure 5.54	M.C.	0.014	0.022	0.028	0.082	0.041
	A.O.E.	0.001	0.026	0.004	0.000	0.006
	A.P.E.	0.525	0.625	0.600	1.300	0.350
Figure 5.55	M.C.	0.083	0.052	0.065	0.076	0.107
	A.O.E.	0.48	0.014	0.010	0.024	0.050
	A.P.E.	5.112	4.338	0.781	3.538	4.611
Figure 5.56	M.C.	0.078	0.060	0.081	0.128	0.312
	A.O.E.	0.045	0.020	0.063	0.084	0.103
	A.P.E.	4.981	4.211	6.225	15.367	20.328

Table 5.13: Quantitative Mismatch between the Original and the Recovered Tetragon in Each Simulated Position (CRS-M Sensor and V.R. Algorithm).

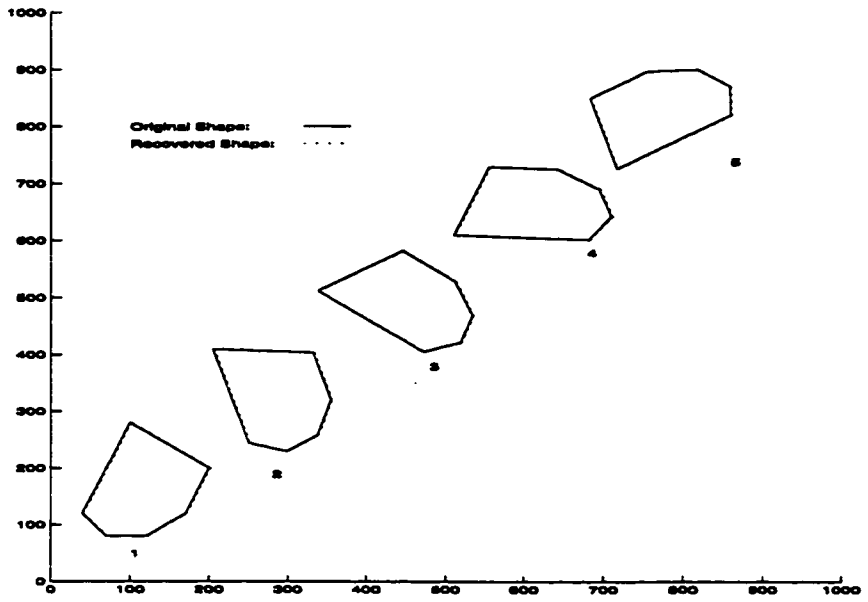

Figure 5.57: Recovering a Hexagon on a ideal CRS-M Sensor by V.R.

The thirteenth set of simulations was done with a hexagon on a CRS-M sensor using Vertex Reconstruction for shape recovery. Figure 5.57 to Figure 5.60 show the simulated results under various error conditions. An ideal sensor was simulated in the first scenario, the algorithm was able to recover the original hexagon perfectly (see Figure 5.57). C.Q.E. and T.E. were then added in the second scenario, only minor errors were found in shape recovery as shown in Figure 5.58. When P.U. profiles I and II were added, noisy signatures caused inaccurate determination of transitional points. Table 5.14 summarizes their quantitative errors.

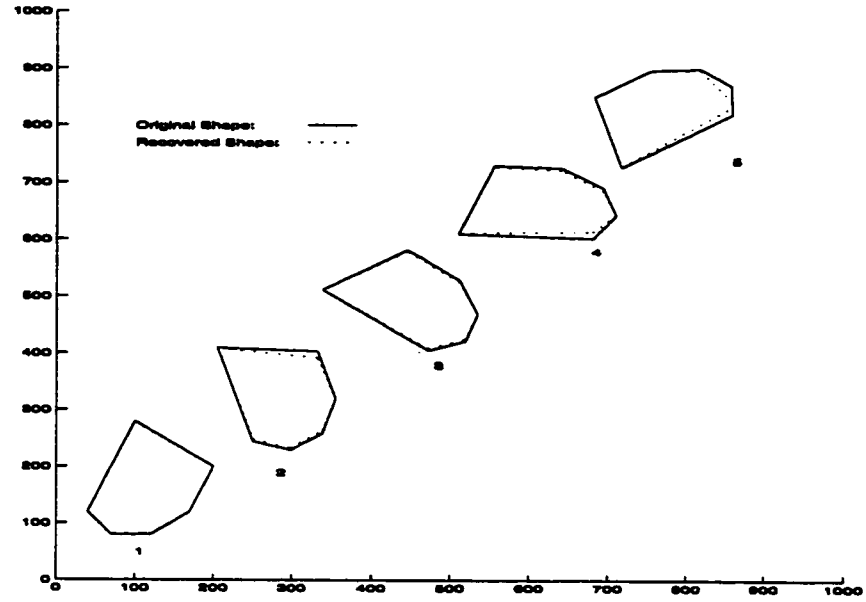

Figure 5.58: Recovering a Hexagon on a CRS-M Sensor (C.Q.E. & T.E.) by V.R.

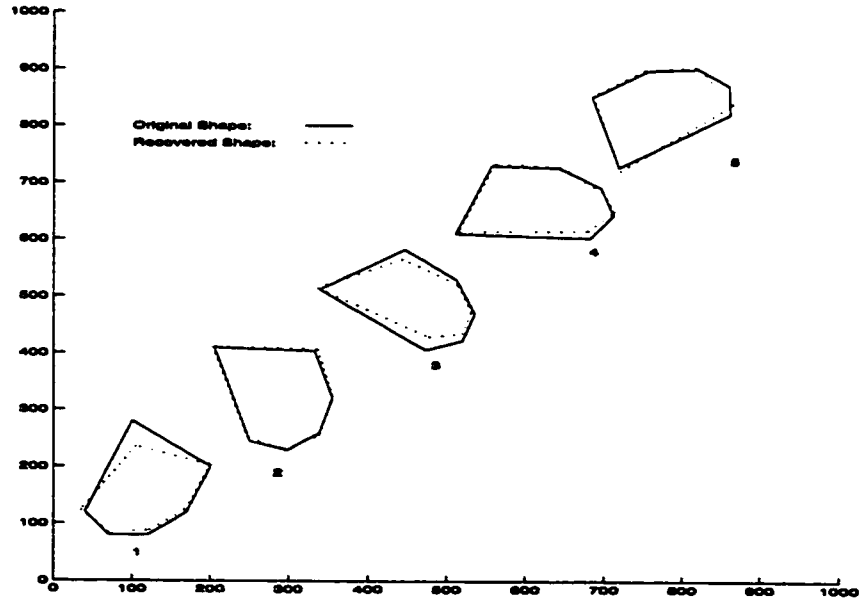

Figure 5.59: Recovering a Hexagon on a CRS-M Sensor (C.Q.E., T.E. & P.U. Profile I) by V.R.

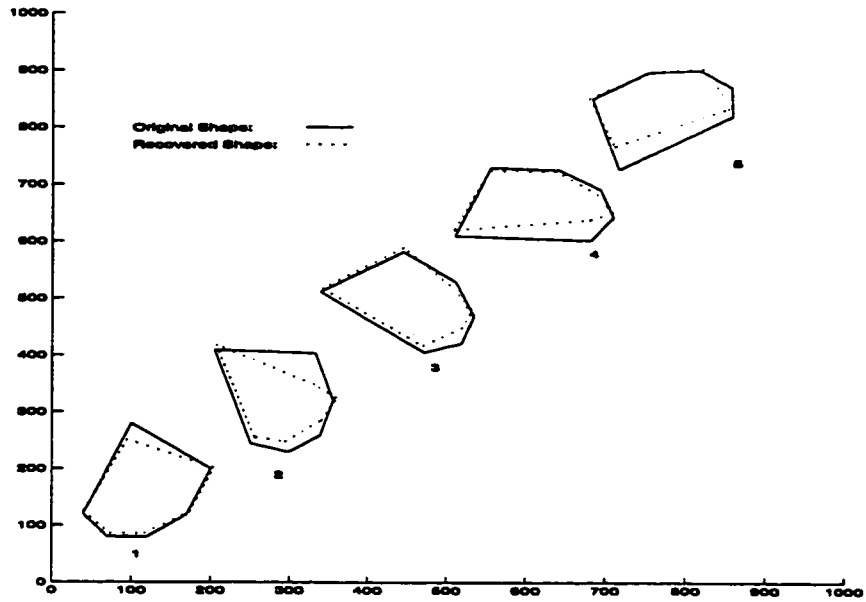

Figure 5.60: Recovering a Hexagon on a CRS-M Sensor (C.Q.E., T.E. & P.U. Profile II) by V.R.

Hybrid Sensor Type: CRS-M Recovery Algorithm: Vertex Reconstruction Simulated Shape: Hexagon						
Reference		Pos. 1	Pos. 2	Pos. 3	Pos. 4	Pos. 5
Figure 5.57	M.C.	0.000	0.000	0.000	0.000	0.000
	A.O.E.	0.000	0.000	0.000	0.000	0.000
	A.P.E.	0.000	0.000	0.000	0.000	0.000
Figure 5.58	M.C.	0.016	0.074	0.042	0.192	0.231
	A.O.E.	0.000	0.001	0.000	0.005	0.029
	A.P.E.	0.133	0.233	0.133	0.350	2.600
Figure 5.59	M.C.	0.320	0.042	0.361	0.187	0.205
	A.O.E.	0.107	0.015	0.048	0.036	0.045
	A.P.E.	13.751	1.687	5.371	2.652	3.065
Figure 5.60	M.C.	0.389	0.325	0.367	0.426	0.438
	A.O.E.	0.097	0.105	0.121	0.114	0.053
	A.P.E.	12.652	15.311	4.365	7.231	10.318

Table 5.14: Quantitative Mismatch between the Original and the Recovered Hexagon in Each Simulated Position (CRS-M Sensor and V.R. Algorithm).

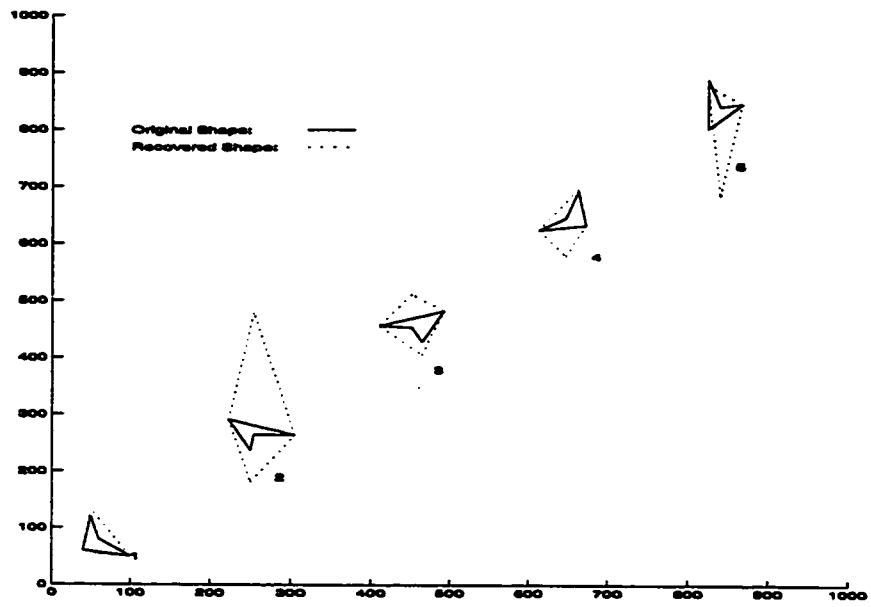

Figure 5.61: Recovering a Concave Polygon on an ideal CRS-M Sensor Using V.R. with k-Pseudo-Signature

As discussed in Chapter 4, the Vertex Reconstruction Algorithm failed to interpret concave shape. Figure 5.61 illustrates the typical ambiguity it caused even when an ideal sensor output was assumed.

5.6 Summary of Simulations

The simulations verified both the Vertex Reconstruction and Profile Reconstruction algorithms. Under ideal conditions, they worked perfectly in recovering the contact shapes. It is shown that Vertex Reconstruction must assume convex polygonal shape, otherwise erroneous shapes were recovered (see Figure 5.19, Figure 5.32 and Figure 5.61). On the other hand, Profile Reconstruction was able to recover those convex polygons simulated for Vertex Reconstruction as well as the concave shapes with the concavity occurred in the digital dimension of the sensor (see Figure 5.45 to Figure 5.48). Vertex Reconstruction depends on the transitional points of a pseudo-signature to recover the vertices of the polygonal shape. It was found that as noise was introduced, pseudo-signatures were distorted. When the noise level was high, P.U. profile II for instance, it was impossible to locate any reliable transitional points for certain configurations of a shape. On the other hand, Pro-

file Reconstruction estimates the lower and upper contact points of each sensing element, which is independent on the outputs from other sensing elements. It is only affected by the error from the concerned sensing element and no transitional point detection is required. Besides, the whole profile of the contact shape was recovered, which is more precise than just the vertices produced by Vertex Reconstruction. As a result, the performance of Profile Reconstruction was better than that of Vertex Reconstruction.

With Vertex Reconstruction, there are choices of k_h, k_l or k, depending on whether a CRS-CRS sensor or CRS-M sensor is used. It was found that under noisy conditions, shape recovery using k_l or k produced similar quantitative errors. Under similar noise conditions, the performance of Vertex Reconstruction using k_h was inferior to that of using either k_l or k. Though it is difficult to compare all the shape recovery case by case, the difference in the general form of coefficients in matrix A and B (see Section 4.2.4) provides some explanations on this phenomenon. In setting up the system of linear equations using k_h, all the coefficients contain the factor k_h. However, in the case of using k_l or k, some of the coefficients are constants such as $2L$ or L, which do not have the factors k_l or k. Hence, the effect of error in k_l or k on the solution of their corresponding system of equations is less serious than the same amount of error in k_h on the solution of its corresponding system of equations.

Chapter 6

Experimental Results

From the simulation results in Chapter 5, it is noted that the shape recovery algorithms are sensitive to noise in the sensor output. Shape recovery becomes unreliable when P.U. profile II is simulated. To see what level of P.U. can be obtained in practice, three prototypes of hybrid sensor were made and some experimental data were collected for analysis.

6.1 Experiments with a CRS-CRS Sensor

The prototype of a CRS-CRS hybrid sensor is shown in Figure 6.1. Conductive silicone rubber of 1 mm thickness was used. It is commercially available as RFI/EMI shielding materials [18] and comes in the form of a sheet. To use it in the prototype, 3 mm wide strips were sliced from the rubber sheet. As the conductivity of silicone rubber changed when it was stretched, the linear conductivity of each strip was adjusted before fixing the two end points. Ten pairs of strips were aligned in parallel and a hard board was used as backing. Non-conductive fabric mesh was laid between the top layer and the bottom layer of strips. These two layers of strips did not touch when no force was applied. When a force was applied on the surface of the sensing elements, their top strips touched the corresponding strips at the bottom through the openings of the fabric mesh. The setup measures 6.5 cm (digital dimension) by 32.5 cm (analog dimension). Since there were only ten columns of sensing elements in the setup, the resolution in the digital dimension was limited to 1.5 sensing element per cm. As visual measurement was done in the analog dimension, its resolution was 0.1 cm, which was limited by the tape measure used. Since the length of each sensing element was 32.5 cm, the equivalent maximum C.Q.E. was $\pm\frac{1}{325}$. For simplicity, only a rectangular object was used in the experiments.

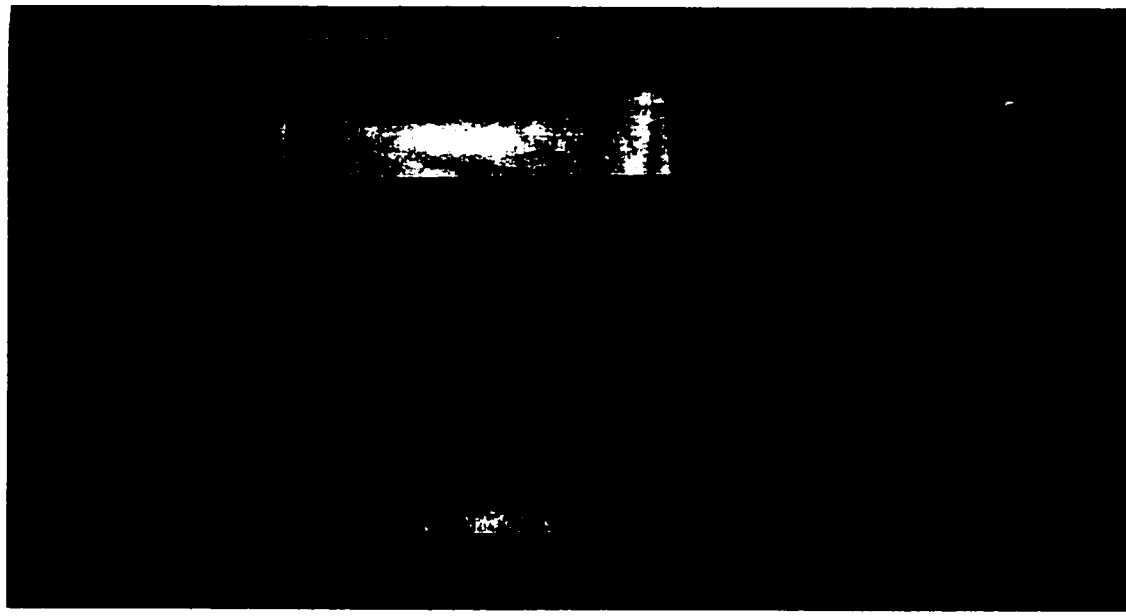

Figure 6.1: Prototype of a CRS-CRS Sensor with Ten Sensing Elements

6.1.1 Calibrations of a CRS-CRS Sensor

As discussed in Chapter 3, it is ideal when conductivities of the two rubber strips in a pair are assumed to be equal and linearly uniform. In practice, ideal conditions are difficult to achieve and calibration is required to compensate major discrepancies. First, each sensor column was equally divided into 32.5 units along the length of the strips. Then, three runs of calibrations with a reference voltage of 6.05V were done as follows:

1. A point contact was made at the 1, 2, 3, ... unit mark in turn. Both V_h and V_l were recorded. They were compared to the expected values according to equations 3.1 and 3.2. Their means were then calculated as $V_{h(w=0)}$ and $V_{l(w=0)}$.
2. A 5-unit long contact was made starting at the 1, 2, 3, ... unit marks. Another pair of means, $V_{h(w=5)}$ and $V_{l(w=5)}$ were obtained.
3. Repeat step 2 above with a 10-unit length of contact and obtain the means, $V_{h(w=10)}$ and $V_{l(w=10)}$.

Figure 6.2 to Figure 6.4 show the calibration graphs for the first strip-pair of the CRS-CRS sensor prototype. It was found that the measured voltages (represented by crosses in the figures) were consistently higher than the expected voltages (represented by solid line in the figures). This discrepancy various slightly with w for a given l. It was impractical and impossible to tabulate the required voltage adjustment for each combination of l and w.

$V_{ref} = 6.05V$	Sensing Element Number									
	1	2	3	4	5	6	7	8	9	10
Calibration Factor for V_h (V)	0.345	0.016	0.353	0.317	0.080	0.161	0.070	0.261	0.168	0.291
Calibration Factor for V_l (V)	0.316	0.006	0.359	0.325	0.073	0.155	0.072	0.243	0.137	0.290

Table 6.1: Calibration Factors for Each Sensing Element of the CRS-CRS Hybrid Sensor Prototype.

Instead, the mean difference between the measured and expected voltages from the above calibration results was used as an calibration factor as follows:

$$V_{hOffset} = \frac{V_{h(w=0)} + V_{h(w=5)} + V_{h(w=10)}}{3} \tag{6.1}$$

$$V_{lOffset} = \frac{V_{l(w=0)} + V_{l(w=5)} + V_{l(w=10)}}{3} \tag{6.2}$$

Table 6.1 lists the calibration factors for all the ten sensing elements. In practice, the corresponding calibration factor was subtracted from the measured voltage of each sensing element before further processing. For example, if the measured outputs are V_h and V_l, the adjusted outputs are given by:

$$V_{hAdj} = V_h - V_{hOffset} \tag{6.3}$$

$$V_{lAdj} = V_l - V_{lOffset} \tag{6.4}$$

Though this calibration is simple, it is a compromise by approximating a non-linear function with a linear function. Over-adjustment exists near the two ends of a sensing element, but it worked reasonably well with the sensor prototype.

6.1.2 Results of Recovering a Rectangle Using the Vertex Reconstruction Algorithm with a CRS-CRS Sensor and k_h-Pseudo-Signature

Experiments were done with a rectangular planar object of dimension 5 cm by 3.5 cm. It was pressed against different positions on the sensor surface. Typical results are illustrated

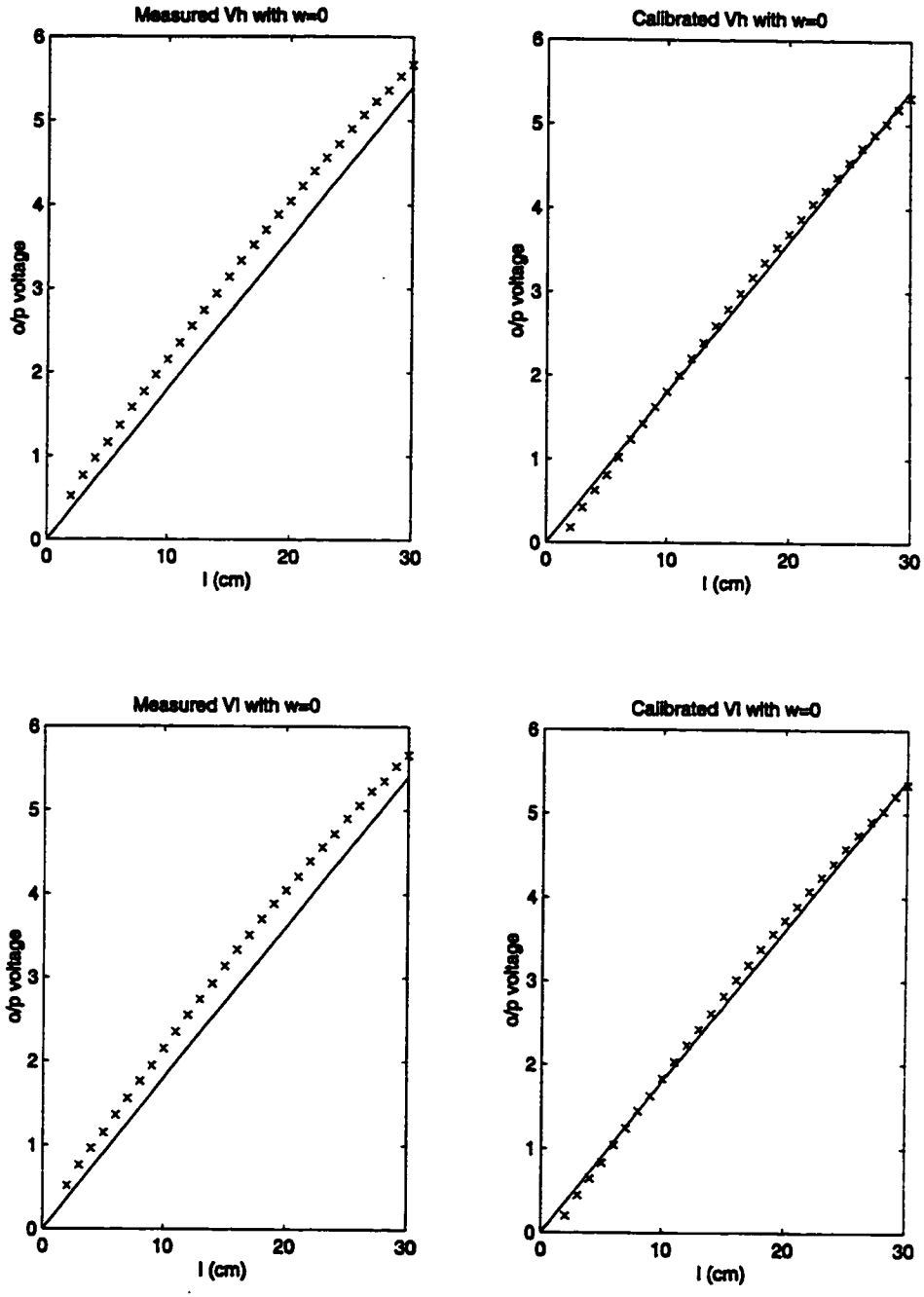

Figure 6.2: Calibration Graphs for the First Sensing Element in the CRS-CRS Hybrid Sensor Prototype ($w = 0$).

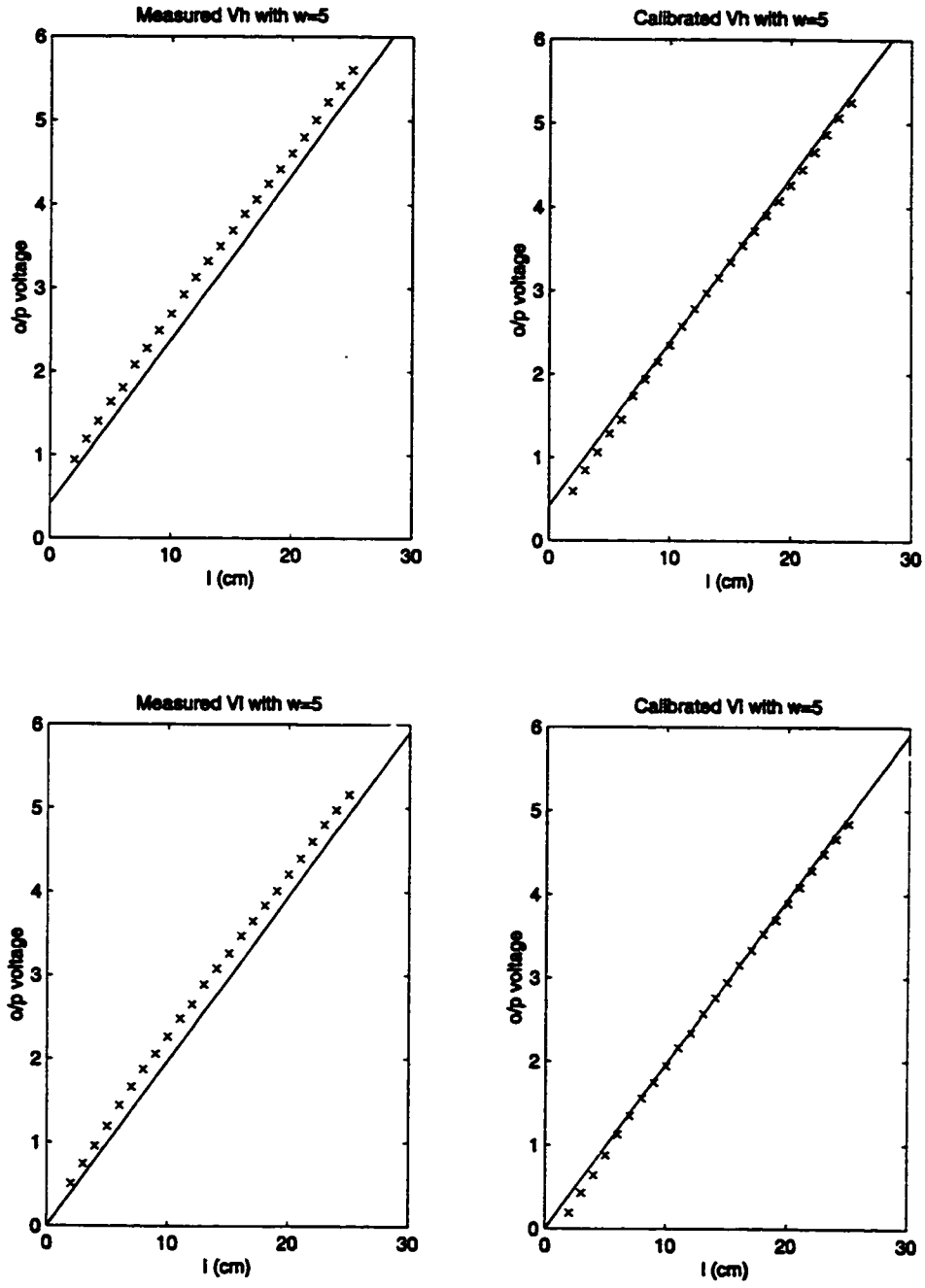

Figure 6.3: Calibration Graphs for the First Sensing Element in the CRS-CRS Hybrid Sensor Prototype ($w = 5$).

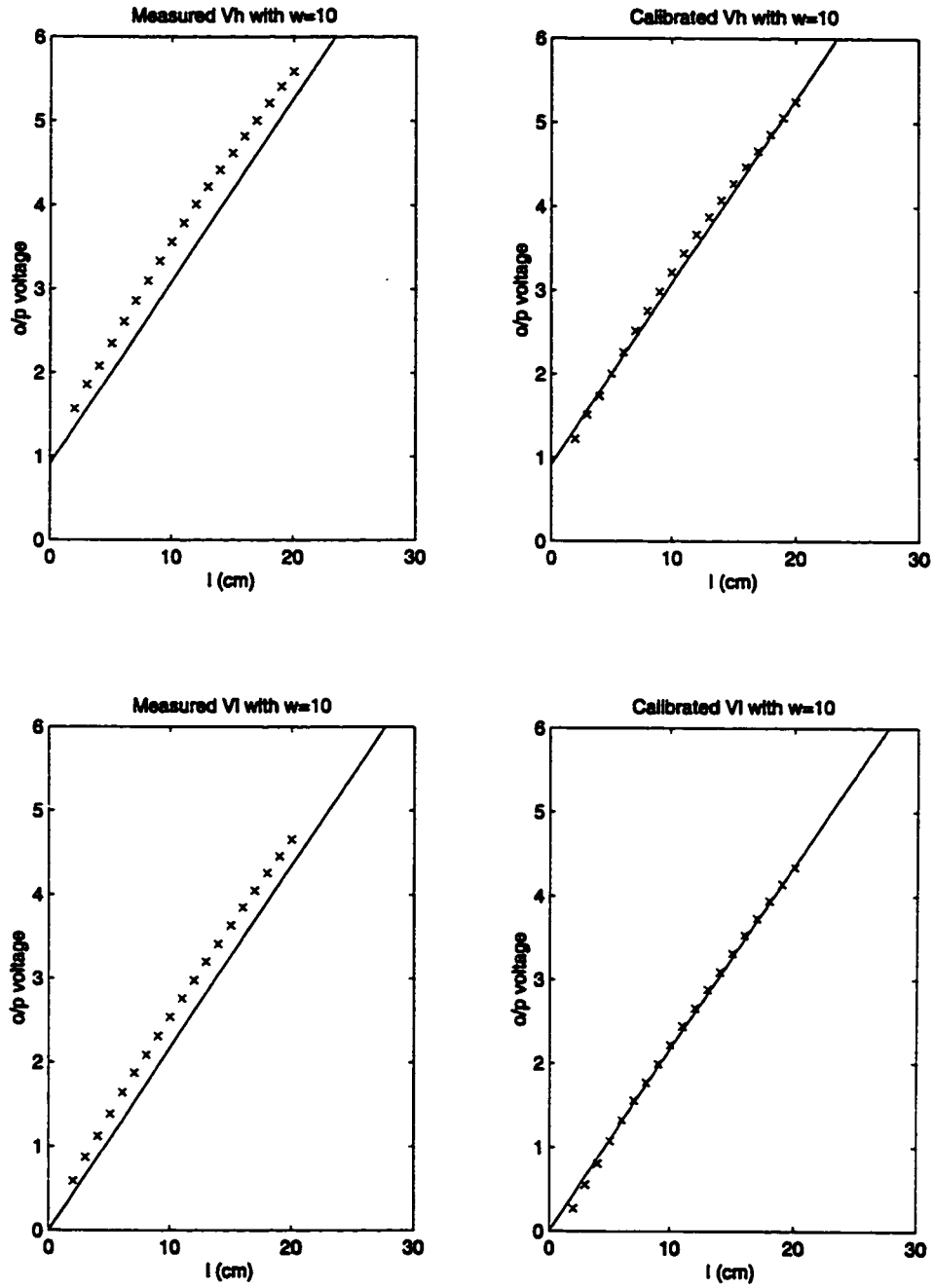

Figure 6.4: Calibration Graphs for the First Sensing Element in the CRS-CRS Hybrid Sensor Prototype ($w = 10$).

	Figure 6.5	Figure 6.6	Figure 6.7	Figure 6.9	Figure 6.10
M.C. (Radian-cm)	0.692	0.985	0.574	0.969	0.996
A.O.E. (Radian)	0.385	0.307	0.116	0.139	0.621
A.P.E. (cm)	1.545	2.925	0.525	0.510	1.617

Table 6.2: Quantitative Mismatch Between the Original and the Recovered Rectangle in Each Experiment (CRS-CRS Sensor Prototype and V.R. Algorithm with k_h-Signature).

in Figure 6.5 to Figure 6.10. In Figure 6.5, the object was put on the lower region of the CRS-CRS sensor. The transitions in the corresponding pseudo-signature was not prominent enough for accurate detection. Moreover, relatively large error in k_h resulted from the fourth sensing element. Hence, the recovered shape significantly deviated from the original. Figure 6.6 is the result of using raw data without calibration. Only slight improvement was noted with calibration. In Figure 6.7, the object was placed on the middle region of the sensor surface. The transition at the seventh sensing element was not distinctive either. However, the measured values of k_h were good enough to give a reasonably recovered shape. In this case, calibration was important to obtain a good signature. Figure 6.8 shows the signature without calibration. It is practically impossible to extract any transitional points. In Figure 6.9, the object was pressed against the upper region of the sensor. Similar to the previous experiments, the transition at the seventh sensing element was not prominent. Hence relatively large discrepancy between the corresponding recovered vertex and the original was produced. However, this result is still better that the one without calibration (see Figure 6.10). Table 6.2 lists the quantitative errors of the recovered shape.

From these experiments, it was noted that shape recovery was easily affected by output noise at the lower region of the sensor. The magnitude of output was relatively small when an object was located near the lower region. Since a mean calibration factor was adopted for output correction, over-adjustment might be done. On the contrary, more accurate output correction was done when the object was put on the middle and upper region of the sensor. Hence the reconstructed vertices were closer to the original. At these regions, the determining factor on the success of the Vertex Reconstruction algorithm was the accuracy in detecting the transitions in a pseudo-signature. Besides, calibration is important to give a properly aligned signature irrespective to different offsets on each sensing element.

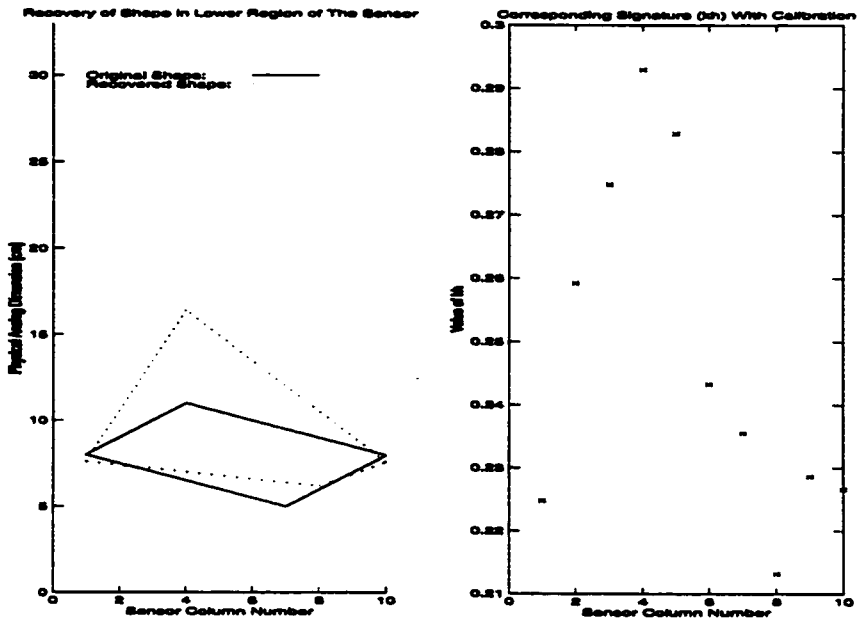

Figure 6.5: Recovering a Rectangle Using V.R. Algorithm with k_h-Signature in the Lower Region of the CRS-CRS Sensor (with Calibration).

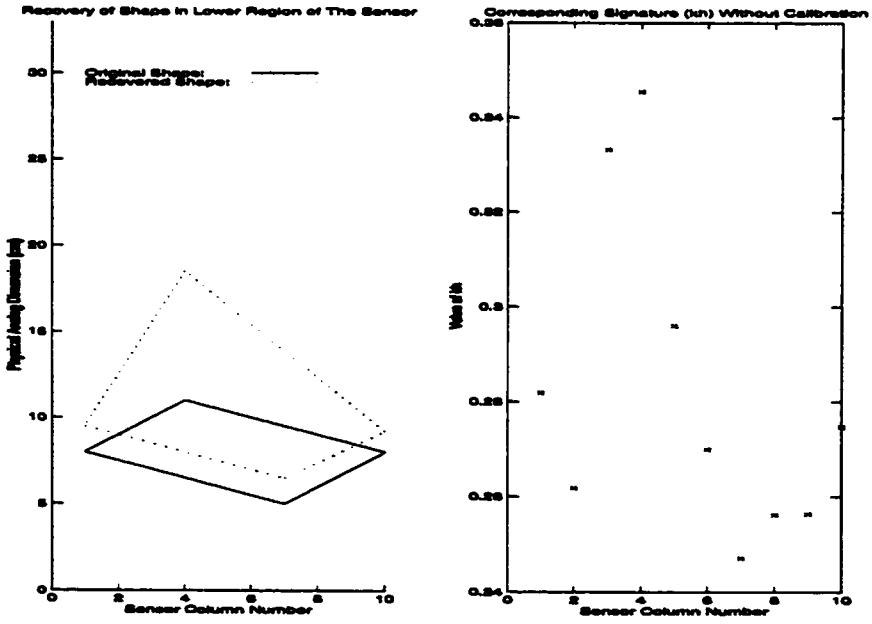

Figure 6.6: Recovering a Rectangle Using V.R. Algorithm with k_h-Signature in the Lower Region of the CRS-CRS Sensor (without Calibration).

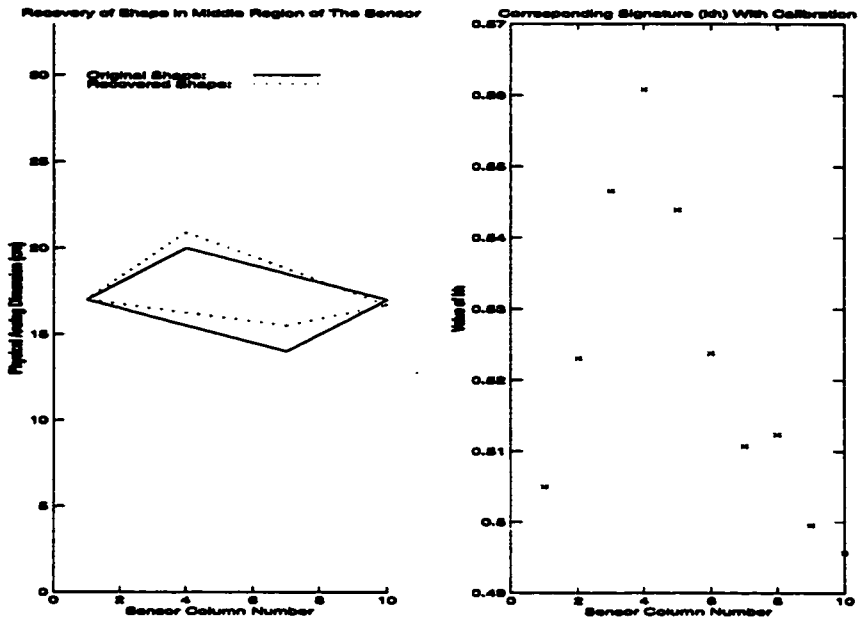

Figure 6.7: Recovering a Rectangle Using V.R. Algorithm with k_h-Signature in the Middle Region of the CRS-CRS Sensor (with Calibration).

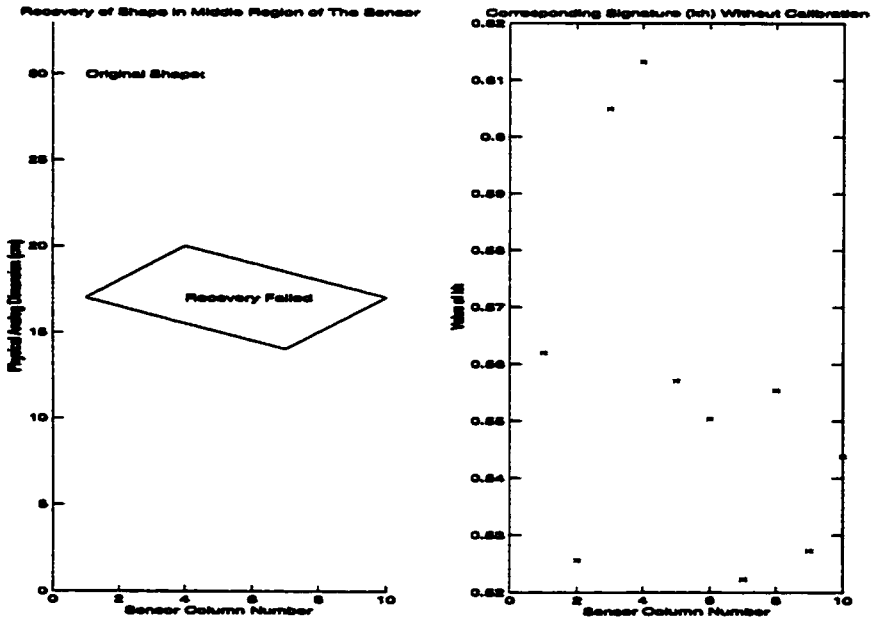

Figure 6.8: Noisy k_h-Signature of a Rectangle in the Middle Region of the CRS-CRS Sensor (without Calibration).

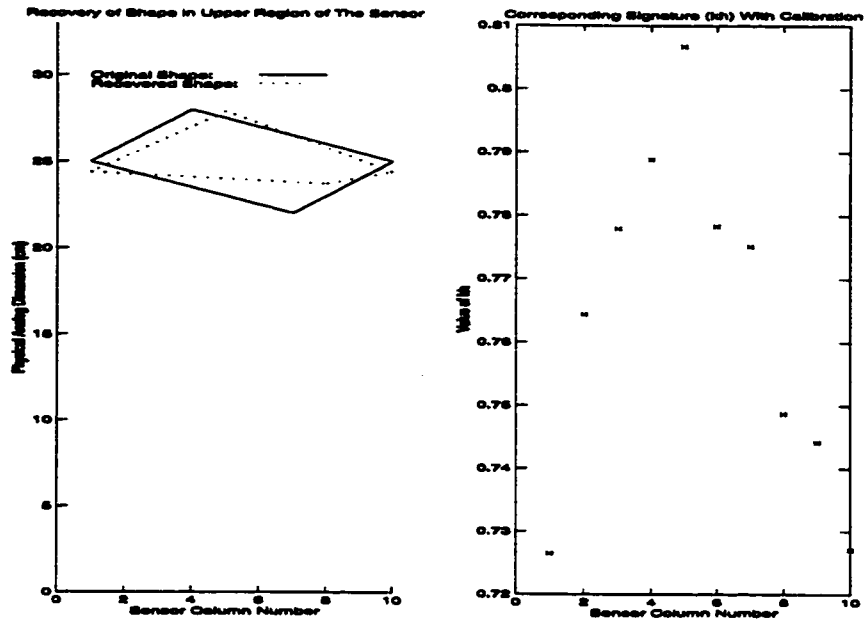

Figure 6.9: Recovering a Rectangle Using V.R. Algorithm with k_h-Signature in the Upper Region of the CRS-CRS Sensor (with Calibration).

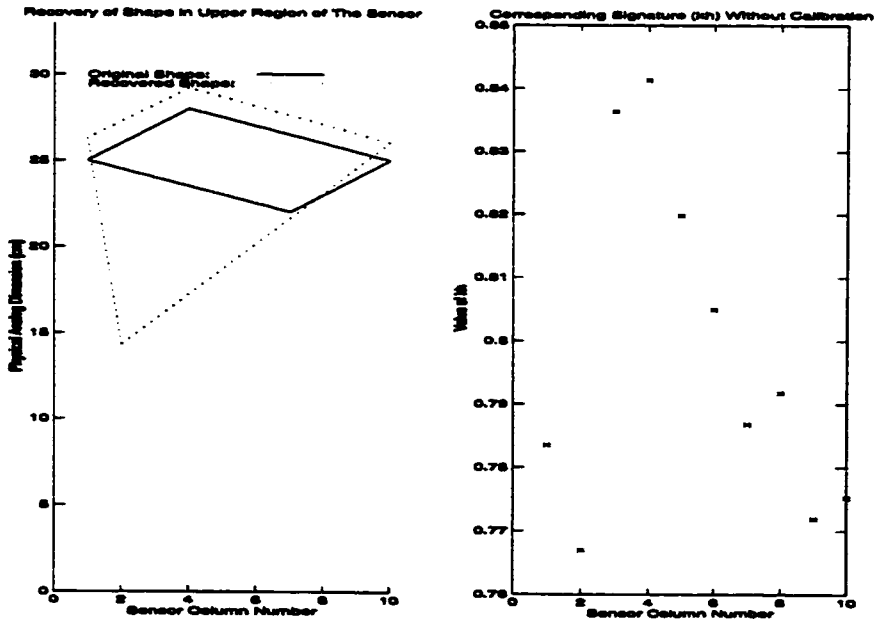

Figure 6.10: Recovering a Rectangle Using V.R. Algorithm with k_h-Signature in the Upper Region of the CRS-CRS Sensor (without Calibration).

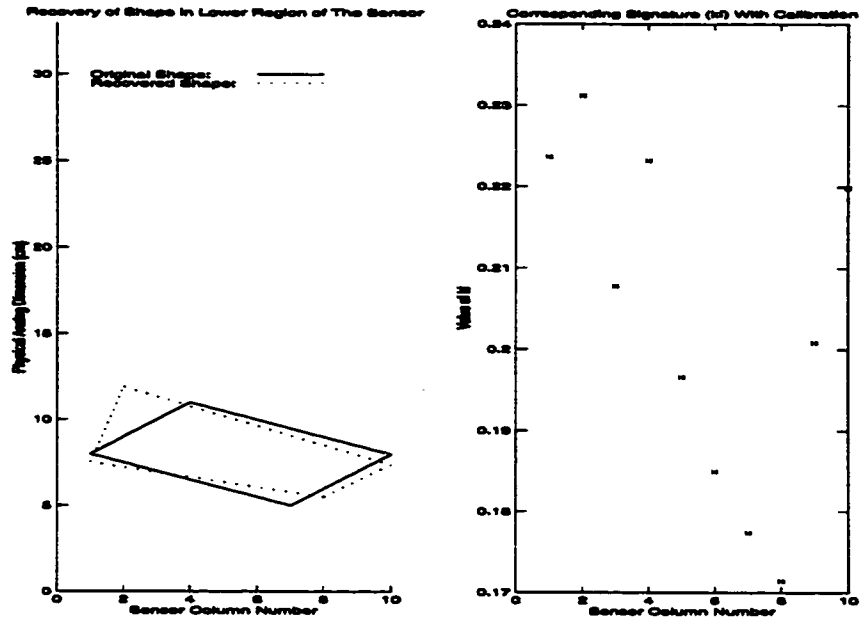

Figure 6.11: Recovering a Rectangle Using V.R. Algorithm with k_l-Signature in the Lower Region of the CRS-CRS Sensor (with Calibration).

6.1.3 Results of Recovering a Rectangle Using the Vertex Reconstruction Algorithm with a CRS-CRS Sensor and k_l-Pseudo-Signature

The values of k_l were also collected from the experiments described in the previous section. Vertex Reconstruction with k_l-signature was applied. Typical results are illustrated graphically in Figure 6.11 to Figure 6.16. In Figure 6.11, the object was put on the lower region of the CRS-CRS sensor. With calibration, the recovered shape was reasonably good. Figure 6.12 shows the corresponding un-calibrated signature, from which it was practically impossible to extract any transitional points. In Figure 6.13, the object was placed on the middle region of the sensor surface. The calibrated signature made it possible to recover a shape close to its original. In this case, calibration was vital and the un-calibrated signature was too noisy (see Figure 6.14). In Figure 6.15, the object was pressed against the upper region of the sensor. Due to relatively large error in the fourth sensing element, the recovered shape deviated quite a lot from the original. Figure 6.16 gives the seriously distorted signature without calibration. Table 6.3 lists the quantitative errors of the recovered shape.

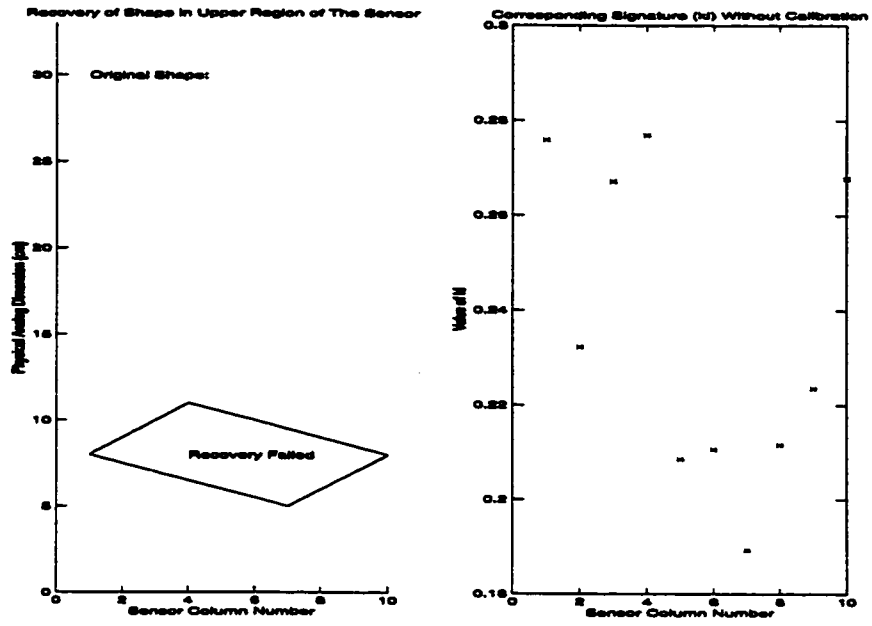

Figure 6.12: Noisy k_l-Signature of a Rectangle in the Lower Region of the CRS-CRS Sensor (without Calibration).

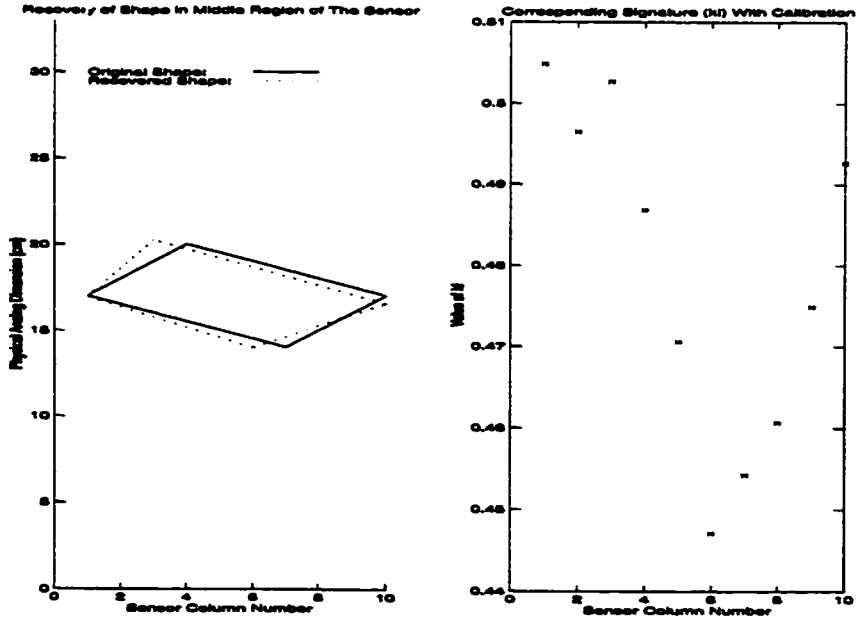

Figure 6.13: Recovering a Rectangle Using V.R. Algorithm with k_l-Signature in the Middle Region of the CRS-CRS Sensor (with Calibration).

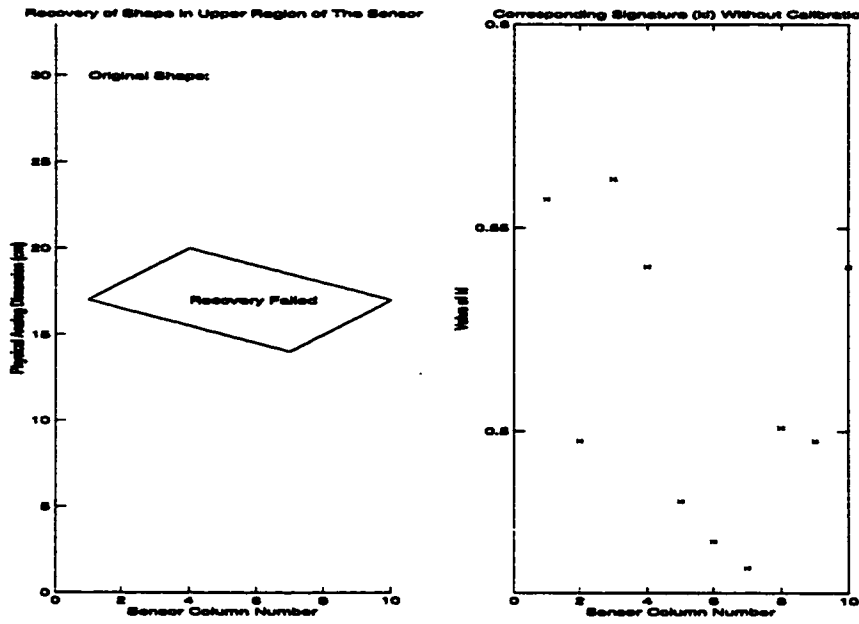

Figure 6.14: Noisy k_l-Signature of a Rectangle in the Middle Region of the CRS-CRS Sensor (without Calibration).

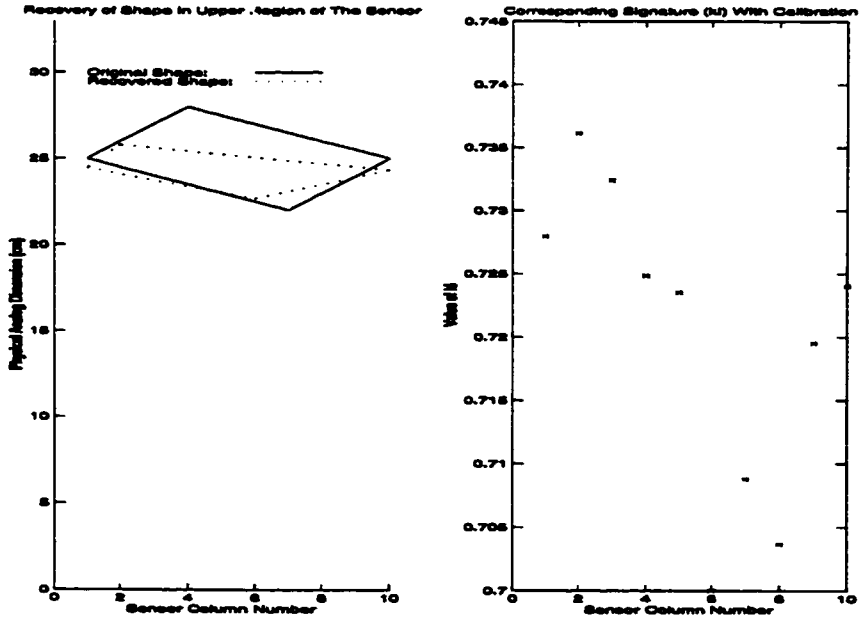

Figure 6.15: Recovering a Rectangle Using V.R. Algorithm with k_l-Signature in the Upper Region of the CRS-CRS Sensor (with Calibration).

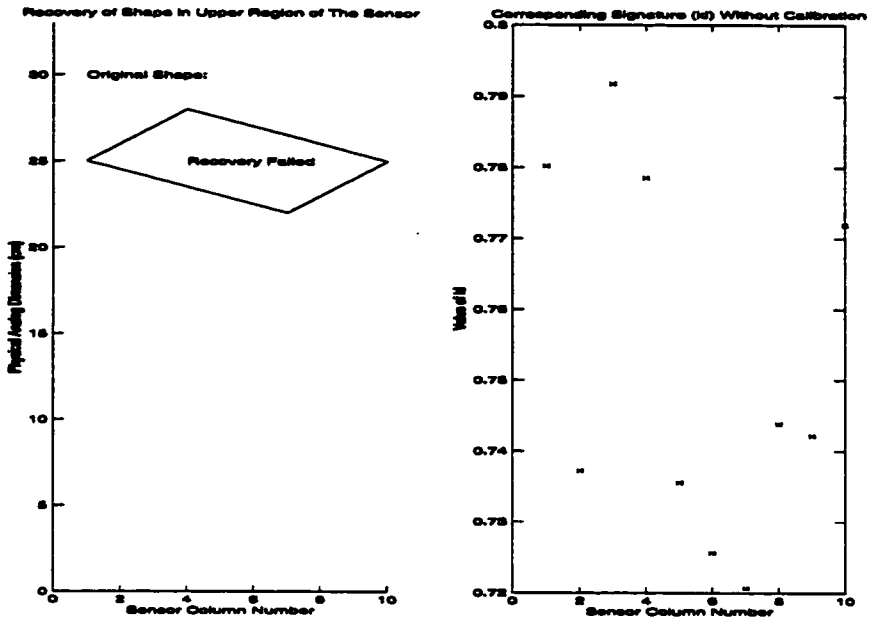

Figure 6.16: Noisy k_l-Signature of a Rectangle in the Upper Region of the CRS-CRS Sensor (without Calibration).

	Figure 6.11	Figure 6.13	Figure 6.15
M.C. (Radian-cm)	0.629	0.266	0.340
A.O.E. (Radian)	0.134	0.012	0.019
A.P.E. (cm)	0.261	0.502	0.656

Table 6.3: Quantitative Mismatch Between the Original and the Recovered Rectangle in Each Experiment (CRS-CRS Sensor Prototype and V.R. Algorithm with k_l-Signature).

6.1.4 Results of Recovering a Rectangle Using the Profile Reconstruction Algorithm with a CRS-CRS Sensor

Both k_h and k_l collected in the experiments described in Section 6.1.2 were fed to the Profile Reconstruction algorithm. Figure 6.17, Figure 6.19 and Figure 6.21 show the corresponding results of shape recovery with calibration. In all cases, the recovered profiles resembled the original closely. However, poor results were found when un-calibrated data were used for shape recovery, as shown in Figure 6.18, Figure 6.20 and Figure 6.22. Table 6.4 lists the quantitative errors in the recover shapes.

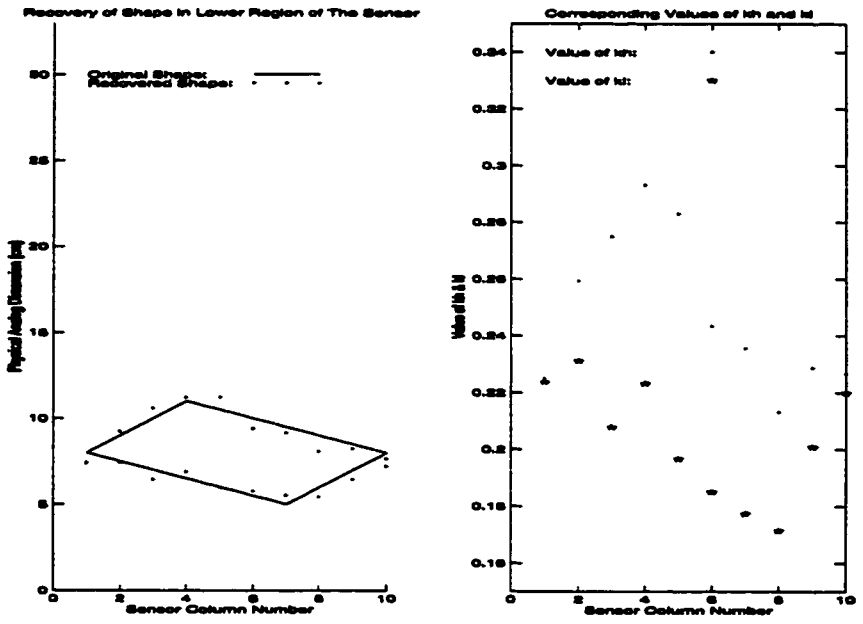

Figure 6.17: Recovering a Rectangle Using P.R. Algorithm in the Lower Region of the CRS-CRS Sensor (with Calibration).

	Figure 6.17	Figure 6.19	Figure 6.21
M.C. (Radian-cm)	0.397	0.223	0.273
A.O.E. (Radian)	0.094	0.011	0.006
A.P.E. (cm)	0.175	0.350	0.925

Table 6.4: Quantitative Mismatch Between the Original and the Recovered Rectangle in Each Experiment (CRS-CRS Sensor Prototype and P.R. Algorithm).

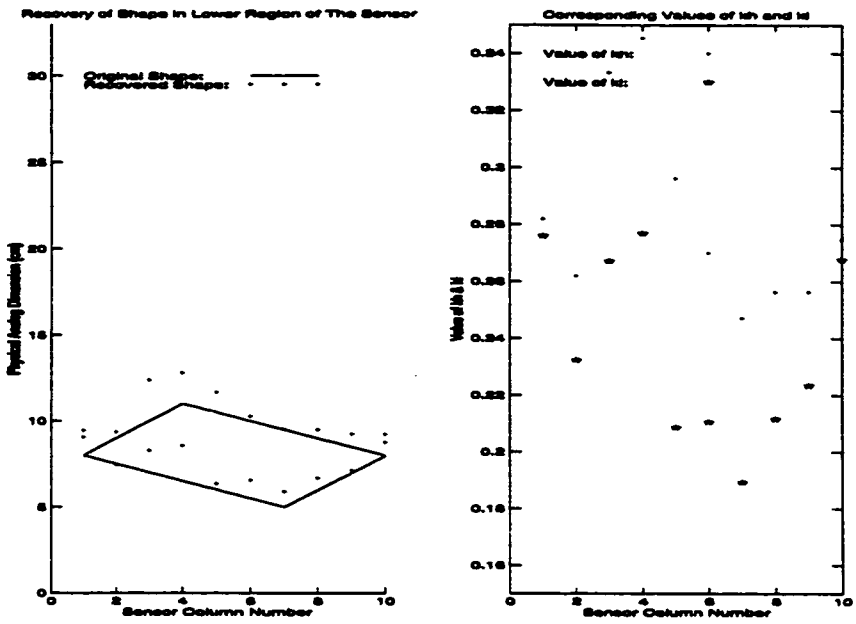

Figure 6.18: Recovering a Rectangle Using P.R. Algorithm in the Lower Region of the CRS-CRS Sensor (without Calibration).

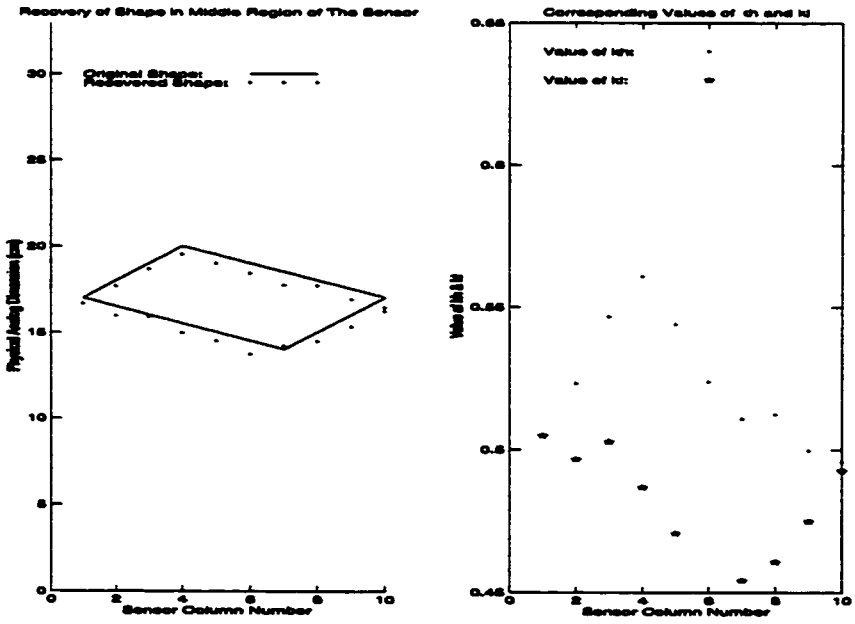

Figure 6.19: Recovering a Rectangle Using P.R. Algorithm in the Middle Region of the CRS-CRS Sensor (with Calibration).

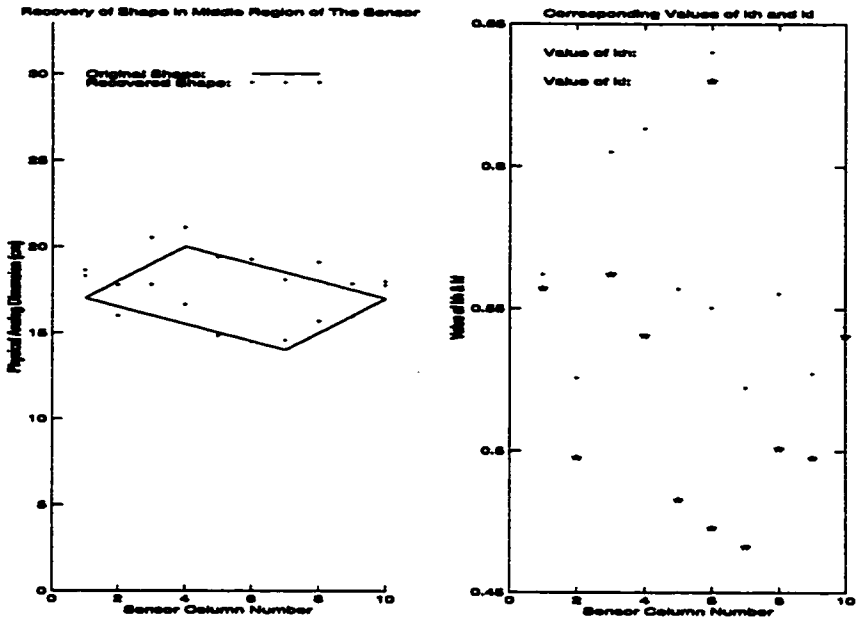

Figure 6.20: Recovering a Rectangle Using P.R. Algorithm in the Middle Region of the CRS-CRS Sensor (without Calibration).

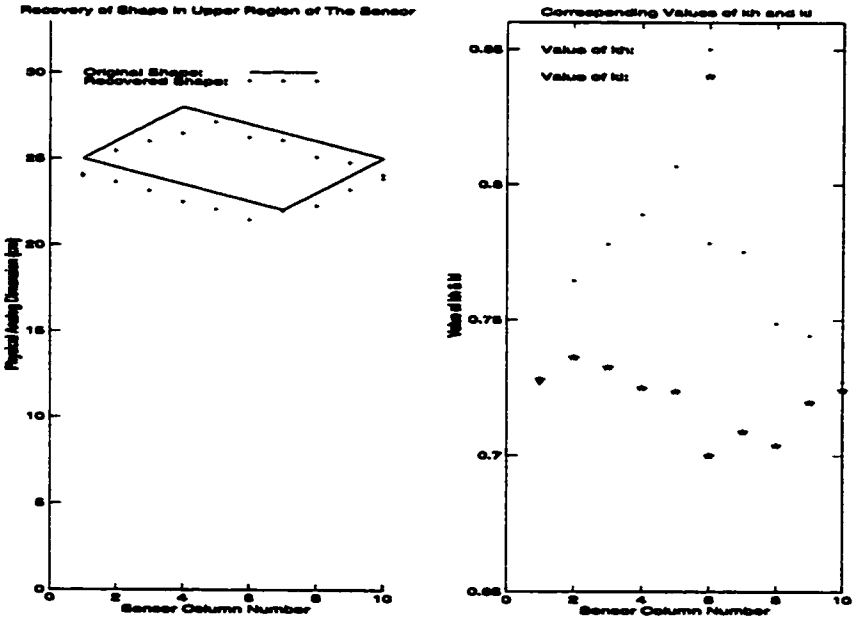

Figure 6.21: Recovering a Rectangle Using P.R. Algorithm in the Upper Region of the CRS-CRS Sensor (with Calibration).

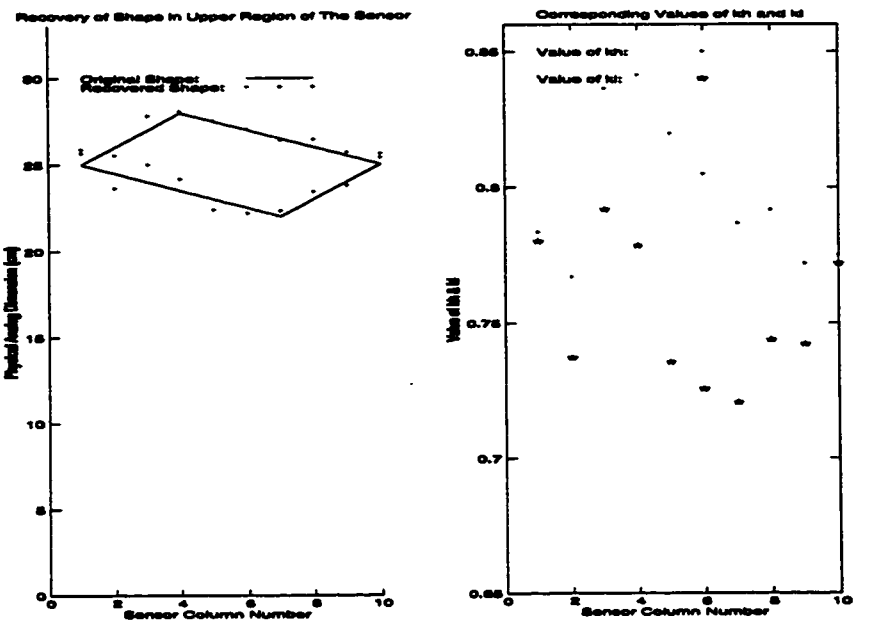

Figure 6.22: Recovering a Rectangle Using P.R. Algorithm in the Upper Region of the CRS-CRS Sensor (without Calibration).

6.2 Experiments with a CRS-M Sensor

The prototype of a CRS-M hybrid sensor is shown in Figure 6.23. It measured 4cm (digital dimension) by 25cm (analog dimension). The same conductive silicone rubber as in the CRS-CRS prototype was used. Strips with 3 mm in width were sliced from the rubber sheet. Nine strips were aligned in parallel on top of a bare clad board. Non-conductive fabric mesh was laid between layer of strips on top and the conductive copper surface at the bottom. When no force was applied, the rubber strips did not touch the metal surface of the clad board. Since there were only nine columns of sensing elements in the setup, the resolution in the digital dimension was limited to 2.25 sensing elements per cm. With visual measurement using a tape measure, the resolution in the analog dimension was 0.1 cm. This is equivalent to a maximum C.Q.E. of $\pm\frac{1}{250}$. For simplicity, only a rectangular object was used in the experiments.

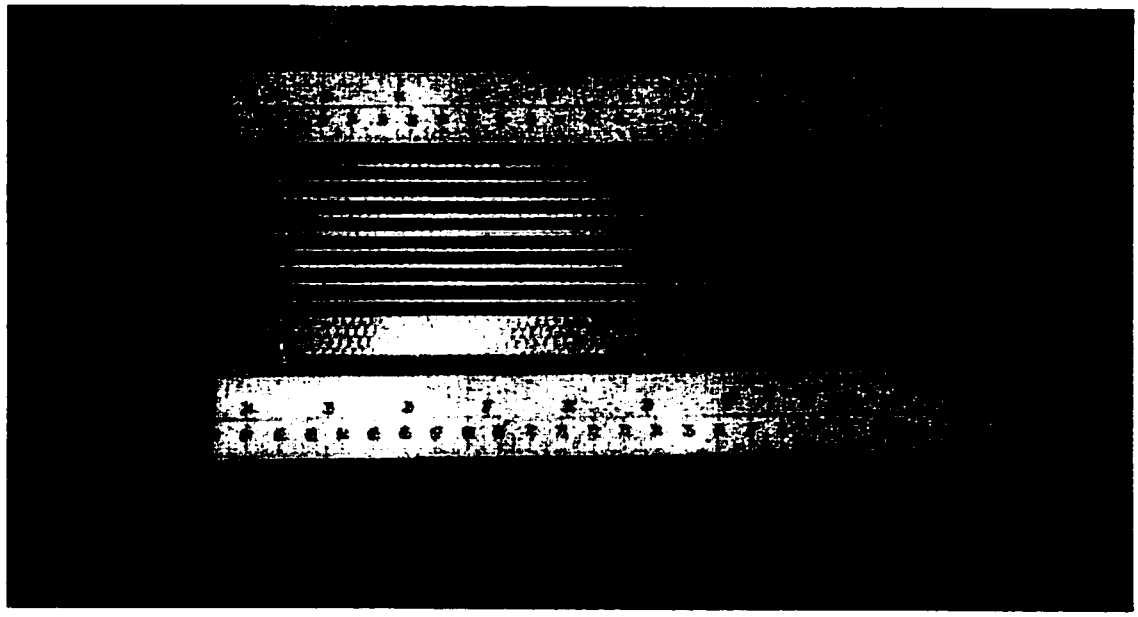

Figure 6.23: Prototype of a CRS-M Sensor with Nine Sensing Elements

6.2.1 Calibrations of a CRS-M Sensor

Calibration procedure similar to that in a CRS-CRS sensor was done. Since there was just a set of V_{out} in case of a CRS-M Sensor, only single-measurement was required. The steps were as follows:

1. A point contact was made at the 1, 2, 3, ... unit mark in turn. Corresponding V_{out} were recorded. They were compared to the expected values according to equation (3.7). The mean was then calculated as $V_{out(w=0)}$.
2. A 5-unit long contact was made starting at the 1, 2, 3, ... unit marks. Another mean, $V_{out(w=5)}$ was obtained.
3. Repeat step 2 above with a 10-unit length of contact and obtain the mean, $V_{out(w=10)}$.

Finally, the calibration factors were calculated as follows:

$$V_{outOffset} = \frac{V_{out(w=0)} + V_{out(w=5)} + V_{out(w=10)}}{3} \tag{6.5}$$

Figure 6.24 to Figure 6.26 show the corresponding calibration graphs of a sensing element in a CRS-M Sensor Prototype. Table 6.5 tabulates the calibration factors for each of the sensing element. These calibration factors are used in a similar way as in the CRS-CRS sensor. It is a compromised approximation of a non-linear function by a linear function, but it works reasonably well with the CRS-M sensor prototype.

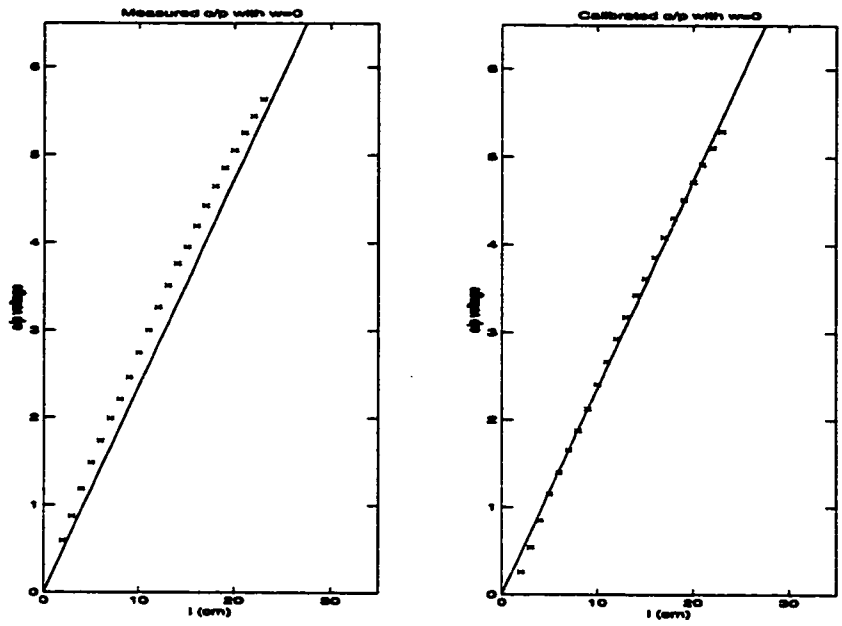

Figure 6.24: Calibration Graphs for the First Sensing Element in the CRS-M Hybrid Sensor Prototype ($w = 0$).

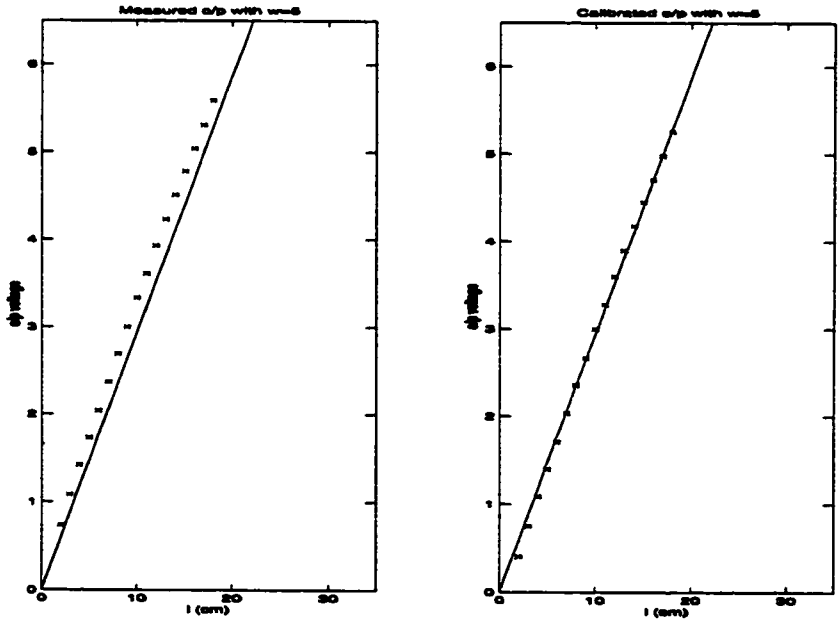

Figure 6.25: Calibration Graphs for the First Sensing Element in the CRS-M Hybrid Sensor Prototype ($w = 5$).

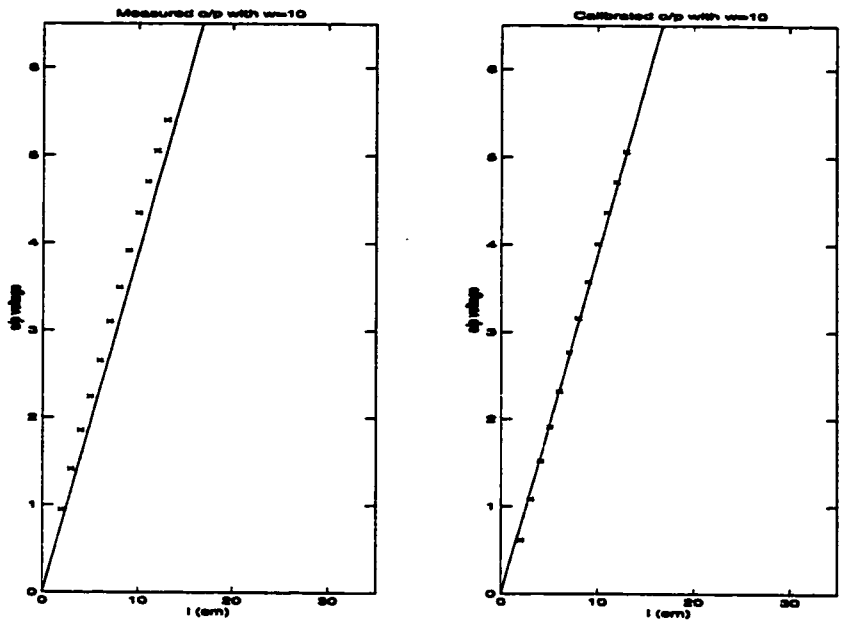

Figure 6.26: Calibration Graphs for the First Sensing Element in the CRS-M Hybrid Sensor Prototype ($w = 10$).

$V_{ref} = 6.05$V	Sensing Element Number								
	1	2	3	4	5	6	7	8	9
Calibration Factor for V_{out} (V)	0.333	0.175	0.068	0.304	0.201	0.199	0.009	0.024	0.087

Table 6.5: Calibration Factors for Each Sensing Element of the CRS-M Hybrid Sensor Prototype.

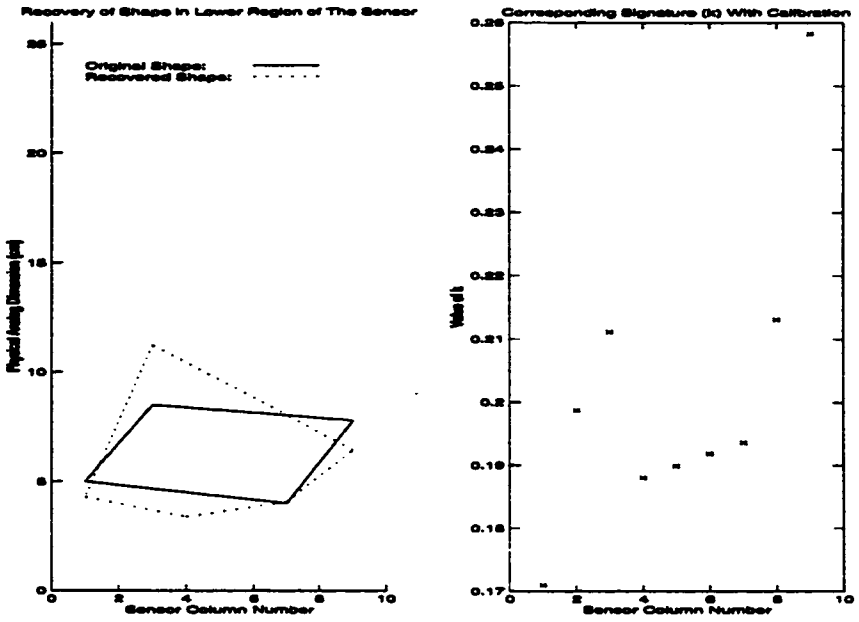

Figure 6.27: Recovering a Rectangle Using V.R. Algorithm in the Lower Region of the CRS-M Sensor (with Calibration).

6.2.2 Results of Recovering a Rectangle Using the Vertex Reconstruction Algorithm with a CRS-M Sensor

Experiments were done with a rectangular planar object of dimension 5 cm by 3.5 cm. Typical results are illustrated graphically in Figure 6.27 to Figure 6.32. In Figure 6.27, the object was placed near the lower region of the CRS-M sensor. Transitions were detected easily. However, errors in k caused relative large discrepancies in estimating the vertices. Figure 6.30 shows that without calibration, the errors in the signature were even worse. In Figure 6.29, the object was located on the middle region of the sensor surface. Accurate transitions were detected and the recovered shape resembled the original closely. Figure 6.30 shows the result of using an un-calibrated signature. In Figure 6.31, the object was put on the upper region of the sensor. Prominent transitions could be identified from the pseudo-signature. However, due to noise in the value of k from the seventh sensing element, relatively large error was resulted in reconstructing the lower right vertex of the rectangular object. For completeness, Figure 6.32 shows the result of shape recovery using an uncalibrated signature. Table 6.6 shows the quantitative errors in shape recovery.

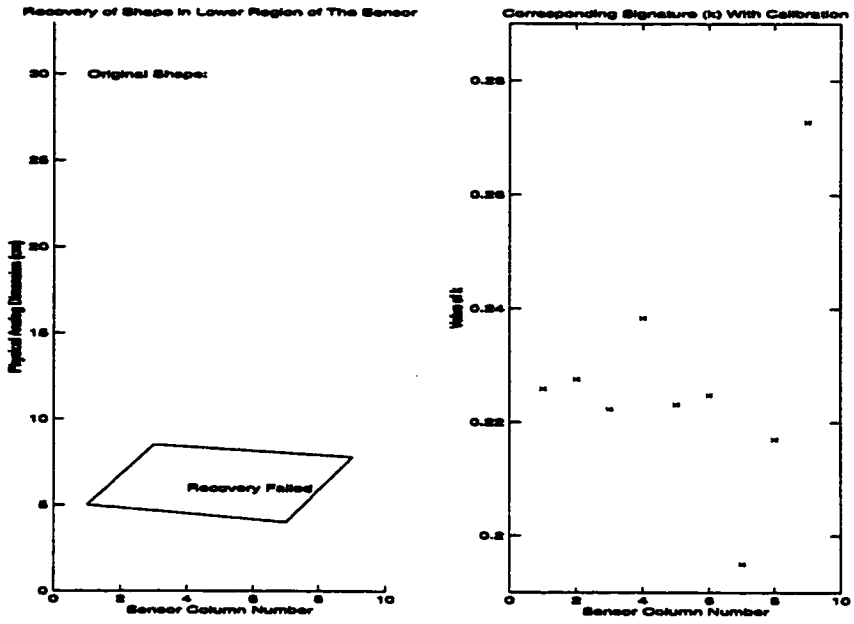

Figure 6.28: Noisy k_l-Signature of a Rectangle in the Lower Region of the CRS-M Sensor (without Calibration).

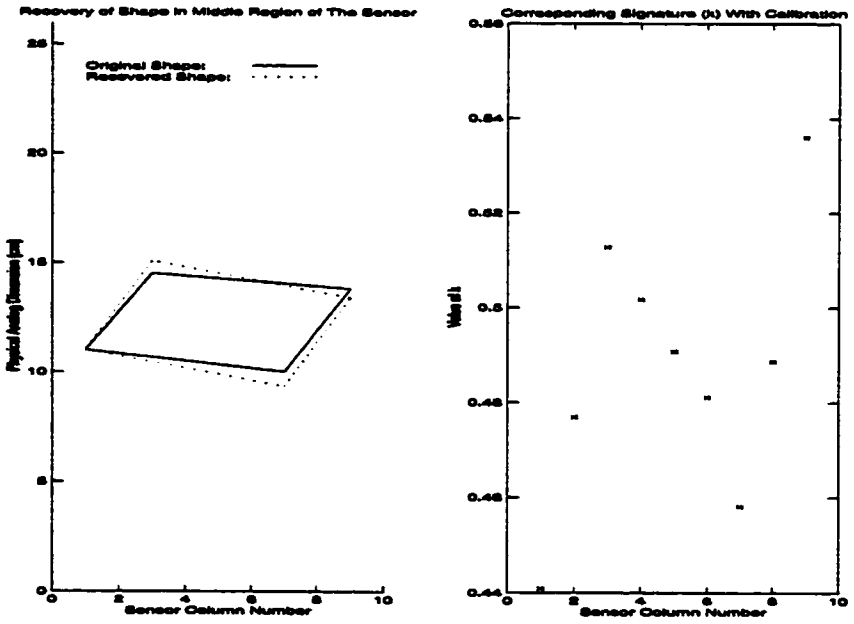

Figure 6.29: Recovering a Rectangle Using V.R. Algorithm in the Middle Region of the CRS-M Sensor (with Calibration).

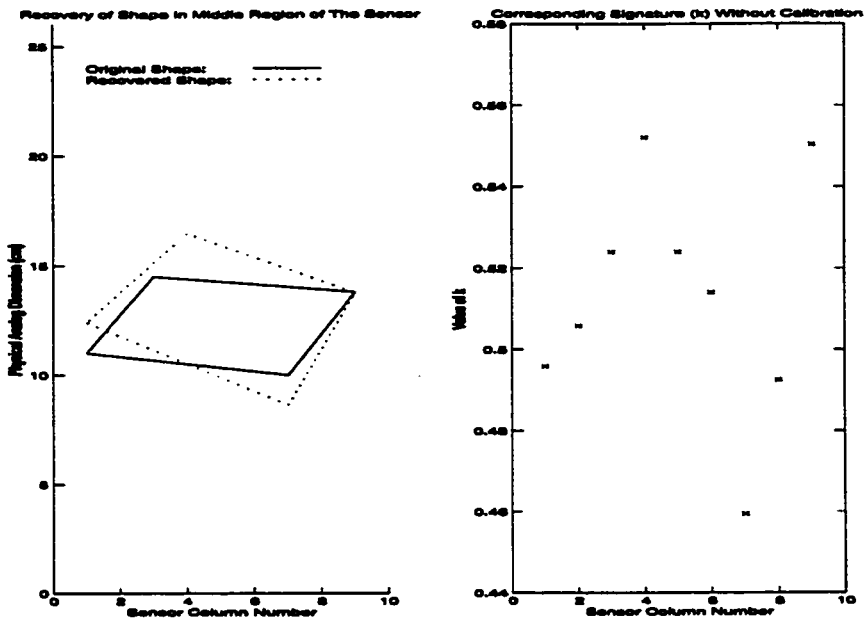

Figure 6.30: Recovering a Rectangle Using V.R. Algorithm in the Middle Region of the CRS-M Sensor (without Calibration).

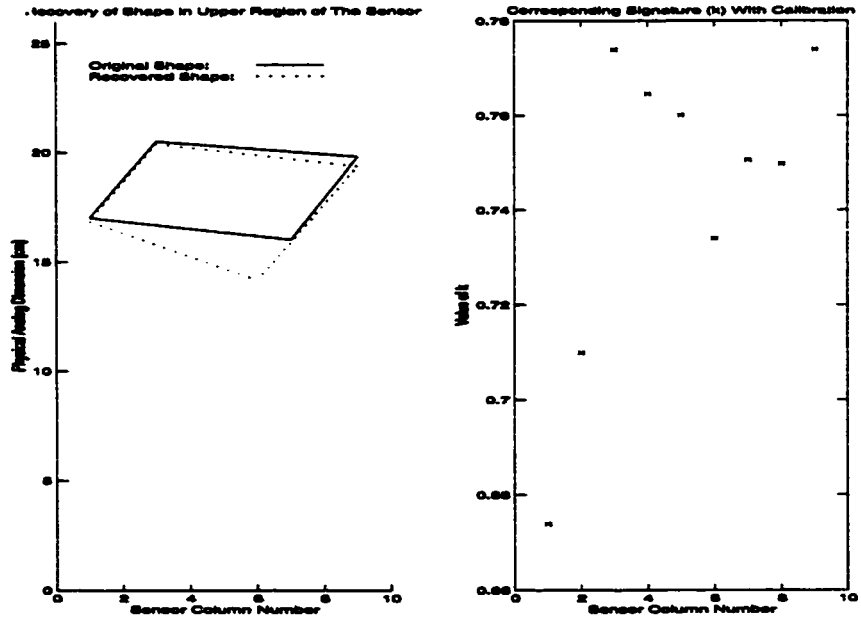

Figure 6.31: Recovering a Rectangle Using V.R. Algorithm in the Upper Region of the CRS-M Sensor (with Calibration).

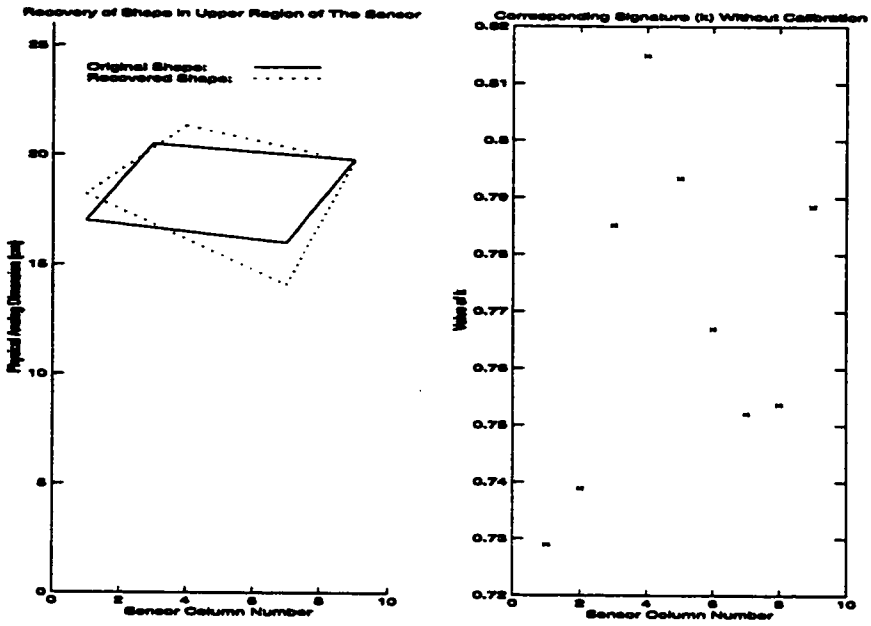

Figure 6.32: Recovering a Rectangle Using V.R. Algorithm in the Upper Region of the CRS-M Sensor (without Calibration).

	Figure 6.27	Figure 6.29	Figure 6.30	Figure 6.31	Figure 6.32
M.C. (Radian-cm)	0.930	0.132	0.390	0.358	0.535
A.O.E. (Radian)	0.050	0.028	0.226	0.084	0.290
A.P.E. (cm)	0.475	0.125	0.707	0.673	0.250

Table 6.6: Quantitative Mismatch Between the Original and the Recovered Rectangle in Each Experiment (CRS-M Sensor Prototype and V.R. Algorithm with k-Signature).

6.3 Experiments with a Cyl-CRS-M Sensor

The prototype of a Cyl-CRS-M hybrid sensor is shown in Figure 6.33. It measured 10 cm in length by 1.8 cm in diameter. The same conductive silicone rubber as in the CRS-M prototype was used. A section of PVC pipe was used for the cylindrical base structure. The metallic bottom layer was a sheet of aluminum foil coated on the PVC pipe surface. Then a fabric mesh was laid on the metallic surface to serve as a separator. Finally, strips with 3 mm in width were sliced from the rubber sheet. Five of these strips were aligned in parallel on top of the fabric mesh. Electrodes were connected to both ends of each rubber strip. To protect the sensing surface, a tough PVC plastic sheet was wrapped around the whole structure. When no force was applied, the rubber strips did not touch the aluminum foil. Since there were only five columns of sensing elements in the setup, the resolution in the

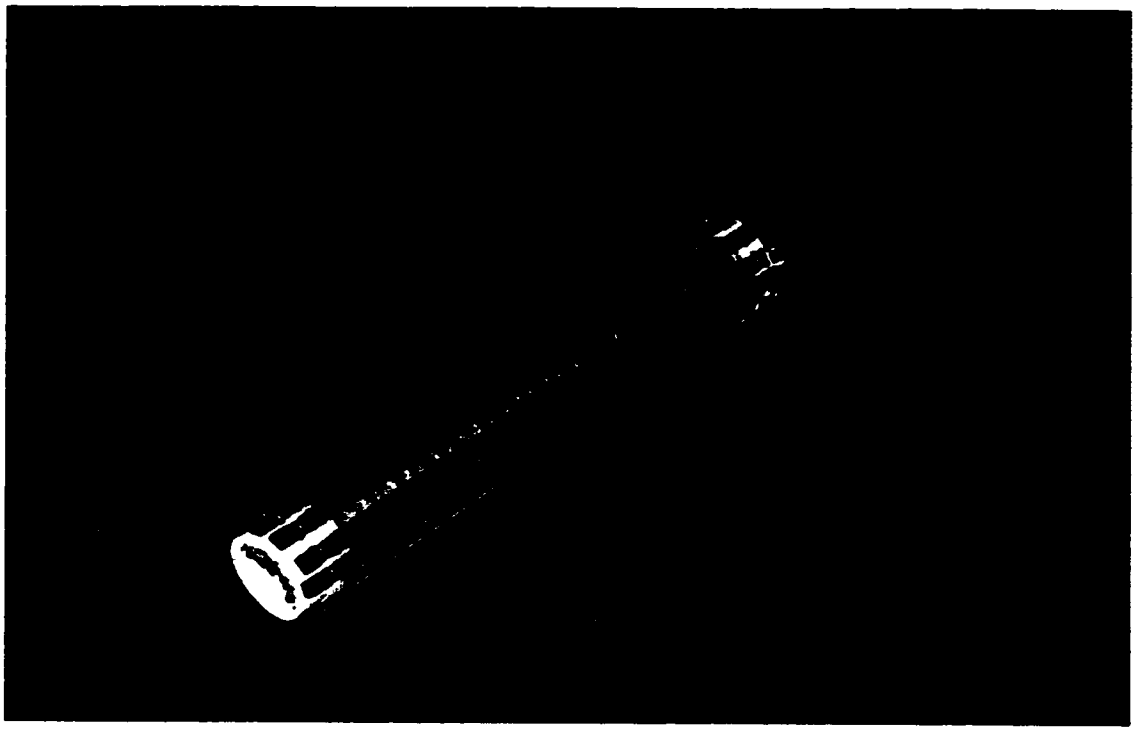

Figure 6.33: Prototype of a Cyl-CRS-M Sensor with Nine Sensing Elements

digital dimension was limited to 2.5 sensing elements per cm on a radius of curvature of 0.9 cm. As measurement was done visually using a tape measure, the resolution in the analog dimension was 0.1 cm. This is equivalent to a maximum C.Q.E. of $\pm\frac{1}{100}$. Only point and line contacts were tested with this prototype.

6.3.1 Calibrations of a Cyl-CRS-M Sensor

As the Cyl-CRS-M Sensor was used to detect point and line contacts, calibration with $w = 0$ was sufficient. Figure 6.34 shows the corresponding calibration graphs of a sensing element in a CRS-M Sensor Prototype and Table 6.7 lists the calibration factors for each of the sensing elements.

$V_{ref} = 6.05$V	Sensing Element Number				
	1	2	3	4	5
Calibration Factor for V_{out} (V)	0.345	0.016	0.353	0.317	0.080

Table 6.7: Calibration Factors for Each Sensing Element of the Cyl-CRS-M Hybrid Sensor Prototype.

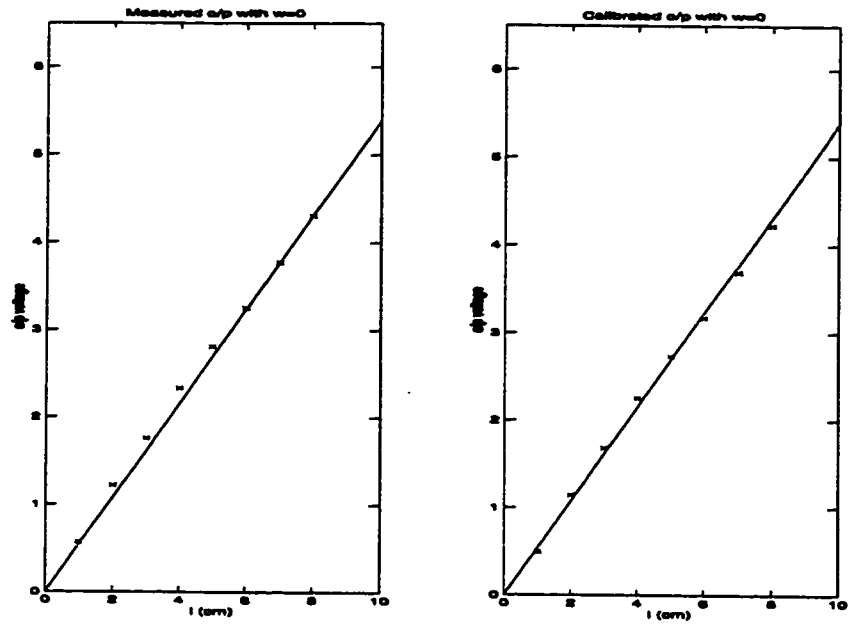

Figure 6.34: Calibration Graphs for the First Sensing Element in the Cyl-CRS-M Hybrid Sensor Prototype ($w = 0$).

6.3.2 Results of Recovering Points/Lines Contacts with a Cly-CRS-M Sensor

Due to curvature of the cylindrical sensing surface of the prototype, any edge of a contact object actually touched two of the sensing elements at most. Any line-contact situation was practically resolved into two-point-contact scenario. Five sets of two-point contacts were made on the Cly-CRS-M sensor and Figure 6.35 shows the results of the experiments. In general, the location of any point contact was extracted from the calibration graph and the recovered points were closely matched to the originals.

6.4 Summary of Experiments

A 12-bit precision A/D conversion is common in practice which means a maximum of $\pm\frac{1}{8192}$ part of error might occur in the output voltage conversion process. This is insignificant as compared to the quantization error due to the length of contact between an object and the hybrid sensor, for instance $\pm\frac{1}{325}$, $\pm\frac{1}{250}$ and $\pm\frac{1}{100}$ in the CRS-CRS, CRS-M and Cyl-CRS-M sensor prototype respectively. Though they were larger than the value of $\pm\frac{1}{1000}$ used in the simulations, no significant impact was found from the experiments. Experiments also

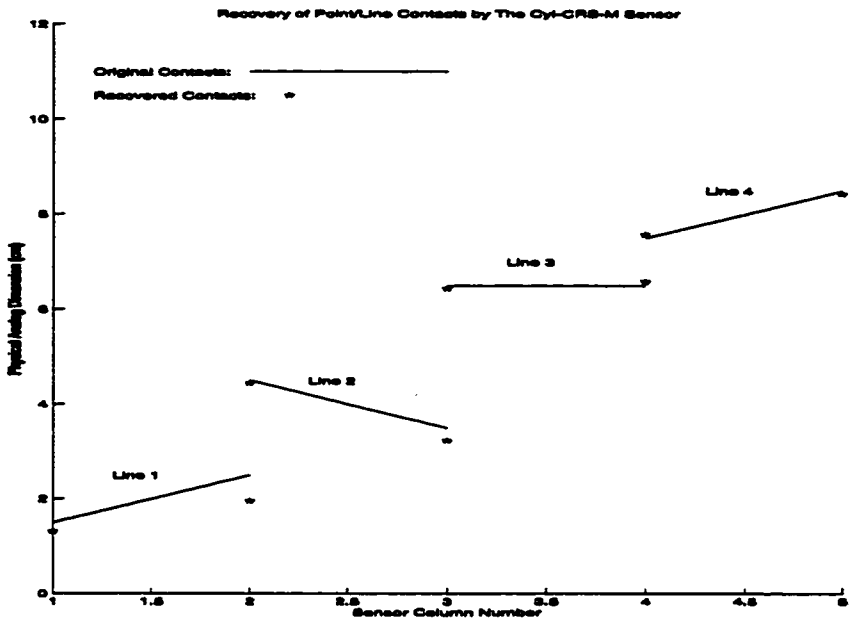

Figure 6.35: Recovering Points/Lines Contacts Using the CRS-M Sensor.

revealed that after calibration was done on the sensor outputs, the errors were similar to that of P.U. profile II used in the simulations. Table 6.8 to Table 6.11 show the corresponding errors of each sensing elements after calibration. The error of V_h w.r.t. V_{ref} in a CRS-CRS sensor was approximately -1.0% to +1.1%. With the same CRS-CRS sensor, the error of V_l w.r.t. V_{ref} was -1.2% to +1.1%. For the CRS-M sensor, the error of V_{out} w.r.t. V_{ref} ranged from -1.1% to +1.0%. For the Cyl-CRS-M sensor, the error of V_{out} w.r.t. V_{ref} was approximately -0.9% to +0.4%. In conclusion, the performance of shape recovery in the experiments matches that in the simulation with a P.U. profile II.

Reference	Sensing Element Number									
	1	2	3	4	5	6	7	8	9	10
Figure 6.5	1.1%	0.9%	1.0%	1.0%	0.9%	0.5%	0.3%	0.4%	1.0%	1.1%
Figure 6.7	0.1%	0.1%	0.3%	0.3%	-0.7%	-1.0%	-0.7%	0.7%	-1.0%	0.7%
Figure 6.9	0.3%	-0.7%	0.4%	-1.0%	-0.9%	-0.1%	-1.0%	-0.8%	-0.1%	0.2%

Table 6.8: Percentage Errors in V_h w.r.t. V_{ref} for Each Sensing Element of the CRS-CRS Hybrid Sensor Prototype in the Experiments (after Calibration).

Reference	Sensing Element Number									
	1	2	3	4	5	6	7	8	9	10
Figure 6.11	0.8%	1.2%	0.3%	0.7%	1.0%	1.1%	0.7%	1.0%	0.5%	1.1%
Figure 6.13	0.1%	-0.1%	0.2%	1.1%	-0.5%	-1.2%	-1.1%	0.9%	-1.0%	1.0%
Figure 6.15	0.1%	-0.7%	0.3%	-1.1%	-0.3%	-0.4%	-0.8%	-0.5%	-0.7%	0.5%

Table 6.9: Percentage Errors in V_i w.r.t. V_{ref} for Each Sensing Element of the CRS-CRS Hybrid Sensor Prototype in the Experiments (after Calibration).

Reference	Sensing Element Number								
	1	2	3	4	5	6	7	8	9
Figure 6.27	1.0%	0.7%	0.3%	0.5%	0.6%	0.7%	1.0%	0.4%	0.5%
Figure 6.29	0.8%	0.1%	0.2%	0.4%	0.3%	0.3%	-0.9%	-0.3%	-0.4%
Figure 6.31	0.4%	1.0%	-0.2%	-0.5%	-0.2%	-0.3%	-1.1%	-0.7%	-0.9%

Table 6.10: Percentage Errors in V_{out} w.r.t. V_{ref} for Each Sensing Element of the CRS-M Hybrid Sensor Prototype in the Experiments (after Calibration).

Reference in Figure 6.35	Sensing Element Number				
	1	2	3	4	5
Line 1	-0.5%	-0.9%	-	-	-
Line 2	-	-0.4%	-0.6%	-	-
Line 3	-	-	-0.3%	0.4%	-
Line 4	-	-	-	0.3%	-0.4%

Table 6.11: Percentage Errors in V_{out} w.r.t. V_{ref} for Each Sensing Element of the Cyl-CRS-M Hybrid Sensor Prototype in the Experiments (after Calibration).

Chapter 7

Conclusions

This thesis presented a new tactile sensor design, called hybrid tactile sensor, and described the two shape interpretation algorithms, the Vertex Reconstruction Algorithm and the Profile Reconstruction algorithm, which reconstruct the contact object's shape from sensor outputs. Four hybrid tactile sensor models, namely, the CRS-CRS, the CRS-M, the CRS-CRP and the Cyl-CRS-M were presented. They were studied in detail, except for the CRS-CRP design which was too complicated for a convenient analytical model. Based on the mathematical models of the sensor designs, simulations were conducted for verification and performance estimation. Three prototypes were constructed using inexpensive materials. Experiments were carried out with each prototype and their results were analyzed and compared.

7.1 Summary of Objectives

This thesis categorized sensor technologies into analog sensing and digital sensing. Analog sensing technology provided a simple and inexpensive means to abstract tactile information. However, it was limited in giving point contact data only. On the other hand, digital sensing technology was capable of giving more detail such as the shape and orientation of an object in touch with the sensing surface. Yet, it involved more complex circuitry, larger amount of raw data and slower sampling operations as compared to its analog counterpart. This research focused on a trade-off between the above two extremes and attempted a new hybrid tactile sensor design with the following advantages:

1. The tactile sensor should be simple in structure and inexpensive to fabricate.
2. The tactile sensor should be able to provide information on the location and the shape of contact.

3. The tactile sensor should be flexible enough to conform to different geometric shapes.

7.2 Summary of Simulations

Simulations were done to verify the behavior of each hybrid sensor model. In addition, the validity of each shape reconstruction algorithm was checked with different error levels in sensor outputs. Polygonal shapes such as triangles, tetragons and hexagons were used in the simulations. Different error conditions were assumed in each simulation set. These conditions include:

1. Ideal Sensor Output (Noise-free Sensor).
2. Sensor Output with C.Q.E. (and T.E., if applicable) Only.
3. Sensor Output with C.Q.E. (and T.E., if applicable) and P.U. profile I.
4. Sensor Output with C.Q.E. (and T.E., if applicable) and P.U. profile II.

It was found that each hybrid sensor model and the applicable shape reconstruction algorithms worked perfectly under ideal conditions. Even with C.Q.E. (and T.E. in case of using the Vertex Reconstruction Algorithm), shape recovery was reasonably good. Two profiles of P.U. were introduced on top of C.Q.E. (and T.E.), the performance of both shape interpretation algorithm deteriorated. P.U. profile I approximated the characteristics of the prototype closely and still produced reasonably good results. P.U. profile II caused much noisy conditions and the algorithms performed poorly or even failed to work.

7.3 Summary of Prototypes and Experiments

As shape reconstruction algorithms were sensitive to sensor output errors, it was necessary to see whether low sensor output errors could be achieved in practice. Three sensor prototypes were made in the research. The CRS-CRS sensor and the CRS-M sensor were two simple planar structures, whereas the Cyl-CRS-M was a cylindrical one. The elastic conductive rubber strips of these sensors were prepared from conductive silicone rubber sheets. These conductive silicone rubber sheets were carbon-based conductive material widely used in RFI/EMI shielding. It was readily available in various resistivities and thickness at very low cost. Besides, rubber strips made from these conductive silicone rubber exhibited extremely good linearity in resistivities. For insulation between the two structural layers of a hybrid sensor, fabric meshes that are easily found in a fabric store were used as separators.

Experiments on shape recovery were done with each prototype and the applicable shape reconstruction algorithms. Since the resolutions in the digital dimensions of the prototypes were small, only a simple rectangular shape was used for the experiments. Calibrations were required to obtain the necessary offset voltage to correct the sensor outputs. From the results of the experiments, the shape reconstruction algorithms gave reasonable shape recovery.

7.4 Summary of Achievement

The new hybrid tactile sensor models combined the advantages of both analog and digital sensing technologies and the following is achieved in the research:

1. The sensor was simple because only n or $2n$ sampling operations are required to cover an area that normally requires n^2 sampling operations. This represents a considerable saving in sampling time especially when n is large.
2. It was shown that very inexpensive materials can be used for fabrication of the hybrid sensors.
3. The flexibility of the materials and the overall sensor structure made it possible for a hybrid sensor to fit into different geometric surfaces.
4. Due to simplicity of a typical hybrid sensor, even sensors with large physical dimensions could be manufactured at relatively low cost.
5. No special circuit was required to eliminate the parallel path problem in a conventional digital sensor.

Through simulation and experiment with the sensor prototypes, the two accompanying shape recovery algorithms were verified. Their behavior under noisy conditions were compared and could serve as guidelines in choosing materials and sensor models in achieving different quality requirement. The sensor prototypes used in the experiments were not in production-quality, but the results in shape recovery were still satisfactory. Since much more precise dimensions and control of materials can be achieved in industrial production process (for instance, resistors with 0.1% tolerance are commercially available), hybrid sensor with lower noise level than the prototypes can easily be made. The hybrid tactile sensor designs discussed in this thesis provide simple and economical alternatives in tactile sensor.

7.5 Further Research

In this thesis, new hybrid tactile sensor designs and the accompanying shape recovery algorithms were presented. Its simplicity provided a new alternative in tactile sensor technologies. Further research on these designs may involve the following:

1. Improvement on the physical construction and materials of the prototypes to minimize error levels of the sensor outputs.
2. Improvement on transition detection in a pseudo-signature when applying the Vertex Reconstruction algorithm for shape recovery.
3. Investigation on the performance of the hybrid sensor model with different geometric structure, for instance, semi-spherical shape such as a finger tip.
4. Investigation on the possibility of shape recovery of multiple objects with overlapping pseudo-signatures.

Bibliography

[1] A. Namiki and M. Ishikawa. Optimal grasping using visual and tactile feedback. In *Proceedings of 1996 IEEE International Conference on Multisensor Fusion and Integration for Intelligent Systems*, pages 584–596, 1996.

[2] M. Charlebois, K. Gupta, and S. Payandeh. Shape description of general, curved surfaces using tactile sensing and surface normal information. In *Proceedings of 1997 IEEE International Conference on Robotics and Automation*, pages 2819–2824, 1997.

[3] M. Hakozaki, H. Oasa, and H. Shinoda. Telemetric robot skin. In *Proceedings of 1999 IEEE International Conference on Robotics and Automation*, pages 957–961, 1999.

[4] Howard R. Nicholls and Mark H. Lee. A survey of robot tactile sensing technology. *The International Journal of Robotics Research*, 8(3):3–30, June 1989.

[5] B. E. Robertson and A. J. Walkden. Tactile sensor system for robotics. In *Robot Sensors, Vol 2: Tactile and Non-Vision*, pages 89–97. IFS (Publications) Ltd, UK, 1986.

[6] M. Inaba, Y. Hoshino, K. Nagasaka, T. Ninomiya, S. Kagami, and H. Inoue. A full-body tactile sensor suit using electrically conductive fabric and strings. In *Proceedings of 1996 IEEE International Conference on Intelligent Robots and Systems*, pages 450–457, 1996.

[7] P. Dario and D. De Rossi. Tactile sensors and the gripping challenge. *IEEE Spectrum*, pages 46–52, August 1985.

[8] J. S. Son, E. A. Monteverde, and R. D. Howe. A tactile sensor for localizing transient events in manipulation. In *Proceedings of 1994 IEEE International Conference on Robotics and Automation*, pages 471–476, 1994.

[9] J. Dargahi, M. Parameswaran, and S. Payandeh. A micromachined piezoelectric tactile sensor for use in endoscopic graspers. In *Proceedings of 1998 IEEE International Conference on Intelligent Robots and Systems*, pages 1503–1508, 1998.

[10] D. M. Siegel, S. M. Drucker, and I. Garabicta. Performance analysis of a tactile sensor. In *Proceedings of 1987 IEEE International Conference on Robotics and Automations*, pages 1493–1499, 1987.

[11] D. De Rossi, A. Nannini, and C. Domenici. Artificial sensing skin mimicking mechanoelectrical conversion properties of human dermis. *IEEE Transactions on Biomedical Engineering*, 35(2):83–92, February 1988.

[12] H. Shinoda, K. Matsumoto, and S. Ando. Acoustic resonant tensor cell for tactile sensing. In *Proceedings of 1997 IEEE International Conference on Robotics and Automation*, pages 3087–3092, 1997.

[13] B. L. Hutchings, A. R. Grahn, and R. J. Petersen. Multiple-layer cross-field ultrasonic tactile sensor. In *Proceedings of 1994 IEEE International Conference on Robotics and Automations*, pages 2522–2528, 1994.

[14] Bert Tise. A compact high resolution piezoresistive digital tactile sensor. In *Proceedings of 1994 IEEE International Conference on Robotics and Automations*, pages 760–764, 1988.

[15] Carroll Touch. *Touch Handbook*. Carroll Touch, P.O. Box 1309, Round Rock, Texas 78680, 1996.

[16] L. D. Harmon. Automated tactile sensing. *The International Journal of Robotics Research*, 1(2):3–31, 1982.

[17] Esther M. Arkin, L. Paul Chew, Daniel P. Huttenlocher, Klara Kedem, and Joseph S. B. Mitchell. An efficiently computable metric for comparing polygonal shapes. *IEEE Transactions on Pattern Analysis and Machine Intelligence*, 13(3):209–216, March 1991.

[18] Fujipoly. *Electronic Packaging Components*. Fujipoly, 365 Carnegie Avenue, P.O. Box 679, Kenilworth, NJ 07033-0679, USA, 1996.

INFORMATION TO USERS

This manuscript has been reproduced from the microfilm master. UMI films the text directly from the original or copy submitted. Thus, some thesis and dissertation copies are in typewriter face, while others may be from any type of computer printer.

The quality of this reproduction is dependent upon the quality of the copy submitted. Broken or indistinct print, colored or poor quality illustrations and photographs, print bleedthrough, substandard margins, and improper alignment can adversely affect reproduction.

In the unlikely event that the author did not send UMI a complete manuscript and there are missing pages, these will be noted. Also, if unauthorized copyright material had to be removed, a note will indicate the deletion.

Oversize materials (e.g., maps, drawings, charts) are reproduced by sectioning the original, beginning at the upper left-hand corner and continuing from left to right in equal sections with small overlaps.

Photographs included in the original manuscript have been reproduced xerographically in this copy. Higher quality 6" x 9" black and white photographic prints are available for any photographs or illustrations appearing in this copy for an additional charge. Contact UMI directly to order.

ProQuest Information and Learning
300 North Zeeb Road, Ann Arbor, MI 48106-1346 USA
800-521-0600

UNIVERSITY OF ALBERTA

FIELD ASSESSMENT OF CROWCHILD TRAIL BRIDGE

by

KONG K. TAING 

A thesis submitted to the Faculty of Graduate Studies and Research in partial fulfillment of the requirements for the degree of Master of Science.

in

STRUCTURAL ENGINEERING

DEPARTMENT OF CIVIL AND ENVIRONMENTAL ENGINEERING

Edmonton, Alberta

Spring, 2000

UNIVERSITY OF ALBERTA

LIBRARY RELEASE FORM

Name of Author: Kong K. Taing

Title of Thesis: Field Assessment of Crowchild Trail Bridge

Degree: Master of Science

Year this Degree Granted: 2000

Kong K. Taing
#201, 5540 44 Avenue,
Red Deer, Alberta
T4N 3J3

Date : December 31, 1999

UNIVERSITY OF ALBERTA

FACULTY OF GRADUATE STUDIES AND RESEARCH

The undersigned certify that they have read, and recommend to the Faculty of Graduate Studies and Research for acceptance, a thesis entitled Field Assessment of Crowchild Trail Bridge submitted by Kong K. Taing in partial fulfillment of the requirements for the degree of Master of Science in Structural Engineering.

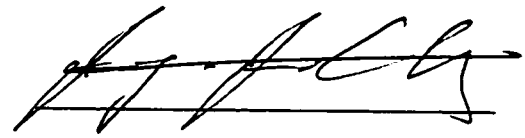

Dr. J. J. R. Cheng, Supervisor

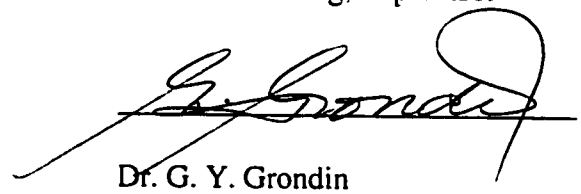

Dr. G. Y. Grondin

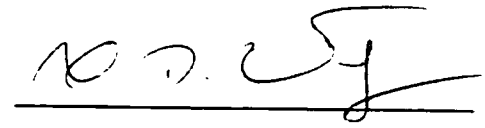

Dr. X. D. Wang

December 17, 1999

ABSTRACT

The Crowchild Trail Bridge in Calgary, Alberta is a three-span, two-lane, one-way traffic overpass. In 1997, its superstructure was replaced by a steel-free concrete deck supported by five steel plate girders. In order to assess the performance of the bridge, the University of Alberta developed an extensive instrumentation and monitoring program at the time of construction. Initial load tests were carried out in August 1997, before the bridge was open to traffic, to establish the baseline structural characteristics of the bridge. The bridge was tested again in August 1998, one year after opening to traffic. The testing programs include ambient vibration test, static and dynamic load tests using trucks with known axle loads and running at various speeds. In addition to the strain gauges, thermistors, and fibre optic strain gauges installed in the first year, cable transducers and accelerometers were added in the second year tests.

Natural frequencies and mode shapes of the bridge were determined by the ambient vibration tests performed in 1997 and 1998. The investigated frequencies and mode shapes show good correlation with theoretical closed form solutions. However, all the investigated frequencies have shown a reduction of approximately 0.20 Hz after the bridge has been in service for one year. The static and dynamic tests show that the composite action in the positive moment region has not changed during the first year of operation, but there is a shift of 98 mm in the neutral axis in the negative moment region due to the cracking of the concrete deck. Since the mass of the structure has not changed, this may indicate that the stiffness of the bridge has been reduced. Good load sharing between the girders was observed in both positive and negative moment regions. The

damping ratio and dynamic amplification factor was obtained from both the strain gauge and deflection data. The local strain gauge data yielded higher dynamic amplification factors than the ones from the overall deflection results. Both transverse and longitudinal cracks were observed on the bottom surface of the bridge deck. As of August 1998, cracks visible on the deck show no serviceability concern.

ACKNOWLEDGEMENTS

This research was conducted under the supervision of Professor Roger J.J. Cheng. The privilege of working with him has been a great source of inspiration for me. His helpful guidance, encouragement and invaluable support are greatly appreciated. Funding from UAEM and ISIS Canada and cooperation from the City of Calgary are appreciated.

Dr. Gilbert Grondin has been extremely helpful in the preparation of this thesis. I am grateful of his timeless effort, technical input, persistence and encouragement.

I would like to thank Dr. Shahab Afhami for his great technical assistance in all instrumentation and countless times he made available for me.

TABLE OF CONTENTS

LIST OF TABLES

LIST OF FIGURES

LIST OF PHOTOS

LIST OF ABBREVIATIONS AND NOTATIONS

NOTATIONS

A, B	Constants
c	Damping Coefficient
c_{cr}	Critical Damping Coefficient
E	Modulus of Elasticity
E_C	Modulus of Elasticity of Concrete
E_S	Modulus of Elasticity of Steel
F	Gauge Factor
F_y	Yield Strength
$f'_{C_{28}}$	Concrete Strength on the 28^{th} day
f_{cr}	Ultimate Concrete Strength
f_D	Damping Force
f_I	Inertia Force
f_S	Stiffness Force
G, r	Constants that Depend on Initial Conditions
G_1, G_2	Constants that Depend on Initial Conditions
I	Moment of Inertia
k	Stiffness
l	Length
M	Moment
m	Mass or Number of Successive Peaks
n	Modulus of Elasticity Ratio
P	Concentrated Load
$P(t)$	Force as a function of time, t
$Q(x)$	Spartial function
$R_{internal}$	Internal Reaction
Rx	Reaction in the X direction

Ry	Reaction in the Y direction
T_D	Damping Period
T_n	Undamped Period
$T(t)$	Time function
t	Time
u	Displacement
$\dot{u}$	Velocity
$\ddot{u}$	Acceleration
$\dot{u}_o$	Initial Velocity
$\ddot{u}_o$	Initial Acceleration
V	Shear Force
ε	Strain
γ_C	Concrete Density
λ	Constant
θ	Phase of Vibration
ρ	Magnitude of Vibration
Ω	Resistance Ohms
w_n	Undamped Angular Frequency
w_D	Damped Angular Frequency
ξ	Damping Ratio

ABBREVIATIONS

AE10	Epoxy for Strain Gauges
CFRP	Carbon Fibre Reinforced Polymers
CHBDC	Canadian Highway Bridge Design Code
GFRP	Glass Fibre Reinforced Polymers
ISIS	Intelligent Sensing of Innovative Structure

NEFMAC	NEw Fiber composite MAterial for reinforcing Concrete
OHBDC	Ontario Highway Bridge Design Code
OBB	Ontario Bridge Barrier
TUNS	Technical University of Nova Scotia
UBC	University of British Columbia
U of A	University of Alberta

1. INTRODUCTION

1.1 Background and Statement of the Problems

Bridges have been built as early as the second century BC. Roman engineers developed and utilized the concept of arching action for centuries (Barker *et al.*, 1997). In fact, some of the oldest stone arch bridges from the ninth century BC still survive and remain functional even today. The basic concept of arching action is shown in Figure 1.1 below. Arch structures have proven themselves to be beautiful, durable and adaptable to ever changing environmental load. Despite its excellent track record, the arch structural form was eventually replaced with lighter weight and cheaper to build structures; such as steel and steel reinforced concrete structures.

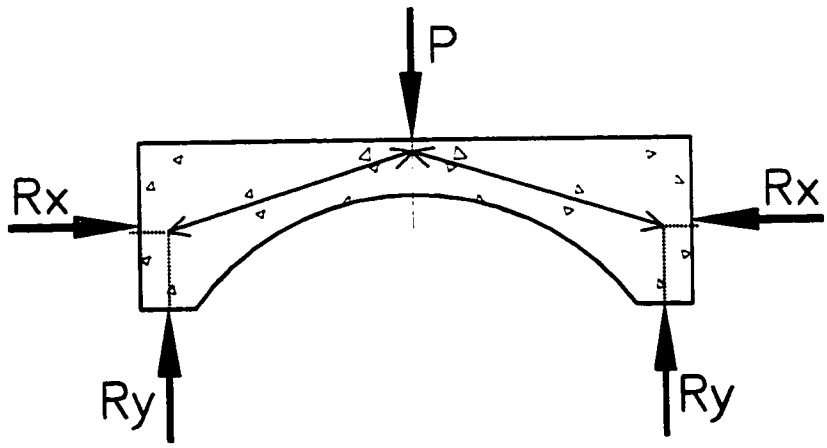

Figure 1.1: Basic Concept of Arching Action

Steel bridges became popular in the mid-eighteenth century, during the Industrial Revolution. By the early nineteenth century, steel reinforced concrete bridges appeared and grew at an exponential rate (Barker *et al.*, 1997). Numerous factors contribute to the popularity of reinforced concrete structures. The cost is competitive and its weight often reduces or eliminates dynamic problems. Nonetheless, reinforced concrete bridges have merely been introduced a few decades ago, yet a great number of them already need to be replaced due to corrosion of steel reinforcement or deterioration of concrete. Costs to

retrofit or replace such structures are both a nuisance to the public and expensive. Because reinforced concrete structures have numerous durability problems in northern climates, an alternative method of construction is needed in such regions.

One of the durability problems encountered with reinforced concrete structures is related to the corrosion of the steel reinforcement inside the concrete deck. Particularly in cold regions where deicing salt is used, the problems are most apparent. Poor quality concrete and inadequate concrete cover for the reinforcing steel account for the majority of the durability problems. Since the steel reinforcement is embedded, it is either difficult or impossible to access without damage to the structure as a whole. Thereby, maintenance, evaluation, and repairs of bridge superstructures are very expensive and sometimes impossible. Therefore, it is necessary to find novel approaches to the use of steel reinforcement and to assess their durability.

1.2 Innovative Structures

A new and innovative approach to bridge deck design is to totally exclude internal reinforcement from the deck, utilizing the steel reinforcement in the form of external tension straps. Figure 1.2 shows the arching action concept with external steel reinforcement. Photo 1.1 shows such innovative concept used in the construction of Crowchild Trail Bridge in Calgary, Alberta. This concept is the same as the traditional reinforced concrete deck except that the steel in tension is now taken out of the deck. The advantages of this system are as follow:

1. It results in a better use of concrete's high compressive strength and steel's high tensile strength;
2. It requires less concrete and therefore material cost is reduced;
3. It reduces the dead weight on the structure;
4. It saves labor cost, since no placement of internal steel reinforcement is needed;

5. It allows for better maintenance of the steel reinforcement since it is exposed and the application of protective coating to the steel straps is no longer an impossible task;

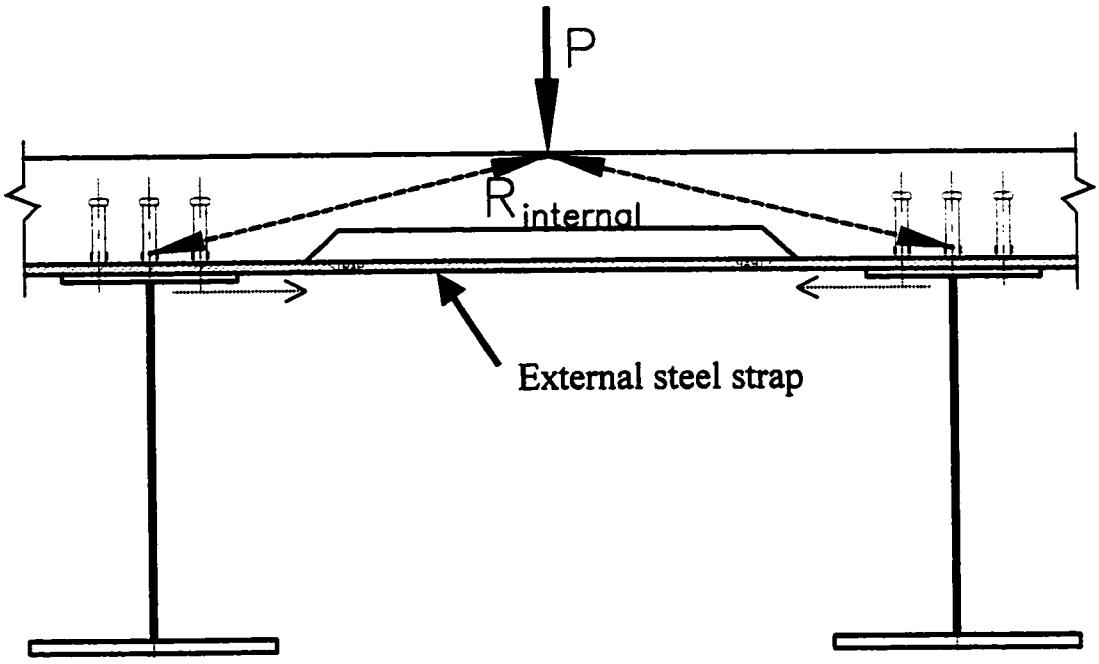

Figure 1.2: Arching Concepts with External Steel Reinforcement

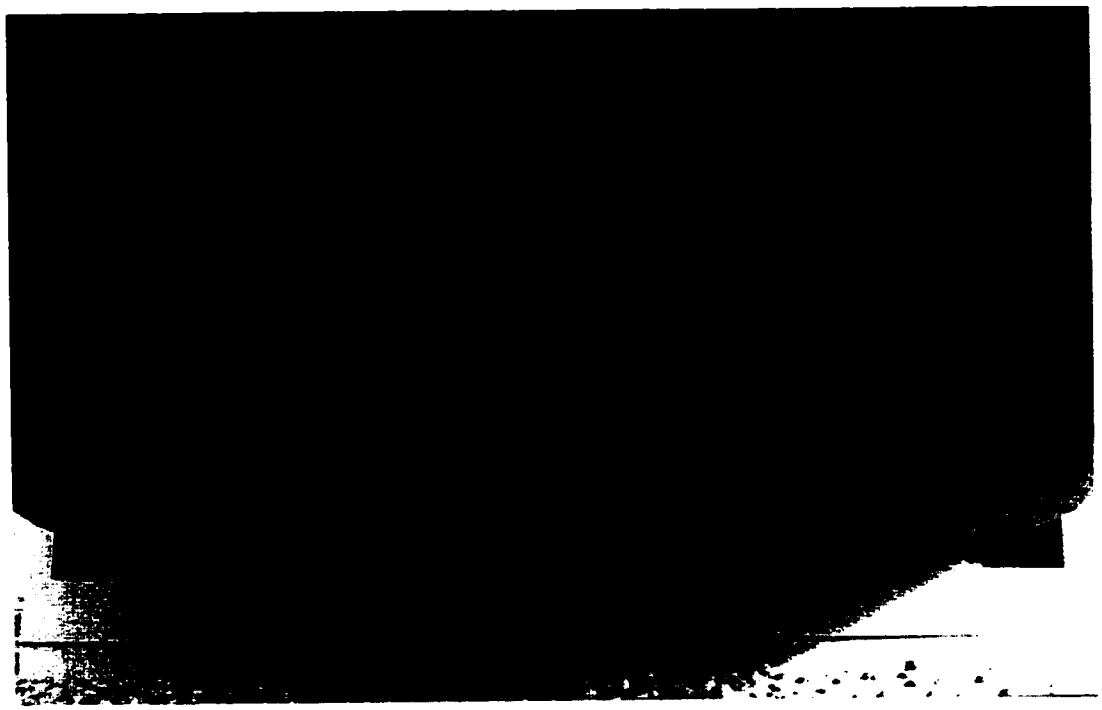

Photo 1.1: Crowchild Trail Bridge's Superstructure at North Abutment.

1.3 Scope and Objectives

The Crowchild Trail Bridge is located at the intersection of Crowchild Trial and University Drive in Calgary, Alberta. It consists of three continuous spans, two-lane, one-way traffic overpass. The total length of the bridge is 92.878 meters with two interior supports. This bridge was built in June 1997 using the innovative steel-free deck approach described in section 1.2, and it is the first of its kind in the world that utilizes this innovative approach of steel-free deck with external reinforcement over the positive and negative moment regions. Photo 1.2 shows the steel-free deck concept used over the negative moment region at Pier No. 1. Although steel-free deck design is believed to solve the internal steel corrosion problem and accessibility of the steel for maintenance and repair issues, it is essential to assess and understand its performance and long-term durability. The objective of this research is to evaluate and assess the performance of Crowchild Trail Bridge by using the field instrumentation and testing on the bridge.

Field assessment of Crowchild Trail Bridge focuses on three main issues: the performance under serviceability conditions, change of major characteristics of the bridge with time, and its long-term durability. In order to assess its performance under serviceability condition, static and dynamic tests were carried out using trucks with known axle loads. Ambient vibration tests were performed to determine the fundamental dynamic characteristics of the bridge. The fundamental structural characteristics obtain from truck tests and ambient vibration tests are evaluated annually and compared to those obtained before the bridge was open to traffic. To study long term durability, the bridge was inspected visually, and the crack patterns were mapped periodically. The scope of this thesis is confined to the field assessment of Crowchild Trail Bridge over its first two years of operation.

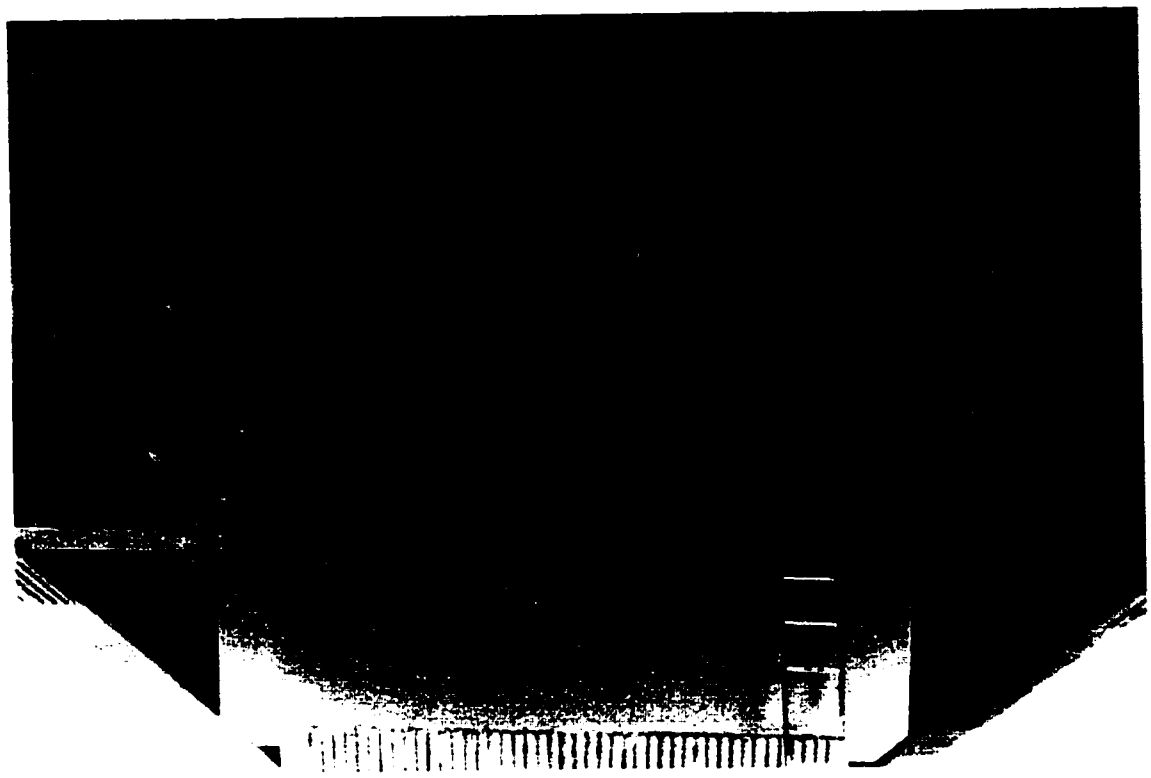

Photo 1.2: Superstructure of Crowchild Bridge at Pier No. 1 (Looking South)

1.4 Thesis Layout

Chapter 2 presents a review of the literature on steel-free decks. Scale model and full-scale model test results on steel-free decks at positive and negative moment region are outlined and summarized. Construction and instrumentation of the Crowchild Trail Bridge are described in detail in Chapter 3. Mechanical properties of materials used, layout of structural elements and final as-built details are documented.

Chapter 4 presents a summary of experimental field test results and experimental analysis obtained from the Crowchild Trail Bridge. Before the bridge was opened to traffic, Phase I test was conducted to establish a reference structural characteristic of the bridge. In Phase II of the tests, static and dynamic tests were performed. Details of Phase II testing are also discussed in terms of fundamental structural characteristics and its changes over time. Crack patterns are also documented and presented in this chapter. The experimental results are used to compare to the theoretical solutions discussed in

Chapter 5. Finally, Chapter 6 presents a summary of the findings for the field assessment of the Crowchild Trail Bridge. Conclusions are drawn and suggestions are made for future research in this field.

2. LITERATURE REVIEW

2.1 Steel-Free Deck in the Positive Moment Region

The concept of steel-free deck started with the work of Kinnunen and Nylander (1960) who proposed a model to predict the punching resistance of simply supported concrete slabs subjected to a concentrated load. Hewitt and Batchelor (1975) later incorporated restraint boundary conditions and the concept of compressive membrane stresses (known as internal arching action) with the model proposed by Kinnunen and Nylander. Hewitt and Batchelor's model, however, was developed for reinforced concrete slabs with internal reinforcement. The proposed restraint factors were empirical and can only be determined through experimentation.

The Technical University of Nova Scotia (TUNS), in collaboration with the Ministry of Transportation of Ontario, initiated a research program on steel-free bridge deck design (Mufti *et al.*, 1993). Five half-scale models of steel-free deck with in-plane restraint provided by external steel straps were constructed and tested. The results of these tests lead Mufti *et al.* (1996) to a gradual refinement of the steel-free deck concept. The majority of their work on this concept has been empirical. Finite element models developed by Wegner and Mufti (1994b) have provided useful guidance to help reduce the amount of experimental work.

Wegner and Mufti (1994b) proposed a method to incorporate internal arching action concept for unreinforced slabs with in-plane restraint provided by external reinforcement. Several of Wegner and Mufti's basic assumptions used in the development of the model were adopted from Kinnunen and Nylander. The finite element results however did not match experimental results with required accuracy and the concept was found to be very complex and sensitive to modeling parameters (Newhook *et al.*, 1995).

After eight years of laboratory studies in the design and testing of steel-free concrete deck concept, the Salmon River Bridge in Halifax, Nova Scotia was built (Newhook *et al.*, 1996). The Salmon River Bridge consisted of two spans, each 31.2 m in length, with a simply supported superstructure. To verify the design, a full-scale model of the superstructure was constructed at the Heavy Structures Laboratory of TUNS. The model was tested for various loading conditions to assess the ultimate strength behaviour.

2.1.1 Half-Scale Model

To optimize the internal arching action in steel-free deck design, Mufti *et al.* (1993) constructed various half-scale models based on the steel-free deck concept as shown in Figure 2.1. The first three of the five half-scale models were constructed as cast-in-place with 100 mm thick concrete deck. The girders were 2.31 m apart and 3.66 m long. A concentrated load was applied to a 127 mm x 254 mm steel plate pad with rubber bearing. The load represented wheel load, and it was applied at half way between the two girders.

In the first half-scale model, three internal diaphragms were used but none at the supports. This specimen failed at 173 kN. The failure mode was a hybrid of flexure and punching shear. Diaphragms were added at the two end supports in the second half-scale model and the failure load increased to 222 kN. The failure mechanism for the second model was similar to the first model; a hybrid of flexure and punching shear. In the third half-scale model, the diaphragm size was increased (Mufti *et al.*, 1993) and eight steel straps were added at 457 mm on centers by welding to the underside of the top flanges of the girders. The third model was tested three times, and the variable was the location of the load along the span. In the first test, the model was loaded at the midspan, this model failed in punching shear at a load of 418 kN. In the second and third tests on this third model, the load was applied at different locations along the span. As the load point approached the edge of the slab, the failure modes again became a hybrid of flexural and punching shear.

Subsequently, a fourth half-scale model was built to investigate the behaviour of a multi-girder system whereby the concrete on top of the interior span may crack under tension due to loads straddling the girder. The test results showed simultaneous punching shear failure under the two loads straddling the interior girder. The failure load was 418 kN for each loading location. Since the failure loads was the same for a single load and dual load straddling the girder, the fourth specimen demonstrated that the proposed design does support multi-girder systems.

Newhook *et al.* (1995) later constructed a fifth half-scale model similar to the fourth model described above. This model was designed to evaluate the following parameters: location of load, edge beams, strap spacing and stiffness, diaphragm contribution, and reduced deck thickness. In the previous four specimens, loads were always applied directly above or adjacent to straps, such that the straps were in the most advantageous position to provide restraint. In the fifth specimen, however, the loads were applied at the midpoint between straps, such that the straps would not be in the optimal position to provide restraint. The fifth specimen was used for serveral ultimate static load tests; all failure modes were punching shear. The authors concluded that the travelling nature of wheel loads does not present a problem in terms of the ability of the straps to provide the required lateral restraint, provided that the strap spacing is not excessive. Newhook *et al.* (1995) removed a portion of the diaphragm, but no significant effect was found in the punching failure mode. The results further reinforced that straps provide more effective lateral restraint than diaphragms. No dynamic testing was performed.

2.1.2 Full-Scale Model

Based on the fifth half-scale model, Mufti *et al.* (1995) proceeded with a full-scale model of the Salmon River Bridge. Two 12 m long girders were simply supported and spaced at 2700 mm on center. Lateral tie was constructed at each end of the girders with C380 x 50 mm channels bolted to top flange of the girders, which were made composite with the deck using shear studs. At the ends, the deck was thickened to 300 mm. Angles

L100 x 100 x 10 mm were used for the remainder of the K-Type diaphragms at the ends. At the mid-span, angles L100 x 100 x 10 mm were used for the X-Type bracing system with a bottom chord. Concrete strengths for this full-scale model and the Salmon River Bridge are listed in Table 2.1 below.

Table 2.1: Concrete Strength

Component with Fibres	Experimental Model	Salmon River Bridge
Compressive Strength	41.8 MPa	39.0 MPa
Modulus of Rupture	5.2 MPa	5.9 MPa

Figure 2.1 shows typical interior cross section and Figure 2.2 shows typical plan view of the deck. The model consisted of a 200 mm thick slab with 100 mm haunches. The slab was supported by two W610 x 241 steel beams tied together at the top flange with 100 mm x 12.5 mm steel straps spaced at 1200 mm along the entire length of the test specimen. The load patch was 250 mm x 500 mm, centered between the girders.

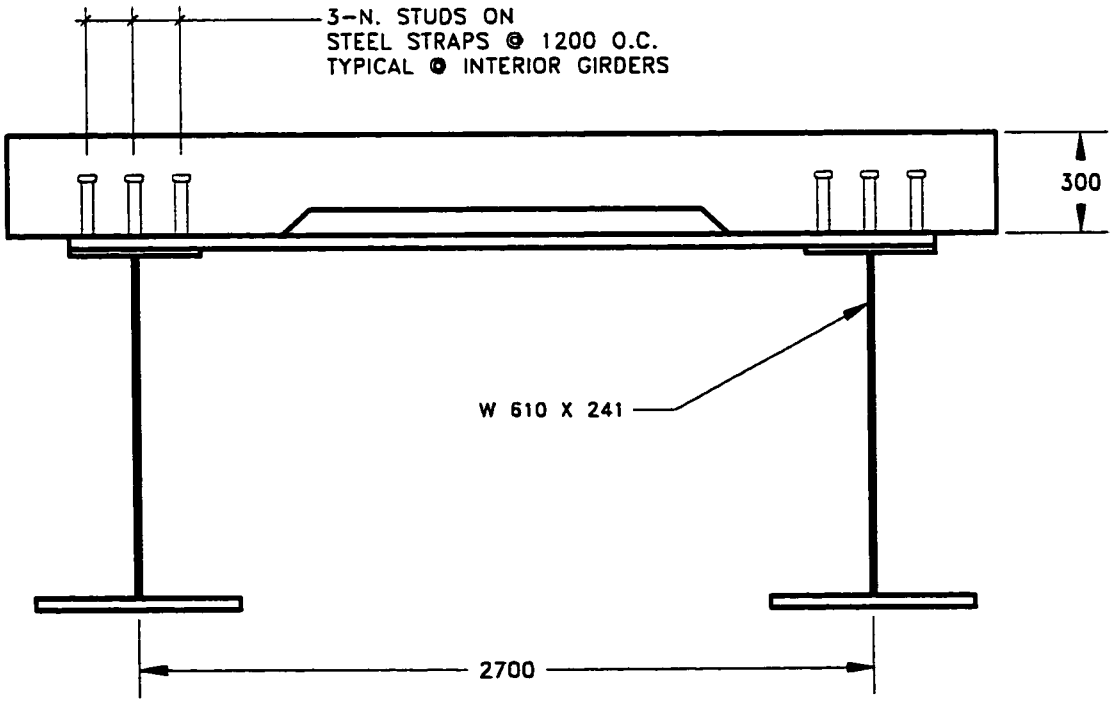

Figure 2.1: Typical Cross Section of the Superstructure.

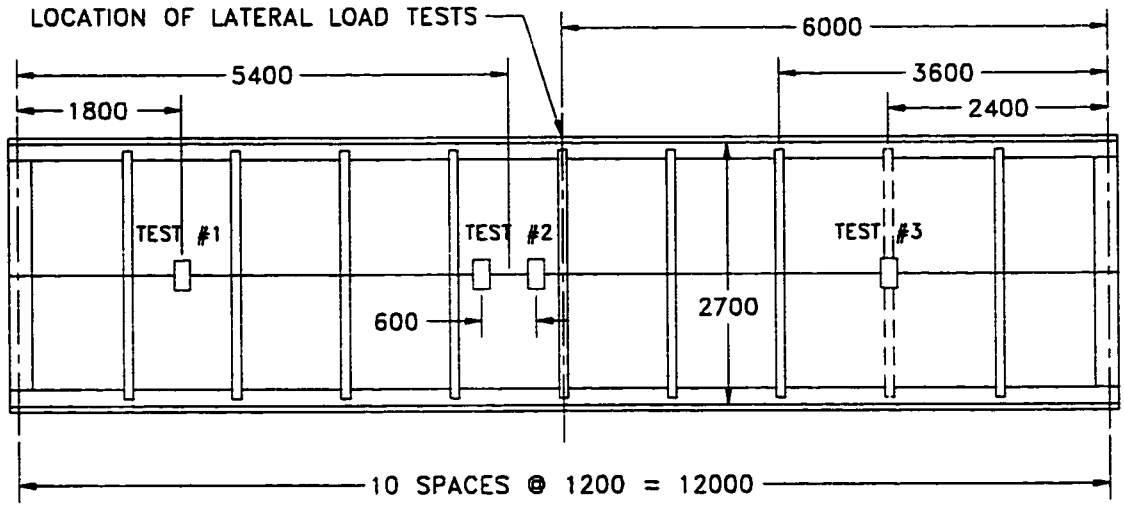

Figure 2.2: Plan View: Location of Load Tests (Newhook *et al.*, 1996)

To determine the contribution of the cross bracing to the lateral stiffness of the system, a series of lateral point loads were applied to the system, as shown in Figure 2.2 above. Before the concrete deck was cast, a series of horizontal loads was applied to the fully braced system, in Test Series 1. Fully braced diaphragms, consisting of K-Type braced plus the top and bottom flanges of the girders were tied together. In the Test Series 2, the bottom chord of the diaphragm was removed leaving K-Type bracing. For Test Series 3, the diaphrgam was completely removed. Results from these tests show that the braced diaphragm provide less than 12 percent of the total lateral restraints stiffness at the diaphragm location and quickly diminishes as the load moves away.

After the concrete deck was cast, Newhook *et al.* (1996) conducted the following three destructive tests. Test #1 was conducted to determine the load capacity of the system. Test #2 was conducted to simulate a very severe tandem axle loading. Test #2 was stopped at a load of 1373 kN for safety reasons. Test #3 was conducted to simulate the failure of the strap. The test was terminated at a load of 863 kN without failure. At this point, the deck was severely damaged and longitudinal cracks ran full length along the underside of the deck. The strap directly beneath the load point was removed to simulate strap failure; the deck was loaded to a maximum of 1118 kN and failed at 951 kN.

Newhook *et al.* (1996) made recommendations for the calculation of the lateral restraint stiffness of steel-free deck system by only considering the contribution from steel straps alone. The steel-free deck on the Salmon River Bridge was designed based on this recommendation. The design approach proposed by Newhook et al. (1996) leads to very conservative results since it does not include the lateral stiffness contribution from girders, cross bracings, outside restraint from straps, and load sharing of the system as a whole. The lateral restraint contribution from straps compared to the total lateral restraint of the model was only 40 percent of the total lateral stiffness of the system. Newhook *et al.* (1996) recommendations are therefore conservative.

Stress-strain curves plotted by Newhook *et al.* (1996) show that the steel-free deck system seems to suggest plastic deformation after 470 kN. In terms of serviceability, this can be a problem. Authors stated that the significant change in behaviour of the system corresponded to the load at the point where the first crack was observed at the underside of the deck beneath the loading point. It is also important to consider the fatigue of concrete, as the maximum service load range is approximately one fifth of the concrete cracking load.

2.1.3 Salmon River Bridge Project

The first steel-free deck bridge was built on the Trans-Canada Highway in Nova Scotia. It was open to traffic on December 5, 1995. The bridge consists of two 31.2 m simply supported spans. The cross section consists of steel plate girders spaced at 2.7 m with diaphragms spaced at 7200 mm supporting a 200 mm deck with haunches of 130 mm and no overhangs. The diaphragms are built-up of C380 x 50 with the strong axis in the plane of the deck as opposed to conventional practice, which would have the strong axis in the vertical plane. With this new concept, Newhook *et al.* (1996) believed that adequate in-plane restraint would be developed to achieve punching failure capacity of the deck. The concrete is reinforced with chopped polypropylene fibre. Lateral confinement is provided by 100 x 14 mm uncoated weathering steel straps welded to the top of the

girders at 1200 mm on center. Although it is believed that the steel straps need to only be 100 x 12 mm, an extra 2 mm is added to allow for the weathering process.

The predicted ultimate capacity for this configuration was 550 kN; this load capacity was limited by the yielding of the strap adjacent to the maximum wheel load. Testing of a full-scale model of this structure, which accounts for lateral stiffness of the girder, deck haunches and post yield capacity in the straps indicated that the actual capacity was in excess of 1200 kN (Newhook *et al.*, 1996). The weld detail used to attach the steel straps to the top flange of the beam was designed based on the following two design considerations (Newhook *et al.*, 1996):

1. Yielding of the steel straps at the factored load level.
2. Under cyclic service loads the stress range in the weld was limited to 48 MPa as per CSA-S6 requirement for Class W connection detail with over 2 million cycles of load reversal.

Salmon River Bridge was instrumented and monitored by TUNS and the Ministry of Transportation of Ontario (Newhook *et al.*, 1996). Strain sensors were mounted on the steel straps and girders to measure their field performance. Sensors consist of electronic resistance foil gauges and Bragg Grating type fibre optic sensors. In addition, three fibre optic sensors were embedded in the NEw Fiber composite MAterial for reinforcing Concrete (NEFMAC) grids. No field data on Salmon River Bridge were presented (Doncaster *et al.*, 1996). Consequently, this fact further reinforced the need to field evaluate such innovative structure.

2.1.4 Kent County Road

Another steel-free deck was built in Chatham, Ontario, in 1996. The bridge consists of four spans of 13 m, 20 m, 20 m, and 13 m length. The two 13 m long spans were built using the steel-free deck concept. The two interior spans used a conventional steel reinforced concrete deck. The deck consists of a 175 mm slab supported by five

girders spaced at 2.1 meters. The deck slab overhangs 0.9 m beyond the outer girder and the overhangs were reinforced with Glass Fibre Reinforced Polymers (GFRP) bars. The barriers are reinforced with double-headed tension bars made of stainless steel for connection between barrier and deck slab. In the negative moment region of the deck, GFRP bars were used as the reinforcement. The bridge barrier wall used was Ontario Bridge Barrier (OBB) is also free of corrodible steel reinforcement. The bridge was also instrumented with strain gauges but no known field data were reported. Again, this innovative approach to steel-free bridge deck design had been put into used on two different superstructures, yet no field data had been reported in regards to its performance in service.

2.2 Steel-Free Deck in the Negative Moment Region

Dorey *et al.* (1996) investigated the suitability of continuous steel-free deck for multi-span structures. A study was conducted to determine whether the steel-free deck concept would have sufficient uncracked moment capacity over the negative moment region to meet the OHBDC. A full-scale model was constructed and tested at TUNS. Dorey *et al.* showed that the uncracked portion of the superstructure had adequate strength for the specified loads, but not for the factored loads. The test by Dorey *et al.* also showed that the uncracked specified serviceability stresses in the concrete did not meet OHBDC-91 limit of $0.4f_{cr}$ for crack control. This is a potential concern in the development of continuous steel-free deck over negative moment regions. However, researchers at TUNS believe that steel-free deck concept over negative moment region has sufficient reserve tensile capacity to carry the specified tensile loads (Dorey *et al.*, 1996).

2.2.1 Full-Scale Model

Dorey *et al.* (1996) constructed a full-scale test specimen of the negative moment region. The length of the test specimen was taken as approximately 0.2 times the span length of the continuous span. A 12.5 m long test specimen was used to model the negative momen region of a two span 31.2 m bridge. The specimens were tested as simply supported beams with the loads applied to create tension in the top fibers. The first crack appeared near the location of the applied load at 314 kN. This was well below the predicted 715 kN capacity based on measured flexural strength of the concrete. With additional load, additional cracks developed in the transverse direction. The cracks that formed during the test ranged in width between 0.50 mm to 2.20 mm at termination of the test. The load at first cracking of the deck corresponds to a stress of 2.9 MPa, which is close to the lower measured splitting strength of concrete, 3.2 MPa. Dorey *et al.* (1996) suggested that size effect is a factor for lower value in the model than in the material tested.

The load versus deflection curve obtained from the tests conducted by Dorey *et al.* (1996) shows linear relationship before cracking, indicating a constant stiffness and elastic behaviour. After cracking, the slope of the load versus deflection curve decreased, indicating a loss of composite action. The slope of the load versus deflection curve continued to decrease until it reached a lower bound (slope again became constant). Dorey *et al.* have successfully correlated the predicted model to the experimental model in regards to composite action before crack and after crack relationship. The test results raised two important concerns: low cracking load capacity and large crack widths in negative moment regions.

The experimental full-scale model had shown that both strength and serviceability cracking limit states were exceeded in the negative moment region. Dorey *et al.* (1996) suggested that the strength limit states could be easily addressed by

- Proportioning the section such that the neutral axis is higher within the section.
- Increasing the concrete strength.

The writer, however, believes that by cambering the support in the negative moment region before placement of the concrete and lowering the support to its desired location after placement of the concrete, beneficial prestressing forces would be developed in the concrete deck to help counteract the negative moment stresses. Of course, creep must be considered in the design.

2.3 Serviceability Issues

Serviceability must also receive due consideration in addition to the strength issues. Many freeze thaw cycles can deteriorate the concrete around the cracks and the deterioration can be severe enough to cause overall deck failure. In addition, excessive cracking in the negative moment region gives the chloride laden water on the top of the deck easy access to the steel girders, leading to their premature deterioration. Finally, aesthetics of structure needs to be considered.

As suggested in the name *'innovative design'* of steel-free deck, it is essential to field evaluate the durability of such design and its' performance. Steel-free deck is an innovative design proposed by Mufti and his associates, and it has been put into use on both the Salmon River Bridge and the Kent County Road. Although these bridges have been instrumented, no field data have been reported on its performance or durability. TUNS had done extensive laboratory research works on the concept of steel-free deck in collaboration with Ministry of Transportation of Ontario. However, all laboratory work on scale model and full-scale model have been focused on the ultimate strength behaviour and little on the serviceability. In addition, no dynamic testing was investigated for a bridge deck that only performed under dynamic loading.

Use of steel-free deck concept has been extended into the negative moment region of the Crowchild Trail Bridge in Calgary, Alberta near the University of Calgary. Crowchild Trail Bridge's construction and instrumentation are described in detail in Chapter 3. The University of Alberta has extensively developed field instrumentation and monitoring program on this bridge. The purpose of this program was to field assess the bridge's static and dynamic behaviour in service. This program, in turn, established a base structural characteristic of the bridge, thereby allowing a future long term monitoring program on the bridge to be developed and evaluated.

3. CONSTRUCTION AND INSTRUMENTATION OF THE CROWCHILD TRAIL BRIDGE

3.1 Background

The Crowchild Trail Bridge is a two-lane, one-way traffic overpass located on the intersection of Crowchild Trail and University Drive near the University of Calgary. The original superstructure was a three-span prestressed concrete box-girder bridge designed for HS20 truck loading. Each span is simply supported, and pretensioned longitudinally. Due to a large increase in traffic loads and rapid deterioration of the superstructure, it was necessary to replace the superstructure of the bridge. Photo 3.1 shows the old Crowchild Trail Bridge concrete box girder system during demolition.

Photo 3.1: Old Crowchild Trail Bridge Superstructure under Demolition

The old Crowchild Trail Bridge was evaluated using Clause 11 of the Ontario Highway Bridge Design Code (OHBDC-1991) and Clause 12 of CSA/CAN–S6-M88 for

a CS-615 design truck. Evaluation showed that the prestressed concrete box girders had insufficient bending capacity. Furthermore, the development and quantity of reinforcement in the draped connection and T-Beam corbel were inadequate. Therefore, the bridge was upgraded in July 1997. Two options for the upgrade were considered. The first option was to replace the concrete box girders with new concrete girders. With this option, it would have been necessary to also strengthen the existing foundations. The second option was to replace the superstructure with lighter structure, thereby eliminating the need to modify the supporting foundation.

After 20 years of operation, the original Crowchild Trail Bridge superstructure was already in need of replacement. It was therefore necessary to find a better method of construction, which would make better use of the concrete strength and would improve durability in northern regions. For economic and durability reasons, it was decided to replace the old Crowchild Trail bridge superstructure by a steel-free deck on steel girders. With this option, the bridge could carry the CS-750 truck load, and the existing piers were reused without any need of modification. The design for the typical overload trucks is based on the Ultimate Limit State load rating, using Clause 12 of CAN/CSA-S6-M88.

Photo 3.2: Crowchild Trail Bridge's Superstructure (Demolition Process)

Photos 3.1 and 3.2 show the demolition process of the previous concrete box girder superstructure. Furthermore, it shows how care was taken to protect the existing piers so that they could be reused in the new construction without any modification. Nonetheless, the steel-free deck concept is relatively new, and it is therefore necessary to field evaluate its performance in the field from the points of view of strength and serviceability.

3.2 Description of Crowchild Trail Bridge

3.2.1 General

Crowchild Trail Bridge has three continuous spans, 29830 mm, 32818 mm, and 30230 mm long from the North abutment. The superstructure is a composite structure with a cast-in-place fiber reinforced concrete deck continuous over positive and negative moment regions. The deck is supported on five built-up steel plate girders. This is the first continuous steel-free deck in the world. Figure 3.1 shows the West elevation of the new Crowchild Trail Bridge. Photo 3.3 shows the new Crowchild Trial Bridge after construction.

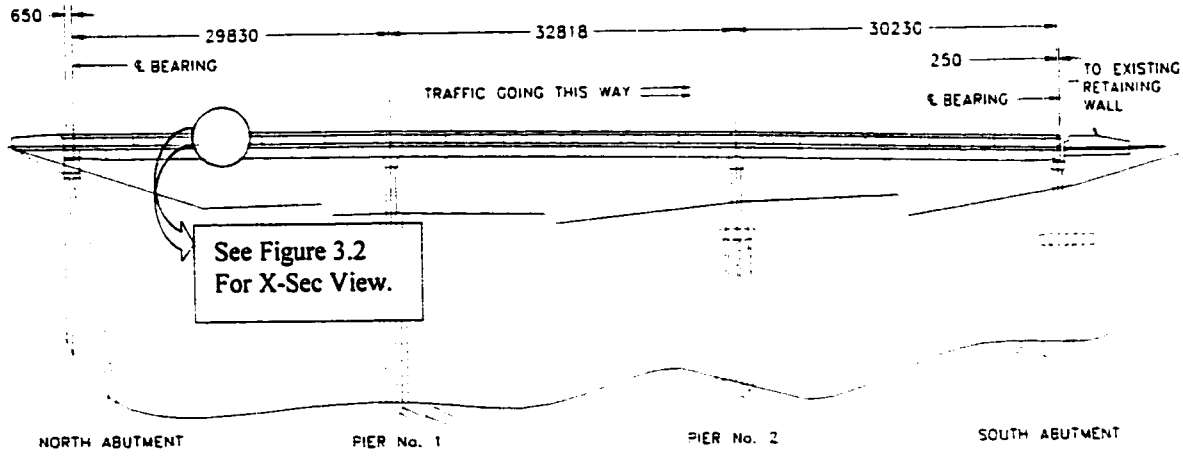

Figure 3.1: Crowchild Trail Bridge: West Elevation

Photo 3.3: New Crowchild Trail Bridge (Looking North-East)

The major problem with the conventional reinforced concrete deck is the corrosion of the internal steel reinforcement in severe winter climates. The new Crowchild Trail Bridge has a deck width of 9030 mm and it has no internal steel reinforcement. Figure 3.2 shows the overall cross-sectional view of the Crowchild Trail Bridge superstructure. Refer to drawing Figure A1 in Appendix A for more detailed information.

Within each span, there are four cross frames equally spaced. These cross frames serve as diaphragms and provide for lateral stability of the girders and load sharing between the girders. The deck behaves much like a conventional reinforced concrete deck, except that there is no internal tension steel reinforcement, which was replaced by external steel straps. Photo 3.4 shows the completed deck view from under the bridge. In this case, the exposed steel reinforcement consists of tension straps as shown in the photo.

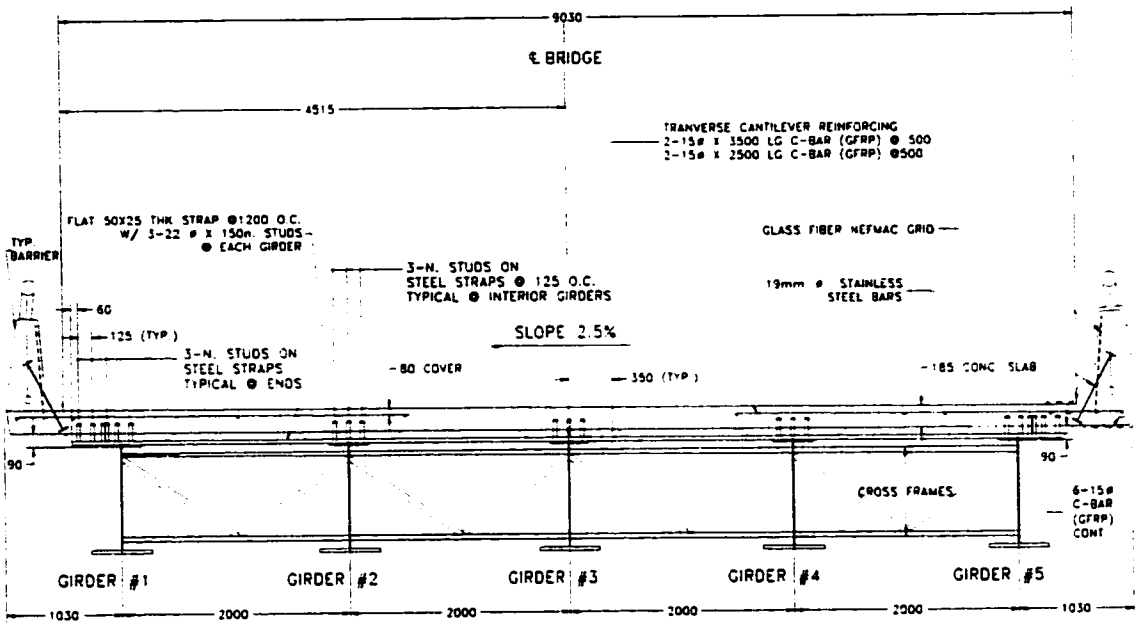

Figure 3.2: Crowchild Trail Bridge--Cross Section

Photo 3.4: Underside of Crowchild Trail Bridge (Looking North)

3.2.2 Concrete Bridge Deck

With the configuration shown in Figure 3.2, the main part of the concrete deck is only 175 mm thick with a 90 mm haunch spanning between the girders parallel to the tension straps. The main purpose of the tension straps is to provide the necessary lateral constraints to develop the internal arching action in the concrete deck. The tension-straps are 50 x 25 mm bars spaced at 1.2 m on center. Loss of section due to the weathering process has been considered in the design of the straps. A plan view of the strap layout is presented in drawing Figure A3 of Appendix A. The drawing also presents the plan view of the girder layout and cross sections of the girders along the length of the bridge.

The primary concern in the use of steel-free deck over negative moment regions is the potential excessive flexural cracks width in the concrete deck, which may affect the internal arching action required for the steel-free deck to function. Tests at TUNS have tried to address this negative moment region issue. Tests confirmed that cracks in the transverse direction do not significantly affect the internal arching capacity of the slab (Dorey *et al.*, 1996). Although transverse cracks consist mainly of shrinkage cracks and do not cause structural concerns, in the negative moment region these cracks could increase beyond the limits set out by the OHBDC (1991). To take care of the concern in regards to transverse crack, Glass Fiber Reinforced Polymer (GFRP) bars are utilized over the piers. Photo 3.5 shows the GFRP bars over the intersection of the bridge Girders and Pier No. 1 diaphragm.

GFRP reinforcement is also used on both sides of the cantilevers of the deck, as shown in Figure 3.2 and in Photo 3.6. Prefabricated glass fiber reinforcing grids, NEFMAC, are used for the reinforcement of bridge barriers and double headed stainless steel bars are used to anchor the barriers to deck.

The specified 28-day concrete compressive strength is 35 MPa. The concrete was mixed with 0.45 percent by volume of chopped polypropylene fibers. Concrete mixes

used are in conformance with CAN3-A23.1-M90. Table 3.2 shows the concrete mix characteristics for the Crowchild Trail Bridge.

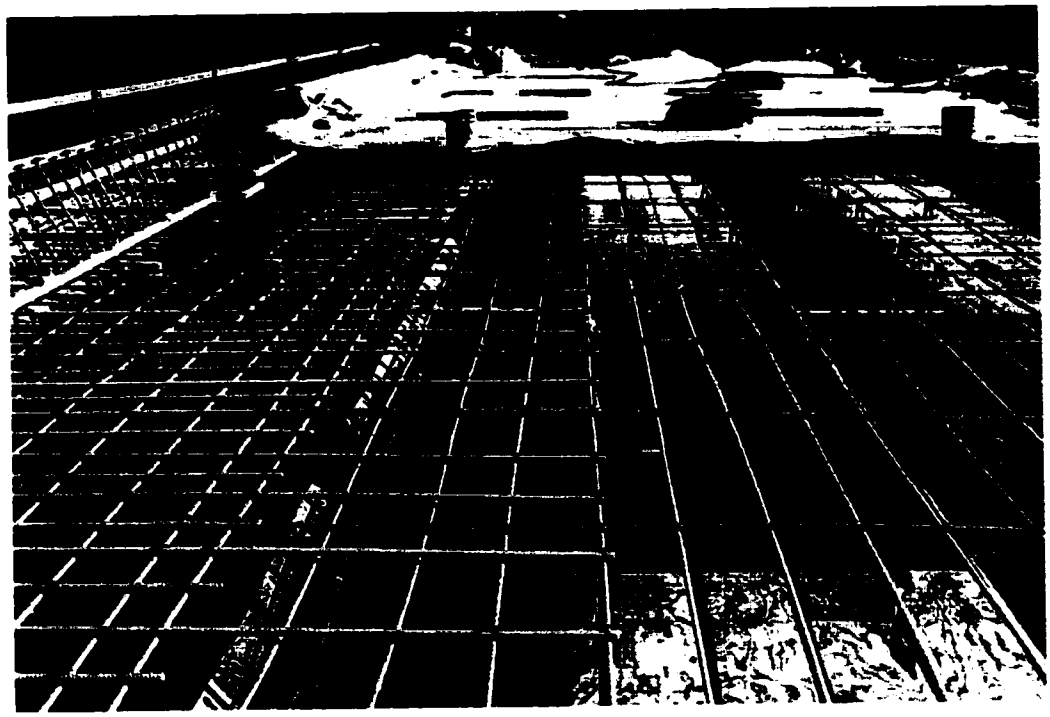

Photo 3.5: Reinforcement in Negative Moment Region

Photo 3.6: Reinforcement at Cantilever Ends

3.2.3 Steel Plate Girders

Built-up steel plate girders were used to replace the old prestressed concrete box girders. The flange, web thickness, and depth of the girders varied between the positive and the negative moment region. Figure 3.3 shows the top flange of the steel girders along the bridge and identifies the location of four different section types described in more detail in Table 3.1.

Table 3.1: Girder Type and Section Dimensions

BRIDGE GIRDER & PIER DIAPHRAGM SCHEDULE			
SECTION TYPE	TOP FLANGE	WEB (d – 2t)	BOTTOM FLANGE
1	18 x 350 mm	10 x 900 mm	30 x 550 mm
2	32 x 600 mm	12 x 900 mm	38 x 600 mm
3	18 x 350 mm	10 x 900 mm	25 x 500 mm
4 (PIER)	40 x 650 mm	28 x 860 mm	40 x 650 mm

Girder section type 1 is used in the positive moment regions of the first and last spans of the bridge. Girder section type 2 is used in the negative moment regions, over the piers. Girder section type 3 is used in the positive moment region of the middle span. The steel grade used for the steel plate girders is CSA-G40.21M 300W.

Steel straps and girders are made composite with the concrete slab by cold-finished carbon steel shear studs, grade 1020. The steel straps were attached to the concrete deck using three shear studs above each girder as depicted in Photo 3.7. Before the placement of the concrete deck, the steel straps were temporarily tied to the top of the girders with light gauge wire.

The five steel girders are braced with cross frames; four equally spaced within each span. Stiffened transverse girders over the two piers form transverse diaphragms between all five girders. Bridging between the superstructure and the foundation supports

are five load bearing plates at each abutment and two load bearing plates at each interior pier. Photos 3.8 and 3.9 show the bearing plates at the abutment and the pier, respectively.

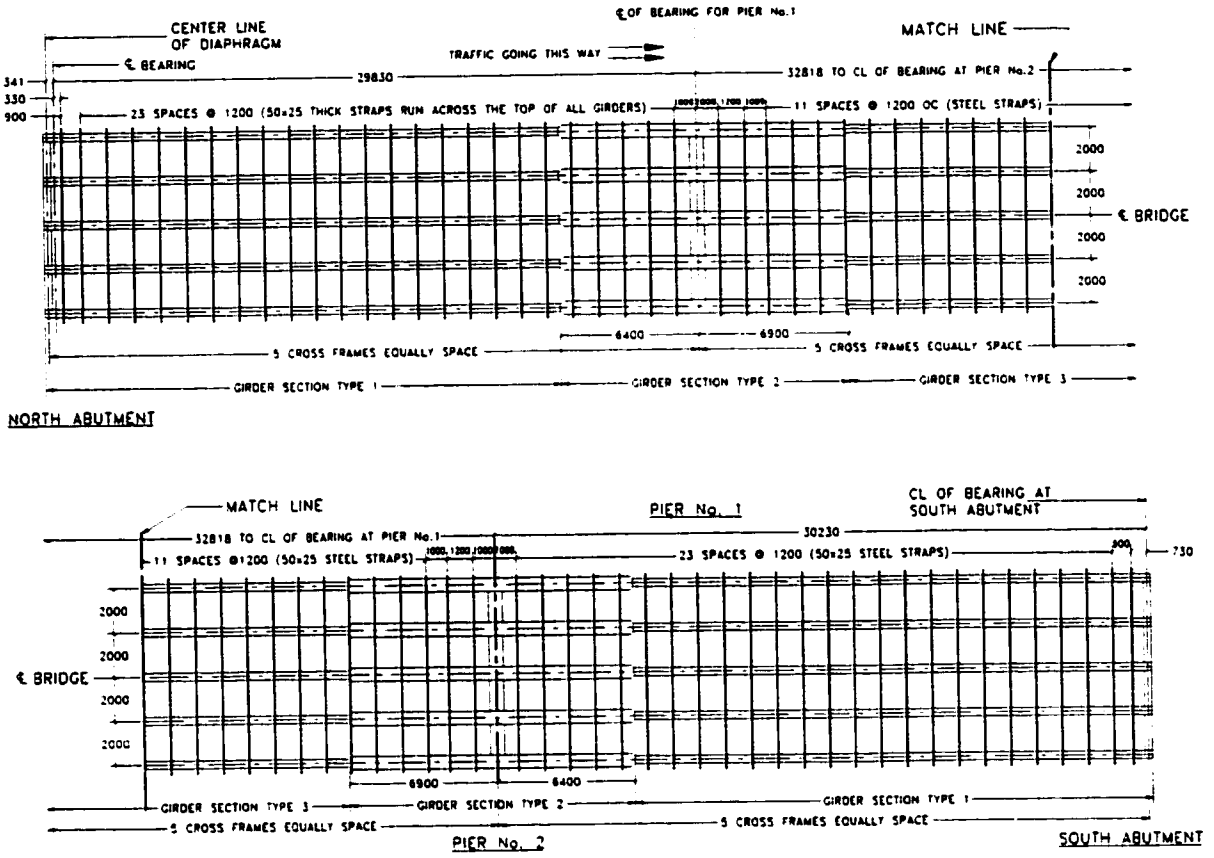

Figure 3.3 Plan View of Girders and Tension Straps

Table 3.2: Crowchild Trail Bridge Concrete Mix Properties/Specifications

CONCRETE MIXES (for 1 m^3)	
Specified Strength, $f_c'_{28}$ = 35 MPa	Fine Aggregates = 680 kg
Water = 155 kg	Air Entrainment = 50 ml / 100 kg
Cement = 430 kg	Superplastizer = 290 ml / 100 kg
Coarse Aggregates = 1080 kg	Polypropylene Fibers = 4.5 kg (0.45% by volume)

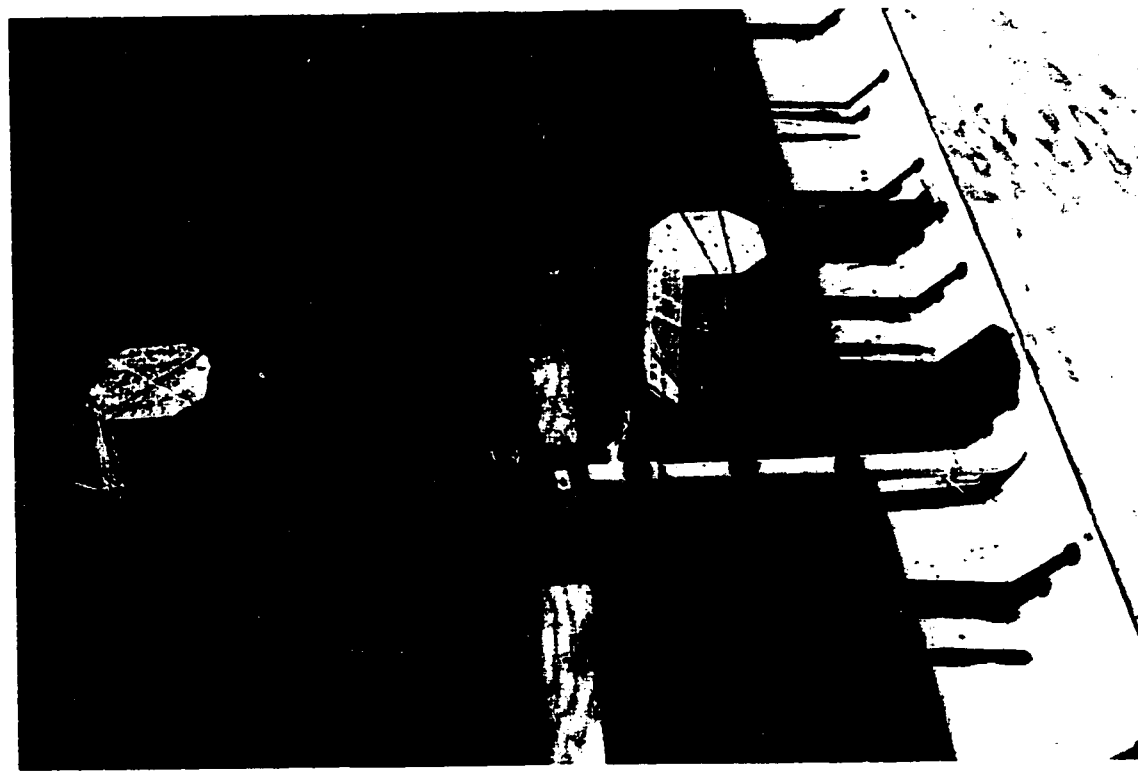

Photo 3.7: Steel Studs on Plate Girders and Steel Straps

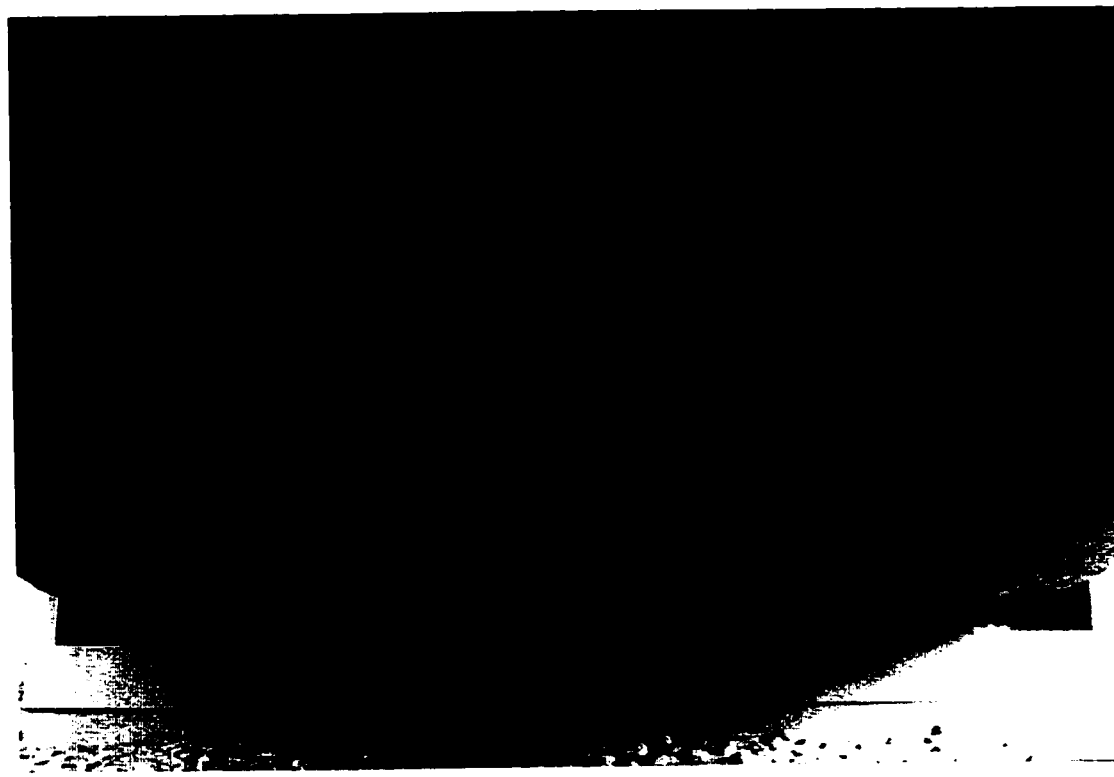

Photo 3.8: Supports at North Abutment

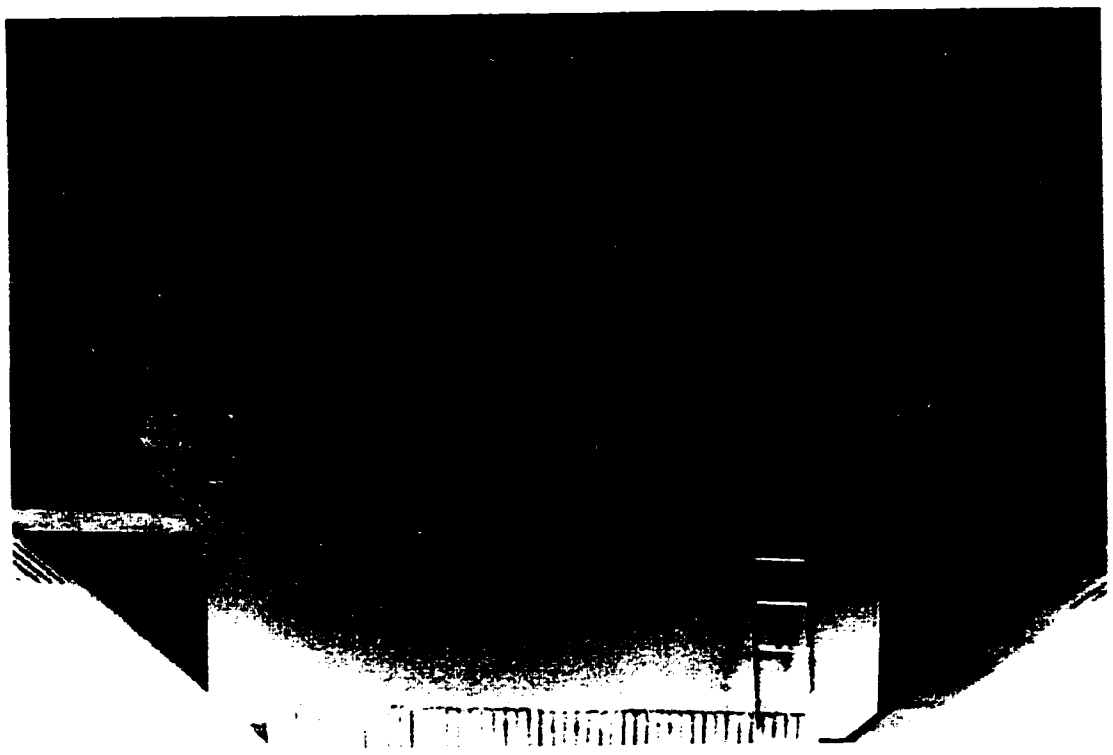

Photo 3.9: Supports at Pier No. 1 (Looking South)

3.3 Instrumentation

To better understand the behavior of the new superstructure of the bridge, a field instrumentation and monitoring program was developed at the University of Alberta in collaboration with ISIS Canada, City of Calgary, and SPECO Consultant. Of particular importance are the studies of static and dynamic behavior under service loading conditions.

3.3.1 Location of Gauges

In the last two weeks of July 1997, the University of Alberta has extensively instrumented the Crowchild Trail Bridge. The instrumentation installed on the Crowchild Trail Bridge consisted of 108 strain gauges and five thermistors. Among the 108 strain gauges, 86 of the strain gauges are 5 mm foil strain gauges, two are glued-on fiber optic strain gauges, three are embedded fiber optic strain sensors in GFRP bars (called smart

bars), and 17 are electrical resistance embedded concrete strain gauges (120 x 10 mm gauge length). Four of the five thermistors were embedded inside the concrete deck and one was used to measure the ambient air temperature near the bridge. Photo 3.10 shows a typical embedded concrete strain gauge, a thermistor and an electrical resistance strain gauge.

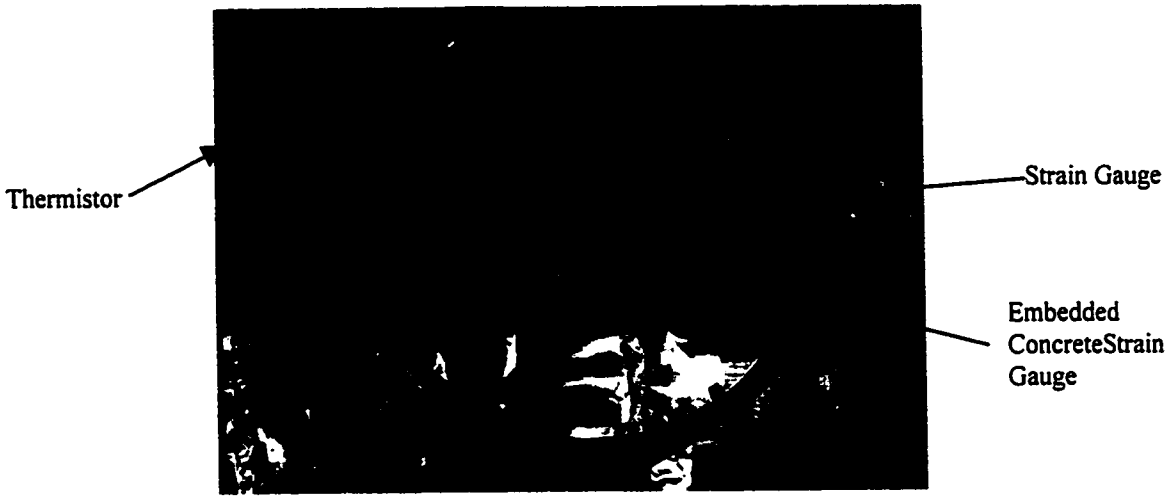

Photo 3.10: Gauging Instruments Used on Crowchild Bridge.

The 86 electrical resistance foil strain gauges were installed on the following structural members: 64 electrical resistance strain gauges on structural steel members, two on the NEFMAC grid, 17 on the GFRP bars, and three on smart bars. Smart bar is a 10 mm GFRP bar, with exterior sand coating, that comes with an embedded fiber optic sensor. TUNS manufactured the bars under an ISIS research project. The smart bars were used in conjunction with the three foil strain gauges for comparison with the fiber optic sensors. The two glued-on fiber optic strain gauges were installed opposite to the two foil strain gauges for comparison of their performance. The 17 electrical resistance concrete strain gauges were embedded inside five precast concrete blocks. Four of the five thermistors were also embedded inside two precast concrete blocks. All precast concrete blocks had higher sand and water content than the concrete mix for the deck, thereby giving the precast concrete blocks lower modulus of elasticity than the deck.

A summary of all the instrumentation used in Crowchild Trail Bridge is presented in Table 3.3. Included in this table are descriptions of the instrumentation, structural members on which the instruments were mounted, notations, descriptions, and quantities.

Table 3.3: Instrumentation

Notation	Structural Members Monitored	Quantities
[I] Electrical resistance foil strain gauges (120Ω, 5 mm in length, F=2.12)		
G	Built-Up Plate Girders	34
T	Steel Straps	18
S	Shear Studs	6
C	Cross Frame	4
N	NEFMAC grid and Stainless Steel Rods in the barriers	4
R	GFRP bars (On deck reinforcement)	15
RC	GFRP bars (Same location as glue-on fiber optic gauges)	2
RS	Smart bar (Same location as embedded fiber optic gauges)	3
[II] Electrical resistance embedded strain gauges (120Ω, 120mm in length, F=2.0)		
E	Embedded in precast concrete blocks	17
[III] Fiber Optic Sensors		
FC	GFRP @ RC gauge (Ser. No. N1001-441, -395)	2
FS	Smart bars @ RS gauge (Ser. No. N1001-163, -356, -186)	3
[IV] Thermistors		
TH	Four in precast concrete blocks and one in open air	5

All the instrumentation was mounted in the North span of the bridge. The overall layout of all the instrumentation used in the Crowchild Trail Bridge is shown in Figure 3.4. The strain gauges placed on the girders are designated as the "G" series. The "T" series strain gauges shown in Figure 3.4 were mounted on the tension straps at mid-length. The "S" series strain gauges were mounted on the shear studs and the "C" series were mounted on the cross frame. The "N", "R", "F", and "TH" series were mounted on

NEFMAC, the reinforcing bars, the fiber optic sensors, and the thermistors, respectively. The gauge notation summarized in Table 3.3 is used in all of the figures that follow.

Detail *region "B"* in Figure 3.4 shows 14 strain gauges and the fiber optic sensors on the glass fiber reinforcement. The goal of *region "B"* instrumentation was to monitor the behavior of the deck in the negative moment region and to evaluate the use of fiber optic sensors. Two Fabry-Perot type of fiber optic sensors, manufactures by Rock Test Inc., were installed on the glass fibre reinforcement at the same location as conventional electrical resistance strain gauges to evaluate the performance of the fiber optic sensors. The fibre optic sensors were non-compensated for temperature, and were installed using the same epoxy as any other gauges (AE10 epoxy). More detail for drawing in *region "B"* can be found in Appendix A, drawing number T200006.

Details for *region* "A" drawing in Figure 3.4 shows the six strain gauges on the glass fiber reinforcements. The purpose of *region "A"* instrumentation was to monitor the behavior in the cantilevers. All the gauges on the glass fiber reinforcement were mounted in the laboratory before shipping out for field installation.

The numbers from 1 to 5 running vertically at the North Abutment shown in Figure 3.4 identify the girders. The numbers from 1 to 25 running across the bottom from North Abutment to Pier No. 1 identify the tension straps. Figure 3.4 depicts a rectangular box between girders 1 and 2 on strap number 16, used as the central box where all the wiring from all of the strain gauges converged. At the intersection of Pier No. 1 and girder number 2, there is another central box for all the fiber optic gauges. Figure 3.4 also shows the location of the six diaphragms between North Abutment and Pier No. 1. Two of the diaphragms, on top of Pier No. 1 and the North Abutment, are stiffened steel plate girders. The other four diaphragms are cross frames. The cross frames are made up of back-to-back angles. The cross frame next to strap number 11 was instrumented as shown in Figure 3.5. The instrumented cross frame is the third diaphragm from the North as shown in Figure 3.4.

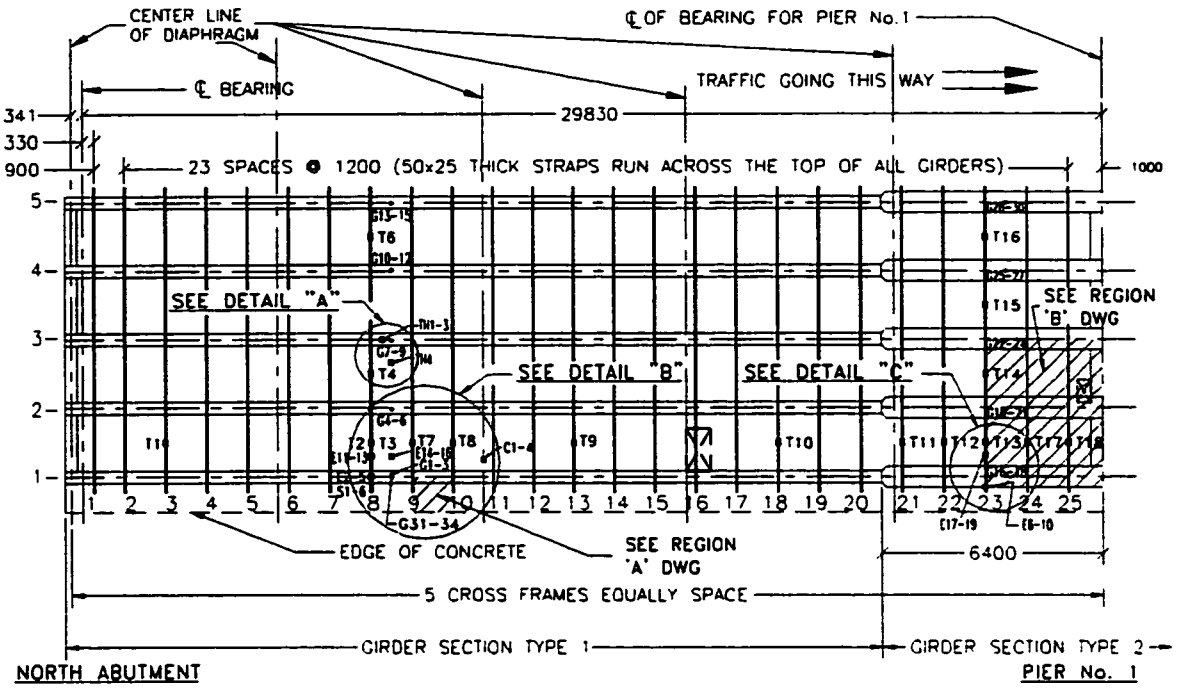

(a) Instrumentation in the North Span

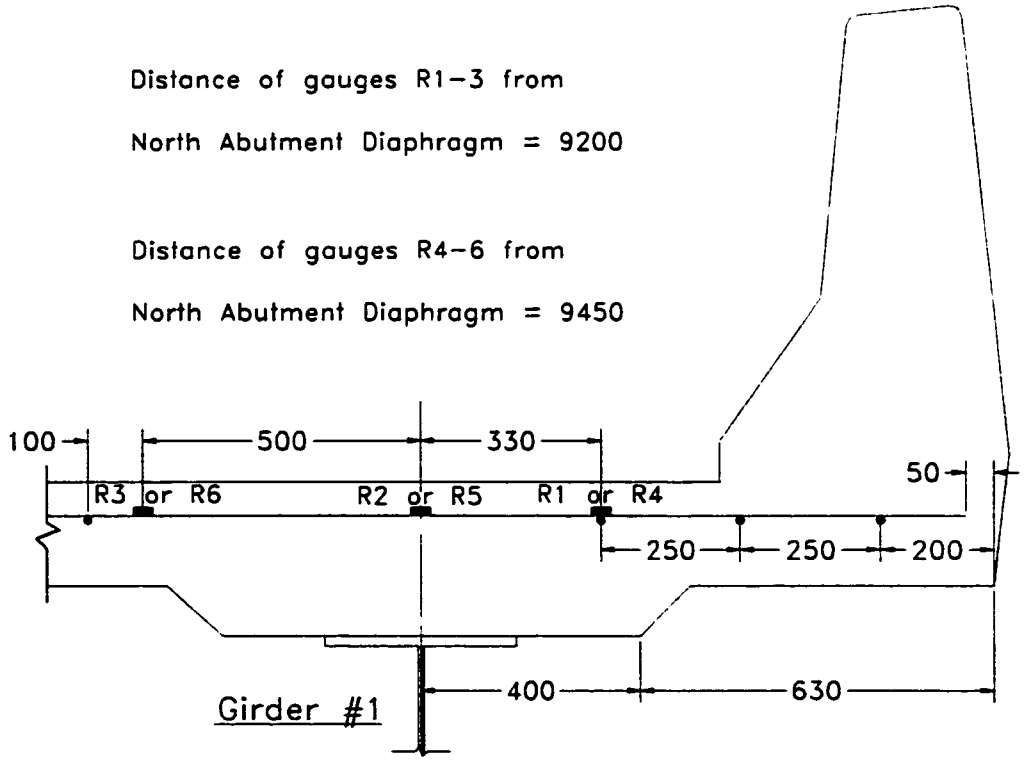

(b) Region "A"

Figure 3.4: Instrumentation Used in the Crowchild Bridge

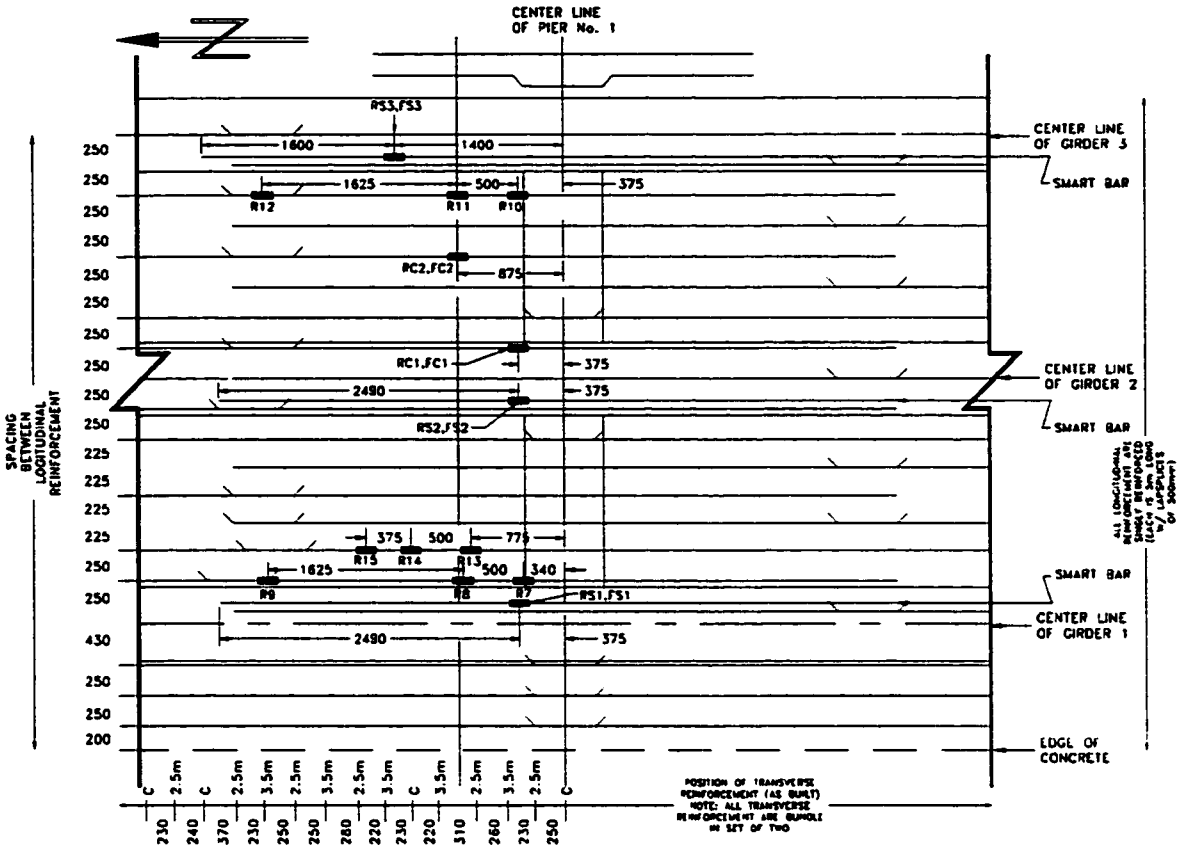

(c) Region "B"

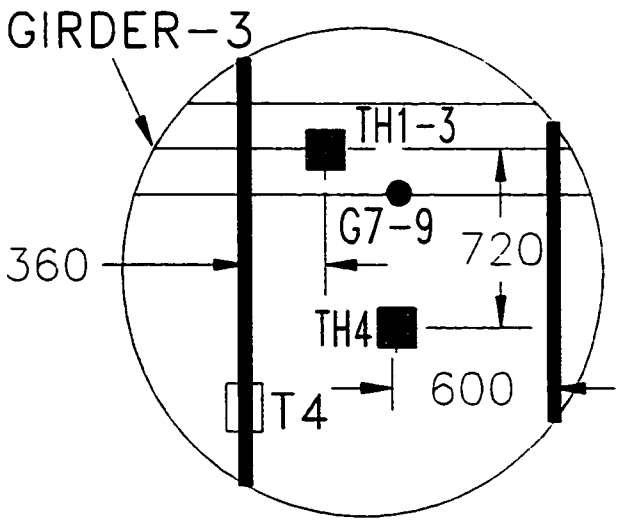

(d) Detail "A"

Figure 3.4: Instrumentation Used in the Crowchild Bridge (Cont'd)

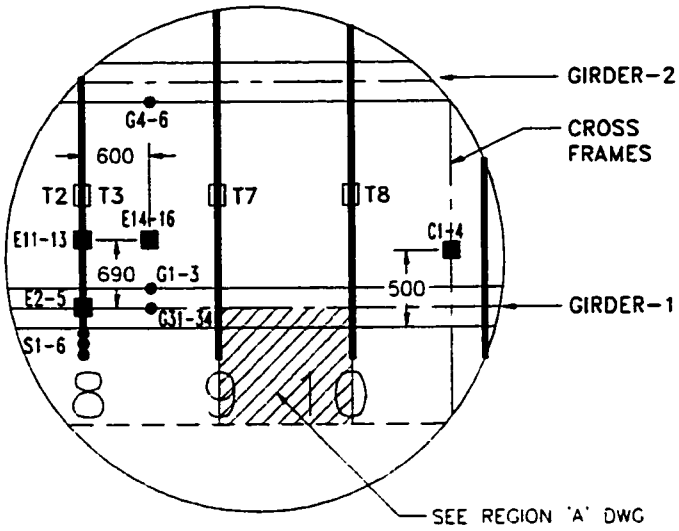

(e) Detail "B"

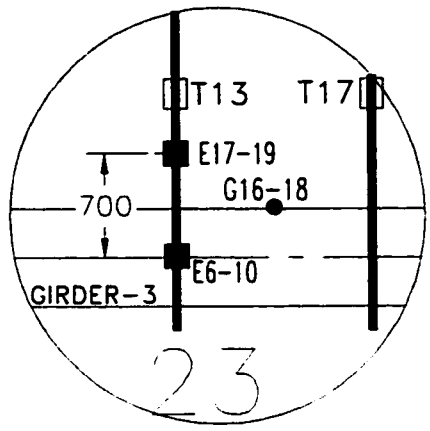

(f) Detail "C"

Figure 3.4: Instrumentation Used in the Crowchild Bridge (Cont'd)

Figure 3.5 shows the North elevation of the cross frame. All the strain gauges on the cross frame were located at one quarter of the distance between the two girders in order to stay away from the region of disturbance at mid-span. Photo 3.8 shows the completed cross frames on Crowchild Bridge.

Detail "A" in Figure 3.5 shows the location of the gauges on the top horizontal member of the cross frame. *Detail "B"* in Figure 3.5 shows the location of the gauges on the bottom horizontal member of the cross frame. Strain gauges C1 and C3 were used to evaluate the load sharing between the girders. Strain gauges C2 and C4 were placed as shown in Figure 3.5 to monitor the out of plane movement of the cross frame under heavy loading. The cross frame members consist of two L90 x 65 x 10 mm back-to-back. The typical space between the two back-to-back angles is 20 mm, as shown in *Detail "B"*. A 100 x 100 x 20 mm gusset plate is bolted between these two angles at the mid-span between the girders.

To control the alignment and position of the concrete strain gauges and the thermistors in the cast-in-place concrete deck, the thermistors and the concrete strain gauges were embedded in precast concrete blocks. The concrete blocks were sand blasted

to improve bond with the deck concrete. Photos 3.11 and 3.12 show the formwork used for the blocks of embedded concrete strain gauges and thermistors, respectively.

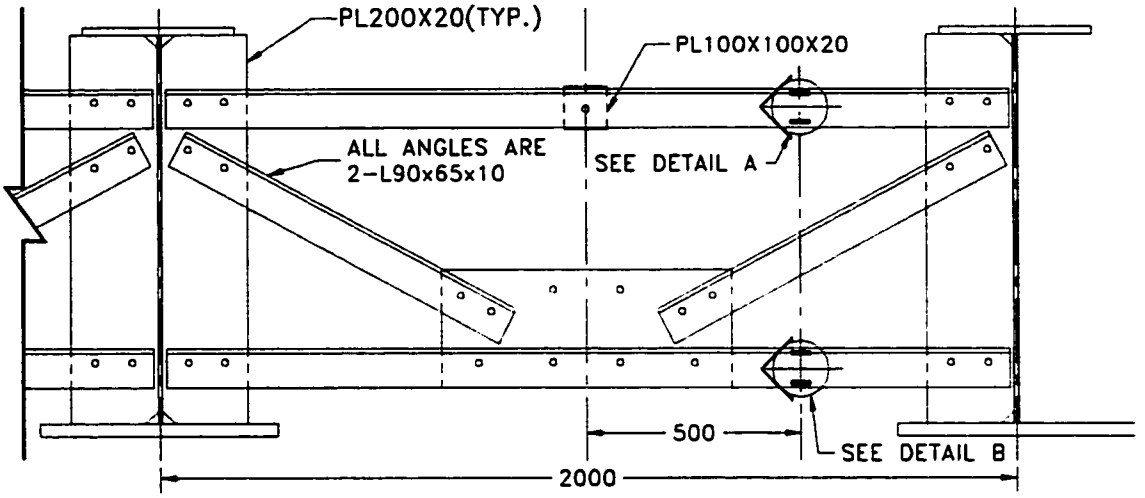

North Elevation View of Typical Cross Frame Layout

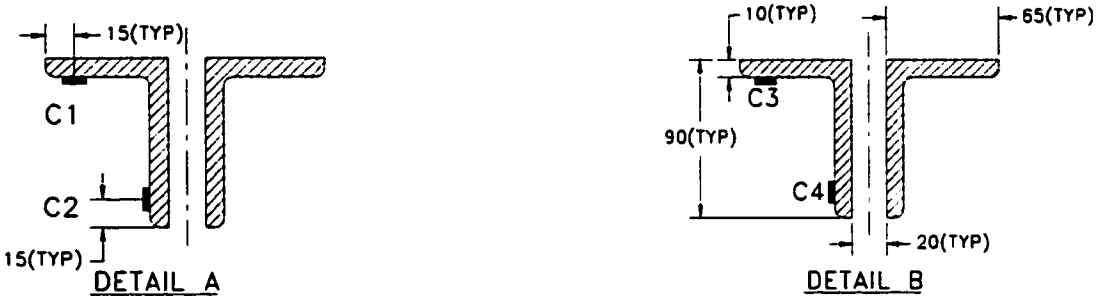

Figure 3.5: Instrumentation on Cross Frame

Photos 3.13 through 3.15 show the completed precast blocks, field placement of these precast blocks and the casting of concrete deck. Figure 3.6 shows the location of the gauges and the precast concrete blocks for the embedded concrete strain gauges. To monitor the arching action in the concrete deck, seventeen embedded concrete strain gauges were installed in five precast concrete blocks. Blocks 1 and 4 each had four strain gauges and blocks 2, 3, and 5 each had three strain gauges as shown in Figure 3.6.

Photo 3.11: Formwork for the Embedded Concrete Strain Gauges

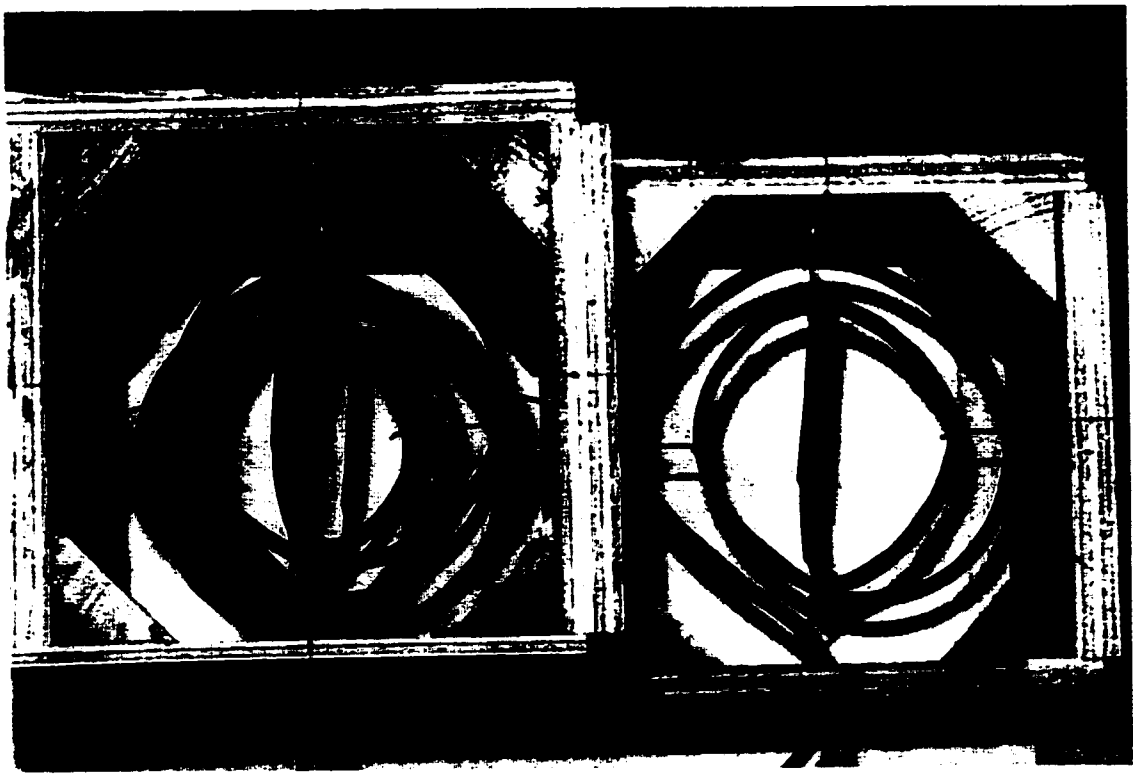

Photo 3.12: Formwork for the Embedded Thermistors

Photo 3.13: Precast Blocks for Embedded Instruments

Photo 3.14: Precast Blocks for Embedded Thermistors (Field Placement)

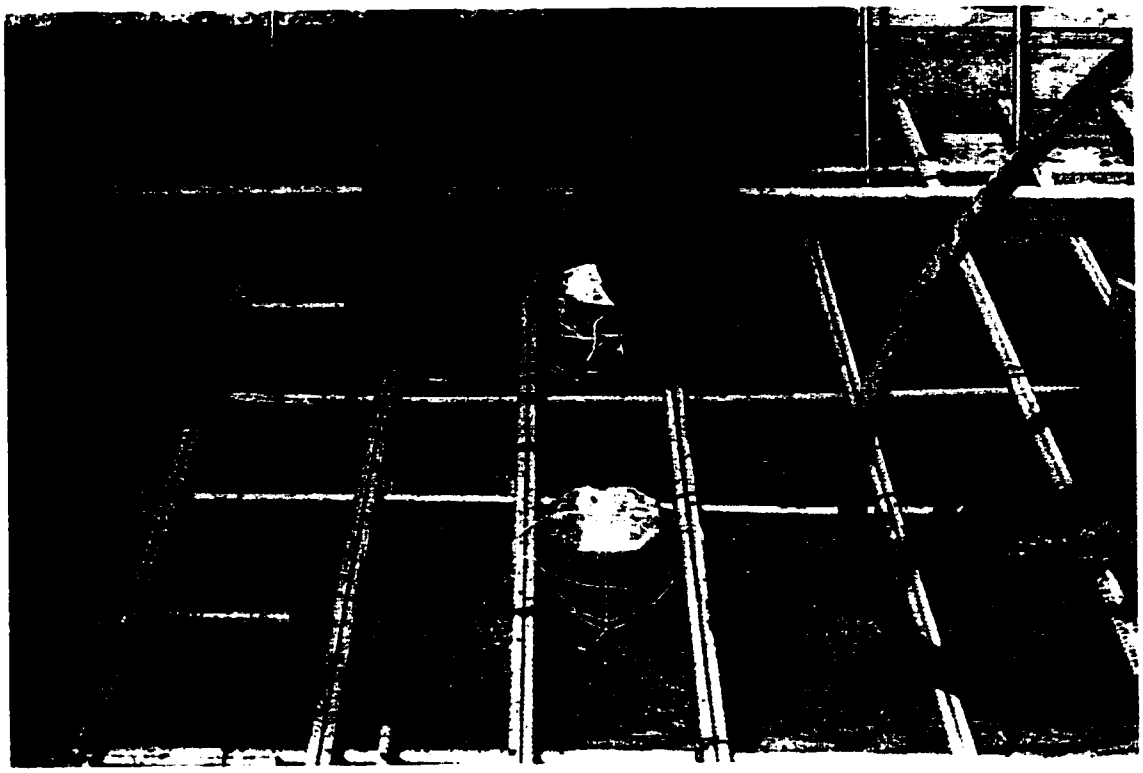

Photo 3.15: Precast Blocks for Embedded Concrete Strain Gauges (Field Placement and Concrete Casting)

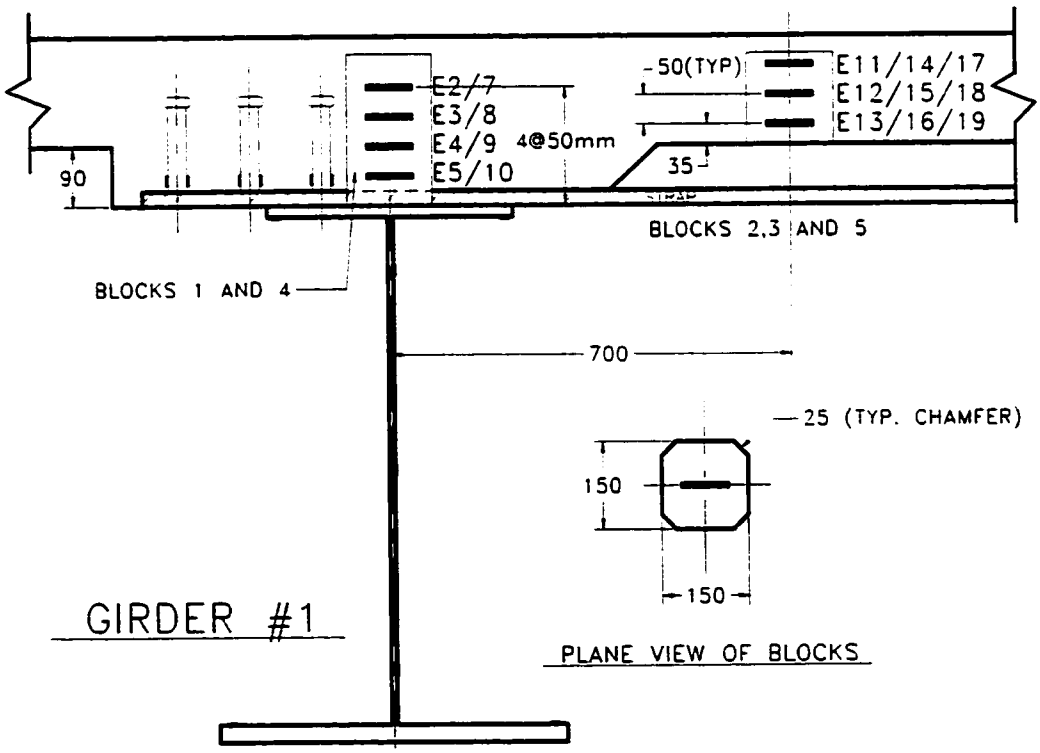

Figure 3.6: Embedded Concrete Strain Gauges

Locating on top of girder #1, as shown in Figure 3.6, Block 1 had gauges E2 to E5 and Block 4 had gauges E7 to E10. Blocks 2, 3 and 5 had guages E11 to E13, E14 to E16, and E17 to E19 respectively. Blocks 1, 2, and 3 shown in Figure 3.6 were placed in the positive moment region. Blocks 1 and 2 were placed on the eighth strap, 8770 mm from the centreline of the North Abutment diaphragm as shown in the layout drawing *Detail "B"* in Figure 3.4. Block 3 was placed 600 mm South of the eighth strap between girders 1 and 2 as shown in *Detail "B"* of Figure 3.4. Photo 3.6 shows the field placement of blocks 1, 2 and 3.

Blocks 4 and 5 were placed in the negative moment region on top of strap number 23 at 3400 mm North of centerline of Pier No. 1 (see *Detail "C"* shown in Figure 3.4 and layout drawing number T200004A in Appendix A). These gauges have an overall length of 120 mm, a nominal gauge factor of 2.0, a resistance of 120 Ω, and are temperature compensated for concrete. The thermal output of these gauges is ±1.8 με/°C between 0 °C and 60 °C.

Four thermistors monitored the temperature profile in the deck and a fifth thermistor measured air temperature. The location of the embedded thermistors is shown in Figure 3.7. Three of the four embedded thermistors namely TH1, TH2 and TH4 were placed inside the concrete deck as shown and TH3 thermistor was placed on the boundary of the concrete deck and steel girder. A plan view of the blocks in Figure 3.7 shows the coil of the thermistors wrapped at least two revolutions inside the concrete block before extending out of the concrete. This precaution is taken to minimize effect of the temperature conductivity through the lead wires of the thermistors. Photos 3.12 and 3.13 show the formwork and completed precast blocks for the themisters and Photo 3.14 shows the field placement of the blocks.

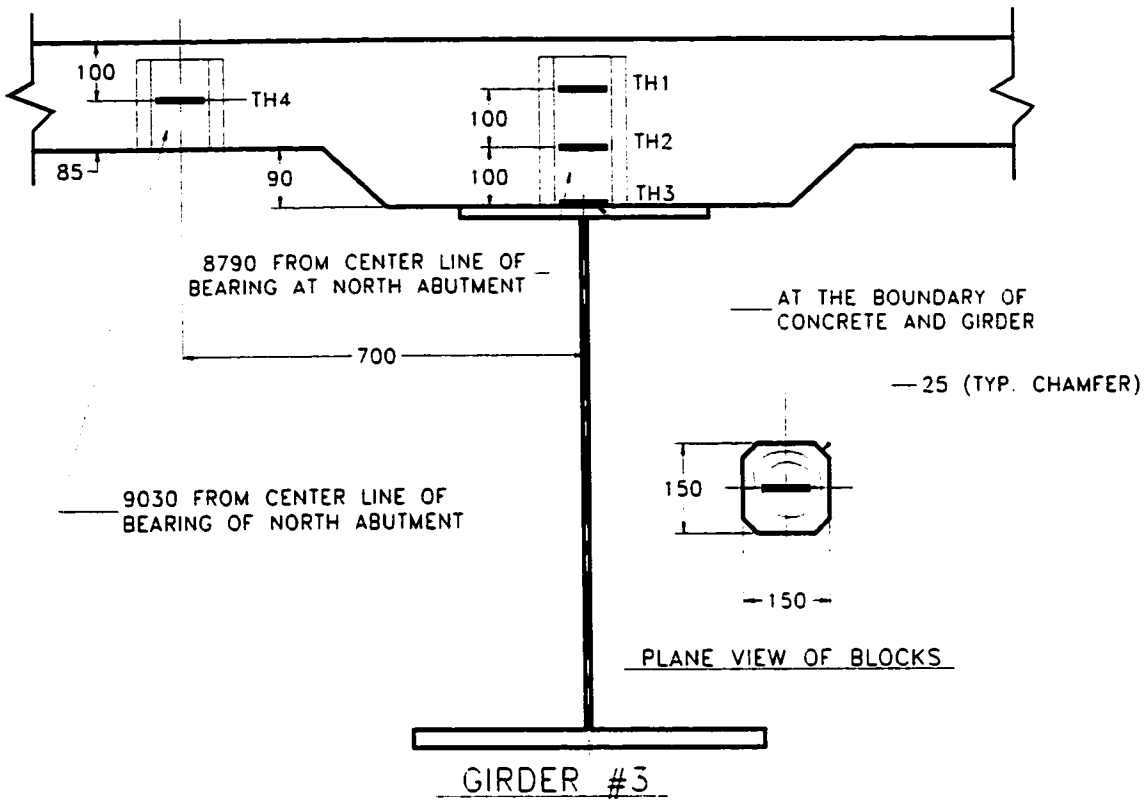

Figure 3.7: Embedded Thermistors

Eighteen strain gauges were used to monitor the performance of the steel straps. Twelve of the gauges, placed between girders 1 and 2, were used to examine the response of the straps along the length of the bridge. Straps close to the supports and cross frames are expected to carry less load than straps that are further away. The other six gauges were used to monitor strain distribution along one steel strap. Three strain gauges were placed on strap # 8 and the other three gauges on strap # 23 in the positive and negative moment region, respectively. Figure 3.8 shows a typical cross sectional view of the straps that were instrumented.

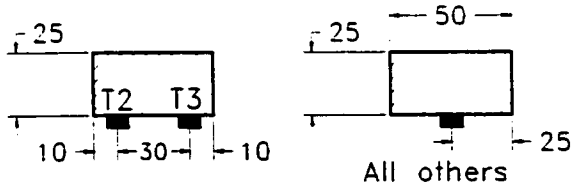

Figure 3.8: Gauges on Steel Straps

Six strain gauges were used to monitor strains in the end shear studs at 8430 mm from centerline of the North end bearing. Figure 3.9 shows the location of these strain gauges.

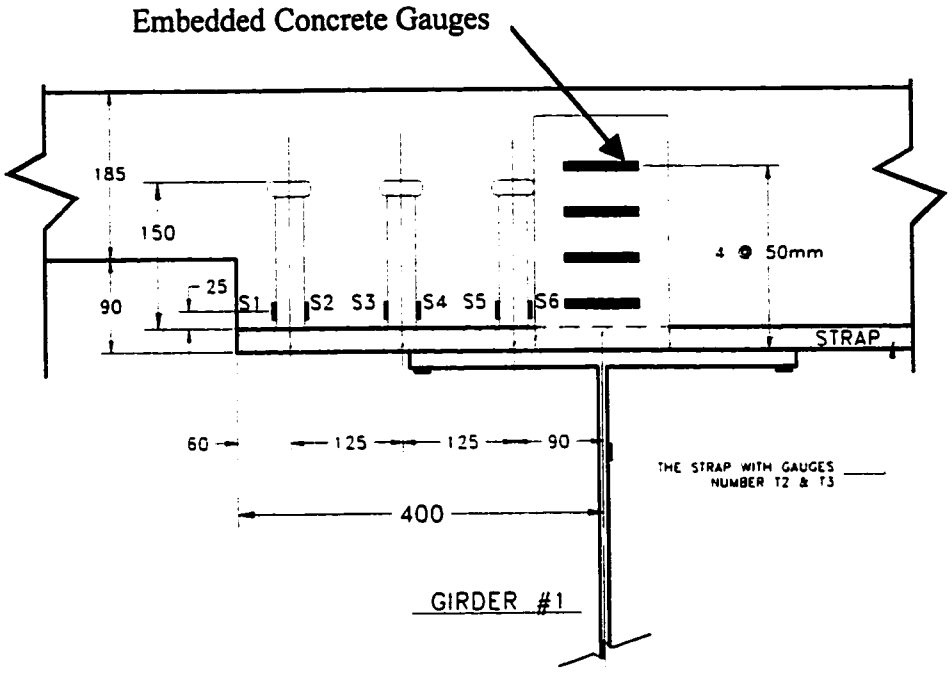

Figure 3.9: Gauges on Shear Studs

Thirty-four strain gauges were used to monitor strains in the steel girders. As shown in Figure 3.10, the webs of all five girders were instrumented with three gauges at both the positive and the negative moment regions to monitor load sharing among the girders and moment distributions along the girders. Furthermore, four gauges were also installed on the flanges of girder 1 to measure any warping of the girders and to better examine the strain distribution at a cross section. Figure 3.10 shows the location of the gauges on the girders.

At the side barriers, two strain gauges were installed on NEFMAC and two on a stainless steel bar. Figure 3.11 and Photo 3.6 show in detail the installed gauges on the NEFMAC and a stainless steel bar.

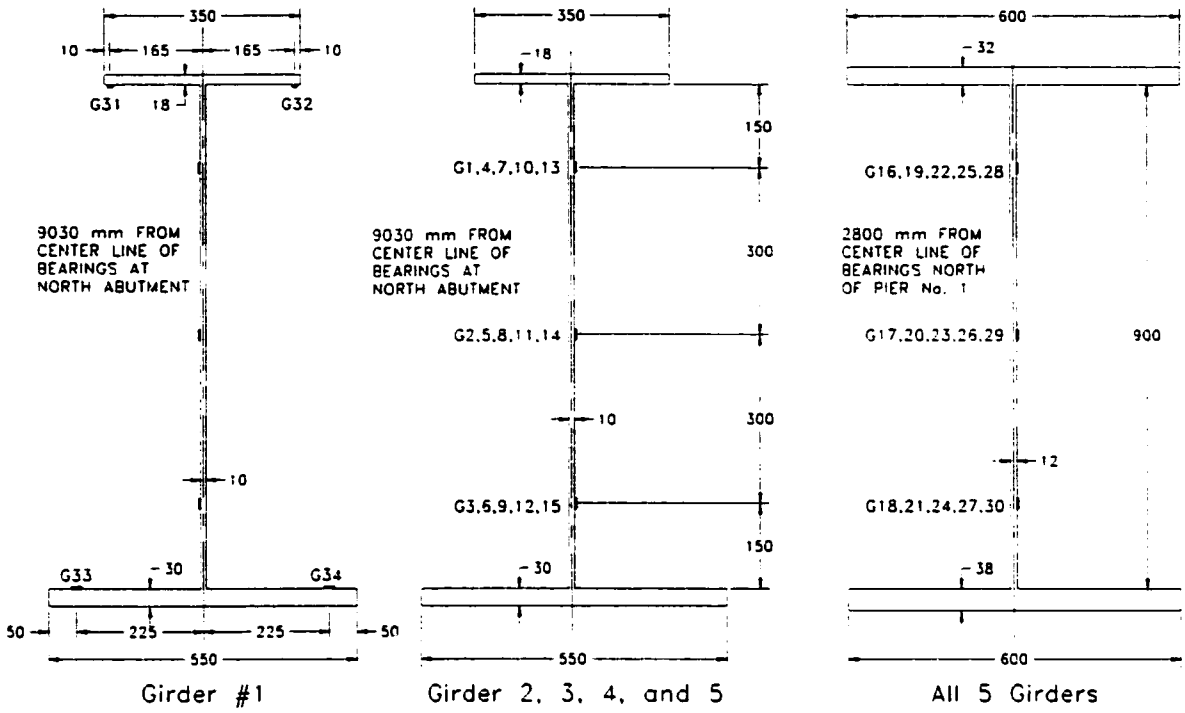

Sections at Positive Moment Region Section At Negative Moment Region

Figure 3.10: Strain Gauges on Girders

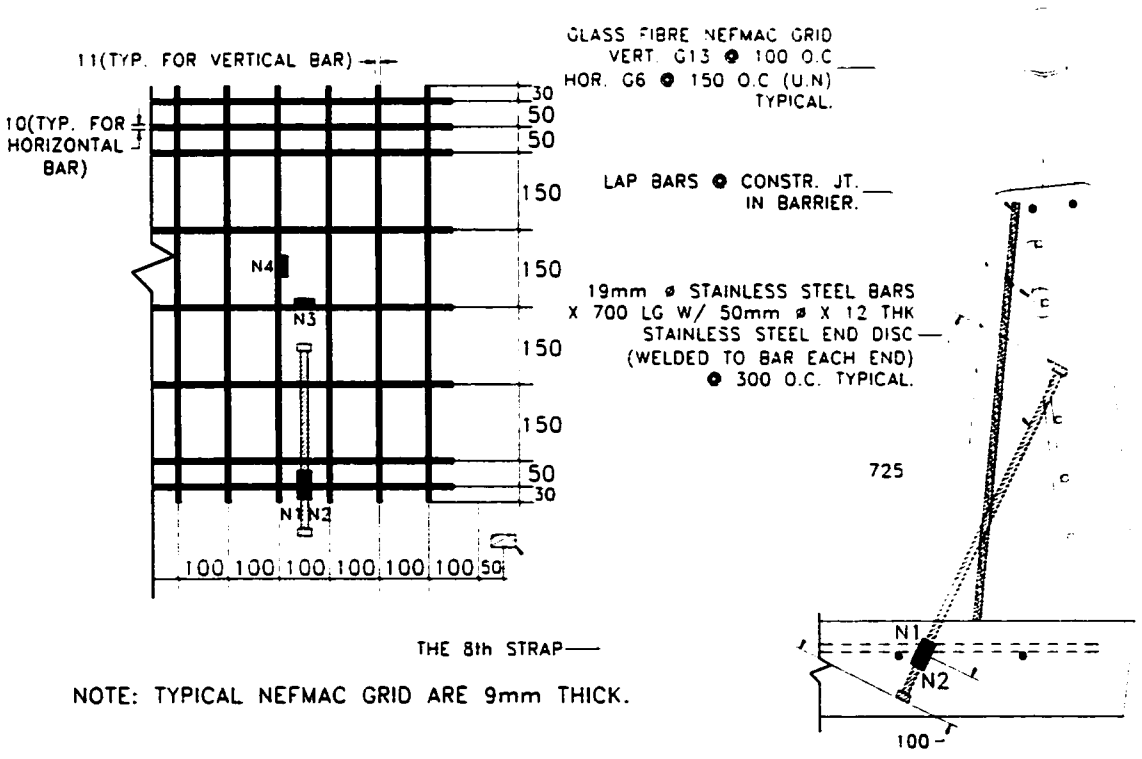

Figure 3.11: Gauges on NEFMAC and Stainless Steel Bar

The distance from the center line of the diaphragm at the North abutment is 9170 mm to the instrumented stainless steel bar or 400 mm South of strap number 8.

3.4 Field Testing

3.4.1 Tests Performed on Crowchild Trail Bridge

Since the superstructure of the Crowchild Bridge was replaced in 1997, five sets of tests have been conducted. All five different sets of tests done on the bridge up to August 1998 are summarized in Table 3.4. Tests in October 1997 and June 1998 were conducted with unknow axles load, speed, and location of load. Some investigation of the October 1997 data on the load sharing due to overall deflection is shown in Appendix B. Tests in October 1997 and June 1998 and the temperature investigation in September 1997 were detailed in the *Field Instrumentation and Monitoring of Crowchild Trail Bridge* report (Cheng and Afhami, 1999) and will not be covered here. Since tests in August 1997 and August 1998 were conducted with know axles load, these two tests are investigated in details as outlined in Chapter 4. Some comparison analysis of August 1997, October 1997 and August 1998 are shown in Chapter 5.

Table 3.4: Tests Performed on Crowchild Bridge

Test	Measurements	Comments
I. August '97		
Ambient Vibration	Acceleration	UBC performed the test before the Bridge was open to traffic
Field Survey	Deflections	Truck load was known accurately
Static Test	Strains	Truck load was known accurately
Mapping Cracks	Mapping Cracks	Mapping of crack patterns
II. September '97		
Temperature Test	Strains, and Temperatures	Test performed under known temperature changes
III. October '97		
Dynamic Test	Strains	Tests performed under unknown traffic loading
IV. June '98		
Dynamic Test	Strains	Tests performed under unknown traffic loading
V. August '98		
Ambient Vibration	Acceleration	U of A tested the bridge after it was in operation for one full year.
Dynamic Test	Strain, Deflection, and Acceleration	Truck load was known accurately
Static Test	Strain and Deflection	Truck load was known accurately
Mapping Cracks	Mapping Cracks	Mapping of crack patterns

4. EXPERIMENTAL RESULTS

4.1 Results of the August 1997 Test

In August 97, just prior to the first opening of the bridge to traffic, a research team from the University of British Columbia (UBC) performed an ambient vibration test on Crowchild Trail Bridge (Ventura *et al.*, 1997). Ambient vibration tests do not involve direct force excitation, but rather just forces from wind, surrounding traffic, human activities etc. Measurements from ambient vibration tests are typically taken over a longer period than for dynamic tests to ensure that all modes of interest have been excited. The peaks in the Averaged Normalized Power Spectral Density of ambient vibration measurements from different locations on the structures are then determined and used to estimate the natural frequencies of the structure. It is worth noting that dynamic properties of structures at low level of excitation may be slightly different from high level of excitation.

Prior to the ambient vibration tests, University of Alberta, the City of Calgary and Speco Consultants performed static tests. Two heavily loaded tractor-trailer trucks were used in the static test. Vertical deflection points were measured by surveying, and strain measurements were recorded using strain indicators. Finally, an initial crack pattern was mapped.

4.1.1 Ambient Vibration Results from UBC

Data acquisition systems used in the ambient vibration test on the Crowchild Trail Bridge by UBC are as follows (Ventura *et al.*, 1997):

- Forced-balanced accelerometers, kinematics model FBA-11 capable of measuring up to ±0.5 g with a resolution of 0.2 μg.

- Signal Conditioners, which used to remove undesired frequency contents and amplify the signals. All filter cards (Kinemetrics AM3) were set to a cut-off frequency of 50 Hz.
- Analog to digital converter used was Keithly Model 575 AMM2 board.

Measurements were obtained when there was no traffic on the bridge, thus the only forces acting on the bridge during the ambient vibration tests were wind, human activity, traffic below and beside the overpass. Due to limited number of accelerometers available, 14 different setups were required. In 11 of the 14 setups two accelerometers were used as references and in the remaining three setups three accelerometers were used as references. In phase analysis, reference accelerometer is required to establish the relationships between the different setups. Eight accelerometers were used to monitor the acceleration at 46 locations. The acceleration was monitored at 44 different locations in the bridge deck, one near the base of Pier No.1 and one near the base of Pier No. 2. Locations of the accelerometers are listed in UBC report EQ97-005 (Ventura *et al.*, 1997). The temperature at the bridge site during the test was approximately 8°C with moderate to heavy rain for the majority of the test. The maximum recorded level of vibration was approximately 1.7 milli-g's.

In identifying natural frequencies, Ventura *et al.* (1997) used an average of 64 records in the vertical direction, 40 records in the transverse direction, and 7 records in the longitudinal direction. The most significant peaks between 0 and 20 Hz were identified. Ventura *et al.* (1997) suggested that the results were preliminary and needed to be complemented with results of finite element analyses. Furthermore, the resolution of higher vibration modes was not as good due to the limited number of measuring points. It was suggested that some modes are highly coupled and current techniques for ambient vibration data analysis have difficulty handling these situations.

The ambient vibration tests were performed by UBC on the Crowchild Trail Bridge on August 15, 1997, between 9:00 AM to 11:00 PM. The tests identified 13

natural frequencies between 0 and 20 Hz. A list of these natural frequencies is given in Table 4.1.

Table 4.1: Natural Frequencies Between 0 - 20 Hz.

Peak	*Frequency (Hz)*	*Mode Shape*
1	2.78	1st Fundamental Vertical
2	3.13	1st Fundamental Torsional
3	3.76	2nd Vertical Mode
4	4.05	2rd Torsional Mode
5	4.64	3rd Vertical Mode
6	5.18	3th Torsional Mode
7	7.13	4th Torsional Mode
8	9.13	4th Vertical Mode
9	10.94	6th Torsional
10	12.99	6th Fundamental Transverse
11	15.63	6th Couple Torsional
12	17.87	5th Vertical
13	19.24	7th Torsional

4.1.2 Static Test Results

For the static tests, two trucks, each weighing approximately 357 kN, as shown in Figure 4.1, were used for nine different load cases, P1 to P9. The two trucks used in the tests; they had approximately the same axles load and spacing of the axles as illustrated in Figure 4.1. Figure 4.2 shows the locations of the truck on the North span of the bridge for the nine different load cases used in the static tests, P1 to P9. The trucks were facing north for all tests. The nine load points are shown by the '*X*' marks running between girder 1 and girder 2. These '*X*' marks are in reference to the front axial of the truck's left wheel. In all the tests, the trucks were moving from South to North. For six of the nine load cases, the two trucks were parked side by side at points P1 to P6 along the bridge as

shown in Figure 4.2. For load points P1 to P6, the layout positions of the two trucks in the transverse direction of the bridge are as follows: facing north, the truck on the West side; its' left wheel of the front axle is at midpoint between girder 1 and girder 2. Since the two trucks were parked side by side, the truck on the East side, its' right wheel of the front axle is at an approximate midpoint between girder 4 and girder 5. The bridge was therefore loaded symmetrically. For the last three load cases, P7 to P9, only one truck was used for the tests. The layout positions of the truck for load cases P7 to P9 in the transverse direction of the bridge are facing north; the truck's left wheel is at an approximate midpoint between girder 1 and girder 2.

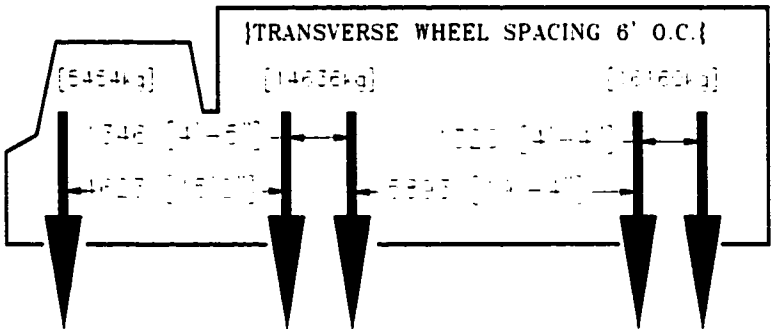

Figure 4.1: Trucks Use in August 97 Test

For all nine load cases, strain readings were recorded at the same time as the surveying measurements. For each loading condition, 25 deflection points were surveyed, namely, five points along each girder in the North span. The survey points are identified as A1-A5, B1-B5, C1-C5, D1-D5, and E1-E5 in Figure 4.2. The field survey results and their corresponding load points are shown in Table 4.2. All the corresponding strain gauge readings are presented in Appendix B.

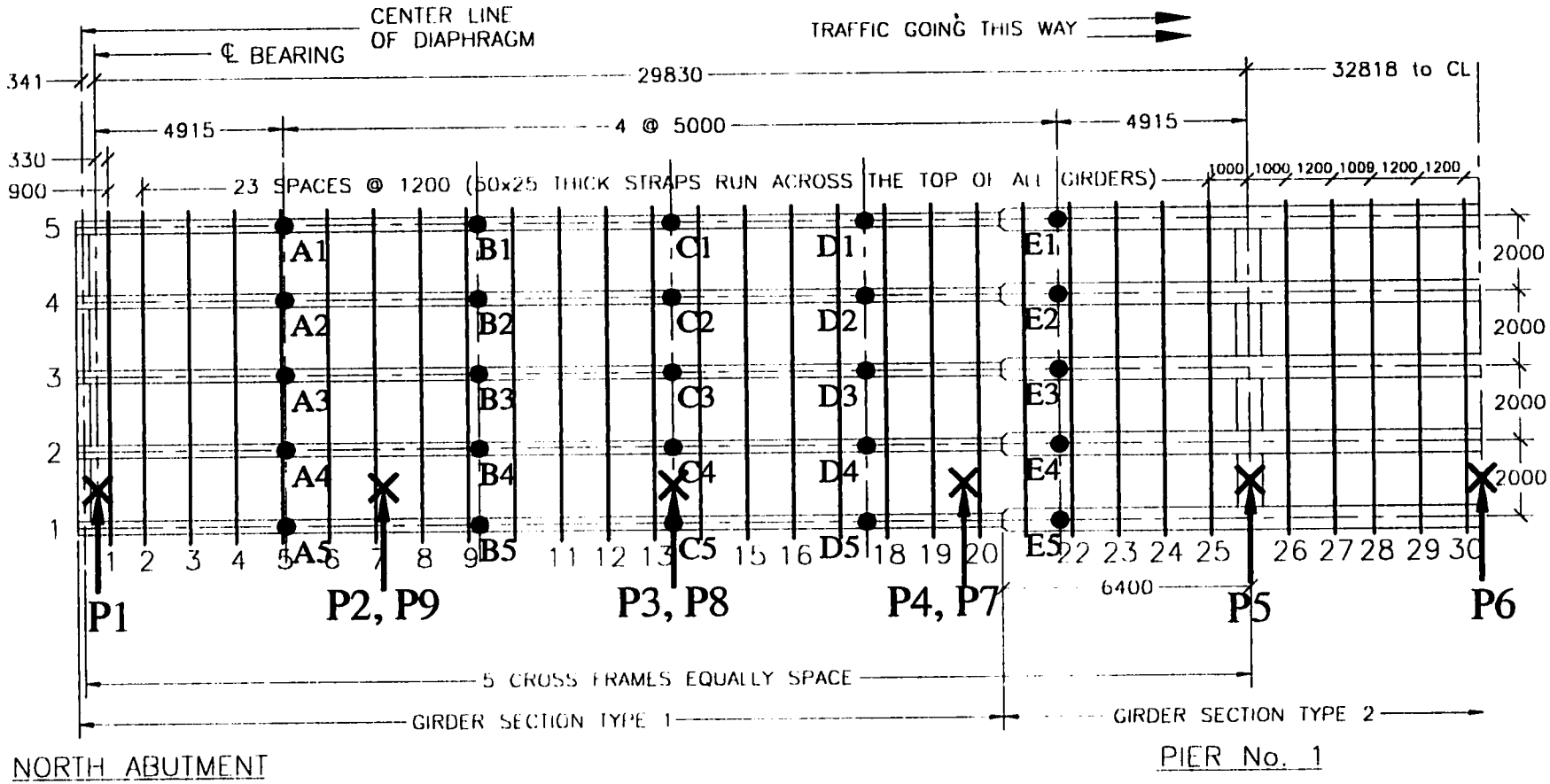

Figure 4.2: Load Points and Survey Points [August 1997]

Table 4.2: Static Tests-Survey Deflections Measurements, mm [August 1997]

	No truck	P1	P2	P3	P4	P5	P6	P7	P8	P9	No truck
A1	1	1	1	-1	-6	-8	-6	1	-1	-1	-1
A2	0	1	1	0	-5	-8	-5	0	-1	-2	0
A3	1	3	3	-1	-3	-6	-6	0	-1	-2	-1
A4	2	3	3	-2	-3	-7	-7	-1	-3	-5	-2
A5	1	2	2	1	-4	-7	-6	-1	-4	-7	-1
B1	2	3	3	-3	-8	-13	-12	-2	-2	-2	-2
B2	1	3	3	-2	-8	-12	-12	-1	-2	-3	-1
B3	2	3	3	-3	-9	-13	-13	-3	-6	-7	-2
B4	2	4	3	-3	-11	-14	-14	-4	-8	-11	-2
B5	1	5	4	-1	-8	-11	-10	-2	-9	-13	-1
C1	1	4	3	-5	-11	-15.0	-12	-1	-1.0	-1.0	-1
C2	2	4	3	-3	-12	-16.5	-14	-2	-3.5	-4.5	-2
C3	2	4	4	-3	-12	-14.5	-13	-2	-5.5	-7.5	-2
C4	2	5	5	-2	-10	-14.5	-12	-2	-7.5	-11.5	-2
C5	2	6.5	6	2	-8	-12.5	-13	-1	-9.5	-13.5	-2
D1	1	4	3	-5	-10	-12	-11	-1	-1	-1	-1
D2	1	6	4	-3	-9	-13	-10	-2	-3	-3	-1
D3	1	5	4	-2	-9	-13	-11	-1	-6	-6	-1
D4	1	6	6	-1	-9	-12	-10	-1	-7	-9	-1
D5	2	7.0	6	0	-7	-8	-8	-2	-8	-11	-2
E1	0	4	2	-2	-6	-8	-6	0	-1	-1	0
E2	1	3	2	-3	-6	-8	-6	0	-2	-3	-1
E3	1	5	4	-1	-7	-8	-7	-1	-4	-5	-1
E4	1	4	4	-1	-6	-6	-6	-1	-5	-6	-1
E5	2	5	4	-1	-5	-7	-5	-2	-7	-7	-2
Max	2	7	6	2	-3	-6	-5	1	-1	-1	0
Min	0	1	1	-5	-12	-17	-14	-4	-10	-14	-2

4.1.2.1 Survey Results

The maximum deflection in the North span was 17 mm downward at survey point C2, when the front axles of the two trucks were placed at load point P5. Figure 4.3 shows the deflections for the five girders at survey points C1 to C5 for this load case. In turns, these deflection measurements can be used to assess the level of load sharing between the girders.

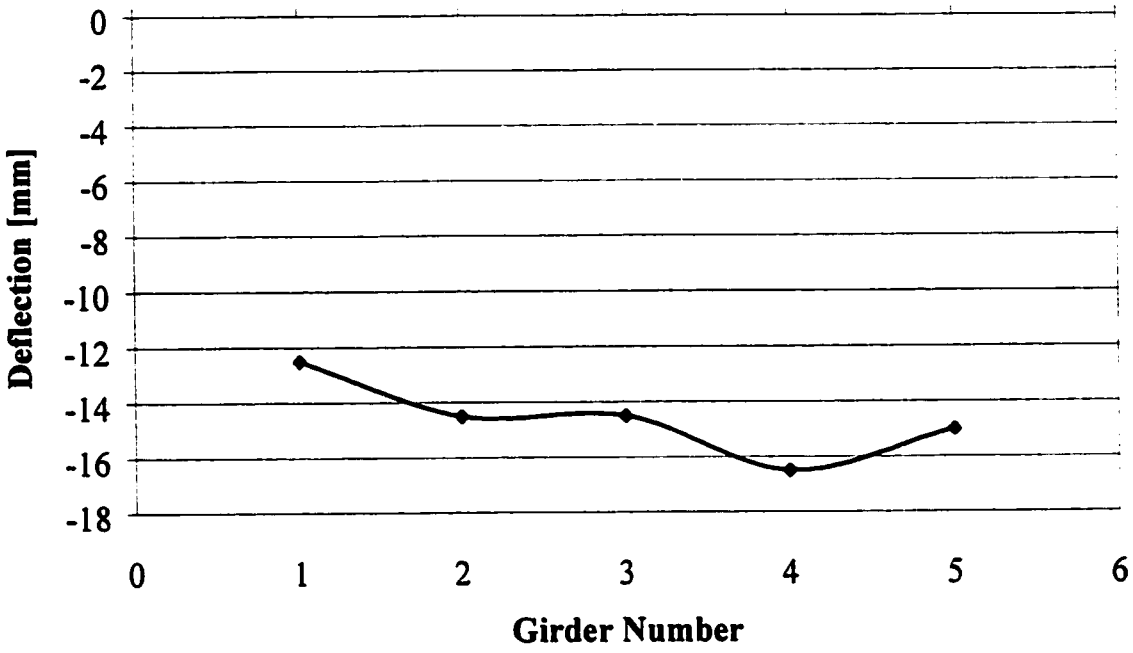

Figure 4.3: Deflection at C1 to C5 for Load Case P5

Figure 4.4 shows the deflection for all five girders at the measurement points C1 to C5 for load case P1. For this load case P1, the two trucks were on the middle span, the maximum deflection in the North span was 7 mm upward at C5 as shown in Figure 4.4. Although the bridge was loaded symmetrically, girder 1 shows the highest deflection of all five girders. Girder 4 in Figure 4.4 shows the least among of deflection among the five girders. Deflection results from August 1997 were done by surveying, thus its may scatter significantly.

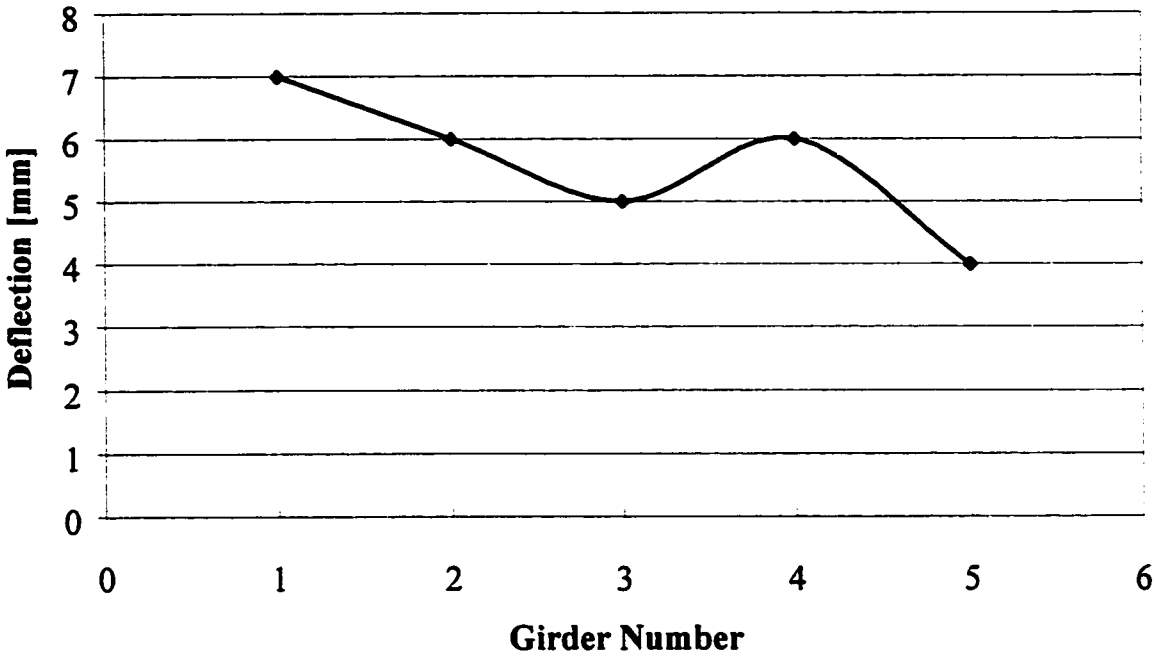

Figure 4.4: Deflection at C1 to C5 for Load Case P1

To impose an eccentric loading on the superstructure, the front axle of a truck is placed at load point P9. The resulting deflection measured in the girders is shown in Figure 4.5 below. The maximum deflection under the truck load is 13.5 mm at C1 for girder 1. At this time, the cross frame between the girders perform very well in redistributing its load among it neighboring girders. Note the slight non-linearity in load sharing among the girders for girder 2. This is expected because under tributary area, it is carrying twice the load as its neighboring girders under this loading condition.

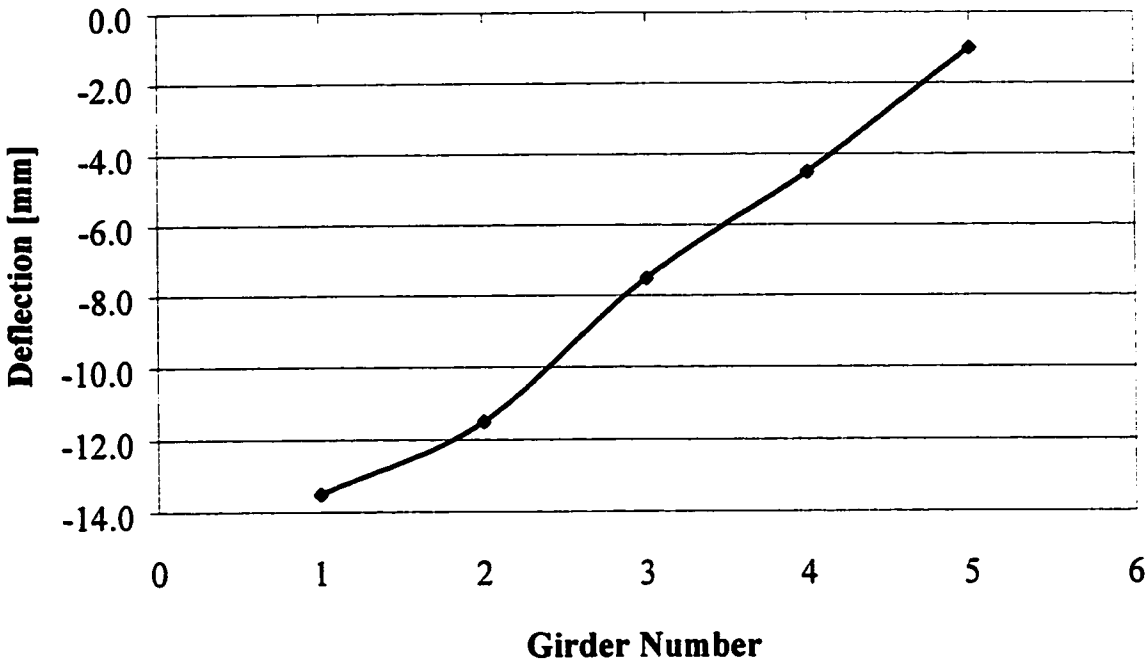

Figure 4.5: Deflection at C1 to C5 for Load Case P9

4.1.2.2 Results from Strain Measurements

A manual switch box was used to record the strains during the static test in August 1997. On August 11th, 1997, the first set of readings was taken at 6:30 a.m., just prior to placing asphalt. The air temperature at the time was 14°C. At 11:20 a.m. on the same day, a second reading was taken after the asphalt was placed and had cooled; the air temperature was 21°C. The strain gauge readings for before asphalt and after asphalt is placed are documented in Appendix B. In addition, strain gauge readings obtained for all the nine load cases are also presented in Appendix B. The strain gauge readings were used to find strain distribution in the cross section, the location of the neutral axis, assess the load sharing between girders, and compare the analysis results with the field test results. Furthermore, it provided the base structural characteristics of the bridge for future studies.

The strain distribution in girder 1 obtained from the measured strains is shown in Figure 4.6. With such loading configuration, the maximum measured strain is 103 με on

strain gauge G3. Although strain gauges G33 and G34 show smaller strain than G3, nonetheless, strain distribution in the cross section is still linear otherwise. Field investigation showed that strain gauges G33 and G34 had poor connections, hence they are unreliable. The small strains indicate that the bridge response was well within the elastic range. Note the neutral axis is at 54.1 mm below the bottom of the top flange.

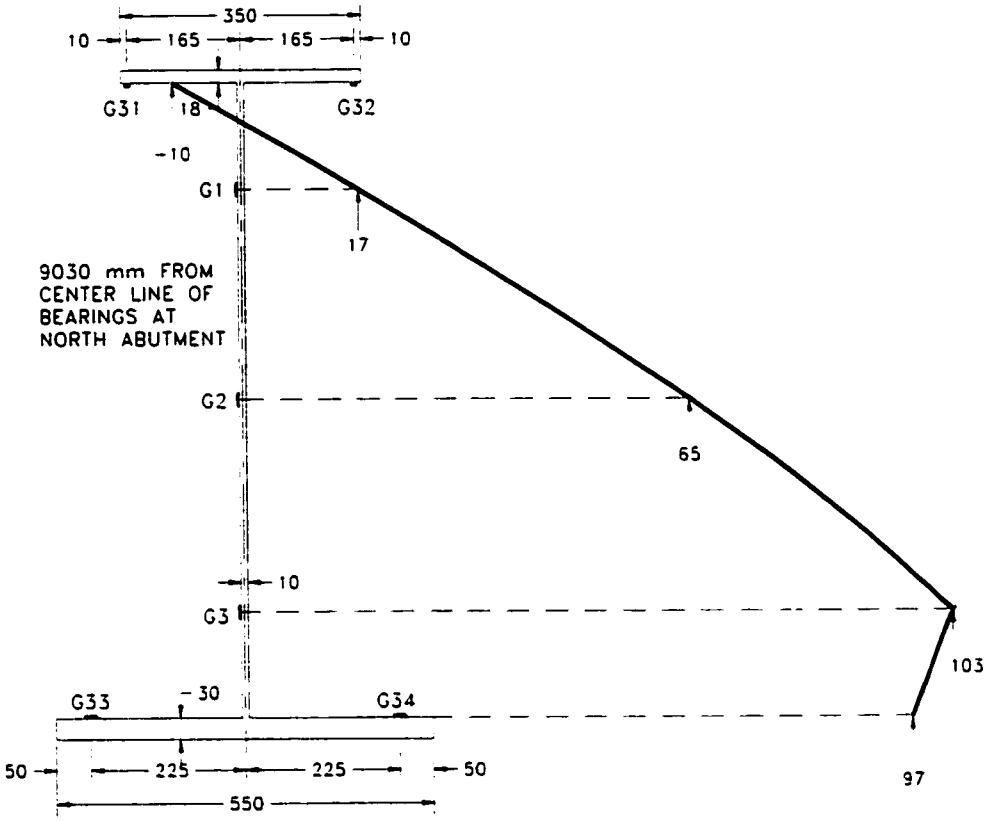

Figure 4.6: Positive Moment Region Strain Distribution in Girder #1

For the same load case P9, the strain distribution in the negative moment region is shown in Figure 4.7. Despite the slight non-linearity, the strain distribution is essentially linear. From extrapolation, the high compressive strain in the bottom flange is 30.7 με. The neutral axis is at 93 mm below the bottom side of the top flange. The change in the location of the neutral axis in the negative moment region reflects the change in composite action of the member.

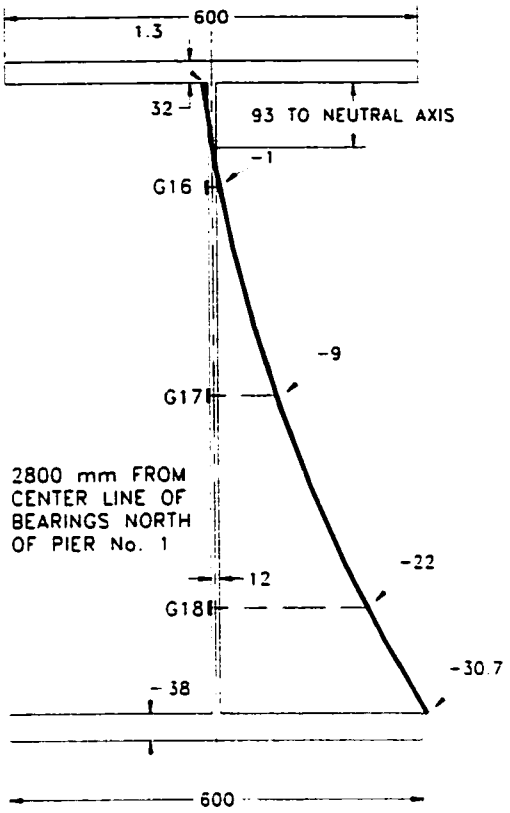

Figure 4.7: Negative Moment Region--Strain Distribution in Girder #1

Load sharing between girders is best examined by using the measured strains in the girders. On all web of the girders in positive and negative moment regions, there are longitudinal strain gauges at 150 mm from the topside of the bottom flanges. When one truck is loaded at load point P9, load sharing among the girders were based on strain gauge measurements as shown in Figure 4.8. The maximum strain under this loading condition is 103 με on girder 1 in the positive moment region. In the negative moment region, the maximum compressive strain is 22 με in girder 1 and girder 2. Note the strains on girders in the negative moment region; almost all have the same magnitude. This would indicate that the load distribution by the diaphragm over the pier is very effective in distributing the load.

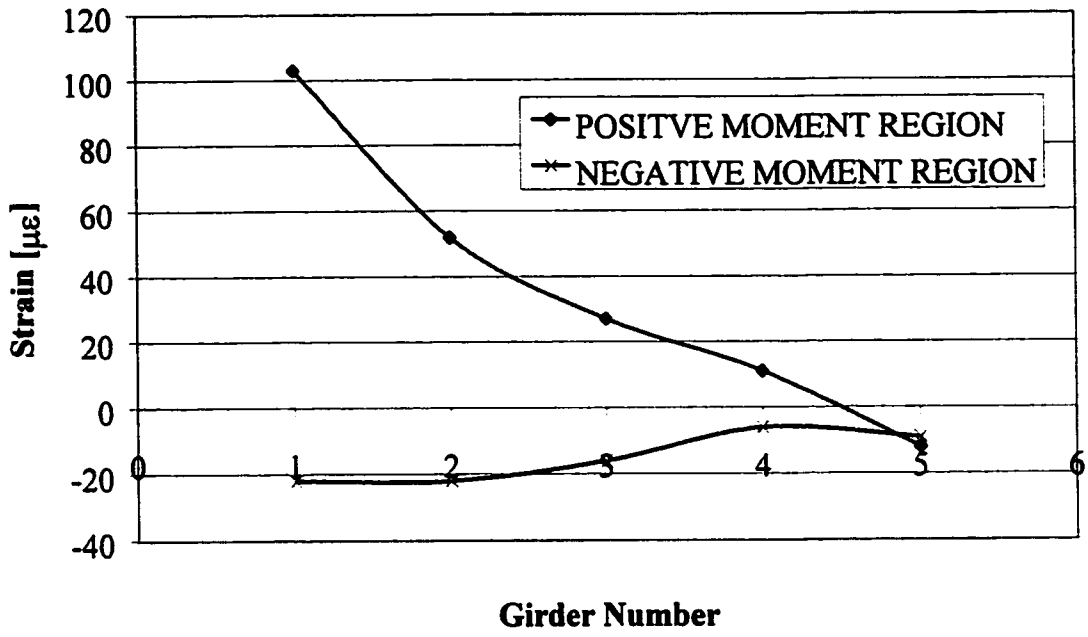

Figure 4.8: Strains in Positive and Negative Moment Regions for August 1997

4.1.3 Crack Pattern for August 1997

Crack patterns on the bottom side were mapped in August 1997 for the first time. The reader should recall that Crowchild Trail Bridge consists of three continuous spans. The South span was reinforced with both GFRP and steel reinforcement. The crack pattern detected in the south span as of August 1997 is shown in Figure 4.9. All cracks formed were transverse cracks. Most cracks at that stage were less than 0.5 mm in width. No longitudinal cracks were detected.

Figure 4.10 shows the crack pattern observed in the middle span, which is partially reinforced with GFRP bars and has no steel reinforcement. This appears to have more transverse cracks than the North or South span. The North span, reinforced only in the cantilever edge, has the least cracks as shown in Figure 4.11. All cracks width was approximately 0.5 mm. As of August 1997, there were no longitudinal cracks in any of the spans.

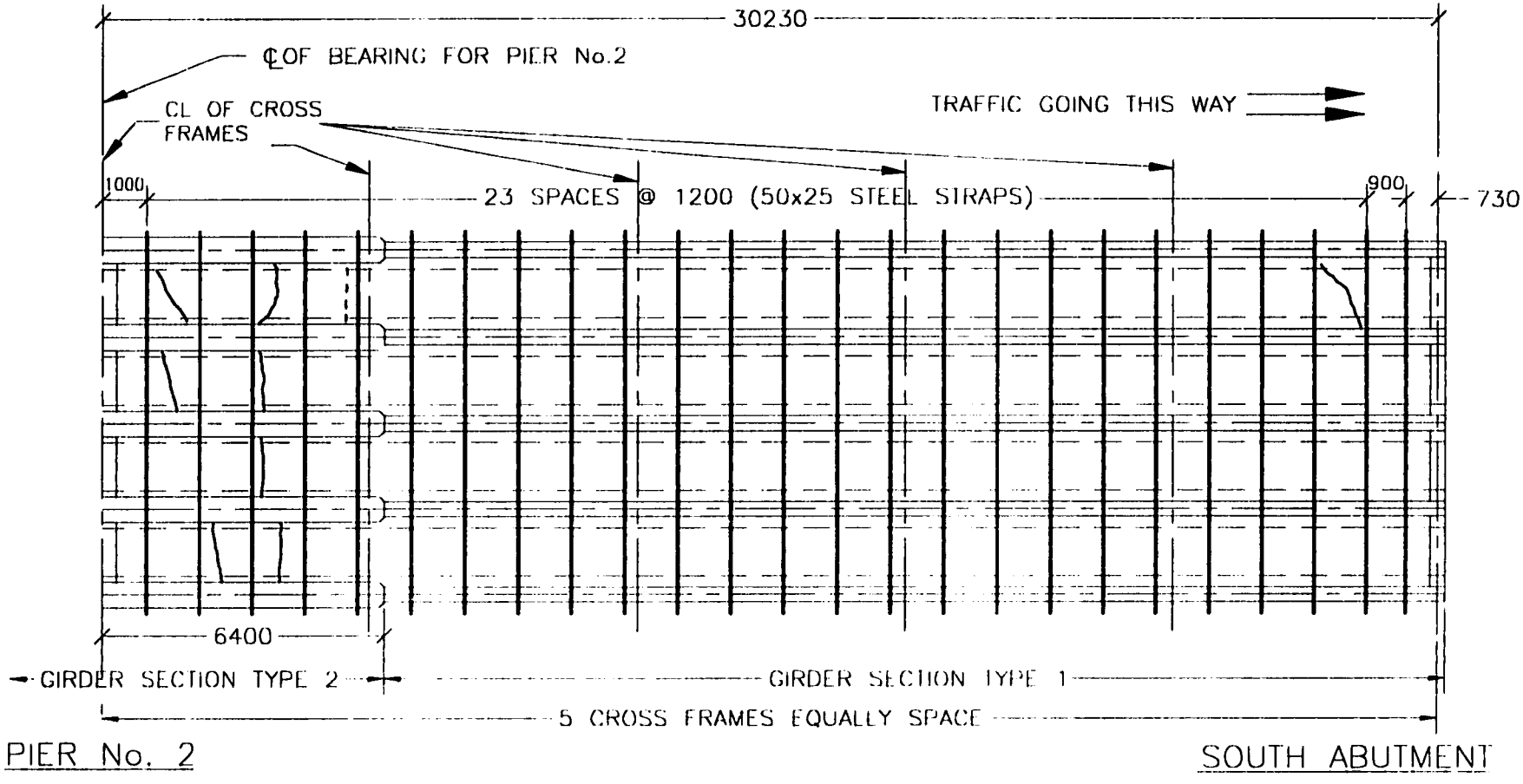

Figure 4.9: South Span Crack Pattern [August 1997]

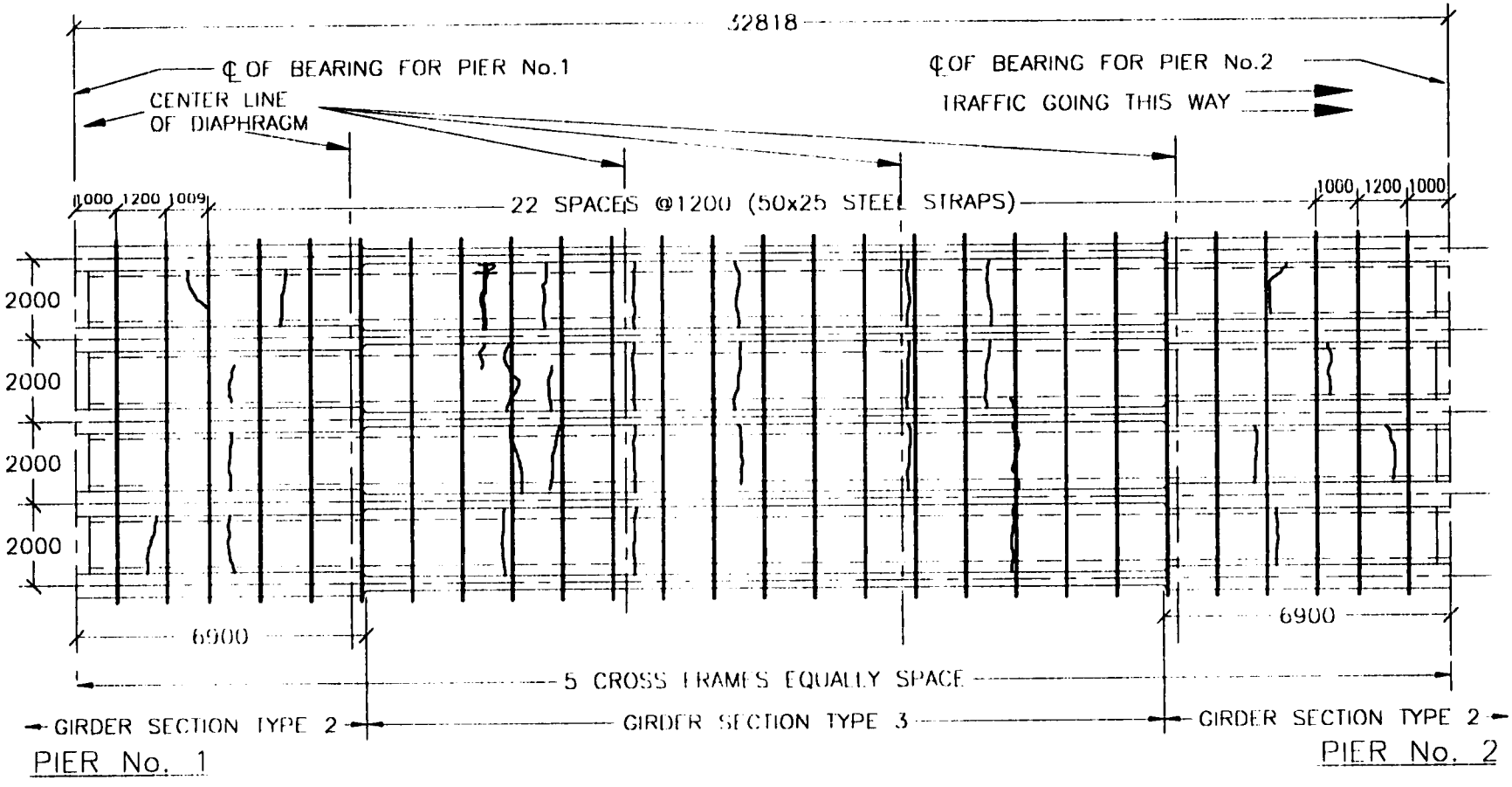

Figure 4.10: Middle Span Crack Pattern [August 1997]

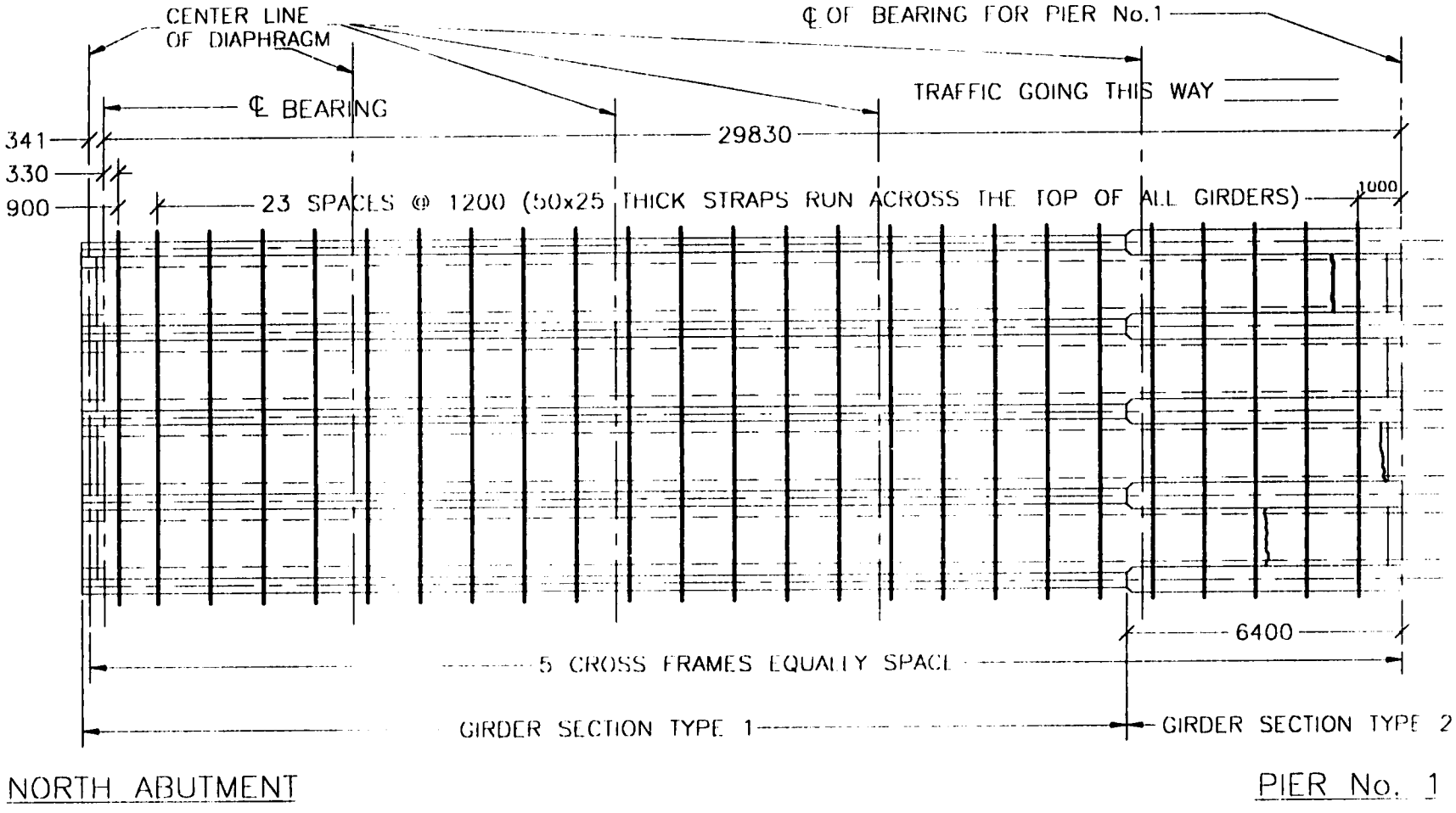

Figure 4.11: North Span Crack Pattern [August 1997]

4.2 Results of the August 1998 Test

By August 1998, Crowchild Trail Bridge had been in operation for one full year. Initial tests were carried out in August 1997, before the bridge was open to traffic, to establish base structural characteristics of the bridge. A second test was conducted in August 1998. The second test included static and dynamic load tests using truck with known axle loads and ran at various speeds. In addition to the electrical strain gauges installed in the first year, cable transducers and accelerometers were added in the second year test. Natural frequencies and mode shapes of the bridge were also determined by the ambient vibration test.

Results from the second test, such as load sharing between girders, dynamic load factor, bridge stiffness, natural frequencies and damping factor of the bridge, are presented. Where applicable, these results are compared to the base test results. In addition, the crack pattern of the concrete deck is mapped and compared to the pattern observed before the bridge was open to traffic. The changes in the bridge structural characteristics are used as an indication of the amount of deterioration of the Crowchild Trail Bridge during the first year of operation.

4.2.1 Ambient Vibration Tests

Field assessment of a full-scale real life structure in service was never an easy task. On August 1998, a second ambient vibration test was performed on the Crowchild Trail Bridge. The tests took less than two hours to perform with only one lane closed to traffic and the other closed only intermittently. The results from this second Ambient Vibration Tests are essential for comparison to the base structural characteristics of the bridge.

4.2.1.1 Objective and Problems

The objective is to use ambient vibration tests to determine the dynamic behavior [frequencies, mode shapes, stiffness, and torsional rigidity of the deck] of the Crowchild Trail Bridge. The selection of the proper tools and procedure was an important part of this investigation. During ambient vibration tests, the bridge is considered to be excited by various random low-level forces. Such random forces can be from wind, passing vehicle underneath the bridge and other human activities. Such random forces cannot be controlled, and the level of excitation is very low. Reliable results are possible, provided that:

1. Strains are small, and the system behaves linear elastically.
2. The level of excitation is such that the structure's mode shapes of interest are significantly excited. Thereby, it is identifiable in the power spectrum.
3. The system is lightly damped.

Thereby, the period of measurements in ambient vibration test is typically longer than in dynamic tests in order to capture all the mode shapes of interest.

4.2.1.2 Field Testing

Due to various limitations for field testing of such bridge in service, testing programs must be very carefully designed to take the least amount of time and create minimal interference to traffic flow. Ideally, 200 accelerometers or more are needed on a bridge this size, thus only one set of reading is needed. Accelerometer instrument is however very expensive, and therefore only four accelerometers were made available. Due to this limitation, the ambient vibration test was broken up into a series of ten sets of tests. Despite limited number of accelerometers available, ambient vibration tests performed in August 1998 took less than two hours. Only one of the two lanes was closed to traffic for the full two hours, where as the other lane was only closed

intermittently for each of the test. All four accelerometers were used in each of the ten sets of reading were taken. For each set of reading, the intermittent closing of the second lane was 3 minutes and 20 seconds. Eight of the ten sets of readings were taken for the vertical modes and two for the transverse modes behaviour of the bridge. In each set of test, the data was acquired for 200 seconds with a scan rate of 200 scans per second. This enabled the capture of frequencies up to 50 Hz with the corresponding mode shapes for a complete phase analysis. However, only frequencies below 10 Hz are of interest in this work and discussed in details.

For ambient vibration tests, all the accelerometers were placed as shown in Figure 4.12. In the transverse direction, the accelerometers were placed directly on top of either girder #1 or girder #2. For each set of reading, one of the four accelerometers was placed at the reference point (see Figure 4.12). This reference accelerometer was later used to normalize the other accelerometers with respect to the magnitude and direction of the vibration. By normalize all other accelerometers' magnitude with respect to the reference accelerometer for each set of test, it had the effect of canceling out the different levels of excitation forces in various sets of tests. In addition, reference accelerometer also serves a vital role in correlating all the different sets of tests for phase analysis to identify the mode shapes. Table 4.3 shows the test #, filename, accelerometer # and its' location on the bridge for each test performed (see Figure 4.12).

Table 4.3: Filenames and Accelerometer Locations

Test #	Filename	Accelerometer #	On Top of Girder #
1	A0825P0952.raw	10(Ref.)	1
		11	1
		12	1
		13	2
2	A0825P1001.raw	10(Ref.)	1
		11	1
		12	1
		13	2
3	A0825P1008.raw	10(Ref.)	1
		11	1
		12	1
		13	2
4	A0825P1019.raw	10(Ref.)	1
		11(Ref.)	1
		12(Ref.)	1
		13(Ref.)	1
5	A0825P1049.raw	10(Ref.)	1
		11	1
		12	1
		13	2
6	A0825P1057.raw	10(Ref.)	1
		11	1
		12	1
		13	2
7	A0825P1121.raw	10(Ref.)	1
		11	1
		12	1
		13	2
8	A0825P1131.raw	10(Ref.)	1
		11	1
		12	1
		13	2
9T	A0825P1041.raw	10(Ref.)	1
		11	1
		12	1
		13	1
10T	A0825P1029.raw	10(Ref.)	1
		11(Ref.)	1
		12(Ref.)	1
		13(Ref.)	1

The eight elliptical-circles shown in Figure 4.12 were referred to the eight sets of tests performed to determine the vertical characteristics of the bridge. These eight elliptical-circles shown from North to South respectively were directly corresponding to *Test #1* to *#8* as shown in Table 4.3. For example for *Test #1*, the three dots shown in the elliptical-circle on the North span were the locations of the accelerometers. The last column in Table 4.3 indicates the location in which the accelerometers were placed. *Tests #1* to *#8* are for vertical mode shapes. Note the Accelerometer # 10 was always placed between the 33rd and the 34th steel strap from the North, and it was not moved for any of the eight tests. Only three of the four accelerometers were moved for each of the test performed. For the transverse mode shapes, only two readings were taken, *Test # 9T* and *#10T*. For *Test #9T*, the location of the accelerometers *#10, #11, #12,* and *#13* were near the 17th, 30th, 33rd, and 43rd steel strap from the North abutment, respectively. For *Test #10T*, all accelerometers were place between the 33rd and the 34th steel strap from the North. All accelerometers were monitored using LabVIEW in combination with a high-speed data acquisition system to obtain data shown in Table 4.3.

4.2.1.3 Data Reduction

Plot of raw data for accelerometer #10 in file A0825P0952.raw is shown in Figure 4.13. It shows the responded of the accelerometer in mV as a function of time in second. The analog signal from the accelerometer was converted to digital signal and sampled at 200 scans per second for 200 seconds. Nyquist frequency rule dictates that the maximum frequency can be determined from any response is half of the sampling rates (McConnell, 1995). Consequently, for a sampling rate of 200 scans per second, the maximum frequency that can be determined is 100 Hz. Hence, the scan rate used was more than sufficient for the interested frequencies of 10 Hz and less.

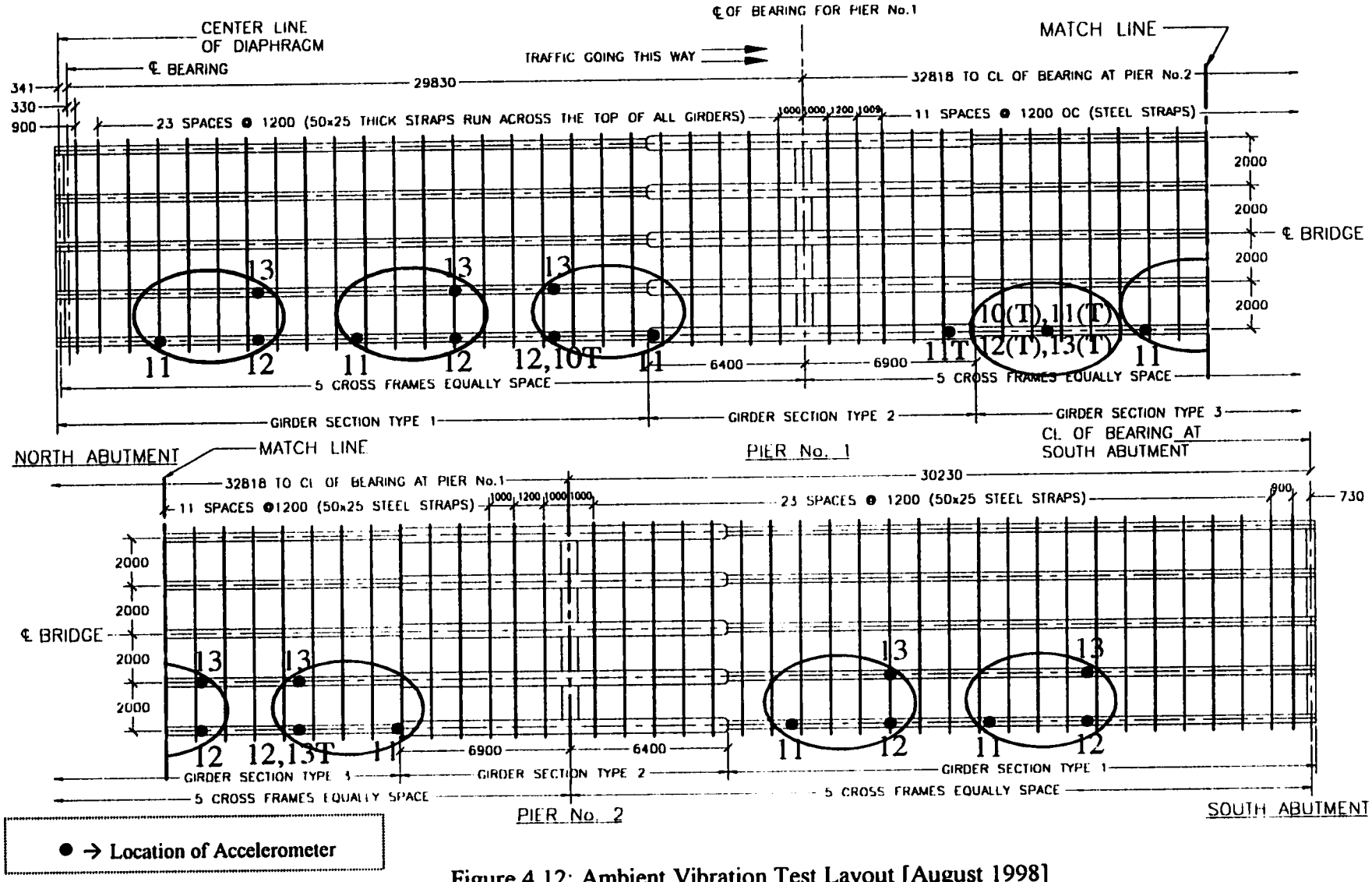

Figure 4.12: Ambient Vibration Test Layout [August 1998]

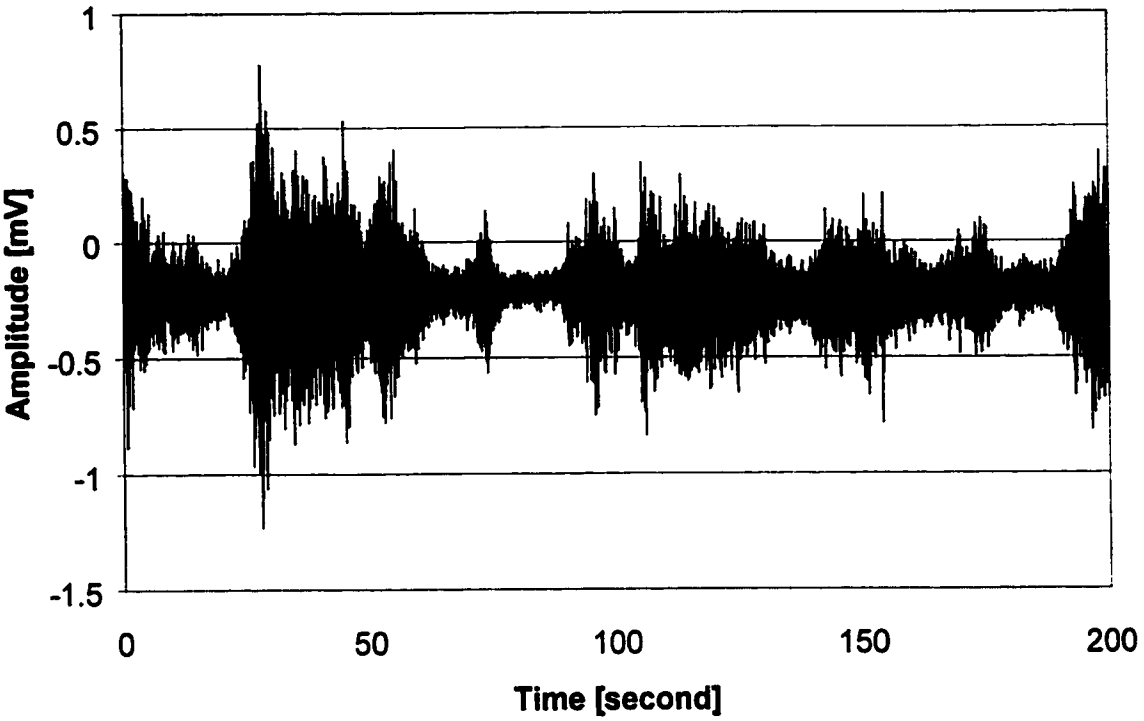

Figure 4.13 Accelerometer #10-- Raw Data

Before the tests begin, several sampling rates were trailed and tested for variation in frequencies response. At 200 scans per second, there was no variation in frequency response for this bridge. Hence, the Aliasing problem had been considered in collecting these data. An example of Aliasing error in data collecting is shown in Appendix B. Despite all precaution had been taken to eliminate all known errors, the background noise from the DC power source render such raw data are of little use. Fortunately, these noises were deterministic and periodic (typically they occurred at a multiple frequency of 20 Hz). Butterworth filter type was chosen to filter out such unwanted frequencies. This filter was chosen for its smooth response at all frequencies and a monotonic decrease from the specified cutoff frequency characteristics. Butterworth filter was applied to all raw data to obtain the final filtered data.

Figure 4.14 shows power spectrum plot of the raw file A0825P0952.raw. The power spectrum of the raw data was computed by applying Fourier Transforms to find the

frequencies of the function. The horizontal axis represents the frequency axis and the vertical axis is the square of the amplitude of the accelerometer response. Commercially available software such as LabVIEW was used to digitally apply Fast Fourier Transforms, FFT and Discrete Fourier Transforms, DFT and plot the power spectrum (National Instruments Corporation, 1996). Since only frequencies between 2 to 10 Hz are of interest, Figure 4.14 below only shows frequency between this range.

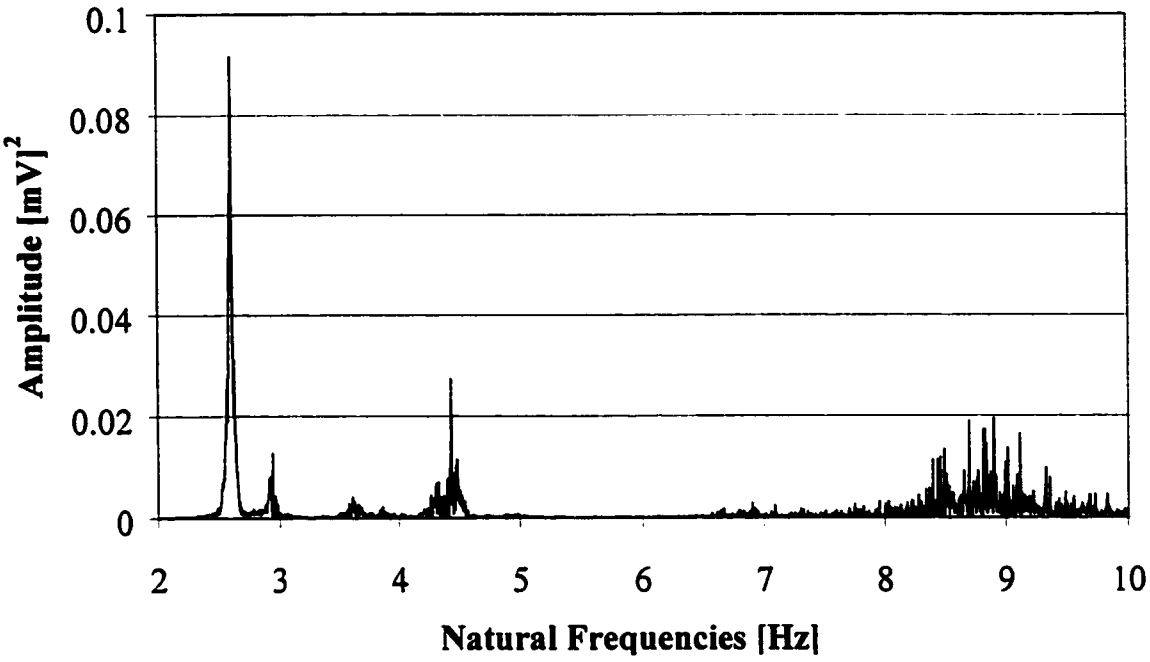

Figure 4.14 Power Spectrum for Accelerometer #10

The actual vibration modes of a structure may be highly coupled. Depending upon the location of the accelerometer placed on the structure, it may see higher magnitude of excitation for some frequencies and little or none of the others frequencies. For example, if an accelerometer is placed at mid-span on a simply supported beam, it may see maximum magnitude of vibration in the first mode and little or none in the second mode. Figure 4.15 is a plot of the accelerometer #11 from the same file as Figure 4.14, which is a plot of accelerometer #10. Note that the frequency of 2.60 Hz is very predominant in Figure 4.14, but very little is showing in Figure 4.15 despite the fact that all the accelerometers were calibrated to have the same output when subjected to the same level of excitation. The significantly lower magnitude of excitation for the 2.60 Hz

frequency shown in Figure 4.15 compared to Figure 4.14 is due to the location of the accelerometer and not the accelerometer itself. To determine the exact mode shape of each frequency, the following parameters are require: the level of excitation as a function of location on the bridge and the direction of excitation at an instant frame of time. Since the vertical axis of the power spectrum plot is amplitude squared, the directions are not known at that particular time frame.

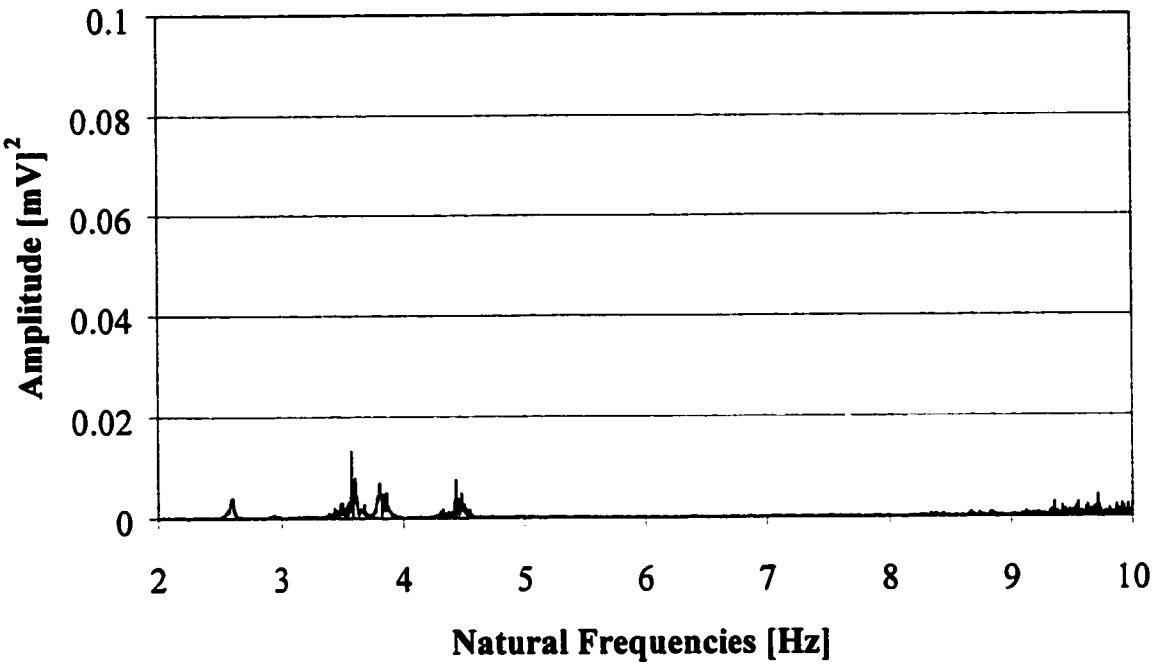

Figure 4.15: Power Spectrum for Accelerometer # 11

In order to determine the mode shape for a particular frequency the magnitude and direction of excitation at different points along the bridge must be known. The magnitude of excitation for each frequency can be found from the power spectrum analysis. The direction of excitation can be determined by comparing the phase of excitation to the reference accelerometer excitation. In raw data, the frequencies are highly coupled. In phase analysis, only one frequency can be examined at a time. Thus, a band-pass filter is used to isolate the frequency of interest. Each file is then filtered for all frequencies of interest in turn. Finally, the phase of each frequency can be compared to the reference accelerometer with the same frequency. Figure 4.16 shows the phase

analysis plots for 2.60 Hz frequency. Clearly for 2.60 Hz, accelerometers #11 to #13 are all moving in the opposite direction compared to the reference accelerometer #10.

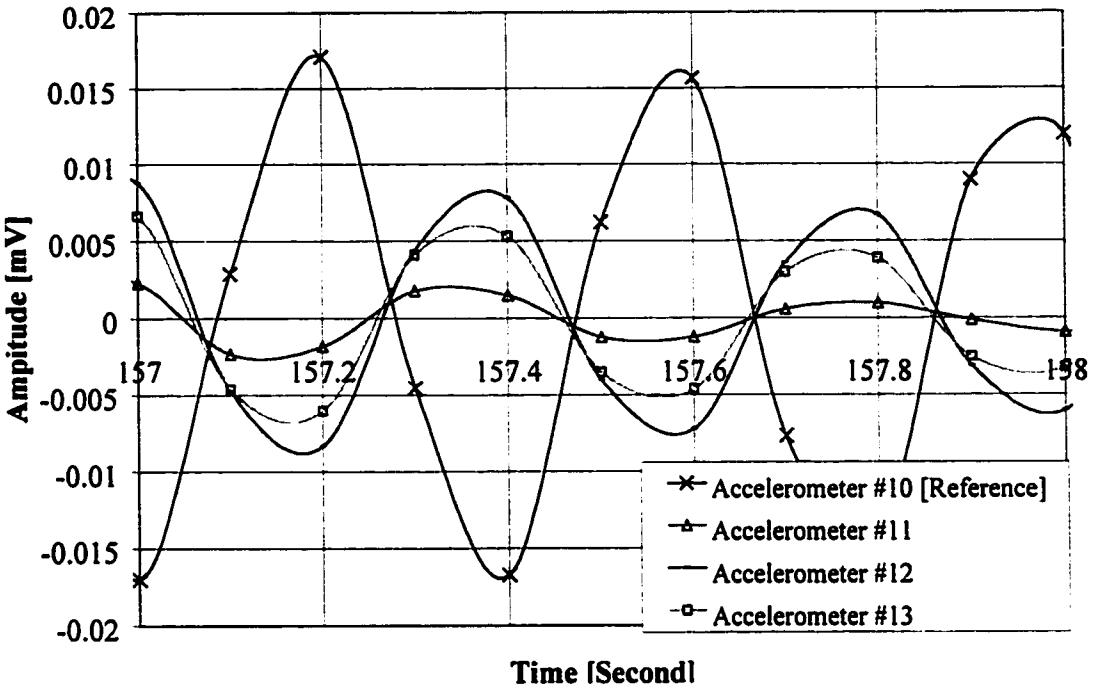

Figure 4.16: Phase Analysis for 2.60 Hz

In order to distinguish between the torsional and vertical mode shapes, the magnitude of excitation of girder #1 is compared to that of girder #2. If both accelerometers on girder #1 and girder #2 located at the same distance along the bridge show a very close magnitude of excitation, the mode of vibration is a vertical mode. Figure 4.17 shows such magnitude comparison. Likewise, if the difference between the magnitudes of excitation is always proportional to the distance between the accelerometers across the width of the bridge at a cross section, the mode of vibration is a torsional mode as shown in Figure 4.17. This method is based on the assumption that the bridge deck is rigid. An improvement in future testing would be to place an accelerometer on every girder, since the bridge deck may not be rigid. Another benefit of this modification is that it allows a closer examination of the stiffness of the individual girders, and the stiffness of the deck.

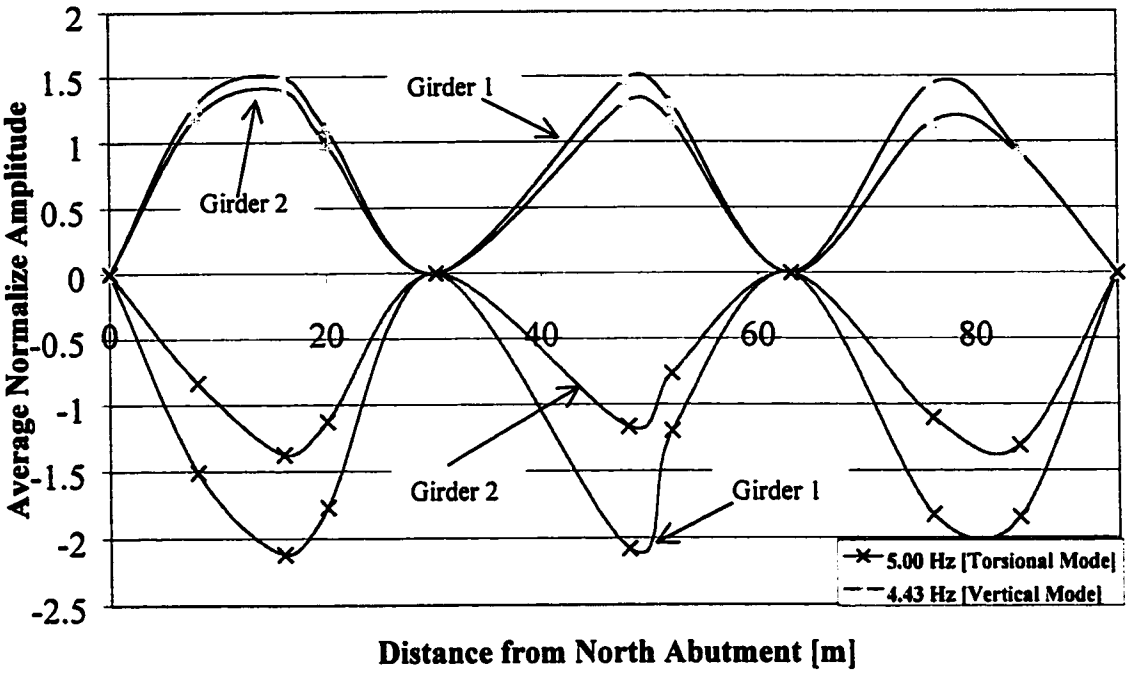

Figure 4.17: Distinguish between Vertical [4.43 Hz] / Torsional [5.00 Hz] Mode Shapes

4.2.1.4 Frequencies and Mode shapes

Due to the nature of mode shapes and the small number of accelerometers used on this bridge, some accelerometers may or may not capture some particular frequencies. For example, the power spectrum for Accelerometer #11 shown in Figure 4.15 practically did not captures the 2.90 Hz frequency, where as Accelerometer #10 shown in Figure 4.14 does. Again, this is due to the location of the accelerometer on the bridge, which determine the frequencies and magnitude of the frequencies captured. It is worth noting that eight different vertical vibration tests were performed, and each test was conducted with the accelerometers at different locations on the bridge. Consequently, if one accelerometer did not capture some particular frequencies, than chances are other accelerometers at other locations on the bridge will captures these missing frequencies. Therefore by summing all four accelerometers in each of the test, from eight different tests, it is possible to capture the majority of the lower modes of vibration without missing any modes. Likewise, if there were enough data gather from infinite number of points from the bridge, then there is no limits to the number of mode shapes in which it

can captures. The power spectrum of all eight files in the vertical mode are summed and plotted in Figure 4.18.

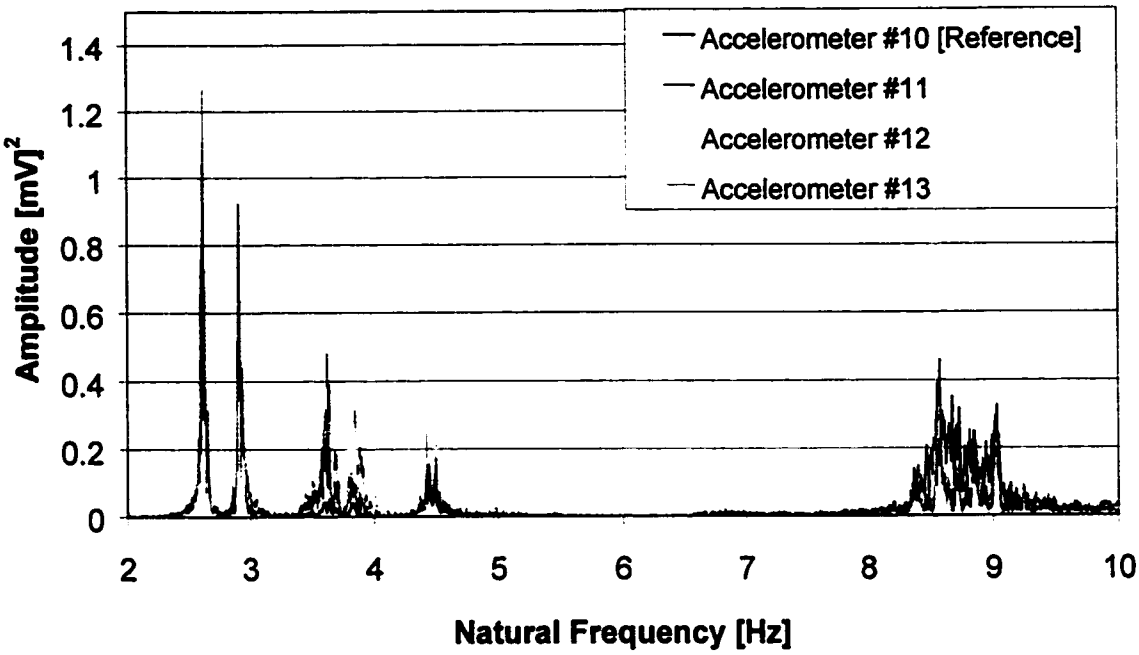

Figure 4.18: Power Spectrum for the Sum of All Accelerometers from Eight Files

The power spectrum shown in Figure 4.18 identifies eight predominant frequencies below 10 Hz as outlined in Table 4.4. The resolution of these frequencies is ±0.01 Hz. Table 4.4 shows the ambient vibration tests done by U of A and UBC yields very close results. In addition, the mode shapes found by both Universities were all matched. In general, the frequencies found in August 1998 were approximately 0.20 Hz lower than the frequencies found in September 1997. Since the mass of the bridge had not changed over the last one year of operation, thus the bridge stiffness could have been reduced.

Table 4.4: Vertical and Torsional Modes

U of A (Aug '98)	UBC Report (Sept '97)	Description
2.60 Hz	2.78 Hz	1st Fundamental Vertical Mode
2.90 Hz	3.13 Hz	1st Fundamental Torsional Mode
3.63 Hz	3.76 Hz	2nd Vertical Mode
3.85 Hz	4.05 Hz	2nd Torsional Mode
4.43 Hz	4.64 Hz	3rd Vertical Mode
5.00 Hz	5.18 Hz	3rd Torsional Mode
6.85 Hz	7.13 Hz	4th Torsional Mode
8.60 Hz	9.13 Hz	4th Vertical Mode

The frequencies in Table 4.4 above and its corresponding mode shapes are shown in Figure 4.19. Both three-dimensional prospective view and the West elevation view of the each mode shape are shown in the figure. For each figure, it consisted of one vertical and one torsional mode shapes. For all figures shown in Figure 4.19, the horizontal axis is the distance along the bridge, and the vertical axis is the average normalized magnitude of excitation for each mode shape. For each frequency list in Table 4.4 above, the corresponding mode shapes are shown in Figure 4.19 as follows:

1. Figure 4.19 (a) 1st fundamental vertical and torsional mode shapes.
2. Figure 4.19 (b) 2nd fundamental vertical and torsional mode shapes.
3. Figure 4.19 (c) 3rd fundamental vertical and torsional mode shapes.
4. Figure 4.19 (d) 4th fundamental vertical and torsional mode shapes.

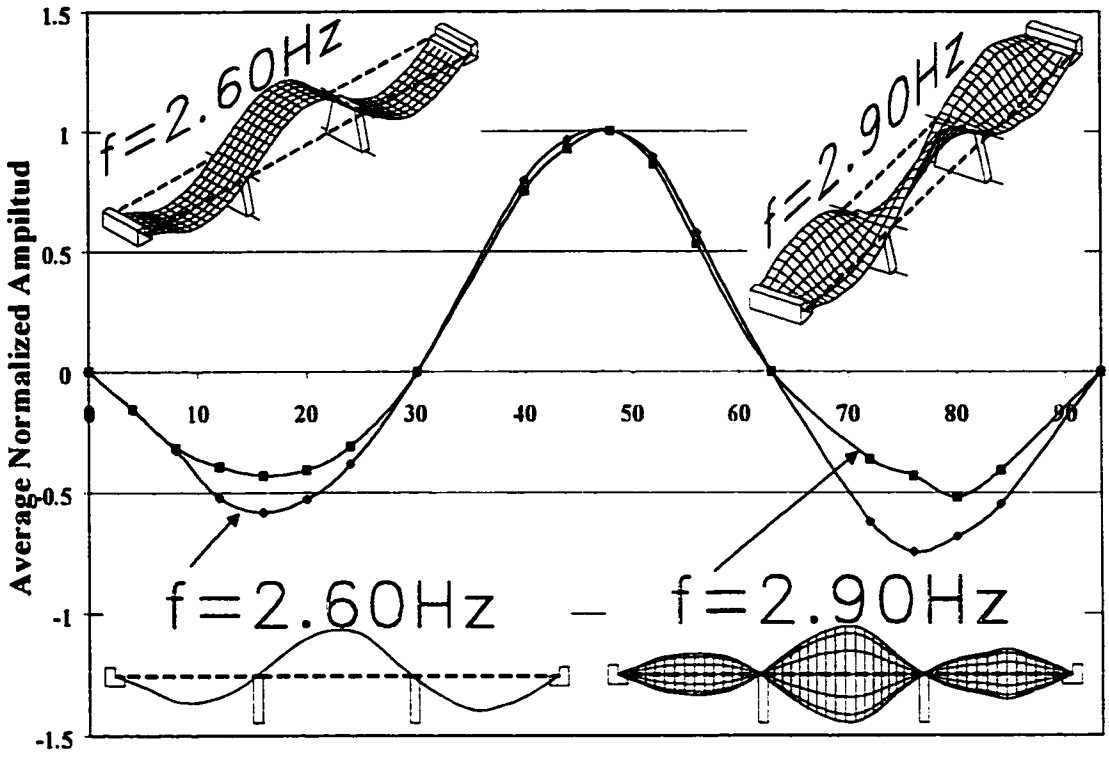

(a) 1st Fundamental Vertical and Torsional Mode Shapes

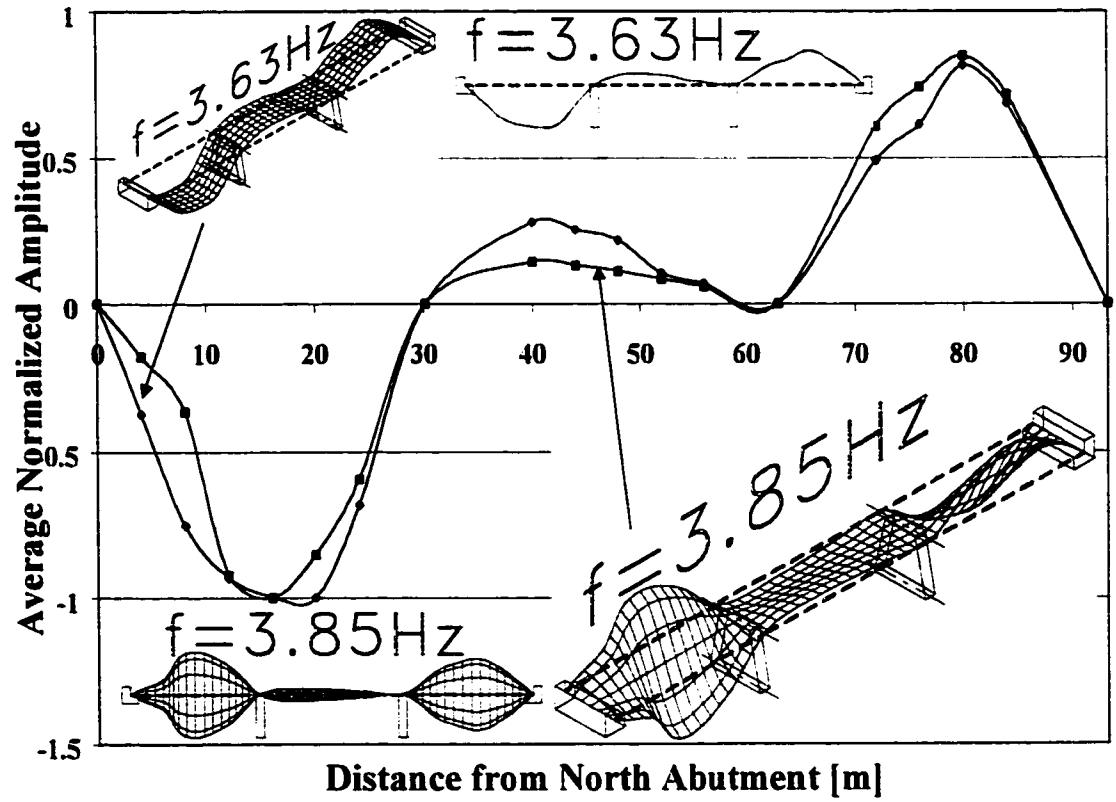

(b) 2nd Vertical and Torsional Mode Shapes

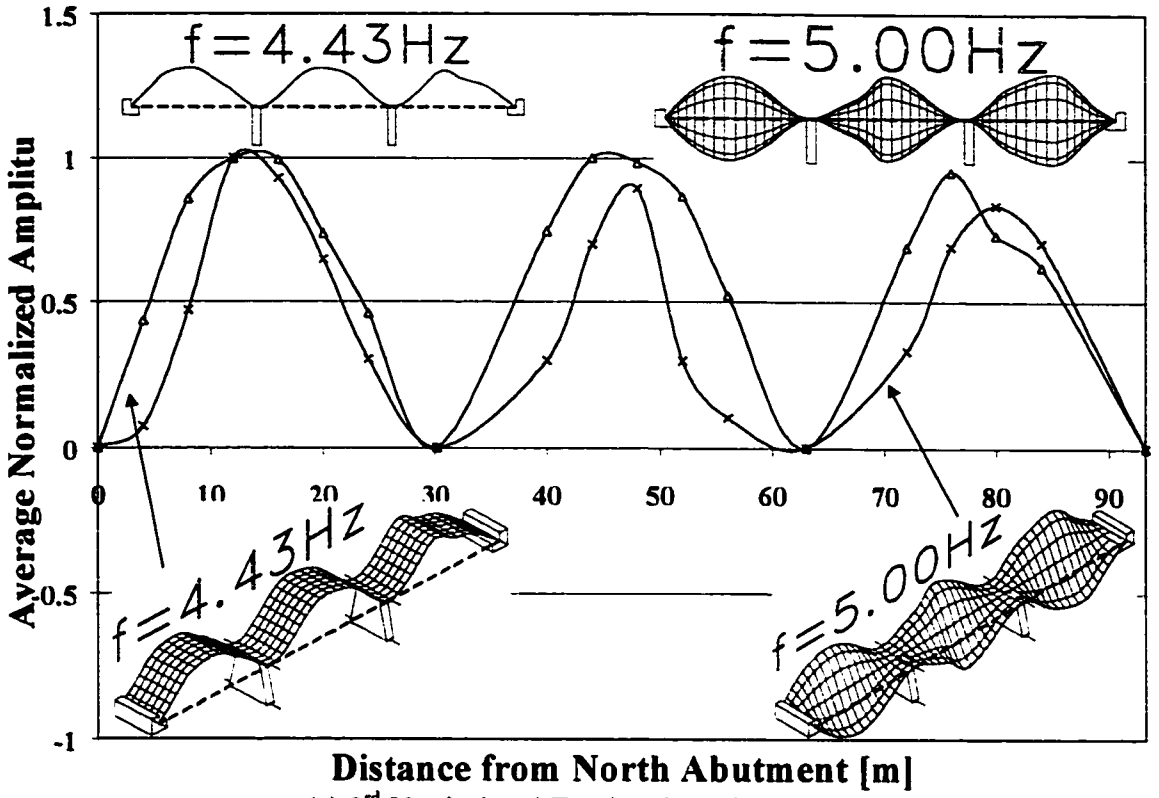

(c) 3rd Vertical and Torsional Mode Shapes

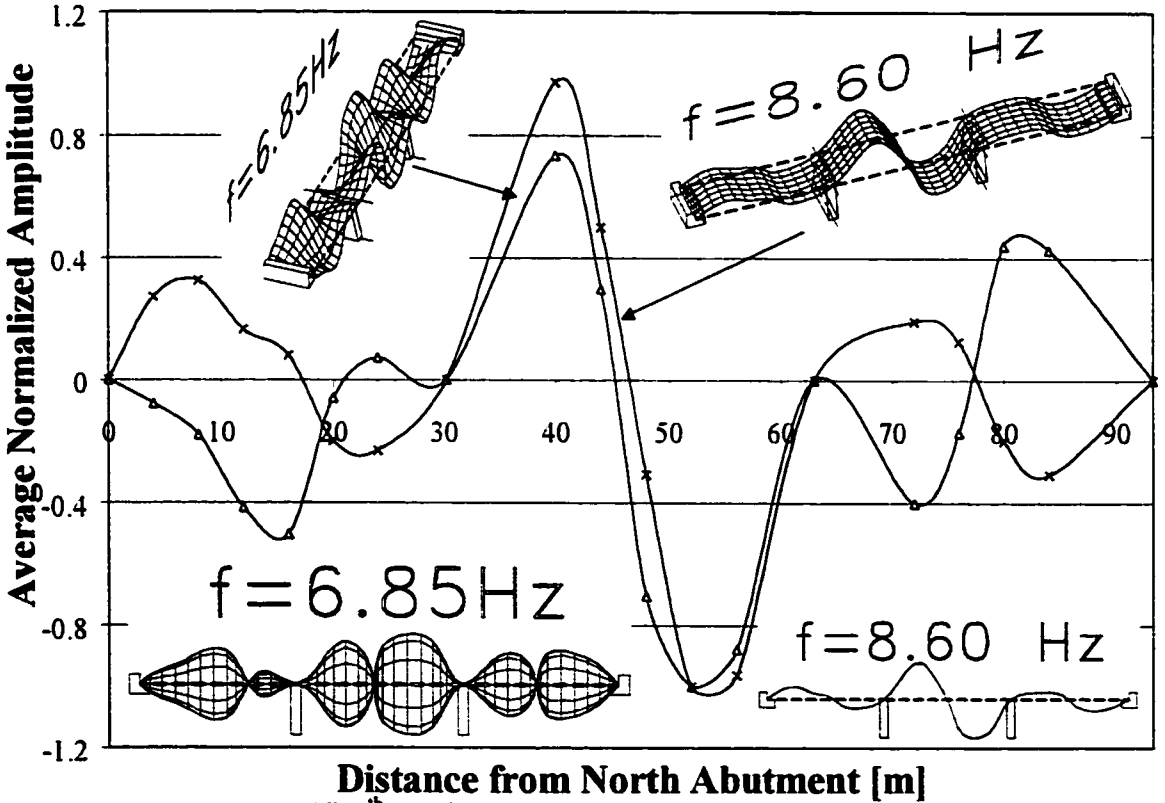

(d) 4th Vertical and Torsional Mode Shapes

Figure 4.19: Frequencies and Mode Shapes

4.2.2 Static Test Results

To establish the static behaviour of the bridge under service load, a truck with known axles load was used in the tests. The static test results in August 1998 were used to monitor the change in the bridge structural characteristics by comparing it to the static test results obtained in August 1997. Subsequently, the results were also used to compare to the dynamic test results in August 1998. The truck had a total gross weight of 395 kN with 42 kN on the front axle, and 154 kN and 199 kN on the second and third tandem axles as shown in Figure 4.20. For all the tests performed in August 1998, the truck was moving from North to South as shown in Figure 4.21. Figure 4.21 shows the position of the right wheel of the front axle along the bridge for each of the static tests. All load points were located at midpoint between girders #1 and #2 as indicated in Figure 4.21.

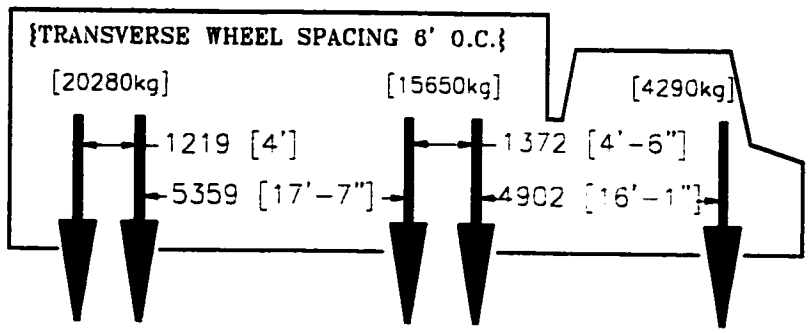

Figure 4.20: Truck Used for August 1998 Static Tests

Initial zero readings were obtained before the test truck moved onto the bridge. Strain gauges and cable transducers were recorded for each load position indicated in Figure 4.21. It tokes approximately 1-2 minutes to complete each set of reading for one load point. After every four to five readings, the truck was moved off the bridge to re-establish zero readings for all the instrumentation to account for possible temperature effects.

The high-speed data acquisition system available was limited to read 50 channels at a time. Due to this limitation, all static and dynamic tests were repeated three times for each load point of interest. Over 100 strain gauges, 10 cable transducers, and four

accelerometers were used for the August 1998 tests. Due to high number of strain gauge channels needed for each load point, these strain gauge channels were divided into three separate sets as follows:

Strain Gauges Set 1	Strain gauges G1 to G34 and T4
Strain Gauges Set 2	Strain gauges T1 to T18, R1 to R15, RC1 and RC2
Strain Gauges Set 3	Strain gauges E2 to E19, N1 to N4, T4, S1 to S6, C1 to C4, and RS1 to RS3

Consequently, each test had to be repeated three times in order to record the three sets of strain gauges. For each test run, the high-speed data acquisition channels were set up to log the following readings:

1. Channels 0 to 34 are for 35 strain gauges (either Set 1, Set 2, or Set 3 was connected for Static and Dynamic tests).
2. Channels 35 is for the one standard strain gauge (Connected at all times for Static and Dynamic tests).
3. Channels 36 to 45 are for the 10 cable transducers (Connected at all times for Static and Dynamic tests).
4. Channels 46 to 49 are for the four accelerometers (These channels were connected for Dynamic test only).

Since all test runs were repeated three times for each load point, data for the ten cable transducers, one standard strain gauge, one *T4* strain gauge and four accelerometers were logged redundantly three times each. Hence, these triplicate sets of data were used to check the consistency of test results. Due to high volume of strain gauge channels needed for each load point, *Strain Gauges Set #1, Set #2, and Set #3*, were logged only once for each test run. Unfortunately, for *Set #3* in the static test, the truck was not positioned on every load point due to time limitation.

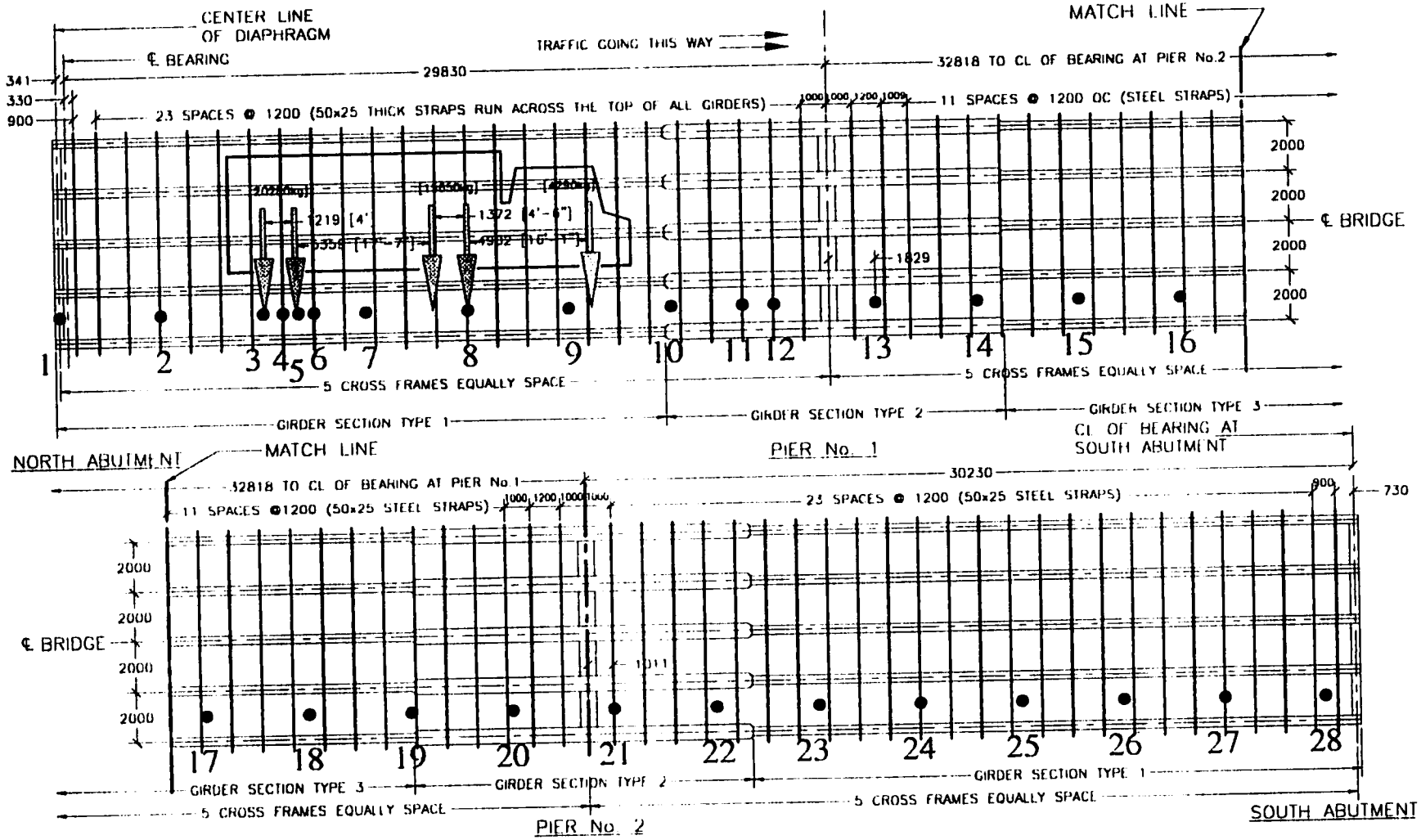

Figure 4.21: Load Points Layout for August 1998 Tests

4.2.2.1 Data Obtained from the Cable Transducers

Cable transducers # 1 to #5 measured the vertical displacement at strap #13 for girders #1 to #5, respectively (see Figure 4.22). Strap numbering system is shown in Figure 4.22 below. Cable transducers #6 to #9 were mounted on girders #1 to #4, respectively at strap # 21. Cable transducer #10 was used to measure the vertical displacement of girder #5 at strap #35, in the middle span.

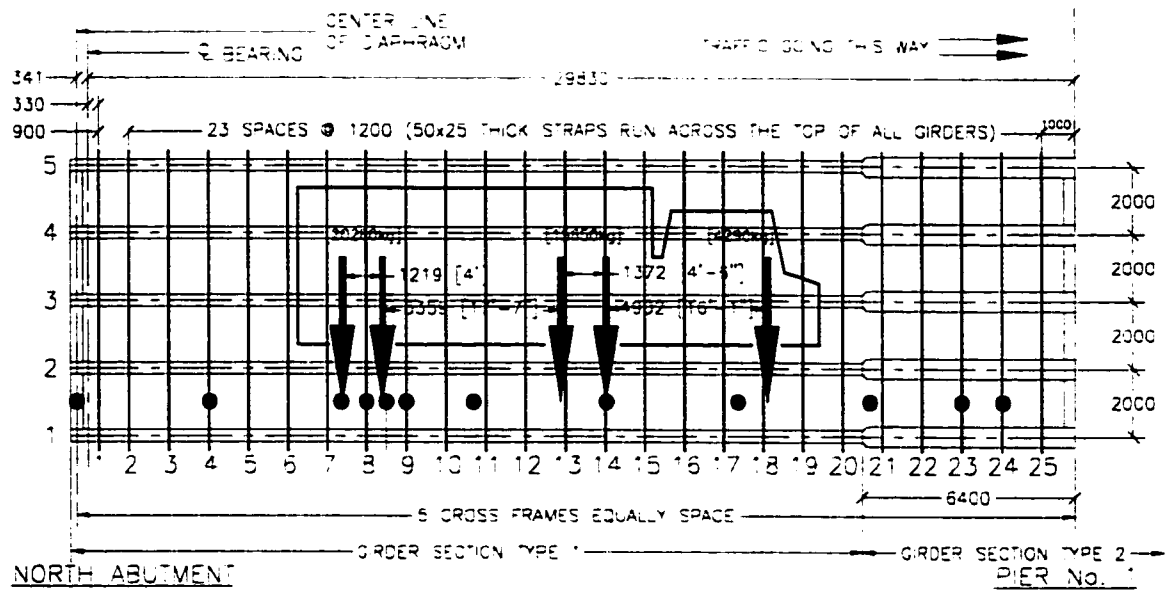

Figure 4.22: North Span Loading Configuration and Strap Numbering.

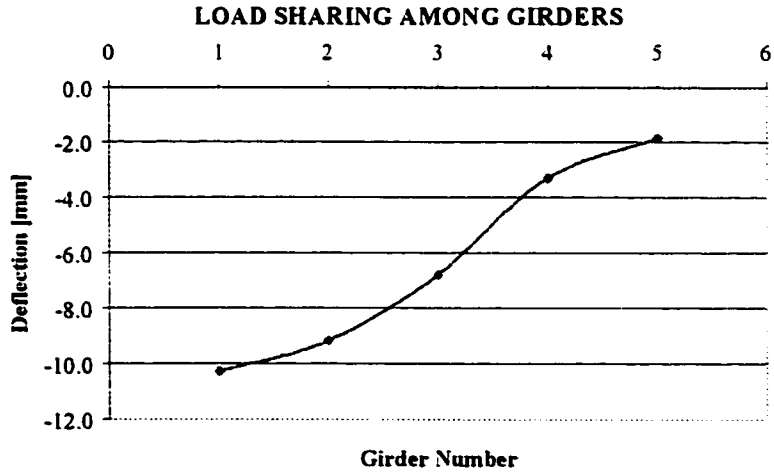

Figure 4.23: Cable Transducers at Strap #13

Load sharing between the girders can be assessed from the cable transducer data collected at Strap #13. As shown in Figure 4.23 the maximum deflection under this one truckload was 10.28 mm for girder #1.

The bridge influence line can be shown from the cable transducer results at strap #13, as shown in Figure 4.24. The locations of the cable transducers at strap #13 is shown in Figure 4.24 by a single vertical line labeled *Cable T*. The vertical axis shows the deflection in millimeters for girders G1 to G5 for different positions of the front axle of the test truck from the North end of the bridge, plotted along the horizontal axis. The horizontal axis is the distance in meters along the bridge from North to South. In addition, the two vertical lines labeled *Pier No.1* and *Pier No.2* indicate the location of the two interior piers with respect to the overall length of the bridge. For the North span, the maximum deflection recorded was 10.3 mm when the truck front axle was 15.90 m from the North abutment (at Strap #14). Assuming the bridge to be a continuous beam, the maximum deflection is expected at strap #14. However, the middle span had a maximum deflection of 4.46 mm when the truck front axel reaches 9.85 meter South of Pier No.1. This was not expected based on Maxwell's reciprocal theorem. Because for a continuous 3 equal spans bridge, assuming the bridge has the same stiffness all along its length, the maximum deflection is expected to be at the midspan. A maximum deflection at 9.85 meter South of Pier No.1 is merely one-third the length of the middle span. This may suggested that the stiffness at this point is lower than its neighboring part. Whereby the same loads at this point had a larger influence effects on the overall structure than its counter part.

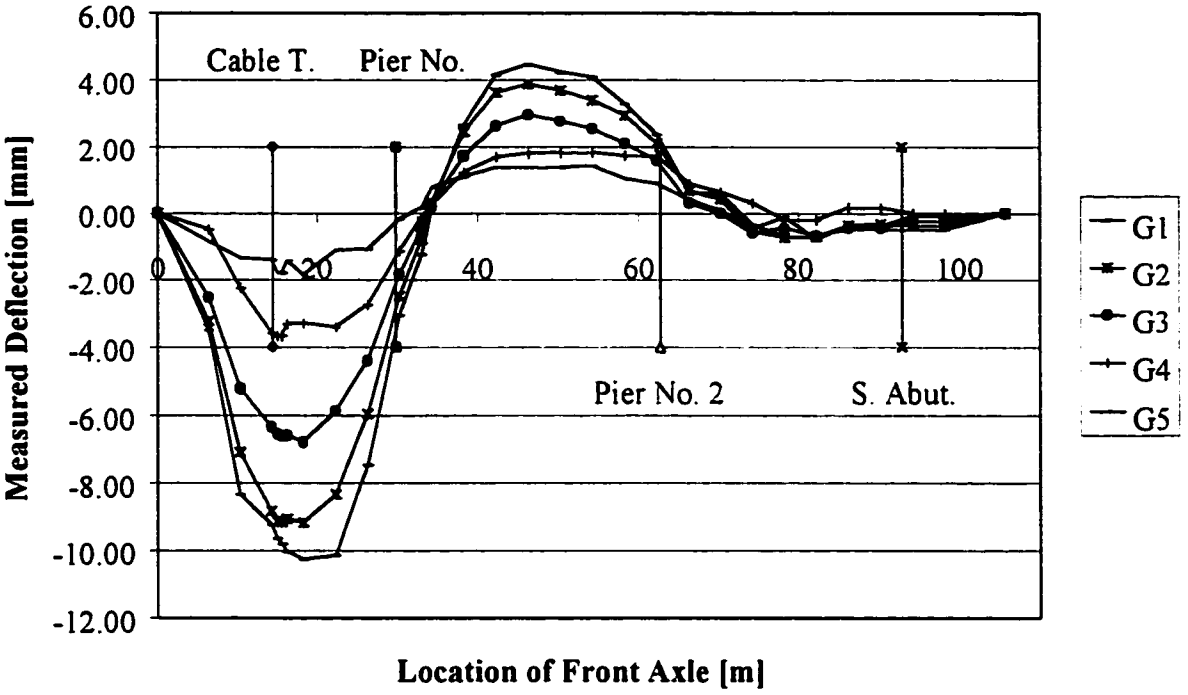

Figure 4.24: Influence Lines from Cable Transducers at Strap #13

4.2.2.2 Results from Strain Measurements

On the bottom side of the strap #8, there were two strain gauges mounted at midpoint between girder #1 and #2, side by side on the strap. This was used to monitor the deviation in the strain gauges readings and arching action in the deck. Results show the maximum difference in the two strain gauges readings on strap #8 was 2 $\mu\epsilon$. This indicated that the variation in the any of the strain gauge readings were quite small. Secondly, when the centerline of the second axel was offset to the South of strap #8 by 1.027 mm, the steel strap #8 gives a maximum strain reading of 85 $\mu\epsilon$ and it cycles between -15 to 85 $\mu\epsilon$ as the truck move across the entire length of the bridge. With such low strain cycle on the steel straps, fatigue is not a concern.

The cross sectional views of the girders *type 1* and *type 2* that was indicated in Figure 4.22 are shown in Figure 4.25. The strain gauges location on all steel girders and its distances from the North Abutment were also detailed as shown below.

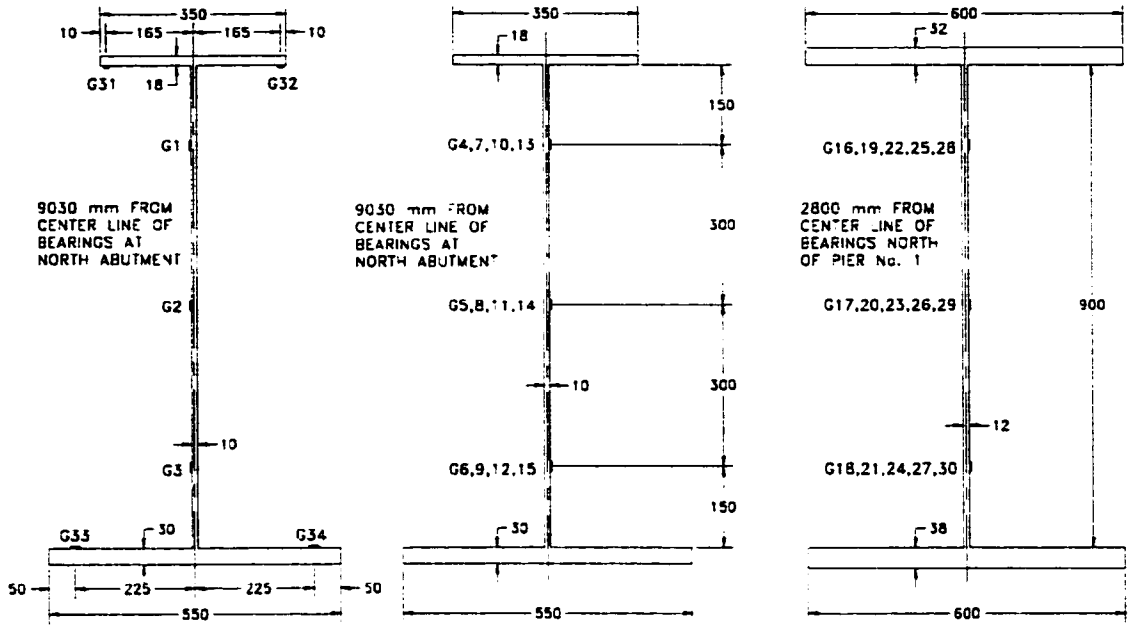

Figure 4.25: The Three Girder Type Used and Strain Gauges Layout

Strain gauges G1 to G3 were mounted on the web of girder 1 and gauges G31 to G34 were mounted on the flange of girder 1 as shown in Figure 4.25. The strain gauges were mounted at 9.03 m from North abutment. When the front axle of the truck reaches 15.05 m from North abutment, the cross sectional strain from top to bottom of the cross section are -10, 18.6, 65.1, 97.1, and 104 $\mu\epsilon$ respectively for August 1998. These recorded strain distribution in girder 1 is shown in Figure 4.26. The location of the neutral axis is 52 mm below the bottom face of the top flange. With such loading configuration, the maximum measured strain is 104 $\mu\epsilon$ on strain gauges G33 and G34. A close examination of the strain gauges indicated strain gauges G33 and G34 had a poor connection, hence their readings were unreliable. Despite the slight non-linearity observed in the strain distribution due to strain gauges G33 and G34, the cross section is linear otherwise. The small strains indicate that the bridge response was well within the elastic range.

Comparison of the cross sectional strain distribution for girder #1 between August 1997 and August 1998 shows practically no change in the location of neutral axis for the positive moment region. The difference between the neutral axes was 2 mm closer to the top flange for August 1998. These results suggested that there is no change in composite action for the positive moment region. Furthermore a shift of 2 mm up closer to the concrete deck may be from the gain in concrete strength over the last one year of curing process or simply instrumentation errors.

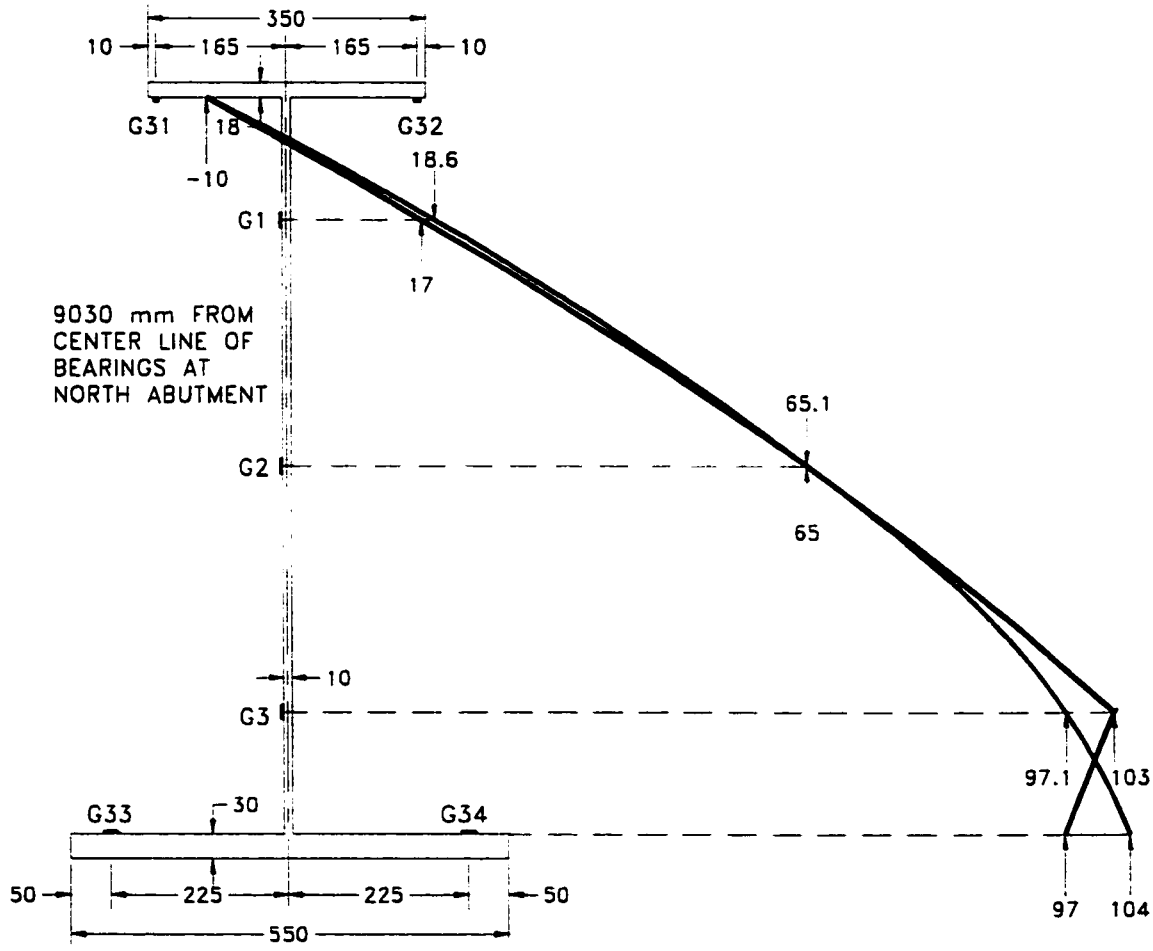

Figure 4.26: Strain Distribution for Aug. '97 and Aug. '98 in Positive Moment Region

For the same load case, the strain distribution in the negative moment region is shown in Figure 4.27. The instrumented section in the negative moment region is 2.8 m North of Pier No.1. As expected, the strain distribution in the cross-section is almost

linear. From extrapolation, the maximum compressive strain in the bottom flange is 14.8 $\mu\epsilon$. The neutral axis is at 191 mm below the bottom face of the top flange. The change in location of the neutral can be interpreted as a measure of the change in composite action of the member. Figure 4.27 clearly shows that the neutral axis had moved from 93 mm to 191 mm between August 1997 and August 1998 respectively. This 98 mm shift in neutral axis suggests that there was a partial loss of composite action in the negative moment region. It should be recalled that the tests performed in August 1997 were done before the bridge was open to traffic. Comparison of the crack patterns between August 1997 and August 1998 (see Figure 4.48) shows a lot of new transverse and longitudinal cracks in the bridge deck in the negative moment region.

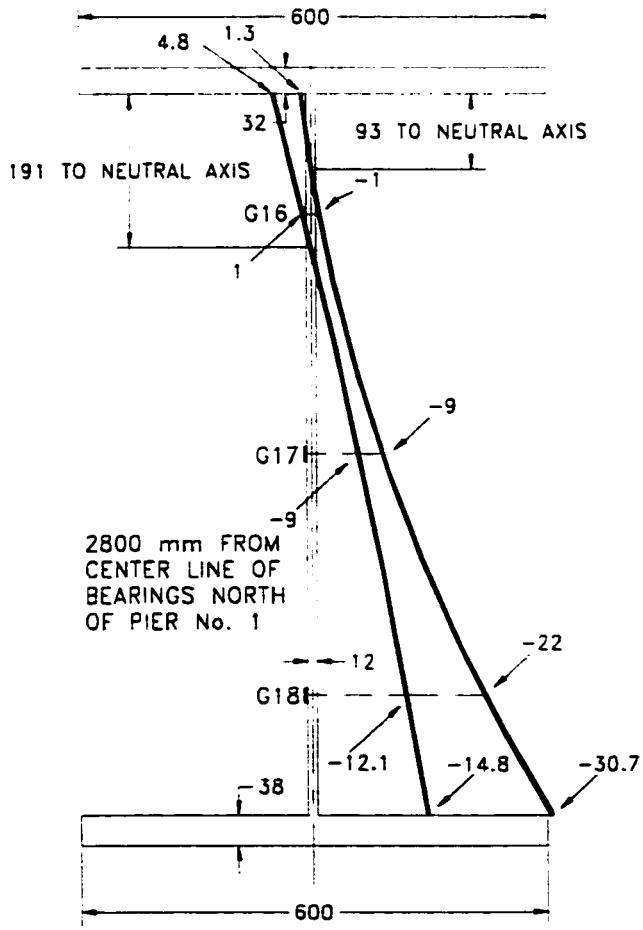

Figure 4.27: Strain Distribution for Aug. '97 and Aug. '98
in the Negative Moment Region

Load sharing between the girders is best examined through strain gauges. On all the girders' web in positive and negative moment region, there is a longitudinal gauge at 150 mm from the topside of the bottom flange. With the truck front axle loaded at 15.05 meter from the North Abutment, load sharing among the girders from strain gauges is shown in Figure 4.28. The maximum strain under this loading condition is 97.1 με for gauge G3 on girder #1 in the positive moment region. In the negative moment region, the maximum compressive strain is 25.3 με for gauge G21 on girder #2. Note that the strains in the negative moment region have almost the same magnitude. This would indicate that the load sharing and the load redistribution by the diaphragm over the pier were very effective in redistributing the load.

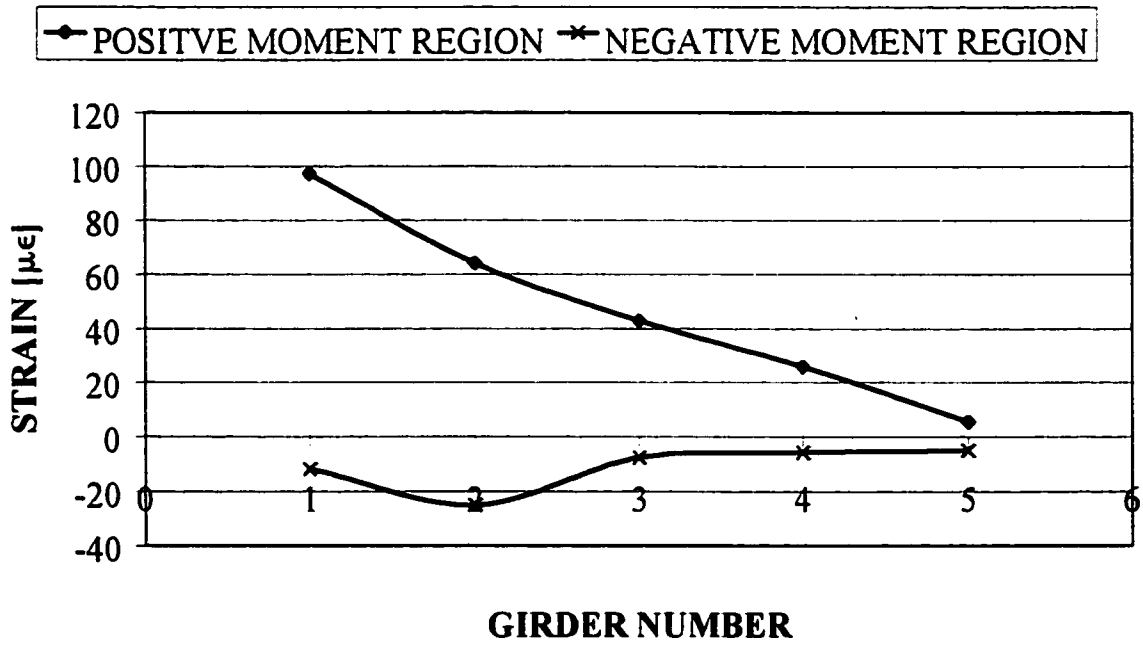

Figure 4.28: Strain Distribution for Positive and Negative Regions in August 1998

4.2.2.3 Influence Line

The bridge influence line under static load test in August 1998 is shown in Figure 4.29. The vertical axis is the strain measurement, and the horizontal axis is the distance in meters along the bridge from North to South. This figure shows the locations of the North and South abutment, Pier No1 and Pier No.2, and the location of the Strain

gauge G3. Clearly, the maximum strain is 97.1 $\mu\epsilon$, when the truck front axle is at 15.05 meters. Although the influence line is slightly jagged in shape, but this is quite acceptable for a static test.

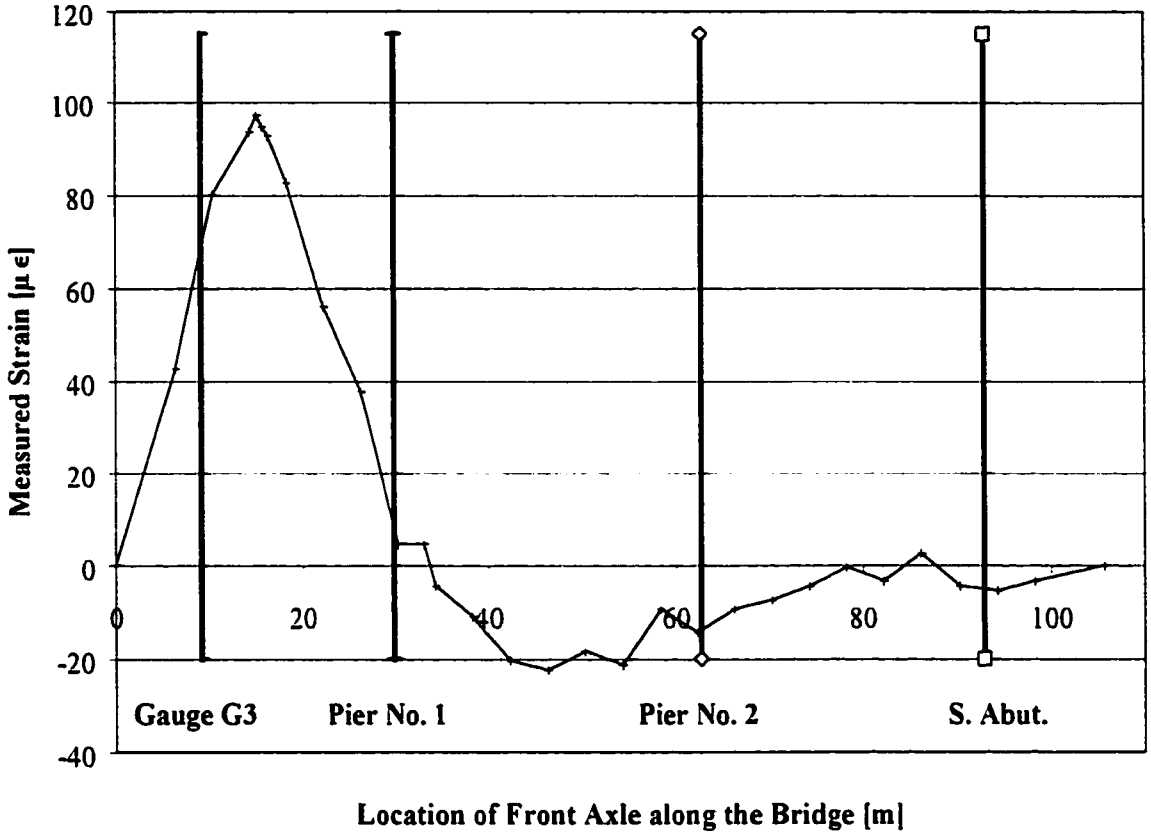

Figure 4.29: Influence Line for Strain Gauge G3

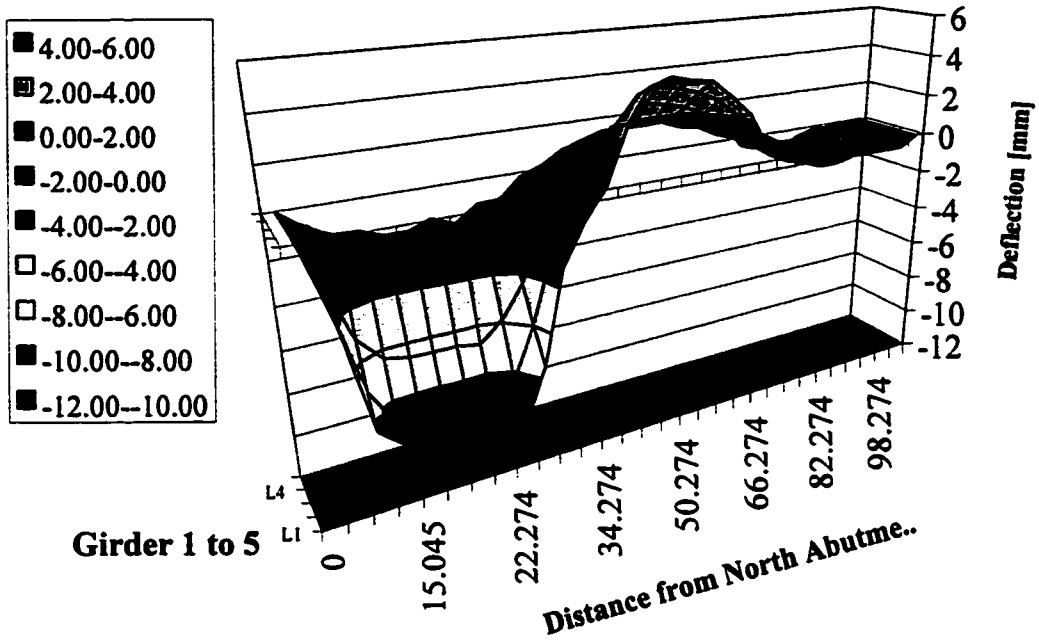

Figure 4.30: 3D Influence Surface for the Bridge from Cable Transducer at Strap #13

Figure 4.30 shows a 3D-influence surface for the entire length and width of the bridge. The vertical axis is the deflection of the girders in millimeters, the horizontal axis is the distance along the length of the bridge in meter, and the third axis is the width of the bridge. The '*Girder 1 to 5*' axis is representing girder #1 to girder #5 in the transverse direction. The '*Distance from North Abutment*' axis represents the location of the front axle of the truck. The legend on the left indicates different ranges of deflection.

4.2.3 Dynamic Tests

It is very important to determine the similarities and differences in the behaviour of the bridge under static and dynamic loading. If there are enough similarities can be established between static and dynamic results; the static test can be eliminated all together. Static test takes almost a full day to perform where as dynamic test takes less than a half-hour. The same truck is use in dynamic test as in static test. Loading conditions are identical, thereby; the results can be monitored and compared between all the tests. Four different speeds were investigated: 15, 30, 40, and 55 km/hr. The longest

test lasted no more than 25 seconds. Hence, the temperature effects can be neglected. Before the truck came onto the bridge, two seconds or more of zero readings were taken. Second zero readings were taken, where scan continued for approximately three or more seconds after the truck had completely move off the bridge.

Dynamic field-testing was done in three stages. Ten cable transducers, four accelerometers, strain gauge T4, and the standard strain gauge are presented in all three stages of the tests. Stages 1 – 3 contain strain gauge sets 1 – 3 as outlined in Section 4.2.2. Table 4.5 shows the three stages, its corresponding filename, speed of the truck, and the size of the file in seconds.

Table 4.5: Filenames, Test Speed and Stage Number

[All files are scanned at 500 scans per second]

Stage	Filename	Speed of Truck [km/hr]	File Size [sec.]
1	C10825P0027.raw	15	30
	C10825P0003.raw	30	20
	C10825P0010.raw	40	20
	C10825P0020.raw	55	20
2	C20825P0207.raw	15	30
	C20825P0210.raw	30	20
	C20825P0216.raw	40	20
	C20825P0223.raw	55	20
3	C30825P0312.raw	15	30
	C30825P0316.raw	30	20
	C30825P0324.raw	40	20
	C30825P0344.raw	55	20

4.2.3.1 Data Reduction

All measurements were recorded by a high-speed data acquisition system. Dynamic data were all scanned at 500 readings per second. Depending upon the location of the strain gauge, the length of the lead wires and the power sources, the environmental noises on raw data can be as high as 400 $\mu\epsilon$ in magnitude. The major sources of noises were power supply and long lead wires. Long lead wire acted as antennas in the system and generated the noises. Figure 4.31 shows the raw data for strain gauges G3. The response is buried in these noises due to small input/output voltage. Fortunately, most of these noises were deterministic and periodic; thereby filtration for the actual response is possible. Figure 4.32 is a plot of the filtered data with a low pass Butterworth filter of 10 Hz. Since frequencies above 10 Hz have very little effect upon the influence line response of the bridge, a low pass filtered limit of 10 Hz was used.

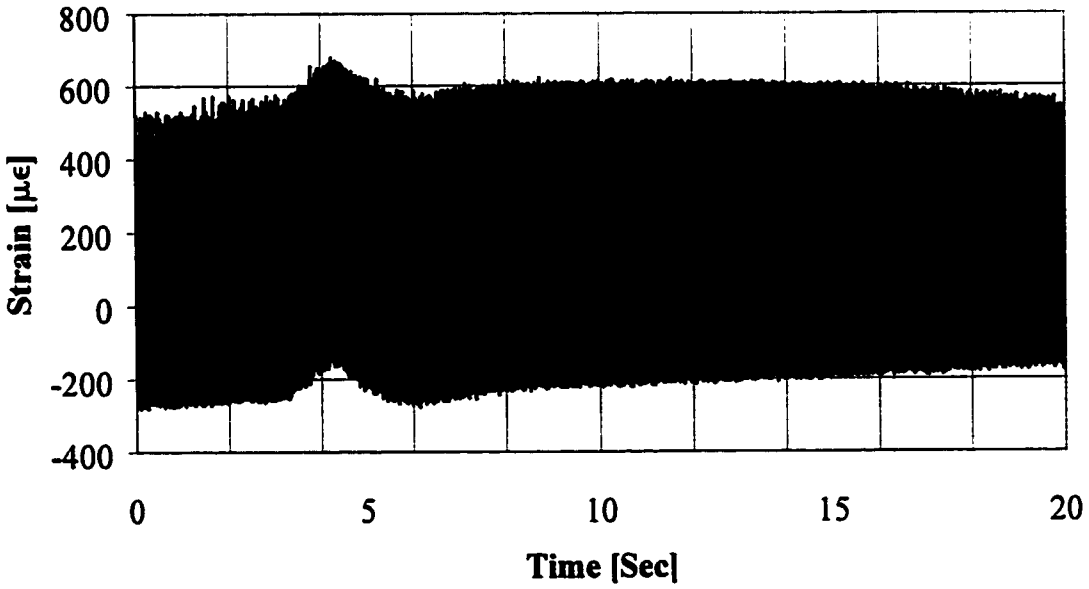

Figure 4.31: Raw Data for Strain Gauges G3 in 55 km/hr test on August 1998

For each test run, raw data were scanned at 500 Hz for 30 second long; render each file size in the magnitude of five megabytes. Although a scan rate of 500 Hz may capture frequency and mode shape as high as 125 Hz, only frequencies up to 10 Hz are of interest. With this frequency range of interest and a file that was scanned at 500 Hz, the

original file size can be reduces by 13 times and still capture up to a 10 Hz frequency. This row averaging of the raw data will not only reduce the file size by 13 times, but also improve the resolution of the amplitude of the 10 Hz frequency over the 125 Hz frequency by a factor of 13 times.

Due to various system limitations, the response drifted over time as shown in Figure 4.32. This drift was a random phenomenon; however, it manifested itself in a very low cycle drift characteristic. Theoretically, a band stop on the low cycle drift is possible thereby leaving the final responses of the gauges. In practice, a digitally filtration on one of the two frequencies that are so very close to each other shall have an effect on the magnitude of the response of the other frequency. Consequently, this phenomenon is best corrected with second order polynomial as shown in Figure 4.32. With this specific truck ran at 55 km/hr, Figure 4.33 shows the final dynamic response for all frequencies under 10 Hz in strain gauge G3.

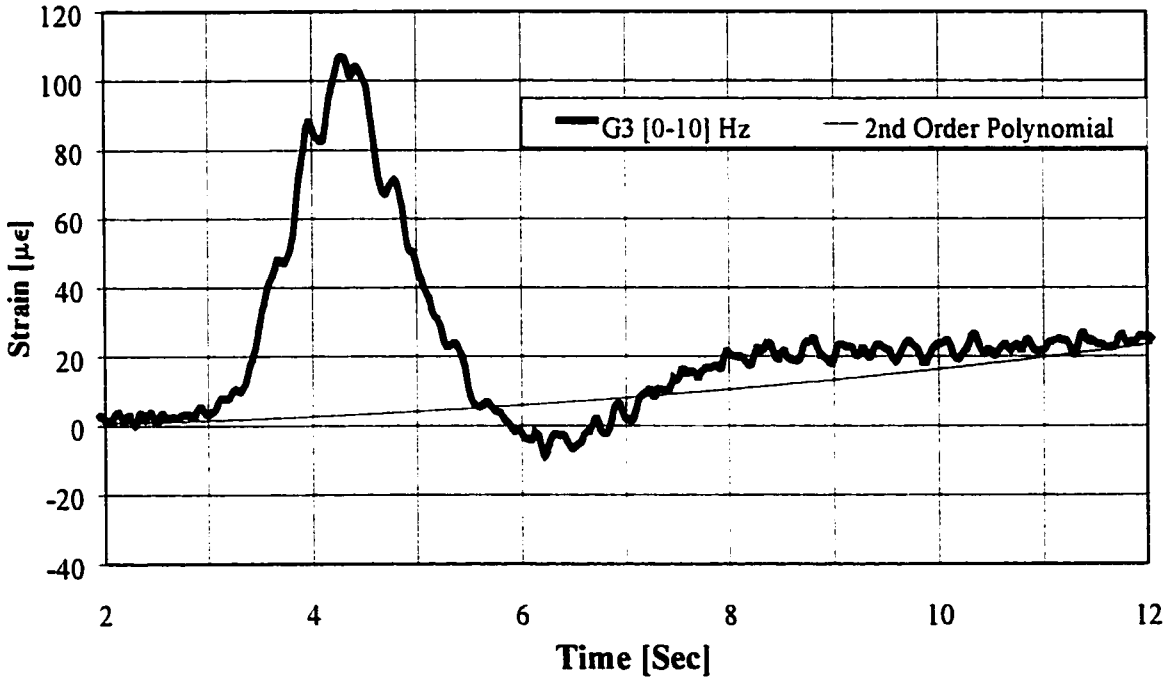

Figure 4.32: Low Pass Filtered Data of 10 Hz for Gauge G3 *[Before correcting for drift]*

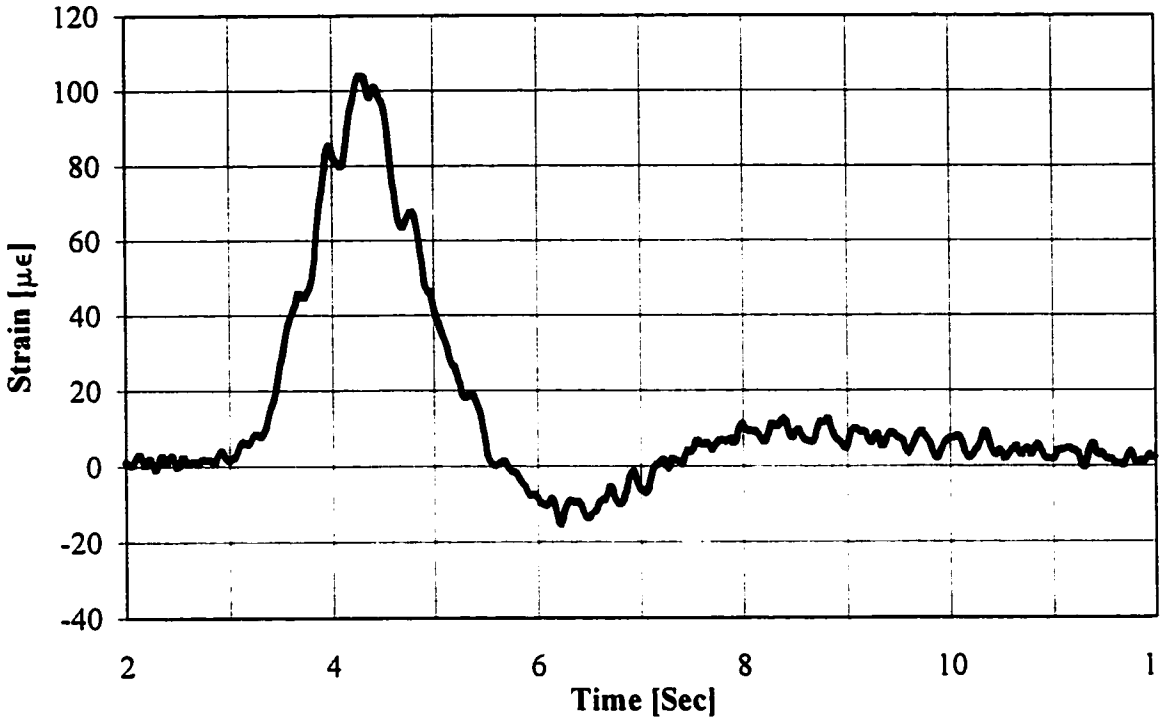

Figure 4.33: Final Filtered Response for Strain Gauge G3 *[After corrected for drift]*

Similar filtering processes and drift correction were applied to the standard strain gauge. The standard strain gauge, ST is mounted on the small 10 x 10 x 100 mm steel bar. This bar was subjected to similar environmental noises as the gauges on the superstructure. The data from standard strain gauge was log simultaneously in correspondence with all the other strain gauges. The only difference is that the small steel bar was not subjected to any load as opposed to other strain gauges on the structure. After applying the same filtering process as the strain gauge G3, the strain gauge ST final response is shown in Figure 4.34.

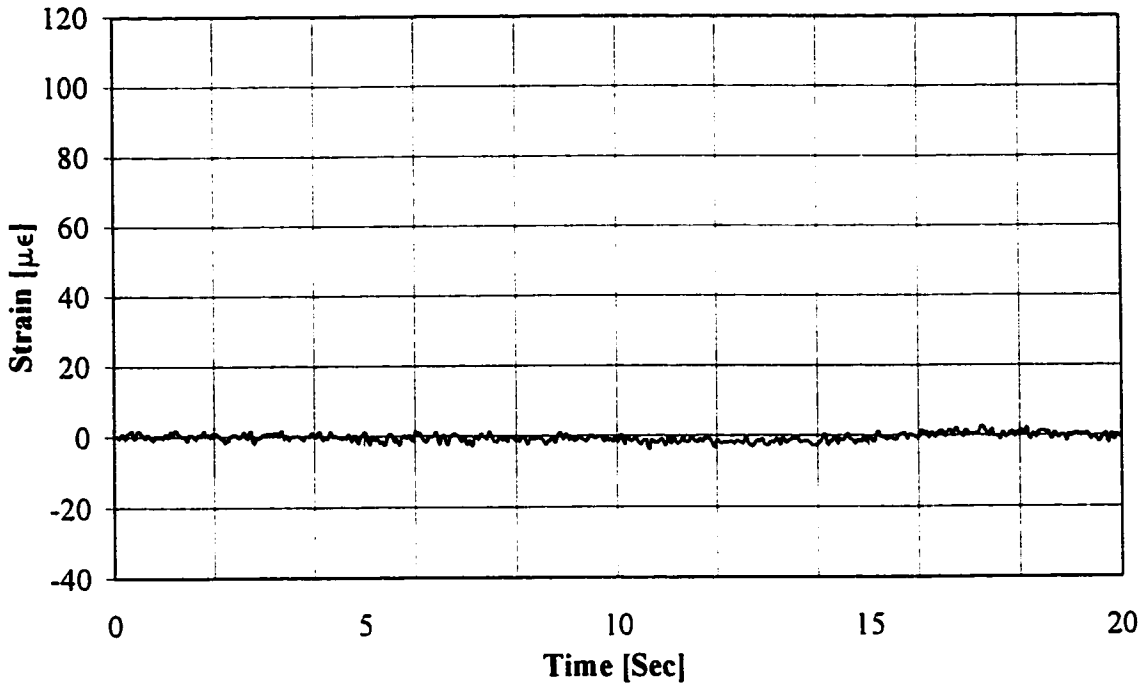

Figure 4.34 Final Filtered Response for Strain Gauge ST

Clearly, the filtering processes do not add any response to the final results. As expected, the standard strain gauge shows practically zero strain. Hence, the response in Figure 4.33 is the actual response due to the truck load only, and not noises or effect of the filter.

Figure 4.33 shows the dynamic response of the bridge for strain gauges G3 between 0 and 10 Hz. In order to compare this dynamic response to the static response, the dynamic response needs to be decoupled into *static component* and *dynamic component*. Commercial software such as LabVIEW can be use to digitally filter out the *dynamic component* thereby leaving the *static component*. However, before this decoupling process can begin, frequency limit needs to be established between the static and dynamic components. The lowest frequency limit is use to set a low pass filter in the LabVIEW program, therefore, any frequencies that passes under this filter will be the static response. Likewise, any frequency that is above this limit is the dynamic response. To establish the lowest frequency limit for the static component, speed of the vehicle that is moving over the bridge, length of the bridge, and number of spans must be known. The

Crowchild Trail Bridge has approximately three equal spans, and the overall length is 92.878 meters. A sum of the first two spans is 62.648 meters. According to influence line behaviour, the first two spans will form one full cycle in the response of the bridge. By knowing the speed of the truck, the time it takes for the truck to pass the first two spans is the approximate period of one cycle for the passing truck.

$$\text{Period,} \qquad T = \frac{\text{Distance}}{\text{Speed}} = \frac{62.648m}{15.2778\,{}^{m}/_{\text{sec.}}} = 4.101\,\text{sec.}$$

$$\text{Frequency} \qquad \therefore f = \frac{1}{T} = \frac{1}{4.101\,\text{sec.}} = 0.244Hz \qquad \text{[for 55 km/hr]}$$

$$\text{Frequency} \qquad \therefore f = \frac{1}{T} = \frac{1}{15.036\,\text{sec.}} = 0.0665Hz \qquad \text{[for 15 km/hr]}$$

For the 15 km/hr and the 55 km/hr, the influence line's frequency of the passing truck over the Crowchild Trail Bridge was 0.0665 Hz and 0.244 Hz respectively. Thus, the highest frequency of the passing truck over the Crowchild Bridge is 0.244 Hz for all the test-speed investigated. Consequently, a low-pass filter of 0.8 Hz will not affect the influence line even at 150 km/hr [0.665 Hz] on this bridge. Since all the speed ranges investigated have a maximum frequency of 0.244 Hz, a band-pass filter between 0 to 0.8 Hz will not affect the static influence line of the truck being investigated here. For the 55 km/hr test speed, the response of strain gauge G3 shown in Figure 4.35 yields identical influence line as in static test (Figure 4.29).

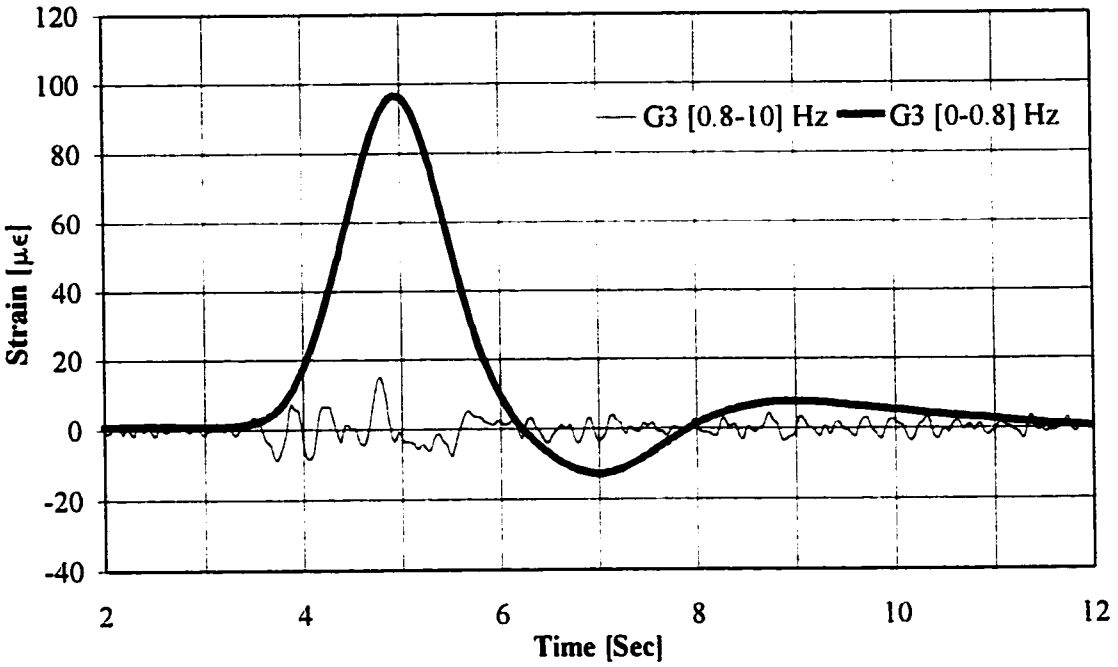

Figure 4.35: Filtered Data with Low Pass of 0.8 Hz and Band Pass of [0.8-10] Hz

Since the truck passes over the bridge at a much lower cycle than 0.8 Hz, a low-pass filtered below this frequency gives the influence line of the structure as shown. The influence line is plotted for strain versus time. This is the static response of the bridge. Final dynamic response of strain gauge G3 from 55 km/hr test is also shown in Figure 4.35. The maximum strain due to the dynamic component is 14.9 με. Clearly, dynamic test results can be filtered and reduced to obtain the static test results. In less than one minute, influence line, strains, length of each span, dynamic amplification factor, static/dynamic behaviour of the bridge can be determined with one truck and one strain gauge.

Cable transducer results from the same dynamic test had much less noises than strain gauge results. This is a result of the input/output voltage ratio that is much smaller in cable transducer than in strain gauge. Figure 4.36 shows the filtered and unfiltered data for the cable transducer. Note the Butterworth filter cause a slight shift in the filtered data of 0.696 second. As shown in Figure 4.37, the filtered data can easily be corrected for the shift of 0.696 second. Clearly, the result in Figure 4.37 shows that Butterworth filtered

has neither effect the shape nor the magnitude of the responses. The raw data shows the jagged curve, and the filtered data shows the smooth curve.

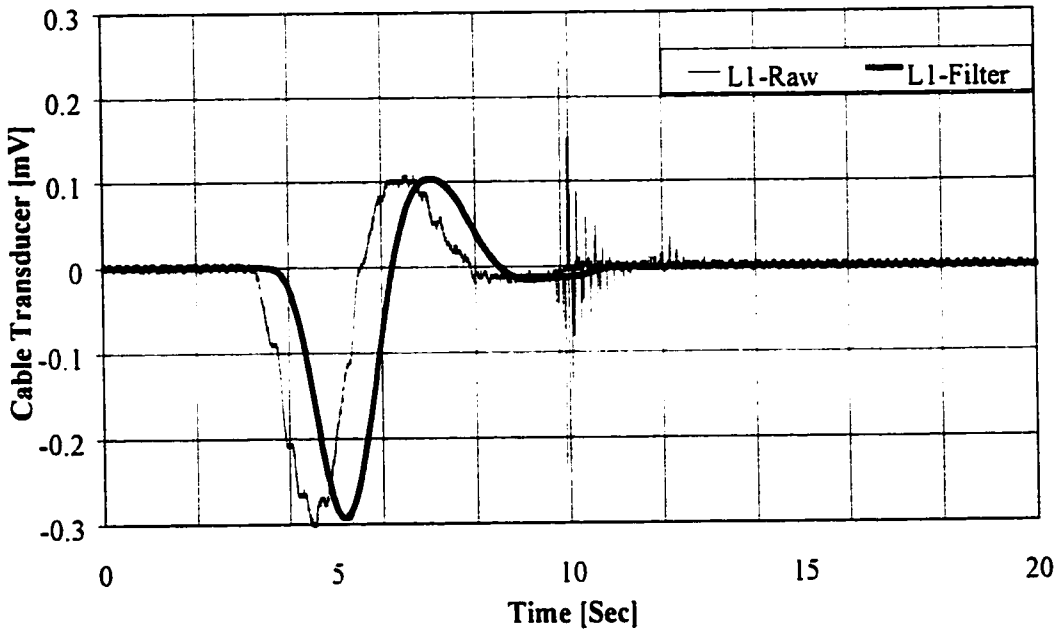

Figure 4.36: Cable Transducer Raw/Filtered Data *[Before Corrected for Shift]*

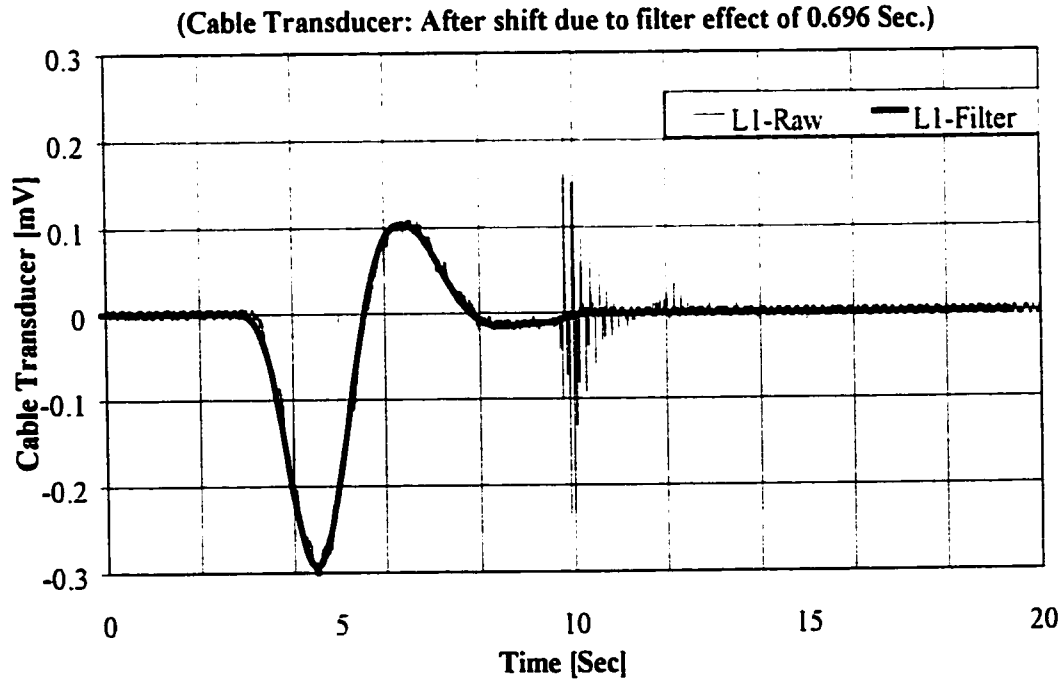

Figure 4.37: Cable Transducer Raw/Filtered Data *[After Corrected for Shift]*

Since the low-speed dynamic results can always be filtered for static results, future static tests can be eliminated altogether for the Crowchild Trail Bridge. Furthermore, results in Figure 4.35 seem to support that dynamic amplification factor can be found without the use of static test. The advantage of this implication translates into a tremendous saving in future field testing, little or no obstruction to traffic flow, hence more structures can be assess and evaluate in a very short time.

4.2.3.2 Damping Coefficient

Damping ratio of the bridge can be found by the decay of the free vibration motion. From the influence line, it is possible to determine the time when the truck comes onto the bridge and the time when the truck has completely left the bridge. Since accelerometer data were taken at the same time as the cable transducer, the free vibration period can easily be determined. Figure 4.38 shows the accelerometer data superimposed on cable transducer data. When the cable transducer data shows approximately zero reading, this would indicated that the truck had completely left the bridge. Thus, free vibration period can be determined. In turn, damping ratio of the structure can be determined. As of August 98, Crowchild Trail Bridge shows a damping ratio of 1.20 percent for the governing vibrating frequency was 3.40 Hz. The closest vertical mode found in ambient vibration test was 3.63 Hz. Figure 4.39 shows a close-up of the free vibration portion of Figure 4.38 and the damping curves for the structure. Damping curves plot in this figure was for accelerometer #48, and it was confirmed with all other accelerometers at the same speed.

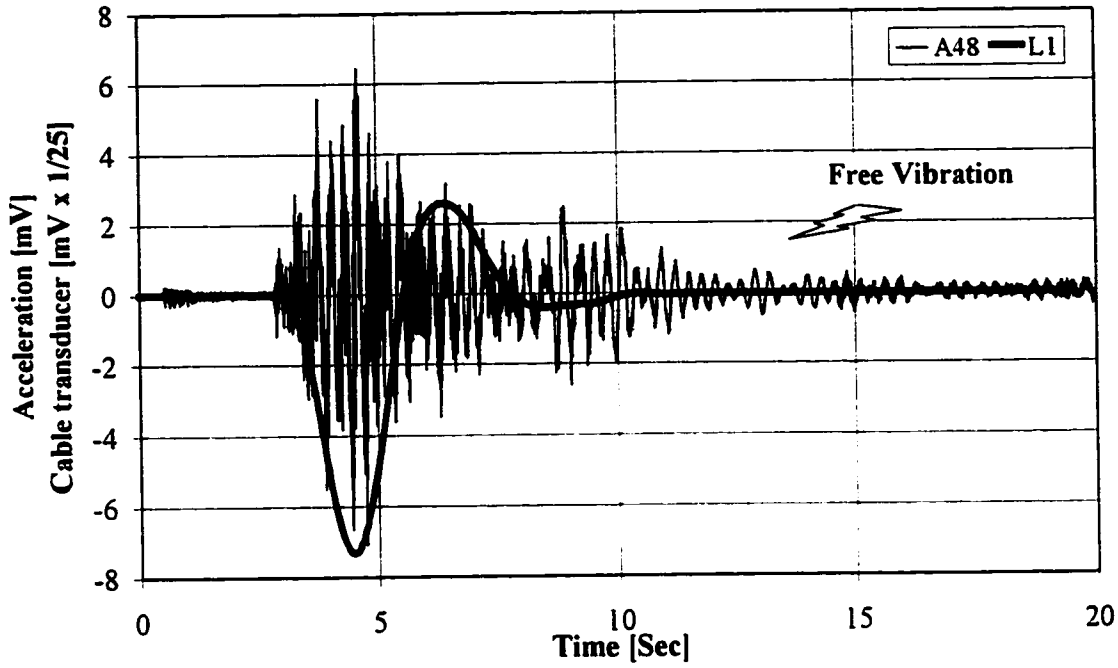

Figure 4.38: Superimposition of Cable Transducer and Accelerometer Data

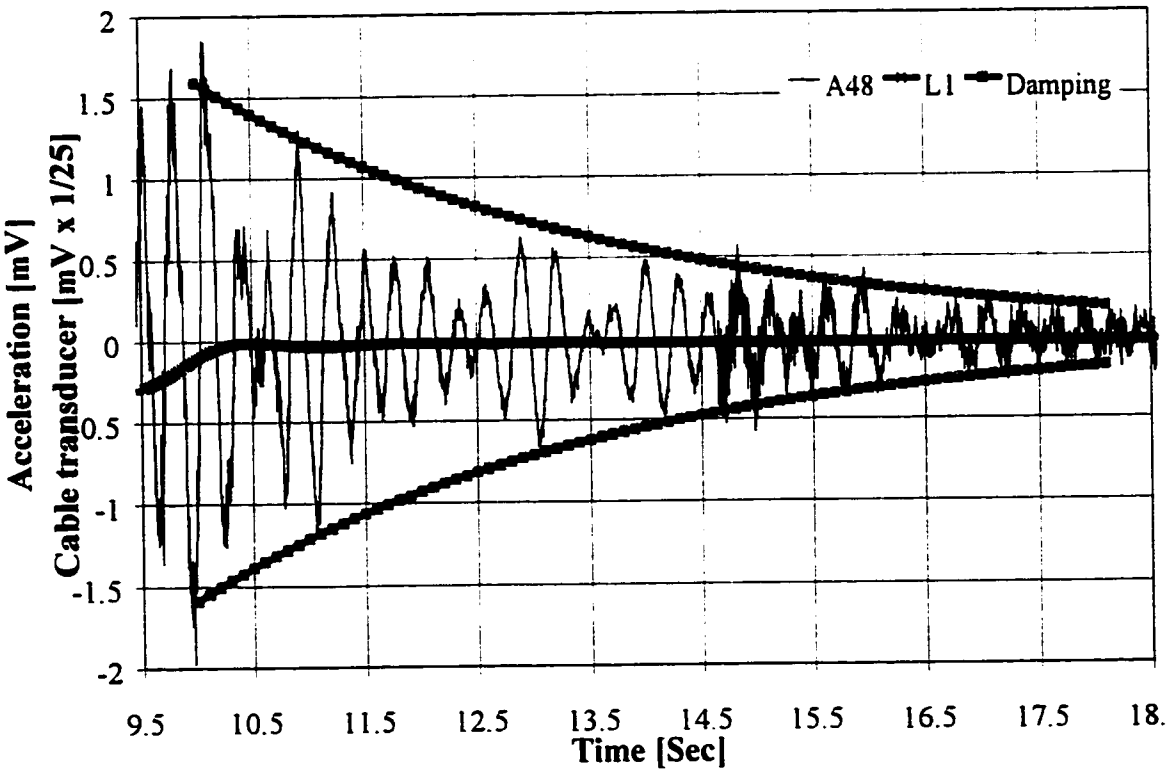

Figure 4.39: Accelerometer and Cable Transducer--Damping Curve

4.2.3.3 Dynamic Amplification Factor

Two approaches can be used to find the dynamic amplification factor. The first approach is to run static and dynamic tests on the structure and measured its responses. To find the dynamic amplification factor, takes the ratio of the maximum dynamic response to maximum static response for the structure. In which case, there must be enough dynamic test runs to ensure that the maximum dynamic effect is in phase with the maximum static response. If they are out of phase, then the maximum dynamic response could be less than the maximum static response. Thus, a true dynamic amplification factor cannot be calculated. However, to ensure that the maximum dynamic effect is in phase with the maximum static response is very time consuming and could be difficult to achieve in actual field-testing. An alternative method to find the dynamic amplification factor is to decouple the dynamic and the static responses. Thereby leaving the dynamic response completely independent of the location along the bridge. Hence, the maximum magnitude in the dynamic response portion is the dynamic amplification factor. With the latter method, only one test run is needed, and it has proved to provide a very reliable result. This method is used throughout all the analysis.

Dynamic amplification factor can be determined from either strain gauge or cable transducer test results. For the dynamic test of 15, 30, 40, and 55 km/hr, both results were used to calculate the dynamic amplification factor and compare it with each other, for all the various speeds tested. Results from the Crowchild Trail Bridge have clearly demonstrated that the dynamic amplification factor can be broken down into two components: the overall vertical deflection component and the local strain component in the bridge members.

4.2.3.3.1 Dynamic Amplification Factor: Local Strain Component

For running speed of 55 km/hr, Figure 4.40(a) shows the maximum strain due to static and dynamic affect are 96.4 $\mu\epsilon$ and 14.9 $\mu\epsilon$ respectively. Thereby giving a dynamic

amplification factor of 1.15. For the 40, 30, and 15 km/hr, the decoupled static/dynamic responses are shown in Figure 4.40(b), (c), and (d) respectively.

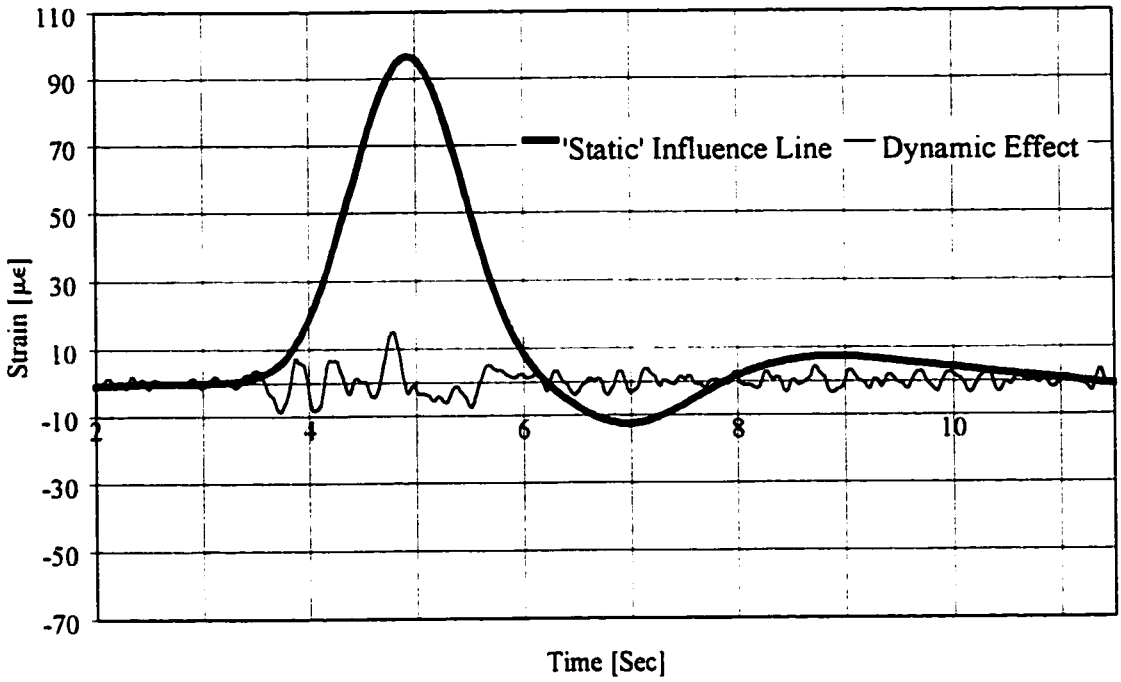

Figure 4.40(a): Decouple Response in Strain Gauges G3 for 55 km/hr Test

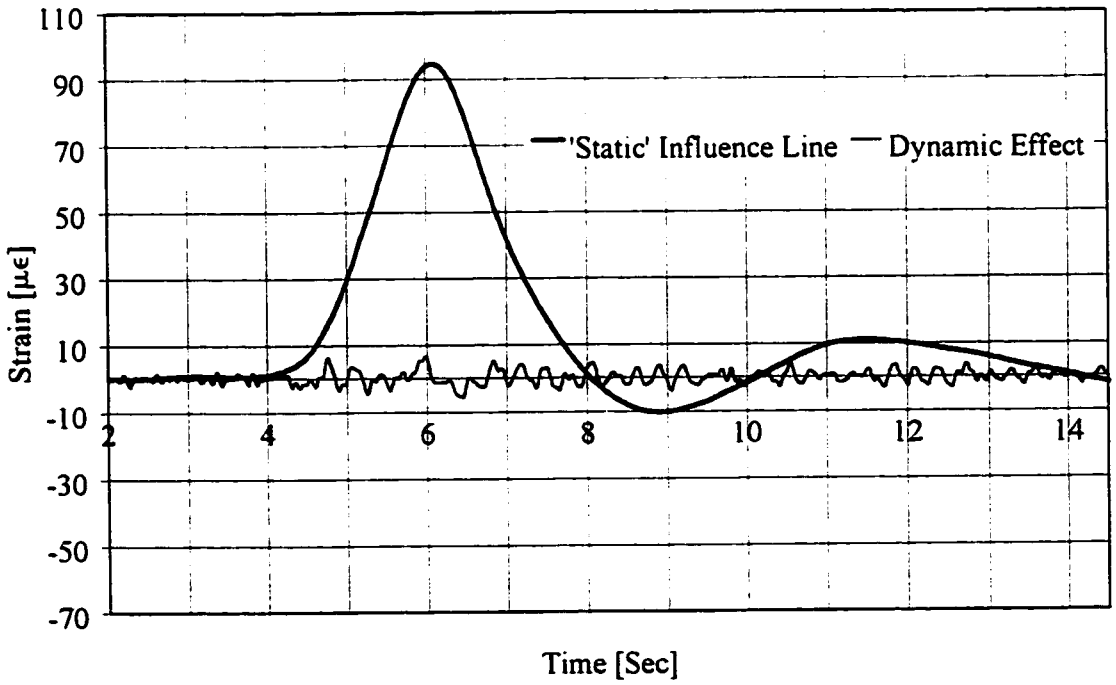

Figure 4.40(b): Decouple Response in Strain Gauges G3 for 40 km/hr Test

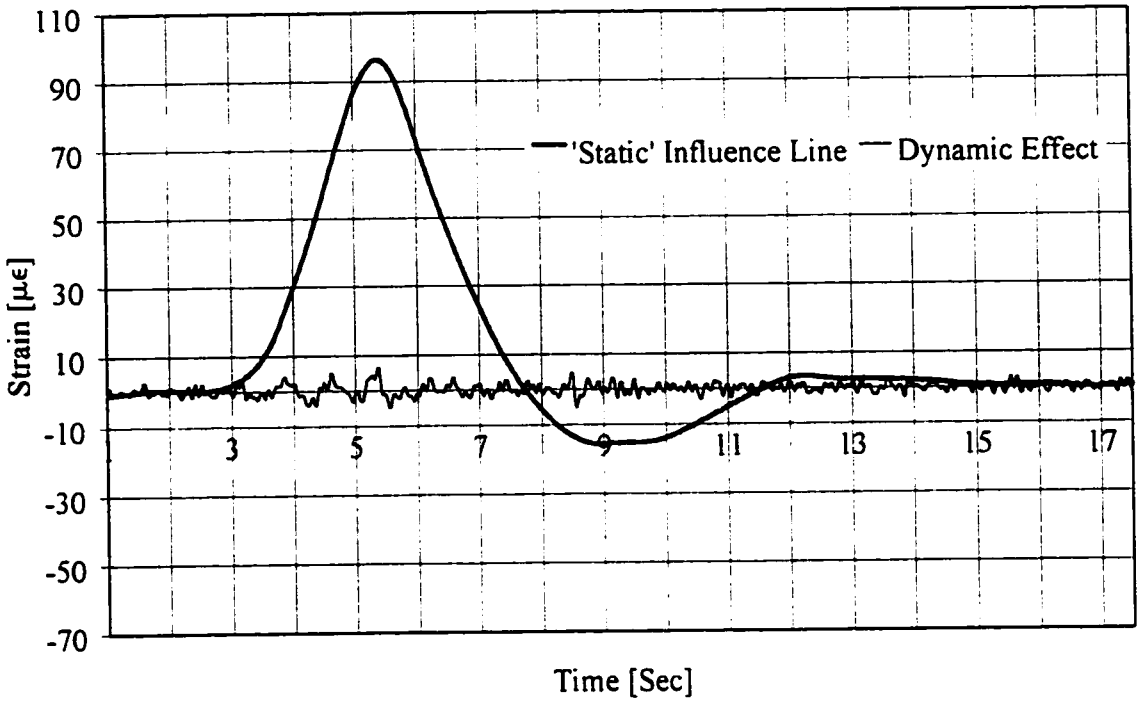

Figure 4.40(c) Decouple Response in Strain Gauges G3 for 30 km/hr Test

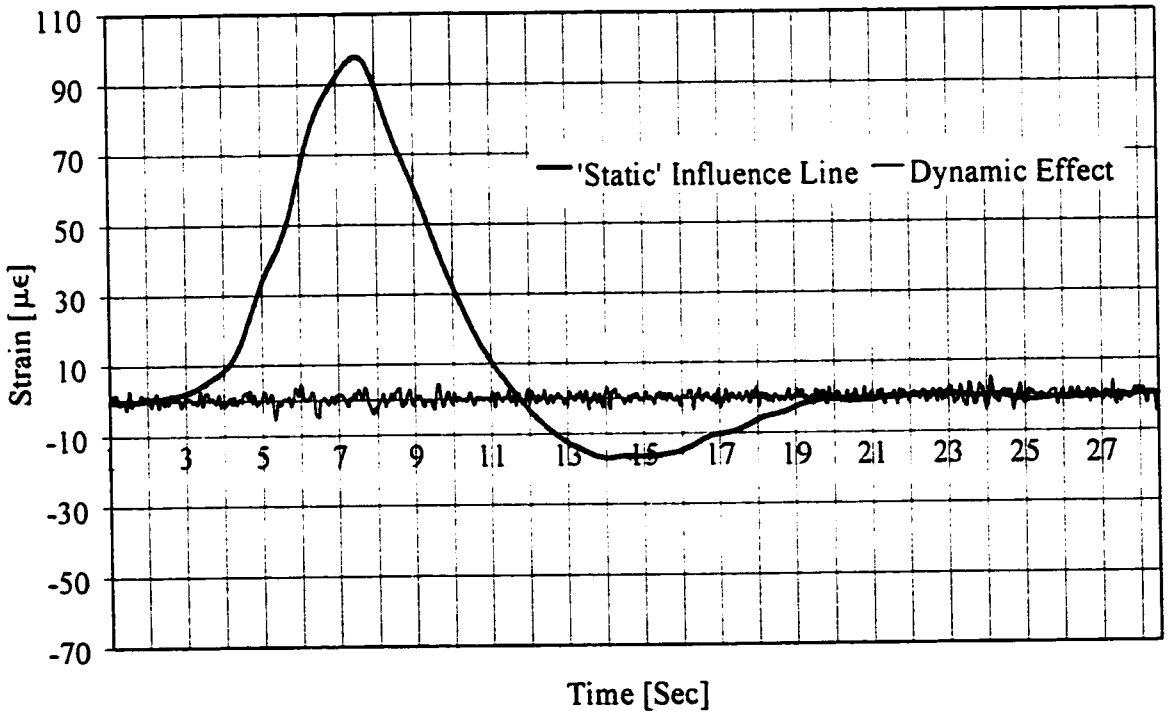

Figure 4.40(d) Decouple Response in Strain Gauges G3 for 15 km/hr Test

These figures suggest that the dynamic amplification factors vary nonlinearly with respect to speed. Table 4.6 shows a summary of the static response, dynamic response, and its' corresponding dynamic amplification factors for the strain gauge G3, G6, G33, and G34.

Dynamic Amplification Factor, DAF, due to local strain effects can be shown to vary with respect to speed in Figure 4.41. For 15 km/hr, the DAF is 5.5% with a variation of less than 0.07% for all the strain gauges investigated. Largest scatters were for 30 and 40 km/hr test speed with a 2.5% and 1.6% variation respectively. Finally, for the 55 km/hr, the maximum spreads for all the strain gauges were 0.7 % as shown in Figure 4.41 below.

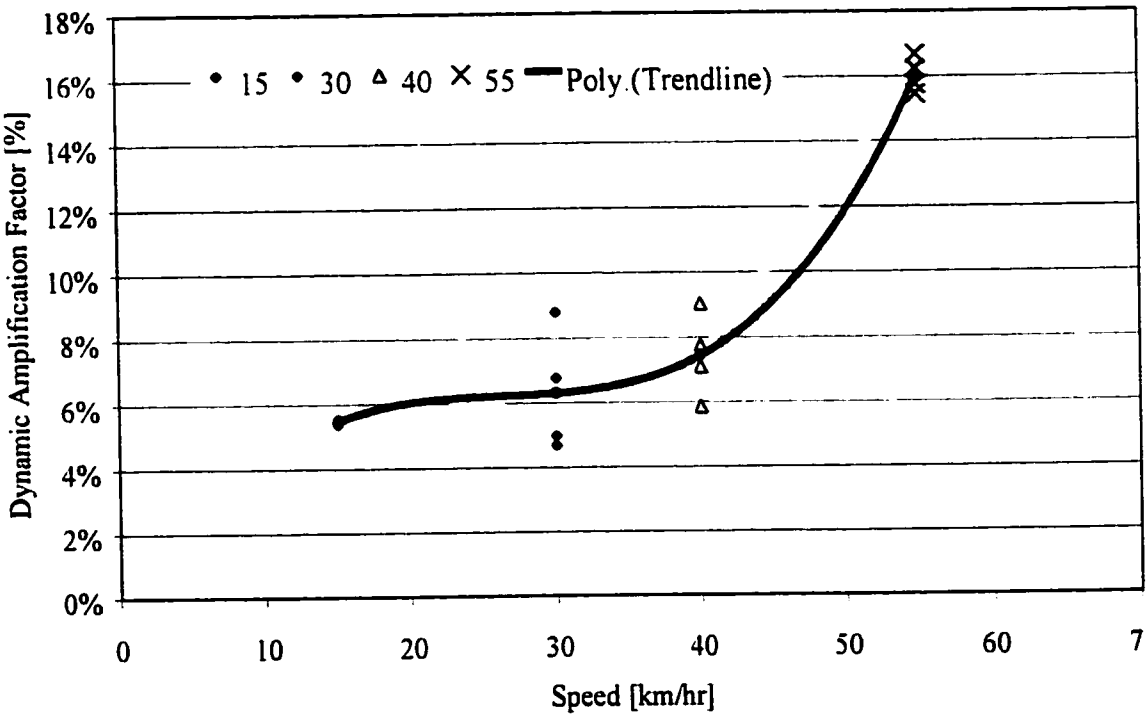

Figure 4.41: Dynamic Amplification Factor – Local Effect

Table 4.6: Dynamic Amplification Factor: Local Strain Effects for [Set 1]

Static Maximum Strain for Gauge G3 = *97.1* $\mu\epsilon$

G3

Speed	Static Response [$\mu\epsilon$]	Dynamic Response [$\mu\epsilon$]	DAF wrt Static	DAF wrt Filtered Response
15	97.83	5.4	6.3%	5.5%
30	96.23	6.5	5.8%	6.8%
40	94.44	6.7	4.1%	7.1%
55	96.51	14.9	14.7%	15.4%

Static Maximum Strain for Gauge G33 = *100.5* $\mu\epsilon$

G33

Speed	Static Response [$\mu\epsilon$]	Dynamic Response [$\mu\epsilon$]	DAF wrt Static	DAF wrt Filtered Response
15	98.8	5.3	3.5%	5.4%
30	106.8	5.3	11.5%	5.0%
40	96.9	7.5	3.8%	7.7%
55	101.5	16.9	17.8%	16.7%

Static Maximum Strain for Gauge G34 = *108.7* $\mu\epsilon$

G34

Speed	Static Response [$\mu\epsilon$]	Dynamic Response [$\mu\epsilon$]	DAF wrt Static	DAF wrt Filtered Response
15	104.8	5.8	1.8%	5.5%
30	117.8	5.5	13.5%	4.7%
40	104.3	6.1	1.6%	5.8%
55	109.2	17.7	16.8%	16.2%

Static Maximum Strain for Gauge G6 = *64.4* $\mu\epsilon$

G6

Speed	Static Response [$\mu\epsilon$]	Dynamic Response [$\mu\epsilon$]	DAF wrt Static	DAF wrt Filtered Response
15				
30	61.5	5.4	3.9%	8.8%
40	63.07	5.7	6.8%	9.0%
55	64.85	10.2	16.5%	15.7%

4.2.3.3.2 Dynamic Amplification Factor: Overall Deflection Component

Second method of examining the dynamic amplification factor is through the overall deflection of the structural components. The bridge was tested three times for each of the four speeds investigated. In set #1, for the 55 km/hr test, readings from cable transducer at the same location as the strain gauge G3 is plotted in Figure 4.42. The Deflections due to static and dynamic response were 11.5 mm and 0.94 mm respectively. Subsequently, the dynamic amplification factor is 1.08. The factor found from cable transducer is slightly lower than that of the suggested by strain gauge results. [However, the maximum response in the filtered data for the cable transducer was a little higher than from the static test. This relationship between the dynamic test and the static test will not be further investigated. Since cars were still allowed to pass in the other lane during the dynamic test, therefore the loads were slightly different in dynamic test as oppose to static.]

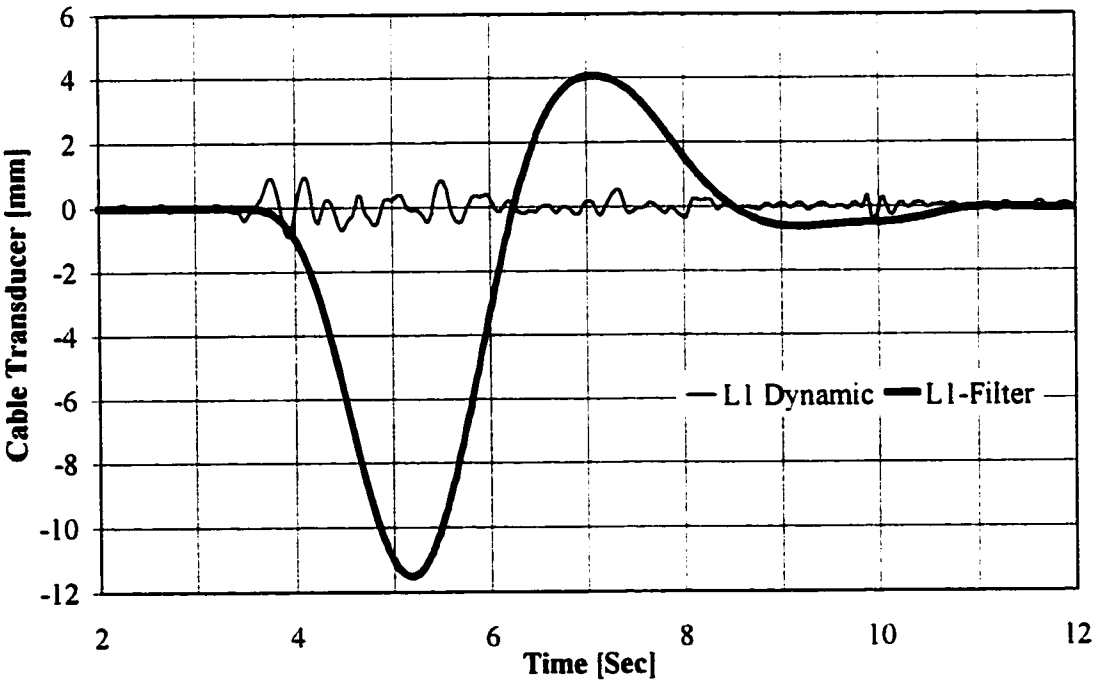

Figure 4.42: Cable Transducer #1 for 55 km/hr Test

Cable transducer plots of all different speeds for all three sets are in Appendix B. Table 4.7 below shows the decoupled responses of the cable transducers tested. It details the static and dynamic responses, and its' corresponding DAF for all the tests.

Table 4.7: Dynamic Amplificaiton Factor: Overall Deflection

Static Maximum Deflection = 10.28 mm

Set 1

Speed	Static Response [mm]	Dynamic Response [mm]	DAF wrt Static	DAF wrt Filtered Response
15	10.02	0.48	2.2%	4.8%
30	10.23	0.61	5.5%	6.0%
40	10.36	0.77	8.3%	7.4%
55	11.49	0.94	21.0%	8.2%

Set 2

Speed	Static Response [mm]	Dynamic Response [mm]	DAF wrt Static	DAF wrt Filtered Response
15	10.61	0.57	8.8%	5.4%
30	10.77	0.57	10.3%	5.3%
40	10.10	0.79	6.0%	7.8%
55	11.30	0.86	18.3%	7.6%

Set 3

Speed	Static Response [mm]	Dynamic Response [mm]	DAF wrt Static	DAF wrt Filtered Response
15	10.26	0.51	4.8%	5.0%
30	12.09	0.93	26.7%	7.7%
40	11.56	0.84	20.7%	7.3%
55	12.04	1.34	30.2%	11.2%

From the above table, the dynamic amplification factor due to overall deflection effects can be shown to vary with respect to speed, as shown in Figure 4.43 below. The overall trend for the DAF as a function of speed seems to be linear. For 15 km/hr test speed, the DAF from the deflection is 5.1%, comparing to the strain gauge of 5.5%. The DAF results from cable transducer and strain gauge give very close results for a low speed of 15 km/hr. In the 30 km/hr and 40 km/hr, the DAF are 6.3% and 7.5% respectively. For the 55 km/hr, the DAF is 9.0%. The overall trend of the DAF obtains from the cable

transducer and strain gauge gives quite vastly different behaviour. The trend from the cable transducers gives a linear relationship with respect to the speed; however, the strain gauge gives a nonlinear relationship that increases exponentially for all the speeds tested. This suggests that the local strain effects are much more severe under dynamic load than that of the overall deflection effects. This implies a 'lag effect' in load distribution under dynamic loading. The differences between the DAF from the overall deflection and the strain gauge clearly show a large portion of DAF that the designer may never have considered in the design.

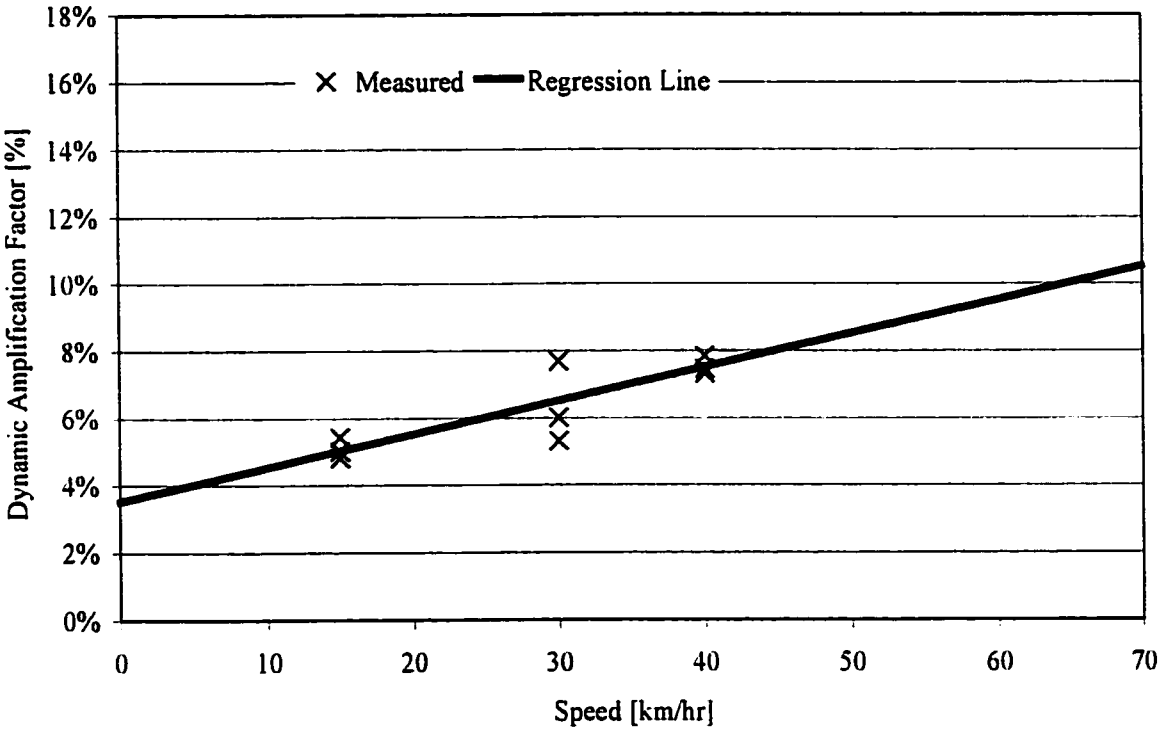

Figure 4.43: Dynamic Amplification Factor – Overall Deflection Effect

4.2.3.4 Load Sharing

Load sharing among girders can be examined through the strain gauges or by cable transducers that were mounted on the superstructure. Comparison of the cable transducer results between static and dynamic tests are shown in Figure 4.44 below. It is important to note that the difference of the sum at a cross section for the deflection measurements in

static and dynamic tests was only 0.7 percent. Hence, the bridge does not overall deflected more in dynamic test than static test; rather it absorbed the energy in a torsional mode as opposed to the vertical mode.

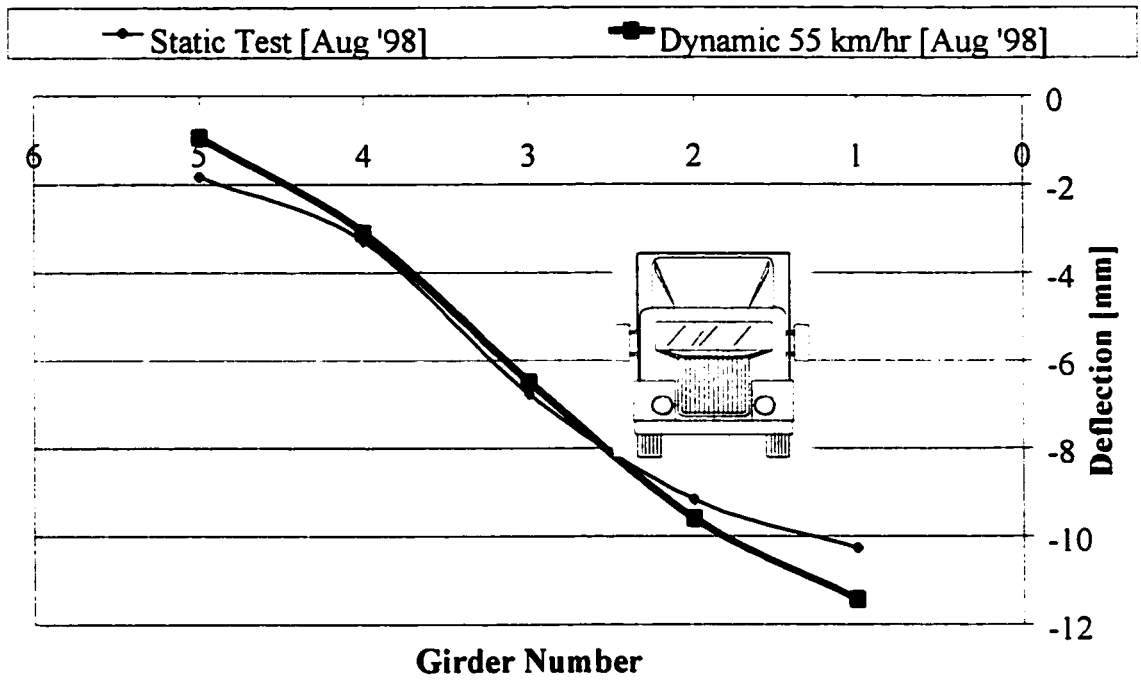

Figure 4.44: Overall Deflection Among Girders

The torsional excitation characteristics manifest itself again in the three-dimensional influence surface plots in Figure 4.45. Figure 45(a) and Figure 45(b) are plots for the static test and the 55 km/hr dynamic test, respectively. The purpose of these plots is for visual aid in the behaviour of the bridge under vertical loads in the transverse as well as longitudinal directions along the bridge. Comparison between the static and the dynamic results shows that they are almost identical. The static curve is more jagged in shape, and it has slightly smaller maximum deflection than that of the dynamic test. Likewise, it has bigger minimum deflection than that of the dynamic test. These facts have further reinforced the torsional excitation in the 55 km/hr test speed.

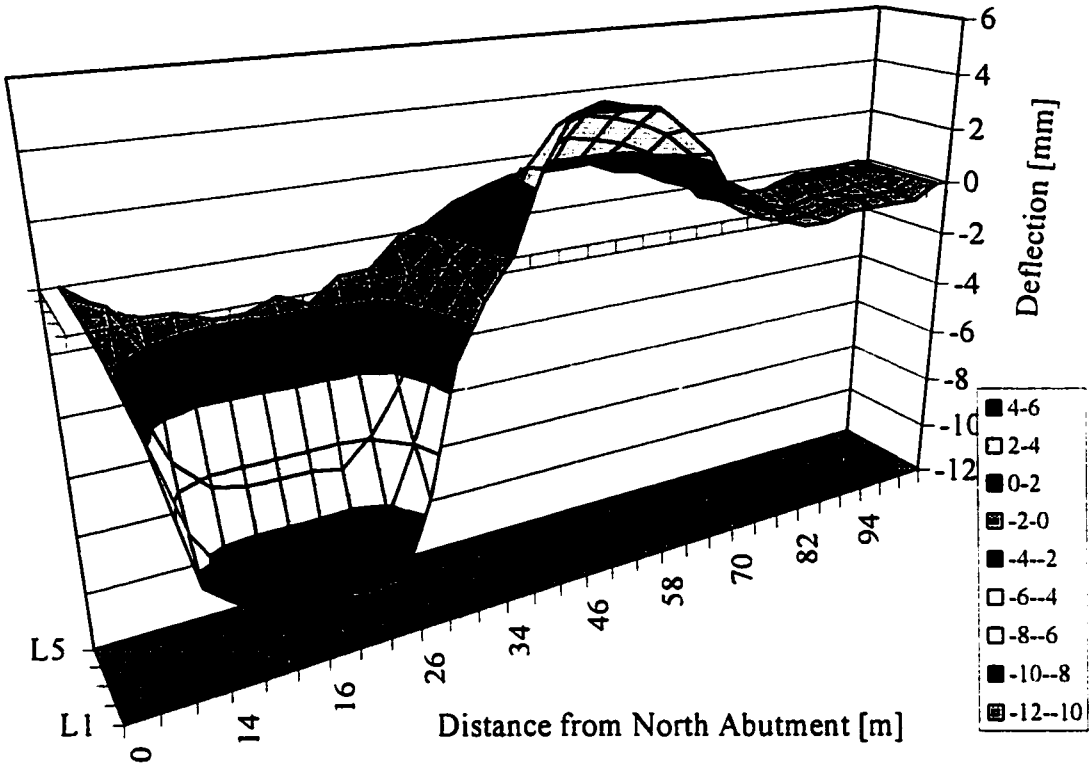

Figure 4.45(a): 3D Influence Surface – Static Test Results

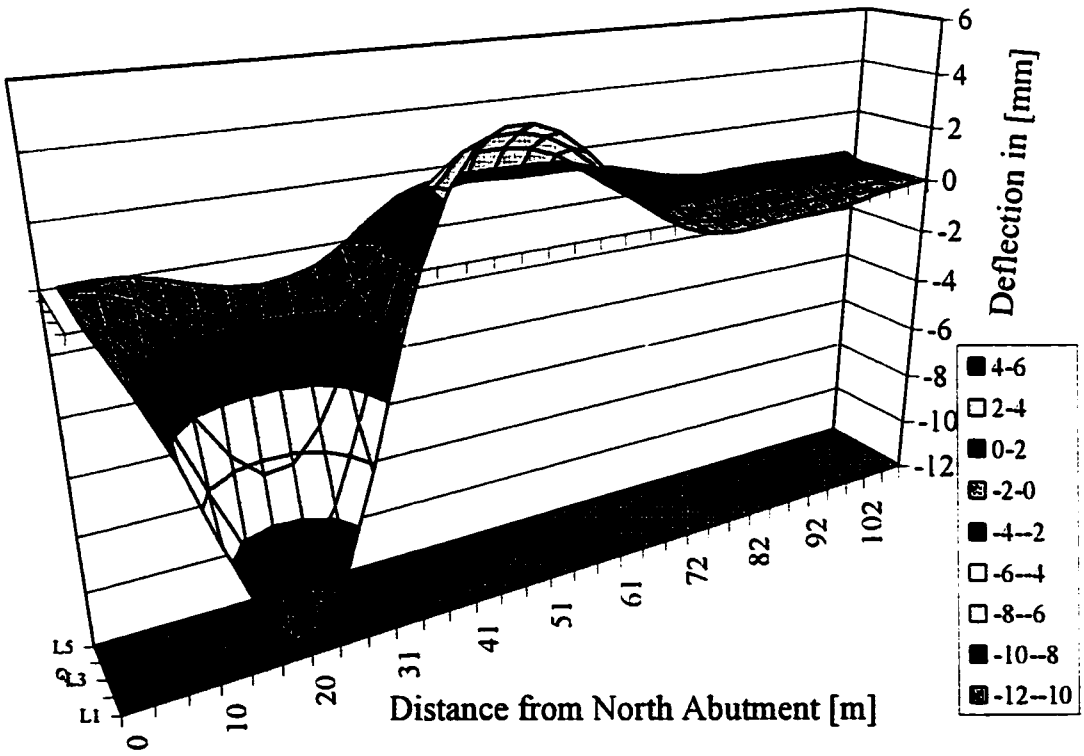

Figure 4.45(b): 3D Influence Surface – Dynamic Test Results

4.2.4 Crack Pattern for August 1998

The first crack patterns were mapped in August 1997. Crowchild Trail Bridge consisted of three continuous spans. The South span was reinforced with both GFRP and steel reinforcement. Crack pattern for the South span to the North span as of August 1997 is shown in Figures 4.9 to 4.11. All cracks were in the transverse direction. Most cracks were approximately 0.5 mm in width. As of August 1997, there was no longitudinal crack.

After one full year of operation, a second crack pattern was mapped in August 1998. Crack pattern for the South span, Middle span and North span are shown in Figures 4.46 to 4.48 respectively. The cracks that were there already from August 1997 seem to have grown twice wider by August 1998. As of August 1998, there were quite a few new cracks had formed on the underside of the bridge. In addition to many new transverse cracks formed, there were quite a few longitudinal beginning to appear. Most longitudinal cracks were formed right at the transition point between the flat part of the deck and the taper part. However, a few longitudinal cracks formed at midway between the two supporting girders in the South span.

Overall, there are quite a few new cracks pattern formed over the last one year of operation. Most of the cracks formed were 0.5 mm and less in width. Cracks that were there already since August 1997 are now a little wider and there existed water stain marks. There appeared to be more transverse cracks in the Middle and the South spans. North span, which was reinforced only in the cantilever edge, now had longitudinal cracks in the sophist and at midway in between the two girders as shown in Figure 4.48.

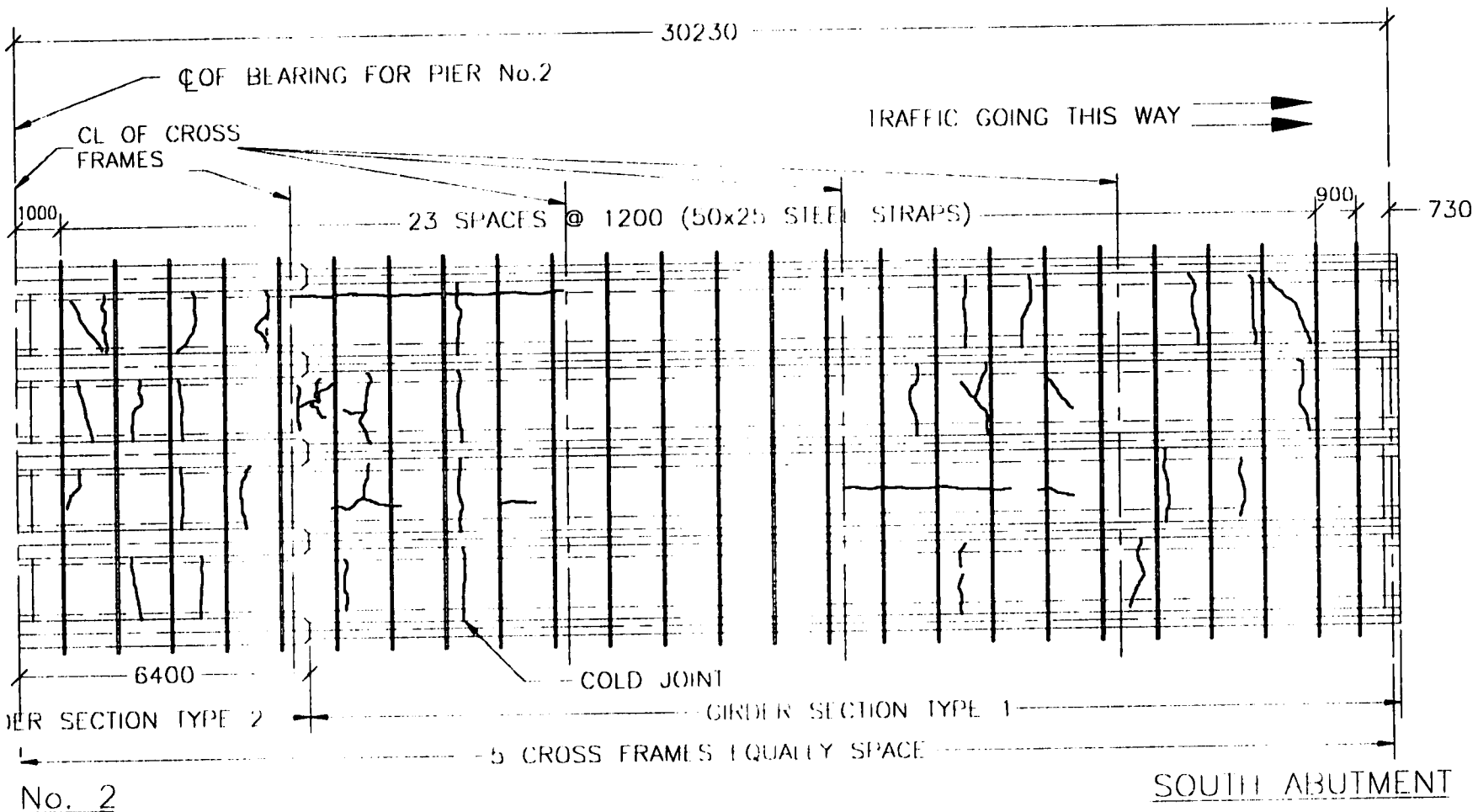

Figure 4.46: South Span Crack Pattern [August 1998]

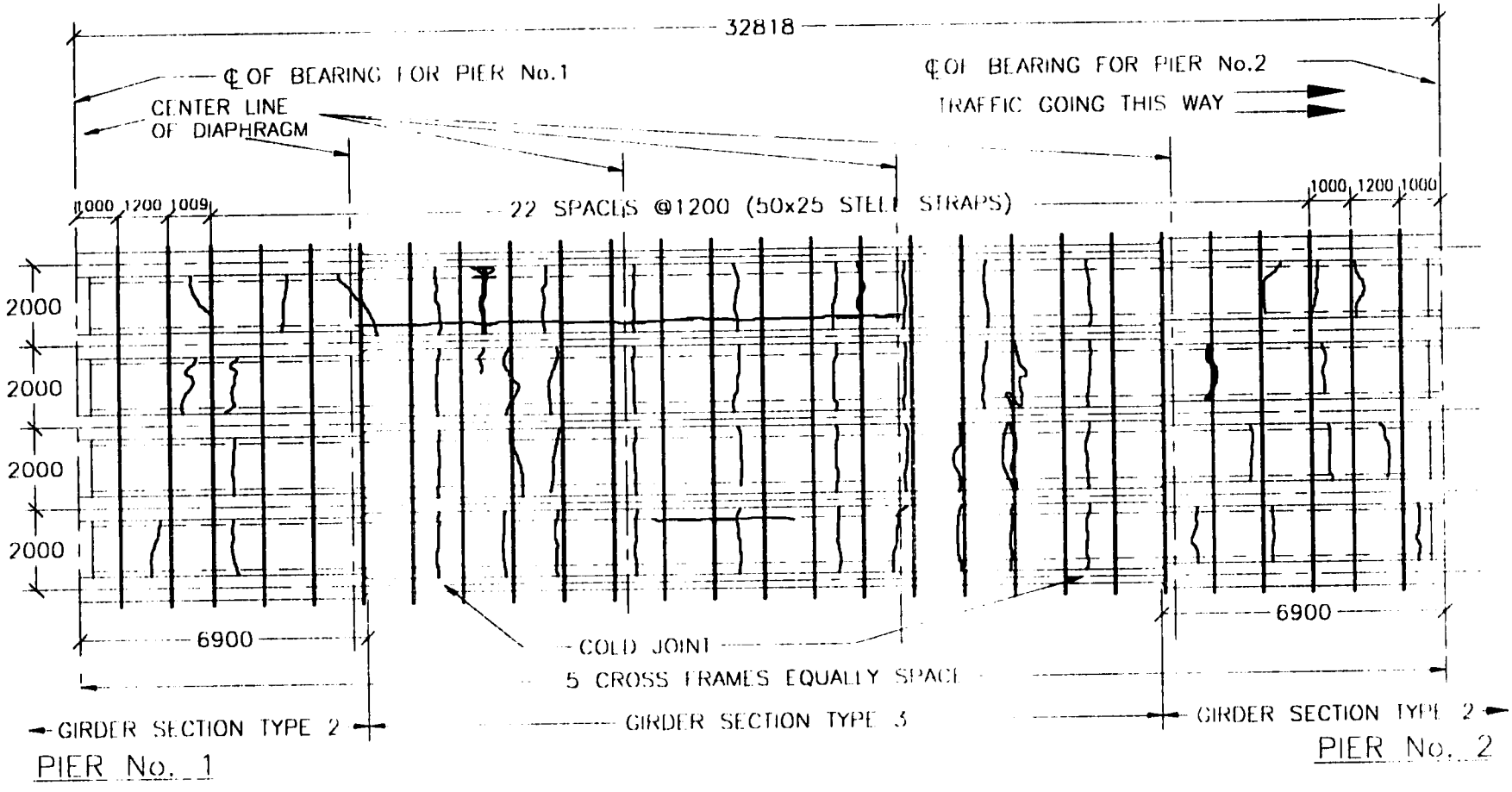

Figure 4.47: Middle Span Crack Pattern [August 1998]

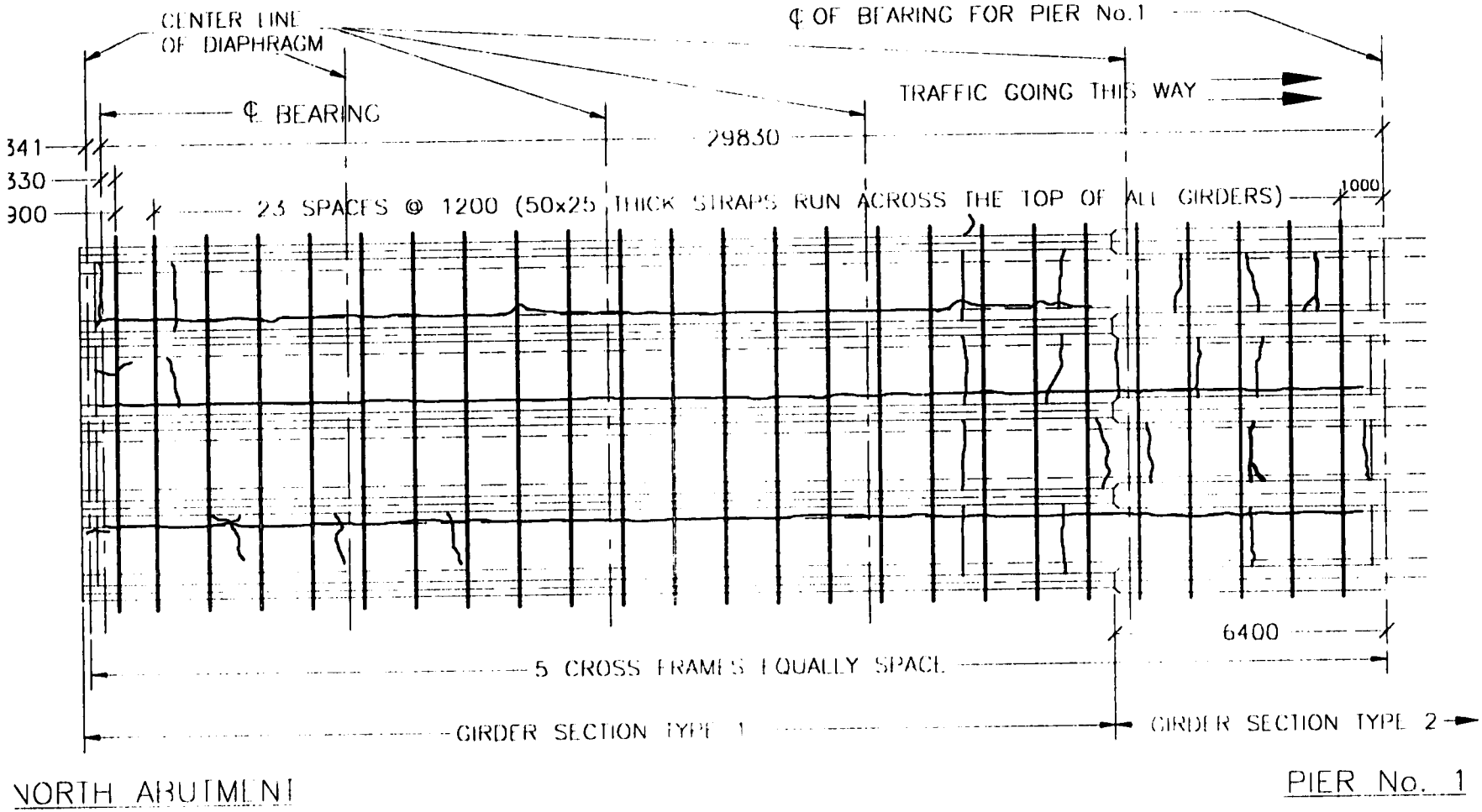

Figure 4.48: North Span Crack Pattern [August 1998]

5. ANALYSIS AND COMPARISON

5.1 Dynamic Behaviour of Crowchild Trail Bridge

5.1.1 Theoretical Background

Structural dynamic problems are often difficult to visualize, design for, and anticipate. Exact modeling of structural dynamic problems is either impossible or impractical. Thus, dynamics problems are idealize and visualize in three pure components. Figure 5.1 below shows the idealized components of a dynamic problem.

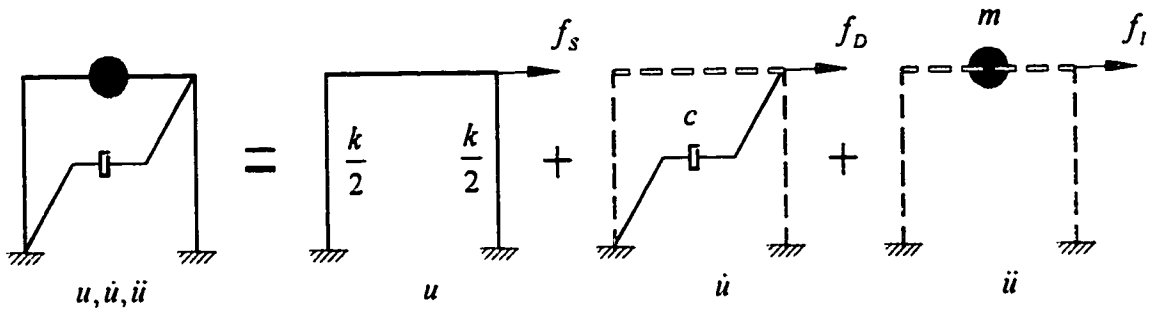

Figure 5.1: Idealized Components

For the force *P(t)* acting on the idealized system above, the governing equation of motion become

$$f_I + f_D + f_S = P(t)$$

$$m\ddot{u} + c\dot{u} + ku = P(t) \qquad \text{for Elastic Systems} \qquad (5.1)$$

$$m\ddot{u} + c\dot{u} + f_S(u, \dot{u}) = P(t) \qquad \text{for Inelastic Systems}$$

where

u	*Displacement*	f_I	*Inertia Force*
$\dot{u}$	*Velocity*	m	*Mass*
$\ddot{u}$	*Acceleration*	k	*Stiffness*
f_S	*Stiffness Force*	c	*Damping Coefficient*
f_D	*Damping Force*	$P(t)$	*Force as a function of time, t*

Equation (5.1) can be solved by four methods: closed form solution, Duhamel's Integral, Transform methods, and Numerical Integration. However, the closed form solution can be very complex and sometimes no solution to the differential equation can

be found. Duhamel's Integral and Transform method are designed to solve for linear differential equations. Only the numerical time-stepping integration method is a practical approach in solving the equation of motion in inelastic systems.

For a damped, free vibration system, and forcing function $P(t) = 0$, the governing second order, linear, homogeneous differential equation of motion with constant coefficients is:

$$m\ddot{u} + c\dot{u} + ku = 0 \tag{5.2}$$

Let $u = Ge^{rt}$, where G *and* r are constants that depend on initial conditions. Equation (5.2) becomes

$$Ge^{rt}(mr^2 + cr + k) = 0$$

Therefore $$mr^2 + cr + k = 0 \tag{5.3}$$

(a) For Undamped System

The solution of equation (5.3) for undamped systems, $c = 0$, is

$$r^2 = \frac{-k}{m} \tag{5.4}$$

Letting $i = \sqrt{-1}$ and $w_n = \sqrt{\frac{k}{m}}$, equation (5.4) becomes

$$r = \pm iw_n \tag{5.5}$$

where w_n *is the natural frequency of the undamped systems.*

Therefore, $$u = G_1 e^{-iw_n t} + G_2 e^{iw_n t} \tag{5.6}$$

$$= A\sin(w_n t) + B\cos(w_n t) \qquad \text{by Euler's Identity} \tag{5.7}$$

$$= \frac{\dot{u}_o}{w_n}\sin(w_n t) + u_o \cos(w_n t) \qquad \text{after initial conditions, } u(0) = u_o \text{ and } \dot{u}(0) = \dot{u}_o \text{ are applied} \tag{5.8}$$

where A, B *constants* $\ddot{u}_o$ *Initial Acceleration*

$\dot{u}_o$ *Initial Velocity* t *time*

(b) For Damped System

The solution of equation (5.3) for damped system is

$$r = \frac{-c}{2m} \pm \frac{\sqrt{c^2 - 4km}}{2m}$$

$$= \frac{-c}{2m} \pm \sqrt{\left(\frac{c}{2m}\right)^2 - \left(\frac{k}{m}\right)} \qquad (5.9)$$

(i) For critically damped systems,

$$\left(\frac{c}{2m}\right)^2 = \left(\frac{k}{m}\right)$$

Thus, $c_{cr} = 2mw_n$ (5.10)

where c_{cr} is the critical damping coefficient.

(ii) For Heavily damped systems,

$$\left(\frac{c}{2m}\right)^2 > \left(\frac{k}{m}\right) \qquad (5.11)$$

(iii) Lightly damped systems,

$$\left(\frac{c}{2m}\right)^2 < \left(\frac{k}{m}\right) \qquad (5.12)$$

Letting $\xi = \frac{c}{c_{cr}} = \frac{c}{2mw_n}$, equation (5.9) becomes

$$r = -w_n\xi \pm \sqrt{(w_n\xi)^2 - w_n^2}$$

$$= -w_n\xi \pm iw_n\sqrt{1-\xi^2} \qquad (5.13)$$

where ξ is the damping ratio.

Letting $w_D = w_n\sqrt{1-\xi^2}$, equation (5.13) can be simplified as

$$r = -w_n\xi \pm iw_D \qquad (5.14)$$

where w_D is the natural frequency of the damped systems.

Therefore $u = G_1 e^{(-w_n\xi + iw_D)t} + G_2 e^{(-w_n\xi - iw_D)t}$

$$= e^{-w_n\xi t}\left(G_1 e^{iw_D t} + G_2 e^{-iw_D t}\right) \qquad (5.15)$$

$$= e^{-w_n\xi t}\left(A\sin w_D t + B\cos w_D t\right) \quad \text{by Euler's Identity} \qquad (5.16)$$

Applying Initial Conditions, $u(0) = u_o$ and $\dot{u}(0) = \dot{u}_o$

$$u(t) = e^{-\xi w_n t}\left[u(0)\cos w_n t + \left(\frac{\dot{u}(0) + w_n \xi u(0)}{w_D}\right)\sin w_D t\right] \tag{5.17}$$

Finally, $$u(t) = \rho\cos(w_D t - \theta)e^{-\xi w_n t} \tag{5.18}$$

where $$\rho = \sqrt{\left(\frac{\dot{u}_o + u_o w_n \xi}{w_D}\right) + u_o^2}$$

$$\theta = tan^{-1}\left[\frac{(\dot{u}_o + u_o w_n \xi)}{w_D u_o}\right]$$

(c) Damping Coefficient

Equation (5.17) shows that the ratio of the amplitude between each successive peak is defined as follow (Chopra, 1995):

$$\frac{u(t)}{u(t+T_D)} = e^{\frac{2\pi\xi}{\sqrt{1-\xi^2}}} \tag{5.19}$$

Similarly, the ratio for the acceleration between each successive peak is,

$$\frac{\ddot{u}(t)}{\ddot{u}(t+T_D)} = e^{\frac{2\pi\xi}{\sqrt{1-\xi^2}}} \tag{5.20}$$

Solving for the damping ratio, ξ

$$\ln\left(\frac{\ddot{u}(t)}{\ddot{u}(t+T_D)}\right) = \frac{2\pi\xi}{\sqrt{1-\xi^2}}$$

$$\xi = \pm\frac{\ln\left(\frac{\ddot{u}(t)}{\ddot{u}(t+T_D)}\right)}{\sqrt{\left[\ln\left(\frac{\ddot{u}(t)}{\ddot{u}(t+T_D)}\right)\right]^2 + 4\pi^2}} \tag{5.21}$$

However, it is more accurate to select multiple peaks, such that the amplitude has decreased at least 50%. Similarly, for multiple successive peaks, we can derive the relationship as follow:

$$\frac{u(t)}{u(t+mT_D)} = e^{\frac{2\pi m\xi}{\sqrt{1-\xi^2}}} \tag{5.22}$$

$$\xi = \pm \frac{\ln\left(\frac{u(t)}{u(t+mT_D)}\right)}{\sqrt{\left[\ln\left(\frac{u(t)}{u(t+mT_D)}\right)\right]^2 + 4\pi^2 m^2}} \tag{5.23}$$

(d) Simply Supported Beams

A simply supported beam is shown in Figure 5.2. The frist three frequncies and mode shapes of this free simply supported beam are shown in Table 5.1. Obviously, Table 5.1 is valid only for free vibration with zero initial velocity and an initial displacement (Chopra, 1995).

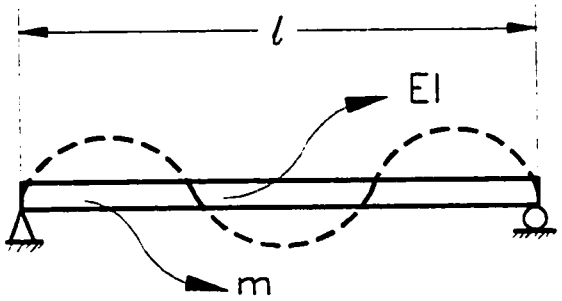

Figure 5.2: Simply Supported Beam

Table 5.1: Frequency of Single Span and Simply Supported

Mode	Mode Shape	Angular Velocity, ω	Period, T	Frequency
1		$\omega_1 = \frac{\pi^2}{l^2}\sqrt{\frac{EI}{m}}$	$\frac{2\pi}{\omega_1}$	$\frac{\omega_1}{2\pi}$
2	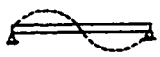	$\omega_2 = \frac{4\pi^2}{l^2}\sqrt{\frac{EI}{m}}$	$\frac{2\pi}{\omega_2}$	$\frac{\omega_2}{2\pi}$
3		$\omega_3 = \frac{9\pi^2}{l^2}\sqrt{\frac{EI}{m}}$	$\frac{2\pi}{\omega_3}$	$\frac{\omega_3}{2\pi}$

(e) Continuous Beams

Unlike a simply supported beam shown above, the dynamic analysis of continuous beams is more cumbersome. Due to the complexity of its' mode shapes, derivation of a mathematical equivalent is not an easy task. Take the case of three continuous span, simply supported as shown in Figure 5.3. Assuming three identical spans, the first three vertical-fundamental mode shapes of the beam are shown in Table 5.2 (Biggs, 1964).

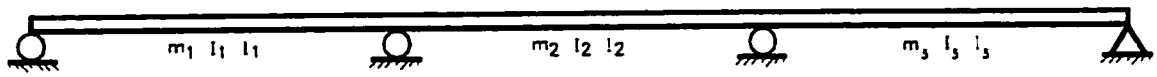

Figure 5.3: Three Continuous Span

Table 5.2: Frequency of Three Continuous Span and Simply Supported

Mode	Mode Shape	Angular Velocity, ω	Period, T	Frequency
1		$\omega_1^2 = \frac{EI\pi^4}{ml^4}$	$\frac{2\pi}{\omega_1}$	$\frac{\omega_1}{2\pi}$
2	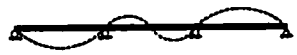	$\omega_2^2 = \frac{EI(3.55)^4}{ml^4}$	$\frac{2\pi}{\omega_2}$	$\frac{\omega_2}{2\pi}$
3		$\omega_3^2 = \frac{EI(4.30)^4}{ml^4}$	$\frac{2\pi}{\omega_3}$	$\frac{\omega_3}{2\pi}$

5.1.2 Natural Frequencies and Mode Shapes of the Crowchild Trail Bridge

To analyze the Crowchild Trail Bridge, the following assumptions are made:

1. All five girders have the same stiffness;
2. Barrier rail and asphalt have no contribution to the stiffness;
3. Each girder has the same stiffness along the length and is continuous in all three spans;
4. All three spans are equal, with span length = 30 230 mm;
5. Small deformation and elastic behaviour are assumed;
6. Shear deformation is ignored;
7. Rotational inertia of masses is considered to be negligible;

8. Damping is negligible;
9. Full composite action is assumed;
10. Steel Strength, $F_y = 350MPa$ is used;

Table 5.3: Crowchild Trail Bridge Concrete Mix Properties

CONCRETE MIXES (for 1 m^3)	
Specified Strength, fc'_{28} = 35 MPa	Fine Aggregates = 680 kg
Water = 155 kg	Air Entrainment = 50 ml / 100 kg
Cement = 430 kg	Superplastizer = 290 ml / 100 kg
Coarse Aggregates = 1080 kg	Polypropylene Fibers = 4.5 kg (0.45% by volume)

From Table 5.3 above, the concrete density is determined to be $\gamma_C = 2350^{kg}/_{m^3}$.

Based on the secand modulus, the elastic modulus of concrete can be determined by

$$E_C = (3300\sqrt{f'_C} + 6900)\left(\frac{\gamma_C}{2300}\right)^{1.5} = 27290MPa$$

$$n = \frac{E_C}{E_S} = \frac{27290}{207000} = 0.131836$$

Figure 5.4 shows a simplified model of the Crowchild Trail Bridge. The diagram shown on the left in Figure 5.4 shows the section before conversion to steel equivalent, and the diagram shown on the right is the steel equivalent after conversion. The distance from the bottom side of the bottom flange to the neutral axis is at 916 mm. Moment of inertia is $I_x = 24489.3 \times 10^6 mm^4$. Assuming the density of concrete, steel, and asphalt are 2350, 7850, and 2293 kg/m^3 respectively. Thus, the simplified model to the left has a mass of 1864 kg/m.

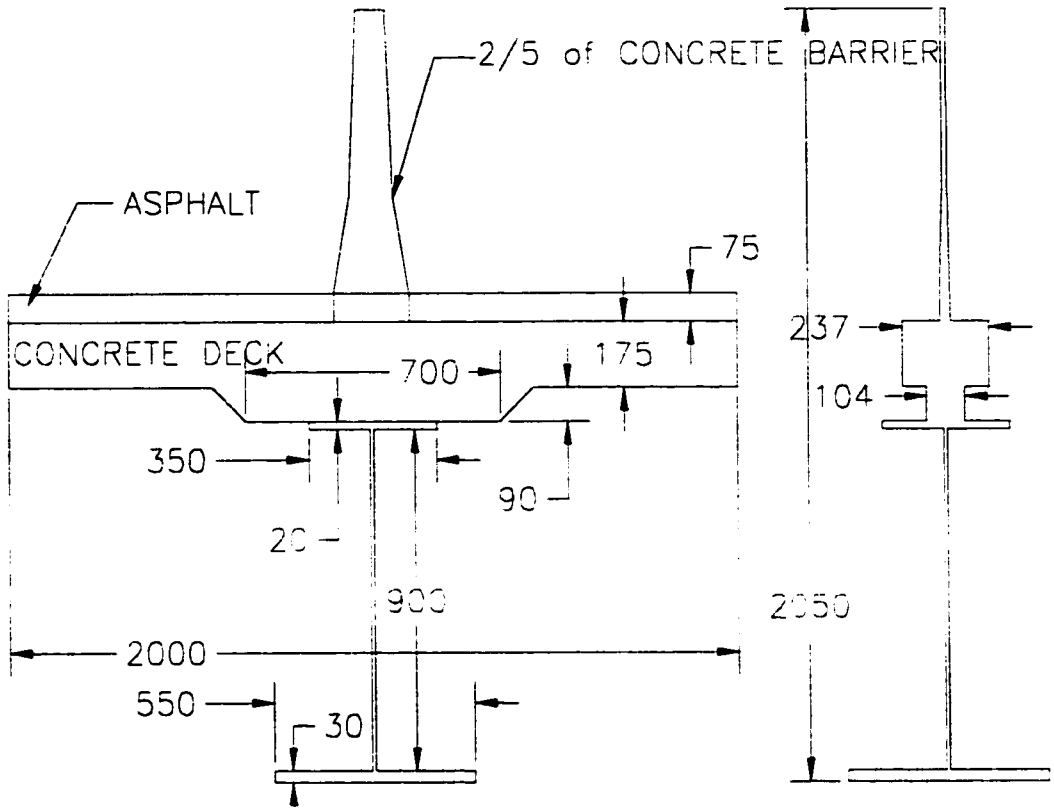

Figure 5.4: Simplified Model of Bridge Deck

Natural frequencies of the above simplify model is calculated with the following variables substituted into the equations in Table 5.2:

$$E_s = 207000MPa, \quad I_x = 24489.3 \times 10^6 mm^4,$$

$$l = 30.23m, \quad m = 1864\,{}^{kg}/_{m}$$

Therefore,

$$\omega_1 = 17.84\,{}^{rad}/_{s} \quad \text{and} \quad f_1 = 2.83Hz$$

$$\omega_2 = 22.74\,{}^{rad}/_{s} \quad \text{and} \quad f_2 = 3.62Hz$$

$$\omega_3 = 33.37\,{}^{rad}/_{s} \quad \text{and} \quad f_3 = 5.31Hz$$

Comparing the results of the ambient vibration tests done by the University of Alberta in 1998 and University of British Colombia in 1997 with the theoretical solutions shows very good agreement, as indicated in Table 5.4.

Table 5.4: Comparison of Natural Frequencies Results

U of A [August '98]	UBC Report [September '97]	Analysis [Section Properties]	Description
2.60 Hz	2.78 Hz	2.83 Hz	1st Vertical Mode
3.63 Hz	3.76 Hz	3.62 Hz	2nd Vertical Mode
4.43 Hz	4.64 Hz	5.31 Hz	3rd Vertical Mode

5.1.3 Damping of the Crowchild Trail Bridge

The damping curve shown in Figure 5.5, along with the test curves, is derived from equation (5.22). It can be seen that the two curves agree with the free vibration portion of the test curve very well. [The conversion factors for the accelerometer, A48, and the cable transducer, L1 are 1 V = 10 mg and 1 V = 1.57 mm, respectively.]

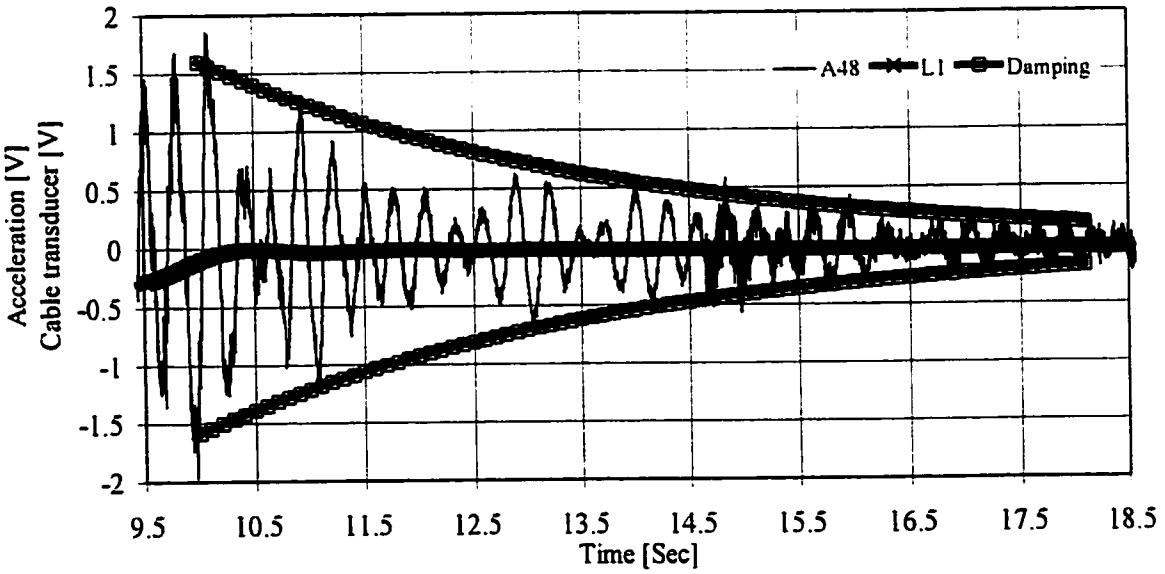

Figure 5.5: Damping Curve

Damping in real structures is from internal friction as solids deformed, friction at connection, open and close of micro-cracks in concrete, etc. It is impossible to identify and describe mathematically every individual energy dissipation mechanisms. Even for system that is vibrating within linear elastic range the damping coefficient '*c*' can still

vary with respect to amplitude of deformation. The effects of damping will reduce the natural frequency of an undamped system, w_n to a damped system, w_D. Likewise, period of an undamped system, T_n is increased to period of a damped system, T_D. However, the effects are negligible for a damping ratio of $\xi \leq 20\%$, a range that includes most of structures. A plot the relationship of $w_D = w_n\sqrt{1-\xi^2}$ in equation (5.16) is shown in Figure 5.6. Clearly, for low damping ratio, neglecting damping effects are quite acceptable, such as a structure with $\xi \leq 20\%$ produces only a 2% error in frequencies if the damping is neglected. To determine the damping ratio analytically is either impossible or impractical. On the other hand, a simple force vibration test can not only easily determine the damping ratio, but also the stiffness, and the natural frequency of the structures.

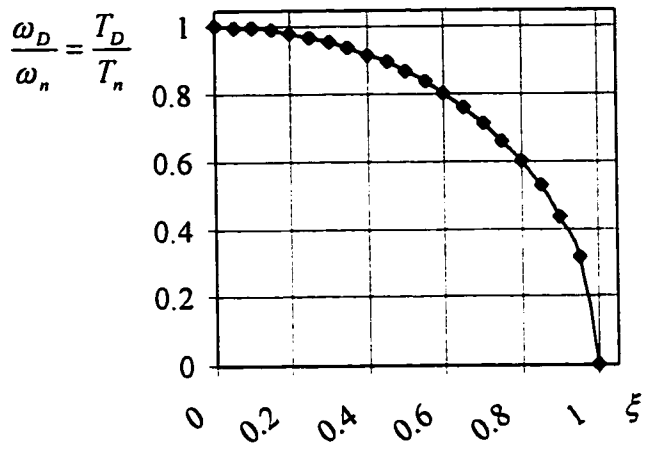

Figure 5.6: Effect of Damping

5.2 Static Behaviour of Crowchild Trail Bridge

Four issues of static behaviour of Crowchild Trail Bridge are being discussed in this section: 1) shear transfer inside the concrete deck in the transverse direction, 2) rigidity of the deck and load sharing among the girders, 3) composite action between the concrete deck and the steel girders in the longitudinal direction, and 4) change in the stiffness of the bridge.

5.2.1 Shear Transfer in the Transverse Direction

In a one way flexural member, shear is the gradient of bending moment along the length of the member, and consists of two components: beam action and arching action. Shear resulting from a gradient in tensile force acting on a constant moment arm is

referred to as beam action. Beam action is a characteristic of slender flexural members. Shear resulting from a constant tensile force acting on a varying moment arm is called arching action. It requires only remote anchorage of the reinforcement and, unlike beam action, the transfer of shear flow will not be prevented by the inclined cracks. Shear transfer by means of arching action is usually associated with deep beams and regions adjacent to discontinuities or disturbances in either the loading or the geometry of the member.

The concrete deck of the Crowchild Bridge is designed so that, at ultimate load, shear is mainly transferred by the arching action. As illustrated in Figure 5.7, near the ultimate load, the concrete cracks at the mid-span. Hence, the applied load is transferred to the supporting girders by means of compressive struts. The horizontal component of the compressive arch is resisted partly by the tension ties (i.e. steel straps) and partly by the restraints provided by the lateral stiffness of the girders. At service loads, however, shear is transferred by a combination of beam action and arching action. Beam action is the governing mechanism before cracking of the concrete deck, as it is the stiffer mechanism of the two.

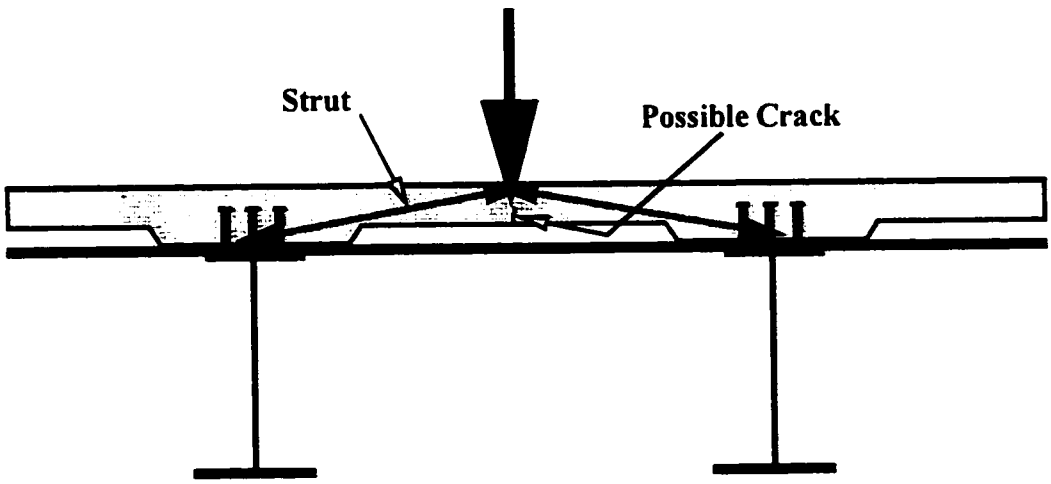

Figure 5.7: Shear Transfer in the Concrete Deck

In 1997 tests and measurements, the largest measured strain for the straps was 40 με. Recalled the steel straps had a rectangular cross section of 25 mm x 50 mm; therefore the steel strap carried an axial load of 10 kN. Recalled from chapter 3, the heaviest tandem axel was 160 kN; each wheel set weighted 80 kN per side. Assuming only one strap was carrying the applied load by arching action alone, the strap must carried 144 kN. Since the strap only carried 10 kN as measured under the applied load, arching action was obviously not the sole load carrying mechanism in the system. In addition, no longitudinal crack was visible on the bottom surface of the deck. It is then concluded that as of late October 97, the shear transfer inside the concrete deck in the transverse direction was mainly by the beam action.

Strains in the straps, however, had increased to about 80 με in 1998. The increased strain, together with the existence of the longitudinal cracks, suggests that the contribution of tensile concrete in transferring shear has reduced in the second year.

5.2.2 Rigidity of the Deck and Load Sharing between Girders

The stiffness of the bridge deck in the transverse direction (or the rigidity of the deck) is the most important factor controlling the load sharing between the girders. Load sharing between the girders is of great importance since it illustrates the contribution of the girders that are not directly loaded. It is impractical to quantify any of these two terms. Consequently, any discussion in this regard is subject to engineering judgment.

The deflection measurements in the 1997 static tests with two trucks sides by side was used to evaluate the rigidity of the bridge deck. Neglecting the small transverse slope of the bridge, the centerline of the middle girder becomes an axis of symmetry. In the extreme case of a rigid deck, any symmetric load about this axis results in equal deflections for all the girders. This is not necessarily the case with poor stiffness of the deck in the transverse direction. As shown in Figure 4.3, the deflection of the girders in cases with two side by side trucks is almost uniform, suggesting a good stiffness in the transverse direction. Note that in Figure 4.3 the deflection of girder 5 was slightly higher

than the deflection of girder 1. This may be a result of the misalignment of the two trucks.

The case of asymmetric loading, such as a single truck in one lane, can be replaced by a concentric load and a torque. Often, torque caused by the eccentricity of the load results in additional downward movements in girders on one side and uplift on the other side. With a rigid deck, the deflected shape remains very close to a straight line. In a deck with poor stiffness, however, the deflection of the girders that are not directly loaded is close to zero.

Any significant change in the stiffness of the superstructure with time, therefore, can be detected by plotting the load sharing between girders for similar truck positions. Figure 5.8 shows the load sharing between girders based on the deflection measurements for 1997 and 1998. Similarity, the two figures suggest that the load sharing between the girders has not changed. Note that the truck specifications as well as its eccentricity from centerline of torsion (Girder #3) were slightly different in each year.

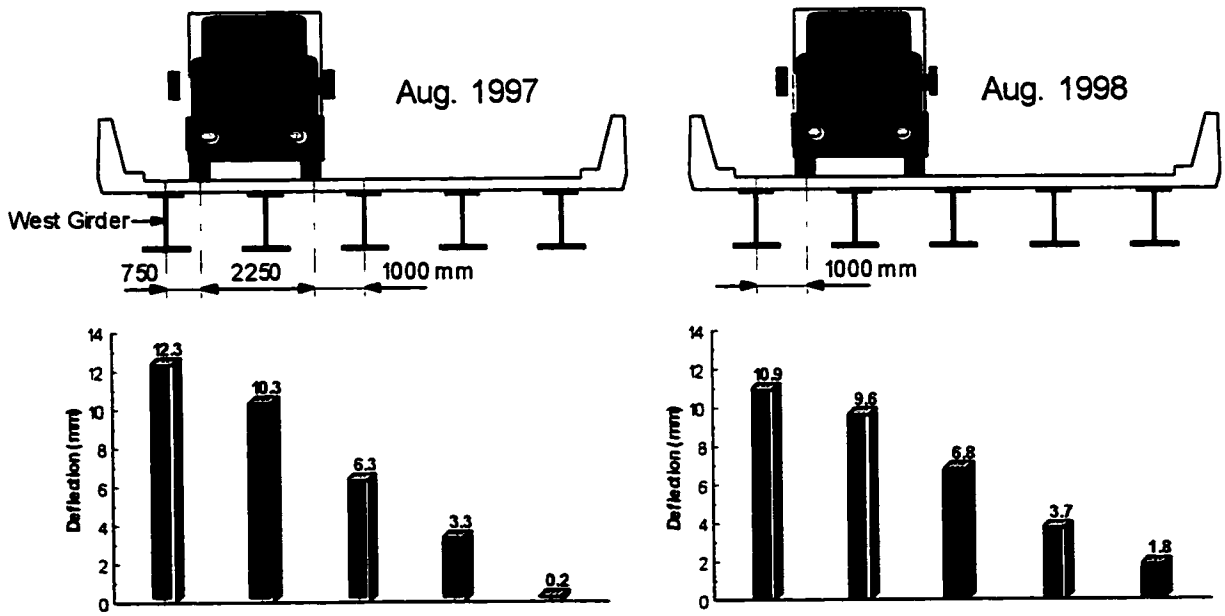

Figure 5.8: Load Sharing between Girders Based on the Deflection Measurements

5.2.3 Composite Action in the Longitudinal Direction

Composite action between the concrete deck and the steel girders in the longitudinal direction is being studied for two regions in the North span, namely the positive moment region where the concrete is mostly in compression and the negative moment region where the concrete is mostly in tension. The contribution of the concrete to the stiffness and load carrying can be evaluated based on the measured location of the neutral axis in each region.

Figure 5.9 illustrates the location of the neutral axis for Girder #1 in the positive moment region. To investigate any changes in the location of the neutral axis with time, four load cases were considered: August 1997, October 1997, June 1998, and August 1998. Note that the specification of the trucks was different from one load case to another, with the August 98 truck being the heaviest. As a result, the maximum strain in each load case is different. However, the location of the neutral axis is approximately 50 mm from the bottom face of the top flange. For all four tests conducted up to the end of August 1998, the composite action between the concrete deck and the steel girders in the longitudinal direction has not deteriorated significantly in the positive moment region.

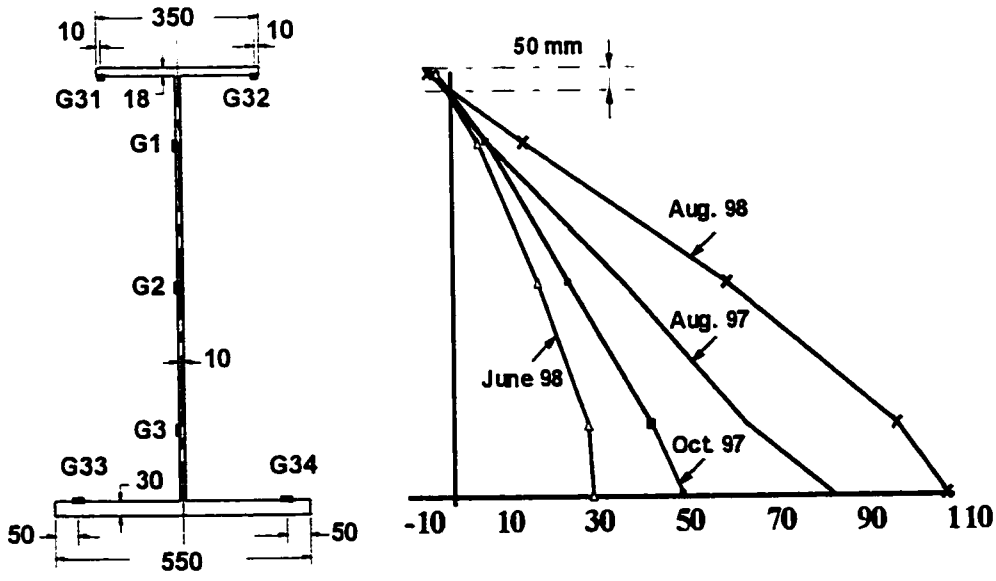

Figure 5.9 Location of the Neutral Axis in the Positive Moment Region

Figure 5.10 illustrates the location of the neutral axis for girder 1 in the negative moment region for the four load cases. Note that the accuracy in determining the location of the neutral axis is lower compared to the positive moment region, due to the magnitude of the strain were much smaller. In addition, there were no strain measurements on the flanges. The neutral axis has moved from 93 mm in 1997 to 191 mm in 1998 with reference to the bottom face of the top flange. The 98 mm shift in the location of neutral axis indicates a loss in the composite action between the concrete deck and the steel girders in the negative moment region.

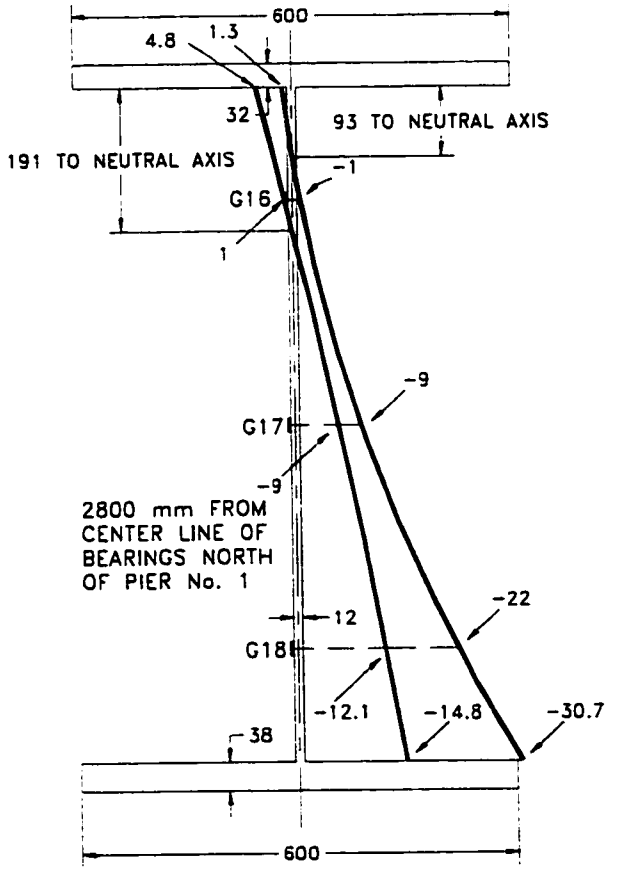

Figure 5.10 Location of the Neutral Axis in the Negative Moment Region

5.2.4 Change in the Stiffness of the Bridge

Any losses in the composite action of the concrete deck and the steel girders in the negative moment region associates with a reduced moment of inertia in that region.

Consequently, the stiffness of the bridge in the longitudinal direction is affected. To evaluate the change in the stiffness with time, the bridge has been modeled as a continuous beam. A primary concern with any analytical model is to model the contribution of the concrete, especially at the negative moment region where the transverse cracks propagate with time. To overcome this problem, the cross sectional properties were determined based on the measured location of the neutral axis for each year. The thickness of the concrete deck was assumed 200 mm. The equivalent contributing width of concrete for segment types 1 and 2 were determined so that the calculated location of the neutral axis matches those based on the strain measurements. The width of the concrete for segment type 3 is assumed equal to that for type 1. Cross sectional properties obtained are presented in Table 5.5.

Segment type 1 is used at the positive moment regions of the exterior spans. Segment type 2 is used at the negative moment regions of both piers, and extends 6.4m and 6.9m from the centerline of the piers into the exterior and middle spans, respectively. Segment type 3 is used at the positive moment regions of the middle span.

Three cases are studied using a simple two-dimensional beam analysis: 1) beam and truck of 1997, 2) beam and truck of 1998, and 3) beam of 1997 but truck of 1998. Deflections in the first two cases can be compared directly to the test results. As the model is only a two-dimensional analysis, the average of the deflection of all the girders is used (6.5mm and 6.56mm for the years 1997 and 1998, respectively as shown in Figure 5.8). Comparison of the last two cases, however, demonstrates the change in the stiffness of the bridge with time.

Table 5.5: Section Properties of the Girders

Segment	Component	b (mm)	h (mm)	Neutral Axis (mm)	A ($mm^2 \times 10^3$)	I ($mm^4 \times 10^6$)
	Concrete & GFRP	521	200			
Type 1	Top flange	350	18	50	136	17700
Aug. 97	Web	10	900			
& 98	Bottom flange	550	30			
	Concrete & GFRP	380	200			
Type 2	Top flange	600	32	120	129	21900
Aug. 97	Web	12	900			
	Bottom flange	600	38			
	Concrete & GFRP	140	200			
Type 2	Top flange	600	32	270	80.8	16870
Aug. 98	Web	12	900			
	Bottom flange	600	38			
	Concrete & GFRP	521	200			
Type 3	Top flange	350	18	23.5	132	14560
Aug. 97	Web	10	900			
& 98	Bottom flange	500	25			

The calculated deflections (at the locations where measurements were conducted for each year) were 6.69, 6.91, and 6.67 mm respectively for the 3 cases. The calculated deflections in the first two cases are in good agreement with their corresponding measured deflections. Comparison of the last two cases suggests that the stiffness of the bridge has reduced approximately 3.5% from 1997 to 1998.

6. SUMMARY AND CONCLUSIONS

6.1 Summary

The Crowchild Trail Bridge is an experimental bridge located at the intersection of Crowchild Trail and University Drive in Calgary, Alberta. It is a three-span, two-lane, one-way traffic overpass. It is spanning 92.878 meters with two interior supports. This bridge was built using the innovative steel free – fibre reinforced concrete deck design. This is the first of its kind in the world to utilize this innovative approach over the positive and negative moment regions. Field assessment of the Crowchild Trail Bridge focused on two main issues: performance under serviceability conditions and long-term durability. University of Alberta had extensively developed field instrumentation and monitoring program on this bridge. To assess its performance, static and dynamic tests were carried out using trucks with known axle loads. Based on the results of tests, the bridge fundamental structural characteristics, both static and dynamic, were determined under such service load conditions. For long-term durability study, the bridge is then monitored at various time intervals. The bridge fundamental structural characteristics are then re-evaluated and compared to the time before it was put into service. The scope of this thesis is the field assessment of the Crowchild Trail Bridge over the first years of its operation.

Since the superstructure of the Crowchild Trail Bridge was replaced in August 1997, two major phases of testing were completed by the end of August 1998. Tests consisted of ambient vibration, field survey, static load test, dynamic load test, and mapping of crack patterns. Strains, deflections and acceleration behaviour were measured. In August 1998, static and dynamic tests were performed using a truck with known axle loads and ran at various speeds. Natural frequencies and mode shapes of the bridge were determined by ambient vibration tests. Load sharing between girders, the dynamic load factor, stiffness, natural frequencies and damping factor of the bridge, were analyzed.

Comparison of the neutral axis in the positive moment region between August 1997 and August 1998 shows no change in the neutral axis. This result suggested no changes in composite action for the positive moment region. In the negative moment region, there was a 98 mm shift in the neutral axis, which suggested a partial loss in the composite action.

In August 1997, field survey indicated a maximum deflection of 17 mm in the North span, when two 357 kN trucks was loaded symmetrically in the North span. For asymmetric loading, one 357 kN truck was used, the maximum deflection was 13.5 mm. The steel strap had a maximum strain reading of 85 με and it varied between -15 to 85 με as the truck moved along the entire length of the bridge. With a maximum strain of 104 με in the girder and 85 με in the straps, the bridge clearly was behaving well within linear elastic range.

University of British Colombia performed an ambient vibration test on Crowchild Trail Bridge in September 1997. After it had been in operation for one full year, the University of Alberta did a second ambient vibration test at the end of August 1998. In the ambient vibration tests, eight predominant frequencies below 10 Hz were found. Comparison of the field-testing done by the University of Alberta and the University of British Colombia with the theoretical closed form solution shows very good agreement. Result comparison between UBC and U of A results shows that all the natural frequencies found have been reduce by approximately 0.20 Hz. The resolution of the measured frequency is ±0.01 Hz.

Both static and dynamic tests were conducted on the Crowchild Trail Bridge in August 1998. The same truck was used in both tests. Four different speeds, 15, 30, 40, and 55 km/hr, of truck were investigated in the dynamic tests. Results show that the dynamic test results can be filtered and reduced to obtain the identical static test results. The advantages of this implication translate into tremendous saving in future field testing

since little or no obstruction to traffic flow due to the dynamic testing; hence more structures can be assess and evaluate in a very short time.

Damping ratio of the bridge can be found by the decay of the free vibration motion. Since accelerometer data are taken at the same time as the cable transducer, the free vibration period can easily be determined. As of August 98, the Crowchild Trail Bridge had a damping ratio of approximately 1.20 percent.

Dynamic amplification factor can be determined from either strain gauges or cable transducers test results. The results from Crowchild Trail bridge have clearly demonstrated that there are two distinct dynamic amplification factors: the *overall vertical deflection component* and the *local strain component* in the bridge members. For the 55 km/hr test, the maximum strain components due to static and dynamic are 96.5 με and 14.9 με respectively. Thereby giving the dynamic amplification factor of 1.16 with a scatter of 0.7% for all the strain gauges investigated. Dynamic amplification factor due to the local strain effects varies non-linearly with respect to speed. For the *overall deflection component* in the 55 km/hr test, the deflections due to static and dynamic response are 11.5 mm and 0.94 mm, respectively. This gives a dynamic amplification factor of 1.08. The factor found from cable transducer is lower than that suggested by the strain gauge results. The overall trend of the DAF obtains from cable transducer and the strain gauge give quite vastly different behaviour. The dynamic amplification factors from the cable transducers give a linear relationship with respect to the speed; however, the strain gauges give a nonlinear relationship that increases exponentially for the speed tested. This suggested that the local strain effects are much more severe under dynamic load than that of the overall deflection component.

Good load sharing among girders was found from both deflection and strain gauge results. The deflected shapes of the girders were close to a straight line. No deterioration with time has been observed for the load sharing among the girders.

The first crack patterns were mapped at the end of August 1997 after removal of concrete formwork. All cracks were running in transverse direction, and were approximately 0.5 mm in width. No longitudinal crack in any of the three spans was found. After one full year of operation, a second crack patterns were mapped in August 1998. Those cracks existed from August 1997 seem to become twice wider by August 1998. As of August 1998, there were quite a few new cracks formed on the underside of the bridge. In addition to many new transverse cracks formed, there were quite a few longitudinal cracks developed. Most longitudinal cracks are formed right at the transition point between the flat part of the deck and the taper part. However, a couple longitudinal cracks were formed at midway between the two supporting girders in the South span.

6.2 Conclusions

The following conclusions and major observations are found based on ambient vibration, static, and dynamic tests carried out on Crowchild Trail Bridge in August 1997, before the bridge was open to traffic, and August 1998, after the bridge has been in operation for one full year,

1. Composite Action in the positive moment region has not changed during this period, while in the negative moment region there is a shift of 98 mm in the neutral axis due to the cracking of the concrete deck. According to a simple beam analysis, this loss of composite action in the negative moment region associates with almost 3.5% decrease in the overall stiffness of the bridge.

2. As of August 1998, wheel loads are transferred inside the concrete deck to the steel girders mainly by means of beam action. The share of arching action in the transfer of shear, however, has almost doubled in 1998 compared to that in 1997. Under 80,000 lbs triple axle truck load, the tension strap has a strain cycled between 85 and −15 με. At this low strain cycle, fatigue would not be a concern.

3. All the natural frequencies and mode shapes investigated show good correlation between both fields testing results and theoretical closed form solutions. The field ambient vibration tests show that all the natural frequencies investigated have been reduced by approximately 0.20 Hz after the bridge has been in service for one year. Since the mass of the structure has not changed, this may indicate stiffness of the bridge has reduced.

4. Based on the dynamic test results, the damping ratio and dynamic amplification factor can be obtained from both strain gauges and deflection data. The local strain gauge data yielded higher dynamic amplification factors than the ones based on the overall deflection results. Furthermore, dynamic test results can be filtered for static results, thus future static tests can be eliminated for the Crowchild Trail Bridge.

5. At a transverse section, the deflected shape of the girders has been very close to a straight line. This suggests a relatively stiff deck in the transverse direction, and hence, a good load sharing among the girders. No deterioration with time has been observed for the load sharing among the girders.

6. Overall, there are quite a few new cracks pattern formed over the one year of operation. Most cracks formed are 0.5 mm and less in width. Only few transverse cracks were observed in August 1997 while some longitudinal cracks with more transverse cracks were detected in August 1998. As of August 1998, cracks visible on the bottom surface of the bridge deck show no serviceability concern.

6.3 Recommendations for Future Research

It is recommended to conduct a yearly inspection and testing of the Crowchild Trail Bridge. The tests should include both ambient vibration test and dynamic load test. This ongoing periodic monitoring of the superstructure will eventually lead to a better

understanding of the performance of the bridge over time, which in turn lead to more effective maintenance and repair techniques.

A continuous monitoring of the performance of the bridge will enable engineers to a better understanding of the effects of truck load, temperature variations, and crack propagation on the long term performance of the bridge on a daily basis. Therefore, it is recommended to install a wireless remote monitoring system on the bridge to monitor a few selected key sensors in the bridge.

Recommendation for future ambient vibration testing is to place the accelerometers on every girder, since the bridge deck may not be rigid. Figure 6.1 shows the propose location of accelerometer for future testing. With such testing configuration, it minimizes the work and time of testing and maximizes the results. The results from the ambient vibration tests allow for closer examination of the changes in stiffness of individual girders, rigidity of the deck, and capture most of the important frequencies and mode shapes. These changes of the characteristics of the bridge will provide the health status of the bridge over time.

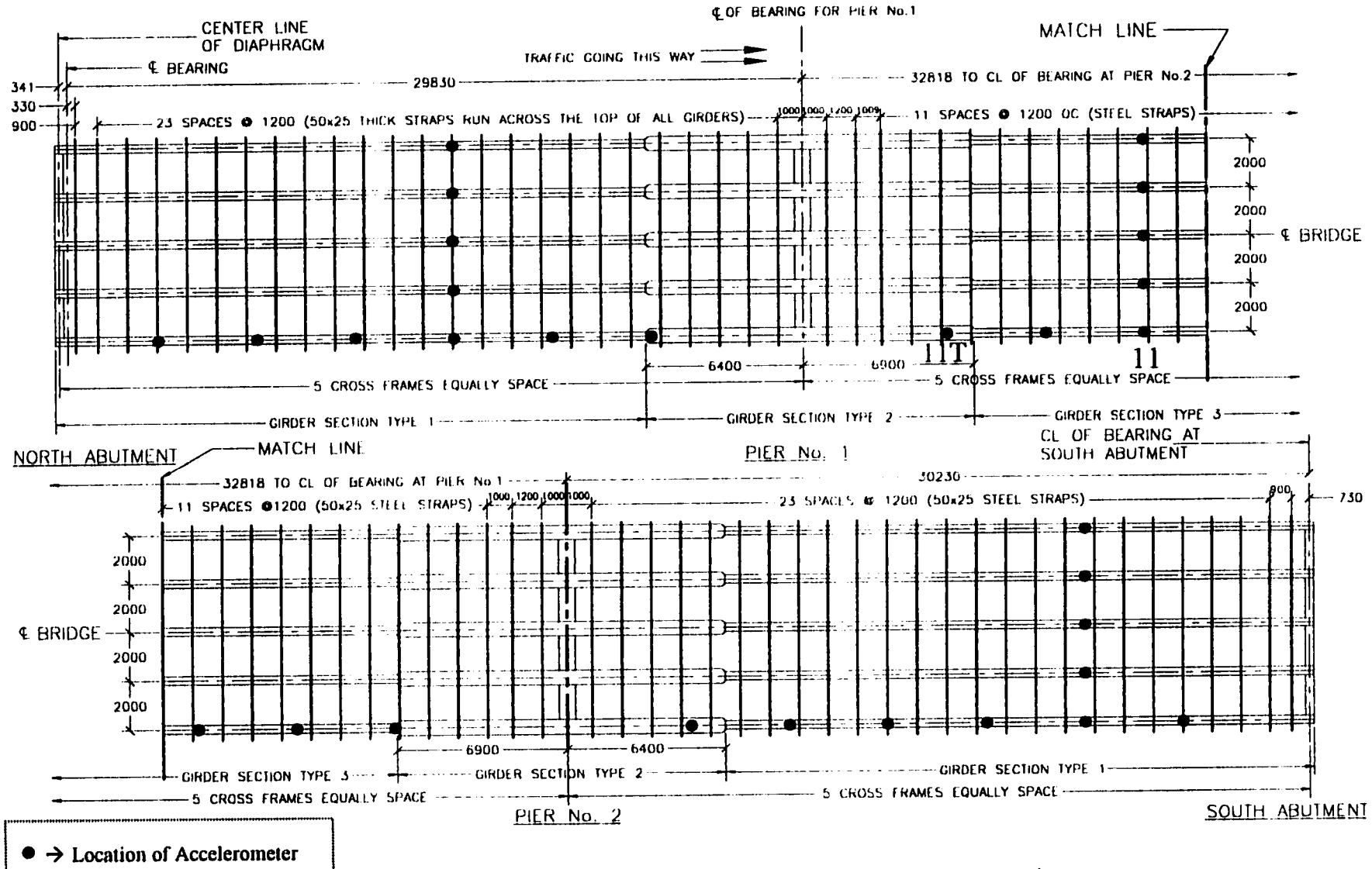

Figure 6.1: Recommended Accelerometer Location for Future Testing

REFERENCES

1. Afhami, S., Alexander, S.D.B., and Cheng, J.J.R., 1998. "Field Instrumentation and Monitoring of Crowchild Bridge in Calgary, Alberta". Proceedings, CSCE Annual Conference held in Calgary, Alberta, Canada.

2. Aly, A., Bakht, B., and Schafer, J., 1997. "Design and Construction of a Steel-Free Deck Slab in Ontario". Proceedings, CSCE Annual Conference held in Sherbrooke, Canada, Vol. 6, pp. 81-90.

3. Barker, R.M., and Puckett, J.A., 1997. *Design of Highway Bridges*. John Wiley & Sons, Inc., New York.

4. Biggs, J.M., 1964. *Introduction to Structural Dynamics*. McGraw-Hill, Inc., New York.

5. Black, C., Tsai, P., and Ventura, C.E., 1997. "Ambient Vibration Measurements of the University Drive/Crowchild Trial Bridge in Calgary, Alberta". UBC Earthquake Engineering Research, Project number EQ 97-005, October.

6. Buckland, P.G., and Barlett, M.F., 1992. "Canadian Highway Bridge Evaluation: A General Overview of Clause 12 of CSA Standard CAN/CSA-S6-88". CAN. J. CIV. ENG. Vol. 19, pp. 981 – 936.

7. Canadian Institute of Steel Construction, 1999. *Handbook of Steel Construction*, 7th Edition, Willowdale, Ontario.

8. Cheng, J.J.R., and Afhami, S., 1999. "Field Instrumentation and Monitoring of Crowchild Trail Bridge in Calgary, Alberta". University of Alberta report for the City of Calgary, July.

9. Chopra, A.K., 1995. *Dynamics of Structures: Theory and Applications to Earthquake Engineering*. Prentice-Hall, Inc., New Jersey.

10. Clough, R.W. and Penzien, J., 1993. *Dynamics of Structures*. Second Edition, McGraw-Hill, Inc., New York.

11. Dimarogonas, A., 1996. *Vibration for Engineers*. Second Edition, Prentice Hall Inc, New Jersey.

12. Doncaster, A., Newhook, J., and Mufti, A.A., 1996. "An Evaluation of Fiber Optic Sensors". Concrete International, Vol.18, No. 6, pp. 215 – 226.

13. Dorey, A.B., Newhook, J.P., and Mufti, A.A., 1996. "The Behaviour of a Reinforcing Steel-Free Bridge Deck Under Negative Moment". Concrete International, V.18, No. 6.

14. McConnell, K.G., 1995. *Vibration Testing: Theory and Practice*. John Wiley & Sons, Inc., New York.

15. Ministry of Transportation, Ontario, 1991. *Ontario Highway Bridge Design Code*, 3rd Edition. MTO Quality and Standard Division.

16. National Instruments Corporation, 1996. LabVIEW: *Analysis VI Reference Manual.*

17. Newhook, J.P., Mufti, A.A., and Wegner, L.D., 1995. "Fibre Reinforced Concrete Deck Slabs Without Steel Reinforcement". Nova Scotia CAD/CAM Centre, Research Report No. 1-1995, February.

18. Newhook, J. P., and Mufti, A. A., 1996. "A Reinforcing Steel-Free Concrete Deck Slab for the Salmon River Bridge". Concrete International, Vol.18, No. 6, pp. 30 – 34. June.

19. Newhook, J.P., and Mufti, A.A., 1996. "Steel –Free Concrete Bridge Deck- the Salmon River Project: Experimental Verification". Concrete International, V.18, No. 6, pp. 123 – 134. June.

20. Newhook, J.P., Mufti, A.A., Jaeger, L.G., MacDonnell, R., and Hamilton, D., 1996. "Steel-Free Concrete Bridge Deck-the Salmon River Project: Design and Construction". Concrete International, V. 18, No. 6, pp. 203 – 214. June.

21. Taing, K.K., Cheng, J.J.R., and Afhami, S., 1999. "Field Assessment of Crowchild Bridge in Calgary, Alberta". Proceedings, CSCE Annual Conference held in Regina, Saskatchewan, Canada.

22. Tartaglione, L. C., 1991. *Structural Analysis*. McGraw-Hill Inc., New York.

Appendix A

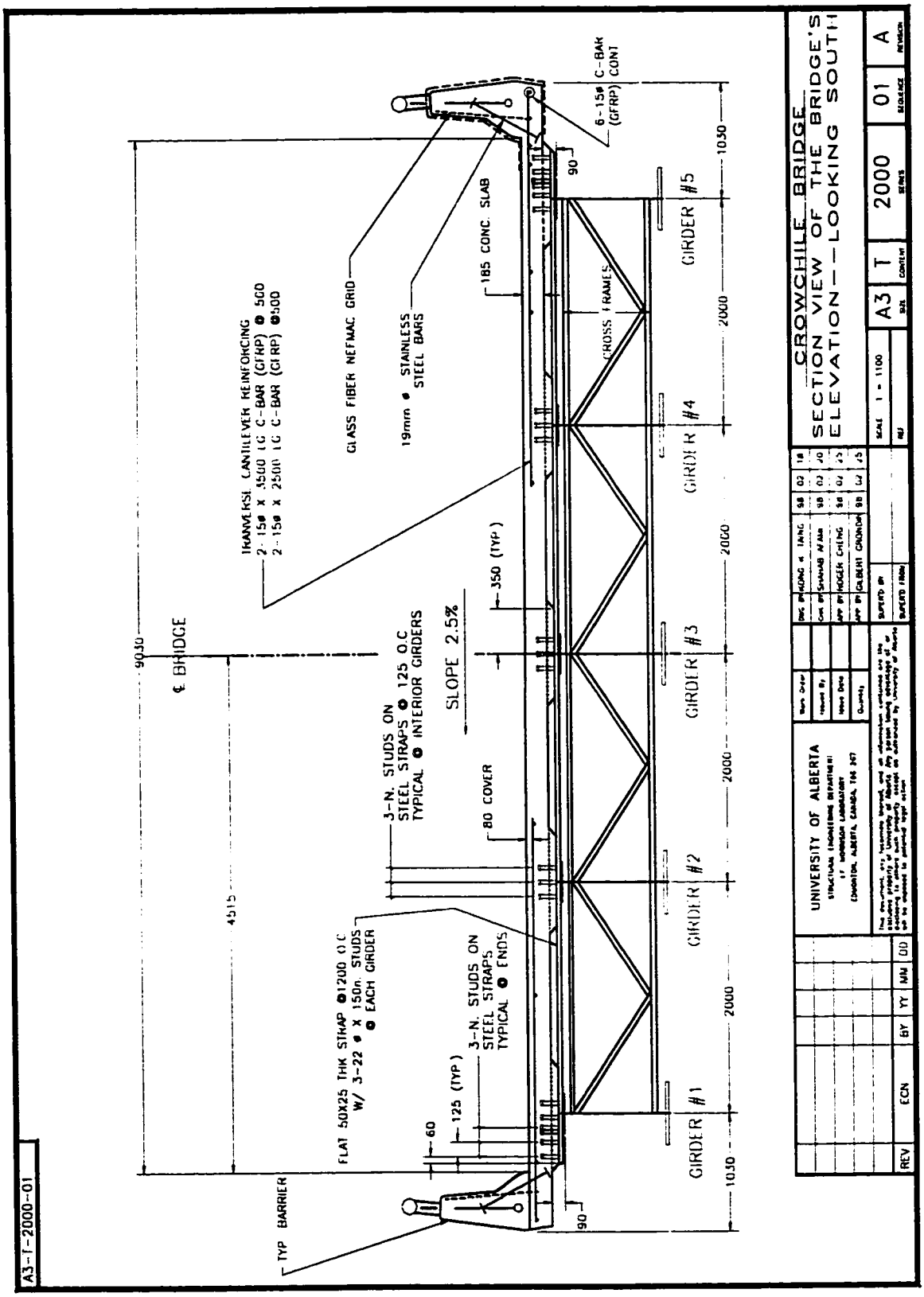

Figure A1: Cross Sectional View of the Crowchild Bridge

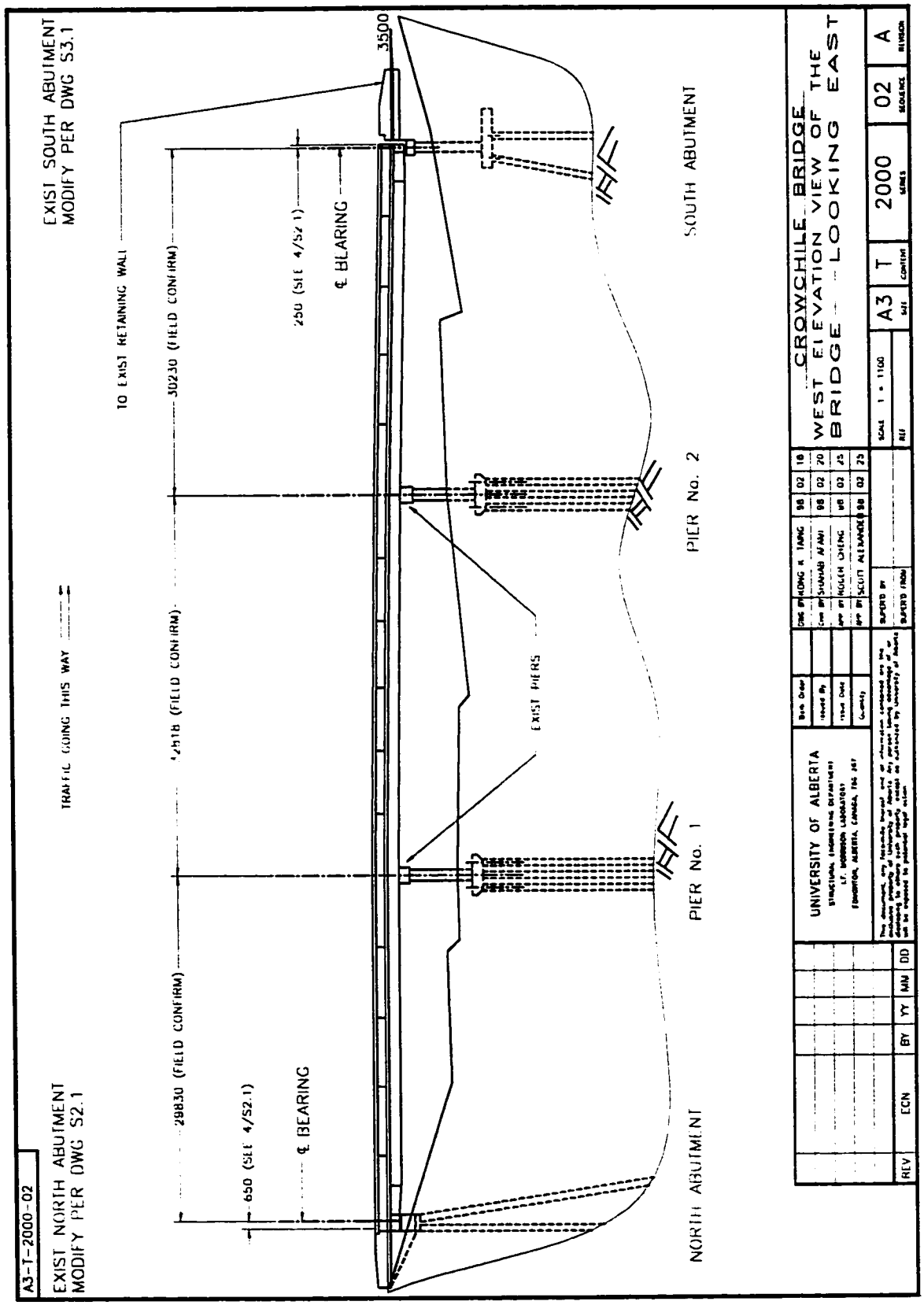

Figure A2: West Elevation View of the Crowchild Bridge

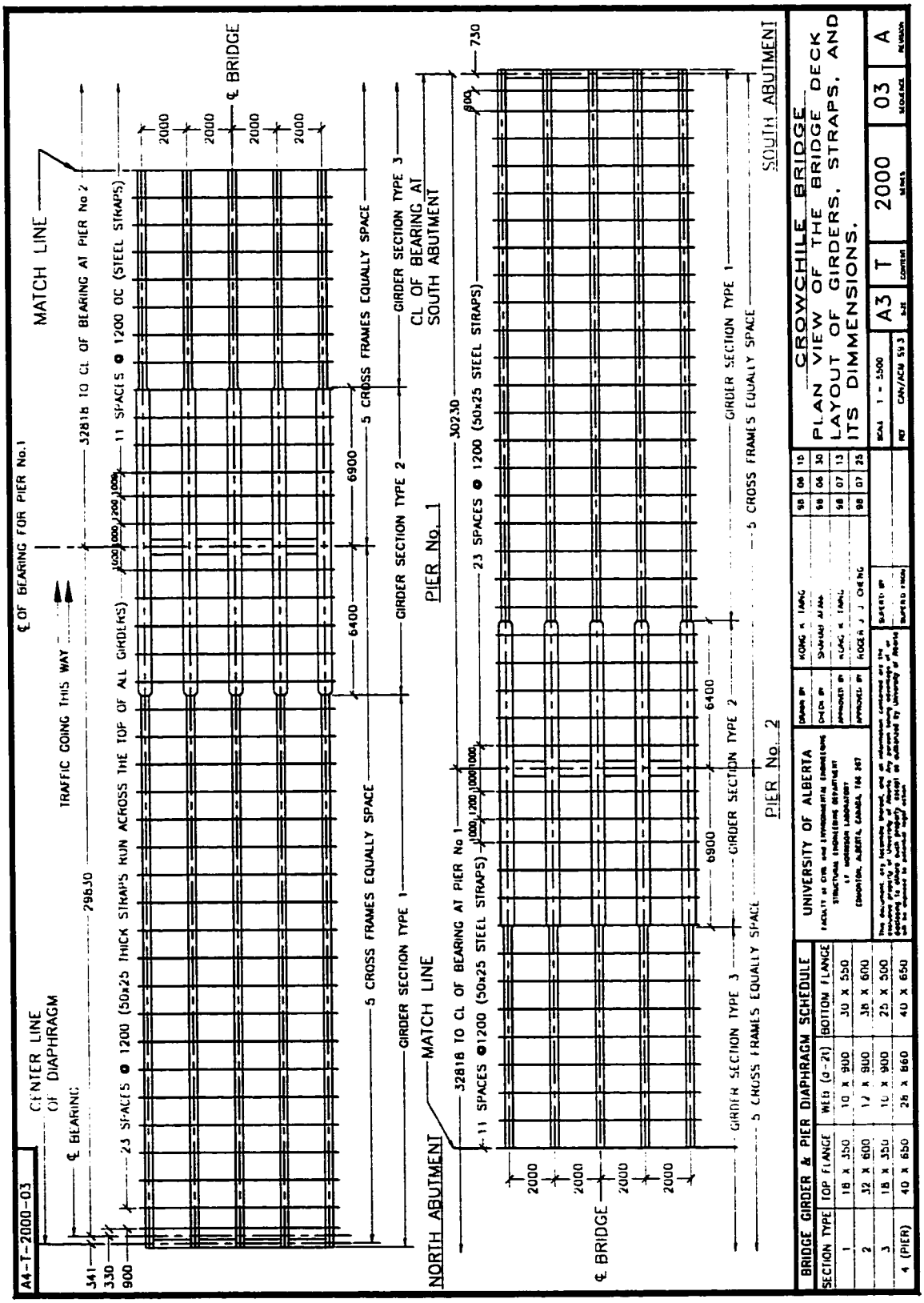

Figure A3: Plan View Layout of the Girders and Straps

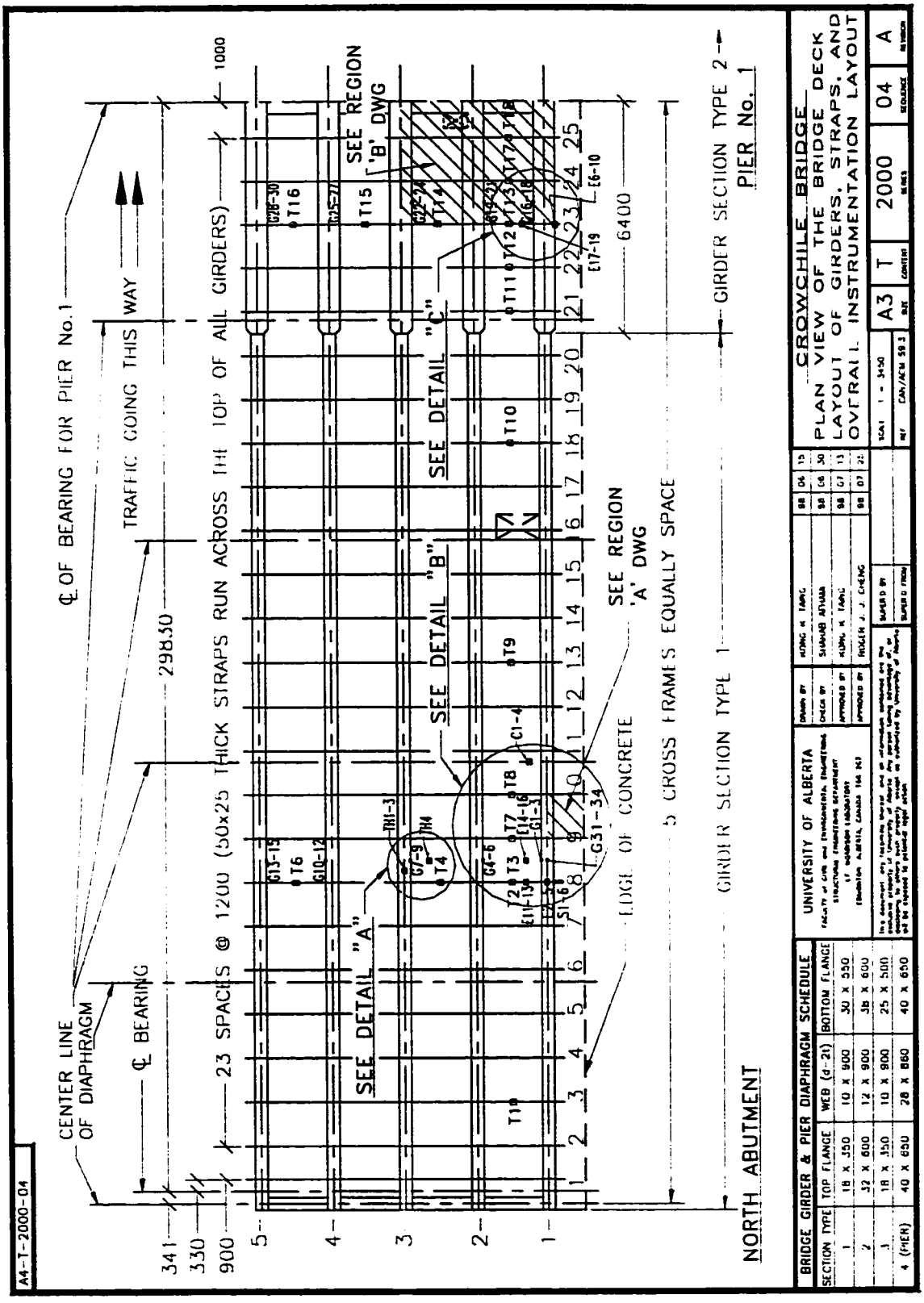

Figure A4: Overall Instrumentation Layout

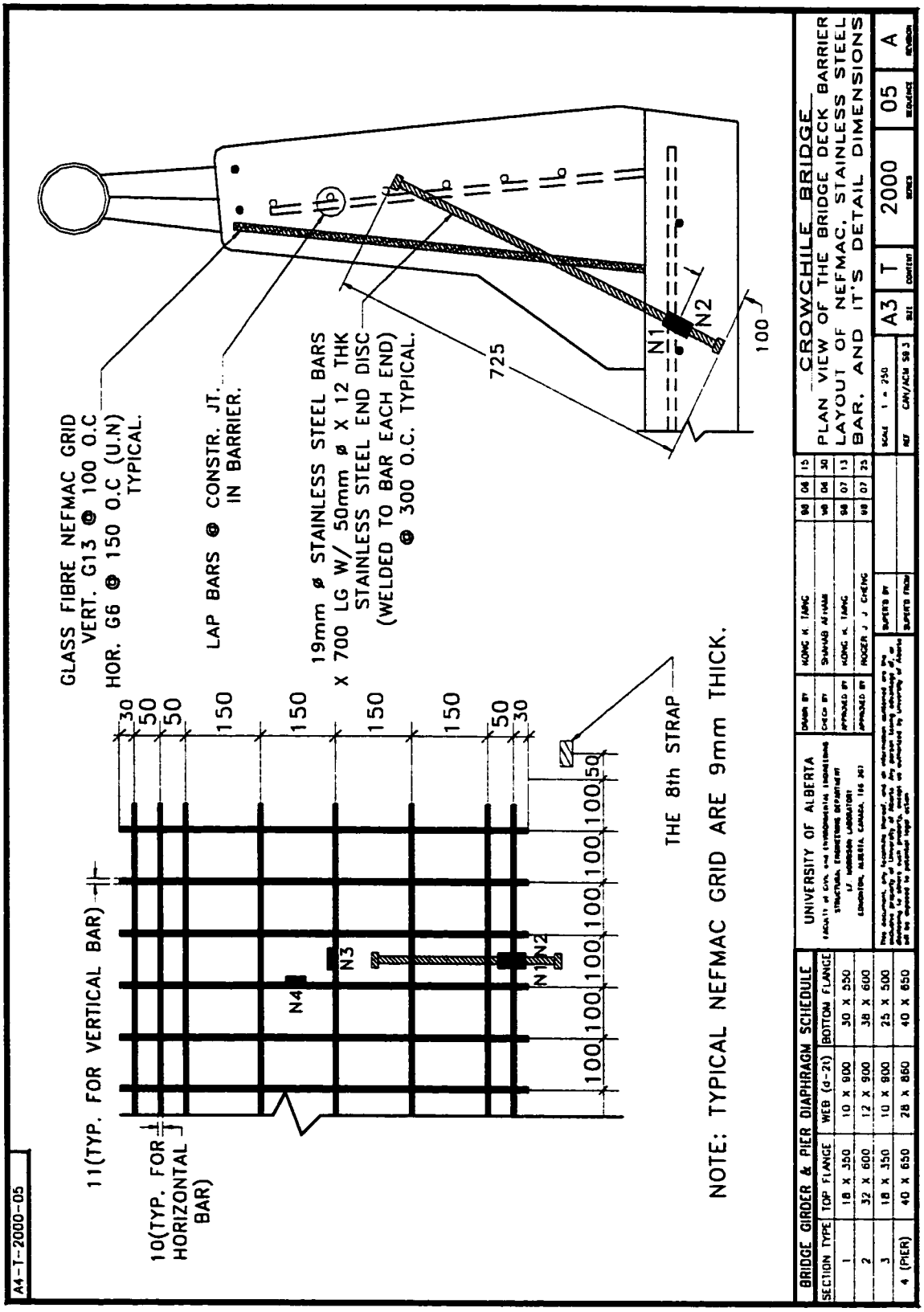

Figure A5: Bridge Deck Barrier

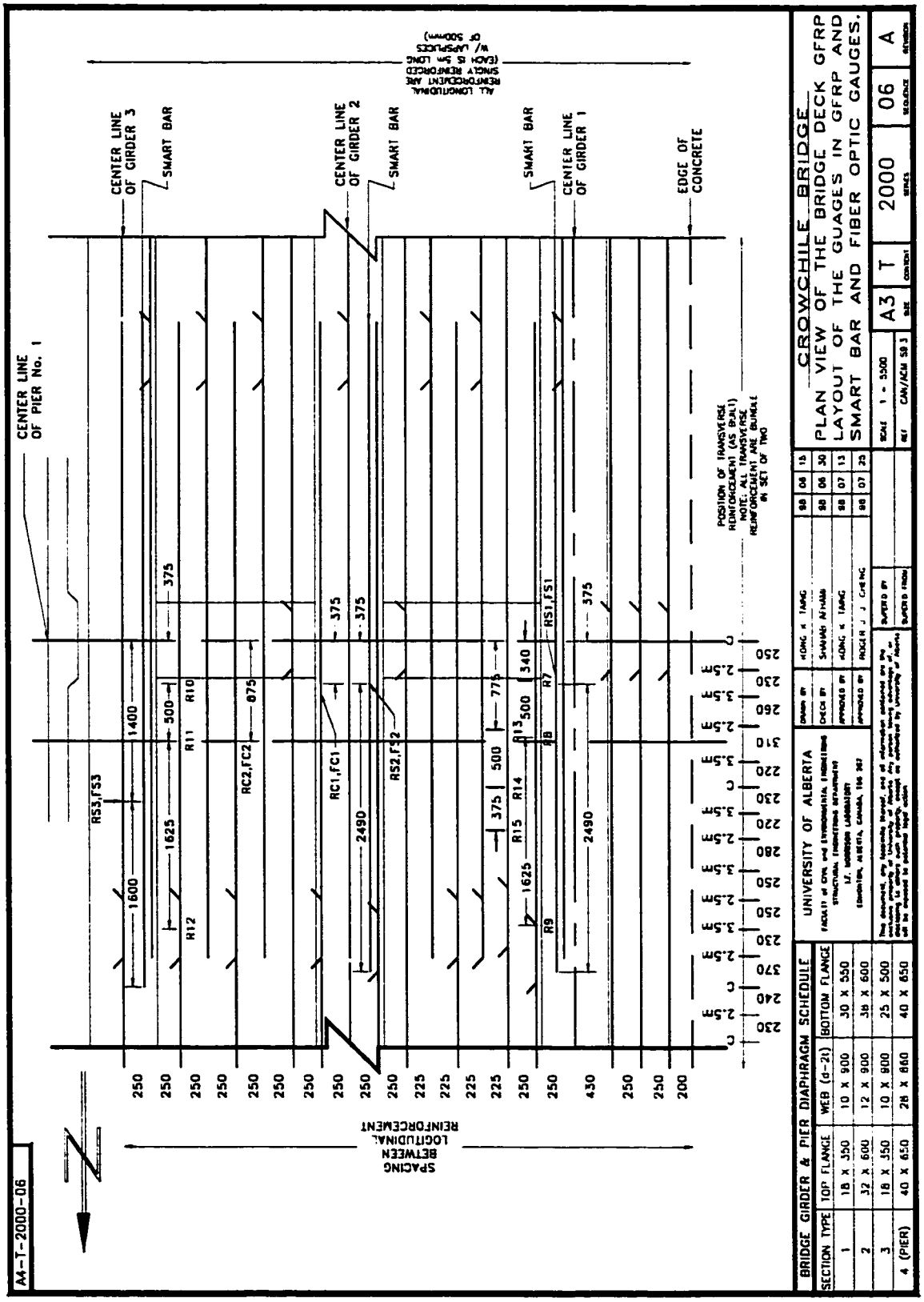

Figure A6: Layout of Gauges that are Embedded in Concrete

APPENDIX B

Table B1: Static Test of August '97, Strain Gauge Reading – by multiplexer

		truck positio	1	2	3	4	5	6	7	8	9	
	No Asphalt	**No Truck**										**No Truck**
Date	Aug. 11, 97	Aug. 13, 97	Aug. 14, 97	Aug. 14, 97	Aug. 14, 97	Aug. 14, 97	Aug. 14, 97	Aug. 14, 97	Aug. 14, 97	Aug. 14, 97	Aug. 14, 97	Aug. 14, 97
At the Beginning :												
Time	6 : 30 am	11 : 20 am	9 : 40 am	10 : 05 am	10 : 35 am	11 : 00 am	11 : 25 am	12 : 00	1 : 20 pm	1 : 45 pm	2 : 00 pm	2 : 25 pm
Standard	42	31	-22	-10	-14	-15	-19	-22	-12	-15	-18	-18
Temperature	14	21	23	21	22	23.5	25	24	23	22	23	24.5
TH1		19.7	18.2	18.9	19.3	20.1	21.6	22.7	22.7	22.8	22.9	23.6
TH2		17.9	18.1	18.2	18.4	18.6	19.1	19.9	21.4	21.5	21.6	21.8
TH3		17.8	18.1	18.2	18.4	18.8	19.4	19.8	20.8	21	21.1	21.5
TH4		17.9	17.4	17.9	18.2	18.8	20.1	21.3	22.7	22.8	22.9	23.4
TH5		21.3	18.1	19.4	20.9	22.5	24.4	24.8	22.8	23.2	23.8	25
G1	-94	-126	-146	-136	-136	-136	-126	-112	-101	-105	-96	-113
G2	-371	-443	-450	-439	-440	-421	-397	-381	-393	-374	-350	-415
G3	-601	-655	-639	-680	-667	-636	-601	-599	-663	-628	-579	-682
G4	-312	-313	-320	-312	-314	-304	-296	-285	-286	-284	-285	-287
G5	-425	-424	-450	-445	-439	-421	-402	-388	-408	-400	-387	-415
G6	-220	-203	-222	-213	-189	-159	-117	-107	-170	-150	-120	-172
G7	-930	-932	-936	-929	-926	-920	-914	-901	-896	-898	-898	-893
G8	-636		-640	-635	-631	-614	-599	-586	-614	-602	-595	-608
G9	-435	-423	-439	-432	-419	-381	-340	-333	-395	-379	-361	-388
G10	-118	-147	-153	-146	-142	-132	-122	-113	-112	-116	-116	-110
G11	325	314	300	306	319	341	368	375	341	345	343	340
G12	538	561	524	526	558	594	632	636	568	569	576	565
G13	247	228	227	221	232	244	249	258	269	262	258	270
G14	745	732	672	697	715	732	743	737	739	738	739	719
G15	471	443	355	394	359	467	511	521	492	485	484	496
G16	-1127	-1141	-1140	-1139	-1144	-1148	-1151	-1135	-1112	-1123	-1124	-1123
G17	-432	-484	-486	-480	-472	-475	-491	-475	-443	-448	-461	-452
G18	-188	-244	-274	-264	-240	-231	-247	-237	-210	-213	-237	-215
G19	-662	-666	-637	-634	-636	-637	-636	-626	-615	-623	-620	-616
G20	-369	-400	-408	-405	-391	-389	-402	-391	-363	-371	-377	-365
G21	140	106	68	75	108	122	103	114	138	135	123	145
G22	370	373	380	380	385	392	393	397	417	406	410	422

Table B1 Cont'd

G23		-442	-453	-478	-475	-458	-447	-461	-455	-433	-438	-437	-432
G24		-450	-538	-576	-572	-535	-512	-540	-533	-510	-511	-512	-496
G25			281	283	287	284	295	283	286	289	288	290	272
G26		532	507	501	505	521	529	519	530	550	546	545	547
G27		285	264	214	222	253	267	248	254	280	277	278	284
G28		306	296	306	312	314	324	324	339	351	343	342	344
G29		482	420	347	399	421	444	442	466	489	482	484	479
G30		206	127	23	60	48	125	131	148	188	184	187	196
G31		-41	-25	178	185	192	202	192	189	191	175	167	187
G32	TRBL						146	144	144	155	143	161	160
G33	TRBL						290	329	324	261	291	348	254
G34		-1027	-1014	-1035	-1004	-984	-917	-890	-890	-957	-917	-851	-948
T4		-468	-532	-562	-562	-545	-526	-509	-504	-525	-526	-531	-514
T1		214	274	245	248	255	269	279	299	286	279	274	302
T2		-392	-305	-321	-317	-308	-282	-251	-235	-270	-276	-253	-268
T3		-1115	-1036	-1063	-1060	-1056	-1037	-1006	-999	-1052	-1042	-1013	-1056
T4		-551	-562	-585	-583	-571	-543	-521	-510	-541	-544	-537	-527
T5		133	217	202	208	217	242	267	281	241	231	231	264
T6		155	243	219	227	232	245	275	283	233	232	219	269
T7		-1333	-1230	-1251	-1241	-1233	-1199	-1161	-1150	-1196	-1197	-1165	-1192
T8		-849	-772	-787	-782	-772	-740	-706	-697	-746	-743	-710	-738
T9		-1644	-1556	-1573	-1568	-1558	-1516	-1494	-1502	-1538	-1517	-1493	-1526
T10		-1306	-1254	-1274	-1269	-1250	-1209	-1208	-1232	-1233	-1199	-1191	-1225
T11		-977	-907	-932	-924	-901	-886	-901	-904	-888	-890	-899	-875
T12		-1044	-950	-1004	-997	-970	-955	-979	-975	-947	-951	-968	-955
T13		-352	-298	-321	-315	-286	-271	-299	-292	-260	-264	-288	-271
T14	TRBL	1580	1650						1616	1614	1605	1592	1592
T15		-174	-103	-117	-114	-117	-107	-112	-111	-92	-115	-102	-91
T16	TRBL	3700	3847						3842	3872	3854	3814	3903
T17		-620	-558	-583	-573	-547	-545	-566	-557	-522	-526	-550	-536
T18		-43	30	-5	12	17	21	25	29	38	28	23	41
R12		1493	1489	1474	1487	1462	1465	1484	1471	1472	1472	1464	1468
R13		1446	1477	1459	1452	1459	1469	1473	1462	1473	1466	1474	1460
R14		-305	-281	-299	-306	-307	-303	-286	-289	-284	-292	-282	-283
R15		669	700	696	698	694	703	711	707	714	706	715	718
R1		19	82	0	11	23	36	40	38	28	30	33	42
R2		-305	-292	-310	-300	-293	-283	-280	-280	-273	-276	-275	-273

Table B1 Cont'd

R3		199	205	164	177	187	187	184	187	174	193	197	180
R4		268	302	273	284	293	306	308	305	299	306	304	316
R5		-410	-384	-417	-401	-393	-387	-385	-386	-380	-380	-369	-370
R6	not reliable		3389	3274	3278	3277	3265	3250	3237	3235	3239	3239	3250
R7		1857	1900	1907	1912	1912	1926	1929	1920	1929	1926	1941	1915
R8		855	886	887	902	898	906	912	907	895	901	912	899
R9		-437	-398	-396	-388	-396	-392	-381	-377	-382	-395	-373	-376
R10	TRBL	1222	1336	1332					1345	1328			1333
R11	TRBL	660	691	672					684	679			680
RC1		164	264	266	308	313	338	274	278	258	244	205	218
RC2		-468	-514	-465	-527	-516	-513	-530	-535	-540	-536	-553	-517
E2		51	81	52	54	75	81	86	86	85	139	92	113
E3		-1411	-1388	-1409	-1405	-1384	-1375	-1370	-1363	-1363	-1341	-1355	-1335
E4		-2714	-2657	-2697	-2691	-2675	-2663	-2673	-2669	-2659	-2630	-2670	-2656
E5		-669	-652	-664	-660	-647	-640	-633	-632	-621	-604	-615	-611
E7		-1875	-1802	-1843	-1839	-1820	-1811	-1817	-1810	-1789	-1772	-1788	-1780
E8		-2215	-2206	-2224	-2221	-2202	-2192		-2159	-2194	-2171	-2194	-2180
E9		-2144	-2135	-2157	-2155	-2129	-2116	-2122	-2119	-2109	-2085	-2111	-2096
E10		673	681	658	663	684	689	690	690	706	724	704	717
E11		-1166	-1060	-1099	-1094	-1064	-1057	-1046	-1042	-1044	-1023	-1038	-1027
E12		-1538	-1519	-1533	-1532	-1507	-1501	-1499	-1497	-1496	-1473	-1488	-1482
E13		-857	-858	-882	-879	-854	-846	-828	-827	-809	-783	-795	-792
E14		-1498	-1411	-1453	-1445	-1422	-1415	-1402	-1398	-1393	-1399	-1394	-1380
E15		-2342	-2286	-2323	-2313	-2285	-2276	-2249	-2245	-2234	-2239	-2231	-2219
E16		-2801	-2794	-2838	-2829	-2810	-2801	-2782	-2786	-2768	-2757	-2756	-2757
E17		-1032	-922	-948	-943		-934	-909	-907	-895	-896	-889	-876
E18		-2738	-2675	-2706	-2699	-2685	-2678	-2674	-2672	-2664	-2667	-2664	-2651
E19		-2199	-2187	-2209	-2196	-2163	-2166	-2168	-2163	-2144	-2144	-2147	-2128
N1		6362	6588	6709	6707	6731	6741	6748	6752	6772	6772	6783	6782
N2		568	757	813	818	837	844	856	858	882	879	884	895
N3		911	914	909	906	914	893	868	873	937	916	891	953
N4		3117	3133	3125	3128	3156	3161	3156	3152	3159	3154	3160	3166
T4		-441	-426	-458	-453	-431	-415	-374	-376	-405	-402	-393	-386
S1		-519	-529	-545	-540	-541	-533	-532	-529	-520	-527	-522	-514
S2		-58	-66	-71	-63	-66	-54	-49	-46	-38	-42	-35	-28
S3		-462	-478	-494	-491	-493	-485	-488	-495	-476	-501	-491	-476

Table B1 Cont'd

S4	138	134	132	135	133	142	145	150	162	157	159	156
S5	-679	-678	-694	-690	-690	-683	-681	-681	-665	-669	-670	-664
S6	-648	-651	-652	-643	-644	-637	-636	-633	-626	-627	-624	-619
C1	-657	-641	-640	-631	-629	-606	-585	-582	-599	-601	-593	-595
C2	-173	-171	-180	-171	-175	-182	-200	-202	-156	-162	-165	-152
C3	-1114	-1118	-1120	-1114	-1115	-1110	-1108	-1110	-1097	-1101	-1100	-1094
C4	-911	-937	-942	-930	-934	-947	-977	-976	-920	-928	-938	-913
RS1	3450	3520	3541	3548	3545	3556	3575	3564	3580	3573	3577	3569
RS2	3062	3143	3155	3149	3170	3194	3186	3174	3192	3182	3188	3183
RS3	2517	2511	2545	2467	2450	2475	2472	2451	2467	2463	2444	2486
At the end :												
Time	7 : 30 am	12 : 10 pm	10 : 00 am	10 : 30 am	10 : 55 am	11 : 20 am	11 : 50 am	12 : 30 pm	1 : 40 pm	2 : 00 pm	2 : 20 pm	2 : 50 pm
Standard	1	-22	-10	29	-15	-19	-22	-19	-15	-18	-18	22
Temperature	15	22.5	21	21	23.5	25	24	23	22	23	24	25
TH1		21.1	18.8	19.3	20.1	21.3	22.6	22.9	22.7	22.9	23.3	24.1
TH2		18.6	18.2	18.4	18.6	19	19.8	20.3	21.4	21.6	21.7	22
TH3		18.5	18.2	18.4	18.8	19.3	19.8	20	20.8	21.1	21.3	21.6
TH4		19.1	17.7	18.2	18.8	19.9	21.2	21.9	22.8	22.9	23.2	23.7
TH5		22.9	19.2	20.7	22.5	24	25	24	23	23.8	24.8	25.2

Fiber optics										
9:15	9:40 am	10:27	10:53	11:20	11:30	11:50	1:15 pm	1:45	2:00	2:25
491	568	568	589	603	609	594	599	607	606	582
422	435	442	448	454	462	469	478	476	481	488
-91	-14	-14	7	21	27	12	17	25	24	0
-66	-53	-46	-40	-34	-26	-19	-10	-12	-7	0
0	77	77	98	112	118	103	108	116	115	91
0	13	20	26	32	40	47	56	54	59	66
-45.5	31.5	31.5	52.5	66.5	72.5	57.5	62.5	70.5	69.5	45.5
-33	-20	-13	-7	-1	7	14	23	21	26	33

Table B2: Strain Gauge Reading for Static Test, August '97—Before and After Asphalt

	No Asphalt	No Truck	No Truck
Date	Aug. 11, 97	Aug. 13, 97	Aug. 14, 97
At the Beginning :			
Time	6 : 30 am	11 : 20 am	2 : 25 pm
Standard	42	31	-18
Temperature	14.5	21	24.5
TH1		19.7	23.6
TH2		17.9	21.8
TH3		17.8	21.5
TH4		17.9	23.4
TH5		21.3	25
G1	-94	-126	-113
G2	-371	-443	-415
G3	-601	-655	-682
G4	-312	-313	-287
G5	-425	-424	-415
G6	-220	-203	-172
G7	-930	-932	-893
G8	-636		-608
G9	-435	-423	-388
G10	-118	-147	-110
G11	325	314	340
G12	538	561	565
G13	247	228	270
G14	745	732	719
G15	471	443	496
G16	-1127	-1141	-1123
G17	-432	-484	-452
G18	-188	-244	-215
G19	-662	-666	-616
G20	-369	-400	-365
G21	140	106	145
G22	370	373	422
G23	-442	-453	-432
G24	-450	-538	-496
G25		281	272
G26	532	507	547
G27	285	264	284
G28	306	296	344
G29	482	420	479
G30	206	127	196
G31	-41	-25	187
G32			160
G33			254
G34	-1027	-1014	-948
T4	-468	-532	-514
T1	214	274	302
T2	-392	-305	-268
T3	-1115	-1036	-1056
T4	-551	-562	-527
T5	133	217	264
T6	155	243	269
T7	-1333	-1230	-1192

Thermal effect	Date	Aug. 11, 97	Aug. 13	Aug. 14, 97
	Avg Temp.	14.75	21.75	24.75

	Asphalt & Temp. With respect to Aug. 13, 97	Aug. 14, 97		Asphalt only
ΔT =	3	ΔT = 7	ΔT = 10		
G1	13	-32	-19	G1	-62
G2	28	-72	-44	G2	-137
G3	-27	-54	-81	G3	9
G4	26	-1	25	G4	-62
G5	9	1	10	G5	-20
G6	31	17	48	G6	-55
G7	39	-2	37	G7	-93
G8			28	G8	
G9	35	12	47	G9	-70
G10	37	-29	8	G10	-115
G11	26	-11	15	G11	-72
G12	4	23	27	G12	14
G13	42	-19	23	G13	-117
G14	-13	-13	-26	G14	17
G15	53	-28	25	G15	-152
G16	18	-14	4	G16	-56
G17	32	-52	-20	G17	-127
G18	29	-56	-27	G18	-124
G19	50	-4	46	G19	-121
G20	35	-31	4	G20	-113
G21	39	-34	5	G21	-125
G22	49	3	52	G22	-111
G23	21	-11	10	G23	-60
G24	42	-88	-46	G24	-186
G25	-9			G25	
G26	40	-25	15	G26	-118
G27	20	-21	-1	G27	-68
G28	48	-10	38	G28	-122
G29	59	-62	-3	G29	-200
G30	69	-79	-10	G30	-240
G31	212	16	228	G31	-479
G32				G32	
G33				G33	
G34	66	13	79	G34	-141
T4	18	-64	-46	T4	-106
					0
T1	28	60	88	T1	-5
T2	37	87	124	T2	1
T3	-20	79	59	T3	126
T4	35	-11	24	T4	-93
T5	47	84	131	T5	-26
T6	26	88	114	T6	27
T7	38	103	141	T7	14

Table B2 Cont'd

T8	-849	-772	-738	34	77	111	T8	-2
T9	-1644	-1556	-1526	30	88	118	T9	18
T10	-1306	-1254	-1225	29	52	81	T10	-16
T11	-977	-907	-875	32	70	102	T11	-5
T12	-1044	-950	-955	-5	94	89	T12	106
T13	-352	-298	-271	27	54	81	T13	-9
T14	1580	1650	1592	-58	70	12	T14	205
T15	-174	-103	-91	12	71	83	T15	43
T16	3700	3847	3903	56	147	203	T16	16
T17	-620	-558	-536	22	62	84	T17	11
T18	-43	30	41	11	73	84	T18	47
R12	1493	1489	1468	-21	-4	-25	R12	45
R13	1446	1477	1460	-17	31	14	R13	71
R14	-305	-281	-283	-2	24	22	R14	29
R15	669	700	718	18	31	49	R15	-11
R1	19	82	42	-40	63	23	R1	156
R2	-305	-292	-273	19	13	32	R2	-31
R3	199	205	180	-25	6	-19	R3	64
R4	268	302	316	14	34	48	R4	1
R5	-410	-384	-370	14	26	40	R5	-7
R6 not reliable		3389	3250	-139			R6 not reliable	
R7	1857	1900	1915	15	43	58	R7	8
R8	855	886	899	13	31	44	R8	1
R9	-437	-398	-376	22	39	61	R9	-12
R10	1222	1336	1333	-3	114	111	R10	121
R11	660	691	680	-11	31	20	R11	57
RC1	164	264	218	-46	100	54	RC1	207
RC2	-468	-514	-517	-3	-46	-49	RC2	-39
								0
E2	51	81	113	32	30	62	E2	-45
E3	-1411	-1388	-1335	53	23	76	E3	-101
E4	-2714	-2657	-2656	1	57	58	E4	55
E5	-669	-652	-611	41	17	58	E5	-79
E7	-1875	-1802	-1780	22	73	95	E7	22
E8	-2215	-2206			9		E8	
E9	-2144	-2135	-2096	39	9	48	E9	-82
E10	673	681	717	36	8	44	E10	-76
E11	-1166	-1060	-1027	33	106	139	E11	29
E12	-1538	-1519	-1482	37	19	56	E12	-67
E13	-857	-858	-792	66	-1	65	E13	-155
E14	-1498	-1411	-1380	31	87	118	E14	15
E15	-2342	-2286	-2219	67	56	123	E15	-100
E16	-2801	-2794	-2757	37	7	44	E16	-79
E17	-1032	-922	-876	46	110	156	E17	3
E18	-2738	-2675	-2651	24	63	87	E18	7
E19	-2199	-2187	-2128	59	12	71	E19	-126
N1	6362	6588	6782	194	226	420	N1	-227
N2	568	757	895	138	189	327	N2	-133
N3	911	914	953	39	3	42	N3	-88
N4	3117	3133	3166	33	16	49	N4	-61
T4	-441	-426	-386	40	15	55	T4	-78
S1	-519	-529	-514	15	-10	5	S1	-45
S2	-58	-66	-28	38	-8	30	S2	-97
S3	-462	-478	-476	2	-16	-14	S3	-21
S4	138	134	156	22	-4	18	S4	-55
S5	-679	-678	-664	14	1	15	S5	-32

Table B2 Cont'd

S6	-648	-651	-619	32	-3	29	S6	-78
C1	-657	-641	-595	46	16	62	C1	-91
C2	-173	-171	-152	19	2	21	C2	-42
C3	-1114	-1118	-1094	24	-4	20	C3	-60
C4	-911	-937	-913	24	-26	-2	C4	-82
RS1	3450	3520	3569	49	70	119	RS1	-44
RS2	3062	3143	3183	40	81	121	RS2	-12
RS3	2517	2511	2486	-25	-6	-31	RS3	52
At the end :				23.63918				
Time	7 : 30 am	12 : 10 pm	2 : 50 pm					
Standard	1	-22	22					
Temperature	15	22.5	25					
TH1		21.1	24.1					
TH2		18.6	22					
TH3		18.5	21.6					
TH4		19.1	23.7					
TH5		22.9	25.2					

Table B3: Static Test, August '97, Survey Reading—Raw Data

	No truck	P1	P2	P3	P4	P5	P6	P7	P8	P9	No truck
a1	1068	1068	1068	1067	1062	1060	1062	1068	1067	1067	1067
a2	1012	1013	1013	1012	1007	1004	1007	1012	1011	1010	1012
a3	955	957	957	953	951	948	948	954	953	952	953
a4	911	912	912	908	907	903	903	909	907	905	908
a5	847	848	848	847	842	839	840	845	842	839	845
b1	2501	2502	2502	2497	2492	2487	2488	2498	2498	2498	2498
b2	2440	2442	2442	2437	2431	2427	2427	2438	2437	2436	2438
b3	2382	2383	2383	2378	2372	2368	2368	2378	2375	2374	2379
b4	2330	2332	2331	2326	2318	2315	2315	2325	2321	2318	2327
b5	2268	2272	2271	2266	2259	2256	2257	2265	2258	2254	2266
c1	2474	2477	2476	2468	2462	2458	2461	2472	2472	2472	2472
c2	2411	2413	2412	2407	2398	2393	2396	2408	2406	2405	2408
c3	2351	2353	2353	2347	2338	2335	2337	2348	2344	2342	2348
c4	2295	2298	2298	2292	2284	2279	2282	2292	2286	2282	2292
c5	2232	2237	2236	2232	2223	2218	2218	2230	2221	2217	2229
d1	2444	2447	2446	2438	2433	2431	2432	2442	2442	2442	2442
d2	2382	2387	2385	2378	2372	2368	2371	2379	2378	2378	2380
d3	2320	2324	2323	2317	2310	2306	2308	2318	2313	2313	2318
d4	2263	2268	2268	2261	2253	2250	2252	2261	2255	2253	2261
d5	2202	2207	2206	2200	2193	2192	2192	2198	2192	2189	2198
e1	2393	2397	2395	2391	2387	2385	2387	2393	2392	2392	2393
e2	2337	2339	2338	2333	2330	2328	2330	2336	2334	2333	2335
e3	2273	2277	2276	2272	2266	2265	2266	2272	2269	2268	2272
e4	2219	2222	2222	2217	2212	2212	2212	2217	2213	2212	2217
e5	2156	2159	2158	2154	2150	2148	2150	2153	2148	2148	2153

Table B4: Static Test, August '97, Reduce Survey Data

	No truck	P1	P2	P3	P4	P5	P6	P7	P8	P9	No truck
A1	1	1	1	-1	-6	-8	-6	1	-1	-1	-1
A2	0	1	1	0	-5	-8	-5	0	-1	-2	0
A3	1	3	3	-1	-3	-6	-6	0	-1	-2	-1
A4	2	3	3	-2	-3	-7	-7	-1	-3	-5	-2
A5	1	2	2	1	-4	-7	-6	-1	-4	-7	-1
B1	2	3	3	-3	-8	-13	-12	-2	-2	-2	-2
B2	1	3	3	-2	-8	-12	-12	-1	-2	-3	-1
B3	2	3	3	-3	-9	-13	-13	-3	-6	-7	-2
B4	2	4	3	-3	-11	-14	-14	-4	-8	-11	-2
B5	1	5	4	-1	-8	-11	-10	-2	-9	-13	-1
C1	1	4	3	-5	-11	-15.0	-12	-1	-1.0	-1.0	-1
C2	2	4	3	-3	-12	-16.5	-14	-2	-3.5	-4.5	-2
C3	2	4	4	-3	-12	-14.5	-13	-2	-5.5	-7.5	-2
C4	2	5	5	-2	-10	-14.5	-12	-2	-7.5	-11.5	-2
C5	2	6.5	6	2	-8	-12.5	-13	-1	-9.5	-13.5	-2
D1	1	4	3	-5	-10	-12	-11	-1	-1	-1	-1
D2	1	6	4	-3	-9	-13	-10	-2	-3	-3	-1
D3	1	5	4	-2	-9	-13	-11	-1	-6	-6	-1
D4	1	6	6	-1	-9	-12	-10	-1	-7	-9	-1
D5	2	7.0	6	0	-7	-8	-8	-2	-8	-11	-2
E1	0	4	2	-2	-6	-8	-6	0	-1	-1	0
E2	1	3	2	-3	-6	-8	-6	0	-2	-3	-1
E3	1	5	4	-1	-7	-8	-7	-1	-4	-5	-1
E4	1	4	4	-1	-6	-6	-6	-1	-5	-6	-1
E5	2	5	4	-1	-5	-7	-5	-2	-7	-7	-2
Max	2	7	6	2	-3	-6	-5	1	-1	-1	0
Min	0	1	1	-5	-12	-17	-14	-4	-10	-14	-2

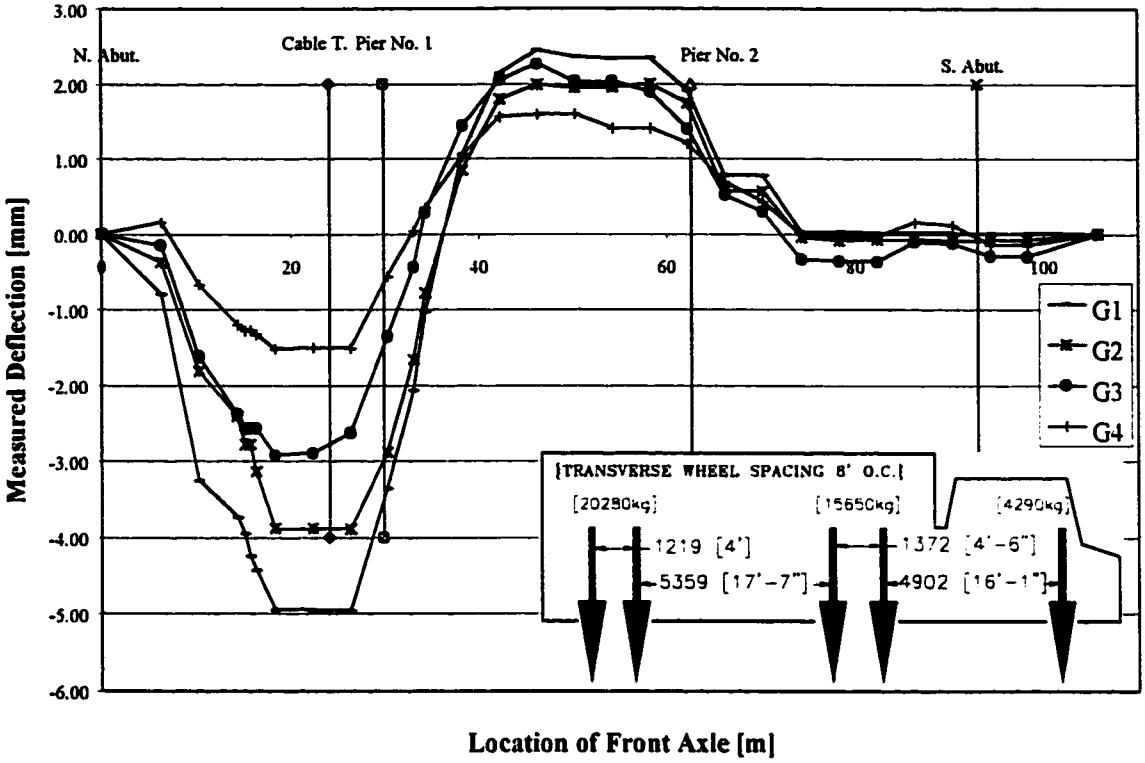

Figure B1: Static Load Test, August '98 for Cable Transducer at Strap #21

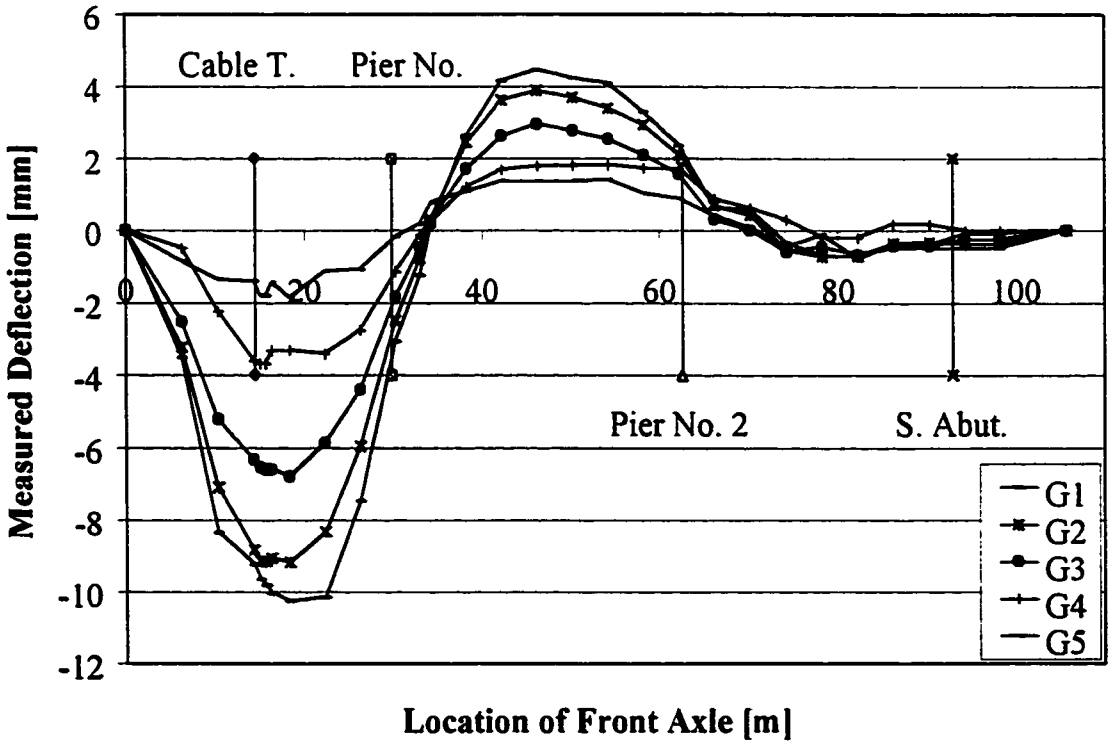

Figure B2: Static Load Test, August '98 for Cable Transducer at Strap #13

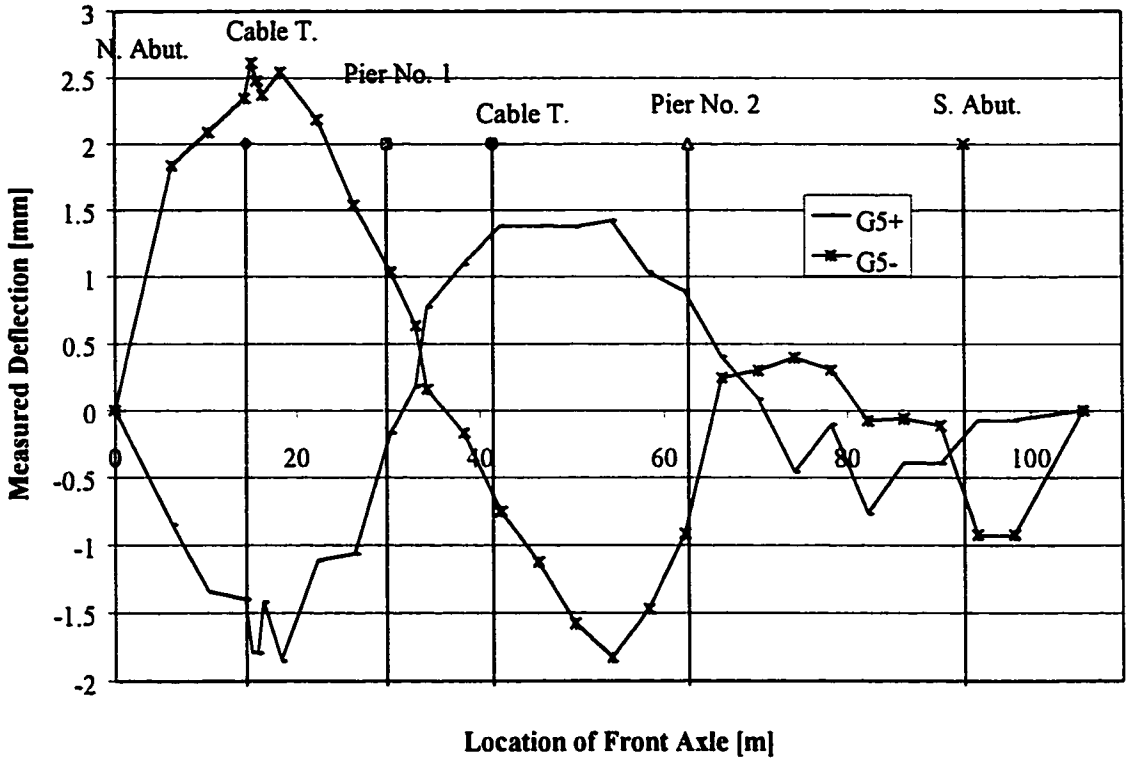

Figure B3: Static Load Test, August '98 for Two Cable Transducers for Girder 5 in the Positive and Negative Moment Region.

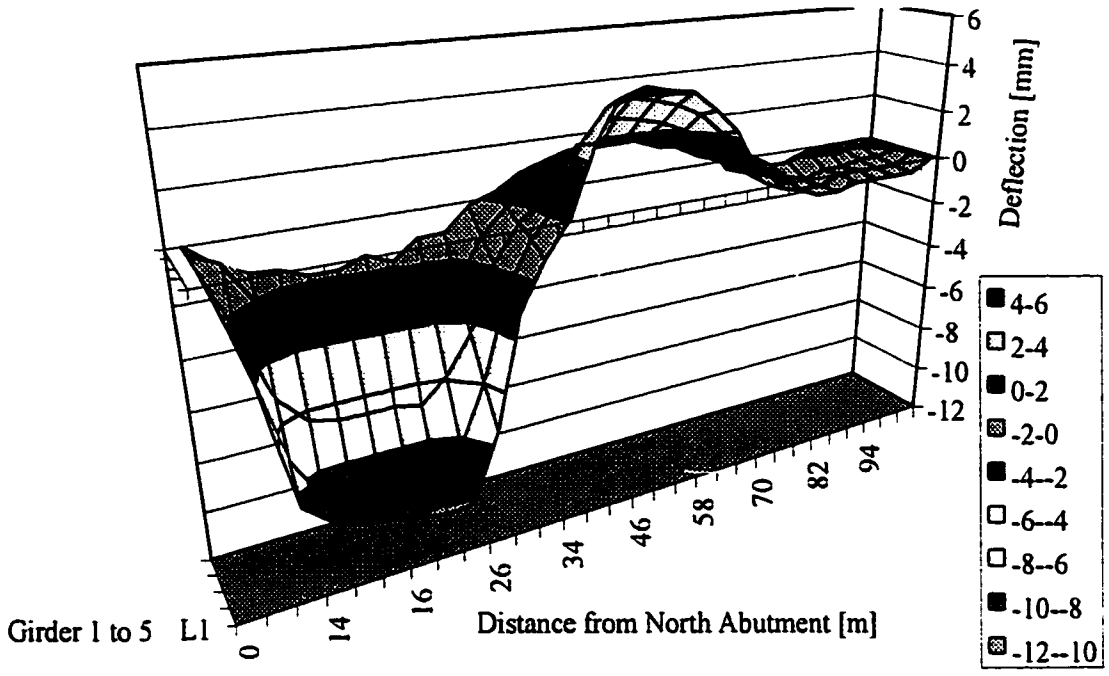

Figure B4: Static Load Test, August '98 from Cable Transducers at Strap #13—3D Plot

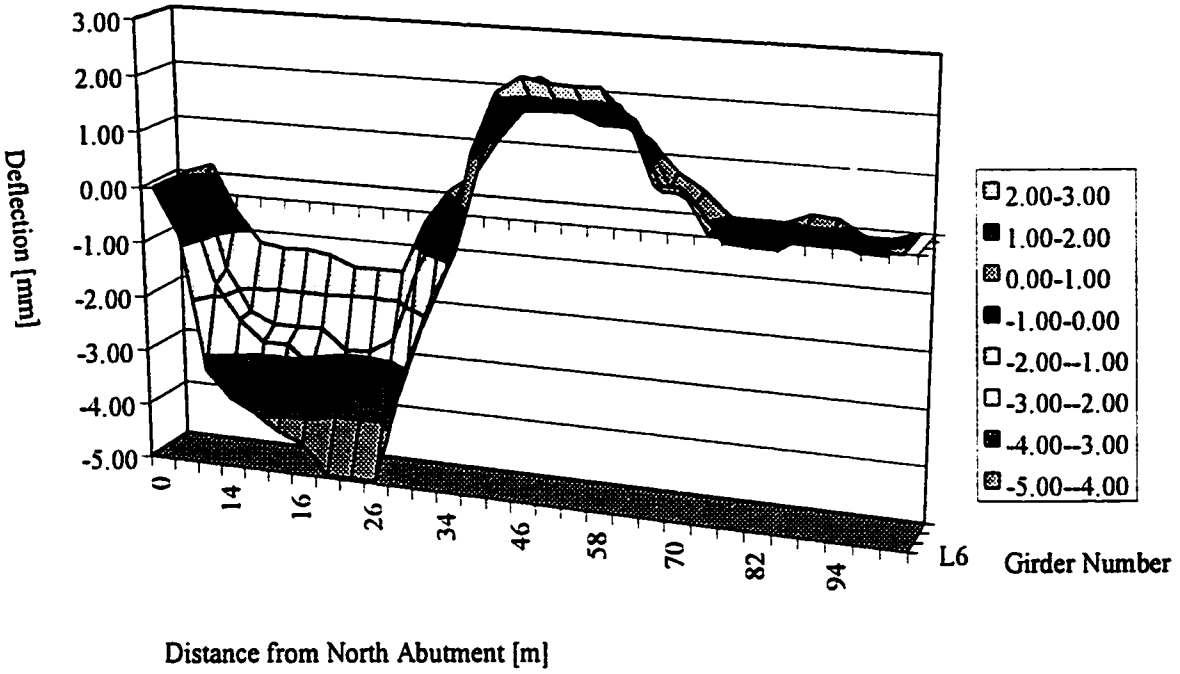

Figure B5: Static Load Test, August '98 from Cable Transducers at Strap #21—3D Plot

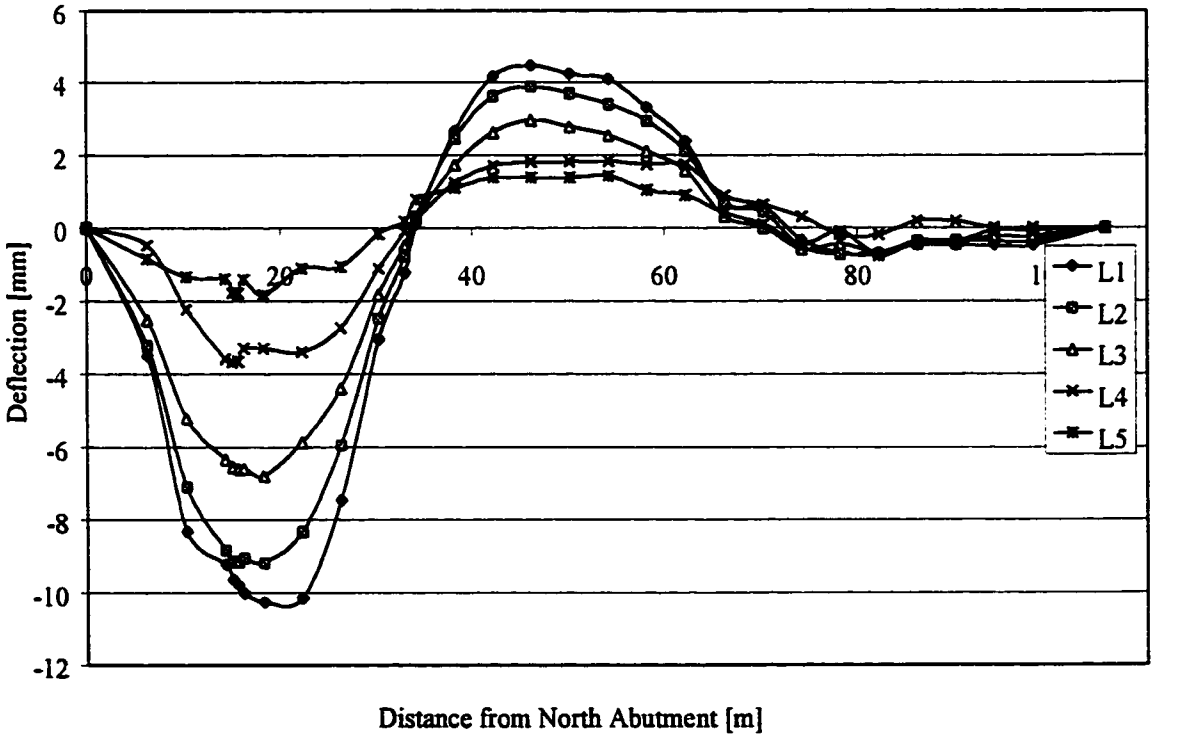

Figure B6: Static Load Test, August '98 from Cable Transducers at Strap #13

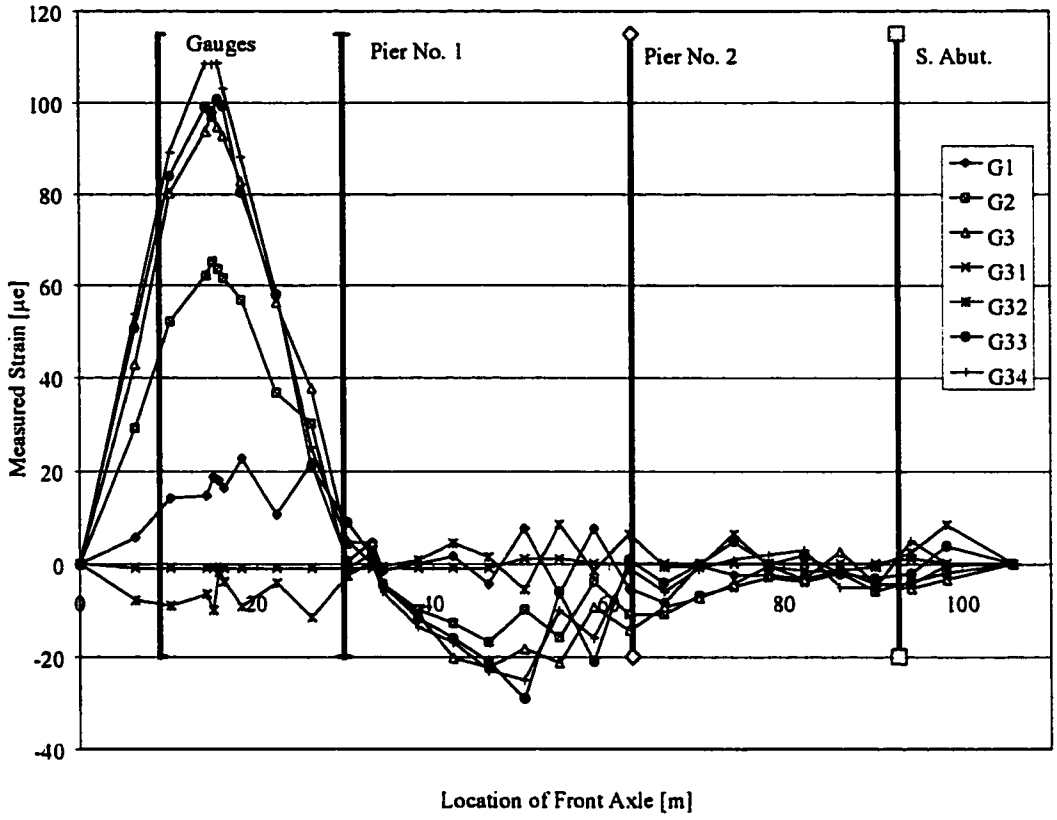

Figure B7: Static Load Test, August '98 for Girder 1 in Positive Moment Region

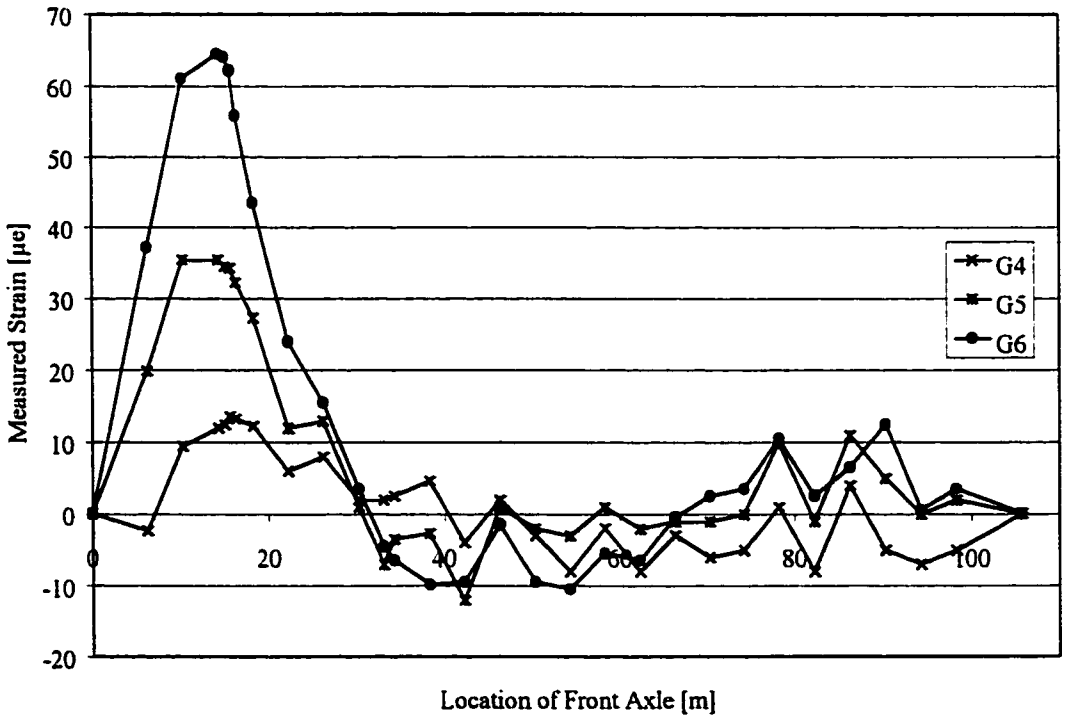

Figure B8: Static Load Test, August '98 for Girder 2 in Positive Moment Region

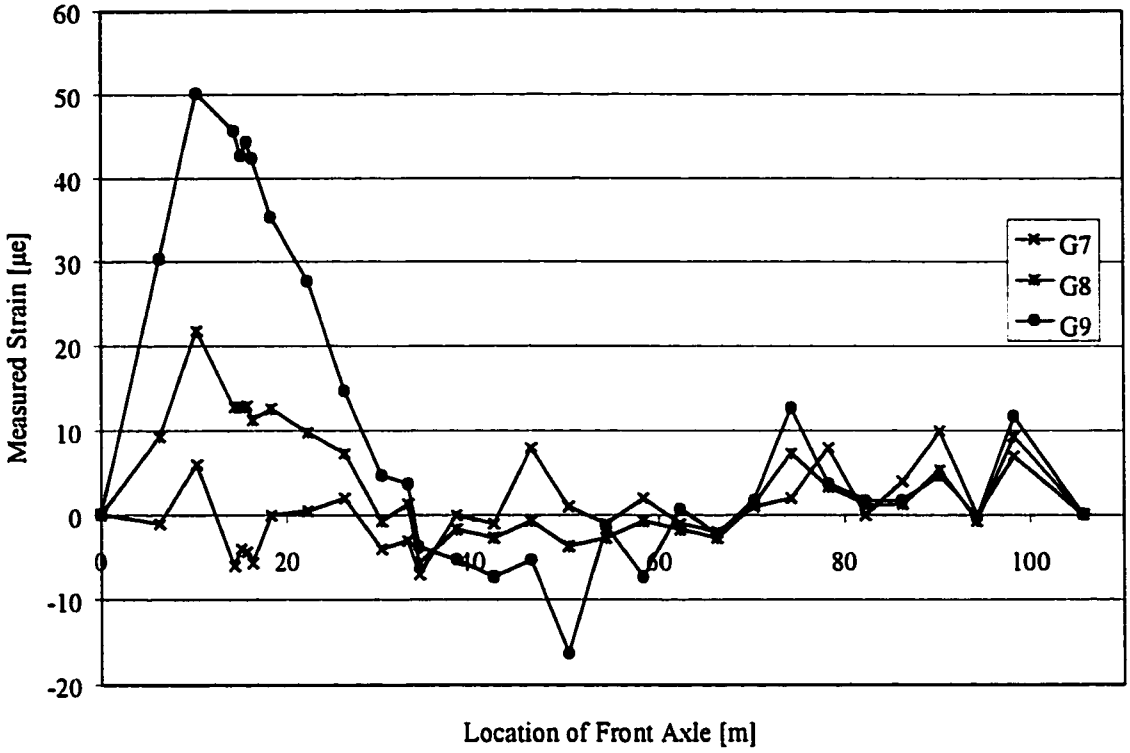

Figure B9: Static Load Test, August '98 for Girder 3 in Positive Moment Region

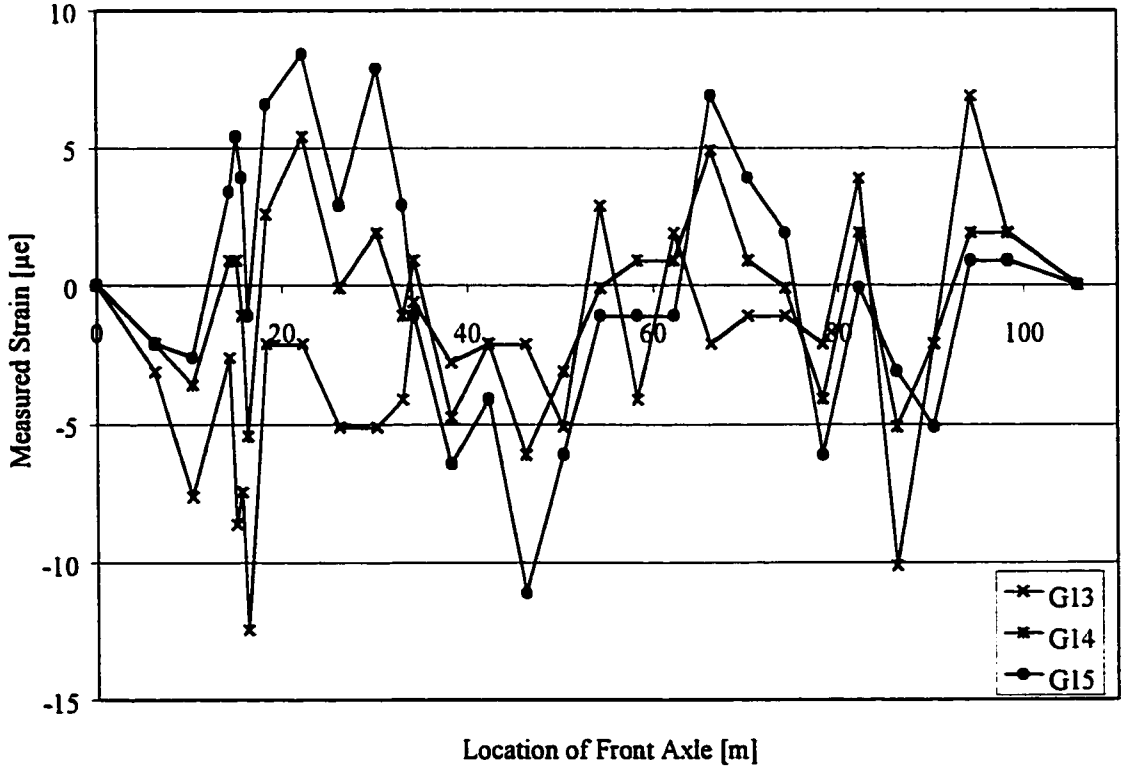

Figure B10: Static Load Test, August '98 for Girder 5 in Positive Moment Region

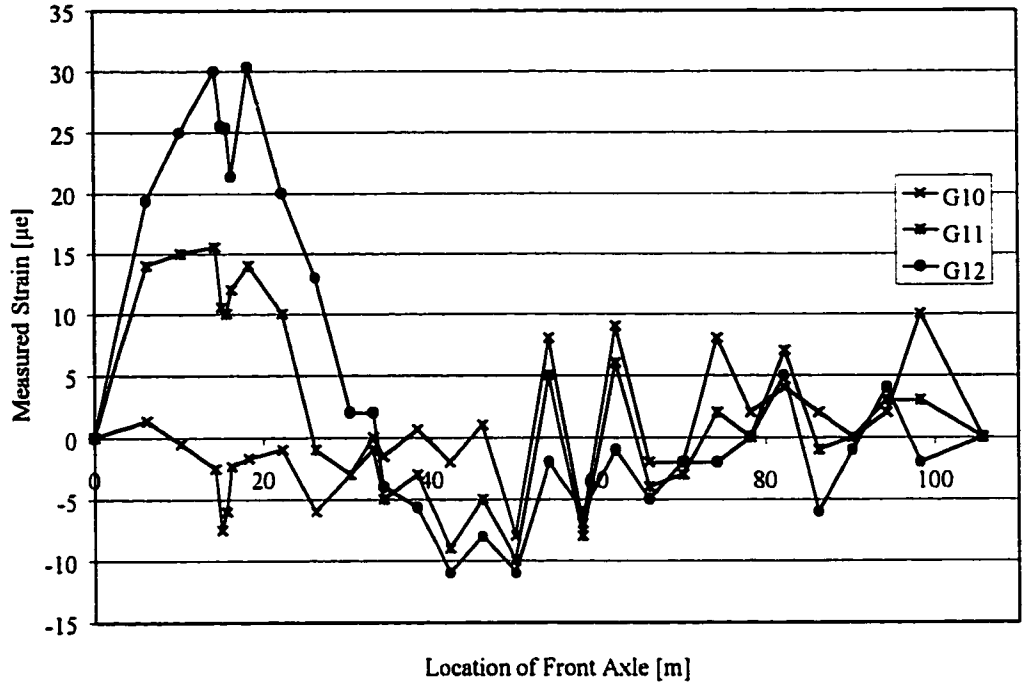

Figure B11: Static Load Test, August '98 for Girder 4 in Positive Moment Region

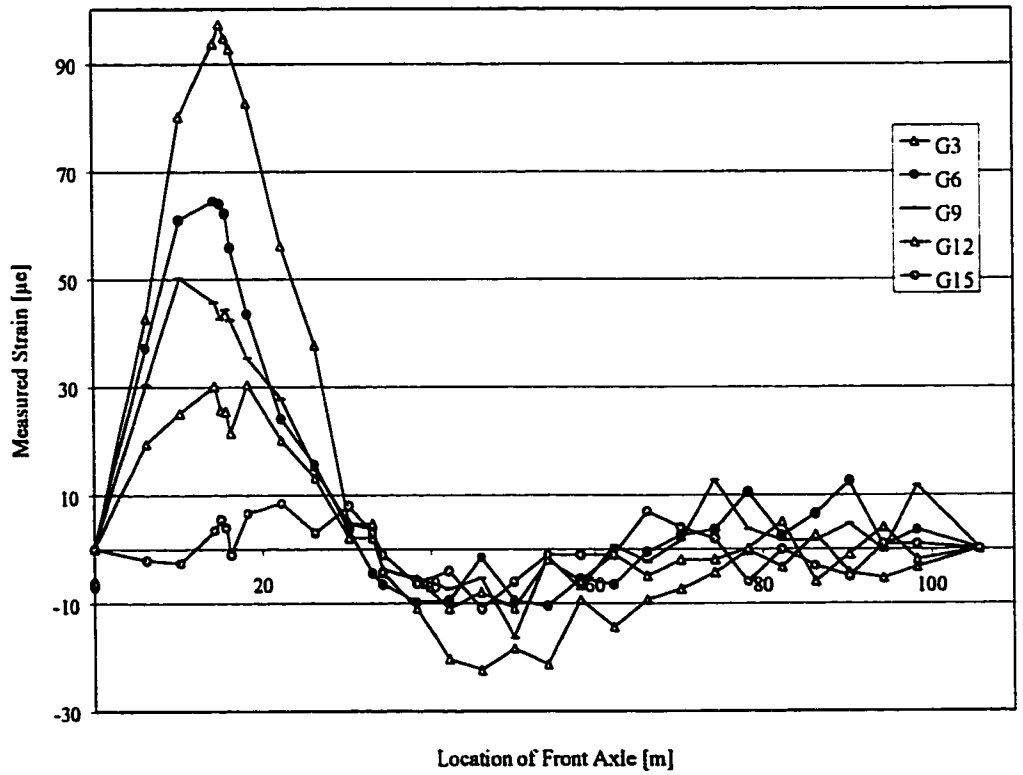

Figure B12: Static Load Test, August '98 for all Bottom Gauges in Positive Moment Region

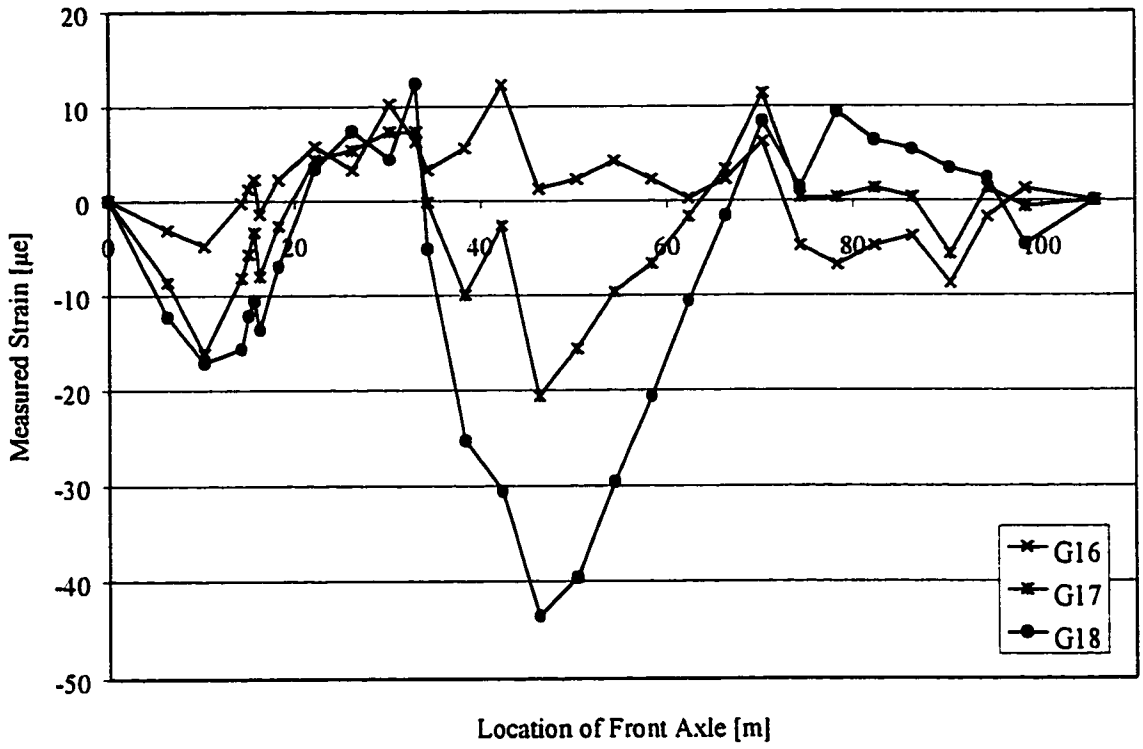

Figure B13: Static Load Test, August '98 for Girder 1 in Negative Moment Region

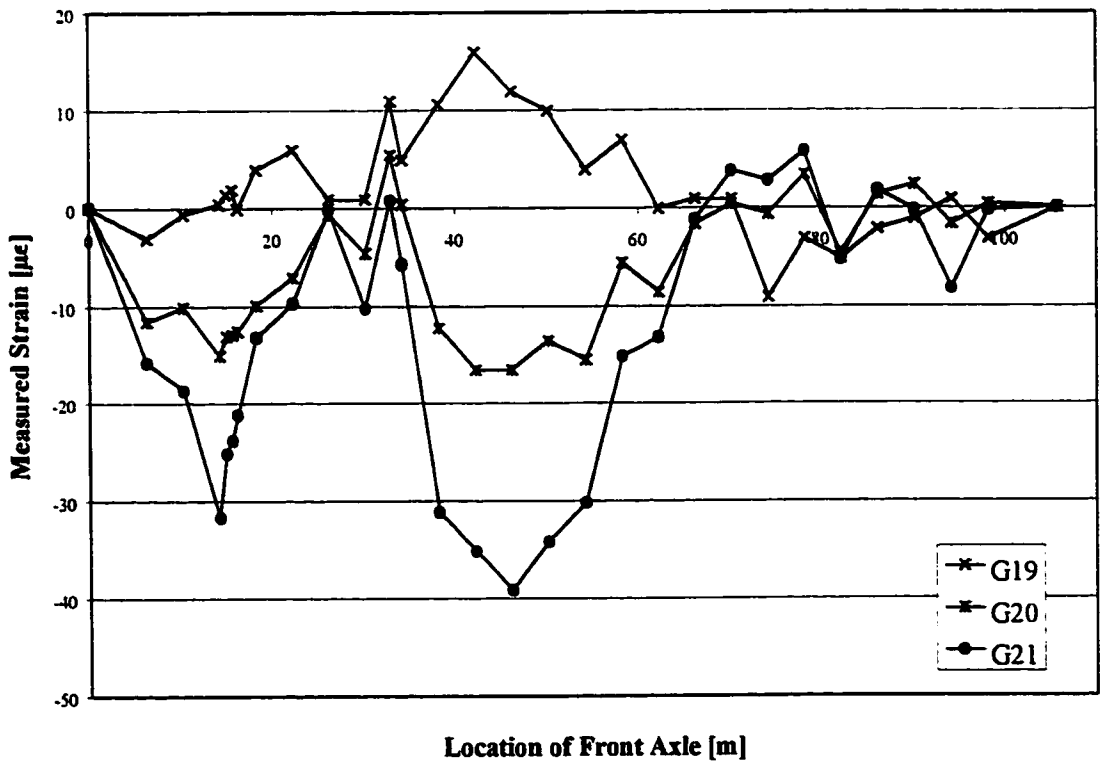

Figure B14: Static Load Test, August '98 for Girder 2 in Negative Moment Region

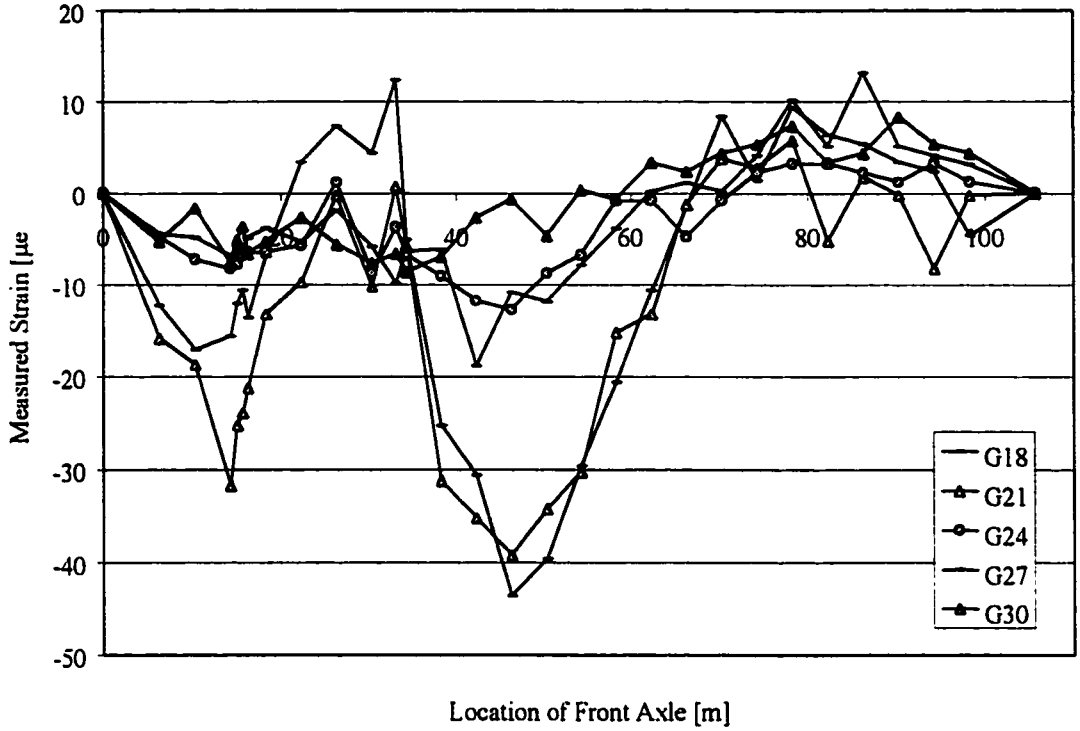

Figure B15: Static Load Test, August '98 for all Bottom Gauges in Negative Moment Region

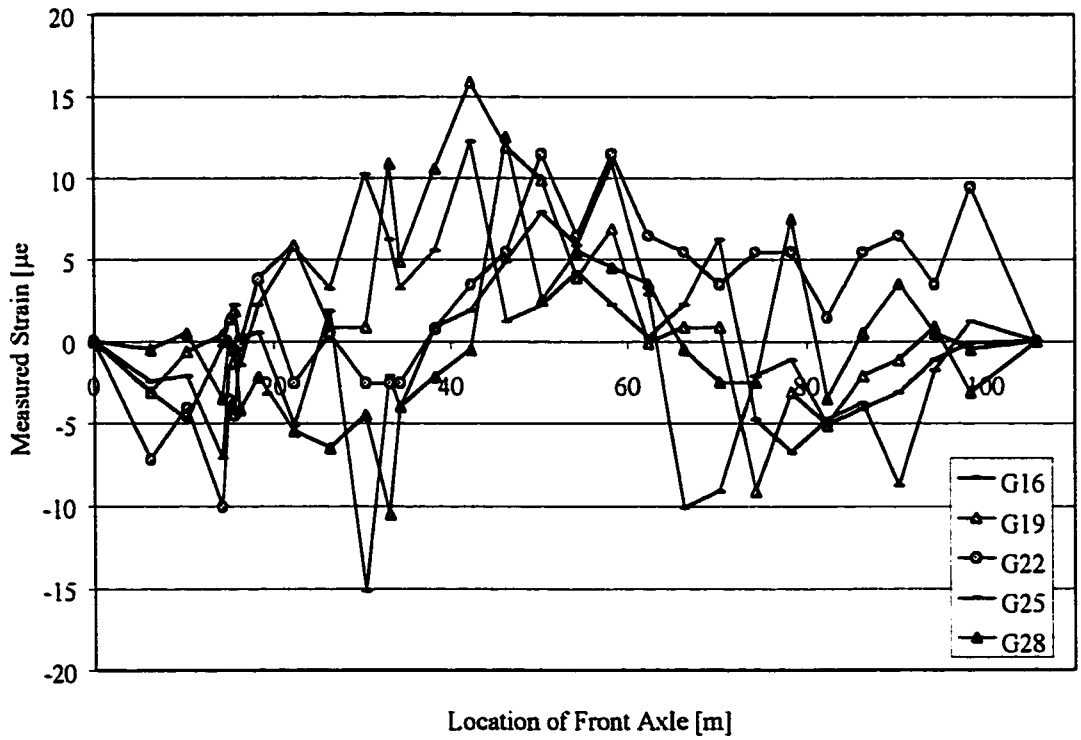

Figure B16: Static Load Test, August '98 for Top Gauges in Negative Moment Region

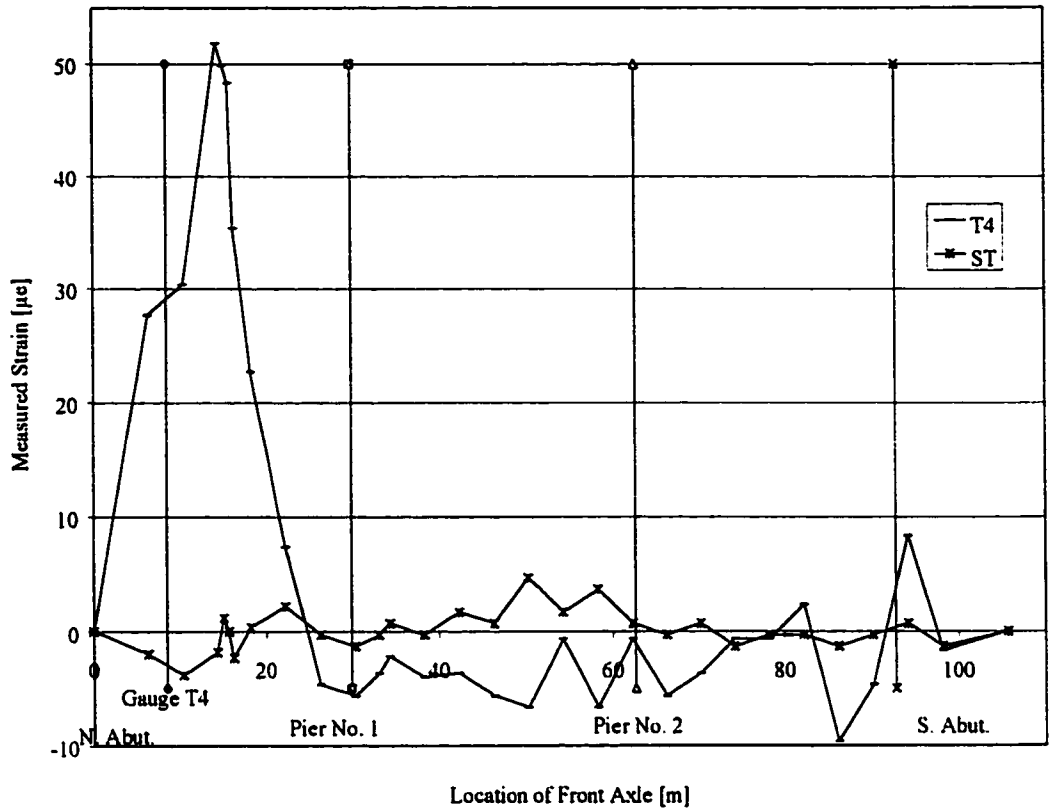

Figure B17: Static Load Test, August '98 for T4 & ST Gauges

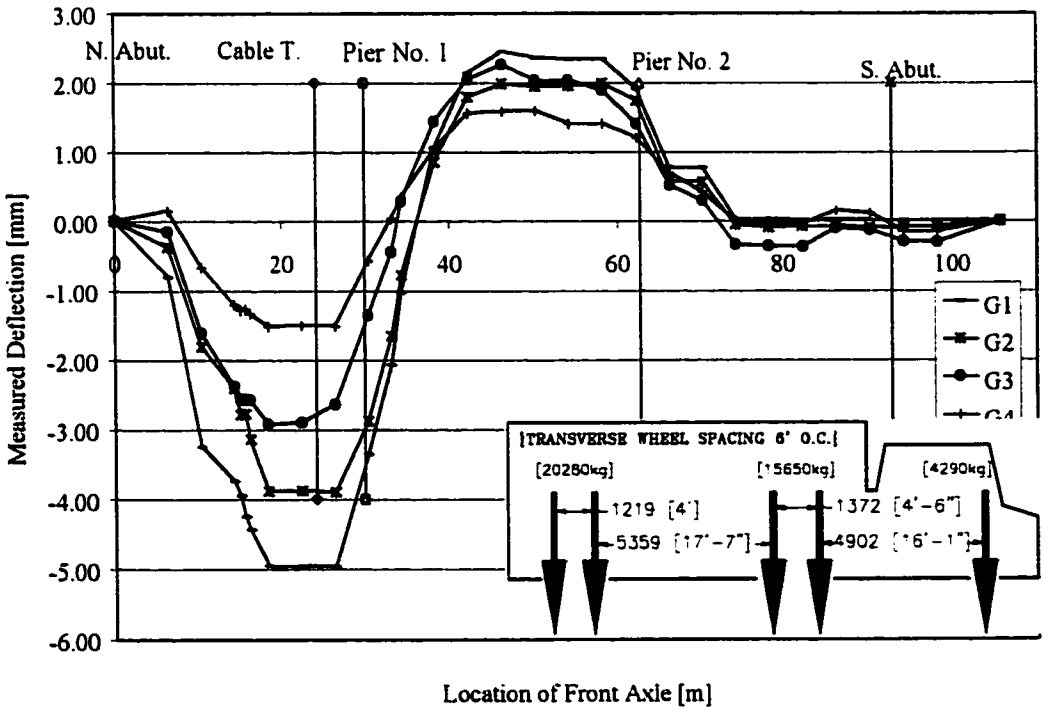

Figure B18: Static Load Test, August '98 for All Cable Transducers at Strap #21

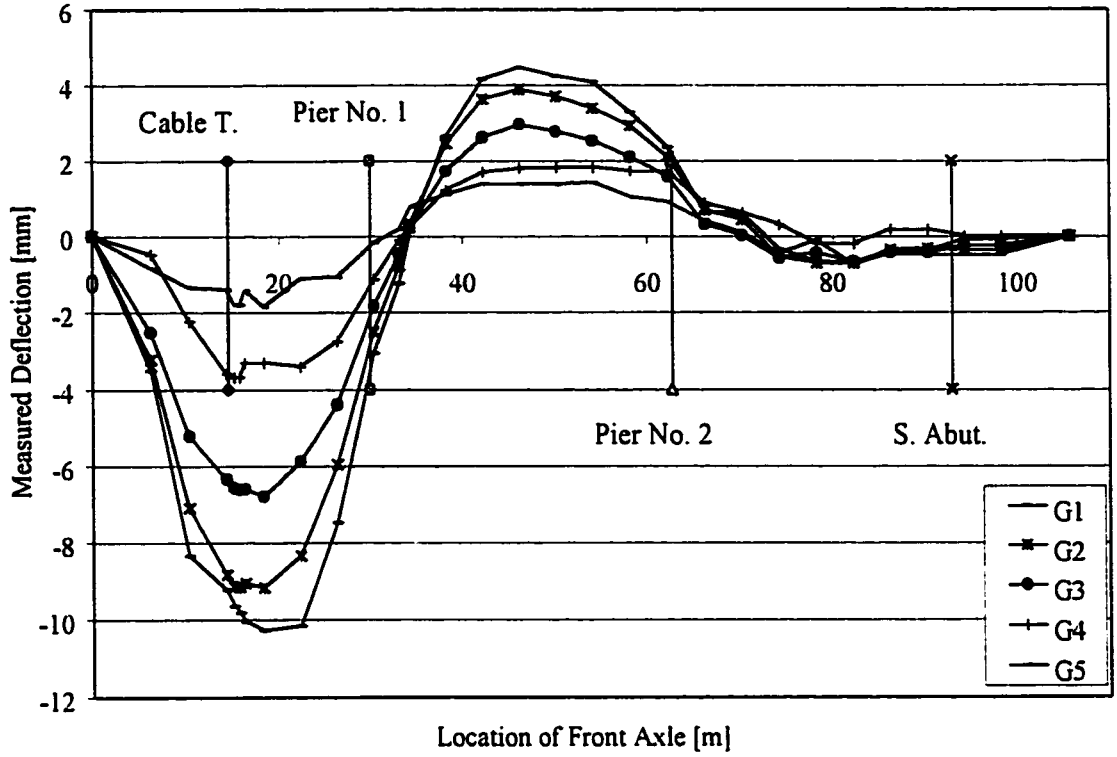

Figure B19: Static Load Test, August '98 for Cable Transducers at Strap #13

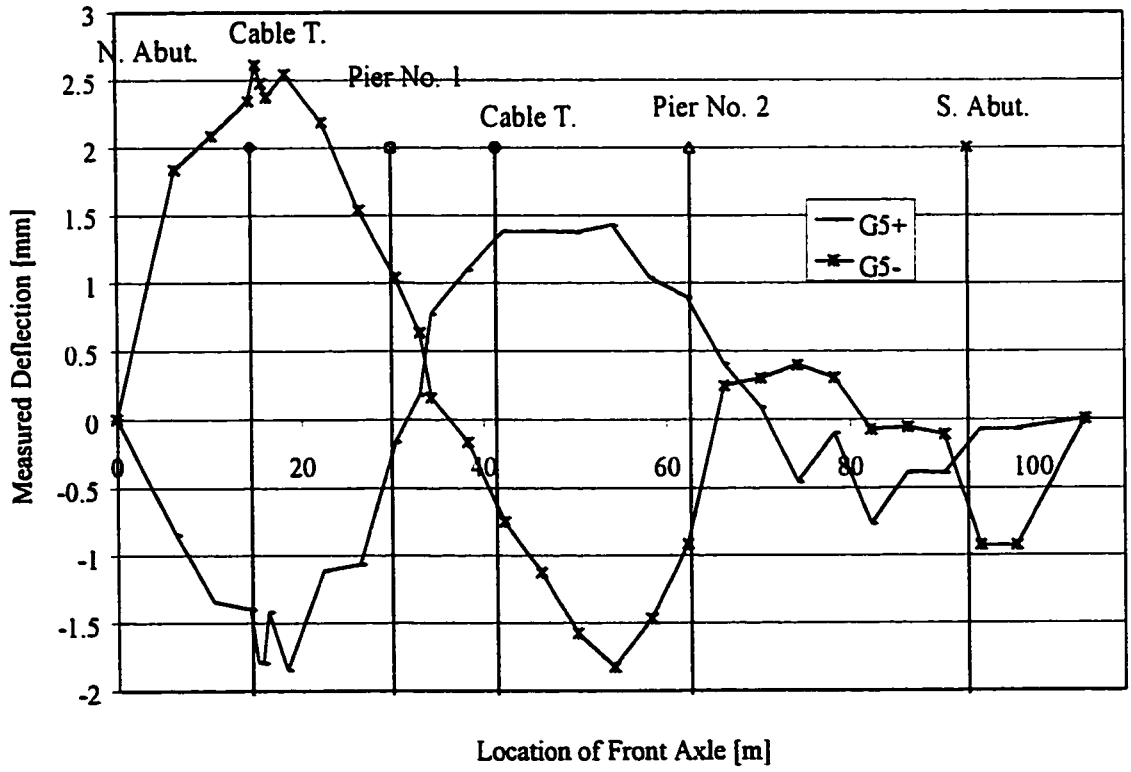

Figure B20: Static Load Test, August '98 for Cable Transducers on Girder 5

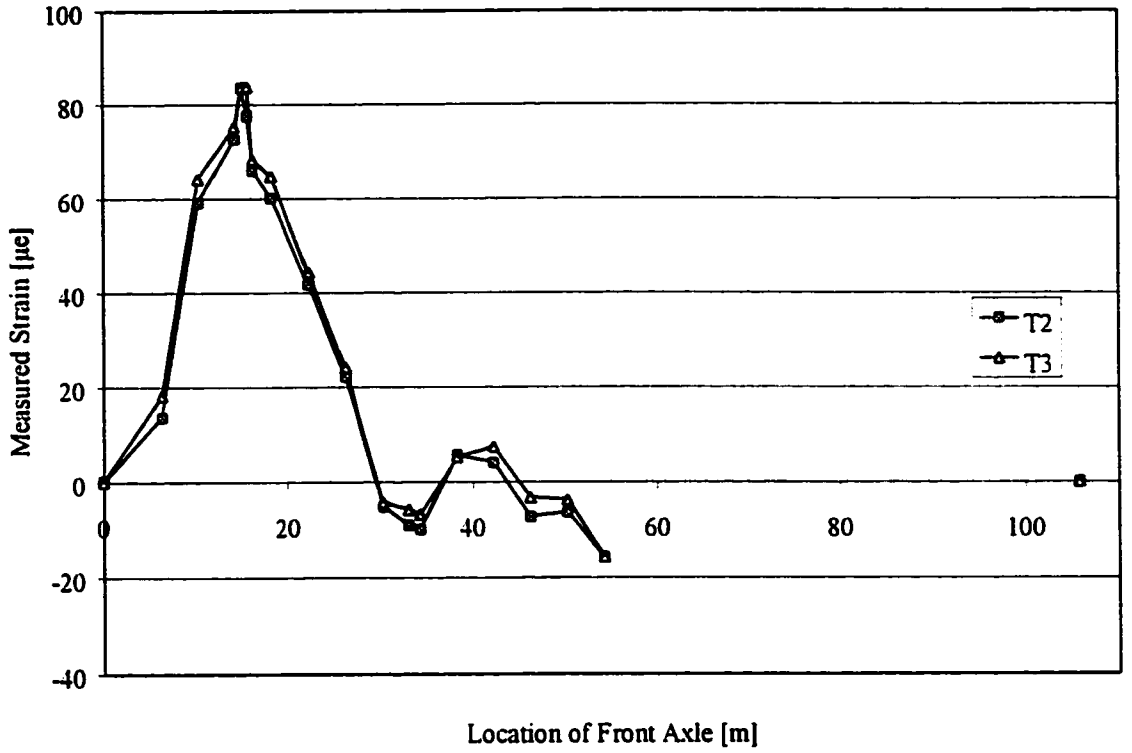

Figure B21: Static Load Test, August '98 for Strap #8 in Positive Moment Region

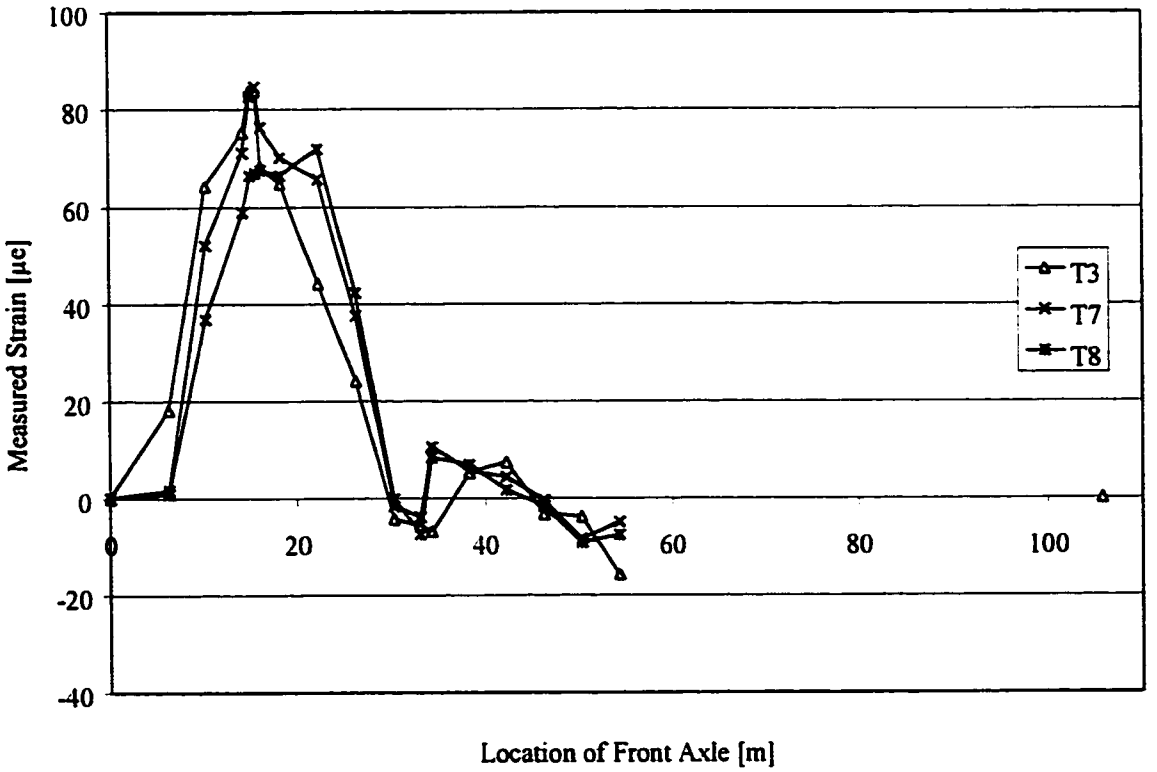

Figure B22: Static Load Test, August '98 for Straps #9, 10, 11 in Positive Moment

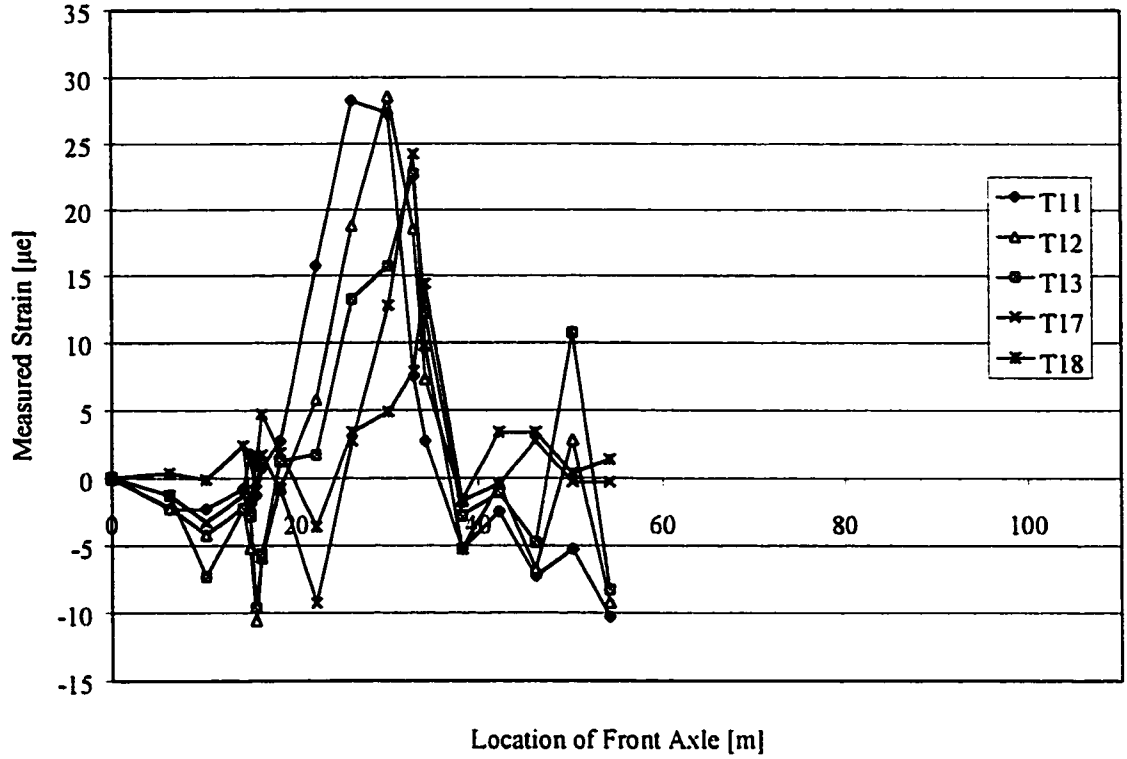

Figure B23: Static Load Test, August '98 for Straps in Positive Moment Region

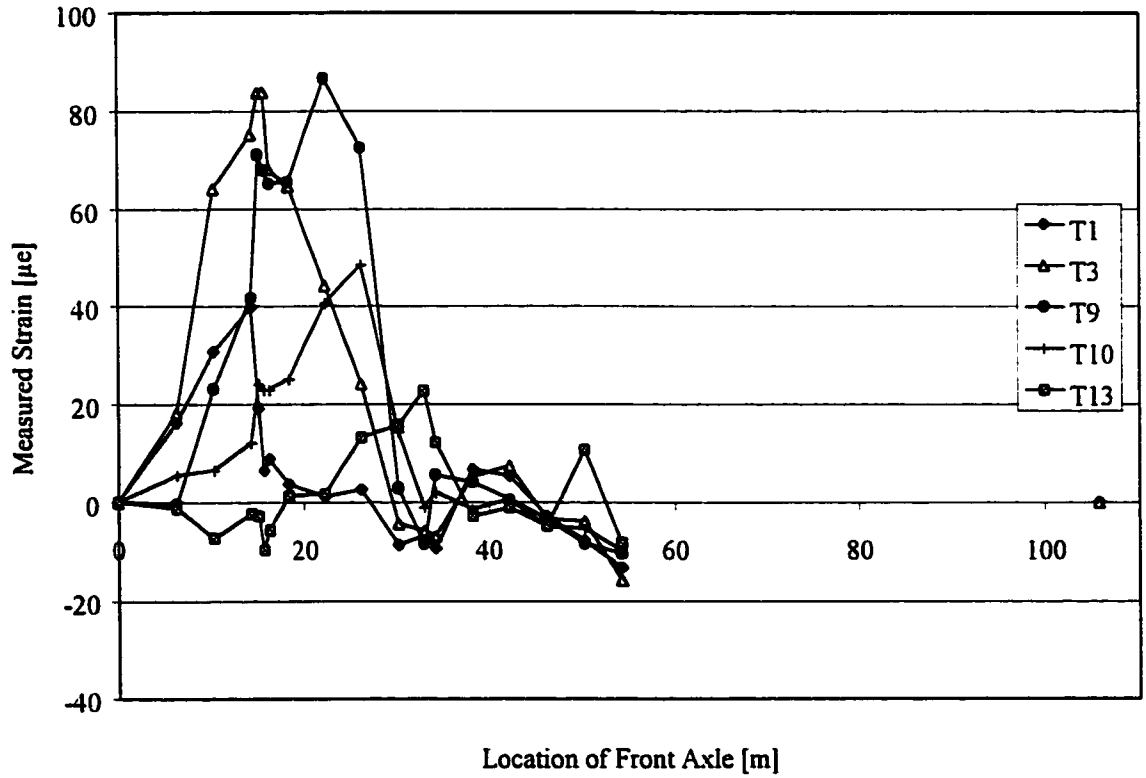

Figure B24: Static Load Test, August '98 for Straps in Positive Moment Region

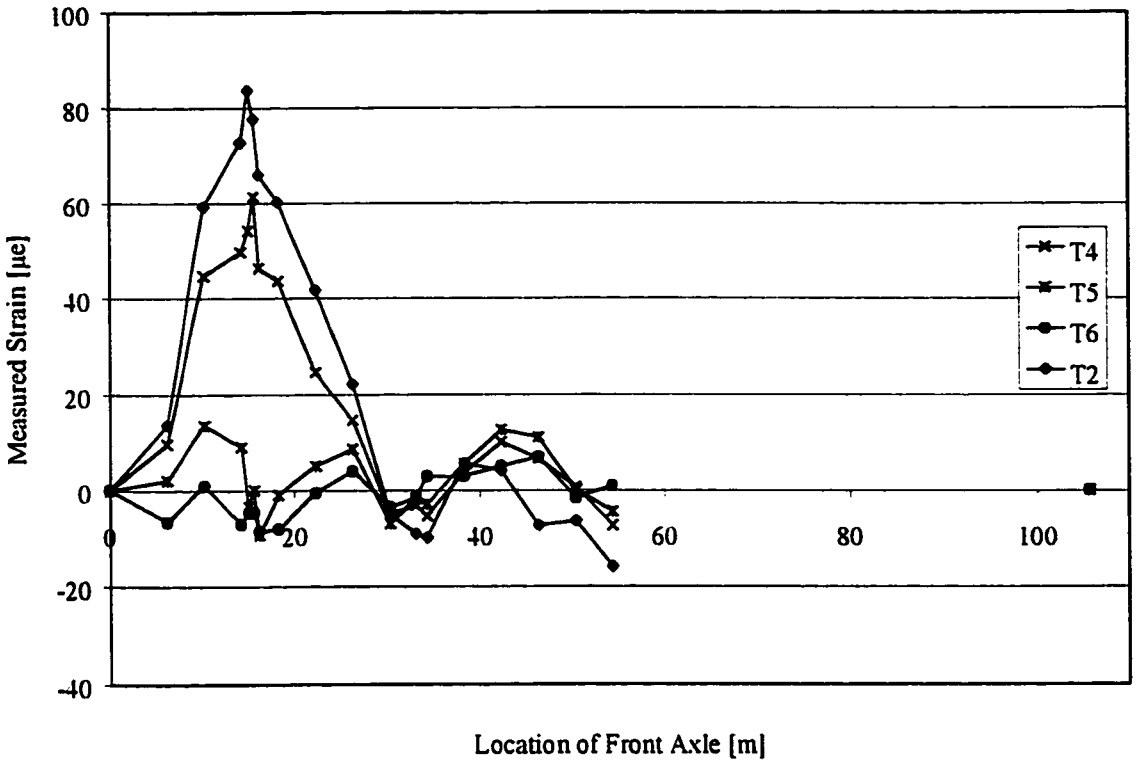

Figure B25: Static Load Test, August '98 for Strap #8 in Positive Moment Region

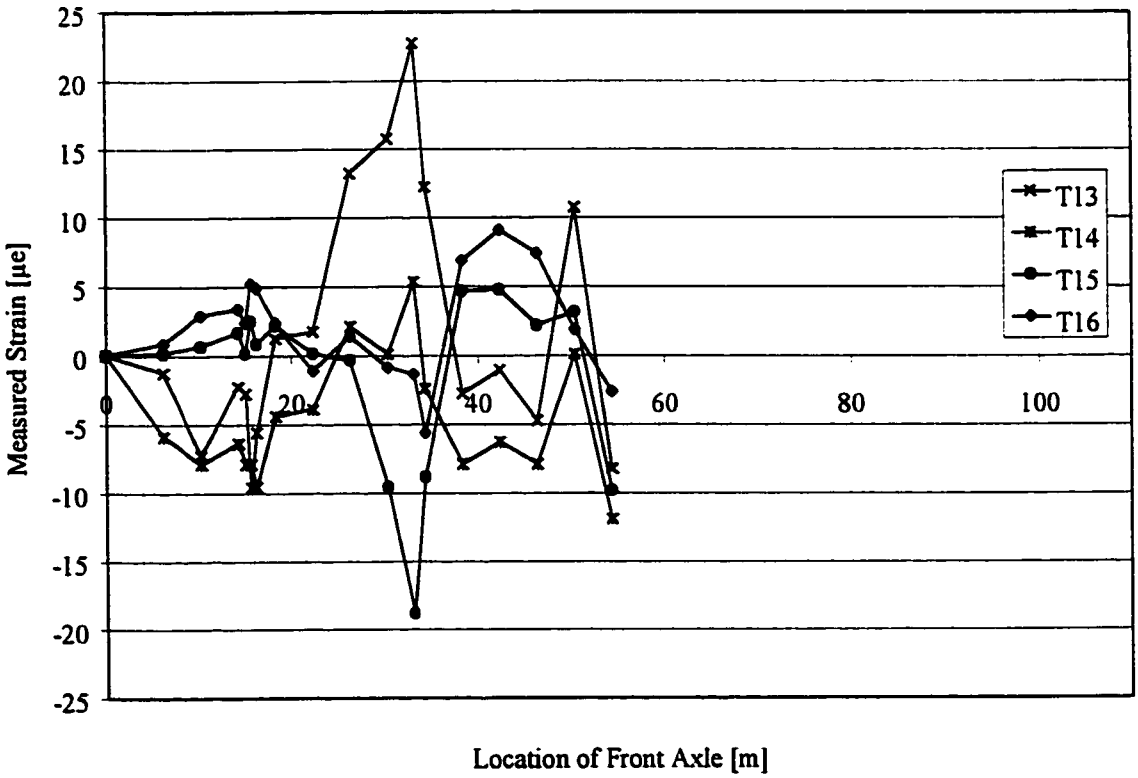

Figure B26: Static Load Test, August '98 for Strap #23 in Positive Moment Region

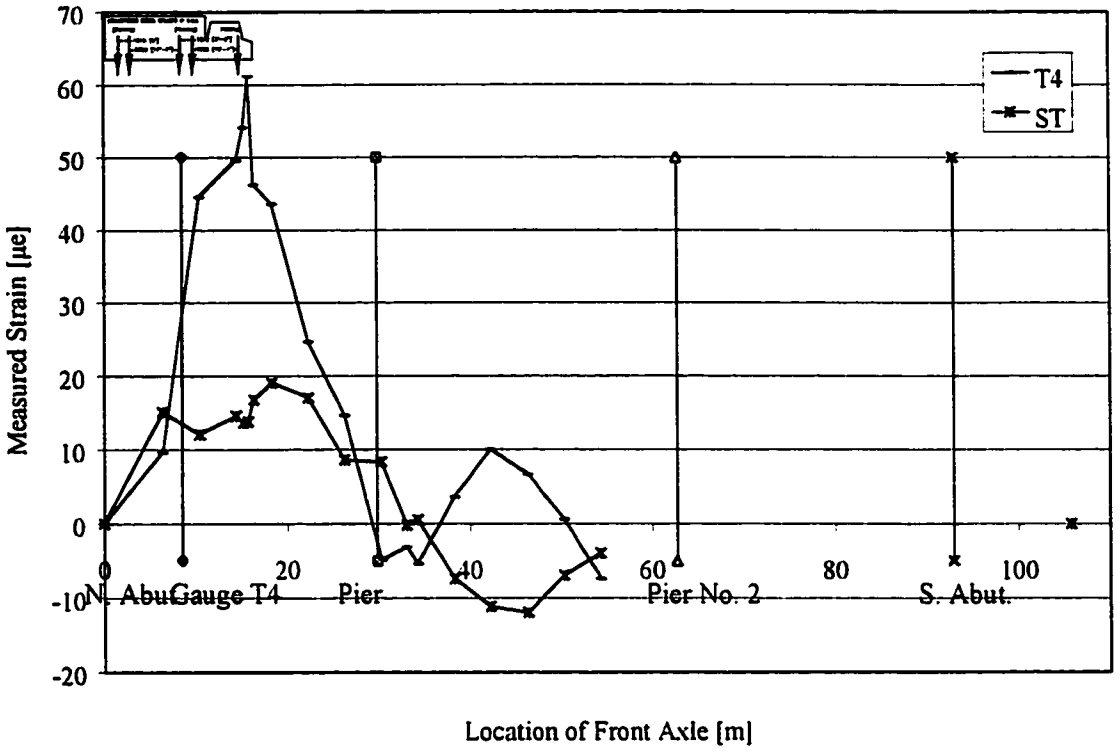

Figure B27: Static Load Test, August '98 for T4 & Standard Gauges

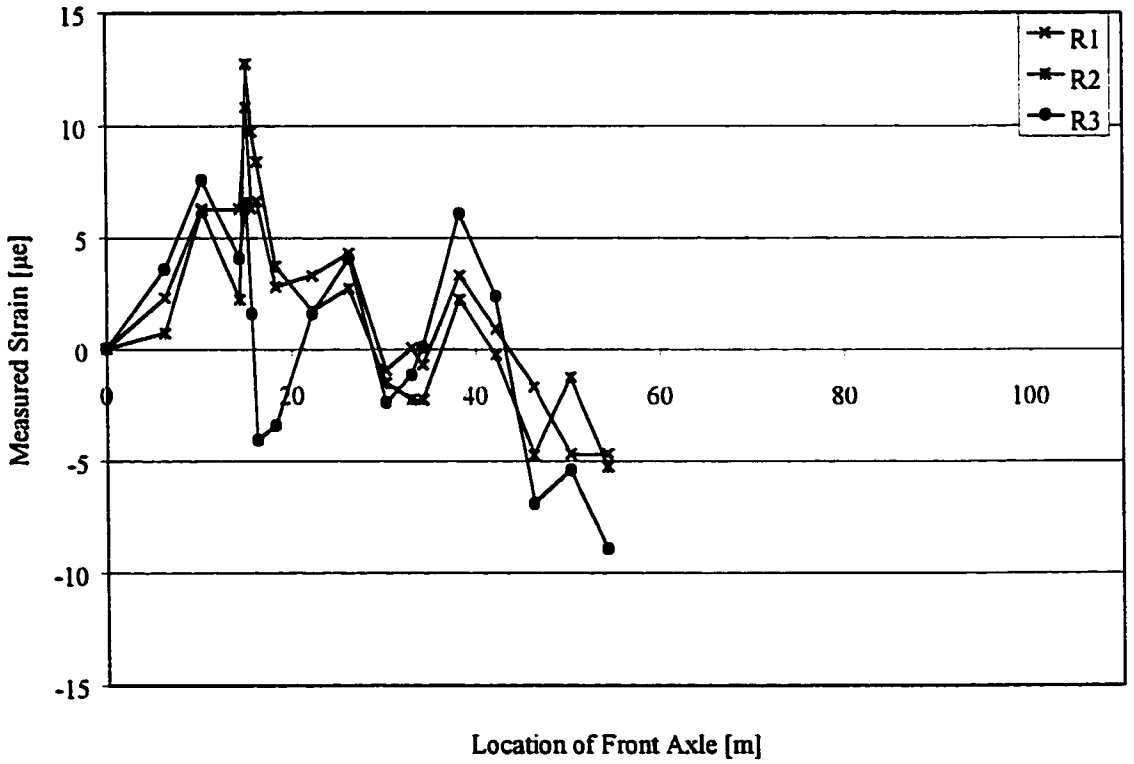

Figure B28: Static Load Test, August '98 for C-Bar at Cantilever

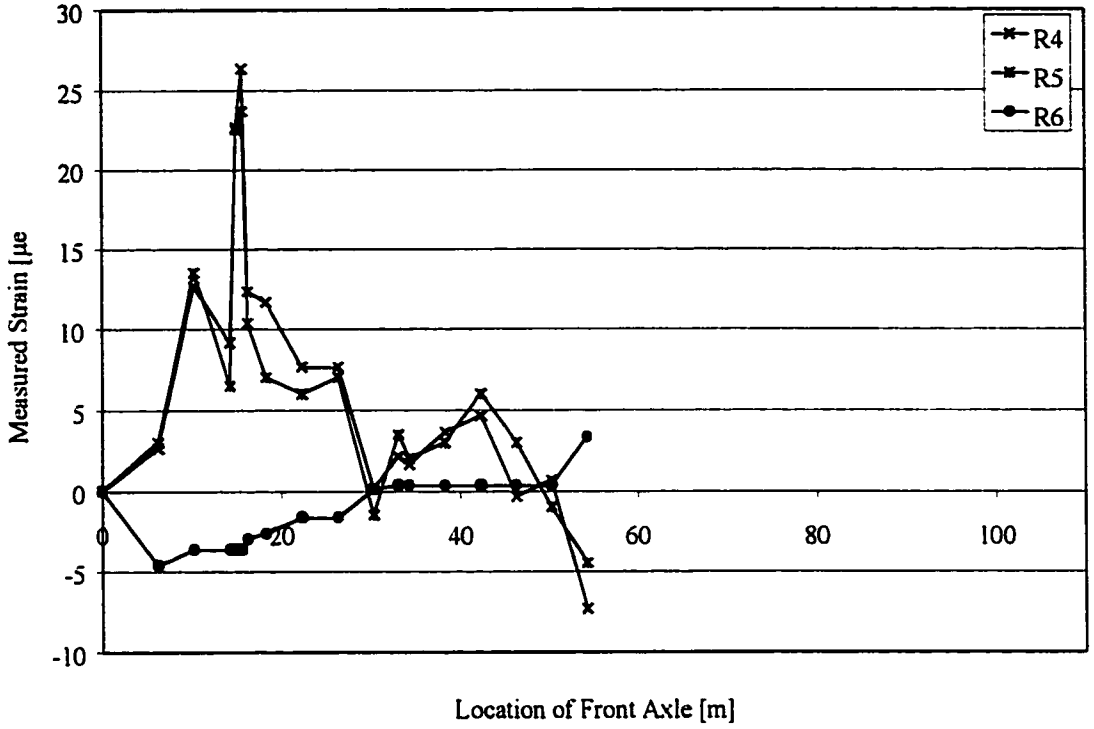

Figure B29: Static Load Test, August '98 for C-Bar at Cantilever

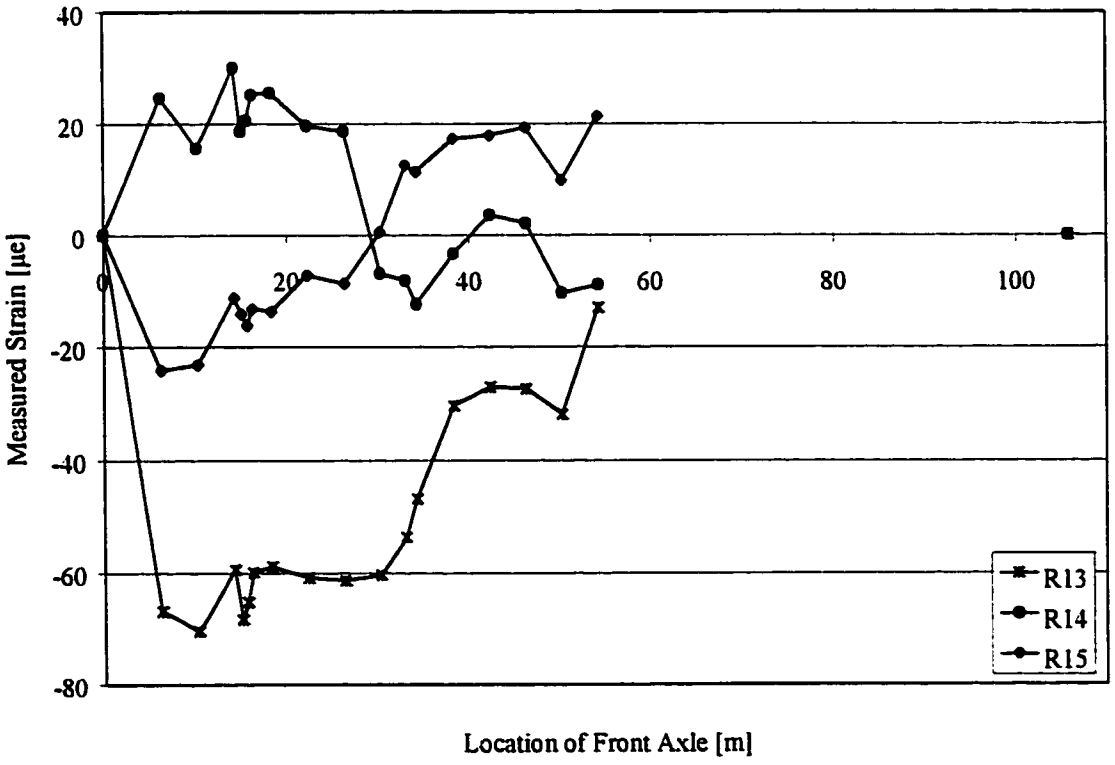

Figure B30: Static Load Test, August '98 for C-Bar at Pier No.1

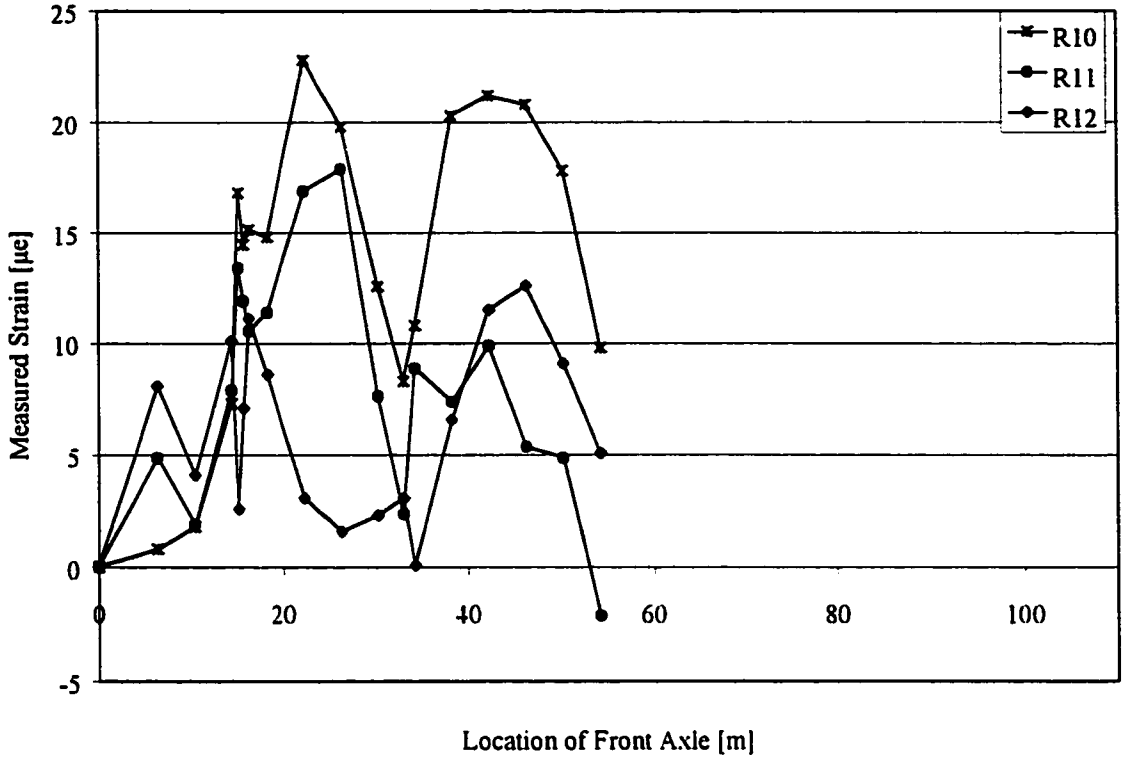

Figure B31: Static Load Test, August '98 for C-Bar at Pier No.1

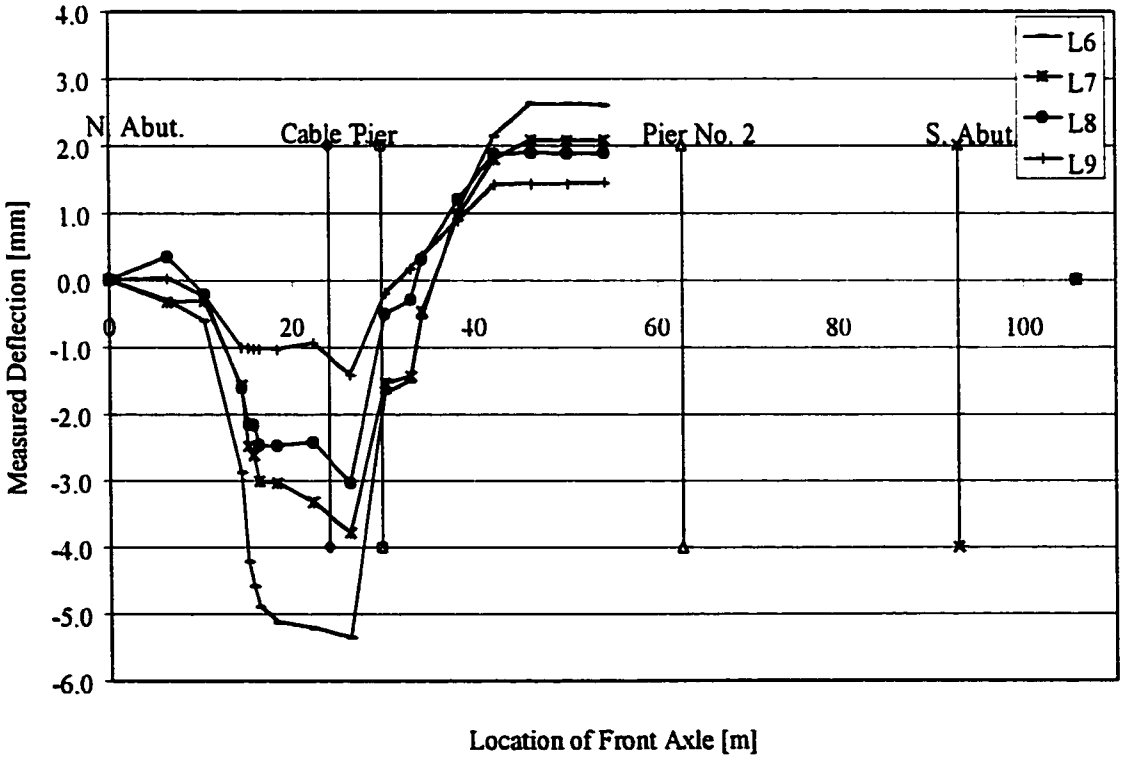

Figure B32: Static Load Test, August '98 for Cable Transducers at Strap #21

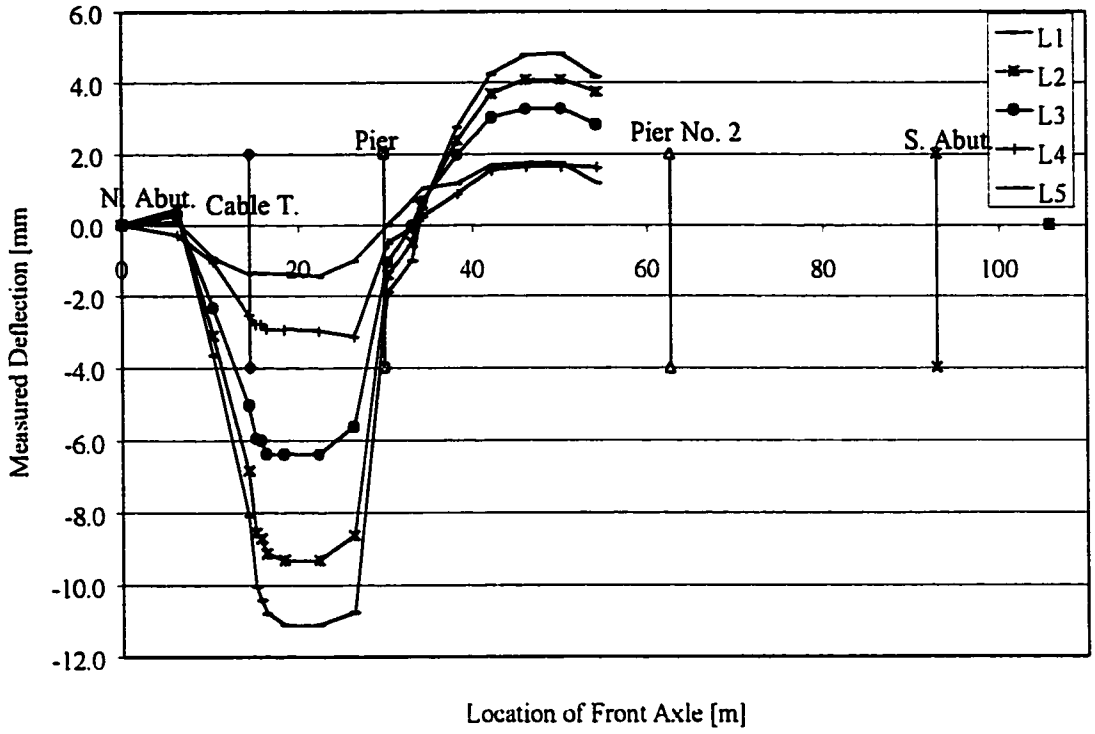

Figure B33: Static Load Test, August '98 for Cable Transducers at Strap #13

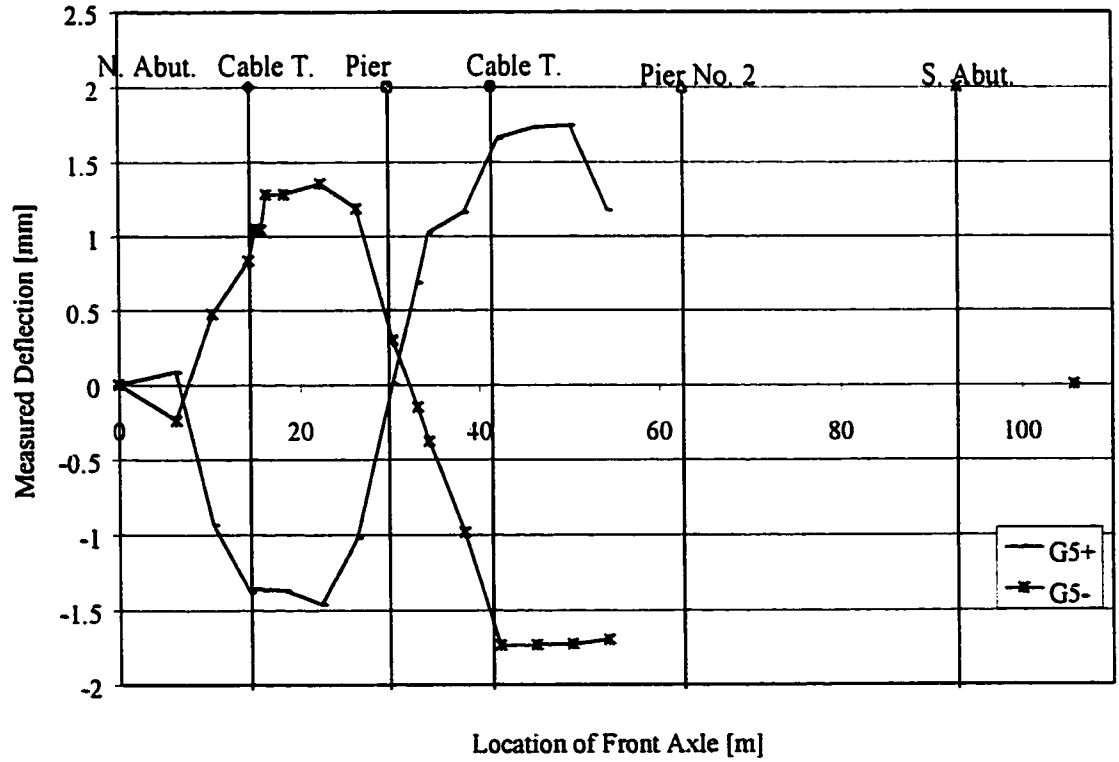

Figure B34: Static Load Test, August '98 for Cable Transducers on Girder 5

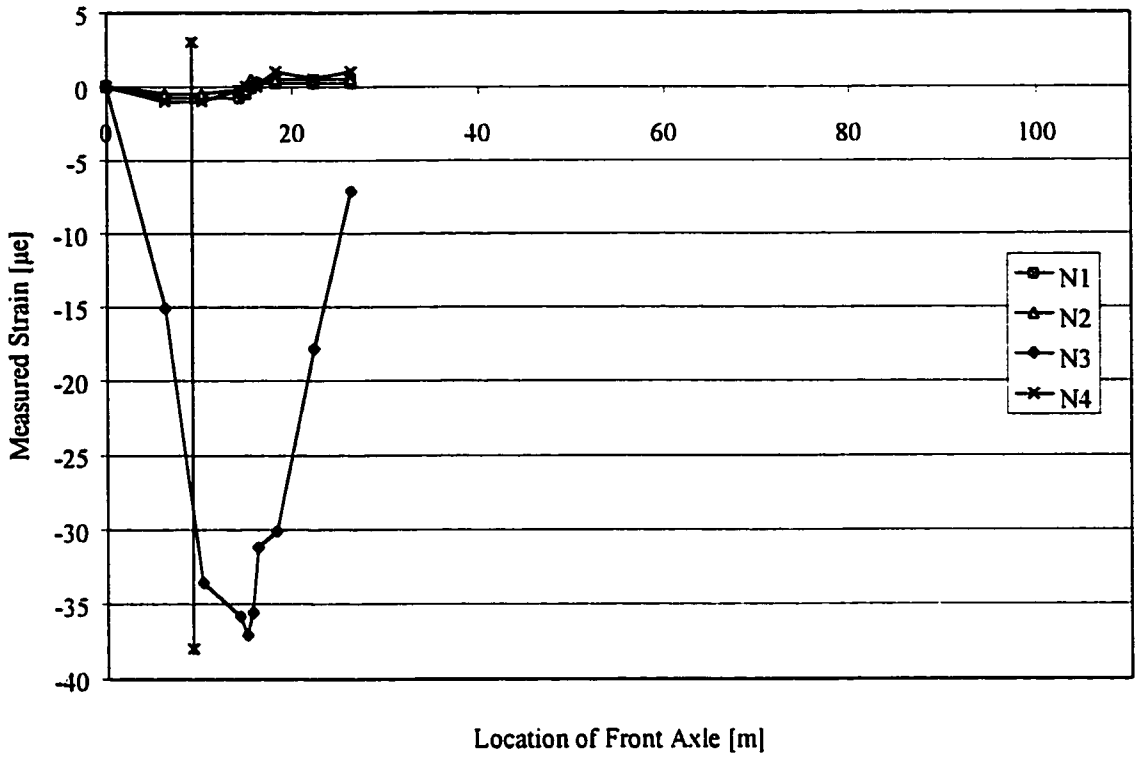

Figure B35: Static Load Test, August '98 for Gauges on NEFMAC & Stainless Bar

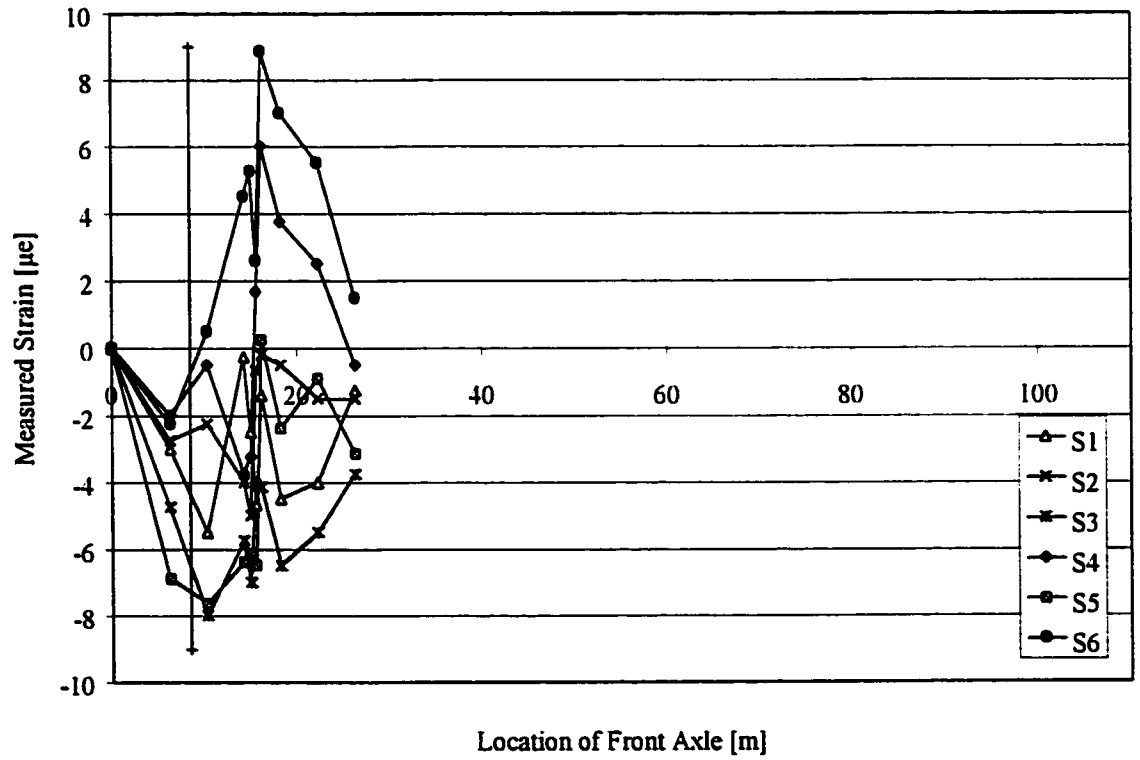

Figure B36: Static Load Test, August '98 for Gauges on Shear Stud

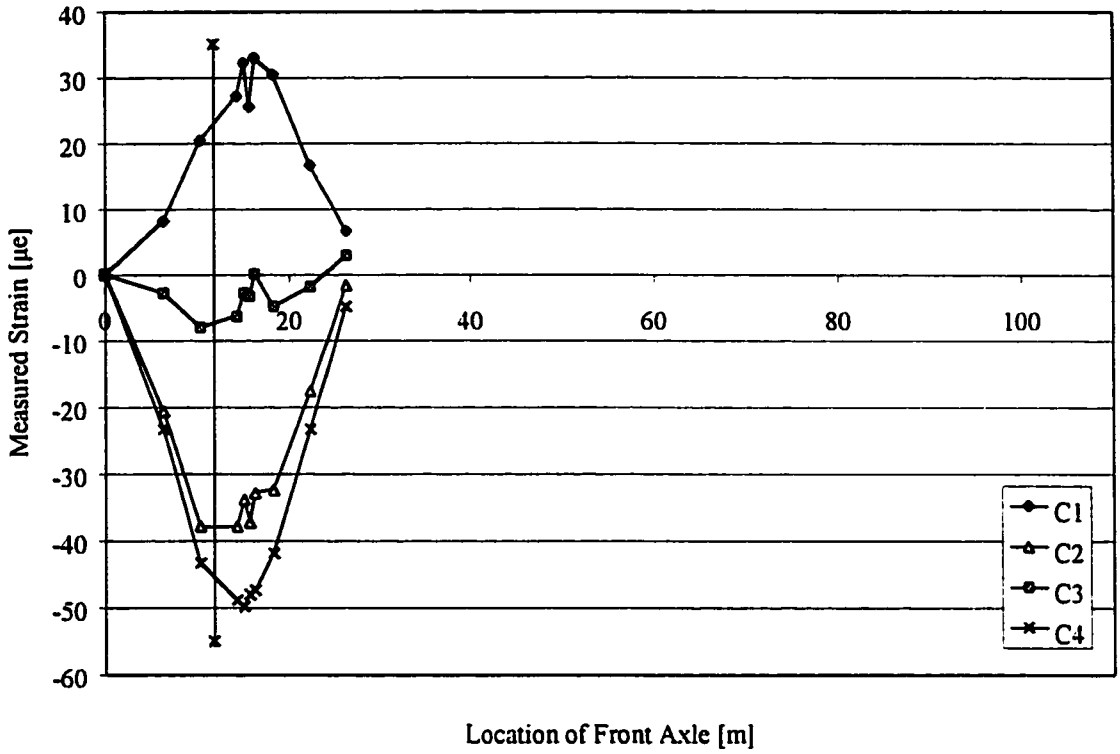

Figure B37: Static Load Test, August '98 for Gauges on Cross Frame

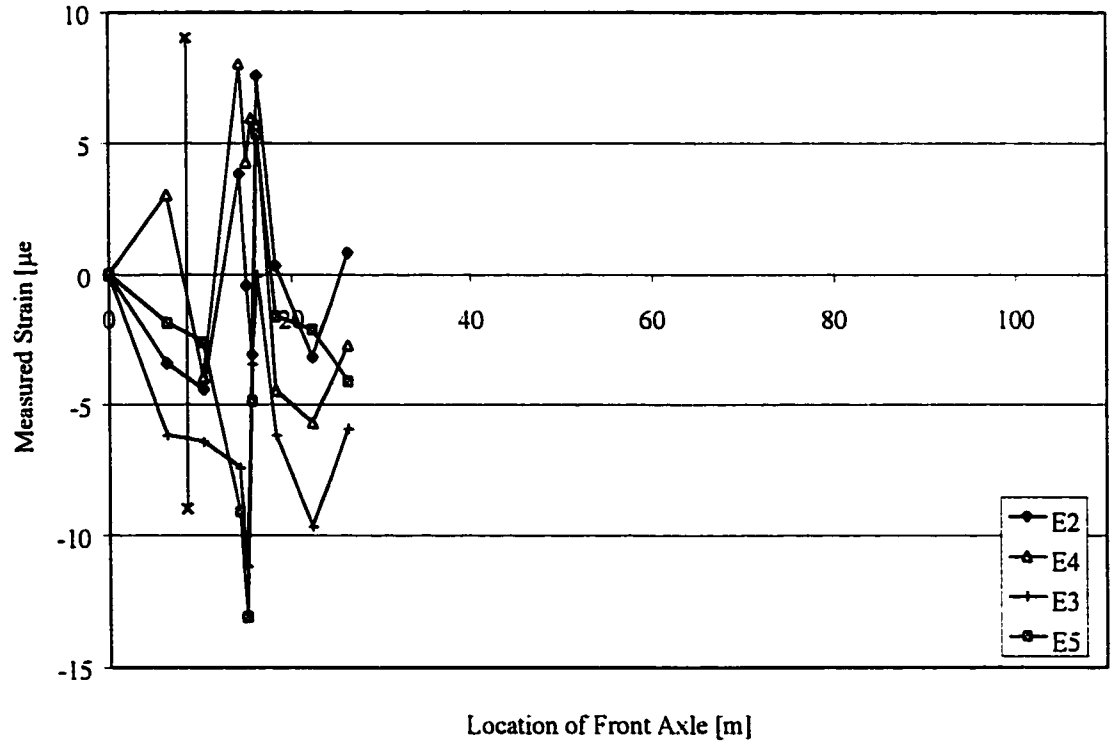

Figure B38: Static Load Test, August '98 for Embedded Concrete Gauges

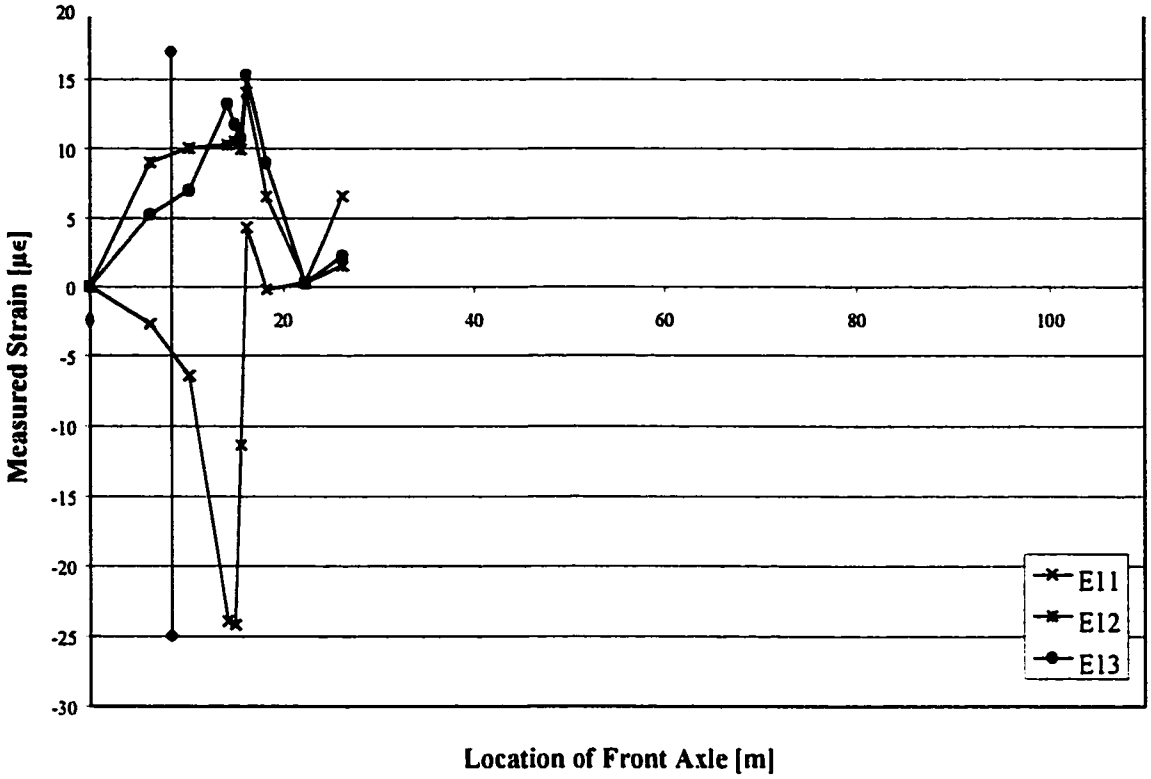

Figure B39: Static Load Test, August '98 for Embedded Concrete Strain Gauges

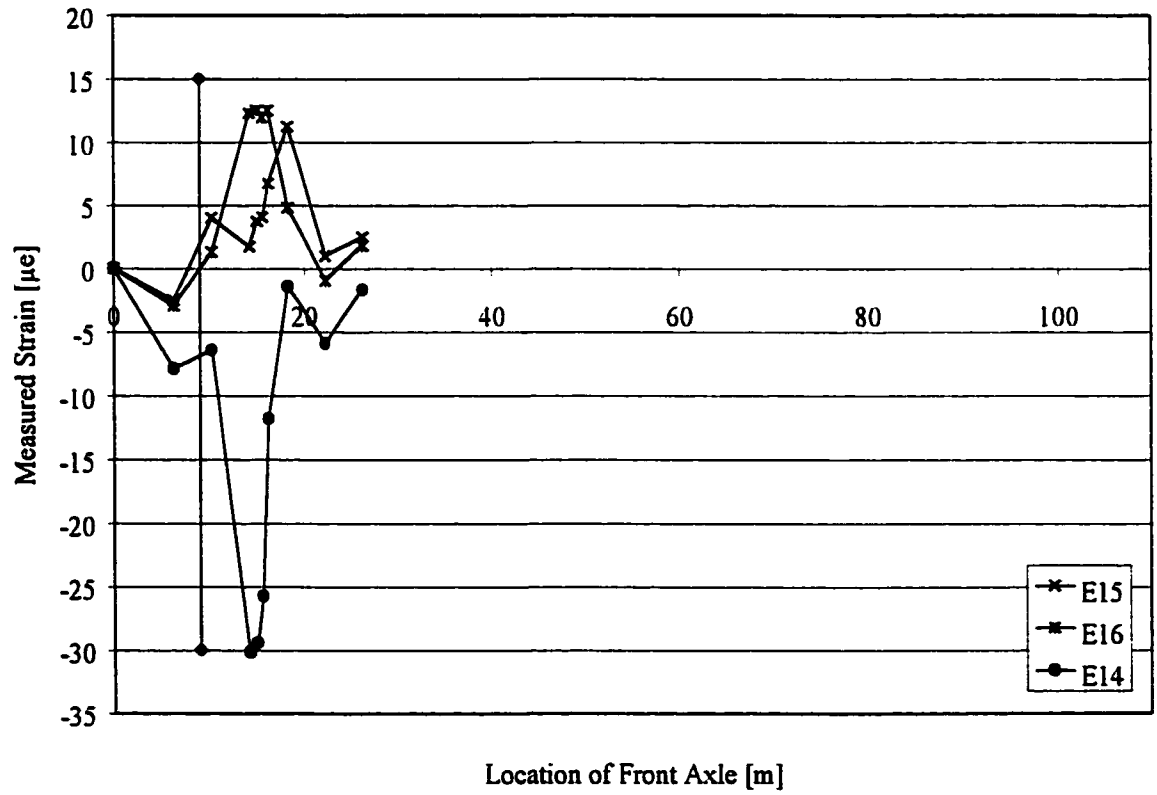

Figure B40: Static Load Test, August '98 for Embedded Concrete Strain Gauges

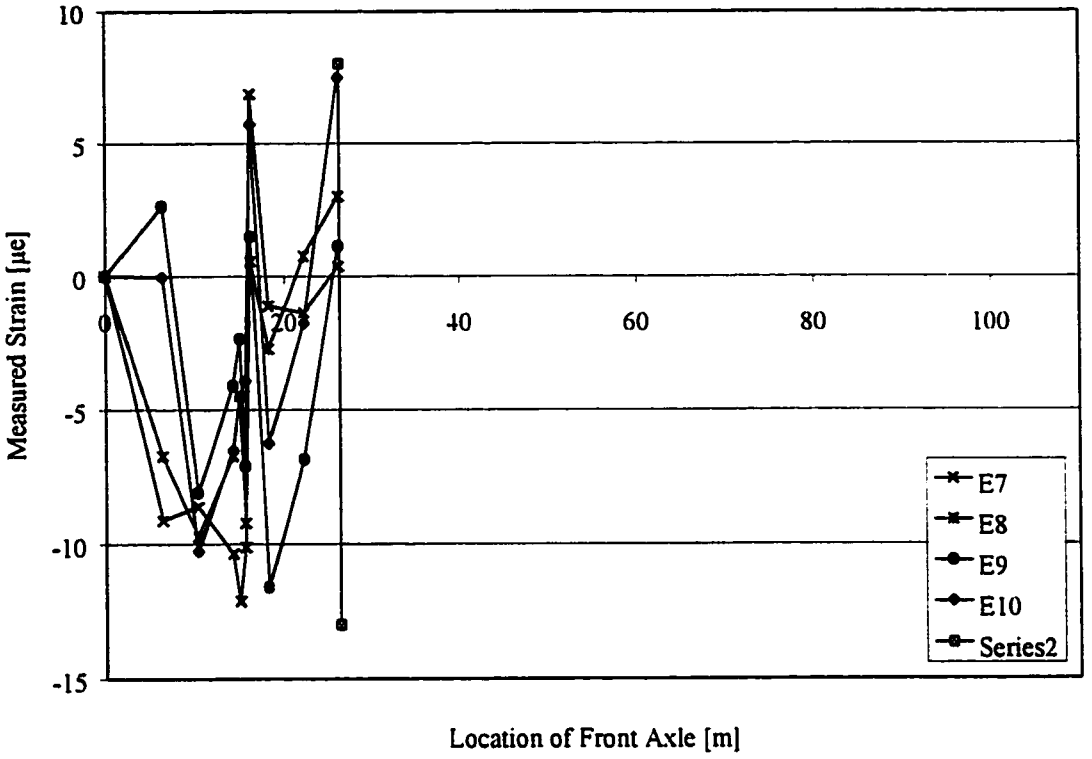

Figure B41: Static Load Test, August '98 for Embedded Concrete Strain Gauges

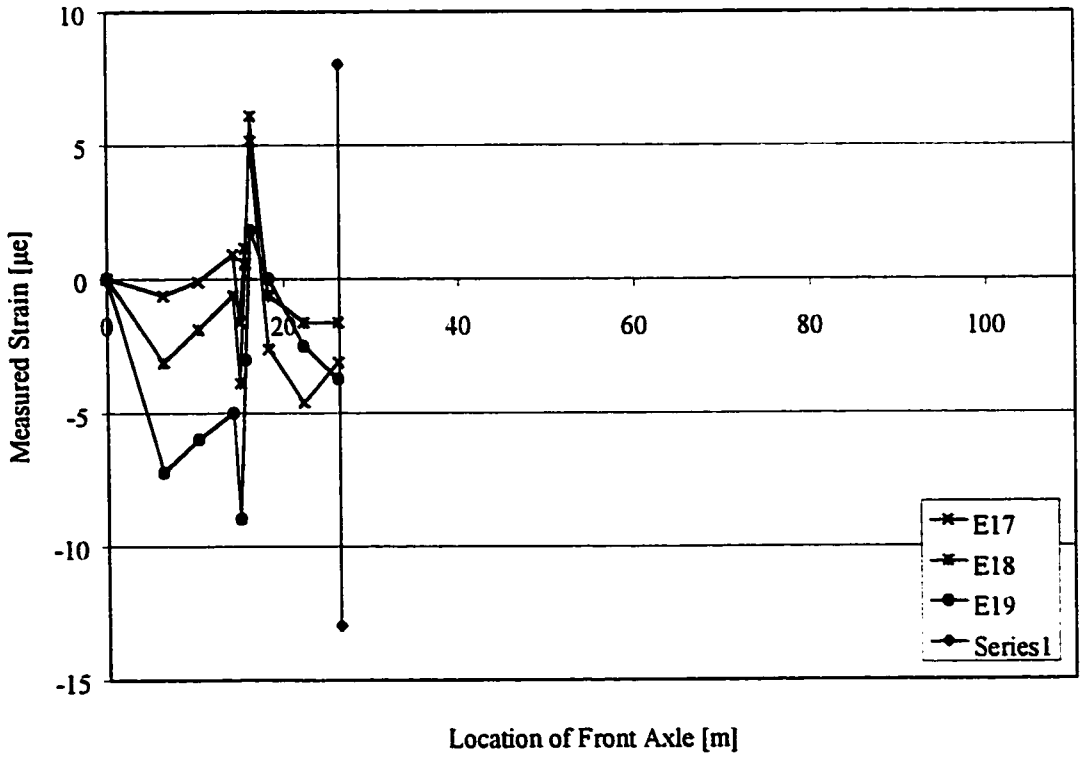

Figure B42: Static Load Test, August '98 for Embedded Concrete Strain Gauges

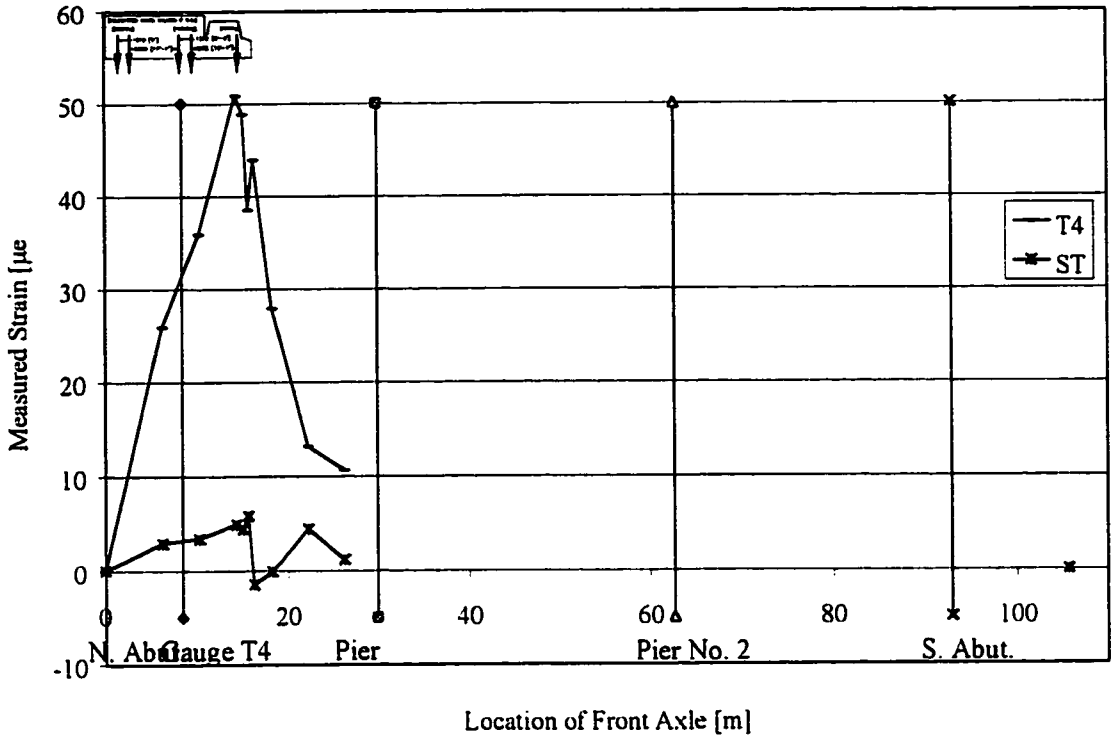

Figure B43: Static Load Test, August '98 for T4 and St Gauges

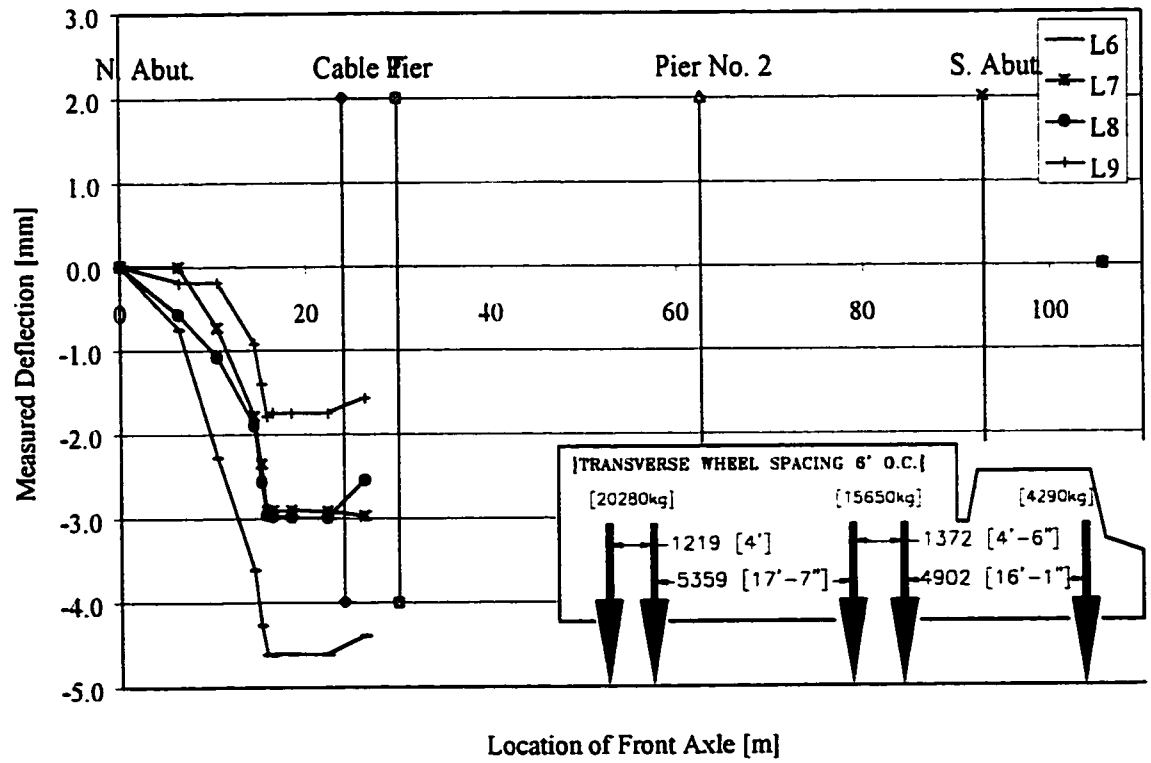

Figure B44: Static Load Test, August '98 for Cable Transducers at Strap #21

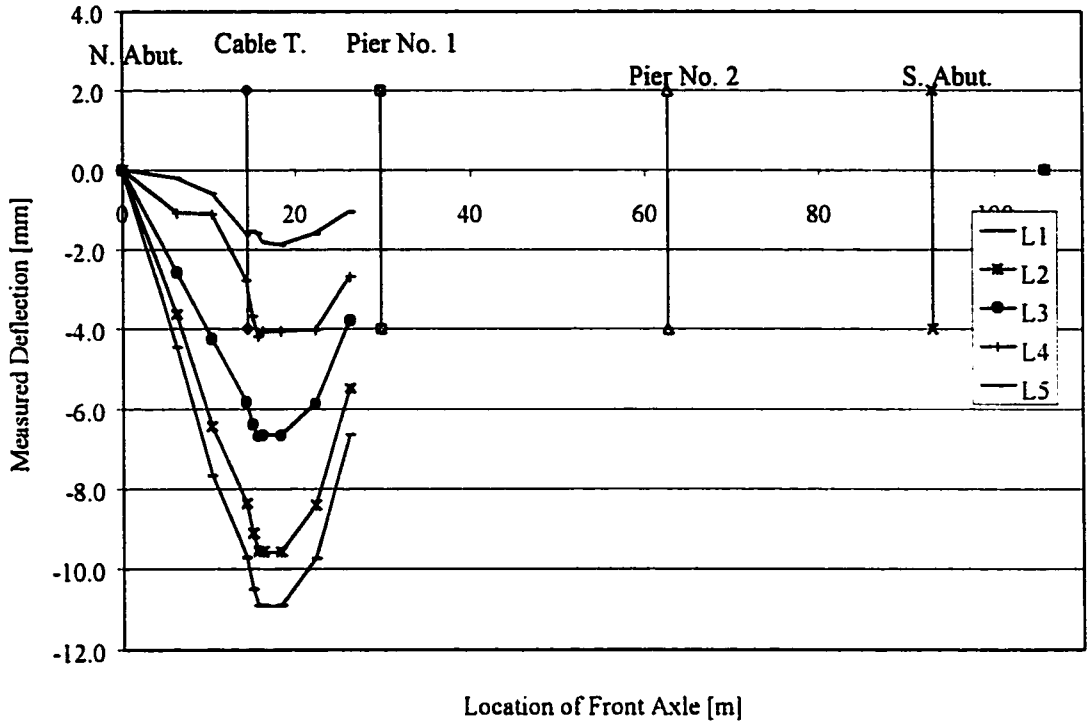

Figure B45: Static Load Test, August '98 for Cable Transducers at Strap #13

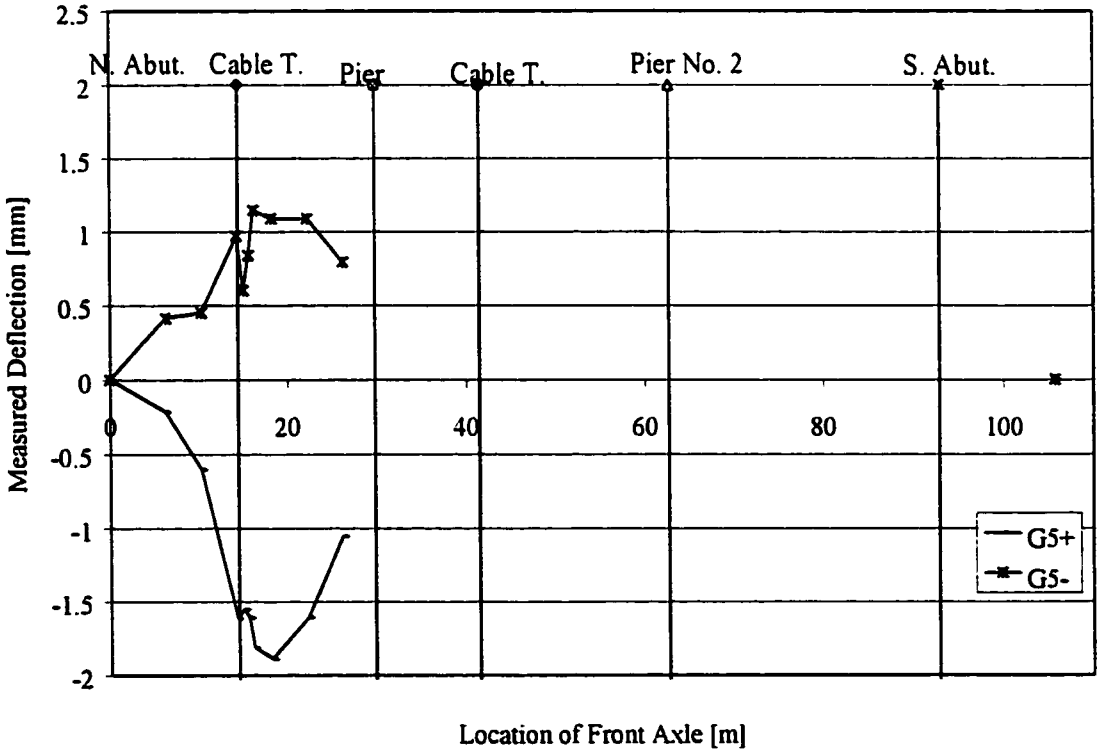

Figure B46: Static Load Test, August '98 for Two Cable Transducers on Girder 5

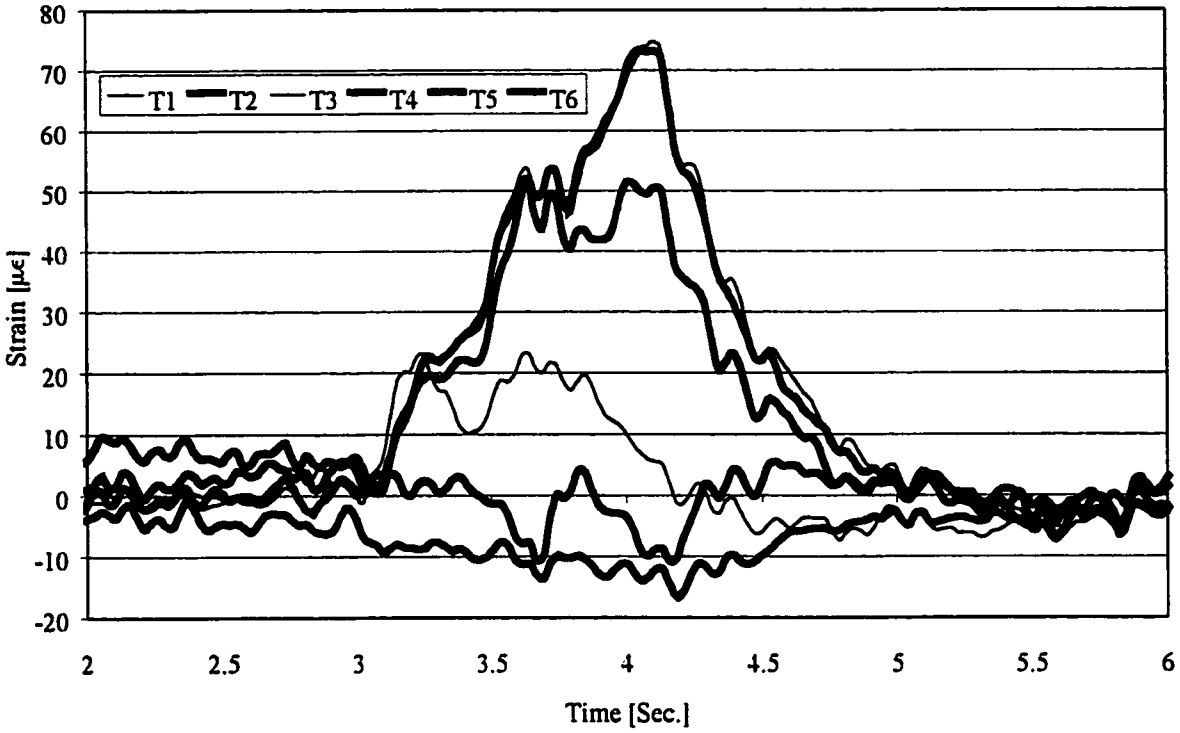

Figure B47: 55 km/hr Test, August '98 for Strap #8 in Positive Moment Region

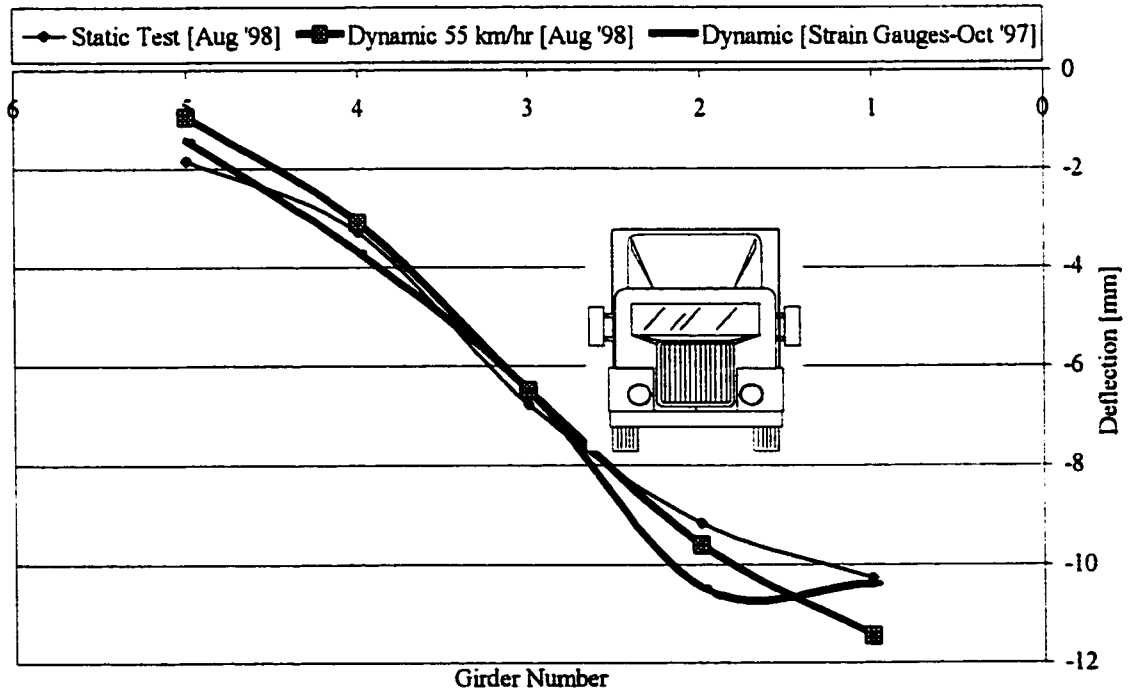

Figure B48: Comparison of Load Sharing in the Positive Moment Region

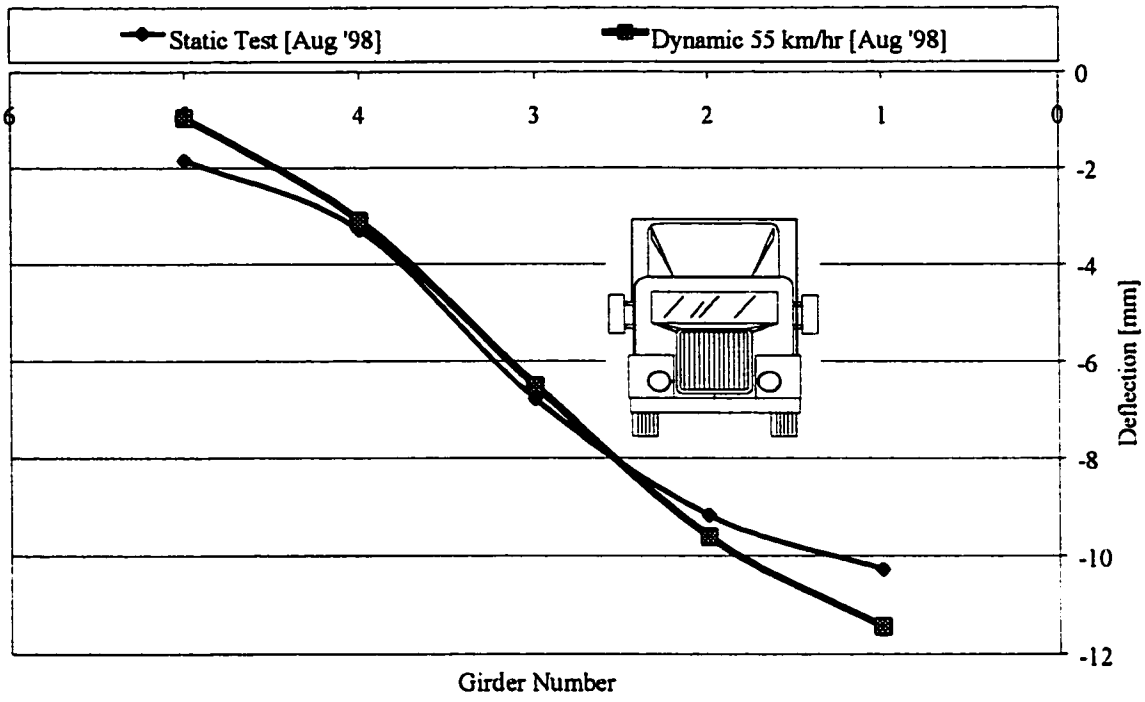

Figure B49: Comparison of Load Sharing in the Positive Moment Region

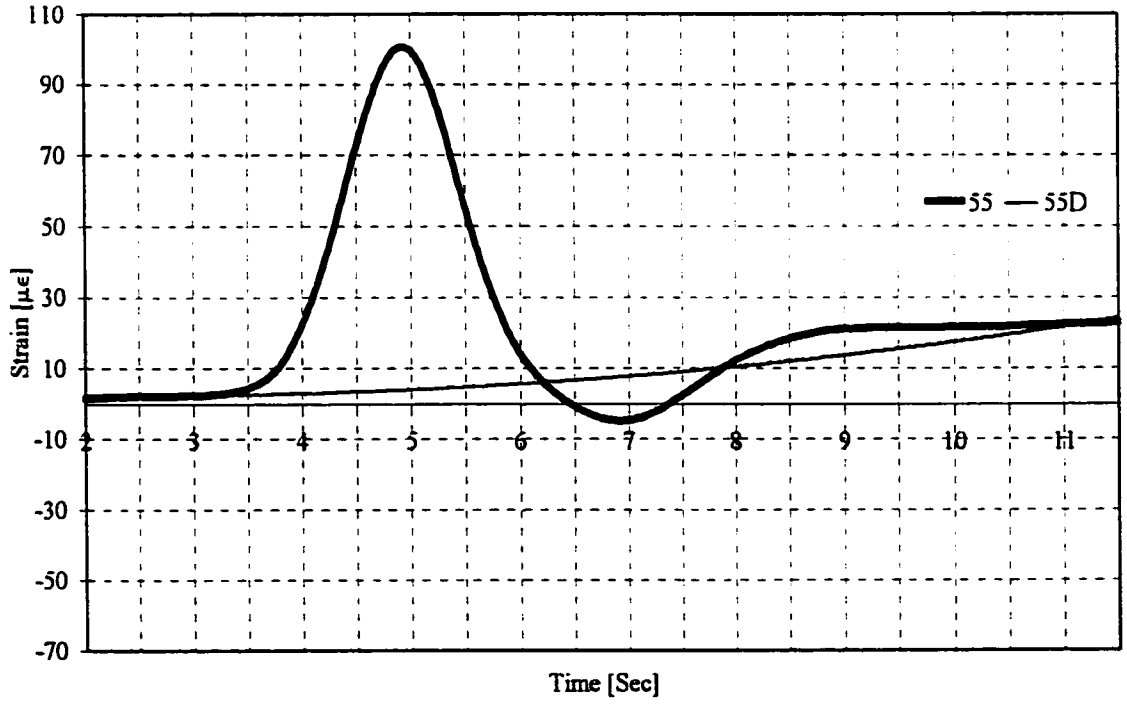

Figure B50: 55 km/hr Test, August '98 for Gauge G3

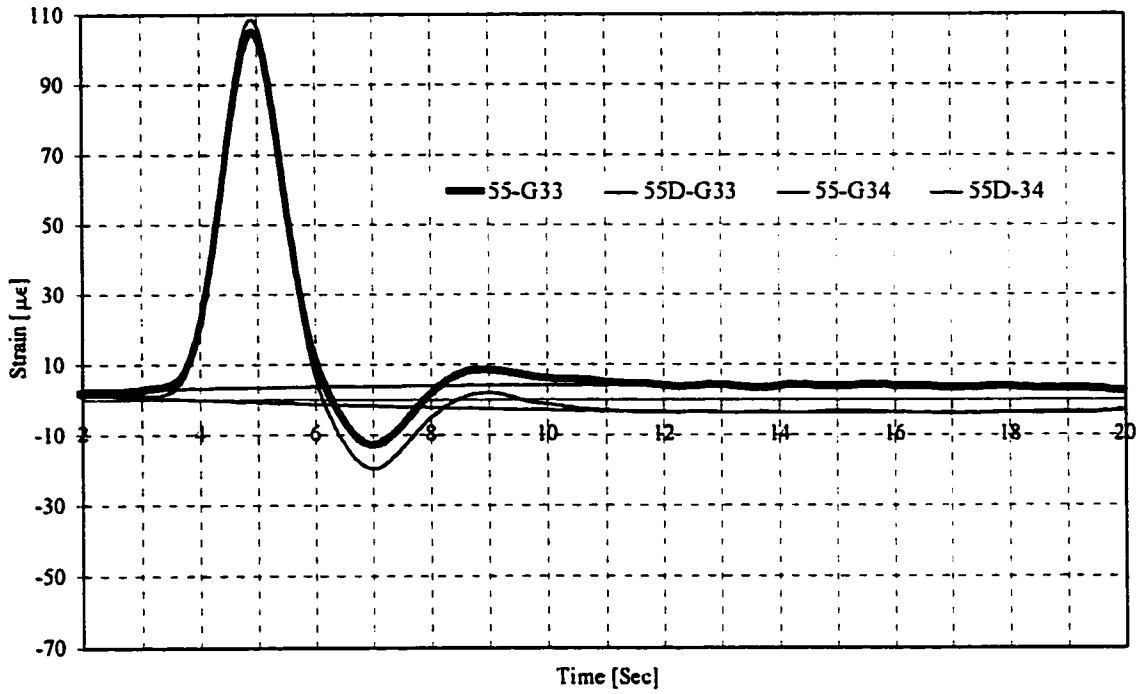

Figure B51: 55 km/hr Test, August '98 for Gauge G33 & G34

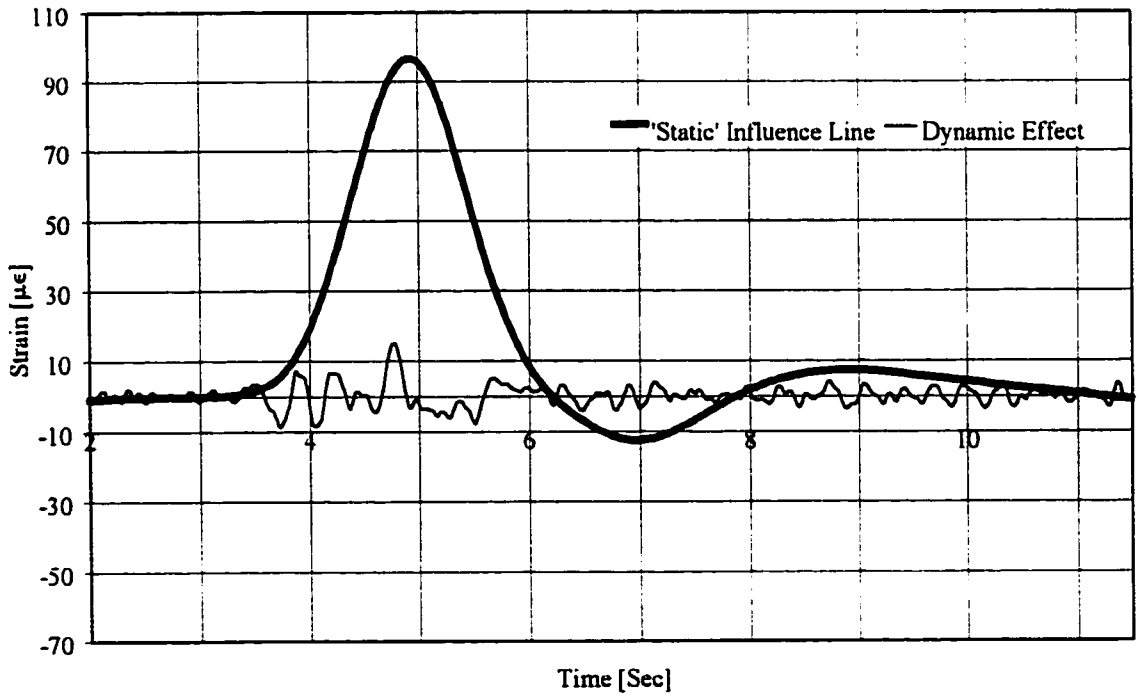

Figure B52: 55 km/hr Test, August '98 for Gauge G3 Filtered Data

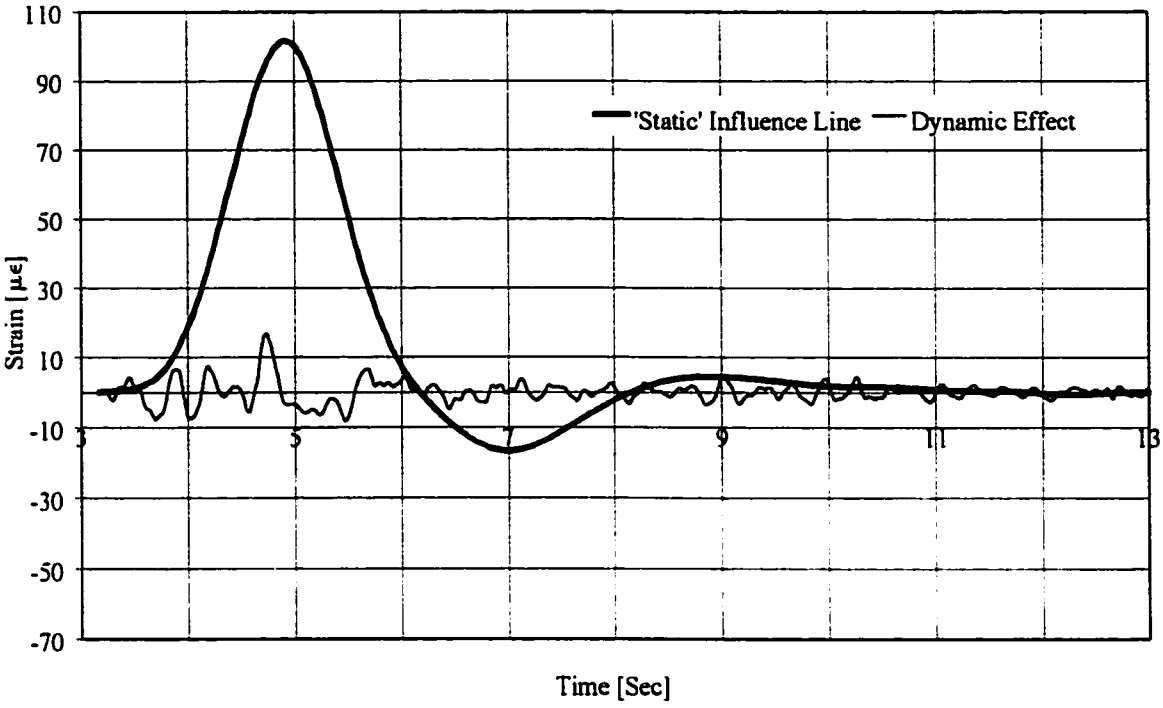

Figure B53: 55 km/hr Test, August '98 for Gauge G33 Filtered Data

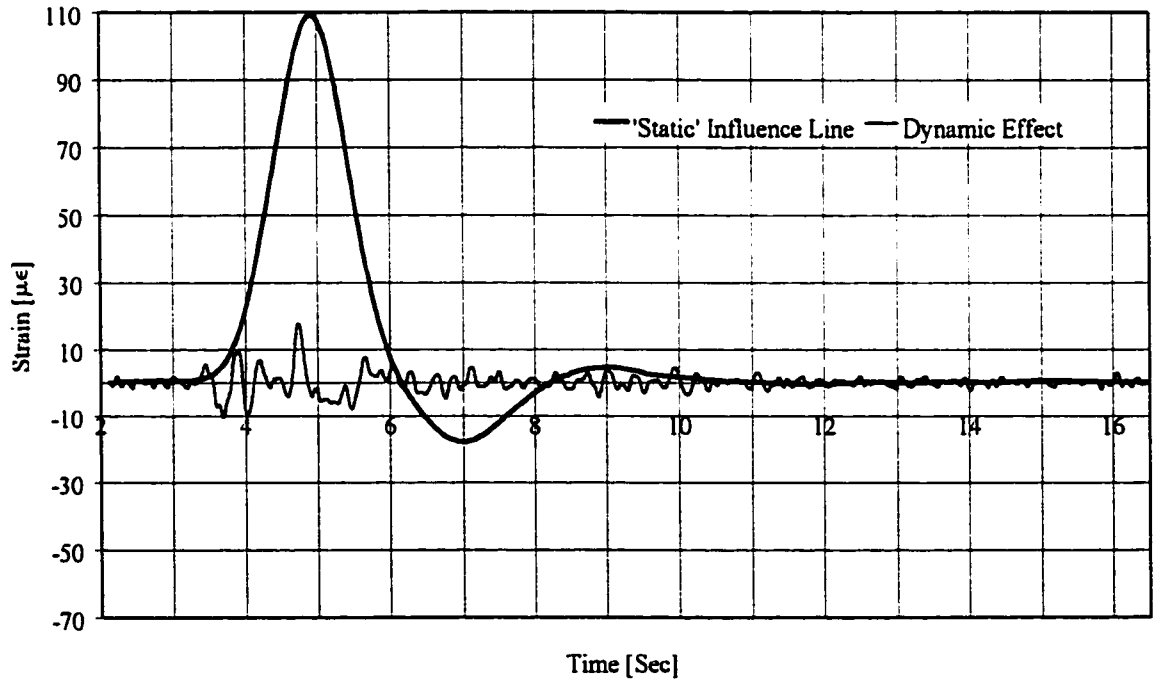

Figure B54: 55 km/hr Test, August '98 for Gauge G34 Filtered Data

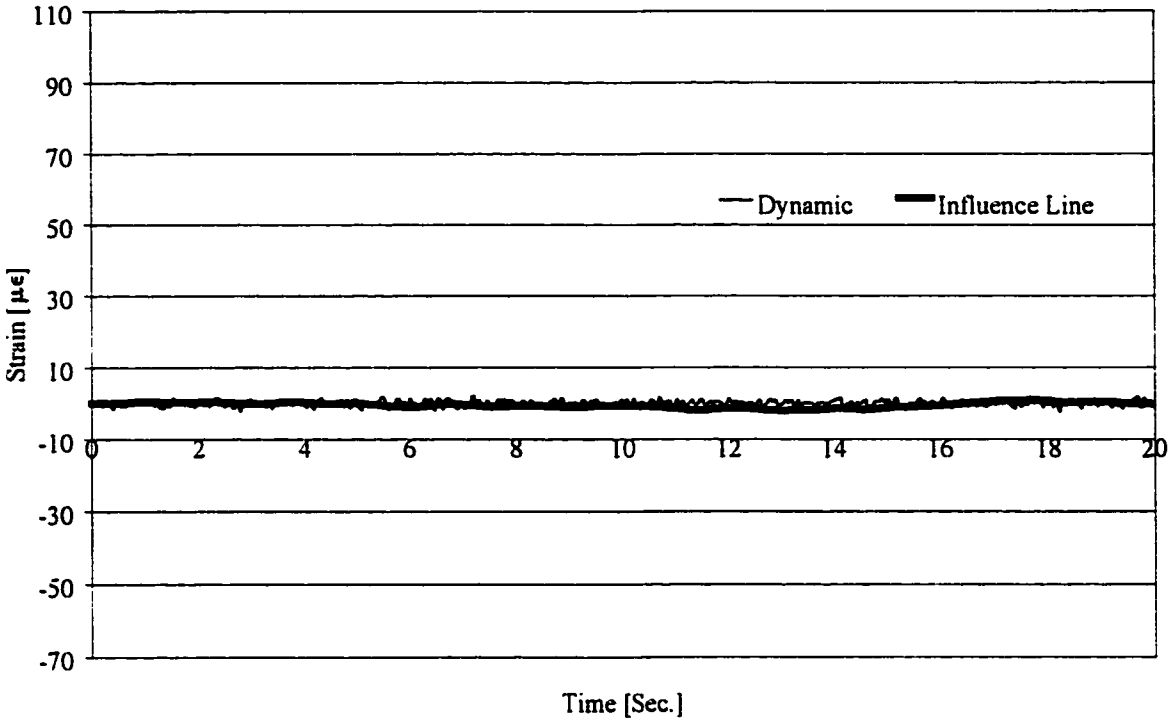

Figure B55: 55 km/hr Test, August '98 for Gauge ST Filtered Data

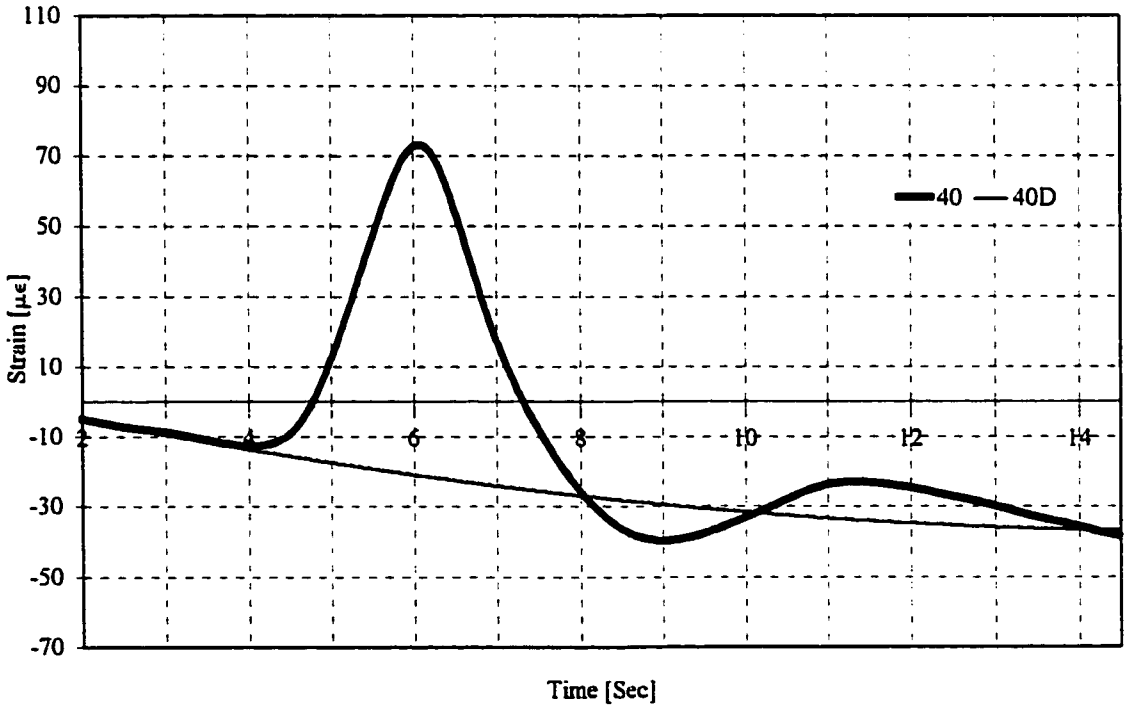

Figure B56: 40 km/hr Test, August '98 for Gauge G3 Filtered Data

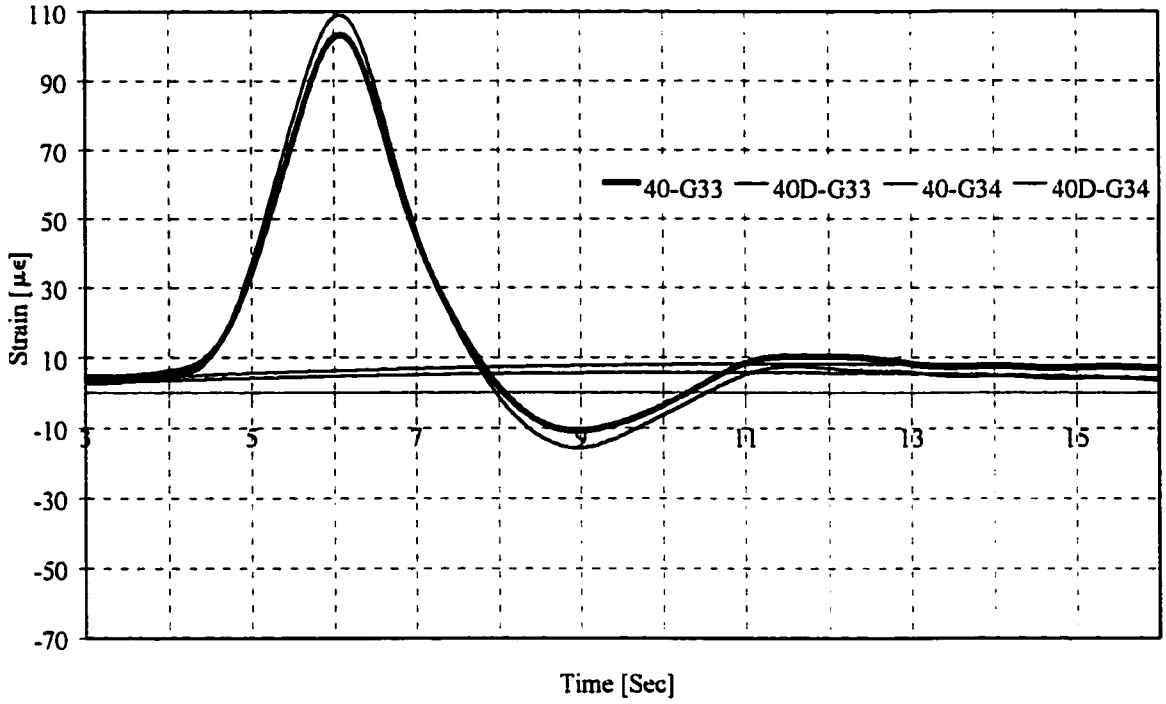

Figure B57: 40 km/hr Test, August '98 for Gauge G33 & G34 Filtered Data

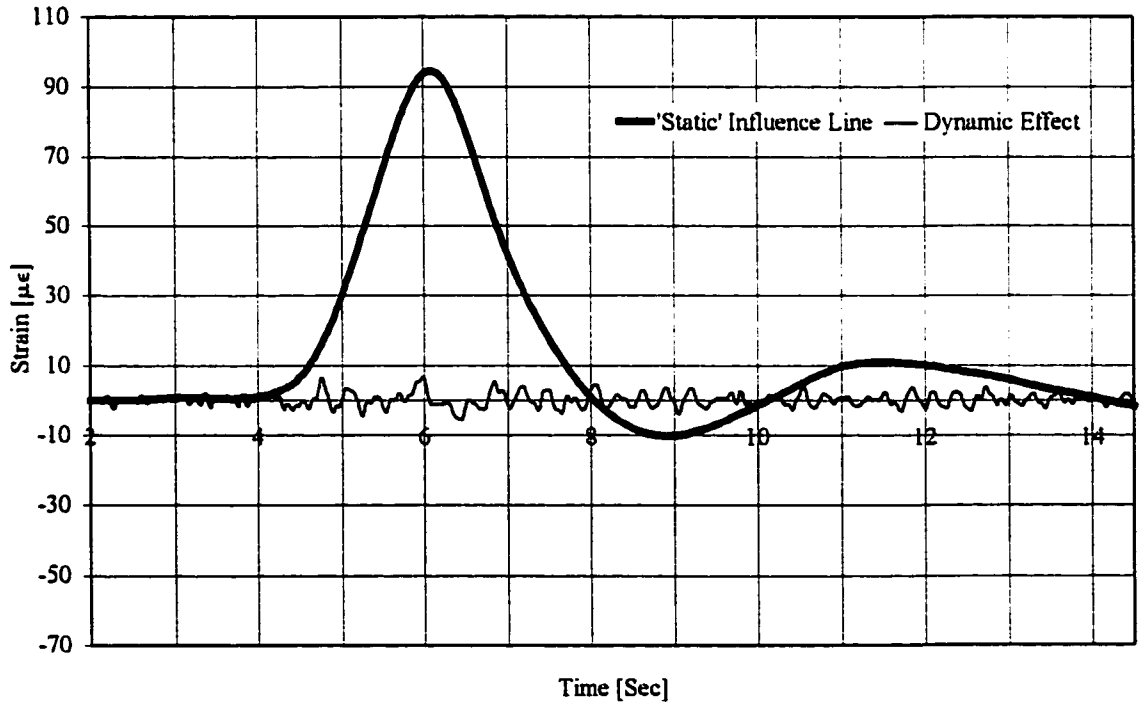

Figure B58: 40 km/hr Test, August '98 for Gauge G3 Filtered Data

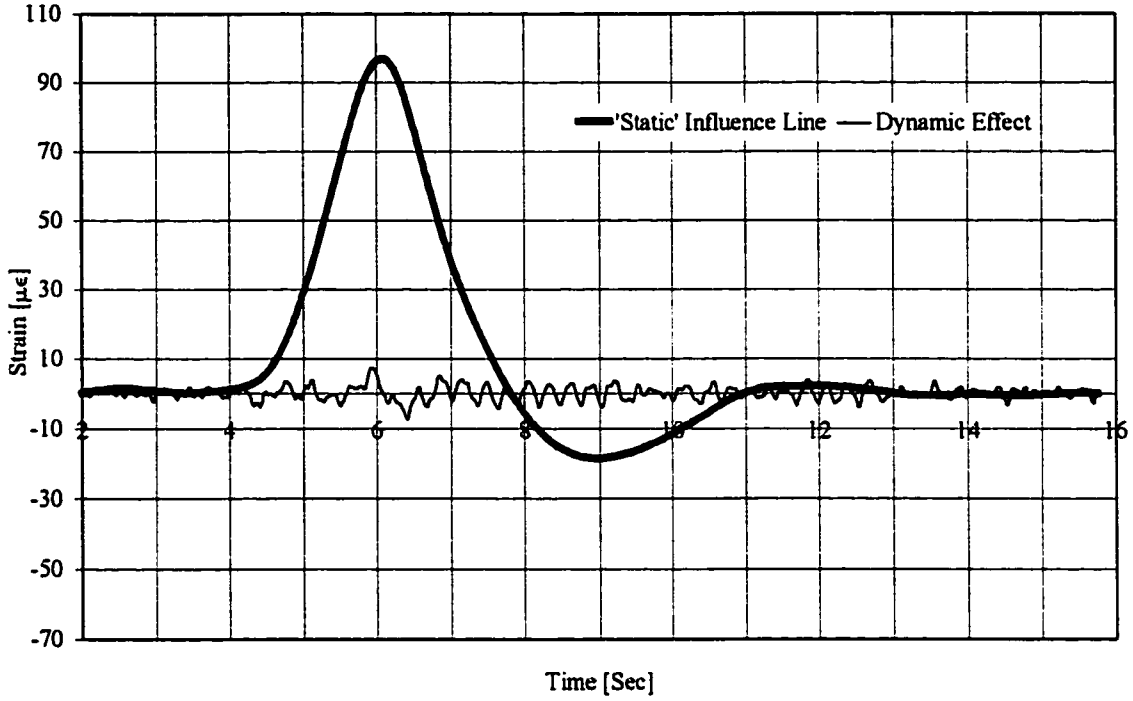

Figure B59: 40 km/hr Test, August '98 for Gauge G33 Filtered Data

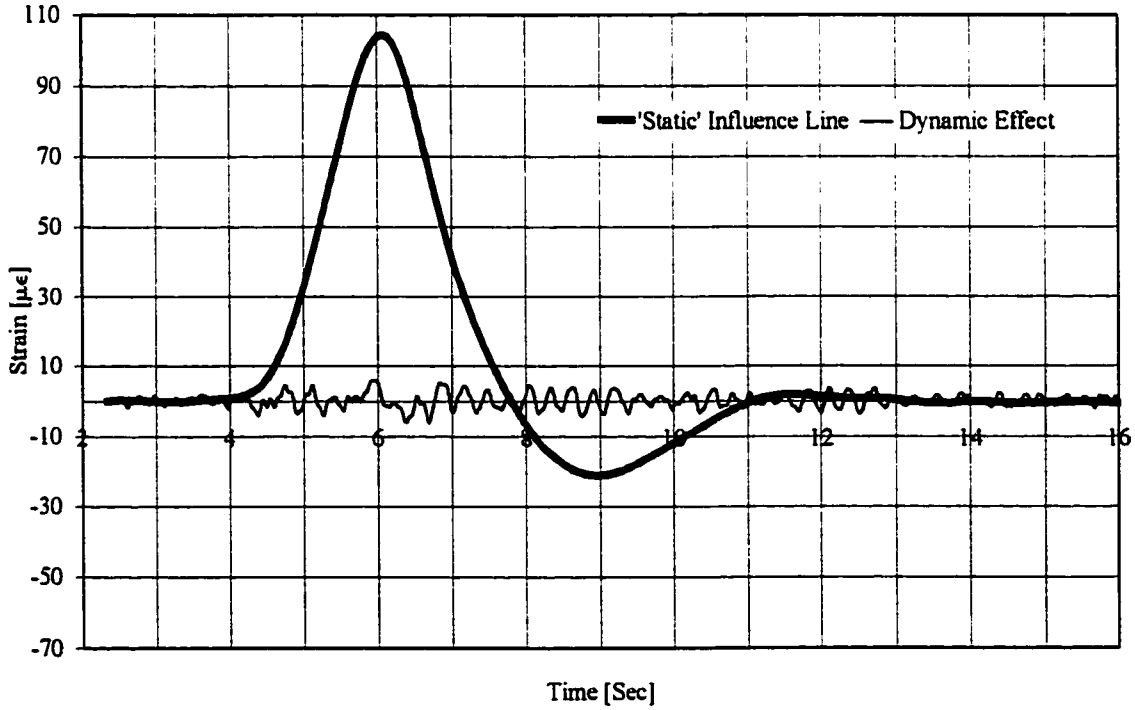

Figure B60: 40 km/hr Test, August '98 for Gauge G34 Filtered Data

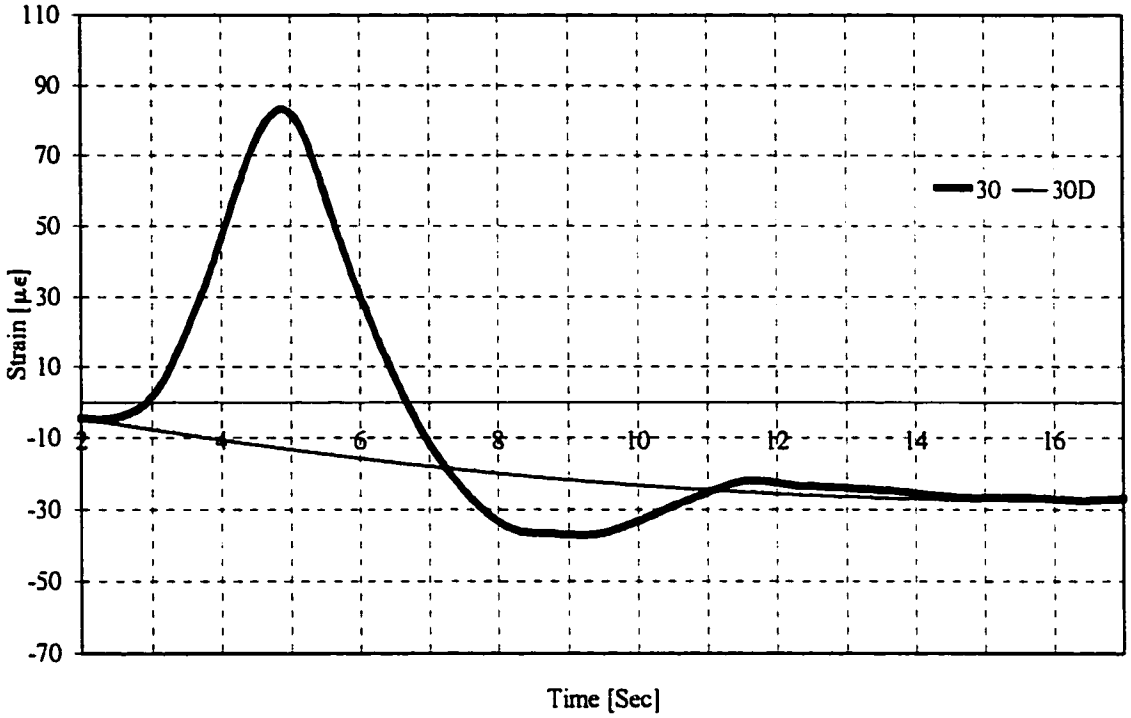

Figure B61: 30 km/hr Test, August '98 for Gauge G3 Filtered Data

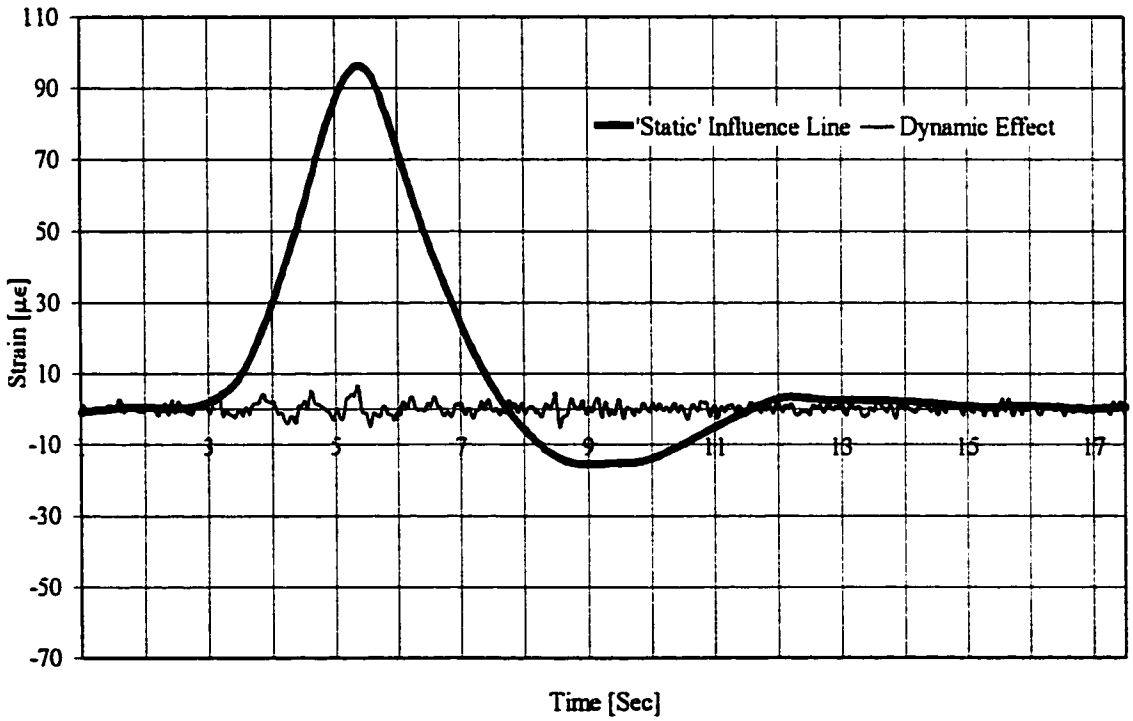

Figure B62: 30 km/hr Test, August '98 for Gauge G3 Filtered Data

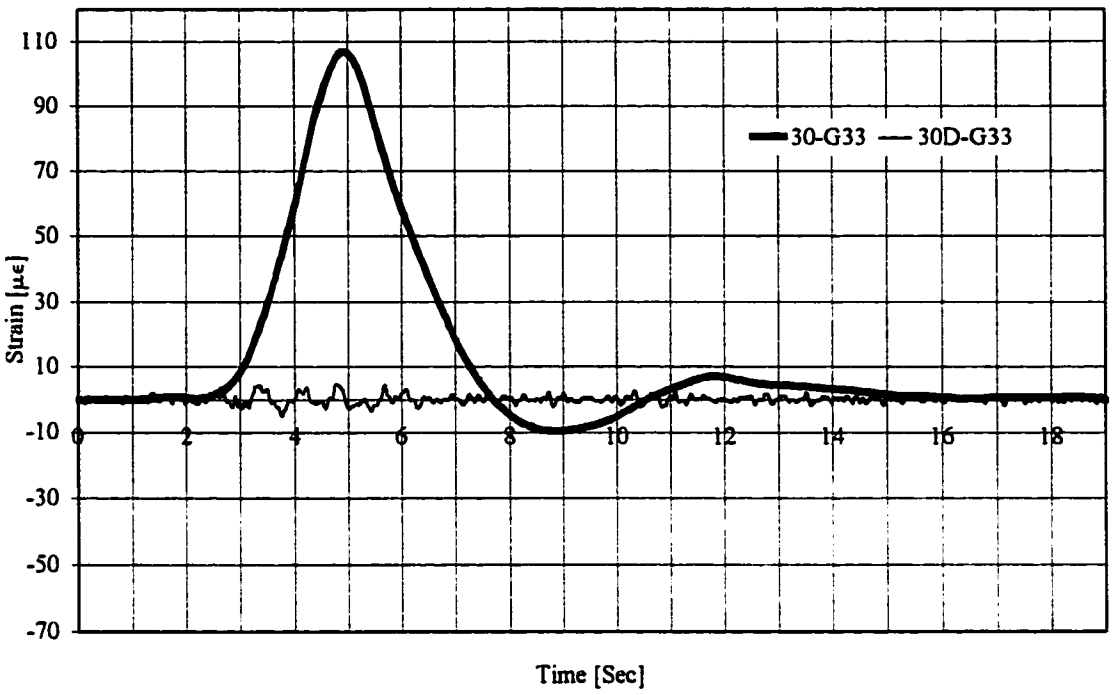

Figure B63: 30 km/hr Test, August '98 for Gauge G33 Filtered Data

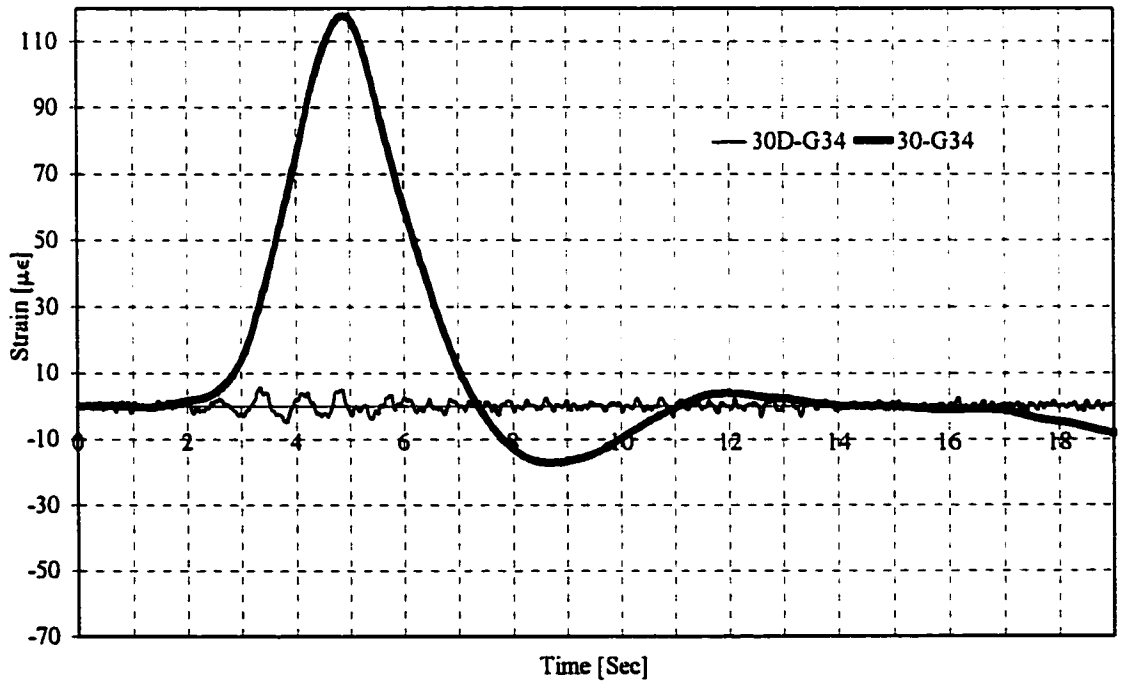

Figure B64: 30 km/hr Test, August '98 for Gauge G33 & G34 Filtered Data

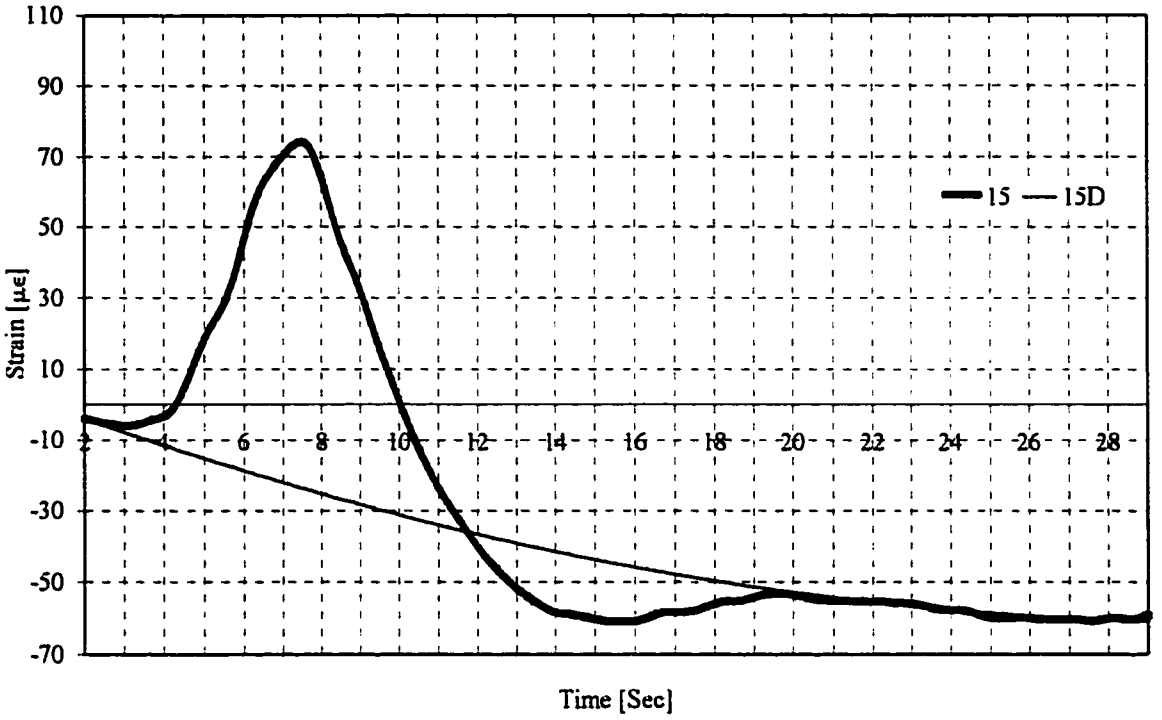

Figure B65: 15 km/hr Test, August '98 for Gauge G3 Filtered Data

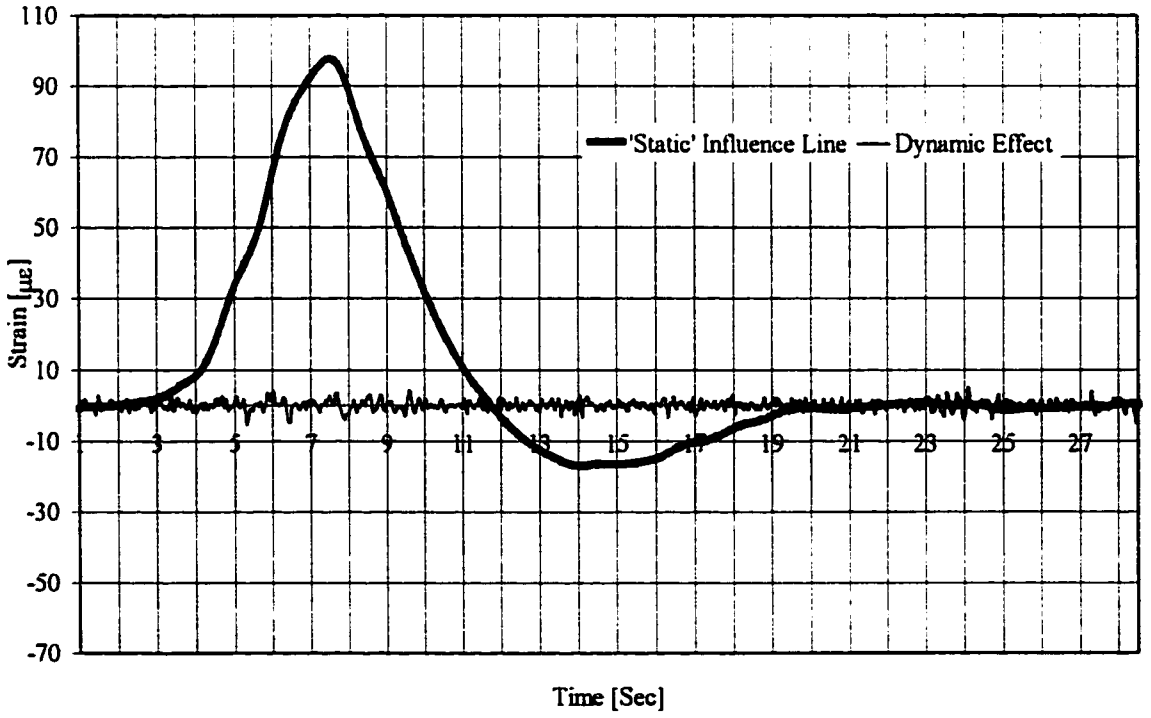

Figure B66: 15 km/hr Test, August '98 for Gauge G3 Filtered Data

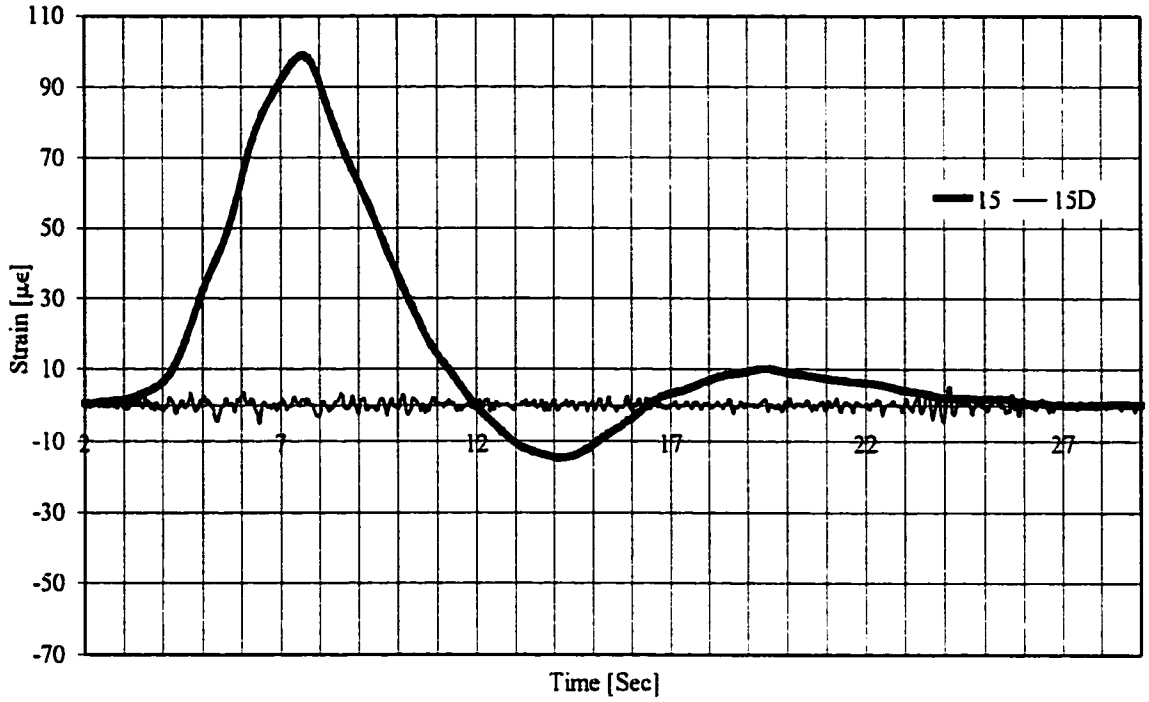

Figure B67: 15 km/hr Test, August '98 for Gauge G33 Filtered Data

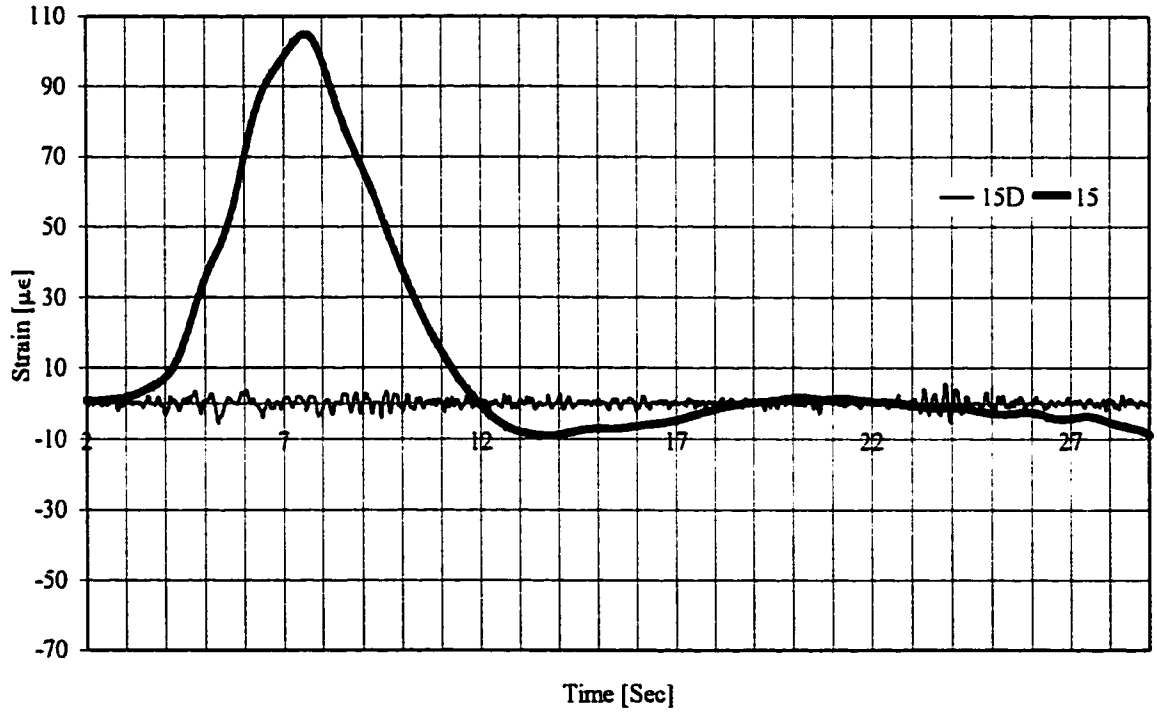

Figure B68: 15 km/hr Test, August '98 for Gauge G34 Filtered Data

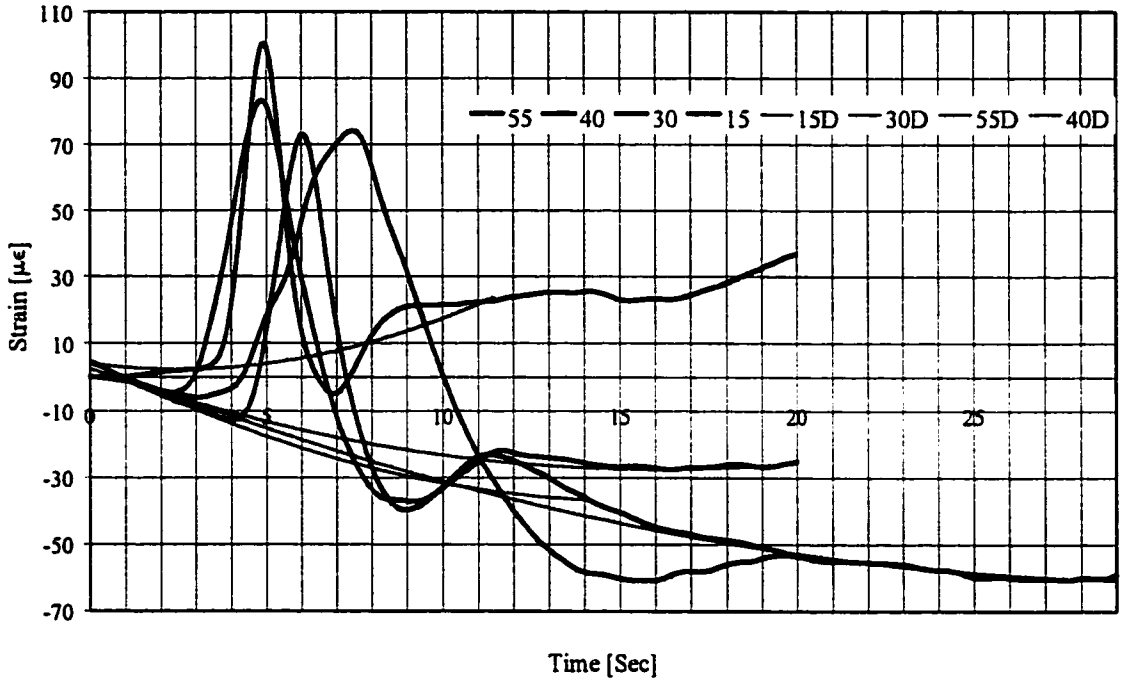

Figure B69: All Four Test Speeds, August '98 for Gauge G3 Filtered Data

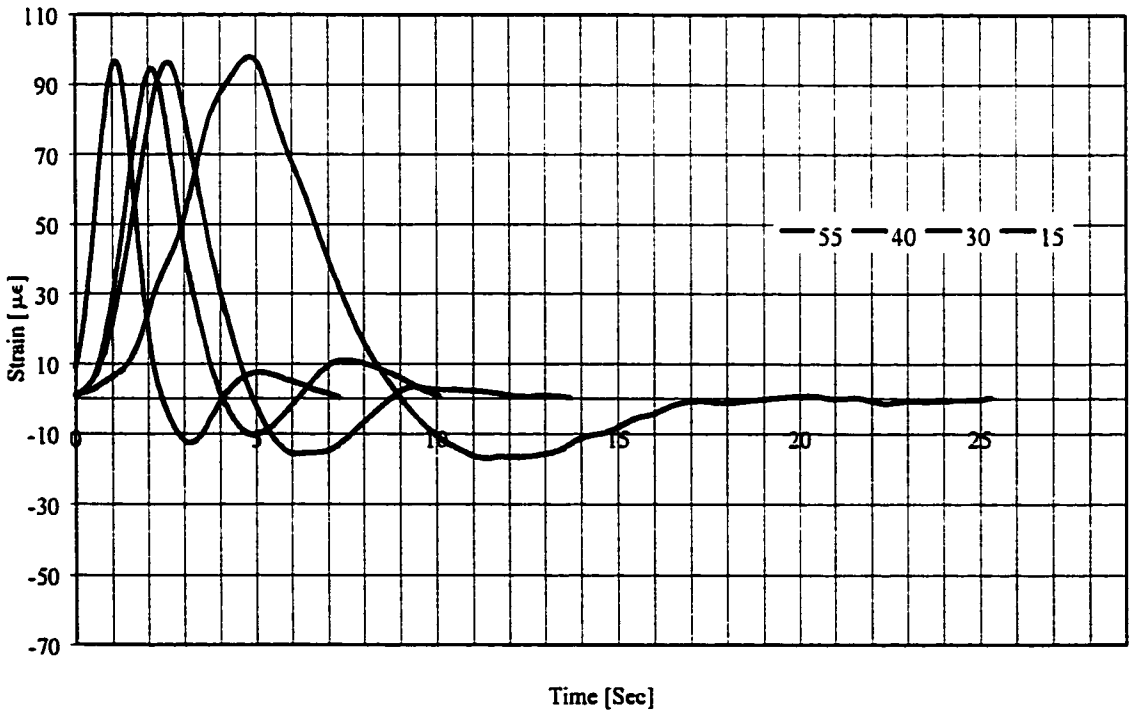

Figure B70: All Four Test Speeds, August '98 for Gauge G3 Filtered Data

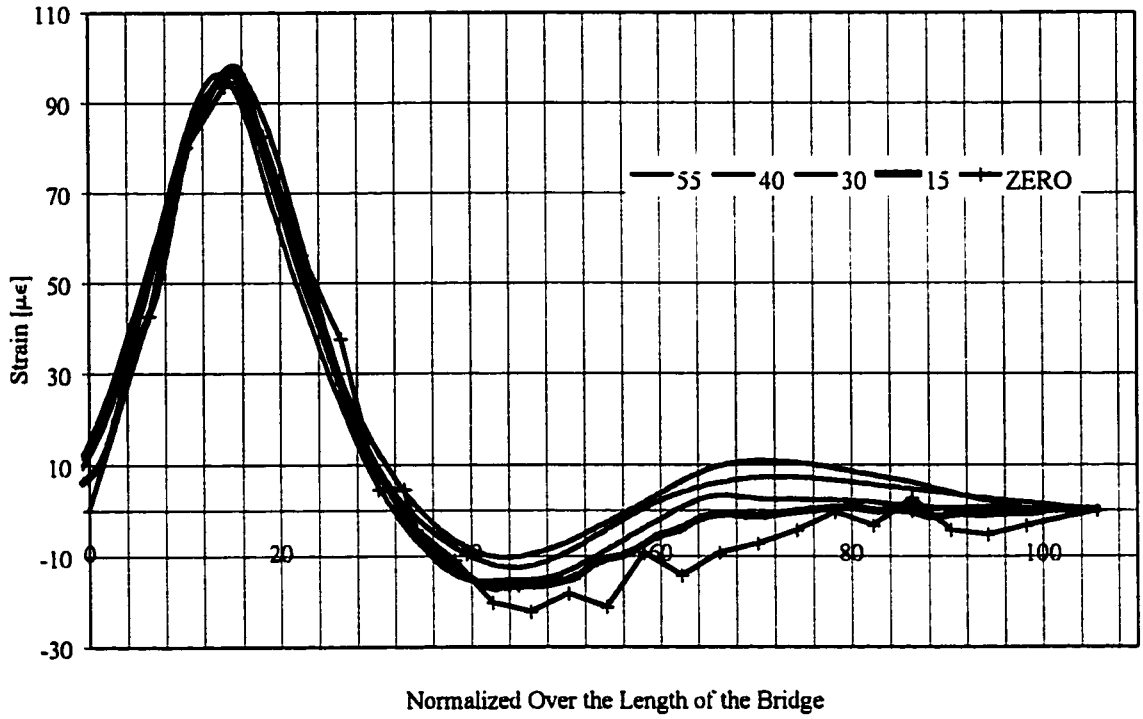

Figure B71: All Four Test Speeds, August '98 for Gauge G3 Filtered Data Superimposed

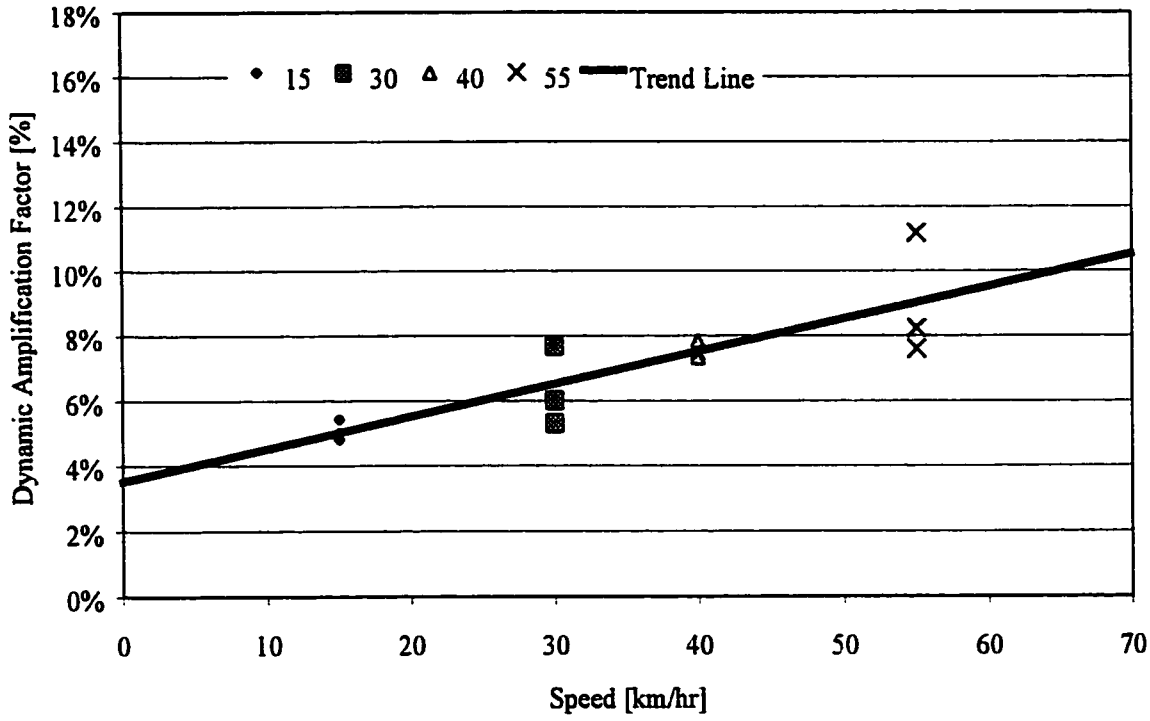

Figure B72: Dynamic Amplification Factor versus Speeds from Cable Transducers

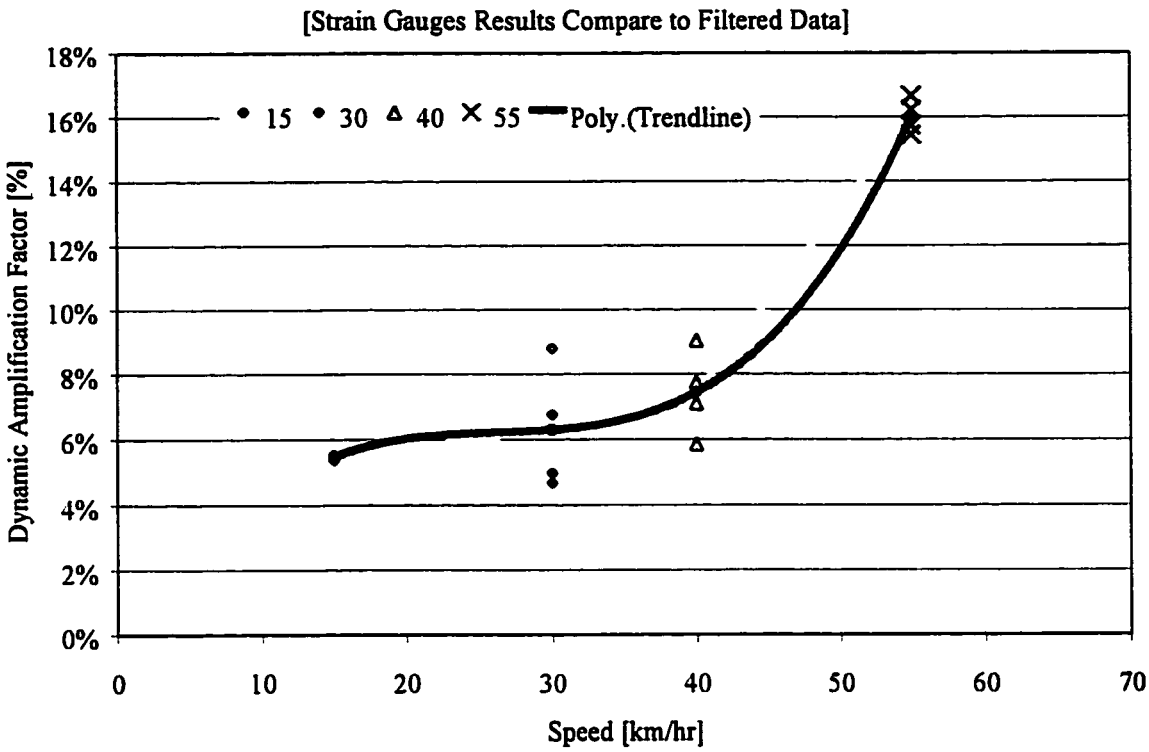

Figure B73: Dynamic Amplification Factor versus Speeds from Strain Gauges

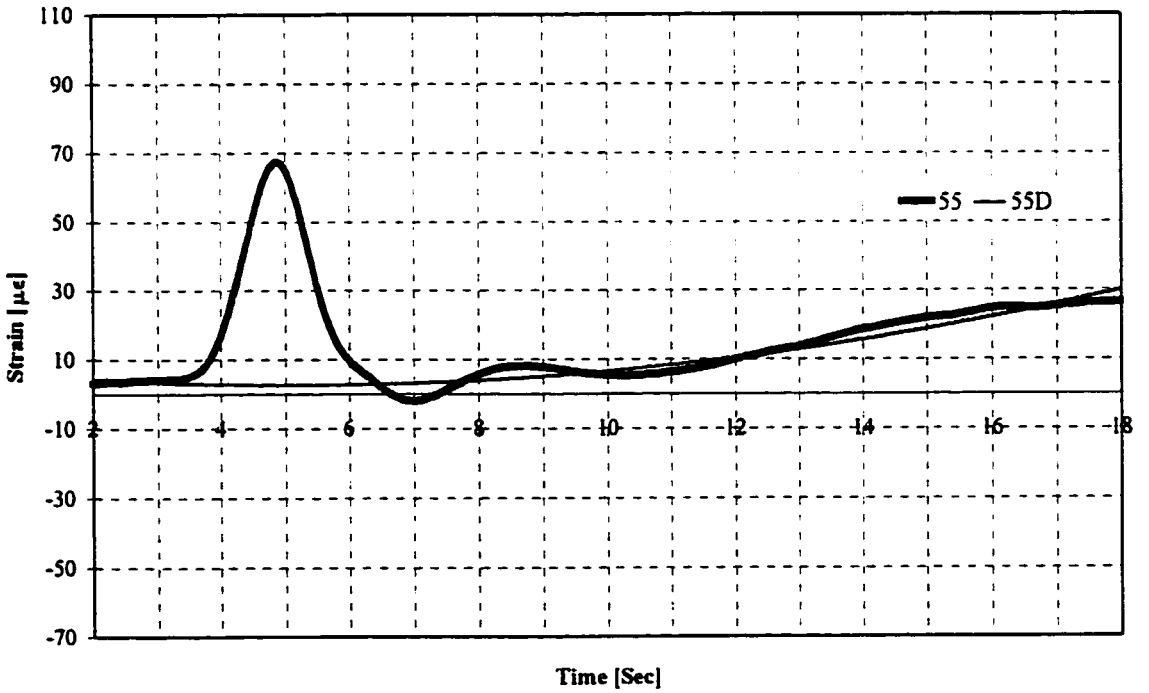

Figure B74: 55 km/hr Test, August '98 for Gauge #6 Before Corrected for Drifts

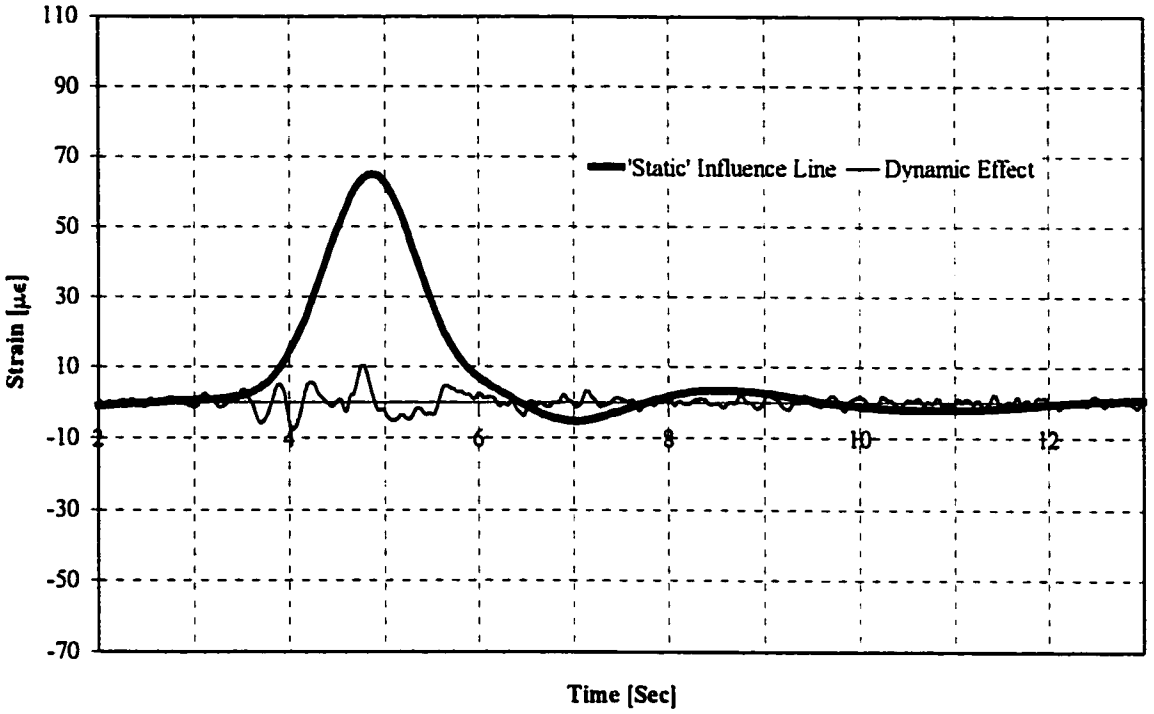

Figure B75: 55 km/hr Test, August '98 for Gauge #6 After Corrected for Drifts

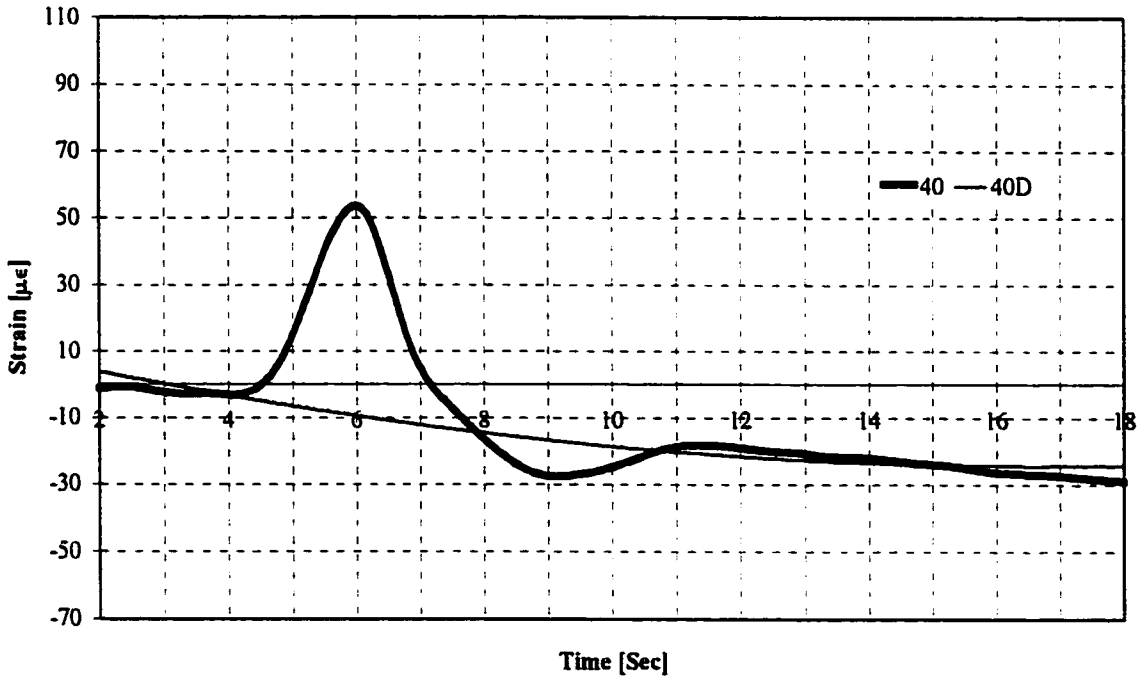

Figure B76: 40 km/hr Test, August '98 for Gauge #6 Before Corrected for Drifts

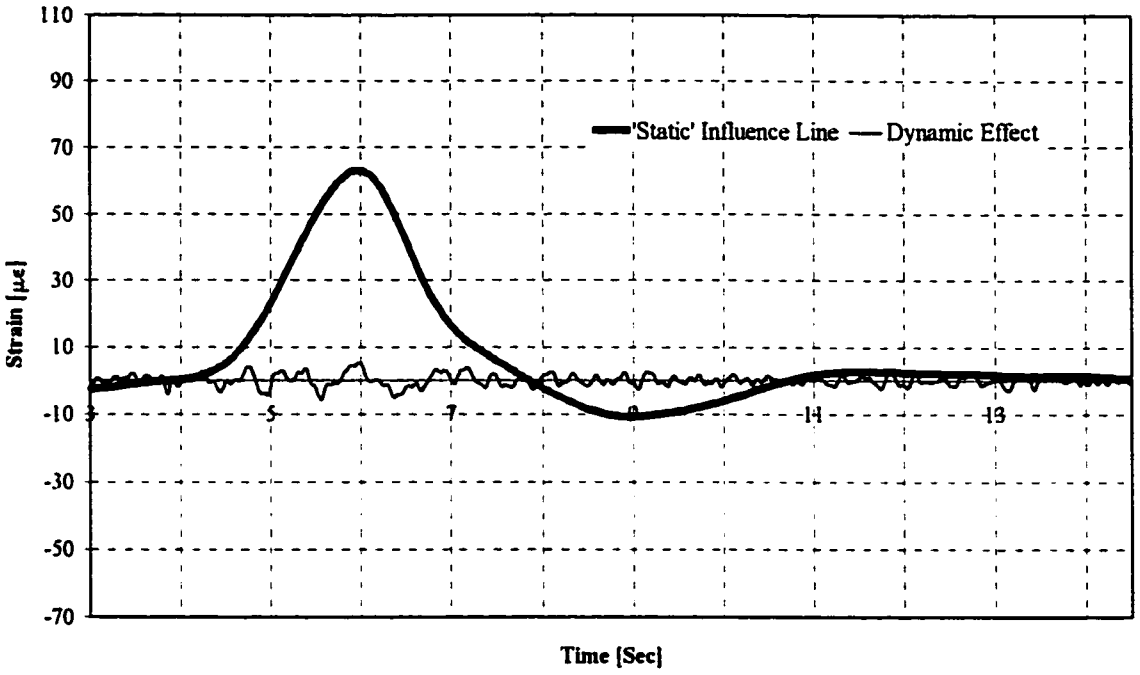

Figure B77: 40 km/hr Test, August '98 for Gauge #6 After Corrected for Drifts

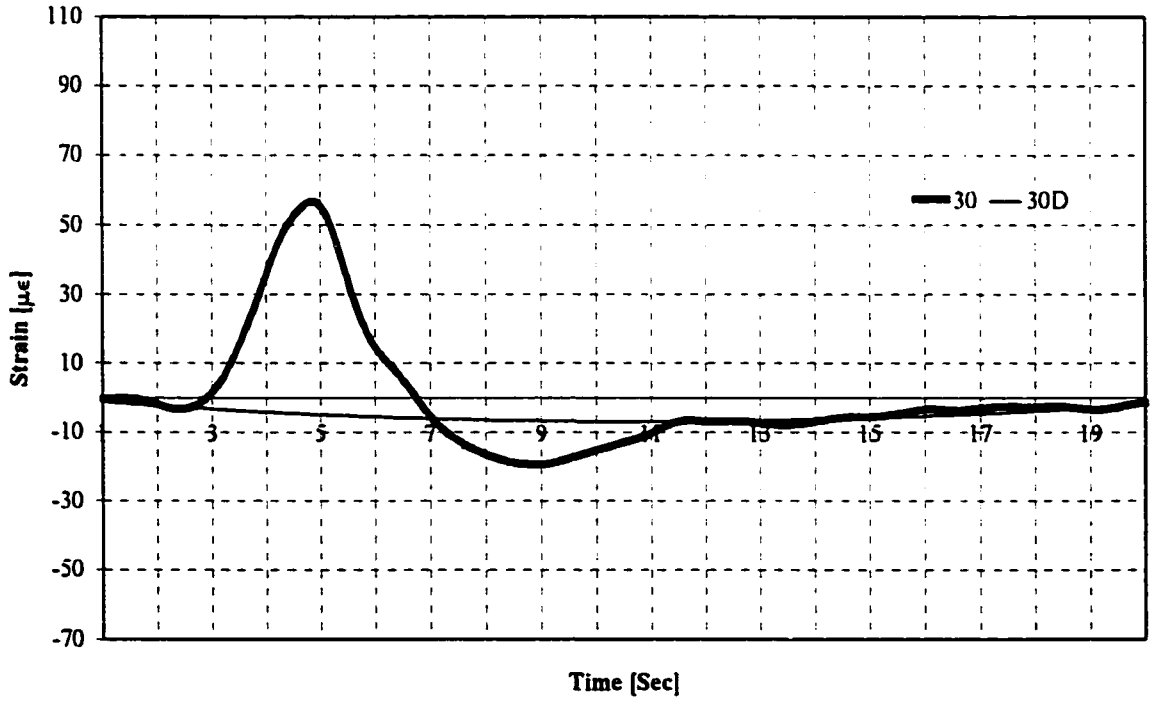

Figure B78: 30 km/hr Test, August '98 for Gauge #6 Before Corrected for Drifts

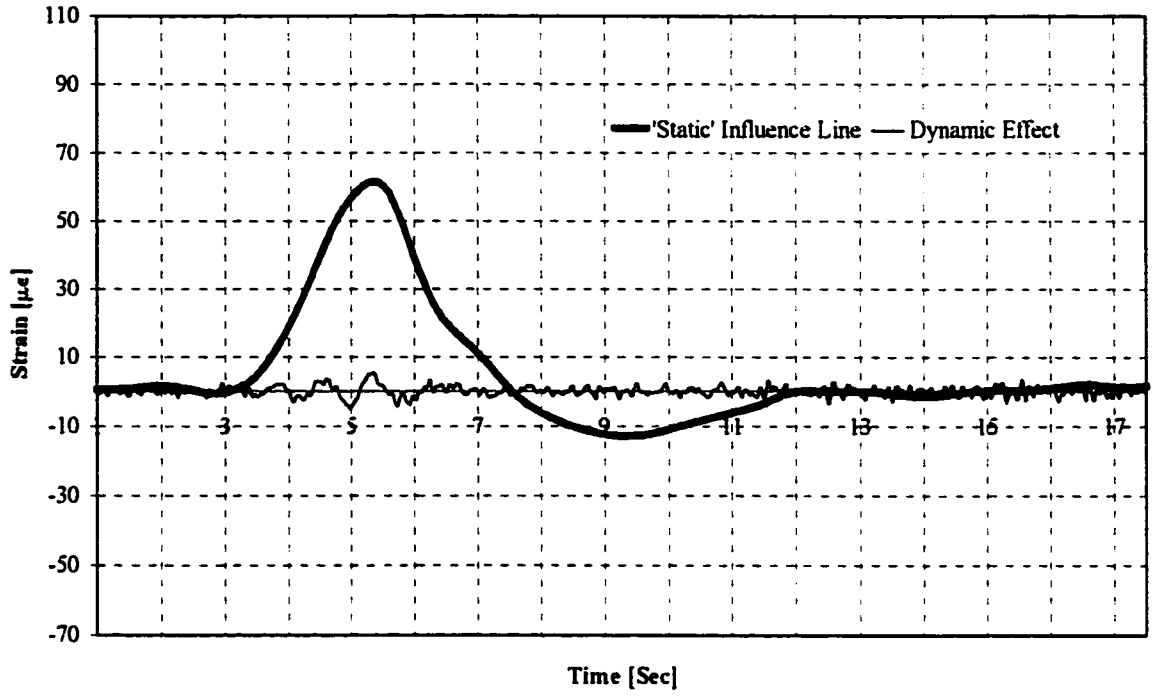

Figure B79: 30 km/hr Test, August '98 for Gauge #6 After Corrected for Drifts

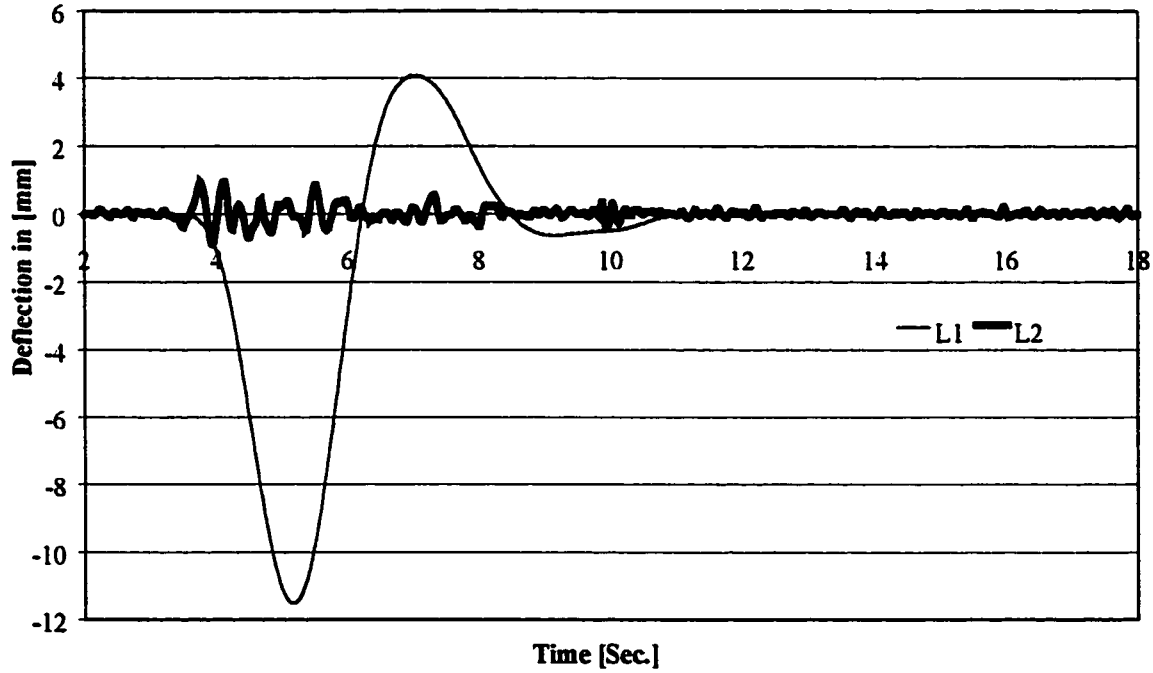

Figure B80: 55 km/hr Test, August '98 for Cable Transducer #1 Filtered Data Set 1

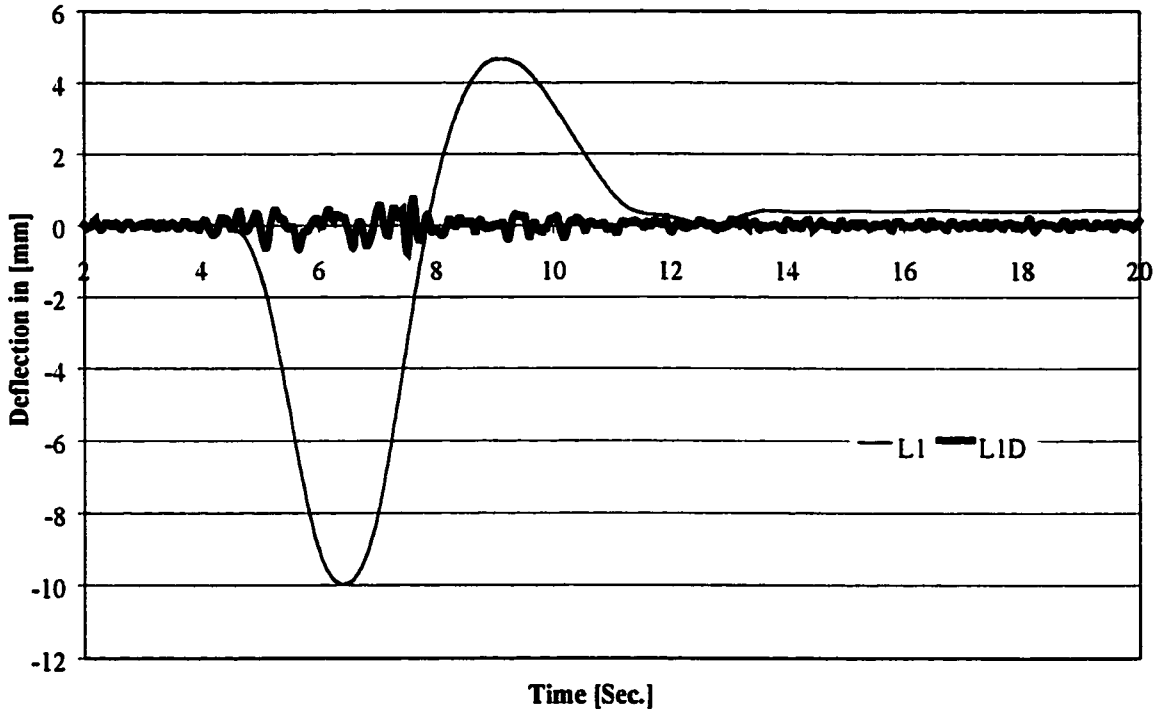

Figure B81: 40 km/hr Test, August '98 for Cable Transducer #1 Filtered Data Set 1

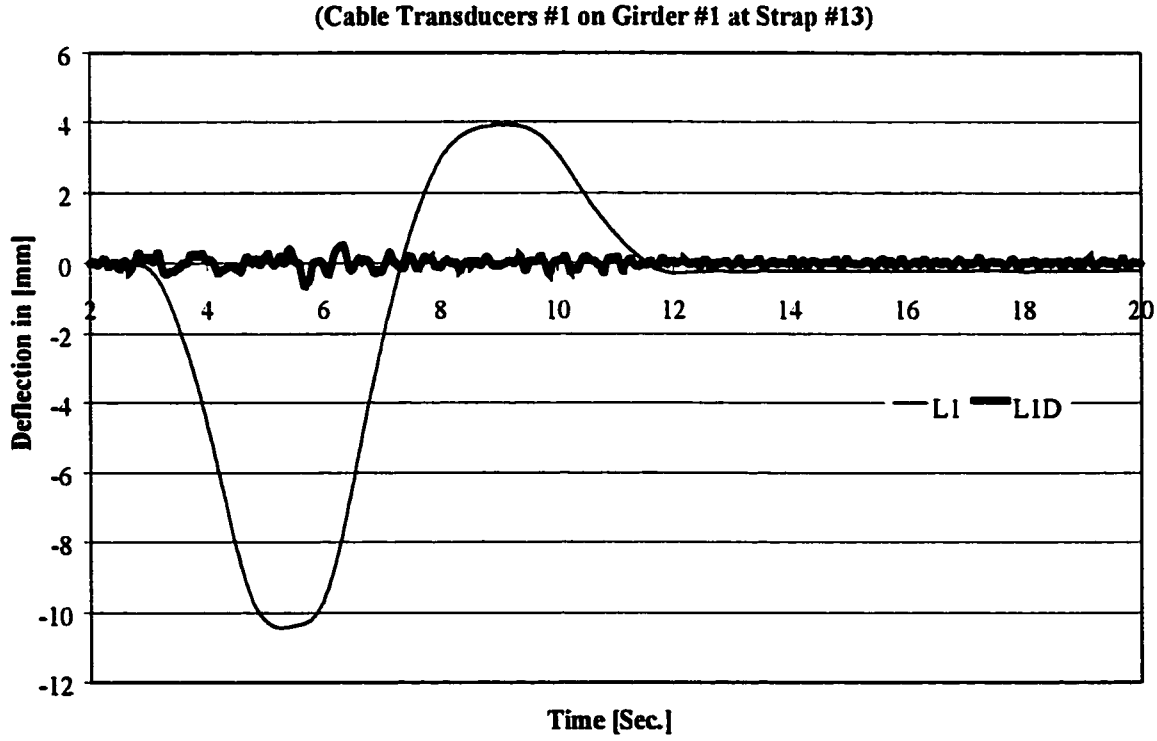

Figure B82: 30 km/hr Test, August '98 for Cable Transducer #1 Filtered Data Set 1

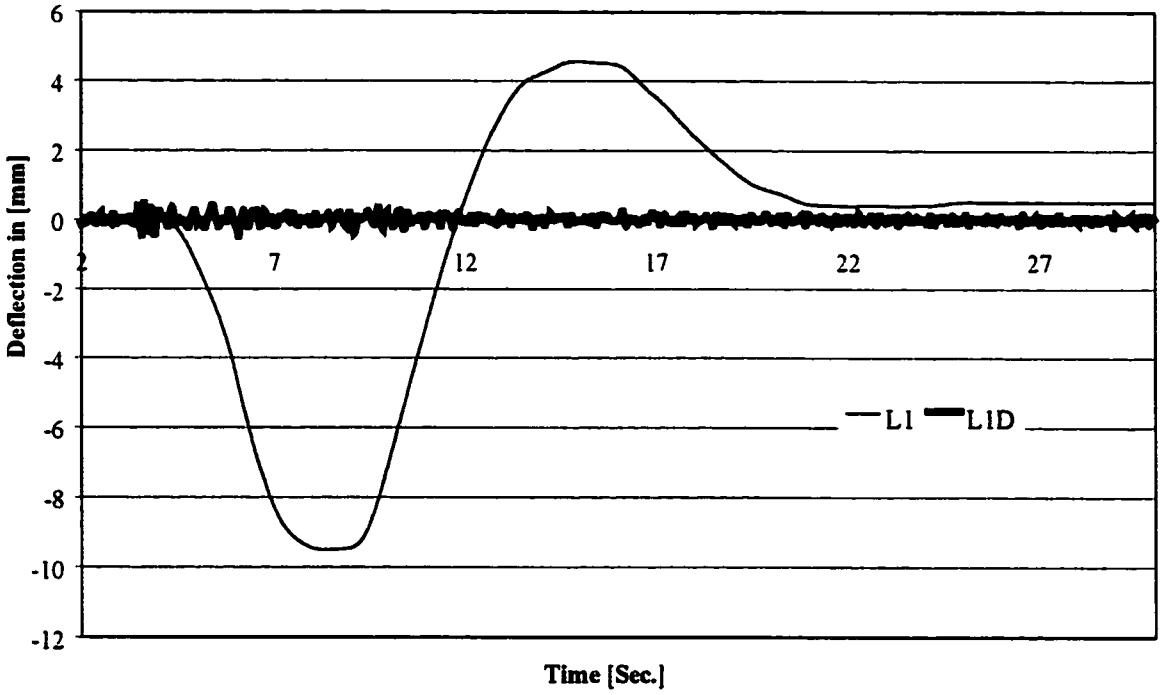

Figure B83: 15 km/hr Test, August '98 for Cable Transducer #1 Filtered Data Set 1

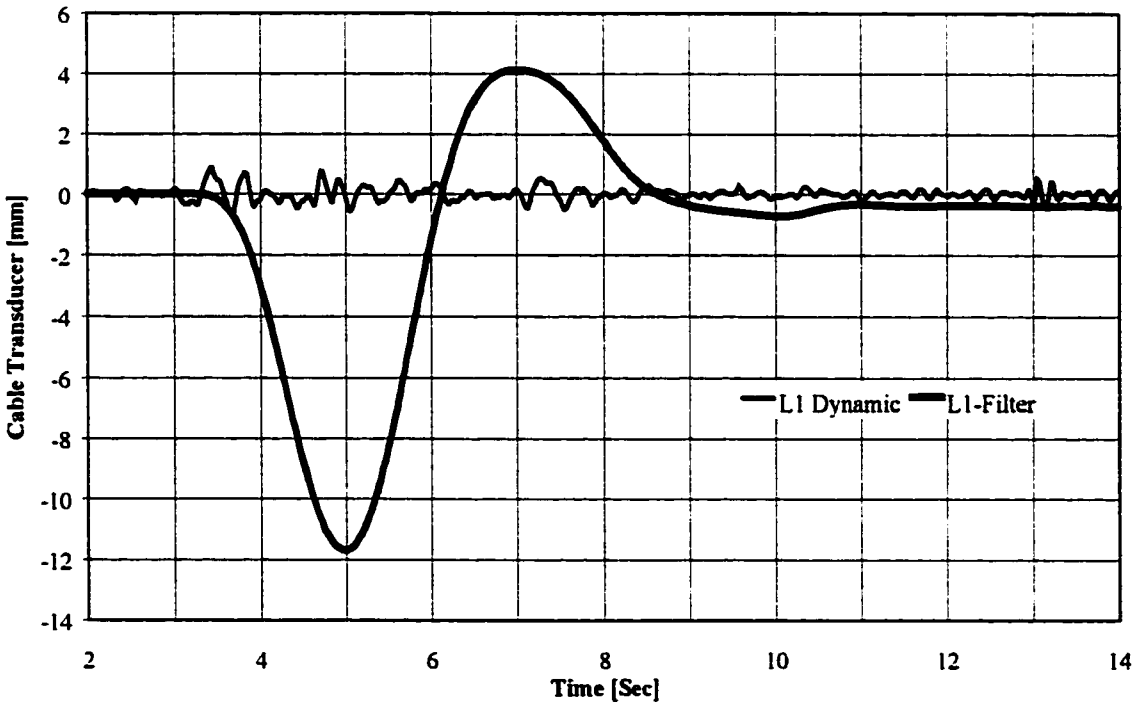

Figure B84: 55 km/hr Test, August '98 for Cable Transducer #1 Filtered Data Set 2

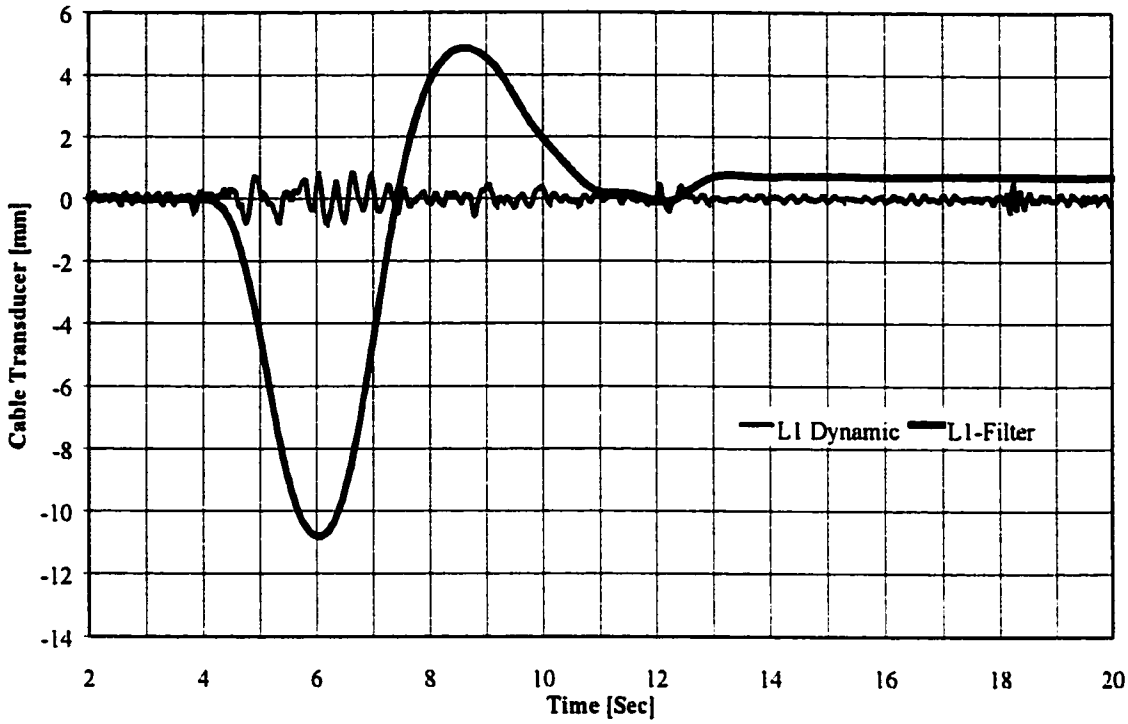

Figure B85: 40 km/hr Test, August '98 for Cable Transducer #1 Filtered Data Set 2

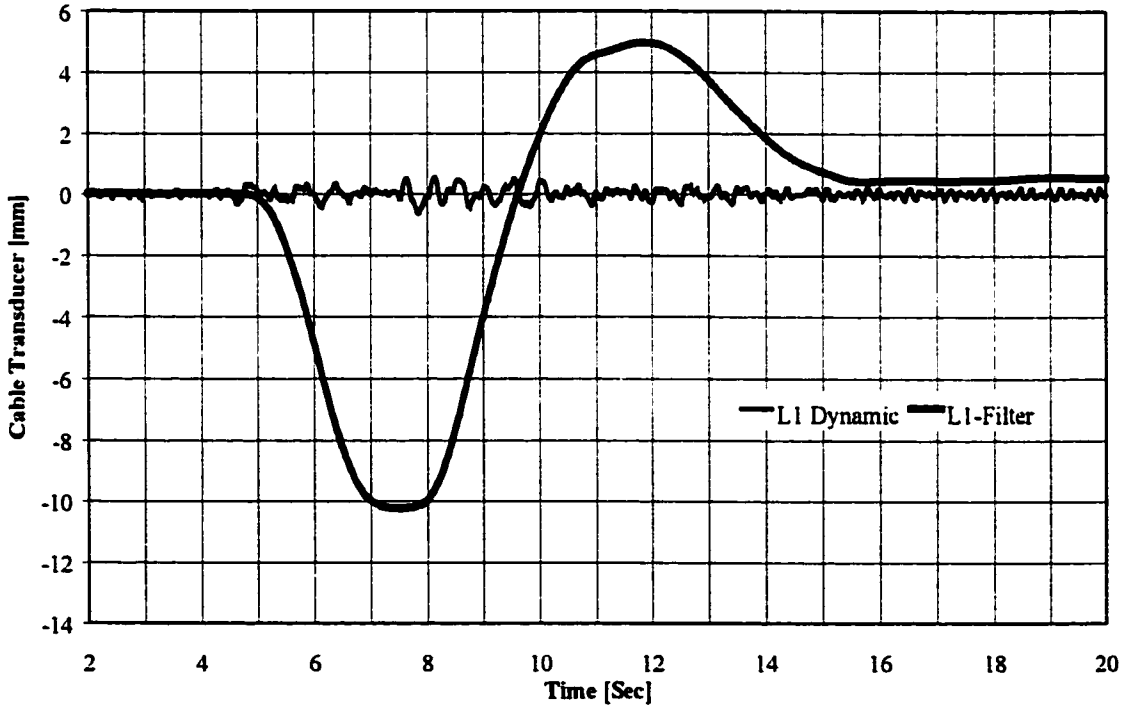

Figure B86: 30 km/hr Test, August '98 for Cable Transducer #1 Filtered Data Set 2

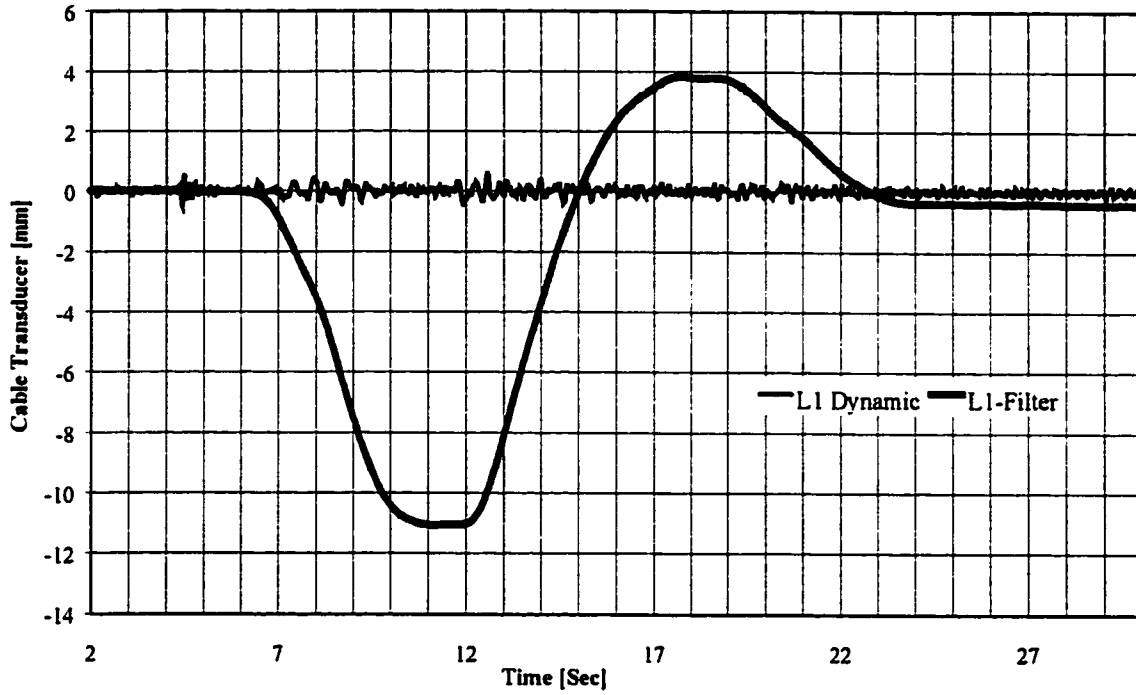

Figure B87: 15 km/hr Test, August '98 for Cable Transducer #1 Filtered Data Set 2

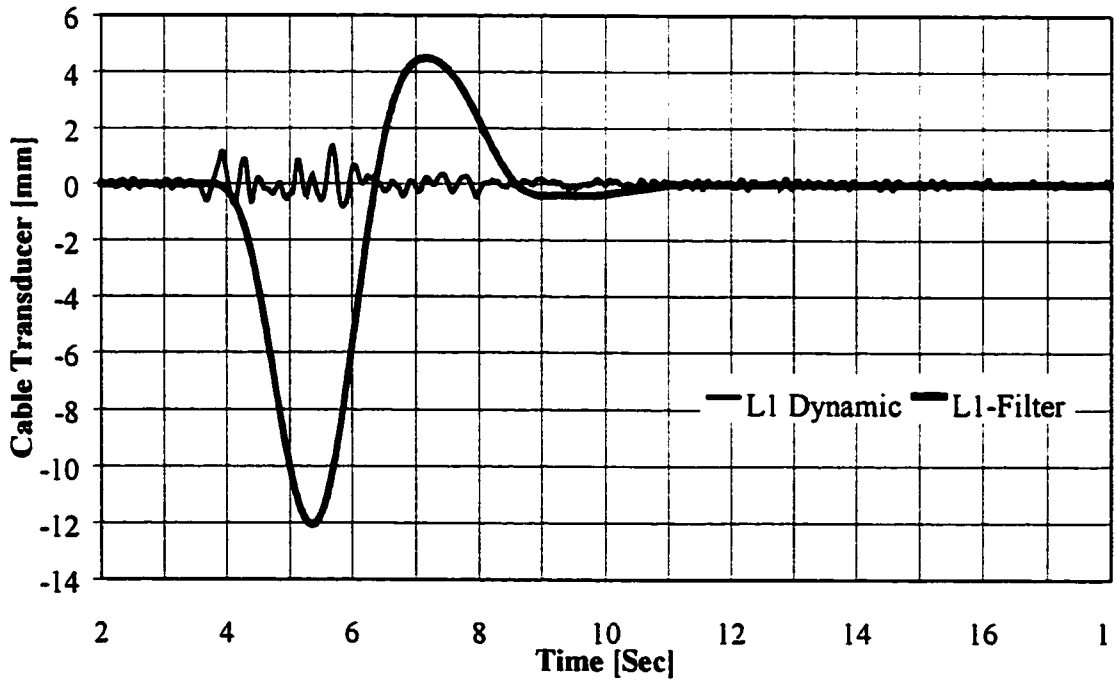

Figure B88: 55 km/hr Test, August '98 for Cable Transducer #1 Filtered Data Set 3

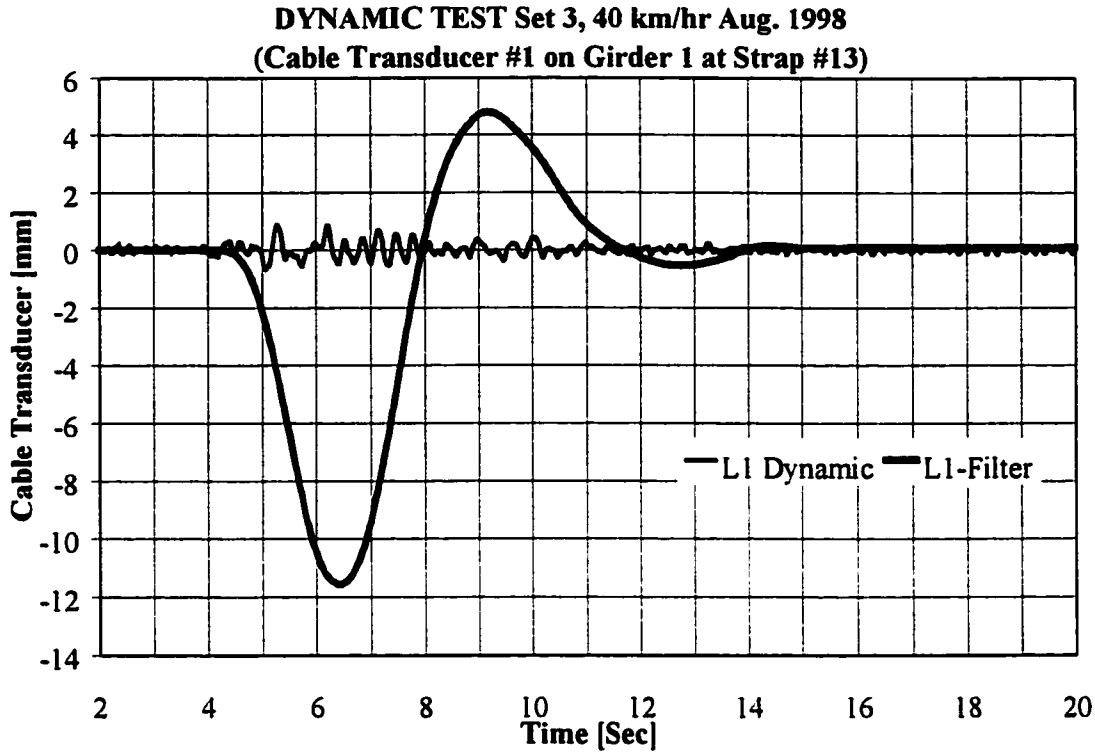

Figure B89: 40 km/hr Test, August '98 for Cable Transducer #1 Filtered Data Set 3

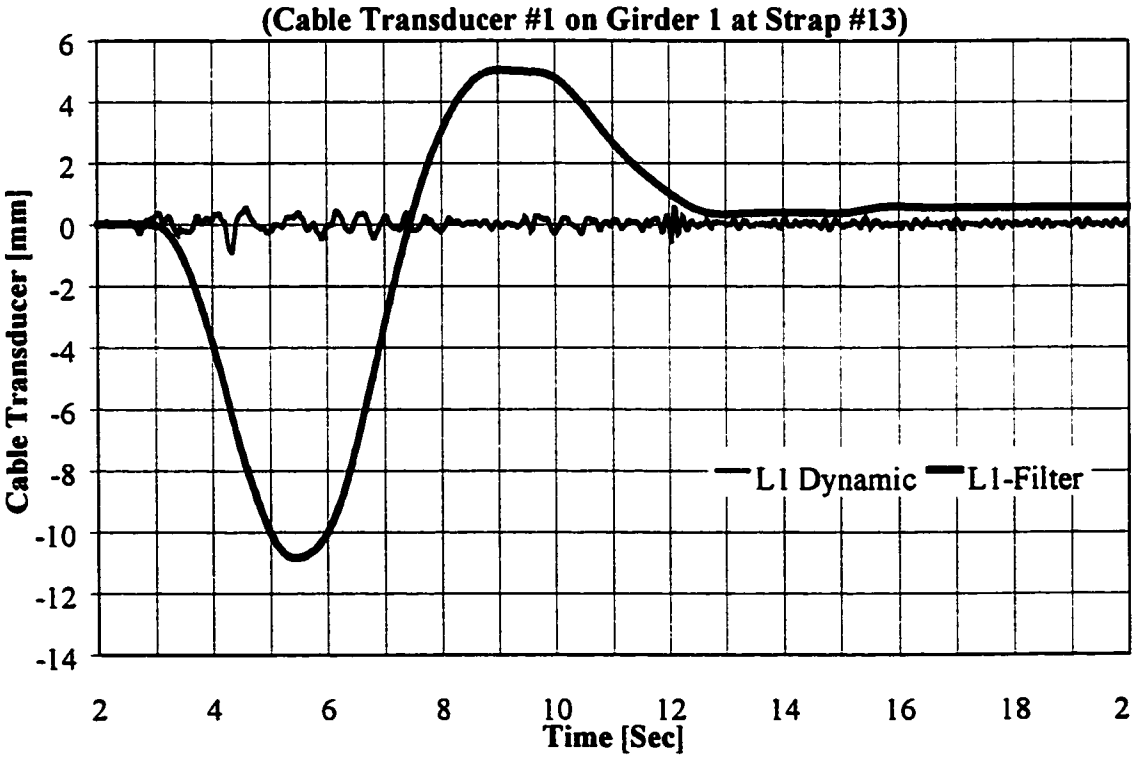

Figure B90: 30 km/hr Test, August '98 for Cable Transducer #1 Filtered Data Set 3

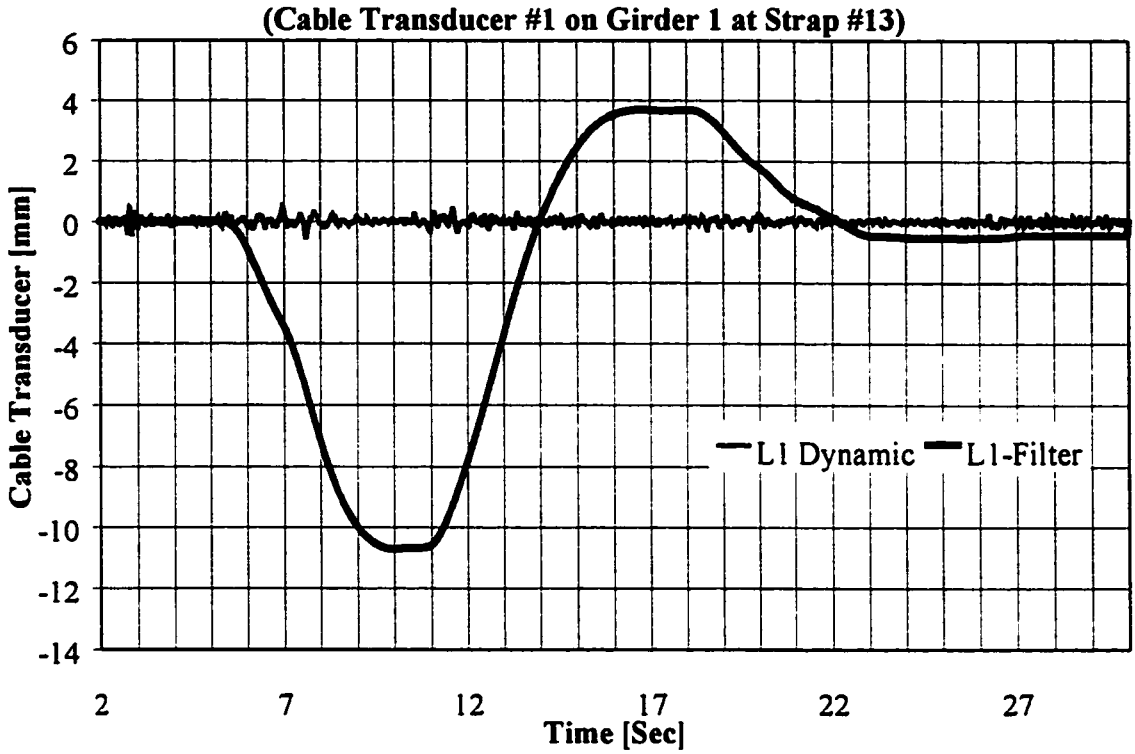

Figure B91: 15 km/hr Test, August '98 for Cable Transducer #1 Filtered Data Set 3

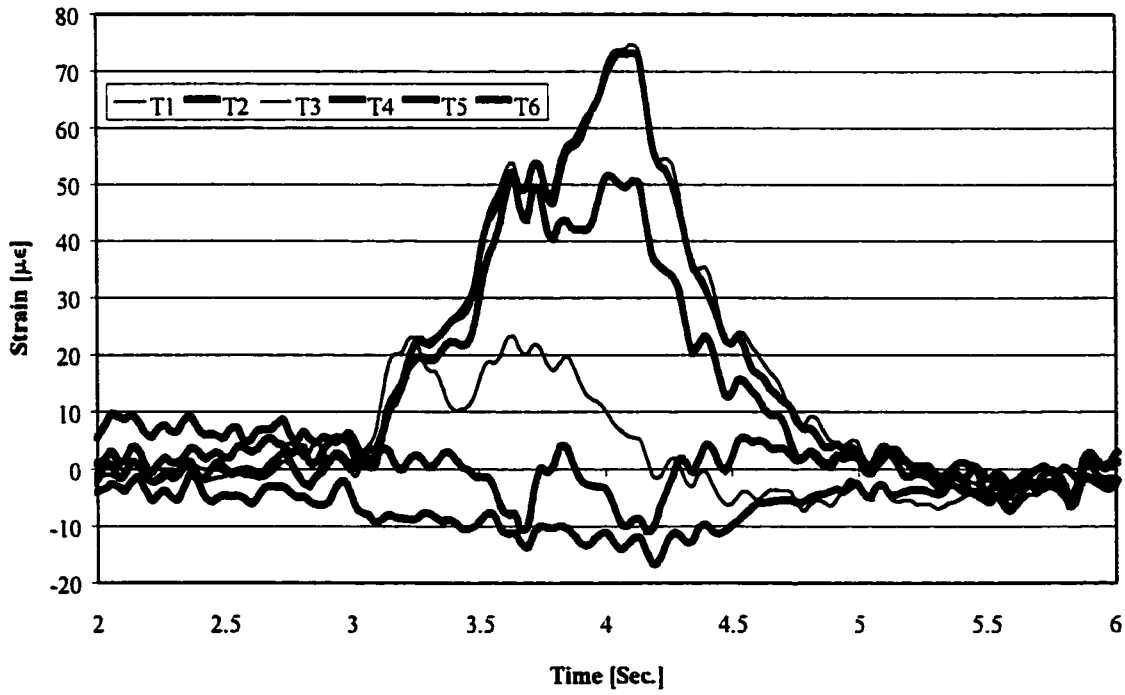

Figure B92: 55 km/hr Test, August '98 for Strain on One Steel Straps, Set 2

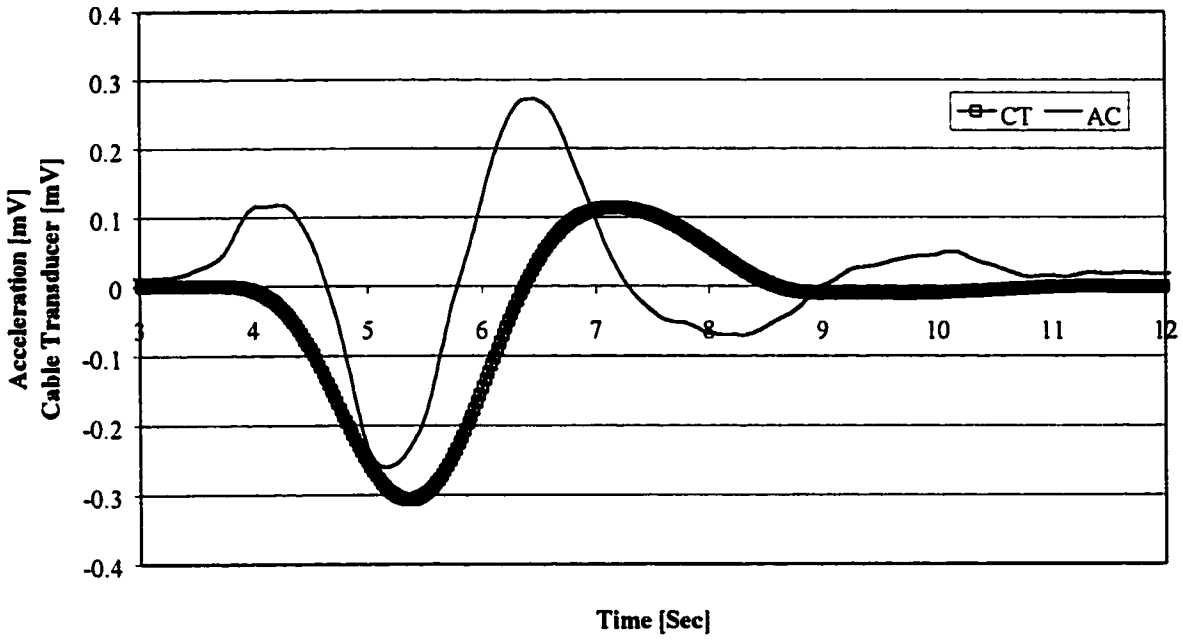

Figure B93: 55 km/hr Test, August '98 for Cable Transducer #1 and Accelerometer #8 Filtered Data Set 3 for a Low Pass Filtered of 0.8 Hz.

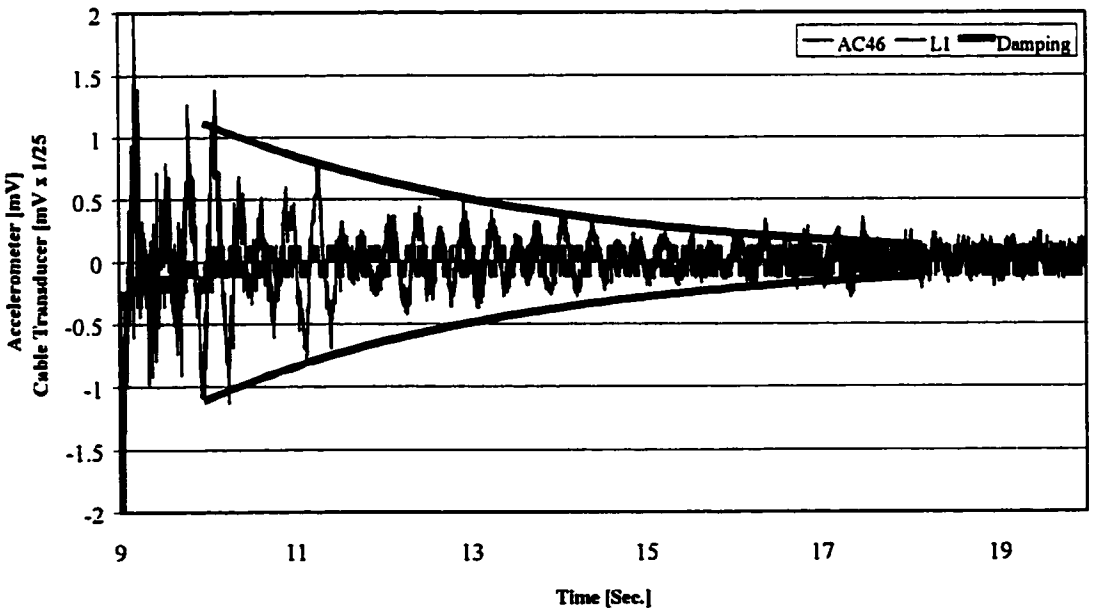

Figure B94: Damping Cure for Free Vibration Phase in Test Set 3

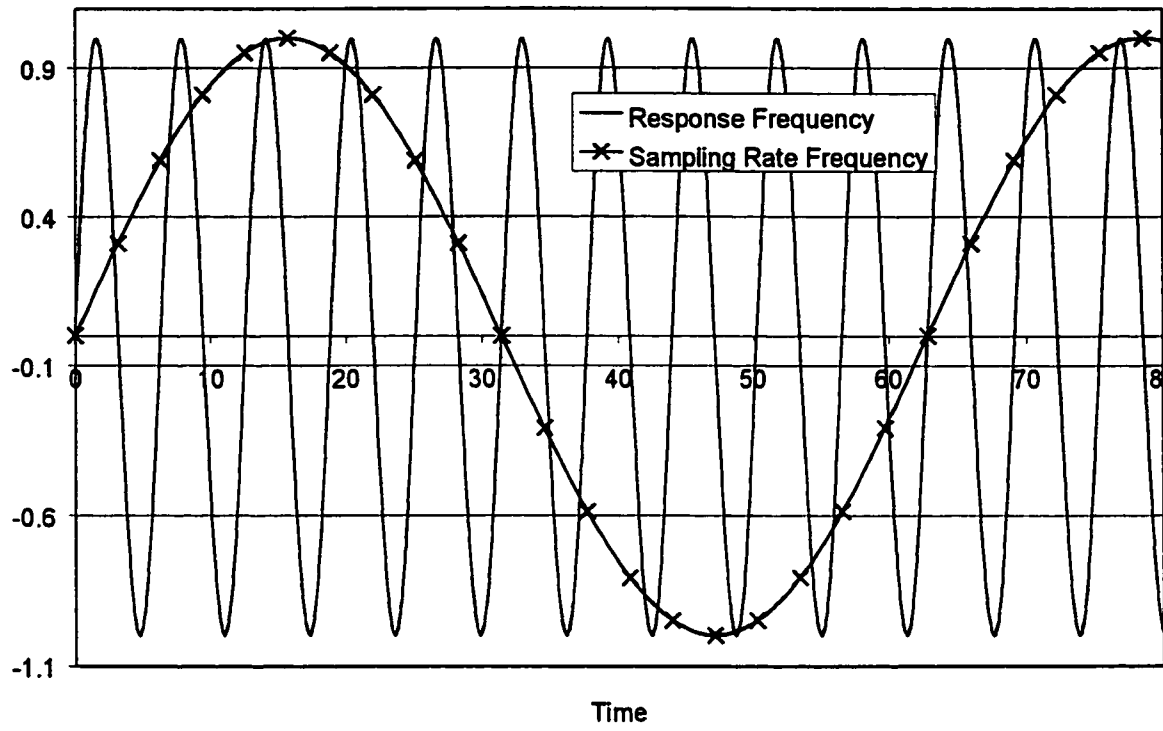

Figure B95: Potential Aliasing Error

INFORMATION TO USERS

This manuscript has been reproduced from the microfilm master. UMI films the text directly from the original or copy submitted. Thus, some thesis and dissertation copies are in typewriter face, while others may be from any type of computer printer.

The quality of this reproduction is dependent upon the quality of the copy submitted. Broken or indistinct print, colored or poor quality illustrations and photographs, print bleedthrough, substandard margins, and improper alignment can adversely affect reproduction.

In the unlikely event that the author did not send UMI a complete manuscript and there are missing pages, these will be noted. Also, if unauthorized copyright material had to be removed, a note will indicate the deletion.

Oversize materials (e.g., maps, drawings, charts) are reproduced by sectioning the original, beginning at the upper left-hand corner and continuing from left to right in equal sections with small overlaps.

Photographs included in the original manuscript have been reproduced xerographically in this copy. Higher quality 6" x 9" black and white photographic prints are available for any photographs or illustrations appearing in this copy for an additional charge. Contact UMI directly to order.

ProQuest Information and Learning
300 North Zeeb Road, Ann Arbor, MI 48106-1346 USA
800-521-0600

THE UNIVERSITY OF ALBERTA

MODELING FLUIDIZED BED JET INTERACTIONS USING COMPUTATIONAL FLUID DYNAMICS

by

JONATHAN JAMES TYLER 

A THESIS

SUBMITTED TO THE FACULTY OF GRADUATE STUDIES AND RESEARCH IN

PARTIAL FUFILMENT OF THE REQUIREMENTS FOR THE DEGREE OF

MASTER OF SCIENCE

IN

CHEMICAL ENGINEERING

DEPARTMENT OF CHEMICAL AND MATERIALS ENGINEERING

EDMONTON, ALBERTA

SPRING, 2000

THE UNIVERSITY OF ALBERTA

Library Release Form

NAME OF AUTHOR: Jonathan James Tyler

TITLE OF THESIS: Modeling Fluidized Bed Jet Interactions Using Computational Fluid Dynamics

DEGREE: Master of Science

YEAR THIS DEGREE GRANTED: 2000

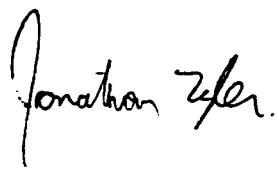

8 Hythe Ave. South
Burnaby, British Columbia
V5A 3B4

Date: January 28, 2000

THE UNIVERSITY OF ALBERTA

FACULTY OF GRADUATE STUDIES AND RESEARCH

The undersigned certify that they have read, and recommend to the Faculty of Graduate Studies and Research, for acceptance, a thesis entitled MODELING FLUIDIZED BED JET INTERACTIONS USING COMPUTATIONAL FLUID DYNAMICS submitted by Jonathan James Tyler in partial fufilment of the requirements for the degree of Master of Science in Chemical Engineering.

Dr. P.A.J. Mees, Supervisor

Dr. K. Nandakumar

Dr. J. Yokota

Date: November 26, 1999

ABSTRACT

Computational fluid dynamic (CFD) simulations were conducted using CFX 4.2 from AEA Technology in order to verify and validate the two fluid multiphase flow models against experimental results. A fully three dimensional fluidized bed simulation with a side injection gas nozzle was constructed and simulations performed at various jet velocities, aeration rates and with different model parameters.

Based on these simulations it was determined that the Superbee TVD discretization scheme should be used on a well designed discretization mesh of at least 50,000 nodes. Particular care must be taken when specifying the nozzle inlet boundary condition.

Predicted bubble behavior and jet penetration into the fluidized bed agreed well with literature and experimental results. Two large recirculation zones were predicted to form within the fluidized bed; the simulations tended to over predict these recirculation zones. The two fluid model within CFX 4.2 gives results that agree qualitatively with experiments.

ACKNOWLEDGEMENTS

The author would like to extend his gratitude to Dr. Philip Mees for his supervision, guidance and support throughout this project. It has been a challenging and rewarding project.

Additional support and discussion has been provided from members at Syncrude Canada Limited from Dr. Barry Bara, Dr. Larry Hackman and Dan Bulbuc. Without these people this project would not have been possible. Thanks to Dr. Berutti and Jason Cowpan from the University of Saskatchewan for sharing their experimental apparatus and for the enjoyable time that I spent in their company gathering observations from the apparatus.

Financial support was provided from Syncrude Canada Limited; without whom my experience as a graduate student and an engineer would have been much diminished. Scholarships from NSERC Canada and the University of Alberta have been greatly appreciated and contributed to the overall successes enjoyed in this project. I am very grateful for this support.

I would like to thank Bob Barton and Jacques Gibeau for maintaining and troubleshooting the computer systems. Without their help and expertise my work would not have been completed.

Finally, I would like to thank my family and friends for their support and patience throughout this project. A special thanks to Catherine for making sure that my weekends were spent in the mountains and not in front of the computer screen.

TABLE OF CONTENTS

LIST OF TABLES

LIST OF FIGURES

NOMENCLATURE

Arabic Letters

Symbol	Description
$\bar{r}$	Position vector
$\hat{e}_i$	Unit direction basis vector
$\bar{\bar{J}}$	Jacobian
$\bar{v}$	Velocity vector
$\hat{n}$	Unit normal vector
$\bar{\bar{I}}$	Identity matrix
$\bar{f}_b$	Body force vector
$\bar{\bar{A}}$	General matrix
$\bar{F} = (F_1, F_2, F_3)$	Continuous vector function
$\hat{i}, \hat{j}, \hat{k}$	Unit basis vectors in Cartesian coordinates
$\dot{m}_{\alpha\beta}$	Thermodynamic phase change from phase α to β
$\bar{U}$	Velocity vector
$\dot{M}$	General mass flux (used in Rhie-Chow interpolation)
$\bar{B}$	Cell average of other terms in momentum equation over point P
ΔU	System relative velocity
Δx, Δy, Δz	Mesh spacing in X, Y and Z directions
(X_1, X_2, X_3)	Particle origin point
(x_1, x_2, x_3)	Current position
A	Bounding area
a_i	Particle radii in a specific group

A_i	Area of control volume face at position i=N,E,S,W
a_i	Advection and transient coefficients for phase i
a_{ij}	General *ij* element of matrix $\overline{\overline{A}}$
A_{ij}	Cofactor of matrix $\overline{\overline{A}}$
$A_{O.C}$	Orifice area in simulation
$A_{O.E}$	Orifice area in experiment
b_i	Interphase transfer coefficient for phase *I*
B_P	Other terms in momentum equation at node P
c	Local characteristic velocity
$c_{\alpha\beta}$	Drag coefficient of phase β on phase α
C_D	Drag coefficient
C_i	Convection coefficient at node i
c_i	Source linearization term for phase *i*
Cn	Courant number
D	Denominator
D	Nozzle orifice diameter in simulation
D_0	Nozzle orifice diameter
D_{32}	Sauter mean diameter
D_i	Diffusion coefficient at position i
D_p	Particle diameter (μm)
d_p	Particle diameter (μm)
ds	Cell miss-match
dV	Change of volume in curvilinear coordinate system.

dV_0	Change of volume in Cartesian coordinate system
e	Restitution coefficient
f	Transported quantity
$F(t)$	Integrated quantity, f, over a volume
$f(x,t)$	Integrable function representing conserved quantity
$f_1 f_2$	Bounding surface functions
f_{12}	Collisional force between particles 1 and 2
f_i	Mapping function from x to ξ coordinate system
f_i	Transport quantity at node i
Fr^*	Modified Froude number
$G(\varepsilon)$	Solids pressure function
G_0	Solids compaction modulus
g_0	Radial distribution function
G_s	Solids stress
h,P,k	Parameters defining the fit of parabola Q_i
h_i	Magnitude of curvilinear transform
i,j,k	Control volume indices
$ilen$	Total length of 1-D discretization mesh
k	Empirical parameter
k	Gidaspow dense-phase drag correction multiplicative factor
l	Average interparticle spacing (m)
M	Particle laden jet parameter from Guedon *et al.* (1994)
m^*	System relative mass

m_i	Individual particle mass
n	Number density
n	Iterate count or time step
N	Numerator
N,E,S,W	Relative position of neighboring nodes to central node P
n,e,s,w	Control volume interfaces
P	Particle, general
P	Pressure
p	Gidaspow drag correction exponent
p^*	Pseudo-pressure
p'	Pressure correction
P_i	Pressure at node i
P_s	Solids pressure
Q_i	Parabola built off of point i
r	Radius
r	Flux limiter ratio
R	Residual
Re_P	Particle Reynolds number
R_{min}	Minimum control volume radius (m)
S	Entropy
S	Volumetric source term
S_C, S_P	Linearized source terms
S_{ij}	Velocity strain rate tensor

t	Time (s)
T	Absolute temperature
U	Internal energy of a powder
u^*, v^*, w^*	Pseudo-velocities in pressure correction method
U_b	Bubble rise velocity
U_{mf}	Minimum fluidization velocity
U_p	Particle approach velocity
$v(t)$	Volume at time t in n-space
V_b	Specific volume, volume weighted specific bulk volume
v_k	Volume occupied by phase k.
v_p	Volume of one particle
X	Value at node X

Greek Letters

$\bar{\xi} = (\xi_1, \xi_2, \xi_3)$	Curvilinear coordinate system
$\overline{\overline{\tau}}$	Shear stress tensor
ε_P^C	Calculated volume fraction based on a volume average
ψ	Diffusional flux vector of f
Φ	Volumetric rate of production of f
ρ	Density (kg/m^3)
μ	Molecular (fluid) viscosity
ζ	Bulk viscosity
δ	Error bound on CV

β	Drag force exerted on a single sphere
Γ	Diffusivity
ψ	Flux limiter
$\phi()$	Lagrangian position function
ε^*	Compaction volume fraction
α,β,γ	Direction cosine angles
δ_{ij}	Kronecker delta
ε_{mf}	Volume fraction at minimum fluidization
λ_{mfp}	Mean free path between particle collisions
ε_p	Phase average volume fraction (true value)
ϕ_s	Sphericity
Θ_s	Granular temperature

Superscripts

*	Pseudo value
C,PARABOLIC	Central differencing using parabolic interpolation
CENTRAL	Lax-Wendroff central differencing
n	Time step
n+1/2	Half time step or pseudo time step
UP	Upwinding
UP2	Second order upwinding

Subscripts

i+1/2, i-1/2	Half cell values

Abbreviations

CV	Control Volume
DNS	Direct numerical simulation
FCC	Fine cracking catalyst
FD	Flow domain
FOUW	First order upwinding
IPSA	Interphase Slip Algorithm
LW	Lax-Wendroff Central Differencing
PEA	Partial Elimination Algorithm
SIMPLE	Semi-Implicit Method for Pressure Linked Equations
WB	Warming-Beam Differencing

Chapter 1

Introduction

This project studied the use of a two-fluid multiphase computational fluid dynamics model for simulating the interaction of a horizontal gas feed jet on the hydrodynamics of a gas/solid fluidized bed. Two of the largest fluidized bed reactors are located in Fort McMurray, north Alberta to hydrocrack the oil from the rich oil sands reserves. Design modifications to these units or construction of an additional reactor is a very costly undertaking and requires the best available design tools. The main aim of this project was to provide a review of the current state of the art multiphase flow modeling software from AEA Technology to model a two phase gas fluidized bed and provide information about model limitations, requirements and predicted flow behavior in a much smaller pseudo-two dimensional fluidized bed. These studies will be used to continue the modeling work with a reacting gas/solid/liquid fluidized bed system. Work from this study will provide a theoretical basis from which to continue.

Theoretical work requires comparison against experimental observations for validation. It also requires internal model verification to ensure that the model assumptions and solution methods are reliable under different operating conditions. Both model verification and validation has been carried out in this work to provide a basis on which to continue multiphase flow modeling.

A fully three dimensional, transient incompressible two fluid simulation model was set up and solved using the CFX 4.2 solver from AEA Technologies. The solids phase was assumed to consist of completely spherical, monosized particles of constant density. The gas phase was assumed to be incompressible and behave as a laminar air flow. No turbulence model was used for these simulations.

A single phase gas jet was discharged into a rectangular computational domain representing an incipently fluidized two-phase bed. The nozzle was modeled to be at the end of a length of solid pipe with an orifice of comparable area to that used in the experimental apparatus at the University of Saskatchewan. Fluidization gas was injected through the distributor at the bottom of the bed providing aeration for the solids phase. Only gas was allowed to pass out of the top section of the bed thereby ensuring a constant mass of solids within the fluidized bed. All geometric parameters of the fluidized bed simulation were adjustable through use FORTRAN routines.

Simulation data was recorded every 0.05 seconds for analysis. The analysis of multiphase flow simulations can be very complicated and several different techniques to observe the data were used. One of the most useful ways to study the data was in the form of animated movies that provided flow information about the formation of the jet plume and bubble formation within the fluidized bed. Instantaneous streamlines for the solids and gas phase were also plotted to determine how the flow field might look at an instant in time. Time averaged volume fraction data over the width of the bed provided information about the transient behavior of gas and solids voidage.

This thesis is broken into three main parts concerning theoretical background and derivations, experimental observations and computational results. Chapter 2 deals with an introduction to fluidization technology and the related flow phenomena that have been observed. In Chapter 3, rigorous derivations of single phase hydrodynamic equations are discussed and their extension to multiphase flow systems are outlined. Chapter 4 touches on numerical methods available for solving the partial differential equations derived in Chapter 3 and goes on to discuss the merits and weaknesses of the current state-of-the-art computational methods. Chapter 5 details the set up and assumptions used when performing the fluidized bed simulations in this study. Chapter 6 describes the experimental facilities and the results that were obtained for validating the simulation results. Chapter 7 focuses on validation and verification of the computational results against those listed in Chapter 6. Chapter 8 provides a conclusion and recommendations for future work.

Chapter 2

Literature Review

This thesis focuses on the application of computational fluid dynamics to multiphase flow modeling with the specific intention of verifying and validating the application of such models to the interaction of a horizontal gas jet within a gas-solid fluidized bed. Fundamental governing equations for single-phase flow models are reviewed and extended for multiphase flow systems. Current state-of-the-art numerical methods for solving the resulting transient, three-dimensional partial differential equations are presented and contrasted. Experimental results are used to compare against the simulation studies for validation of the solution and modeling methods. This chapter provides a brief overview of the rich body of research that has been conducted concerning fluidization technology and some of the approaches available for simulation.

2.1 Flow Behavior within a Fluidized Bed

2.1.1 General Flow Behavior

The understanding of the overall flow patterns within fluidized beds has been given great attention over the past decade due to the use of this technology in a wide range of industries. In the petroleum industry the development of more active catalysts for the production of gasoline requires the replacement of older bubbling fluidized beds with circulating fluidized beds. Fluidized bed nuclear fission reactors are even being investigated as an alternative to traditional designs (Rots *et al.*, 1996). New emissions standards are forcing the electric power industry to burn coal with much lower emissions of sulfur and nitrogen oxides (Miller and Gidaspow, 1992; Lyczkowski *et al.*, 1993). Erosion of internal fluidized bed surfaces, and even of the particulate phase itself (Werther and Xi, 1993), remains a challenge and needs to be addressed in more detail for continued widespread commercial application of this technology (Lyczkowski *et al.*, 1993; Bouillard *et al.*, 1989). Berruti *et al.* (1995) present a good review of the hydrodynamics of circulating fluidized beds and some of the current research requirements. Many studies have focussed on the gas-particle flow in vertical pipes (Sinclair and Jackson, 1989; Nakamura and Capes, 1973). It has been suggested that the overall flow patterns within multiphase flow systems, including gas in liquid and solid in gas flows, might be more dependent upon coherent structures present in the flow field. An excellent review of these coherent structures present in multiphase flows is presented by Van Den Akker (1998).

Fluidized beds operate over a wide range of flow regimes which are set by both the fluidization gas velocity and the nature of the particles being fluidized (Fan and Zhu,

1998). A general overview of these flow regimes and their dependence on fluidization velocity is shown in Figure 2.1.

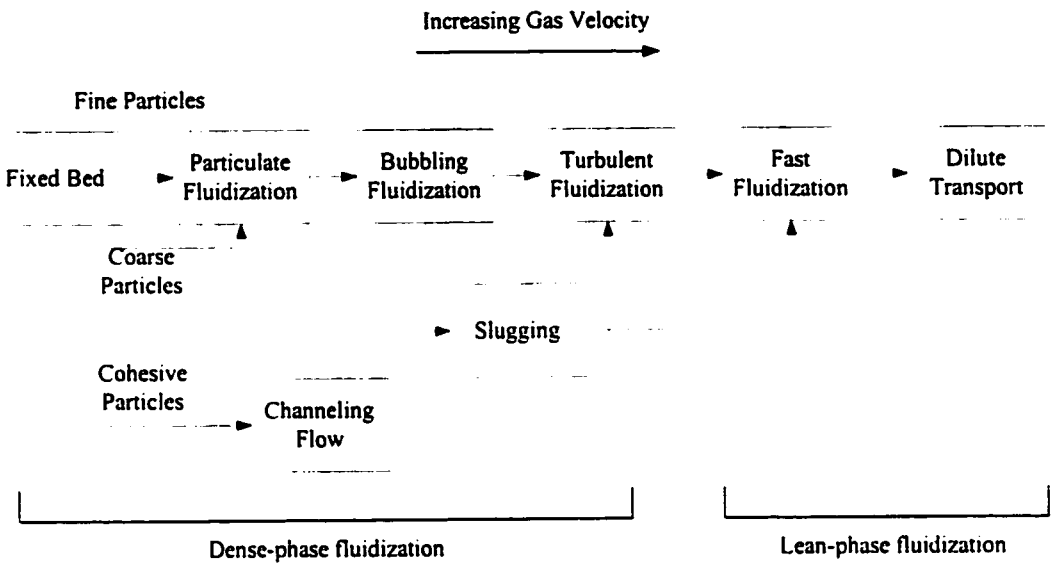

Figure 2.1 – Different fluidization flow regimes in a fluidized bed. Adapted from Chyang *et al.* (1998).

Dense-phase fluidization encompasses particulate fluidization, bubbling fluidization and turbulent fluidization. Above these gas flow velocities the behavior of the bed changes to a more dilute system and can be classified as being lean-phase fluidization. Fixed beds represent a percolating flow through a packed bed of particles. At higher fluidization velocities between minimum fluidization and minimum bubbling fluidization the bed is said to behave in the particulate fluidization regime. The bed appears homogeneous and the gas flows through the interstitial spacing between particles. This regime only exists for Geldart Type A particles (Geldart 1973) under a narrow operating range of gas velocities. Increasing the fluidization velocity above the minimum bubbling velocity leads to the formation of bubbles within the fluidized bed or the so called bubbling

fluidization regime. In the bubbling fluidization regime bubbles are readily observed within the dense phase of the bed. Higher fluidization velocities lead to the turbulent fluidization regime where there is vigorous movement of the particles within the bed but distinct bubbles are not discernible. The surface of the bed becomes more diffuse due to the increased entrainment of solid particles into the freeboard section of the reactor (Figure 2.2 c).

Vessel geometry can also lead to a change in the fluidization behavior observed with increased fluidization velocity. Slugging refers to the regime where bubble sizes comparable to the width of the vessel are present (Figure 2.2 d). This behavior is most noticeable when the ratio of bed width to height is quite low. In this case particles are moved up through the bed as slugs. Increasing fluidization velocity in the slugging regime can lead directly to turbulent fluidization or fast fluidization.

In addition to fluidization gas velocity dependencies, the method of delivery of aeration gas will affect the fluidized bed flow behavior. Spouting fluidization occurs when a central jet is introduced into a fluidized bed. Solids are entrained in the central core region and accelerated upwards along the axis of the reactor forming a dilute core flow region. Entrained solids fall on to the top of the bed where they recirculate back down along the dense annular region forming a solids circulatory pattern (Figure 2.2 e).

Channeling within a fluidized bed is usually due to the cohesive nature of particles. Particle shape, size and density can also have effect on the channeling effects. Channeling can also occur in a bed when the fluidization gas is not evenly distributed across the distributor plate (Figure 2.2 f).

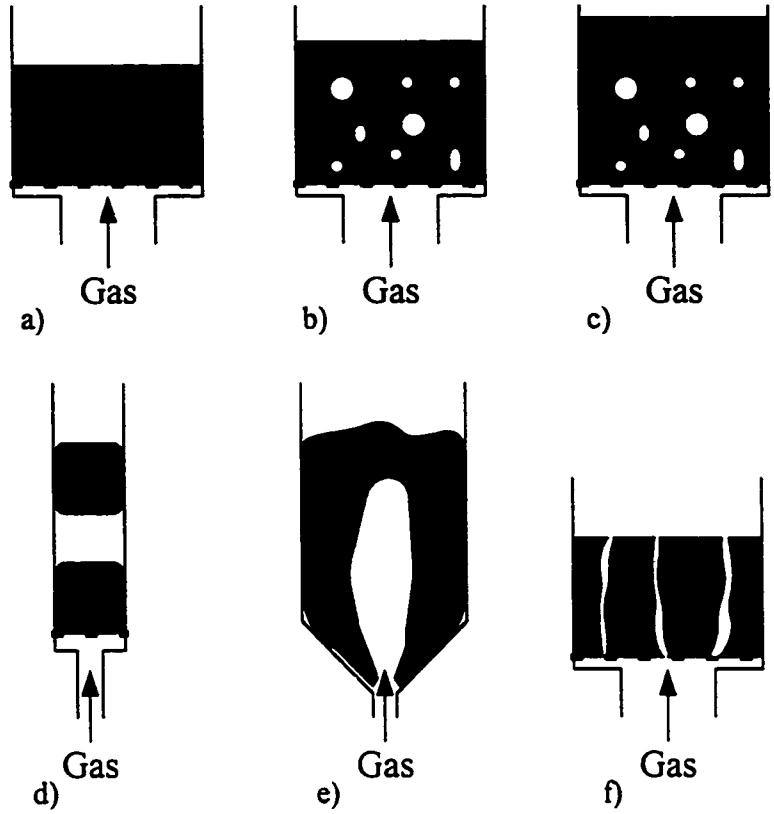

Figure 2.2 – Gross characteristic flow regimes in a fluidized bed. Adapted from Chyang *et al.* (1998)

Circulating fluidized beds represent one of the most versatile types of industrial fluidized beds and find application in coal combustion, incineration and petroleum upgrading. Solids are taken from the freeboard section of the reactor and recycled (or recirculated) back to the dense phase region of the reactor using a nonmechanical or L-valve. Tsuo and Gidaspow (1990) report that experimental observations by several authors (Weinstein *et al.*, 1986; Hartge *et al.*, 1986) show a nonhomogeneous radial distribution of solids volume fraction that increases monotonically with radius. A core-annulus type of flow pattern in circulating fluidized beds has been shown to exist in several experimental reports (Capes and Nakamura, 1973; Gajdos and Bierl, 1978; Bader *et al.*, 1988; Miller and Gidaspow, 1992). Solids radial fluxes are measured in a fluidized

bed using a probe which is inserted into the flow with the collection port facing upwards (to measure downwards flux) or downwards to measure upwards flux. Since the fluidized bed is a transient system, measurements must be time averaged and the upwards and downwards fluxes subtracted to get the total flux and direction. Many early attempts at mathematically modeling two phase flow behavior have used one dimensional formulations; however, care must be taken when observing early one dimensional attempts (Yerushalmi *et al.*, 1976) since the flow was assumed to be unidirectional and this has been shown to be an incorrect assumption. Sinclair and Jackson (1989) further cite that a one dimensional analysis can be inappropriate when the single dimension is not at right angles (90° or 180°) to the gravity vector in which case particles will tend to be distributed nonuniformly over the cross section as a result of gravitational sedimentation.

Gidaspow *et al.* (1989) have carried out an experimental study of the formation and descent of solids clusters within a circulating fluidized bed apparatus. This work was complemented by a later study (Tsuo and Gidaspow, 1990) using a two dimensional computational fluid dynamics model studying the flow patterns within a circulating fluidized bed. With these numerical studies they observed cluster formation along the walls of the vessel measuring approximately 2 to 3 cm in size and traveling downwards at 1.1 m/s. Clusters were observed to combine and grow in size. From this study they have concluded that for the dilute circulating fluidized bed regime their two dimensional model can predict the formation of clusters in agreement with observations. For dense phase fluidization regimes the flow system behaves as a core annulus type of system with solids down flow along the vessel walls. This too was in agreement with experimental observations.

2.2.2 Bubble Movement within a Fluidized Bed

Considerable effort has been concentrated on formulating the hydrodynamic models describing multiphase flows in industrial equipment such as fluidized beds and pneumatic transport riser systems. Davidson (1961) first formulated multiphase flow hydrodynamics by constructing two continuity equations (one each for the gas and solids phases) and expressed the relative velocity between the two phases in terms of Darcy's law for flow in porous media. He also assumed that the solids flow around bubbles was irrotational ($\nabla \times \bar{v} = 0$); this assumption can be justified based on the mixture momentum balance (Gidaspow and Solbrig, 1976; Lyczkowski *et al.*, 1982). Bubbles within the fluidized bed play a significant role in the dispersion, mixing and contact between the gas and solids phases. Jackson (1963) carried out perturbation analyses of his governing equations and showed that a small perturbation in voidage will grow without bound. Davidson and Harrison (1963) analyzed bubble formation on the assumption that there must be some stable bubble size that will form within the fluidized bed. This stability was defined in terms of bubble size that had to be greater than the terminal velocity of the particles for the formation of a stable bubble. Rietema and Mutsers (1973) used a small perturbation analysis, reviewed in detail by Jackson (1985), to obtain a criterion for bubbling. Rietema and Mutsers' work has been continued by Mutsers and Rietema (1977), Piepers *et al.* (1984) and Rietema (1984). The analysis of bubbles as shocks, or flow instabilities, within the fluidized bed domain is in addition to the question of stability of the governing hydrodynamic equations as analyzed by Lyczkowski *et al.* (1978).

The question of the formation of bubbles within a fluidized bed has been studied by many people (Fanucci *et al.*, 1979; El-Kaissy and Homsy, 1976; Jackson, 1963; Pigford and Baron, 1965; Garg and Pritchett, 1975). However, as pointed out by Jackson (1963) most stability studies have used linear stability theory to predict the onset of bubbles. There is no guarantee that a small perturbation will grow when the nonlinearities of the governing equations can no longer be neglected. Verloop and Heertjes (1970) were the first to show that shock waves will form within a fluidized bed when porosity waves rise faster than an equilibrium disturbance. Foscolo and Gibilaro (1984) determined an expression for this velocity based on particle properties and the gravitational constant by neglecting inertial effects. This work was extended by Rowe (1986) for Geldart Type A and B powders (Geldart, 1973).

Fanucci *et al.* (1979) presented a rigorous characteristic analysis of the governing partial differential equations. Assuming a sinusoidal particle velocity variation with time at the distributor plate they determined that the characteristic paths intersected and shocks formed. This type of analysis was repeated by Rasouli (1981) using the relative velocity equations; similar intersecting characteristic paths were also observed. Each of these analyses have used the somewhat unrealistic formulation where the inlet velocity has varied sinusoidally with time. Harris and Crighton (1994) have considered the evolution of an initially small voidage disturbance in a gas fluidized bed; their analysis resulted in the prediction of gas slugs which are common in flow systems where the ratio of the height of the vessel is large when compared to its diameter. Gidaspow (1994) dedicates a chapter to the formation of bubbles and their treatment as shocks within a fluidized bed for a one dimensional analysis using a slip velocity formulation of the void propagation

equation. He starts by defining a one dimensional continuity equation for both the solids and gas phases; these equations are linked by the definition of the void fraction which must sum to one in order to satisfy continuity. The gradient of the relative velocity between the two phases is expressed in terms of the relative velocity model of Gidaspow (1994) which includes terms for gravity, drag, vessel wall friction and solids normal stress. A limiting case of a fluidized bed at minimum fluidization is assumed so that the Ergun equation can be applied for the drag relationship. Gidaspow also assumed that the flow was fully developed and that the relative velocity was based on a balance between the buoyant and drag forces within the bed. Based on these assumptions a characteristic void propagation can be determined and compared with the convective void propagation velocity in the bed. If this characteristic velocity is greater than that of the bed, then shocks, hence bubbles, will form. However if this velocity is less, then the bubble will dissipate into the bed and bubbles will not form.

Much experimental work has been carried out to study single bubbles within gas fluidized beds at minimum fluidization. Single bubble dynamics within a fluidized bed are similar to those in a liquid medium (Clift and Grace, 1985; Fan and Tsuchiya, 1990; Krishna, 1993). Most bubbles within a fluidized bed are either of spherical cap or elliptical cap shape. Two basic types of bubbles have been observed, the fast bubble and the slow bubble, each is shown in Figure 2.3 a and b, respectively.

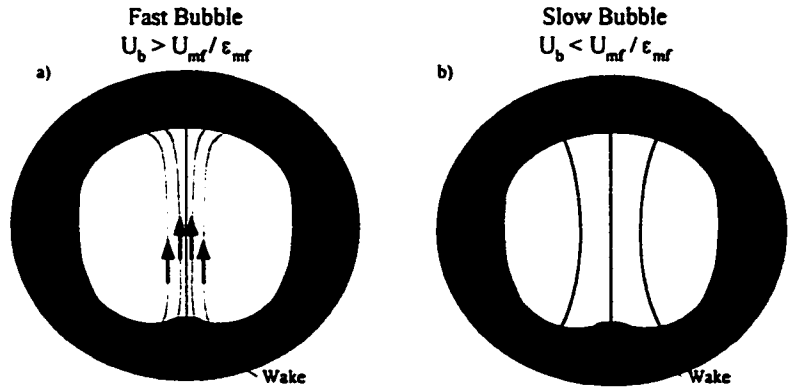

Figure 2.3 – Flow patterns within voids formed in fluidized beds. a) fast bubble, b) slow bubble.

A cloud region is formed around the periphery of the bubble and circulates in a closed loop between the bubble and the fluidized bed. Rowe (1971) visualized this cloud by injecting a coloured NO_2 tracer gas near the periphery of the bubble. When the bubble propagation rise velocity, U_b, is greater than that of the interstitial fluid, a "clouded" fast bubble forms and the gas recirculates up through the centre of the bubble and out of the top of the void. As the gas rise velocity increases significantly higher than the interstitial fluid velocity the cloud becomes very thin and internal recirculation of the gases within the bubble takes place. However, when the gas rise velocity is less than the interstitial fluid velocity, a cloud does not form around the bubble. Instead the interstitial gas flows through the bubble (Fan and Zhu, 1998). Gabor (1972) reported experimental observations of the bubble movement within a freely bubbling fluidized bed and how this movement affected a horizontal line of coloured tracer particles within the bed. As the bubble moves up through the bed the particles did not pulse upward during bubble formation on the distributor plate. The particles remained at rest until a rising bubble came into their vicinity. Particles near the bubble but not along the axis of bubble rise were initially moved upward and then followed a curved trajectory downward.

Therefore, actual bubble rise in a fluidized bed causes particles to move with a net downward displacement unless the particles fall through the bubble roof and get carried upwards in the bubble wake.

Bubbles play a significant role in the solids movement throughout fluidized bed reactors and for the contact of solids with the gas phase; it has been suggested that the solids transport in the wakes of rising voids is *the* essential mixing mechanism (Kunii and Levenspiel, 1991). The importance of locating feed materials within the bubble zone has been stressed by Guedon *et al.* (1994) for the proper mixing of prepolymer materials within fluidized beds and for the avoidance of hot spots within the reactor. The rising voids within the fluidized bed causes some lateral drift of solids within the fluidized bed (Grace *et al.*, 1997; Valenzuela and Glicksman, 1984; Eames and Duursma, 1997) as solids particles are displaced radially with void passage. Eames and Duursma (1997) carried out theoretical calculations and report that it is the ratio of initial bubble distance from the bed surface to vessel width and not the ratio of bubble diameter to vessel width that has a marked effect mixing. Bubble wakes in single-phase flow are defined as the streamline enclosing the region beneath the bubble base (Fan and Zhu, 1998). In a gas-fluidized bed this single phase can be considered to be the emulsion phase, a combination of the gas and solids phases within the fluidized bed. Hence, a bubble wake is defined as the area enclosed by a streamline at the base of the bubble. Littman and Homolka (1973) made pressure measurements around a bubble moving through a fluidized bed and concluded that the pressure wake is also closed and can trail as much as twelve bubble radii. As the bubble rises through the bed the solids in the wake are entrained and carried up the bed. This provides a mechanism for the overall mixing of the solids within the

bed. Bubble formation within small laboratory apparatus typically form slugs with solids trickling through the top of the bubble (Figure 2.2 d); however, in larger industrial units bubbles are often formed away from the walls and will proceed rapidly up the reactor thereby decreasing residence time (Behie *et al.*, 1970).

Two different views can be applied when studying bubble wakes within a fluidized bed. The first view, attributed to Clift (1986), is based on analogy to gas bubbles in liquids. The bubble Reynolds number Re_b is of the order of 100. At this flow regime it would be expected that the bubble rise through the fluidized bed would lead to a vortical motion of particles and gas within its wake. The second view indicates that the wake is produced by gas and solids entering the wake from the outer boundary, flowing radially inward toward the bubble center and vertically downward out of the wake (Kozanoglu and Levy, 1991). At this time more thorough experiments are needed to clarify either of these views. It has been reported (Rowe and Partridge, 1965; Rowe, 1971) that vortex shedding may occur in gas fluidized beds in the wake region of a bubble.

Models have been proposed to solve the governing equations of multiphase flows to predict bubble behavior within the fluidized bed. Two-fluid models have been formulated by many researchers (Kuipers *et al.*, 1992; Gidaspow, 1986; Tsuo and Gidaspow, 1990; Bouillard *et al.*, 1991; Ding and Gidaspow, 1990; Gidaspow and Ettehadieh, 1983); this particular approach to modeling is described in detail in Chapter 2. Lagrangian approaches have also been attempted whereby each particle within the fluidized bed is tracked according to Newtonian physics and the interstitial gas flow field is calculated based on Eulerian field mechanics. Hoomans *et al.* (1995) have carried out

such simulations using 40,000 particles and compared these results with experimental results for bubble formation and rise times. Their model involved a hard sphere approach with the input of a restitution and friction coefficients. Other exotic forms of solving the governing equations have been attempted with varying degrees of success. Andrews and O'Rourke (1996) have implemented a Multiphase Particle in Cell (MP-PIC) method employing both a two fluid model but with a clumping of solids particles in a Lagrangian sense.

2.2.3 Vertical Jet Behavior

Much research has focussed on the penetration of vertical jets into fluidized beds (Merry, 1975; Gidaspow *et al.*, 1983; Filla *et al.*, 1983). The high speed impingement of particulate on vessel internals can lead to attrition and eventual wear of the structures. For beds with fast chemical reactions much of the conversion may occur in the jetting zone near the distributor plate (Behie and Kehoe, 1973; Behie *et al.*, 1975). Merry (1975) analyzed data for vertical jet penetration into fluidized beds from several sources (Markhevka *et al.*, 1971; Basov *et al.*, 1969; Zenz, 1968; Shakhova, 1968; Yang and Kearns, 1970) and proposed an expression that correlates a wide range of data.

$$\frac{L}{d_0} = 5.2\left(\frac{\rho_f d_0}{\rho_p d_p}\right)^{0.3}\left[1.3\left(\frac{u_0^2}{g d_0}\right)^{0.2} - 1\right] \qquad (2.1)$$

Expression (2.1) is quite general and correlates a wide range of data for gas and liquid fluidized beds, with nozzles up to 35 mm diameter and jets of up to 0.5 m in length. All of the data used were for beds of effectively uniform particle size and for Merry's correlation it was not clear at present exactly how the mean particle size D_p in the

correlation should be specified for a bed with a very wide range of particle sizes. Wen *et al.* (1981) have stated that it is important to set up experiments whereby wall effects are minimized and a more realistic interaction of several jets is studied. In some situations the physical implementation of this is very difficult. Computer simulations have been shown to be effective for predicting the overall behavior and pressure distributions within circulating fluidized bed reactors fluidized with a central vertical jet (Benyahia *et al.*, 1996).

2.2.3 Horizontal Jets in Fluidized Beds

One of the most common ways of introducing feed into a fluidized bed is the use of nozzles which are inserted into the vessel; this approach is common for petroleum upgrading. Lummi and Baskakov (1967) injected a CO_2 tracer with an air jet to measure tracer concentrations within the bed. Zenz (1968) presented a curve to predict horizontal penetration depth. Shakhova (1968) derived an expression for horizontal jet penetration based on a simple momentum balance. Kozin and Baskakov (1967) proposed a correlation for horizontal jet penetration based on specific air distributor designs. Two of the earliest reports for predicting the penetration of a horizontal gas jet into fluidized beds were conducted by Shakhova (1968) and Merry (1971). Early investigations by Merry (1971) used a series of pseudo-two dimensional fluidized beds with transparent face plates to visually measure the penetration of a horizontal gas feed jet into the fluidized bed. Merry investigated using beds of sand, kale seed and steel shot under atmospheric conditions. Nozzle diameters of 2.54 to 14.3 mm were used with jet exit velocities of between 40 and 300 m/s. He found maximum penetrations of 30 cm and proposed a

semi-theoretical expression for predicting maximum jet penetration into the bed based on fluid properties (viscosity, density), nozzle diameter, inlet jet velocity and bed properties (density, particle diameter and void fraction). This expression has been applied to a wide range of data reasonably well and predicts horizontal penetrations to within ±30%.

A horizontal gas jet injected into a fluidized bed essentially becomes a two-phase jet of gas and entrained solid particles. Solids particles from the jet are entrained in the jet and accelerated in the gas jet stream. Abramovich (1963) analyzed a two-phase jet in air by assuming that the motion of the admixture particles approximated the local air velocity and that the transverse cross-section of the jet was similar to the temperature profiles observed in jets of non-uniform temperature. His analysis only applies to tiny liquid droplets and dust in a jet which are said to be one way coupled and have an insignificant impact on the jet flow field. In a fluidized bed there are often considerable relative velocity differences between the gas and solid phases and this dilute jet analysis is not appropriate. The situation is complicated by the fact that the relative velocity will vary both along the length of the jet and also across the jet. Merry presented a well thought out approach for modeling jet discharge into a fluidized bed as follows: treat the two-phase jet as if it were a homogeneous jet in which the density varies only along the axis (this variation is due to the change in relative velocity between particle and gas as the particle travels through the jet region). This expression is then modified to account for the fact that particles of different size will be accelerated from rest at different rates. This simplification is justified by the fact that the pressure gradient along the jet axis in a fluidized bed is small.

Bubbles are assumed to form only at the end of the jet region and an insignificant number of bubbles actually come off of the jet plume. The jet acts as a sink with particles becoming entrained and then accelerated to the jet velocity. These high-speed particles will bump into slower moving particles that have just been entrained into the jet and as such the slower moving particles will rebound back out into the boundary of the jet. Merry contends that this is the mechanism by which the top surface of the jet void is supported within the fluidized bed. By balancing the drag force with the weight that is exerted on the particle Merry determined that the jet boundary is in a state of stable equilibrium with the local gas velocity.

Three zones can be defined for the particle movement within the fluidized bed region adjacent to the jet/bed boundary. Region A is where the jet acts like a sink and the particles are entrained into the jet. Region B is the path of the particles within the jet which either travel downwards towards the bottom of the jet or get rebounded back into the jet boundary. Where momentum transfer to the entrained particles is greater, deceleration of the gas stream is greater and jet penetration is less. Merry reported that particles in the region near the nozzle orifice at the inception of the jet actually appear to migrate in a direction opposite to that of the flow of the gas jet; this has been confirmed by Xuereb *et al.* (1991).

An approximate solution for the discharge of a turbulent jet into a fluidized bed was presented by Shakhova (1968). He assumed that the jet plume and the fluidized bed are separated by a two-phase boundary layer consisting of plume gas (the jet) and the fluidized bed emulsion phase. This boundary layer between the jet plume and the fluidized bed is divided into two zones and showed the validity of this model with

experimental results. Based on his calculations, as the thickness of this two phase zone increases the mean density of the jet plume also increases. Due to boundary layer growth, the transverse jet density changes with increasing jet penetration into the bed. Shakhova assumed that Schlichting's equation governs the jet cross sectional velocity profile and used expressions for boundary layer thickness and an integral momentum balance to determine the axial velocity distribution. As the axial velocity decreases, the fluidized bed density exerts an ever-increasing influence on the jet surface and the plume begins to collapse. Based upon these relationships, he developed an expression for the horizontal jet penetration into the bed. Unfortunately, Shakhova chose to neglect the observed hydrodynamic effect of bubble formation and fluidization velocity. Fluidization gas velocity has an effect on the overall bed porosity, which would impact on the average bed density and hence the two-phase boundary layer in his model. His final working equation was based upon a simple turbulence model and required an empirical parameter for turbulence values.

A summary of several expressions for horizontal jet penetration is listed in Table 2.1. Not all of the expressions were developed for horizontal gas jets being discharged into a fluidized bed. The study by Hong *et al.* (1997) investigated the penetration from an inclined nozzle but their expression treats the horizontal penetration as a special case. Guedon *et al.* (1994) investigated the penetration depth of inclined solids laden jets into fluidized beds and their relationship listed is also a special case of their more general expression. Only the expressions of Merry, Shakhova and Zenz were used to compare against simulation results.

Table 2.1

Horizontal Penetration Expressions from Literature

Expression	Author
$\frac{L_{max}-L_{min}}{2d_0}=7.8\left[\frac{\rho_g}{\rho_p}\frac{U_0}{(gd_0)^{1/2}}\right]$	Shakhova (1968)
$0.044\frac{L_{max}}{d_0}+1.57=0.5\log\left(\rho_g u_0^2\right)$	Zenz (1968)
$\frac{L_{max}}{d_0}=\left[5.25\left(\frac{\rho_0 u_0^{\,2}}{(1-\varepsilon)\rho_p g d_p}\right)^{0.4}\left(\frac{\rho_f}{\rho_p}\right)^{0.2}\left(\frac{d_p}{d_0}\right)^{0.2}-4.5\right]$	Merry (1971)
$L_{max}=9.7\times10^{14}M^{1.83}U_j^{2.82}\rho_b^{-6.23}$	Guedon *et al.* (1994) (from a solids laden jet)
$\frac{L_{max}}{d_0}+3.80=1.89\times10^6\left[\frac{\rho_j U_j^2}{(1-\varepsilon_g)\rho_s g d_p}\right]^{0.327}\left(\frac{\rho_g}{\rho_s}\right)^{1.974}\left(\frac{d_p}{d_0}\right)^{-0.040}$	Hong *et al.* (1997) (horizontal jet special case)

More recent investigations by Xuereb *et al.* (1991) have included detailed observations about the formation of bubbles from the tip of the jet region and particle migration along the surface of the jet plume boundary. These experiments were carried out in a two-dimensional bed with a transparent face plate in order to study the behavior of horizontal or inclined jets in a gas-solids fluidized system. The use of cinematographic techniques has enabled them to point out the interactions between the jet and the bubbles resulting from the fluidization, as well as the inherent fluctuations of the jet. Values of morphological parameters which characterize the jet were found from pictures and movies: penetration length and expansion angle, corresponding to three

positions of the nozzle: inclined upwards, inclined downwards, or horizontal. The effect of the fluidization velocity, the gas injection velocity and the particle diameter was studied in these configurations. The existence of a dragging zone, previously reported by Merry (1971), of particles from the dense phase into the jet, close to the injection point, was confirmed.

Xuereb *et al.* (1991) defined three zones along the length of the horizontal jet into a fluidized bed: i) the particle entrainment zone, ii) the linear jet expansion zone and iii) the bubble zone. Jet penetration fluctuations were caused by the natural formation of bubbles within the fluidized bed and were reported to occur at frequencies between 2 and 5 Hz. As shown by their experimental photographs, it was very difficult to get a good idea of the bubble shape, size, etc... They also observed that naturally occurring bubbles within the fluidized bed will cause the jet to move towards the bubble even if it has to bend downwards.

The late nineties have seen a renewed interest in studying the size and shape of the void formed within a fluidized bed created by the use of a horizontal gas jet. Chen and Weinstein (1993) employed an X-ray technique to measure instantaneous solids void fractions through the depth of a fluidized bed. This method gave a chord (or depth) averaged view of the solids volume fraction and is used for identifying the location and size of the jet plume. Nozzle orifice diameters of 0.64 and 1.27 cm were investigated at jet velocities of 23, 46 and 69 m/s. Maps of the mean solid fraction and of statistical properties of the fluctuating component show that there are three discernible regions in the jet influenced area of the bed: coherent void, bubble trains and a surrounding compaction zone.

Chen and Weinstein (1997) conducted measurements of jet penetration into a fluidized bed using a heated horizontal gas jet and correlating temperature with gas voidage. These data provided a comparison of the picture of the jet structure obtained from the spread of the jet momentum (Chen and Weinstein, 1993) to that of the spread of the heated gas. Gas temperatures were measured in a vertical plane containing the axis of the nozzle jet. Also, the effect of the superficial velocity through the bed distributor was studied. Measurements were made with the thermocouple traverses providing the temperature field in a vertical plane containing the jet axis. Even with a jet velocity of over 30 m/s, the jet was observed to bend upwards a few centimeters from the nozzle. Their data show that there is a bubble train leaving the upper surface of the jet at about 2 cm from the jet entry wall and that bubbles do not typically leave from the tip of the jet plume. This observation is somewhat inconsistent with other studies. Solids were observed to remain stagnant within a zone below the jet. This zone below the jet was inferred from a relatively high temperature zone which is consistent with the existence of a stagnant compaction zone below the jet which is formed by the gas entrained through the zone into the jet. One of the main conclusions of this paper is that Merry's (1971) correlation gives reasonable estimates of horizontal jet penetration over a wide range of fluidized bed operating conditions. Fluidization gas was varied from 0.03m/s to 0.21 m/s and the fluidized particles were FCC with ρ=1450 kg/m^3 and D_p=60 μm.

Chyang *et al.* (1997) continued studies of the gas discharge modes including bubbling and jetting formed at a single horizontal nozzle into a two-dimensional gas fluidized bed by visual observation. Nozzles of diameter 3.0, 4.5, 6.0, 7.5 and 9.0 mm were investigated. Jet velocities were varied from 1 to 130 m/s. Gas discharge modes

were determined for different jet flow velocity ranges as follows: For high velocities a permanent flame-like cavity stands in front of the orifice and is called a jet. However, when the jet velocity is low, bubbles are formed at the nozzle orifice and proceed up along the reactor wall. When particles are light and small or the nozzle diameter is large, the gas discharge mode at the orifice will be unstable. These authors call this the "transition state". However, the behavior of a two dimensional system is expected to be quite different from that of a three dimensional system (Chen and Weinstein, 1993; Guedon *et al.*, 1994; Tyler and Mees, 1999) because in the latter case, there is a path by which the gas and solid can move around the sides of the jet. This prevents the jet ceiling from becoming a stagnant zone as it does in the 2D geometry where the jet and the bubble track isolate the ceiling from the rest of the bed. This observation is of significance when using computational fluid dynamics to predict fluidized bed and horizontal gas jet interactions.

Chyang *et al.* (1997) observed that fluidization gas velocity has an effect on the maximum penetration of the jet and are shown in Figure 2.4. At U_f / U_{mf} equal to 0.6-1.0 there was a maximum observed in the jet penetration. Based on this result they decided to continue all tests at minimum fluidization. Jet penetration increased with increased nozzle diameter for a fixed velocity. This result is not surprising as the jet momentum flux increases with increasing orifice size at constant jet velocity. Most authors tend to use the dimensionless number L/D_o as a measure of jet penetration length.

Penetration decreased with increased particle size within the fluidized bed. The literature correlations under estimated the penetration that was measured in this study. Chyang *et al.* (1997) attribute this to the various definitions used for penetration length

for the correlations. Some experimentalists use maximum penetration while others use jet curvature or "pinch points" to define the end of the jet plume.

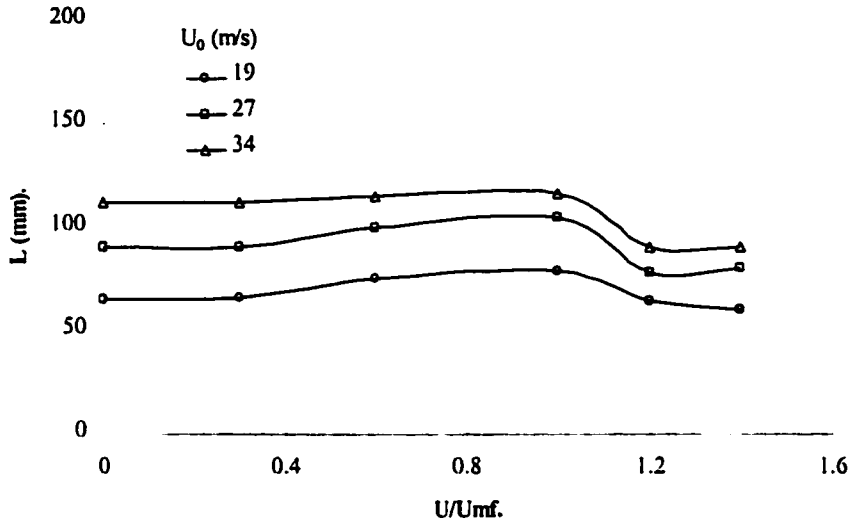

Figure 2.4 – Horizontal jet penetration as a function of fluidization velocity. Adapted from Chyang *et al.* (1997)

Two nondimensional numbers were used to classify the nozzles. The modified Froude number: $Fr^* = \frac{2\rho_g D_0^2 U_0^2}{3\rho_p D_p^3 g}$ which is the ratio of gas inertial force at the jet to the gravity force acting on the particles, and the ratio of the nozzle diameter to the particle diameter. Based on these dimensionless numbers and their test runs they determined a nozzle flow regime phase diagram consisting of bubble, jet and transition regimes; see Figure 2.5.

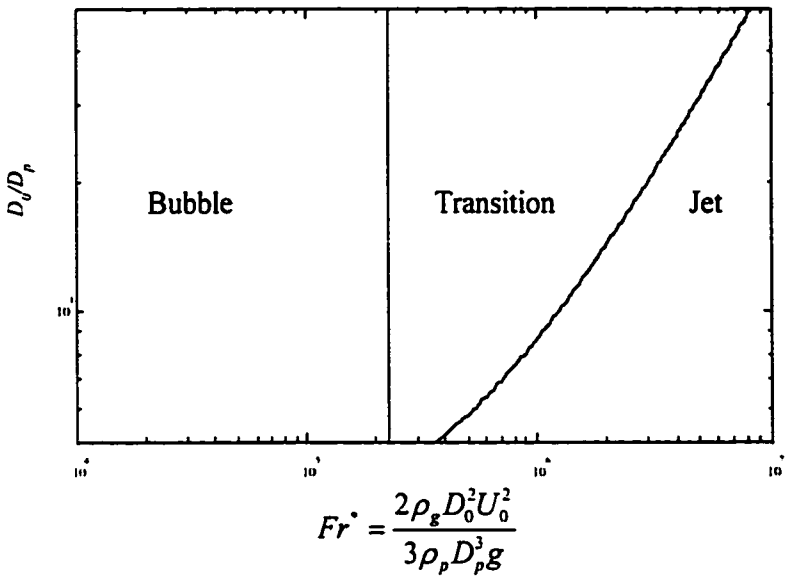

Figure 2.5 - Flow regimes of the gas discharge mode for horizontal nozzles. Group B particles. From Chyang *et al.* (1997) Figure 23.

At high Fr^* numbers a jet is readily observed while at low Fr^* numbers a bubbling regime is encountered on the phase diagram. From the experiments of Chyang *et al.* (1997) it can be concluded that the gas discharge mode will be changed from bubbling to jetting while as the gas velocity (inertia force / moment) is increased. The dominating factor for gas discharge mode from a horizontal nozzle is the inertial force of the gas flow through the nozzle.

An in depth study of horizontal gas jet penetration was conducted by Hong *et al.* (1997) using a small experimental apparatus of 314x25 mm two-dimensional gas-solid fluidized bed with a vertical jet in the center and an inclined jet at the side of the bed. Millet and two kinds of silica sand were used as the bed material. These particles are quite large, on the order of 1 to 2 mm in diameter, and have a density ranging between 808 and 878 kg/m^3. These researchers also developed a computer code for predicting the

penetration depth of the horizontal gas jet into a fluidized bed. First order upwind (FOUW) was used to discretize advection terms (see Chapter 3 for a discussion of numerical methods). Their formulation of the governing multiphase hydrodynamic equations is similar to that used in the software package CFX 4.2.

Hong *et al.* (1997) state that there are two processes occurring near the nozzle. The first being the formation of a torch-like vacant space, which is the jet. This is due to the gas phase drag force being exerted on the solids and creating a volume for the gas. Concurrently, particles are entrained into the jet due to the high gas velocity and the low gas pressure at the bottom of the jet. Therefore, the bottom of the jet is compressed by the entrainment process and to some degree further compression leads to the detachment of the jet from the nozzle and the subsequent formation of bubbles.

Gross bed properties predicted with their computer code, such as horizontal gas jet penetration, agreed well with their experimental results. They also note that at lower jet velocities there is a greater difference between the predicted and measured penetration lengths. One major drawback when using CFD to model the fluidized bed with a horizontal nozzle is discretization of the nozzle inlet. As the nozzle orifice becomes smaller, a finer mesh is required to properly define the orifice. A finer mesh leads to an increase in mesh density and increased computational demands. There are merits to both the empirical correlation and the CFD simulations.

By decreasing the submergence of the nozzle within the bed, Hong *et al.* (1997) observed a slight increase in gas jet penetration with both their experiments and simulations. Unfortunately simulation results regarding only the jet penetration were reported and not overall predicted flow patterns or solids volume fraction distributions.

One of the main conclusions of their study was that simulations take a long time and produced penetration results that agreed well with experiment and literature correlation. So the question is: why do CFD for a nozzle penetration length when a simple correlation will give a value to within 25%?

Fluidized beds are also used in the exothermic production of base polymers. The formation of "hot spots" within the reactor can lead to product degradation, internal fouling and run away reactions. Obviously the understanding and control of the injection of feed material into these reactors has a significant impact on the overall operation. Guedon *et al.* (1994) conducted tests to see how the intermittent injection of solid particles into a fluidized bed affected bed performance and mixing parameters. Most of the injected particles ended up at the tip of the jet plume and were mixed into the bed only through the motion of the bubbles within the fluidized bed. In such a case it is very important to ensure that the jet penetrates into the bubbling part of the fluidized bed. Although visual observations are invaluable, the 2D nature of a bed required to take such observations can have significant wall effects which are not present in a true three dimensional industrial reactor. Guedon *et al.* (1994) decided to use a semi-cylindrical column made of steel with a Perspex face plate. Experiments were conducted at 25 bars. Polyurethane particles with a density of 650 kg/m^3 and a Sauter mean diameter, D_{32}, of 754 μm. Superficial velocity was varied from 0.4 to 0.6 m/s. Injected pre-polymer particles had a similar density to the particles already present in the bed; D_{32}=628 μm. Injected particles were colored for easier visual observations.

Particles were injected into the fluidized bed from a pressurized holding vessel with a pneumatic valve and traveled along a 1.1 m 0.0127 m ID line and into the bed

through 0.0127 m ID nozzle. The nozzle injection system was modeled using a force balance on the particle slug as it moved along the injection line. From this model an injection velocity could be calculated and subsequent penetration results correlated to this velocity and the holding vessel pressure.

Guedon *et al.* (1994) concluded that using an intermittent feed jet to feed solids into the fluidized bed can be used to good effect to deliver feed particles to specific areas within a fluidized bed. Injected particles tended to end up near the tip of the jet and could only be dispersed through the bed by gas bubbles. Therefore the tip of the jet should be positioned within the bubbling part of the fluidized bed. The injection system was successfully modeled and the injected particles were shot into the bed as a solid slug of particles. The length of the injection line should be kept below a certain critical value. An empirical correlation was derived to predict the penetration depth of the injected solids into a dense fluidized bed.

Chapter 3

Governing Equations of Single and Multiphase Flows

For years the flow of fluids in, around and over objects has been the fascination of many researchers. This chapter deals with the general conservation equation(s) and its (their) application to single and multiphase flow systems. Extensions and constitutive relationships required for modeling system closure are presented and the different approaches are discussed. The perception and approaches used to average these continuous equations are described and some of the limitations involved with the assumptions are described.

3.1 Approaches to Flow Modeling

There are several different approaches for modeling flow scenarios. Each method has its set of strengths and weaknesses but may find favor for application in specific areas.

3.1.1 Eulerian Continuum Approach

Most engineers are comfortable with using the Eulerian approach for observing data. Process equipment performance typically requires field data, such as velocity fields, pressure fields and the distribution of basic flow properties such as mass concentrations, temperatures and mass fluxes. The Eulerian approach is typically the most suitable approach when information of this kind is required. Flow variables at discrete points within the domain are reported. This is probably the easiest to grasp presentation of flow data. Experiments typically report certain measured values at points within the flow being studied.

Multiphase Eulerian models are formulated by regarding both the continuous (gas) and dispersed (solids) phases as interpenetrating continua. A momentum balance for the solids phase is determined by some form of averaging method. Single-phase flow equations describing the continuous phase are coupled with the solids momentum equation using additional source and interaction terms within the model equations. Although each phase is not explicitly continuous for multiphase models, assumptions are made so that the equations can be applied to multiple phases. Transport quantities of each of the pseudo-continuous phases have to be determined and applied in a continuum approach.

Important to the application of a continuum model is the definition of an infinitesimal control volume (CV) within the flow domain (FD). The CV must be small enough compared to a characteristic length to accurately represent the small scale flow phenomena. From a macroscopic point of view the CV must be small enough so that the concept of a continuous phase can be adopted. Additionally this CV must be large enough so that a statistically valid number of particles within the CV are present to represent the continuous properties of pressure, temperature, density and velocity for both the continuous (usually the gas phase) and the dispersed phases (solid particles). Too small a CV and an insufficient number of particles can be captured within the model; this is explored in more detail in a following section.

3.1.2 Lagrangian Trajectory Approach

The Lagrangian approach treats each particle within the flow domain as an individual entity whose path is explicitly tracked throughout. Particle motion is governed by ordinary differential equations describing the motion of the particle in a Lagrangian coordinate system. As such, the particle velocity and corresponding path can be determined by integrating these equations. This approach is suitable when it is required to predict the motion of individual particles and how their flow patterns are affected by transient effects. Simulations of this type can be applied to follow tracer particles, such as radioactive tracers, deposition studies and erosion impact studies. Currently these types of simulations are extremely computationally demanding and realistic results are only possible for very dilute solids flows with simplifying assumptions.

Particles are labeled and set to occupy an initial position within the flow domain under study. The particle P can be considered to have an origin point (X_1,X_2,X_3) and at

times $t>0$ the particle P occupies a new position (x_1,x_2,x_3). Therefore the new position x_i is a function of the original position and time $\bar{x} = \phi(\overline{X},t)$. All of the particles are assumed to be distinct and to remain distinct by not agglomerating. A continuous inverse transformation must also be defined to map the current particle location and time back to the original particle position.

Two general approaches are applied to the Lagrangian simulation of multiphase flows, stochastic and deterministic models. The deterministic Lagrangian trajectory model neglects the effect of the instantaneous fluctuating velocity field of the carrier phase turbulence and its effects on the transport processes of the particle phase. Stochastic models take this instantaneous gas turbulence into account and formulate the instantaneous gas velocity in the formulation of the motion of the particles. Statistical methods are applied in the stochastic approach.

In order to be able to solve the individual particle trajectories the carrier gas flow field must be calculated a priori. Eulerian computations are usually applied to calculate the flow field under study. Velocity field results are then coupled with the Lagrangian prediction of the particle movement within the flow and the affects of particle to particle and particle to carrier phase are calculated. In order to achieve convergence many iterations are required to obtain solutions for each of the phases.

The Lagrangian approach is extremely computationally intensive and requires large computing facilities for simulations that model reasonable physical situations.

3.1.3 Kinetic Theory Approach

In dense gas/solids flows the approach of the kinetic theory of gases can be applied. It is assumed that most, if not all, of the transfer of energy within the flow

domain occurs due to particle to particle interaction in the form of collisions. Each particle is likened to a "molecule" and the collisional properties of these particles are used to predict the flow behavior.

Certain constitutive relationships have to be included with the model to account for properties analogous to those of the gas molecular kinetic theory approach. Some of these properties include the restitution coefficient, solids viscosity terms and a granular temperature which appears as a new transported quantity.

The frequency distribution of particles within the flow domain are assumed to obey a Maxwellian distribution and to be a function of time, position and instantaneous velocity. The Maxwellian distribution for particles in three dimensions can be determined and the treatment of particle collisions and transport coefficients can be included. The Boltzmann integral-differential equation can be determined using the Reynolds Transport theorem and equates the rate of change of f for a system of a number of particles to the rate at which f is altered by encounters. A transport equation can be determined from this Boltzmann integral-differential equation resulting in Maxwell's transport equation. The latest version of CFX 5.0 will include a kinetic theory model of multiphase flows. It will not be discussed further in this thesis work.

3.1.4 Ergun Equation and Other Empirical Approaches

The classic Ergun equation gives a relationship between the pressure drop in a packed bed to the flow rate and the properties of particle and gas. This equation has been very successfully applied to predict pressure drops and required flow rates for many industrial fluidized bed applications and still finds relevance in all areas of fluidized bed work. Other empirical results predict jet penetrations, bed expansion heights and voidage

distribution functions for a number of different geometries. Empirical results are very important to get a feel for how a flow system will behave and should be used to gain an insight into the flow domain in question by using well established and verified relationships.

3.1.5 Direct Numerical Simulation

Direct numerical simulation (DNS) involves solving the entire set of Navier Stokes equations on a very fine grid to model all of the nonlinear interaction terms. In the case of multiphase flows each particle is tracked and advanced through the flow domain by calculating all of the interaction forces around the particle including particle-particle interactions, particle-fluid interactions and fluid-particle interactions. DNS is extremely computationally intensive and has not found wide spread application. It is hoped that large DNS runs will provide correlations that can be used in other less demanding methods such as the Eulerian two-fluid models.

3.2 Single Phase Flows

3.2.1 Derivation of the General Transport Theorem

To describe fluid flow phenomena, governing equations based on the conservation of mass, momentum and energy must be constructed for single phase flow (Aris, 1962) and then generalized to multiphase flow systems. Each of these three conserved quantities can be expressed in the more general transport theorem governing conservation. For these discussions the conservation of angular momentum will not be elaborated on. An infinitesimally small fluid element is considered within the flow

domain. All conservation equations in continuum mechanics can be derived from the general transport theorem. A variable *F(t)* is defined as a volume integral over an arbitrary volume element *v(t)* in an n-space as shown in Equation 3.1.

$$F(t) = \iiint_{v(t)} f(\bar{x}, t)\, dv \tag{3.1}$$

where $f(\bar{x}, t)$ is an integrable function representing a parameter such as mass, momentum or energy; t is the time; and $\bar{x}$ is a position vector. In three dimensions the vector $\bar{x} = (x_1, x_2, x_3)$. In order to be able to calculate the total rate of change of *F(t)* it is necessary to introduce an ξ-space where the volume of *F(t)* is fixed with respect to time so that the interchange of differentiation and integration is possible for the total derivative of *F*. In order to be able to do this we define the relationship of the change of volume with time to that of a new coordinate system $\bar{\xi}$ such that this new coordinate system has no volume change associated with it. Figure 3.1 defines the control volume in this new curvilinear coordinate system.

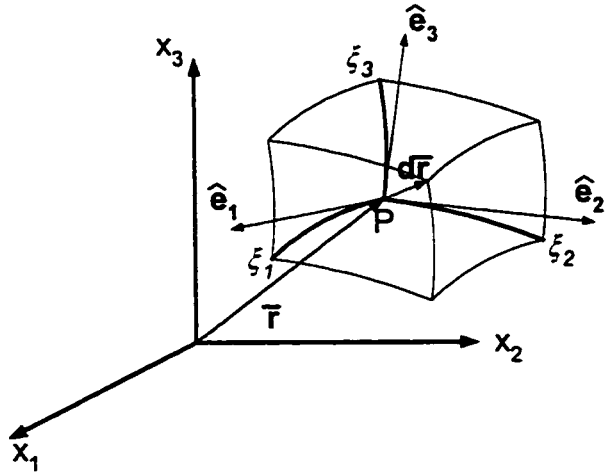

Figure 3.1 – General control volume in curvilinear coordinates.

The point P can be located in coordinate systems as Cartesian (x_1,x_2,x_3) and also as curvilinear (ξ_1, ξ_2, ξ_3). Subsequently the point (x_1,x_2,x_3) can be described as $x_1=f_1(\xi_1, \xi_2, \xi_3)$, $x_2= f_2(\xi_1, \xi_2, \xi_3)$ and $x_3= f_3(\xi_1, \xi_2, \xi_3)$ where it is assumed that f_i are continuous functions with continuous partial derivatives.

If ξ_2 and ξ_3 are held constant, then as ξ_1 varies the position vector **r** traces a curve called the ξ_1 coordinate curve; this treatment can be applied for both ξ_2 and ξ_3. Therefore:

$$d\bar{r} = \frac{\partial \bar{r}}{\partial \xi_1} d\xi_1 + \frac{\partial \bar{r}}{\partial \xi_2} d\xi_2 + \frac{\partial \bar{r}}{\partial \xi_3} d\xi_3 \tag{3.2}$$

The vector $\partial\bar{r}/\partial\xi_1$ defines a tangent at the point P which can be assigned a directional unit vector of $h_1\hat{e}_1$ with $h_1 = |\partial\bar{r}/\partial\xi_1|$; similar expressions can be determined for $\hat{e}_2$ and $\hat{e}_3$. Therefore the previous expression can be written as:

$$d\bar{r} = h_1 d\xi_1 \hat{e}_1 + h_2 d\xi_2 \hat{e}_2 + h_3 d\xi_3 \hat{e}_3 \tag{3.3}$$

If the orthogonal basis vectors $\hat{e}_1$, $\hat{e}_2$ and $\hat{e}_3$ are mutually perpendicular at any point P, then the curvilinear coordinates are orthogonal. In this case the volume of the parallelepiped formed by the infinitesimal position vector $d\bar{r}$ is given by:

$$dV = \left| \frac{\partial \bar{r}}{\partial \xi_1} \cdot \frac{\partial \bar{r}}{\partial \xi_2} \times \frac{\partial \bar{r}}{\partial \xi_3} \right| d\xi_1 d\xi_2 d\xi_3 = \left| \frac{\partial(x,y,z)}{\partial(\xi_1,\xi_2,\xi_3)} \right| d\xi_1 d\xi_2 d\xi_3 \tag{3.4}$$

In which case,

$$dV = \bar{\bar{J}} dV_0 \tag{3.5}$$

Where the Jacobian is defined as:

$$\bar{\bar{J}} = \begin{vmatrix} \frac{\partial x_1}{\partial \xi_1} & \frac{\partial x_1}{\partial \xi_2} & \frac{\partial x_1}{\partial \xi_3} \\ \frac{\partial x_1}{\partial \xi_1} & \frac{\partial x_1}{\partial \xi_2} & \frac{\partial x_1}{\partial \xi_3} \\ \frac{\partial x_1}{\partial \xi_1} & \frac{\partial x_1}{\partial \xi_2} & \frac{\partial x_1}{\partial \xi_3} \end{vmatrix} \tag{3.6}$$

and represents the change in volume of an element when transforming from one coordinate system to another.

We now have an expression to transform the initial deforming coordinate system to one where the volume element is not dependent on time.

$$F(t) = \iiint_{v(t)} f(\bar{x},t)\, dv = \iiint_{v_0} f(\bar{\xi},t)\, \bar{\bar{J}}\, dv_0 \tag{3.7}$$

The total derivative of $F(t)$ can now be calculated by bringing the differentiation with respect to time into the integrand which is now being calculated over constant volume, v_0.

It can be shown that $\frac{d\bar{\bar{J}}}{dt} = \left(\nabla \cdot \bar{v}\right)\bar{\bar{J}}$ where $\bar{v} = \frac{d\bar{x}}{dt}$, please see *Appendix A.1*. Therefore, the expression of the total derivative now becomes:

$$\frac{dF}{dt} = \frac{d}{dt}\iiint_{v(t)} f\left(\bar{x},t\right)dv = \frac{d}{dt}\iiint_{v_0} f\left[\bar{x}\left(\bar{\xi},t\right)\right]\bar{\bar{J}}dv_0$$

$$\begin{aligned} &= \iiint_{v_0}\left(\frac{df}{dt}\bar{\bar{J}} + f\frac{d\bar{\bar{J}}}{dt}\right)dv_0 \\ &= \iiint_{v_0}\left(\frac{df}{dt} + f\left(\nabla \cdot \bar{v}\right)\right)\bar{\bar{J}}dv_0 \\ &= \iiint_{v(t)}\left(\frac{df}{dt} + f\left(\nabla \cdot \bar{v}\right)\right)dv \end{aligned} \tag{3.8}$$

Note that the full derivative df/dt can be expressed as

$$\frac{df}{dt} = \frac{\partial f}{\partial t} + \bar{v} \cdot \nabla f \tag{3.9}$$

And substituting into the general transport theorem (3.8)

$$\frac{dF}{dt} = \iiint_{v(t)}\left(\frac{\partial f}{\partial t} + \nabla \cdot f\bar{v}\right)dv \tag{3.10}$$

The rate of change of F can be found from the net flow of f across the closed surface of $v(t)$ and the generation of f within $v(t)$. Defining ψ as the (diffusional) flux vector of f across the closed surface of $v(t)$ and Φ as the volumetric rate of production of f, the rate of change of F can be specified as:

$$\frac{dF}{dt} = -\iint_{A} \hat{n} \cdot \psi dA + \iiint_{v(t)} \Phi dv \tag{3.11}$$

Where $\hat{n}$ is the outward facing normal to the closed surface, A, bounding the volume $v(t)$. Gauss' theorem can be applied to this surface integral to change it into a volume integral, please see *Appendix A.2: Gauss' Theorem*. The general transport theorem can now be combined with the volumetric production and convective flux terms to obtain:

$$\iiint_{v(t)} \left(\frac{\partial f}{\partial t} + \nabla \cdot f\bar{v} + \nabla \cdot \psi - \Phi \right) dv = 0 \tag{3.12}$$

Since this derivation has been for an arbitrary volume, the integration operator can be removed and the general conservation equation in a single phase of fluid can be written as follows:

$$\frac{\partial f}{\partial t} + \nabla \cdot \left(f\bar{v} \right) + \nabla \cdot \psi - \Phi = 0 \tag{3.13}$$

There are four different behavior to address in the general conservation equation: i) discretization in time, ii) advection terms, iii) diffusion based terms and iv) source terms. Each of these terms will be dealt with in Chapter 3 Computational Techniques.

3.2.2 Continuity Equation

Based on the general conservation equation, an expression for the conservation of mass can be formulated by setting f equal to the fluid density ρ, there is no diffusive mass flux, $\psi=0$, and there is no volumetric mass production, $\Phi=0$.

$$\frac{\partial \rho}{\partial t} + \nabla \cdot \left(\rho \bar{v}\right) = 0 \tag{3.14}$$

3.2.3 Momentum Equation

To derive the momentum equation, f is set to the momentum per unit volume, $\rho\bar{v}$. Diffusive momentum flux is due to shear stresses within the fluid. This term is generally lumped with the static pressure of the fluid, P and is expressed as $\psi = \left(P\bar{\bar{I}} - \bar{\bar{\tau}}\right)$. Source term is the action of body and other forces acting on the fluid (including gravitational and magnetic fields); this is a force per unit mass and is expressed as $\Phi = -\rho\bar{f}_b$.

$$\frac{\partial\left(\rho\bar{v}\right)}{\partial t} + \nabla \cdot \left(\rho\bar{\bar{v}}\bar{v}\right) = \rho\bar{f}_b - \nabla P + \nabla \cdot \bar{\bar{\tau}} \tag{3.15}$$

Different expressions for the stress tensor, $\overline{\overline{\tau}}$, refer to fluids with different properties. Many fluids can be characterized as Newtonian where the shear stress within the fluid is only proportional to the gradient of velocity. For this discussion a Newtonian fluid will be assumed and the stress tensor will simply be stated and not derived:

$$\overline{\overline{\tau}} = \mu\left(2S_{ij} - \frac{2}{3}\delta_{ij}S_{ll}\right) + \zeta\delta_{ij}S_{ll} \tag{3.16}$$

S_{ij} is the velocity strain rate tensor, μ is the fluid viscosity and ζ is the bulk viscosity coefficient, which is usually assumed to be insignificant.

3.3 Multiphase Flows

Multiphase flows are characterized from single phase flows in that there is interaction between different thermodynamic phases present within the flow system. Multiphase flows include gas-solids flows (fluidized beds, pneumatic transport, granular and chute flows), gas-liquid (bubble columns, atmospheric flows, application of sprays, etc...), liquid-solid flows and gas-liquid-solid flows (three phase biological contact units, three phase fluidized beds, etc...). Multicomponent flows are flows in which there are different chemical species interacting. Multicomponent flows can also be multiphase flows such as the pneumatic transport of benzoic acid in solid form – in this case the benzoic acid is present as solid particles and as a sublimated gas phase within the carrier gas phase for transport. Multiphase flow is a very common phenomenon and is the topic

of this study. Gas-solids flows within a fluidized bed reactor has been the focus of this research.

Much work has been carried out to formulate the correct equations governing two-phase flows within fluidized beds. Sinclair (1997) has done an extensive review of the many different formulations and presents a list of the most important governing equations used by different authors. Only the two-fluid models will be discussed in this report. Early attempts at modeling fluidized bed hydrodynamics are attributed to Davidson (1961) for assuming that the particulate phase behaves as an incompressible fluid with a constant porosity outside of bubbles. The gas was assumed ideal and pressure drop was calculated using Darcy's law for flow in a porous medium. Original formulations of the two-fluid model (Anderson and Jackson, 1967) formulate the equation of motion for the center of mass of a single particle agreeing with the control volume size as already discussed. This averaging procedure leads to terms that describe the interactions associated with the velocity fields of the two phases. One of the most confusing aspects of multiphase flow modeling is that there still exist differences in the *fundamental* governing equations used by different investigators in the literature. Some of the earliest investigations using a two fluid formulation were carried out by Arastoopour and Gidaspow (1979) and Arastoopour *et al.* (1982). Gidaspow and co-workers have done extensive work with computer simulations of circulating fluidized beds and bubbling beds using two fluid models. However, over the years Gidaspow has used several different formulations for the momentum equations. Hydrodynamic model A (Bouillard *et al.*, 1989) contained gas-phase pressure drops in both the gas and solids momentum equations. Hydrodynamic model B (Lyczkowski *et al.*, 1978) retained the

entire pressure drop only in the gas momentum equation and Gidaspow's relative velocity model (Gidaspow, 1994; Arastoopour and Gidaspow, 1979) uses a formulation based on the slip velocity between the two phases. It was recognized that with Hydrodynamic model A the inclusion of the continuous phase pressure in the solids momentum equation leads to an initial value problem that is ill-posed (Fanucci *et al.*, 1979). In order to overcome this problem a normal component of solids stress based on a solids shear stress modulus was added to stabilize numerical solution.

The equations governing multiphase flow systems such as those studied in this report can be derived from first principles; however, in the previous section a detailed derivation of the single phase general conservation equations have been presented. Extension to multiphase fluid dynamics is straightforward but requires the inclusion of additional transfer terms between the momentum equations for each phase. The governing equations will be stated without derivation.

Gas Continuity:

$$\frac{\partial}{\partial t}\left(\varepsilon_g \rho_g\right)+\nabla\cdot\left(\varepsilon_g \rho_g \overline{U}_g\right)=\left(\dot{m}_{gs}-\dot{m}_{sg}\right)=0 \tag{3.17}$$

The gas continuity is similar to that of the single phase continuity equation; however, the gas volume fraction is now included as an unknown within the equation and must be taken into account. The thermodynamic mass transfer terms (the last term on the right hand side of the continuity equation) from one phase to another is included but is not used for this work.

Gas Momentum:

$$\frac{\partial}{\partial t}\left(\varepsilon_g \rho_g \overline{U}_g\right)+\nabla\cdot\left(\varepsilon_g\left(\rho_g \overline{U}_g \otimes \overline{U}_g-\mu_g\left(\nabla\overline{U}_g+\left(\nabla\overline{U}_g\right)^T\right)\right)\right.$$

$$=\varepsilon_g\left(\overline{B}-\nabla p_g\right)+c_{gs}^{(d)}\left(\overline{U}_g-\overline{U}_s\right)+\overline{F}_g+\dot{m}_{gs}\overline{U}_s-\dot{m}_{sg}\overline{U}_g \qquad (3.18)$$

Coupling of the two sets of equations is carried out by the use of momentum transfer in the form of drag on one phase exerted by the other. Momentum transfer due to phase change is listed in the last two terms; however, this was not considered in this study.

Solids Continuity:

$$\frac{\partial}{\partial t}\left(\varepsilon_s \rho_s\right)+\nabla\cdot\left(\varepsilon_s \rho_s \overline{U}_s\right)=\left(\dot{m}_{sg}-\dot{m}_{gs}\right)=0 \qquad (3.19)$$

Solids Momentum:

$$\frac{\partial}{\partial t}\left(\varepsilon_s \rho_s \overline{U}_s\right)+\nabla\cdot\left(\varepsilon_s\left(\rho_s \overline{U}_s \otimes \overline{U}_s-\mu_s\left(\nabla\overline{U}_s+\left(\nabla\overline{U}_s\right)^T\right)\right)\right.$$

$$=\varepsilon_s\left(\overline{B}-\nabla p_g\right)+c_{sg}^{(d)}\left(\overline{U}_s-\overline{U}_g\right)+\overline{F}_s+\dot{m}_{sg}\overline{U}_g-\dot{m}_{gs}\overline{U}_s+\nabla p_s \qquad (3.20)$$

The solids momentum equation (3.20) has several additional terms which are not found in the gas phase momentum equation (3.18). Simulations were conducted with the gas phase pressure shared between the two momentum equations thereby making these equations conform to Gidaspow's Hyrodynamic model A. Several comparison simulations were also conducted with the gas pressure removed from the solids

momentum equation agreeing with Gidaspow's Hydrodynamic model B. In order to make this initial value problem well posed a solids pressure term was included in the solids momentum equation. The form of this expression is described subsequently.

There are a total of nine unknowns (three velocity components for each of the solids and gas phases, two volume fractions and the continuous, or thermodynamic, pressure) and eight equations available for solution (six momentum and two continuity equations). Since the flow is assumed to be incompressible, there is not an equation of state for the pressure and it must be solved iteratively using a pressure correction method. The pressure correction method used in CFX is described in Chapter 3 Computational Methods. Constitutive relationships for the solids viscosity, drag coefficient and solids pressure are required. These and other more general factors are discussed below.

3.3.1 Forces Acting on Solids in a Gas-Solid Multiphase Flow System

Influences affecting the flow of a single phase flow system can be broken into those forces resulting from body forces (gravitational, magnetic, etc...) and internal forces resulting from viscous interaction of the flow "particles" and pressure. Multiphase flow systems have an added influence due to the interaction of the phases with one another and also upon themselves (much as viscous shears affect single phase flows). The following is a brief description of those forces influencing multiphase flows. Not all of these forces have been explicitly modeled in this study but are included here for completeness.

3.3.2 Drag Forces

In a fluidized bed the solids particles are kept in suspension by the action of the fluidization gas passing up through the reactor and counteracting the force of gravity. One of the ways in which the gas and solids interact is through the transfer of momentum between the phases. This leads to a two way coupling of the momentum equations. Drag forces for single spheres falling in a stationary liquid (similar to sedimentation) have been studied and very good correlations have been found for the drag factor over a sphere over a wide range of Reynolds numbers (Bird, Stewart and Lightfoot, 1960).

Figure 3.2 shows some commonly used drag models for multiphase flow systems including the correlation used for this study. For this study the drag model of Gidaspow (1994) was chosen. This model was chosen based on the work done by Witt and his colleagues (Witt, Perry and Schwarz, 1998; Witt and Perry, 1995a; Witt and Perry, 1995b) at CSIRO, Australia. Witt *et al.* have used CFX and produced good comparison between fluidized bed experiments and simulation results. Other modern simulation studies have also used this correlation to good effect, see Hong *et al.* (1997). For solids volume fractions less than 0.2 the correlation of Wen and Yu (1966) is followed. Above this volume fraction the Ergun equation is used to calculate the drag factor. As pointed out by van Wechem *et al.* (1999) the rationale for this model is unclear especially as there is a discontinuity at the solids volume fraction of 0.2. This particular drag model was used for these simulations based on the drag models used in the work of Witt *et al.* More importantly the correlation of Wen and Yu (1965) was based on data that spanned the entire operating conditions.

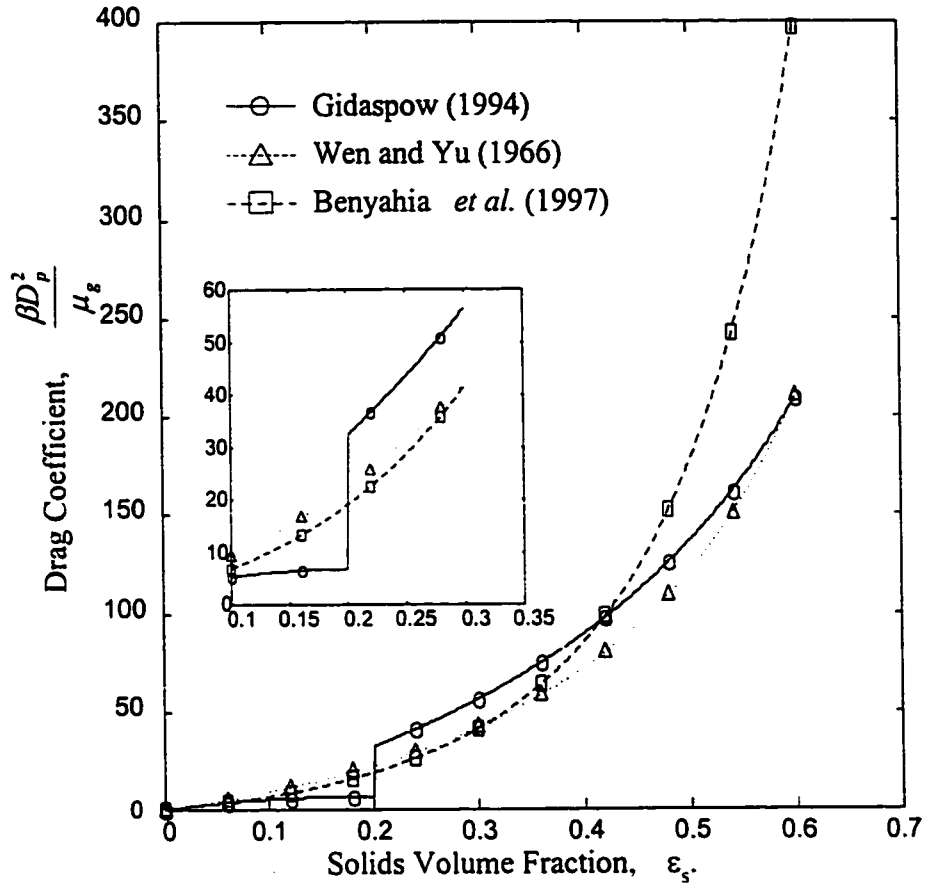

Figure 3.2 - Drag coefficient correlation based on $Re_p=45$ using the drag correlation of Schiller and Nauman (1933) for particles in gas flows.

The equations used to describe the drag correlation used for this work are obtained from a modified form (Richardson and Zaki, 1954) of the drag force exerted on a single particle and is given by:

$$\beta_v = 150\frac{(1-\varepsilon)^2}{\varepsilon(d_p\phi_s)^2} + 1.75\frac{\rho_g|V_g - V_s|(1-\varepsilon)}{\phi_s d_p} \qquad \text{for } \varepsilon_s > 0.2 \tag{3.21}$$

$$\beta = \frac{3}{4} C_d \frac{\varepsilon_g \rho_g |u_g - u_s| (1-\varepsilon_g)}{D_p} G(\varepsilon_g) \qquad \text{for } \varepsilon_s \leq 0.2 \qquad (3.22)$$

where the drag coefficent C_d is defined based on the particle Reynolds number, Re_p, and corelations for the drag coefficient of a single sphere falling through a quiescent fluid as follows:

$$C_D = \frac{24}{\mathrm{Re}} \qquad 0 \leq \mathrm{Re} \leq 0.2 \qquad (3.23)$$

$$C_D = \frac{24}{\mathrm{Re}} (1 + 0.1 \mathrm{Re}^{0.75}) \qquad 0 \leq \mathrm{Re} \leq 500\text{-}1000$$

(Schiller and Nauman, 1933) (3.24)

$$C_D = 0.44 \qquad 500\text{-}1000 \leq \mathrm{Re} \leq 1\text{-}2 \times 10^5 \qquad (3.25)$$

$$\mathrm{Re}_p = \frac{D_p |U_s - U_g| \rho_g}{\mu_g} \qquad (3.26)$$

Since these relationships are for a single sphere drag coefficient, they have to be corrected to take the interaction of other particles into account. These expressions are corrected for the interaction of particles based on the multiplicative factor given by Gidaspow (1994):

$$k = (1 - \varepsilon_s)^p \qquad (3.27)$$

where p = -1.65. When the gas volume fraction falls below 0.8, this Gidaspow modification to the drag factor becomes inadequate. In this case the drag is calculated based on the Ergun equation (3.21).

3.3.3 Solids Pressure

Solids particles within fluidized beds come into intimate contact with one another and these interactions have to be taken into account. It was realized that in order to solve the equations governing dense multiphase gas-solids flows, terms must be included in the solids momentum equation to ensure that the solids do not reach physically unrealizable volume fractions. Coulombic stress, also known as solids pressure and/or the normal component of solids stress, has been introduced as a source term in the solids momentum equation. This coulombic stress acts as a repulsive force that increases with particle volume fraction.

The solids pressure gradient in equation (3.20) is considered to be a function of local volume fraction and is expressed as

$$-\nabla P_S = G(\varepsilon_g)\nabla \varepsilon_g \tag{3.28}$$

G is commonly referred to as the solids elastic bulk modulus and can be shown to be a thermodynamic property of powders. Several attempts at measuring G have been reported. Gough (1979) and more recently Bouillard *et al.* (1989) have determined a convenient form for the modulus G as:

$$G = G_0 e^{-k(\varepsilon_g - \varepsilon^*)} \tag{3.29}$$

with typical values of k=600, G_0=1.0 Pa and ε^*=0.376. This form is similar to that used in the CFX package.

Figure 3.3 is a plot of some commonly used approximations of G versus gas volume fraction. The correlation G_1 of Bouillard *et al.* (1989) was used for the simulations in this study. Some sensitivity studies were conducted using the relationship of Ettehadieh *et al.* (1984) and is discussed in Chapter 5; this function is very similar in value to Benyahia *et al.* (1997) shown in Figure 3.3. Values for the specific functions are listed in Table 3.1. For each solids pressure function there exists a point where the repulsive force increases exponentially. This occurs near the minimum solids packing fraction and prevents solids from reaching volume fractions that are physically unreasonable.

Table 3.1

Common Solids Pressure Functions in Literature

Expression	Reference
$G(\varepsilon_g) = 10^{-8.76\varepsilon_g + 5.43}$	Ettehadieh *et al.* (1984)
$G_1(\varepsilon_g) = e^{-600(\varepsilon_g - 0.376)}$	Bouillard *et al.* (1989)
$G_2(\varepsilon_g) = e^{-500(\varepsilon_g - 0.422)}$	
$G_3(\varepsilon_g) = e^{-20(\varepsilon_g - 0.62)}$	
$G(\varepsilon_g) = e^{-100(\varepsilon_g - 0.45)}$	Kuipers *et al.* (1992)
$G(\varepsilon_g) = e^{-600(\varepsilon_g - 0.39)}$	Lyczkowski *et al.* (1993)
$G(\varepsilon_g) = 10^{-8.5\varepsilon_g + 5.43}$	Benyahia *et al.* (1997)

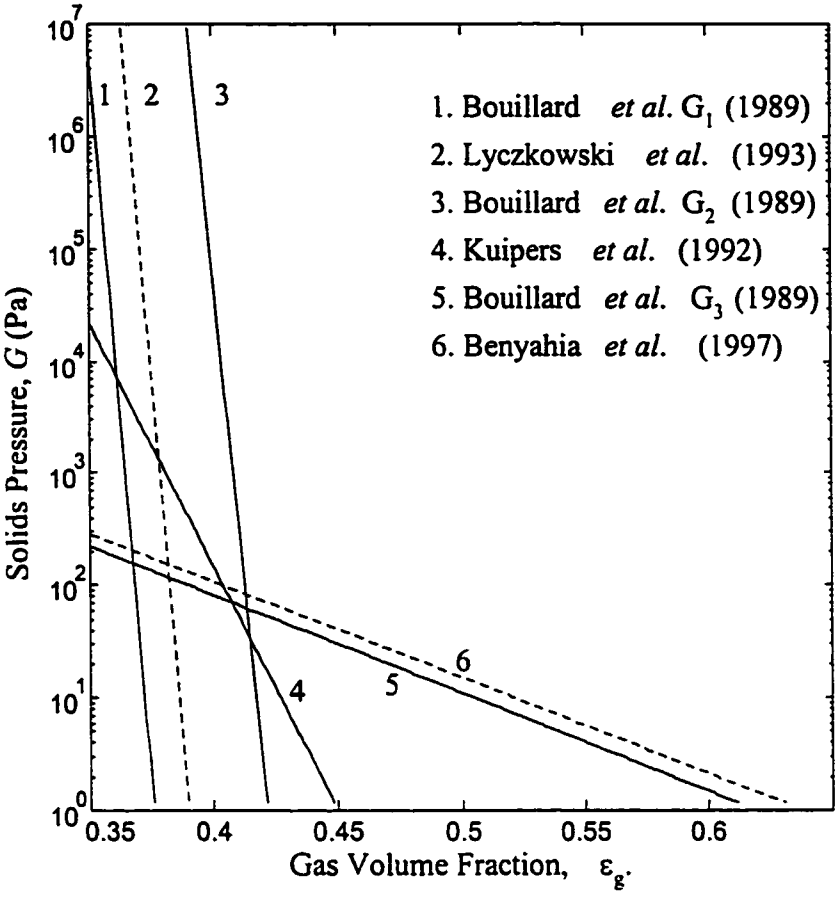

Figure 3.3 – Solids pressure functions used in literature.

Thermodynamic variables that define the state of a powder can include: specific entropy, bulk specific volume, composition and possibly several other variables that must account for the strains in a solid in more than one direction. The internal energy of a powder can be defined as:

$$U = U(S, v_B) \tag{3.30}$$

where

$$v_B = 1/\rho_s \varepsilon_s \tag{3.31}$$

Which is the volume weighted specific bulk volume of the solids. The solids stress, σ_s, can be defined like the pressure for a fluid:

$$\sigma_s = -\frac{\partial U}{\partial v_B} \tag{3.32}$$

Assuming a constant particle density of the solid, ρ_s, at constant entropy this equation can be rewritten as:

$$dU = \frac{\sigma_s}{\rho_s} \frac{d\varepsilon_s}{\varepsilon_s^2} \tag{3.33}$$

Therefore, the internal energy of the solids phase (powder) decreases with expansion. Since the only new variable that has been introduced is the bulk powder specific volume, the temperature of the powder is still given by:

$$T = \left(\frac{\partial U}{\partial S} \right)_{v_B} \tag{3.34}$$

Using thermodynamic stability, see Smith, Van Ness and Abbott (1949):

$$d^2U > 0 \tag{3.35}$$

which leads to the well known relation for fluids:

$$\left(\frac{\partial \sigma_s}{\partial v_B}\right)_{T\_or\_S} < 0$$

$$or \tag{3.36}$$

$$\left(\frac{\partial \sigma_s}{\partial \rho_B}\right)_{T\_or\_S} > 0$$

Since at constant temperature or entropy,

$$\sigma_s = \sigma_s(\varepsilon_s), \left(\frac{\partial \sigma_s}{\partial \rho_B}\right) = \frac{1}{\rho_s}\left(\frac{\partial \sigma_s}{\partial \varepsilon_s}\right) \tag{3.37}$$

The elastic bulk modulus G, similar to the Young's modulus for solids, is defined to be:

$$G = \left(\frac{\partial \sigma_s}{\partial \varepsilon_s}\right)_{T\_or\_S} \tag{3.38}$$

Based upon this analysis it is seen that G is a thermodynamic property of the powder.

3.3.4 Friction

Interaction of solids particles with one another also leads to the transfer of kinetic to thermal energy within the fluidized bed. This transfer of energy will be considered to be a loss of kinetic energy as the simulations in this study do not include a mechanism for the transfer of that thermal energy back to kinetic energy. Frictional forces between the solids particles have taken the form of a solids viscosity term that is similar to the gas viscosity as defined by the kinetic theory of gases.

3.3.5 Particle Viscosity Due to Interparticle Collisions

At high solids concentrations the shear motion of particles can lead to a large number of collisions between particles. These collisions lead to the transfer of momentum and can be described in terms of a solids shear stress (based on the continuum and not internal solids shear stress as experienced when studying solids deformations). Constitutive relationships for these stresses were first put forth by Lun *et al.* (1984) based on a gas kinetic theory approach allowing for the inelastic collision of particles. Gidaspow (1994) presents a solids viscosity relationship which varies little from that of Lun *et al.* (1984). Hrenya and Sinclair (1997) follow the treatment of Lun *et al.* (1984) but add a modification that sets the particle viscosity to zero at zero solids volume fraction. The original work of Lun *et al.* (1984) was derived for particles in an infinite medium. As the particles move further apart their mean free path becomes infinite and the solids viscosity at zero solids volume fraction takes on a finite value. The solids

viscosity relationship of Syamlal *et al.* (1993) neglects the kinetic or streaming effect of the particles on the solids viscosity which is dominant at low solids volume fractions. As this is so, this treatment departs markedly from other models available in the literature. Since Syamlal *et al.* (1993) chose to neglect these low solids volume fraction effects, their model does correctly reduce to zero solids viscosity at zero solids volume fraction. All models coincide at higher solids volume fractions where the flow is collision dominated. The available correlations are listed in Table 3.2 and a plot of the different viscosity functions is shown in Figure 3.4.

Table 3.2

Solids Viscosity Correlations Available in Literature

Hrenya and Sinclair (1997)

$$\mu_s = \frac{4}{5}\varepsilon_s^2 \rho_s D_p g_0 (1+e)\sqrt{\frac{\Theta_s}{\pi}} + \frac{10}{96}\sqrt{\Theta\pi}\frac{\rho_s D_p}{(1+e)\left(\frac{3}{2}-\frac{1}{2}e\right)\left(1+\frac{\lambda_{min}}{R}\right)g_0} + \frac{1}{6}\sqrt{\Theta\pi}\frac{\rho_s D_p \varepsilon_s \left(\frac{1}{2}\left(1+\frac{\lambda_{min}}{R}\right)+\frac{3}{4}e-\frac{1}{4}\right)}{\left(\frac{3}{2}-\frac{1}{2}e\right)\left(1+\frac{\lambda_{min}}{R}\right)} + \frac{1}{15}\sqrt{\Theta\pi}\frac{\rho_s D_p g_0 (1+e)\left(\frac{3}{2}e-\frac{1}{2}\right)\varepsilon_s^2}{\left(\frac{3}{2}-\frac{1}{2}e\right)}$$

Gidaspow (1994)

$$\mu_s = \frac{4}{5}\varepsilon_s^2 \rho_s D_p g_0 (1+e)\sqrt{\frac{\Theta_s}{\pi}} + \frac{10}{96}\sqrt{\Theta\pi}\frac{\rho_s D_p}{(1+e)g_0} + \frac{1}{6}\sqrt{\Theta\pi}\rho_s D_p \varepsilon_s + \frac{1}{15}\sqrt{\Theta\pi}\rho_s D_p g_0 (1+e)\varepsilon_s^2$$

Syamlal *et al.* (1993)

$$\mu_s = \frac{4}{5}\varepsilon_s^2 \rho_s D_p g_0 (1+e)\sqrt{\frac{\Theta_s}{\pi}} + \frac{\varepsilon_s D_p \rho_s \sqrt{\pi\Theta}}{6(3-e)} + \frac{1}{15}\sqrt{\Theta\pi}\rho_s D_p g_0 \varepsilon_s^2 \frac{(1+e)\left(\frac{3}{2}e-\frac{1}{2}\right)}{\left(\frac{3}{2}-\frac{e}{2}\right)}$$

Lun *et al.* (1984)

$$\mu_s = \frac{4}{5}\varepsilon_s^2 \rho_s D_p g_0 (1+e)\sqrt{\frac{\Theta_s}{\pi}} + \frac{10}{96}\sqrt{\Theta\pi}\frac{\rho_s D_p}{(1+e)\left(\frac{3}{2}-\frac{1}{2}e\right)g_0} + \frac{1}{6}\sqrt{\Theta\pi}\frac{\rho_s D_p \varepsilon_s \left(\frac{3}{4}e+\frac{1}{4}\right)}{\left(\frac{3}{2}-\frac{1}{2}e\right)} + \frac{1}{15}\sqrt{\Theta\pi}\frac{\rho_s D_p g_0 (1+e)\left(\frac{3}{2}e-\frac{1}{2}\right)\varepsilon_s^2}{\left(\frac{3}{2}-\frac{1}{2}e\right)}$$

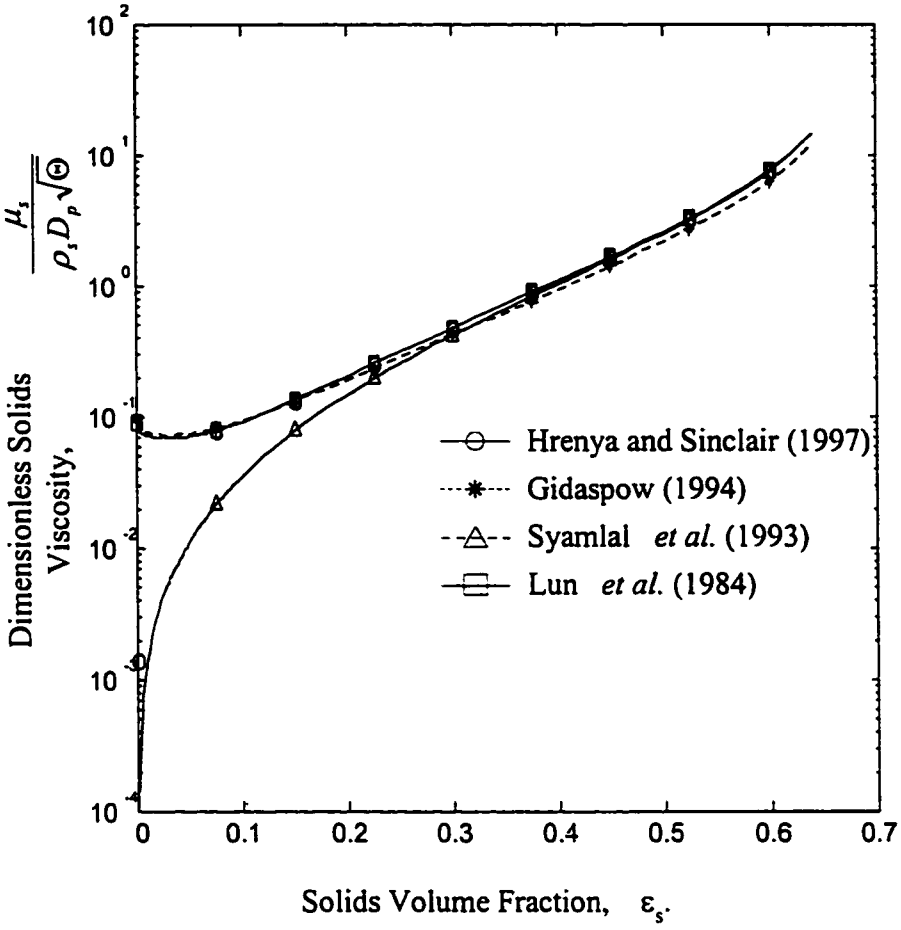

Figure 3.4 - Plot of solids viscosity versus solids volume fraction for different correlations available in the literature. Restitution coefficient set equal to 0.9. Sinclair (1997) radial distribution function used.

Consider the elastic collision of two particles of different sizes in a two dimensional *rx*-plane (Arastoopour *et al.* 1982) as shown in Figure 3.5.

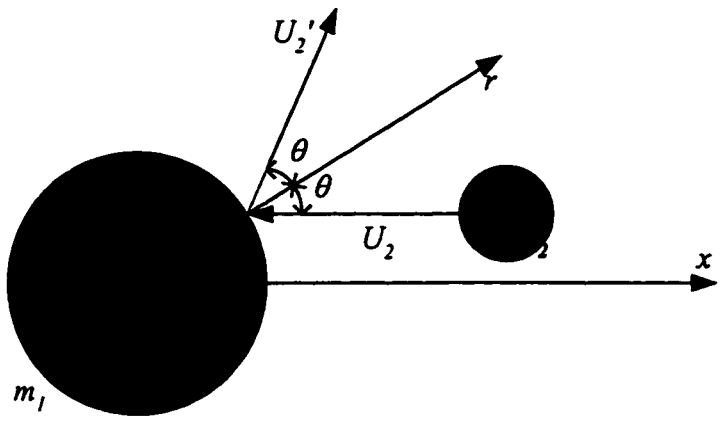

Figure 3.5 – Elastic collision of two solid spherical particles of different sizes.

Particle 2 with mass m_2 initially has momentum in the negative x direction and impacts on the stationary particle 1 with mass m_1 from which it undergoes an elastic collision resulting in specular reflection about the axis r and its subsequent velocity is in the rx plane. The rate of change of the x-component of the momentum between the two particles is given by:

$$m_2 U_2 - [m_2 U_2 \cos(\pi - 2\theta)] = 2m_2 U_2 \cos^2\theta \tag{3.39}$$

with θ the contact angle in the rx-plane. Next consider a collision between two particles 1 and 2 with masses m_1 and m_2 and velocities U_1 and U_2. From Newton's law

$$m_1 \frac{dU_1}{dt} = f_{12} \qquad m_2 \frac{dU_2}{dt} = -f_{12} \tag{3.40}$$

with f_{12} being the collisional force. For such a system a relative mass, m^*, can be defined as $\frac{1}{m^*} = \frac{1}{m_1} + \frac{1}{m_2}$ and a relative velocity as $\Delta U = U_1 - U_2$, simplifying to the following expression for the completely elastic collision between two particles.

$$m^* \frac{d\Delta U}{dt} = f_{12} \tag{3.41}$$

Therefore, the collision of two particles moving with independent velocities can be likened to the collision of a particle colliding with a fixed particle with the same relative mass and relative velocity. This result will be important when relating the collision of a single particle with a cloud of particles in shear flow.

Now consider the collision of a single particle with a cloud of particles as shown in the Figure 3.6. A representative particle of radius r is shown traveling to the left and is subjected to a shear flow within a particle cloud with a velocity gradient $\partial U_p / \partial y$. The particle number density is n, and the mass of this particle is m. For analysis the velocity U_p is set to zero in the center plane of the sphere and the previous conclusions can be applied. The relative velocity (based on the shear velocity gradient and the distance, y, above the zero line) can be estimated as

$$\Delta U_p = \frac{\partial U_p}{\partial y} y = \frac{\partial U_p}{\partial y} r \sin\theta \cos\phi \tag{3.42}$$

with the angles defined as shown in the diagram.

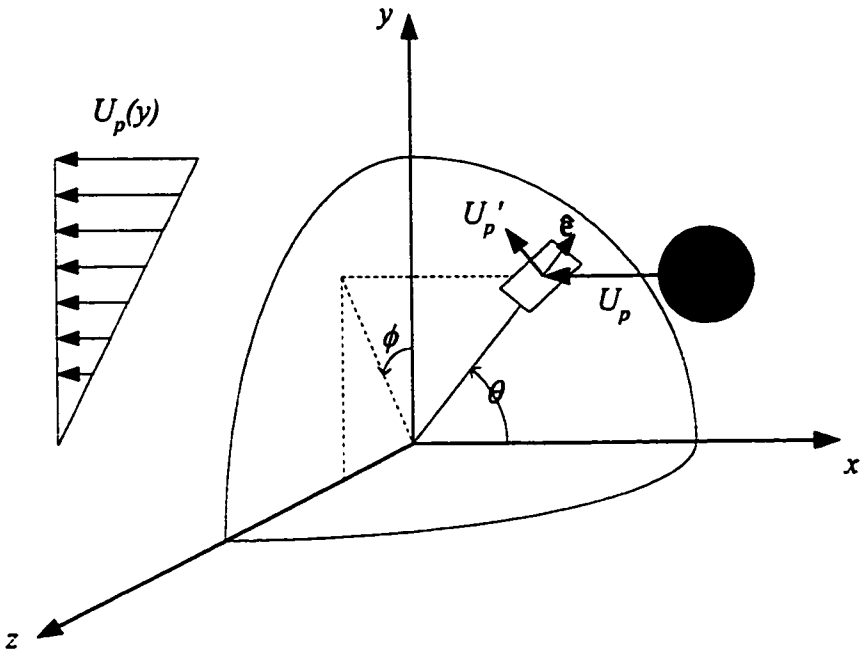

Figure 3.6 – Collision of a single particle with a cloud of particles in shear flow.

The differential area of impact of this particle on the solids cloud shown by the shaded patch is $r^2 \sin\theta d\theta d\phi$. The projected area normal to the incoming velocity U_p is $r^2 \sin\theta \cos\theta d\theta d\phi$. It has been previously shown that the momentum change from impact of two particles moving with different velocities can be expressed in terms of the relative mass and the relative velocity of the system. Based on this proof, the rate of change of x-momentum for a particle can be expressed as $2m\Delta U_p \cos^2\theta$ assuming single scattering and specular reflection. The total force acting upon the quarter sphere can be expressed in terms of the total impact of particles on the bounding area; this being a function of particle number density, approach velocity and mass.

$$F = 4\int_0^{\pi/2}\int_0^{\pi/2} n(\Delta U_p)^2 mr^2 \sin\theta\cos\theta d\theta d\phi \tag{3.43}$$

This expression for the force is made up of the change in x-momentum of the particles of mass m impacting on the semisphere (i.e. a quarter sphere, since U_p is zero at $y=0$) multiplied by the velocity. The number density n is required to take into account all of the particles impacting on the surface. Integrating this expression gives

$$F = \frac{\pi}{12} nm\left(\frac{\partial U_p}{\partial y}\right)^2 r^4 \tag{3.44}$$

With this expression for the force acting on the semisphere consider a mixture of two groups of particles with radii a_1 and a_2 and corresponding number densities of n_1 and n_2. Particles in group 1 are subjected to a shear flow of particles in group 2. The x-component of the collision force between particles 1 and 2 can be obtained as

$$F_{12} = \frac{\pi^2}{18} n_1 n_2 m^*\left(\frac{\partial U_p}{\partial y}\right)^2 (a_1 + a_2)^7 \tag{3.45}$$

This force can be projected onto an area normal to the y-axis and a shear stress for the solids phase can be defined as

$$(\tau_{xy})_{12} = \frac{2F_{12}}{\pi(a_1 + a_2)^2} = \frac{\pi}{9} n_1 n_2 m^*\left(\frac{\partial U_p}{\partial y}\right)^2 (a_1 + a_2)^5 \tag{3.46}$$

Soo (1989) generalized this expression to the following

$$\tau_{12} = -\frac{\pi}{9}\frac{n_1 n_2 m_1 m_2}{(m_1 + m_2)}(a_1 + a_2)^3 (\Delta_{p2} : \Delta_{p2})^{1/2} \Delta_{p2} = -\mu_{p12}\Delta_{p2} \tag{3.47}$$

where Δ_p has the Cartesian components of

$$\Delta_{pij} = \frac{\partial U_{pi}}{\partial x_j} + \frac{\partial U_{pj}}{\partial x_i} \tag{3.48}$$

and the : operator refers to the dyadic product. The viscosity due to the particle collision is defined from the expression for the solids shear stress and for the special case of identical particles reduces to

$$\mu_p = \frac{1}{3}\varepsilon_p \rho_p D_p^2 (\Delta_p : \Delta_p)^{1/2} \tag{3.49}$$

3.3.6 Radial Distribution Functions

Expressions for the solids viscosity all depend upon a radial distribution function g_0 at contact. A brief summary of the review given by van Wachem *et al.* (1999) is presented here for completeness. Several investigators have proposed solids distribution functions for use with the determination of the solids viscosity. Early models by

Carnahan and Starling (1969) did not tend to the correct limit as solids volume fraction approached the solids packing limit. Alternate expressions have been proposed by other authors such as Gidaspow (1994), Lun and Savage (1986), and Sinclair and Jackson (1989). Van Wachem *et al.* (1999) report that Gidaspow's expression most closely follows the experimental data of Alder and Wainright (1960); however, the impact of using these different expressions in calculating the solids viscosity is at most a factor of two, excluding the model of Syamlal *et al.* (1993).

3.3.7 Basset Force

The original form of the Basset force was derived in 1888 (Basset, 1888). The Basset force occurs when a particle is accelerated in a fluid and has importance with respect to Stokes drag. The Basset force can be substantial when particles are accelerated at a high rate as is the case at the boundary of the gas jet being discharged into a fluidized bed.

3.3.8 Magnus Force

Particle rotation in low Reynolds flow leads to fluid entrainment resulting in an increase in the velocity on one side of the particle and a decrease in velocity on the other side. Due to the velocity imbalance a net lift force is exerted on the particle causing it to move towards the higher flow velocity (Magnus, 1852).

3.3.9 Saffman Force

The Saffman force falls into a category of forces exerted on particles present in a gradient such as temperature, velocity and pressure gradients. In such cases these

gradient effects can have as much an importance as drag forces. Velocity gradients lead to the Saffman lift force (Saffman 1965) being exerted on a particle travelling with constant velocity.

Other gradient related forces include: Radiometric force as a result of a temperature gradient in a gas (thermophoresis) or nonuniform radiation (photophoresis). At room conditions these forces are typically only important for submicrometer particles (Fan and Zhu, 1999).

3.3.10 Pressure Gradient Induced Forces

Pressure gradients may have an impact on a force being exerted on a particle (Tchen, 1947). The significance of this force is evident when a shock wave propagates through a fluidized bed.

3.3.11 Response Times

The response time of a particle to changes in flow field variables are important for determining dimensionless numbers to characterize the flow. The momentum response time relates the time required by a particle to respond to changes in velocity. Crowe *et al.* (1998) give a detailed analysis of particle response times as follows. Consider the equation of motion for a particle in a gas phase

$$m\frac{dU_s}{dt} = \frac{1}{2}C_D\frac{\pi D_p^2}{4}\rho_g\left(U_g - U_s\right)\left|U_g - U_s\right| \tag{3.50}$$

Using the definition of the particle Reynolds number and dividing equation (3.50) by the particle mass gives

$$\frac{dU_s}{dt} = \frac{18\mu_g}{\rho_g D_p^2}\frac{C_D \mathrm{Re}_p}{24}\left(U_g - U_s\right) \tag{3.51}$$

In Stokes flow the drag factor $\frac{C_D \mathrm{Re}_p}{24}$ approaches unity leaving the Stokes relaxation time

$$\tau_S = \frac{\rho_g D_p^2}{18\mu_g} \tag{3.52}$$

and the original formulation of the equation of motion for a particle in gas flow can be written as:

$$\frac{dU_s}{dt} = \frac{1}{\tau_S}\left(U_g - U_s\right) \tag{3.53}$$

This first order differential equation can be solved by assuming an initial condition of zero particle velocity, giving:

$$U_s = U_g\left(1 - e^{-t/\tau_S}\right) \tag{3.54}$$

The Stokes relaxation time is the time required for a particle released from rest to reach 63% $\left(\frac{e-1}{e}\right)$ of the free stream velocity. For simulations in this report the Stokes relaxation time was calculated to be 0.0005 seconds.

3.4 Modeling and Averages

Basic assumptions governing the equations describing fluid flow within an infinitesimal volume element are subject to certain restraints. The general conservation equation is a balance of transported quantities over a definable, although infinitesimal, volume element within the flow domain. This continuum approach is applicable for situations where continuum mechanics can be applied. Continuum approaches might not be applicable for rarefied gas flows where the flow is dominated by interparticle spacing and not by the continuous distribution of the particles. In such cases another type of fundamental approach must be taken to formulate the governing equations using some type of statistical or kinetic theory approach. With this consideration it is also necessary to study the effect of the size of the averaging volume used to solve and model the equations. Three different averages will be discussed: temporal averaging, ensemble averaging (phase lock averaging) and volume averaging. Volume averaging was used for the work in this thesis and the emphasis of this discussion will be on that method.

Multiphase flows usually occur within a confined volume such as a reactor, pipe, tributary, etc... or some sort of bounded domain. A mathematical description of this domain is desired and as such the Eulerian approach is an ideal method. In single phase flows the transported quantities are considered to be continuous throughout the entire domain. However, for multiphase flows there is a dispersed and a continuous phase. Averaging techniques must be applied to construct a continuum description of each of the phases involved so that single phase flow models can be extended to multiphase flow models.

3.4.1 Volume Averaging

Multiphase flows consist of different phases each interacting at different length and time scales. The continuum approach can be constructed either using a temporal average such as a fractional residence time or by using a volume average technique where the phase properties are distributed using a volume fraction variable. Thermodynamic properties such as pressure, temperature and density are cumulative with volume fraction but not so with fractional residence times. Volume averaging is intuitive and linked with the control volume approach used when deriving the general conservation equation.

3.4.2 Phase Average and Intrinsic Average

Fan and Zhu (1998) define two volume averages for transport quantities within a continuum model. For a given transported quantity f within a specific control volume of size v a phase average quantity can be defined as:

$$\langle f_k \rangle = \frac{1}{v} \iiint_{v_k} f_k \, dv \tag{3.55}$$

where v_k is the volume occupied by phase k within the control volume v. An intrinsic average can be defined as the quantity of f within the volume v_k.

$$^{i}\langle f_k \rangle = \frac{1}{v_k} \iiint_{v_k} f_k \, dv \tag{3.56}$$

Intrinsic volume averages refer to the control volume independent value of the transport quantity such as density and velocity. Phase averages are dependent upon the size of the control volume.

Volume averages can only be applied to quantities per unit volume and other flow properties must be constructed based on ratios of these averages. The intrinsic average velocity of the phase k can be defined as (see Appendix A.3)

$$ {}^{i}\langle \bar{v}_k \rangle = \frac{1}{{}^{i}\langle \rho_k \rangle}\left[\frac{1}{v_k}\iiint_{v_k}\rho_k \bar{v}_k dv\right] = \frac{\langle \rho_k \bar{v}_k \rangle}{\langle \rho_k \rangle} \tag{3.57} $$

3.4.3 Minimum Control Volume Sizes for Phase Averages

Multiphase continuum models must be set up so that the volume averages are small enough when compared to the overall gross characteristic length that they can safely be neglected and not interfere with the overall macroscopic behavior of the flow. At the same time, the control volume must be large enough to capture a statistically significant number of particles. Therefore, to have a statistically meaningful phase average there exists a minimum averaging volume. This information runs contrary to the accepted view that in order to get "better" results from a computational fluid dynamics simulation it is necessary to increase the grid resolution, i.e. by increasing the number of nodes and shrinking the control volume size. This is true for a completely continuous fluid such as a single phase continuum model; however, with the addition of particles to these volume averaged continuum models a certain size limit must be observed.

Consider a simple repeating pattern of monosized spherical particles as shown in Figure 3.7.

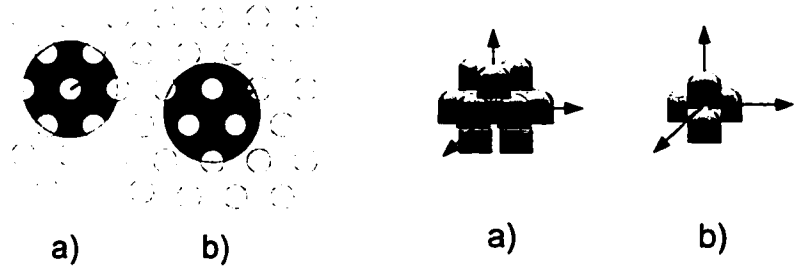

Figure 3.7 – Limiting cases for solids volume averaging analysis. Plan view on left, three dimensional view on right.

The center of the spherical control volume can be placed arbitrarily within the monosized particles; however, two limiting cases can be identified by locating the centroid of the control volume at a) the center of a particle, or b) at the symmetric center of four neighboring particles (three particles in plane and another particle to the top of these three).

The computed volume fraction of particles within a control volume invariably includes particles completely within the bounding surface and some particles which are only partially enclosed. With increasing control volume size, the number of particles within the control volume will increase and the calculated volume fraction will asymptotically approach the bulk volume fraction ε_p within the domain. Calculation of this volume fraction is based upon three geometric parameters including the diameter of the particles, inter-particle spacing and the radius of the control volume. An error margin can be defined based on this asymptotic value and the value calculated using a specified

control volume size as $\delta = \left|\varepsilon_p^c - \varepsilon_p\right| / \varepsilon_p$. Average inter-particle spacing can be estimated from the particle number density, n, using:

$$l \approx n^{-1/3} = \left(\frac{\pi}{6} \frac{D_p^3}{\varepsilon_p} \right)^{\frac{1}{3}} \tag{3.58}$$

The ratio of l/D_p must only be a function of $f(\varepsilon_p)$. The relationship of the control volume radius can be expressed as a functional relationship of $R/D_p = f(\varepsilon_p)g(\varepsilon_p)$. The minimum control volume radius R_{min} is only a function of ε_p for a given δ. Celmins (1988) has formulated a quantitative relationship between minimum control volume radius for a given tolerance δ as

$$\frac{R_{\min}}{D_p} = \frac{\varepsilon_p^{-\frac{1}{3}}}{\sqrt{2\delta}} \left(1 - \varepsilon_p\right) \tag{3.59}$$

For a tolerance of δ=1% a three dimensional plot of the minimum volume fraction can be plotted against the particle diameter D_p and solid volume fraction ε_p, see Figure 3.8. As can be seen from this diagram there is a minimum volume fraction below which the continuum assumption for gas particle flows is not applicable. A short MATLAB routine was written to create this plot and is included in *Appendix B.1*.

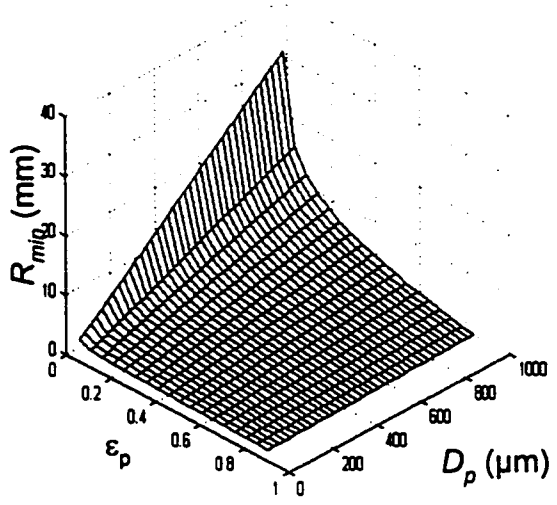

Figure 3.8 – Minimum control volume size for statistically valid multiphase averaging.

For the simulations that were carried out for this study a minimum control volume size can be calculated based on the particles size of 370 μm with a 1, 2 and 5% tolerance on the asymptotic volume fraction, assumed to be 0.42. The resulting minimum CV sizes are 2.64×10^{-5}, 1.26×10^{-5} and 5.31×10^{-6} m^3 respectively. Each of these minimum CV sizes is much smaller than those used in the simulations for this study, so the CV formulation can be considered acceptable in this case.

Chapter 4

Computational Methods

Governing equations of fluid mechanics are transient, three dimensional partial differential equations linked through inter-phase transfer terms. Solution of these systems of equations for geometries of engineering interest requires the use of numerical methods. This chapter deals with the discretization, organization and solution of these governing equations. General discretization schemes are described and their relative strengths and weaknesses are compared. Pressure correction methods, linked equation acceleration schemes and Rhie-Chow interpolation techniques are discussed.

4.1 Computational Techniques

Solution of the equations governing multiphase flows cannot be done analytically and the use of numerical methods has to be employed. Computational Fluid Dynamics (CFD) refers to the use of some sort of numerical solution method of the governing hydrodynamic equations to predict flow patterns within a given flow geometry. In addition to the question of the physics to be modeled with the governing equations and the simplifying assumptions and approximations that have to be included, choice of the numerical solution scheme can have a significant impact on the overall accuracy, solution time and stability of the simulation. Discussion in this section will deal explicitly with the conventions used in the CFX 4.2 simulation package from AEA Technology.

4.1.1 Representing Flow Fields in CFX 4.2

Governing equations of multiphase fluid dynamics (see Chapter 2) are partial differential equations representing a continuous flow phenomena and the solution of which will result in a continuous description of the flow field. These equations are coupled, highly nonlinear and involve several dimensions; analytical solution is not possible and solutions must be obtained using numerical methods. As previously shown in Chapter 2 the equations governing the multiphase flow in this study are:

Gas Continuity:

$$\frac{\partial}{\partial t}\left(\varepsilon_g \rho_g\right)+\nabla\cdot\left(\varepsilon_g \rho_g \overline{U}_g\right)=\left(\dot{m}_{gs}-\dot{m}_{sg}\right)=0 \qquad (2.17)$$

Gas Momentum:

$$\frac{\partial}{\partial t}\left(\varepsilon_g \rho_g \overline{U}_g\right)+\nabla\cdot\left(\varepsilon_g\left(\rho_g \overline{U}_g \otimes \overline{U}_g-\mu_g\left(\nabla\overline{U}_g+\left(\nabla\overline{U}_g\right)^T\right)\right)\right.$$

$$=\varepsilon_g\left(\overline{B}-\nabla p_g\right)+c_{\alpha\beta}{}^{(d)}\left(\overline{U}_\beta-\overline{U}_\alpha\right)+\overline{F}_g+\dot{m}_{gs}\overline{U}_s-\dot{m}_{sg}\overline{U}_g \qquad (2.18)$$

Solids Continuity:

$$\frac{\partial}{\partial t}\left(\varepsilon_s \rho_s\right)+\nabla\cdot\left(\varepsilon_s \rho_s \overline{U}_s\right)=\left(\dot{m}_{sg}-\dot{m}_{gs}\right)=0 \qquad (2.19)$$

Solids Momentum:

$$\frac{\partial}{\partial t}\left(\varepsilon_s \rho_s \overline{U}_s\right)+\nabla\cdot\left(\varepsilon_s\left(\rho_s \overline{U}_s \otimes \overline{U}_s-\mu_s\left(\nabla\overline{U}_s+\left(\nabla\overline{U}_s\right)^T\right)\right)\right.$$

$$=\varepsilon_s\left(\overline{B}-\nabla p_g\right)+c_{sg}{}^{(d)}\left(\overline{U}_s-\overline{U}_g\right)+\overline{F}_s+\dot{m}_{sg}\overline{U}_g-\dot{m}_{gs}\overline{U}_s+\nabla p_s \qquad (2.20)$$

These eight equations cannot be solved analytically and must be solved using numerical techniques. The continuous flow field is broken up into a discrete number of points at which solutions to the governing equations are found. The continuous derivatives are approximated using field variables at neighboring nodes.

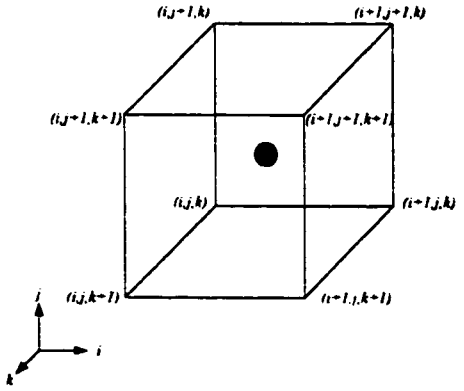

Figure 4.1 – Control volume indices in CFX 4.2

Control volumes within the CFX solver code are located by the lower, back vertex of a quadrilateral shape (in this case a cube) by the coordinates *(i,j,k)* see Figure 4.1. Control volume centers are not explicitly specified but are calculated based on the arithmetic mean of all eight vertices as defined by the discretization mesh. All variables are located at the centroids of the control volumes and represent an average value over the entire control volume. Flux properties, which have to be calculated at the surfaces of control volumes, need to be determined based on surrounding control volume averages. This has a significant impact on the overall solution accuracy and involves the use of interpolation between the centroids of control volumes.

4.2 Discretizing the Governing Equations

The basis of the CFX 4.2 Solver code (CFX 4.2 Solver manual. AEA Technology, UK) is a conservative finite-difference, or finite volume, method with all of the variables defined at the centroid of the control volumes. Conservative variables use combinations of the simple flow variables (ρ, u, v, etc...) to express quantities in terms of fluxes across boundaries. This formulation is required when solving the discretized equations across shocks or other discontinuities in the flow. For example, consider the one dimensional nonconservative form of the momentum equation:

$$\rho \frac{Du}{Dt} = \rho\left(\frac{\partial u}{\partial t} + u\frac{\partial u}{\partial x}\right) = -\frac{\partial P}{\partial x} + \left(\frac{\partial F_v}{\partial x} + S\right) \tag{4.1}$$

In flows containing shocks the simple variables are not continuous over shock boundaries. In this case $\rho_1 \neq \rho_2$, $u_1 \neq u_2$ and $P_1 \neq P_2$, Figure 4.2.

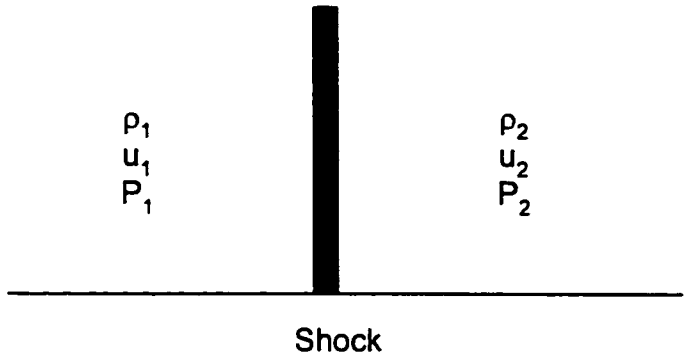

Figure 4.2 – Simple flow variables either side of a shock.

Discretization of the derivative $\rho u \frac{\partial u}{\partial x} \approx \rho u \left(\frac{u_2 - u_1}{\Delta x} \right)$ leads to an incorrect solution. What value should be taken for ρu? Values on either side of the shock over which the derivative is formed are not continuous and will cause convergence problems. By reformulating the one dimensional momentum equation in conservative form by bringing the density into the total derivative the derivative can be recast as follows:

$$\frac{\partial F}{\partial x} \approx \frac{F_r - F_l}{\Delta x} = \frac{F_2 - F_1}{\Delta x} = \frac{\left(\rho_2 u_2^2 + P_2\right) - \left(\rho_1 u_1^2 + P_1\right)}{\Delta x} \qquad (4.2)$$

This formulation will give the correct physical answer in this flow situation and not result in discontinuous flux variables.

Control volumes are formed over the entire flow domain in question and the governing equations (derived in Chapter 3) are integrated and solved for the flow variables. In CFX, all spatial terms are discretized using second order central

differencing but the advection terms (those involving a velocity gradient) have several different schemes available for discretization both for convenience and solution speed. Convection coefficients are obtained using Rhie-Chow interpolation formulae (discussed below).

4.2.1 Diffusion Terms:

Terms involving gradient diffusion and advection can be explained with reference to Figure 4.3. Capital letters represent the actual position of the flow variable node at the intersection of the solid mesh lines. Lower case letters represent the position of the boundaries between the actual control volumes with the dashed line representing the control volume centered on node P. For this discussion the diagonal arrow represents the two dimensional flow velocity.

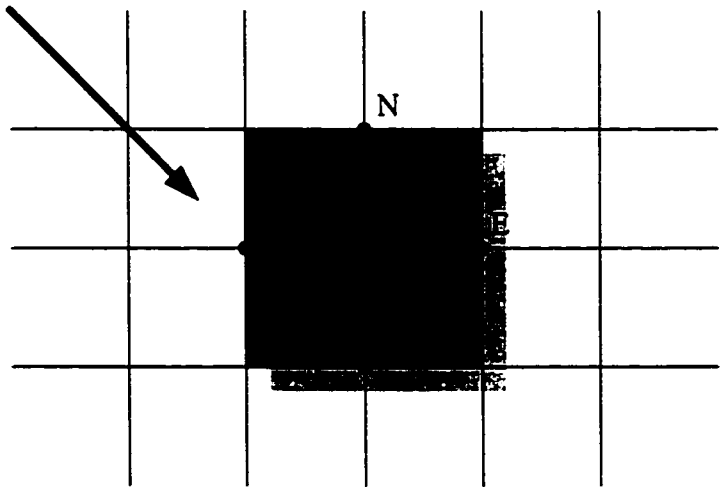

Figure 4.3 – Variable locations at mesh intersections.

Control volume centroids are represented by the solid circles where the flow variables in question are stored. The CV of interest is located at point P and has surrounding

interphases with its neighbours at *n*, *e*, *s* and *w*. Consider the diffusional terms at the west face, *w*, of the control volume and discretize them as follows:

$$\iint_{A_w} \Gamma \nabla f \cdot \hat{n} dA = \frac{\Gamma A_w}{\Delta x}(f_P - f_W) \equiv D_w(f_P - f_W) \tag{4.3}$$

Here A_w is the area of the west face, Δx is the distance between the west (W) and central (P) nodes and D_w is the west diffusion coefficient. Similar expressions can be derived for the remaining three faces and when summed form the diffusive contribution to the governing equation as follows:

$$D_w(f_P - f_W) + D_e(f_E - f_P) + D_n(f_P - f_N) + D_s(f_S - f_P) + other\_terms = 0 \tag{4.4}$$

4.2.2 Advection Terms:

Discretization of the advection terms determines the overall accuracy of the solutions of the model equations used in the CFX solver. For the work presented in this thesis the HYBRID and higher order SUPERBEE schemes were used. Advection terms, which describe the convective flux of the conserved variable across the phase boundary, are required at the interfaces between control volumes; however, since the flow variables are stored at the centroids of control volumes, there has to be some sort of interpolation to determine the interface flux values. Many different schemes have been proposed over the years to deal with this issue and some of the methods available in CFX are discussed below.

4.2.3 Upwind Differencing (UDS):

When the flow is from left to right (i.e. from W to E), the advected value of the variable f at the west face of the control volume (f_w) is taken to be f_W, so that, at the west face:

$$\int \rho f \bar{U} \cdot \hat{n} dA = \rho U_w A_w f_W \equiv C_W f_W \tag{4.5}$$

Here C_W is the convection coefficient at the west face. As can be seen from the discussion on diffusion, all factors involving f_W can be collected together and a matrix coefficient for the west node can be determined

$$A_W = MAX(C_W, 0) + D_W \tag{4.6}$$

This scheme is first order accurate. Convection coefficients for the other faces (in the case of three dimensional flow this would include top, bottom, east, west, front and back faces, Figure 4.1) can be constructed in the same manner and a summation of the terms carried out to form the set of matrix equations governing the flow phenomena.

4.2.4 Hybrid Differencing (HDS):

This is a modification to the first order upwind differencing in which central differencing is used if the mesh Peclet number (C/D) (ratio of convection to diffusion) is

less than 2, and upwind differencing, but ignoring diffusion, is used if the mesh Peclet number is greater than 2. In this case, the west matrix coefficient is:

$$A_W = MAX\left(\frac{1}{2}C_W, D_W\right) + \frac{1}{2}C_W \tag{4.7}$$

This scheme is also first order accurate, but is slightly better than upwind differencing because second order central differencing will be used across streams and in regions of low flow. This is the default discretization scheme used in CFX 4.2.

4.2.5 Total Variation Diminishing Schemes:

Total variation diminishing (TVD) schemes are modifications to the higher order upwind schemes in CFX with flux limiters to ensure the boundedness of the solution. The Superbee TVD scheme was chosen for these studies due to its properties of compression, shock sharpening and low asymmetry. These properties are demonstrated in the following section and have a significant impact on the overall simulation results (also please see Chapter 7 Results and Discussion).

In TVD schemes f_w is given by:

$$f_w = \left(1 + \frac{1}{2}\psi\right) f_W - \frac{1}{2}\psi f_{WW} \tag{4.8}$$

Where the flux limiter, ψ, which is given in terms of the ratio $r = \frac{f_P - f_W}{f_W - f_{WW}}$ for Superbee is:

$$\psi = \max(0, \min(2r,1), \min(r,2)) \tag{4.9}$$

In fact, any scheme which falls within the regions to the right of the dashed line outlined in the Figure 4.4 is guaranteed to be TVD and subsequently non-oscillatory. Half cell values, those involving indices with $_{i+1/2}$ have to be constructed.

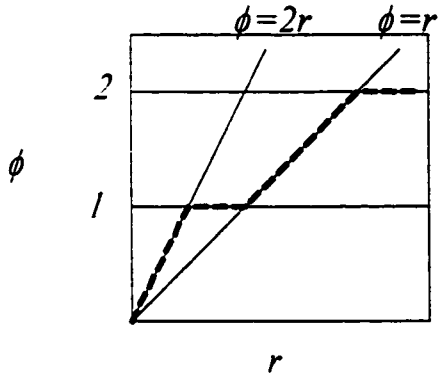

$\phi=0 \rightarrow f_{i+1/2} = f_i$

$\phi=1 \rightarrow f_{i+1/2} = f^{Central}_{i+1/2}$

$\phi=r \rightarrow f_{i+1/2} = f^{Up}_{i+1/2}$

$\phi=2 \rightarrow f_{i+1/2} = f_{i+1}$

$\phi=2r \rightarrow f_{i+1/2} = f^{Up2}_{i+1/2}$

$$f_{i+1/2} = median(f_i, f^{Central}_{i+1/2}, f_{i+1}, f^{Up}_{i+1/2}, f^{Up2}_{i+1/2})$$

Figure 4.4 – Superbee TVD scheme.

Each of the terms present in this expression have to be constructed based on finite difference approximations. These are outlined next.

4.3 Constructing Finite Difference Schemes

Important in the use of CFD is the formulation of the difference equations that are used to represent the continuous differential equations governing the flow field. As a simple example, a 1D wave equation was discretized in space and time to study the characteristics of the differencing equations that have been proposed and some that are implemented in CFX.

Uniform second order accurate non-oscillatory schemes are attributed to Harten and Osher. The methods of Lax-Wendroff (LW) related to upwind methods which lead to the total variation diminishing (TVD) schemes (Van Leer and Roe). Sweby found flux limited TVD-LW methods that lead to improved TVD-LW schemes. A brief discussion of this progression is given below.

Consider the one dimensional wave equation

$$\frac{\partial u}{\partial t} + c\frac{\partial u}{\partial x} = 0 \tag{4.10}$$

and approximate the derivatives using the midpoint rule in both space and time; however, discretization of the spatial terms is expressed using half cell or intermediary values:

$$\frac{f_i^{n+1} + f_i^n}{\Delta t} + c\frac{\left[f_{i+1/2}^{n+1/2} - f_{i-1/2}^{n+1/2}\right]}{\Delta x} = 0 \tag{4.11}$$

It is necessary to construct values for the half cells $f_{i+1/2}^{n+1/2}$ and $f_{i-1/2}^{n+1/2}$. Consider Figure 4.5 showing nodes at time *n* and *n+1* and at positions *i-1*, *i*, and *i+1*. Half cell values can be determined at *n+1/2* and at *i+1/2*.

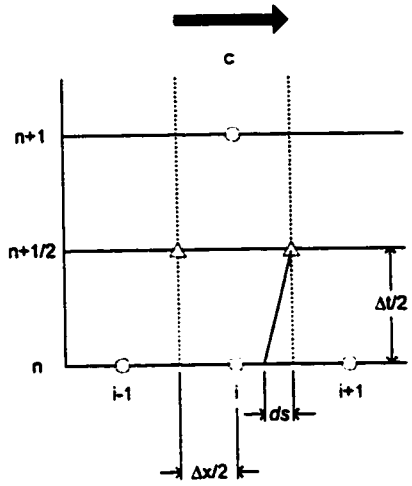

Figure 4.5 – TVD half cell construction in forward direction.

$$ds = c\frac{\Delta t}{2} \tag{4.12}$$

The data at the base of the interpolation between locations $_i$ and $_{i+1/2}$ must come from some interpolation as follows:

$$f_{i+1/2}^{n+1/2} = f_{i+1/2}^{n} - (slope)ds \tag{4.13}$$

where

$$slope = \frac{f_{i+1/2}^{n} - f_{i}^{n}}{\Delta x/2} \tag{4.14}$$

simplifying:

$$f_{i+1/2}^{n+1/2} = f_{i+1/2}^{n} - \left[\frac{f_{i+1/2}^{n} - f_{i}^{n}}{\Delta x/2}\right]\left[c\frac{\Delta t}{2}\right] = f_{i+1/2}^{n} - \frac{c\Delta t}{\Delta x}\left[f_{i+1/2}^{n} - f_{i}^{n}\right] \tag{4.15}$$

In a similar manner the $f_{i-1/2}^{n+1/2}$ half cell value can be calculated as shown in Figure 4.6:

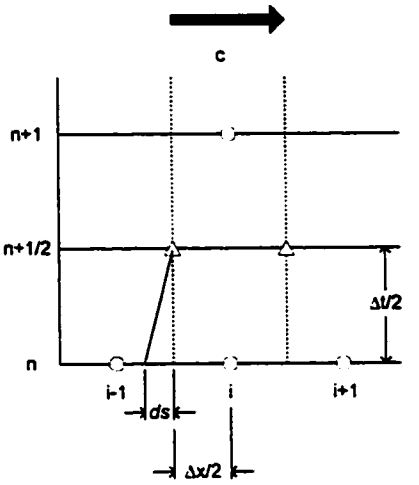

Figure 4.6 - TVD half cell construction in backward direction.

$$ds = c\frac{\Delta t}{2} \tag{4.16}$$

$$f_{i-1/2}^{n+1/2} = f_{i-1/2}^{n} - (slope)ds \tag{4.17}$$

$$slope = \frac{f_{i-1/2}^{n} - f_{i-1}^{n}}{\Delta x/2} \tag{4.18}$$

after substitution this gives:

$$f_{i-1/2}^{n+1/2} = f_{i-1/2}^{n} - \left[\frac{f_{i-1/2}^{n} - f_{i-1}^{n}}{\Delta x/2}\right]\left[c\frac{\Delta t}{2}\right] = f_{i-1/2}^{n} - \frac{c\Delta t}{\Delta x}\left[f_{i-1/2}^{n} - f_{i-1}^{n}\right] \tag{4.19}$$

These interpolations for the half cell values are substituted back into equation (4.11) to give the new expression for f_i^{n+1}.

$$f_i^{n+1} = f_i^n - \frac{c\Delta t}{\Delta x}\left[\left(f_{i+1/2}^n - \frac{c\Delta t}{\Delta x}\left[f_{i+1/2}^n - f_i^n\right]\right) - \left(f_{i-1/2}^n - \frac{c\Delta t}{\Delta x}\left[f_{i-1/2}^n - f_{i-1}^n\right]\right)\right] \tag{4.20}$$

$$f_i^{n+1} = f_i^n - \frac{c\Delta t}{\Delta x}\left[f_{i+1/2}^n - f_{i-1/2}^n\right] + \left(\frac{c\Delta t}{\Delta x}\right)^2\left[f_{i+1/2}^n - f_i^n - f_{i-1/2}^n + f_{i-1}^n\right] \tag{4.21}$$

It is necessary to define the $f_{i+1/2}^n$ and $f_{i-1/2}^n$ terms. Calculation of these half cell values determines the accuracy of the numerical scheme.

Several different methods have been proposed for constructing the half cell values in the discretization scheme just described. Schemes listed below are used for the implementation of SUPERBEE and MINMOD TVD Schemes.

Lax-Wendroff Central Difference

$$f_{i+1/2}^n = f_{i+1/2}^{n,Central} = \frac{1}{2}\left(f_i^n + f_{i+1}^n\right)$$

$$f_{i-1/2}^n = f_{i-1/2}^{n,Central} = \frac{1}{2}\left(f_{i-1}^n + f_i^n\right) \tag{4.22}$$

Warming-Beam Upwind

$$f_{i+1/2}^n = f_{i+1/2}^{n,Up} = f_i^n + \left(f_i^n - f_{i-1/2}^{n,Central}\right)$$

$$f_{i-1/n}^2 = f_{i-1/2}^{n,Up} = f_{i-1}^n + \left(f_{i-1}^n - f_{i-3/2}^{n,Central}\right) \tag{4.23}$$

Second Order Upwind

$$f^n_{i+1/2} = f^{n,Up2}_{i+1/2} = f^n_i + \left(f^n_i - f^n_{i-1}\right)$$

$$f^n_{i-1/2} = f^{n,Up2}_{i-1/2} = f^n_{i-1} + \left(f^n_{i-1} - f^n_{i-2}\right) \tag{4.24}$$

The TVD schemes can be reconstructed based on the formulations using the half cell values as follows:

MINMOD: $$f^n_{i+1/2} = median(f^n_i, f^{n,Central}_{i+1/2}, f^{n,Up}_{i+1/2}) \tag{4.25}$$

SUPERBEE: $$f^n_{i+1/2} = median(f^n_i, f^{n,Central}_{i+1/2}, f^{n,Up}_{i+1/2}, f^n_{i+1}, f^{n,Up2}_{i+1/2}) \tag{4.26}$$

4.3.1 Higher Order Non-oscillatory Schemes (SONIC and UNO)

Harten and Osher are credited with formulating the higher order schemes by realizing that the problems associated with the TVD schemes are caused by the Lax-Wendroff central differences approximation (see equation 4.22). To alleviate these problems, they introduced a quadratic interpolation scheme based on fitting parabolas between node values and then interpolating the half cell values, Figure 4.7.

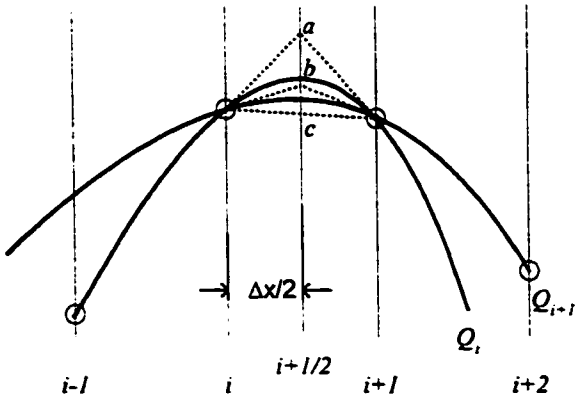

Figure 4.7 – Construction of the parabolic interpolation.

$$f_{i+1/2}^{c,parabolic} = median(a,b,c) \tag{4.27}$$

Q_i and Q_{i+1} are parabolas fitting points ($_{i-1}$, $_i$, $_{i+1}$) and ($_i$, $_{i+1}$, $_{i+2}$), respectively. Points a, b, c, which will define the half cell values, are at the intersection of the tangents of the parabolas directly at $_{i+1/2}$ half cell. The parabola is defined as $(x-h)^2 = 4P(y-k)$ and it is necessary to find h, P, k. Calculations for parabola Q_i :

$$\begin{aligned} X_{i+1}^2 - 2hX_{i+1} + h^2 &= 4P(f_{i+1} - k) \\ X_i^2 - 2hX_i + h^2 &= 4P(f_i - k) \\ X_{i-1}^2 - 2hX_{i-1} + h^2 &= 4P(f_{i-1} - k) \end{aligned} \tag{4.28}$$

Subtracting equation 2 from 1 and 3 from 2 results in:

$$\begin{aligned} X_{i+1}^2 - X_i^2 - 2h(X_{i+1} - X_i) &= 4P(f_{i+1} - f_i) \\ X_i^2 - X_{i-1}^2 - 2h(X_i - X_{i-1}) &= 4P(f_i - f_{i-1}) \end{aligned} \tag{4.29}$$

For a uniform grid the distance between neighboring grid points is ΔX and the off index $_i$ can be substituted as follows:

$$\begin{aligned} (X_i + \Delta X)^2 - X_i^2 - 2h(X_i + \Delta X - X_i) &= 4P(f_{i+1} - f_i) \\ X_i^2 - (X_i - \Delta X) - 2h(X_i - (X_i - \Delta X)) &= 4P(f_i - f_{i-1}) \end{aligned} \tag{4.30}$$

These equations simplify to:

$$\begin{aligned} \Delta X(2X_i + \Delta X) - 2h\Delta X &= 4P(f_{i+1} - f_i) \\ \Delta X(2X_i - \Delta X) - 2h\Delta X &= 4P(f_i - f_{i-1}) \end{aligned} \tag{4.31}$$

Two such higher order nonoscillatory schemes have been devised. UNO2 and SONIC both use quadratic interpolation of the Law-Wendroff central differences approximation; however, UNO2 implements Van Leer's MINMOD scheme and replaces the $f^{C}_{i+1/2}$ expression with the quadratic interpolation. The SONIC scheme uses Roe's SUPERBEE scheme in the same manner and replaces the $f^{Central}_{i+1/2}$ with the quadratic interpolation. These two methods are not implemented in the current version of CFX4.2. Having been introduced to the methods used to construct the difference approximations it is necessary to observe the effect that the different schemes have on simulation results.

4.4 Analysis of Several Different Discretization Schemes

With the various choices available for discretizing the governing equations it is necessary to study the behavior of these different schemes. A Flux-Limited Lax-Wendroff scheme was constructed for the 1D linear wave equation:

$$\frac{\partial f}{\partial t} + c\frac{\partial f}{\partial x} = 0 \tag{4.32}$$

on a grid of 900 mesh cells of size $\Delta x = 1.0$. The performance of First Order Upwinding, Lax Wendroff Central Differencing, Warming-Beam Upwinding, Minmod, MUSCL and SUPERBEE schemes were compared by convecting a simple initial wave form consisting of a parabola, spike and shock at time equal to zero along the mesh for 500 time steps. The results of the final wave form were compared with the initial waveform for each of the different schemes.

TVD is representative of the changes in total wave form height as the simulation progresses. TVD ensures no creation of any oscillations and no growth of the amplitude of the wave form. Nonoscillatory (or essentially nonoscillatory) schemes do not allow any creation of oscillations and allow some growth of the amplitude. The total variation is defined as:

$$TV(f)=\sum_{i=1}^{ilen}|f_{i+1}-f_i| \tag{4.33}$$

Numerical schemes are said to be Total Variation Diminishing (TVD) if the total variations satisfy the inequality $TV(f^{n+1})\leq TV(f^n)$ for all time. Satisfying this conditions also ensures that there will be no oscillations produced in the solution. For conditions contrary to this inequality, oscillations will be present. Oscillations can lead to nonphysical values produced by the discretization scheme. This can be a problem when predicting values that are bounded (such as the volume fraction ε) - it is not reasonable to expect a volume fraction less than zero or greater than one. TVD schemes can be guaranteed to be present if the flux limiter is limited to lie within the area to the right of the *2r* line on the Superbee diagram, Figure 4.4. All of the TVD schemes can be constructed by choosing the correct flux limiter expression.

4.4.1 FIRST ORDER UPWINDING (FOUW)

Figure 4.8 is an overlay plot of the initial wave train given by the initial conditions in the assignment and that same wave train after being convected for n=500 time steps using

FOUW. As can be seen from the Figure, this method is highly dissipative and leads to a smearing of the three distinct shapes that were initially present. Characteristic of a first order scheme, there are no oscillations in the numerical solution.

The final normalized total variation for n=800 of FOUW at C_N=0.75 is 0.29947. Although this scheme satisfies the TVD criterion, it performs poorly due to the dissipative effects (Figure 4.14).

4.4.2 LAX-WENDROFF Central Differencing (LW)

Figure 4.9 is also an overlay plot showing the initial wave train and the wave train after being convected for n=500 time steps using LW. Most notable of this scheme are the oscillations that are present. The convected wave train also shows a slight asymmetry to the right.

The final normalized total variation for n=800 of LW at C_N=0.75 is 1.24. Since this value is greater than 1.0, the LW scheme does not satisfy the TVD criterion and is not a TVD scheme (Figure 4.14).

4.4.3 WARMING-BEAM (WB)

Figure 4.10 shows that the WB scheme leads to oscillations in the convected solution. Asymmetries are not as apparent as in the LW scheme. Sharp edges (such as those shown for the n=1 plot in Figure 4.10 on the top hat) show that oscillations using WB are most pronounced at abrupt edges (such as shocks or phase boundaries that would be present in multiphase flow simulations).

The final normalized total variation for n=800 of LW at C_N=0.75 is 1.46. Since this value is greater than 1.0, the WB scheme does not satisfy the TVD criterion and is not a TVD scheme (Figure 4.14).

4.4.4 Minmod TVD (MINMOD)

Figure 4.11 is the MINMOD solution to the convection equation at n=1 and n=500 time steps. This scheme is somewhat dissipative as shown by the longer trailing edges between the three different pulses. Due to this dissipation the pulses tend to merge into each other; however, this is not as pronounced as in the FOUW scheme.

The final normalized total variation for n=800 of LW at C_N=0.75 is 0.77. Since this value is less than 1.0, the MINMOD scheme does satisfy the TVD criterion and is a TVD scheme (Figure 4.14).

4.4.5 MUSCL TVD (MUSCL)

Figure 4.12 shows the fairly good results obtained using the MUSCL scheme. Each pulse is preserved and there is very little dissipation between them at n=600. All of the pulses are symmetric and the method is not overly compressive. Characteristic of the TVD schemes, there are no oscillations in the solution.

The final normalized total variation for n=800 of LW at C_N=0.75 is 0.89. Since this value is less than 1.0, the MUSCL scheme does satisfy the TVD criterion and is a TVD scheme (see Figure 4.14).

4.4.6 SUPERBEE

Figure 4.13 for the SUPERBEE scheme shows that all of the pulses are very well preserved; however, this method is over compressive and tends to turn all of the pulses into a "top hat" sort of shape. There is very little dispersion and the three pulses are easy to distinguish. This method has been selected for the multiphase flow modeling as the higher order discretization because it tends to sharpen shocks which are present within the flow domain.

The final normalized total variation for n=800 of LW at C_N=0.75 is 0.944. Since this value is less than 1.0, the SUPERBEE scheme does satisfy the TVD criterion and is a TVD scheme (see Figure 4.14).

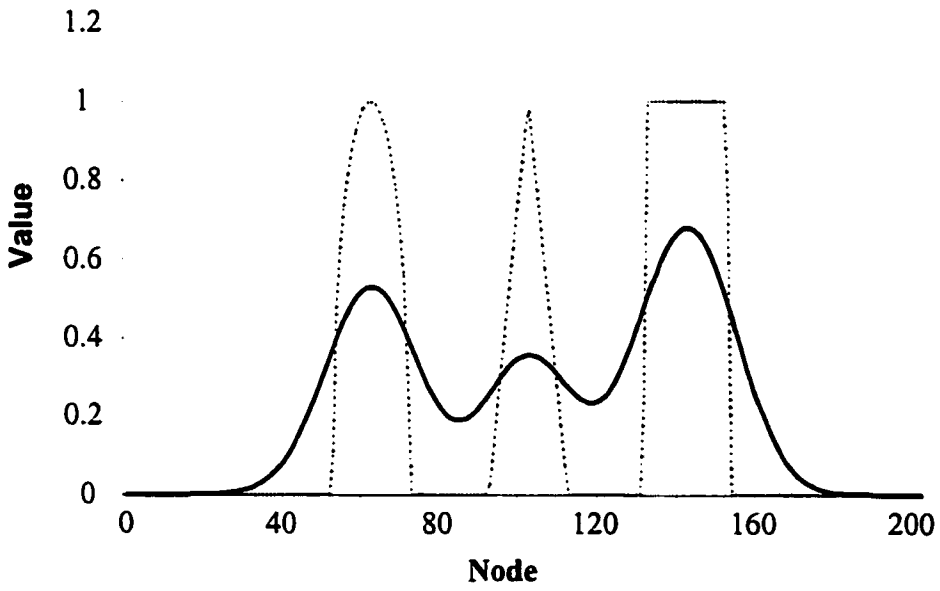

Figure 4.8 – First order upwinding test. Dashed line represents the initial wave form and the solid line represents the wave form after convecting for 500 time steps.

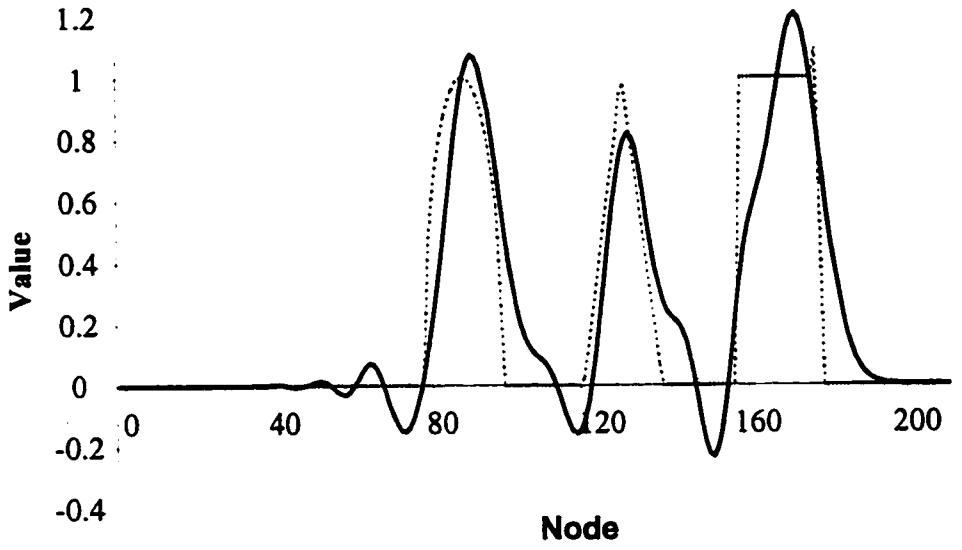

Figure 4.9 – Lax-Wendroff Test. Dashed line represents the initial wave form and the solid line represents the wave form after convecting for 500 time steps.

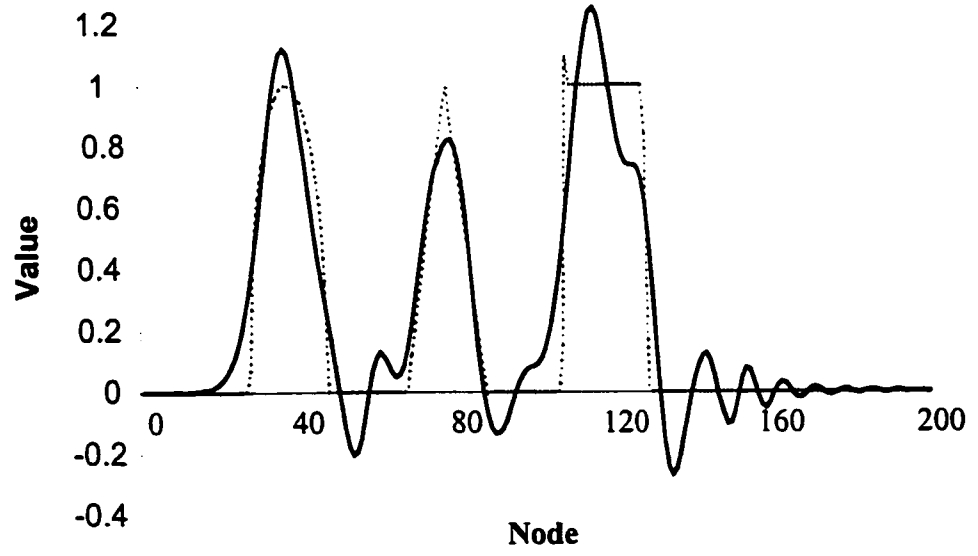

Figure 4.10 – Warming-Beam upwinding test. Dashed line represents the initial wave form and the solid line represents the wave form after convecting for 500 time steps.

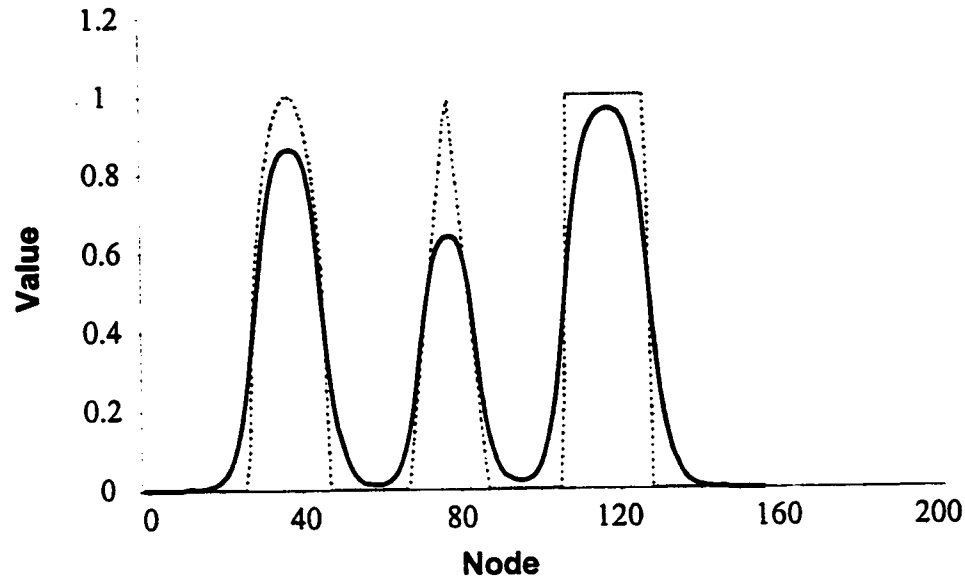

Figure 4.11 – MINMOD test. Dashed line represents the initial wave form and the solid line represents the wave form after convecting for 500 time steps.

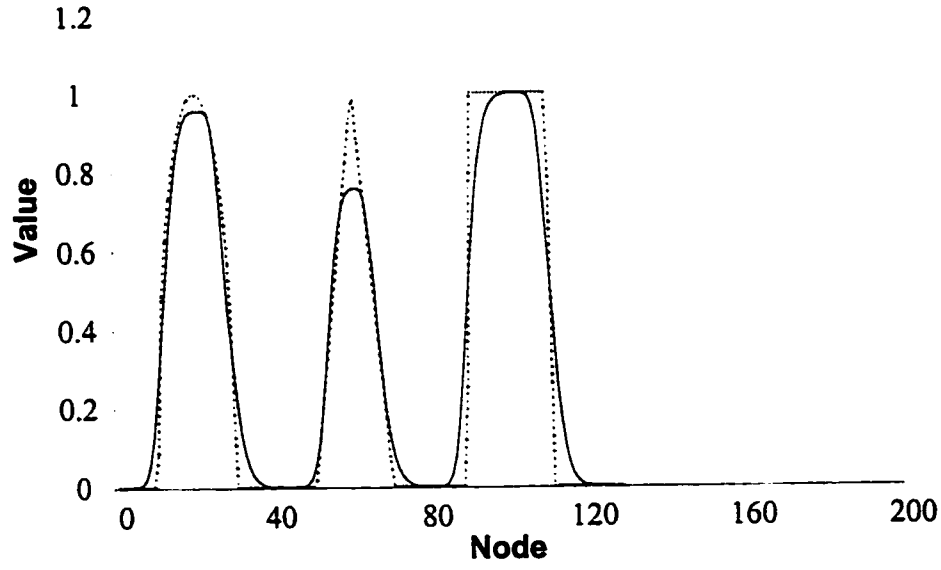

Figure 4.12 – MUSCL TVD test. Dashed line represents the initial wave form and the solid line represents the wave form after convecting for 500 time steps.

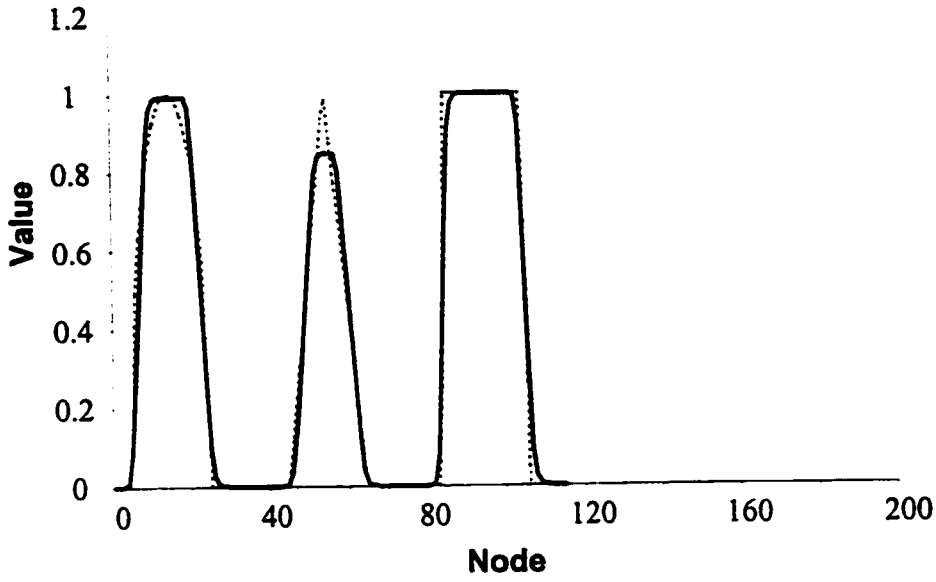

Figure 4.13 – SUPERBEE TVD test. Dashed line represents the initial wave form and the solid line represents the wave form after convecting for 500 time steps.

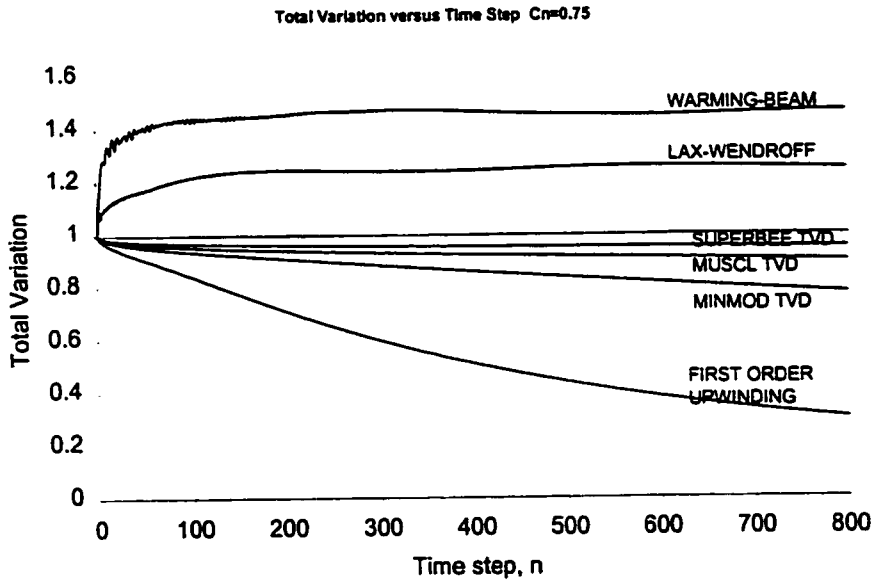

Figure 4.14 – Total variation plots with time step for each of the discretization schemes studied.

Figure 4.14 showing the total variation with time step indicates that the schemes introducing oscillations into the advected wave form had normalized total varizations that

were greater than one. Dissipative schemes (such as FOUW and MINMOD) appear to have TVDs which are much lower than one. SUPERBEE and MUSCL schemes with TVDs of approximately one retained the original wave form structure the best.

4.5 Source Terms

The terms appearing as sources in the general conservation equation are split into two parts when integrated over the control volume.

$$\iiint_{v} \Phi dv = S_C + S_P f_P \tag{4.34}$$

The S_P term must be negative to ensure that the source term does not grow and create convergence problems (Patankar, 1980). This term tends to enhance the diagonal of the matrix resulting in diagonal dominance and a faster solution procedure. Source terms, including solids pressure, have been discussed in Chapter 3.

4.6 Coupling Difference Equations with IPSA

Momentum equations for the gas and solids phases must be linked through momentum transfer terms. The numerical solution of these two sets of equations requires an algorithm for solution. This section describes some of the numerical procedures used in CFX 4.2 to solve the multiphase flow equations.

4.6.1 Semi-Implicit Method for Pressure-Linked Equations (SIMPLE)

The numerical solution of the multiphase flow equations used in the CFX 4.2 solver is that of the InterPhase Slip Algorithm (IPSA) which is an extension of the SIMPLE (Semi-Implicit Method for Pressure-Linked Equations) of Patankar and Spalding (1972) which was developed for single-phase flow problems. The SIMPLE method was devised to solve for the pressure terms appearing in the momentum equations. For incompressible flow there is no equation of state for pressure and so the pressure field has to be solved iteratively. If the pressure field is given, there is no difficulty in constructing and solving the momentum equations. However, if the pressure field is not known (as is usually the case), then a pressure correction algorithm must be employed.

In the SIMPLE method, an estimated pressure field is created and a pseudo velocity field is created based upon relating the pressure in the momentum equations to reducing the continuity error. The pressure is then recalculated using a pressure correction equation and the scheme is iterated as follows:

1. Guess p^* (the estimated pressure field);
2. Solve the momentum equations to get u^*, v^*, w^*;
3. Solve the pressure correction equation;
4. Correct the pressure and velocities;
5. Solve for any other flow variables which might influence the flow field;
6. Return to step 2 with the corrected pressure as the new p^* field. Repeat until convergence.

4.6.2 Inter Phase Slip Algorithm (IPSA)

IPSA also employs an iterative solution scheme in which the pressure-correction method is used to satisfy the conservation at each iteration. In general the transport equations are coupled via the interphase transfer terms (in this case through the drag terms in the momentum equations). Accordingly, convergence could be very slow when the coupling terms are very large. For two-phase flows the Partial Elimination Algorithm (PEA) by Spalding can be employed. For the sake of argument and build up of the methods used for multiphase flows with more than two phases the development of PEA will be demonstrated.

For a particular computational cell within the solution domain, the transport equations (momentum and energy) can be simplified as (Lo, 1989):

$$\begin{aligned} a_1\phi_1 &= b(\phi_2 - \phi_1) + c_1 \\ a_2\phi_2 &= b(\phi_1 - \phi_2) + c_2 \end{aligned} \tag{4.35}$$

where a contains the advection and transient coefficients; b is the interphase transfer coefficient and c represents all other terms not yet accounted for (i.e. source terms, etc...), subscripts 1 and 2 represent each of the phases. These equations can be rearranged to give the following:

$$\begin{aligned} (a_1 + b)\phi_1 &= b\phi_2 + c_1 \\ (a_2 + b)\phi_2 &= b\phi_1 + c_2 \end{aligned} \tag{4.36}$$

When the interphase transfer coefficient, b, is large, then the value of ϕ_1 is very close or equal to ϕ_2. Also, the values of the variables have changed little from their starting values; therefore, the rate of convergence would be quite slow. PEA minimizes this slow rate of convergence by eliminating ϕ_2 from the first equation and ϕ_1 from the second equation to give:

$$\left[a_1+\frac{b}{a_2}(a_1+a_2)\right]\phi_1=\frac{b}{a_2}(c_1+c_2)+c_1$$
$$\left[a_2+\frac{b}{a_1}(a_1+a_2)\right]\phi_2=\frac{b}{a_1}(c_1+c_2)+c_2 \qquad (4.37)$$

Taking the limit as the interphase transfer coefficient becomes large, both of the variables tend to:

$$\phi_1=\phi_2=\frac{c_1+c_2}{a_1+a_2} \qquad (4.38)$$

The two phases have the same value but are not necessarily maintained at their initial points.

4.6.3 Volume Fraction Equations

Volume fraction equations can simply be written as the ratio of the denominator over the numerator:

$$\varepsilon_1 = \frac{N_1}{D_1}$$
$$\varepsilon_2 = \frac{N_2}{D_2} \tag{4.39}$$

To ensure that the sum of the volume fractions always equals one, the two equations can be rewritten as:

$$\varepsilon_1 = \frac{N_1 D_2}{N_1 D_2 + N_2 D_1}$$
$$\varepsilon_2 = \frac{N_2 D_1}{N_1 D_2 + N_2 D_1} \tag{4.40}$$

With further manipulation the above equation can be rearranged to the following:

$$\varepsilon_1 = \frac{N_1}{D_1 + \left[(N_1 - \varepsilon_1 D_1) + \frac{D_1}{D_2}(N_2 - \varepsilon_2 D_2) \right]} \tag{4.41}$$

The terms within the square brackets represent the continuity error of the two phases in question.

4.6.4 Pressure Correction Equation

The IPSA solution method makes use of a single pressure-correction equation for correcting the pressure field based on satisfying the continuity and momentum equations.

Therefore, this method yields a single pressure field that is shared between the two phases.

The momentum equations are first solved based upon an initial pressure field estimate. As a result of this, the computed velocities may not satisfy continuity. Pressure-correction is carried out to adjust the velocity and pressure fields to correct the continuity imbalance. The phase one continuity equation can be simplified to:

$$a_{1,P}\varepsilon_{a,P} - \left[\sum_i \left(a_{1,i}\varepsilon_{a,i}\right) + \dot{m}_i\right] = 0 \tag{4.42}$$

Where subscript p refers to the computational cell under consideration and i refers to the neighbouring points; $a(=\rho Au)$ is the convection coefficient; A is the mass flow area and m is the mass source term. The transient term is not considered in this discussion. Corrections are introduced into the equations by expressing the velocity as:

$$u_1 = u_1^* + \frac{\partial u_1}{\partial p} p' \tag{4.43}$$

where the superscript * denotes values before the correction step and p' $(=p-p^*)$ is the pressure correction. Substituting the pressure corrected velocity component into the above simplified continuity equation gives:

$$a_{1,P}^*\varepsilon_{1,P} - \left[\left(\sum_i a_{1,i}^*\varepsilon_{1,i}\right) + m_i\right] + a_{1,P}^{'}P_P^{'}\varepsilon_{1,P} - \sum_i a_{1,P}^{'}P_P^{'} \tag{4.44}$$

where $a' = \rho A \frac{\partial u}{\partial P}$. A similar expression can be formulated for the second phase. By adding together the phase-1 and 2 equations a joint-continuity equation is obtained in terms of the pressure correction.

4.6.5 IPSA in Harwell-FLOW3D Computer Code: now CFX 4.2

The IPSA method previously described has been incorporated into the FLOW3D code and the solution sequence is as follows (Lo, 1989):

1. Guess field values;
2. Solve momentum equations (using PEA if necessary);
3. Calculate convection coefficients using Rhie-Chow algorithm;
4. Solve one volume fraction equation using the implicit formulation;
5. Obtain the second volume fraction;
6. Set up the pressure-correction using the joint-continuity;
7. Solve the pressure-correction equation and apply the correction to velocities, pressures and convection coefficients
8. Check convergence and repeat from 2 if necessary.

In this form, the IPSA solution method is formulated for a two phase flow and can easily be extended to multiphase flows with little difficulty. For example, the PEA solution technique only applies to two phase flows and is not general enough

4.6.6 Rhie-Chow Interpolation

All variables in the CFX code are stored at the centroid of control volumes using a non-staggered grid. The pressure correction method used for incompressible flows requires the calculation of the pressure derivative to the second order which can lead to an oscillatory pressure field which satisfies continuity but makes no physical sense (Patankar, 1980). Rhie-Chow interpolation is used to overcome this problem with non-staggered gridding. A brief description of this method is included below based on the original formulation by Rhie and Chow (1983). With reference to Figure 4.3 the flow variables are all stored at nodes with the control volume boundaries defined by the dashed lines. Consider the steady one dimensional continuity equation over the control volume centered at P

$$\rho_g u A_e - \rho_g u A_w = 0 \tag{4.45}$$

The momentum equation now uses a central difference formulation to discretize the pressure gradient. Please note that in equation (4.46) the convective mass flux term has been expressed as $\dot{M}$ and not explicitly as a combination of nodal values. The convective mass flux can be calculated using any of the aforementioned methods in this chapter, B_P represents all other terms including friction, body forces and sources.

$$\dot{M}(u_P - u_W) = \frac{1}{2}(P_W - P_E)A_P + B_P \tag{4.46}$$

The velocity at node P can be more conveniently written as

$$u_P = -\frac{A_P}{\dot{M}} \left.\frac{dp}{dx}\right|_P \Delta x + B_P \tag{4.47}$$

The velocity at the east face, e, is the average of the u_P and u_E nodes

$$u_e = \frac{u_P + u_E}{2} = -\frac{A_e}{\dot{M}} \frac{1}{2} \left(\left. \frac{dp}{dx} \right|_P + \left. \frac{dp}{dx} \right|_E \right) \Delta x + \overline{B} \tag{4.48}$$

Substituting expressions from (4.48) into the continuity equation (4.45) can result in an oscillatory pressure field. Rhie and Chow (1983) recognized this problem and suggested formulating the pressure gradient on the control volume boundaries using first order approximations so that the first order pressure variations can be detected.

$$u_e + \frac{A_e}{\dot{M}} (P_E - P_P) = \frac{u_P + u_E}{2} + \frac{A_e}{\dot{M}} \frac{1}{2} \left(\left. \frac{dP}{dx} \right|_P + \left. \frac{dP}{dx} \right|_E \right) \Delta x \tag{4.49}$$

Expansion of the pressure derivatives using central differences and collection of like terms results in a scheme that can detect first order pressure variations on a non-staggered mesh.

4.7 Numerical Errors and Convergence

The CFX solver solves linearized transport equations. As shown previously these equations are derived by integrating the transport equations over control volumes (cells), thus each equation may be regarded as 'belonging' to a particular variable and to a particular cell. These equations describe the influence on that particular variable in that particular cell of:

a) other variables in the same cell;

b) values of the same variable in neighboring cells; and

c) values of the other variables in neighboring cells.

Iteration is used to solve for the variables within each cell that are governed by these equations. An inner iteration solves for the spatial coupling for each variable and an outer iteration is used to solve for the coupling between variables. Thus each variable is taken in sequence, regarding all other variables as fixed, a discrete transport equation is formed for every cell in the flow domain and the problem is handed over to a linear equation solver which returns the updated values of the variable. The non-linearity of the original differential equations is simulated by reforming the diffusion and convection coefficients of the discrete equations, using the most recently calculated values of the variables, before each outer iteration.

4.7.1 Output File Summary of CFX 4.2 Simulations

There are several ways to specify control of the outer iteration. A maximum number of iterations can be specified for the outer iteration. For transient calculations the maximum number of iterations might be between 5 and 50 whereas for a steady state calculation the number of outer iterations might be up to several tens of thousands depending upon the desired accuracy.

A second criterion determining whether the solution procedure has converged is the satisfaction of a tolerance on some residual. The default convergence criterion is based upon the satisfaction of a mass source residual. The mass source residual is not dimensionless but is the sum of the absolute values of the net mass fluxes into or out of every cell in the flow domain and has units of mass/time. An example of the calculation of the mass source residual is as follows:

$$R = \sum_i |\rho A_i \hat{u}_i| \text{ with i cycling through all of the control volumes} \quad (4.50)$$

A reasonable non-dimensionalization of this residual would be to divide R by the total sum of the mass flow rates through all of the inlets.

With each simulation an output file is created summarizing the residual reduction for the inner iterations and outer iterations (time step). A sample from one of these output files is shown in Figure 4.15; labels have been added to this figure to show items of interest. Included in this file is a summary of the flow variables at a monitoring point. The values at the monitoring point should converge to constants with increasing numbers of inner iterations.

For each inner iteration the absolute residuals for each of the flow variables is listed. These values should decrease with progressing inner iterations to ensure that convergence is being achieved. All data for the grid refinement studies in section 7.1.3 have used these inner iteration absolute residuals for comparison purposes. Also provided in this output file is a list of the flow variables at a monitoring point within the flow domain.

Once the convergence criteria has been achieved for the inner iteration, in this study reduction of the gas mass continuity residual to 5 x 10^{-6} was chosen as the convergence criterion, statistics for the outer iteration are presented. The average reduction factor achieved by the linear solvers presents the ratio of the last inner iteration residual to that of the first inner iteration residual. These ratios must be less than one for convergence. Maximum absolute time derivatives are also summarized.

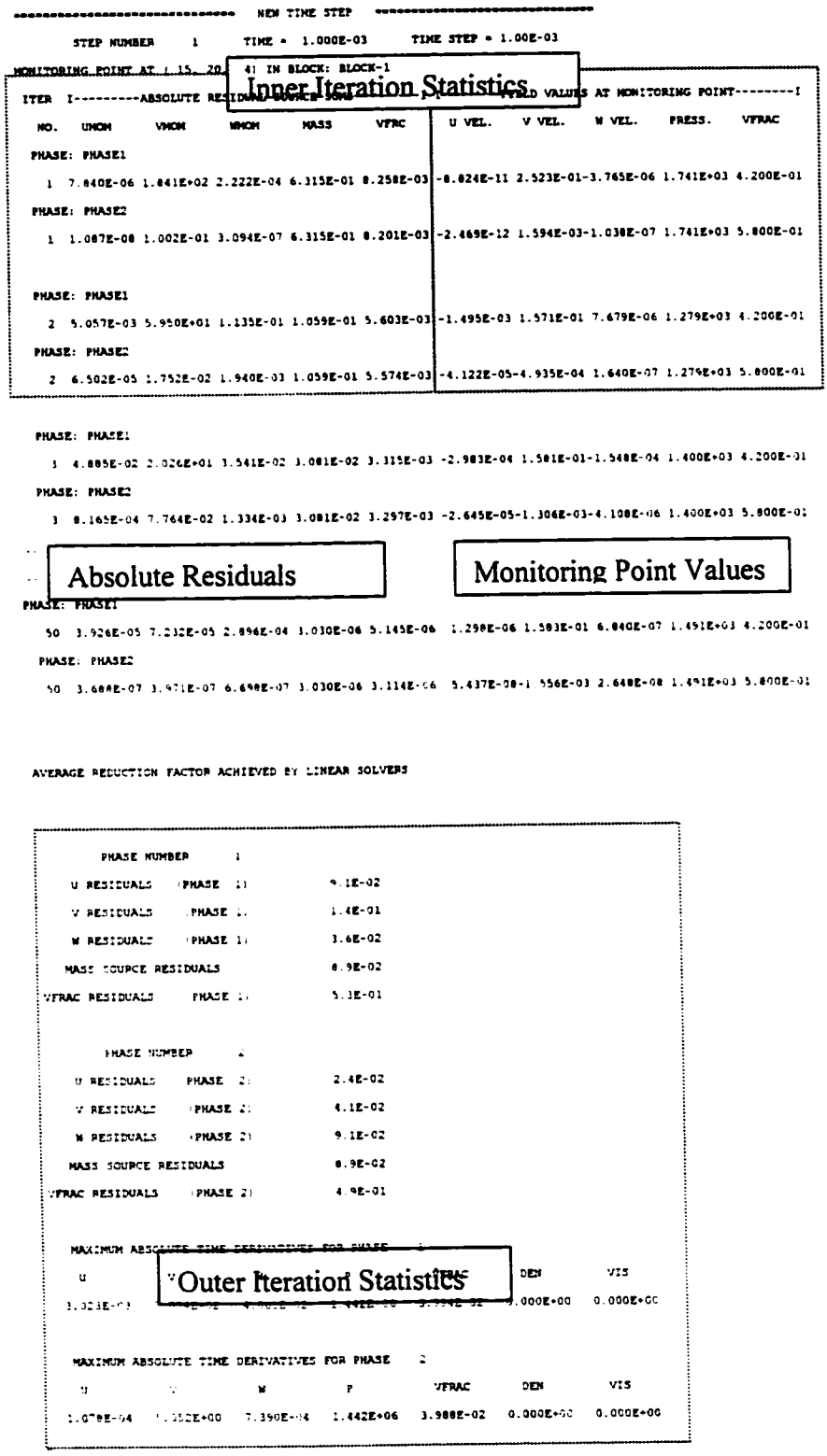

Figure 4.15 – Inner and outer iteration error summaries in CFX 4.2

Summary of Computational Methods

This chapter has shown the approach to solving the governing hydrodynamic equations of fluid mechanics for multiphase flows. Theoretical considerations of discretization scheme comparison were presented and the different schemes were compared and contrasted. Limitations of the schemes were also explored and the interpretation of numerical performance in terms of residual reduction and monitoring point values were discussed. Strengths of using the conservative formation for numerical modeling were briefly discussed and the problems associated with interpolating continuous flow field variables at points other than control volumes were elaborated on.

Chapter 5

CFX 4.2 Model Set-Up

This chapter describes the use and set-up of AEA Technology's CFX 4.2 computational fluid dynamics package. The command file and FORTRAN subroutines used for the simulations are discussed. Boundary, initial and other assumptions and conditions are described in detail. Adjustable parameters used for accelerating the simulations are discussed (Courant false time stepping, relaxation factors, double versus single precision calculations, Algebraic Multigrid acceleration, etc...).

5.1 CFX 4.2 Model Set Up

Running simulations with the CFX 4.2 flow solver requires writing a user FORTRAN file for special routines and also writing a command file to set up the desired simulation type and other solver settings. A general copy of both of the fortran (.f) and command (.fc) files are included in Appendix C. Specific details requiring explanation are elaborated in this chapter.

All simulations were of a gas-solid two-phase, three dimensional transient laminar flow situation in a rectangular fluidized bed geometry. Both phases were assumed to be incompressible and maintain constant hydrodynamic properties, such as viscosity, density and particle size. A time step of 0.001 seconds was used in all of the simulations with full flow field data output every 0.05 seconds. Convergence tolerance was set to a mass tolerance of 5.0×10^{-6} kg/s on the gas phase. This value represents the residual on the continuity equation after the outer (nonlinear) iteration.

5.1.1 Geometry

Geometry was chosen to reflect that of the experimental two dimensional bed used at the University of Saskatchewan under the direction of Dr. Berruti and operated by Jason Cowpan. A photograph of the experimental apparatus is shown in Figure 5.1; a more detailed description of the experimental apparatus is included in Chapter 6. Simulations were carried out in a Cartesian or rectangular coordinate system. The geometry was 1.2 m x 1.2 m x 0.10 m in the X, Y and Z directions corresponding with the experimental set up. The nozzle was placed on the left hand side of the fluidized bed domain and the orifice exit gas was shot towards the right. All dimensions of the

simulation geometry could be changed: orifice size, nozzle insertion, nozzle submergence and also the overall bed size. Figure 5.2 shows the location and all geometry variables that could be altered for simulations.

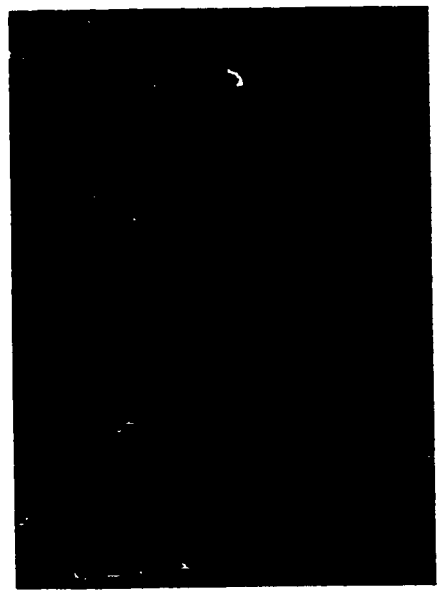

Figure 5.1 - Photograph of the experimental two dimensional bed filled with coke particles.

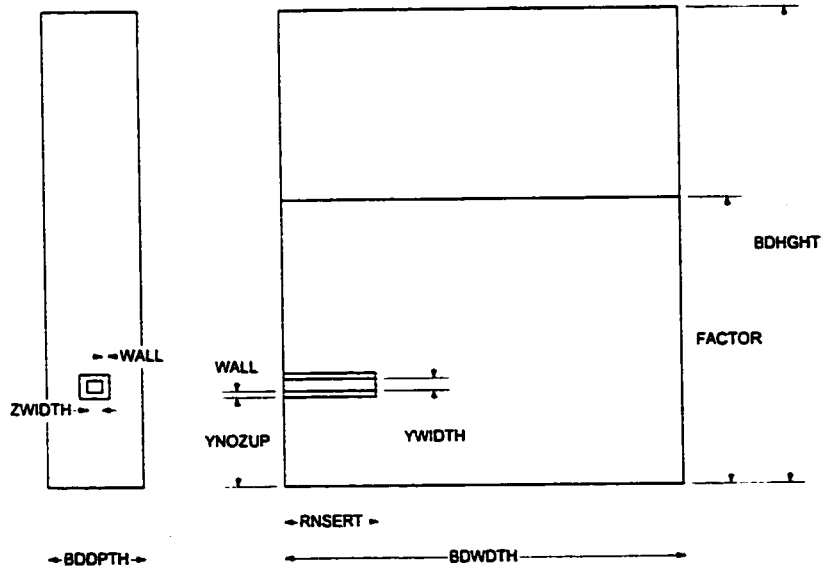

Figure 5.2 – Definition of geometry variables used in the FORTRAN user file.

Each of the variables specified in the diagram are used in the user FORTRAN routines which automatically generate the mesh. Changing the variables in the COMMON /UCBLOK/ section at the head of the user FORTRAN file sets the geometry to be used in the simulations; these variables are summarized in Table 5.1.

Table 5.1:

User FORTRAN Geometry Variables for Simulations

Variable Name	**Type**	**Description**
BDDPTH	Float	Physical depth (Z direction) of reactor.
BDHGT	Float	Physical height (Y direction) of reactor.
BDWDTH	Float	Physical width (X direction) of reactor.
DIAM	Float	Particle diameter.
FACTOR	Float	Desired initial fluidized bed height. This value is overwritten by user FORTRAN.
FINES	Float	Mesh parameter, must be set equal to YNOZUP.
NTOP	Integer	Mesh parameter. This value determines the overall number of mesh points in the entire domain. Usually set to 30 or 40.
NUMZ	Integer	Mesh parameter. Odd number of mesh points in Z direction.
RNSERT	Float	Nozzle insertion into bed. Distance from left wall to tip of nozzle.
WALL	Float	Nozzle pipe wall thickness.
YNOZUP	Float	Distance from bottom of nozzle to distributor.
YWIDTH	Float	Physical size of square orifice in Y direction.
ZWIDTH	Float	Physical size of square orifice in Z direction.

Particular care was taken to generate a reasonable representation of the nozzle pipe and orifice used in the simulations. The rectangular section representing the pipe is a solid block defined in the simulation through which no flow could pass. Inclusion of this pipe has lead to certain recirculatory flow patterns beneath the nozzle due to the down flowing nature of the solids along the wall.

Since a rectangular coordinate system was chosen, the nozzle orifice could not be made round in shape. It was necessary to match the square orifice area with that of a round area used in the experimental apparatus. The correct orifice size to use in the simulations was defined as follows:

$$A_{0.E} = \pi r^2 = \frac{\pi}{4} D_0^2 \qquad A_{0.C} = D^2 \tag{5.1}$$

The area of the square orifice in the simulations, $A_{O.C}$, must be the same as the area of the round orifice, $A_{O.E}$, used in the experiments to ensure the correct momentum transfer and gas mass flow rate.

$$A_{0.C} = A_{0.E} \Rightarrow D = \frac{\sqrt{\pi}}{2} D_0 \tag{5.2}$$

Problems involving the meshing of this small dimension, D_0, within the simulation were encountered and tests were conducted to investigate this.

5.1.2 Grid Generation

Analytical solution of the governing equations of multiphase fluid mechanics is not possible so the continuous domain has to be split into a discrete mesh where approximate solutions are obtained at the intersections of the mesh lines. As pointed out

by Anderson (1995), "the determination of a proper grid for the flow over or through a given geometric shape is a serious matter-one that is by no means trivial...the type of grid you choose for a given problem can make or break the numerical solution." The discretization mesh must be formulated to ensure numerical stability of the numerical solution technique while at the same time it must be structured such that mesh density is concentrated in regions of flow interest. Poor choice of mesh density can lead to incorrect solutions or solutions that are too coarse to resolve fine scale flow features. Too dense a mesh will lead to wasted computing resources.

In consideration of these facts a gridding routine was programmed in user FORTRAN as part of the CFX code to make a fine grid around the nozzle area. Figure 5.3 is a diagram of a typical discretization mesh generated with this code.

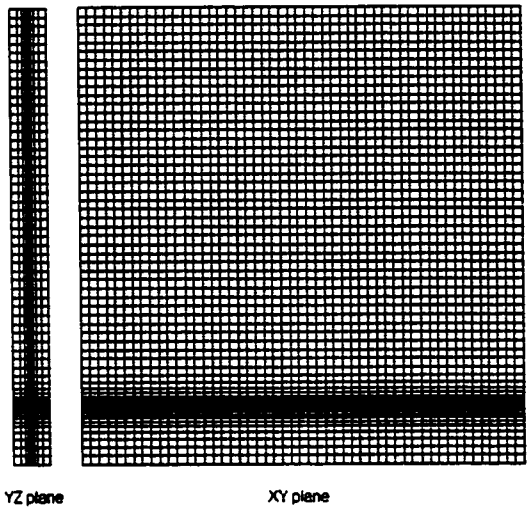

Figure 5.3 – Typical mesh used for simulations.

A geometric gridding scheme was used to mesh above and below the orifice location (typically the smallest division in the vertical direction). Two subroutines were created in the USRGRD user FORTRAN routines to facilitate meshing; these subroutines would automatically determine the number of mesh nodes and node spacing required to

ensure a smooth grid progression. Specific details of these routines are included as comments in the FORTRAN listing in Appendix C.

The mesh is generated automatically based upon the dimensions that are input to specify the location and size of the nozzle orifice. Some control is afforded for selecting the overall number of mesh points by specifying the desired number of linear mesh points in the freeboard area of the domain; see Table 5.1 NTOP variable.

The general approach to creating the discretization mesh is shown in Figure 5.4. The Y direction mesh is created first by determining the largest node spacing based on a linear step in the freeboard section of the bed. A subroutine then determines a mesh spacing above and below the nozzle orifice to ensure a gradual progression from the smallest node size (usually YWIDTH) to the linear step size in the freeboard. The linear step size in the freeboard is then recalculated based on the geometric progression above the nozzle orifice. This is to ensure that the total height of the reactor is kept at the value specified by BDHGT. The same approach is applied to calculate the mesh spacing in the X direction based on linearizing the nozzle insertion (RNSERT) and then following a linear step size to the right of the nozzle pipe. This general algorithm has been applied to the generation of all grids for the fluidized bed simulations.

5.1.2 Boundary Conditions

Boundary conditions were specified both in the command file and also in user FORTRAN. It was necessary to set some boundary conditions in user FORTRAN to allow for the flexibility of specifying the positions for the pipe boundary and nozzle orifice. An isometric view of the various boundary conditions and computational geometry are shown in Figure 5.5.

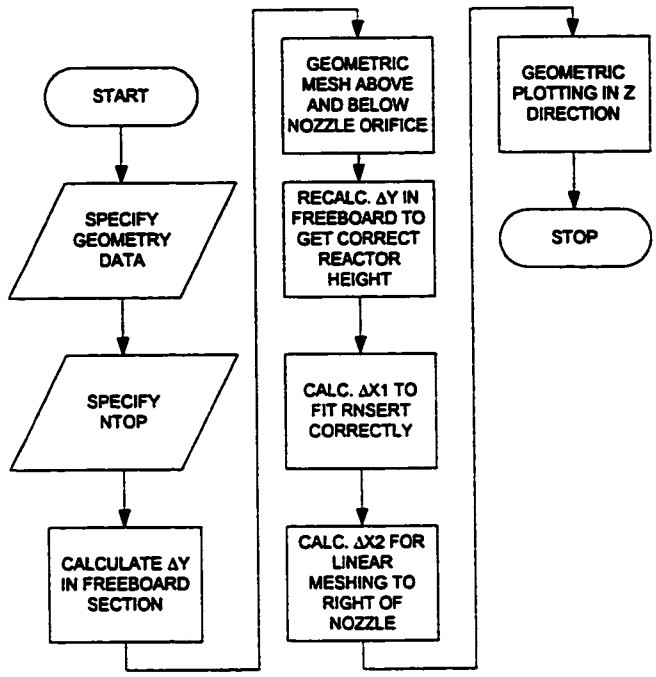

Figure 5.4 – Meshing algorithm.

The simulation domain is bounded by walls that have zero momentum flux through them. It is assumed that there is a slip boundary condition for the solids at the wall and a no slip boundary condition for the gas phase at the walls. The solids slip boundary condition is required so that when a solid particle 'strikes' the wall it does not 'stick' and cause numerical problems.

Two inlets were specified for the simulations: the nozzle inlet at the tip of the nozzle pipe and the distributor plate at the bottom of the computational domain. For both of these boundary conditions the gas normal velocity was specified. Only the gas phase was fed in through the inlets as the jet was not laden with solid particles.

The top of the fluidized bed domain consisted of a pressure boundary condition which was not specified with an absolute pressure as this was an incompressible

simulation. There was no solids carry over out of the domain and the gas flow into the simulation was exactly balanced by that flowing out through the pressure boundary face.

The rectangular pipe leading to the nozzle orifice was specified as a solid boundary with no flow present at the nodes where this solid exists. It was necessary to make the solid inlet pipe at least 3 by 3 control volumes in cross section due to the way in which CFX implements a solid boundary within the flow domain. More information can be found in the CFX Solver Manual.

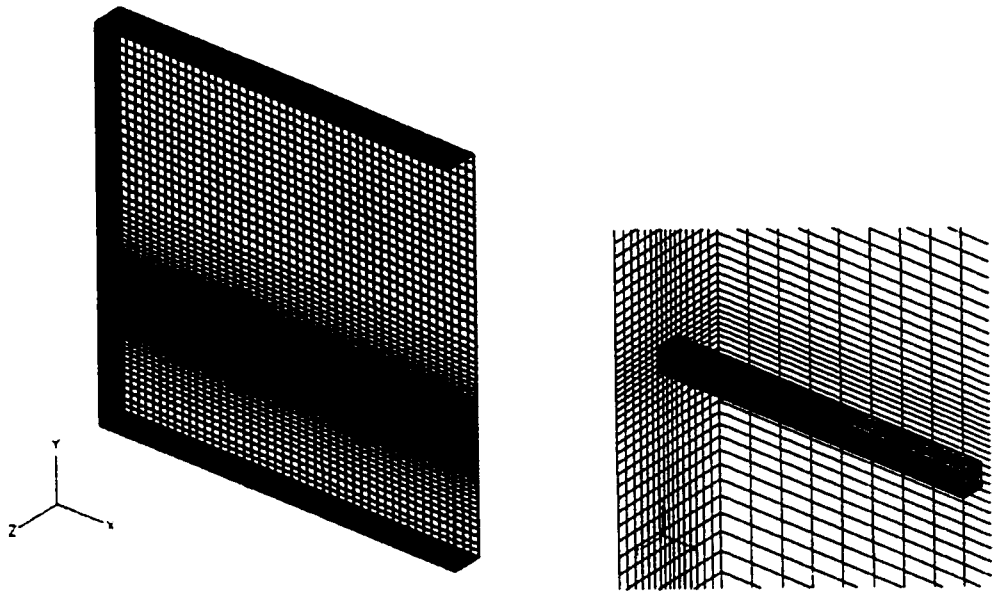

Figure 5.5 – Boundary conditions and discretization mesh in three dimensions.

5.2 Initial Conditions

Initial conditions were required to start the simulation. For all of these simulations the initial conditions were set with the user FORTRAN routine USRINT. All nodes within the computational domain were first filled completely with a gas volume fraction of 1. Next the height of the fluidized bed was determined by finding the node in the Y direction that was closest in height to that specified in the UCCOMMON block

under the FRACTION variable. In all cases a desired bed height of 0.71m was set; however, due to the automatic gridding routines this height actually varied to within ±0.01 m. This was not considered to be a problem. All nodes within this height were set to have an initial solids volume fraction of 0.42.

The bed was assumed to be incipently fluidized by setting the gas phase Y velocity to that of minimum fluidization using the same equation which determines the fluidization gas velocity for the distributor plate boundary condition. The solids velocity in all directions was set to zero. McCabe, Thiele and Smith (1989) give an expression for predicting the minimum fluidization velocity as:

$$U_{mf} = \frac{0.091(\rho_s - \rho_g)gD_p^2}{150\mu_g} \tag{5.3}$$

At t=0 the gas jet was initiated at the specified normal velocity for the required simulation.

5.3 Phase Properties

5.3.1 Gas Phase Properties

The continuous phase in these simulations was assumed to be air with a density, ρ_g, equal to 1.2 kg/m^3 and viscosity, μ_g, equal to 1.8 x 10^{-5} Pa·s.

5.3.2 Solids Phase Properties

The dispersed solids phase was set to have a density, ρ_s, of either 1450 or 950 kg/m^3 depending upon the simulations that were being carried out (see Chapter 7; Tables 7.1 and 7.4). The solids viscosity, μ_s, was kept constant at 1.0 x 10^{-12} Pas. This value was chosen based on the example fluidized bed simulation in the CFX 4.2 examples directory, example 28. Solids were assumed to be monosized spherical particles of diameter, D_p, of 370 μm.

The solids compaction modulus was set to –600 with a compaction volume fraction of 0.376 agreeing with the parameters used by Bouillard *et al.*(1989) equation G_1. To avoid numerical overflow errors a solids volume cut off was set to 0.0001 in the solids momentum equation. Any control volumes with solids volume fractions less than this were considered to have only the gas phase present. No significant loss of solids mass from the simulation domain was observed by using this numerical adjustment. The drag model relationships and solids volume fraction cut off values have been discussed in Chapter 3.

5.3 CFX Flow Solver Acceleration

All simulations were implemented using algebraic multi-grid acceleration as implemented in the CFX solver code. The set up parameters are included in the command file listed in Appendix C.

5.3.1 Under Relaxation Factor Studies

Under relaxation parameters can be specified in the control file so that certain terms within the momentum equations are relaxed relative to the other terms. Relaxing certain terms can lead to an improvement in convergence rates. Some tests were conducted after choosing a suitable discretization scheme (see Chapter 7: Results and Discussion) and mesh density to accelerate the convergence of inner iterations. Using single precision it appeared that the gas continuity residual would stabilize at approximately $3x10^{-5}$ kg/s. Based on this value the "best" combination of relaxation factors would be those which decrease the gas continuity residual with the least number of iterations. For all simulations each of the momentum equation terms were set with a relaxation factor of 0.6; this seemed to be the most appropriate relaxation factor to use when compared with the other relaxation factor combinations tested. Figures 5.6 to 5.14 show the residual reductions for a single outer iteration when different combinations of relaxation factors are used. An outline of the relaxation factor tests is listed in Table 5.2.

Table 5.2

Under Relaxation Parameter Tests

Run	X Momentum Relaxation	Y Momentum Relaxation	Z Momentum Relaxation
1	0.6	0.6	0.6
2	0.3	0.3	0.3
3	0.3	0.7	0.7
4	0.7	0.3	0.7
5	0.7	0.7	0.3
6	0.3	0.7	0.3
7*	0.3	0.7	0.3
8	0.8	0.8	0.8
9	0.9	0.9	0.9

*Courant false time stepping implemented

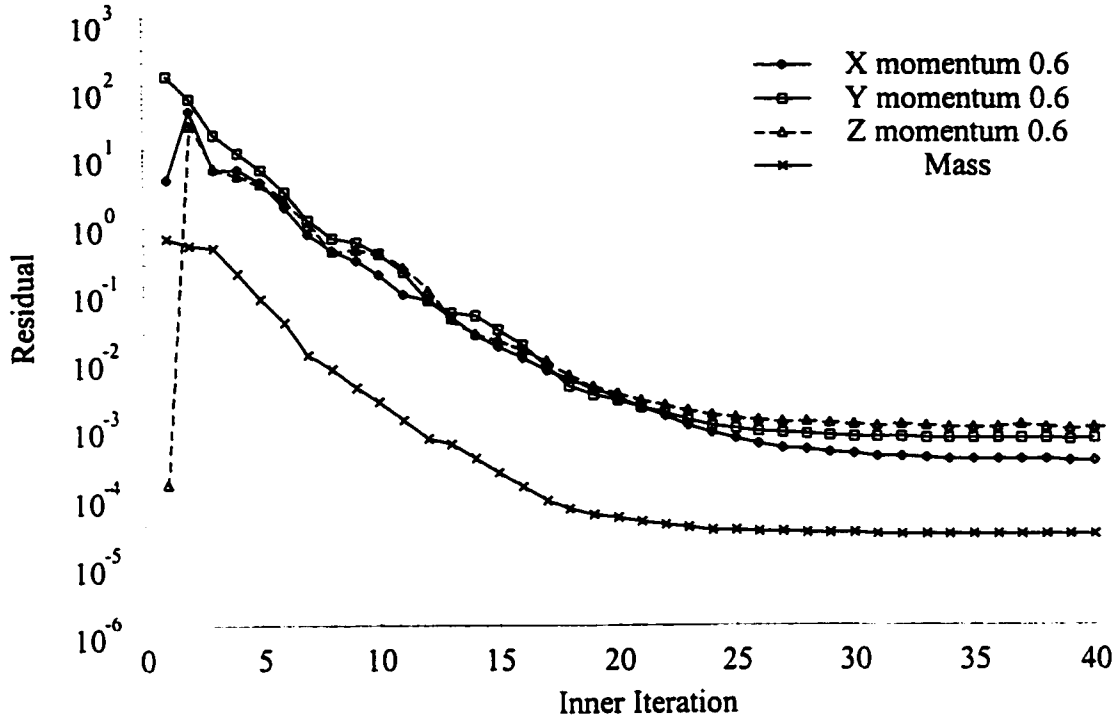

Figure 5.6 – Inner residual reduction with under relaxation test for Run 1, Table 5.2.

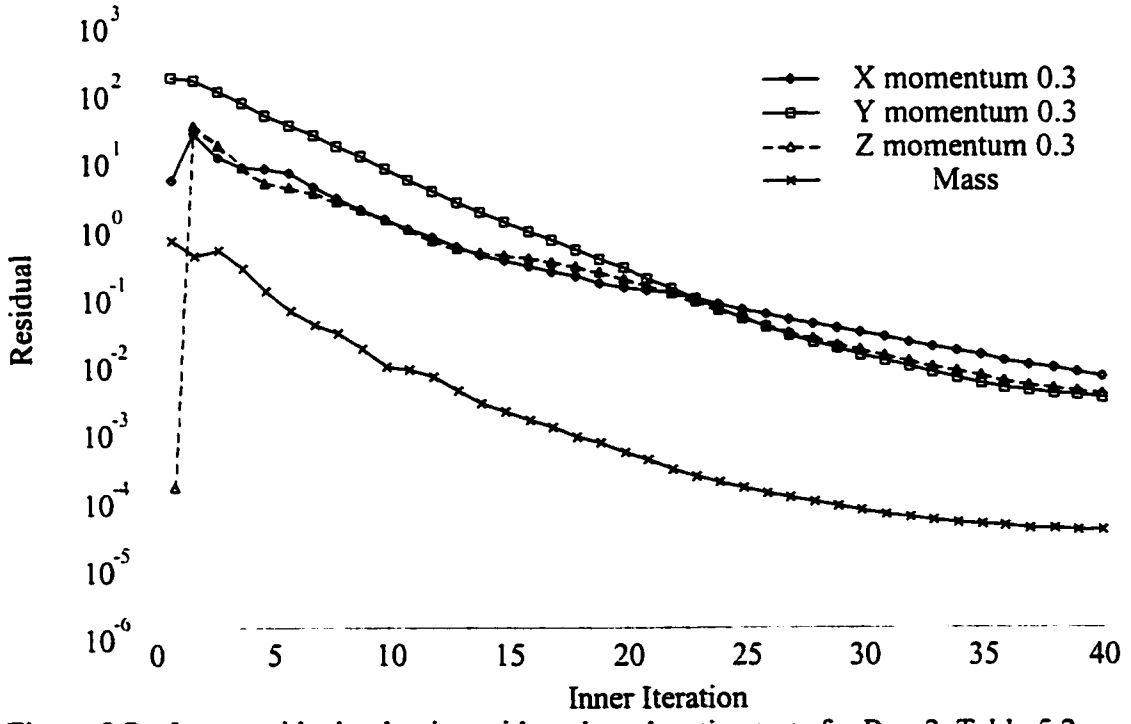

Figure 5.7 – Inner residual reduction with under relaxation tests for Run 2, Table 5.2.

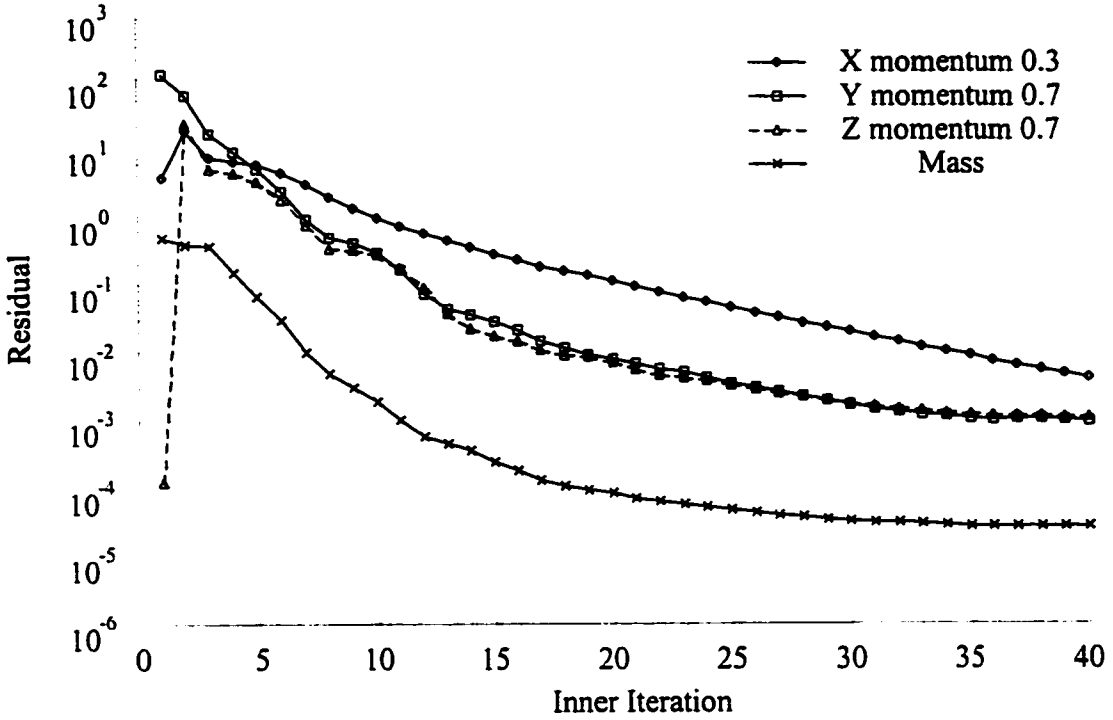

Figure 5.8 – Inner residual reduction with under relaxation tests for Run 3, Table 5.2.

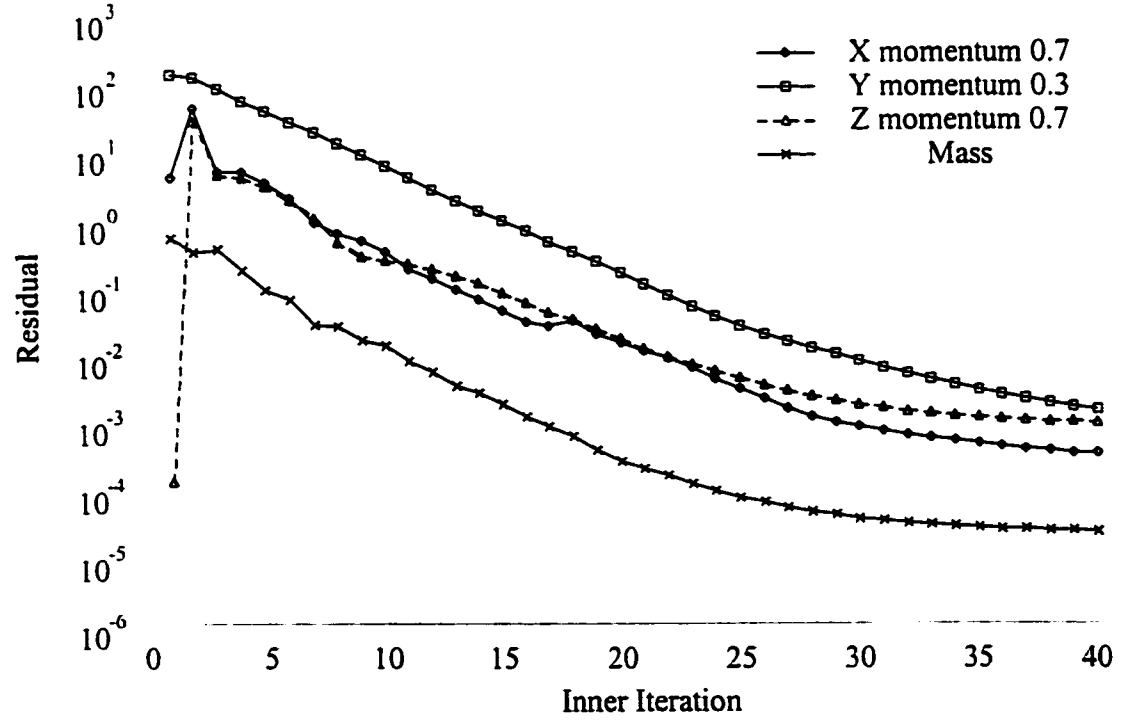

Figure 5.9 – Inner residual reduction with under relaxation tests for Run 4, Table 5.2.

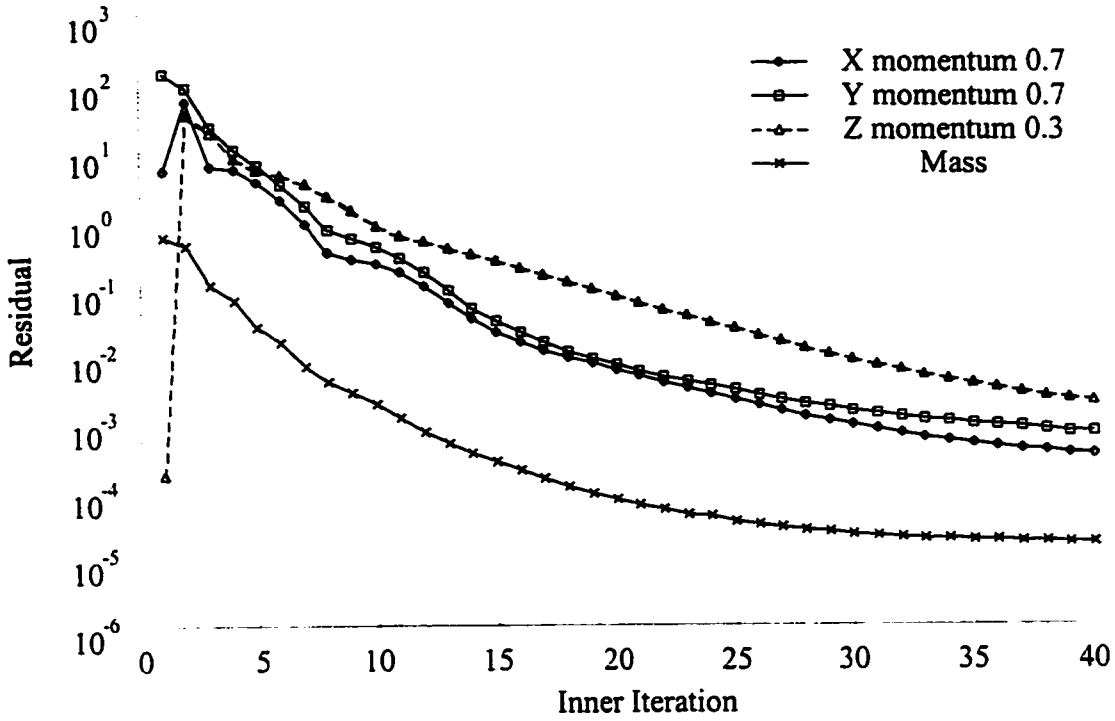

Figure 5.10 – Inner residual reduction with under relaxation tests for Run 5, Table 5.2.

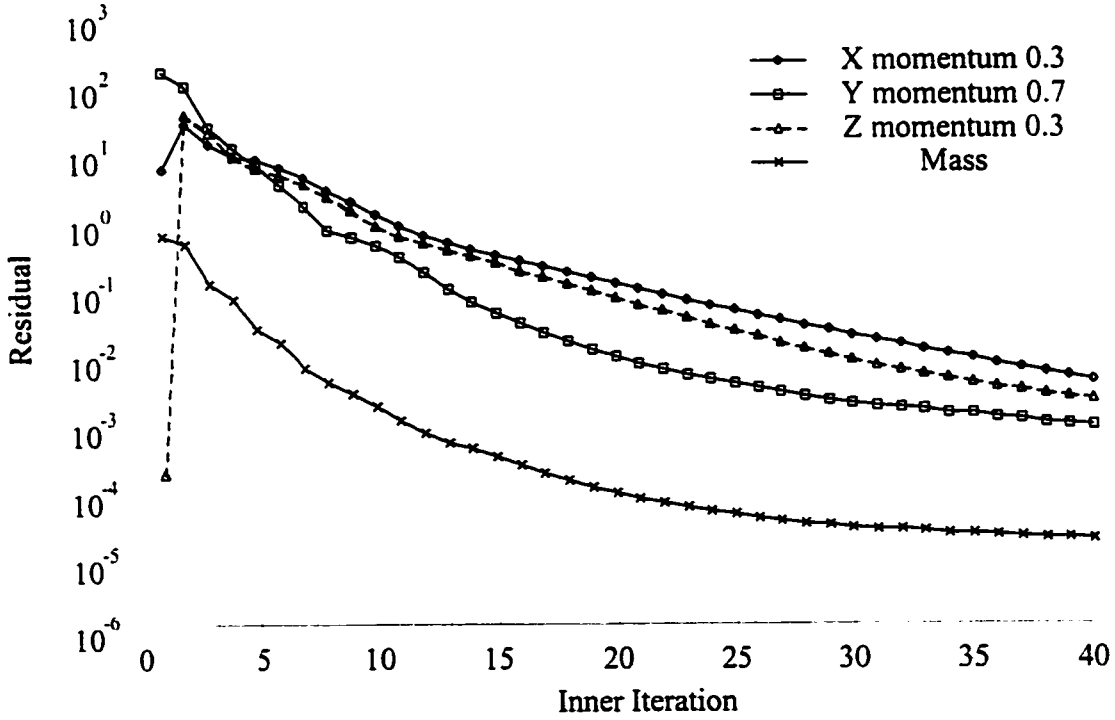

Figure 5.11 – Inner residual reduction with under relaxation tests for Run 6, Table 5.2.

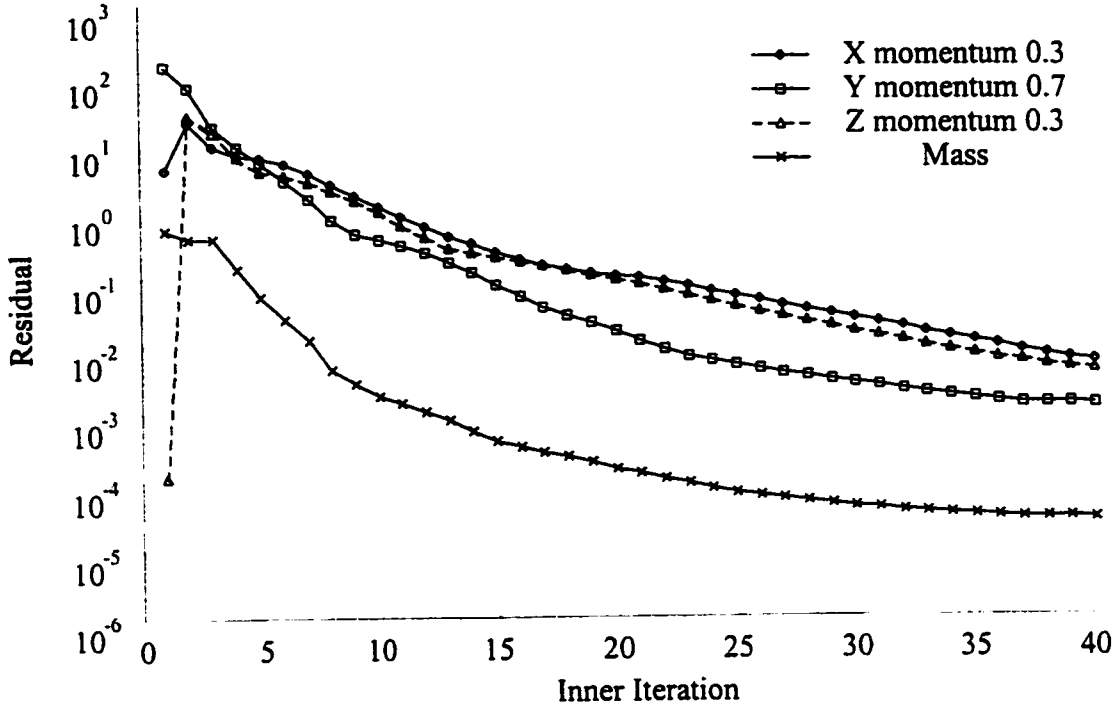

Figure 5.12 – Inner residual reduction with under relaxation tests for Run 7, Table 5.2.

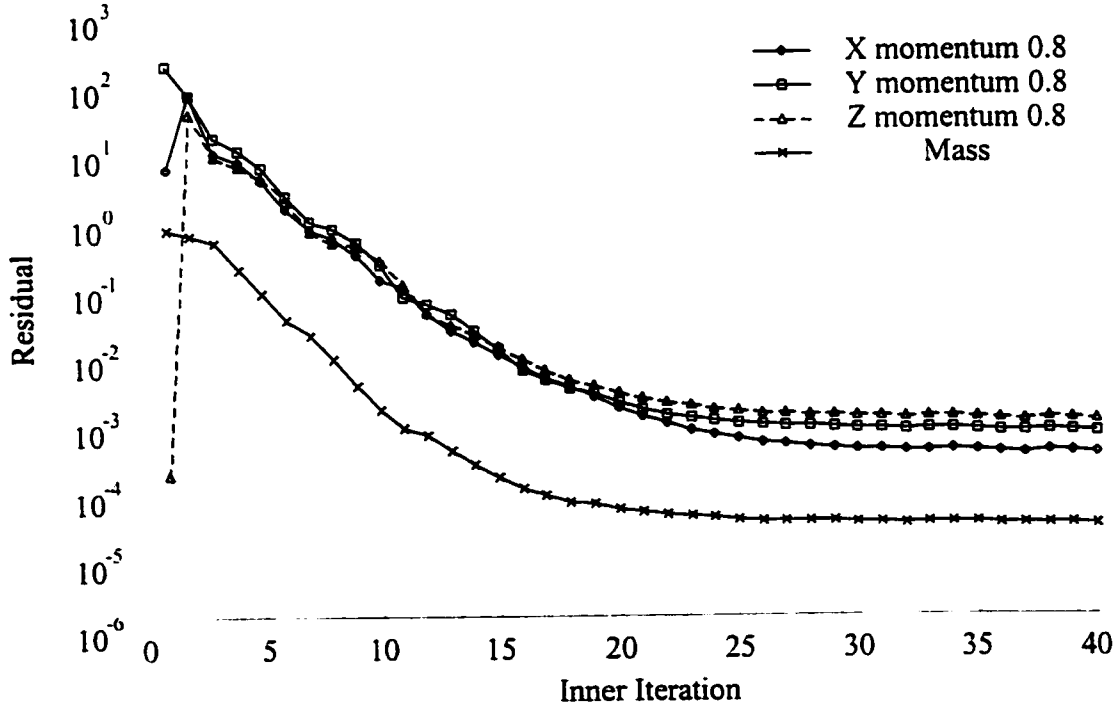

Figure 5.13 – Inner residual reduction with under relaxation tests for Run 8, Table 5.2.

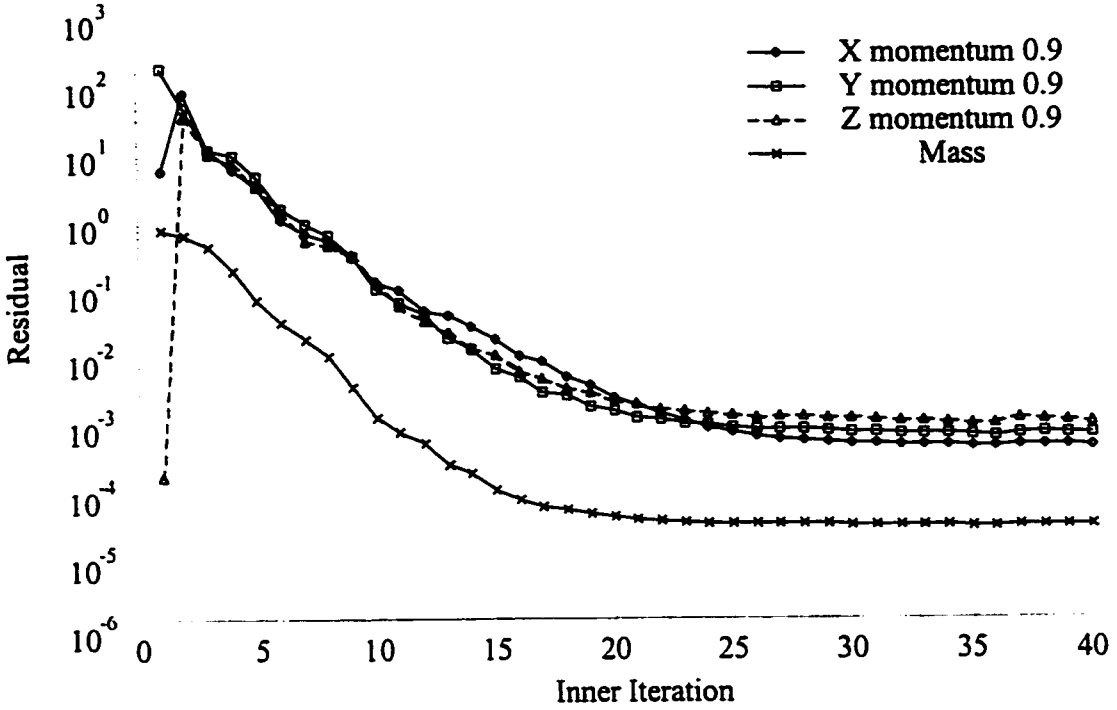

Figure 5.14 – Inner residual reduction with under relaxation tests for Run 9, Table 5.2.

5.3.2 Single versus Double Precision

The choice of single or double precision has an effect on both the solution time and numerical accuracy associated with the flow field variable representation. All runs in this report have used single precision because of the very long run times required to get substantial data from the simulations. Figure 5.15 shows the residuals from an identical run to that of run 9 Table 5.2 but using double precision. In this case the gas continuity residual is reduced by six orders of magnitude over 65 iterations. Conversely there is only a four order of magnitude reduction after 30 iterations which is slightly worse than the 15 iterations required for the same residual reduction using single precision; compare with Figure 5.14. A reduction of the gas continuity residual by four orders of magnitude is approximately equal to a 0.1 % error on the overall gas mass inlet flows within the

computational domain. In this case the use of double precision numerics could lead to improved residual reduction; however, at the expense of increased iteration counts with more involved computational and memory demands. Single precision calculations should be sufficient for the desired accuracy for these simulations.

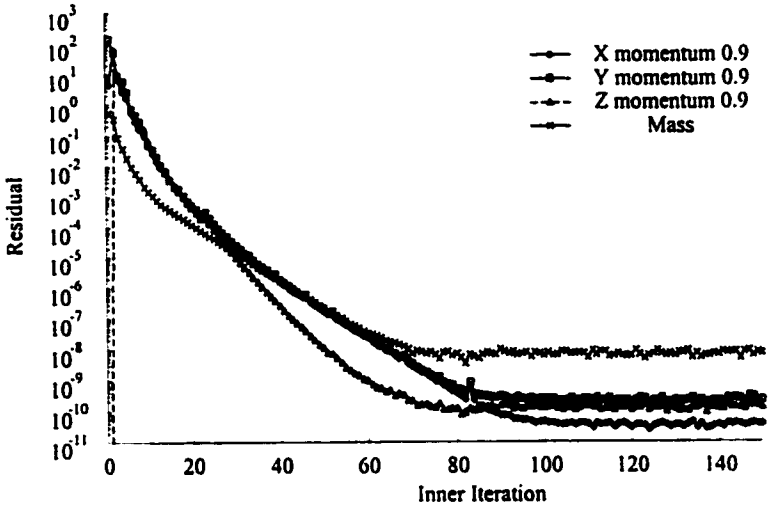

Figure 5.15 – Double precision residuals comparable to Table 5.2 Run 9.

5.3.3 Courant False Time Stepping

As previously mentioned in Chapter 3, there exists a minimum control volume size below which the continuum assumptions are not statistically valid for multiphase flows. All control volumes in these simulations were created so as to be larger than the minimum control volume size. In addition to checking for the valid control volume size, a Courant number analysis was carried out. The Courant number can be thought of as an indication of how far a flow particle (general sense of an infinitesimal control volume) has moved between nodes in a single time step. It is a dimensionless number based upon a characteristic flow velocity, mesh spacing and time step. For three dimensions, three local Courant numbers can be defined for each unit direction.

$$Cn = v\frac{\Delta t}{\Delta x_i} \qquad (5.4)$$
$$i = 1,2,3$$

Ideally the Courant number should be equal to one, in which case the information at a node has traveled exactly the same distance as the grid spacing. However, for stability with most discretization schemes it is necessary to have a Courant number less than one.

Courant numbers for simulations on two different mesh sizes are reported in Table 5.3. The characteristic Y velocity is based upon the characteristic velocities found from analyzing the experimental results. The characteristic X velocity has been assumed to be the same as the jet velocity at the nozzle orifice.

Table 5.3

Courant Number Analysis for $\Delta t = 0.001$ s

	Cn_y*		Cn_x**	
Grid	Maximum	Minimum	Maximum	Minimum
56 x 117 x 21	0.500005	0.0623438	15.83336	15.55543
44 x 96 x 9	0.609366	0.0494302	15.55566	1.46249

*based on a characteristic y velocity of 1.0 m/s

**based on a characteristic maximum x velocity of 250 m/s

From Table 5.3 it is seen that the Cn_x values were as high as 15. Ideally this value should be less than or equal to one. Tests were conducted using the automatic Courant false time stepping routines that are available in the CFX solver. This option analyzes the local velocity and mesh spacing and determines the "best" pseudo-time step to use

between the outer iterations to satisfy the Courant number requirement. In effect, this method does more false time steps between each real time step to arrive at the converged solution. Unfortunately using Courant false time stepping increases the amount of time required to do simulations. Figure 5.16 shows the gas continuity residual reductions when the Courant false time stepping was enabled. With no additional modifications to the solver settings a reduction of about four orders of magnitude in the gas continuity residual was realized after 25 outer iterations. This residual reduction is of the same order as that using the solver with Courant false time stepping. Based on this observation Courant false time stepping was not used for simulations.

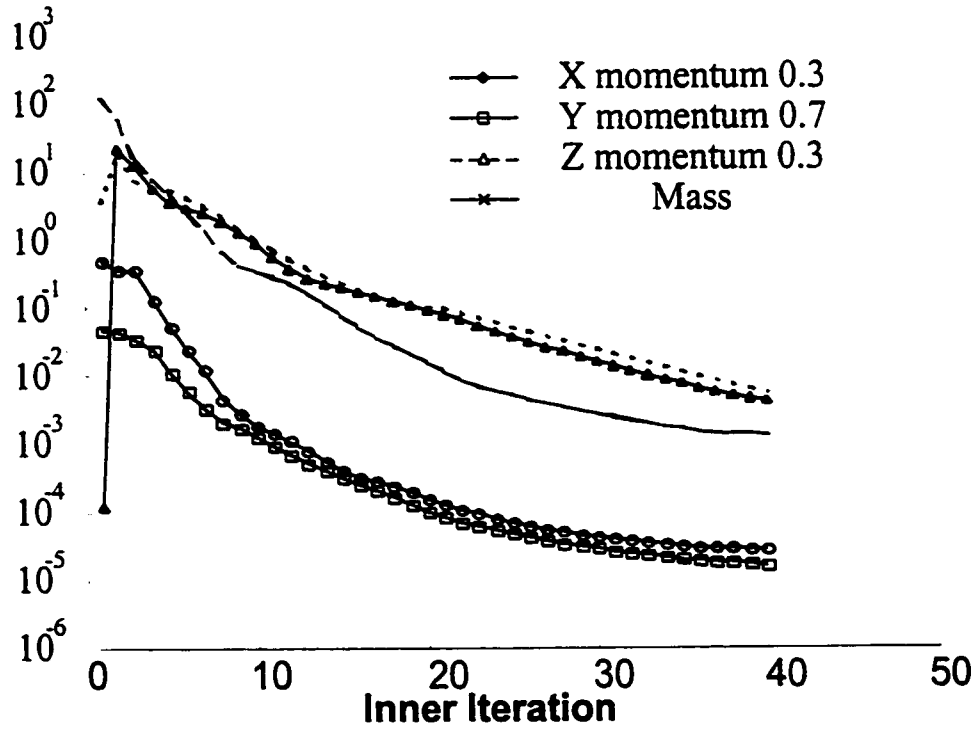

Figure 5.16 – Gas continuity residual using Courant false time stepping.

5.4 SUMMARY OF SIMULATION SET-UP

A summary of the CFX 4.2 solver set up was described in this chapter. Preliminary results from the under relaxation studies have shown that all under relaxation factors should be set to 0.6. Courant false time stepping was not shown to be useful for these simulations and will not be implemented. For efficient use of computer time, all simulations will be run using single precision. Boundary and initial conditions were described.

Chapter 6

Experimental Section

Experiments were conducted at the University of Saskatchewan to compare with some of the results from the simulation studies in this report. This chapter describes the two-dimensional fluidized bed, the methods used to record observations and descriptions of the general flow patterns observed with this apparatus.

6.1 EXPERIMENTAL SET UP

6.1.1 Geometry

The two dimensional fluidized bed was fabricated and operated at the University of Saskatchewan under the direction of Dr. Berutti. The fluid bed was rectangular in cross-section with length and depth dimensions of 1.2 m x 0.1 m, respectively, and a height of 1.2 m, see Figure 6.1. Both the front and rear faces of the bed were constructed of clear acrylic sheets to facilitate visual observations of the jet and use of a high-speed video camera. The sides of the bed were constructed of aluminum and a port was located on the left side to accommodate a horizontal injection nozzle for experiments. The axis of the nozzle was located 0.39 m above the top of the distributor plate, and 0.0117 m from the acrylic front sheet. The nozzle port allowed easy adjustment of the nozzle insertion into the fluidized bed. For all experiments carried out for this study, the nozzle insertion was held constant at 0.070 m. The cyclone return dipleg entered the bed on the left side above the nozzle at a 45° angle and extended 0.08 m horizontally into the bed.

All fluidization air and horizontal feed jet gas for these experiments was provided from an oil free compressor. The windbox below the distributor plate was split to allow for different aeration rates to be set for both the left and right sides of the distributor plate, see Figure 6.2. To provide even distribution of the fluidization gas, deflector caps were placed over the fluidization gas inlets. The right and left aeration rates were kept equal for the experiments in this study. The distributor plate had a felt covering attached to prevent particles from falling through the aeration holes and to enhance flow distribution across the distributor.

The nozzle was attached onto the end of a steel pipe and inserted into the fluidized bed. The nozzle orifice was round with an internal diameter of 3.81mm. Jet air was provided from the compressor and a mass flow controller was used to meter the jet air supply. Construction and design details of this nozzle can be requested from Dr. Berruti at the University of Saskatchewan and will not be described further here.

6.1.2 Particle Properties

The solid particles used for the experiments were medium density polyethylene particles supplied by NOVA Chemicals (Calgary, Alberta). The particles were white in colour with a density of 930 kg/m^3. Mean particle diameter was determined to be 370 μm. Minimum fluidization velocity was reported to occur at about 4.4 cm/s. Based on mass measurements for a given volume of particles, assuming negligible particle porosity, the minimum fluidization voidage was found to be 0.5.

To facilitate visualization of the particle flow patterns within the fluidized bed, a portion of the particles were coloured with paint. To colour the particles, a thin layer of particles was laid out on a large sheet and a light layer of spray paint was applied to the particles. Several coats of paint were required to completely colour these particles. It is not known if this painting changed the particle size and/or density.

6.1.3 Experimental Procedure

A NAC High Speed System Model HSV-100 camera was used for filming the experiments. The camera was able to capture colour images at 500 frames per second on

super VHS videotapes. These images were then digitized and analyzed on a computer. Video observations were taken of the overall flow patterns within the fluidized bed and

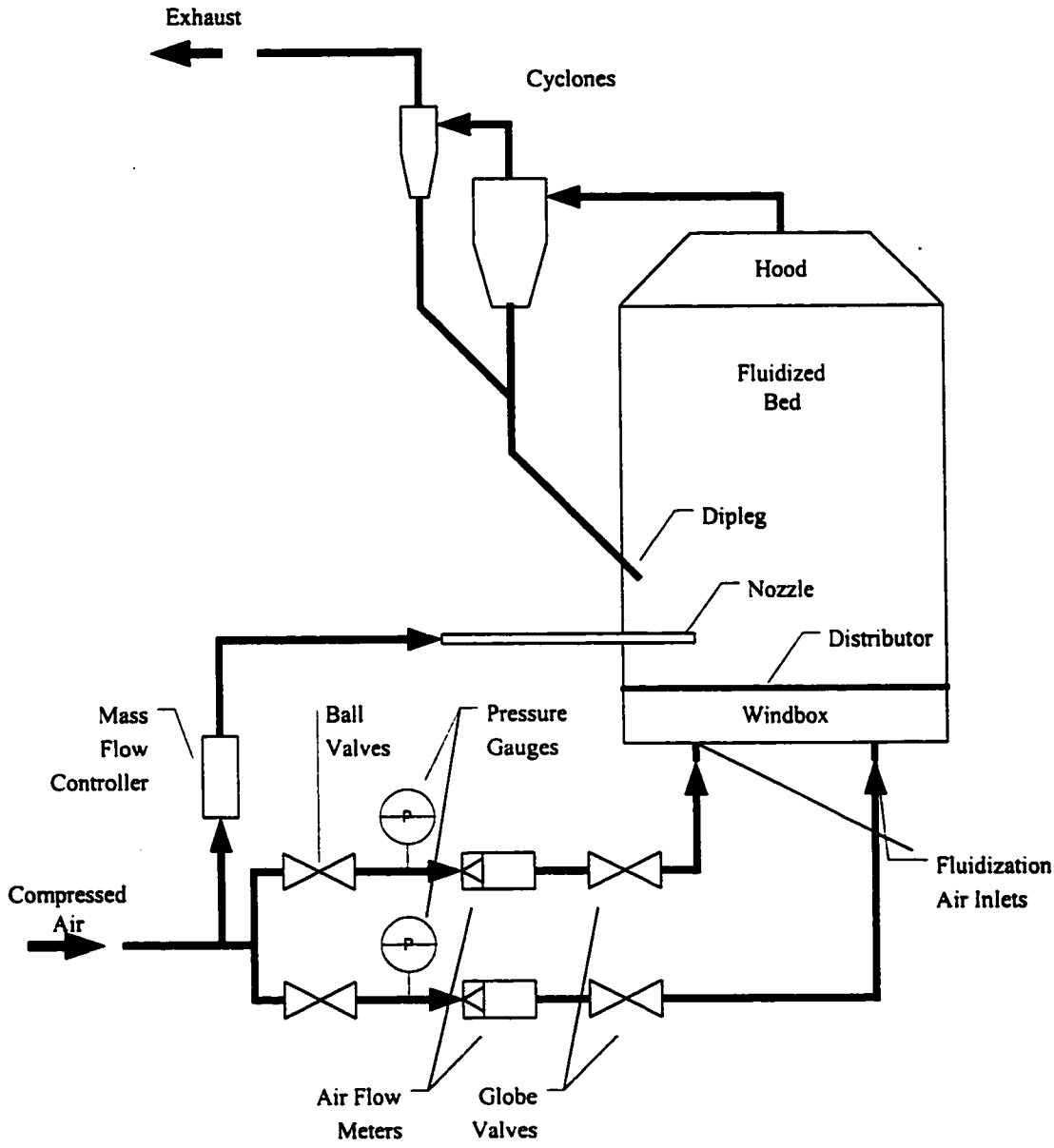

Figure 6.1 – Diagram of the fluidized bed experimental apparatus. Modified from Jason Cowpan's M.Sc. thesis, University of Saskatchewan, 1999.

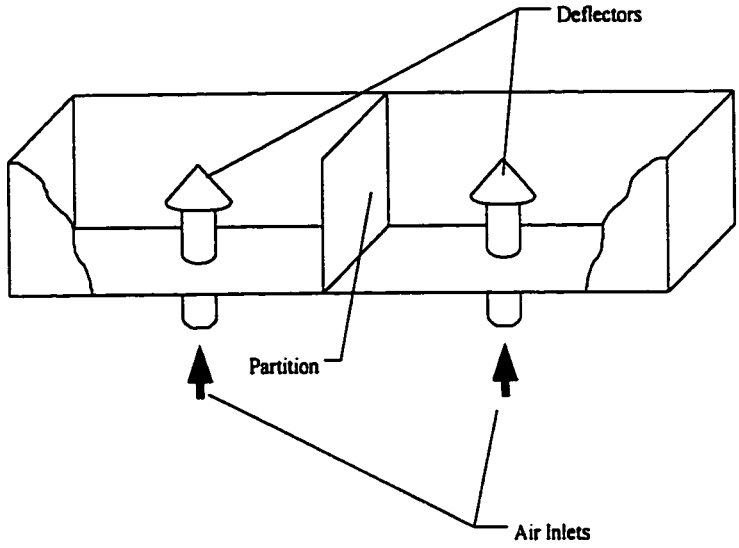

Figure 6.2 – Cut away diagram of the windbox. Courtesy Jason Cowpan M.Sc. thesis, University of Saskatchewan, 1999.

more detailed recordings were taken by zooming in on the horizontal jet region within the fluidized bed. For each of the runs approximately 10 seconds of footage was taken; this length of time was adequate to capture important jetting phenomena.

For each set of experiments the fluid bed was assembled, filled with particles to a height of 0.85 m above the distributor and all flow lines were connected. The compressor was started and the buffer tank filled. Fluidization gas was then set using the globe and ball valves to adjust and control the pressure and flow rate to the windbox. Once the fluidization gas was set, the air supply to the nozzle was adjusted using the mass flow controller. The only variables adjusted for these runs were the fluidization gas flow rate and the gas flow rate to the horizontal nozzle. The experimental operating conditions that were investigated are listed in Table 6.1 and reflect the conditions which were used in the CFD simulations. The numbers listed in the table refer to the digital time stamp in the upper right corner of the video recording.

Table 6.1:

Experimental Operating Conditions and Video Reference Numbers

	U_j (m/s)				
U_0 (cm/s)	229.2	327.5	425.7	524	589.5
0	301	302	303	304	305
	318C	319C	320C		
3.1	314	315	316	317	
	323C	322C	321C		
4.4	306	307	308	309	
	324C	325C	326C		
5.7	310	311	312	313	
	327C	328C	329C		

U_{mf} = 4.4 cm/s
C refers to video recording at the tip of the jet plume in the near field

Data can be extracted from the images recorded on the video tape by digitizing the images and then processing the images on a computer. Distinguishing markers with a set distance were always recorded on the video. These markers allowed the distance per pixel to calculated for each of the images analyzed. It is assumed that the aspect ratio of the pixels in the Y and X directions is the same when the video was converted to digital format. Pixel measurements with respect to distances in centimeters are listed in Table 6.2. These values were used to determine the average bubble size and rise velocity discussed in section 6.2.4.

6.2 Observations

The general flow patterns within the experimental fluidized bed could be broken into three main types: those below U_{mf}, those at U_{mf} and those at fluidization velocities much above U_{mf}. Observations of the fluidized bed were taken with a high speed video camera recording 500 frames per second. Video tapings were taken at a far field to

observe the entire fluidized bed in operation and also zoomed to observe the end of the jet plume. Four high power white lights were shone onto the face of the fluidized bed to provide lighting for the recordings. Without these lights there was not enough ambient lighting to make any meaningful recordings. Attempts were also made to shine the light through the bed to illuminate individual bubbles within the fluidized bed. This attempt didn't work very well as the bed was too dense and didn't allow enough light to penetrate.

Table 6.2:

Summary of Video Capture Image Dimension Conversions from Pixels to Centimeters

Image Data Name:	Xstart (pixel)	Xend (pixel)	dx (pixel)	Measure (m)	Conversion (m/pixel)
311.09	298	441	143	0.1	0.000699
312.06	302	442	140	0.1	0.000714
313.06	298	440	142	0.1	0.000704
314.08	255	412	157	0.1	0.000637
315.08	252	413	161	0.1	0.000621
316.06	252	411	159	0.1	0.000629
317.09	253	413	160	0.1	0.000625
318.07	224	779	555	0.1	0.000180
319.05	224	780	556	0.1	0.000180
320.09	110	674	564	0.1	0.000177
323.07	165	681	516	0.1	0.000194
322.08	274	846	572	0.1	0.000175
321.10	184	705	521	0.1	0.000192
324.06	130	697	567	0.1	0.000176
325.08	114	680	566	0.1	0.000177
326.05	103	620	517	0.1	0.000193
327.07	240	754	514	0.1	0.000195
328.09	136	641	505	0.1	0.000198
329.05	113	630	517	0.1	0.000193

6.2.1 Below U_{mf}

With zero fluidization gas the bed acted as a packed bed and the jet was discharged into the medium. With increasing fluidization gas velocity (below U_{mf}) the bed would slowly start to expand and the solids particles started to make very small movements in place. No overall flow patterns within the fluidized bed were observed. The bulk bed particles seemed to remain at a fixed position but tended to vibrate with increasing fluidization gas velocity.

At fluidization velocities below minimum fluidization the particle entrainment into the jet was from above the jet plume. No particle entrainment was observed below the jet. With zero fluidization gas the bed acted as a packed bed and the jet would discharge into the bed and "carve" the region above the jet plume and bubbles would form once the roof of this carving zone collapsed back on the jet. This intermittent carving and roof collapse lead to a periodic extension and then decrease in the jet penetration length into the bed.

6.2.2 At U_{mf}

As soon as the fluidization gas was increased to U_{mf} the bed height increased and bubbles were seen to occur on the top surface of the bed. An overall slight recirculating bed pattern was observed with the particles descending along the center of the bed and then moving towards the sides (along the X axis direction). Small triangular shaped mounds of particles appeared to form at two positions on the distributor plate. These stagnant zones were not expected to form and are thought to have formed because of poor flow distribution through the distributor. Since the distributor was split to allow for a

weakly recirculating bed to be set up, a deflector plate had to be placed over both of the fluidization air inlet jets to ensure that the flow would not exit at the location directly above these nozzles, see Figure 6.2. These plates might have lead to the flow patterns being observed on top of the distributor.

Particles were entrained from above and below the jet plume at U_{mf}. The flow appeared to be a line sink starting on the left at the approximate location of the tip of the nozzle and continuing to where the gas jet impinged on the front face of the reactor.

6.2.3 Above U_{mf}

At fluidization velocities much greater than U_{mf} the bed operated in the bubbling or turbulent fluidization regime. The overall recirculating pattern within the fluidized bed was still observed; however, due to the increase in the bubbles forming from the distributor and progressing up through the bed it was very difficult to ascertain any particular flow patterns.

Particles were still entrained from above and below the jet plume and then accelerated into the fluidized bed. Bubbles from the distributor moved up from below the jet and might have had some impact on entraining particles into the jet zone.

6.2.4 Bubble Sizes and Rise Velocities

From the experimental video tapes the behavior of the bubbles can be determined by using a simple geometric argument as follows. Bubble boundaries are located based on the width and height of each bubble. Since the bubbles being tracked are the same

coordinate system for each run, a geometric bubble center can be identified based on the maximum width and height positions of the bubbles. Tracking this centroid over a fixed period of time will give the bubble rise velocity. By using the center of the bubble and not the bubble boundary this should negate (somewhat) the effects of bubble shape distortion. These concepts are shown in the following figure. Identical analyses were carried out on the simulation results. The perimeter points are labeled as X_1, X_2, Y_1 and Y_2; the approximate center is shown with a cross. Selected video recordings of the operating fluidized bed were digitized and then broken into individual frames as 24-bit grayscale bitmaps and the bubble information was extracted.

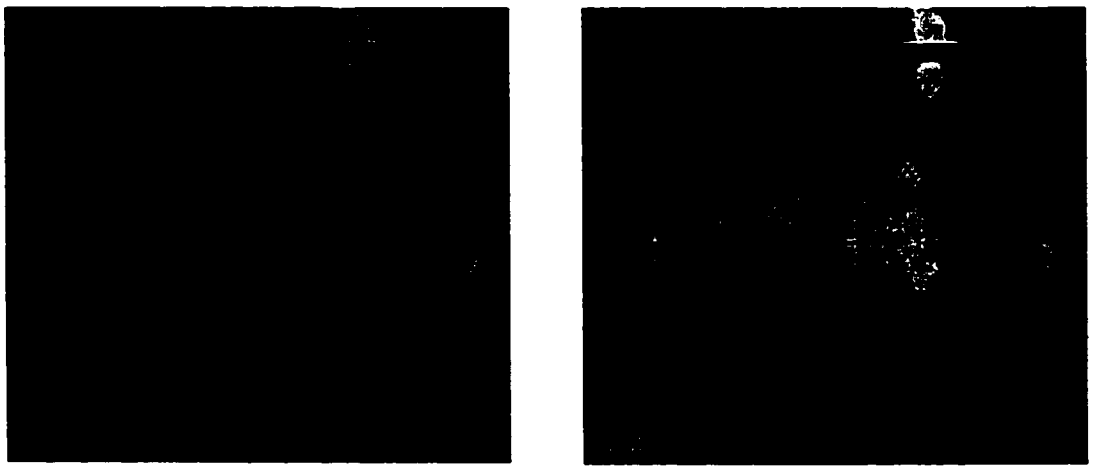

Figure 6.3 – Definition of the bubble dimensions from digitized video observations.

Bubbles would form at the tip of the jet and then wrap slightly back to the left (over the jet plume). Figure 6.4 shows this particular bubble behavior. Just above the tip of the jet plume a long tongue would progress vertically upwards creating a slender void. Once the roof of the jet collapsed in on itself this void would form into a more spherical bubble

shape and progress up towards the top of the bed. Occasionally the jet would catch up to the bubble and cleave it through the center forming a mushroom shaped void. Internal recirculation of solids through the bubbles was observed from the center to the top of the bed.

Figure 6.4 - Demonstration of "fingers", round bubbles and bubbles cleaving into mushrooms.

Results from the average bubble rise velocity, horizontal velocity and bubble size are listed in Table 6.3. From the results presented in this table it can be seen that a characteristic rise velocity of the order of 1 m/s can be defined for bubbles, which can be considered to be flow disturbances. Likewise a characteristic horizontal velocity of approximately 0.1 m/s can be defined. These velocities can be used to determine the correct mesh spacing in the numerical simulation outside of the gas jet zone adjacent to the nozzle inlet based on Courant number.

6.2.5 Transient Analysis

The flow within the fluidized bed is highly transient showing flow behavior over a wide range of characteristic times. Bubble movement occurs on time scales larger than the behavior of the jet while the behavior of individual particles within the jetting zone

have much shorter time scales associated with them. The particle Stokes relaxation time, assuming a very low slip velocity between the gas and solids phase, is calculated to be 0.4014 seconds.

Table 6.3:

Bubble Rise Velocity, Horizontal Velocity and Size from Experiments

Run	Rise Velocity (m/s)*	Horizontal Velocity (m/s)**	Bubble Area (m^2)+
306	1.38	-0.034	0.010
307	1.25	-0.072	0.017
308	0.80	-0.194	0.024
309	0.34	0.183	0.012
310	0.84	0.114	0.009
311	1.12	-0.098	0.020
312	0.83	0.032	0.012
313	0.44	0.200	0.038
314	1.46	0.218	0.008
315	1.25	0.021	0.017
316	1.35	-0.103	0.019
317	0.66	0.021	0.023

*standard deviation is as high as 0.62
**standard deviation is as high as 0.36
+standard deviation is as high as 0.004

Chapter 7

Results and Discussion

This chapter deals with the results from the simulations and a comparison with experimental results taken at the University of Saskatchewan. Chapter 7 is broken into two parts: The first part deals with numerical considerations such as discretization scheme, grid refinement studies and the governing hydrodynamic equations. Numerical considerations must be taken into account so that there is confidence in the physical predictions. Part 2 deals with the physical predictions obtained from the simulations. Predicted flow behavior is compared and contrasted against experimental and literature results.

A simulation naming convention using two letters followed by two numbers was followed for book keeping purposes. The first letter refers to the type of simulations used for that particular set of simulations; the second letter refers to the jet velocity and the last two digits refer to individual runs within that test set. For example:

AA01 – refers to:

A – simulation using discretization scheme as the key parameter;

A – jet velocity of 150 m/s;

01 – first run in this set using Hybrid discretizaton.

7.1 Part I: Numerical Considerations

Computational fluid dynamic simulation work requires the use of a computer to solve the governing flow equations for flow geometries of engineering interest. Since computers are limited to fixed finite number systems, errors are introduced due to rounding and truncation. This will introduce numerical errors. As shown in Chapter 3 there are many different ways to approach the volume averaging of the governing flow equations. With so much choice there are certain approaches which may be "better" than others for certain flow modeling scenarios. This first part of the chapter deals with some of the simulations that were carried out to explore the different modeling possibilities available within the CFX 4.2 flow solver. Numerical issues such as residual reduction, computational effort, discretization scheme and grid density are explored. All simulations dealing with numerical considerations are listed in Table 7.1. Each run has its own unique four character identification string.

7.1.1 Three Dimensions and Symmetry

The literature abounds with simulations of fluidized beds in two dimensions; however, preliminary simulations using a two-dimensional bed and a horizontal feed jet were found to produce unrealistic results. Two dimensional simulations with side injection of the gas into the fluidized bed would cause the bed above the jet to lose fluidization and slump. This is not observed in the experimental apparatus because the bed can be thought of as being pseudo-two dimensional. Although the experimental apparatus is very narrow in comparison with its height and width, there still exists a depth

Table 7.1: Numerical Simulations Summary

Axxx series: Discretization Scheme Comparison (section 7.2)								
CFD Run	Scheme	U_f	D_o	S	I	D_p	ρ_p	*Nozzle CVs*
U_{inf}=150 m/s			(m)	(m)	(m)	(μm)	(kg/m³)	(size)
AA01	Hybrid	U_{inf}	0.0099	0.145	0.1175	370	1450	2x2
AA02	Minmod	U_{inf}	0.0099	0.145	0.1175	370	1450	2x2
AA03	SB	U_{inf}	0.0099	0.145	0.1175	370	1450	2x2
U_{inf}=250 m/s								
AB01	Hybrid	U_{inf}	0.0099	0.145	0.1175	370	1450	2x2
AB02	Minmod	U_{inf}	0.0099	0.145	0.1175	370	1450	2x2
AB03	SB	U_{inf}	0.0099	0.145	0.1175	370	1450	2x2
U_{inf}=300 m/s								
AC01	Hybrid	U_{inf}	0.0099	0.145	0.1175	370	1450	2x2
AC02	Minmod	U_{inf}	0.0099	0.145	0.1175	370	1450	2x2
AC03	SB	U_{inf}	0.0099	0.145	0.1175	370	1450	2x2

Dxxx series: Grid Refinement Studies (section 7.3)										
CFD Run	Scheme	U_f	D_o	S	I	D_p	ρ_p	*Nozzle CVs*	*Grid*	*Nodes*
U_{inf}=250 m/s			(m)	(m)	(m)	(μm)	(kg/m³)	(size)		
DA01	SB	U_{inf}	0.0099	0.145	0.1175	370	1450	1x1	Coarse	11270
DA02	SB	U_{inf}	0.0099	0.145	0.1175	370	1450	1x1	Normal	30000
DA03	SB	U_{inf}	0.0099	0.145	0.1175	370	1450	1x1	Medium	60480
DA04	SB	U_{inf}	0.0099	0.145	0.1175	370	1450	1x1	Fine	83600
DA05	SB	U_{inf}	0.0099	0.145	0.1175	370	1450	1x1	Fine	83600
U_{inf}=250 m/s										
DB01	SB	U_{inf}	0.0099	0.145	0.1175	370	1450	2x2	Medium	71280
DB02	SB	U_{inf}	0.0099	0.145	0.1175	370	1450	2x2	Fine	98010
U_{inf}=250 m/s										
DC01	SB	U_{inf}	0.0099	0.145	0.1175	370	1450	3x3	Medium	86670
DC02	SB	U_{inf}	0.0099	0.145	0.1175	370	1450	3x3	Fine	116640
DD01	SB	U_{inf}	0.0099	0.145	0.1175	370	1450	3x3	Fine	116640
DD02	SB	U_{inf}	0.0099	0.145	0.1175	370	1450	3x3	Fine	116640

Exxx series: Continuous Phase Pressure Sensitivity Analysis (section 7.4)										
CFD Run	Scheme	U_f	D_o	S	I	D_p	ρ_p	*Nozzle Nodes*	*Grid*	*Nodes*
U_{inf}=250 m/s			(m)	(m)	(m)	(μm)	(kg/m³)	(size)		
EA01	SB	U_{inf}	0.0099	0.145	0.1175	370	1450	1x1	Coarse	11270
EA02	SB	U_{inf}	0.0099	0.145	0.1175	370	1450	1x1	Normal	30000
EA03	SB	U_{inf}	0.0099	0.145	0.1175	370	1450	1x1	Fine	83600

Hxxx series: Solids Pressure Sensitivity Analysis									
CFD Run	Scheme	U_f	D_o	S	I	D_p	ρ_p	*Nozzle Nodes*	*Restart*
U_{inf}=150 m/s			(m)	(m)	(m)	(μm)	(kg/m³)	(size)	
HA01	SB	$2.0U_{inf}$	0.00292	0.145	0.1175	370	950	2x2	GA01
HA02	SB	$3.0U_{inf}$	0.00292	0.145	0.1175	370	950	2x2	GA02
U_{inf}=250 m/s									
HB01	SB	$2.0U_{inf}$	0.00292	0.145	0.1175	370	950	2x2	GB01
HB02	SB	$3.0U_{inf}$	0.00292	0.145	0.1175	370	950	2x2	GB02
U_{inf}=300 m/s									
HC01	SB	$2.0U_{inf}$	0.00292	0.145	0.1175	370	950	2x2	GC01
HC02	SB	$3.0U_{inf}$	0.00292	0.145	0.1175	370	950	2x2	GC02

through which fluidization gas can pass around the sides of the jet. Two-dimensional simulations on a computer completely lack this third dimension, so no fluidization gas can pass around the jet and reach the top of the bed. Further analysis of the flow domain predicted with the simulations have shown that vortex cores around the jet region in vertical YZ planes (the ω_x vorticity) have been observed to shift from side to side (in the Z direction). Without the third dimension in the Z direction this behavior would not have been predicted.

In addition to the three-dimensional requirement the flow domain was allowed to be asymmetric. Symmetry conditions allow the computational effort to be significantly decreased because half or axisymmetric pieces of the flow domain can be studied. However, for these studies it has been found that the zones around the jet in the X direction do not show symmetric behavior on either side of the jet. Plots of the local jet X vorticity in the YZ plane, ω_x, show that the vorticity cores actually shift from side to side with bubble formation at the tip of the jet. Gas void fraction across the depth of the bed (in the Z direction) was also observed to be asymmetric. The flow domain is not symmetric and requires a full three dimensional field description with no symmetry boundary conditions imposed.

7.1.2 Discretization Scheme Comparison

As shown in the discussion on computational techniques, the choice of discretization method has a significant impact on the overall results obtained from a numerical simulation. In light of this fact several simulations were conducted to compare the results obtained from using different discretization schemes. Three different

discretization schemes were chosen for comparison: Hybrid, MINMOD TVD and Superbee TVD. A list of the simulation conditions is shown in Table 7.1.

The best way to observe the effect of discretization scheme on the simulation results is to use a qualitative comparison of the jet plume formation within the fluidized bed over several time steps. Figures 7.1-7.3 show a side-by-side comparison of the gas volume fraction iso-surface (ε_g=*0.8*) at times of 0.25, 0.5, 0.75 and 1.0 seconds of real time for jet velocities of 150, 250 and 300 m/s, respectively. Gas volume fraction iso-surfaces at ε_g=*0.8* represent the bubble and jet plume boundaries within the fluidized bed. Although flow velocities are not represented with these figures the overall behavior of the bubbles and jet plumes are well indicated.

With increases in jet velocity from 150 to 300 m/s there is an increase in jet penetration into the fluidized bed. This result is expected due to the increased momentum of the jet. One interesting observation is for Run AA01 (Hybrid) where the jet does not seem to detach from the wall but instead traces up along the wall to form a "finger" of gas out the top surface of the bed.

Characteristic of the first order Hybrid scheme (AA01, AB01, AC01) a large, diffuse mushroom shaped void forms from the tip of the jet and a trailing finger connects the top of the bed to the jet plume. No small bubbles were observed to form when using this type of discretization. The first order nature of the Hybrid scheme has previously been shown in Chapter 3 to be overly diffusive leading to a smearing of waveforms which in turn leads to a smearing of phase boundaries. This probably explains why no bubbles are seen to form when using the Hybrid scheme. Bubble boundaries are smeared

leading to large void formation due to the over diffusive nature of the Hybrid discretization scheme.

MINMOD TVD gave results similar to those obtained using the Hybrid scheme especially for jet velocities of 300 m/s, see Figure 7.3. MINMOD is also diffusive and leads to a smearing of phase boundaries. At the higher jet velocities the jet shear with the fluidized bed would be expected to be quite high leading to the entrainment of particles and subsequent formation of bubbles. A trend opposite to this was observed with these preliminary runs (AA02, AB02, AC02); very few bubbles were seen to form with increased jet velocity suggesting that the diffusive nature of the MINMOD scheme does not adequately predict bubble formation.

Superbee TVD results are shown in Figures 7.1-7.3 (runs AC01, AC02, AC03) and a distinct instability is seen forming on the initial jet plume at $t=0.25$s for all inlet jet velocities. This instability leads to the formation of three bubbles off of the initial jet plume and subsequent detachment of the jet plume from the bubbles. The long "finger" and "mushroom" bubble shapes observed with the previous two schemes were not seen with the Superbee scheme. The over compressive nature of Superbee TVD results in a sharpening of the phase boundaries. After discussion with colleagues at the University of Saskatchewan, it was decided that the Superbee TVD scheme gave results which agreed best with experimental observations.

Although it appears that the Superbee discretization scheme is the best choice of the three discretization schemes investigated, there is a tradeoff. Superbee TVD requires more computations per iteration and leads to an increase in overall computation time to produce the same number of outer iterations. To investigate this increased computational

demand a work ratio was determined by dividing the amount of real time results by the total computational time to arrive at an expression of work units. Table 7.2 lists the different CPU time demands and related work ratios for the three discretization schemes investigated. The CPU time was taken from the total processing time reported in the OUT file that is automatically generated from a CFX simulation.

Table 7.2:

CPU Demand and Discretization Scheme

Scheme	**CPU Time (s)**	**Real Time (s)**	**Work (Real s / CPU s)·10^{-5}**
Hybrid	708600	3.693	1.92
Hybrid	694200	3.353	2.07
MINMOD	257700	0.922	2.80
Superbee	411300	1.297	3.17
Superbee	423500	1.322	3.20

Based upon these values, the SUPERBEE scheme requires 1.5 times more CPU time than the HYBRID scheme for comparable real time predictions. The MINMOD scheme lies between the work demands of Hybrid and Superbee schemes.

7.1.3 Grid Refinement Studies

Care must be taken in specifying the correct grid size and number of control volumes used to define the nozzle inlet boundary condition. Several runs were conducted to study the effect of mesh density and nozzle boundary condition control volume density. These runs are summarized in Table 7.1. Gas continuity error, or residual, was chosen as the basis for comparison; validation of the different grid densities investigated and continuity

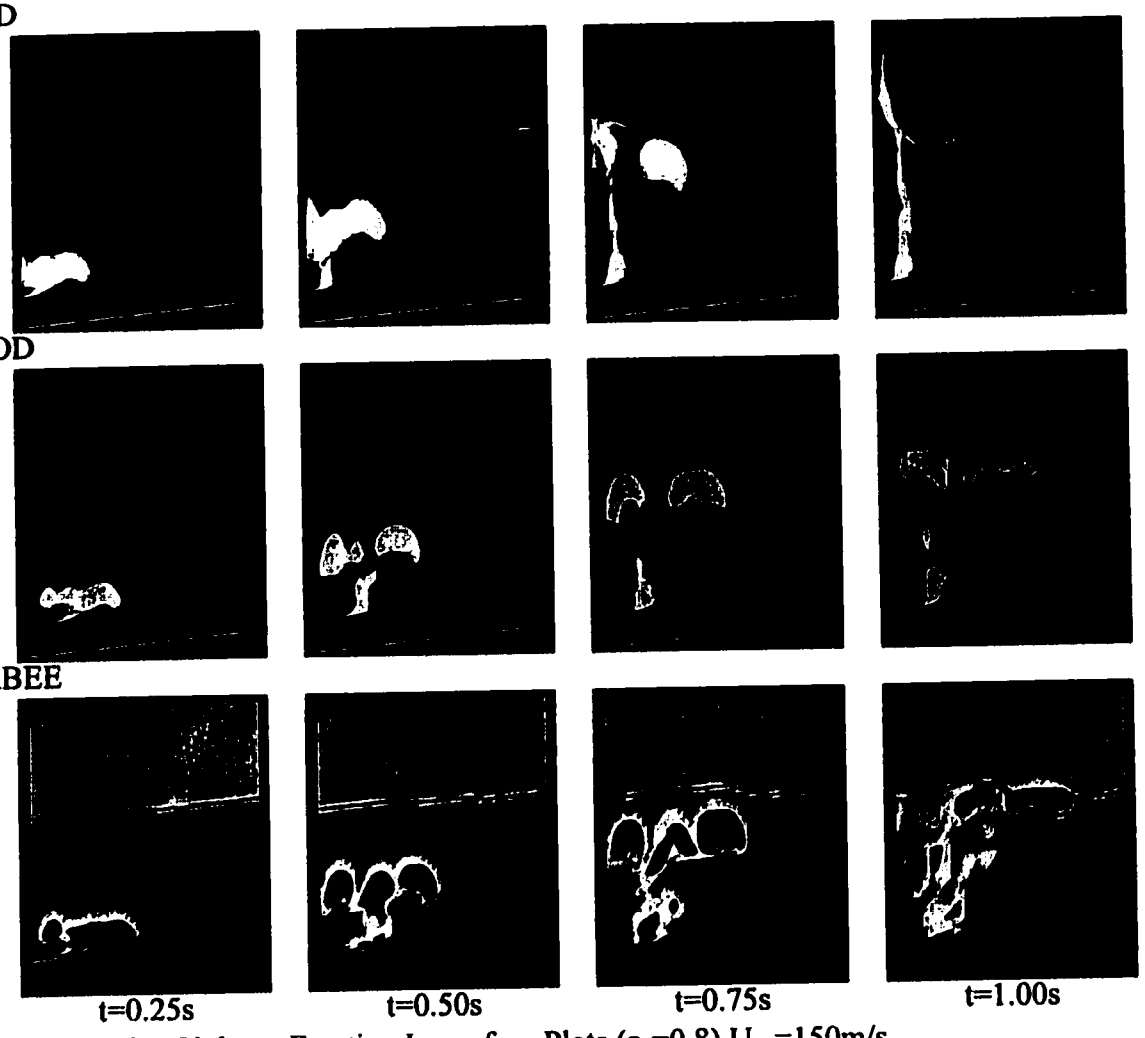

Figure 7.1: Time Series Gas Volume Fraction Isosurface Plots (ε_g=0.8) U_{jet}=150m/s

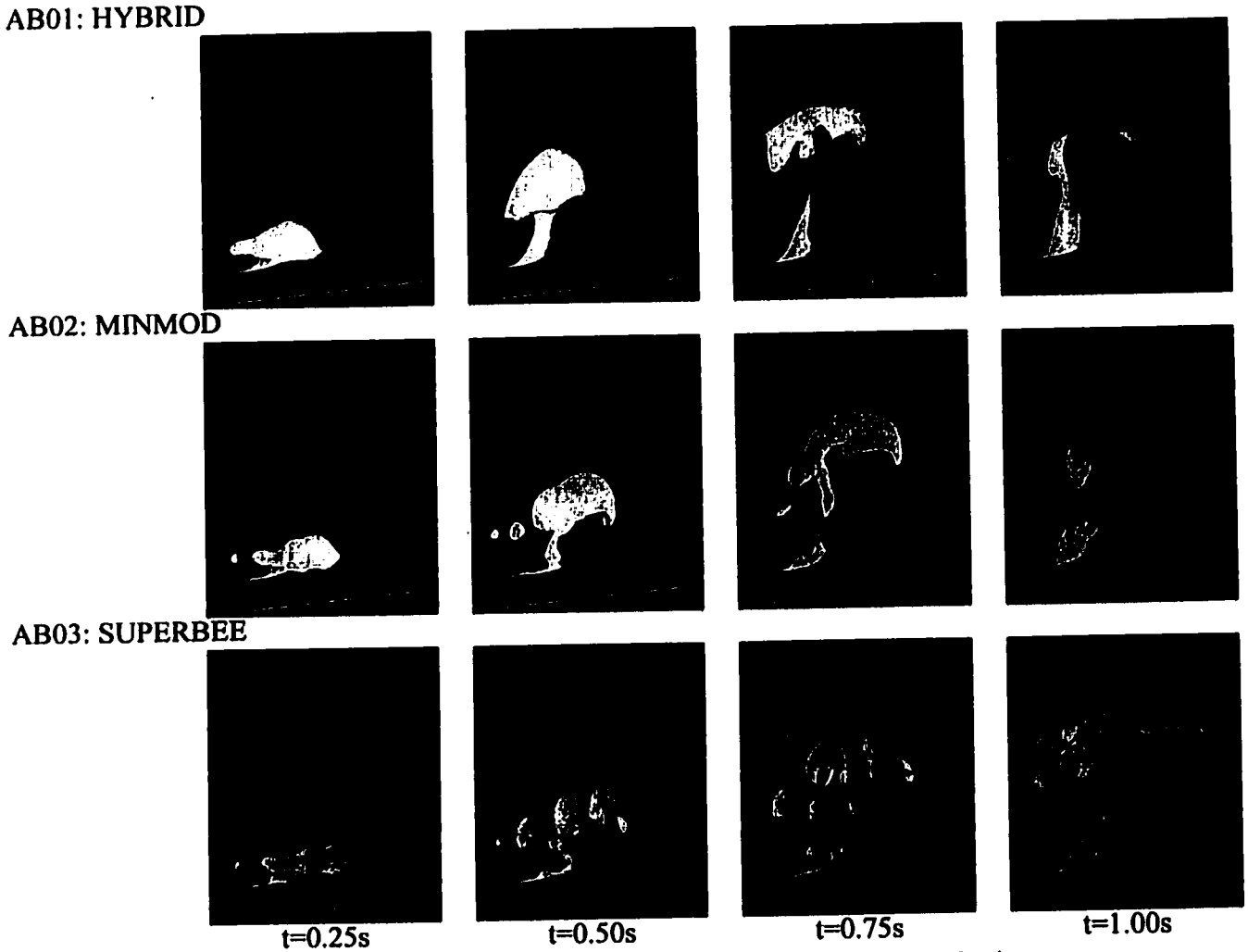

Figure 7.2: Time Series Gas Volume Fraction Isosurface Plots (ε_g=0.8) U_{jet}=250m/s

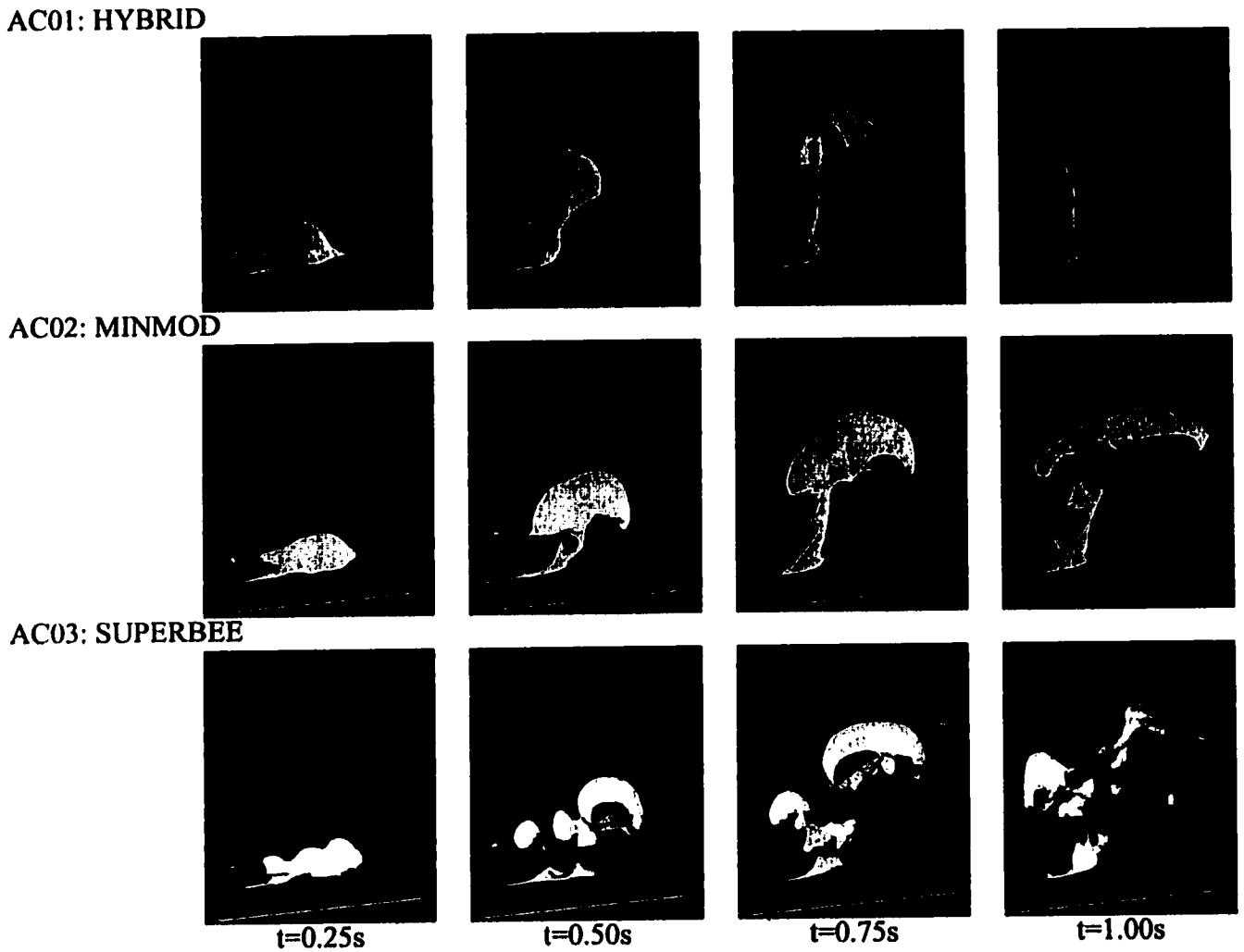

Figure 7.3: Time Series Gas Volume Fraction Isosurface Plots (ε_g=0.8) U_{jet}=300m/s

residuals are presented for runs up to series DC02. Simulations with very fine grids were too costly to generate results for comparison. Simulations for this study were allowed to run for approximately three seconds of real time and comparisons of the residuals were made after the first 1.5 seconds of real time. By comparing results from this time onwards it is expected that any flow instabilities due to initial condition specification have been minimized and the simulations are running in a "steady-state" condition, for further comments about "steady-state" assumption please see section 7.2.5 describing the solids flow patterns with time. The comparison of the gas continuity residuals allows a verification of the model results but does not provide meaningful physical predictions. The aim of this section is to provide a comparative basis on which the grid densities can be contrasted to determine the best and most economical grid density to use for simulations. Comparison of the continuity residuals between different runs should ensure that the numerical schemes are verified between different mesh densities. This analysis assumes that any errors on the coarse grids are decreased by increasing grid density.

Another concern that arose with these simulations is the specification of the nozzle inlet boundary condition. Since the nozzle orifice is small relative to the overall dimensions of the reactor, it is very important to ensure that a smooth grid density variation is realized close to the nozzle orifice. From an economics point of view it is most desirable to have a single control volume for specifying the nozzle inlet boundary condition to minimize the number of control volumes in the entire flow domain resulting in faster production of results. However, a single control volume leads to problems when interpolating and discretizing the derivatives of the transport quantities close to the nozzle orifice, see section 4.2 for a discussion of interpolating convective properties at control

volume boundaries. To investigate the influence of control volume number used to specify the nozzle inlet boundary condition three different schemes were set up and solved using identical solver settings. Nozzle inlet boundary conditions were specified using different numbers of control volumes; these three different orifice boundary conditions used 1 x 1, 2 x 2 and 3 x 3 control volumes. Column one in Figure 7.4 shows the three different mesh densities used to specify the nozzle inlet boundary condition; the nozzle orifice is shown by the central gray area. X's on the mesh lines represent the locations of the control volume boundaries at which point the velocity components are interpolated for use in the discretization scheme (see Chapter 4). For the 1 x 1 control volume it can be seen that the interpolated values occur only at four locations; therefore, the interpolated values are based on the central value (directly in the center of the gray square which would represent the desired jet velocity at that point) and from values from outside of the jet boundary condition (i.e. values that don't have anything to do with the desired jet inlet velocity boundary condition). The 2 x 2 control volume specification of the nozzle inlet boundary condition is better because more control volumes are used within the jet inlet boundary condition for the interpolations; the same argument applies for the 3 x 3 specification and even finer grids.

The additional two columns in Figure 7.4 show the horizontal gas phase jet velocity over the width of the bed (in the Z direction) exactly at the nozzle orifice outlet and at a position slightly to the right of the nozzle but at the same elevation as the nozzle. The 1 x 1 nozzle orifice control volume specification is not adequate for specifying the jet inlet velocity and does not even allow the correct velocity to be specified. In this case the maximum interpolated velocity for the 1 x 1 nozzle boundary condition is only about

80 m/s – much smaller than the required boundary condition of 250 m/s. This problem is due to the fact that the jet velocity at that point is based on interpolated values outside of the jet boundary condition. A slight improvement is realized with the 2 x 2 nozzle boundary condition with a velocity spike of 250 m/s located directly at the center of the nozzle boundary condition. A more realistic jet velocity profile is seen with the 3 x 3 nozzle boundary condition. The more control volumes used to specify the nozzle inlet boundary condition will lead to better definition of the initial jetting region into the fluidized bed. It must be remembered, however, that there is a minimum control volume size below which the two fluid continuum model breaks down, see section 3.4.3, Chapter 3. Additionally the increased resolution of the nozzle boundary condition in the Z direction leads to a dramatic increase in the total number of control volumes used in the entire computational domain by adding on another layer of control volumes in the XY plane. Considering the 1 x 1 control volume specification for the nozzle boundary condition it can be concluded that the 1 x 1 control volume for the nozzle inlet boundary condition is not acceptable.

Figures 7.5 to 7.12 are plots of the gas continuity residuals for the simulations on the related meshes with nozzle control volume densities as shown in Table 7.1. These figures show the absolute residual for each of the inner iterations; outer iterations occur when the residuals spike sharply upwards. As expected in Figure 7.5 for run DA01 the residuals show a random pattern in their reduction suggesting that the grid is too coarse to capture the flow phenomena between outer iterations (i.e. between each time step) and as such the data being provided for the next time step is poor. A slight improvement is

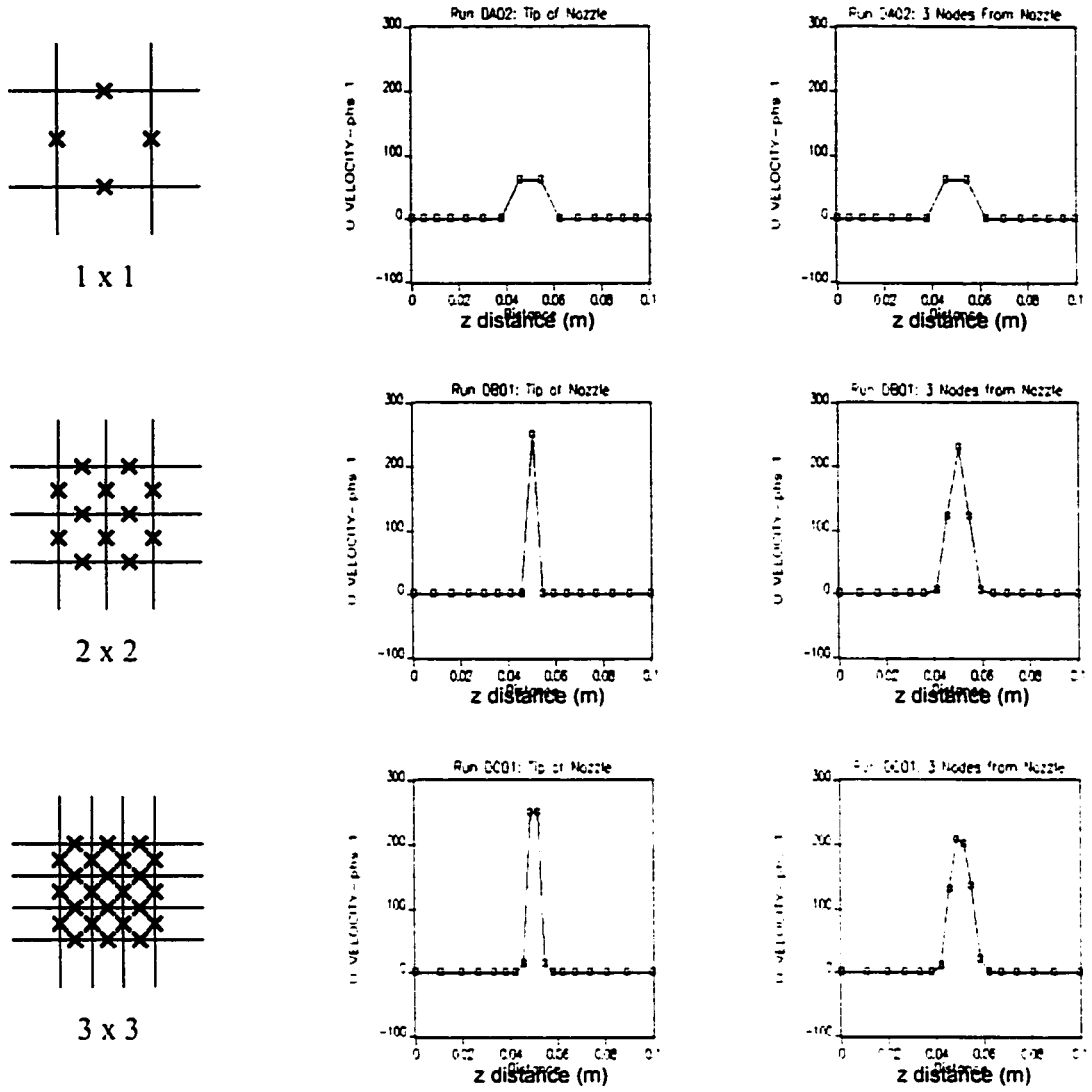

Figure 7.4 – Nozzle inlet boundary control volume specification and jet velocity.

realized with run DA02; however, the residuals still do not show a consistent reduction. These problems might be compounded by the specification of a 1x1 control volume for the nozzle inlet boundary condition. Residual reduction for run DA04 shows the best type of reduction for the first set of simulation results; however, it must be remembered that the nozzle inlet patch is only specified as a 1 x 1 control volume making the use of the mesh in DA04 unacceptable.

Figures 7.9 and 7.10, runs DB01 and DB02 show a marked improvement in residual reduction with iteration; however, contrary to expected CFD experience the increased mesh density of DB02 lead to a flattening out of the residual profile with iteration. These effects are even more pronounced for runs DC01 and DC02 where the tail becomes quite long and residual reduction falls to below one order of magnitude for every 20 iterations performed. The increased resolution of the nozzle inlet boundary condition for these runs at 3 x 3 control volumes might lead to problems when changing from the very fine mesh within the nozzle boundary condition to the coarser mesh used above the nozzle orifice.

Based on these studies it was decided that a nozzle inlet boundary condition of 2 x 2 control volumes is sufficient to properly specify the inlet jet gas velocity. A mesh of approximately 50,000 nodes is sufficient to capture flow detail without being overly computationally expensive and produces control volumes of sizes that are still valid for the two fluid continuum model.

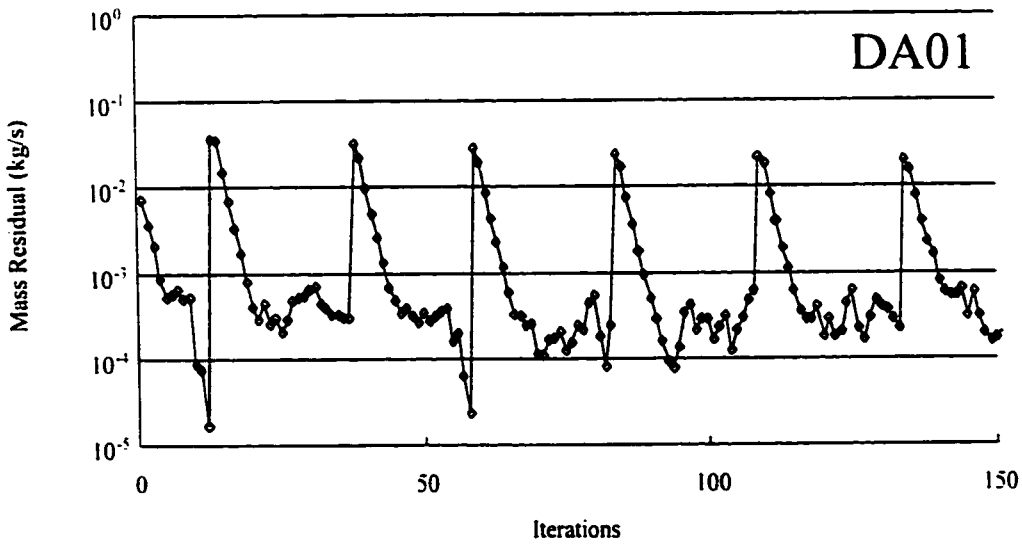

Figure 7.5 - Gas mass residuals versus iteration count for run DA01.

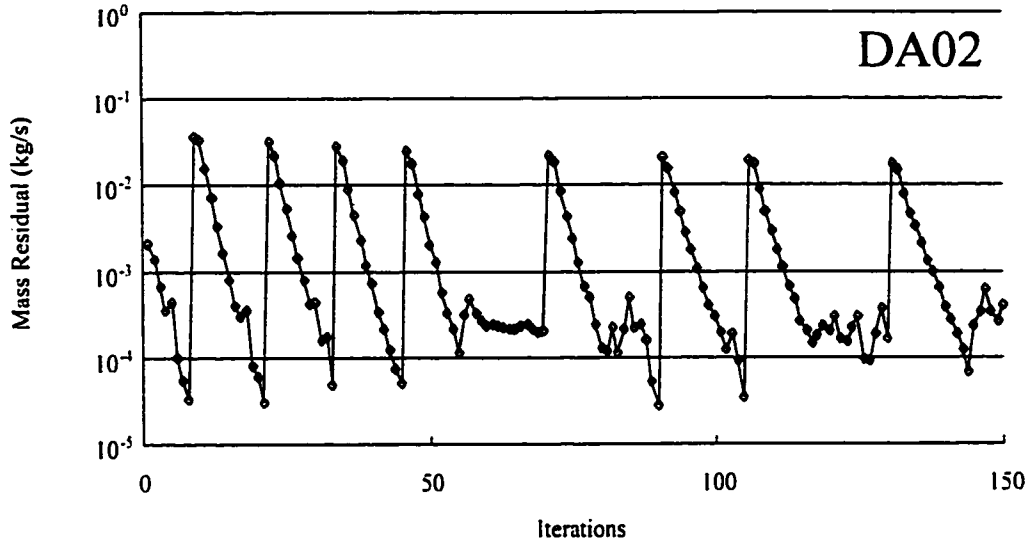

Figure 7.6- Gas mass residuals versus iteration count for run DA02.

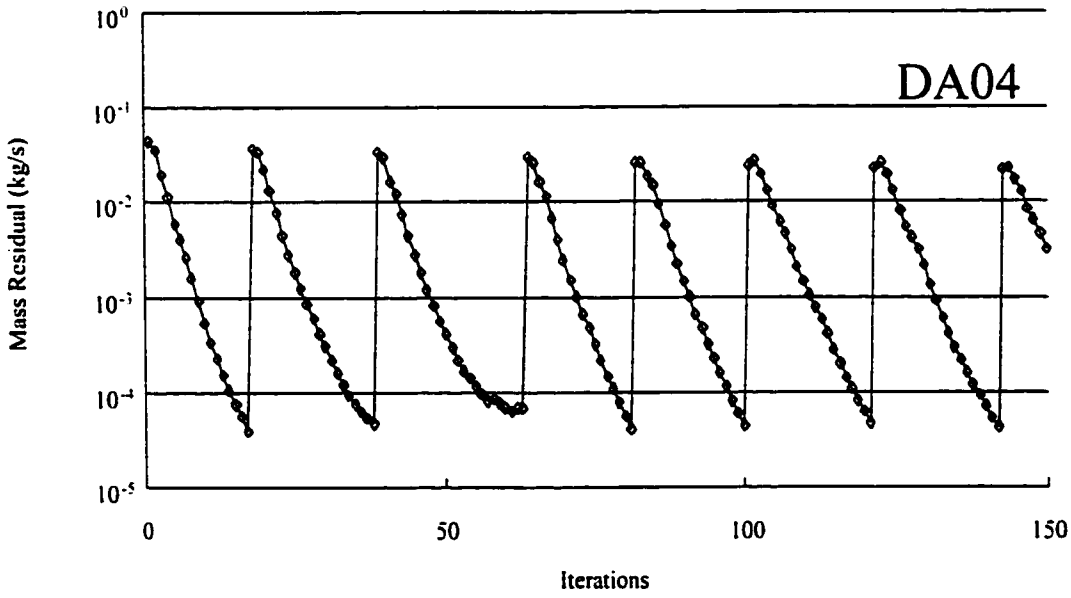

Figure 7.7- Gas mass residuals versus iteration count for run DA04.

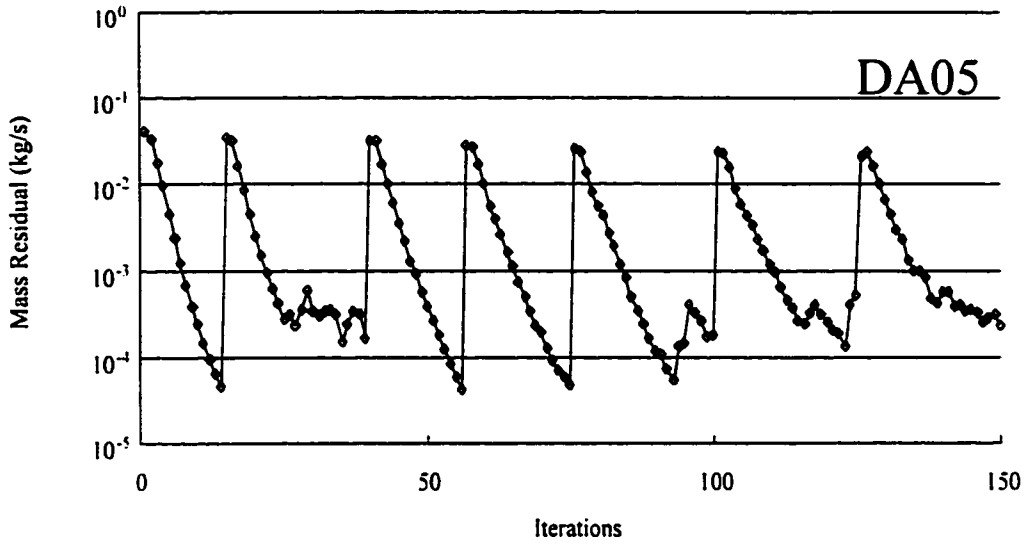

Figure 7.8- Gas mass residuals versus iteration count for run DA05.

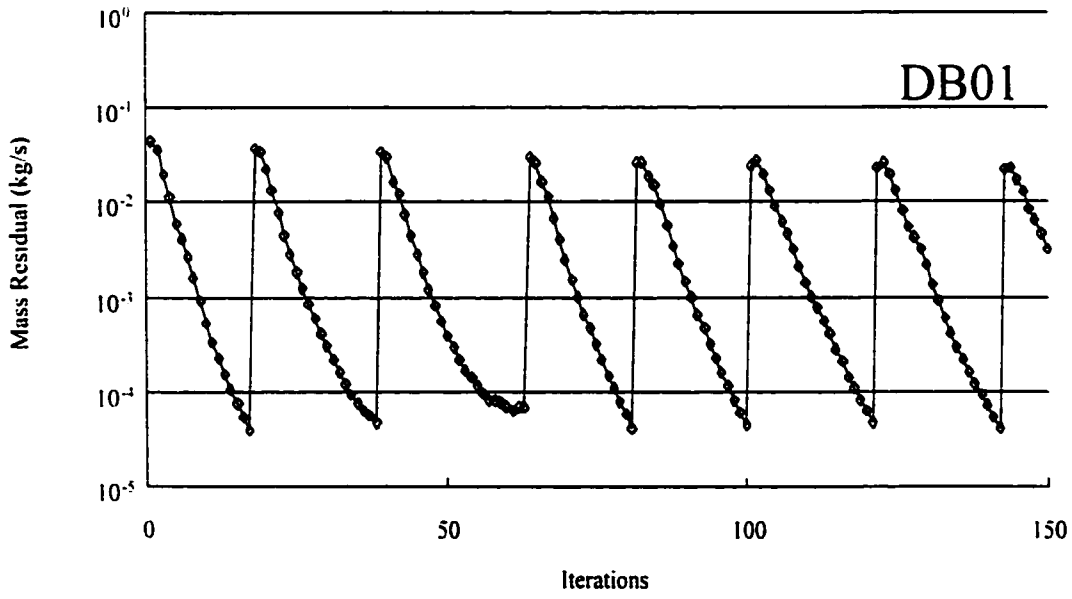

Figure 7.9- Gas mass residuals versus iteration count for run DB01.

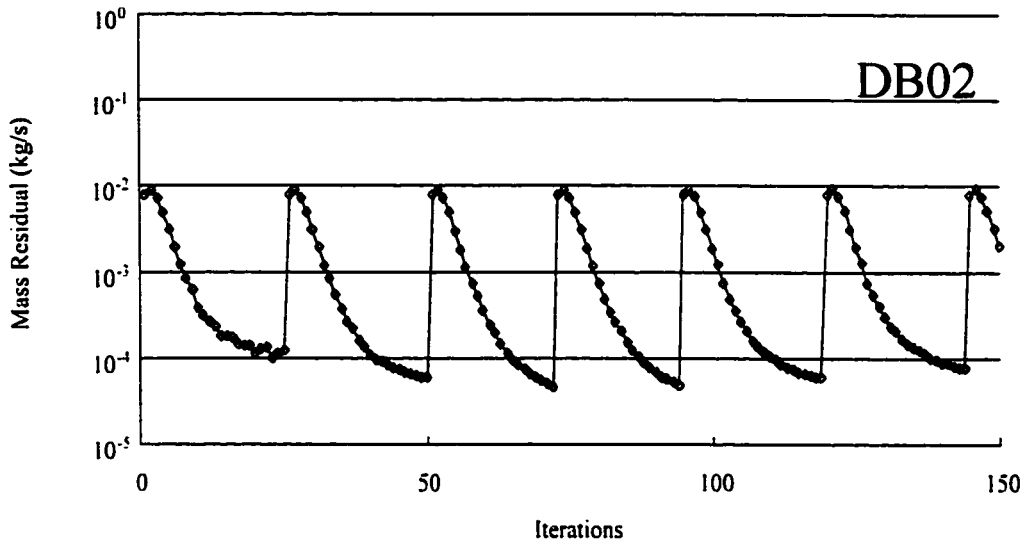

Figure 7.10- Gas mass residuals versus iteration count for run DB02.

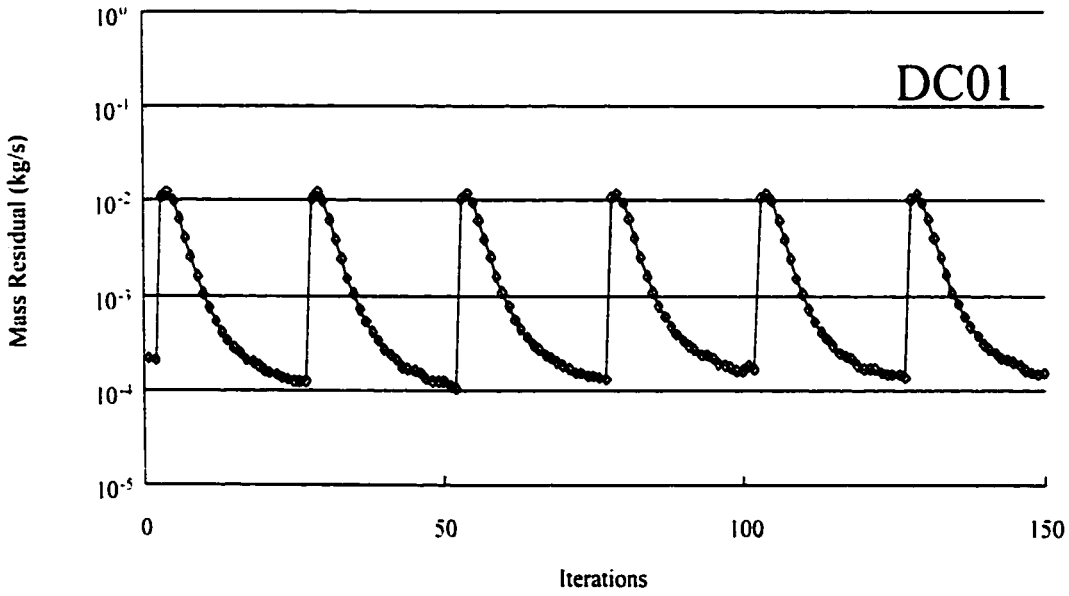

Figure 7.11- Gas mass residuals versus iteration count for run DC01.

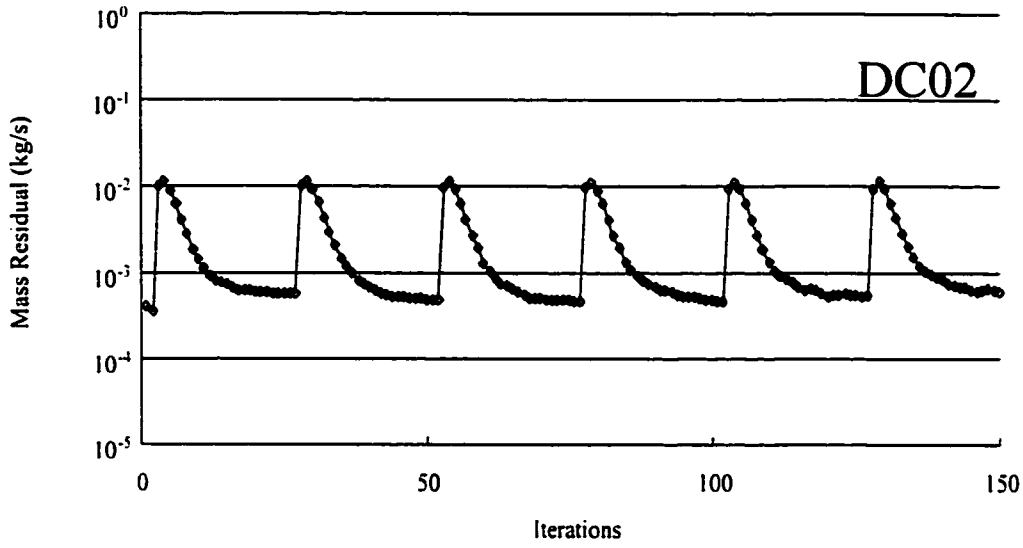

Figure 7.12 - Gas mass residuals versus iteration count for run DC02.

Additional physical arguments can be made as a further comparison of the validity of the grid density used in the simulations. The jet velocity is known and can therefore be interpreted based on the vorticity field that can be calculated from the curl of the velocity field. Figure 7.13 shows the expected vorticity field to be generated around the jet as it issues into the fluidized bed. By relating the strength of the vorticity in each of the coordinate planes and measuring the distance between the vortex cores the Biot-Savart law can be applied to calculate the induced velocity field which should be present centrally between the vortex cores. This comparison offers benefits over the velocity field as a region average of the vorticity can be used to infer the velocity field – only a single value will be used to calculate the jet velocity. The vorticity field thus calculated should be a good representation of the jet velocity condition if the mesh density is sufficient to transport the vorticity information into the surrounding nodes.

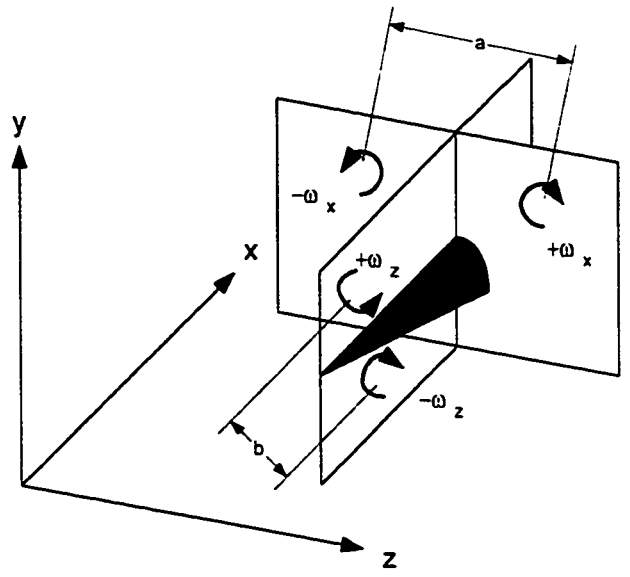

Figure 7.13 – Generalized sense of vorticity in the near jet region.

Table 7.3 summarizes the vorticity contributions calculated for each of the planes shown in Figure 7.13. With much finer grids a secondary vorticity pattern was observed to form near the jet region. In addition to the $\pm\omega_x$ contributions causing the jet to deflect upwards a secondary set of smaller vortices on the top of the jet were observed; these secondary structures are shown in Figure 7.14.

Table 7.3

Vorticity In the Near Jet Region

Run	$+w_x$	$-w_x$	*u (m/s)*	$+w_y$	$-w_y$	*v (m/s)*	$+w_z$	$-w_z$	w (m/s)
DA01	-1.16	1.14		-2.40	2.61		-1.16	1.14	
DA02	-1.04	1.10		-4.81	4.82		-1.04	1.10	
DA04	-0.93	0.91		-24.57	24.57		-0.93	0.91	
DA05	-1.14	1.17		-4.44	4.47		-4.83	5.36	
DB01	-0.50	0.44		-28.73	28.70		-15.00	12.42	
DB02	-0.12	0.11		-26.84	26.84		-13.56	11.76	
DC01	-0.09	0.10		-43.08	44.60		-36.27	43.96	
DC02	-0.21	0.21		-40.51	40.51		-33.52	39.48	

The vortex pair atop of the jet induces a net downward velocity while the vortex pair below the jet induces a net upward velocity. Secondary vortices were observed in simulations DA04, DA05 (very slightly for both of the previous runs), DB01, DB02, DC01 and DC02. After looking at these runs at a time of 0.35 seconds and then comparing the results for a much later time in the simulations, it can be assumed that these secondary vortex structures might actually be start up phenomena; however, it is important to note that for very coarse grids these secondary vortex structures were not predicted.

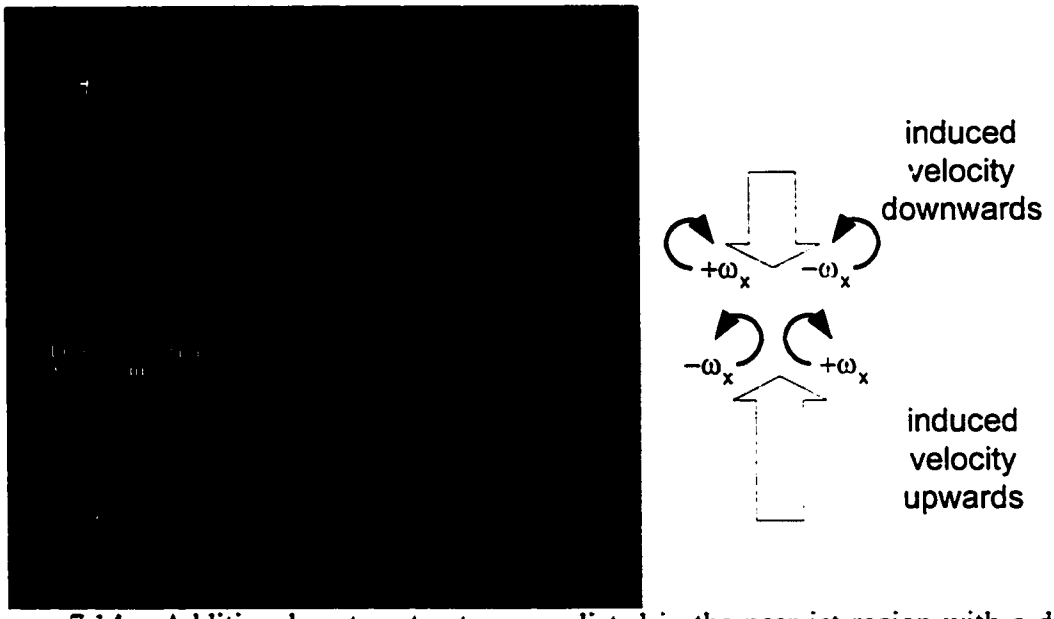

Figure 7.14 – Additional vortex structures predicted in the near jet region with a dense computational mesh.

7.1.4 Sensitivity Analysis: Continuous Phase Pressure Removed from Solids Momentum Equation

Several different formulations for the governing hydrodynamic equations for multiphase flow can be formulated and have been discussed in Chapter 3. Hydrodynamic model A was used for all of the simulations in this study with the exception of those runs

in this section which follow the formulation of hydrodynamic model B. Hydrodynamic model A includes the continuous phase pressure (gas phase) in the dispersed phase (solids) momentum equation whereas hydrodynamic model B does not include the continuous phase pressure in the dispersed phase momentum equation. Simulations for this study are listed in Table 7.1. Please note that the nozzle inlet boundary was specified as 1 x 1 to allow for fast solutions. Although this does not provide results of physical significance it does provide a set of data for model verification.

Figure 7.15 shows a series of gas phase volume fraction plots over a series of time steps for simulations EA01 and DA01 (Model B and Model A) in the first and second columns, respectively. These side-by-side pictures allow a qualitative comparison of the predicted jet plume results from the simulations using Model B and Model A. Results for the first 0.50 s of real time (500 outer iterations; Figure 7.15 a-b) appear to give results which are in good qualitative agreement with each other. However, some slight differences are discernible after 0.75 s of real time solution results with discrepancies in the surface of the fluidized bed surface. Although there are slight differences between the simulation results from Model A and Model B they do not appear to be significant for this simulation study. Based on this analysis all of the simulations were continued with the hydrodynamic Model A with the inclusion of the continuous phase pressure in the solids momentum equation.

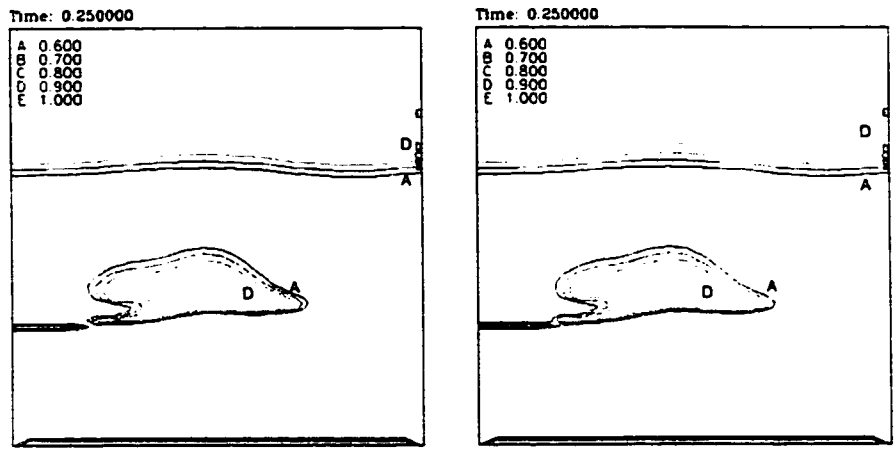

Figure 7.15 a) - Comparison of hydrodynamic model B (left) and model A (right). Plot of gas volume fraction contours, t=0.25 s.

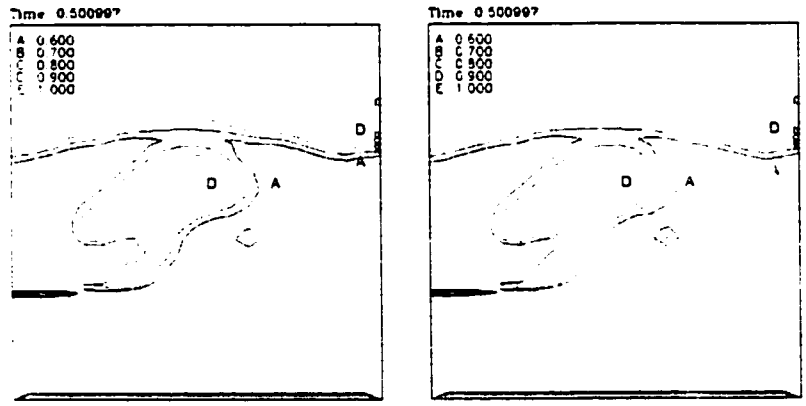

Figure 7.15 b) - Comparison of hydrodynamic model B (left) and model A (right). Plot of gas volume fraction contours, t=0.50 s.

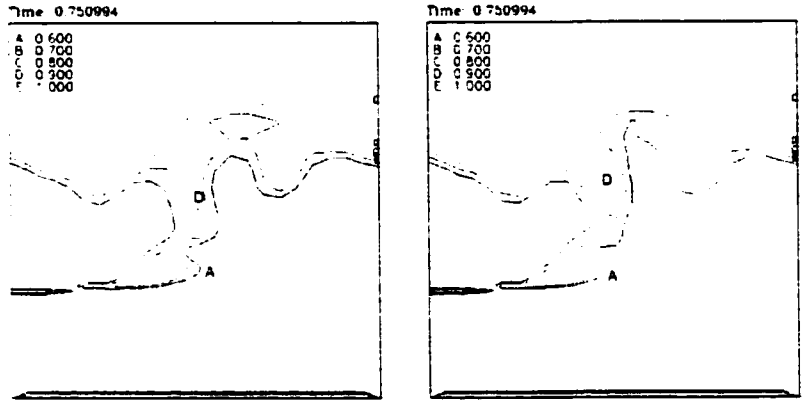

Figure 7.15 c) - Comparison of hydrodynamic model B (left) and model A (right). Plot of gas volume fraction contours, t=0.75 s.

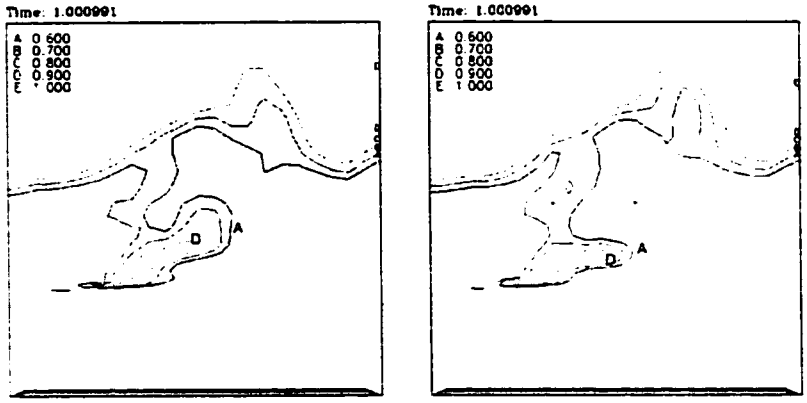

Figure 7.15 d) - Comparison of hydrodynamic model B (left) and model A (right). Plot of gas volume fraction contours, t=1.00 s.

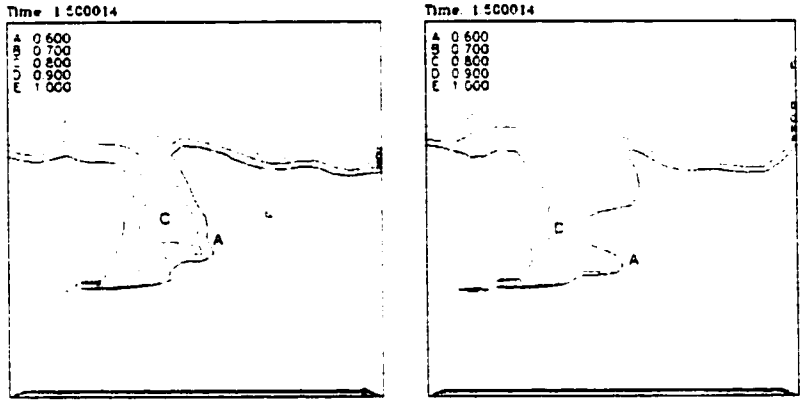

Figure 7.15 e) - Comparison of hydrodynamic model B (left) and model A (right). Plot of gas volume fraction contours, t=1.50 s.

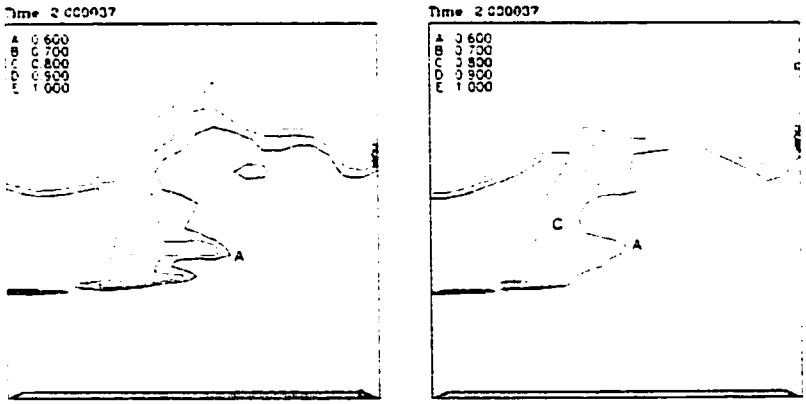

Figure 7.15 f) - Comparison of hydrodynamic model B (left) and model A (right). Plot of gas volume fraction contours, t=2.00 s.

7.1.5 Solids Pressure Sensitivity Analysis

Solids pressure is included in the solids momentum equation as a source to ensure that the solids volume fraction does not reach impossibly high values, see section 3.3.3. Most simulations in this study have used the correlation G_1 of Bouillard *et al.* (1989) see Figure 3.3, page 52. The results in this section are for the correlation of Ettehadieh *et al.* (1984) which is very similar to that used by Benyahia *et al.* (1997), relation number 6 Figure 3.3, page 52. Figure 3.3 shows that each of these functions adds a solids repulsion force as the solids volume fraction increases to a maximum packing fraction; however, the expression of Benyahia *et al.* (1997) has a more gradual affect over a wider range of volume fraction. The correlation of Bouillard *et al.* (1989) rapidly increases for solids volume fractions approaching the maximum packing fraction. It is expected that the Benyahia *et al.*(1997) correlation used for the studies in this section will lead to an increase in the number of voids predicted because of the wider range of solids volume fraction that the correlation takes effect. As the solids volume fraction increases the solids pressure or repulsive forces will increase leading to a condition that prefers gas void formation. The simulations in this set of experiments have used a 2 x 2 nozzle inlet boundary condition; however, since the constitutive relationship for the solids pressure has been altered these results must be considered only to be a set of verification test cases.

In order to be able to compare the complex flow phenomena and how the solids pressure function might be affecting the results it is necessary to determine some measurable quantity. For these simulations the flow domain was broken into four regions and the solids circulation was calculated based on each of these regions. The circulation

will give some sense of solids residence time in each of the zones. A summation of the magnitude of the particular vorticity contribution was determined for said regions within the flow domain. This pseudo-circulation for the solids can be used as a direct comparison of the solids type residence time within the reactor.

Many of the overall flow patterns were similar for the different solids pressure functions; however, at higher aeration rates there was a definite difference in the formation of bubbles. Jet penetrations did not seem to be affected by the use of the different solids pressure functions.

A series of time animations of the simulations for both Gxxx and Hxxx series were compared side by side to study the effect of the solids pressure function on the production and propagation of bubbles. Iso-surfaces of gas volume fractions 0.8 and 0.7 were plotted on the same animations to study how the voids formed and propagated through the bed.

Comparison of GC01 (Bouillard) with HC01 (Benyahia): Jet plume formation and penetration into the fluidized bed are both predicted equally well with both solids pressure expressions. However, there is a significant difference in the bubble behavior predicted from each of these two different simulations. Bubbles predicted with the GC01 simulation tended to be small and sharp in shape with pointed vertices. Bubbles predicted with simulation HC01 showed coalescing behavior forming larger bubbles above the jet plume boundary. The bubbles predicted with this simulation were round or cap shaped and distributed fairly evenly above the plane of the jet.

Comparison of GB02 and HB02: Both simulations appear to give similar results for jet penetration and plume shape into the fluidized bed. The top surface of the bed also

appears to be similar in shape, position and surface disturbances. One of the differences is in the formation and shape of bubbles above the jet zone. For simulation GB02 with the solids pressure expression of Bouillard *et al.* (1989) G_l the bubbles appear to be oblong in shape with major axis parallel to the X axis. The bubbles also have a more jagged or pointed shape at their vertices. Bubbles predicted with the HB02 simulation tend to be rounder, more numerous and more evenly spread above the jet plume within the fluidized bed.

7.1.6 Summary of Numerical Studies

These numerical studies were used to investigate the CFX 4.2 solver options. Based on these results the settings for the physical predictions were determined. A description of the solver settings has already been covered in Chapter 5. In order to maintain reasonable solution accuracy and solution time a discretization mesh of approximately 50,000 nodes is created for the simulations. The nozzle inlet boundary condition is specified using a 2 x 2 control volume. It is felt that this boundary condition is large enough to represent the inlet flow conditions through the nozzle orifice without increasing the grid density and computational expense. The discretization scheme should be the Superbee TVD scheme and implemented on a completely three-dimensional grid with no symmetry assumptions.

For these simulations there was no noticeable qualitative difference between the use of hydrodynamic model A or hydrodynamic model B. However, the use of a different solids pressure function does seem to have an impact on the bubbling behavior especially with aeration rates higher than minimum fluidization. The expression of Bouillard *et al.* (1989) has been observed to produce fewer bubbles than the expression of

Ettehadieh *et al.* (1984) when used with similar geometry, grid spacing and model set up conditions. Further work needs to be done in classifying which relationships to use for specific multiphase simulations.

7.2 Part II: Physical Predictions

Now that studies for the effect of the choice of numerical scheme, hydrodynamic model and mesh refinement have been completed it is possible to continue with analysis of results for predicting real physical behavior. Simulations were carried out to study the effect of nozzle submergence and insertion, the effect of fluidization velocity, and tests under similar experimental operating conditions. All of the simulations used for the physical predictions are listed in Table 7.4. The standard four character simulation identification scheme has been used.

7.2.1 Tests Below U_{mf}

Simulations run at aeration velocities less than U_{mf} were conducted to determine whether the present simulation models could cope with these different operating conditions. Simulations using $0.5U_{mf}$ produced results which agree well with literature predictions of how the jet behavior should change; however, simulations using zero fluidization velocity proved difficult to achieve acceptable converge on the gas continuity residual. This simulation set is listed in Table 7.4 under the Cxxx series.

Description of run CA01: Contour plots of gas volume fraction at $\varepsilon_g=0.8$ provided information about the surface of the bed and bubble formation from the tip of the nozzle. Predominantly the surface of the bed decreased slightly with a decrease in fluidization velocity. Bubbles only present above the jetting region and not in the bulk of the bed – also expected for a lower aeration rate. Bubbles grew in size when rising up through the

bed. Less bed material above the bubble leads to a decrease in pressure thereby decreasing the pressure constraining the bubble resulting in an increase in bubble size with distance from the distributor. Bed surface heights above the distributor were measured and plotted against time to observe transient behavior. Unfortunately the formation and explosion of bubbles out of the surface of the bed and into the freeboard area lead to skewed data for the bed surface. While most of the surface of the bed remained at a fixed level, the bubbles over top of the jet tended to increase the overall average bed height. This problem can be averted somewhat by averaging only those values to the right of the bubble zone. Figures 7.16 and 7.17 show bed heights over time as the fluidization gas is halved and then set to zero. Data for the CCxx series of runs was no longer available. Each graph shows that the average bed height decreased for approximately 1.5 seconds as the effects of the reducing the aeration rate to $0.5U_{mf}$ are propagated throughout the bed. On the average the bed surface level is decreasing in height but there are several upsets where the bed level appears to increase. These upsets are caused by the ejection of bubbles out of the top of the bed surface leading to an increase in the bed surface height where the bubble escapes and deforms the bed surface. These upsets are larger for run CB01 relative to run CA01 because the jet velocity in CB01 is 100 m/s faster than that in CA01 leading to an increased gas flux and greater voidage being injected into the fluidized bed. When the fluidization gas was decreased to half minimum fluidization both of the bed surfaces for runs CA01 and CB01 decreased by approximately 6 cm. The bed surface for run CA01 settled to a height of approximately 70 cm while the bed surface for simulation CB01 settled to a height of 73 cm. This difference in bed heights can be explained based on the amount of gas that is

Table 7.4: Physical Predictions Simulation Summary

Bxxx series: Insertion and Submergence Tests								
CFD Run	Scheme	U_f	D_o	S	I	D_p	ρ_p	*Nozzle CVs*
U_{inf}=250 m/s			(m)	(m)	(m)	(μm)	(kg/m³)	(size)
BA01	SB	U_{mf}	0.0099	0.25	0.10	370	1450	2x3
BA02	SB	U_{mf}	0.0099	0.25	0.15	370	1450	2x3
BA03	SB	U_{mf}	0.0099	0.2	0.10	370	1450	2x3
BA04	SB	U_{mf}	0.0099	0.2	0.15	370	1450	2x3

Cxxx series: Tests Below U_{mf}										
CFD Run	Scheme	U_f	D_o	S	I	D_p	ρ_p	*Nozzle CVs*	t_{start}	t_{end}
U_{inf}=150 m/s			(m)	(m)	(m)	(μm)	(kg/m³)	(size)	(s)	(s)
CA01	SB	0.5U_{mf}	0.0099	0.145	0.1175	370	1450	2x2	1.45	4.40
CA02	SB	0.0	0.0099	0.145	0.1175	370	1450	2x2	4.45	5.10
U_{inf}=250 m/s										
CB01	SB	0.5U_{mf}	0.0099	0.145	0.1175	370	1450	2x2	1.35	4.17
CB02	SB	0.0	0.0099	0.145	0.1175	370	1450	2x2	4.2	4.87
U_{inf}=300 m/s										
CC01	SB	0.5U_{mf}	0.0099	0.145	0.1175	370	1450	2x2	1.3	4.1
CC02	SB	0.0	0.0099	0.145	0.1175	370	1450	2x2	4.1	5.0
CC03	SB	0.25U_{mf}	0.0099	0.145	0.1175	370	1450	2x2	4.1	5.0

Fxxx series: Tests Above U_{mf}								
CFD Run	Scheme	U_f	D_o	S	I	D_p	ρ_p	*Nozzle CVs*
U_{inf}=150 m/s			(m)	(m)	(m)	(μm)	(kg/m³)	(size)
FA01	SB	2.0U_{mf}	0.0099	0.145	0.1175	370	1450	2x2
FA02	SB	3.0U_{mf}	0.0099	0.145	0.1175	370	1450	2x2
U_{inf}=250 m/s								
FB01	SB	2.0U_{mf}	0.0099	0.145	0.1175	370	1450	2x2
FB02	SB	3.0U_{mf}	0.0099	0.145	0.1175	370	1450	2x2
U_{inf}=300 m/s								
FC01	SB	2.0U_{mf}	0.0099	0.145	0.1175	370	1450	2x2
FC02	SB	3.0U_{mf}	0.0099	0.145	0.1175	370	1450	2x2

Gxxx series: Runs Conforming to Experimental Operating Conditions								
CFD Run	Scheme	U_f	D_o	S	I	D_p	ρ_p	*Nozzle CVs*
U_{inf}=150 m/s			(m)	(m)	(m)	(μm)	(kg/m³)	(size)
GA01	SB	2.0U_{mf}	0.00292	0.145	0.1175	370	950	2x2
GA02	SB	3.0U_{mf}	0.00292	0.145	0.1175	370	950	2x2
U_{inf}=250 m/s								
GB01	SB	2.0U_{mf}	0.00292	0.145	0.1175	370	950	2x2
GB02	SB	3.0U_{mf}	0.00292	0.145	0.1175	370	950	2x2
GB03	SB	3.0U_{mf}	0.00292	0.145	0.1175	370	950	2x2
U_{inf}=300 m/s								
GC01	SB	2.0U_{mf}	0.00292	0.145	0.1175	370	950	2x2
GC02	SB	3.0U_{mf}	0.00292	0.145	0.1175	370	950	2x2
GC03	SB	3.0U_{mf}	0.00292	0.145	0.1175	370	950	2x2

being injected by the gas feed jet. For run CA01 the jet velocity is 150 m/s while for run CB01 the jet velocity is 250 m/s. The additional gas being injected for CB01 will augment the fluidization gas and cause the surface of the bed to be at a higher level than for run CA01 due to increased bed voidage.

A vertical line was drawn in both figures at the time when the fluidization gas was set to zero; from this point onwards the bed is no longer fluidized and operates as a packed bed. Unfortunately due to the short duration of the runs at zero fluidization the transient effects of turning off the fluidization gas have probably not been transmitted into the bulk of the bed and the simulation results are showing transition behavior. No meaningful observations can be drawn about the steady state behavior of the predicted bed behavior. It is not possible to tell how the bed surface decreases with no aeration. Observations of the predicted flow field just above the jet plume for zero fluidization show that large bubbles are no longer present within the packed bed. A large jet plume region forms from the nozzle orifice and smaller bubbles occasionally break off of the jet plume and propagate up to the surface of the bed. Observations of the experimental apparatus at the UofS under similar operating conditions show that the packed bed condition does not allow the formation of bubbles. Gas from the jet tends to form a void which carves the bulk bed phase and occasionally the bed would collapse in on this void forming a funnel region from the top of the bed to the jet plume.

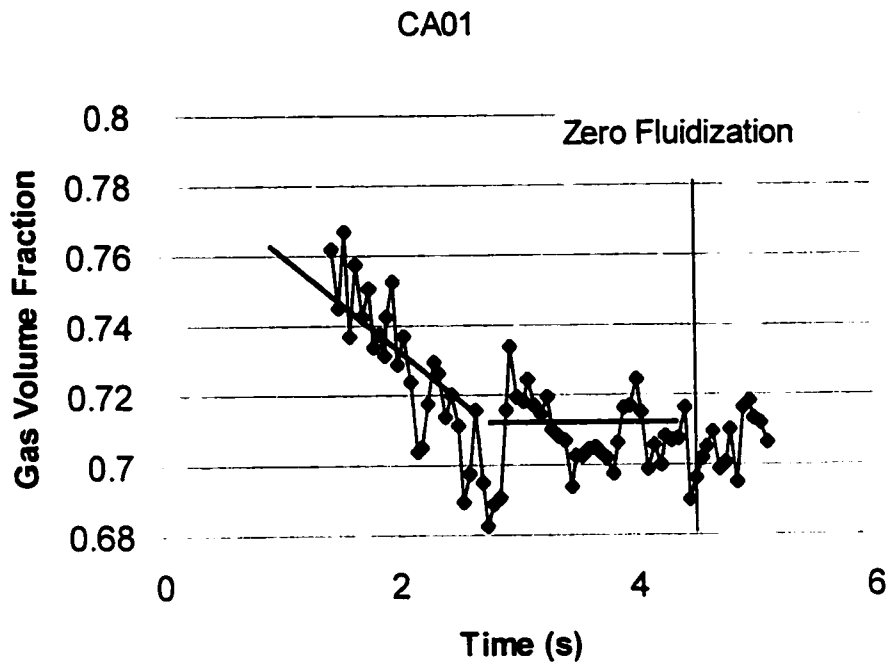

Figure 7.16 – Bed surface height over time for run CA01.

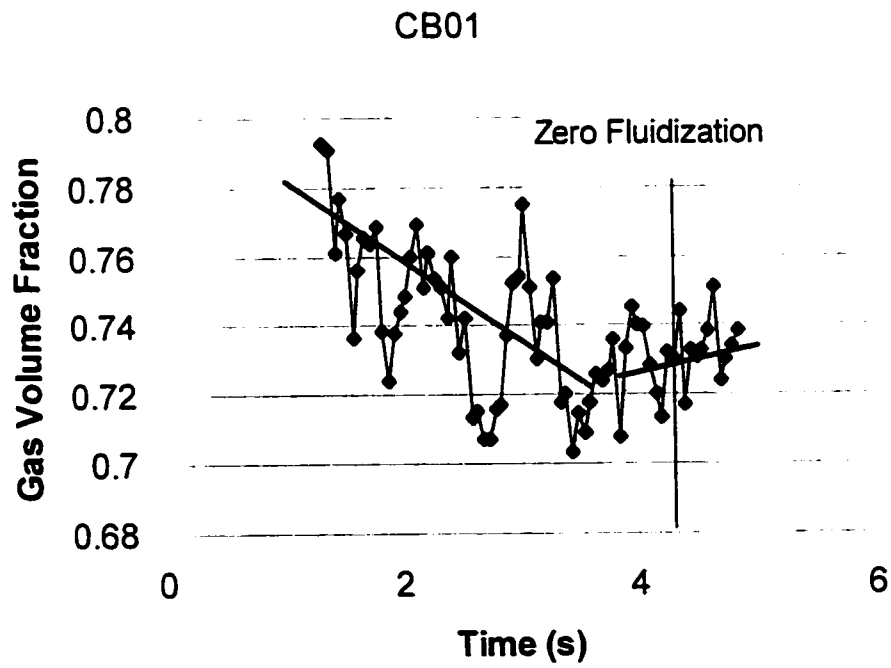

Figure 7.17 – Bed surface height over time for run CB01.

Additional insight into flow development with decreasing fluidization velocity can be found by observing how the jet plume and predicted solids flow patterns change over time. A series of time steps from simulation CA01 was taken at times of 1.45 seconds (just when the aeration rate was decreased to $0.5U_{mf}$), 4.4 seconds (just before the aeration was shut off) and at 5.1 seconds (zero fluidization; packed bed condition). Each of these three figures have solid lines showing predicted instantaneous solids streamlines and shaded iso-surfaces of gas volume fraction of $\varepsilon_g=0.8$. Figure 7.18 shows how the fluidized bed is predicted to behave within an established steady state minimum fluidization flow regime. Two recirculating zones are present; a counter clockwise zone above and to the left of the nozzle and a clockwise zone in bulk of the bed. Bed surface is approximately 76 cm above the distributor. Predicted instantaneous solids streamlines are presented in Figure 7.19 for half minimum fluidization. Two recirculation zones are still present; however, the overall bulk bed circulation is more pronounced and the gas jet has receeded closer to the low X wall. The average bed height has also fallen to approximately 70 cm above the distributor plate. Results for predicted solid flow patterns are shown in Figure 7.20 for a packed bed condition with zero fluidization gas. The large over turning region within the bed has moved closer to the low X wall and the top surface of the bed appears to have sunk near the low X wall. A slight mound has formed on the bed surface due to solid particles being entrained in the jet and carried up to the top surface of the bed where they are deposited; this is the so called "funnel" behavior. This type of behavior was also observed with the experimental apparatus at the UofS under similar operating conditions.

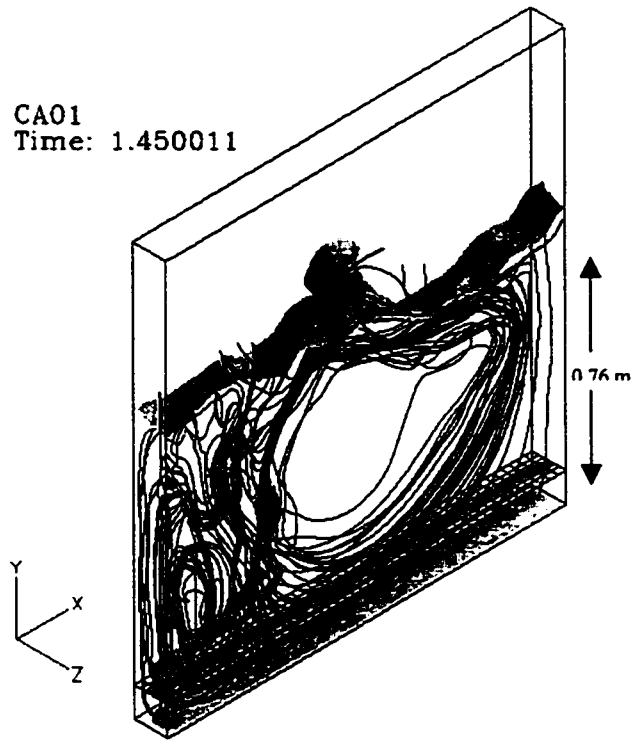

Figure 7.18 – Predicted solids streamlines and bed surface at minimum fluidization.

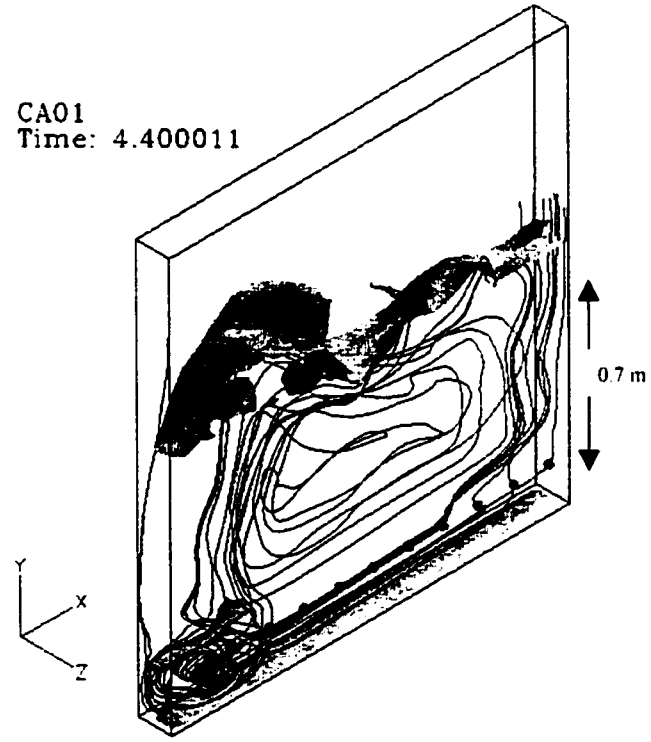

Figure 7.19 – Predicted solids streamlines and bed surface below minimum fluidization.

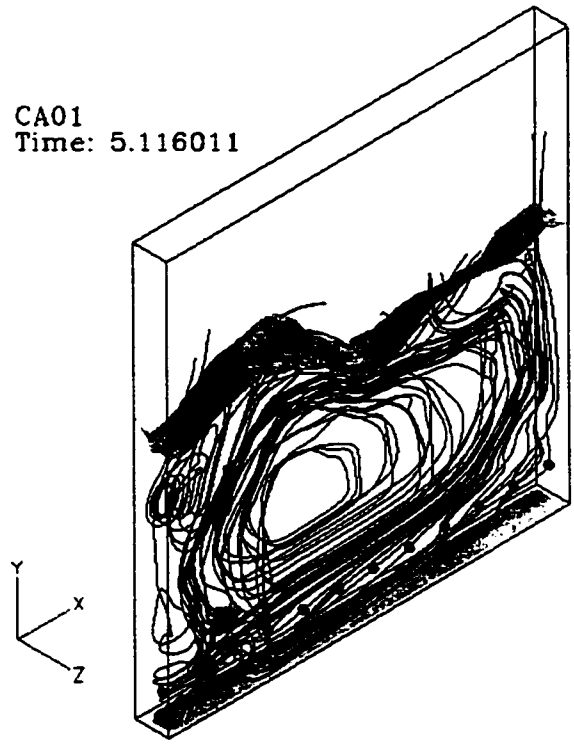

Figure 7.20 – Predicted solids streamlines and bed surface with zero aeration; packed bed condition.

7.2.2 Tests Above U_{mf}

Several simulations were conducted above minimum fluidization to study the effect of increased aeration on the predicted bed behavior. One of the most striking features of these simulations is the transition from minimum fluidization to a higher fluidization velocity over a period of approximately 0.25 seconds. Start up conditions for these simulations above minimum fluidization were provided by restarting previous simulations after 1.2 seconds. Using a set of initial conditions from previous runs allowed the transient start up behavior for the first second to be avoided. Upon initiation of the simulation with the increased fluidization rate a flat gas volume fraction iso-surface of 0.6 was observed to propagate upwards from the distributor plate and into the fluidized bed. Approximately three of these flat surfaces were seen to form and when the top most

plane coincided with the Y height of the nozzle orifice all of the following surfaces are seen to form disturbances along their lengths and a series of complete bubbles ensues. Figure 7.21 shows four frames from this behavior for run FB02. Gas volume fraction iso-surfaces of 0.6 are plotted in an isometric view. Simulation results start from minimum fluidization and at time equal to 1.25 seconds the fluidization velocity is increased to three times minimum fluidization; this 1.25 seconds coincides with the first frame of the sequence shown in Figure 7.21 a. Figure 7.21 b shows the three flat volume fraction iso-surfaces forming below the height of the nozzle orifice. These planes move up in the next frame and begin to form waves. Wave amplitude grows in Figure 7.21 c to a point that the successive planes have started to touch; this is the initial formation of bubbles below the jet height. Complete bubbles form in Figure 7.21 d in the lower part of the bed and the simulation has predicted bubbling fluidization behavior. This predicted transitional behavior seems to follow that observed with the experimental apparatus. When the experimental apparatus at the UofS was first fluidized, a plug flow of gas was present which caused the bed surface to rise before homogeneous fluidization was achieved. This plug flow might be the same as that predicted in the simulation. Distinct surfaces on the top and bottom of the plug would rise and then spontaneously break apart into bubbles. This type of behavior was not observed for simulations at or below minimum fluidization. Step changes from minimum fluidization to half minimum fluidization do not show this behavior.

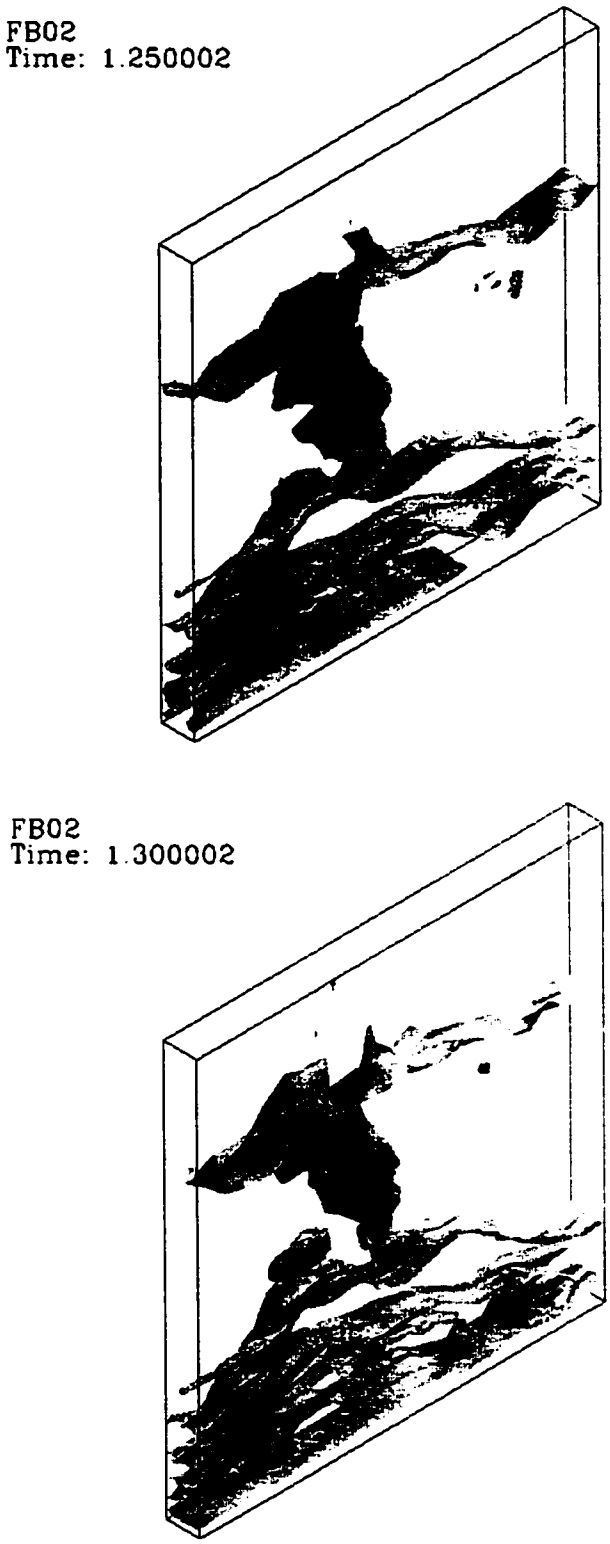

Figure 7.21 – Transient bed behavior with a step change in fluidization velocity.

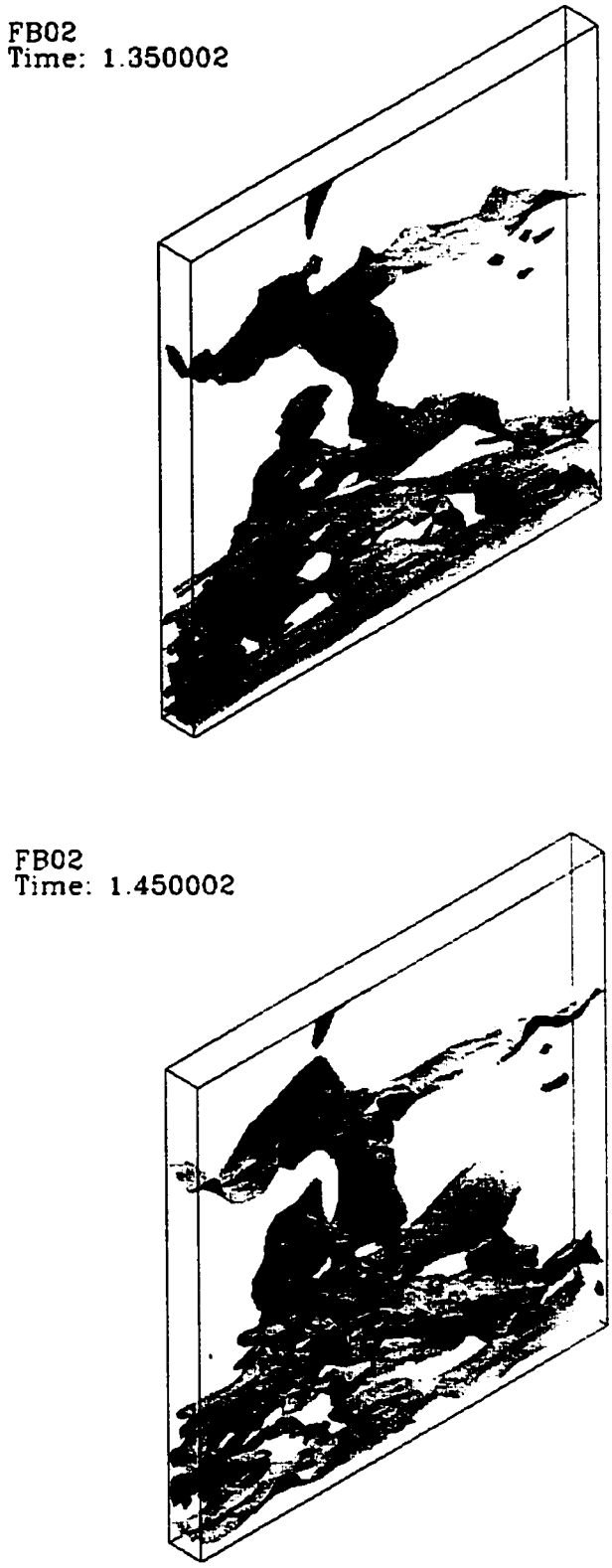

Figure 7.21 continued – Transient bed behavior with a step change in fluidization velocity.

7.2.3 Jet Behavior and Penetration Results

One of the most important parameters for design and placement purposes of the horizontal gas feed jet is the penetration to which the gas jet plume reaches into the fluidized bed. To be able to carry out a meaningful evaluation of jet penetration into the fluidized bed it was necessary to determine whether the simulation operating conditions agreed with the jet regime phase diagram of Chyang *et al.* (1997). Figure 7.22 shows in which flow regime each of the simulations documented in this report fall. All simulations with jet velocities greater than 150 m/s fell within the stable jetting region, and should, therefore, provide results which can be analyzed based on jet penetration depths into the fluidized bed.

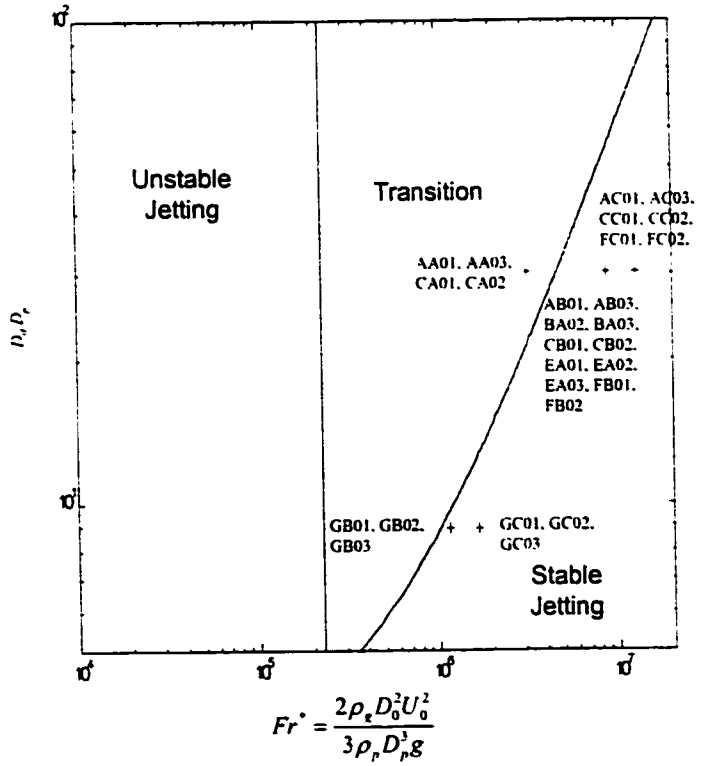

Figure 7.22 – Jet regime phase diagram of Chyang *et al.*(1997) for all simulations.

Penetration results were taken for all simulations by observing the gas volume fraction along the jet axis in the center XY plane. A gas volume fraction of 0.8 was arbitrarily chosen to be the boundary between the fluidized bed and the jet plume. Jet penetration was defined as the distance from the tip of the nozzle (i.e. the location of the nozzle inlet boundary condition) to the furthest gas volume fraction contour of 0.8. In cases where the gas jet curved upwards or began to pinch off to form a bubble the maximum penetration was defined to occur at the end of curvature or the pinch point itself as shown in Figure 7.23. Based on this penetration criteria results were obtained for the jet penetration every 0.05 seconds and then averaged to determine a representative penetration depth for that simulation. The first second of data was ignored to avoid transient start up phenomena. In many cases determining the actual jet penetration was very difficult due to jet curvature, bubble formation and gas volume fractions that changed along the length of the jet. This problem was compounded by the fact that simulation results were only saved every 0.05 seconds and the average behavior between these times is lost whereas with experimental results a continuous measurement can be taken very quickly using a ruler. Defining the penetration depth has been a problem for many researchers and can account for the different results obtained from different studies at similar operating conditions. Penetration results were compared with the correlation of Merry (1971) and nondimensionalized with nozzle diameter; results from this analysis are shown in Figure 7.24. Maximum and minimum penetration depths are also plotted on this figure with abscissa error markers off of each data point. Data markers have been grouped into gross groups representing simulations at minimum fluidization (series

Axxx, Bxxx and Exxx), those results from below minimum fluidization (series Cxxx) and those runs above minimum fluidization (series Fxxx and Gxxx).

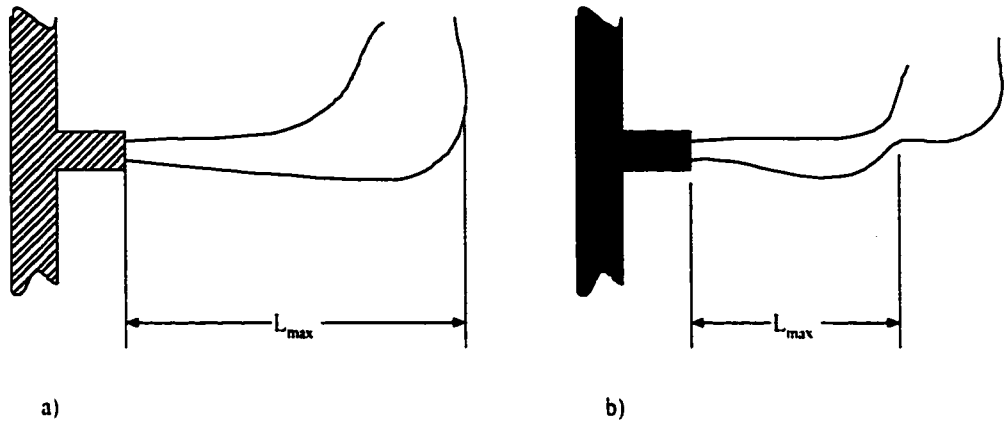

Figure 7.23 - Maximum jet penetration defined on a gas iso-contour of 0.8 from tip of nozzle to a) jet curve and b) jet pinch point.

Predicted penetrations from the Axxx series of simulations show the merits of using the Superbee TVD (open triangles Δ) discretization scheme over the Hybrid scheme (closed triangles ▲). All of the Superbee predicted penetration depths lie on top of Merry's correlation. Maximum and minimum error bounds on each of these data markers are also very narrow when compared with those for the Hybrid scheme. Predicted penetration depths for the case of zero fluidization, series Cxxx, ◇ show that the penetration depth remains relatively small for lower jet velocities of 150 and 250 m/s. At 300 m/s the penetration increases but is still over predicted when compared to Merry's correlation. Similar results are found for the series Cxxx ◆ at half minimum fluidization. Jet penetration increases dramatically for the 300 m/s inlet jet velocity but all of the predicted penetration results are greater than that predicted from the correlation.

Interesting results are obtained for the test of Hydrodynamic model B with the Exxx series of simulations symbol +. All of the predicted penetration depths are identical for different jet velocities as shown by the constant L/d_0 value for all three Exxx

simulations. This result seems contrary to physical expectation since an increase in inlet jet velocity should lead to an increase in jet penetration into the fluidized bed. Although qualitative results comparing Hydrodynamic model A (series Dxxx) and Hydrodynamic model B (series Exxx) in section 7.1.4 showed very little variation in the predicted gas volume fraction contours within the fluidized bed it appears that the physical predictions with Model B do not give results that are in accordance with expected physical behavior.

Results from the Gxxx series, those with a much smaller nozzle orifice size and solids properties agreeing with the experimental fluidized bed, under predicted the gas jet penetration into the fluidized bed when compared with Merry's expression. Additionally the error bounds representing maximum and minimum penetration depths showed a greater range than most other simulations. Only the GC03 and GB03 simulations predicted penetration depths within expected error ranges. Both of these simulations used a jet velocity of 300 m/s which might explain why the penetration was greater and hence closer to that predicted with the Merry's expression. The much smaller nozzle orifice size might contribute to problems associated with simulations for the Gxxx series. This small inlet boundary condition decreased the gas flux across the orifice area subsequently leading to a decrease in jet momentum. Decreased jet momentum will lead to a decrease in jet penetration into the fluidized bed.

By creating animated movies of the gas volume fraction iso-surface of 0.8 it was possible to observe how the jet plume and penetration progressed with time. In general the jet would penetrate into the bed at start up forming large bubbles which would progress upwards and out of the bed surface. After this initial start up regime, the jet would settle down into a characteristic fluctuating behavior. First the jet would penetrate

into the bed and then a bubble would form at the tip from a "pinch point". The jet would then recede slightly (the penetration would decrease somewhat) and this cycle would be repeated. This periodic increase and then decrease in jet penetration was also observed in the experimental tests at the University of Saskatchewan.

7.2.4 Overall Flow Patterns

Simulation results tended to over predict recirculatory flow patterns within the fluidized bed both above and to the right of the jet within the flow domain when compared with the observations taken at the UofS. These large recirculating cells were not observed in the experimental apparatus under any operating conditions. A representative solids velocity field is shown in Figure 7.25. A counter clockwise (CCW) rotating area is seen to form above the jet with solids moving down along the wall and becoming entrained in the jet. A large clockwise (CW) recirculation flow pattern is present to the right of the jet and the fluidized bed is seen to slowly turn over with solids recirculating into the bottom of the jet after being carried along to the left just above the distributor plate. Solids entrained in the central part of the jet were carried upwards and deposited on the top of the bed surface.

Similar recirculating zones were found in Figure 7.26 for the BA03 simulations although the counter clockwise recirculation zone above the jet appears to be more elongated in the Y direction. As shown in Table 7.4, the insertion for BA03 is 0.05 m less than for run BA02. This decrease in fluidized bed above the jet inlet might cause the dragging zone above the jet to be shortened thereby forming a shorter recirculation zone.

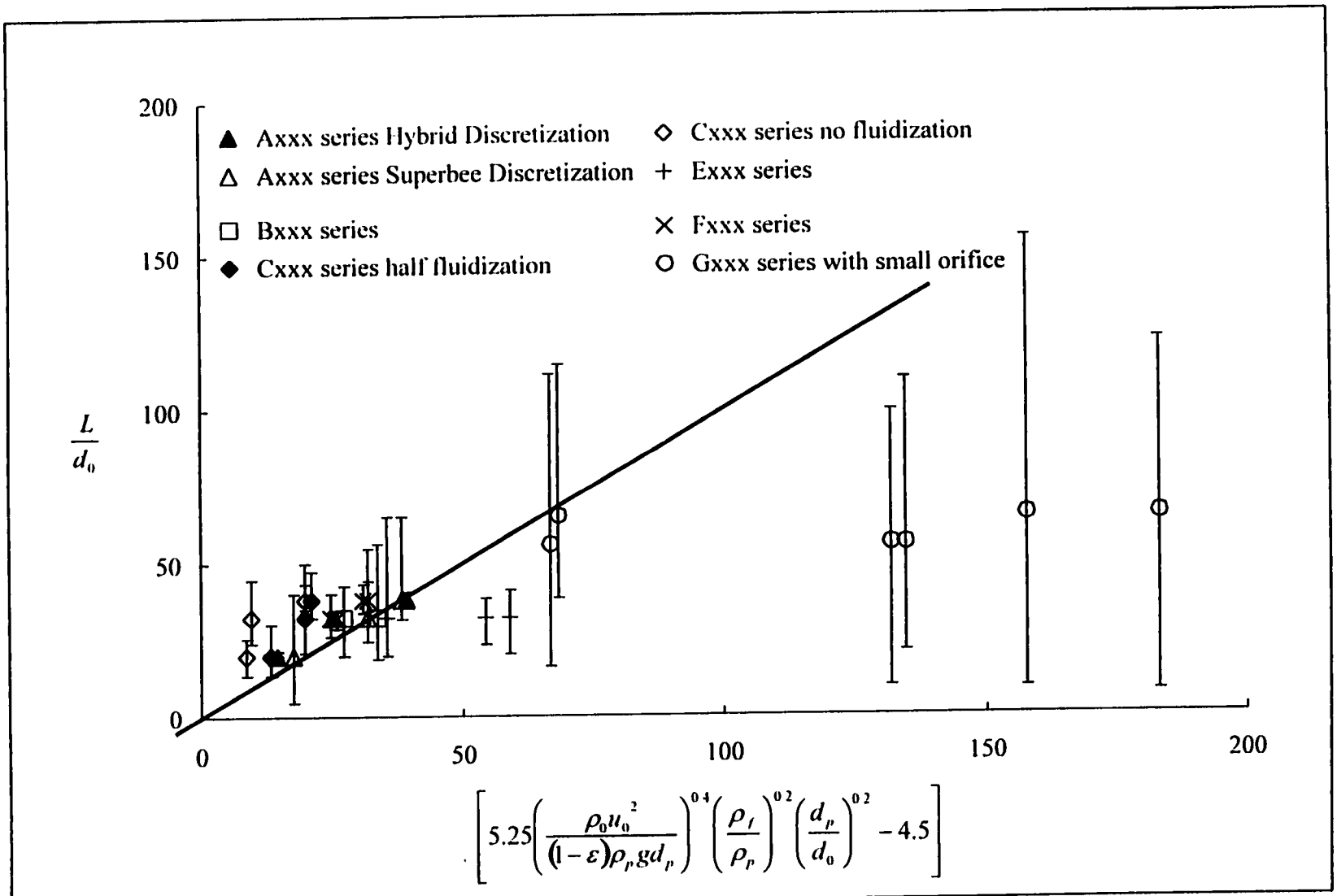

Figure 7.24 - Penetration results from simulations compared with the expression of Merry (1971). Error bars denote maximum and minimum penetrations based on a solids volume fraction iso-surface plot of 0.8.

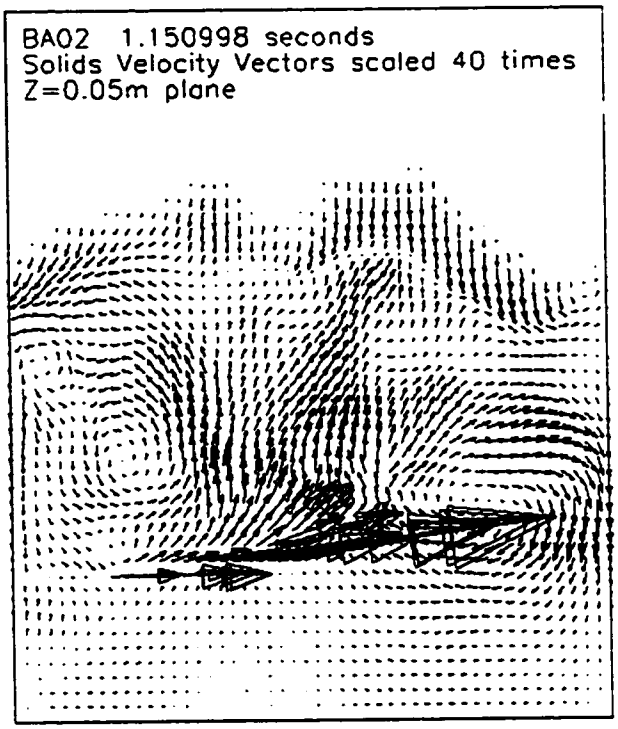

Figure 7.25 - BA02 solids flow pattern vectors in the fluidized bed.

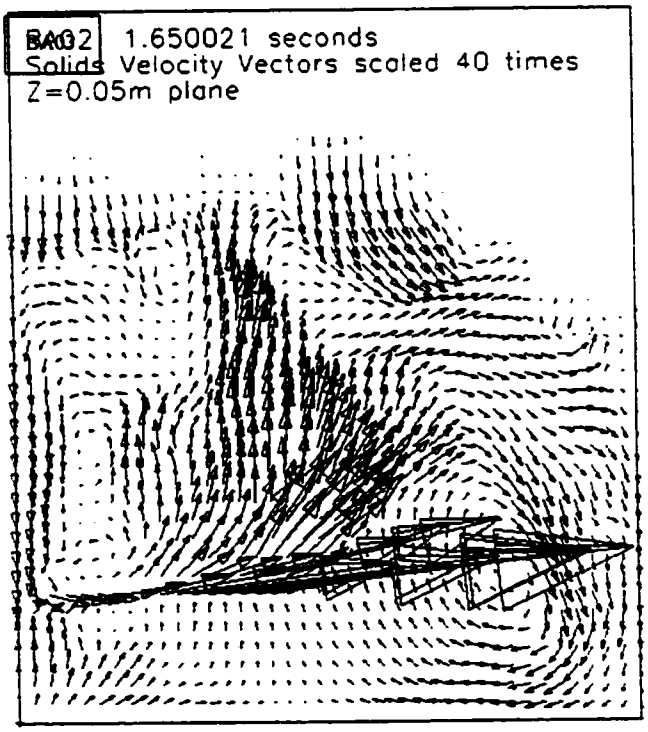

Figure 7.26 - BA03 solids flow pattern vectors in the fluidized bed.

A pair of counter rotating vortices were also predicted to form below the nozzle inlet pipe and close to the low X wall, see Figure 7.27. Solids down flow along the wall impacts on the nozzle inlet pipe and is forced to either side of the pipe leading to a wake region just behind (or below) the nozzle pipe. This behavior was predicted for all simulations and is in agreement with the experimental observations of how the solids behaved close to the nozzle pipe. Solids appeared to be entrained into the gas jet through a line sink shown schematically in Figure 7.28. The entrainment from below the nozzle pipe might be due to this wake region that was predicted in the simulations. Solids are carried down and then back up directly below the pipe being entrained into the gas jet and forming the solids sink.

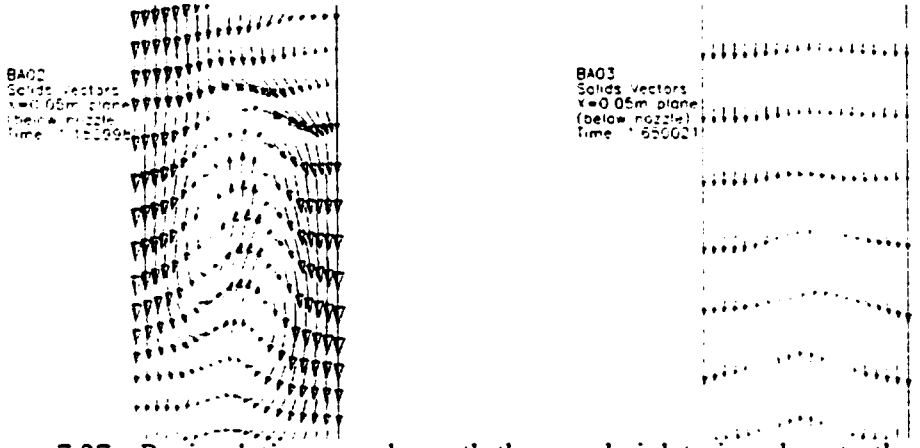

Figure 7.27 - Recirculation zone beneath the nozzle inlet pipe close to the low X wall of the simulation.

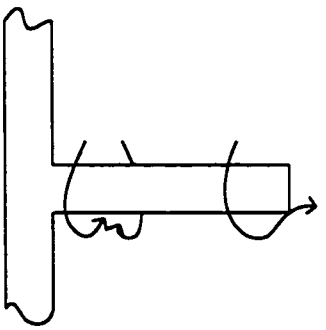

Figure 7.28 – Solids wake region behind nozzle pipe and entrainment into jet.

7.2.5 Particle Tracking

Using FIELDView (FIELDView User Manual, 1999) from Intelligent Light software it is possible to seed a simulated flow field with virtual particles to track how they would move within that given flow field. It has to be emphasized that these particle tracks are not Lagrangian but merely show how particles would move within that flow field at that given instant in time and represent instantaneous streamlines. Ten virtual seed particles were randomly scattered on a gas iso-surface of 0.8 in the region where the jet plume issues into the fluidized bed. Two streamline patterns were seeded with one set of ten particles on the top surface of the gas jet and another set of ten particles being seeded on the lower surface of the jet. After randomly seeding the top and bottom parts of the jet plume, an integration of the velocity field was carried out to predict where these virtual massless particles move.

Figures 7.29-30 are isometric views showing how virtual particles would move if they were to follow the predicted *solids* velocity field. The seed particles above the jet, shown in Figure 7.29, are seen to be carried predominantly up and to the left of the jet into a counter clockwise recirculation zone. Seed particles on the lower surface of the jet plume, shown in Figure 7.30, are also entrained into the jet and carried into a larger clockwise circulating zone which represents a gradual turn over of the fluidized bed material. It appears from these analyses that solids particles within this fluidized bed will be segregated into two zones: a CCW recirculation zone to the left and above the jet and a larger CW zone to the right of the jet representing a gradual turn over of the bed material. It is possible that solids particles along the wall of the reactor are becoming trapped in a recirculatory pattern. This increased residence time could lead to catalyst

degradation in the commercial unit which in turn could further lead to reactor fouling by the action of coke build-up above the nozzle pipe.

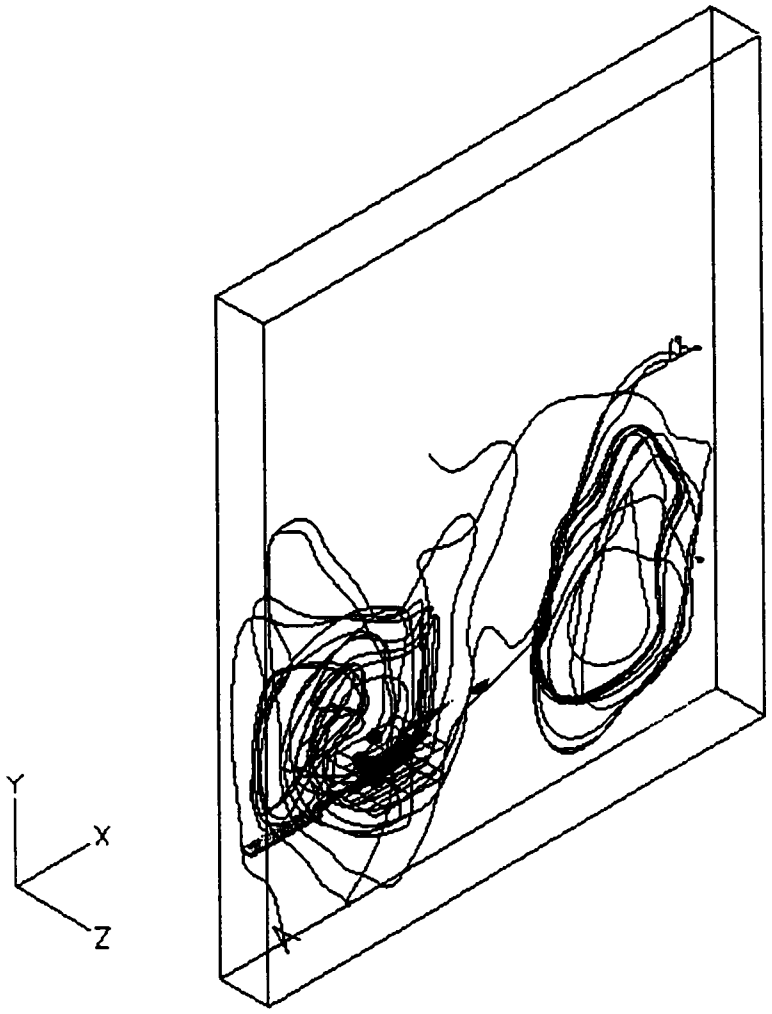

Figure 7.29 – Instantaneous solids flow patterns for seeding above the jet plume. Run BA02, t=2.0 s.

A set of predicted flow patterns was created over a time period to provide visualization of the transient predicted flow patterns within the fluidized bed. Figure 7.31 shows the predicted gas and solids particle tracking in the left and right columns respectively at time increments of 0.25 seconds. All of the seed particles were placed in a straight line at Z=0.05 m along the lower section of the fluidized bed. The gas particles were seeded on the distributor plate while the solids particles were placed slightly higher.

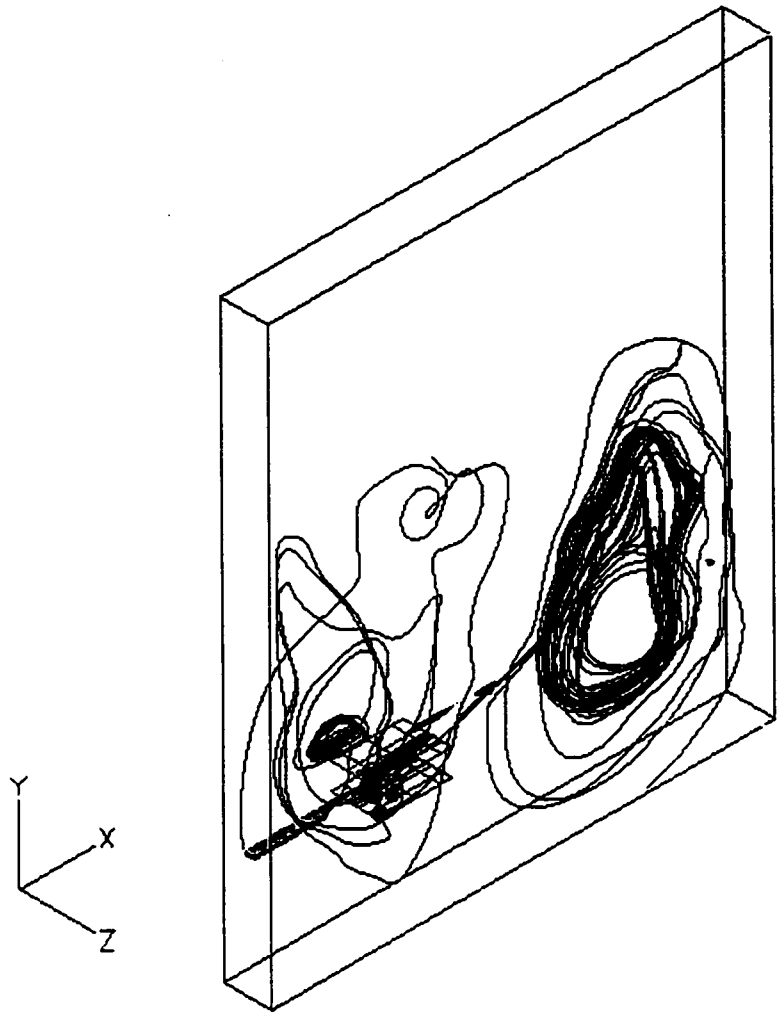

Figure 7.30 – Instantaneous solids flow patterns for seeding below the jet plume. Run BA02, t=2.0 s.

Each row of visualizations is for the same real time step. Start up conditions are evident for Figure 7.31 a at a time of 0.05 seconds. Most of the gas channels directly out of the fluidized bed and the solids move towards the jet plume region. After 0.5 seconds (Figure 7.31 c) two solids recirculation zones have formed and the gas flow behavior has become more chaotic. Fluidization gas appears to bypass the region above the jet plume and become caught in the recirculation zone in the bulk of the bed. Problems with loss of fluidization above the gas jet in two-dimensional simulations were discussed previously

in section 7.1.1. Depth in the three dimensional simulation allows the fluidization gas to pass around the jet fluidizing the top section and can be observed for the gas flow for all predicted gas streamlines at times greater than 0.75 seconds. The prediction that the fluidization gas flow above the jet is affected in three dimensions suggests that there might be a slight loss of fluidization due to the presence of the jet in the bed. All simulation results for times greater than 0.5 seconds show that the two solids recirculation zones persist and become even more pronounced, see Figure 7.31e 1.0 seconds. Gas channeling up through the center of the bed is evident in Figure 7.31 g. Channeling will lead to poor gas-solid contacting and decrease the residence time of the gas phase resulting in decreased reactor performance and yield.

a

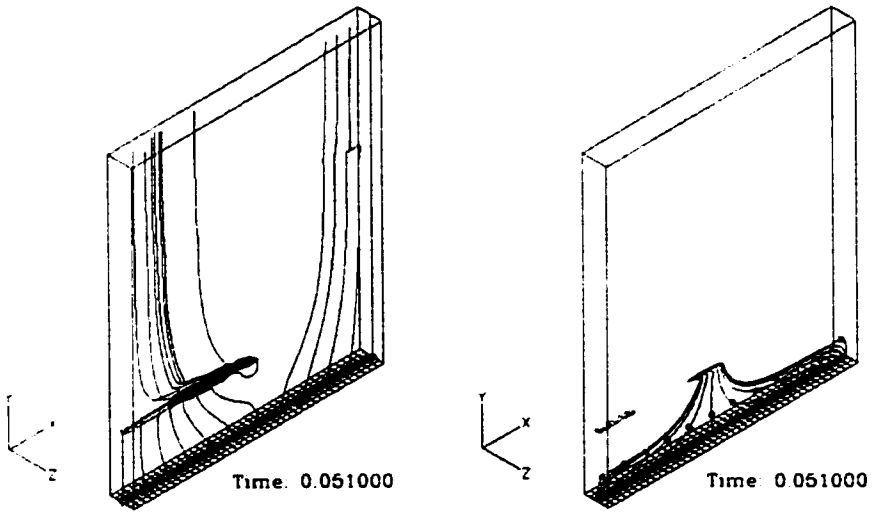

Figure 7.31– Predicted gas (left) and solids (right) instantaneous streamlines.

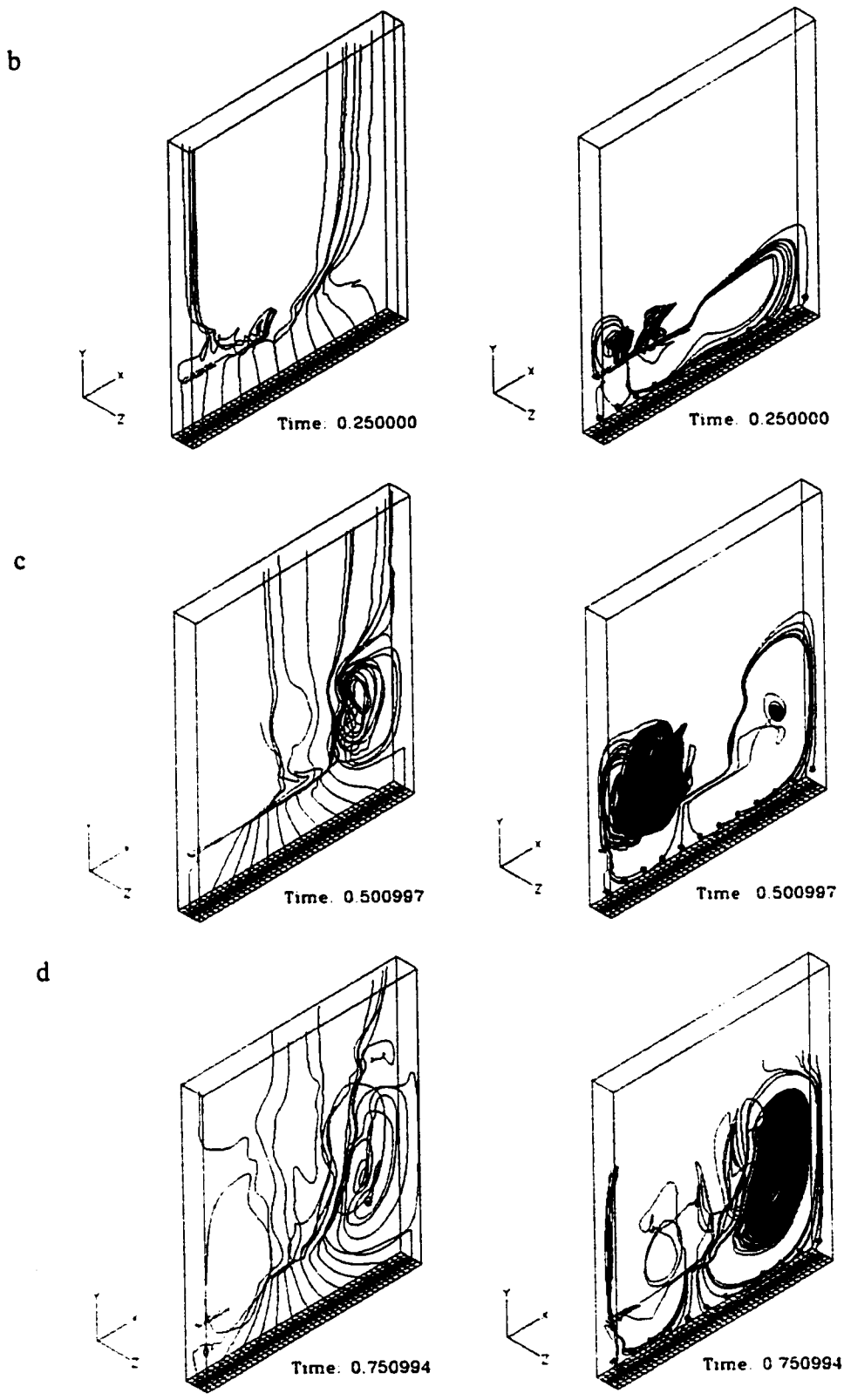

Figure 7.31 continued – Predicted gas (left) and solids (right) instantaneous streamlines.

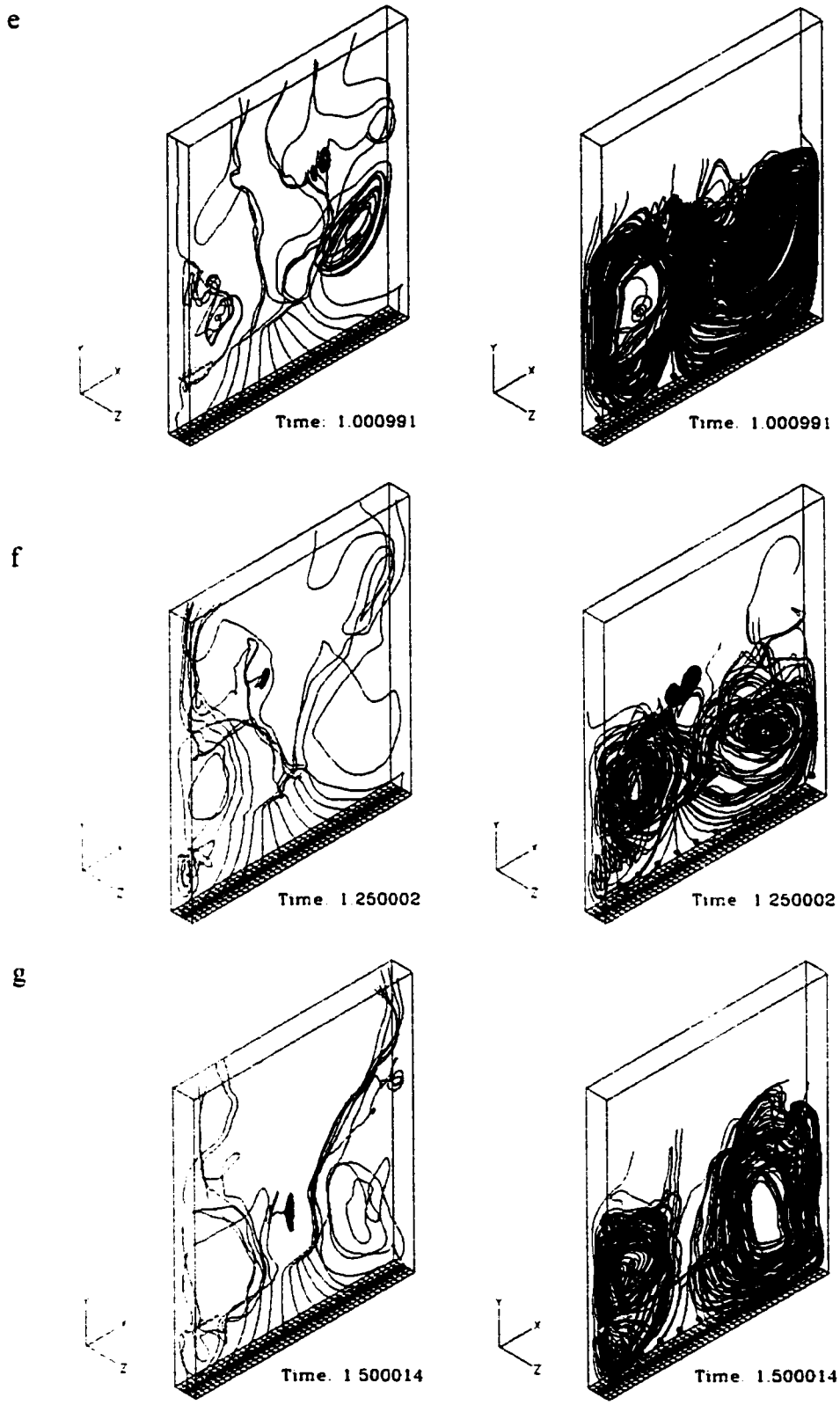

Figure 7.31 continued – Predicted gas (left) and solids (right) instantaneous streamlines.

h

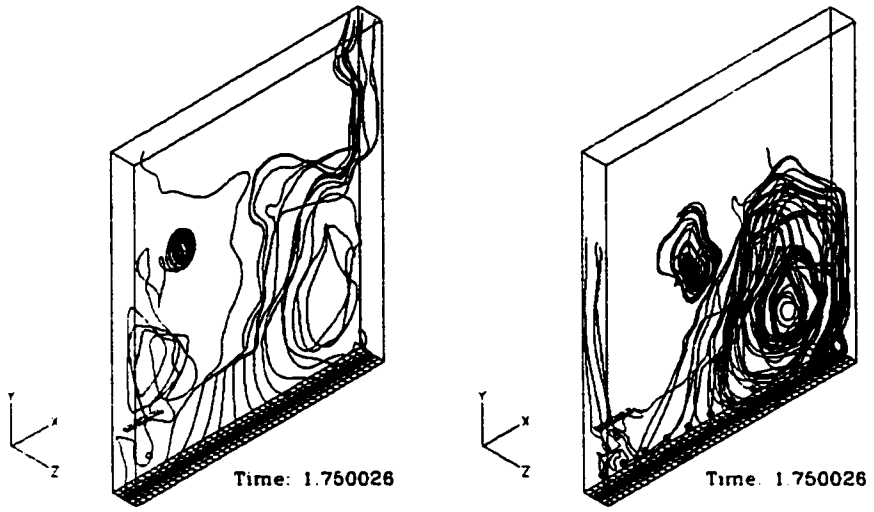

i

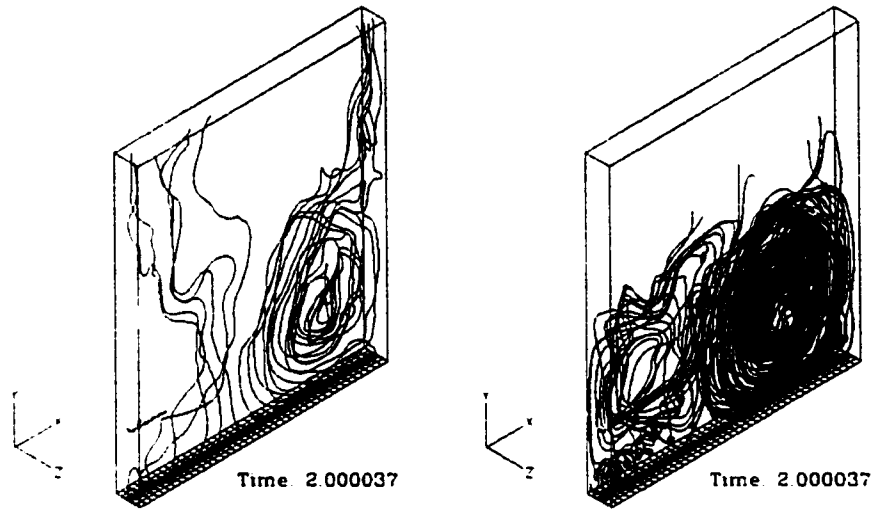

Figure 7.31 continued – Predicted gas (left) and solids (right) instantaneous streamlines.

7.2.6 Bubble Shapes

Bubbles were isolated based on a gas volume fraction contour of 0.8 and the solids velocity vector field was plotted through the central plane of the bubble. Four different flow scenarios were chosen to study bubble shapes:

i) startup conditions at minimum fluidization (the unsteady behavior) - simulation AB03;

ii) $<U_{mf}$ conditions where bubbles were formed below minimum fluidization after allowing enough time for a steady state flow field to be set up (approximately 1.5 seconds) - simulation CB01;

iii) $>U_{mf}$ conditions where bubbles were formed above minimum fluidization after allowing enough time for a steady state flow field to be set up - simulation FB02;

iv) $0U_{mf}$ jet discharge into the fluidized bed with no aeration assuming that the flow field had attained a steady state – simulation CB02.

Bubbles were selected above the jet plume region in the upper section of the bed almost directly above where the jet plume discharges.

Case i) *Bubbles at Start Up*: Run AB03 was chosen to study the bubble shape and solids velocity vector field around the bubble. Figure 7.32 shows gas volume fraction contours and an overlay of the solids vector field for a bubble present at simulation start up. Bubbles at start up were typically observed to be spherical cap shape with strong solids recirculation up through the bubble, sweeping down from the top and sides. This behavior is similar to that of fast bubbles where bubble rise velocity is greater than the fluidization velocity.

Case ii) *Bubbles in a bed with* $<U_{mf}$. Run CB01 was chosen to study bubble shape below minimum fluidization; results from this analysis are shown in Figure 7.33. In this case the bubbles were round in shape and solids were observed to flow through the bubbles with no recirculation back around to the base of the bubble. This behavior is

characteristic of slow bubbles in fluidized beds where the bubbles rise more slowly than the fluidization gas.

Case iii) *Bubbles in a bubbling fluidized bed.* Simulation FB02 was chosen to study bubbles at greater than minimum fluidization; results are shown in Figure 7.34. Above minimum fluidization most of the bubbles assumed an oblong shape. Solids flowed up and through the bubbles with some slight down flow around the edges of the bubbles. At these higher fluidization velocities more bubbles were observed to form than for minimum and lower than minimum fluidization. Many of the bubbles present in the lower part of the bed below the nozzle orifice height tended to coalesce in the upper part of the bed. This behavior seems to have been induced by the presence of the jet void. Similar behavior was observed with the experimental apparatus at the UofS. Bubbles formed below the jet tended to move towards the jet and amalgamate with the voids formed from the jet plume.

Case iv) *Bubbles in a packed bed* $0U_{mf}$. Simulation CB02 was chosen to study bubbles in the packed bed. With zero aeration very few bubbles were formed within the fluidized bed. The jet plume was still present and formed a large void into the bed but bubbles were not observed to pinch off regularly from the tip of the jet. Figure 7.35 shows a small void variation within the fluidized bed. The solids particles have a very strong horizontal velocity and are being swept to the right of the bed by the action of the gas jet. Bubble motion within the packed bed has little effect on the overall solids motion.

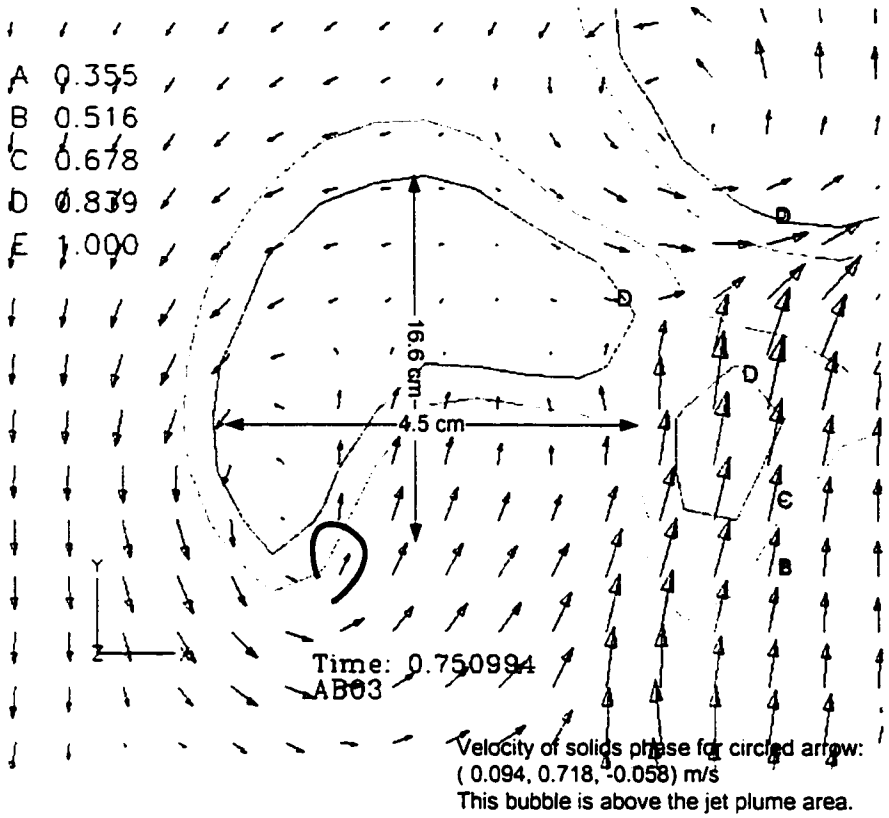

Figure 7.32 – Predicted bubble in a fluidized bed at start up.

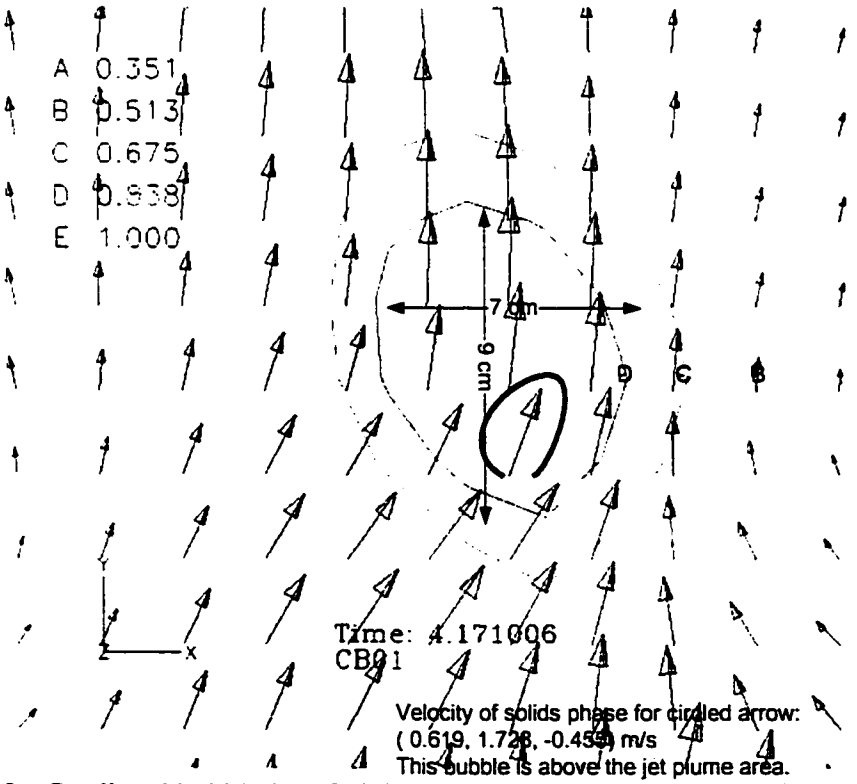

Figure 7.33 – Predicted bubble in a fluidized bed at less than minimum fluidization.

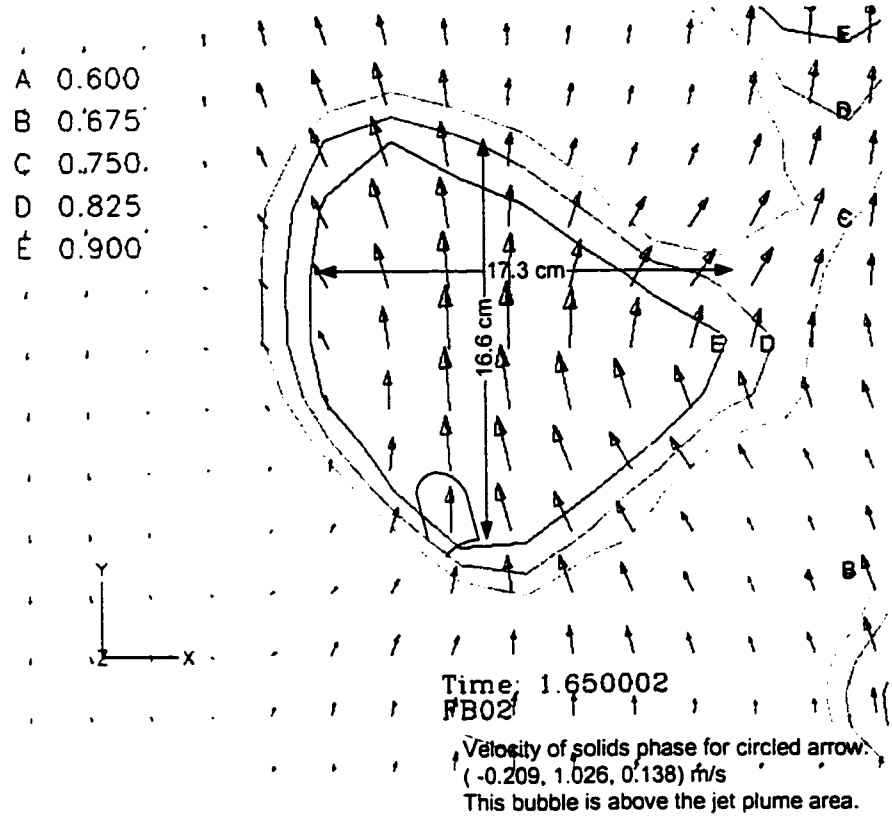

Figure 7.34 – Predicted bubble in a fluidized bed at greater than minimum fluidization.

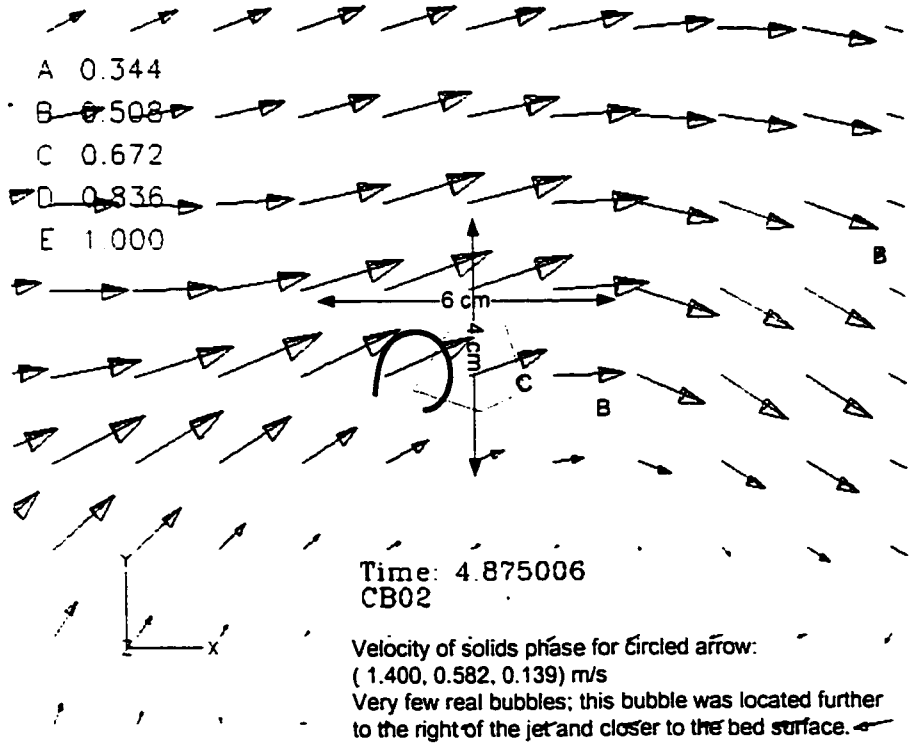

Figure 7.35 – Predicted bubble in a packed bed or zero fluidization.

7.2.7 Bubble Velocities

Quantitative comparison between different simulations based on the size and velocity of bubbles was conducted to determine any trends. Bubble dimensions were determined using the same technique outlined in the Chapter 6 on experimental data whereby the horizontal and vertical boundaries of the bubbles were recorded and a centroid calculated.

Bubble horizontal and vertical velocities in the Z=0.05 m XY plane were calculated based on the difference in bubble centroid between time steps. For these analyses the data was analyzed every 0.05 seconds and average bubble velocities were determined for each run listed in Table 7.5. Most of the data from this analysis suggests that the bubble rise velocities were of the order of 0.1 m/s with some data showing a negative upward velocity. This negative velocity was not observed in the experimental apparatus because all of the bubbles exit through the top of the bed and should have a net positive average vertical velocity. One possible explanation for this is that the use of data spaced every 0.05 seconds could lead to some bias with the results.

Horizontal velocities show more variation than the vertical velocity results and can be attributed to the deformation of bubbles as they progress up the bed. This deformation created difficulties when trying to determine the correct edge of the bubble in the simulation results and lead to errors in horizontal bubble velocities.

7.2.8 Time Averaged Data

Many researchers have presented time averaged data to ascertain the flow characteristics within fluidized beds. This approach might shed some light on certain regions where large scale flow patterns dominate. A set of comparison graphs are

Table 7.5

Average Bubble Rise Velocities from Simulations

Run	V velocity (m/s)	U Velocity (m/s)
FB01	0.300	0.030
FB02	0.039	0.045
FC01	0.026	0.258
FC02	-0.094	-0.136
GB01	0.471	-0.016
GB02	1.459	2.100
GB03	0.673	0.426
GC01	-0.291	-0.020
GC03	0.084	-0.015

included to compare the different time averaged volume fraction profiles for several different simulations. Figures 7.36 to 7.38 show time averaged results for runs below minimum fluidization. At conditions lower than minimum fluidization the bed acted like a packed medium and few bubbles were formed. In these cases the only region within the bed to be affected by the jet is that directly above the jet plume shown by the distinct maximum located between approximately X=0.2 to 0.3 m increasing with increased jet velocity. Beyond this region the bed tended to remain at a constant voidage of approximately ε_g=0.36. Bed surface tilt is present for all of the simulations under taken below minimum fluidization. It appears that the bed surface forms a mound to the right of where the jet plume exits out of the top surface. This is the so called "funnel behavior that was described in section 7.2.2.

With an increase in aeration to twice minimum fluidization the bulk bed voidage increased to approximately ε_g=0.45, see Figures 7.39 to 7.40. The void fractions around

the jet are seen to increase in size and shift slightly right to between X=0.2 and 0.8 showing that the gas jet is penetrating more easily into the fluidized bed. Increased aeration resulted in increased bed voidage and a subsequent decrease in bulk bed density. A decrease in bed density reduces the local grid Reynolds number decreasing the local drag forces exerted on the gas phase thereby decreasing the momentum transfer from the jet to the fluidized bed resulting in an increase in jet penetration for similar jet momentum fluxes through the nozzle orifice. Further increase in aeration velocity to three times minimum fluidization, Figures 7.41 to 7.42 resulted in erratic voidage levels across the width of the bed. At this high aeration velocity the fluidized bed is operating in the bubbling regime bed and the formation of voids or bubbles from the distributor plate propagate up through the bed making the average gas volume fractions erratic. A time averaged analysis of volume fraction data across the bed is not entirely applicable to a bubbling bed regime. Instead point averages within the bed with respect to time should be used to give an indication of bubble frequency. From these data it is unclear whether the jet penetration decreases with increasing fluidization as reported by Chyang *et al.*(1997), see Figure 2.4.

Time averaged data for the Gxxx series of runs show unexpected behavior with increased jet velocity. Comparing Figures 7.43 and 7.44 suggests that the influence of the jet on the fluidized bed is more pronounced for the lower jet velocity of 150 m/s than for the simulations using a jet velocity of 300 m/s; the same trend is seen for three times minimum fluidization in Figures 7.45 to 7.46. This behavior is contrary to that observed from the previous comparison of time averaged data. Two possible factors may be contributing to these results. First the density and size of the solids particles used in these

simulations is lower than that for the previous set of simulations. There is a possibility that the smaller particle size and density influences the flow behavior within the fluidized bed and/or affects the jet behavior. Referring to the jet phase diagram Figure 7.22 shows that simulations GB01, GB02 and GB03 lie very close to the border between transition and stable jetting. It is possible that the small nozzle orifice size with the possible overlap of flow regimes produced with this set of operating conditions is not properly resolved with the numerical simulations. Further investigation of these problems are required to draw significant conclusions.

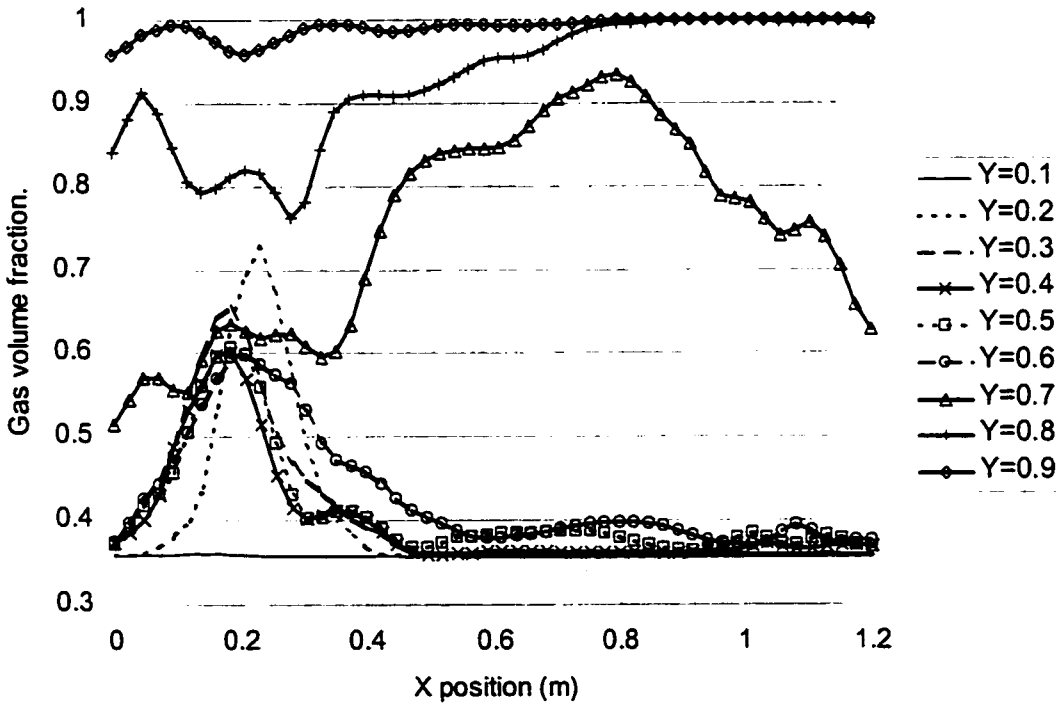

Figure 7.36 – Predicted time averaged gas volume fraction data for run CA01 across the width of the bed. $0.5U_{mf}$ U_{jet}=150m/s.

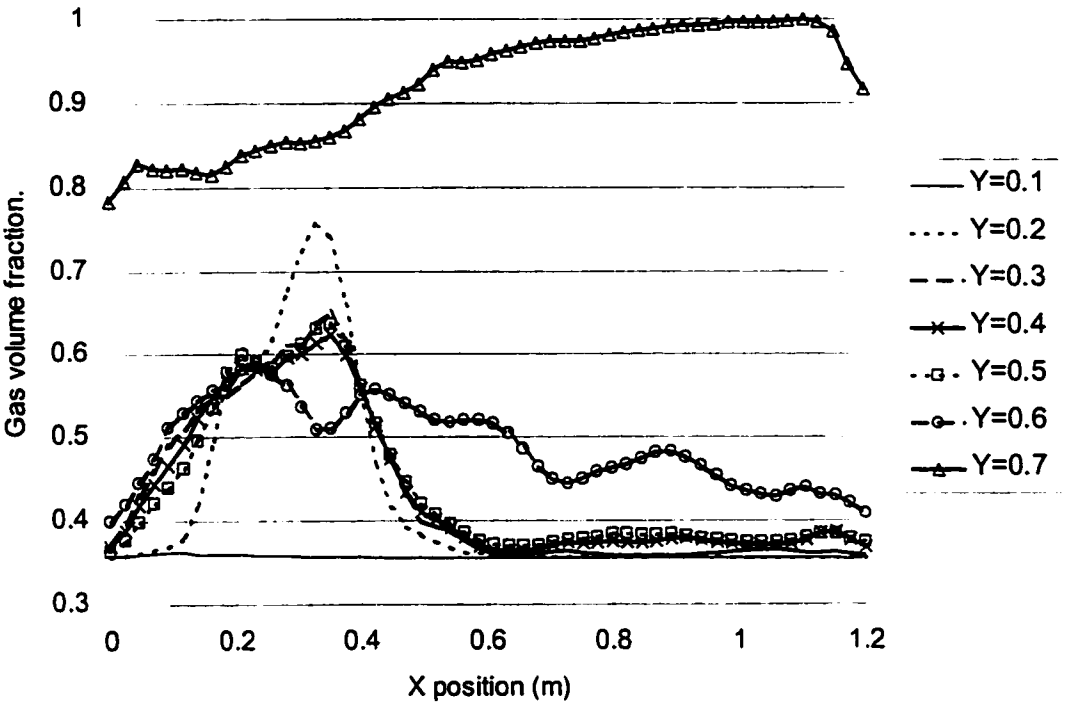

Figure 7.37 - Predicted time averaged gas volume fraction data for run CB01 across the width of the bed. $0.5U_{mf}$ U_{jet}=250m/s.

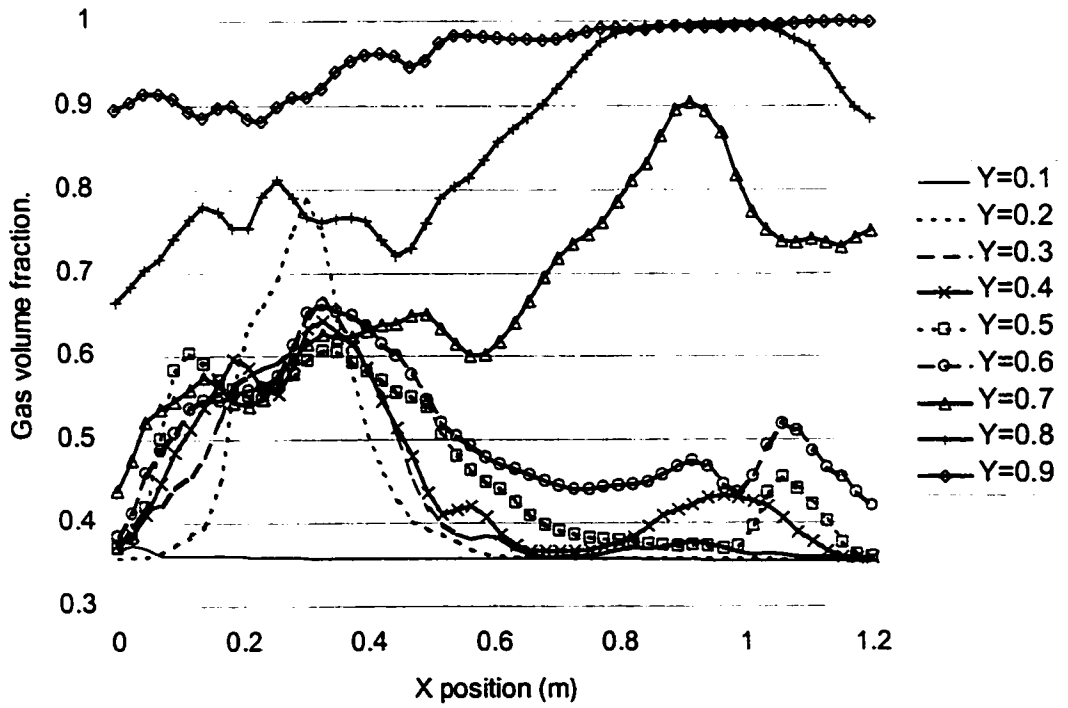

Figure 7.38 - Predicted time averaged gas volume fraction data for run CC01 across the width of the bed. U_{mf}=$0.5U_{mf}$ U_{jet}=300m/s.

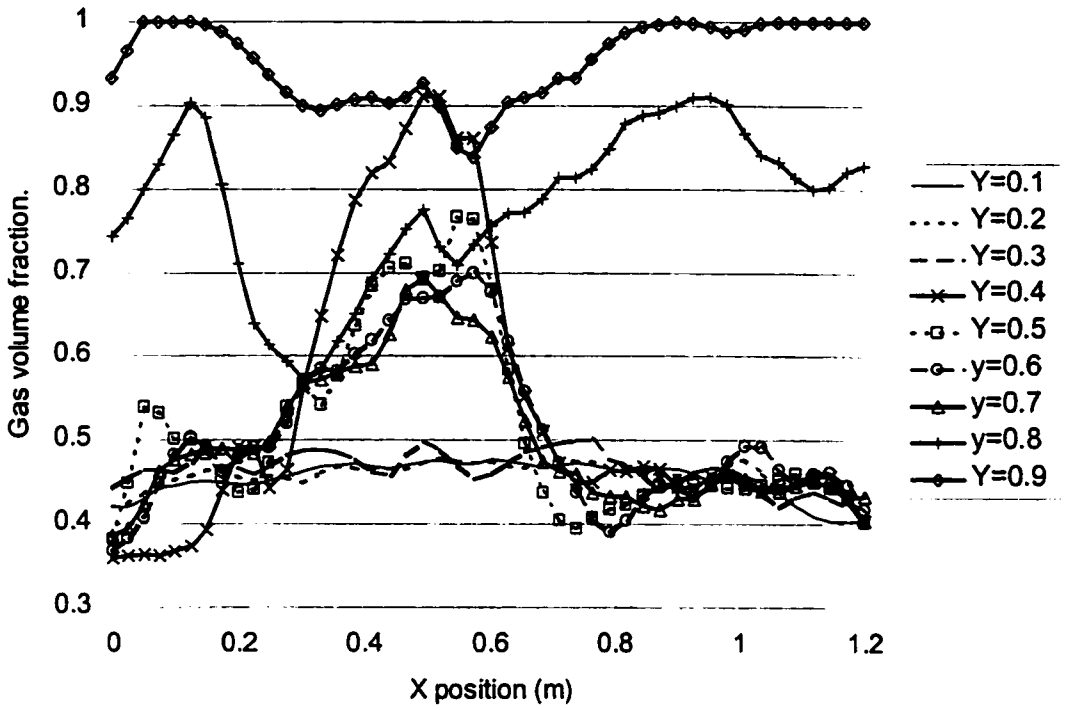

Figure 7.39 – Predicted time averaged gas volume fraction data for run FB01 across the width of the bed. $2U_{mf}$ U_{jet}=250m/s.

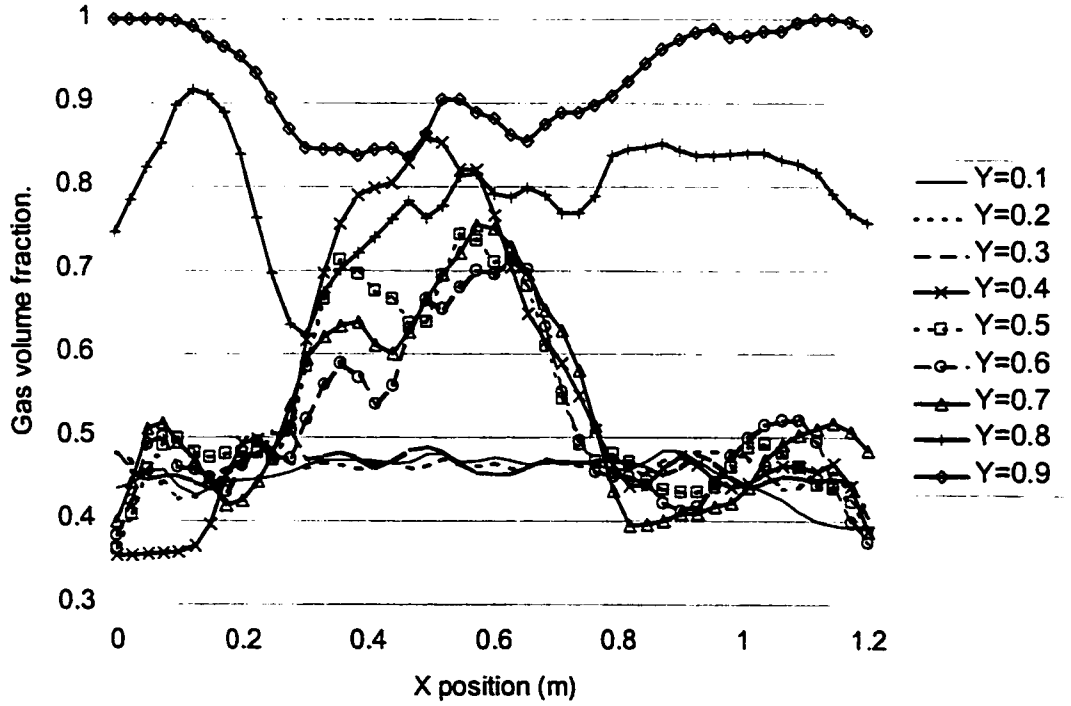

Figure 7.40 – Predicted time averaged gas volume fraction data for run FC01 across the width of the bed. $2U_{mf}$ U_{jet}=300m/s.

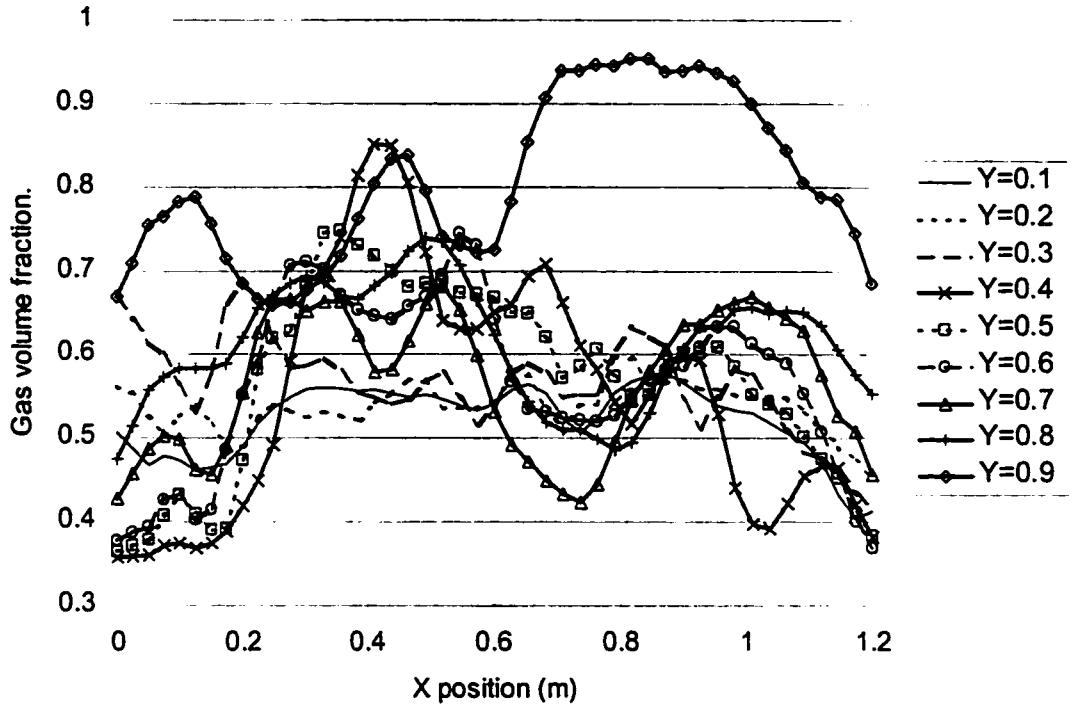

Figure 7.41 – Predicted time averaged gas volume fraction data for run FB02 across the width of the bed. $3U_{mf}$ U_{jet}=250m/s.

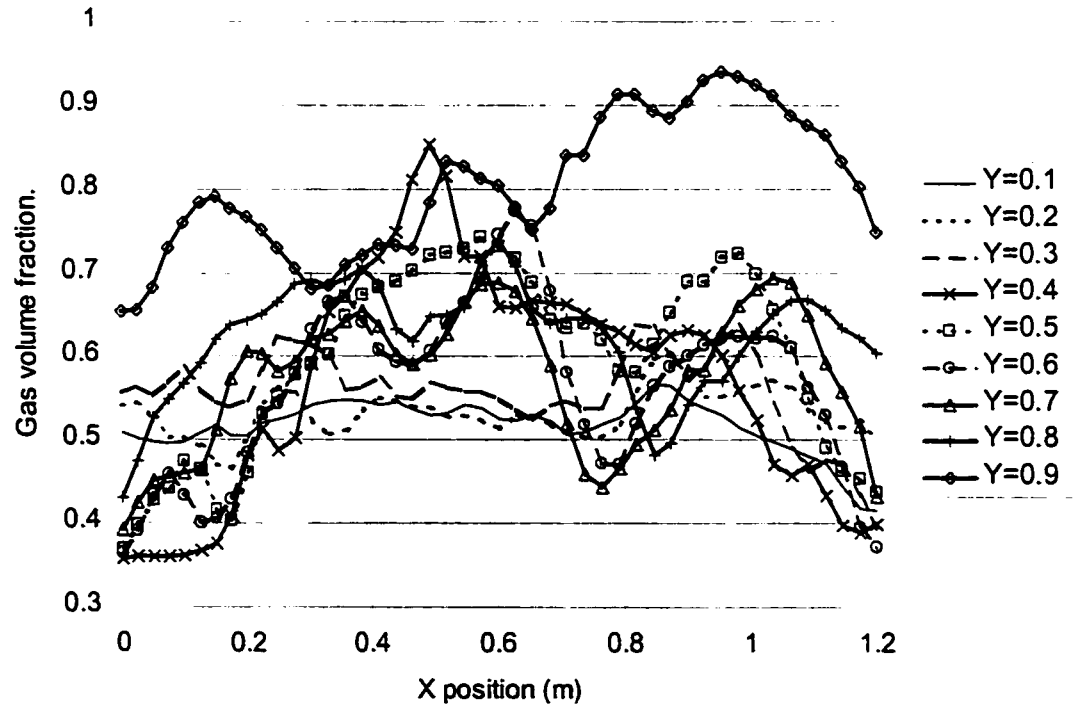

Figure 7.42 – Predicted time averaged gas volume fraction data for run FC02 across the width of the bed. $3U_{mf}$ U_{jet}=300m/s.

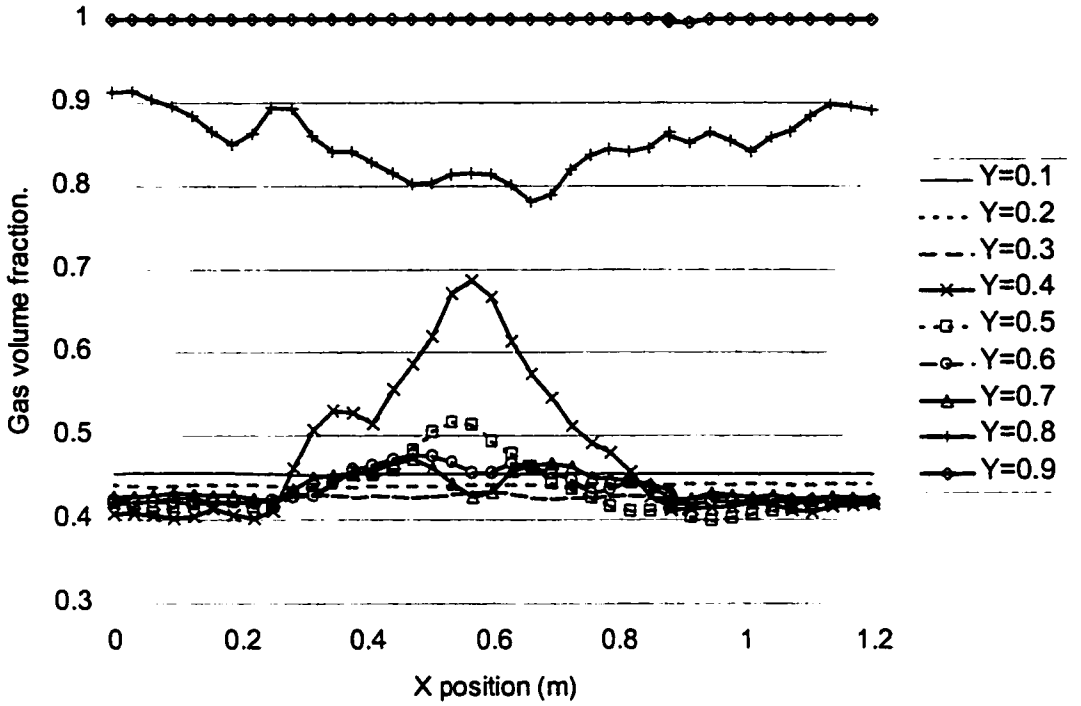

Figure 7.43 – Predicted time averaged gas volume fraction data for run GB01 across the width of the bed. $2U_{mf}$ U_{jet}=150m/s.

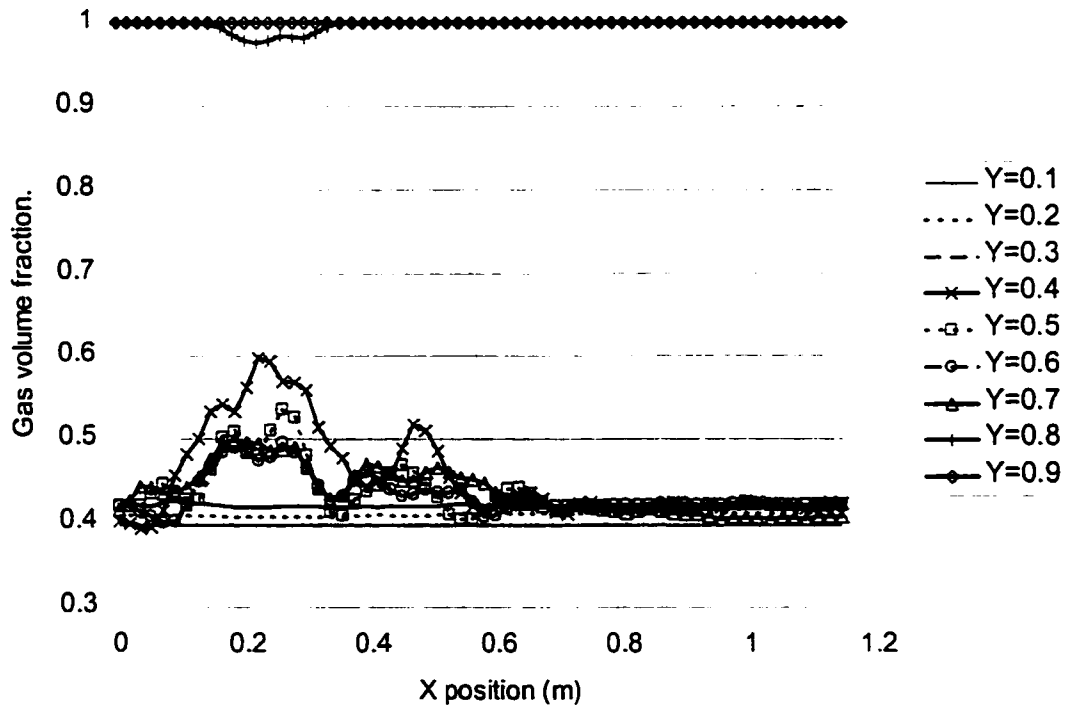

Figure 7.44 – Predicted time averaged gas volume fraction data for run GB03 across the width of the bed. $2U_{mf}$ U_{jet}=300m/s.

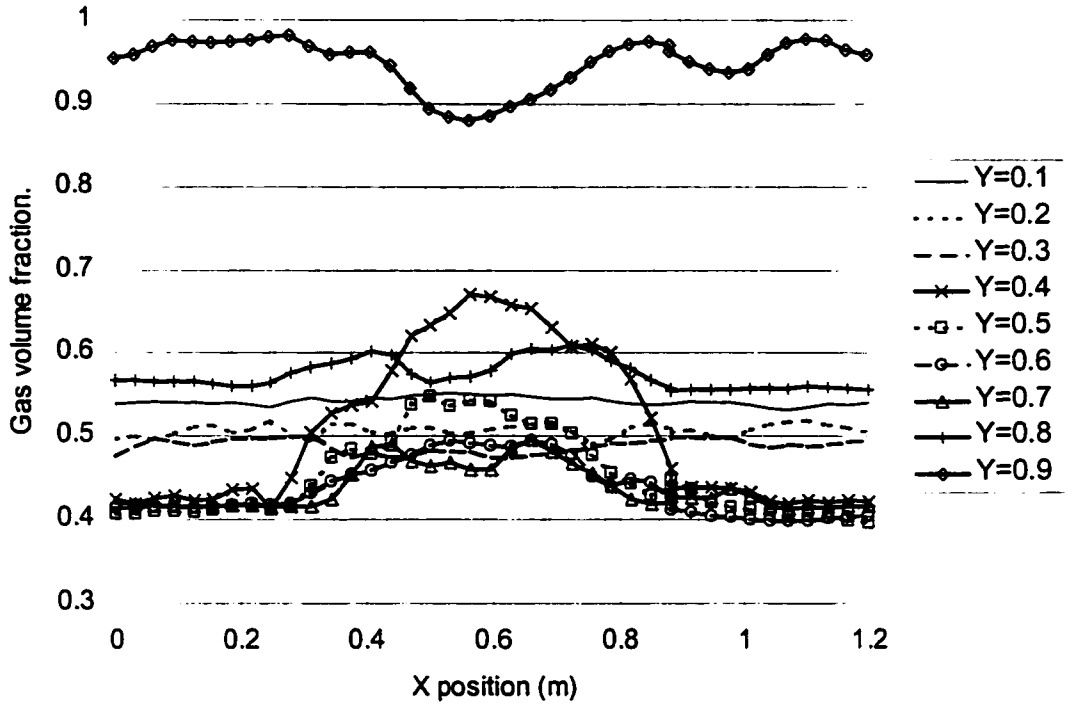

Figure 7.45 – Predicted time averaged gas volume fraction data for run GC01 across the width of the bed. $3U_{mf}$ U_{jet}=150m/s.

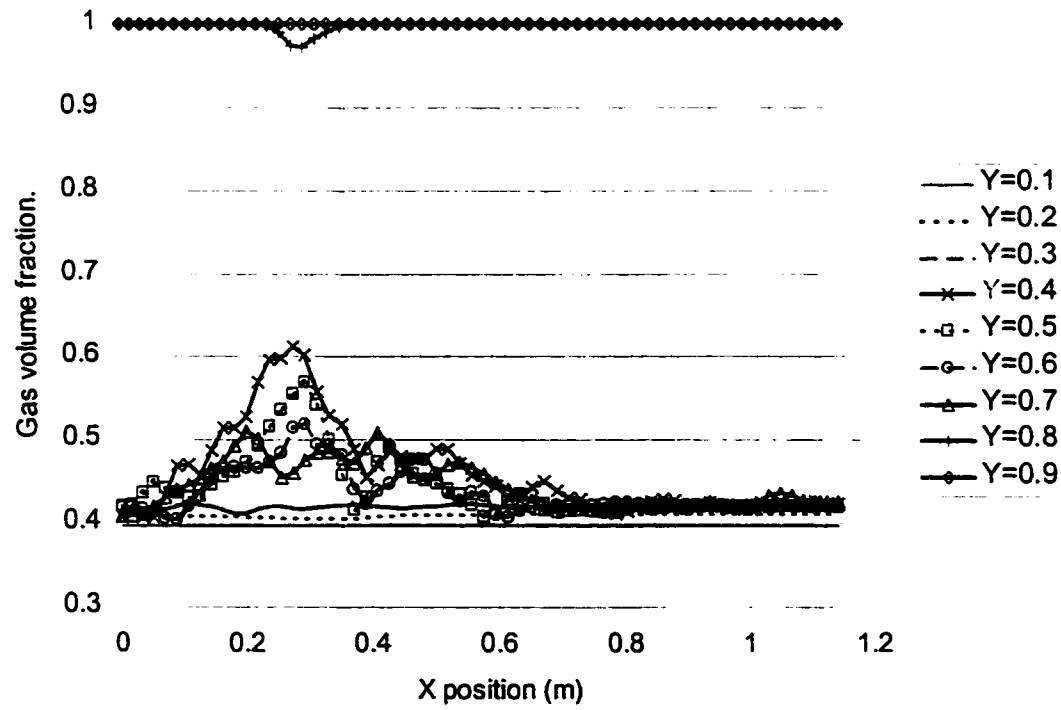

Figure 7.46 – Predicted time averaged gas volume fraction data for run GC03 across the width of the bed. $3U_{mf}$ U_{jet}=300m/s.

7.2.9 Summary of Physical Predictions

Results from the physical predictions have shown that the flow within the fluidized bed is extremely complicated and poses certain difficulties with modeling and interpretation of results. Overall flow patterns within the fluidized bed are characterized by two recirculating zones either side of the region through which the jet plume escapes upwards out of the surface of the fluidized bed. A smaller, elongated counter clockwise rotating recirculation zone is present above and to the left of the nozzle pipe. This recirculation zone has been shown to entrain solids from the top surface of the jet with the possibility of a dead zone within which entrained solids particles are constantly recirculated. This dead zone could lead to the formation of buildup on top surface of the nozzle pipe resulting in coking problems within the commercial reactor unit. A large clockwise solids recirculation zone was predicted in the bulk of the bed to the right of the nozzle. Solids in this zone have been predicted to be entrained from the lower surface of the gas jet. When operating in the bubbling fluidized bed regime the gas to solids contacting should be fairly good within the bulk of the bed due to the slow bed turnover and formation of bubbles within the bulk of the bed.

Fluidized bed behavior has been well predicted for different fluidization velocities with the CFX 4.2 solver. Aeration rates below minimum fluidization resulted in the formation of slow bubbles showing solids carrying through the bubble. Aeration rates at zero fluidization, or in the packed bed regime, proved difficult to achieve good numerical convergence. However, void fractions for this operating condition collapsed to the solids

packing fraction and very few bubbles were predicted to form within the bulk of the bed. This behavior appears to agree with expected physical behavior in this flow regime.

Simulations above minimum fluidization resulted in the bed operating as a bubbling bed and predicted the formation of bubbles off of the distributor plate. This behavior is in agreement with experimental observations. The transition from minimum fluidization to higher fluidization rates showed interesting plug flow like behavior and the formation of bubbles from flat gas volume fraction iso-surfaces. Bubbles within this flow regime exhibited slow bubble behavior. Bed surface heights behaved in accordance with expected experimental observations when the fluidization velocity was decreased. Decreased fluidization velocity caused a decrease in bed height; however, the ejection of bubbles out of the surface of the bed caused problems when trying to evaluate an average bed height.

Jet penetration depths agreed well with the literature correlation of Merry (1971); however, the simulations in the Gxxx series consistently underpredicted penetrations. Further problems occurred when trying to relate time averaged data for the Gxxx series to previous runs with larger orifice sizes. Continued efforts need to be expended to properly classify the flow regime within the Gxxx series of runs to get properly converged and reliable data.

Chapter 8

Conclusions and Recommendations

This chapter summarizes the findings from the simulation studies that were conducted using CFX 4.2 from AEA Technologies. The two fluid models available in CFX 4.2 appear to produce predictions which are in good qualitative agreement with gross bed properties such as jet penetration and bubble formation. More work is required to build confidence in the predictive capabilities of the much smaller scales within the fluidized beds.

8.1 Numerical Considerations

The two fluid model used in CFX 4.2 to predict the behavior of a multiphase gas/solids flow within a fluidized bed produced bubble and jet behavior qualitatively similar to that observed in the companion two dimensional fluidized bed at the University of Saskatchewan. Through extensive validation tests the following conclusions and recommendations are made in regard to using CFX 4.2 to model multiphase flows:

- Superbee discretization should be used with the solver so that bubble boundaries become distinct;
- A grid size of at least 30,000 control volumes should be used for the 1.2 x 1.2 x 0.1 m rectangular reactor geometry;
- Under relaxation parameters should be set to 0.6 for all momentum equations;
- The nozzle inlet boundary condition must be specified to be at least 2 x 2 control volumes in size to avoid interpolation problems associated with the velocity fields;
- Control volume sizes must be chosen so that the continuum modeling assumption is still statistically valid;
- Little difference in produced results was observed for Hydrodynamic model A or B. Use of either of these model for these simulations is acceptable;
- Further work needs to be done to investigate the effect of the solids pressure functions. Results for two different functions resulted in significant differences in bubble shape and formation within the fluidized bed. It is felt that the solids pressure function given by Benyahia *et al.* (1997) produces bubbles which are more realistic than those predicted with the function of Bouillard *et al.* (1989).

8.2 Physical Predictions

Qualitatively the predicted results agreed quite well with literature and experimental observations. Jet penetration depths agreed well with the correlation of Merry (1971); however, for much smaller nozzle diameters these predictions were poor. Continued work needs to address the effect of very small nozzle inlet diameters on the predicted penetration depth of the jet.

Two recirculation zones were predicted to form within the fluidized bed for all jet velocities at fluidization velocities greater than zero. A large clockwise rotating circulation zone was present in the bulk of the bed and a smaller counter clockwise recirculation zone was present above and to the left of the nozzle inlet pipe. Virtual seed particles have shown that solids above the jet plume within the fluidized bed were predicted to become "entrapped" in the counter clockwise recirculation zone above and to the left of the nozzle pipe. Those particles entrained into the jet from below tended to be swept into the larger clockwise recirculation zone in the bulk of the bed. The simulations tended to over predict this recirculatory behavior in comparison with observations from the experimental apparatus.

8.3 Recommendations

Computational fluid dynamic simulations of a two phase gas/solid fluidized bed are possible with the two fluid models available in CFX 4.2. The following are recommendations and future directions that should be pursued when implementing these models:

- First order discretization schemes must not be used for predictions. Higher order bounded schemes should be implemented. For these studies the Superbee TVD scheme was found to be most applicable. It is recommended that studies using the UNO and SONIC schemes be carried out to investigate the use of a completely second order discretization scheme;
- For larger simulations involving several feed nozzles in a more complicated geometry it is recommended that a nonstructured mesh be used. This facility is not currently available in CFX 4.2; however, AEA technology should be implementing this within the next year. Nonstructured meshing will allow greater flexibility for grid refinement close to the nozzle inlet boundary;
- Multiphase simulations produce vast quantities of data that must be interpreted. Visualization of this data is a problem and can be misleading. It is recommended that complete flow field data be saved every 0.05 seconds for analysis and rendering as animated movies. These movies provide a qualitative means by which the quality and realism of the simulations can be judged in addition to the question of numerical convergence. Saving point data from simulations can be very valuable to study time transients; however, if the simulation is predicting flow fields which look unreasonable, then there might be little value in these point measurements. Experimentalists are fortunate in that mere visual observation of an apparatus can be enough to determine whether it is functioning reasonably. This same approach should be applied to the computational results;
- There is a need for more thorough observations from experimental studies. Simulation results are only as good as the physical models, boundary and initial

conditions provided to the solver. It is recommended that all numerical simulations be validated against some experimental data.

REFERENCES

Abramovich, G.N. (1963) The Theory of Turbulent Jets. *MIT Press*, Massachusetts Institute of Technology. Cambridge, Massachusetts.

Alder, B.J., and Wainright, T.E. (1960) *J. Chem. Phys.*, **33**, 1439-1451.

Anderson, T.B., and Jackson, R. (1967) A Fluid Mechanical Description of Fluidized Beds. *I&EC Fund.*, **6**, 4, 527-539.

Andrews, M.J., and O'Rourke, P.J. (1996) The Multiphase Particle-In-Cell (MP-PIC) Method for Dense Particulate Flows. *Int. J. Multiphase Flow*, **22**, 2, 379-402.

Arastoopour, H., Lin, S.-C., and Weil, S.A. (1982) Analysis of Vertical Pneumatic Conveying of Solids Using Multiphase Flow Models. *AIChE J.*, **28**, 3, 467-473.

Arastoopour, H., and Gidaspow, D. (1979) Analysis of IGT Pneumatic Conveying Data and Fast Fluidization Using a Thermodynamic Model. *Powder Technology*, **22**, 77-87.

Aris, R. (1962) Vectors, Tensors and the Basic Equations of Fluid Mechanics. Dover Publications Inc., New York.

Bader, R., Findlay, J., and Knowlton, T.M. (1988) Gas/Solid Flow Patterns in a 30.5cm Diameter Circulating Fluidized Bed. *2nd Int. Circulating Fluidized Bed Conf.*, March 14-18, Compeigne, France.

Basov, V.A., Markhevka, V.I., Melik-Akhnazarov, T.Kh., and Orochko, D.I. (1969). Investigation of the Structure of a Non-uniform Fluidized Bed. *Int. Chem. Eng.*, **9**, 263.

Basset, A.B. (1888). *A Treatise on Hydrodynamics*, **2**. Cambridge: Deighton, Bell; (1961) New York: Dover.

Behie, L.A., Bergougnou, M.A., and Baker, C.G.J. (1975), Heat Transfer From a Grid Jet in a Large Fluidized Bed. *The Can. J. of Chem. Engr.*, **53**, 25-30.

Behie, L.A., and Kehoe, P. (1973). Grid Region in a Fluidized Bed Reactor. *AIChE J.*, **19**, 5, 1070-1072.

Behie, L.A., Bergougnou, M.A., Baker, C.G.J., and Bulani, W. (1970) Jet Momentum Dissipation at a Grid of a Large Gas Fluidized Bed. *The Can. J. of Chem. Eng.*, **48**, 158-161.

Benyahia, S., Arastoopour, H., and Knowlton, T. (1997) Numerical Analysis of Two-Dimensional Transient Gas-Solid Flow in a Pneumatic Conveying Line and in a Fluidized Bed with a Central Jet. *1997 ASME Fluids Engineering Division Summer Meeting FEDSM'97* June 22-26, 1997.

Berruti, F., Chaouki, J., Godfroy, L., Pugsley, T.S., and Patience, G.S. (1995) Hydrodynamics of Circulating Fluidized Bed Risers: A Review. *The Can. J. of Chem. Engr.*, **73**, 579-602.

Bird, R.B., Stewart, W.E., and Lightfoot, E.N. (1960) Transport Phenomena. John Wiley and Sons Inc.

Bouillard, J.X., Gidaspow, D., and Lyczkowski, R.W. (1991) Hydrodynamics of Fluidization: Fast-Bubble Simulation in a Two-Dimensional Fluidized Bed. *Powder Technology*, **66**, 107-118.

Bouillard, J.X., Lyczkowski, R.W., and Gidaspow, D. (1989) Porosity Distributions in a Fluidized Bed with an Obstacle. *AIChE J.*, **35**, 6, 908-922.

Capes, C., and Nakamura, K. (1988) Vertical Pneumatic Conveying: An Experimental Study with Particles in the Intermediate and Turbulent Flow Regimes. *The Can. J. of Chem. Engr.*, **51**, 31.

Carnahan, N.F., and Starling, K.E.(1969). *J. Chem. Phys.*, **51**. 635-636.

CFX 4.2 Solver Manual. AEA Technology, UK.

Chen, L., and Weinstein, H. (1997) Temperature Distribution Around Heated Horizontal Jet in Fluidized Bed. *AIChE J.*, **43**, 2373-2375.

Chen, L., and Weinstein, H. (1993) Shape and Extent of the Void Formed by a Horizontal Jet in a Fluidized Bed. *AIChE J.*, **39**, 12, 1901-1909.

Chyang, C.S., Chang, C.H., and Chang, J.H. (1997). Gas Discharge Modes at a Single Horizontal Nozzle in a Two Dimensional Fluidized Bed. *Powder Technology*. **90**, 71-77.

Clift, R. (1986). Hydrodynamics of Bubbling Fluidized Beds. In *Gas Fluidization Technology*. Ed. D. Geldart. New York: John Wiley & Sons.

Clift, R., and Grace, J.R. (1985). Continuous Bubbling an Slugging. In *Fluidization*, 2nd ed. Ed. Davidson, Clift and Harrison. London: Academic Press.

Crowe, C., Sommerfield, M., and Tsuji, Y. (1998) Multiphase Flows with Droplets and Particles. CRC Press LLC, 2000 Corporate Blvd., N.W., Boca Raton, Florida.

Davidson, J.F., and Harrison, D. (1963) Fluidized Particles. Cambridge, UK: Cambridge University Press.

Davidson, J.F. (1961a) Symposium on Fluidization - Discussion. *Trans. Inst. Chem. Eng.*, **39**, 230-232.

Davidson, J.F. (1961b) *Trans. Inst. Chem. Eng.*, **39**, 230.

Ding, J., and Gidaspow, D. (1990) A Bubbling Fluidization Model Using Kinetic Theory of Granular Flow. *AIChE J.*, **36**, 4, 523-538.

Eames, I., and Duursma, G. (1997) Displacement of Horizontal Layers by Bubbles Injected into Fluidized Beds. *Chem. Eng. Sci.*, **56**, 16, 2697-2705.

El-Kaissy, M.M. and Homsy, G.M. (1976). Instability Waves and the Origin of Bubbles in Fluidized Beds. *Int. J. Multiphase Flow.* **2**, 379-395.

Ettehadieh, B., Gidaspow, D. and Lyczkoski, R.W. (1984) Hydrodynamics of Fluidization in a Semicircular Bed with a Jet. *AIChE J.*, **30**, 4, 529-536.

Fan, L.-S., and Zhu, C. (1998) Principles of Gas-Solid Flows. *Cambridge University Press*. Cambridge, UK.

Fan, L.-S., and Tsuchiya, K. (1990). Bubble Wake Dynamics in Liquids and Liquid-Solid Suspensions. Boston: Butterworths.

Fanucci, J.B., Ness, N., and Yen, R.-H. (1979) On the Formation of Bubbles in Gas-Particulate Fluidized Beds. *J. Fluid Mech.*, **94**, part 2, 353-367.

FIELDView Manual (1999), Intelligent Light Visualization Solutions, 1290 Wall Street West, Third Floor, Lyndhurst, NJ 07071.

Filla, M., Massimilla, L., and Vaccaro, S. (1983) Gas Jets in Fluidized Beds and Spouts: A Comparison of Experimental Behavior and Models. *The Can. J. of Chem. Engr.* **61**, 370-376.

Foscolo, P.U., and Gibilaro, L.G. (1984). A Fully Predictive Criterion for the Transition between Particulate and Aggregate Fluidization. *Chem. Eng. Sci.* **39**, 1667-1675.

Gabor, J.D. (1972) On the Mechanics of Fluidized Particle Movement. *Chem. Eng. J.*, **4**, 118-126.

Gajdos, L., and Bierl, T. (1978) Studies in Support of Recirculating Bed Reactors for the Processing of Coal. Topical rept. for U.S. Dept. of Energy, Carnegie-Mellon Univ., Contract No. EX-76-c-01-2449.

Garg, S.K., and Pritchett, J.W. (1975). Dynamics of Gas-Fluidized Beds. *J. Appl. Phys.* **46**, 4493-4500.

Geldart, D. (1973) Types of Gas Fluidization. *Powder Technology*, **7**, 285-292.

Gidaspow, D. (1994). Multiphase Flow and Fluidization. San Diego, California. Academic Press.

Gidaspow, D., Tsuo, Y.P., and Luo, K.M. (1989) Computed and Experimental Cluster Formation and Velocity Profiles in Circulating Fluidized Beds. *Fluidization IV*, Int. Fluidization Conf., Banff, Alberta, Canada, May.

Gidaspow, D. (1986) Hydrodynamics of Fluidization and Heat Transfer: Supercomputer Modeling. *Appl. Mech. Rev.*, **39**, 1, 1-23.

Gidaspow, D., Lin, C., and Seo, Y.C. (1983a). Fluidization in Two-Dimensional Beds with a Jet. 1. Experimental Porosity Distributions. *Ind. Eng. Chem. Fundam.*, **22**, 187-193.

Gidaspow, D., and Ettehadieh, B. (1983b) Fluidization in Two-Dimensional Beds with a Jet. 2. Hydrodynamic Modeling. *Ind. Eng. Chem. Fundam.*, **22**, 193-201.

Gidaspow, D., and Solbrig, C.W. (1976) Transient Two Phase Flow Models in Energy Production. State of the Art Paper presented at the AIChE 81st National Meeting, 11-14 April 1976.

Grace, J.R., Avidan, A.A., and Knowlton, T.M. (1997). Circulating Fluidized Beds. London, UK: Blackie Academic and Professional.

Guedon, M.O., Baron, M.O.G., Briens, C.L., and Knowlton, T.M. (1994). Intermittent Injection of Prepolymer in a Pressurized Fluidized Bed. *Powder Technology*, **78**, 25-32.

Harris, S.E., and Crighton, D.G. (1994) Solitons, Solitary Waves and Voidage Disturbances in Gas-Fluidized Beds. *J. Fluid Mech.*, **266**, 243-276.

Hartge, E., Li, Y., and Werther, J. (1986) Analysis of the Local Structure of the Two-Phase Flow in a Fast Fluidized Bed. *Circulating Fluidized Bed Technology*, ed. P. Basu, Pergamon, Oxford.

Hong, R., Li, H., Li, H,. and Wang, Y. (1997) Studies on the Inclined Jet Penetration Length in a Gas-Solid Fluidized Bed. *Powder Technology*. **92**, 202-212.

Hoomans, B.P.B., Kuipers, J.A.M., Briels., W.J., and Van Swaaij, W.P.M. (1996) Discrete Particle Simulation of Bubble and Slug Formation in a Two-Dimensional Gas-Fluidized Bed: A Hard Sphere Approach. *Chem. Eng. Sci.*, **51**, 99-118.

Hrenya, C.M. and Sinclair, J.L. (1997) *AIChE J.*, **43**, 853-869.

Jackson, R. (1963). The Mechanics of Fluidized Beds. *Trans. Inst. Chem. Eng.* **41**, 13-38.

Kozanoglu, B., and Levy, E.K. (1991). Transient Mixing of Homogeneous Solids in a

Bubbling Fluidized Bed. *AIChE Symp. Ser.*, **87** (281), 58.

Krishna, R. (1993). Analogies in Multiphase Reactor Hydrodynamics. In *Encyclopedia of Fluid Mechanics*. Supplement 2. *Advances in Multiphase Flow*. Ed. N.P. Chereminisoff. Houston: Gulf Publishing.

Kuipers, J.A.M., Van Duin, K.J., Van Beckum, F.P.H. and Van Swaaij, W.P.M. (1992) A Numerical Model of Gas-Fluidized Beds. *Chem. Eng. Sci.*, **47**, 8, 1913-1924.

Kunii, D., and Levenspiel, O. (1991). Fluidization Engineering, 2nd ed., Butterworth-Heinemann, Boston.

Littman, H., and Homolka, G.A.J. (1973) The Pressure Field Around a Two-Dimensional Gas Bubble in a Fluidized Bed. *Chem. Eng. Sci.*, **28**, 2231-2243.

Lo, S.M. (1989) *Mathematical Basis of a Multi-Phase Flow Model.* United Kingdom Atomic Energy Authority. Report #AERE-R13432.

Lummi, A.P., and Baskakov, A.P. (1967) *Khim. Prom.*, **43**, 7, 522.

Lun, C.K.K. and Savage, S.B. (1986). *Acta Mechanica*, **63**, 15-44.

Lun, C.K.K., Savage, S.B., Jeffrey, D.J., and Chepurniy, D. (1984) Kinetic Theories for Granular Flow: Inelastic Particles in Couette Flow and Slightly Inelastic Particles. *J. Fluid Mech.*, **140**, 223-256.

Lyczkowski, R.W., Gamwo, I.K., Dobran, F., Ai, Y.H., Chao, B.T., Chen, M.M., and Gidaspow, D. (1993) Validation of Computed Solids Hydrodynamics and Pressure Oscillations in a Bubbling Atmospheric Fluidized Bed. *Powder Technology*, **76**, 65-77.

Lyczkowski, R.W., Gidaspow, D., and Solbrig, C.W. (1982) Multiphase Flow-Models for Nuclear, Fossil and Biomass Energy Production. Chapter in *Advances in Transport Processes*, ed. Mujumdar and Mashelkar, Wiley-Eastern, New York, 198-351.

Lyczkowski, R.W., Gidaspow, D., Solbrig, C.W., and Hughes, E.D. (1978) Characteristics and Stability Analyses of Transient One-Dimensional Two-Phase Flow Equations and Their Finite Difference Approximations. *Nucl. Sci. and Eng.*, **66**, 378-396.

Magnus, G. (1852). *Uber die Abweichung der geschosse, nebst einem Anhange: Uber eine auffallende Erscheinung bei rotirenden Korpern.* Berlin: F. Dummler.

Markhevka, V.I., Basov, V.A., Melik-Akhnazarov, T.Kh., and Orochko, D.I. (1971). The Flow of a Gas Jet into a Fluidized Bed. *Theor. Found. Chem. Eng.* **5**, 80.

Merry, J.M.D. (1975). Penetration of Vertical Jets into Fluidized Beds. *AIChE J.*, **21**, 3, 507-510.

Merry, J.M.D. (1971) Penetration of a Horizontal Gas Jet Into a Fluidised Bed. *Trans. Instn. Chem. Engrs.* **49**, 189-195.

Miller, A., and Gidaspow, D. (1992) Dense, Vertical Gas-Solid Flow in a Pipe. *AIChE J.*, November, **38**, 11, 1801-1815.

Mutsers, S.M.P, and Rietema, K. (1977). The Effect of Interparticle Forces on the Expansion of a Homogeneous Gas Fluidized Bed. *Powder Technology*. **18**, 239-248.

Nakamura, K., and Capes, C.E. (1973) Vertical Pneumatic Conveying: A Theoretical Study of Uniform and Annular Particle Flow Models. *The Can. J. of Chem. Engr.*, **51**, 39-46.

Patankar, S.V. (1980) Numerical Heat Transfer and Fluid Flow. Taylor and Francis.

Patankar, S.V., and Spalding. (1972) *Int. J. Heat and Mass Transfer*, **15**, 1787-1806.

Piepers, H.W., Cottar, E.J.E., Verkooijen, A.H.M., and Rietema, K. (1984). Effects of Pressure and Type of Gas on Particle-Particle Interaction and the Consequences for Gas-Solid Fluidization Behavior. *Powder Technology*, **37**, 55-70.

Pigford, R.L., and Baron, T. (1965) Hydrodynamic Stability of a Fluidized Bed. *Ind. Eng. Chem. Fundamentals*, **4**, 81-87.

Rasouli, R. (1981). One Dimensional Transient Unequal Velocity Two-Phase Flow by the Method of Characteristics. Ph.D. Thesis. Chicago, Illinois: Illinois Institute of Technology.

Rhie, C.M., and Chow, W.L. (1983) Numerical Study of the Turbulent Flow Past an Airfoil with Trailing Edge Separation. *AIAA Journal*, **21**, 11, 1525-1532.

Richardson, J.F., and Zaki, W.N. (1954) *Trans. Inst. Chem. Eng.*, **32**, 35-53.

Rietema, K. (1984). Powders: What are They? *Powder Technology*. **37**, 5-23.

Rietema, K. and Mutsers, S.M.P (1973). The Effect of Interparticle Forces on Expansion of a Homogeneous Gas-Fluidized Bed. pp. 32-33 in *Proceedings of International Symposium on Fluidization*. Toulouse, France.

Rots, P.E.A., Mudde, R.F., Van Den Akker, H.E.A., Van Der Hagen, T.H.J.J., and Van Dam, H. (1996) Fluidized Bed Nuclear Fission Reactor. *Chem. Eng. Sci.*, **51**, 11, 2763-2768.

Rowe, P.N., and Partridge, B.A. (1965). An X-Ray Study of Bubble in Fluidized Beds. *Trans. Instn. Chem. Engrs.*, **43**, 157.

Saffman, P.G. (1965) The Lift on a Small Sphere in a Slow Shear Flow. *J. Fluid Mech.*, **22**, 385.

Schiller and Nauman (1933) *Verein Deutscher Ingenieure*, **77**, 318.

Shakhova, N.A. (1972). Aerodynamics of Jets Discharged into Fluidized Beds. *Heat Transfer – Soviet Research*, **4**, 1, 133-142.

Shakhova, N.A. (1968) Discharge of Turbulent Jets into a Fluidized Bed. *J. Eng. Phys.*, **14**, 61-69.

Sinclair, J.L. (1997) *Hydrodynamic Modeling* in Circulating Fluidized Beds. Ed. Grace, J.R., Avidan, A.A., and Knowlton, T.M. Blackie Academic and Professional. London, England.

Sinclair, J.L., and Jackson, R. (1989) Gas-Particle Flow in a Vertical Pipe with Particle-Particle Interactions. *AIChE J.*, September, **35**, 9, 1473-1486.

Smith, J.M., Van Ness, H.C. and Abbott, M.M. (1949) Introduction to Chemical Engineering Thermodynamics. The McGraw-Hill Companies, Inc. 501-525.

Soo, S.L. (1989) *Particulates and Continuum: Multiphase Fluid Dynamics*. New York: Hemisphere.

Syamal, M., Rogers, W., and O'Brien, T.J. (1993) MFIX Documentation Theory Guide, U.S. Dept. of Energy, Office of Fossil Energy, DOE/METC-94/1004 DE94000087, Technical Note.

Tchen, C.M. (1947). *Mean Value and Correlation Problems Connected with the Motion of Small Particles in a Turbulent Field*. Ph.D. dissertation. Delft University, Netherlands.

Tsuo, Y.P,. and Gidaspow, D. (1990) Computation of Flow Patterns in Circulating Fluidized Beds. *AIChE J.*, **36**, 6, 885-896.

Tyler, J., and Mees, P.A.J. (1999) Computer Modeling of the Effect of a Horizontal Feed Jet on the Hydrodynamics of a Two-Dimensional Fluidized Bed. *Proceedings of the 3rd ASME/JSME Joint Fluids Engineering Conference*, July 18-23, San Francisco, California. Paper #FEDSM99-7905

Valenzuela, J.A.. and Glicksman, L.R. (1984) An Experimental Study of Solid Mixing in a Freely Bubbling Two-Dimensional Fluidized Bed. *Powder Technology*. **38**, 63-72.

Van Den Akker, H.E.A. (1998) Coherent Structures in Multiphase Flows. *Powder Technology.*, **100**, 123-136.

Van Wachem, B.G.M., Schouten, J.C., Krishna, R., van den Bleek, C.M., and Sinclair, J.L. (1999). CFD Modeling for Gas-Solid Flows: Qualitative and Quantitative Analysis of the Various Treatments. Proceedings of the 3rd ASME/JSME Joint Fluids Engineering Conference, July 18-23, San Francisco, California. Paper #FEDSM99-7899

Verloop, J., and Heertjes, P.M. (1970). Shock Waves as a Criterion for the Transition from Homogeneous to Heterogeneous Fluidization. *Chem. Eng. Sci.***25**, 828-832.

Weinstein, H., Shao, M., Schnitzlein, and Graff, R.A. (1986) Radial Variation in Void Fraction in a Fast Fluidized Bed. *Fluidization V, Proc. 5th Eng. Found. Conf. Fluidization, Elsinore, Denmark,* K. Ostergaard, A. Sorensen, eds., 329.

Wen, C.Y., Deole, N.R., and Chen, L.H. (1981) A Study of Jets in a Three-Dimensional Gas Fluidized Bed. 175-184.

Werther, J. and Xi, W. (1993) Jet Attrition of Catalyst Particles in Gas Fluidized Beds. *Powder Technology*, **76**, 39-46.

Witt, P.J., and Perry, J.H. (1995a) A Study in Multiphase Modeling of Fluidized Beds. *Proceedings of Computational Techniques and Applications: CTAC95.* July 3-5, 1995.

Witt, P.J., and Perry, J.H. (1995b) Prediction of the Hydrodynamic Behavior and Outlet Gas Composition of a Fluidized Bed Coal Gasifier. *Proceedings of Australian Symposium on Combustion including 4th Australian Flame Days*, Adelaide, November 9-10, 1995.

Witt, P.J., Perry, J.H., and Schwarz, M.P. (1998) A Numerical Model for Predicting Bubble Formation in a 3D Fluidized Bed. *Appl. Math.. Mod.*, **22**, 1071-1080.

Xuereb, C., Laguérie, and Baron, T. (1991) Etude du comportement de jets continus horizontaux ou inclines introduits dans un lit fluidisé par un gaz I: Morphologie des jets. *Powder Technology*, **67**, 43-56.

Yang, W.C., and Keairns, D.L. (1970). Recirculating Fluidized Bed Reactor Data Utilizing a Two-Dimensional Cold Model. *IAChE Symp. Ser. No. 141*, **70**, 27.

Yerushlmi, J., Turner, D.H., and Squires, A.M. (1976) The Fast Fluidized Bed. *Ind. Eng. Chem Process Des. Dev.*, **15**, 1, 47.

Zenz, F.A. (1968a). Bubble Formation and Grid Design. In *J.M.* Ed. Pirie, *Fluidization*, 136, Inst. Chem. Eng., London.

Zenz, F.A., (1968b) *Inst. Chem. Eng. Symp.* ser. 30, p 136.

APPENDIX A: Mathematical Proofs

A.1: Total Derivative of the Jacobian

As shown previously in Chapter 3 concerning the general conservation equation the transformation from a coordinate system to another results in the Jacobian matrix to account for volume changes. In this new coordinate system the volume of integration does not vary with time and as such the total derivative can be brought inside of the integral.

$$\frac{d}{dt}\bar{\bar{J}} = \frac{d}{dt}\left(\frac{\partial \bar{x}}{\partial \bar{\xi}}\right) = \frac{\partial}{\partial \bar{\xi}}\frac{d\bar{x}}{dt} = \frac{\partial \bar{v}}{\partial \bar{\xi}} \tag{A1.1}$$

Since $\bar{\xi}$ is constant with respect to time, the order of integration can be interchanged. The velocity vector $\bar{v}$ is considered to only be a function of the position vector $\bar{x}$ and the above expression can be expanded to:

$$\frac{\partial \bar{v}}{\partial \bar{\xi}} = \frac{\partial \bar{v}}{\partial x_1}\frac{\partial x_1}{\partial \bar{\xi}} + \frac{\partial \bar{v}}{\partial x_2}\frac{\partial x_2}{\partial \bar{\xi}} + \frac{\partial \bar{v}}{\partial x_3}\frac{\partial x_3}{\partial \bar{\xi}} \tag{A1.2}$$

Recall from the definition of a determinant of an *n x n* matrix:

$$\det \bar{\bar{A}} = \left|\bar{\bar{A}}\right| = \sum \pm a_{1i}a_{2j}\ldots a_{np} \tag{A1.3}$$

Where summation is over all permutations of *i,j,....,p* of *1,2,....,n* and the sign agrees with the parity of the permutation (i.e. negative for out of order permutation and positive for ordered permutations). The determinant of a *3 x 3* matrix would then have the following value:

$$\left|\bar{\bar{A}}_{3,3}\right| = a_{11}a_{22}a_{33} + a_{12}a_{23}a_{31} + a_{13}a_{21}a_{32} - a_{12}a_{21}a_{33} - a_{11}a_{23}a_{32} - a_{13}a_{22}a_{31} \quad \text{(A1.4)}$$

If the elements of the matrix are functions of some variable, in this case functions of t, differentiation of the matrix determinant will have to be expanded with respect to each variable using the chain rule resulting in a summation of determinants. The derivative of $\left|\bar{\bar{A}}\right|$ with respect to $\bar{x}$ is the sum of the n determinants obtained by replacing one row (or column) by the derivatives of its elements.

Continuing with the discussion of the full derivative of the Jacobian matrix and expressing it in terms of cofactors, A_{ij}:

$$\frac{d\bar{\bar{J}}}{dt} = \frac{d}{dt}\left(\frac{\partial x_1}{\partial \xi_1}\right)A_{11} + \frac{d}{dt}\left(\frac{\partial x_1}{\partial \xi_2}\right)A_{12} + \frac{d}{dt}\left(\frac{\partial x_1}{\partial \xi_3}\right)A_{13} +$$
$$\frac{d}{dt}\left(\frac{\partial x_2}{\partial \xi_1}\right)A_{21} + \frac{d}{dt}\left(\frac{\partial x_2}{\partial \xi_2}\right)A_{22} + \frac{d}{dt}\left(\frac{\partial x_2}{\partial \xi_3}\right)A_{23} +$$
$$\frac{d}{dt}\left(\frac{\partial x_3}{\partial \xi_1}\right)A_{31} + \frac{d}{dt}\left(\frac{\partial x_3}{\partial \xi_2}\right)A_{32} + \frac{d}{dt}\left(\frac{\partial x_3}{\partial \xi_3}\right)A_{33} \quad \text{(A1.5)}$$

This expression is most easily represented using tensor notation as follows:

$$\frac{d\bar{\bar{J}}}{dt} = \frac{d}{dt}\left(\frac{\partial x_i}{\partial \xi_\alpha}\right)A_{\alpha i} \quad \text{(A1.6)}$$

Interchanging the order of differentiation and using the cofactor property of determinants:

$$\frac{d}{dt}\left(\frac{\partial x_i}{\partial \xi_\alpha}\right)A_{\alpha i} = \frac{\partial}{\partial \xi_\alpha}\left(\frac{dx_i}{dt}\right)A_{\alpha i} = \frac{\partial v_i}{\partial \xi_\alpha}A_{\alpha i} \quad \text{(A1.7)}$$

$$= \frac{\partial v_i}{\partial x_j}\frac{\partial x_j}{\partial \xi_\alpha}A_{\alpha i} = \frac{\partial v_i}{\partial x_j}\delta_{ij}\bar{\bar{J}} \quad \text{(A1.8)}$$

$$= \frac{\partial v_i}{\partial x_i} \bar{\bar{J}} = \bar{\bar{J}}\left(\nabla \cdot \bar{v}\right) \tag{A1.9}$$

The material or total derivative of the Jacobian is:

$$\frac{d\bar{\bar{J}}}{dt} = \bar{\bar{J}}\left(\nabla \cdot \bar{v}\right) \tag{A1.10}$$

A.2: Gauss' or the Divergence Theorem

Let A be a closed surface bounding a volume v. A positive outward normal is defined on the surface A as $\hat{n}$ and define a vector function $\bar{F}$ to be continuous in this volume. The divergence theorem states:

$$\iiint_v \nabla \cdot \bar{F} dv = \iint_A \hat{n} \cdot \bar{F} dA \tag{A2.1}$$

Proof:

If we write $\bar{F}$ and $\hat{n}$ in components,

$\bar{F} = F_1\hat{i} + F_1\hat{j} + F_3\hat{k}$ and $\hat{n} = \cos\alpha\hat{i} + \cos\beta\hat{j} + \cos\gamma\hat{k}$ where α, β and γ are the angles between $\hat{n}$ and the unit axes, then the formula takes the form:

$$\iiint_v \left(\frac{\partial F_1}{\partial x} + \frac{\partial F_2}{\partial y} + \frac{\partial F_3}{\partial z} \right) dxdydz = \iint_A \left(F_1 \cos\alpha\hat{i} + F_2 \cos\beta\hat{j} + F_3 \cos\gamma\hat{k} \right) dA \tag{A2.2}$$

The above expression must be true if each of the vector components can be shown to be equivalent. That is:

$$\iiint_v \frac{\partial F_1}{\partial x} dxdydz = \iint_A F_1 \cos\alpha dA \qquad \text{(A2.3)}$$

The proof is for a special region v that is bounded by a piecewise smooth orientable surface A and has the property that any straight line parallel to any one of the coordinate axes and intersecting v has at most one segment (or a single point) in common with v. This implies that v can be represented in the form

$$f_1(x,y) \le z \le f_2(x,y) \qquad \text{(A2.4)}$$

where (x,y) varies in the orthogonal projection S of v in the xy-plane; see Figure A2.1.

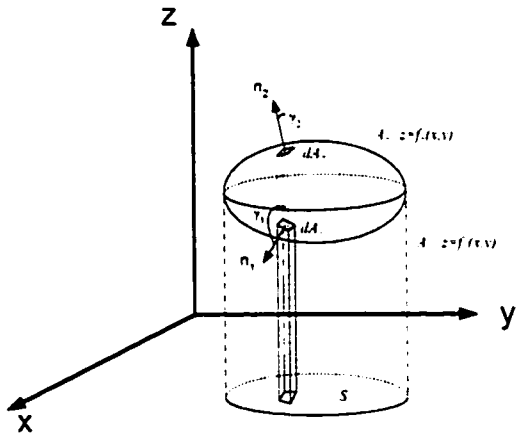

Figure A2.1 – Orientable surface showing projected area on plane axes.

The integration over z can be replaced using functional integrations as the limits

$$\iiint_v \frac{\partial F_1}{\partial x} dxdydz = \iint_A \left[\int_{z=f_1(x,y)}^{z=f_2(x,y)} \frac{\partial F_1}{\partial x} dz \right] dydx \qquad \text{(A2.5)}$$

$$= \iint_S F_1(x,y,z)\Big|_{z=f_1}^{f_2} dydx = \iint_S \left[F_1(x,y,f_2) - F_1(x,y,f_1) \right] dydx \qquad \text{(A2.6)}$$

For the upper bounding surface A_2, $dydx=cos\gamma_2 dA_2=\hat{k}\cdot\hat{n}_2 dA_2$ since the normal forms an acute angle γ_2 with the Cartesian basis vector $\hat{k}$. The same arguments can be applied to the lower bounding surface A_1 but since the normal forms an obtuse angle with the Cartesian basis vector $\hat{k}$ the sign of the cosine function is negative:

$$dydx=-cos\gamma_1 dA_1=-\hat{k}\cdot\hat{n}_1 dA_1 \tag{A2.7}$$

Making these substitutions into the previous expression gives:

$$\begin{aligned}&=\iint_S\left[F_1(x,y,f_2)-F_1(x,y,f_1)\right]dydx=\iint_{A_2}F_1\hat{k}\cdot\hat{n}_2 dA_2-\iint_{A_1}-F_1\hat{k}\cdot\hat{n}_1 dA_1\\&=\iint_A F_1\hat{k}\cdot\hat{n}dA\end{aligned} \tag{A2.8}$$

It has been shown that

$$\iiint_V\frac{\partial F_1}{\partial x}dv=\iint_A F_1\hat{k}\cdot\hat{n}\alpha dA \tag{A2.9}$$

for a single component. By projecting the surface onto the other axes, it can be shown to be true for the other components.

A.3: Number Density

The number density, n, is a statistical measure of the number of particles within a specific volume. As this volume increases an asymptotic number density is reached. Figure A3.1 defines the three different volumes (in this case shown as shaded areas) that are required to define the averages.

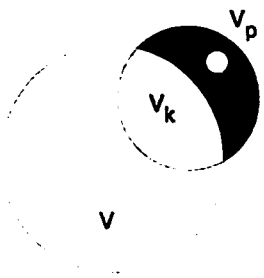

Figure A3.1 – Definition of local and intrinsic volume fractions.

$$n = \frac{\#\,particles}{unit\_volume} \tag{A3.1}$$

$$n = \frac{volume\_of\_one\_particle}{(volume\_of\_particles/total\_volume)} = v_p \frac{v}{v_k} \tag{A3.2}$$

$$= \frac{4}{3}\pi r^3 \frac{1}{\varepsilon_p} = \frac{\pi}{6}\frac{D_p^3}{\varepsilon_p} \tag{A3.3}$$

The number density has units of number of particles per unit volume.

APPENDIX B: Computer Codes

B.1: Minimum Control Volume MATLAB .M File

This MATLAB .M file will create the minimum control volume radius, R_{min}, based on a convergence tolerance bound of $\delta=1\%$ over a particle diameter range $50\mu m \le D_p \le 950\mu m$ and particle volume fraction of $0.01 \le \varepsilon_p \le 0.95$. A three dimensional surface plot is created; axes are not automatically labeled.

```
%[Z]=minimum_radius(delta,Dp,Alpha)
% Z  is a Dp x Alpha Matrix of the minimum CV radius
% delta is the required accuracy
% Dp is a vector of particle diameters in µm
% Alpha is the range of particle volume fractions

function [Z]=minimum_radius(delta,Dp,Alpha)

delta=0.01;
Dp=50:25:975;
Alpha=0.01:0.05:0.9;

for ni=1:size(Dp,2)
   for nj=1:size(Alpha,2)
      Z(ni,nj)=Dp(ni)*(Alpha(nj)^(-1/3)/sqrt(delta*2))*(1-
Alpha(nj));
   end
end

Z=Z/10^3;
%convert Z to units of mm from µm

surf(Alpha,Dp,Z)
view([10,-10,10])
colormap(white)
```

B.2: C Computer Code for Comparison of Different Discretization Schemes

The following computer code was used to discretize the one dimensional convection equation (Equation XXX in Chapter 3). Comments within the code should be sufficient to explain the purpose of each routine and the construction of the various discretization schemes.

```
//MECE 639: Assignment 4
//
// Jonathan Tyler
// November 19, 1998
//
// Revision:  003
// 11/06/98    Rewrote numerical routines to be float and
//             not double
//             Changed double 2D U array to a 1D array
//             calculate_TV routine corrected to use fabs
//             function, not abs
// 11/08/98   Rewrote file routine to write columnar data
//             as opposed to row data
//             Set up a new C++ project to work on the TVD
//             method.  All routines are the same as those
//             used for the flux limiter equations.
// 11/10/98    Rewrote all numerical schemes to share the
//             general flux limited equations.  TVD methods
//             now included in computation.
// 11/19/98    Nonoscillatory higher order upwind schemes
//             implemented on the old TVD code from
//             assignment 3
//             New routines added: MINMOD, MEDIAN3,
//             MEDIAN5, SIGN


#include <stdio.h>
#include <math.h>
#include <string.h>
#include <conio.h>
#include <stdlib.h>

//Define Subroutines
void set_initial_conditions(float *);
void display(float *);
void flux_limiter(int,float *,float *,float);
void calculate_TV(float *,float *,int);
```

```
FILE *create_output_file(int method,float Courant,int
frequency);
void write_data(FILE *,float *,float *,int,int);
void display2 (float *,float *);

//Routines added 11/19/98
float median5(float, float, float, float, float);
float median3(float, float, float);
float sign(float);
float minmod(float, float);



void main (void)
{

//Define variables

     int n;                    //number of time steps
     int frequency;            //every frequency iterations,
                               //write data
     int window=100;           //width of the window for
                               //writing
     FILE *fp;                 //output file pointer

     float *U1,*U2,*TV;
     U1=new float[900];        //Solution array1
     U2=new float[900];        //Solution array2
     TV=new float[3000];       //Total Variation array

     float Courant;            //Courant number
     int i,j,k,r,method=5;     //Generic counters and method
                               //select

/*   METHOD = 1 ==>  FIRST ORDER UPWIND
     METHOD = 2 ==>  LAX WENDROFF
     METHOD = 3 ==>  WARMING BEAN
     METHOD = 4 ==>  MINMOD TVD
     METHOD = 5 ==>  MUSCL TVD
     METHOD = 6 ==>  SUPERBEE TVD
     METHOD = 7 ==>  JONATHAN TVD*/

     char temp[19],key;

     do{
     printf("\n\nEnter method number (1-8)\n");
     printf("\t1.\tFIRST ORDER UPWIND\n");
```

```
      printf("\t2.\tLAX WENDROFF\n");
      printf("\t3.\tWARMING-BEAM\n");
      printf("\t4.\tMINMOD TVD\n");
      printf("\t5.\tMUSCL TVD\n");
      printf("\t6.\tSUPERBEE TVD\n");
      printf("\t7.\tJonathan TVD\n");
      printf("\t8.\tNonoscillatory MINMOD\n");
      printf("\t9.\tNonoscillatory SUPERBEE\n");
      printf("\t10.\tUNO2\n");
      printf("\t11.\tSONIC\n");

      scanf("%i",&method);

      printf("\nEnter the Courant number: ");
      scanf("%f",&Courant);

      n=int(600.0/Courant);

printf("\nMaximum number of time iterations is calculated
to be %i",n);

      printf("\nOutput data every ???? iterations: ");
      scanf("%i",&frequency);

      printf("\nContinue? (y/n)");
      } while((key=getch())!='y');



      fp=create_output_file(method,Courant,frequency);

      set_initial_conditions(U1);
      set_initial_conditions(U2);

      for(i=1;i<=3000;i++) TV[i]=0.0;     //Zero the TV
                                          //variable

//write file header data
          switch(method)
          {
          case 1:
               strcpy(temp,"FIRST ORDER UPWIND");
               break;
          case 2:
               strcpy(temp,"LAX WENDROFF      ");
               break;
```

```
            case 3:
                 strcpy(temp,"WARMING-BEAM      ");
                 break;
            case 4:
                 strcpy(temp,"MINMOD TVD        ");
                 break;
            case 5:
                 strcpy(temp,"MUSCL TVD         ");
                 break;
            case 6:
                 strcpy(temp,"SUPERBEE TVD      ");
                 break;
            case 7:
                 strcpy(temp,"JONATHAN TVD      ");
                 break;
            case 8:
                 strcpy(temp,"NOI MINMOD        ");
                 break;
            case 9:
                 strcpy(temp,"NOI SUPERBEE      ");
                 break;
            case 10:
                 strcpy(temp,"UNO2              ");
                 break;
            case 11:
                 strcpy(temp,"SONIC             ");
                 break;
            case 12:
                 strcpy(temp,"Jon's power scheme");
                 break;
            }
            fprintf(fp,"CFD method: %s\n",temp);
            fprintf(fp,"Courant=%f\n",Courant);
            fprintf(fp,"Output every %f
iterations\n",frequency);




      for(i=1;i<=n;i++)         //Time iteration n steps
      {


            for(k=2;k<=800;k++)
                 TV[i]=TV[i]+fabs(U1[k]-U1[k-1]);
```

```
          flux_limiter(method,U1,U2,Courant);

          for (j=1;j<=900;j++)      //Exchange old with new
               U1[j]=U2[j];

     if(fmod(i,frequency)==0||i==1)
          write_data(fp,U1,TV,i,window);

     }
     fprintf(fp,"\nCourant=%f",Courant);

     for(i=1;i<=n;i++)
          fprintf(fp,"\nTV[%i]=\t%f",i,TV[i]/TV[1]);


     delete U1;           //clean up memory allocations
     delete U2;
     delete TV;

     fclose(fp);
}



     /*****************************************
     **          SUBROUTINES                  **
     *****************************************/

void set_initial_conditions(float *U)
{
//This subroutine sets the initial parabola, spike and
//top hat wave form on the one dimensional mesh.
     int i;
     float dx=1.0;
     float x=0.0;

     for (i=1;i<=900;i++)U[i]=0.0;
//Zero all values on the mesh

     for (i=20;i<=40;i++)
//Create the parabola
     {
          x=float(i)*dx;
          U[i]=sqrt(1.0 - pow(x-30.0*dx,2.0) /
(pow(10.0*dx,2.0)) );
     }
```

```
     for (i=60;i<=70;i++)
//Create the spike
     {
          x=float(i)*dx;
          U[i]=(x-60.0*dx)/(10.0*dx);
     }

     for (i=70;i<=80;i++)
     {
          x=float(i)*dx;
          U[i]=1.0-(x-70.0*dx)/(10.0*dx);
     }

     for (i=100;i<=120;i++)
//Create the top hat (square or shock wave)
     {
          U[i]=1.0;
     }
}

void display (float *U)
{
     int i,j;

     for (j=0;j<=20;j++)
     {
          for (i=1;i<20;i++)
          {
               printf("\nU[%i,1]=%f",j*20+i,U[j*20+i]);
          }
          getchar();
     }
}



void flux_limiter(int method,float *U1,float *U2,float
Courant)
{
     float
r1,r2,phi1,phi2,temp1,temp2,eps,hold,hold1,hold2;
     float UC,Uup,Uup2,U_plus_half,U_minus_half;
     float Uc_minus_half,Uc_plus_half,Uc_minus_3half,

     Uup_plus_half,Uup_minus_half,Uup2_plus_half,Uup2_minus
_half,
```

```
        modify1,modify2,modify;

    int i;                      //generic counter to run
                                //through grid
    modify=0.25;
    eps=1.0e-12;

    for(i=5;i<=899;i++)
    {

    switch (method)
    {
    case 1:
         //FIRST ORDER UPWINDING
         phi1=0.0;
         phi2=0.0;
         break;

    case 2:
         //LAX-WENDROFF UPWINDING
         phi1=1.0;
         phi2=1.0;
         break;

    case 3:
         //WARMING-BEAM 2ND ORDER UPWIND
         temp2=0.5*Courant*(1-Courant)*(U1[i]-2.0*U1[i-
1]+U1[i-2]);
         phi2=1.0;
         phi1=0.0;
         break;

         //TVD METHODS BELOW
    case 4:
         //MIN-MOD TVD
         r1=(U1[i-1]-U1[i-2])/(U1[i]-U1[i-1]+eps);
         r2=(U1[i]-U1[i-1])/(U1[i+1]-U1[i]+eps);

         hold=min(float(1.0),r1);
         phi1=max(float(0.0),hold);

         hold=min(float(1.0),r2);
         phi2=max(float(0.0),hold);
         break;

    case 5:
         //MUSCL TVD
```

```
      r1=(U1[i-1]-U1[i-2])/(U1[i]-U1[i-1]+eps);
      r2=(U1[i]-U1[i-1])/(U1[i+1]-U1[i]+eps);

      phi1=(fabs(r1)+r1)/(1.0+fabs(r1));
      phi2=(fabs(r2)+r2)/(1.0+fabs(r2));
      break;

case 6:
      //SUPERBEE TVD
      r1=(U1[i-1]-U1[i-2])/(U1[i]-U1[i-1]+eps);
      r2=(U1[i]-U1[i-1])/(U1[i+1]-U1[i]+eps);

      hold=min(float(2.0*r1),float(1.0));
      hold1=min(r1,float(2.0));
      hold2=max(hold,hold1);
      phi1=max(float(0.0),hold2);

      hold=min(float(2.0*r2),float(1.0));
      hold1=min(r2,float(2.0));
      hold2=max(hold,hold1);
      phi2=max(float(0.0),hold2);
      break;

case 7:
      //JONATHAN TVD
      r1=(U1[i-1]-U1[i-2])/(U1[i]-U1[i-1]+eps);
      r2=(U1[i]-U1[i-1])/(U1[i+1]-U1[i]+eps);

      hold=min(float(1.7*r1),float(1.0));
      hold1=min(r1,float(1.5));
      hold2=max(hold,hold1);
      phi1=max(float(0.0),hold2);

      hold=min(float(1.7*r2),float(1.0));
      hold1=min(r2,float(1.5));
      hold2=max(hold,hold1);
      phi2=max(float(0.0),hold2);
      break;



//Nonoscillatory schemes below
case 8:
//Nonoscillatory MINMOD

Uc_plus_half=0.5*(U1[i]+U1[i+1]);
Uc_minus_half=0.5*(U1[i-1]+U1[i]);
```

```
      Uc_minus_3half=0.5*(U1[i-2]+U1[i-1]);

      Uup_plus_half=U1[i]+(U1[i]-Uc_minus_half);
      Uup_minus_half=U1[i-1]+(U1[i-1]-Uc_minus_3half);

      Uup2_plus_half=U1[i]+(U1[i]-U1[i-1]);
      Uup2_minus_half=U1[i-1]+(U1[i-1]-U1[i-2]);

      U_plus_half=median3(U1[i],Uc_plus_half,Uup_plus_half);
      U_minus_half=median3(U1[i-
1],Uc_minus_half,Uup_minus_half);
      break;

      case 9:
      //Nonoscillatory SUPERBEE
      Uc_plus_half=0.5*(U1[i]+U1[i+1]);
      Uc_minus_half=0.5*(U1[i-1]+U1[i]);
      Uc_minus_3half=0.5*(U1[i-2]+U1[i-1]);

      Uup_plus_half=U1[i]+(U1[i]-Uc_minus_half);
      Uup_minus_half=U1[i-1]+(U1[i-1]-Uc_minus_3half);

      Uup2_plus_half=U1[i]+(U1[i]-U1[i-1]);
      Uup2_minus_half=U1[i-1]+(U1[i-1]-U1[i-2]);

      U_plus_half=median5(U1[i],Uc_plus_half,Uup_plus_half,U
1[i+1],Uup2_plus_half);
      U_minus_half=median5(U1[i-
1],Uc_minus_half,Uup_minus_half,U1[i],Uup2_minus_half);
      break;



      case 10:
      //UNO2

      //Calculate LW parabolic interpolation of central
difference
      temp1=U1[i+1]-2.0*U1[i]+U1[i-1];              //Di
      temp2=U1[i+2]-2.0*U1[i+1]+U1[i];              //Di+1

      Uc_plus_half=0.5*(U1[i]+U1[i+1])-
0.25*minmod(temp1,temp2);

      temp1=U1[i]-2.0*U1[i-1]+U1[i-2];              //Di-1
      temp2=U1[i+1]-2.0*U1[i]+U1[i-1];              //Di
```

```
     Uc_minus_half=0.5*(U1[i-1]+U1[i])-
0.25*minmod(temp1,temp2);

     temp2=U1[i-1]-2.0*U1[i-2]+U1[i-3];          //Di-2
     temp1=U1[i]-2.0*U1[i-1]+U1[i-2];            //Di-1

     Uc_minus_3half=0.5*(U1[i-2]+U1[i-1])-
0.25*minmod(temp1,temp2);

     //Calculate first order upwinding based on parabolic
     //interpolation
     Uup_plus_half=U1[i]+(U1[i]-Uc_minus_half);
     Uup_minus_half=U1[i-1]+(U1[i-1]-Uc_minus_3half);

     //Calculate second order upwinding
     Uup2_plus_half=U1[i]+(U1[i]-U1[i-1]);
     Uup2_minus_half=U1[i-1]+(U1[i-1]-U1[i-2]);

     U_plus_half=median3(U1[i],Uc_plus_half,Uup_plus_half);
     U_minus_half=median3(U1[i-
1],Uc_minus_half,Uup_minus_half);


     break;

     case 11:
//SONIC
//Calculate LW parabolic interpolation of central
// difference
     temp1=U1[i+1]-2.0*U1[i]+U1[i-1];          //Di
     temp2=U1[i+2]-2.0*U1[i+1]+U1[i];          //Di+1

     Uc_plus_half=0.5*(U1[i]+U1[i+1])-
C.25*minmod(temp1,temp2);

     temp1=U1[i]-2.0*U1[i-1]+U1[i-2];           //Di-1
     temp2=U1[i+1]-2.0*U1[i]+U1[i-1];           //Di

     Uc_minus_half=0.5*(U1[i-1]+U1[i])-
0.25*minmod(temp1,temp2);

     temp2=U1[i-1]-2.0*U1[i-2]+U1[i-3];          //Di-2
     temp1=U1[i]-2.0*U1[i-1]+U1[i-2];            //Di-1

     Uc_minus_3half=0.5*(U1[i-2]+U1[i-1])-
0.25*minmod(temp1,temp2);
```

```
     //Calculate first order upwinding based on parabolic
     //interpolation
     Uup_plus_half=U1[i]+(U1[i]-Uc_minus_half);
     Uup_minus_half=U1[i-1]+(U1[i-1]-Uc_minus_3half);


     //Calculate second order upwinding
     Uup2_plus_half=U1[i]+(U1[i]-U1[i-1]);
     Uup2_minus_half=U1[i-1]+(U1[i-1]-U1[i-2]);

     U_plus_half=median5(Uc_plus_half,Uup_plus_half,U1[i],U
1[i+1],Uup2_plus_half);

     U_minus_half=median5(Uc_minus_half,Uup_minus_half,U1[i
-1],U1[i],Uup2_minus_half);

     break;


     case 12:
     //jon's scheme

     if(fabs(U1[i+1]-U1[i]) > fabs(U1[i-1]-U1[i]))
          modify=0.40;
     if(fabs(U1[i+1]-U1[i]) < fabs(U1[i-1]-U1[i]))
          modify=0.1;

//Calculate LW parabolic interpolation of central
//difference
     temp1=U1[i+1]-2.0*U1[i]+U1[i-1];              //Di
     temp2=U1[i+2]-2.0*U1[i+1]+U1[i];              //Di+1


     Uc_plus_half=0.5*(U1[i]+U1[i+1])-
modify*minmod(temp1,temp2);

     temp1=U1[i]-2.0*U1[i-1]+U1[i-2];              //Di-1
     temp2=U1[i+1]-2.0*U1[i]+U1[i-1];              //Di

     Uc_minus_half=0.5*(U1[i-1]+U1[i])-
modify*minmod(temp1,temp2);

     temp2=U1[i-1]-2.0*U1[i-2]+U1[i-3];            //Di-2
     temp1=U1[i]-2.0*U1[i-1]+U1[i-2];              //Di-1
```

```
     Uc_minus_3half=0.5*(U1[i-2]+U1[i-1])-
modify*minmod(temp1,temp2);

     //Calculate first order upwinding based on parabolic
     //interpolation
     Uup_plus_half=U1[i]+(U1[i]-Uc_minus_half);
     Uup_minus_half=U1[i-1]+(U1[i-1]-Uc_minus_3half);



     //Calculate second order upwinding
     Uup2_plus_half=U1[i]+(U1[i]-U1[i-1]);
     Uup2_minus_half=U1[i-1]+(U1[i-1]-U1[i-2]);

     U_plus_half=median5(Uc_plus_half,Uup_plus_half,U1[i],U
1[i+1],Uup2_plus_half);

     U_minus_half=median5(Uc_minus_half,Uup_minus_half,U1[i
-1],U1[i],Uup2_minus_half);

     break;
     }

          if(method<9)
          {
          temp1=U1[i]-Courant*(U1[i]-U1[i-1]);
//first half of flux equation
          temp2=0.5*Courant*(1-Courant)*(U1[i+1]-
2.0*U1[i]+U1[i-1]);
//second half of flux equation

          U2[i]=temp1-0.5*Courant*(1-
Courant)*(phi2*(U1[i+1]-U1[i])-
                         phi1*(U1[i]-U1[i-1]));
          //put the flux limited equation together
          }

          else
          {
          U2[i]=U1[i]-Courant* (U_plus_half - U_minus_half)
+ pow(Courant,2.0) *(U_plus_half-U1[i] - U_minus_half+U1[i-
1]);
          //working equation for the nonoscillatory schemes
          }

          U2[1]=0.0;
          U2[900]=0.0;
```

```
          //reset boundary conditions

     }

}

void calculate_TV(float *U1,float *TV,int step)
{
     int i;
     TV[step]=0.0;
     for (i=2;i<=900;i++)
          TV[step]=TV[step]+fabs(U1[i]-U1[i-1]);

}



FILE *create_output_file(int method,float Courant,int
frequency)
{
     FILE *fp;
     char filename[40];              //File name and path
     char temp[19];                       //Just a string


     printf("\nPlease enter filename and dos path:\n");
     scanf("%s",&filename);


     if ((fp = fopen(filename, "w"))
          == NULL)
     {
          fprintf(stderr, "Cannot open input file.\n");
     }



          if (fp!=NULL)
     {
          printf("\nFile opened, writing header");


     }
     return fp;
}
```

```
void write_data(FILE *fp,float *U1,float *TV,int i,int
window)
{
     int j;

     fprintf(fp,"\n\nITERATION IS %i and window
%f",i,window);

     for (j=1;j<=900;j++)
     {
          fprintf(fp,"%i\t%f\n",j,U1[j]);
     }
}


void display2 (float *U1,float *U2)
{
     int i,j;

     for (j=0;j<=20;j++)
     {
          for (i=0;i<20;i++)
          {

     printf("\nU1[%i]=%f\tU2[%i]=%f",j*20+i,U1[j*20+i],j*20
+i,U2[j*20+i]);
          }
          getchar();
     }
}

float sign(float value)
{
/* Sign function returns the sign of the argument passed to
it*/
/* -1 is for a negative argument
      1 is for a positivie argument*/

     if (value<0.0) return -1.0;
          return 1.0;
}


float minmod(float A, float B)
{
/*MINMOD function which is defined as:
      SIGN(A)*MAX(0,SIGN(AB)MIN(|A|,|B|) */
```

```
     return
(sign(A)*max(0.0,sign(A*B)*min(fabs(A),fabs(B))));
}

float median3(float A, float B, float C)
{
     return(A+minmod(B-A,C-A));
}

float median5(float A, float B, float C, float D, float E)
{
//Returns the median value from a list of five numbers
     float X1, X2,temp1,temp2;
     X1=median3(A,B,C);
     temp1=max(A,B);
     temp2=max(C,D);
     X2=A+B+C+D-max(temp1,temp2);
     temp1=min(A,B);
     temp2=min(C,D);
     X2=X2-min(temp1,temp2)-X1;
     return (median3(X1,X2,E));
}
```

Appendix C: CFX 4.2 Command and Fortran Files

These two files are a representative sample of the command and FORTRAN files used to set up the computational fluid dynamics simulation. Comments in the code will provide information about modifications for future tests.

*C.2: CFX 4.2 Command File *.fc*

More information about the structure of the CFX command file can be found in the CFX Solver Manual.

```
/* CFX 4.2 Command File for Fluidized Bed Simulations*/

/* September 22, 1999*/
/* Jonathan Tyler*/
/* Dept of Chemical and Materials Engineering*/
/* University of Alberta*/
/* Edmonton, Alberta, Canada*/

/* Two phase fluidized bed simulation with side injection*/
/* horizontal gas feed jet.  Part of Jonathan Tyler's*/
/* Masters thesis work.*/


/* JUNE 17, 1999*/
/* GRID REFINEMENT TESTS: PARTICLE DENSITY SET TO*/
/* 1450KG/M^3*/


/* JUNE 11, 1999*/
/* 3X3 NOZZLE, PARTICLE DENSITY CHANGED TO 930KG/M^3*/
/* NOZZLE DIAMETER NOW SET AT 2.9245E-3M TO MORE */
/* ACCURATELY REPRESENT DR. BERUTTI'S NOZZLE*/

/* MAY 18, 1999 */
/* CONTINUATION RUNS OF PREVIOUS SIMULATIONS FROM CDROM 2*/
/* THIS RUN CONTINUES FROM CD2/SUPERBEE/V_AT_300/M05.DMP */
/* FLUIDIZATION GAS REDUCED TO 50% OF MINIMUM*/
/* FLUIDIZATION*/
/* AMG AND UNDERRELAXATION FACTORS SET*/
/* MAX ITERATIONS REDUCED TO 30*/

/* RUN TO SIMULATE DR BERRUTI'S SIMULATIONS */
```

```
/* FEB 16, 1999 */


/* RUN TO SIMULATE DR BERRUTI'S SIMULATIONS */
/* FEB 16, 1999 */


/*  Physical Properties  */
#CALC
DP=3.7E-4;
RHOP=950;
VISCP=1.0E-12;
EMIN=0.49;

EPTCEL=0.0001;
G=-600;
CMPVF=0.376;

RHOG=1.2;
VISCG=1.8e-5;

GASVL=RHOG*(RHOP-RHOG)*9.81*DP*DP*0.091/(150*VISCG);
GASVEL=2.0*GASVL/RHOG;
#ENDCALC


/*  INLET BOUNDARY CONDITIONS  */
#CALC
VELNOZ=300.0;
#ENDCALC

/*  PROGRAM CONTROL  */
#CALC
MASSTOL=5.0E-6;
MAXITER=30;
MINITER=1;
#ENDCALC

>>CFX4
  >>SET LIMITS
    LARGE
    TOTAL REAL WORK SPACE 30000000
    TOTAL INTEGER WORK SPACE 30000000
    END
  >>OPTIONS
    THREE DIMENSIONS
    NUMBER OF PHASES     2
```

```
    TRANSIENT FLOW
    BUOYANT FLOW
    END
  >>USER FORTRAN
    USRINT
    USRGRD
    USRTPL
    END
>>MODEL TOPOLOGY
>>MODEL DATA
  >>DIFFERENCING SCHEME
    ALL EQUATIONS 'SUPERBEE'
    VOLUME FRACTION 'SUPERBEE'
    PRESSURE 'CENTRAL'
    END
  >>TITLE
    PROBLEM TITLE 'RUN GC02'
    END
  >>WALL TREATMENTS
    SLIP
    END
  >>RHIE CHOW SWITCH
    STANDARD
    END
  >>PHYSICAL PROPERTIES
    >>BUOYANCY PARAMETERS
      GRAVITY VECTOR 0.0 -9.81 0.0
      BUOYANCY REFERENCE DENSITY 1.2
      END
    >>FLUID PARAMETERS
      PHASE NAME 'PHASE1'
      VISCOSITY #VISCG
      DENSITY #RHOG
      END
    >>FLUID PARAMETERS
      PHASE NAME 'PHASE2'
      VISCOSITY #VISCP
      DENSITY  #RHOP
      END
    >>TRANSIENT PARAMETERS
      >>FIXED TIME STEPPING
        TIME STEPS 2000 * 0.001
     END
    >>MULTIPHASE PARAMETERS
      >>INTER PHASE TRANSFER MODELS
        >>MOMENTUM
          >>PARTICLE DRAG MODEL
```

```
        FLOW REGIME 'AUTOMATIC'
        VISCOUS REGIME CORRELATION 'SCHILLER-NAUMANN'
        NEWTON COEFFICIENT 0.44
           DENSE PARTICLE EFFECTS 'GIDASPOW'
           END
     >>PHASE DESCRIPTION
     PHASE NAME 'PHASE1'
        GAS
     CONTINUOUS
     END
     >>PHASE DESCRIPTION
     PHASE NAME 'PHASE2'
     SOLID
     DISPERSE
     MEAN DIAMETER #DP
     SOLID PRESSURE
     SOLID COMPACTION MODULUS #G
     COMPACTION VOLUME FRACTION #CMPVF
     MODIFY EMPTY CELL VELOCITY #EPTCEL
     END
>>SOLVER DATA
  >>UNDER RELAXATION FACTORS
    U VELOCITY 0.6
    V VELOCITY 0.6
    W VELOCITY 0.6
    END
  >>ALGEBRAIC MULTIGRID PARAMETERS
    CONNECTIVITY TOLERANCE 1.0E-14
    SINGULARITY TOLERANCE 1.0E-3
    WORK SPACE FACTOR 2.0
    JACOBI SMOOTHER
    END
  >>PRESSURE CORRECTION
    PISO
    NUMBER OF PISO CORRECTION STEPS 2
    END
  >>EQUATION SOLVERS
    ALL PHASES
    U VELOCITY 'AMG'
    V VELOCITY 'AMG'
    W VELOCITY 'AMG'
    PRESSURE 'ICCG'
    VOLUME FRACTION 'AMG'
    END
  >>PROGRAM CONTROL
    MINIMUM NUMBER OF ITERATIONS   #MINITER
    MAXIMUM NUMBER OF ITERATIONS   #MAXITER
```

```
    PRESSURE REFERENCE POINT BLOCK 'BLOCK-1'
    PRESSURE REFERENCE POINT 10 10 3
    OUTPUT MONITOR POINT 15 20 4
    MASS SOURCE TOLERANCE #MASSTOL
    END
>>CREATE GRID
>>MODEL BOUNDARY CONDITIONS
  >>PRESSURE BOUNDARIES
    PATCH NAME 'OUTLET'
    PHASE NAME 'PHASE1'
    VOLUME FRACTION 1.0
    PRESSURE 0.0
    END
  >>PRESSURE BOUNDARIES
    PATCH NAME 'OUTLET'
    PHASE NAME 'PHASE2'
    VOLUME FRACTION 0.0
    PRESSURE 0.0
    END
  >>INLET BOUNDARIES
    PATCH NAME 'DISTRIBUTOR'
    PHASE NAME 'PHASE1'
    VOLUME FRACTION 1.0
    V VELOCITY #GASVEL
    U VELOCITY 0.0
    W VELOCITY 0.0
    END
  >>INLET BOUNDARIES
    PATCH NAME 'DISTRIBUTOR'
    PHASE NAME 'PHASE2'
    VOLUME FRACTION 0.0
    U VELOCITY 0.0
    V VELOCITY 0.0
    W VELOCITY 0.0
    END
  >>INLET BOUNDARIES
    PATCH NAME 'NOZZLE'
    PHASE NAME 'PHASE1'
    VOLUME FRACTION 1.0
    U VELOCITY #VELNOZ
    V VELOCITY 0.0
    W VELOCITY 0.0
    END
  >>INLET BOUNDARIES
    PATCH NAME 'NOZZLE'
    PHASE NAME 'PHASE2'
    VOLUME FRACTION 0.0
```

```
    U VELOCITY 0.0
    V VELOCITY 0.0
    W VELOCITY 0.0
    END
>>OUTPUT OPTIONS
  >>FRONTEND PRINTING
    NO TOPOLOGY STRUCTURE
    END
  >>LINE GRAPH DATA
    XYZ  0.30 0.37 0.05
    EACH TIME STEP
    FILE NAME 'PLOT_1'
    PHASE NAME 'PHASE1'
    U VELOCITY
    VOLUME FRACTION
    END
  >>LINE GRAPH DATA
    XYZ  0.35 0.37 0.05
    EACH TIME STEP
    FILE NAME 'PLOT_2'
    PHASE NAME 'PHASE1'
    U VELOCITY
    VOLUME FRACTION
    END
  >>LINE GRAPH DATA
    XYZ  0.40 0.37 0.05
    EACH TIME STEP
    FILE NAME 'PLOT_3'
    PHASE NAME 'PHASE1'
    U VELOCITY
    VOLUME FRACTION
    END
  >>LINE GRAPH DATA
    XYZ  0.45 0.37 0.05
    EACH TIME STEP
    FILE NAME 'PLOT_4'
    PHASE NAME 'PHASE1'
    U VELOCITY
    VOLUME FRACTION
    END
  >>LINE GRAPH DATA
    XYZ  0.60 0.37 0.05
    EACH TIME STEP
    FILE NAME 'PLOT_5'
    PHASE NAME 'PHASE1'
    U VELOCITY
    VOLUME FRACTION
```

```
    END
  >>LINE GRAPH DATA
    XYZ  0.35 0.70 0.05
    EACH TIME STEP
    FILE NAME 'PLOT_6'
    PHASE NAME 'PHASE1'
    U VELOCITY
    VOLUME FRACTION
    END
  >>PRINT OPTIONS
    >>WHAT
      NO VARIABLES
      NO WALL PRINTING
      NO GEOMETRIC INFORMATION
      END
  >>DUMP FILE OPTIONS
    ALL VARIABLES
    TIME INTERVAL 0.05
    END
>>STOP
```

C.2: CFX 4.2 Fortran File

This is the accompanying fortran file that must be used in conjunction with the CFX 4.2 command file to set up the fluidized bed simulations used for this work. Values used in this fortran file are typical and can be changed to specify new geometry and flow conditions. Please note that some incorrect formatting may have resulted form importing this source code into the word processor.

```
C Fortran File for CFX 4.2 Fluidized Bed Simulations
C Jonathan Tyler
C September 22, 1999
C Dept of Chemical and Materials Engineering
C University of Alberta
C Edmonton, Alberta, Canada
C
C This fortran file creates the discretization mesh,
C maps related patches for nozzle inlets, pipes, etc…
C and sets the initial conditions for the CFX 4.2
C multiphase flow solver.  It is included as part
C of Jonathan Tyler's Masters thesis.
C
C JUNE 28, 1999
C RUNS FOR GB01,GB02,GC01,GC02
```

```
C MODIFIED JUNE 16, 1999
C MODIFICATION C - FIXED X GRIDDING

C MODIFIED JUNE 16, 1999
C MODIFICATION A:
C NOW THE Z GRIDDING IS MATCH TO THE DZ VALUE CALCULATED
C USING THE NOZDEN VARIABLE.  THIS SHOULD BETTER MATCH THE
C SIZE IN THE Z DIRECTION.
C
C MODIFICATION B:
C Y GRIDDING SECTION CORRECTED SO THAT THE GEOMETRIC
PROGRESSION
C IS BASED ON THE SMALLEST MESH DIVISION WITHIN THE NOZZLE
C INLET PATCH.

C MODIFIED JUNE 11, 1999
C NOZZLE CV DENSITY CAN NOW BE SPECIFIED USING THE
C NOZDEN VARIABLE IN THE /UCBLOK/ COMMON AREA
C THIS WILL CONTROL HOW MANY CVS ARE USED IN THE
C NOZZLE INLET PATCH BC.


C MODIFIED JUNE 10, 1999
C THE ERROR WITH PLACEMENT OF THE NOZZLE INLET AND THE
C PIPE HAVE BEEN CORRECTED.  THE LOWER LEFT CORNER OF CVS
C ARE USED TO LOCATE THE POSITION OF THE BOUNDARIES.

C MODIFIED MARCH 11, 1999
C MODIFIED MARCH 26, 1999
C *************** DATA BLOCKS ************************
      BLOCK DATA BDATA

      COMMON /UCBLOK/ YNOZUP,YWIDTH,FINES,BDHGHT,NTOP,
      +          BDWDTH,BDDPTH,
      +          ZWIDTH,NUMZ,
      +           FACTOR,DIAM,
      +           RNSERT,WALL,
      +           NOZDEN

C SET THE FOLLOWING VARIABLES TO DEFINE GEOMETRY:

C YNOZUP    -  DISTANCE FROM DISTRIBUTOR TO BOTTOM OF NOZZLE
C YWIDTH    -  Y DIMENSION OF THE RECTANGULAR NOZZLE
C FINES     -  SHOULD BE SET EQUAL TO YNOZUP
C BDHGHT    -  TOTAL HEIGHT OF THE REACTOR
C NTOP      -  NUMBER OF GRID SPACES IN LINEAR FREEBOARD
```

```
C BDWDTH    -  X DIMENSION OF THE REACTOR
C BDDPTH    -  Z DIMENSION OF THE REACTOR
C ZWIDTH    -  Z DIMENSION OF THE RECTANGULAR NOZZLE
C NUMZ      -  ODD NUMBER OF CONTROL VOLUMES IN K DIRECTION
C FACTOR    -  DESIRED HEIGHT OF BED INITIALLY FILLED WITH
SOLIDS
C DIAM      -  PARTICLE DIAMETER
C RNSERT    -  NOZZLE INSERTION FROM WALL
C WALL      -  NOZZLE PIPE WALL THICKNESS
C NOZDEN    -  GRID DENSITY AT NOZZLE
C              1  USE A SINGLE CV
C              2  USE A 3 X 3 CV
C              3  USE A 4 X 4 CV

      DATA YNOZUP,YWIDTH,FINES,BDHGHT,NTOP,
     +          BDWDTH,BDDPTH,
     +          ZWIDTH,NUMZ,
     +           FACTOR,DIAM,
     +           RNSERT,WALL,
     +           NOZDEN
     +          /0.35 ,  0.00292 , 0.35, 1.2 ,18,
     +           1.2 , 0.1 ,
     +           0.00292 ,  15 ,
     +            0.71,3.7e-4,
     +            0.25,0.002,
     +            1/

         COMMON /UCGRID/ XGRID(200),YGRID(200),ZGRID(200),
     +          NI,NJ,NK,NNOZUP,NNOZDP


      END
C *****************************************************



       SUBROUTINE
 USRINT(U,V,W,P,VFRAC,DEN,VIS,TE,ED,RS,T,H,RF,SCAL
      +                  ,CONV,XC,YC,ZC,XP,YP,ZP
      +
 ,VOL,AREA,VPOR,ARPOR,WFACT,DISWAL,IPT
      +
 ,IBLK,IPVERT,IPNODN,IPFACN,IPNODF,IPNODB,IPFACB
      +                  ,WORK,IWORK,CWORK)
 C
```

```
C*************************************************************
************
C     FORTRAN ROUTINES MODIFIED BY TAKING OUT THE USRBCS
ROUTINE ON JULY 27/98
      LOGICAL LDEN,LVIS,LTURB,LTEMP,LBUOY,LSCAL,LCOMP
     +       ,LRECT,LCYN,LAXIS,LPOROS,LTRANS
      LOGICAL LRDISK,LWDISK
C
      CHARACTER*(*) CWORK
C
C+++++++++++++++ USER AREA 1
++++++++++++++++++++++++++++++++++++++++
C---- AREA FOR USERS EXPLICITLY DECLARED VARIABLES
C
C+++++++++++++++ END OF USER AREA 1
++++++++++++++++++++++++++++++++
C
      COMMON
     + /ALL/     NBLOCK,NCELL,NBDRY,NNODE,NFACE,NVERT,NDIM
     + /ALLWRK/ NRWS,NIWS,NCWS,IWRFRE,IWIFRE,IWCFRE
     + /ADDIMS/ NPHASE,NSCAL,NVAR,NPROP
     +
,NDVAR,NDPROP,NDXNN,NDGEOM,NDCOEF,NILIST,NRLIST,NTOPOL
     + /CHKUSR/ IVERS,IUCALL,IUSED
     + /DEVICE/ NREAD,NWRITE,NRDISK,NWDISK
     + /IDUM/    ILEN,JLEN
     + /IOLOGC/ LRDISK,LWDISK
     + /LOGIC/   LDEN,LVIS,LTURB,LTEMP,LBUOY,LSCAL,LCOMP
     +          ,LRECT,LCYN,LAXIS,LPOROS,LTRANS
     + /MLTGRD/ MLEVEL,NLEVEL,ILEVEL
     + /SGLDBL/ IFLGPR,ICHKPR
     + /TRANSI/ NSTEP,KSTEP,MF,INCORE
     + /TRANSR/ TIME,DT,DTINVF,TPARM
C
C+++++++++++++++ USER AREA 2
++++++++++++++++++++++++++++++++++++++++
C---- AREA FOR USERS TO DECLARE THEIR OWN COMMON BLOCKS
C     THESE SHOULD START WITH THE CHARACTERS 'UC' TO ENSURE
C     NO CONFLICT WITH NON-USER COMMON BLOCKS
C
      COMMON /UCBLOK/ YNOZUP, YWIDTH, FINES, BDHGHT, NTOP,
     +          BDWDTH, BDDPTH,
     +          ZWIDTH, NUMZ,
     +           FACTOR,DIAM,
     +           RNSERT,WALL,
     +           NOZDEN
```

```
      COMMON /UCGRID/ XGRID(200),YGRID(200),ZGRID(200),
     +          NI,NJ,NK,NNOZUP,NNOZDP


C+++++++++++++++++ END OF USER AREA 2
++++++++++++++++++++++++++++++++++
C
       DIMENSION
      + U(NNODE,NPHASE),V(NNODE,NPHASE),W(NNODE,NPHASE)
      +,P(NNODE,NPHASE),VFRAC(NNODE,NPHASE)
      +,TE(NNODE,NPHASE),ED(NNODE,NPHASE),RS(NNODE,NPHASE,6)
      +,T(NNODE,NPHASE),H(NNODE,NPHASE),RF(NNODE,NPHASE,4)
      +,SCAL(NNODE,NPHASE,NSCAL)

+,DEN(NNODE,NPHASE),VIS(NNODE,NPHASE),CONV(NFACE,NPHASE)
       DIMENSION
      +
XC(NVERT),YC(NVERT),ZC(NVERT),XP(NNODE),YP(NNODE),ZP(NNODE)
      +,VOL(NCELL),AREA(NFACE,3),VPOR(NCELL),ARPOR(NFACE,3)
      +,WFACT(NFACE),DISWAL(NCELL)
       DIMENSION
      + IPT(*),IBLK(5,NBLOCK)

+,IPVERT(NCELL,8),IPNODN(NCELL,6),IPFACN(NCELL,6),IPNODF(NF
ACE,4)
      +,IPNODB(NBDRY,4),IPFACB(NBDRY)
       DIMENSION
      + IWORK(NIWS),WORK(NRWS),CWORK(NCWS)
C
C+++++++++++++++ USER AREA 3
++++++++++++++++++++++++++++++++++++++++
C---- AREA FOR USERS TO DIMENSION THEIR ARRAYS
C
C---- AREA FOR USERS TO DEFINE DATA STATEMENTS
C
C+++++++++++++++++ END OF USER AREA 3
++++++++++++++++++++++++++++++++++
C
C---- STATEMENT FUNCTION FOR ADDRESSING
       IP(I,J,K)=IPT((K-1)*ILEN*JLEN+(J-1)*ILEN+I)
C
C----VERSION NUMBER OF USER ROUTINE AND PRECISION FLAG
C
       IVERS=3
       ICHKPR = 1
C
```

```
C+++++++++++++++ USER AREA 4
++++++++++++++++++++++++++++++++++++++++
C---- TO USE THIS USER ROUTINE FIRST SET IUSED=1
C
       IUSED=1
C
C+++++++++++++++ END OF USER AREA 4
++++++++++++++++++++++++++++++++
C
       IF (IUSED.EQ.0) RETURN
C
C---- FRONTEND CHECKING OF USER ROUTINE
      IF (IUCALL.EQ.0) RETURN
C
C+++++++++++++++ USER AREA 5
++++++++++++++++++++++++++++++++++++++++
C
C---- AREA FOR INITIALISING VARIABLES
U,V,W,P,VFRAC,TE,ED,RS,T,SCAL
C     ONLY.
C
C PHASE 1 = CONTINUOUS PHASE - GAS
C PHASE 2 = DISPERSED PHASE  - SOLID
      IC=1
      ID=2
C FLAG IS USED TO FIND THE DESIRED BED HEIGHT
      FLAG=.TRUE.
C
C  GET SOLID AND GAS PHASE DENSITY SET IN COMMAND FILE
C
       CALL GETADD('USRINT','RPHYS ','DENSIT',ILEVEL,JDENS)
       DENSOL=WORK(JDENS-1+ID)
       DENGAS=WORK(JDENS-1+IC)
C
C  GET GAS VISCOSITY SET IN COMMAND FILE
C
       UGAS=1.8E-5
C
C  GET PARTICLE DIAMETER SET IN COMMAND FILE
C
c      CALL GETADD('USRINT','RPHYS ','D     ',ILEVEL,JDIA)
C

C  SET INITIAL BED GAS VELOCITY TO MINIMUM FLUIDISATION
VELOCITY
        VELP1=(DENSOL-
DENGAS)*9.81*DIAM**2.0*0.091/(150.0*UGAS)
```

```
C  SET INITIAL BED GAS VOLUME FRACTION
      VFINIT=0.42
      VELP2=0.001
C
      EMPTY=1.0E-10
      FULL=1.0-EMPTY
C
C
C ONLY SET INITIAL CONDITIONS IF NOT DOING A RESTART
      IF(.NOT.LRDISK) THEN
C
C ----  GET OUTLET PATCH - PRESSURE BOUNDARY
C
        CALL
IPREC('OUTLET','PATCH','CENTRES',IPT,ILEN,JLEN,
     +           KLEN,CWORK,IWORK)
C ----  FIND THE OUTLET PRESSURE
        INODE=IP(1,1,1)
        POUT=P(INODE,IC)
C
C ----  GET CELL VERTICES TO CALCULATE BED HEIGHT
C
        CALL IPREC('BLOCK-
1','BLOCK','VERTICES',IPT,ILEN,JLEN,
     +           KLEN,CWORK,IWORK)
C ----  FIND POINTERS TO TOP & BOTTOM OF BED

C NEW PART FEB 10, 1999
C BASED ON FACTOR VALUE SCAN FROM TOP OF YGRID TO FIND GRID
CELL VALUE
C THAT IS CLOSEST TO THE DESIRED INITIAL BED HEIGHT.  ONCE
THIS IS
C FOUND, TAKE THE K VALUE TO FEED INTO THE SOLIDS FILLING
ROUTINE
        FLAG=.TRUE.
        DO 90 J=JLEN,1,-1
           IF( (FACTOR .GT. YGRID(J)) .AND. (FLAG .EQ.
.TRUE.) ) THEN
                KHOLD=J+1
                FLAG=.FALSE.
           END IF
90      CONTINUE

        IVBOT=IP(1,1,1)
```

```
        IVTOP=IP(1,KHOLD,1)

C ----  TOTAL BED HEIGHT
        TOTHIG=YC(IVTOP)-YC(IVBOT)
C
C ====  START SETTING VARIABLES
====================================
C
C ----  GET CELL NODES
C
        CALL IPREC('BLOCK-
1','BLOCK','CENTRES',IPT,ILEN,JLEN
     +            ,KLEN,CWORK,IWORK)

C ----  FIRST SET ALL CELLS ASSUMING NO SOLIDS
C
        DO 103 K=1,KLEN
          DO 102 J=1,JLEN
            DO 101 I=1,ILEN
              INODE=IP(I,J,K)
C
              VFRAC(INODE,IC)=FULL
              VFRAC(INODE,ID)=EMPTY
C ----  AIR VELOCITY SET TO MIN. FLUIDIZATION VEL.
              V(INODE,IC)=VELP1
              V(INODE,ID)=VELP2
C ----  SET PRESSURES TO OUTLET PRESSURE
              P(INODE,IC)=POUT
              P(INODE,ID)=POUT
 101        CONTINUE
 102      CONTINUE
 103    CONTINUE
C
C ----  SET INITAL CONDITIONS IN LOWER SECTION OF BED
C
        PCONST=DENSOL*(1-VFINIT)*9.81
C
        DO 203 K=1,KLEN
          DO 202 J=1,KHOLD
            DO 201 I=1,ILEN
              INODE=IP(I,J,K)
C
              VFRAC(INODE,IC)=VFINIT
              VFRAC(INODE,ID)=1.0-VFRAC(INODE,IC)
C ----   SET VELOCITIES
C              V(INODE,IC)= V(INODE,IC) / VFRAC(INODE,IC)
              V(INODE,IC)=0.33
```

```
              V(INODE,ID)=VELP2
C ----    SET PRESSURE - ASSUMING CONSTANT DENSITY & VF IN
BED
              P(INODE,IC)=PCONST*(YC(IVTOP)-YP(INODE))+POUT
              P(INODE,ID)=P(INODE,IC)
 201        CONTINUE
 202      CONTINUE
 203    CONTINUE
C
C ----  END OF INITIAL CONDITION SETUP
C
      ENDIF
C
C+++++++++++++++ END OF USER AREA 5
+++++++++++++++++++++++++++++++++
C
      RETURN
      END



      SUBROUTINE
USRGRD(U,V,W,P,VFRAC,DEN,VIS,TE,ED,RS,T,H,RF,SCAL,
     +                   XP,YP,ZP,VOL,AREA,VPOR,ARPOR,WFACT,
     +                   XCOLD,YCOLD,ZCOLD,XC,YC,ZC,IPT,
     +
IBLK,IPVERT,IPNODN,IPFACN,IPNODF,IPNODB,IPFACB,
     +                   WORK,IWORK,CWORK)
C
C************************************************************
************
C
C   USER SUBROUTINE TO ALLOW USERS TO GENERATE A GRID FOR
CFX-4
C
C   >>> IMPORTANT
<<<
C   >>>
<<<
C   >>> USERS MAY ONLY ADD OR ALTER PARTS OF THE SUBROUTINE
WITHIN  <<<
C   >>> THE DESIGNATED USER AREAS
<<<
C
C************************************************************
************
C
```

```
C   THIS SUBROUTINE IS CALLED BY THE FOLLOWING SUBROUTINES
C      CREATE  CUSR
C
C************************************************************
************
C   CREATED
C      27/04/90  ADB
C   MODIFIED
C      05/08/91  IRH  NEW STRUCTURE
C      09/09/91  IRH  CORRECT EXAMPLE
C      01/10/91  DSC  REDUCE COMMENT LINE GOING OVER 72
COLUMNS.
C      29/11/91  PHA  UPDATE CALLED BY COMMENT, ADD RF
ARGUMENT,
C                     CHANGE LAST DIMENSION OF RS TO 6 AND
IVERS TO 2
C      03/06/92  PHA  ADD PRECISION FLAG AND CHANGE IVERS
TO 3
C      03/07/92  DSC  CORRECT COMMON MLTGRD.
C      23/11/93  CSH  EXPLICITLY DIMENSION IPVERT ETC.
C      03/02/94  PHA  CHANGE FLOW3D TO CFDS-FLOW3D
C      03/03/94  FHW  CORRECTION OF SPELLING MISTAKE
C      22/08/94  NSW  MOVE 'IF(IUSED.EQ.0) RETURN' OUT OF
USER AREA
C      19/12/94  NSW  CHANGE FOR CFX-F3D
C      02/07/97  NSW  UPDATE FOR CFX-4
C
C************************************************************
************
C
C   SUBROUTINE ARGUMENTS
C
C     U       - U COMPONENT OF VELOCITY
C     V       - V COMPONENT OF VELOCITY
C     W       - W COMPONENT OF VELOCITY
C     P       - PRESSURE
C     VFRAC   - VOLUME FRACTION
C     DEN     - DENSITY OF FLUID
C     VIS     - VISCOSITY OF FLUID
C     TE      - TURBULENT KINETIC ENERGY
C     ED      - EPSILON
C     RS      - REYNOLD STRESSES
C     T       - TEMPERATURE
C     H       - ENTHALPY
C     RF      - REYNOLD FLUXES
C     SCAL    - SCALARS (THE FIRST 'NCONC' OF THESE ARE MASS
FRACTIONS)
```

```
C     XP      - X COORDINATES OF CELL CENTRES
C     YP      - Y COORDINATES OF CELL CENTRES
C     ZP      - Z COORDINATES OF CELL CENTRES
C     VOL     - VOLUME OF CELLS
C     AREA    - AREA OF CELLS
C     VPOR    - POROUS VOLUME
C     ARPOR   - POROUS AREA
C     WFACT   - WEIGHT FACTORS
C  *  XC      - X COORDINATES OF CELL VERTICES
C  *  YC      - Y COORDINATES OF CELL VERTICES
C  *  ZC      - Z COORDINATES OF CELL VERTICES
C     XCOLD   - X COORDINATES OF CELL VERTICES AT START OF
TIME STEP
C     YCOLD   - Y COORDINATES OF CELL VERTICES AT START OF
TIME STEP
C     ZCOLD   - Z COORDINATES OF CELL VERTICES AT START OF
TIME STEP
C
C     IPT     - 1D POINTER ARRAY
C     IBLK    - BLOCK SIZE INFORMATION
C     IPVERT  - POINTER FROM CELL CENTERS TO 8 NEIGHBOURING
VERTICES
C     IPNODN  - POINTER FROM CELL CENTERS TO 6 NEIGHBOURING
CELLS
C     IPFACN  - POINTER FROM CELL CENTERS TO 6 NEIGHBOURING
FACES
C     IPNODF  - POINTER FROM CELL FACES TO 2 NEIGHBOURING
CELL CENTERS
C     IPNODB  - POINTER FROM BOUNDARY CENTERS TO CELL
CENTERS
C     IPFACB  - POINTER FROM BOUNDARY CENTERS TO BOUNDARY
FACESS
C
C     WORK    - REAL WORKSPACE ARRAY
C     IWORK   - INTEGER WORKSPACE ARRAY
C     CWORK   - CHARACTER WORKSPACE ARRAY
C
C   SUBROUTINE ARGUMENTS PRECEDED WITH A '*' ARE ARGUMENTS
THAT MUST
C   BE SET  BY THE USER IN THIS ROUTINE.
C
C   NOTE THAT OTHER DATA MAY BE OBTAINED FROM CFX-4 USING
THE
C   ROUTINE GETADD, FOR FURTHER DETAILS SEE THE VERSION 4
C   USER MANUAL.
C
```

```
C*************************************************************
************
C
      LOGICAL LDEN,LVIS,LTURB,LTEMP,LBUOY,LSCAL,LCOMP
     +       ,LRECT,LCYN,LAXIS,LPOROS,LTRANS
C
      CHARACTER*(*) CWORK
C
C+++++++++++++++++ USER AREA 1
++++++++++++++++++++++++++++++++++++++++
C---- AREA FOR USERS EXPLICITLY DECLARED VARIABLES
C
     LOGICAL SHOW
c    SHOW=.FALSE.
C
C+++++++++++++++++ END OF USER AREA 1
++++++++++++++++++++++++++++++++
C
      COMMON
     + /ALL/     NBLOCK,NCELL,NBDRY,NNODE,NFACE,NVERT,NDIM
     + /ALLWRK/ NRWS,NIWS,NCWS,IWRFRE,IWIFRE,IWCFRE
     + /ADDIMS/ NPHASE,NSCAL,NVAR,NPROP
     +
,NDVAR,NDPROP,NDXNN,NDGEOM,NDCOEF,NILIST,NRLIST,NTOPOL
     + /CHKUSR/ IVERS,IUCALL,IUSED
     + /CONC/    NCONC
     + /DEVICE/ NREAD,NWRITE,NRDISK,NWDISK
     + /IDUM/    ILEN,JLEN
     + /LOGIC/   LDEN,LVIS,LTURB,LTEMP,LBUOY,LSCAL,LCOMP
     +          ,LRECT,LCYN,LAXIS,LPOROS,LTRANS
     + /MLTGRD/ MLEVEL,NLEVEL,ILEVEL
     + /SGLDBL/ IFLGPR,ICHKPR
     + /SPARM/
SMALL,SORMAX,NITER,INDPRI,MAXIT,NODREF,NODMON
     + /TIMUSR/ DTUSR
     + /TRANSI/ NSTEP,KSTEP,MF,INCORE
     + /TRANSR/ TIME,DT,DTINVF,TPARM
C
C+++++++++++++++++ USER AREA 2
++++++++++++++++++++++++++++++++++++++++
C---- AREA FOR USERS TO DECLARE THEIR OWN COMMON BLOCKS
C     THESE SHOULD START WITH THE CHARACTERS 'UC' TO ENSURE
C     NO CONFLICT WITH NON-USER COMMON BLOCKS
C *************** START OF MAIN **********************

          COMMON /UCBLOK/ YNOZUP, YWIDTH, FINES, BDHGHT,
NTOP,
```

```
     +          BDWDTH, BDDPTH,
     +          ZWIDTH, NUMZ,
     +           FACTOR,DIAM,
     +           RNSERT,WALL,
     +           NOZDEN

          COMMON /UCGRID/ XGRID(200),YGRID(200),ZGRID(200),
     +           NI,NJ,NK,NNOZUP,NNOZDP


C+++++++++++++++++ END OF USER AREA 2
++++++++++++++++++++++++++++++++++
C
       DIMENSION
      +
U(NNODE,NPHASE),V(NNODE,NPHASE),W(NNODE,NPHASE),P(NNODE,NPH
ASE)

+,VFRAC(NNODE,NPHASE),DEN(NNODE,NPHASE),VIS(NNODE,NPHASE)
      +,TE(NNODE,NPHASE),ED(NNODE,NPHASE),RS(NNODE,NPHASE,6)
      +,T(NNODE,NPHASE),H(NNODE,NPHASE),RF(NNODE,NPHASE,4)
      +,SCAL(NNODE,NPHASE,NSCAL)
       DIMENSION
      +
XP(NNODE),YP(NNODE),ZP(NNODE),XC(NVERT),YC(NVERT),ZC(NVERT)
      +,XCOLD(NVERT),YCOLD(NVERT),ZCOLD(NVERT)
      +,VOL(NCELL),AREA(NFACE,3),VPOR(NCELL),ARPOR(NFACE,3)
      +,WFACT(NFACE)
      +,IPT(*),IBLK(5,NBLOCK)

+,IPVERT(NCELL,8),IPNODN(NCELL,6),IPFACN(NCELL,6),IPNODF(NF
ACE,4)
      +,IPNODB(NBDRY,4),IPFACB(NBDRY)
      +,IWORK(*),WORK(*),CWORK(*)
C
C+++++++++++++++++ USER AREA 3
++++++++++++++++++++++++++++++++++++++++
C---- AREA FOR USERS TO DIMENSION THEIR ARRAYS
C
C---- AREA FOR USERS TO DEFINE DATA STATEMENTS
C
C+++++++++++++++++ END OF USER AREA 3
++++++++++++++++++++++++++++++++++
C
C---- STATEMENT FUNCTION FOR ADDRESSING
       IP(I,J,K)=IPT((K-1)*ILEN*JLEN+(J-1)*ILEN+I)
C
```

```
C---- VERSION NUMBER OF USER ROUTINE AND PRECISION FLAG
C
      IVERS=3
      ICHKPR = 1
C
C+++++++++++++++++ USER AREA 4
++++++++++++++++++++++++++++++++++++++++
C---- TO USE THIS USER ROUTINE FIRST SET IUSED=1
C
       IUSED=1
       SHOW=.FALSE.

C
C+++++++++++++++++ END OF USER AREA 4
++++++++++++++++++++++++++++++++
C
       IF (IUSED.EQ.0) RETURN
C
C---- FRONTEND CHECKING OF USER ROUTINE
       IF (IUCALL.EQ.0) RETURN
C
C+++++++++++++++++ USER AREA 5
++++++++++++++++++++++++++++++++++++++++
C
       CALL IPREC('BLOCK-
1','BLOCK','VERTICES',IPT,ILEN,JLEN,
     +             KLEN,CWORK,IWORK)


C-- LOOP OVER BLOCK
      DO 100 K=1,KLEN
        DO 120 J=1,JLEN
          DO 130 I=1,ILEN
C-- USE STATEMENT FUNCTION IP TO GET ADDRESSES
            IVERT = IP(I,J,K)
C-- DEFINE LOCATION OF GRID VERTICES
            XC(IVERT)=XGRID(I)
            YC(IVERT)=YGRID(J)
            ZC(IVERT)=ZGRID(K)
 130        CONTINUE
 120    CONTINUE
 100  CONTINUE
C
C+++++++++++++++++ END OF USER AREA 5
++++++++++++++++++++++++++++++++
C
```

```
      RETURN
      END


C
C ****************** SUBROUTINES *****************
C

C
C ****************** SUBROUTINES *****************
C
          SUBROUTINE GEO1(SMALL,RLARGE,RL,FRAC,N)

C DATE: 19/10/98
C AUTHOR: JONATHAN TYLER, UNIV OF ALBERTA
C
C DESCRIPTION: SUBROUTINE TO CALCULATE APPROXIMATE
C  GEOMETRIC PROGRESSION BASED ON SIZE OF SMALLEST
C  RLARGE  LARGEST DIVISION
C  SMALL   SMALLEST DIVISION
C  RL  LENGTH TO SOLVE TO
C
C RETURNS: ZFRAC() THE STEP FRACTIONAL VALUES
C          N      THE INTEGER NUMBER OF GRIDS


C      AUTHOR:  JONATHAN TYLER
C      DATE:    NOVEMBER 15, 1998
C      REVISION: 000
C                001  FEB 10, 1999 FINAL DO LOOP INDICES
C                     INCREASED TO RANGE FROM 3 TO N+2


       DIMENSION FRAC(100)

       PLENGTH=0.0
          LENGTH=RL
          BIG=RLARGE
          ALPHA=0.0
          N=0
          FLAG=0
       TEMP=0.0

          DO J=1,100
          ALPHA=(SMALL/BIG)**(1.0/FLOAT(J))
                PLENGTH=BIG*(1.0-(ALPHA)**FLOAT(J))/(1.0-
ALPHA)
```

```
                ERROR=PLENGTH-LENGTH

                IF (ERROR .GE. 0.0 .AND. FLAG .NE. 1) THEN
               RALPHA=ALPHA
                        N=J+1
                        FLAG=1
          END IF
          END DO

c          N=N+2
          N=N+1
          DO J=1,N
                FRAC(J)=SMALL*RALPHA**(1.0-FLOAT(J))
          END DO

         END


C ****************************************
      SUBROUTINE US_GEO(RSEED,RLNGTH,RDELTA,NUMB,ZFRAC)
C
C AUTHOR: JONATHAN TYLER, UNIVERSITY OF ALBERTA
C DATE:   AUGUST 16, 1998
C DESC:   SUBROUTINE WILL DETERMINE THE GRID SPACING VALUES
FOR A
C         GEOMETRIC PROGRESSION BASED ON THE NUMBER OF
GRIDS, THE
C         SIZE THAT THE FINAL GRID WILL BE EQUAL TO.
C VARIABLES:
C     RSEED    INITIAL GUESS VALUE FOR NEWTON'S METHOD (USU
1.15)
C     RLNGTH   LENGTH OVER WHICH TO GRID
C     RDELTA   VALUE THAT LAST GEOMETRIC GRID SHOULD MAP TO
C     NUMB     NUMBER OF GRID SPACES
C     ZFRAC     RETURNED ARRAY OF STEP VALUES
C
      DIMENSION ZFRAC(100)

      RALPHA=RSEED
      RL=RLNGTH
      RB=RDELTA
      N=NUMB
C IMPLEMENTATION OF NEWTON'S METHOD FOR SOLVING FOR ALPHA
      DO 30 J=1,30
         TEMP1=(RB*RALPHA**(-N)-RB)/(1.0-RALPHA)-RL
         TEMP2=-N*RB*RALPHA**(-N-1)/(1.0-RALPHA)
         TEMP3=(1.0-RALPHA)**(-2)*(RB*RALPHA**(-N)-RB)
```

```
         RALPHA2=RALPHA-TEMP1/(TEMP2+TEMP3)
         RALPHA=RALPHA2
30       CONTINUE

C DETERMINE THE SIZE OF THE FIRST GRID
         H1=RB/RALPHA**N

C DETERMINE THE SIZE OF EACH AND STORE IN ZFRAC ARRAY
      DO 40 J=1,N+2
         ZFRAC(J)=H1*RALPHA**(J-1)
40    CONTINUE

700   FORMAT ('ALPHA = ',F12.8)
      END



     SUBROUTINE DISPLAY(GRID,NUMB,STRING)
     DIMENSION GRID(100)
     CHARACTER *5 STRING

     DO 10 J=1,NUMB
          PRINT 8,STRING,J,GRID(J)
10   CONTINUE
8    FORMAT(A5,'(',I3,')=',F12.6)

     END



      SUBROUTINE USRTPL(NBLOCK,NPATCH,NGLUE
     +
,NDBLK,CBLK,INFPCH,CPATCH,INFGLU,IBBPP,IBBPD
     +                  ,WORK,IWORK,CWORK)
C
      CHARACTER*(*) CBLK,CPATCH,CWORK
C
C+++++++++++++++ USER AREA 1
++++++++++++++++++++++++++++++++++++++++
C---- AREA FOR USERS EXPLICITLY DECLARED VARIABLES
C
C     THESE FOLLOWING CHARACTER VARIABLES ARE USED IN THE
USER EXAMPLES
       CHARACTER*32
CNAME,CNAME1,CNAME2,CLIST1,CLIST2,CBLOCK
       CHARACTER*6 CTYPE
C
```

```
C+++++++++++++++ END OF USER AREA 1
+++++++++++++++++++++++++++++++++
C
      COMMON
     + /ALLWRK/ NRWS,NIWS,NCWS,IWRFRE,IWIFRE,IWCFRE
     + /BBCYCL/ XCYCLE(3)
     + /BBDIM/  MBB, MBBPAT, MBBNOD, MBBNBR,
     +          MBB1, MBB2, MBB3, MBB4, MBB5,
     +          MBB6, MBB7, MBB8, MBB9, MBB10,
     +          MBB11, MBB12, MBB13, MBB14, MBB15,
     +          MBB16, MBB17, MBB18, MBB19, MBB20
     + /CHKUSR/ IVERS,IUCALL,IUSED
     + /DEVICE/ NREAD,NWRITE,NRDISK,NWDISK
     + /LIMTPL/ NBLMAX,NPCMAX,NGLMAX
     + /SGLDBL/ IFLGPR,ICHKPR
C
        COMMON /UCGRID/ XGRID(200),YGRID(200),ZGRID(200),
     +         NI,NJ,NK,NNOZUP,NNOZDP

        COMMON /UCBLOK/ YNOZUP,YWIDTH,FINES,BDHGHT,NTOP,
     +          BDWDTH,BDDPTH,
     +          ZWIDTH,NUMZ,
     +          FACTOR,DIAM,
     +          RNSERT,WALL,
     +          NOZDEN



C
      DIMENSION WORK(NRWS),IWORK(NIWS),CWORK(NCWS)

+,NDBLK(3,*),CBLK(*),INFPCH(9,*),CPATCH(2,*),INFGLU(5,*)
     +,IBBPP(MBB1,MBB2),IBBPD(MBB3)
C
          DIMENSION FRAC(100),RTEMP(200)
C
      IVERS=3
      ICHKPR = 1
C
       IUSED=1
C
C+++++++++++++++ END OF USER AREA 4
+++++++++++++++++++++++++++++++++
C
       IF (IUSED.EQ.0) RETURN
C
C---- FRONTEND CHECKING OF USER ROUTINE
```

```
      IF (IUCALL.EQ.0) RETURN
C
C+++++++++++++++++ USER AREA 5
++++++++++++++++++++++++++++++++++++++++

C ***************************************************
C **                                               **
C **      ADJUST DIMENSION VARIABLES               **
C **                                               **
C ***************************************************
C THIS IS NECESSARY TO ENSURE PROPER NUMERICAL ACCURACY
C WHEN USING NEWTON'S METHOD TO DETERMINE SOME OF THE
C GRID PARAMETERS

      YNOZUP=YNOZUP*10.0
      YWIDTH=YWIDTH*10.0
      FINES=FINES*10.0

      INSERT=INSERT*10.0
      WALL=WALL*10.0
      RNSERT=RNSERT*10.0

      BDHGHT=BDHGHT*10.0
      BDWDTH=BDWDTH*10.0

      BDDPTH=BDDPTH*100.0
      ZWIDTH=ZWIDTH*100.0


C ***************************************************
C **                                               **
C **      Y GRIDDING SECTION                       **
C **                                               **
C ***************************************************

C JUNE 16, 1999
C MODIFICATION B
        DY = YWIDTH/(NOZDEN+1)
        WALL=DY

        DELTA=(BDHGHT-(FINES+YWIDTH+YNOZUP+2.0*WALL))/NTOP
C         CALCULATE THE FIRST LINEAR DELTA FOR FREEBOARD

     CALL GEO1(WALL,DELTA,YNOZUP+WALL,FRAC,NNOZUP)
C         DETERMINE GEOMETRIC GRID SPACING BASED ON
SMALLEST
C         UNIT (WALL) TO LARGEST (DELTA) OVER A DISTANCE
```

```
C          YNOZUP+WALL


      YGRID(NNOZUP+1)=YNOZUP+WALL
         YGRID(NNOZUP+2)=YNOZUP+WALL+YWIDTH
      YGRID(NNOZUP)=YNOZUP
      YGRID(1)=0.0
C SET THE VALUES THAT ARE SPECIFIED


      DO 10 J=NNOZUP-1,1,-1
           TEMP=YGRID(J+2)
           YGRID(J+1)=TEMP-FRAC(NNOZUP-J)
10    CONTINUE


         DO 11 J=1,NNOZUP-1
                TEMP=YGRID(NNOZUP+J+1)
                YGRID(NNOZUP+J+2)=TEMP+FRAC(J)
11       CONTINUE


      N1=NNOZUP+1


      DELTA=(BDHGHT-YGRID(2*NNOZUP))/NTOP
C          NEW DELTA VALUE ENSURES THAT THE TOTAL REACTOR
C          HEIGHT IS CORRECT

      DO 15 J=1,NTOP+1
           YGRID(J+2*NNOZUP)=YGRID(2*NNOZUP)+FLOAT(J)*DELTA
15    CONTINUE
C          FINISH LINEAR GRIDDING IN THE FREEBOARD


C INCREASE THE DENSITY OF THE GRIDDING IN THE Y DIRECTION
FOR NOZZLE

         DY = (YGRID(NNOZUP+2)-YGRID(NNOZUP+1))/(NOZDEN+1)
C THIS IS THE DELTA Y VALUE FOR INCREASED GRID DENSITY

C TEMPORARILY HOLD YGRID(NNOZUP+2) TO
YGRID(2*NNOZUP+NTOP+1)
         DO 16 J=NNOZUP+2,2*NNOZUP+NTOP+1
            RTEMP(J)=YGRID(J)
16       CONTINUE
```

```
        DO 17 J=1,NOZDEN
           YGRID(NNOZUP+1+J)=YGRID(NNOZUP+1)+J*DY
17      CONTINUE

        DO 18 J=NNOZUP+2,2*NNOZUP+NTOP+1
           YGRID(J+NOZDEN)=RTEMP(J)
18      CONTINUE
        NTOP=NTOP+NOZDEN


     DO 20 J=1,2*NNOZUP+NTOP+1
          YGRID(J)=YGRID(J)/10.0
20   CONTINUE
C         DIVIDE THE Y DIMENSI :S BY 10 TO GET PROPER
C         PHYSICAL DIMENSIONS

C REVISION: CORRECT IF YGRID(2) IS GREATER THAN
C           YGRID(3)-YGRID(2)

        IF (YGRID(2).GT.(YGRID(3)-YGRID(2))) THEN
            YGRID(1)=YGRID(2)/2.0
            NTOP=NTOP+1

            DO 22 J=2*NNOZUP+NTOP+1,2,-1
               YGRID(J)=YGRID(J-1)
22          CONTINUE
            YGRID(1)=0.0
        ENDIF


        NJ=2*NNOZUP+NTOP



C ***************************************************
C **                                               **
C **        X GRIDDING SECTION                     **
C **                                               **
C ***************************************************

        XGRID(1)=0.0
        CALL MERRY(RL,0.0029245,1.2,1450.0,0.000374,250.0)

     XGRID(1)=0.0
     NXTOP=NINT((BDWDTH-RNSERT)/DELTA)

C         THE NUMBER OF X DIVISIONS IS EQUAL TO
```

```
C          BEDWITH-RNSERT  DIVIDED BY THE LINEAR STEP IN
C          THE Y DIRECTION
      XDELTA=(BDWDTH-RNSERT)/NXTOP

         IJ=1

         DO WHILE(RNSERT/IJ .GT. XDELTA)
            IJ=IJ+1
         END DO


C GRID THE NOZZLE SECTION
         DO 24 J=1,IJ+1
               XGRID(J+1)=XGRID(J)+RNSERT/IJ
24       CONTINUE



      DO 30 J=1,NXTOP+1
           XGRID(J+IJ+1)=RNSERT+XDELTA*FLOAT(J)
30    CONTINUE

      DO 32 J=1,NXTOP+2+IJ
           XGRID(J)=XGRID(J)/10.0
32    CONTINUE
C          DIVIDE THE X DIMENSIONS BY 10 TO GET
C          THE PROPER PHYSICAL DIMENSIONS

         NI=NXTOP+1+IJ


C ***************************************************
C **                                               **
C **       Z GRIDDING SECTION                      **
C **                                               **
C ***************************************************


      INHALF=(NUMZ-1)/2
      DHALF=(BDDPTH-ZWIDTH)/2.0

      ZGRID(1)=0.0
      ZGRID(INHALF+1)=DHALF
      ZGRID(INHALF+2)=DHALF+ZWIDTH

C JUNE 16, 1999
         DZ=ZWIDTH/(NOZDEN+1.0)
```

```
      CALL US_GEO(0.85,DHALF,DZ,INHALF,FRAC)

C        CALL US_GEO(0.85,DHALF,ZWIDTH,INHALF,FRAC)

      DO 35 J=1,INHALF
           ZGRID(J+1)=ZGRID(J)+FRAC(J)
           ZGRID(INHALF+J+2)=ZGRID(INHALF+J+1)+
     +               FRAC(INHALF+1-J)
35    CONTINUE

      ZGRID(2*INHALF+2)=DHALF*2.0+ZWIDTH

C CHECK NOZDEN VARIABLE TO SEE IF THE NOZZLE INLET
C PATCH MUST BE DENSIFIED FOR IMPLEMENTATION.

         NK=NUMZ+NOZDEN
         NNOZDP=INHALF+1


         DZ= (ZGRID(NNOZDP+1) - ZGRID(NNOZDP) ) / (NOZDEN+1)
C DELTA Z FOR INCREASING DENSITY OF THE NOZZLE GRID

C TEMPORARILY HOLD NNOZDP+1 TO NUMZ+1 FOR INSERTION
         DO 36 J=NNOZDP+1,NUMZ+1
            RTEMP(J)=ZGRID(J)
36       CONTINUE

         DO 37 J=1,NOZDEN
            ZGRID(NNOZDP+J)=ZGRID(NNOZDP)+J*DZ
37       CONTINUE

         DO 38 J=NNOZDP+1,NUMZ+1
            ZGRID(J+NOZDEN)=RTEMP(J)
38       CONTINUE


      DO 40 J=1,NK+1
           ZGRID(J)=ZGRID(J)/100.0
40    CONTINUE
C          DIVIDE THE Z DIMENSIONS BY 100 TO GET
C          THE PROPER PHYSICAL DIMENSIONS

C
C+++++++++++++++++ END OF USER AREA 5
++++++++++++++++++++++++++++++++++
C
```

```
C+++++++++++++++ USER AREA 6
++++++++++++++++++++++++++++++++++++++++
C
C ******************************************************
C **                                                  **
C **    TOPOLOGY SECTION                              **
C **                                                  **
C ******************************************************

        CBLOCK='BLOCK-1'
        CALL BLOCK(CBLOCK,NI,NJ,NK,NBLOCK,NDBLK,CBLK)
C CREATE THE SINGLE BLOCK IN THIS USER FORTRAN ROUTINE

        LABEL=1
        CTYPE='INLET '
        CNAME='DISTRIBUTOR'

        CALL PATCH (CTYPE,CNAME,CBLOCK,LABEL,
     +              1,NI,1,1,1,NK,5,
     +              NBLOCK,NPATCH,NDBLK,CBLK,INFPCH,CPATCH)
C CREATE THE DISTRIBUTOR PATCH

C MARCH 11, 1999 ADDITIONS HERE

        CTYPE='SOLID '
        CNAME='PIPE'

        NPI1=1
        NPI2=IJ
        NPJ1=NNOZUP+1
        NPJ2=NNOZUP+3+NOZDEN
        NPK1=NNOZDP-1
        NPK2=NNOZDP+1+NOZDEN

        CALL PATCH (CTYPE,CNAME,CBLOCK,LABEL,
     +              NPI1,NPI2,NPJ1,NPJ2,NPK1,NPK2,0,
     +              NBLOCK,NPATCH,NDBLK,CBLK,INFPCH,CPATCH)


        CTYPE='INLET '
        CNAME='NOZZLE'

      NI1=IJ+1
        NI2=IJ+1
        NJ1=NNOZUP+2
        NJ2=NNOZUP+2+NOZDEN
        NK1=NNOZDP
```

```
      NK2=NNOZDP+NOZDEN

      CALL PATCH (CTYPE,CNAME,CBLOCK,LABEL,
     +            NI1,NI2,NJ1,NJ2,NK1,NK2,4,
     +            NBLOCK,NPATCH,NDBLK,CBLK,INFPCH,CPATCH)


      CTYPE='PRESS '
      CNAME='OUTLET'

      CALL PATCH (CTYPE,CNAME,CBLOCK,LABEL,
     +            1,NI,NJ,NJ,1,NK,2,
     +            NBLOCK,NPATCH,NDBLK,CBLK,INFPCH,CPATCH)
C CREATE THE PRESSURE OUTLET PATCH


      YWIDTH=YWIDTH/10.0
      FINES=FINES/10.0

      BDHGHT=BDHGHT/10.0
      BDWDTH=BDWDTH/10.0

      BDDPTH=BDDPTH/100.0
      ZWIDTH=ZWIDTH/100.0

C *****************************************************
C **                                                 **
C **    GEOMETRY FILE SECTION                        **
C **                                                 **
C *****************************************************

      OPEN (UNIT=1,FILE='GEOMETRY',FORM='FORMATTED',
     +     ACCESS='SEQUENTIAL',STATUS='NEW')

      DO 45 J=1,INHALF
         WRITE(UNIT=1,FMT=800)J,FRAC(J)
45     CONTINUE
         WRITE(UNIT=1,FMT=801)'OVERALL DATA',1

         WRITE(UNIT=1,FMT=801)'YNOZUP=',YNOZUP
         WRITE(UNIT=1,FMT=801)'MERRY=',RL
         WRITE(UNIT=1,FMT=804)'NI=',NI
         WRITE(UNIT=1,FMT=804)'NJ=',NJ
         WRITE(UNIT=1,FMT=804)'NK=',NK
         WRITE(UNIT=1,FMT=805)'IJ=',IJ

         WRITE(UNIT=1,FMT=805)'++++++++',5
```

```
            WRITE(UNIT=1,FMT=805)'PIPE I1:',NPI1
            WRITE(UNIT=1,FMT=805)'PIPE I2:',NPI2
            WRITE(UNIT=1,FMT=805)'PIPE J1:',NPJ1
            WRITE(UNIT=1,FMT=805)'PIPE J2:',NPJ2
            WRITE(UNIT=1,FMT=805)'PIPE K1:',NPK1
            WRITE(UNIT=1,FMT=805)'PIPE K2:',NPK2
            WRITE(UNIT=1,FMT=805)'++++++++',5
            WRITE(UNIT=1,FMT=805)'NOZZLE I1:',NI1
            WRITE(UNIT=1,FMT=805)'NOZZLE I2:',NI2
            WRITE(UNIT=1,FMT=805)'NOZZLE J1:',NJ1
            WRITE(UNIT=1,FMT=805)'NOZZLE J2:',NJ2
            WRITE(UNIT=1,FMT=805)'NOZZLE K1:',NK1
            WRITE(UNIT=1,FMT=805)'NOZZLE K2:',NK2
            WRITE(UNIT=1,FMT=805)'++++++++',5
            WRITE(UNIT=1,FMT=801)'DZ = ',DZ


         DO 50 J=1,NJ

            WRITE(UNIT=1,FMT=802)'YGRID',J,YGRID(J)
50       CONTINUE

         DO 55 J=1,NI
            WRITE(UNIT=1,FMT=802)'XGRID',J,XGRID(J)
55       CONTINUE

         DO 56 J=1,NK
            WRITE(UNIT=1,FMT=802)'ZGRID',J,ZGRID(J)
56       CONTINUE


         KHOLD=0
         FLAG=.TRUE.

         DO 60 J=NJ,1,-1
            IF( (FACTOR .GT. YGRID(J)) .AND. (FLAG .EQ.
.TRUE.) ) THEN
                 KHOLD=J+1
                 FLAG=.FALSE.
            END IF
60       CONTINUE

         WRITE(UNIT=1,FMT=803)KHOLD,YGRID(KHOLD),FACTOR


800      FORMAT('FRAC(',I3,')= ',F12.8)
801      FORMAT(A,F12.8)
```

```
802     FORMAT(A,'('I3,') = ',F12.8)
803     FORMAT('AT ',I3,' YGRID=',F12.8' CLOSE TO ',F12.8)
804     FORMAT(A,I3)
805     FORMAT(A,I3)
        END FILE(UNIT=1)
        CLOSE(UNIT=3)
C
      RETURN
      END

      SUBROUTINE MERRY(RL,D0,RHOG,RHOP,DP,U0)

      RA=(RHOG/RHOP)**0.2
      RB=(DP/D0)**0.2
      RC=5.25*((RHOG*U0**2)/(0.45*9.81*DP))**0.4

      RL=D0*(RA*RB*RC-4.5)
      END
```

INFORMATION TO USERS

This manuscript has been reproduced from the microfilm master. UMI films the text directly from the original or copy submitted. Thus, some thesis and dissertation copies are in typewriter face, while others may be from any type of computer printer.

The quality of this reproduction is dependent upon the quality of the copy submitted. Broken or indistinct print, colored or poor quality illustrations and photographs, print bleedthrough, substandard margins, and improper alignment can adversely affect reproduction.

In the unlikely event that the author did not send UMI a complete manuscript and there are missing pages, these will be noted. Also, if unauthorized copyright material had to be removed, a note will indicate the deletion.

Oversize materials (e.g., maps, drawings, charts) are reproduced by sectioning the original, beginning at the upper left-hand corner and continuing from left to right in equal sections with small overlaps.

Photographs included in the original manuscript have been reproduced xerographically in this copy. Higher quality 6" x 9" black and white photographic prints are available for any photographs or illustrations appearing in this copy for an additional charge. Contact UMI directly to order.

ProQuest Information and Learning
300 North Zeeb Road, Ann Arbor, MI 48106-1346 USA
800-521-0600

University of Alberta

Towards the Complete Backbone Chemical Shift Assignments of HAV 3C Protease

by

Michael Scott Watson ©

A thesis submitted to the Faculty of Graduate Studies and Research in partial fulfillment of the requirements for the degree of

Master of Science

in

Pharmaceutical Sciences

Faculty of
Pharmacy and Pharmaceutical Sciences
Edmonton, Alberta
Spring,2000

University of Alberta

Library Release Form

Name of Author: Michael Scott Watson

Title of Thesis: Towards the Complete Backbone Chemical Shift Assignments of HAV 3C Protease

Degree: Master of Science

Year this Degree Granted: 2000

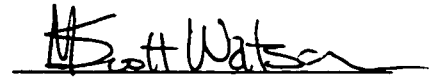

Faculty of Pharmacy and
Pharmaceutical Sciences
University of Alberta
Edmonton, Alberta
T6G 2C2

Date: Jan. 27, 2000

University of Alberta

Faculty of Graduate Studies and Research

The undersigned certify that they have read, and recommend to the Faculty of Graduate Studies and Research for acceptance, a thesis entitled "Towards the Complete Backbone Chemical Shift Assignments of HAV 3C Protease" by Michael Scott Watson in partial fulfillment of the requirements for the degree of Master of Science in Pharmaceutical Sciences.

Dr. David S. Wishart

Dr. Brian D. Sykes

Dr. Steve McQuarrie

Dr. Jim Diakur

Date: Jan. 27, 2000

Abstract

The medically significant Hepatitis A Virus (HAV) 3C protease processes the polyprotein produced by HAV. In this thesis, we describe our efforts at characterizing HAV 3C protease using various approaches including analytical ultracentrifugation, isotopic labeling and NMR spectroscopy with the specific goal of completing the backbone ^{1}H, ^{13}C, and ^{15}N assignments of the HAV 3C protease. Chapter 2 discusses the analytical ultracentrifugation, ^{15}N T_2-relaxation, and ^{1}H linewidth studies that identified sample conditions where HAV 3C protease exists as a monomer at suitable concentrations for NMR spectroscopy. Chapter 3 describes the strategies that facilitated the expression and purification of large quantities (>30 mg/l) of uniformly (^{15}N, $^{13}C/^{15}N$, and $^{2}H/^{13}C/^{15}N$) and ^{15}N-residue specific labeled HAV 3C protease from *E. coli.* Finally, chapter 4 discusses the heteronuclear multidimensional NMR experiments performed that permitted ^{1}H, ^{13}C and ^{15}N chemical shift assignments for ~ 85% of the backbone.

Acknowledgements

First and foremost, I would like to express my gratitude to my supervisor, Dr. David Wishart, for his encouragement, enthusiasm and help. Without the first impressionable discussion I had with him in September of 1996 and his encouragement throughout this program, I would never have been able to accomplish this work.

I would also wish to express my whole-hearted thanks to all my colleagues and fellow students that I have had the pleasure of associating with over the past three years. In particular, I would like to thank Alan Gibbs, Don Husereau, Gary Van Domselaar, Ashenafi Abera and Mesfin Fanta who have all been tremendous friends, providing scientific assistance, many intellectual conversations and a continual source of emotional support. I would also like to thank Ashenafi Abera, Scott Ellerbeck, Hassan Monzavi, YunJun Wang, Alex Nip, Yamini Rammamoortha and Trent Bjorndahl for all their assistance on the HAV 3C Project.

I am very grateful to Dr. Brian Sykes, Dr. Carolyn Slupsky, Dr. Leo Spyracopoulos and Dr. Stephane Gagne for their spectroscopic help and their valuable teachings over the past three years. I am also grateful to Dr. Bruce Malcolm who supplied the E. coli expression system with which we initiated this work and with whom I have had many helpful, insightful discussions as well. In addition, I would like to thank Dr. M.N.G. James, Dr. John Vederas and members of their respective groups for their valued contributions to this study. For technical assistance, I would like to Les Hicks (Sedimentation Analysis), Robert Boyko and Lee Willard (Computational) and all the members of PENCE. I would also like to express my appreciation to members of the Faculty of Pharmacy, Dr. Steve McQuarrie, Dr. John Bachynsky, Dr. Jim Diakur and Dr. Brian Amsden, for their friendship, advice and assistance throughout my studies.

I particularly wish to express my deep gratitude to my entire family, Anthony, Laurie, Hugh, Shannon and Dan for their love, sacrifice and encouragement over the past three years.

Finally, I would like to acknowledge Bristol Myers Squibb and PENCE for financial and technical support throughout my graduate career.

Table of Contents

List of Tables

Page

List of Figures

List of Abbreviations

Amino acids:

A (Ala)	=	L-alanine
C (Cys)	=	L-cysteine
D (Asp)	=	L-aspartic acid
E (Glu)	=	L-glutamic acid
F (Phe)	=	L-phenylalanine
G (Gly)	=	L-glycine
H (His)	=	L-histidine
I (Ile)	=	L-isoleucine
K (Lys)	=	L-lysine
L (Leu)	=	L-leucine
M (Met)	=	L-methionine
N (Asn)	=	L-asparagine
P (Pro)	=	L-proline
Q (Gln)	=	L-glutamine
R (Arg)	=	L-arginine
S (Ser)	=	L-serine
T (Thr)	=	L-threonine
V (Val)	=	L-valine
W (Trp)	=	L-tryptophan
Y (Tyr)	=	L-tyrosine

2D	=	two dimensional
3D	=	three dimensional
CHAPS	=	3-[(3-cholamidopropyl)-dimethyl-ammonio]-1-propanesulfonate
COSY	=	correlation spectroscopy
CSA	=	chemical shift anisotropy
CT	=	constant time
DD	=	dipole-dipole
DLVO	=	Deryagin-Landau-Verwey-Overbeek theory of colloids
DTT	=	dithiothreitol
E. coli	=	Esherichia coli
EDTA	=	ethylenediaminetetraacetic acid
FID	=	free induction decay
HAV	=	hepatitis A virus

HMQC	=	heteronuclear multiple quantum correlation spectroscopy
HSQC	=	heteronuclear single quantum correlation spectroscopy
INEPT	=	insensitive nuclei enhanced polarization transfer
IPTG	=	isopropyl β-D thiogalactopyranoside
J	=	coupling constant
kDa	=	kilodalton
MM294	=	prototrophic strain of E. coli containing pHAV-3CEX
ncyc	=	number of cycles
NMR	=	nuclear magnetic resonance
NOE	=	nuclear Overhauser effect
NOESY	=	nuclear Overhauser effect spectroscopy
OD_{280}	=	optical density at 280 nm
OD_{600}	=	optical density at 600 nm
PDB	=	Protein Data Bank
PW_SHPSS	=	cosine-modulated 180° ^{1}H pulse
PWN	=	90° ^{15}N pulse
SAR by NMR	=	structure activity relationships by nuclear magnetic resonance
SDS-PAGE	=	sodium dodecyl sulfate polyacrylamide gel electrophoresis
T_1	=	longitutinal or spin-lattice relaxation rate
T_2	=	transverse or spin-spin relaxation rate
TFE	=	trifluoroethanol
TOCSY	=	total correlation spectroscopy
γ	=	gyromagnetic constant
$\Delta\nu_{1/2}$	=	half-height linewidth
τ_C	=	correlation time

Chapter 1

Introduction

Over the past two decades, advances in structural biology have radically transformed the ways in which drugs are designed and discovered. Today, rather than treating protein drug targets as simple "black boxes", scientists are now treating them as complex molecular entities that possess well-defined three dimensional structure and specific sites that can be activated or deactivated by small molecule ligands. Innovations in structure determination methods and computer-aided molecular rendering techniques have led to the development of 'structure based drug design' or 'rational drug design'. These are drug development techniques that use the structure of a protein target as an essential template in the design or construction of protein-specific small molecule ligands (Goody, 1995).

One class of proteins that is particularly applicable to rational drug design is the proteases. Proteases are enzymes that cut or cleave peptides and proteins at specific sites (Voet and Voet, 1995). They are critical to many vital processes including digestion, protein turnover, immune recognition, and protein processing. Proteases have been classified into four families: cysteine proteases, metalloproteases, aspartic proteases, and serine proteases based on their catalytically active residues. It is known that a number of proteases are involved in a variety of human diseases (Table 1.1). Consequently, many proteases could serve as excellent targets for the development of inhibitors and new therapeutic agents.

Interestingly, the first "rationally designed" drug (developed by researchers at Squibb) inhibited a protease known as angiotensin converting enzyme (ACE) (Rubin et al., 1978). This drug, named captopril, was the first of a number of impressive ACE-based antihypertensive medications that have appeared over the

last 20 years. In fact ACE inhibitors are by far the most significant rationally designed drugs to have reached the market. Since 1975, there have been several other successful examples of rational designed drugs including the HIV protease inhibitors (DesJarlais et al., 1990; Olson and Goodsell, 1998) and anti-tumor agents such as capecitabine (Verweij, 1999).

Table 1.1 Protease Families

Family	**Representative Enzyme**	**Disease**
Serine Proteases	Neutrophil elastase	Pulmonary emphysema
	Thrombin	Platelet dependent thrombus formation
Metalloproteases	Angiotensin converting enzyme (ACE)	Hypertension
	Stromelysin	Inflammatory disorders
Cysteine Proteases	HAV 3c protease	Hepatitis A
	Cathepsin B	Tumor formation
	Calpain	Stroke
Aspartic Proteases	Renin	Hypertension

The rational design of any given drug depends on a precise knowledge of the three-dimensional (3D) structure of the protein target. To date, the most prominent technique for 3D structure determination has been X-ray crystallography (Blundell and Johnson, 1976). More recently, structure-determination techniques based on nuclear magnetic resonance (NMR) spectroscopy have emerged as a powerful alternative to X-ray crystallography (Wider and Wuthrich, 1999). NMR spectroscopy is often complementary to X-ray crystallography, with one method providing structural or dynamic information that is not as easily obtained with the other. This was demonstrated recently as information derived from both techniques was used in the structural refinement of

bovine pancreatic trypsin inhibitor (BPTI) (Schiffer et al, 1994). Using NMR spectroscopy to derive solution structures of proteins can also provide a check for the correctness of a previously determined crystal structure (and vice versa). Indeed, discrepancies detected between NMR and X-ray structures have increased awareness about the possible mistakes that can be made using either technique (Wagner, 1993). What makes NMR spectroscopy particularly attractive is that the protein of interest is normally studied in solution as opposed to the solid-state that is required for X-ray crystallography. For these reasons structural analysis by NMR is clearly a worthwhile endeavor, even in cases where an X-ray structure of the same protein has already been solved.

This dissertation describes the use of NMR spectroscopy to characterize a large, medically significant protein that could serve as a suitable target for rational drug design. Specifically, it centers on the 217 residue 3C protease from the Hepatitis A virus. This particular 3C protease is responsible for processing the polyprotein produced by the translation of viral mRNA and therefore is essential to the propagation of this virus. Consequently, it serves as an excellent "model" protein target for the rational design of an anti-viral drug.

Although the HAV 3C protease structure has been previously determined by X-ray crystallography (Allaire et al., 1994), we have chosen to characterize this protein via NMR spectroscopy. The intention is to use this technique to help screen for putative inhibitors via a process called "SAR (Structure Activity Relationships) by NMR" (Shuker et al., 1996). More specifically, this thesis describes the efforts to characterize and "condition" HAV 3C protease which, ultimately resulted in the near-complete backbone assignments of this protein. These assignments will serve as a critical first step for future SAR by NMR studies. In particular, chapter 2 describes the techniques that were used to determine sample conditions at which HAV 3C protease existed as a monomer – a prerequisite for the collection of "good" NMR spectra. Chapter 3 describes the protocols that were developed to isotopically label the protein, both uniformly and

site specifically. Chapter 4 describes the heteronuclear multidimensional experiments that were used to facilitate the near complete backbone assignments for this protein, while the final chapter summarizes the results and discusses prospects for future studies.

1.1 NMR Spectroscopy of Proteins

Over the past 15 years, high-resolution NMR spectroscopy has become one of the most powerful techniques for biomolecular structure determination and analysis. The development of pulsed Fourier Transform NMR spectroscopy (Ernst and Anderson, 1966) in conjunction with multidimensional NMR spectroscopy (Jeener, 1971) has made it possible to determine the 3D structure of macromolecules such as proteins and DNA. Using protocols that were developed principally by Wuthrich and his collaborators in the early 1980's, the first 3D protein structure was determined by Williamson et al (1985). Improvements in NMR spectrometer technology such as increased field strength, improved computer speed and increased probe sensitivity coupled with isotopic labelling and improved pulse sequences (Kay and Gardner, 1997; Kay, 1995) have allowed proteins and protein complexes as large as 64 kilodaltons to be characterized by NMR (Shan et al., 1998). To date, NMR spectroscopy has been used to solve more than 1500 biomolecular structures, many of which are available from the Protein Data Bank (PDB) (Bernstein et al., 1977) and Nucleic Acid Database (NDB) (Berman et al., 1992).

Physical principles of NMR. The first commercial NMR spectrometers were available in 1953. The early instruments used permanent magnets rated at 60, 80, 90 or 100 MHz and operated in a continuous wave (CW) or "frequency scan" mode. Historically, the low sensitivity and low resolution of this technique limited the NMR spectroscopy of macromolecules. However, Fourier Transform (FT) NMR (Ernst and Anderson, 1966), introduced in the late 1960s, was shown to be

capable of greatly enhancing the sensitivity of NMR. This sensitivity enhancement was achieved by exciting and subsequently collecting signals from all nuclei (^{1}H or ^{13}C) in a given molecule simultaneously, rather than sequentially as in the CW mode. An equally important development in the late 1960s was the introduction of superconducting magnets that operated with fields of 200 to 500 MHz. These superconducting magnets improved both sensitivity and resolution of NMR spectrometers. Today, the desire for enhanced sensitivity and resolution still remains and there are now 500, 600, 800, and 900 MHz instruments with helium-cooled superconducting magnets that operate in pulsed FT mode.

Simply stated, an NMR spectrometer (Figure 1.1) consists of: (1) a strong magnet with a very homogeneous field, (2) a radio-frequency (RF) oscillator that generates the electromagnetic (EM) radiation, (3) a RF receiver to pick up changes in EM absorbance or emission, (4) an amplifier to enhance the weak signal emanating from the sample, (5) a recording device and/or computer to convert or deconvolute the data, (6) a sample holder surrounded by a transmitter coil and receiver coil, and (7) a sample spinner that spins the sample to increase the apparent homogeneity of the magnetic field.

NMR spectroscopy involves the measurement of the interaction of magnetic moments of atomic nuclei with the surrounding magnetic field (Kessler et al., 1988). The magnetic moment of a nucleus is associated with the nuclear spin quantum number I. Quantum mechanics states that each nuclear particle (proton or neutron) has a spin value of I = ½. Combinations of multiple particles in the nucleus results in an overall spin value that is specific for each atomic isotope. Isotopes possessing even numbers of protons and neutrons will have I = 0 (i.e. ^{4}He, ^{12}C, ^{16}O). Isotopes having an odd number of protons and an even number of neutrons or vice versa will have I = ½ or a multiple of ½ (i.e. ^{1}H, ^{13}C, ^{15}N, or ^{19}F). Those isotopes having odd numbers of both protons and neutrons will have I = 1 (i.e. ^{2}H). For NMR spectroscopy of biomolecules, the most important nuclei are those having I = ½ and I = 1.

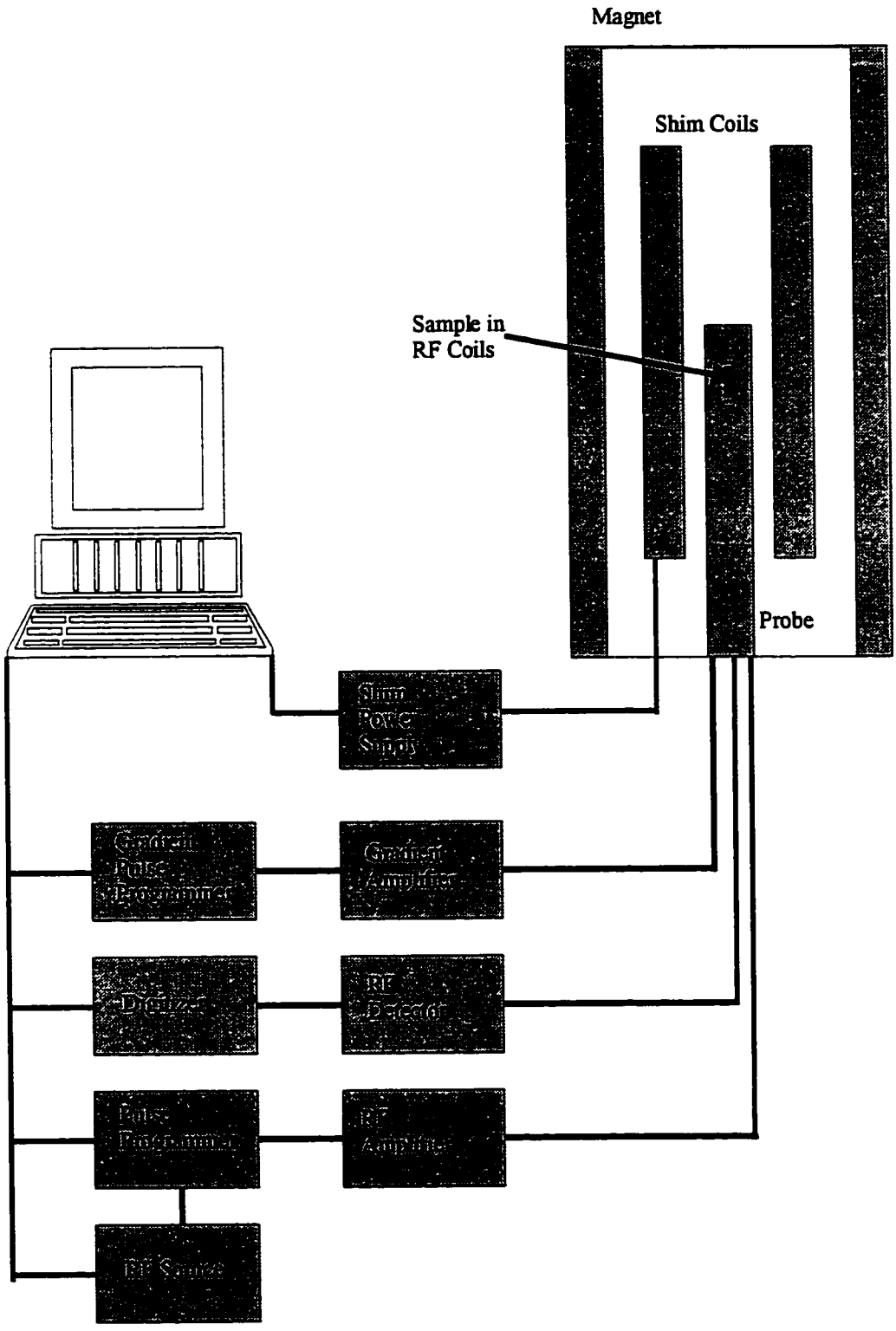

Figure 1.1. Basic outline of a modern, high field NMR spectrometer.

In the presence of an external magnetic field, the spin angular momentum of a nucleus with an overall non-zero spin will undergo a cone-shaped rotational motion called precession (Figure 1.2). The rate of precession for each isotope is referred to as the Larmor frequency (ω_0), which is dependent on the strength of the external field (B_0) and the intrinsic properties of the nucleus reflected in its gyromagnetic ratio (γ). The Larmor frequency may be represented by the following equation:

$$\omega_0 = \gamma B_0 \qquad [1.1]$$

Each magnetic nucleus has 2I+1 possible orientations and 2I+1 corresponding energy levels with respect to the external magnetic field. Therefore, a nucleus with spin I = ½ will have two possible orientations which, in the absence of an external magnetic field, will be of equal energy. However, if a magnetic field is applied, the energy levels split (Figure 1.2). The energy difference (ΔE) between these two orientations is directly proportional to the strength of the magnetic field.

$$\Delta E = \gamma \, h \, B_0/2\pi \qquad [1.2]$$

Where h is Plancks's constant.

At any given magnetic field, a nucleus can jump from one energy level to the other by absorbing or emitting a discrete amount of energy at its Larmor frequency. In NMR, it is important to remember that one is not looking at a single nucleus, but a population of nuclei (~10^{20}). Therefore, at room temperature, the two energy states are unequally populated and the population ratio can be expressed by the Boltzmann equation:

$$N_\beta/N_\alpha = \exp(-\Delta E/kT) \qquad [1.3]$$

Where N_α and N_β (Figure 1.2) are the populations of the lower and upper states respectively, k is Boltzmann's constant and T is temperature in degrees Kelvin.

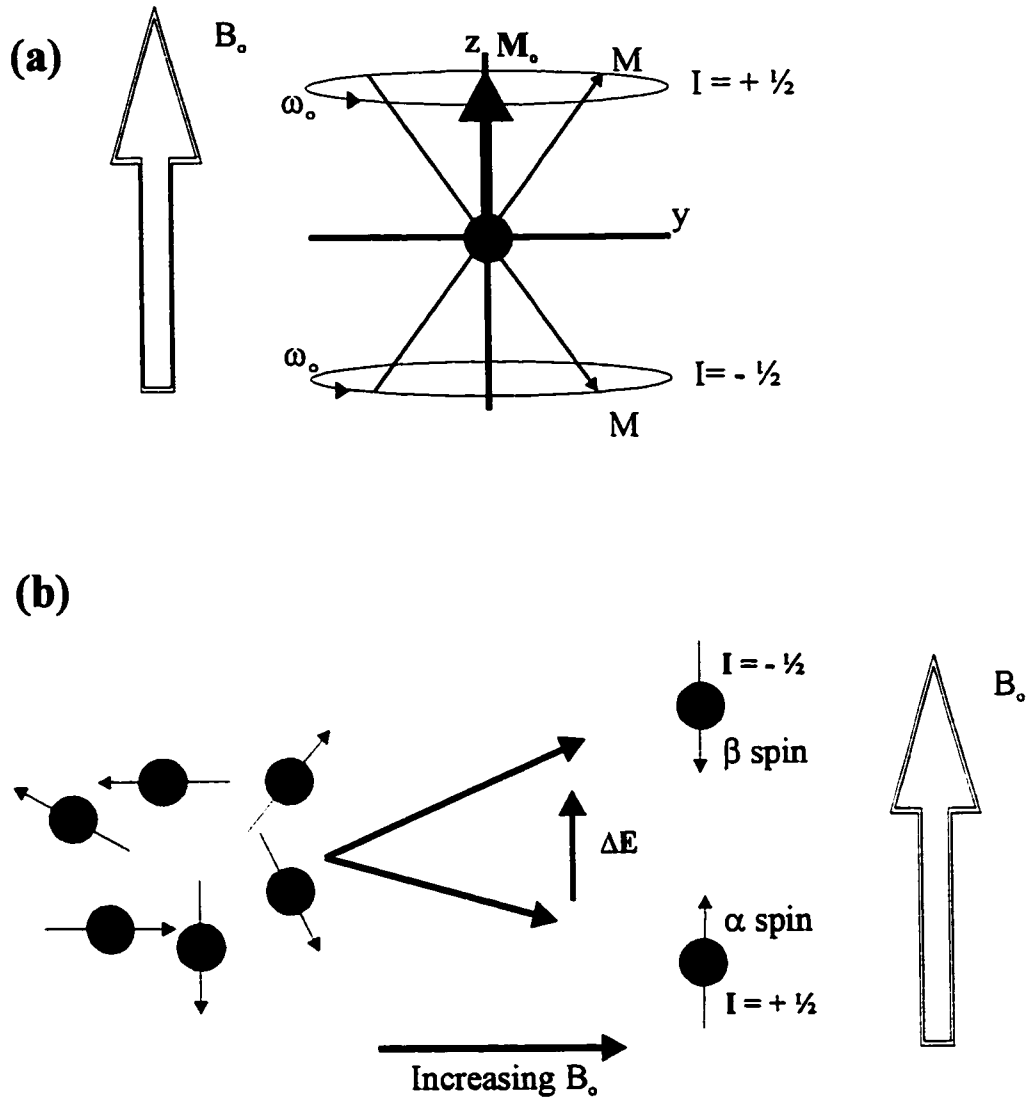

Figure 1.2. Nucleus with spin I = ½ in an applied magnetic field. (a) The two allowed spin states and (b) energy level diagram displaying α and β spin populations.

This population difference generates a net magnetization (M), aligned with the external magnetic field, which will remain static unless the system is disturbed in some way. If a magnetic pulse is applied for a short period of time in such a way that it produces a second magnetic field B_1 perpendicular to the static field B_0, this pulse will drive M away from its equilibrium position by a so-called "flip angle". This flip angle depends on the time, period and the field strength of B_1. A 90° pulse or a 90° flip angle is defined as the time it takes a particular field strength to rotate the equilibrium magnetization 90° with respect to its equilibrium direction (the direction of the applied magnetic field, is usually set along the z axis). Having a metal coil in the xy-plane allows the recording of the oscillating current generated by the precessing magnetization. The precessing magnetization eventually returns to equilibrium, with the xy magnetization slowly fading and the z magnetization growing. This oscillating magnetic field can be detected by a coil, converted to an electrical signal and recorded. This signal is called the free-induction decay (FID). Using a mathematical operation called a Fourier transform;

$$\mathbf{f(\omega) = \int f(t)\, e^{i\omega t}\, dt} \qquad \mathbf{[1.4]}$$

the FID can then be converted from an exponentially decaying oscillation, which is in the time (t) domain, into the more familiar spectrum, which is in the frequency (ω) domain. This whole process is illustrated in Figure 1.3.

Chemical Shifts. The magnetic field at a nucleus will tend to differ from the applied magnetic field due to the "nuclear shielding" effect of the surrounding electrons.

$$\mathbf{B = B_0 (1 - \sigma)} \qquad \mathbf{[1.5]}$$

Where σ is the shielding constant, B_0 is the applied field and B is the net magnetization.

As electron density increases around a nucleus, so does the "shielding" (σ) and consequently, a stronger magnetic field is required to bring the nucleus into resonance. The shielding constant (σ) is related to the electron density (ρ) at a distance (r) from the nucleus as described by Lamb's formula;

$$\sigma = \frac{4\pi e^2}{3mc^2} \int r\rho(r)\, dr \qquad [1.6]$$

Where m is the mass of an electron (9.11×10^{-31} kg), e is the electron charge (-1.6×10^{-19} Coulombs) and c is the speed of light (2.998×10^8 m/s).

The density of the electrons surrounding a nucleus is a function of the type and proximity of chemical groups neighboring the nucleus of interest. In peptides and proteins, the chemical shifts of nuclei depend on the covalent chemistry of individual amino acids as well as the non-bonded environment (McDonald and Phillips, 1967; Allerhand et al., 1973; de Dios et al., 1993). Involvement in hydrogen bonding and proximity to aromatic and carbonyl groups tend to cause the largest deviations of chemical shifts from the values they would otherwise display in an unstructured (i.e. random coil) peptide (Wishart et al., 1995a).

In practical terms, chemical shifts (δ) are measured by the difference between the frequency (Hz) at which a particular nucleus absorbs (ν_{OBS}) relative to the frequency of a given chemical shift standard (ν_{REF}) such as DSS (2,2'-dimethyl-2-silapentane-5-sulfonate). Chemical shifts are most commonly reported in parts per million (ppm) and are calculated using the equation below.

$$\delta\ (\text{ppm}) = \{(\nu_{OBS} - \nu_{REF}) / \nu_{REF}\} \times 10^6 \qquad [1.7]$$

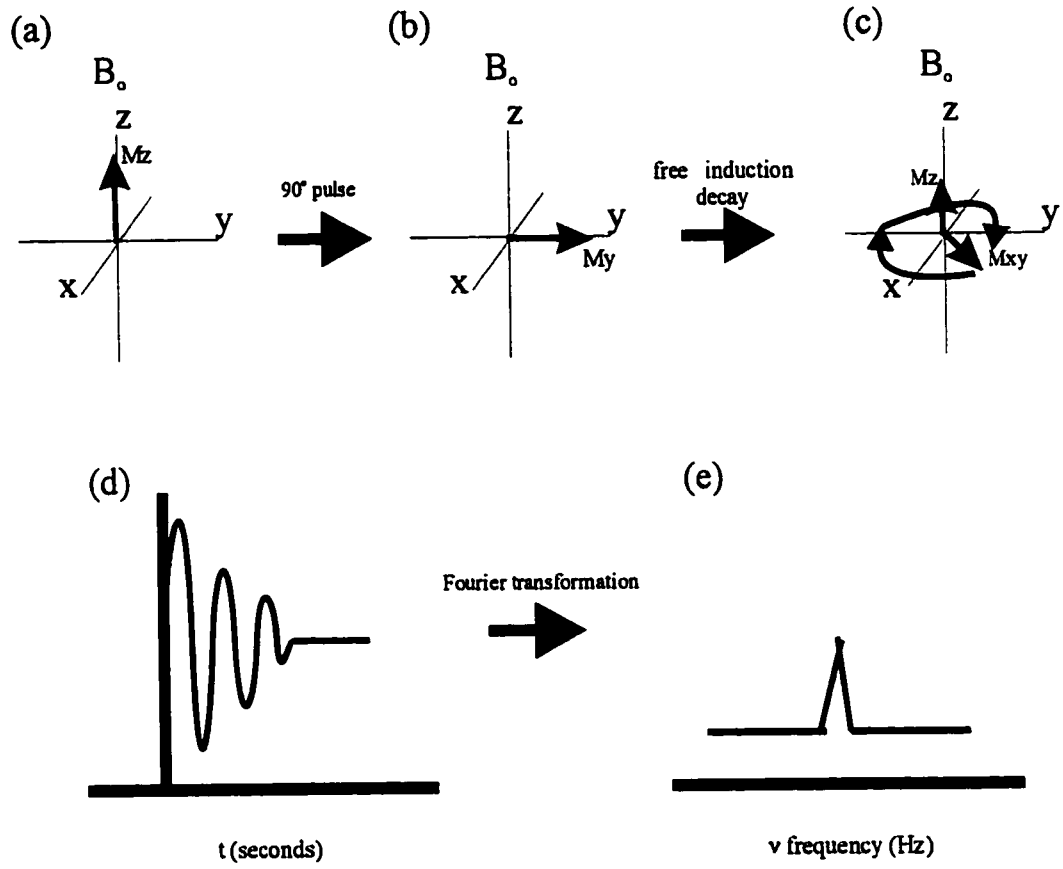

Figure 1.3. Vector picture of pulse NMR. (a) Bulk magnetization (M_z) at equilibrium in magnetic field (B_o), (b) M_z rotates M_y after 90° pulse, (c) M precesses at the Larmor frequency and returns back to equilibrium, (d) free induction decay (FID), (e) fourier transformation of FID yields familiar NMR spectrum.

Chemical shifts are exquisitely sensitive markers of protein structure and protein-ligand interactions. ^{1}H, ^{13}C and ^{15}N chemical shifts are the most widely studied and the dependence of these shifts on protein secondary structure is well established (Wishart et al., 1991; Wishart and Sykes, 1994b). SAR by NMR (Shuker et al., 1996), a method of screening protein-ligand interactions, also relies on chemical shift information. SAR by NMR relies on measuring the effects of ligands binding to protein targets by analyzing the two-dimensional (2D) ^{15}N-^{1}H Heteronuclear Single Quantum Coherence (HSQC) spectrum of the target protein. From perturbations in amide chemical shifts, one can readily identify whether binding has occurred. If the peaks in the 2D ^{15}N-^{1}H HSQC have previously been assigned, then the perturbed peaks also indicate the site(s) on the protein where the ligand is binding.

Spin-Spin Coupling. Nuclei that are coupled through chemical bonds exert an influence on each other's effective magnetic field. This effect shows up in a NMR spectrum as a splitting of the main resonance peak and is termed spin-spin coupling, scalar coupling or J coupling. The strength of this interaction is measured by the scalar coupling constant, $^{n}J_{ab}$, where n designates the number of covalent bonds separating the two nuclei, a and b. The magnitude of $^{n}J_{ab}$ is expressed in Hz and the most important interactions occur when n = 1 to 4.

Spin-spin coupling results from the pairing of an observed nucleus to the electrons in its attached bonds. This pairing sensitizes a nucleus to the spin orientation of neighboring nuclei. When the spin of a bonding electron is influenced, it will in turn influence the spin of other bonding electrons that will then affect an adjacent nucleus and so on down the length of the molecule. This coupling cascade is the basis of through-bond NMR experiments such as COSY and TOCSY.

For proteins, homonuclear experiments such as TOCSY and COSY typically depend on $^{3}J_{HH}$-couplings (such as backbone ^{H}N to backbone H_{α}) to

effect magnetization (polarization) transfer between spins. Significant magnetization transfer via these couplings requires a delay on the order of 1/J. Thus, smaller J coupling values ($^3J_{HH}$ = 3-10 Hz versus $^1J_{CH}$ = 125-160 Hz) require longer periods of time to transfer magnetization ($^3J_{HH}$ – 0.33-0.10 s versus $^1J_{CH}$ – 0.008-0.006 s). This can be problematic in the NMR spectroscopy of larger proteins that possess more efficient relaxation for their NMR active nuclei. An advantage of heteronuclear NMR spectroscopy is the efficient magnetization or polarization transfer enabled by using one- and two-bond J_{CH}, J_{NH}, J_{CC}, and J_{CN} couplings. This concept will be explored in more detail in the next section, which discusses triple resonance spectroscopy.

It is important to note that structural information can also be derived from these coupling constants. As was first described by Karplus (1959), the magnitude of a $^3J_{ab}$ coupling constant contains information about the dihedral angle (θ) formed by the three covalent bonds between nuclei a and b. This relationship is characterized by the following equation:

$$^3J_{ab} = A\cos^2\theta + B\cos(\theta) + C \qquad [1.8]$$

Where A, B, and C are empirically derived constants for each type of coupling constant. $^3J_{HNH\alpha}$ and $^3J_{HAH\beta}$ are the two main coupling constants that provide structural information about dihedral angles in peptides and proteins (Pardi et al., 1984; Bystrov, 1976; Wang and Bax, 1995 and 1996).

Spin Relaxation and Linewidth. Spin relaxation is defined as the return to equilibrium of the projection of the magnetic moment of a large number of spins after an initial perturbation or excitation. This is demonstrated in Figure 1.3(c), which shows transverse magnetization (M_y) returning to its equilibrium magnetization (M_o) along the magnetic field axis (longitudinal - M_z) and perpendicular to it (transverse - M_{xy}). This phenomenon is of great importance to

NMR spectroscopy as the measure of relaxation rates can provide information about the motion or dynamics of the molecules being studied (Kay et al., 1989).

For spin I = ½ nuclei in proteins (such as ^{1}H, ^{13}C and ^{15}N), the two prominent relaxation mechanisms are chemical shift anisotropy (CSA) and dipole-dipole (DD) interactions. As stated earlier, chemical shifts reflect the local magnetic fields experienced by different nuclei. These local fields are anisotropic and consequently the components of the local fields vary as the molecule reorients itself as a result of molecular motion. These varying magnetic fields are what cause CSA relaxation. The second important relaxation mechanism arises from dipole-dipole (DD) interactions. Any NMR active nucleus in a molecule generates a magnetic dipolar field that is proportional to the magnetic moment of the nucleus. As a molecule tumbles in solution, this field fluctuates constituting a mechanism for relaxation of nearby spins.

Dipolar relaxation plays a prominent role in the NMR spectroscopy of proteins. ^{1}H relaxation is dominated by dipolar interaction between nearby protons that are within approximately 5 Å. Similarly, the relaxation of protonated ^{13}C and ^{15}N nuclei also arises primarily from dipolar interactions with directly bonded protons. CSA plays a secondary role in the relaxation of most nuclei. However, it is an important relaxation mechanism for nuclei with large chemical shift ranges. Therefore ^{13}C, ^{15}N and ^{31}P nuclei experience significant CSA contributions to relaxation whereas protons experience negligible effects.

Both CSA and DD interactions play a role in the macroscopically observable relaxation rates known as spin-lattice (longitudinal or T_1) and spin-spin (transverse or T_2) relaxation. T_1 relaxation is the measure of the efficiency with which excited nuclear spins (spins that have experienced a 90° pulse) return to thermal equilibrium by exchanging energy with the "lattice" or surroundings. T_2 relaxation describes the loss of transverse magnetization due to the exchange of spin energies between excited spins. In general, T_1 is always greater than or equal

to T_2 because there are additional contributions to transverse relaxation such as non-uniformity of the static magnetic field, B_0. When the sample is divided into regions such that the field is uniform (regions known as isochromats), then the total magnetization is the sum of these regions. Inherently, there will be differences in sample uniformity that blur the bulk magnetization leading to inhomogeneous line broadening or enhanced transverse relaxation.

In NMR, linewidth ($\Delta\nu_{1/2}$) is defined as the full-width at half-height of the resonance line-shape (Figure 1.4, p.17). Linewidth is a key factor affecting both resolution and signal-to-noise ratio of NMR spectra. Spectral linewidths are intricately related to T_2 relaxation, which is approximately proportional to the overall rotational correlation time (τ_c) of the molecule (Figure 1.5, p.18). τ_c is defined as the approximate average time for the molecule to rotate by one radian (57°). Note that τ_c varies with molecular size, molecular shape, solvent viscosity and temperature (Cavanagh, 1996).

Table 1.2 outlines the relationships between, molecular weight (MW), rotational correlation time (τ_c), backbone ^{15}N- and $^{13}C_\alpha$-T_2 relaxation times and half-height linewidths ($\Delta\nu_{1/2}$). These values are estimated by the following convenient equations (Spyracopoulos et al., 1999). The rotational correlation time (τ_c) of a spherical protein (in nanoseconds) can be estimated from the MW (in kilodaltons) of the protein via

$$\tau_c = \tfrac{1}{2} \times MW \qquad [1.9]$$

In addition, the transverse relaxation times (in seconds) of backbone ^{15}N and $^{13}C_\alpha$ can be conveniently estimated from the correlation time (in nanoseconds) via the following equations.

$$1/T_{2,NH} = 1.11\tau_c \qquad [1.10]$$

$$1/T_{2,CH} = 4.32\ \tau_c \qquad [1.11]$$

Estimates of the half height linewidths ($\Delta\nu_{1/2}$) are calculated from the T_2 values using the following equation.

$$\Delta\nu_{1/2} = 1/\pi T_2 \qquad [1.12]$$

As can be noted in Table 1.2, increased molecular weight corresponds to increased transverse relaxation rates (more rapid decay of transverse magnetization) and broader linewidths. Consequently, larger proteins experience greater sensitivity losses (signal loss) during NMR data acquisitions when compared to smaller proteins. This loss of sensitivity accounts, in large part, for the molecular weight limit imposed on solution NMR methods.

Table 1.2: Relationships between molecular weight, correlation time (τ_c,) backbone ^{15}N-T_2, $^{13}C_\alpha$-T_2, and half-height linewidths ($\Delta\nu_{1/2}$) of backbone ^{15}N and $^{13}C_\alpha$ nuclei.

MW (kDa)	τ_c **(ns)**	^{15}N-T_2 **(s)**	$^{13}C_\alpha$-T_2 **(s)**	^{15}N - $\Delta\nu_{1/2}$ **(Hz)**	$^{13}C_\alpha$ - $\Delta\nu_{1/2}$ **(Hz)**
5	2.5	0.360	0.093	0.88	3.42
10	5	0.180	0.046	1.76	6.91
24	12	0.075	0.019	4.24	16.75
48	24	0.037	0.010	8.60	31.83

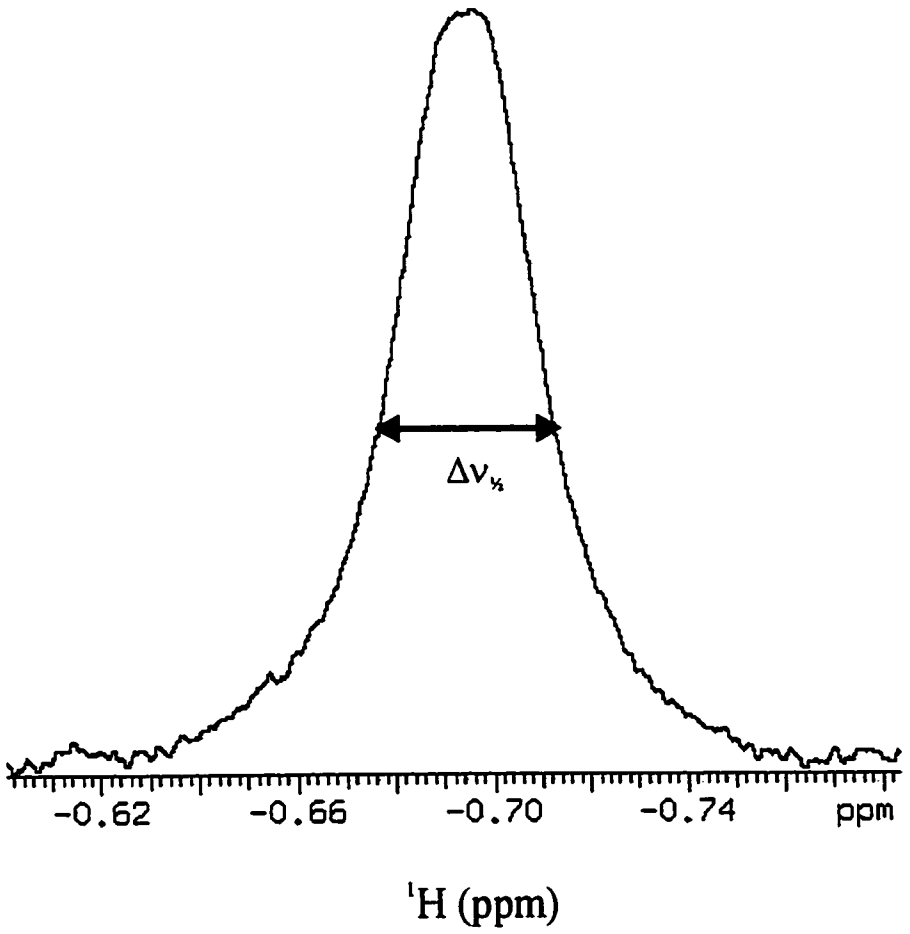

Figure 1.4. A resonance in a 1D ^{1}H NMR spectrum displaying half-height linewidth ($\Delta\nu_{1/2}$).

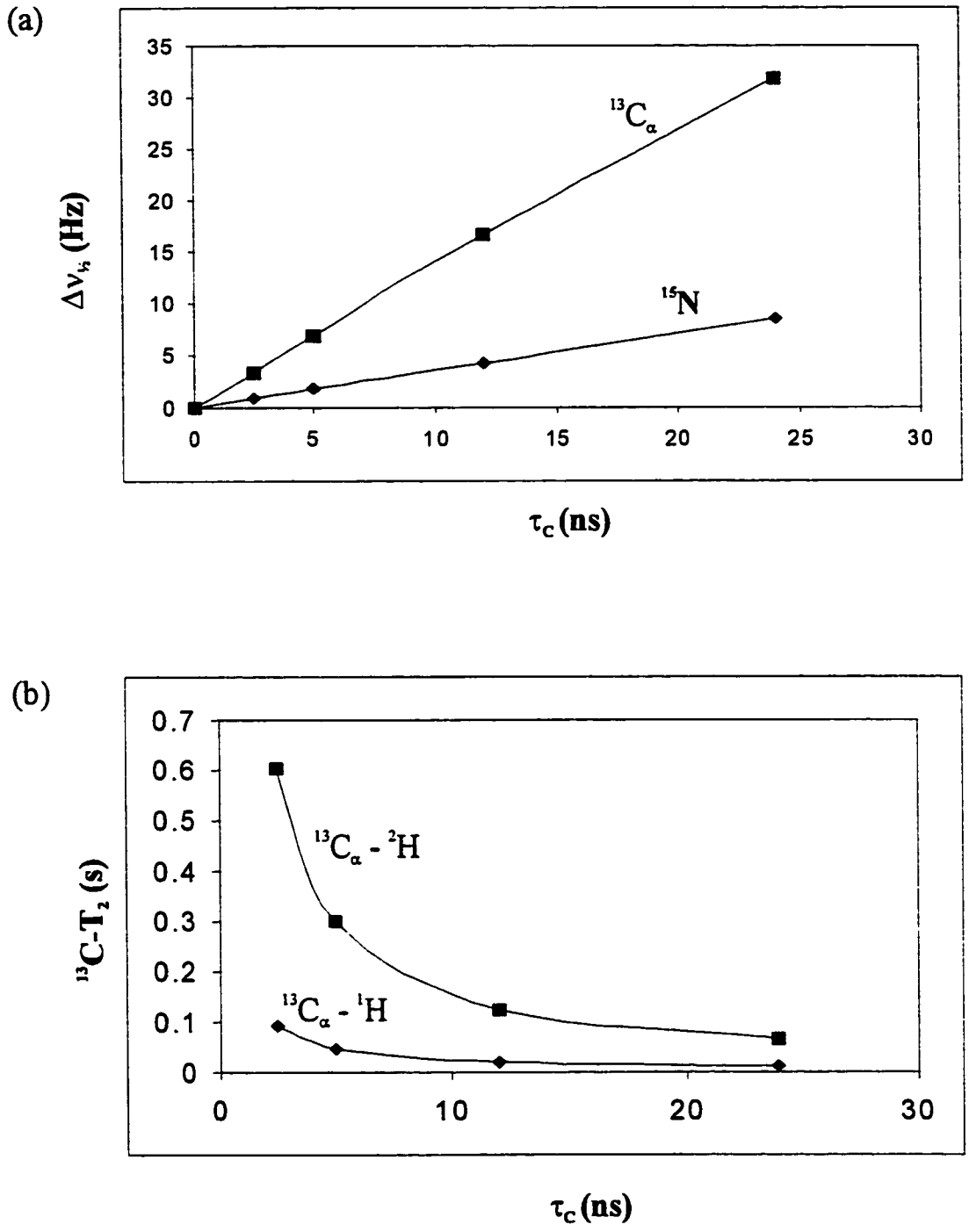

Figure 1.5. Relationships between τ_C, T_2 and $\Delta\nu_{1/2}$. (a) Backbone $^{13}C_\alpha$- and ^{15}N-$\Delta\nu_{1/2}$ in relation to τ_C, (b) backbone $^{13}C\alpha$-T_2 when attached to ^{1}H and ^{2}H in relation to τ_C.

1.2 Sequence-Specific Assignment of Larger Proteins

In NMR, the first step in determining the three dimensional structure of a protein is to assign as many resonances as possible to specific nuclei in the individual amino acid residues. For proteins of approximately 100 amino acids or less, two-dimensional ^{1}H NMR experiments developed during the 1970s and 1980s are usually sufficient to permit unambiguous assignment (Wuthrich, 1986). However, due to problems of overlap and sensitivity, ^{1}H homonuclear NMR spectroscopy is usually insufficient for proteins having a molecular weight exceeding 10 kilodaltons. To permit the sequential assignments of larger proteins, a spectroscopist must often resort to isotopic labelling and very careful sample preparation to overcome three major problems: 1) protein aggregation, 2) spectral overlap and 3) loss of sensitivity. The following three sections will briefly discuss strategies and techniques that have evolved over the past 10 years in order to overcome these three obstacles.

Protein Conditioning. A critical step in the sequential assignment process is the acquisition of "good" spectra to facilitate analysis. Many proteins tend to aggregate far below the concentrations required for NMR experiments. This aggregation is problematic in that it leads to significantly broadened lines, poor resolution and loss of signal, all of which complicate spectral analysis. Possible reasons for aggregation include electrostatic or hydrophobic interactions present between protein molecules (Wagner, 1993). "Protein conditioning" is a term that encompasses the strategies used to prevent protein aggregation in NMR samples (Wagner, 1993). Typically, these strategies include the screening samples where the pH, temperature, buffer, and ionic strength are varied in order to determine the appropriate conditions where the protein behaves as a monomer. There have also been instances where the addition of detergents, such as CHAPS (Anglister et al., 1993), and the introduction of point mutations (Kaarsholm and Ludvigsen, 1994) have been shown to prevent protein aggregation.

Isotopic Labelling. Because of the limited chemical shift dispersion of protons (~10 ppm), the complexity of 2D ^{1}H homonuclear spectra increase roughly as the square of the molecular weight. If it was possible to either increase the chemical shift dispersion or the "dimensionality" of the spectra, this problem of spectral complexity or spectral overlap could be greatly reduced. For this reason isotopic labelling with ^{13}C, ^{15}N (both have large chemical shift ranges), and in some instances ^{2}H, has become standard practice for larger proteins. Normally, these isotopes must be incorporated at levels greater than 90% to achieve satisfactory results (Mossakowska and Smith, 1997). Furthermore, by uniformly or site specifically labelling a protein with either ^{13}C or ^{15}N, a set of nuclei other than ^{1}H can be detected by NMR. This adds new dimensionality to the experiments, thereby reducing spectral overlap and facilitating spectral analysis (Figure 1.6, p.21).

In order to achieve this high degree of isotopic labelling, one must have a high-yield expression system (usually bacterial) in which the cells can grow efficiently on minimal nutrient media composed of simple organic carbon sources (such as ^{13}C enriched glucose), nitrogen sources (such as ^{15}N enriched ammonium chloride) and ^{2}H in the form of $^{2}H_2O$ (Reid et al., 1997). Such a biosynthetic system can be used to either uniformly label proteins or to site-specifically label them with individual amino acids (McIntosh et al., 1990; LeMaster and Richards, 1985).

Because of the beneficial effects of line narrowing, deuterium labelling has played a beneficial role in the solution NMR studies of larger macromolecules (Gardner and Kay, 1998). For heteronuclei (such as ^{13}C and ^{15}N) that are directly bonded to protons, the major source of relaxation is due to dipolar fields caused by the ^{1}H spins (Kay, 1997). The size of these dipolar fields is related to the gyromagnetic constants of the nuclei responsible for them. By substituting ^{13}C-bound protons for deuterons, the size of these dipolar fields can be reduced by a

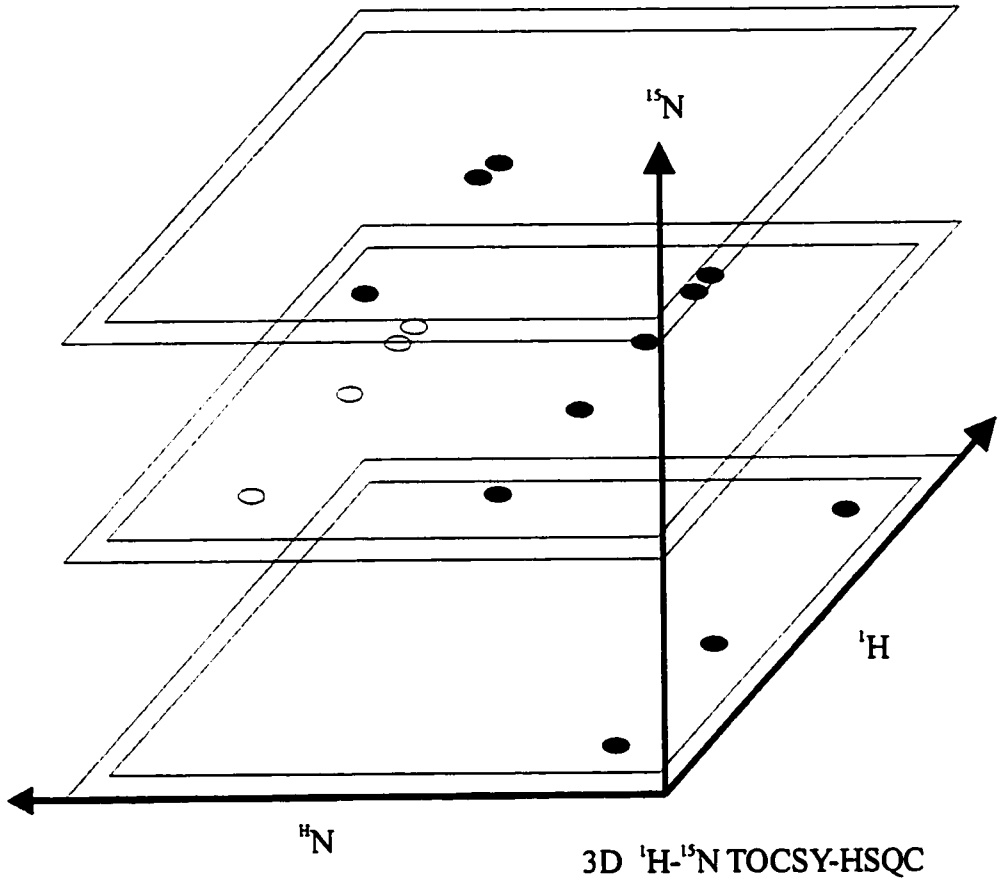

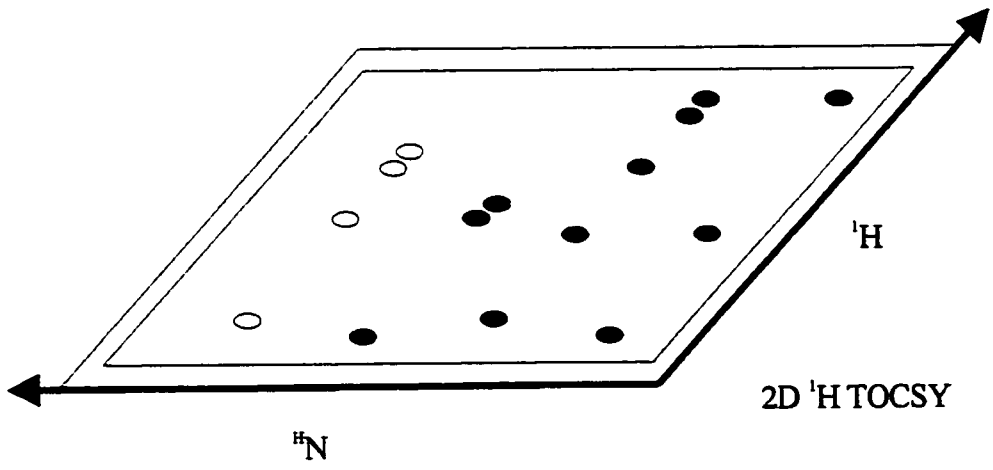

Figure 1.6. Adding a third dimension to NMR experiments.

factor of ~ 6.5. This is because the gyromagnetic constant of deuterium is ~ 6.5 times smaller than that of hydrogen. This results in a substantial decrease in the ^{13}C relaxation rate. In addition, any remaining protons in the protein will also experience a decrease in their T_1 and T_2 decay rate. This is because some of the neighboring protons causing dipolar relaxation (those within 5 Å) have been replaced by deuterons. Figure 1.5 (p.18) illustrates the increase in backbone $^{13}C_\alpha$ carbon T_2's that can be expected upon deuteration (Kay, 1997). These larger T_2 values correspond to slower relaxation rates and therefore a concomitant narrowing in linewidths for the affected nuclei.

Triple Resonance NMR Spectroscopy. Many of the NMR experiments designed for the analysis of larger proteins require uniform labelling with ^{15}N and ^{13}C. These experiments are called triple resonance techniques because three resonances (^1H, ^{13}C and ^{15}N) are recorded in a single experiment. Triple resonance techniques represent a significant advance over homonuclear ^1H techniques because they exploit the large couplings that exist between the ^{15}N and ^{13}C nuclei and their directly bonded protons. They also exploit the sensitivity enhancement that can be achieved with polarization transfer techniques such as INEPT (Morris and Freeman, 1979) which enhance the signals that can be detected from low sensitivity nuclei such as ^{15}N and ^{13}C.

A typical multidimensional NMR experiment can be represented as a series of magnetization or polarization transfer steps, such as:

$$A \rightarrow B \rightarrow C \rightarrow D \rightarrow \ldots. \rightarrow Z$$

where the transfer of magnetization (through combinations of INEPT and reverse INEPT pulses) proceeds from A to B to C and so on until it reaches Z where signal is acquired. The amount of time necessary to transfer significant magnetization along each link in the chain is a function of the strength of the coupling between the two nuclei. This time is given by 1/J (s). Therefore larger couplings lead to

more efficient transfer of magnetization. During this transfer, the signal decays via relaxation processes that become more rapid as the size of the protein increases. If the decay rate is on the same order as the magnetization transfer rate, sensitivity of the experiments will be seriously compromised.

Advantages of Triple Resonance NMR Spectroscopy. For ^{1}H homonuclear NMR experiments, $^{3}J_{HH}$ coupling (approximately 5 – 12 Hz) are normally used to effect magnetization transfer between spins in the protein. In these cases, significant magnetization transfer via this coupling would require 80 – 200 ms delays. During this time, the efficient relaxation rates of nuclei in large proteins would lead to significant loss of signal intensity.

In contrast to ^{1}H homonuclear NMR, triple resonance NMR spectroscopy utilizes two techniques to increase signal at the end of magnetization transfer. First, triple resonance NMR utilizes one and two bond $^{1}J_{CH}$, $^{1}J_{NH}$, $^{1}J_{CC}$, $^{1}J_{CN}$ and $^{2}J_{CN}$ couplings to effect efficient magnetization transfer. Using these couplings, the approximate time necessary for efficient magnetization transfer between backbone nuclei can easily be approximated as 1/J (Table 1.3) (Delaglio et al., 1991; Powers et al., 1992). Therefore, efficient magnetization transfer is the first mechanism by which triple resonance NMR experiments optimize signal intensity.

Table 1.3. Coupling constants and coherence transfer rates for ^{1}H-^{1}H homonuclear, ^{15}N-edited and triple resonance NMR experiments

J coupling	**Coupling Constant (Hz)**	**Coherence Transfer Time (s)**
$^{3}J_{H\alpha H\beta}$	~ 3 – 11	0.333 – 0.091
$^{1}J_{NH}$	~ 95	0.011
$^{2}J_{NH\alpha}$	~ 3 – 11	0.333 – 0.091
$^{1}J_{NC\alpha}$	~ 9 – 13	0.111 – 0.076
$^{2}J_{NC\alpha}$	~ 5 – 10	0.200 – 0.100
$^{1}J_{NCO}$	~ 15	0.067
$^{1}J_{C\alpha CO}$	~ 55	0.018
$^{1}J_{CC}$	~ 30 – 40	0.033 – 0.025
$^{1}J_{CH}$	~ 140	0.007

The second mechanism to optimize signal intensity involves removing the primary source of relaxation in proteins, the protons. Labelling a large protein with deuterium plays an adjunctive role to triple resonance experiments to increase sensitivity of NMR experiments. In the context of pulse sequences, the rate at which a resonance signal decays is of great significance to the success of any NMR experiment. For triple resonance experiments, deuterium (bonded to ^{13}C nuclei) can significantly reduce the relaxation rate of ^{13}C nuclei thereby decreasing the rate at which the ^{13}C signal decays. This reduction in relaxation rate, in combination with efficient magnetization transfer via large one and two bond couplings, ensures that signal is still discernible at time of acquisition. Indeed, many triple resonance pulse schemes have been "deuterium modified" to take advantage of the reduced ^{13}C relaxation rates in highly deuterated proteins (Gardner and Kay, 1998: Yamazaki et al., 1994a/b).

A prototypical triple resonance NMR experiment. A useful triple resonance experiment for sequential assignments of larger proteins is called the HNCA experiment (Kay et al., 1990c; Grzesiek and Bax, 1992). A description of this experiment serves to illustrate the relevant features of heteronuclear multidimensional experiments. As the name implies, this experiment provides protein backbone information by correlating amide proton (^1H_N), attached amide ^{15}N and intraresidue and preceding residue $^{13}C_\alpha(i, i-1)$ chemical shifts.

The flow of magnetization transfer in this experiment can be described concisely by

$$^{H}N \xrightarrow{J_{HN}} {}^{15}N\,(t_1) \xrightarrow{J_{NC^\alpha}} {}^{13}C_\alpha(i,i-1)\,(t_2) \xrightarrow{J_{NC^\alpha}} {}^{15}N \xrightarrow{J_{HN}} {}^{H}N\,(t_3),$$

where the relevant couplings involved in each of the magnetization transfer steps are indicated above the arrows and t_1, t_2 and t_3 denote acquisition times.

This can be more formally denoted using product operator notation as follows:

$I_zJ_zK_z \rightarrow I_yJ_zK_z \rightarrow I_zJ_yK_z\,[t_1] \rightarrow I_zJ_zK_y\,[t_2] \rightarrow I_zJ_yK_z \rightarrow I_yJ_zK_z\,[t_3]$.

Where I, J, K represent ^1H, ^{15}N, and $^{13}C_\alpha$ respectively and t_1, t_2 and t_3 are acquisition periods for ^{15}N, $^{13}C_\alpha$ and ^1H chemical shifts respectively. The y and z subscripts describe when the nucleus' magnetic moment is transverse and longitudinal to B_0 respectively.

In the HNCA experiment (Figure 1.7, p.26), magnetization is first generated on the amide proton (^1H_N) ($I_yJ_zK_z$). An INEPT pulse sequence transfers magnetization to ^{15}N via $^1J_{NH}$ (~90 Hz) coupling. ^{15}N chemical shifts ($I_zJ_yK_z$) are recorded over the acquisition time t_1. A second INEPT pulse sequence is used to transfer magnetization to the intraresidue and the preceding residue $^{13}C_\alpha$ via $^1J_{NC\alpha}$ (8 – 12 Hz) and $^2J_{NC\alpha}$ (~ 7 Hz) couplings respectively. The two $^{13}C_\alpha$ chemical shifts ($I_zJ_zK_y$) are recorded over the acquisition period t_2. Magnetization is then transferred back to the protons using two reverse INEPT sequences and the proton chemical shift ($I_yJ_zK_z$) is collected over the third and final acquisition period t_3. Fourier transformation of the resultant FID yields a frequency domain map with both intra- and interresidue correlations between $^{13}C_\alpha$, ^{15}N, and ^1H_N.

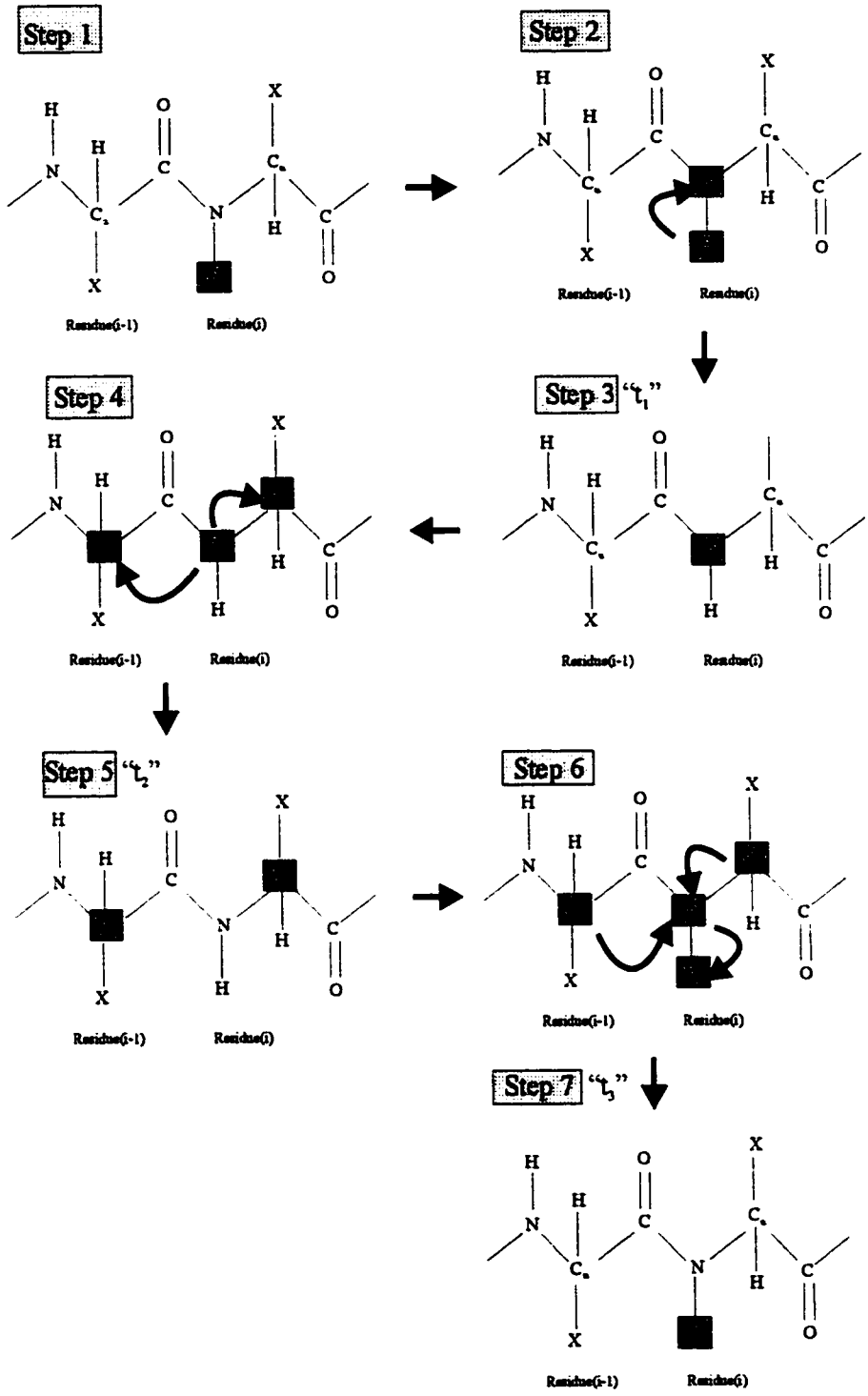

Figure 1.7. Outline of magnetization transfer in HNCA experiments.

1.3 Hepatitis A Virus 3C Protease

Viral Hepatitis A. Hepatitis A is one of the most common forms of acute viral hepatitis in the world. Seroprevalence rates approaching 100% have been noted in the economically developing countries of Africa, Asia, and Latin America. On the other hand, because of improved sanitation, hepatitis A rates have been declining in North America, western Europe and many Mediterranean countries (Koff, 1998). Nonetheless, in 1992 – 1994, of all notifiable infectious diseases in the USA, hepatitis A ranked third amongst children and adolescents, and fifth and sixth amongst men and women respectively (http://www.cdc.gov/). Hepatitis A usually begins with the abrupt onset of non-specific, premonitory constitutional and gastrointestinal symptoms. Symptoms include a combination of fever, malaise, weakness, anorexia, nausea, vomiting, arthralgias (joint pain), and myalgias (muscle pain). Unlike hepatitis B or C, hepatitis A is not linked to chronic liver disease and it does not result in persistent viraemia or an intestinal carrier state. Rather, infection is maintained by serial transmission from acutely infected individuals (Koff, 1998). While effective vaccines for Hepatitis A have recently been introduced (Thiel, 1998), there is no available drug therapy at this time. In most cases, Hepatitis A infections are relatively harmless. However, if individuals are co-infected with chronic hepatitis, the hepatitis A infection is often more dangerous (Sjorgren, 1998; Vento et al., 1998).

Picornaviridae. Hepatitis A virus (HAV) is a member of the picornavirus family (Jia et al., 1991). More than 200 known viruses belong to this family including many that are responsible for human disease (Rueckert, 1996). Each member of the picornavirus family shares the same major events of the viral replication cycle, including specific "self" proteolytic processing of the viral polyprotein (Palmenberg, 1990). Differences in viral replication and polyprotein processing have been used to differentiate the Picornaviridae family into six different genera (Table 1.4).

Table 1.4. The Picornaviruses.

Genus	Number of Serotypes	Viruses	Diseases caused in Humans
Entero	> 90	Poliovirus Coxsackievirus Echovirus	Intestinal infections Poliomyelitis Myocarditis Meningitis Encephalitis
Rhino	> 100	Rhinovirus	Common cold
Aphtho	7	FMDV Equine rhinovirus	Foot and mouth disease of cloven-hoofed animals
Cardio	2	Encephalomyocardiovirus Theiler's murine encephalitis virus	None known
Hepato	1	Hepatitis A virus	Infectious hepatitis
Parecho	2 (perhaps 3)	Parechovirus 1 Parechovirus 2 Ljungan river virus	Myocarditis Intestinal infections

Polyprotein Processing. At the time of the initial infection, the Hepatitis A virus will attach itself to a host cell via specific cell surface receptors and undergo conformational changes that allows it to release its genome into the cytosol of the host cell (Bergmann and James, 1999). Translation of the viral single-stranded RNA yields a large ~ 251 kDa polyprotein (Linemeyer et al., 1985; Najarian et al., 1985) that is co-translationally and sequentially cleaved into individual proteins (Palmenberg, 1990). Once these proteolytic cleavages have been performed, the capsid proteins undergo the conformational changes necessary to allow them to assemble into the procapsid and eventually into the provirion (Rueckert, 1996). A simplified scheme describing the polyprotein processing is shown in Figure 1.8 (p.30).

In hepatoviruses, the 3C gene product is the only protease responsible for polyprotein processing as it is known to cleave all the specific cleavage sites within the polyprotein (Graff et al., 1999; Martin et al., 1999; Jia et al., 1993). The HAV 3C protease typically cleaves between a glutamine residue (P1) and a smaller residue (P2) such as alanine, serine, or glycine (Petithory et al., 1991). Residues in the P4 to P2' positions (following the nomenclature of Schechter and Berger 1967) play a role in cleavage specificity, but a glutamine in the P1 position of the substrate is the most important determinant (Figure 1.9, p.31) (Jewell et al., 1992). X-ray crystallographic studies of the HAV 3C protease (Bergmann et al., 1997) indicate that the other substrate positions of importance are: (1) P2 being occupied by a serine, threonine (2) P3 being occupied by phenylalanine, tryptophan, or glutamate, and (3) P4 being occupied by a large hydrophobic aliphatic residue such as leucine, isoleucine, or valine.

Structure of HAV 3C protease. The structure of the Hepatitis A Virus 3C protease was initially determined by X-ray crystallography in 1994 (Allaire et al., 1994) and later refined by Bergmann et al., in 1997. As can be seen in Figure 1.10 (p.34), HAV 3C protease is composed of two antiparallel β-barrel domains with the active-site and substrate-binding region lying in the surface groove between the two β-barrel domains (Bergmann et al., 1997). Structural comparisons indicate that the 3C proteases belong to the superfamily of chymotrypsin-like serine proteases (Gorbalenya and Snijder, 1996). In this structural family, both domains participate in the binding of peptide substrate. The N-terminal domain participates in binding residues following the scissile peptide bond (P1' to P3') whereas certain C-terminal domains form the pockets that interact with the residues in the P2 to P4 positions of the substrate (Perona and Craik, 1995).

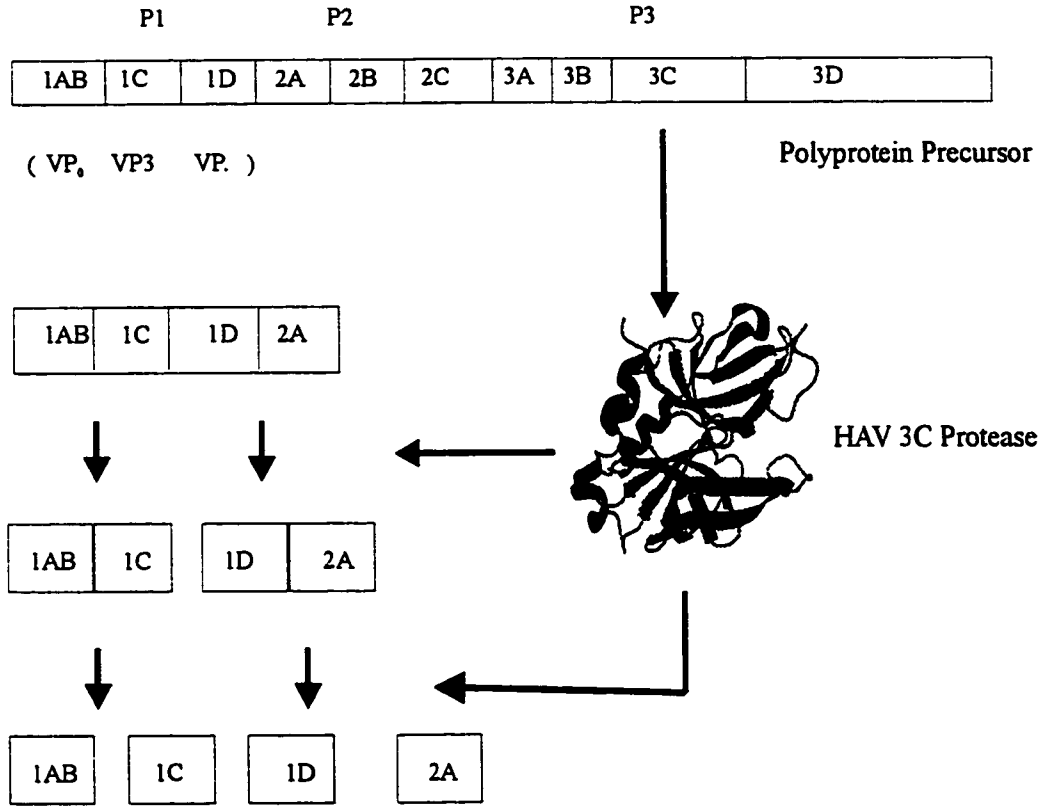

Figure 1.8. Simplified scheme of polyprotein processing by HAV 3C Protease.

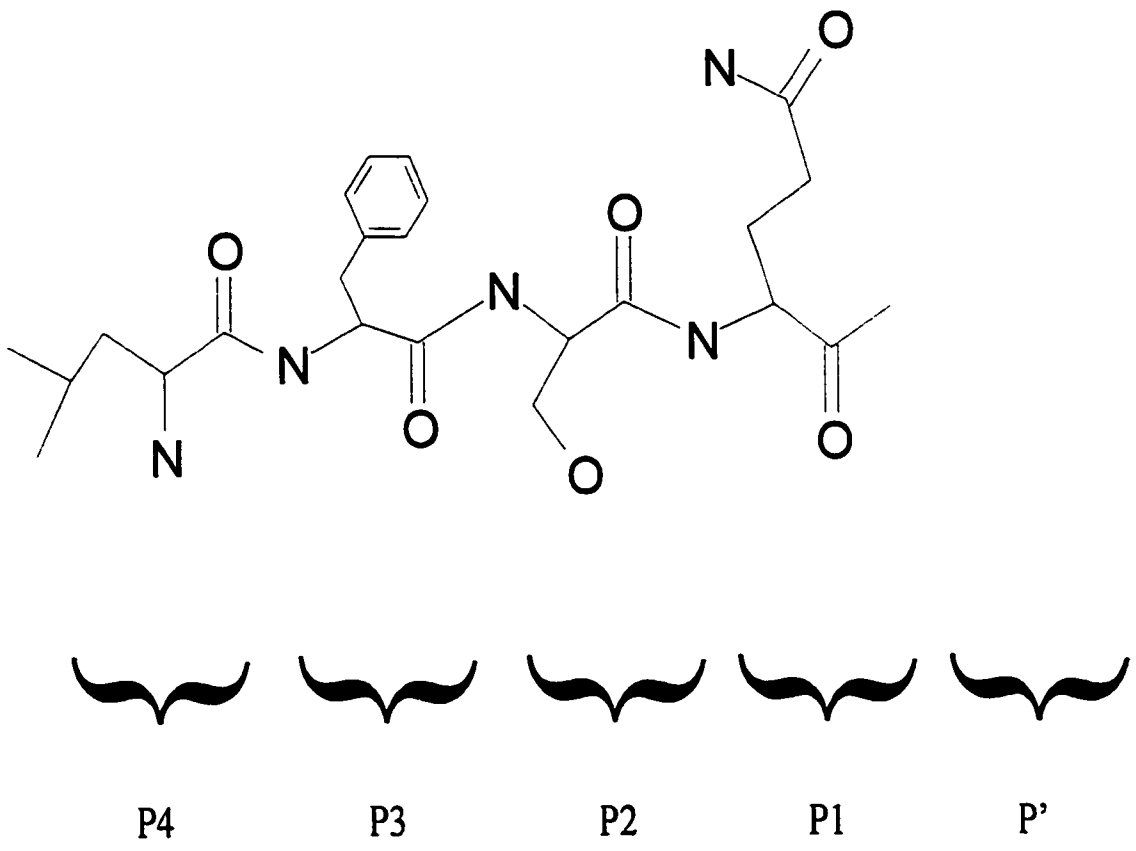

Figure 1.9. Substrate specificity of HAV 3C protease. Cleavage preferences have been shown for P1 - P4 positions although HAV 3C protease is much less specific for P' residues (Bergmann et al., 1997).

Mechanism of HAV 3C protease. In general, there are three chemical groups that function in the active sites of proteolytic enzymes (James, 1993). These include: (1) a nucleophile that attacks the carbonyl of the scissile peptide bond, (2) a general acid-base catalyst that assists in the attack and protonates the leaving group, and (3) an electrophilic structure (oxyanion hole) that stabilizes the negative charge that develops on the carbonyl (Bergmann and James, 1999; James, 1993).

The active site residues of the 3C protease are shown in Figure 1.11 (p.35). Cys172 and His44 form the cysteine-histidine dyad (nucleophile-acid base catalyst) while the oxyanion hole (Pro169, Gly170, Met171 and Cys172) is just above the dyad and to the right (Bergmann et al., 1997). This catalytic-triad arrangement is similar to that observed in the chymotrypsin-like serine proteases but due to the large size of the cysteine sulfur atom, the 3C protease active site is larger (Bergmann and James, 1999). While HAV 3C protease seems to have a mechanism or structure similar to chymotrypsin-like serine proteases, the presence of a cysteine instead of a serine appears to make it something of a hybrid cysteine/serine protease.

HAV 3C protease has four pockets (S1 – S4) that interact with four peptide substrate positions (P1 to P4). The S1-binding pocket is comprised of the main chain atoms of Ala193, Gly194, Gly167, and Leu168 along with the side chains of Leu199 and Met171 and the imidazole of His191. The side chains of Tyr143, His145, and Ala193 form the S2 pocket while the S3 pocket is thought to be formed by Val144, Lys146. The S4 pocket is formed by the side chains of A141, Val144, A198 and Val200 (Bergmann et al., 1997).

The active site residues and the residues comprising the S1 through S4 binding pockets will be very important for future "SAR by NMR" studies of the HAV 3C protease. Using 2D ^{15}N-^{1}H HSQC experiments it should be possible to note where inhibitors are binding to the protease. It is hoped that compounds will be found that cause perturbations to the resonances corresponding to the active site

residues as well as to those resonances corresponding to the S1 through S4 binding pockets.

Inhibitors of the Hepatitis A Virus 3C Protease. Inhibitors of the 3C proteases are generally comprised of a chemical group that covalently attaches to the nucleophilic thiol in the active site and a second group those blocks some other interactions between the protease and its substrates (Figure 1.12, p.36). Typical cysteine protease inhibitors are iodoacetamide, N-ethylmaleimide, epoxides, and aldehydes (Malcolm, 1995). However, recently it was shown that the fluoromethylketones and γ-aminovinylsulfones (Rasnik, 1996) display greater promise than typical cysteine protease inhibitors. A combination of a fluoromethylketone and peptide that mimics the natural peptide specificity such as Acetyl-Leu-Ala-Ala-Gln-FMK has been shown to be an effective inhibitor to the HAV 3C protease both in vitro and in vivo (Morris et al., 1997) (Figure 1.13). Other types of compounds that are being studied as potential inhibitors include α,β-unsaturated carboxylesters, β- and γ-lactones, lactams, isatins (2,3-dioxindoles), and triterpene sulfates (Skiles and McNeil, 1990; Brill et al., 1996).

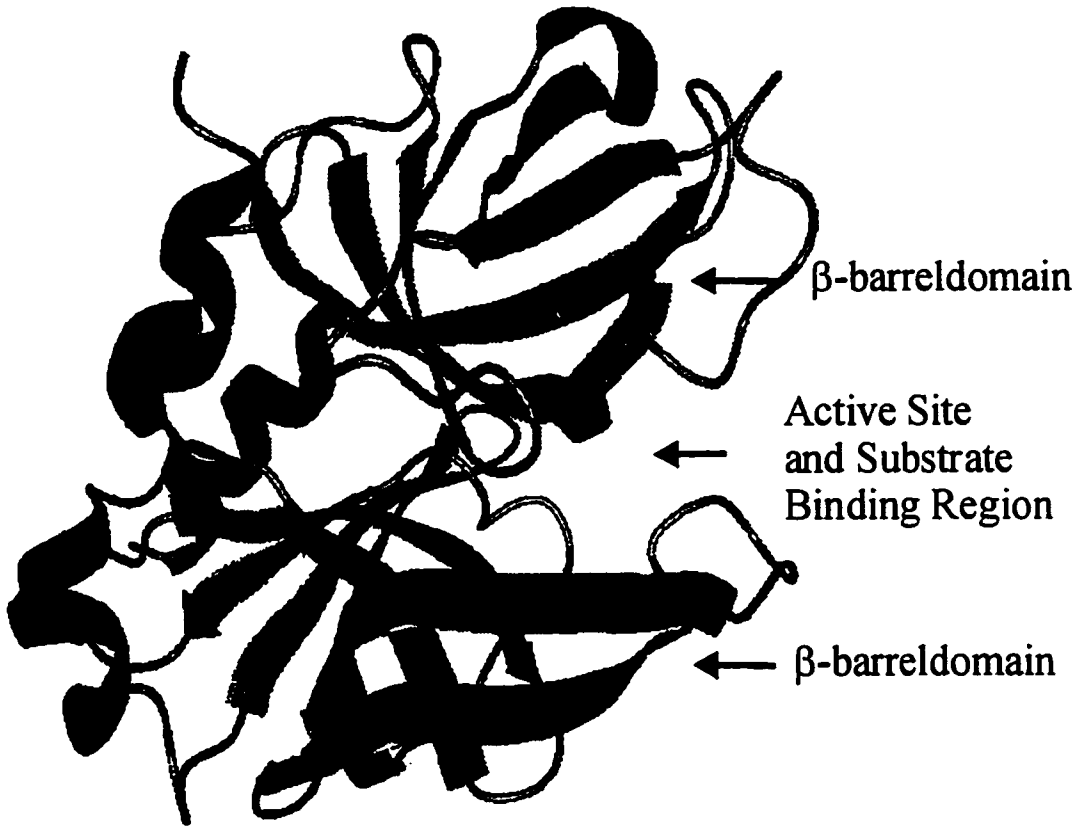

Figure 1.10. Ribbon diagram of the 3D model of HAV 3C protease as determined by X-ray crystallography (Bergmann et al., 1997).

Figure 1.11. Active site residues of HAV 3C protease.

Phthalamide inhibitors

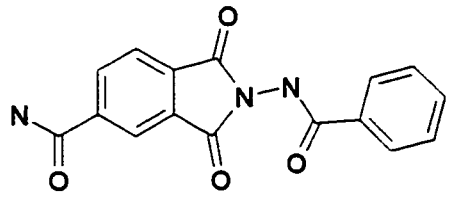

Fluoromethylketone inhibitors

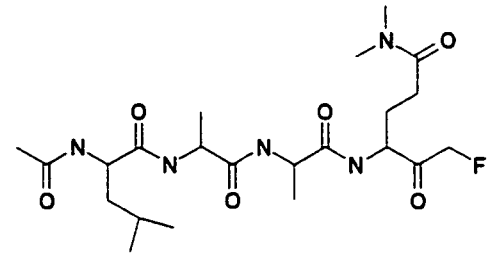

Figure 1.12. Examples of inhibitors to HAV 3C protease. The "pthalamide inhibitor" is positioned in the active site such that it's aldehyde reacts with the nucleophilic thiol of Cys172.

Chapter 2

Determining solution conditions that minimize aggregation of HAV 3C protease

2.1 Introduction

A key prerequisite for determining the sequential assignments of a protein by NMR is that the protein should be soluble and non-aggregating (mono-disperse) at concentrations approaching 1 mM or higher. The increase in molecular weight associated with protein aggregation (particularly for larger proteins) will invariably lead to increases in both the rotational correlation time (τ_C) and half-height linewidths ($\Delta\nu_{1/2}$) of observed resonances. In addition, the rapid transverse relaxation (T_2) associated with such large complexes makes magnetization transfer, even via large heteronuclear couplings, a very inefficient process. Ultimately, for highly aggregated proteins, the sensitivity of NMR experiments drops dramatically and in many cases it is impossible to discern or assign resonances.

Protein aggregation may result from inter-protein electrostatic interactions, the presence of surface hydrophobic patches or the presence of mobile tails (Wagner, 1993). The extent of aggregation may depend on: pH, temperature, amount and type of salts added, addition of reducing agents such as DTT (dithiothreitol), addition of detergents such as CHAPS (3-[(3-cholamidopropyl)-dimethyl-ammonio]-1-propanesulfonate), and the addition of ligands, substrates or cofactors (Schein, 1990). Different combinations of these solution characteristics can reduce protein aggregation. However, there are no hard and fast rules to follow because each protein reacts differently to various conditions. Therefore, as a general rule, the first step in every protein NMR study should involve the optimization of the solution conditions, via thorough screening of many buffer combinations. This screening process is often termed "protein conditioning" (Wagner et al., 1993). Protein conditioning is usually geared towards finding

sample conditions for the protein that produce the narrowest linewidths possible without adversely affecting the structure of the protein.

Indications that the HAV 3C protease may be aggregating at NMR sample concentrations (~ 1 mM) were obtained after a series of NMR experiments (^{1}H-^{15}N TOCSY-HSQC, the HNCACB, and the CBCACONNH) yielded spectra that were devoid of all but a handful of the expected resonances. It was postulated that efficient relaxation rates reflecting the molecular weight of an aggregated complex would account for the disappearance of the ^{1}H and ^{13}C signals. In further support of this premise, X-ray crystallographic experiments had earlier shown that there are two HAV 3C protease molecules present in the crystal unit cell (Bergmann et al., 1997) (Figure 2.1, p.39). Finally, previous NMR studies with the HAV 3C protease indicated protein "self-association" was a definite concern especially after the sample was left in an NMR tube for an extended period of time (Dr. Bruce Malcolm, personal communication).

To facilitate further multidimensional NMR studies with the HAV 3C protease, we decided to employ NMR spectroscopy and analytical ultracentrifugation to: (1) identify optimal sample conditions that produce the narrowest half-height linewidths, (2) determine if the protease is monomeric under these optimal sample conditions, (3) determine the maximal concentration where HAV 3C protease remains monomeric, and finally (4) determine the length of time that the protease would remain monomeric after being prepared for NMR.

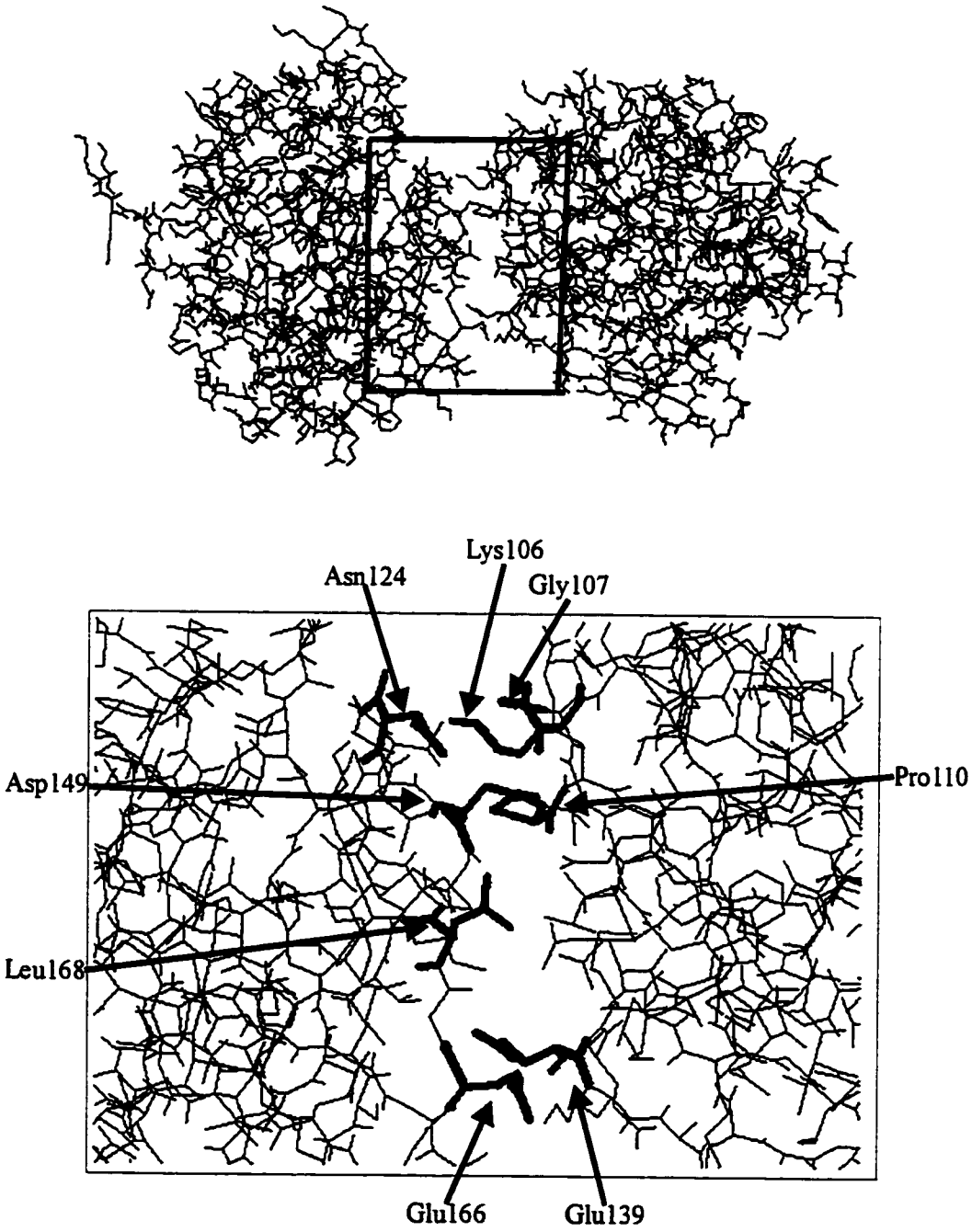

Figure 2.1. Residues involved at the dimer interface of two HAV 3C protease molecules in the unit cell as determined by X-ray crystallography (Bergmann et al., 1997).

2.2 Materials and Methods

HAV 3C Protease Expression System. The HAV 3C expression system was a generous gift from Dr. Bruce Malcolm. The expression plasmid was prepared by cloning the HAV 3C protease gene into a pBR-based plasmid (pHAV-3CEX) containing a tac promoter to enhance expression (Malcolm et al., 1992). The HAV 3C gene was modified at position 24 (C24S) to reduce problems associated with aggregation and disulfide bridge formation noted with the wild type. The pHAV-3CEX vector was transformed into a prototrophic E. coli strain (MM294) that expressed high levels of HAV 3C protease upon induction with isopropyl β-D thiogalactopyranoside (IPTG).

HAV 3C Protease Expression and purification. The following protocol has been optimized from that originally presented by Malcolm et al. (1992). In general, this protocol entailed initially growing the bacterial expression system in a small (25-30 mL) "overnight" starter culture. The "overnight" culture was grown on either rich (Terrific Broth) or minimal media (M9). If sufficient bacterial growth had occurred in this overnight culture, 10 mL of this culture was used to inoculate a larger (1 L) batch of minimal media ("expression media") which was used for HAV 3C protease expression. A detailed description of this protocol follows.

Step 1. MM294 Growth and HAV 3C Protease Expression. MM294 cells, containing the HAV 3C protease gene, from -80°C freezer stock were streaked onto a LB plate containing ampicillin (150 μg/ml). The plate was incubated for ~24 hours at 37°C. A single colony was selected using a fired platinum wire and aseptically transferred into a 25-30 mL volume of media. The media was grown overnight (12-14 hours) in an incubator-shaker at 37°C and 325 rpm. 10 mL of overnight culture was used to inoculate 1 L of minimal media. Bacterial growth was monitored using optical absorbance measurements at 600 nm. When the

OD_{600} reached 0.6 (~2-3 hours), IPTG was added to a final concentration of 2 mM to induce the over-expression of HAV 3C protease. Immediately after induction, the temperature of the incubator-shaker was reduced to 30°C and growth was allowed to continue for an 8 hour induction period. Bacteria were harvested by centrifuging for 10 minutes at 5,000 rpm. The supernatant was discarded and the bacterial pellet was stored at -20°C overnight.

Step 2. MM294 Lysis and HAV 3C Protease Collection. The cell pellet was resuspended in 100 mL of cell resuspension buffer. Lysozyme was added to a concentration of ~80 μg/mL lysate and the mixture was incubated on ice for approximately 30 minutes. Three continuous freeze-thaw cycles (freeze in a dry ice/ethanol mixture and thaw in 30°C water bath) were used to lyse the cells. After the freeze-thaw steps, the lysate was centrifuged for 1 hour at 18,000 rpm and the supernatant was collected. About six drops of 10% polyethylenimine was added to each 25 mL of lysate to precipitate the nucleic acids and the lysate was then centrifuged again for 30 minutes at 12,000 rpm. The supernatant was pooled and kept on ice prior to final purification.

Step 3. Purification of HAV 3C Protease. An ion-exchange chromatography column was prepared by packing a 60 mL syringe with ~ 30 mL CM Sepharose resin (Pharmacia). The column was pre-equilibrated by running ~120 mL phosphate buffer (20 mM KH_2PO_4, 0.5 mM EDTA, 1.0 mM DTT at pH 5.4) through the column using a peristaltic pump. The protein supernatant was loaded onto the column at 1mL/min. Proteins passing through the column were monitored by UV_{280} absorbance using a single path monitor. After the column was loaded, the column was extensively washed with the same phosphate buffer at 1 mL/min until no further protein could be detected passing through the column. The remaining protein was then eluted with a linear gradient of NaCl (0 – 0.5 M) in the same phosphate buffer. The HAV 3C protease normally eluted at ~ 0.35 M NaCl.

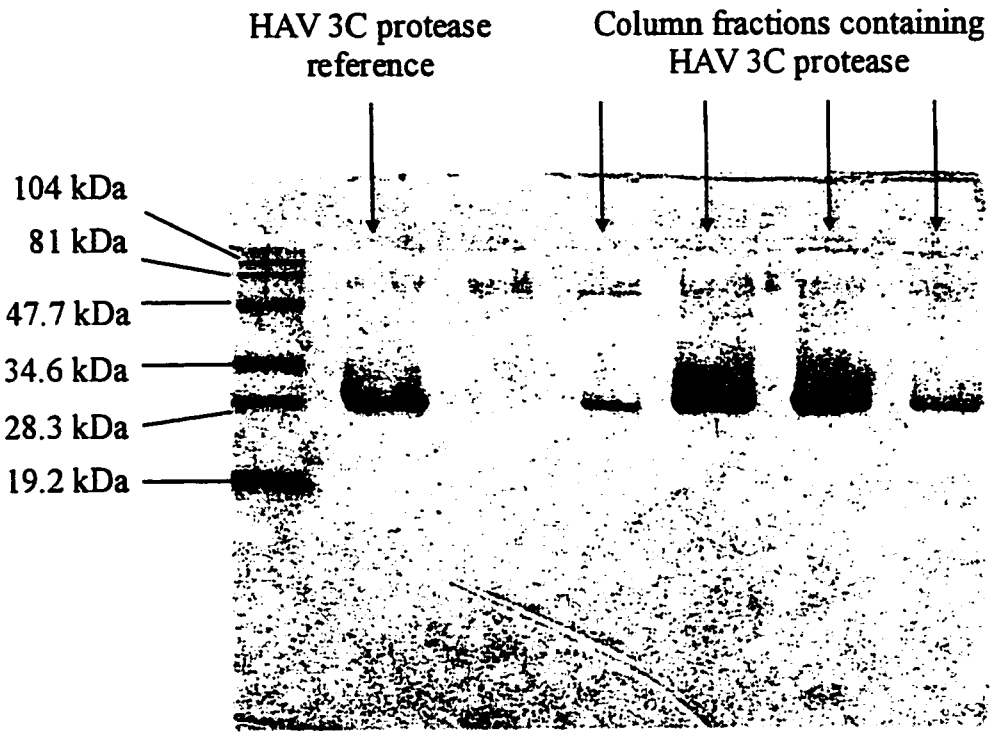

Figure 2.2. SDS-PAGE showing column fractions containing HAV 3C protease.

Step 4. HAV 3C Protease Quantification and Storage. The OD_{280} was recorded for all column fractions by a UV/Visible spectrophotometer using the first fraction as a reference. All column fractions were analyzed by sodium dodecyl sulfate polyacrylamide gel electrophoresis (SDS-PAGE) according to the method of Laemmli (1970). Those fractions containing 3C protease, as judged by the appearance of a protein band similar to the HAV 3C protease reference (Figure 2.2, p.42), were pooled into a 50 mL centrifuge tube. The quantity of HAV 3C protease (mg/mL) in each fraction was calculated by dividing the fraction 'OD_{280} value' by 1.2. 25 μL of 3% w/v sodium azide was added to inhibit bacterial growth and nitrogen gas was instilled into the tube. The sealed tube was stored at 4°C. HAV 3C protease was generally found to be stable for one month under these storage conditions.

1D ^{1}H NMR studies. The concentration of the HAV 3C protease stock solution was determined by recording the OD_{280} for the solution using a phosphate buffer (20 mM KH_2PO_4, 0.5 mM EDTA, 1.0 mM DTT at pH 5.4) as a reference. It is important to note that if pH changes were required they had to be done at this (pre-concentrated) stage as it was found changing the pH of highly concentrated protease solutions led to precipitation. Changes in pH changes were accomplished by adding drops (in the required amount) of 0.1 M KOH or 0.1 M HCl. An appropriate volume of stock solution (containing 6 mg of HAV 3C protease) was used in the preparation of each NMR sample. When 6 mg of HAV 3C protease was concentrated to 500 μL (NMR sample volume) it would provide ~ 0.5 mM NMR samples. This was the approximate concentration of HAV 3C protease that was tested under most buffer conditions. The protease solution was concentrated to 400 – 500 μL using a 10K centrifugal filter device (Millipore) having a MW cutoff of 10 kDa. In the series of experiments looking at salt concentration effects, the stock solution containing 350 mM NaCl was concentrated to 1.0 mL then reconstituted with 2.5 mL phosphate buffer (20 mM KH_2PO_4, 0.5 mM EDTA, 1.0 mM DTT, and pH 5.4) and then concentrated again. This yielded samples with 100 mM NaCl. To prepare samples with higher

concentrations of NaCl, the appropriate mass of NaCl was added to the already concentrated samples. Appropriate quantities of TFE, CHAPS, $CaCl_2$, and glycine were all added to the previously concentrated HAV 3C protease solutions in order to prepare the samples listed in Table 2.1 (p.43). Each NMR sample was prepared to a volume of 500 μL by combining 10 μL DSS (5 mM), 50 μL D_2O (99%) and 440 μL of concentrated protease in each condition set. The final step was to transfer this volume to a 5 mm NMR tube.

A 1D ^1H NMR spectrum was collected for each sample (if possible) on a Varian VXR 500 MHz NMR spectrometer equipped with a 5 mm triple resonance probe. A sweepwidth of 8000 Hz was used with 2048 transients being collected for each sample. A relaxation delay of 1.0 s was used between transients. Spectra were processed and analyzed using VNMR software version 5.1 with a line-broadening constant (lb) of 0.5.

The Val25 γCH_3 resonance at -0.7 ppm was examined and the half-height linewidth of this resonance (Figure 2.3, p.47) was recorded for each sample. Half-height linewidths were determined using the Varian "dres" macro after suitable phasing, drift and baseline correction. The linewidths values are listed in Table 2.1.

2D ^1H-^{15}N HMQC-J and ^{15}N T_1/T_2-Envelope Experiments. NMR samples of the HAV 3C protease were prepared as discussed above. Four samples (A,B,C, and D) were prepared containing 1.5 mM, 1.0 mM, 0.75 mM and 0.46 mM of ^{15}N labelled HAV 3C protease. Sample C (0.75 mM HAV 3C protease) was prepared using enzymatic assay conditions of 350 mM NaCl, 20 mM KH_2PO_4, 0.5 mM EDTA at pH 7.0. Samples A, B, and D were prepared in the ideal conditions identified by the 1D ^1H NMR linewidth studies (100 mM NaCl, 20 mM KH_2PO_4, 0.5 mM EDTA, 1.0 mM DTT at pH 5.4). Samples B and C were prepared from frozen stock (-20°C) while the other two were prepared from fresh stock stored at 4°C.

Table 2.1 Solution conditions tested in 1D ^{1}H NMR studies with HAV 3C protease.

Sample #	Solution Conditions	$\Delta\nu_{1/2}$ (Hz)
1	0.5 mM HAV 3C Protease / 20 mM KH_2PO_4 / 350 mM NaCl 0.5 mM EDTA / pH 7.0 / 25.0 °C	18
2	0.5 mM HAV 3C Protease / 20 mM KH_2PO_4/ 350 mM NaCl 0.5 mM EDTA / pH 7.0 / 25.0 °C / Y143G	--
3	0.5 mM HAV 3C Protease / 20 mM KH_2PO_4 / 350 mM NaCl 0.5 mM EDTA / pH 7.0 / 25.0 °C / Y143G with Inhibitor	--
4	0.5 mM HAV 3C Protease / 20 mM KH_2PO_4 / 350 mM NaCl 0.5 mM EDTA / pH 7.0 / 25.0 °C / 9.1 % (v/v) TFE	--
5	0.5 mM HAV 3C Protease / 20 mM KH_2PO_4 / 350 mM NaCl 0.5 mM EDTA / pH 7.0 / 25.0 °C / 4.5 % (v/v) TFE	--
6	0.5 mM HAV 3C Protease / 20 mM KH_2PO_4 / 350 mM NaCl 0.5 mM EDTA / pH 7.0 / 25.0 °C / 25.0 mM CHAPS	--
7	0.5 mM HAV 3C Protease / 20 mM KH_2PO_4 / 350 mM NaCl 0.5 mM EDTA / pH 7.0 / 25.0 °C / 7.0 mM CHAPS	19
8	0.5 mM HAV 3C Protease / 20 mM KH_2PO_4 / 350 mM NaCl 0.5 mM EDTA / pH 5.4 / 25.0 °C	18
9	0.5 mM HAV 3C Protease / 20 mM KH_2PO_4 / 100 mM NaCl 0.5 mM EDTA / 1.0 mM DTT / pH 5.4 / 25.0 °C	16
10	0.5 mM HAV 3C Protease / 20 mM KH_2PO_4 / 350 mM NaCl 0.5 mM EDTA / 1.0 mM DTT / pH 5.4 / 25.0 °C	17
11	0.5 mM HAV 3C Protease / 20 mM KH_2PO_4 / 450 mM NaCl 0.5 mM EDTA / 1.0 mM DTT / pH 5.4 / 25.0 °C	18
12	0.5 mM HAV 3C Protease / 20 mM KH_2PO_4 / 750 mM NaCl 0.5 mM EDTA / 1.0 mM DTT / pH 5.4 / 25.0 °C	20
13	0.5 mM HAV 3C Protease / 20 mM KH_2PO_4 / 1.0 M NaCl 0.5 mM EDTA / 1.0 mM DTT / pH 5.4 / 25.0 °C	20
14	0.75 mM HAV 3C Protease / 20 mM KH_2PO_4 / 100 mM NaCl 0.5 mM EDTA / 1.0 mM DTT / pH 5.4 / 25.0 °C	17
15	0.5 mM HAV 3C Protease / 20 mM KH_2PO_4 / 1.0 M NaCl 0.5 mM EDTA / 1.0 mM DTT / pH 5.4 / 25.0 °C	20
16	0.5 mM HAV 3C Protease / 20 mM KH_2PO_4 / 1.0 M NaCl 0.5 mM EDTA / 1.0 mM DTT / pH 5.4 / 30.0 °C	19
17	0.5 mM HAV 3C Protease / 20 mM KH_2PO_4 / 1.0 M NaCl 0.5 mM EDTA / 1.0 mM DTT / pH 5.4 / 35.0 °C	19
18	0.5 mM HAV 3C Protease / 20 mM KH_2PO_4 / 1.0 M NaCl 0.5 mM EDTA / 1.0 mM DTT / pH 5.4 / 40.0 °C	19
19	0.5 mM HAV 3C Protease / 20 mM KH_2PO_4 / 1.0 M NaCl 0.5 mM EDTA / 1.0 mM DTT / pH 5.4 / 45.0 °C	19
20	0.5 mM HAV 3C Protease / 20 mM KH_2PO_4 / 100 mM NaCl 0.5 mM EDTA / 1.0 mM DTT / pH 5.4 / 25.0 °C	16
21	0.5 mM HAV 3C Protease / 20 mM KH_2PO_4 / 100 mM NaCl 0.5 mM EDTA / 1.0 mM DTT / pH 5.4 / 30.0 °C	16
22	0.5 mM HAV 3C Protease / 20 mM KH_2PO_4 / 100 mM NaCl 0.5 mM EDTA / 1.0 mM DTT / pH 5.4 / 35.0 °C	16
23	0.5 mM HAV 3C Protease / 20 mM KH_2PO_4 / 100 mM NaCl 0.5 mM EDTA / 1.0 mM DTT / pH 5.4 / 25.0 °C/ with Inhibitor	17
24	0.5 mM HAV 3C Protease / 20 mM KH_2PO_4 / 100 mM NaCl 0.5 mM EDTA / 1.0 mM DTT / pH 5.4 / 25.0 °C/ 20 mM $CaCl_2$	18
25	0.5 mM HAV 3C Protease / 20 mM KH_2PO_4 / 100 mM NaCl 0.5 mM EDTA / 1.0 mM DTT / pH 5.4 / 25.0 °C/ 100 mM $CaCl_2$	18
26	0.5 mM HAV 3C Protease / 20 mM KH_2PO_4 / 100 mM NaCl 0.5 mM EDTA / 1.0 mM DTT / pH 5.4 / 25.0 °C/ 9.1 % (v/v) Saturated Glycine Solution	--

2D ^{15}N-^{1}H HMQC-J experiment. The 2D ^{15}N-^{1}H HMQC-J experiment (Kay et al., 1989; Kay and Bax, 1990) was used to determine $^{3}J_{HNH\alpha}$ coupling constants. This experiment differs from the 2D ^{15}N-^{1}H HMQC in that it utilizes a 90°γ purge pulse (Frey et al., 1985) to eliminate the dispersive contributions to lineshape that are associated with J modulation present during the acquisition time, t_1. A key to this experiment was collecting a high number of transients to allow for good spectral resolution. In the ^{15}N-^{1}H HMQC-J experiment (Figure 2.4, p.48), magnetization is generated on $^{1}H_N$ [Step 1]. An HMQC pulse sequence transfers magnetization to ^{15}N via the $^{1}J_{NH}$ (~90 Hz) coupling [Step 2]. ^{15}N chemical shifts are recorded over the acquisition time t_1 [Step 3]. A second HMQC pulse sequence transfers magnetization back to $^{1}H_N$ [Step 4] and the proton chemical shift is collected over the second acquisition time t_2 [Step 5]. Fourier transformation of the resultant FID yields a frequency domain map showing all $^{1}H_N$ and ^{15}N correlations.

^{15}N T_1/T_2-Envelope Experiments. The ^{15}N T_1 and T_2 relaxation data for the amide envelope were obtained by recording a series of 1D ^{15}N inverse detected NMR spectra for a series of T_1 and T_2 delays (Farrow et al., 1994). In these experiments, an INEPT sequence was used to transfer the magnetization from $^{1}H_N$ to the directly attached ^{15}N. The ^{15}N magnetization was refocused in either the z plane (for T_1-envelope) or the xy plane (for T_2-envelope). Then the ^{15}N magnetization was allowed to evolve for a period of time (T_{xd}) specified by

$$\mathbf{T_{1d} = ncyc\ \{PW\_SHPSS + (2 \times 2.5 \times 10^{-3})\}} \qquad \mathbf{[2.1]}$$

$$\mathbf{T_{2d} = ncyc\ \{(32 \times PWN) + (32 \times 450 \times 10^{-6})\}} \qquad \mathbf{[2.2]}$$

where ncyc was the number of cycles used (1 to10), PW_SHPSS (cosine-modulated 180° ^{1}H pulse) = 550×10^{-6} s, and PWN (90° ^{15}N pulse) = 59×10^{-6} s. This corresponded to T_{1d} values of 0.0056 s, 0.0112 s, 0.0168 s, 0.0224 s, 0.0280 s, 0.0336 s, 0.0392 s, 0.0448 s, 0.0504 s and 0.0560 s. T_{2d} values were 0.0163 s, 0.0326 s, 0.0489 s, 0.0652 s, 0.0815 s, 0.0978 s, 0.1141 s, 0.1304 s, 0.1467 s and 0.1630 s. After incrementally increasing the amount of time, a

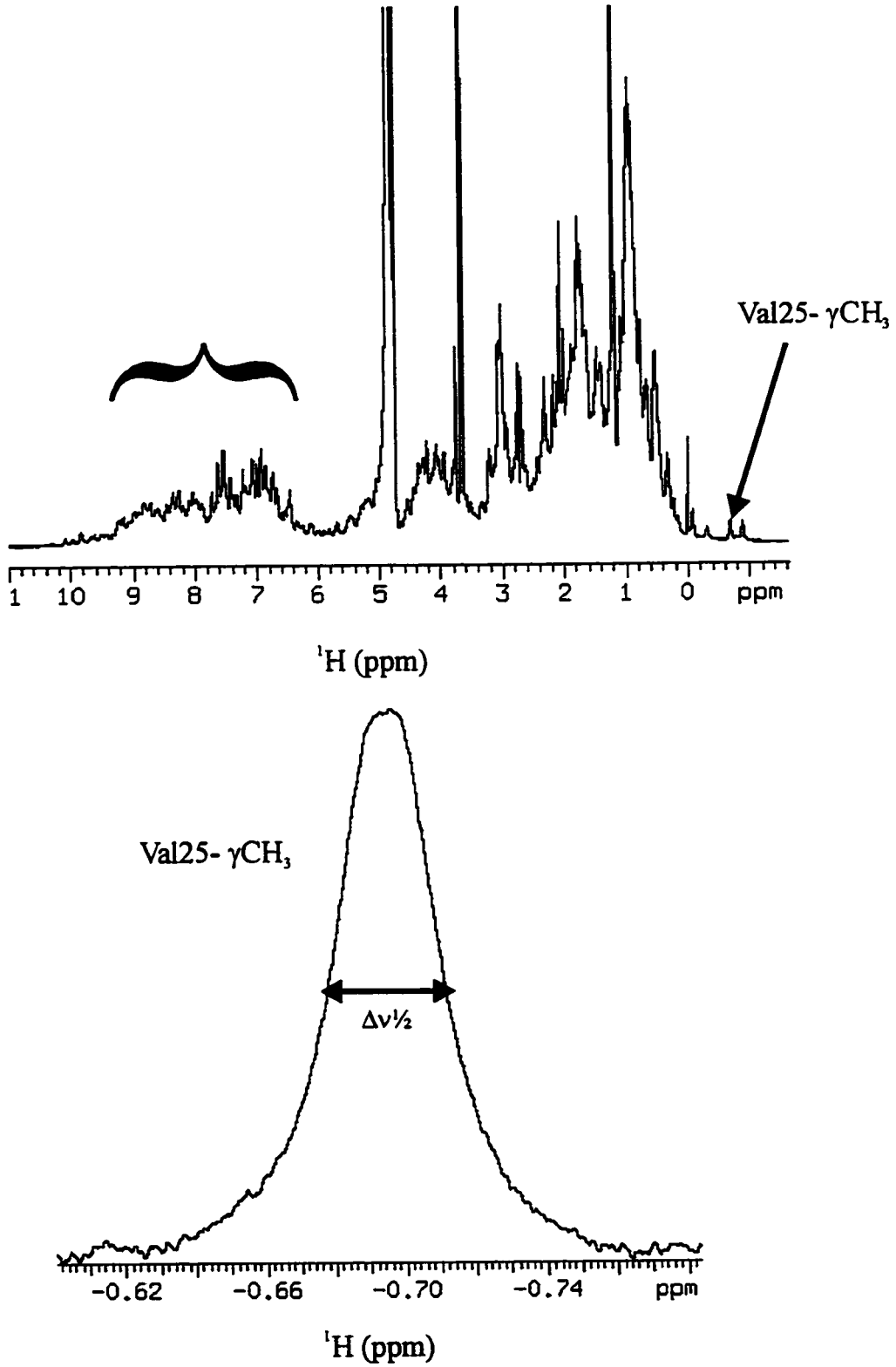

Figure 2.3. Comparing the effect of NMR buffer conditions on the HAV 3C protease by using 1D ^{1}H NMR studies.

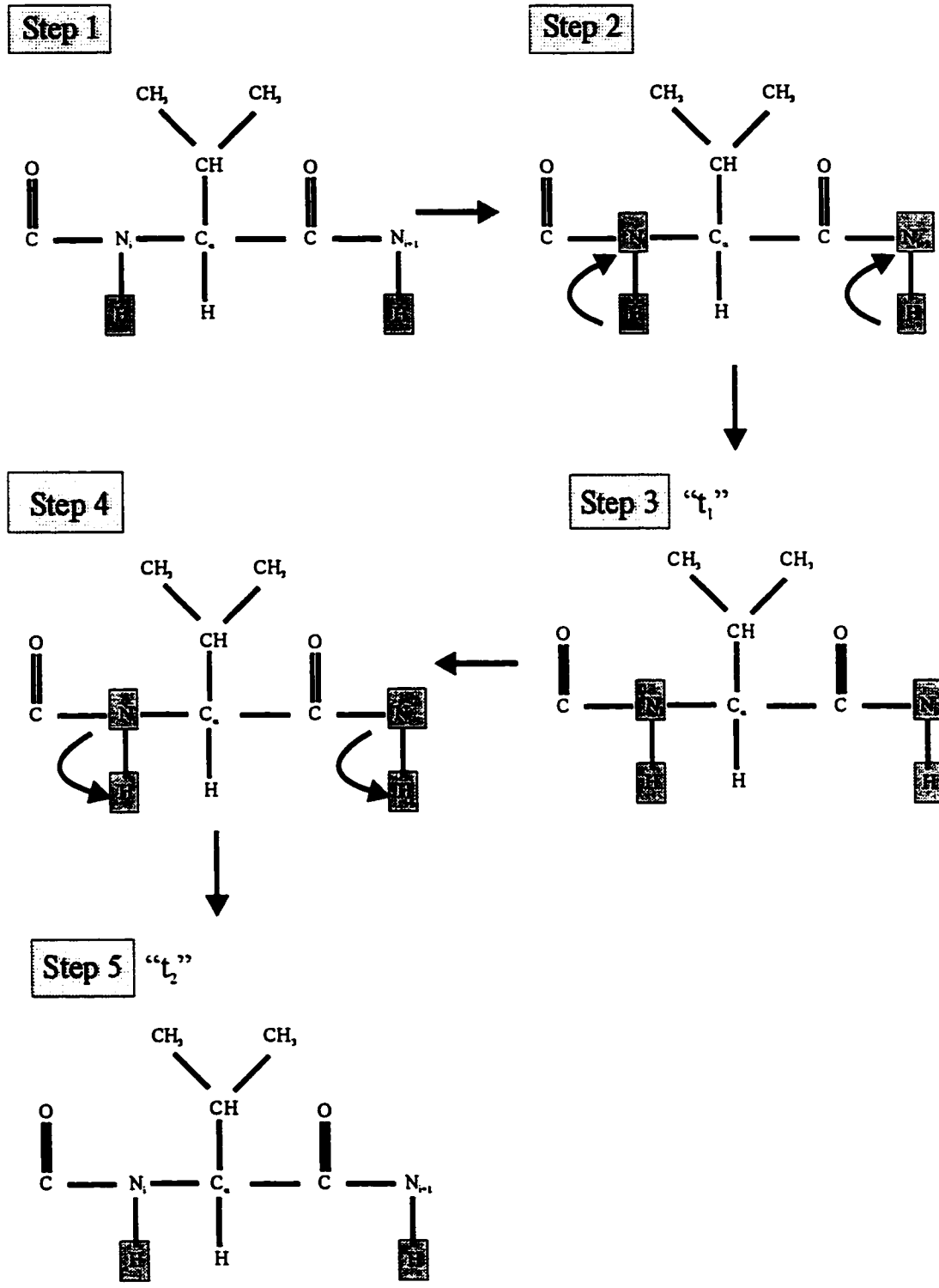

Figure 2.4. Outline of magnetization transfer in the HMQC-J experiment.

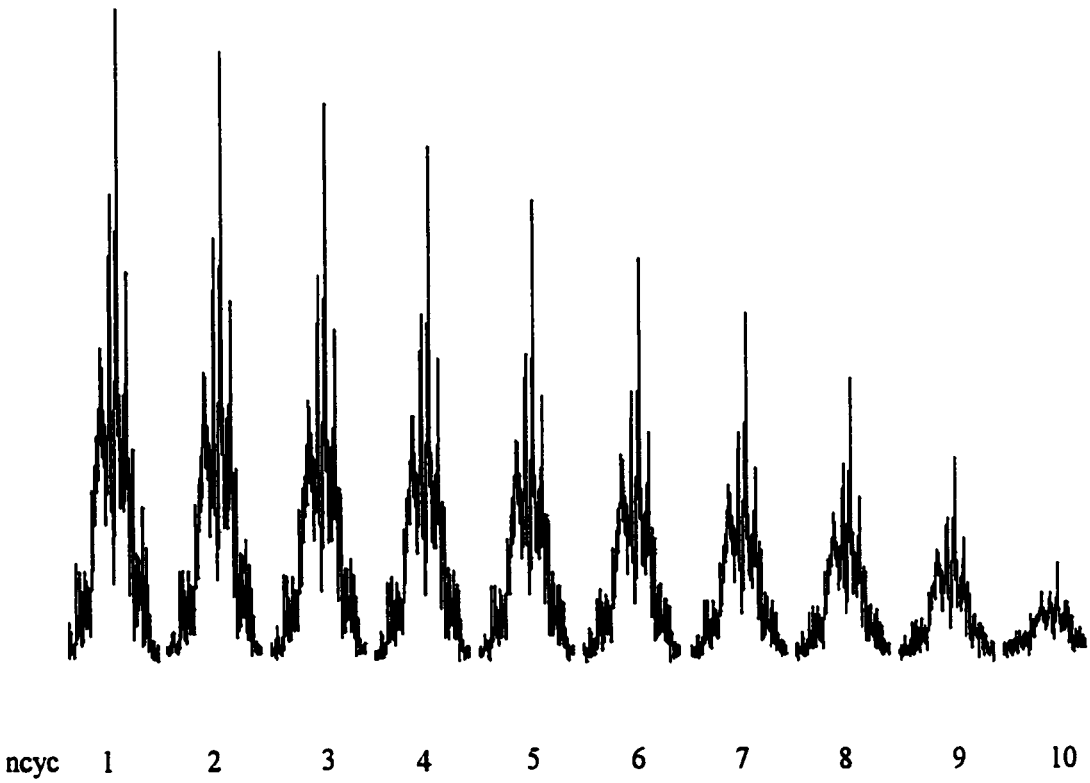

Figure 2.5. A typical result for ^{15}N T_1- and T_2-envelope experiments. The amide envelope is shown decreasing logarithmically as ncyc increases from 1 to 10 (successive increases in T_{1d} or T_{2d}).

reverse INEPT pulse sequence was used to transfer magnetization back to the proton for signal acquisition.

^{15}N-T_1 and ^{15}N-T_2 values were obtained by integrating the area under the entire ^1H_N envelope for each cycle in the experiment (Figure 2.5, p.49). As magnetization evolved on the ^{15}N during the delay, the magnetization would also undergo relaxation. A longer delay corresponded to a greater period of relaxation and a further decay of magnetization. Therefore, each cycle would transfer less and less magnetization back to the proton for detection. Consequently, the integral of the amide envelope would decrease in an exponential fashion throughout the experiment. The '$T_{1d \text{ or } 2d}$ - normalized integral value' values (Table 2.2) were entered into the program "xcrvfit" (performed at PENCE, University of Alberta) which calculated values for ^{15}N-T_1 and ^{15}N-T_2. Xcrvfit (Robert Boyko, unpublished) calculates these values using iterative numerical methods to determine the best-fit curve to the predicted exponential.

Table 2.2. Example of normalized "amide-envelope" integral data used to calculate T_1 and T_2 values using 'xcrvfit'. This data set was collected from a 0.75 mM HAV 3C protease sample in 350 mM NaCl, 20 mM KH_2PO_4, 0.5 mM EDTA and pH 7.0.

ncyc	**^{15}N-T_1 Envelope**		**^{15}N-T_2 Envelope**	
	T_{1d} (s)	**^{1H}N Integral**	**T_{2d} (s)**	**^{1H}N Integral**
1	0.0056	1.00	0.0163	1.00
2	0.0112	0.93	0.0326	0.64
3	0.0168	0.86	0.0489	0.51
4	0.0224	0.78	0.0652	0.36
5	0.0280	0.71	0.0815	0.32
6	0.0336	0.63	0.0978	0.23
7	0.0392	0.54	0.1141	0.20
8	0.0448	0.45	0.1304	0.14
9	0.0504	0.33	0.1467	0.12
10	0.0560	0.18	0.1630	0.08

Experimental Set Up. Dr. Carolyn Slupsky and Dr. Stephane Gange performed the NMR experiments. ^{1}H-^{15}N HMQC-J and ^{15}N T_1- and T_2-envelope spectra were recorded at 25°C on a Varian Unity 600 spectrometer equipped with a triple resonance probe. ^{1}H-^{15}N HMQC-J experiments were performed with a ^{15}N sweepwidth of 2000 Hz and a ^{1}H sweepwidth of 6000 Hz. A total of 2048 complex points were collected along the t_2 domain (^{1}H) and 640 increments along the t_1 domain (^{15}N). The relaxation delays for these experiments were 1.1 s and the refocusing delay was set at 0.0024 s. ^{15}N T_1- and T_2-envelope experiments were performed with a ^{15}N sweepwidth of 1500 Hz and a ^{1}H sweepwidth of 8000 Hz. A total of 1216 complex points were collected in the t_2 domain (^{1}H) and 2 increments in the t_1 domain (^{15}N). Relaxation delays of 2.0 s and 2.5 s were employed for ^{15}N T_1- and T_2-envelope experiments respectively.

Analytical Ultracentrifugation studies. Two solutions of HAV 3C protease (5 mg/mL) were prepared by concentrating HAV 3C protease stock solution (1-3 mg/mL) using a 10K centrifugal filter device (Millipore) with a MW cutoff of 10 kDa. The first buffer (the original storage conditions or enzymatic assay conditions) contained 350 mM NaCl, 20 mM KH_2PO_4, 0.5 mM EDTA at pH 7.0. The second buffer (optimized storage conditions minus 250 mM NaCl) contained 100 mM NaCl, 20 mM KH_2PO_4, 0.5 mM EDTA, 1.0 mM DTT, at pH 5.4. In the second buffer, salt was removed by concentrating the stock solution, reconstituting with an appropriate volume of phosphate buffer (20 mM KH_2PO_4, 0.5 mM EDTA, 1.0 mM DTT, and pH 5.4), and then concentrating again to 5 mg/mL HAV 3C protease.

Les Hicks, of Dr. Cyril Kay's laboratory, performed the sedimentation equilibrium experiments. They were carried out at 20°C using a Beckman XLI Analytical Ultracentrifuge and interference optics following procedures outlined in the XLI Instruction Manual. 110 μL aliquots of HAV 3C protease solution were loaded into 6-sector CFE (charcoal filled epon) sample cells, allowing three

concentrations (5.48 mg/mL, 3.28 mg/mL, and 1.1 mg/mL) of sample to be run simultaneously. Runs were performed at a 16,000 and 20,000 rpm and were continued until there was no significant difference in scans taken approximately three hours apart. The sedimentation equilibrium data was evaluated using a nonlinear least-squares curve-fitting algorithm (Johnson et al., 1981) contained in the NonLin analysis package.

HAV 3C Protease NMR Sample Stability Study. HAV 3C protease stock (2 mg/mL) was stored at 4°C in the optimized post-column buffer (350 mM NaCl, 20 mM KH_2PO_4, 0.5 mM EDTA and 1 mM DTT at pH 5.4). After a month of storage, this stock was used to prepare two 0.63 mM HAV 3C protease NMR samples in a buffer containing 100 mM NaCl, 20 mM KH_2PO_4, 0.5 mM EDTA, 1.0 mM DTT at pH 5.4. A 1D ^1H NMR spectrum was collected for each of these samples on days 1, 4, 7, 9, and 27. In between collection days, one sample was stored at 4°C and the other at room temperature (25°C). All 1D ^1H NMR spectra were recorded and analyzed as described previously.

2.3 Results and Discussion

Self-association measurements of HAV 3C protease. While ^1H-^{15}N HSQC and ^1H-^{15}N TOCSY-HSQC spectra of the ^{15}N labelled HAV 3C protease generally yielded good spectra with well-resolved resonances, later experiments conducted on doubly labelled ($^{13}C/^{15}N$) protease generally gave disappointing results. In particular, the HNCACB and CBCACONNH triple resonance experiments displayed only a few intense peaks that were presumably from the C-terminal residues.

Initially, a low level of isotopic substitution was thought to be the cause of these poor results. However, subsequent electrospray mass spectrometry analysis revealed that isotopic incorporation was >95% for both ^{13}C and ^{15}N. This result is

presented in Chapter 3 that discusses isotopic incorporation into HAV 3C protease. As low labelling efficiency could be ruled out, an alternative explanation was that the HAV 3C protease was aggregating into a polymeric state. Aggregation or increased apparent MW could account for the poor quality of those spectra that depended on multiple polarization transfers (HNCACB etc.) while at the same time it could explain the relatively good quality HSQC spectra (where only two polarization transfers are used) observed for the ^{15}N labelled material.

Another source of information that indicated that the HAV 3C protease may have a tendency to associate came from the analysis of the ^{1}H-^{15}N HMQC-J experiments. ^{1}H linewidths in the range of 18 to 30 Hz, were measured from a ^{1}H-^{15}N HMQC-J spectrum collected from a 0.75 mM HAV 3C protease sample in 350 mM NaCl, 20 mM KH_2PO_4, 0.5mM EDTA at pH 7.0 (high salt/high pH). Three-bond H_NH_α coupling constants ($J_{HNH\alpha}$) can be calculated using the following formula:

$$\mathbf{J_{HNH\alpha} = 0.50(\Delta\nu_{1/2}) - MW/10\ 000} \qquad \mathbf{[2.3]}$$

Where $\Delta\nu_{1/2}$ is the ^{1}H half height linewidth and MW is the molecular weight (Wishart and Wang, 1998). Using this formula and the measured ^{1}H linewidths, H_NH_α coupling constants were calculated to be in the range of 6.77 – 13.10 Hz when a MW of 23.87 kDa (monomeric species) was used. If the same formula was used with a MW of 47.64 kDa (dimeric species), coupling constants in the range of 4.37 – 10.7 Hz were calculated. This latter range is more typical for proteins (between 3 Hz and 10 Hz) and therefore this result suggested dimerization was likely occurring.

To further ascertain if HAV 3C protease aggregation was the primary cause of our poor NMR results, we performed a sedimentation equilibrium study using analytical ultracentrifugation. This study clearly showed that the protease was associating in the original high salt/high pH conditions (5mg/mL HAV 3C

protease, 350 mM NaCl, 20 mM KH_2PO_4, 0.5 mM EDTA, pH 7.0). The results of this study, displayed in Figure 2.6 (p.55), show that the solution behavior of this protease doesn't fit to a single species model. The absence of a 'shotgun appearance' for the residuals is a key indicator of a poor fit. In addition, the standard deviation is 0.087 when it should be less than 0.02 for a good fit. Many different 'species' models (monomer, monomer-dimer, monomer-trimer, monomer-dimer-trimer) were tested and it was found that the "single-species" (monomer) model yielded the best result. Using this model, the apparent molecular weight was determined to be 34,547 daltons whereas the theoretical mass of HAV 3C protease was 23,876.59 daltons based on the amino acid sequence and the natural abundance of all isotopes. This result indicated that the HAV 3C protease was "self-associating" to some degree, even at the low concentrations (~0.04 – 0.30 mM) used for ultracentrifugation. Consequently, a large scale screening of NMR sample conditions was performed to determine optimal NMR sample conditions that might reduce the self-association tendency of HAV 3C protease.

Identification of optimal NMR sample conditions. In order to do determine optimal conditions for NMR analysis, two different HAV 3C protease mutants and nearly 30 different solution conditions were studied. These conditions included different temperatures, varying salt concentrations, varying pH, and the addition of organic solvents and detergents. The actual solution conditions for each NMR sample tested are listed in Table 2.1. Qualitative information about the presence of aggregation can be obtained by monitoring the broadening of NMR linewidths (Akiyoshi et al., 1993). Even though the analysis of the half-height linewidth ($\Delta\nu_{1/2}$) does not provide easily quantifiable information about the size of the protein aggregates, the narrowing of linewidths qualitatively corresponds to longer T_2 values and/or a decreases in molecular weight. Table 2.1 outlines these solution studies and the recorded half-height linewidth ($\Delta\nu_{1/2}$) of the upfield Val25 CH_3 resonance (at –0.7 ppm) for each sample.

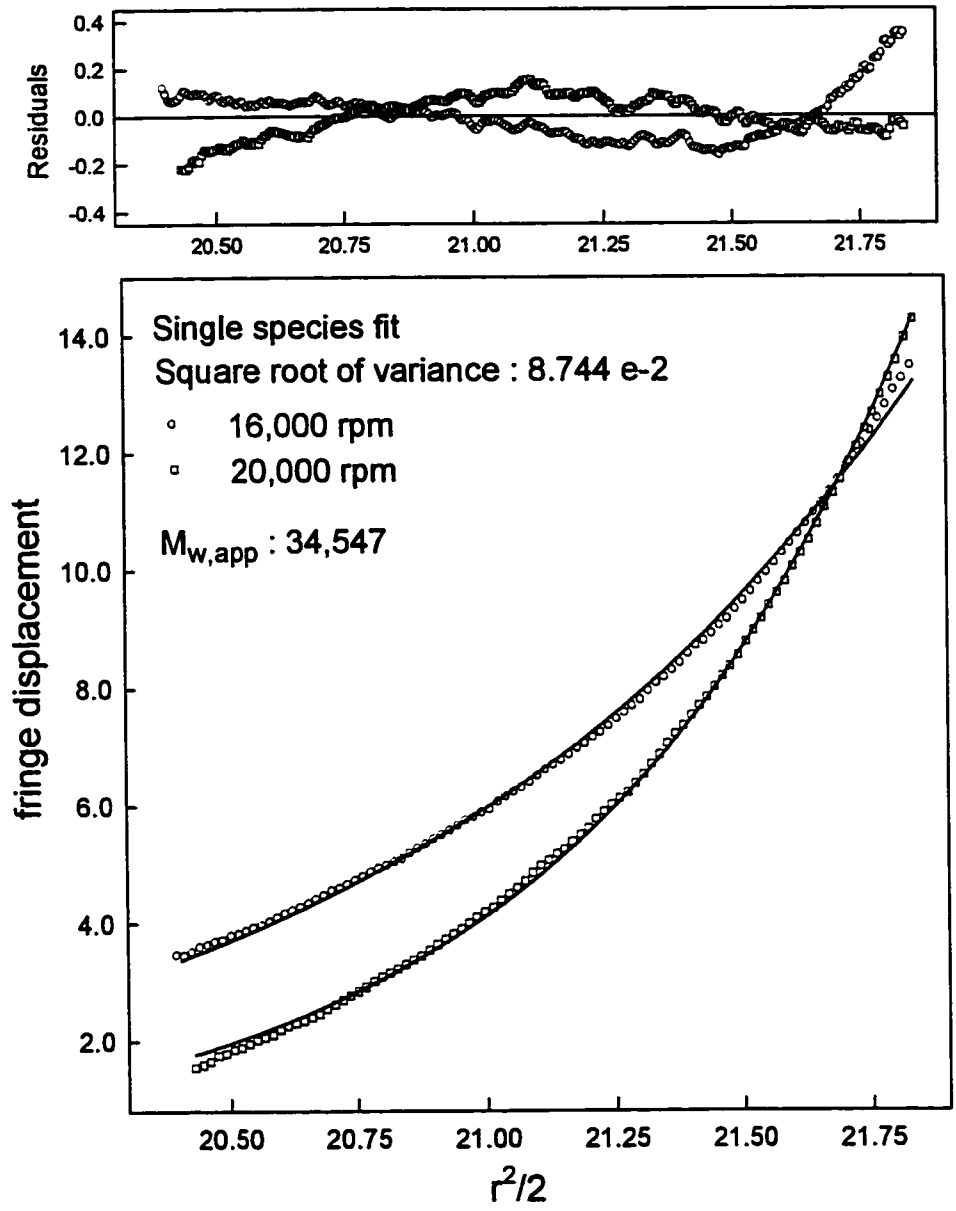

Figure 2.3: Sedimentation Analysis of HAV 3C protease in 350 mM NaCl, 20 mM KH_2PO_4, 0.5 mM EDTA, and pH 7.0.

Frozen vs. unfrozen HAV 3C protease stock solutions. During the initial analysis of these 1D ^{1}H NMR spectra, it was observed that better resolved spectra were obtained when HAV 3C protease samples were prepared from pooled protease stock that had not been previously frozen. Figure 2.7 (p.57) shows how the amide region of the unfrozen spectrum displayed sharper peaks than the sample that had been previously frozen. "Freeze-thaw" induced aggregation has been previously observed with other proteins such as recombinant human factor XIII. This was attributed to interfacial adsorption and denaturation at the air-liquid and ice-liquid interfaces (Kreilgaard et al., 1998). With respect to the HAV 3C protease, it is likely that as ice crystals formed during the freezing process, protease molecules were forced too close together (Martin, 1993). Upon thawing, precipitation was not observed but it could have been that some degree of freeze-induced or interfacial denaturation had taken place. This "freeze-thaw" induced denaturation, accompanied with the proximity of other HAV 3C protease molecules in the frozen state, likely led to an increased tendency to self-associate. After this observation was made, all pooled protease stock was stored in the refrigerator at 4°C instead of freezing it at – 20°C.

Preventing hydrophobic interactions between HAV 3C protease molecules. If protein aggregation arises from the interaction of hydrophobic interfaces between monomers, site-directed mutagenesis at the hydrophobic regions can be used to alleviate the aggregation problem (Schein, 1990). This method has been used successfully for the solution structure determination of the insulin monomer (Kaarsholm and Ludvigsen, 1994). To investigate whether site-directed mutants of HAV 3C protease could be prepared (or found) that would have a reduced tendency to aggregate, we analyzed the X-ray structure of HAV 3C protease (Bergmann et al., 1997). Interestingly this structure shows two molecules interacting as a dimer (Figure 2.1). To analyze the dimer interface, a program called VADAR was used (Wishart, 1994). VADAR provides information on accessible surface area and packing volumes and can be used to quantify the interactions between amino acids in domains or interfaces. Structural analysis was

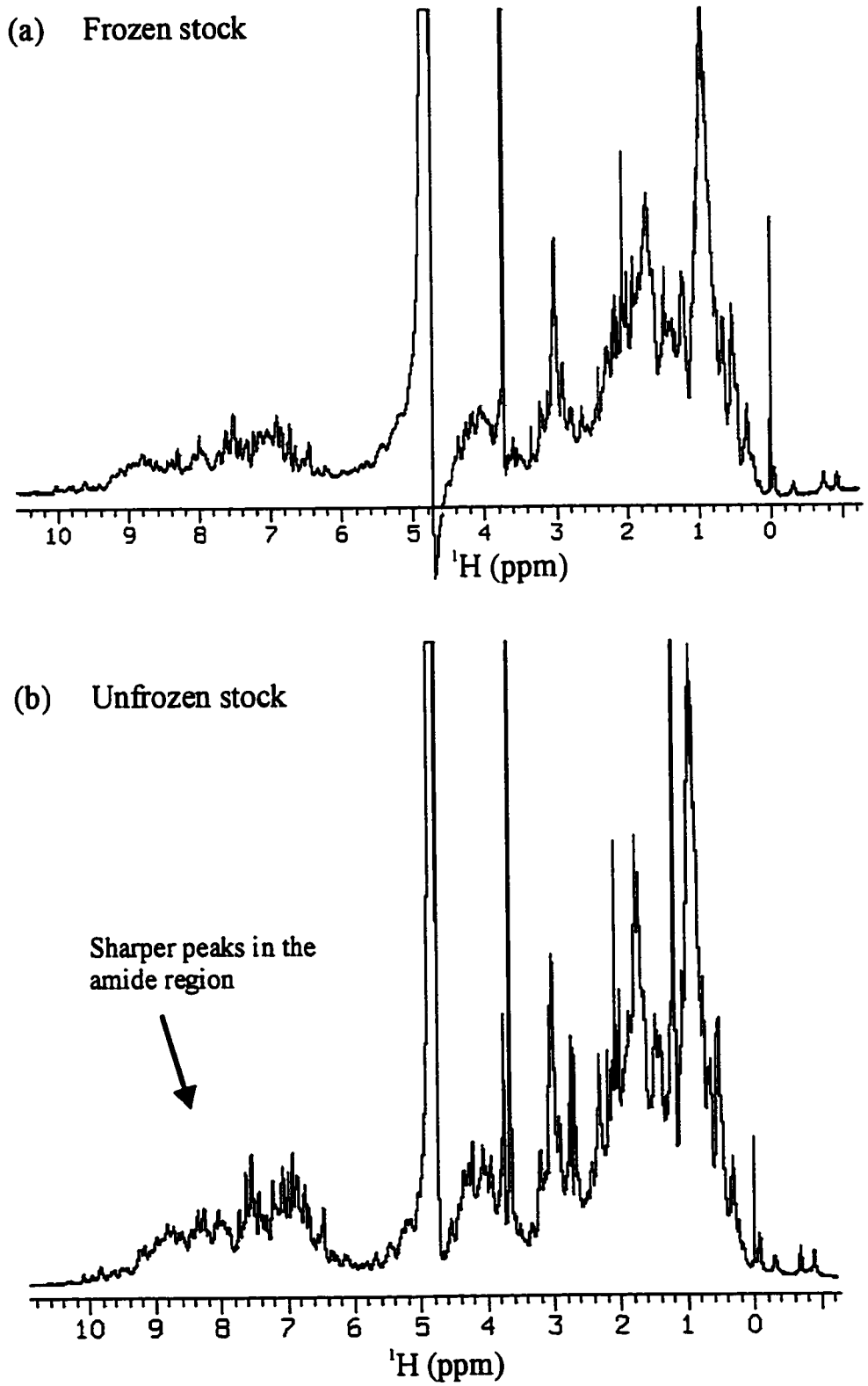

Figure 2.7. Comparison of 1D ^{1}H NMR spectra collected from 0.5 mM HAV 3C protease sample (20mM KH_2PO_4, 350 mM NaCl, 0.5 mM EDTA at pH 7.0) prepared with (a) frozen and (b) un-frozen stock solutions at 25 °C on a Varian VXR 500 MHz NMR Spectrometer.

performed on HAV 3C protease's PDB file (1HAV) to determine which residues appear to be interacting at the interface. By running VADAR on the crystallographic dimer and then taking out the coordinates of one of the species and rerunning the VADAR surface area analysis, we were able to determine which amino acids are most likely involved in the dimeric interfaced interactions. The residues that showed the greatest change in surface area were Asn124, Glu166, Leu168, Gly107, Pro110, and Glu139. For a study involving site-directed mutagenesis, it would appear that replacing the most hydrophobic residue, in this case Leu168, with a hydrophilic residue type (perhaps lysine) might potentially reduce the tendency to dimerize. Additionally, because electrostatic interactions were suspected for the HAV 3C protease, it may have been beneficial to substitute Glu166 (or Glu139) with an alanine in order to prevent this interaction. While the Leu168Lys (L168K), Glu166Ala (E166A) or Glu139Ala (E139A) mutants were not available to investigate this hypothesis, we were able to analyze another mutant (Y143G) that had been previously found to exhibit "better than average" spectra (Dr. W. Bachovchin, personal communication).

Mutants of HAV 3C protease. Spectra from the Y143G mutant had unusual lineshapes that appeared very narrow in the upper portions of the resonance but broad in the lower portions (Figure 2.8, p.60). This baseline broadening could be due to the final structure being composed of two slightly different molecular conformations. An additional problem arose with this mutant as well. In particular, the HAV 3C Y143G mutant protease could only be expressed and purified in cells grown in rich (TB) media and not in minimal media which is required for isotopic labelling. For reasons of the baseline broadening and expression problems, we decided not to pursue further NMR studies with the Y143G mutant and, instead, focused on improving conditions for the original HAV 3C protein.

Effect of solvents or detergents. Another method of treating aggregation is to add detergents or organic solvents (Schein, 1990). Detergents are amphiphilic compounds that lower the surface tension of water and bind to hydrophobic areas

on proteins thereby preventing aggregation. CHAPS is a detergent that has been shown to be quite effective in reducing aggregation and it was successfully used in the multidimensional studies of calcineurin B (Anglister, et al., 1993). Two HAV 3C protease samples were prepared with 25.0 and 7.0 mM concentration of CHAPS. In both cases, the C24S mutant showed no narrowing of half-height linewidth. Denaturing solvents such as trifluoroethanol (TFE) have also assisted in reducing aggregation by providing a competitive interaction for the intramolecular hydrophobic interactions responsible for stable tertiary structure (Schein, 1990). TFE was successfully used for the NMR study of troponin C (Slupsky, et al., 1995). However, in our hands, any amount of TFE added to HAV 3C protease caused immediate precipitation of the protein. The fact that CHAPS did not lead to half-height linewidth narrowing suggests that electrostatic interactions, rather than hydrophobic interactions, may be the predominant factor leading to self-association of the HAV 3C protease.

Effect of pH. To determine the effect of pH on HAV 3C protease spectra, we also prepared a sample at pH 5.4. While there was no appreciable narrowing of linewidth at the lower pH, the amide region of spectra appeared to have sharper peaks. In addition, a ^{1}H-^{15}N HSQC spectra of a doubly labelled HAV 3C protease (^{13}C labelled Glycine and ^{15}N labelled Leucine) taken at pH 5.4 was compared to a similar spectra collected at pH 7.0 of the protease specifically labelled at leucine. The spectra collected at lower pH appeared to be better resolved than those spectra recorded at higher pH. The lower pH likely increases the amide signal due to the slower hydrogen exchange rate at acidic pHs'. Based on these results, It was decided that all further experiments would be performed at pH 5.4.

Effect of salt concentration. Salt concentrations played a critical role in defining the optimal solution conditions for HAV 3C protease. In Table 2.1 (p. 45), it is noted that decreasing the NaCl concentration from 1.0 M to 0.1 M narrowed the half-height linewidth from 20 Hz to 16 Hz. The reason salt concentration had such

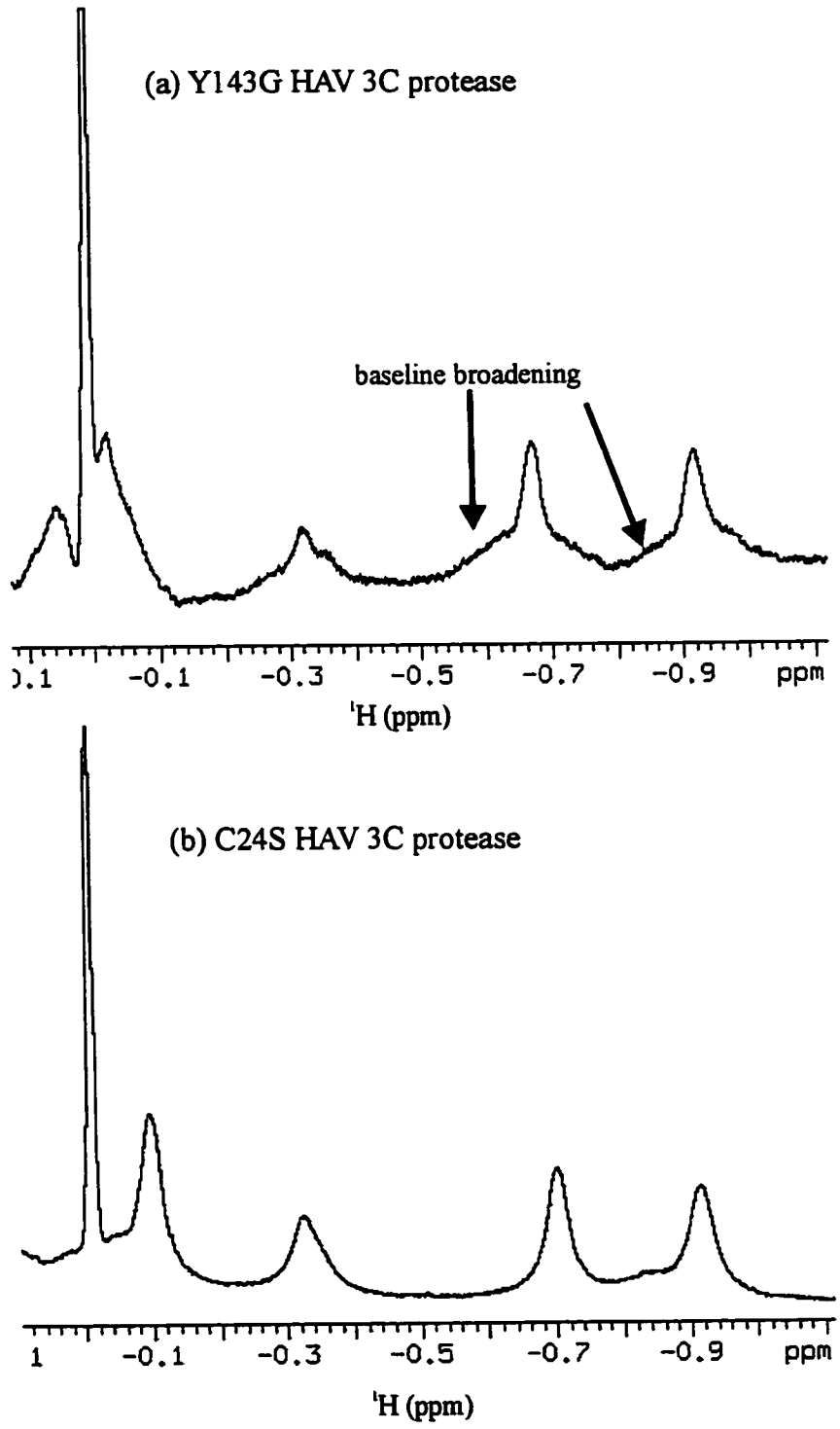

Figure 2.8. Comparison of 1D ^{1}H NMR spectra collected from 0.5 mM (a) Y143G and (b) C24S mutants of HAV 3C protease samples (20 mM KH_2PO_4, 350 mM NaCl, 0.5 mM EDTA at pH 7.0) at 25°C on a Varian VXR 500 Mhz NMR Spectrometer.

an impact on the half-height linewidth can potentially be explained by the DLVO (Deryagin-Landau-Verwey-Overbeek) theory of colloids (De Young et al., 1993). This theory relates the attractive van der Waals and repulsive electrostatic forces as a function of intermolecular distance (Figure 2.9, p.62). As the protease concentration increases, the distance between molecules would decrease. In order to retain electrostatic repulsive forces between molecules at high concentration (smaller distances between molecules), this theory states that a low salt concentration is required. At high salt concentrations, the electrostatic charges on the protease are shielded from each other and the van der Waals (attractive) forces dominate. This results in an attraction between molecules that ultimately leads to aggregation. Lowering the salt concentration ensures that electrostatic repulsive forces would remain between molecules thereby preventing a polymeric state from arising. Although the linewidth change from 20 Hz to 16 Hz does not by itself mean that an aggregated state has been transformed into a monomeric state, it does suggest that the protease is behaving better in NMR samples with low salt concentrations.

As can be seen in Table 2.1 (p. 45), certain solution properties didn't appear to affect the half-height linewidth. These factors were temperature and the addition of DTT and $CaCl_2$ to the solution. However, the temperature studies did teach us something about the stability of the protein. Increasing the temperature generally led to more rapid precipitation. Performing NMR experiments above 25°C would typically cause the protein to precipitate within hours (depending on the temperature). The highest temperature that could be tolerated for extended periods of time (10 days) was 25°C. While DTT didn't appear to have an effect on linewidth it was added to the samples to prevent disulfide bridge formation. In the C24S HAV 3C protease, there is still the active site Cys172 that could potentially lead to the formation of intermolecular disulfide linkages. Erring on the side of caution, we decided to add DTT to all samples to keep the Cys172 in the reduced form.

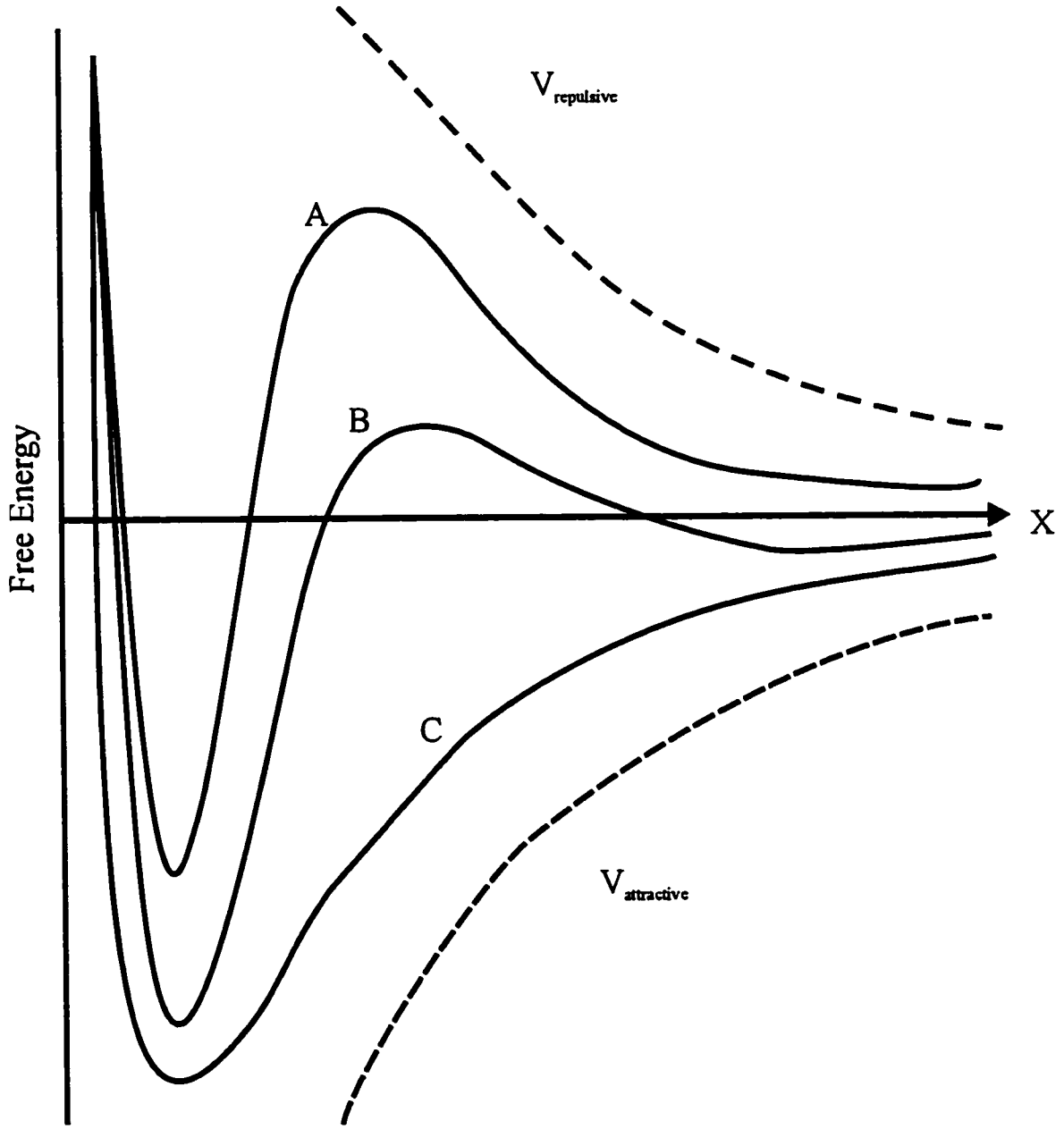

Figure 2.9. DLVO Theory. Van der Waals electrostatic forces ($V_{attractive}$ and $V_{repulsive}$) are plotted as a function of intermolecular distance (x). (a) Low salt, (b) medium salt and (c) high salt.

In conclusion, the 1D ^{1}H NMR half height line width studies indicate that the optimum NMR sample conditions for the HAV 3C protease are: 100 mM NaCl, 20 mM KH_2PO_4, 0.5 mM EDTA , 1.0 mM DTT , at pH 5.4

Confirmation of a HAV 3C protease monomer. Once optimal solution conditions were determined, analytical ultracentrifugation of HAV 3C protease under the new conditions was performed to determine if the protein was monomeric. The results of the second ultracentrifugation study are presented in Figure 2.10 (p.64). Under these low salt, low pH conditions, HAV 3C protease clearly adhered to a single species fit. The fit in this study is 'good' because of the shotgun appearance of the residuals and the standard deviation is just 0.017. The results show an apparent molecular weight of 24,719 daltons which is significantly closer to the theoretical molecular weight of 23,876.59 daltons based on the amino acid sequence and the natural abundance of all isotopes. Fitting the data to a monomer-dimer species model, a dissociation constant (Kd) of 13 mM was determined. This means that at 13 mM, under these solution conditions, 50 per cent of the HAV 3C protease molecules would be dimerized.

^{15}N-T_1 and ^{15}N-T_2 envelope studies (Farrow et al., 1995) were also performed to confirm the results of analytical ultracentrifugation and to investigate the maximal allowable concentration for the HAV 3C protease. Table 2.3 shows the backbone ^{15}N-T_1/T_2 results for one sample (C) in the high salt, high pH conditions and three samples (A,B,D) collected under optimal (low salt, low pH) conditions. Interestingly, these data agree very well with those from the analytical ultracentrifugation studies. Both techniques indicate that the molecular weight has decreased from ~ 32 to ~24 kDa (approximately monomeric) when the protein was moved from high salt, high pH conditions to low salt, low pH conditions. If the protease was existing as a dimer in the original NMR sample conditions the estimated molecular weight would have been ~ 48 kDa. This implies that the protease was not fully dimerized in the high salt, high pH conditions but a certain percentage of self-association was evident. This percentage was ~ 45% and

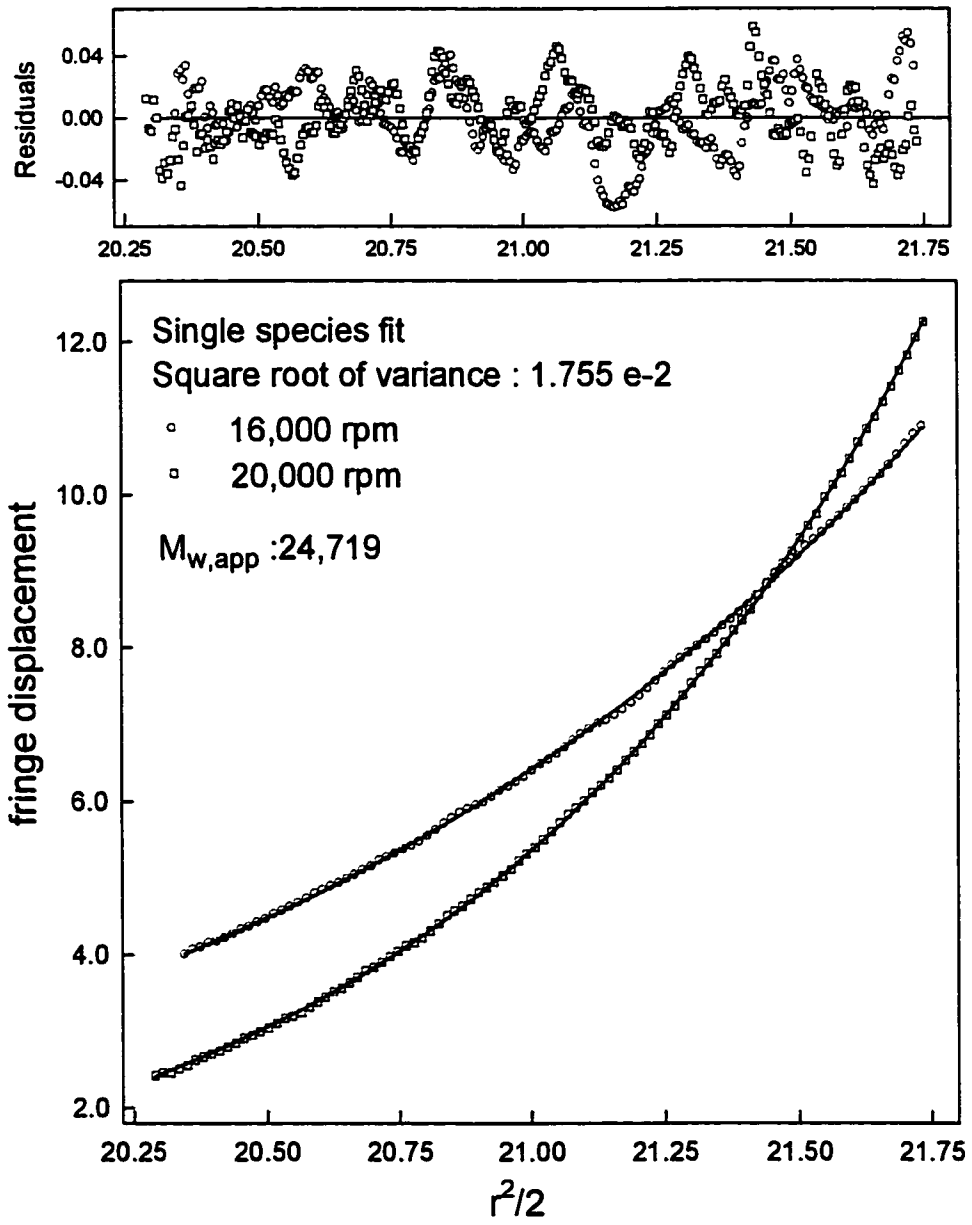

Figure 2.8: Sedimentation Analysis of HAV 3C protease in 100 mM NaCl, 20 mM KH_2PO_4, 0.5 mM EDTA, 1.0 mM DTT and pH 5.4.

~ 33% as calculated from analytical ultracentrifugation and ^{15}N-T_2 enveloped studies respectively.

Table 2.3. Analysis of the ^{15}N-amide envelope of HAV 3C Protease at four different concentrations and two sets of conditions. τ_C and MW are estimated using equations found in Spyracopoulos et al., 1999. ($1.11\tau_C = 1/T_{2NH}$, $MW = 2 \times \tau_C$)

	Sample A	**Sample B**	**Sample C**	**Sample D**
^{15}N T_1 (ms)	~ 1015	~ 1003	~ 944	~ 964
^{15}N T_2 (ms)	~ 74	~ 59	~ 57	~ 77
τ_C (ns)	~ 12.1	~ 15.3	~ 15.8	~ 11.7
MW (kDa)	~ 24.2	~ 30.6	~ 31.6	~ 23.4

Sample A: 1.40 mM HAV 3C Protease / 100 mM NaCl / 20 mM KH_2PO_4 / 0.5 mM EDTA / 1.0 mM DTT / pH 5.4
Sample B: 1.0 mM HAV 3C Protease / 100 mM NaCl / 20 mM KH_2PO_4 / 0.5 mM EDTA / 1.0 mM DTT / pH 5.4
Sample C: 0.75 mM HAV 3C Protease / 350 mM NaCl / 20 mM KH_2PO_4 / 0.5 mM EDTA / pH 7.0
Sample D: 0.46 mM HAV 3C Protease / 100 mM NaCl / 20 mM KH_2PO_4 / 0.5 mM EDTA / 1.0 mM DTT / pH 5.4

Samples A, B and D in Table 2.3 were studied to determine if increasing protease concentrations would increase ^{15}N-T_2 times which in turn would reflect increased levels of aggregation. Of these three samples, sample B (1.0 mM) yielded results that did not fit with samples A (1.4 mM) and D (0.46 mM). Sample B was prepared from frozen stock and had an estimated ^{15}N-T_2 of ~ 59 ms which is very similar to the ^{15}N T_2 (~ 57 ms) of the protease in the original high salt/high pH conditions. It appears that freezing and thawing prior to sample preparation can lead to problems with aggregation, even when the protein is under optimal low salt, low pH conditions (100 mM NaCl, 20 mM KH_2PO_4, 0.5 mM EDTA , 1.0 mM DTT , and pH 5.4). This observation supports the observations

from the 1D ^{1}H NMR linewidth studies that protease stock should be kept chilled at 4°C and not frozen at –20°C. Sample D (0.46 mM) and sample A (1.40 mM) had very similar ^{15}N-T_2 times and therefore it appears that increasing the concentration of the protease to maximum of 1.40 mM does not lead to any significant aggregation. It is important to note that the 1.40 mM protease sample had exhibited some precipitation after 48 hours as the sample was cloudy with flakes. Preparing NMR samples at this high concentration may be risky for longer 3D NMR experiments that take three days to complete. In contrast, sample D (0.46 mM) showed no precipitate for several weeks after it was prepared.

Stability Study of the HAV 3C Protease. This stability study attempted to address two key issues; (1) the length of time the protease stock solution would be stable when stored at 4°C and (2) the length of time a concentrated (0.63 mM) sample (stored at 4°C and 25°C) would remain monomeric after preparation. The results of this study are shown in Table 2.4. HAV 3C protease was expressed and purified as described previously and stored in a stock solution (2mg/mL) for a month prior to preparing the two samples used in this study. Spectra collected for the two 0.63 mM samples on days 1 through 9 displayed a half-height linewidth of 16 Hz. Therefore, the concentrated protease sample appears to be stable for nine days regardless of whether it is stored at 4°C or 25°C. The increase in half-height linewidth noted on day 27 (2 Hz at 4°C and 1 Hz at 25°C) could be due to self-association although the extent of aggregation is not known.

Table 2.4. Stability Study of (~0.6 mM) HAV 3C protease NMR samples at 4°C and 25°C.

Day #	**$\Delta\nu_{1/2}$ (Hz) of Sample at 4°C**	**$\Delta\nu_{1/2}$ (Hz) of Sample at 25°C**
1	16 Hz	16 Hz
4	16 Hz	16 Hz
7	16 Hz	16 Hz
9	16 Hz	16 Hz
27	18 Hz	17 Hz

The results of this study indicate that HAV 3C protease can be stored at 4°C at low concentrations (2 mg/mL) in the elution buffer for at least one month with no evidence of aggregation. This study also shows that the concentrated (0.63 mM) protease samples are stable for at least nine days and that after this time, some degree of 'self-association' is noted. This suggests that concentrated HAV 3C protease samples should be prepared and analyzed by NMR within 10 days of preparation. These samples yield the best results within the first nine days although it may be that well resolved spectra can be recorded up to ~ one month after preparation.

2.4 Conclusion

To summarize, solution conditions have been found where the HAV 3C protease remains monomeric at high (> 0.5 mM) sample concentrations. To identify these conditions a number of solution variables (salt, pH, temp, detergents, addition of ligands) were screened via half-height linewidth measurements. Subsequent studies using two techniques, analytical ultracentrifugation and ^{15}N-T_2 relaxation studies, clearly established that the HAV 3C protease was monomeric at low salt (100 mM NaCl) and low pH (pH 5.4) condtions. Our ^{15}N NMR relaxation studies indicate that NMR samples up to 1.4 mM can remain monomeric although some precipitation typically occurs from more concentrated samples after 48 hours. Finally, stability studies indicate that after the protease has been expressed and purified, it can be stored at ~2-3 mg/mL in the elution buffer at 4°C for up to one month and that concentrated (~0.63 mM) HAV 3C protease samples show no sign of aggregation for at least nine days. This information proved to be vital for the success of the triple resonance experiments that are described later in this thesis.

Chapter 3

^{2}H, ^{13}C and ^{15}N isotopic labelling of HAV 3C protease

3.1 Introduction

^{2}H, ^{13}C and ^{15}N isotopic labelling of proteins has become a standard practice in biomolecular NMR spectroscopy. It is primarily used to facilitate the study of larger (>12 kDa) proteins. If a protein can be biosynthesized by a bacterial (or a simple eukaryotic) expression system, ^{15}N and ^{13}C can be readily incorporated by growing the cells in minimal media containing isotopically enriched nitrogen and carbon sources (McIntosh and Dahlquist, 1990; Pardi 1992). Similarly, ^{2}H can be incorporated by growing cells in $^{2}H_2O$-based media (Venters et al., 1995). When ^{13}C and ^{15}N are incorporated into proteins, multidimensional heteronuclear NMR experiments can be acquired to alleviate the peak overlap problems often found in 2D ^{1}H NMR spectra of unlabelled proteins. Concomitantly, these heteronuclear spectra are easier to work with, owing to the large chemical shift dispersion inherent to ^{13}C and ^{15}N nuclei (Clore and Gronenborn, 1991; Kay et al., 1990a; Bax et al., 1989). Incorporation of ^{2}H into bio-molecules is primarily used to improve the relaxation properties of larger proteins (Gardner and Kay, 1998) leading to better spectral resolution. By using a suite of triple-resonance experiments developed in Dr. Lewis Kay's laboratory for deuterated proteins (Yamazaki et al., 1994a/b), several large proteins including the 29 kDa human carbonic anhydrase II (Venters et al., 1995) and a 37 kDa trp repressor/DNA ternary complex (Yamazaki et al., 1994a/b) have been successfully assigned.

While uniform incorporation of ^{2}H, ^{13}C and ^{15}N is the predominant strategy for labelling proteins, residue selective ^{15}N labelling is a useful alternative as it can assist in defining which resonances in heteronuclear NMR spectra belong to a

specific amino acid type. This information can be invaluable, as it can be difficult to assign spin systems to residue types on the basis of chemical shift information alone. For example, when using HNCA and HN(CO)CA spectra to obtain backbone sequential chemical shift assignments, ambiguities may arise due to the similarities in $^{13}C_{\alpha}$ chemical shifts displayed by certain groups of amino acids. One such group includes histidine, leucine, methionine and glutamine as they all display $^{13}C_{\alpha}$ chemical shifts near ~53 ppm (Wishart et al., 1995b). By using ^{1}H-^{15}N HSQC spectra collected from residue-specific ^{15}N labelled samples, unambiguous assignment of spin systems to a given residue type is possible, provided that these types of specifically labelled samples can be successfully bio-synthesized. This type of labelling strategy has aided in the NMR study of several proteins including α-lytic protease (Bachovchin, 1985), E. coli thioredoxin (LeMaster and Richards, 1985), T4 lysozyme (McIntosh et al., 1990) and a M13 coat protein (Henry and Sykes, 1992).

In this study, several biosynthetic strategies were employed to introduce isotopes into the HAV 3C protease. Single (^{15}N), double ($^{13}C/^{15}N$), triple ($^{2}H/^{13}C/^{15}N$) and residue-specific (^{15}N) labelled protease samples were all successfully produced. This was accomplished by growing the E. coli cells containing the HAV 3C protease expression system in $^{1}H_2O$- or $^{2}H_2O$-based minimal media supplemented with $^{15}NH_4Cl$, $^{13}C_6$-glucose and/or amino acid mixtures containing ^{15}N-amino acids. These strategies produced protease samples with high levels (>95%) of ^{13}C and ^{15}N and moderate levels (~70 %) of ^{2}H incorporation. In addition, a simple residue-specific labelling strategy with a prototrophic strain of E. coli, produced "good" results with HAV 3C protease labelled specifically at alanine, leucine, isoleucine, lysine, and valine.

3.2 Materials and Methods

Isotopes and Reagents. $^{15}NH_4Cl$ (98%), ^{13}C-C_6-Glucose (>98%), and sterile filtered $^{2}H_2O$ (>97%) were purchased from Martek Biosciences Corpoation (Columbia, MD). ^{15}N-Alanine, ^{15}N-Glycine, ^{15}N-Isoleucine, ^{15}N-Leucine, ^{15}N-Lysine, ^{15}N-Phenylalanine, and ^{15}N-Valine (all 95-99%) were purchased from Cambridge Isotope Laboratories, Inc (Andover, MA). Unlabelled amino acids were obtained from Sigma Chemical Co. (St. Louis, MO). Reagents used for the expression and purification of HAV 3C protease are listed in Table 3.1.

Table 3.1. List of reagents used for the expression and purification of HAV 3C protease.

Reagent	**Ingredient**	**Quantity**
M9 Minimal Media Add ingredients to sufficient double distilled (dd) H_2O to make 1 L.	$NaHPO_4$	6.80 gm
	NaCl	0.50 gm
	NH_4Cl	1.00 gm
	Glucose	4.00 gm
	$MgSO_4$ (1.0M)	2.00 mL
	$CaCl_2 \bullet 2H_2O$ (1.0M)	0.10 mL
	Thiamine (1% w/v)	1.00 mL
	Ampicillin (75mg/mL)	2.00 mL
	$FeSO_4$ (1 mM)	2.00 mL
Cell Resuspension Buffer Add ingredients to sufficient dd H_2O to make 100 mL.	Tris-HCl (1.0M / pH 8.5)	5.00 mL
	EDTA (0.5 M / pH 8.0)	0.50 mL
	DTT (1.0M / pH 5.2)	0.20 mL
Phosphate Buffer Add ingredients to sufficient dd H_2O to make 1 L. Correct solution pH to 5.4 with 1.0 M KOH or 1.0 M HCl.	KH_2PO_4	2.72 gm
	0.5 M EDTA (pH 8.0)	1.00 mL
	1.0 M DTT (pH 5.2)	2.00 mL

HAV 3C protease expression and purification. All HAV 3C protease samples were isolated from a prototrophic E. coli strain MM294 containing the overexpression plasmid pHAV-3CEX (Malcolm et al., 1993) with a C24S mutation (to facilitate protein stability). The four types of isotopically labelled HAV 3C protease have been prepared by growing the E. coli expression system in four different minimal media preparations as described below. The expression and purification of HAV 3C protease was performed as outlined in Chapter 2. Expected yields and parameters used to obtain each type of isotopically labelled HAV 3C protease sample are outlined in Table 3.2.

Table 3.2. Comparison of strategies used in the isolation of HAV 3C protease. T1 is the approximate time used for the overnight culture growth. T2 is the approximate time between inoculation of the "expression" media and induction with IPTG. T3 is the "induction period" that cells were allowed to grow prior to harvesting. M9* is minimal media (1 L) prepared with 1.0 gm of ^{13}C-C_6-glucose and 1.0 gm $^{15}NH_4Cl$. M9** is minimal media (1 L) prepared with an amino acid mixture substituted for NH_4Cl. M9*** is minimal media (300 mL) prepared with 90 % $^{2}H_2O$:10% $^{1}H_2O$, 0.6 gm of ^{13}C-C_6-glucose and 0.3 gm of $^{15}NH_4Cl$.

Isotopic Label	Overnight media	Expression media	T1 (hrs)	T2 (hrs)	T3 (hrs)	Yield of HAV 3C protease (mg/L)
^{15}N	TB	M9	12-14	2-4	8	~ 20
$^{13}C/^{15}N$	TB	M9*	12-14	2-4	8	~ 8
^{15}N residue specific	TB	M9**	12-14	2-4	8	~ 40
Unlabelled	M9	M9	12-14	2-4	8	~ 80
$^{2}H/^{13}C/^{15}N$	M9***	M9***	48	6	12	~ 25

^{15}N uniformly labelled HAV 3C protease. To uniformly incorporate ^{15}N into HAV 3C protease, 1 L of M9 minimal media was prepared by substituting 1 gm of $^{15}NH_4Cl$ for 1 gm of unlabelled NH_4Cl. E. coli cells (containing the overexpression plasmid pHAV-3CEX) were grown overnight in a 25 mL rich

media (TB) starter culture. If growth occurred, 10 mL of this starter culture was used to inoculate the 1 L batch of $^{15}NH_4Cl$-minimal media. The E. coli cells utilized $^{15}NH_4Cl$ similarly to unlabelled NH_4Cl therefore no adaptation period or change in protocol was necessary. Therefore, isolation and purification of the uniformly ^{15}N labelled HAV 3C protease was done as outlined in Chapter 2.

$^{13}C/^{15}N$ uniformly labelled HAV 3C protease. In order to limit the expense of ^{13}C-C_6-glucose used to prepare a doubly labelled $^{13}C/^{15}N$ HAV 3C protease, several trials were performed to determine the minimal amount of glucose (per 1 L batch) that the E. coli cells could successfully grow on. These studies indicated that a sufficient quantity of HAV 3C protease (for a NMR sample) could be obtained by growing cells in a 1 L batch of minimal media having 1.0 gm glucose (data not shown). With this information, 1 L of M9 minimal media was prepared by substituting 1.0 gm of $^{15}NH_4Cl$ for 1.0 gm of unlabelled NH_4Cl and 1.0 gm of ^{13}C-C_6-glucose for 4 gm of glucose. As before, E. coli cells were grown overnight in a 25 mL rich media starter culture. If growth occurred, 10 mL of this starter culture was used to inoculate the 1 L batch of minimal media. The E. coli cells utilized ^{13}C-C_6-glucose similarly to unlabelled glucose therefore no adaptation period or change in protocol was necessary. Therefore, isolation of the $^{13}C/^{15}N$ labelled HAV 3C protease was done as outlined in Chapter 2.

$^{2}H/^{13}C/^{15}N$ uniformly labelled HAV 3C protease. Triple labelling ($^{2}H/^{13}C/^{15}N$) HAV 3C protease with a high level of deuterium required an initial adaptation period as outlined in Figure 3.1. This involved growing our E. coli expression system in minimal media prepared with increasing concentrations of sterile filtered $^{2}H_2O$ (>97%). Two mL quantities of minimal media, composed of 50, 80, and 85 percent $^{2}H_2O$, were prepared and filtered through a 0.22 μm Millex GV filter (Millipore) to ensure sterilization. A single colony was selected from a LB/amp plate and transferred to minimal media containing 50% $^{2}H_2O$:50%$^{1}H_2O$. This mixture was grown at 37°C for 20 hours at which time the OD_{600} reached 1.6. It was then stored overnight at 4°C. The next day, 20 μL of this mixture was added

to two additional (2.0 mL) media preparations having 80 and 85 percent ^2H_2O. The 80 percent ^2H_2O minimal media was used to ensure the expression system had not lost the HAV 3C protease vector. This culture was grown at 37°C and when the OD_{600} of this culture reached 0.6, IPTG was added to a final concentration of 2 mM to induce the overexpression of HAV 3C protease. Immediately after induction, the temperature was lowered to 30°C and the cells were allowed to grow for a period of 8 hours. The cells were collected and lysed via the freeze-thaw method described in Chapter 2. The presence of HAV 3C protease was confirmed by SDS-Page gel electrophoresis. The 85 percent ^2H_2O culture was grown for 20 hours at 37°C to an OD_{600} of 1.8. The ^2H_2O-adapted MM294 cells from this culture were used to prepare several –80°C freezer stocks by mixing 1 mL of the culture with 1 mL of sterile 30 percent glycerol.

To triple label ($^2H/^{13}C/^{15}N$) the protease, 300 mL of 90% ^2H_2O:10% ^1H_2O based minimal media was prepared using only 0.6 gm ^{13}C-C_6-glucose and 0.3 gm $^{15}NH_4Cl$. Cells taken from the "^2H_2O adapted" -80°C freezer stock were transferred directly into 30 mL of this deuterated minimal media. Due to the slow growth in deuterated minimal media (Table 3.2, p.71), the 12-14 hour period for previous overnight cultures was extended to 48 hours. After this period, the entire volume (30 mL) of overnight culture was transferred into the remaining 270 mL of prepared minimal media. In approximately six hours the OD_{600} reached 0.77 and IPTG was added to a final concentration of 2 mM to induce the culture. The temperature was lowered to 30°C and growth was allowed to continue for an extended induction period of 12 hours. After this stage, the triply labelled HAV 3C protease was isolated and purified as described previously in Chapter 2.

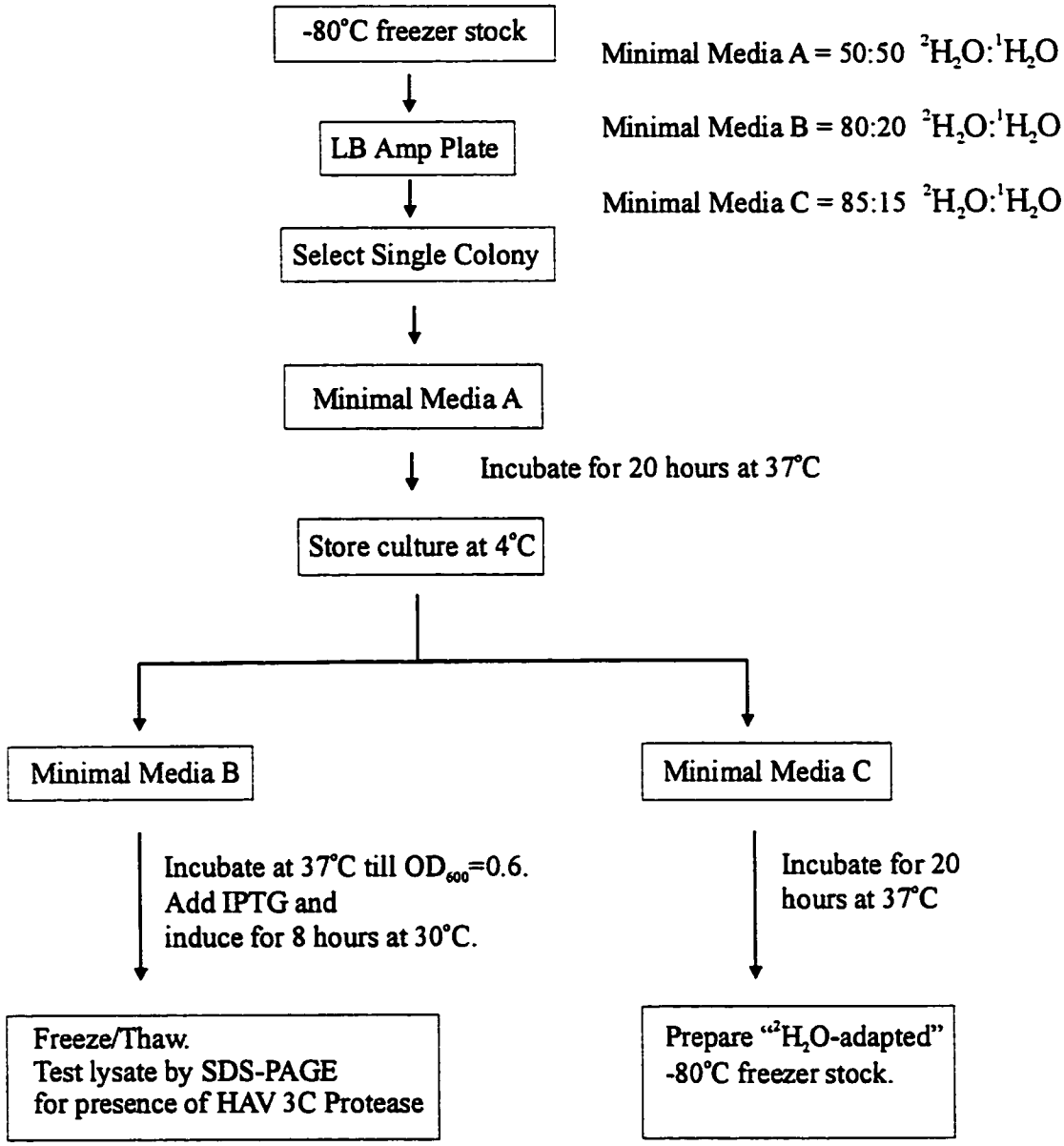

Figure 3.1. Protocol to adapt bacteria to ^2H_2O:^1H_2O based minimal media.

Residue-specific ^{15}N Labelling of HAV 3C Protease. HAV 3C protease was labelled at specific residues (alanine, glycine, leucine, lysine, isoleucine, phenylalanine, and valine) by growing E. coli cells (containing the overexpression plasmid pHAV-3CEX) in a 1 L batch of minimal media supplemented with 100 mL of an amino acid mixture instead of NH_4Cl (Muchmore et al., 1989). This amino acid mixture consisted of 19 unlabelled L-amino acids and one ^{15}N-L-amino acid that had to be specially prepared as outlined in Table 3.3. 10 mL of each of the 10 amino acid solutions (100mg/10 mL) was combined and filter sterilized through a 0.22 m Millex GV filter (Millipore) to ensure sterilization. As before, E. coli cells were grown overnight in a 25 mL rich media starter culture. If growth occurred, 10 mL of this starter culture was used to inoculate this 1 L batch of minimal media. The E. coli cells grew efficiently on this "amino acid" minimal media producing greater quantities (Table 3.2) of HAV 3C protease than seen before although no adaptation period or change in protocol was necessary. Therefore, isolation of the residue-specific ^{15}N labelled HAV 3C protease followed identically the protocol outlined in Chapter 2.

2D ^{15}N-^{1}H HSQC studies of uniform and residue-specific labelled HAV 3C protease. These experiments were performed by Dr. Carolyn Slupsky and Dr. Brian Sykes. NMR samples (~1.0 mM) of all residue specific and uniform labelled HAV 3C protease were prepared in 90% $^{1}H_2O$:10% $^{2}H_2O$, 350 mM NaCl, 20 mM KH_2PO_4, 0.5 mM EDTA at pH 6.8 except for the uniform and ^{15}N l-isoleucine sample that were prepared in 90% $^{1}H_2O$:10% $^{2}H_2O$, 100 mM NaCl, 20 mM KH_2PO_4, 0.5 mM EDTA, 1.0 mM DTT at pH 5.4. ^{15}N-^{1}H HSQC experiments (Kay et al., 1992: Zhang et al., 1994) were carried out at 25°C on a Varian Unity 600 spectrometer equipped with three channels and a 5 mm pulse-field gradient triple resonance probe. The spectra were acquired with 64 to 128 complex points in the F1 (^{15}N) dimension and 512 complex points in the F2 (^{1}H) dimension. Depending on the concentration and quality of the sample 96-224 transients were collected. The spectral widths were typically 2000 Hz in F1 (^{15}N) and 8000 Hz in the F2 (^{1}H) dimension. Samples were directly (^{1}H) and indirectly (^{15}N) referenced

to DSS as described by Wishart et al. (1995). Spectra were processed and peak-picked on a Sun Ultra 1 workstation, using the NMRPipe (Delaglio et al., 1995) and PIPP (Garrett et al., 1991) software packages.

Table 3.3. Preparation of 1% (w/v) amino acid stock solutions. 500 mg of each amino acid in each amino acid group was dissolved in sufficient dd H_2O to make 50 mL. Solutions were filtered through a 0.22 μm Millex GV filter (Millipore) to ensure sterilization. Store all at 4°C except for Cys-Asn-Gln which is stored at room temperature.

Amino Acid Group	**Special Requirements**
Trp	Add sufficient drops of 1.0 M HCl to dissolve.
Tyr	Add sufficient drops of 1.0 M KOH to dissolve.
Asp-Glu	Add sufficient drops of 1.0 M KOH to dissolve.
Cys-Asn-Gln	
Leu-Ile-Val	
Met	
Ala-Thr-Phe-Pro-Ser	
Arg-Lys	
Gly	
His	

Mass Spectral Analysis. Four 100 μL aliquots of HAV 3C protease (non-labelled, ^{15}N-labelled, $^{13}C/^{15}N$-labelled and $^{2}H/^{13}C/^{15}N$-labelled) were examined via mass spectral analysis. These aliquots (0.5 - 2.0 mg/mL HAV 3C protease) were in the post-column elution buffer which was either 350 mM NaCl, 20 mM KH_2PO_4, 0.5 mM EDTA at pH 6.8 or 350 mM NaCl, 20 mM KH_2PO_4, 0.5 mM EDTA, 1.0 mM DTT at pH 5.4. The 100 μL aliquot was taken from the purest post-column fraction (containing HAV 3C protease) as judged by SDS-PAGE. The four protease samples were submitted to PENCE "as-is" to determine the experimental mass of each sample by electrospray mass spectrometry using a Fisons VG Quattro LCMS. The obtained experimental masses are reported in Table 3.4.

3.3 Results and Discussion

Adapting bacteria to chemically defined media. Initially, the protocol for the expression and purification of HAV 3C protease involved growing our bacterial expression system in a rich (TB) media overnight. 10 mL of this culture was used to inoculate 300 mL to 1 L of minimal media ("expression" media) prepared with ^{13}C or ^{15}N enriched components. This protocol usually led to the expression of HAV 3C protease in yields of ~ 15-25 mg/L.

When attempting to label the protein with $^{2}H/^{13}C/^{15}N$, concerns arose over the use of the rich media as an "overnight" culture and the possible carry over of protonated nutrients to the deuterated media. To eliminate this problem, we tested and later confirmed that minimal media could be used in the initial starter culture. Interestingly, 12 months prior to this, many attempts to grow the same cells in minimal media proved unsuccessful. One explanation for our later success could be that at some point in the study, the MM294 cells harboring the pHAV-3CEX vector had mutated allowing them to grow better in minimal media. Conversely, the latter efforts differed from the earlier efforts in that a much longer growth period was used to allow cellular adaptation to the minimal media. Regardless, the use of minimal media in the starter culture proved to be very fruitful as it led to significantly higher yields (~ 75-100 mg/l) of HAV 3C protease as compared to those yields seen before (Table 3.2, p.71). The improved yields of HAV 3C protease is likely the result of adapting bacteria to minimal media prior to using them to inoculate the 1.0 L minimal ("expression") media. This agrees with Mossakowska and Smith (1997) who report that swapping from rich complex media, in which all the E. coli requirements are provided, to minimal media in which E. coli have to synthesize key intermediary metabolites, usually results in much poorer and slower growth.

Table 3.4. ^{2}H, ^{13}C and ^{15}N incorporation levels in singly, doubly and triply labelled HAV 3C protease as determined by electrospray mass spectrometry.

Isotopic Label	Theoretical Mass	Observed Mass	% isotope enrichment
Unlabelled	23 876.59	23 923.92 ± 13.78	--
^{15}N	24 165.36	24 149.39 ± 12.35	~95.5 (^{15}N)
$^{13}C/^{15}N$	25 240.77	25 184.76 ± 15.82	~95.5 (^{15}N) ~96.3 (^{13}C)
$^{2}H/^{13}C/^{15}N$	26 621.00	26 184.01 ± 19.66	~95.5 (^{15}N) ~96.3 (^{13}C) ~72.4 (^{2}H)

Isotopic Incorporation. Electrospray mass spectrometry was used to determine the mass for the unlabelled and three uniformly labelled types of HAV 3C protease. These results are reported in Table 3.4. The mass of the unlabelled protease was measured to be 23,923.92 ± 13.78 which is in good agreement (± 1 % or ± 23.8 Da) with the theoretical mass of 23,876.59 based on the amino acid sequence and the natural abundance of all isotopes. The protease contains 287 nitrogen nuclei therefore if all ^{14}N nuclei were replace by ^{15}N nuclei the mass should increase by 288.77 mass units. The measured mass of 24,149.39 ± 12.35 for the ^{15}N labelled protease is 15.97 mass units less than the theoretical mass therefore ^{15}N incorporation was estimated to be (272.80/288.77) 95.5 percent. The protease contains 1069 carbon nuclei therefore replacing all carbons with ^{13}C should increase the mass by 1075.41 mass units. The measured mass of 25,184 ± 15.82 for the $^{13}C/^{15}N$ labelled protease is 56.01 mass units less than the expected mass. Assuming that 15.97 mass units could be attributed to ^{15}N deficiency, the incorporation of ^{13}C was said to be (1035.37/1075.41) 96.3 percent. The protease has ~ 1707 protons (which varies with pH) therefore if all except for the 335 attached to nitrogen (backbone and sidechain) were exchanged with ^{2}H, the protease would increase in mass by 1380.23 mass units. An observed mass of 26,184.01 ± 19.66 was measured for the triply labelled protease which is 437.00 mass units less than the theoretical. Assuming that 56.01 could be attributed to ^{15}N

and ^{13}C deficiencies, the level of isotopic incorporation for ^{2}H was said to be (999.24/1380.23) 72.39 percent.

The less-than-perfect (96 %) labelling for the uniformly ^{15}N and $^{13}C/^{15}N$ labelled proteases could be attributed to the contamination arising from the 10 mL of unlabelled TB used to inoculate the 1L minimal media "expression" media. However, this level of incorporation was deemed satisfactory since any level >90% is the normal requirement for satisfactory heteronuclear experiments (Mossakowska and Smith, 1997). For the triply labelled sample, deuterium incorporation was estimated to be approximately 70 % which, initially seemed quite low considering the M9 media was composed of 90 % $^{2}H_2O$. Usually the level of ^{2}H incorporation reflects the percentage of $^{2}H_2O$ used to prepare the minimal media (Gardner and Kay, 1998). Therefore, using 90 % $^{2}H_2O$ minimal media we should have expected approximately 90 % ^{2}H incorporation. It is thought that several factors lead to this less-than-expected distribution of deuterium throughout the protease. One factor could be that protonated glucose instead of deuterated glucose was used. This is of importance because during biosynthesis, protons from these molecules can be efficiently retained at the side chains of aromatic amino acids and other specific sites within several amino acids (Gardner and Kay, 1998). Additionally, metabolic and biosynthetic enzymes may have preferentially used protons over deuterons, since both were in the medium. This preference is thought to be due to kinetic and thermodynamic isotope effects (Galimov, 1985). Regardless, this level of deuteration was deemed to be satisfactory since other proteins, such as a 37 kDa trp repressor/DNA ternary complex (Yamazaki et al, 1994b), have been successfully studied at ^{2}H incorporation levels of approximately 70 %.

^{15}N Labelling at Specific Amino Acids in the HAV 3C Protease. Amino acid biosynthesis in bacteria is regulated by enzymatic activity and at the level of gene expression (Neidhardt, 1987). Endogenous synthesis of unlabelled amino acids and transaminase-catalysed nitrogen exchange often can be minimized by

supplying the host bacteria with sufficient quantities of various amino acids in the "expression" medium (McIntosh and Dahlquist, 1990). Therefore the simplest approach, and the strategy we used in this study was to use a defined "expression" medium (minimal media minus NH_4Cl) containing one ^{15}N labelled amino acid mixed with 19 unlabelled amino acids. The extent to which a ^{15}N labelled amino acid will be incorporated depends on many factors including the amino acid in question and the growth characteristics of the bacterial host.

The ^{1}H-^{15}N HSQCs recorded for the ^{15}N specifically labelled alanine, glycine, isoleucine, leucine, lysine, phenylalanine and valine HAV 3C protease samples are shown in Figures 3.2 (p.81) and 3.3 (p.82). Inspection of this group of ^{1}H-^{15}N HSQC spectra will allow one to discern two characteristics that are generally conserved. First, all seven spectra show some degree of ^{15}N being incorporated into the side chain nitrogen nuclei of arginine, lysine, glutamine, and asparagine. This is evident as the "hourglass-shaped" peaks between 6.4 and 7.8 ppm in the ^{1}H dimension and 110 and 114 ppm in the ^{15}N dimension. Second, in addition to the strong peaks, which are assumed to be the intended amino acid, there are usually a few extra less intense peaks found in each spectrum. One of these extra peaks (^{15}N = 130.20 ppm, ^{1}H = 8.01 ppm) corresponds to the C-terminal residue E217. Likewise, there are three other peaks (120.80/7.72, 123.95/8.40, 123.99/8.32) found in most of the spectra corresponding to the other C-terminal residues K214, K215, and I216.

This non-specific ^{15}N incorporation, otherwise known as "scrambling", can be caused by enzymes that convert the exogenously supplied ^{15}N labelled amino acid into a metabolic precursor or it can be caused by transaminases which catalyze nitrogen exchange into undesired sites of other amino acids (Muchmore et al., 1989). It is likely that all of the specific labels experienced "scrambling" to some degree since an auxotrophic strain of bacteria was not used to prepare the specifically labelled samples. The reason that the C-terminal resonances are

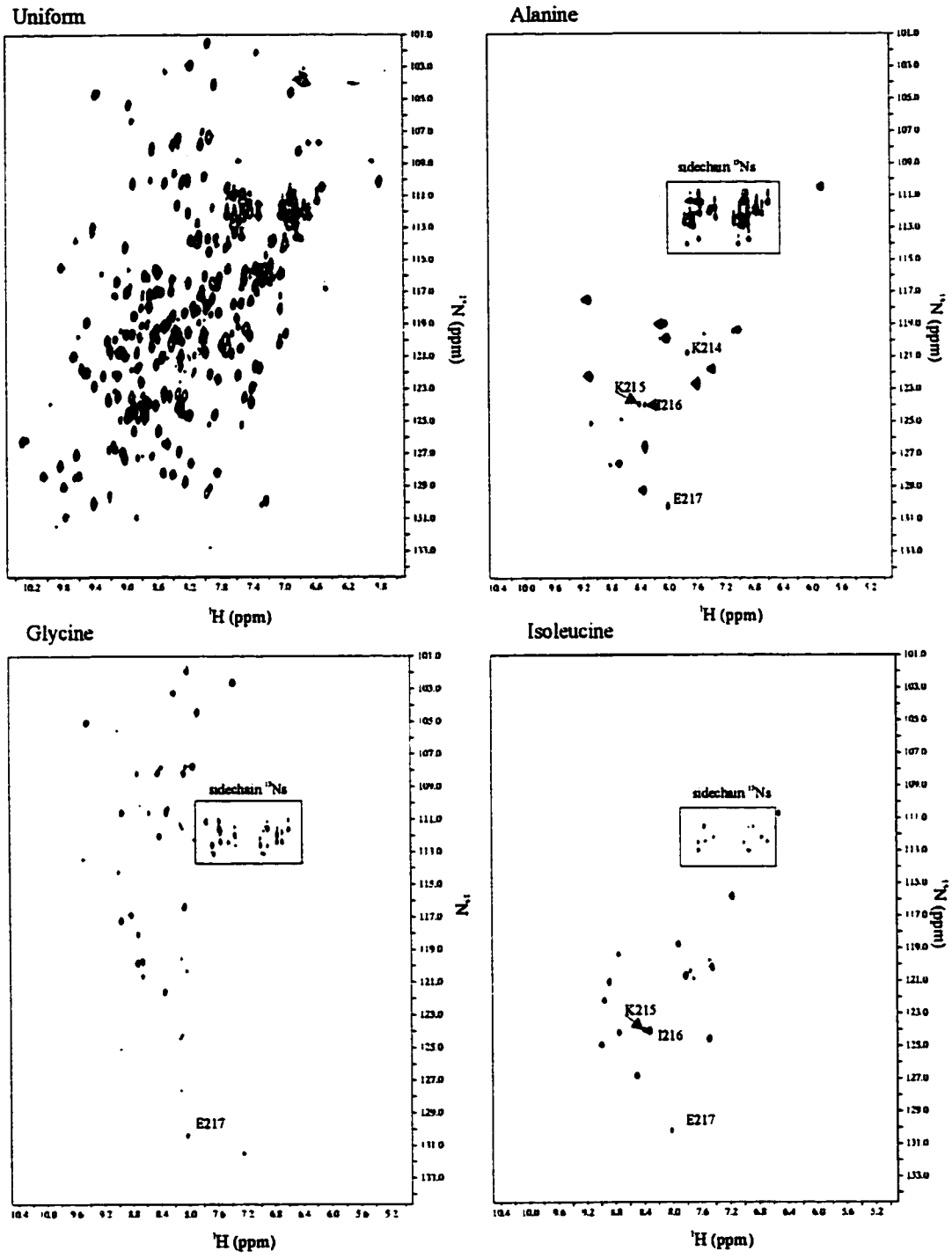

Figure 3.2. ^{1}H-^{15}N HSQC spectra of (~1 mM) uniform ^{15}N and ^{15}N-isoleucine labelled HAV 3C protease in 'low salt-low pH' conditions and ^{15}N-alanine and ^{15}N-glycine labelled HAV 3C protease in 'high salt-high pH' conditions collected at 25°C on a Varian Unity 600 spectrometer.

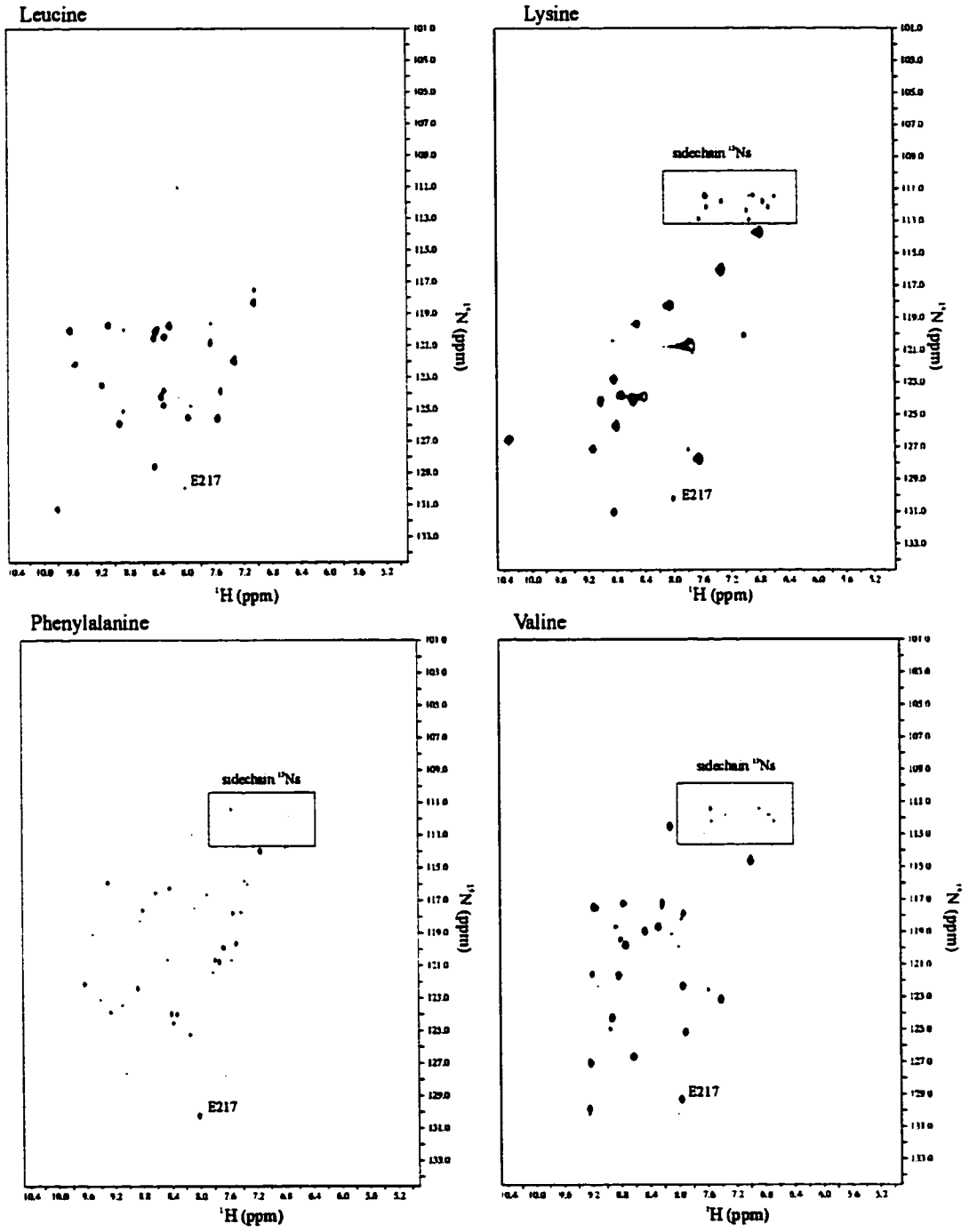

Figure 3.3. ^{1}H-^{15}N HSQC spectra of (~1 mM) ^{15}N-leucine, ^{15}N-lysine, ^{15}N-phenylalanine and ^{15}N-valine labelled HAV 3C protease in 'high salt-high pH' solution conditions collected at 25°C on a Varian Unity 600 MHz spectrometer.

visible is likely due to their very high mobility. Because of this mobility, they display very sharp intense peaks that exaggerate their level of ^{15}N incorporation.

The relative success of this simple specific labelling strategy (without the use of auxotrophic strains of E. coli) is reported in Table 3.5. Five of the seven trials gave very good results (showing greater than 80% of the expected peaks). In particular, the spectra collected for alanine, isoleucine, leucine, lysine, and valine labelled HAV 3C protease were generally good. Of these, the isoleucine and leucine samples gave the best results (although leucine must have scrambled preferentially into one other residue in the sequence) showing 100% of the expected peaks. The reason that these two samples displayed all of the expected peaks is likely due to the fact that they were prepared at a lower pH (5.4) which led to a slower rate of hydrogen exchange and improved amide ($^{1}H/^{15}N$) signals. It is possible that if the other samples had been prepared at this lower pH, they too would have displayed all (or at least more) of the expected peaks. Attempts to label HAV 3C protease at glycine and phenylalanine were the least useful as it is quite clear that scrambling occurred for both samples. However, of these two, the glycine spectrum was of some utility as 15 of the 22 expected peaks could still be discerned.

Table 3.5. Success of residue-specific ^{15}N labelling studies.

Amino Acid type	Total number in sequence	Number of intense peaks in ^{1}H-^{15}N HSQC spectrum
Alanine	12	11
Glycine	22	"scrambled"
Isoleucine	13	13
Leucine	19	20
Lysine	17	15
Phenylalanine	8	"scrambled"
Valine	23	18

3.4 Conclusion

To summarize, nearly all of our isotopic labelling attempts proved to be very successful. For the three uniformly labelled protease samples ($^{2}H/^{13}C/^{15}N$, $^{13}C/^{15}N$, and ^{15}N), incorporation levels of >95% were noted for both ^{13}C and ^{15}N and ~ 70 % for ^{2}H. It was determined that careful adaptation of the bacterial expression system to chemically defined media played a major role in optimizing our yields of the labelled HAV 3C protease. This was demonstrated in the higher yields (75-100 mg/L versus 20 mg/L) of protease when using minimal media instead of rich media in the "overnight" culture. Cellular adaptation was also important in producing HAV 3C protease in deuterated media. This was demonstrated in the success of the step-wise approach to progressively higher percentages of $^{2}H_2O$ content which we used to select "$^{2}H_2O$-adapted" bacteria in the production of the triple ($^{2}H/^{13}C/^{15}N$) labelled protease. Finally, the ^{15}N residue-specific labelling schemes, even without the use auxotrophic strains of E. coli, were successful in five of the seven attempted residue-specific trials.

Chapter 4

^{1}H, ^{13}C and ^{15}N backbone assignments of HAV 3C protease

4.1 Introduction

Preclinical drug discovery generally involves two processes: 1) lead generation and 2) lead optimization. In the lead generation process, candidate molecules are identified that appear to bind to a protein target and inhibit the *in vitro* activity of the protein. In the lead optimization process, potential drug leads are optimized with respect to detailed structural information, *in vitro* potency and other important parameters such as bioavailabity, pharmacokinetic or toxicological properties. In recent years, NMR spectroscopy has been applied to both lead generation and lead optimization (Moore, 1999; Roberts, 1999; Fesik, 1993; Hajduk et al., 1997; Shuker et al., 1996). In the area of lead generation, NMR has been used to detect weak binding of small molecules to a number of protein drug targets. Subsequently, this binding information can be used to design much tighter-binding inhibitors. The method, known as "SAR by NMR" (Shuker et al., 1996), screens a large library (10^{3}-10^{4}) of small molecules against an ^{15}N labelled protein target by using information derived from 2D ^{1}H-^{15}N HSQC spectra. Using this technique, protein-ligand binding can be discerned by noting perturbations in the target protein's amide chemical shifts. In the area of lead optimization, NMR has been used to characterize the detailed structure and dynamics of both the protein target and the small molecule leads. Such studies typically involve the solution structure determination of either the protein, the protein-ligand complex or the ligand structure using either isotope edititing/filtering or transferred NOE techniques (Roberts, 1999).

For NMR spectroscopy to be used in either of the processes described above, it is critical that complete backbone ^{1}H, ^{13}C and ^{15}N chemical shift

assignments be available for the protein target of interest. This is because the sequential assignments serve as the basis of any strategy employed to solve protein 3D structure via NMR spectroscopy (Clore and Gronenborn, 1994). Additionally, having the backbone amide ($^{1}H_{N}$, ^{15}N) chemical shifts assigned in the ^{1}H-^{15}N HSQC spectra is of utmost importance for "SAR by NMR" because knowing which residue(s) experience amide chemical shift perturbations indicate which site(s) on the protein are involved in ligand binding (Shuker et al., 1996).

This chapter describes the NMR experiments that were performed to obtain nearly complete ^{1}H, ^{13}C and ^{15}N backbone chemical shift assignments for HAV 3C protease. Early efforts using ^{15}N-edited and triple resonance experiments (^{1}H-^{15}N TOCSY-HSQC, ^{1}H-^{15}N NOESY-HSQC, HNCACB and CBCA(CO)NNH) using single (^{15}N) and double ($^{13}C/^{15}N$) labelled HAV 3C protease were thwarted by problems with macromolecular aggregation in 'high salt/high pH' solution conditions. The efficient relaxation rates typical of aggregated proteins led to spectra that were devoid of much of the expected chemical shift information. However, identifying solution conditions that minimized aggregation (low salt/low pH) and preparing a triply ($^{2}H/^{13}C/^{15}N$) labelled HAV 3C protease sample (to combat efficient relaxation rates) solved the "poor spectral quality" problem. With this triple labelled sample, we collected three "deuterium-modified" triple resonance experiments that yielded spectra displaying nearly all of the expected chemical shifts. As a result, these final CT-HNCA, CT-HN(CO)CA and HN(CA)CB spectra were used in conjunction with previously collected residue-specific HSQC data to complete about 85 percent of the sequential backbone assignments.

The assignments were found to be in good agreement with a set of predicted chemical shifts calculated from SHIFTX (Neal, Nip and Wishart, unpublished) and TOTAL (Williamson et al., 1992,1995). These programs use semi-empirical methods (using ring-current shifts, shifts arising from magnetic anisotropies of bonds, and shifts arising from the polarizing effect of polar atoms

on the C H bond) to calculate ^{1}H, ^{13}C and ^{15}N chemical shifts for HAV 3C protease based on the 3D coordinates from its X-ray crystal structure (Bergmann et al., 1997). Finally, the backbone chemical shifts that have been assigned were analyzed by the CSI program (Wishart et al., 1994) and preliminary calculations show that the locations of 2 α-helices and 11 β-strands are in good agreement with X-ray crystallographic data.

4.2 Heteronuclear NMR experiments used to obtain sequential backbone assignments for HAV 3C protease

Due to the complexity and number of NMR experiments performed in these studies, a concise description of each experiment follows. These experiments include: 1) ^{1}H-^{15}N HSQC (Kay et al., 1992: Zhang et al., 1994), 2) ^{1}H-^{15}N TOCSY-HSQC (Zhang et al., 1994), 3) ^{1}H-^{15}N NOESY-HSQC (Zhang et al., 1994), 4) (constant-time) CT-HNCO (Muhandiram and Kay, 1994), 5) deuterium-modified CT-HNCA (Yamazaki et al., 1994a), 6) deuterium-modified CT-HN(CO)CA (Yamazaki et al., 1994b), and 7) deuterium-modified HN(CA)CB (Yamazaki et al., 1994b) experiments.

2D ^{1}H-^{15}N HSQC. 2D ^{15}N-^{1}H HSQC experiments (Kay et al., 1992: Zhang et al., 1994) were used to correlate the chemical shift of each ^{15}N nucleus and its covalently bonded proton ($^{1}H_N$). In the ^{15}N-^{1}H HSQC experiment, depicted in Figure 4.1 (p.93), magnetization is initially generated on $^{1}H_N$ [Step 1]. An INEPT pulse sequence transfers magnetization to the attached ^{15}N via $^{1}J_{NH}$ (~90 Hz) coupling [Step 2] and all ^{15}N chemical shifts are recorded over the acquisition time t_1 [Step 3]. A reverse INEPT pulse sequence transfers magnetization back to the attached $^{1}H_N$ [Step 4] and all $^{1}H_N$ chemical shifts are collected over the second acquisition time t_2 [Step 5]. Fourier transformation of the resultant FID yields a frequency domain map showing all $^{1}H_N$ and ^{15}N correlations.

3D ^{1}H-^{15}N TOCSY-HSQC. The 3D ^{1}H-^{15}N TOCSY-HSQC experiment (Zhang et al., 1994) is illustrated in Figure 4.2 (p.94). Presaturation of the water resonance was avoided by using 'water-selective pulses' and gradients and by ensuring that water magnetization is placed along the +z-axis prior to acquisition (Grzesiek and Bax, 1993; Kay et al., 1994). Compared to ^{1}H-^{15}N HSQC-TOCSY experiments that utilize water presaturation, the advantage of the TOCSY-HSQC is that it avoids saturation of the $^{1}H_{\alpha}$ spins, allowing observation of important $^{1}H_{\alpha}$ cross peaks. Initially this experiment is a homonuclear TOCSY experiment with ^{15}N spin decoupling during the t_1 period [Step 1]. Isotropic mixing transfers magnetization between ^{1}H spins within each spin system and ^{1}H chemical shifts are recorded over the acquisition time t_1. An INEPT pulse sequence then transfers magnetization to ^{15}N via $^{1}J_{NH}$ (~90 Hz) coupling [Step 2] and all ^{15}N chemical shifts are recorded over the acquisition time t_2 [Step 3]. Finally, a reverse INEPT pulse sequence is used to transfer magnetization back to $^{1}H_{N}$ [Step 4] and all $^{1}H_{N}$ chemical shifts are collected over the final acquisition time t_3 [Step 5]. Fourier transformation of the resultant FID yields a frequency domain map showing all $^{1}H_{N}$, ^{15}N and ^{1}H resonances within each spin system.

3D ^{1}H-^{15}N NOESY-HSQC. The 3D ^{1}H-^{15}N NOESY-HSQC experiment (Zhang et al., 1994) is illustrated in Figure 4.3 (p.95). Presaturation of the water resonance was avoided by using 'water-selective pulses' and gradients and by ensuring that water magnetization is placed along the +z-axis prior to acquisition (Grzesiek and Bax, 1993; Kay et al., 1994). The advantage discussed above for the TOCSY-HSQC applies to the NOESY-HSQC as well. Initially the sequence is a homonuclear NOESY experiment with ^{15}N spin decoupling during the t_1 period [Step 1]. Magnetization transfer occurs via dipolar mediated cross-relaxation for a mixing period τ_M. All NOEs (through space magnetization transfers to ^{1}H nuclei within 5Å of each other) are recorded over the acquisition period t_1. Although all protons are frequency-labelled during t_1, only magnetization from $^{1}H_{N}$ is transferred to the attached ^{15}N by an INEPT pulse sequence via the

$^1J_{NH}$ (~90 Hz) coupling [Step 2]. All ^{15}N chemical shifts are recorded over the acquisition time t_2 [Step 3]. A reverse INEPT pulse sequence is used to transfer magnetization back to the attached ^1H_N [Steps 4] and all ^1H_N chemical shift are collected over the final acquisition time t_3 [Step 5]. Fourier transformation of the resultant FID yields a frequency domain map showing all ^{15}N and ^1H_N correlations as well as ^1H correlations that cross-relaxed with each ^1H_N.

3D CT-HNCO Experiment. The 3D CT-HNCO experiment (Muhandiram and Kay, 1994) was used to correlate the ^1H_N and ^{15}N chemical shifts of residue 'i' with the carbonyl carbon (^{13}CO) chemical shift of the preceding residue 'i-1'. In the HNCO experiment, depicted in Figure 4.4 (p.96), magnetization is initially generated on ^1H_N [Step 1]. An INEPT pulse sequence transfers magnetization to ^{15}N via $^1J_{NH}$ (~90 Hz) coupling [Step 2] and all ^{15}N chemical shifts are recorded over the acquisition time t_1 [Step 3]. This experiment is optimized through the use of a constant time interval that allows overlap of the period needed to encode ^{15}N frequencies (t_1) and the period needed for dephasing of the ^{15}N spins with respect to the ^{13}CO. The introduction of this constant time period is advantageous as it results in a reduction of relaxation losses and a concomitant improvement in sensitivity. A second INEPT pulse sequence is used to transfer magnetization to the preceding residue ^{13}CO via $^1J_{NCO}$ (~15 Hz) coupling [Step 4] and all ^{13}CO chemical shifts are recorded over the acquisition period t_2 [Step 5]. Magnetization is then transferred back to ^1H_N using two reverse INEPT sequences [Step 6] and all ^1H_N chemical shift are collected over the third and final acquisition period t_3 [Step 7]. Fourier transformation of the resultant FID yields a frequency domain map with correlations between $^{13}CO(i-1)$, $^{15}N(i)$, and $^1H_N(i)$.

"Deuterium-modified" NMR experiments. Triple-resonance (^{15}N, ^{13}C, ^1H) experiments applied to proteins with molecular weights in excess of 20 kDa may experience a number of significant limitations (Gardner and Kay, 1998). The first problem relates to the rapid T_2 relaxation rates of nuclei (particularly ^{13}C) that participate in the magnetization transfer steps during the course of these

experiments. These rapid relaxation rates can lead to significant signal loss in these multiple step triple resonance experiments. The second problem, according to Gardner and Kay, (1998), is the lack of resolution in these spectra, particularly in the carbon dimension, due to the short acquisition times that must be used as a consequence of efficient ^{13}C T_2 relaxation rates. The ^{13}C T_2 relaxation rate is dominated by the strong dipolar interaction with its attached protons (Browne et al., 1973). As discussed in Chapter 1, replacing protons with deuterium, whose magnetogyric ratio is ~6.5 times lower than that of protons, greatly reduces the dipolar interaction and consequently lessens the ^{13}C T_2 relaxation rates (or increases ^{13}C T_2 relaxation times). This increases in ^{13}C T_2 relaxation times provides a solution to the above problems by reducing signal loss and increasing the time allotted for acquiring ^{13}C chemical shifts.

In general, the following experiments (CT-HNCA, CT-HN(CO)CA, CT-HN(CA)CB) have been modified by incorporating deuterium decoupling during periods in which transverse carbon magnetization is present (Gardner and Kay, 1998). At high magnetic field strengths, the ^{2}H spin lattice relaxation time, T_1, in proteins is in the millisecond range due to the large ^{2}H quadrupolar interaction (~170 kHz) (Grzesiek et al., 1993). As a consequence, the ^{2}H-^{13}C J coupling (~22 Hz) gives rise to a ^{13}C resonance that is broadened by scalar relaxation of the second kind (Abragam, 1961; London, 1990). However, incorporating deuterium decoupling into these pulse sequences during ^{13}C chemical shift acquisition effectively removes this broadening. This results in ^{13}C linewidths that are much narrower than those noted for protonated ^{13}C nuclei (Grzesiek et al., 1993).

3D "deuterium-modified" CT-HNCA. The deuterium-modified CT-HNCA (Yamazaki et al., 1994) was used to provide protein backbone information by correlating the $^{1}H_N$ with directly attached ^{15}N, $^{13}C_\alpha$ and preceding $^{13}C_\alpha(i-1)$ chemical shifts. In the HNCA experiment, shown in Figure 4.5 (p.97), magnetization is initially generated on the $^{1}H_N$ [Step 1]. An INEPT pulse sequence transfers magnetization to ^{15}N via the $^{1}J_{NH}$ (~90 Hz) coupling [Step 2]. A second

INEPT pulse sequence is used to transfer magnetization to the attached and preceding $^{13}C_\alpha$ via the $^{1}J_{NC\alpha}$ (8 – 12 Hz) and $^{2}J_{NC\alpha}$ (~ 7 Hz) couplings respectively [Step 3]. The two $^{13}C_\alpha$ chemical shifts are then recorded over the acquisition period t_1 [Step 4]. This experiment is optimized through the use of a constant time interval that allows overlap of the period needed to encode $^{13}C_\alpha$ frequencies (t_1) and the period needed for dephasing of the $^{13}C_\alpha$ spins with respect to the ^{15}N. This results in a reduction of relaxation losses and a concomitant improvement in sensitivity. Magnetization is then transferred back to ^{15}N using a reverse INEPT sequence [Step 5] and all ^{15}N chemical shifts are recorded over the acquisition time t_2 [Step 6]. Magnetization is then transferred back to $^{1}H_N$ using a reverse INEPT sequence [Step 7] and all $^{1}H_N$ chemical shifts are collected over the third and final acquisition period t_3 [Step 8]. Fourier transformation of the resultant FID yields a frequency domain map with correlations between $^{13}C_\alpha$(i, i -1), ^{15}N(i), and $^{1}H_N$(i).

3D "deuterium-modified" CT-HN(CO)CA. The deuterium modified 3D HN(CO)CA (Yamazaki et al., 1994) was used to complement the deuterium-modified HNCA by correlating $^{1}H_N$ chemical shifts with attached ^{15}N chemical shifts and preceding $^{13}C_\alpha$(i-1) chemical shifts. In the HN(CO)CA experiment, shown in Figure 4.6 (p.98), magnetization is initially generated on $^{1}H_N$ [Step 1]. An INEPT pulse sequence transfers magnetization to ^{15}N via the $^{1}J_{NH}$ (~90 Hz) coupling [Step 2]. A second INEPT pulse sequence is used to transfer magnetization to the preceding residue ^{13}CO(i-1) via the $^{1}J_{NCO}$ (15 Hz) coupling [Step 3]. A third INEPT pulse sequence is used to transfer magnetization to the preceding residue $^{13}C_\alpha$(i-1) via the $^{1}J_{C\alpha CO}$ coupling (55 Hz) [Step 4]. The preceding $^{13}C_\alpha$(i-1) chemical shifts are then recorded over the acquisition period t_1 [Step 5]. This experiment is optimized through the use of a constant time interval that allows overlap of the period needed to encode $^{13}C_\alpha$ frequencies (t_1) and the period needed for dephasing of the $^{13}C_\alpha$ spins with respect to the ^{13}CO. This results in a reduction of relaxation losses and a concomitant improvement in sensitivity. Magnetization is then transferred back to ^{15}N(i) using two reverse

INEPT sequence [Step 6] and all ^{15}N chemical shifts are recorded over the acquisition time t_2 [Step 7]. Finally, magnetization is transferred back to $^{1}H_N$ using a reverse INEPT sequence [Step 8] and all $^{1}H_N$ chemical shifts are collected over the third and final acquisition period t_3 [Step 9]. Fourier transformation of the resultant FID yields a frequency domain map with correlations between $^{13}C_\alpha$(i-1), ^{15}N(i), and $^{1}H_N$(i).

3D "deuterium modified" HN(CA)CB. The deuterium modified 3D HN(CA)CB (Yamazaki et al., 1994) is illustrated in Figure 4.7 (p.99). This experiment provides protein backbone information by correlating the $^{1}H_N$ chemical shifts with the attached ^{15}N chemical shifts and $^{13}C_\beta$(i, i-1) chemical shifts. In this experiment, magnetization is first generated on $^{1}H_N$ [Step 1]. INEPT pulse sequences are used to transfer magnetization to ^{15}N via the $^{1}J_{NH}$ (~90 Hz) coupling [Step 2], the attached and preceding $^{13}C_\alpha$(i, i-1) via the $^{1}J_{NC\alpha}$ (8 – 12 Hz) and $^{2}J_{NC\alpha}$ (~ 7 Hz) couplings [Step 3] and finally to the $^{13}C_\beta$(i, i-1) [Step 4] via the $^{1}J_{CC}$ (~30-40 Hz) coupling. The two $^{13}C_\beta$(i, i-1) chemical shifts are then recorded over the acquisition period t_1 [Step 5]. Magnetization is then transferred back to ^{15}N using two reverse INEPT pulse sequences [Steps 6-7] and all ^{15}N chemical shifts are recorded over the acquisition time t_2 [Step 8]. Magnetization is finally transferred back to $^{1}H_N$ using a reverse INEPT sequence [Step 9] and all $^{1}H_N$ chemical shifts are recorded over the third and final acquisition period t_3 [Step 10]. Fourier transformation of the resultant FID yields a frequency domain map with correlations between $^{13}C_\beta$(i, i-1), ^{15}N(i), and $^{1}H_N$(i).

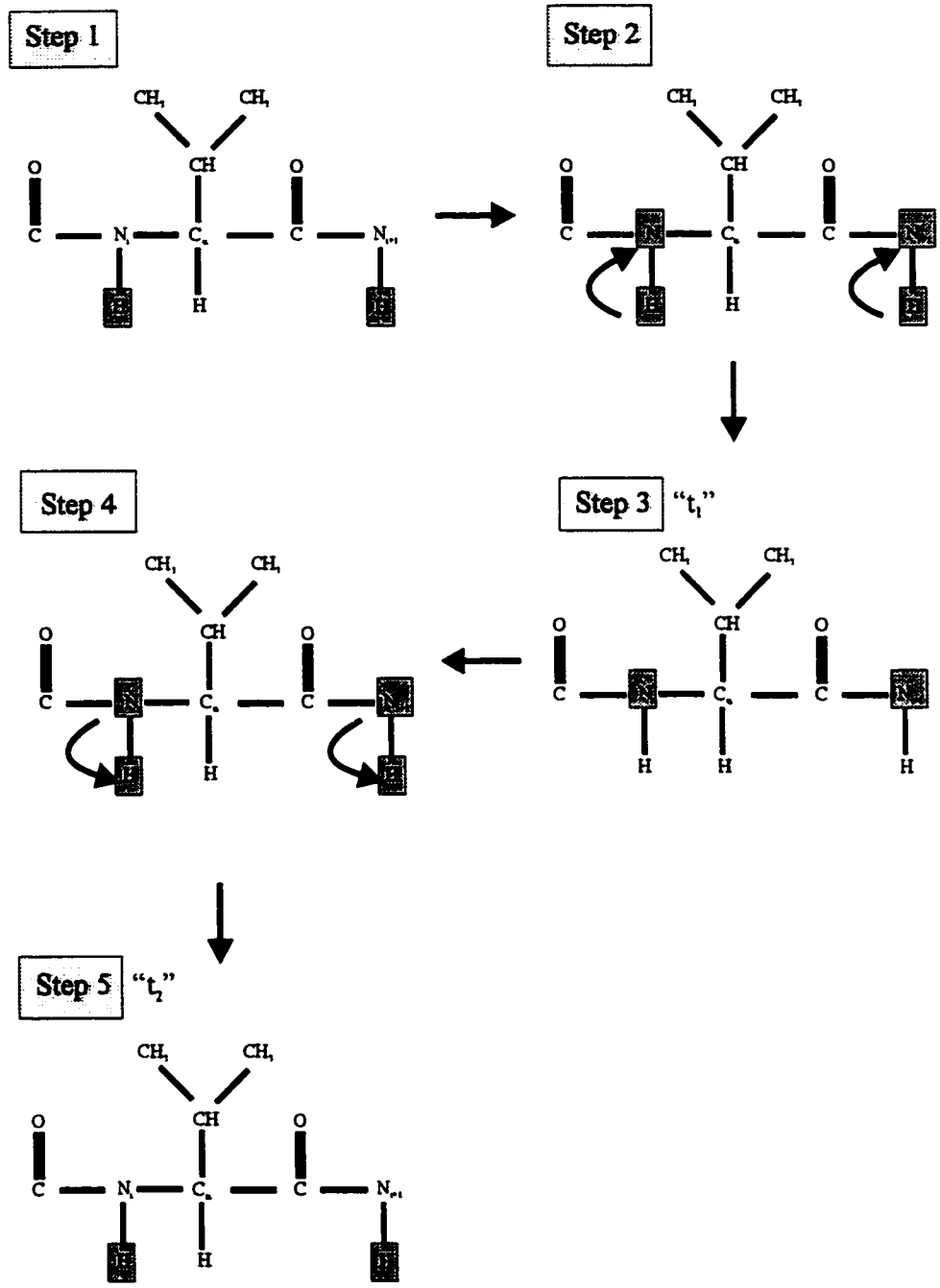

Figure 4.1. Outline of magnetization transfer in the ^{1}H-^{15}N HSQC experiment.

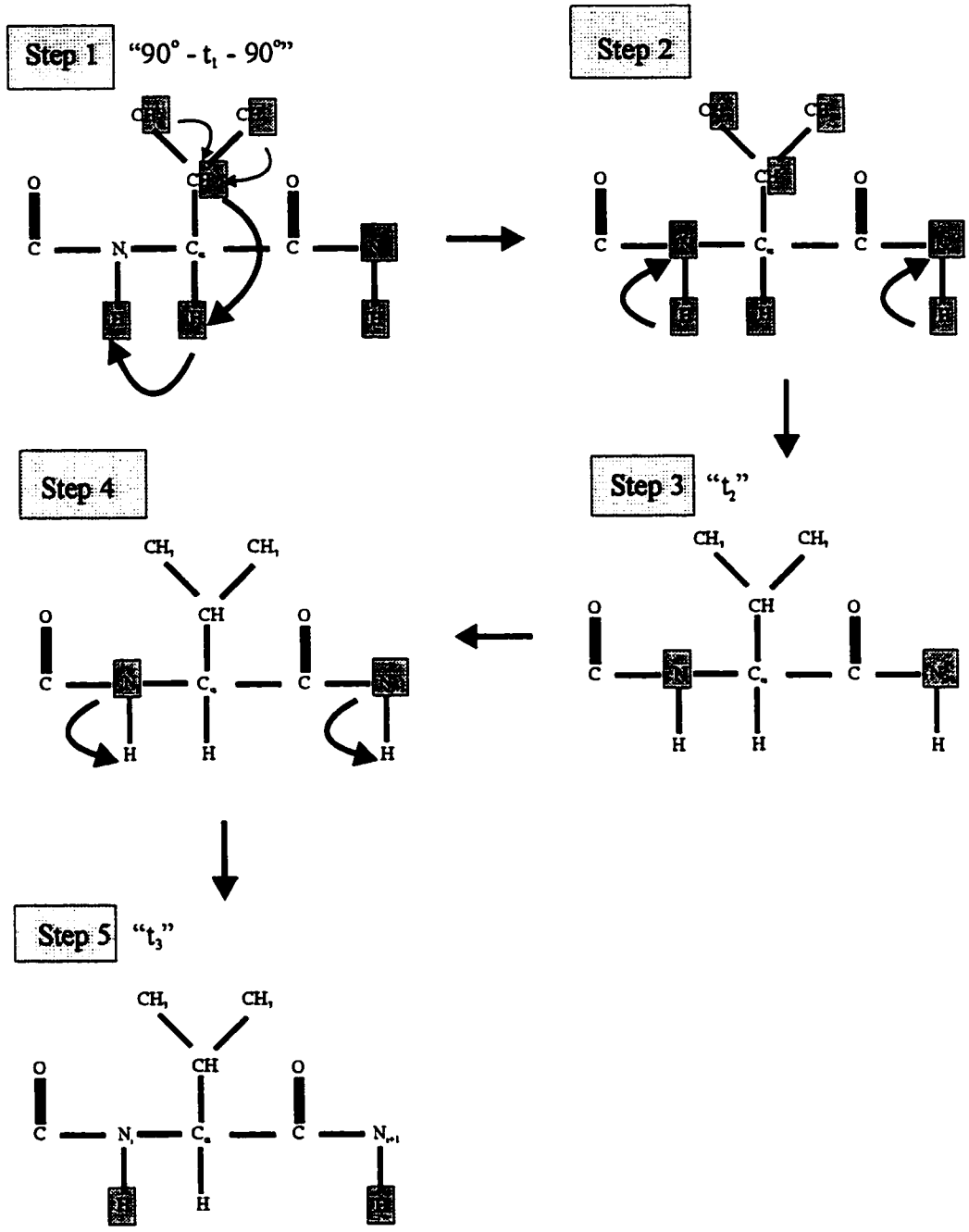

Figure 4.2. Outline of magnetization transfer in the ^{1}H-^{15}N TOCSY-HSQC experiment.

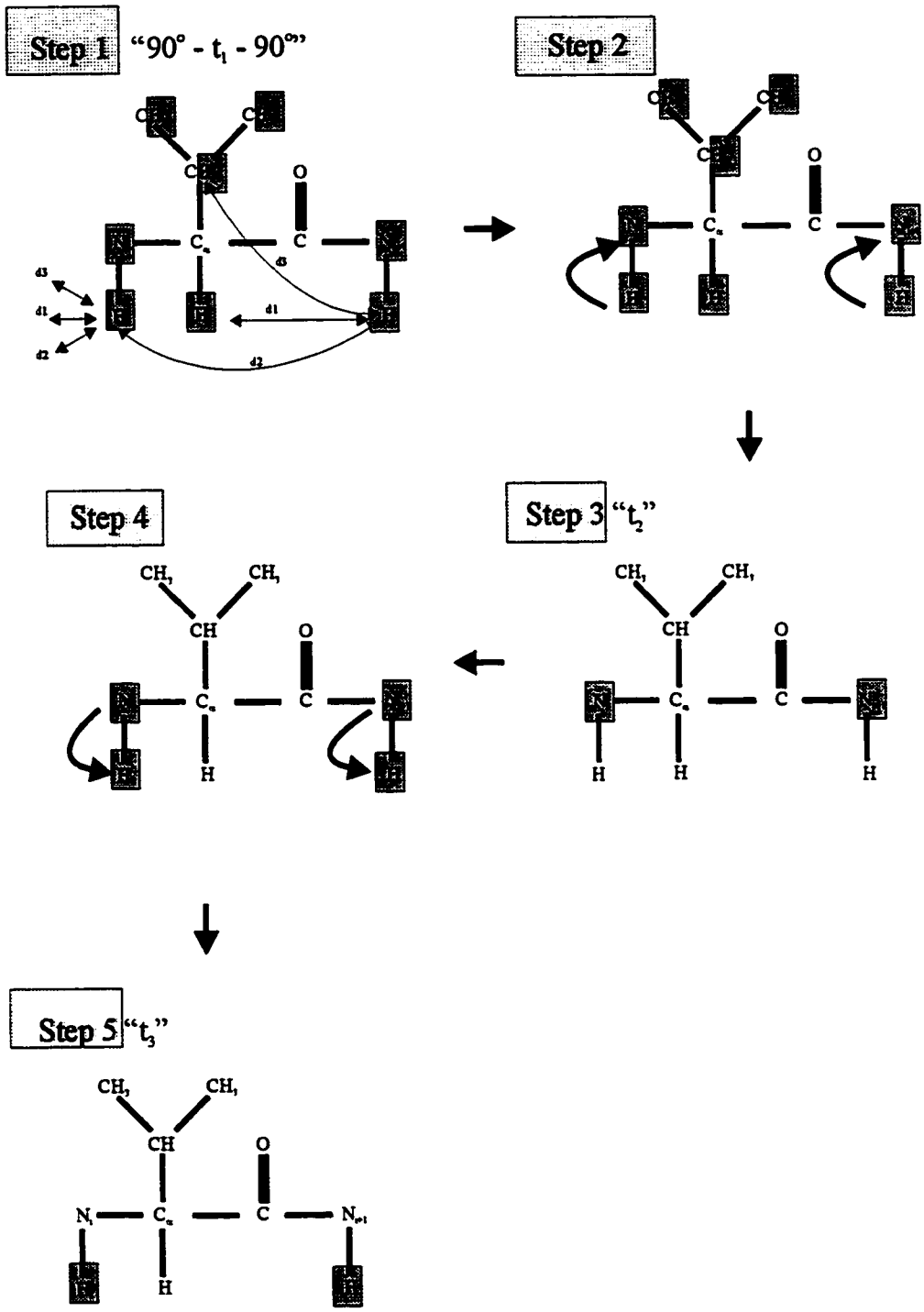

Figure 4.3. Outline of magnetization transfer in the ^{1}H-^{15}N NOESY-HSQC experiment.

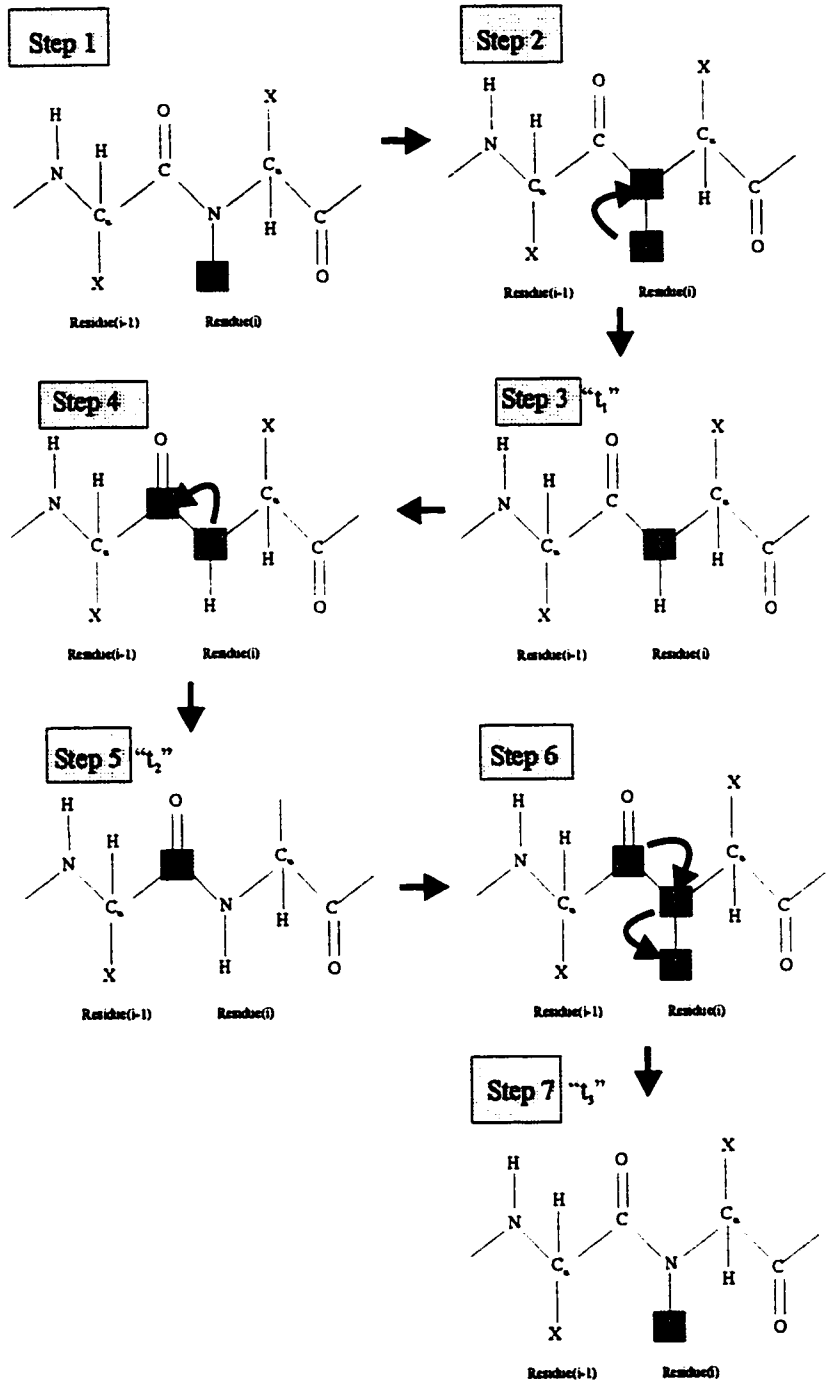

Figure 4.4. Outline of magnetization transfer in the CT-HNCO experiment.

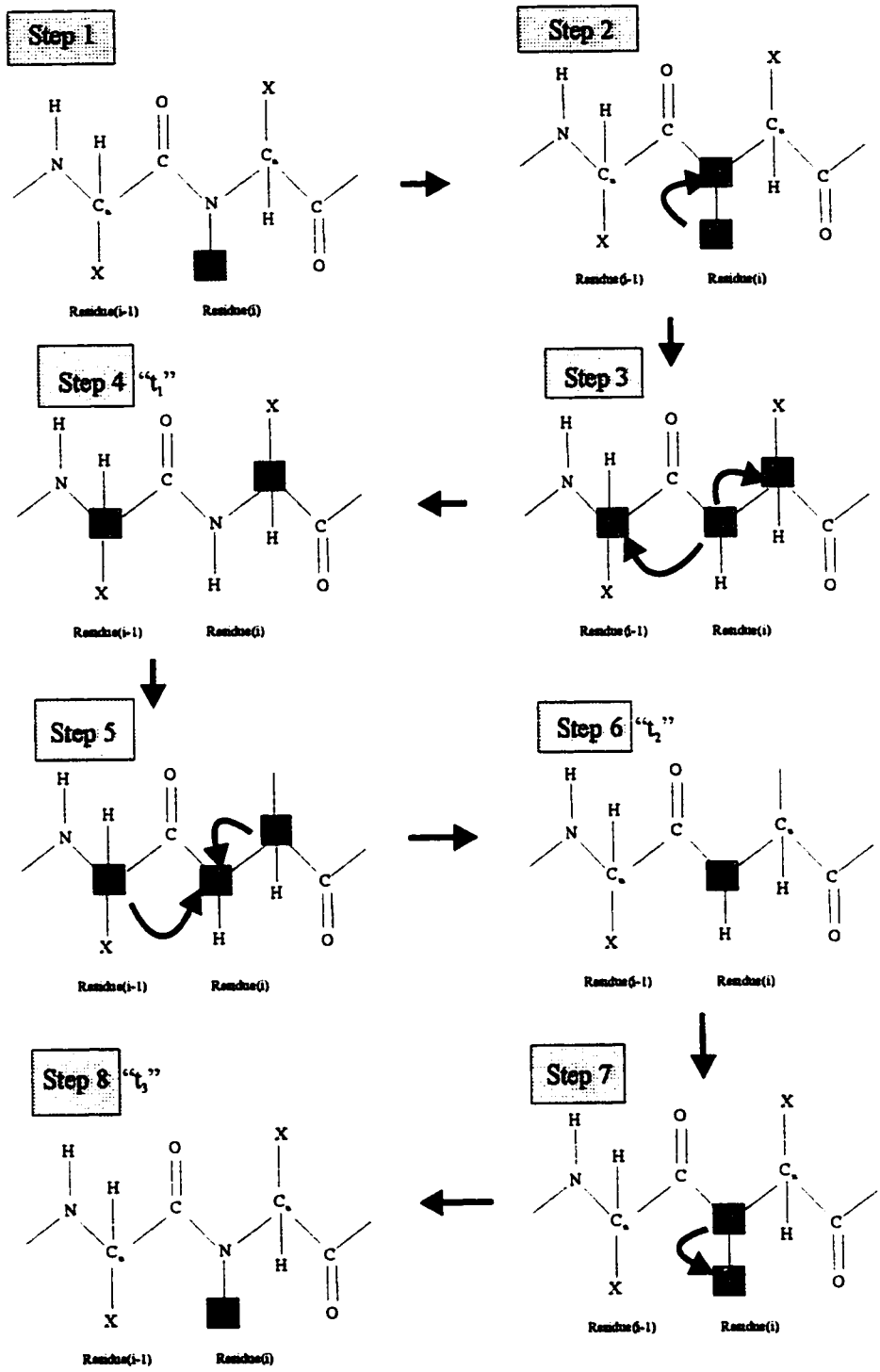

Figure 4.5. Outline of magnetization transfer in the "deuterium modified" HNCA experiment.

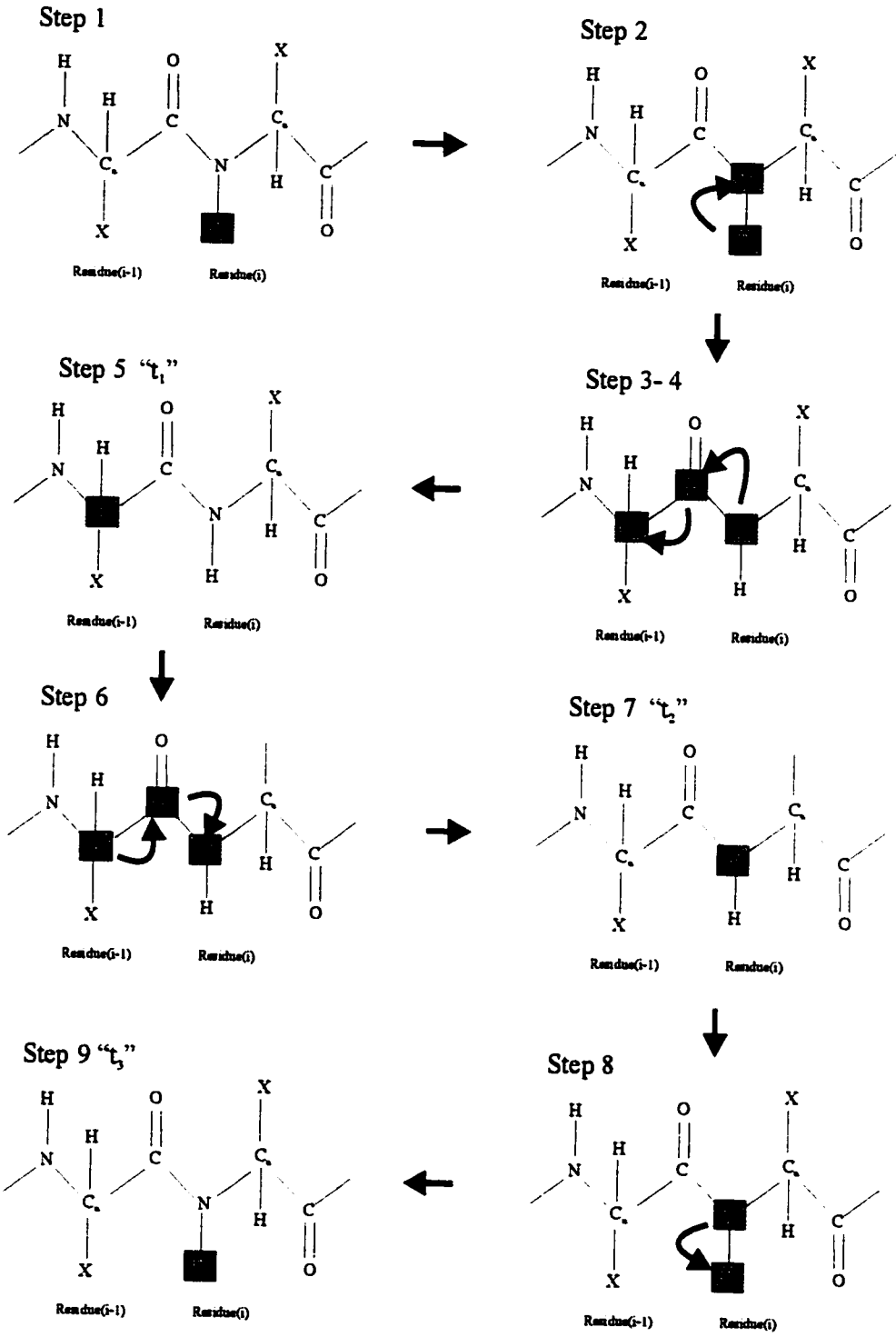

Figure 4.6. Outline of magnetization transfer in the "deuterium modified" HN(CO)CA experiment.

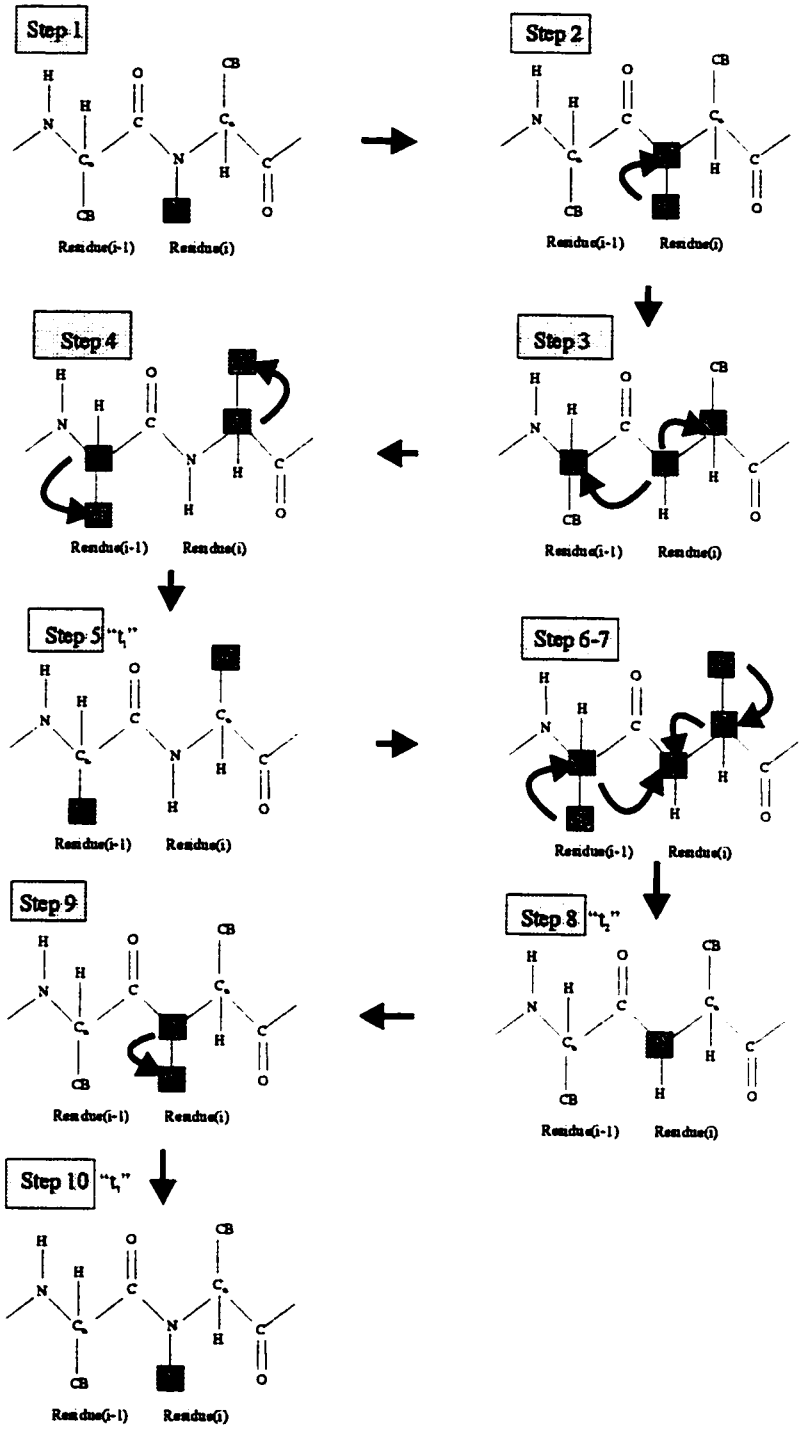

Figure 4.7. Outline of magnetization transfer in the "deuterium modified" HN(CA)CB experiment.

4.3 Materials and Methods

Preparation of HAV 3C protease NMR samples. ^{15}N, $^{13}C/^{15}N$, $^{2}H/^{13}C/^{15}N$ and residue-specific ^{15}N labelled HAV 3C protease samples were isolated from the prototrophic E. coli strain MM294 containing the overexpression plasmid pHAV-3CEX (Malcolm et al., 1993) with a C24S mutation (to facilitate protein stabilization). Media was prepared, bacteria cultures were grown and the HAV 3C protease was isolated as described in Chapters 2 and 3. The NMR sample used for $^{1}H-^{15}N$ HSQC, $^{1}H-^{15}N$ TOCSY-HSQC and $^{1}H-^{15}N$ NOESY-HSQC experiments contained 0.75 mM HAV 3C protease (uniformly ^{15}N labelled) dissolved in 350 mM NaCl, 20 mM KH_2PO_4, 0.5 mM EDTA at pH 7.0. The sample was prepared to a volume of 500 µL by combining 10 µL DSS, 100 µL D_2O (99%) and 390 µL concentrated protease solution. The resulting sample had a $H_2O:D_2O$ ratio of 8:2. The NMR sample used for the CT-HNCO experiment contained 1.0 mM HAV 3C protease (uniformly $^{13}C/^{15}N$ labelled) dissolved in 350 mM NaCl, 20 mM KH_2PO_4, 0.5 mM EDTA at pH 7.0. The sample was prepared to a volume of 500 µL by combining 10 µL of 3% (w/v) sodium azide, 10 µL DSS, 50 µL D_2O (99%) and 430 µL concentrated protease solution. The resulting sample had a $H_2O:D_2O$ ratio of 9:1. The NMR sample used for the deuterium-modified CT-HNCA, CT-HN(CO)CA and HN(CA)CB experiments contained 1.0 mM HAV 3C protease (uniformly $^{2}H/^{13}C/^{15}N$ labelled) dissolved in 100 mM NaCl, 20 mM KH_2PO_4, 0.5 mM EDTA, 1.0 mM DTT at pH 5.4. The sample was prepared to a volume of 500 µL by combining 10 µL of 3% (w/v) sodium azide, 10 µL DSS, 50 µL D_2O (99%) and 430 µL concentrated protease solution. The resulting sample had a $H_2O:D_2O$ ratio of 9:1.

Experimental set up for NMR experiments. Experiments were set up and performed by Dr. Stephane Gange, Dr. Carolyn Slupsky, Dr. Leo Spyracopoulos and Dr. Brian Sykes. $^{1}H-^{15}N$ HSQC, $^{1}H-^{15}N$ TOCSY-HSQC and $^{1}H-^{15}N$ NOESY-HSQC experiments were carried out at 25°C on a Varian Unity 600 MHz spectrometer equipped with three channels and a pulse-field gradient triple

Table 4.1. Acquisition parameters for NMR experiments.

Experiment	Nucleus			No. of complex points			Spectral widths (Hz)			Scans
	F1	F2	F3	F1	F2	F3	F1	F2	F3	
^{1}H-^{15}N HSQC (pH 7.0)	^{15}N	$^{1}H^{N}$		256	1024		2000	8000		224
^{1}H-^{15}N TOCSY HSQC	^{1}H	^{15}N	$^{1}H^{N}$	240	64	1024	7000	1885	8000	12
^{1}H-^{15}N NOESY HSQC	^{1}H	^{15}N	$^{1}H^{N}$	256	64	1024	7000	1885	8000	16
HNCO	^{15}N	^{13}CO	$^{1}H^{N}$	64	128	1024	1625	1541	6000	24
^{1}H-^{15}N HSQC (pH 5.4)	^{15}N	$^{1}H^{N}$		256	1024		1600	8000		32
HNCA	$^{13}C_{\alpha}$	^{15}N	$^{1}H^{N}$	168	56	1024	3268	1600	8000	16
HN(CO)CA	$^{13}C_{\alpha}$	^{15}N	$^{1}H^{N}$	168	56	1024	3268	1600	8000	16
HN(CA)CB	$^{13}C_{\beta}$	^{15}N	$^{1}H^{N}$	128	56	1024	7650	1600	8000	16

resonance probe. Mixing times in the ^{15}N-^{1}H TOCSY-HSQC and ^{15}N-^{1}H NOESY-HSQC experiments were 32 ms and 72 ms respectively. All triple resonance experiments were acquired at 25°C on a Varian Unity 500 MHz spectrometer equipped with three channels and a pulsed-field gradient triple resonance probe (with sequential quadrature detection during the detection period). The acquisition parameters for all experiments are listed in Table 4.1 (p.101). Chemical shifts were directly (^{1}H) and indirectly (^{13}C,^{15}N) referenced to DSS at 0 ppm as described by Wishart et al. (1995). Spectra were processed and peak-picked on a Sun Ultra 1 workstation, using the NMRPipe (Delaglio et al., 1995) and PIPP (Garrett et al., 1991) software packages.

Assignment strategy. A two-step approach was adopted to achieve the sequential polypeptide backbone resonance assignments. The first step was to use the ^{1}H-^{15}N HSQC (Figures 4.8 and 4.9, p.104-105) spectrum of HAV 3C protease to make unambiguous assignments for a number of amino acid types and use them as starting and check-points in later data tracing. This required the use of ^{1}H-^{15}N HSQC spectra from residue-specific ^{15}N labelled HAV 3C protease samples (as discussed in Chapter 3). Using these spectra, $^{1}H_N$ and ^{15}N assignments were made for a significant portion of the alanine, glycine, leucine, lysine, isoleucine and valine residue types. It is important to note that all ^{1}H-^{15}N HSQC spectra for the residue-specific ^{15}N labelled HAV 3C protease samples, except the isoleucine sample, were collected at pH 7.0 whereas the ^{1}H-^{15}N HSQC spectra of uniform and isoleucine ^{15}N-labelled HAV 3C protease were collected at pH 5.4. This was somewhat problematic due to differences in the amide chemical shifts observed at different pH values. Only those resonances in the residue-specific HSQC spectra that could be unambiguously assigned to peaks in the uniformly labelled HSQC spectrum were used.

The second step in the assignment process was to find sequential connectivities of the backbone resonances. Initially, chemical shift "clusters" were assembled by comparing spin system data collected from HNCA, HN(CO)CA,

HN(CA)CB and the residue-specific HSQC data. This process began by using the residue-specific HSQC data to assign a residue type to a peak in the uniformly labelled HSQC spectrum. Next its $^{1}H_{N}$, ^{15}N, $^{13}C_{\alpha}$ and $^{13}C_{\beta}$ chemical shifts ('i' chemical shifts) would be determined along with the $^{13}C_{\alpha}$ and $^{13}C_{\beta}$ chemical shifts of the preceding residue ('i-1' chemical shifts). This 'spin system' assignment process was repeated for all peaks in the uniformly labelled HSQC spectrum. Chemical shift clusters were built in the 'i-1' direction by correlating the $^{13}C_{\alpha}$(i) and $^{13}C_{\beta}$ (i) chemical shifts from one spin system with the original (known residue-type) spin system's $^{13}C_{\alpha}$ (i-1) and $^{13}C_{\beta}$ (i-1) chemical shifts. Similarly, clusters could be built moving in the 'i + 1' direction by reversing the above protocol. This process is demonstrated in Figure 4.10 (p.106), which shows sequential connectivities being made between G195 to L199 using information afforded by the HNCA spectrum. When a sizeable cluster was built (4-6 residues long), we would observe what residue type we started with (eg. Lys) and observe the other spin systems involved in the cluster. Usually, one of the other spin systems would also have been assigned to a specific residue type. Additionally, ideas about what residues were responsible for the other spin systems in the cluster could be generated by comparing the observed chemical shifts of the spin system to expected random coil chemical shifts for residue-type spin systems (Wishart et al., 1995). Once this was accomplished for a given cluster, the string of residues (known residue types and hypothesized residue types) was then fitted into the HAV 3C sequence. When a positive match for a given sequential cluster could be made, the sequential backbone chemical shift information was inserted into Table 4.2 (p.109).

Because of the large size of the HAV 3C protease (23.8 kDa), chemical shift degeneracy often posed a challenging problem. In the process of either building up one cluster or linking two clusters together, it was always necessary to match up one or two chemical shifts (^{13}C and ^{13}C). In some cases, multiple choices were available. When a positive decision could not be made, we would stop and start from another marker, that being of a known residue type.

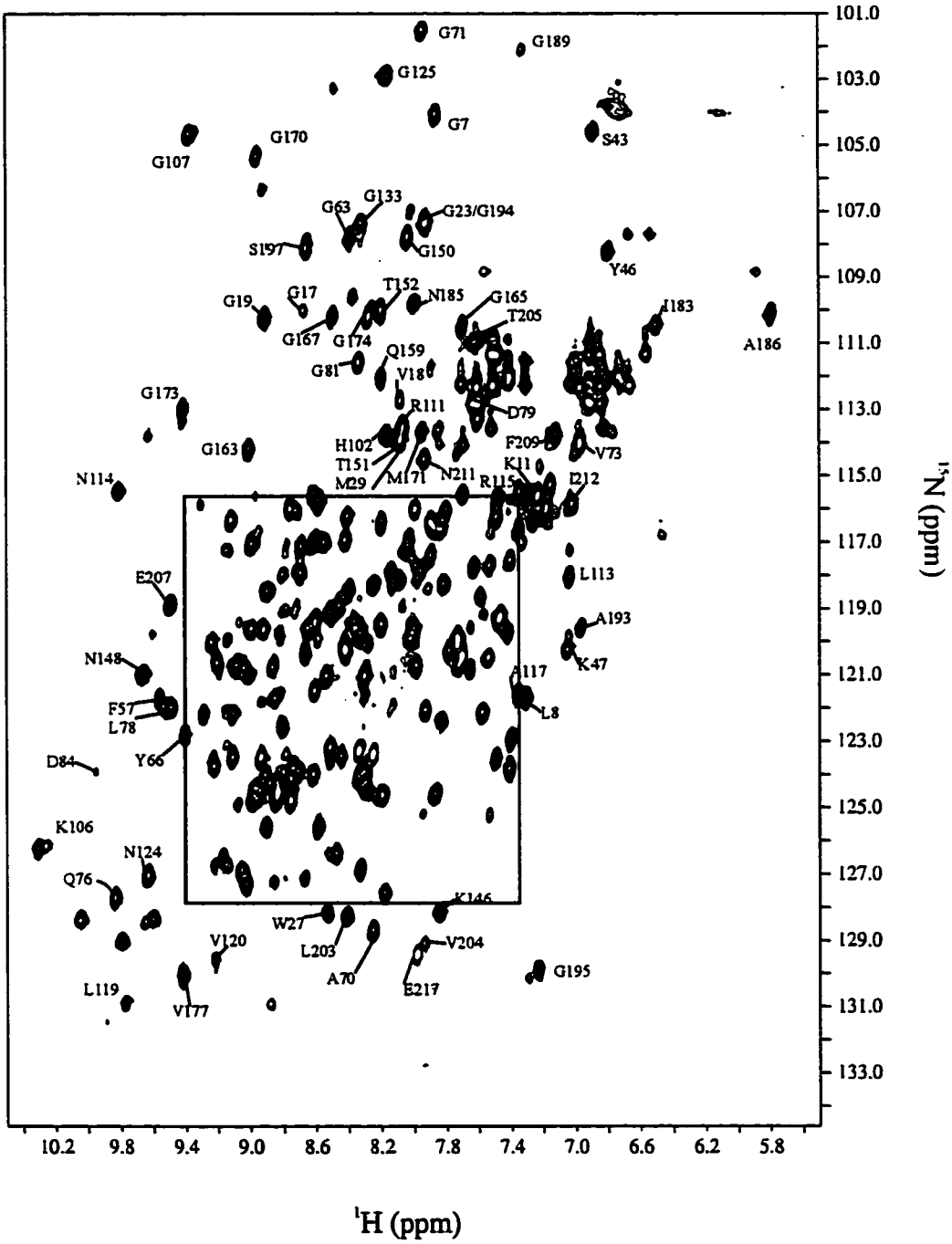

Figure 4.8. ^{1}H-^{15}N HSQC spectrum from 1 mM HAV 3C protease in 20 mM KH_2PO_4, 100 mM NaCl, 0.5 mM EDTA, 1.0 mM DTT at pH 5.4 collected at 25°C on a Varian Unity 600 MHz spectrometer.

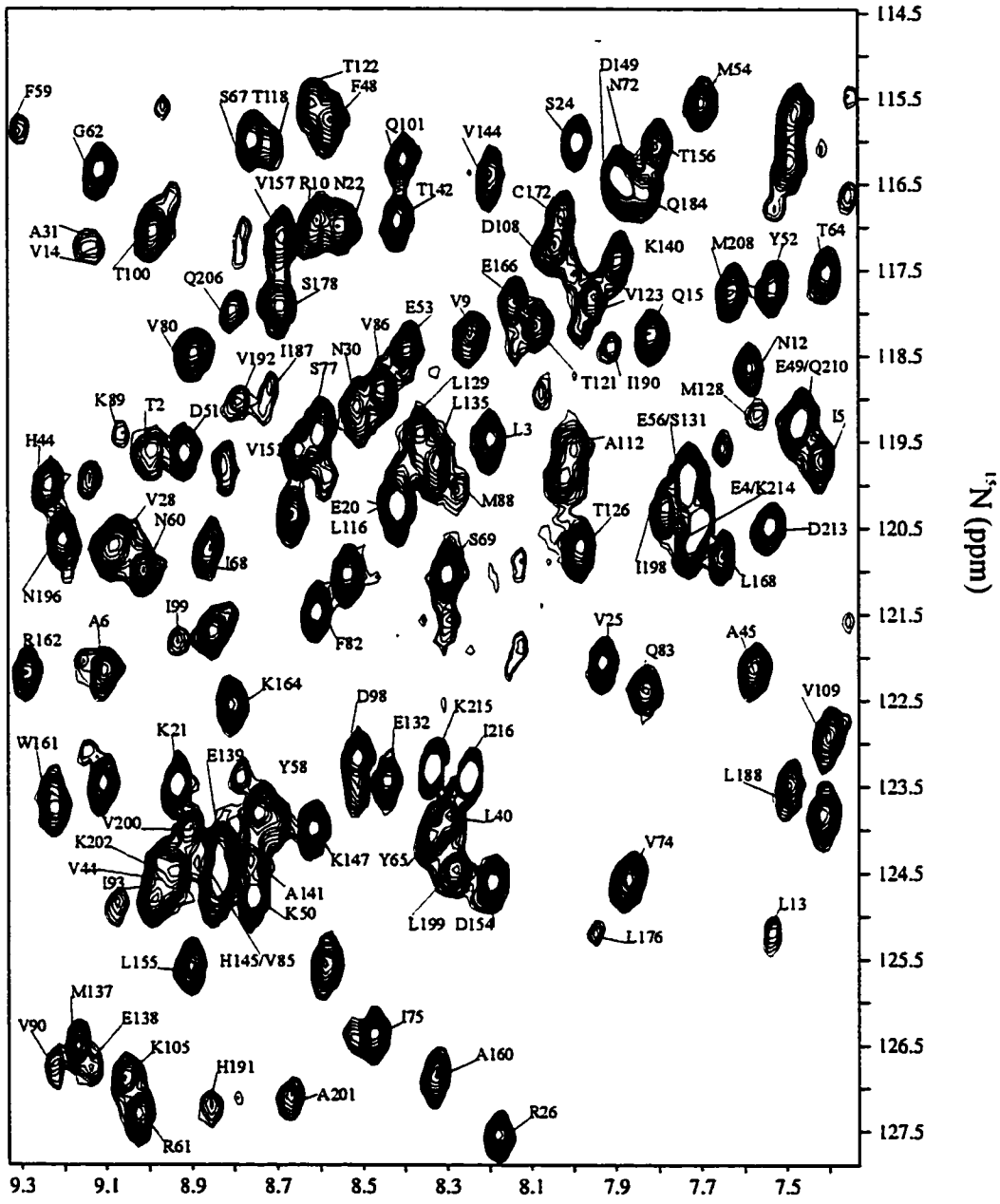

Figure 4.9. Expanded region of ^{1}H-^{15}N HSQC spectrum from 1 mM HAV 3C protease in 20 mM KH_2PO_4, 100 mM NaCl, 0.5 mM EDTA, 1.0 mM DTT at pH 5.4 collected at 25°C on a Varian Unity 600 MHz spectrometer.

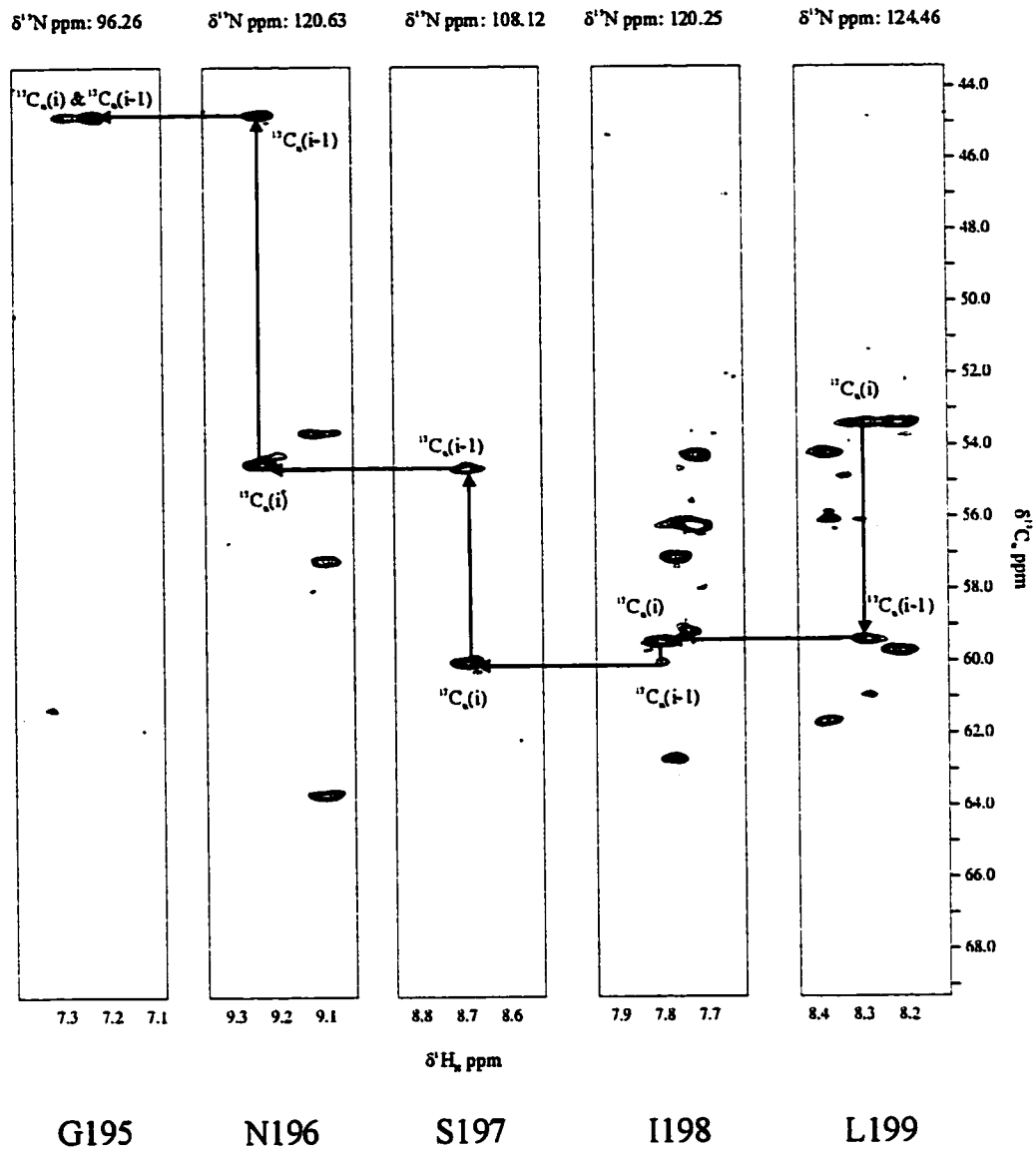

Figure 4.10. Polypeptide backbone assignments of Gly195, Asn196, Ser197, Ile198 and Leu199. An example how assignments could be extended in both directions using the 3D HNCA. The HNCA experiment was performed on the ^{2}H, ^{13}C, ^{15}N uniformly labelled HAV 3C protease (1mM) in 20 mM KH_2PO_4, 100 mM NaCl, 0.5 mM EDTA, 1.0 mM DTT, 10%D_2O, pH 5.4 at 25°C using a Varian Unity 500 MHz spectrometer.

4.4 Results and Discussion

Spin system assignments. The general approach for assigning the backbone spin system resonances ($^{1}H_N$, ^{15}N, $^{13}C_\alpha$, $^{13}C_\beta$, $^{1}H_\alpha$ and $^{13}CO(i-1)$) was based on the use of the ^{1}H-^{15}N HSQC spectrum collected at pH 5.4 (Figure 4.8) as a chemical shift fingerprint of the observable amides. This spectrum displayed 204 of the expected 210 resonances (217 – 7 prolines). This less-than-perfect result is due to several amide resonances having the same (or very similar) $^{1}H_N$ and ^{15}N chemical shifts. Amide HN pairs identified in the HSQC were correlated to the backbone ^{13}C resonances using HNCA and HN(CO)CA spectra. The HNCA spectrum provided both intraresidue (i) and interresidue (i-1) $^{13}C_\alpha$ resonances with the intraresidue resonance usually being of a noticeably higher intensity. The HN(CO)CA spectrum was used to unambiguously determine which resonance in the HNCA spectrum belonged to the interresidue $^{13}C_\alpha$ resonance. Using these two spectra, 205 $^{13}C_\alpha$ resonances could be identified. Similarly, HN pairs were correlated to $^{13}C_\beta$ resonances using the HN(CA)CB spectrum. This spectrum provided both intraresidue and interresidue $^{13}C_\beta$ resonance information. The intraresidue $^{13}C_\beta$ resonance was assumed to be the more intense of the two. The HN(CA)CB experiment was not as sensitive as the HNCA and HN(CO)CA experiments and consequently only 170 $^{13}C_\beta$ resonances could be identified.

Determining $^{1}H_\alpha$ and ^{13}CO (i-1) resonances for each spin system required the use of ^{1}H-^{15}N HSQC, ^{1}H-^{15}N TOCSY-HSQC, ^{1}H-^{15}N NOESY-HSQC, and HNCO spectra, all of which were acquired at pH 7.0. This was done after the sequential assignments had been made using the HNCA, HN(CO)CA, HN(CA)CB and residue-specific HSQC spectra. To determine $^{1}H_\alpha$ and ^{13}CO (i-1) resonance assignments, it was necessary to determine which HN resonances in the 'high-pH' ^{1}H-^{15}N HSQC could be unambiguously equated to HN resonances in the 'low-pH' ^{1}H-^{15}N HSQC. Differences in the amide chemical shifts between these two spectra likely arose from differences in protonation states of acidic (aspartate, glutamate, cysteine and tyrosine) and basic (arginine, lysine, histidine) amino acids.

Changing the protonation-state will invariably change the surrounding electronic environment which amide chemical shifts are notoriously sensitive to (MacLachlan et al., 1997). Consequently, with so many differing amide resonances, equivalency could only be established for 71 HN pairs between the 'high-pH' and 'low-pH' HSQC spectra.

The equivalent, 'high-pH' HN pairs were subsequently correlated to ^{1}H resonances using ^{1}H-^{15}N TOCSY-HSQC and ^{1}H-^{15}N NOESY-HSQC spectra. It is important to note that these spectra were of much lower quality than the other triple resonance spectra. If a ^{1}H chemical shift was not present in the TOCSY spectrum, the NOESY spectrum was used to determine the most likely $^{1}H_{\alpha}$ chemical shift based on the NOEs observed for that spin system (i.e. presence detected in the 'i + 1' spin system). Similarly, the equivalent HN pairs (at high pH) were correlated to $^{13}CO(i-1)$ resonances using the HNCO spectrum. Because the HNCO was a triple resonance experiment, this spectrum was significantly more sensitive than the ^{15}N-edited experiments (TOCSY and NOESY) and nearly all expected ^{13}CO resonances could be observed. However, only those $^{13}CO(i-1)$ chemical shifts that correlated to the 71 HN pairs are reported. The last step was to assign the ^{13}CO (i-1) resonances to their own respective (i) spin system according to the HAV 3C protease sequence.

Sequential assignments. Chemical shift information from HNCA, HN(CO)CA, HN(CA)CB and information from the ^{1}H-^{15}N HSQC spectra of the ^{15}N residue-specific labelled proteases have allowed 175 sequential assignments to be made (Table 4.2). Initially, HNCA, HN(CO)CA and residue-specific HSQC spectra were used to link up $^{13}C_{\alpha}(i)$ and $^{13}C_{\alpha}(i-1)$ resonances (Figure 4.10). However, many ambiguities arose due to similarities in the $^{13}C_{\alpha}$ resonances of amino acids such as histidine, leucine, methionine and glutamine. All of these residues typically have $^{13}C_{\alpha}$ random coil chemical shifts at approximately 53 ppm (Wishart et al., 1995b). Using this method, about 65 percent of the sequential assignments could be made. The $^{13}C_{\beta}$ resonance information collected from the HN(CA)CB

Table 4.2. Sequential backbone chemical shifts assignments of HAV 3C protease.

Residue		^{15}N	$^{1}H_N$	$^{13}C_\alpha$	$^{13}C_\beta$	^{15}N*	$^{1}H_N$*	$^{1}H_\alpha$*	^{13}CO*
1	S			56.89	63.69				
2	T	119.60	8.99	66.49	67.75				
3	L	119.46	8.19	57.33	40.38				
4	E	120.75	7.73	58.66	28.79				
5	I	119.71	7.41	61.01	34.25				178.54
6	A	122.15	9.10	55.08	17.60	122.26	9.10	3.92	179.58
7	G	104.03	7.86	46.68		104.34	7.85	3.92	176.12
8	L	121.68	7.30	57.12	40.78	122.31	7.34	4.05	180.09
9	V	118.24	8.24	66.16	30.93	118.68	8.24	3.35	178.14
10	R	116.91	8.60	59.51	28.61	117.1	8.58	3.83	179.11
11	K	115.62	7.29	57.75	31.41	116.04	7.32	4.25	176.58
12	N	118.63	7.58	51.96	38.32	118.99	7.60	5.03	174.11
13	L	125.20	7.53	55.40	42.66	125.45	7.55	4.98	177.25
14	V	117.25	9.17	58.29		117.50	9.11	5.17	175.47
15	Q	118.25	7.81	56.39	30.93	118.30	7.76	5.14	
16	F			54.0					
17	G	109.99	8.67	43.64					169.59
18	V	112.74	8.08	58.56	35.01	112.33	8.12	5.25	
19	G	110.22	8.90	45.32					
20	E	120.24	8.46	54.59	30.93				
21	K	123.48	8.93	58.04	31.02				
22	N	116.99	8.55	53.55	37.12				175.18
23	G	107.32	7.94	44.30		107.60	7.92	4.23	173.83
24	S	116.01	7.99	57.46	63.94	116.20	8.04	4.40	173.06
25	V	122.05	7.93	61.13	32.02	122.32	7.93	3.46	174.48
26	R	127.54	8.18	53.73	30.14	128.11	8.25	4.36	
27	W	128.14	8.52	57.02	28.05				
28	V	120.68	9.07	63.55	34.33				
29	M	113.6	8.06	56.04	29.43				
30	N	119.09	8.51	52.55	42.03				
31	A	117.25	9.14	50.73	22.64				
32	L								
33	G								
34	V								
35	K								
36	D								
37	D								
38	W								
39	L								
40	L								
41	V								
42	P								
43	S								
44	H	119.98	9.23	57.73	26.01				
45	A	122.11	7.57	54.22	19.29				
46	Y	108.20	6.79	56.63	41.35				
47	K	120.22	7.04	57.27	31.1				
48	F	115.75	8.57	56.97	37.28				
49	E	119.23	7.46	54.15	28.86				
50	K	124.78	8.75	57.03	31.69				
51	D	119.64	8.91	54.68	38.72				

Residue		^{15}N	$^{1}H_N$	$^{13}C_\alpha$	$^{13}C_\beta$	^{15}N*	$^{1}H_N$*	$^{1}H_\alpha$*	^{13}CO*
52	Y	117.69	7.53	60.03	37.27				
53	E	118.42	8.39	58.19	27.45				
54	M	115.54	7.69	54.30	31.83				
55	M								
56	E								
57	F	121.72	9.56	57.33	39.88				
58	Y	123.8	8.74	55.88	39.90				
59	F	115.88	9.30	55.09	42.46				
60	N	120.99	9.01	51.45	38.55				
61	R	127.30	9.02	53.99	31.19				
62	G	116.34	9.11	46.79					174.95
63	G	107.79	8.38	44.59		108.00	8.41	4.01	173.87
64	T	117.52	7.40	61.40	69.68	117.72	7.41	4.20	
65	Y	124.07	8.33	53.93	37.43				
66	Y	122.77	9.40	57.17	40.58				
67	S	116.00	8.75	55.89	66.79				
68	I	120.73	8.86	59.50	41.02				
69	S	121.04	8.30	58.30	62.94				
70	A	128.67	8.24	54.59	18.40				
71	G	101.48	7.94	45.35					
72	N	116.55	7.87	52.26	39.33				175.08
73	V	114.02	6.97	60.35	32.43	114.75	7.00	4.56	175.14
74	V	124.57	7.87	62.13	32.42	125.14	7.89	4.25	174.35
75	I	126.37	8.47	58.80	39.40	126.84	8.49	5.27	176.44
76	Q	127.72	9.83	53.42	31.59	128.09	9.84	4.94	
77	S	119.41	8.60	57.77	64.24				
78	L	121.97	9.49	55.93	41.86				
79	D	112.82	7.60	51.51	42.43				
80	V	118.47	8.89	62.50	31.73				
81	G	111.59	8.33	43.85					
82	F	121.47	8.60	58.46	38.80				
83	Q	122.38	7.83	52.97	27.85				175.50
84	D	123.93	9.95	53.70		123.86	9.95	5.51	
85	V	124.6	8.83	63.02					178.20
86	V	118.89	8.45	58.66		119.41	8.50	4.86	
87	L								
88	M								
89	K								
90	V								
91	P								
92	T								
93	I								
94	P								
95	K								
96	F								
97	R			55.88	29.69				
98	D	123.16	8.51	53.24	39.58				
99	I	121.81	8.93	60.88					177.89
100	T	117.06	8.98	65.22	68.85	117.02	8.99	3.60	177.03
101	Q	116.21	8.40	56.24	26.70	116.24	8.42	4.20	
102	H	113.75	8.16	55.39	27.60				
103	F								
104	I			59.88	39.61				
105	K	126.89	9.05	55.93	31.90				179.34

Residue		^{15}N	$^{1}H_N$	$^{13}C_\alpha$	$^{13}C_\beta$	^{15}N*	$^{1}H_N$ *	$^{1}H_\alpha$*	^{13}CO*
106	K	126.30	10.3	60.01	31.30	126.56	10.33		179.86
107	G	104.65	9.37	45.48		104.88	9.43	3.94	174.35
108	D	117.20	8.04	53.99	41.83	117.49	8.07	5.06	177.05
109	V	122.92	7.40	68.65	30.00	123.17	7.42	3.93	
110	P			65.10					
111	R	113.49	8.06	56.97					
112	A	119.59	7.99	51.09	20.88				177.85
113	L	118.07	7.03	55.29	42.24	118.27	7.04	4.10	176.71
114	N	115.46	9.81	54.53	36.95	115.75	9.85	4.26	173.30
115	R	115.47	7.34	52.54	31.64	115.77	7.37	4.83	176.00
116	L	120.24	8.42	55.09	40.37	120.64	8.45	4.73	
117	A	121.56	7.35	51.31	23.78				
118	T	116.00	8.75	61.12	71.31				172.36
119	L	130.88	9.77	53.78	40.46	131.19	9.77	5.66	173.76
120	V	129.51	9.21	61.06	30.79	129.90	9.25	4.35	
121	T	118.15	8.08	58.31	68.86				
122	T	115.56	8.61	60.61	71.11				
123	V	117.81	7.95	61.73	32.74				
124	N	127.05	9.63	53.67	36.98				175.18
125	G	102.87	8.15	44.64		103.09	8.18	4.25	174.41
126	T	120.70	7.98	60.23	69.33	120.97	8.00	4.60	
127	P								
128	M								
129	L								
130	I								
131	S	120.02	7.73	58.90					
132	E	123.44	8.44	55.63	28.45				
133	G	107.36	8.32	44.80					
134	P			62.76	31.48				
135	L	119.73	8.32	54.59	36.87				
136	K			53.75					
137	M	126.50	9.16	53.45					
138	E	126.76	9.13	53.45	29.94				
139	E	124.6	8.83	59.24	28.71				
140	K	117.40	7.89	54.63	35.10				
141	A	124.36	8.75	50.63	21.96				
142	T	116.92	8.41	60.02	70.47				
143	Y			54.82	38.55				
144	V	116.38	8.19	60.63	33.66				
145	H	124.28	8.83	54.76	32.24				
146	K	128.13	7.84	54.87	32.10				176.76
147	K	123.99	8.61	55.84	32.47	124.36	8.70	4.51	178.22
148	N	121.00	9.66	55.49	37.18	122.11	9.63	4.60	
149	D	116.39	7.89	52.82	39.35				
150	G	107.77	8.03	44.90					174.62
151	T	113.92	8.08	61.65	69.98	114.05	8.08	4.47	173.50
152	T	110.00	8.19	59.87	71.03	109.66	8.17	5.28	174.53
153	V	119.59	8.64	59.47	34.16	119.76	8.74	4.31	172.95
154	D	124.60	8.19	53.13	40.40	125.26	8.13	4.89	175.15
155	L	125.58	8.90	53.22	41.87	125.96	8.89	4.43	
156	T	116.06	7.80	60.62	71.04				
157	V	117.11	8.68	57.89	34.43				
158	D			53.45	42.23				
159	Q	112.02	8.19	57.40	26.37				172.26

Residue		^{15}N	$^{1}H_N$	$^{13}C_\alpha$	$^{13}C_\beta$	^{15}N*	$^{1}H_N$*	$^{1}H_\alpha$*	^{13}CO*
160	A	126.84	8.32	49.43	21.57	126.54	8.31	4.98	
161	W	123.75	9.22	55.17	31.14				
162	R	122.18	9.28	54.44	33.03				
163	G	114.20	9.00	43.15					172.35
164	K	122.55	8.80	55.14	33.82	122.83	8.83	5.04	
165	G	110.45	7.69	44.17					
166	E	117.87	8.13	54.32	29.34				175.22
167	G	110.18	8.49	43.99		110.43	8.54	4.48	172.74
168	L	120.82	7.65	51.73	43.45	120.77	7.65	3.80	
169	P			65.44	31.38				
170	G	105.33	8.96	45.64					
171	M	113.64	7.94	56.16	33.11				176.17
172	C	116.86	8.02	61.60	28.52	116.61	8.04	4.61	
173	G	112.95	9.41	44.81					172.62
174	G	110.20	8.27	44.55		110.41	8.31	4.33	171.59
175	A	118.93	8.07	49.79	23.11	119.03	8.09	5.29	174.60
176	L	125.20	7.95	52.89		125.47	7.97	4.63	
177	V	130.05	9.41	58.03	28.08				
178	S	117.92	8.69	61.12	62.36				
179	S								
180	N								
181	Q								
182	S				61.12				
183	I	110.44	6.50	59.95	35.44				
184	Q	116.60	7.83	56.58	24.95				175.14
185	N	109.79	7.99	55.50	36.87	109.69	7.96	3.79	171.34
186	A	110.04	5.79	52.21	19.04	110.53	5.86		
187	I	118.85	8.71	61.49					
188	L	123.49	7.49	55.60	43.98				178.90
189	G	102.05	7.32	45.32		102.44	7.35	4.14	171.14
190	I	118.40	7.91	55.35	39.87	118.46	7.92	5.25	
191	H	127.19	8.85	58.89	32.33				
192	V	119.03	8.78	61.34	34.93				
193	A	119.55	6.96	52.30	21.21				175.18
194	G	107.32	7.92	44.88		107.60	7.92	4.23	
195	G	96.26	7.23	44.54					
196	N	120.63	9.20	54.32	36.97				
197	S	108.12	8.65	59.75	62.11				
198	I	120.25	7.78	59.16	39.98				
199	L	124.46	8.28	53.12	41.87				
200	V	123.98	8.90	60.58	33.64				173.59
201	A	127.08	8.66	49.33	21.12	127.61	8.69	5.27	
202	K	124.0	8.70	54.27	29.74				176.27
203	L	128.24	8.40	56.55	41.62	128.81	8.41		175.82
204	V	129.08	7.93	60.94	34.73	129.27	7.97		
205	T	110.95	7.62	57.49	71.23				
206	Q	117.98	8.80	58.45	28.78				179.29
207	E	118.87	9.49	60.34	27.41	119.04	9.51	3.93	179.17
208	M	117.76	7.62	57.95	30.41	118.00	7.65	4.00	176.97
209	F	113.74	7.12	57.32	36.94	113.99	7.14	4.32	176.98
210	Q	119.31	7.47	57.92	27.84	119.65	7.48	4.09	
211	N	114.48	7.93	54.01	38.01	114.83	7.96	4.60	176.04
212	I	115.26	7.15	62.65	36.80	115.99	7.16	3.54	175.55
213	D	120.47	7.54	53.94	40.35	120.70	7.55	4.44	175.74

Residue		^{15}N	$^{1}H_N$	$^{13}C_\alpha$	$^{13}C_\beta$	^{15}N*	$^{1}H_N$*	$^{1}H_\alpha$*	^{13}CO*
214	K	120.74	7.71	55.93	32.39	120.79	7.71	4.27	176.21
215	K	123.29	8.33	55.83	32.21	123.99	8.40	3.83	176.34
216	I	123.37	8.24	60.69	37.81	124.02	8.33	4.35	175.32
217	E	129.40	7.98	57.20	30.33	130.23	8.01	4.19	

Chemical shifts were directly (^{1}H) and indirectly (^{13}C,^{15}N) referenced to DSS at 0.00 ppm as described by Wishart et al., (1995). * Chemical shifts at pH 7.0.

experiment sorted out many ambiguities that arose from problems of $^{13}C_\alpha$ chemical shift overlap. Using both $^{13}C_\alpha$ and $^{13}C_\beta$ chemical shift information helped define and differentiate spin systems much better as random coil $^{13}C_\beta$ chemical shifts for histidine, leucine, methionine, and glutamine are 29.0, 41.7, 32.4 and 29.2 ppm respectively. This $^{13}C_\beta$ information was particularly useful when trying to identify what residue type was responsible for a given spin system. It also provided an additional data point when building chemical shift clusters.

The amide peak in the ^{1}H-^{15}N HSQC spectrum that displayed the greatest intensity (at 129.40/7.98 ppm) corresponded to the C-terminus (Glu217). This intense peak was a favorable starting point and connectivities, in the 'i-1' direction, were made using information contained in HNCA, HN(CO)CA and HN(CA)CB spectra. This initial stretch continued until Ala193 where the resonance intensity in all spectra began to drop off. Resonance assignments (A193, G194, G195, I198, L199, etc.) were confirmed with the HSQC spectra collected from ^{15}N residue-specific labelled HAV 3C protease. This integrated approach to sequentially assigning the backbone was repeated throughout the assignment process. Other starting points were Lys11 and Val109, as they belonged to helical regions that had been assigned using the initial ^{15}N-edited experiments. Sequential stretches were assigned from these starting points and confirmed with residue-specific HSQC data. Once these sequentially assigned stretches could no longer be extended, other peaks were selected from the residue-specific HSQC spectra to serve as new starting points. Generally, the best check for correctness of a sequentially assigned cluster was to simply note the difference in $^{13}C_\alpha$ and $^{13}C_\beta$ chemical shift

values between residues 'i' and 'i-1'. A correctly assigned cluster would rarely show chemical shift difference greater than 0.1 ppm.

Table 4.2 displays a couple regions (32-43, 87-96, 127-130 and 179-181) that could not be assigned. Generally, the residues that have been assigned on either side of these regions displayed very weak or no $^{13}C_{\alpha}$ and $^{13}C_{\beta}$ chemical shifts and it is likely that those residues within the unassigned regions also have weak resonances. The weak resonance intensity could be due to the fact those residues are in mobile regions in some kind of intermediate or slow exchange process.

'Observed' versus 'predicted' HAV 3C protease chemical shifts. Comparisons between the observed and predicted chemical shifts for HAV 3C protease are displayed in Figure 4.11 (p.115). Predicted chemical shifts for ^{15}N, $^{1}H_{N}$, $^{13}C_{\alpha}$, $^{13}C_{\beta}$ and ^{13}CO shifts were obtained from SHIFTX, whereas the predicted ^{1}H chemical shifts were calculated using TOTAL (Williamson et al., 1995). Correlation coefficients of 0.76, 0.60, 0.97, 0.99, 0.78 and 0.78 were determined for ^{15}N, $^{1}H_{N}$, $^{13}C_{\alpha}$, $^{13}C_{\beta}$, $^{1}H_{\alpha}$ and ^{13}CO chemical shifts respectively. Although all these values indicate a 'good' correlation between observed and predicted data, the $^{13}C_{\alpha}$ and $^{13}C_{\beta}$ correlations are nearly perfect. It is likely that these chemical shifts, relative to their chemical environment and structure, are more easily predicted than the other types of chemical shifts.

Correlation coefficients for ^{15}N, $^{1}H_{N}$,$^{1}H_{\alpha}$ and ^{13}CO are lower than those noted for the $^{13}C_{\alpha}$ and $^{13}C_{\beta}$. For this reason, we studied the eight residues that showed the greatest difference between observed and predicted ^{15}N, $^{1}H_{N}$,$^{1}H_{\alpha}$ and ^{13}CO chemical shifts (Table 4.3, p.116). This was done to determine if any trends could be found that might indicate structural differences between the solution and X-ray structures of HAV 3C protease. Trends that can be noted in Table 4.3 are I212 appearing in 3 (^{15}N, $^{1}H_{N}$, and ^{13}CO) of the 4 categories and 50 percent of the residues showing the greatest difference in ^{13}CO chemical shifts are glycines. I212

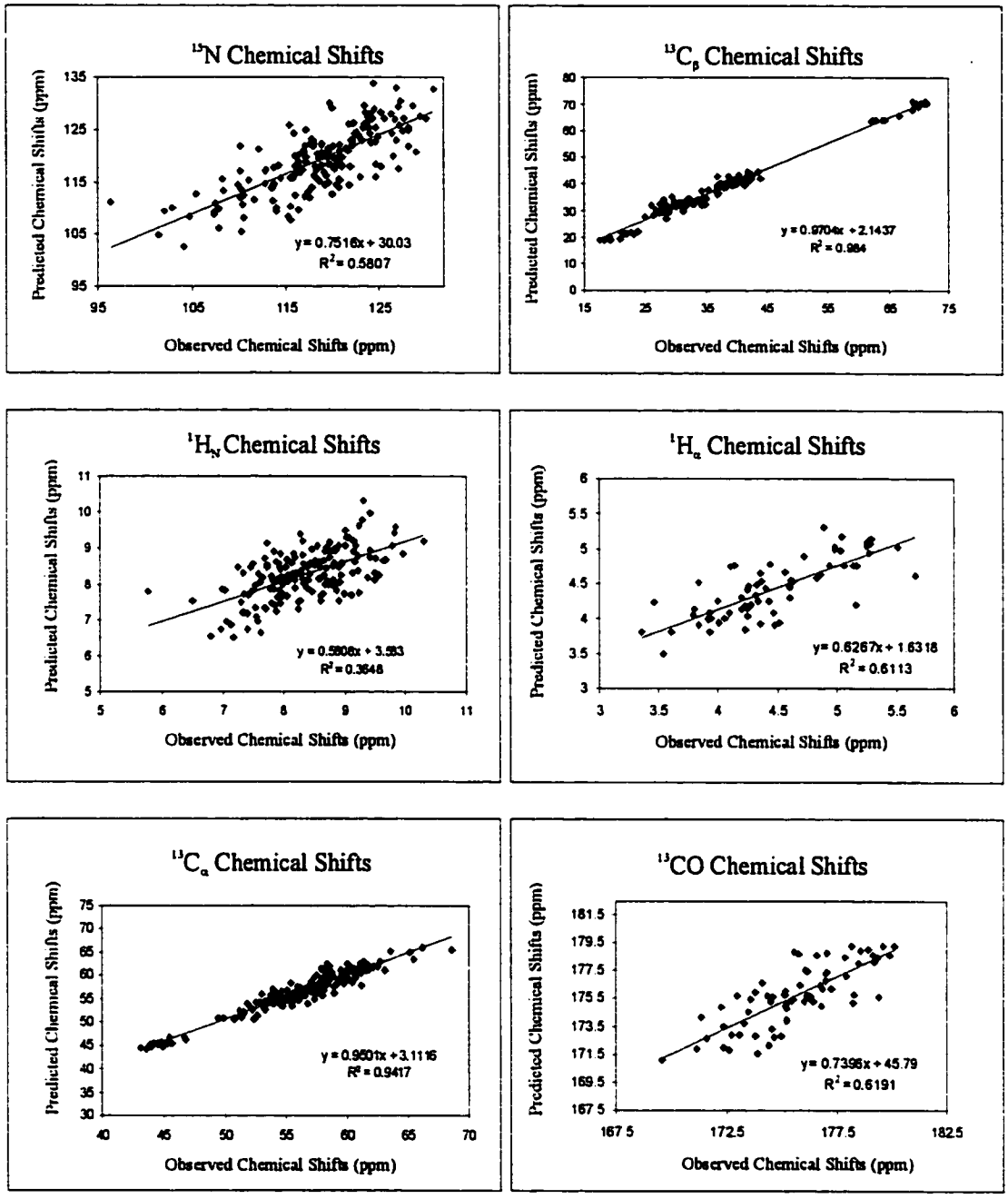

Figure 4.11. Predicted versus observed chemical shifts for HAV 3C protease. Predicted chemical shifts for ^{15}N, $^{1}H_N$, $^{13}C_\alpha$, $^{13}C_\beta$ and ^{13}CO shifts were obtained from SHIFTX, whereas the $^{1}H_\alpha$ predicted chemical shifts came from the TOTAL program (Williamson et al., 1992).

Table 4.3. The 8 residues showing the greatest differences between observed and predicted ^{15}N, $^{1}H_N$, $^{1}H_\alpha$ and ^{13}CO chemical shifts.

^{15}N			$^{1}H_N$		
Residue	Observed	Predicted	Residue	Observed	Predicted
N114	115.46	125.74	H44	9.23	7.75
N124	127.05	117.60	F59	9.30	10.34
L135	119.73	129.93	Y66	9.40	9.96
A141	124.36	133.84	L155	8.90	7.55
Q159	112.02	121.23	A186	5.79	7.78
A186	110.04	121.80	L199	8.28	9.38
G194	96.26	111.14	M208	7.62	6.63
I212	115.26	108.29	I212	7.15	6.51
$^{1}H_\alpha$			^{13}CO		
Residue	Observed	Predicted	Residue	Observed	Predicted
V25	3.46	4.23	G62	174.95	172.80
R111	5.16	4.21	G63	173.87	171.60
L113	4.10	4.74	V85	178.20	175.21
L119	5.66	4.61	K105	179.34	175.61
D154	4.89	5.30	G125	174.41	172.10
G167	4.48	3.91	G173	172.62	171.80
G189	4.14	4.77	I212	175.55	178.84
K215	3.83	4.51	D213	175.74	178.69

was assigned using all of our spectra (^{15}N-edited and triple resonance) therefore it is unlikely that it is assignment incorrectly. This result may be indicating that the environment surrounding I212 is different in the solution-state compared to that in the solid-state. The result that 50 percent of the residues showing greatest differences in ^{13}CO chemical shifts are glycines may indicate that glycine ^{13}CO chemical shifts are more difficult to predict than other residue types. Otherwise,

those residues that are present in Table 4.3 do not show any obvious trends. As a result, it is very likely that there is no indication of structural differences, between solution and solid states of HAV 3C protease, that can be inferred from the differences found between our observed and predicted chemical shift sets.

Secondary structure of HAV 3C protease. The $^{13}C_{\alpha}$,$^{13}C_{\beta}$,$^{1}H_{\alpha}$ and ^{13}CO chemical shifts are sensitive to secondary structure. In fact, the secondary structure can be accurately predicted from these chemical shifts using the CSI method (Wishart et al., 1992, 1994). The CSI program (Wishart et al., 1994) was used to calculate indices for most amino acid residues in HAV 3C protease using available chemical shift information. Consequently, some stretches of secondary structure were predicted based on information from only one type of chemical shift and certain stretches (32-43, 87-96, 127-130 and 179-181) had no chemical shift assignments therefore no structure could be predicted. Obviously, a more accurate prediction of secondary structure could be attained as soon as all chemical shifts have been assigned. However, Table 4.4 displays the results of the CSI predictions based on the current set of chemical shift assignments. As can be seen, 11 β-strands and 2 α-helices have been predicted. The position and extent of these structural elements are in good agreement with structural elements in HAV 3C proteases crystal structure (Bergmann et al., 1997), as calculated by VADAR. VADAR (Wishart et al., 1994) used the 3D coordinates of the HAV 3C protease PDB file (1HAV) to calculate the secondary structure elements. It is likely that the differences between the CSI predictions and secondary structure from X-ray data would be significantly less if complete chemical shift assignments were present.

Table 4.4. Comparison of secondary structure features of HAV 3C protease obtained from CSI and X-ray diffraction methods. VADAR (Wishart, 1994) was used to calculate secondary structure from the PDB file (1HAV) of the X-ray crystal structure of HAV 3C protease (Bergmann et al., 1997). *From the PDB file (1HAV) as this α-helix was not calculated by VADAR.

β-Strands					α-Helices				
CSI				Vadar	CSI				Vadar
C_α	C_β	H_α	CO		C_α	C_β	H_α	CO	
					6-11		6-11	2-10	2-11
				12-18					
24-27				23-25					
				28-33					
				37-41					
58-61				55-60					
64-68	66-68			65-69					
72-76	73-76	73-76		73-76					
				84-90					
				95-97					
								105-108	108-111
				103-105					
115-123	121-123			115-122					
140-147	140-143			127-146					
149-157	151-153	151-155	150-154	152-158					
160-168	160-168			160-165					
175-177				174-179					
				186-188					
	191-194			190-193					
198-202				197-204					
					206-209		208-215	206-212	*206-213

4.5 Conclusion

In conclusion, 175 of the 210 (217 residues – 7 prolines) sequential backbone assignments have been made although a majority of the ^{1}H and ^{13}CO assignments are still missing due to ^{1}H-^{15}N TOCSY-HSQC, ^{1}H-^{15}N NOESY-HSQC and HNCO experiments being performed on a HAV 3C protease sample at high pH. The three key experiments that enabled the near complete backbone assignments to be made were the "deuterium modified" HNCA, HN(CO)CA and the HN(CA)CB experiments as they yielded spectra with nearly all expected resonances. There were two reasons why these experiments were so successful. The first reason lies in the fact that we prepared this HAV 3C protease sample in solution conditions that minimized aggregation. The second reason was incorporating high levels of deuterium into the protease to combat the efficient relaxation rates of nuclei present in non-deuterated samples. The sequential

assignments that have been made are in good agreement with those chemical shifts that have been predicted by SHIFTX and TOTAL software packages based on the X-ray crystal structure of the HAV 3C protease. Finally, based on the 'Chemical Shift Index' and our present sequential assignments, secondary structure elements have been predicted that are in relatively good agreement with those structural elements determined by X-ray crystallography.

CHAPTER 5

General Discussion and Conclusion

This thesis centers on the 3C protease from Hepatitis A virus, the causal agent of one of the most common forms of acute, infectious hepatitis in the world. HAV 3C protease is a large, 217 residue protein that could serve as an excellent target for 'structure based drug design'. It is an excellent drug target because it is responsible for processing the polyprotein produced by the translation of viral mRNA and therefore, it is essential to the propagation of this virus (Linemeyer et al., 1985; Najarian et al., 1985; Palmenberg, 1990; Rueckert, 1996). The intent of this thesis was to obtain near complete ^{1}H, ^{13}C and ^{15}N backbone chemical shift assignments for HAV 3C protease. More specifically, in Chapter 2, I describe how NMR spectroscopy and ultracentrifugation studies were used in consort to identify solution conditions that minimized the macromolecular aggregation noted in our early HAV 3C protease NMR samples. In Chapter 3, I describe four expression and purification protocols that facilitated uniform ($^{2}H/^{13}C/^{15}N$, $^{13}C/^{15}N$, ^{15}N) and residue-specific (^{15}N) isotope incorporation into HAV 3C protease. Finally, in Chapter 4, I describe the heteronuclear NMR experiments, performed with single (^{15}N), doubly ($^{13}C/^{15}N$) and triply ($^{2}H/^{13}C/^{15}N$) labelled HAV 3C protease, that enabled 175 of the 217 backbone chemical shift assignments to be made. It is my contention that the sequential assignments that have been completed to date will enable NMR spectroscopy to be used in future 'drug-screening' efforts, as described in Shuker et al., (1996), to assist in the 'structure based drug design' of a protease inhibitor to fight Hepatitis A.

As I described previously in Chapters 1 and 2, to obtain "good" NMR spectra from larger proteins, it is important to ensure that the protein be mono-disperse at concentrations of 1 mM or higher. Macromolecular aggregation is often problematic in protein NMR spectroscopy as it leads to extremely efficient ^{13}C, ^{15}N and ^{1}H T_2 relaxation rates which in turn leads to significantly broadened

lines, poor resolution and loss of signal. Early NMR experiments (^{1}H-^{15}N TOCSY-HSQC, ^{1}H-^{15}N NOESY-HSQC, HNCACB, CBCA(CO)NNH) performed with HAV 3C protease in 'high salt/high pH' conditions (350 mM NaCl, 20 mM KH_2PO_4, 0.5 mM EDTA at pH 7.0) generally yielded spectra that were devoid of much of the expected chemical shift information. At that time, it was hypothesized that HAV 3C protease was behaving as an aggregate as efficient T_2 relaxation rates of nuclei in an aggregated complex could account for the significant loss of signal in these initial spectra. Additionally, $^{3}J_{HNH\alpha}$ coupling constants calculated from ^{1}H linewidths in a HAV 3C protease HMQC-J spectrum using the method of Wishart and Wang, (1998) indicated that the molecule was behaving as a dimer. Sedimentation analysis and ^{15}N T_1- and T_2-envelope studies eventually confirmed this hypothesis.

To identify solution conditions that minimized HAV 3C protease aggregation, a series of 1D ^{1}H NMR spectra were collected with the protease dissolved in approximately 25 different buffer conditions. Buffer variables that were tested included pH, temperature, NaCl concentration and the addition of CHAPS, TFE, glycine and $CaCl_2$. The quality of the amide region (sharpness and intensity of peaks) and half-height linewidth ($\Delta\nu_{1/2}$) of the Val25 γCH_3 resonance at –0.7 ppm were used to compare and contrast the behavior of HAV 3C protease under various buffer conditions. This was done because qualitative information about the presence of aggregation can be obtained by monitoring the broadening of NMR linewidths (Akiyoshi et al., 1993). Buffer conditions yielding the sharpest peaks in the amide region and the narrowest half-height linewidth for the Val25 γCH_3 resonance were 100 mM NaCl, 20 mM KH_2PO_4, 0.5 mM EDTA and 1.0 mM DTT at pH 5.4. Subsequent sedimentation analysis, ^{1}H-^{15}N HMQC-J and ^{15}N-T_1 and -T_2 envelope studies confirmed that HAV 3C protease was behaving as a monomer under these optimized conditions.

Chapter 2 also describes an important 'time-course' stability study of HAV 3C protease that involved collecting 1D ^{1}H NMR spectra of the protein over a

period of one month. This study determined that HAV 3C protease stock should be stored for up to a month at 4 C in the post-column elution buffer (350 mM NaCl, 20 mM KH_2PO_4, 0.5 mM EDTA, 1.0 mM DTT at pH 5.4) under argon gas with 25 L of 3 % (w/v) sodium azide added to ensure sterility. This study also determined that NMR experiments performed with HAV 3C protease yield the best results within 9 days of making the NMR sample. After the 9 day period, it is likely that some degree of HAV 3C protease aggregation occurs although the extent of this is unknown.

Chapter 3 describes the protocols developed to isotopically label HAV 3C protease with combinations of ^{2}H, ^{13}C and ^{15}N. These protocols were based on the initial expression and purification of unlabelled HAV 3C protease that was published by Malcolm et al., (1993). Single (^{15}N) and double ($^{13}C/^{15}N$) labelled HAV 3C protease was produced by substituting $^{15}NH_4Cl$ and $^{13}C_6$-glucose for $^{14}NH_4Cl$ and ^{12}C-glucose into the media preparations. Obtaining a triple ($^{2}H/^{13}C/^{15}N$) labelled HAV 3C protease required that our E. coli expression system be adapted to deuterium-based minimal media. This process entailed successively growing the bacteria in minimal media prepared with increasing amounts (50, 80 and 85 percent) of $^{2}H_2O$. Bacteria do not metabolize $^{2}H_2O$ as efficiently as $^{1}H_2O$ due to thermodynamic and kinetic isotope effects (Galimov, 1985) therefore growth rates in $^{2}H_2O$ based minimal media were much slower than those seen in pure $^{1}H_2O$ based minimal media. The uniform labelling strategies allowed isotopic incorporation levels of $\geq$ 95% for ^{13}C and ^{15}N and ~ 70 % for ^{2}H.

To obtain ^{15}N labelled HAV 3C protease with specific amino acids (alanine, glycine, leucine, lysine, isoleucine, phenylalanine and valine), we chose to use our prototrophic strain of E. coli and substitute an amino acid mixture (19 unlabelled and a single ^{15}N labelled amino acid) for $^{14}NH_4Cl$ in the minimal media (Muchmore et al., 1989). This simple residue-specific labelling protocol yielded good results with 5 of our 7 trials as only glycine and phenylalanine showed significant amounts of ^{15}N 'scrambling'.

Chapter 4 reports the near complete (~85%) backbone sequential assignments of HAV 3C protease and the NMR experiments that were used to obtain them. Progress on the sequential assignments was greatly accelerated after we identified the 'low-salt/low-pH' solution conditions that minimized aggregation and after we prepared a triple ($^{2}H/^{13}C/^{15}N$) labelled HAV 3C protease to reduce efficient T_2 relaxation rates of ^{1}H, ^{13}C and ^{15}N nuclei. After preparing a 1 mM $^{2}H/^{13}C/^{15}N$ labelled HAV 3C protease sample in the optimized 'low salt/low pH' solution conditions, "deuterium modified" CT-HNCA, CT-HN(CO)CA and HN(CA)CB experiments, designed in Dr. Lewis Kay's laboratory (Gardner and Kay, 1998; Yamazaki et al., 1994b), were completed that yielded spectra with nearly all of the expected resonances present. These spectra were used in consort with data from six (alanine, glycine, leucine, lysine, isoleucine and valine) ^{15}N residue-specific HSQC spectra to make the sequential backbone assignments.

Presently, backbone sequential assignments ($^{1}H_N$, ^{15}N, $^{13}C_\alpha$, $^{13}C_\beta$, ^{13}CO and $^{1}H_\alpha$) have been made for 175 of the 217 residues. ^{13}CO and ^{1}H resonances were acquired from HNCO, ^{1}H-^{15}N TOCSY-HSQC and ^{1}H-^{15}N NOESY-HSQC spectra collected at high pH. To determine ^{13}CO and $^{1}H_\alpha$ chemical shifts it was necessary to equate amide chemical shifts collected at low pH with those collected at high pH. For many amide resonances this relationship could not be unambiguously established, therefore a majority of these shifts are missing from the table of reported backbone chemical shifts in Chapter 4.

In Chapter 4 we also show that the backbone assignments exhibit good agreement with a set of predicted chemical shifts that had been estimated by SHIFTX and TOTAL (Williamson et al., 1995) software packages. These programs predicted ^{1}H, ^{13}C and ^{15}N chemical shifts based on the PDB file (1HAV) of the X-ray crystal structure of HAV 3C protease (Bergmann et al., 1997). In addition, the backbone chemical shifts were analyzed by the CSI program (Wishart

et al., 1994) demonstrating 2 α-helices and 11 β-strands. These structural elements are in good agreement with X-ray crystallographic data.

The efforts to obtain the sequential assignments of HAV 3C protease also served to teach an important lesson regarding NMR spectroscopy. Many NMR experiments were performed on HAV 3C protease prior to determining the optimum buffer conditions. Under these suboptimal conditions HAV 3C protease molecules had a tendency to aggregate leading to efficient T_2 relaxation rates and poor quality spectral data. However, significant progress occurred once a triply ($^2H/^{13}C/^{15}N$) labelled HAV 3C protease was prepared and placed in more optimal 'low salt/low pH' conditions. This optimized HAV 3C protease sample addressed the two key problems encountered in this project: 1) aggregation and 2) efficient relaxation rates. Essentially, an important take home message is that taking time to optimize your sample prior to acquiring important NMR spectra is a worthwhile endeavor for any protein study via NMR spectroscopy.

The completion of the sequential backbone assignments of HAV 3C protease will require some time and effort with our present collection of NMR spectra. However, to fill in the ^1H and ^{13}CO chemical shifts it will be necessary to perform other experiments. In order to determine all ^{13}CO chemical shifts, a CT-HNCO spectrum should be collected from a triply labelled HAV 3C protease sample under 'low salt-low pH' conditions. To determine all ^1H chemical shifts will likely require us to prepare a doubly labelled ($^{13}C/^{15}N$) HAV 3C protease sample and then collect a HCCH-TOCSY. It may even be advisable to prepare a new triply labelled protease sample for this last experiment to minimize the $^{13}C_\alpha$ T_2 relaxation rates. This new triply labelled protease should aim for 30-50% levels of deuterium incorporation (to ensure there are protons to be detected) therefore minimal media should be prepared with approximately 50 percent ^2H_2O.

Finally, ligand-binding studies should be initiated using the "SAR by NMR" technique described by Shuker et al., 1996. The first ligand to be tested

should be iodoacetamide (an irreversible inhibitor) followed by the tightest binding inhibitor (as determined by enzymatic assay) that has been synthesized by Dr. John Vederas' group. These two ligands should cause perturbations in amide resonances that indicate binding to active site residues and possibly residues near the active site. This would provide a standard by which to measure other ligands. If the results from this step look good, it would be wise to test all ligands that have been screened enzymatically to determine if there are patterns of chemical shift perturbations that can be noted from inhibitors that bind with varying affinity. Information garnered from these experiments may allow us to hypothesize how the compounds are fitting into the protease and these hypotheses may be of utility to those synthesizing the compounds. Eventually, the solution structure of HAV 3C protease should be determined. Having structural information may allow one to use NMR to determine exactly how the ligands fit into the protease, information that has eluded crystallographers. This type of information would be significantly more attractive to the pharmaceutical companies.

Appendix A

Processing NMR spectra with NMRPIPE software

The following processing guidelines are based on the NMRPIPE software described by Delaglio et al., (1995). Steps that are typically involved in a NMR data processing session can be summarized in the following steps: (1) convert the FID from Varian to nmrPipe format, (2) use available scripts to process the data (this involves editing the processing shell script) and (3) inspect the resulting spectrum to decide if any additional processing is required such as re-phasing, zero-filling, or baseline correction. The NMRDRAW program can be used to view the processed spectrum.

Many processing functions and their associated arguments can be displayed by using function-specific commands. For example the following command will display information regarding the sine window function.

nmrPipe -fn SP -help

Following is a list of some of the functions that are typically used in data processing.

EXT	Extracts a region from the current dimension with specified limits.
FT	Applies a real or complex forward or inverse Fourier transform.
HT	Applies a Hilbert transform to reconstruct imaginary data.
LP	Linear prediction.
POLY	When used in frequency-domain, applies polynomial baseline correction. When used in the time-domain, applies solvent correction.
PS	Applies the zero- and first-order phase corrections.
REV	Reverse data order in given dimension
SOL	Applies solvent correction
SP	Applies sine-bell apodisation
ZF	Applies zero-filling

The following arguments are used by more than one function in the shell scripts above.

-di	Deletes imaginary data after the given processing function is performed.
-hdr	Extracts parameters recorded during previous processing from spectral header.
-in	Specifies the input file or file template.
-inPlace	Specifies replacement of the input data by the output result.
-inv	Activates the inverse mode of a given function.
-out	Specifies the output file or file template.
-ov	Permits overwriting of any pre-existing files.
-sw	Updates the spectral width and other ppm calibration information.
-verb	Permits processing in verbose mode, with status messages.

I Processing 2D NMR experiments.

CALIB. Copy the calib script into the directory containing the Varian procpar. Run the calib script by simply typing calib. This invokes the script to search through the procpar and find the various paramaters required to transform the Varian data into nmrpipe data and store the parameters in a file called pipe.param. An example of a pipe.param file follows.

```
PARAMETERS FOR VAR2PIPE (NMRPIPE)

 xN        1024          yN        128
 xT         512          yT         64
 xsw    6000.150          ysw  1400.000

 1H OBServe frequency :  499.886
 1H CARrier position  :    4.739

 15N OBServe frequency :  50.659
 15N CARrier position  :  118.504
```

FID.COM. Insert parameters listed in pipe.param and the appropriate path to the Varian 'FID' into the fid.com script using an editing program of your choice (eg. nedit). Invoke the script by typing fid.com. When this script is run it will take the fid (Varian FID) as input and transform it into nmrpipe format (eg. 15NHSQC.fid). A typical fid.com script follows.

```
var2pipe -in fid \
         -xT          512   -yT          64          \
         -xMODE    Complex  -yMODE    Complex        \
         -xSW      6000.150  -ySW     1400.000       \
         -xOBS      499.886  -yOBS      50.659       \
         -xCAR        4.739   -yCAR    118.504       \
         -xLAB           HN   -yLAB          N       \
         -ndim            2   -aq2D      States      \
| nmrPipe -fn MAC -macro $NMRTXT/ranceY.M -noRd -noWr -out 15NHSQC.fid --verb -ov
```

FT2D.COM. The ft2d.com script will transform '15NHSQC.fid' into the '15NHSQC.ft2' which is in a format that can be viewed by nmrDraw. It is important to know what portion of the spectra (i.e. the amide region) that requires processing. Insert this defined region into the EXT or extract function of this script. A typical ft2d.com script follows.

```
#!/bin/csh
nmrPipe  -in 15NHSQC.fid                                    \
| nmrPipe -fn POLY -time                                     \
| nmrPipe  -fn SP -off 0.33 -end 0.98 -pow 1 -c 1.0          \
| nmrPipe  -fn ZF -auto                                      \
| nmrPipe  -fn FT                                            \
| nmrPipe  -fn PS -p0 8.0  -p1 -35.0                         \
| nmrPipe  -fn EXT -x1 12.5PPM -xn 5.5PPM  -sw -verb -di     \
| nmrPipe  -fn TP                                            \
| nmrPipe  -fn LPC -fb -auto                                 \
| nmrPipe  -fn SP -off 0.417 -end 0.98 -pow 2 -c 1.0         \
| nmrPipe  -fn ZF -auto -verb                                \
| nmrPipe  -fn FT                                            \
| nmrPipe  -fn PS -p0 303.0 -p1 133.0 -di                    \
| nmrPipe  -fn POLY -auto                                    \
| nmrPipe  -fn TP                                            \
| nmrPipe  -fn POLY -auto                                    \
  -verb -ov -out 15NHSQC.ft2
```

You will see this script has two 'PS' lines. The first is for phasing in the X dimension ($^{1}H_{N}$) and the second is for phasing in the Y dimension (^{15}N).

If the spectrum is out of phase in the X or Y dimension, phase the spectrum appropriately in nmrDraw with p0 and p1 slide bars. Note the numbers associated with your phasing in nmrDraw and insert them (taking into consideration what their previous values) into the ft2d.com script. Rerun your ft2d.com script.

II Processing 3D NMR experiments

CALIB. Run the calib script in the directory containing the 3D Varian procpar. Invoke by typing calib. Ensure that both ^{15}N and ^{13}C information is collected when asked by the script. This searches the procpar file to find the parameters that are necessary to convert the Varian FID to nmrpipe format. A typical pipe.param file for 3D experiments follows.

PARAMETERS FOR VAR2PIPE (NMRPIPE)

xN	**1024**	**yN**	**100**	**zN**	**64**
xT	**512**	**yT**	**50**	**xT**	**32**
xsw	**6000.150**	**ysw**	**7794.232**	**zsw**	**1600.000**

1H OBServe frequency :	**499.886**
1H CARrier position :	**4.739**
15N OBServe frequency :	**50.659**
15N CARrier position :	**117.821**
13C OBServe frequency :	**125.701**
13C CARrier position :	**43.016**

FID_EXPERIMENT.COM. Insert parameters into the 'fid_experiment.com' script using an editor of your choice. Run the script by typing fid_experiment.com. The input is the varian 'fid' which will be transformed and stored into several nmrpipe format 'fids' in a directory called FID. Following is a typical fid_experiment.com script.

```
#!/bin/csh
var2pipe -in  fid                                                    \
 -xN              1024    -yN              100  -zN                64  \
 -xT               512    -yT               50  -zT                32  \
 -xMODE        Complex    -yMODE        Complex  -zMODE        Complex  \
 -xSW          6000.150   -ySW          7794.232  -zSW           1600.0  \
 -xOBS          499.886   -yOBS          125.701  -zOBS           50.659 \
 -xCAR            4.739   -yCAR           43.016  -zCAR          117.821 \
 -xLAB                H   -yLAB                C  -zLAB                N  \
 -ndim                3   -aq2D           STATES  -aqORD               0  \
#| nmrPipe -fn MAC -macro $NMRTXT/ranceZ.M -noRd -noWr                   \
| pipe2xyz -out FID/experiment%03d.fid -verb -ov
```

FT2D_EXPERIMENT.COM. Processing in 3 dimensions takes a very long time. It is a good idea to observe your data in 2 dimensions prior to processing the experiment fully in 3 dimensions. For this use the ft2d_experiment.com script. This allows you to view the full experiment in one xy plane. Invoke the script as before.

```
#!/bin/csh
nmrPipe  -in FID/experiment001.fid                  \
| nmrPipe -fn SOL                                   \
| nmrPipe -fn SP -off 0.33 -end 0.99 -pow 1 -c 1.0  \
| nmrPipe -fn ZF -size 512                          \
| nmrPipe -fn FT  -verb                             \
| nmrPipe -fn PS -p0 -0.0 -p1  0  -di               \
| nmrPipe -fn EXT -x1 10.5PPM -xn 5.75PPM  -sw      \
| nmrPipe -fn TP                                    \
| nmrPipe -fn LP -fb                                \
| nmrPipe -fn SP -off 0.43 -end 0.99 -pow 2 -c 1.0  \
| nmrPipe -fn ZF -size 512                          \
| nmrPipe -fn FT  -verb                             \
| nmrPipe -fn PS -p0  -90.0  -p1 180.0  -di         \
| nmrPipe -fn TP                                    \
| nmrPipe -fn POLY -auto                            \
       -ov -out experiment.ft2
```

The 'experiment.ft2' (output) file can be viewed by nmrDraw. It is likely that this spectrum will have to be phased with the p0 and p1 toggle bars. Insert the appropriate values back into the ft2d_experiment.com script and rerun.

FT3D.COM. Initially it is important to transfer all the relevant values from the ft2d.com script to the ft3d.com script. Likely, this will just be the phasing values you have determined. Invoke the script to fully process your 3D experiment by typing ft3d.com. An example script follows.

```
#!/bin/csh
#
#   Processing of F3 dimension (HN)
#
xyz2pipe -in FID/experiment%03d.fid -x  -verb              \
| nmrPipe  -fn SOL                                        \
| nmrPipe  -fn SP -off 0.33 -end 0.99 -pow 1 -c 1.0       \
| nmrPipe  -fn ZF -auto                                   \
| nmrPipe  -fn FT                                         \
| nmrPipe  -fn PS -p0 0.0 -p1 0.0                         \
| nmrPipe  -fn EXT -x1 5.75PPM -xn 10.5PPM -di -sw        \
| pipe2xyz -out DAT/experiment%03d.DAT -x -ov
#
#   Processing of F2 dimension (N) without LP
#
xyz2pipe -in DAT/experiment%03d.DAT -z  -verb              \
| nmrPipe  -fn SP -off 0.5 -end 0.95 -pow 1 -c 1.0        \
| nmrPipe  -fn ZF -size 72                                \
| nmrPipe  -fn FT -di                                     \
| pipe2xyz -out DAT/experiment%03d.DAT -z -inPlace
#
#   Processing of F1 dimension (C) with LP
#
xyz2pipe -in DAT/experiment%03d.DAT -y -verb              \
| nmrPipe  -fn LP -fb -ps90-180                           \
| nmrPipe  -fn SP -off 0.5 -end 0.99 -pow 2 -c 1.0        \
| nmrPipe  -fn ZF -auto                                   \
| nmrPipe  -fn FT                                         \
| nmrPipe  -fn PS -p0 -90.0 -p1 180.0 -di                 \
| pipe2xyz -out DAT/experiment%03d.DAT -y -inPlace
#
#   Processing of F2 dimension (N) with LP
#
xyz2pipe -in DAT/experiment%03d.DAT -z -verb              \
| nmrPipe  -fn HT                                         \
| nmrPipe  -fn FT                  -inv                   \
| nmrPipe  -fn ZF -size 72           -inv                 \
| nmrPipe  -fn SP -off 0.5 -end 0.95 -pow 1 -c 1.0 -inv   \
| nmrPipe  -fn LP -fb -ps0-0                              \
| nmrPipe  -fn SP -off 0.417 -end 0.98 -pow 2 -c 1.0      \
| nmrPipe  -fn ZF -auto                                   \
| nmrPipe  -fn FT  -di                                    \
| pipe2xyz -out DAT-2/experiment%03d.DAT -z -inPlace
```

First run the ft3d.com commenting out the LP (linear prediction) and ZF (zero filling) commands which are very time intensive. Have a look at your final data from this initial processing. If things seem to be appropriate, run the script with LP and ZF. This will take a couple of hours. To be considerate to others use the following command.

nice +19 ft3d_experiment.com > & ft3d.log &

You can then periodically check the progress by viewing the ft3d.log.

References

Abragam, A. *The Principles of Nuclear Magnetism*, Clarendon Press, Oxford, 1961. pp. 309.

Akiyoshi, K., Deguchi, S., Moriguchi, N., Yamaguchi, S., and Sunamoto, J. (1993) *Macromolecules* 26:3062-3068.

Allaire, M., Chernai, M.M., Malcolm, B.A., and James, M.N. (1994) *Nature* 369:72-76.

Allerhand, A., Childers, R.F. and Oldfield, E., (1973) *Biochemsitry* 12:1335-1341.

Anglister, J., Grzesiek, S., Ren, H., Klee, C.B., and Bax, A. (1993) *Journal of Biomolecular NMR* 3:121-126.

Bachovchin, W.M. (1985) *Proceedings of the National Academy of Sciences of the USA* 82:7948-7952.

Bax, A. and Davis, D.G. (1985) *Journal of Magnetic Resonance* 65:355-360.

Bax, A., Clore, G.M., Driscoll, P.C., Gronenborn, A.M., Ikura, M., and Kay, L.E. (1990) *Journal of Magnetic Resonance* 87:620-627.

Bax, A., Sparks, S.W., and Torchia, D.A. (1989) *Methods in Enzymology* 176:134-150.

Bergmann, E.M., and James, M.N.G. (1999) *Proteases of Infectious Agents: Proteolytic Enzymes of the Viruses of the Family Picornaviridae*. Academic Press.

Bergmann, E.M., Mosimann, S.C., Chernaia, M.M., Malcolm, B.A., James, M.N., (1997) *Journal of Virology* 71(3):2436-2448.

Bernstein, F.C., Koetzle, T.F., Williams, G.J., Meyer, E.F., Brice, M.D., Rodgers, J.R., Kennard, O., Shimanouchi T., Tasumi, M., (1977) *European Journal of Biochemistry* 80(2):319-324.

Billeter, M., Braun, W. and Wuthrich, K. (1982) *Journal of Molecular Biology* 155:321-346.

Blundell, T. L. and Johnson, L. N. (1976) *Protein Crystallography*, Academic Press.

Braunschweiler, L. and Ernst, R.R. (1983) *Journal of Magnetic Resonance* 53:521-528.

Brill, B.M., Kati, W.M., Montogomery, D., Karwowski, J.P., Humphrey, P.E., Jackson, M., Clement, J.J., Kadam, S., Chen, R.H., and McAlpine, J.B. (1997) *Journal of Antibiotics* 49:541-546.

Browne, D.T., Kenyon, G.L., Packer, E.L., Sternlicht, H., and Wilson, D.M. (1973) *Journal of the American Chemical Society* 95:1316-1323.

Bystrov, V.F. (1976) *Progress in NMR Spectroscopy* 10:41-81.

Carpenter, J.F. (1998) *Journal of Pharmaceutical Sciences* 12:1597-1603.

Cavanagh, J., Fairbrother, W.J., Palmer, A.G. III, Skelton, N.J. (1996) *Protein NMR Spectroscopy Principles and Practice*, Academic Press.

Center for Disease Control and Prevention (http://www.cdc.gov/).

Clore, G.M. and Gronenborn, A.M. (1987) *Protein Engineering* 1:275-288.

Clore, G.M., and Gronenborn, A.M. (1991) *Progress in NMR Spectroscopy* 23:43-92.

Clore, G.M. and Gronenborn, A.M. (1994) *Protein Science* 3:372-290.

de Dios, A.C., Pearson, J.G. and Oldfield, E., (1993) *Science* 260:1491-1495.

Delaglio, F., Grzesiek, S., Vuister, G.W., Zhu, G., Pfeifer, J. and A. Bax (1995) *Journal of Biomolecular NMR* 6:277-293.

Delaglio, F., Torchia, D.A. and Bax, A. (1991) *Journal of Biomolecular NMR* 1:439-446.

Derman, H.M., Olson, W.K., Beveridge, D.L., Westbrook, J., Gelbin, A., Demeny, T., Hsieh, S.H., Srinivasan, A.R., Schneider, B., (1992) *Biophysical Journal* 63(3):751-759.

DesJarlais, R.L., Seibel, G.L., Kuntz, I.D., Furth, P.S., Alvarez, J.C., Ortiz de Monteillano, P.R., Decamp, D.L., Babe, L.M., Craik, C.S., (1990) *Proceeding of the National Academy of Sciences of the USA* 87(17):6644-6648.

Ernst, R.R. and Anderson, W.A., (1966) *Review of Scientific Instruments* 37:93-102.

Farrow, N.A., Zhang, O., Forman-Kay, J.D. and Kay, L.E. (1995) *Biochemistry* 34 (3):868-878.

Fesik, S.W. (1993) *Journal of Biomolecular NMR* 3:261-269.

Fesik, S.W. and Zuiderweg, E.R.P. (1988) *Journal of Magnetic Resonance* 78:588-593.

Frey, M.H., Wagner, G., Vasak, M., Sorensen, O.W., Neuhaus, D., Worgotter, E., Kagi, J.H.R., Ernst, R.R. and Wuthrich, K.J. (1985) *Journal of the American Chemical Society* 107:6847-6851.

Galimov, E.M. (1985) *The Biological Fractionation of Isotopes*, Orlando, Academic, p. 261.

Gardner, K.H. and Kay, L.E. (1998) *Annual Review of Biophysics and Biomolecular Structure* 27:357-406.

Garrett, D.S., Poweres, R., Gronenborn, A.M. and Clore, G.M. (1991) *Journal of Magnetic Resonance* 95:214-220.

Goody, R.S. (1995) *Nature Medicine* 1(6):519-520.

Gorbalenya, A.E. and Snijder, E.J. (1996) *Viral cysteine proteinases. Perspectives Drug Discovery and Design* 6:64-86.

Graff, J., Richards, O.C., Swiderek, K.M., Davis, M.T., Rusnak, F., Harmon, S.A., Jia, X.J., Summers, D.F. and Ehrenfeld, E. (1999) *Journal of Virology* 73:6015-6023.

Grzesiek, S. and Bax, A. (1992) *Journal of Magnetic Resonance* 96:432-440.

Grzesiek, S. and Bax, A. (1993) *Journal of the American Chemical Society* 115:12593-12594.

Grzesiek, S., Aglister, J., Ren, H. and Bax, A. (1993) *Journal of the American Chemical Society* 115:4369-4370.

Hajduk, P.K., Meadows, R.P. and Fesik, S.W. (1997) *Science* 278:497-499.

Heinz, B.A., Tang, J., Labus, J.M., Chadwell, F.W., Kaldor, S.W., Hammond, M., (1996) *Antimicrobial Agents and Chemotherapy* 40(1):267-270.

Henry, G.D. and Sykes, B.D. (1992) *Biochemistry* 31(23):5284-5297.

Ikura, M., Kay, L.E., and Bax, A. (1990) *Biochemistry* 29:4659-4667

James, M.N.G. (1993) *Proteolysis and Protein Turnover: Convergence of active-centre geometries among the proteolytic enzymes.* Bond, J.S. and Barrett, A.J. (eds). Portland Press, London.

Jeener, J., (Lecture, Ampere Summer School, Basko Polje, Yugoslavia, 1971)

Jeener, J., Meier, B.H., Bachmann, P. and Ernst, R.R. (1979) *Journal of Chemical Physics* 71:4546-4550.

Jewell, D.A., Swietnicki, W., Dunn, B.M., and Malcolm, B.A. (1992) *Biochemistry* 31:7862-7869.

Jia, X.Y., Ehrenfeld, E., and Summers, D.F. (1991) *Journal of Virology* 65:2595-2600.

Jia. X.Y., Summers, D.F. and Ehrenfeld, E. (1993) *Virology* 193:515-519.

Johnson, M.L., Correia, J.J., Yphantis, D.A. and Halvorson, H.R. (1981) *Biophysical Journal* 36:575-588.

Kaarsholm, N.C. and Ludvigsen, S. (1995) *Receptor* 5:1-8.

Karplus, M. (1959) *Journal of Physical Chemistry* 30:11-15.

Kay, L.E., Brooks, B., Sparks, S.W., Torchia, D.A. and Bax, A. (1989) *Journal of the American Chemical Society* 111:5488-5490.

Kay, L.E. and Bax, A. (1990) *Journal of Magnetic Resonance* 86:110-126.

Kay, L.E., Clore, G.M., Bax, A., and Gronenborn, A.M. (1990a) *Science* 249:411-414.

Kay, L.E., Ikura, M. and Bax, A. (1990b) *Journal of the American Chemical Society* 112:888-889.

Kay, L.E., Ikura, M., Tschudin, R., and Bax, A. (1990c) *Journal of Magnetic Resonance* 89:496-514.

Kay, L.E., Keifer, P., and Saarinen, T. (1992) *Journal of the American Chemical Society* 114:10663-10665.

Kay, L.E., Xu, G.Y. and Yamazaki, T. (1994) *Journal of Magnetic Resonance*, Series A 109:129-133.

Kay, L.E. (1995) *Progress in Biophysics and Molecular Biology* 63:277-299.

Kay, L.E. (1997) *Biochemistry and Cell Biology* 75:1-15.

Kay, L.E. and Gardner, K.H. (1997) *Current Opinion in Structural Biology* 7:722-731.

Kessler, H., Gehrke, M., Griesinger, C. (1988) *Angewandte Chemie Inernationalt Edition in English* 27:490-536.

Koff, R.S. (1998) *The Lancet* 351:1643-1648.

Kreilgaard, L., Jones, L.S., Randolph, T.W., Frokjaer, S., Flink, J.M., Manning, M.C. and

Kumar, A., Ernst, R.R. and Wuthrich, K. (1980) *Biochemical and Biophysical Research Communications* 95:1-15.

Laemmli, U.K. (1970) *Nature* 227:680-685.

LeMaster, D.M. and Richards, F.M. (1985) *Biochemistry* 24:7263-7270.

Linemeyer, D.L., Menke, J.G., Martin-Gallardo, A., Huges, J.V., Young, A., and Mitra, S.W. (1985) *Jorunal of Virology* 54:347-355.

London, R.E. (1990) *Journal of Magnetic Resonance* 86:410-415.

MacLachlan, L.K., Middleton, D.A., Andrew, E.J. and Reid, D.G. (1997) *Methods in Molecular Biology, Vol. 60: Protein NMR Techniques*, Reid, D.G. (ed), Humana Press Inc., Totowa, NJ, pp. 337-362.

Malcolm, B.A. (1995) *Protein Science* 4:1439-1445.

Malcolm, B.A., Chin, S.M., Jewell, D.A., Stratton-Thomas, J.R., Thudium, K.B., Ralston, R. and Rosenberg, S. (1992) *Biochemistry* 31(13):3358-3363.

Marion, D., Kay, L.E., Sparks, S.W., Torchia, D.A. and Bax, A. (1989) *Journal of the American Chemical Society* 111:1515-1517.

Martin, A. (1993) *Physical Pharmacy, 4th Edition.* Lea and Febiger, Philadelphia, London, Chapter 10, 212-250.

Martin, A., Benichou, D., Chao, S.F., Cohen, L.M. and Lemo, S.M. (1999) *Journal of Virology* 73:6220-6227.

McDonald, C.C. and Phillips, W.D., (1967) *Journal of the American Chemical Society* 89:6332-6336.

McIntosh, L.P., Griffey, R.H., Muchmore, D.C., Neilson, C.P., Redfield, A.G., and Dahlquist, F.W. (1987) *Proceedings of the National Academy of Sciences of the USA* 84:1244-1248.

McIntosh, L.P. and Dahlquist, F.W. (1990) *Quarterly Review of Biophysics* 23:1-38.

McIntosh, L.P., Wand, A.J., Lowry, D.F., Redfield, A.G. and Dahlquist, F.W. (1990) *Biochemistry* 29:6341-6362.

Montelione, G.T., Wuthrich, K., Burgess, A.W., Nice, E.C., Wagner, G., Gibson, K.D., and Scheraga, H.A. (1992) *Biochemistry* 31:236-249.

Moore, J.M. (1999) *Current Opinion in Biotechnology* 10:54-58.

Morris, G.A. and Freeman, R. (1979) *Journal of the American Chemical Society* 101:760-762.

Morris, T.S., Frormann, S., Shechosky, S., Lowe, C., Lall, M.S., Gauss-Muller, V., Purcell, R.H., Emerson, S.U., Vederas, J.C., Malcolm, B.A., (1997) *Bioorganic Medicinal Chemistry* 5(5):797-807.

Mossakoska, D.E., and Smith, R.A.G. (1997) *Methods in Molecular Biology, Vol. 60: Protein NMR Techniques*, Reid, D.G. (ed), Humana Press Inc., Totowa, NJ, pp. 325-335.

Muchmore, D.C., McIntosh, L.P., Russell, C.B., Anderson, D.E. and Dahlquist, F.W. (1989) *Methods in Enzymology* 177:44-73.

Muhandiram, D.R. and Kay, L.E. (1994) *Journal of Magnetic Resonance Series B* 103:203-216.

Najarian, R., Caput, D., Gee, W., Potter, S.J., Renard, A., Merryweather, J., Van Nest, G., and Dina, D. (1985) *Proceedings of the National Academy of Science of the USA* 82:2627-2631.

Neidhardt, F.C., (ED.) (1987) *Escherichia coli and Salmonella typhimurium. Cellular and Molecular Biology, vol. I.* Washington, D.C: Amer. Coc. Microbiol.

NonLinear Least Squares Program for anlalysis of Equilibrium Ultracentrifugation Experiments. Copyright © 1991 by David A. Yphantis. 99 River Rd., Mansfield Center, Connecticutt 06250-1018.

Olson, A.J. and Goodsell, D.S. (1998) *SAR QSAR Environmental Research* 8(3-4):273-285.

Optima XL-I Analytical Ultracentrifuge Instruction Manual. Published by the Spinco Business Center of Beckman Instruments, Inc. Palo Alto, CA. (1997)

Oschkinat, H., Griesinger, D., Kraulis, P.J., Sorensen, O.W., Ernst, R.R., Gronenborn, A.M., Clore, G.M. (1988) *Nature* 332:374-376.

Palmenberg, A.C. (1990) *Annual Review of Microbiology* 44:602-623.

Pardi, A. (1992) *Current Opinion in Structural Biology* 2:832-835.

Pardi, A., Billeter, M. and Wuthrich, K. (1984) *Journal of Molecular Biology* 180:741-751.

Pelton, J.G., and Wemmer, D.E., (1995) *Annual Review of Physical Chemistry* 46:139-167.

Perona, J.J. and Craik, C.S. (1995) *Protein Science* 4:337-360.

Petithory, J.R., Masiarz, F.R., Kirsch, J.F., Santi, D.V., and Malcolm, B.A. (1991) *Proceedings of the National Academy of Sciences of the USA* 88:11510-11514.

Powers, J.C., Odake, S., Oleksyszyn, J., Hori, H., Ueda, T., Boduszek, B., Kam, C., (1993) *Agents and Actions Supplement* 42:3-18.

Powers, R., Garrett, D.S., March, C.J., Frieden, E.A., Gronenborn, A.M. and Clore, G.M. (1992) *Biochemistry* 31:4334-4346.

Rasnick, D. (1996) *Perspectives in Drug Discovery and Design* 6:47-63.

Reid, D.G., MacLachlan, L.K., Edwards, A.J., Hubbard, J.A. and Sweeney, P.J. (1997) *Methods in Molecular Biology, Vol. 60: Protein NMR Techniques*, Reid, D.G. (ed), Humana Press Inc., Totowa, NJ, pp. 1-28.

Richards, F.M. (1974) *Journal of Molecular Biology* 82:1-14.

Richmond, T.J. (1984) *Journal of Molecular Biology* 178:63-89.

Roberts, G.C.K. (1999) *Current Opinion in Biotechnology* 10:42-47.

Roth, S.M., Schneider, D.M., Strobel, L.A., vanBerkum, M.B., Means, A.R. and Wand, A.J. (1992) *Biochemistry* 31:1443-1451.

Rubin, B., Antonaccio, M.J. and Horovitz, Z.P. (1978) *Progress in Cardiovascular Disease* 21(3):183-194.

Rueckert, R.R. (1996) *Fields Virology: Picornaviridae: The Viruses and their Replication.* (Fields, B.N., Knipe, D.M., Howley, P.M., Channock, R.M., Melnick, J.L., Monath, T.P., Roizmann, B. and Straus, S.E. eds). Lippincott-Raven, Philadelphia.

Schecter, T. and Berger, A. (1967) *Biochemical and Biophysical Research Communications* 27:157-162.

Schein, C.H. (1990) *Bio/Technology* 8:308-315.

Schiffer, C.A., Huber, R., Wuthrich, K., van Gunsteren, W.F., (1994) *Journal of Molecular Biology* 241(4):588-599.

Shan, X., Gardner, K.H., Muhandiram, D.R., Kay, L.E., Arrowsmith, C.H., (1998) *Journal of Biomolecular NMR* 3:307-318.

Shuker, S.B., Hajduk, P.J., Meadows, R.P. and Fesik, S.W. (1996) *Science* 274:1531-1534.

Sjogren, M.H. (1998) *Hepatology* 27:887-888.

Skelton, J.J., Aspiras, F., Ogez, J., and Schall, T.J. (1995) *Biochemistry* 34(16):5329-5342.

Skelton, N.J., Aspiras, F., Ogez, J. and Schakk, T.J. (1995) *Biochemistry* 34:5329-5342.

Skiles, J.W., and McNeil, D. (1990) *Tetrahedron Letters* 31:7277-7280.

Spyracopoulos, L., Gagne, S.M., and Sykes, B.D., (1999) P*roceedings for the International School of Structural Biology and Magnetic Resonance. 4th Course on Dynamics, Structure and Function of Biological Macromolecules*

Thiel, T.K. (1998) *American Family Physician* 57:1500-1501.

Tjandra, N., Wingfield, P.T., Stahl, D.J., and Bax, A. (1996) *Journal of Biomolecular NMR* 8:273-284.

Venters, R.A., Huang, C.C., Ramer, B.T., Trolard, R., Spicer, L.D., and Fierke, C.A. (1995) *Journal of Biomolecular NMR* 5:339-344.

Vento, S., Garofano, T., Renzini, C., Cainelli, F., Casali, F., Ghironzi, G., Ferraro, T., and Conaia, E. (1998) *New England Journal of Medicine* 338:286-290.

Voet, D. and Voet, J.G. (1995) *Biochemistry, 2nd Edition.* John Wiley and Sons. New York. pp. 389-400.

Wagner, G. and Wuthrich, K. (1982) *Journal of Molecular Biology* 155:347-366.

Wagner, G., (1993) *Journal of Biomolecular NMR* 3:375-385.

Wang, A.C. and Bax, A. (1995) *Journal of the American Chemical Society* 113:7772-7777.

Wang, A.C. and Bax, A. (1996) *Journal of the American Chemical Society* 117:1810-1813.

Wider, G. and Wuthrich, K. (1999) *Current Opinion in Structural Biology* 9(5):594-601.

Williamson, M.P., Havel, T.F., Wuthrich, K., (1985) *Journal of Molecular Biology* 182(2):295-315.

Williamson, M.P., Asakura, T., Nakamura, E. and Demura, M. (1992) *Journal of Biomolecular NMR* 1:83-98.

Williamson, M.P., Kikuchi, J. and Asakura, T. (1995) *Journal of Molecular Biology* 247(4):541-546.

Wishart, D.S., Sykes, B.D., Richards, F.M. (1991) *Journal of Molecular Biology* 222:311-333.

Wishart, D.S., Sykes, B.D. and Richards, F.M. (1992) *Biochemistry* 31:1647-1651.

Wishart, D.S. and Sykes, B.D. (1994a) *Journal of Biomolecular NMR* 4:171-180.

Wishart, D.S. and Sykes, B.D. (1994b) *Methods in Enzymology* 39:363-392.

Wishart, D.S., Bigam, C.G., Holm, A., Hodges, R.S. and Sykes, B.D. (1995a) *Journal of Biomolecular NMR* 5:67-81.

Wishart, D.S., Bigam, C.G., Yao, J., Abildgaard, F., Dyson, H.J., Oldfield, E., Markley, J.L. and Sykes, B.D. (1995b) *Journal of Biomolecular NMR* 6:135-140.

Wishart, D.S., Fortin, S., Woloschuk, D.R., Wong, W., Rosborough, T., Van Domselaar, G., Schaeffer, J. and Szafron, D. (1997) *CABIOS* 13(5):561-562.

Wishart, D.S. and Wang Y. (1998) *Journal of Biomolecular NMR* 11:329-336.

Wuthrich, K. (1986) *NMR of Proteins and Nucleic Acids*, New York, John Wiley & Sons.

Wuthrich, K., Wider, G., Wagner, G. and Braun, W. (1982) *Journal of Molecular Biology* 155:311-319.

Yamazaki, T., Lee, W., Revington, M., Mattiello, D.L., Dahlquist, F.W., Arrowsmiths, C.H. and Kay, L.E. (1994a) Journal of the American Chemical Society 116:6464-6465.

Yamazaki, T., Lee, W., Arrowsmith, C.H., Muhandiram, D.R. and Kay, L.E. (1994b) *Journal of the American Chemical Society* 116:11655-11666.

Zhang, O., Kay, L.E., Olivier, J.P. and Forman-Kay, J.D. (1994) *Journal of Biomolecular NMR* 4:845-858.

INFORMATION TO USERS

This manuscript has been reproduced from the microfilm master. UMI films the text directly from the original or copy submitted. Thus, some thesis and dissertation copies are in typewriter face, while others may be from any type of computer printer.

The quality of this reproduction is dependent upon the quality of the copy submitted. Broken or indistinct print, colored or poor quality illustrations and photographs, print bleedthrough, substandard margins, and improper alignment can adversely affect reproduction.

In the unlikely event that the author did not send UMI a complete manuscript and there are missing pages, these will be noted. Also, if unauthorized copyright material had to be removed, a note will indicate the deletion.

Oversize materials (e.g., maps, drawings, charts) are reproduced by sectioning the original, beginning at the upper left-hand corner and continuing from left to right in equal sections with small overlaps.

Photographs included in the original manuscript have been reproduced xerographically in this copy. Higher quality 6" x 9" black and white photographic prints are available for any photographs or illustrations appearing in this copy for an additional charge. Contact UMI directly to order.

ProQuest Information and Learning
300 North Zeeb Road, Ann Arbor, MI 48106-1346 USA
800-521-0600

University of Alberta

Damage Investigations of Glass Fibre/Epoxy Resin Composite Laminates Under Cyclic Loading

by

Alan W. Wharmby

A thesis submitted to the Faculty of Graduate Studies and Research in partial fulfillment of the requirements for the degree of Master of Science

Department of Mechanical Engineering

Edmonton, Alberta

Spring, 2000

University of Alberta

Library release form

Name of Author: Alan William Wharmby

Title of Thesis: Damage Investigations of Glass Fibre/Epoxy Resin Composite Laminates Under Cyclic Loading.

Degree: Master of Science

Year this Degree Granted: 2000

11044 80 Ave
Edmonton, AB
T6G 0R3
Canada

January 28, 2000

University of Alberta

Faculty of Graduate Studies and Research

The undersigned certify that they have read, and recommended to the Faculty of Graduate Studies and Research for acceptance, a thesis entitled Damage Investigations of Glass Fibre/Epoxy Resin Composite Laminates Under Cyclic Loading submitted by Alan William Wharmby in partial fullfillment of the requirements for the degree of Master of Science.

Dr. F.Ellyin

Dr. Z. Xia

Dr. R.L. Eadie

2000/01/27

Abstract

This study was separated into two components.

In the first component, cyclic loading of cross-ply and multi-ply specimens was examined. $(0_2/90_3)_s$ and $(\pm 45/90_3)_s$ laminates were tested under quasi-static and cyclic loading. Damage curves for crack initiation, delamination initiation, and final failure were developed. Visual damage growth, transverse crack growth, and stiffness reduction measurements were examined to determine how and why damage grew throughout the specimens.

In the second component, constrained angle ply specimens were examined. Laminates with orientations of $(0/\pm\theta_4/0)_T$ where θ = 25, 45, and 75 degrees were tested under monotonic and cyclic loading. For these specimens damage curves for crack initiation, crack saturation, and delamination initiation were developed. Visual damage growth was compared with stiffness reduction measurements and correlations were observed between the two. Visual damage was examined using a microscope to examine the edges, and an image processor to examine through the width of the specimen.

Acknowledgements

The author wishes to express his appreciation to Dr. F. Ellyin for his guidance and financial support throughout this endeavour.

Gratitude is extended to Dr. John Wolodko for his expertise in the field of advanced composite materials. As well, special thanks is extended to Mr. Bernie Faulkner whose technical know-how is second to none, and who was extremely patient and helpful with all of my questions regarding testing equipment. His influences on me regarding the hobby of photography were also very much appreciated, and a grateful stress reliever.

I am also very grateful to the members of the ACME group, past and present, who offered support, laughter, excitement, and above all excellent technical discussions during group meetings. Yu Chen, Dr. Xueli Han, Jamie Hoover, Yafei Hu, Dr. Chingshen Li, Cecilia Linghede, Yu Liu, Garrett Meijer, Pierre Mertiny, Mike Martens, Dave Thorton, and Dr. Zhihui Xia all became good friends and were a pleasure to be around.

Special thanks go out to my many friends for providing more than adequate stress relief. Nichole Dusyk, Martin Coles, Baljit Dhaliwal, Sarah Haddow, Andru McCracken, Lance Portas, Kevin Reid, Nikhil Rao, Steve Sutankayo, Kent West, and last but not least Kristine Wichuk all provided me with interesting and varied views of life.

I am especially grateful to my parents and brothers for supporting me and believing in me throughout this degree, as well as my life.

List of Tables

List of Figures

1 Introduction

The use of continuous fibre composite materials has grown enormously during the latter half of this century. From their beginnings as a high strength material mainly employed in costly military aviation projects, their use has spread to many different civilian applications. New designs range from aeroplane parts such as rudders and wings for commercial aircraft to sporting equipment such as handlebars and frames for mountain bikes. In recent years composite materials have been studied for applications such as pressure vessels and piping.

Advanced composite materials are unique mainly because of the ability to tailor design the material properties for a required application. By varying the orientation of the fibres in the laminate, it can be optimized for strength and stiffness, or on the other hand optimized for improved ductility. With this ability comes the benefit of a lighter material with better corrosion resistance compared to conventional homogeneous materials such as steel.

One of the drawbacks of composites is an incomplete understanding of their damage characteristics. By studying how damage initiates and propagates in a composite material under both uniaxial and multiaxial loading conditions, during both monotonic and cyclic loading, a clearer concept of how the material behaves can be gained. A better understanding of the material properties could lead to reduced safety factors, lower costs, superior design, and the institution of new applications. The purpose of this thesis is to examine how continuous fibre composite materials behave under cyclic loading conditions.

A large amount of work has already been performed in the area of cyclic loading in composite laminates. Inspite of this, a full understanding of how damage initiates and propagates through a laminate is not yet clear. It is still very difficult to predict how damage will propagate in composites with varying lay-ups. How the damage initiates is also not fully understood. These fundamental problems need to be solved before critical component design with composites can take place.

1.1 Differences between Composite Laminates and Metals

There are many differences between a composite laminate and an isotropic metal that cause conventional damage analysis to be ineffective.

Whereas a metal can usually be considered as an isotropic material, a composite laminate must be considered anisotropic. Since a composite is much stronger in the direction of the fibres, the strength characteristics will vary depending on the orientation examined. In a composite laminate, elastic moduli E_{11}, E_{22}, and E_{33} vary greatly, whereas in a metal these directional properties are relatively close to one another.

The main difference between the behaviour of metals and laminated composites is the failure mode. Whereas a metal has mainly one dominant failure mode that consists of a crack propagating through the material, a composite laminate has many failure modes. These consist of microdamage, transverse cracking, delamination, and fibre-failure and will be discussed in Section 1.2. Also, whereas the damage mode in a metal consists of a single dominant event, the overall damage progression in a composite laminate is a multiplicity of interacting and competing failure modes. Experiments have shown that

these different modes vary between specimens depending on lay-up of the laminae plies with respect to the applied loading conditions, loading rate and amplitude, loading type, dimensions of the specimens and whether the specimens are tubular or coupon in shape. Damage in composites occurs on different scales. The first damage mode, microdamage, is usually defect induced and occurs at the microscopic scale. On the other hand, damage such as transverse cracking, delamination, and fibre failure occur in the macroscopic scale of the specimen.

It is these differences that differentiate examination of composites from that of metals.

1.2 Description of Damage in Composites

Damage growth has different modes during the life of a composite laminate. These do not simply proceed one after the other, but occur as competing events that interact with one another. These different modes of damage can be split into four distinct and different types of damage.

1.2.1 Microdamage

The first type of damage growth in a composite laminate as it is being loaded is microdamage. This damage develops throughout the specimen and is due to defects in the laminate. A noticeable scaling effect can be seen in composite specimens, whereby larger specimens fail under lower stresses than smaller specimens. This is due to the effect of microvoids in the specimen [1-3]. The defects can be in the form of microvoids,

damage caused by residual stresses, areas of high or low fibre content, impurities inserted during the manufacturing of the laminate, and small defects in the initial fibre and matrix mixture that emerge during production of the fibres. This damage is exclusively in the microscale, yet it has been shown that this damage serves as an initiation site for macroscopic scale matrix cracking [4,5].

Microvoids can sometimes appear due to improper lay-up of the laminae in the specimen, which results in trapped air voids between individual plies [6]. They can also emerge due to improper vacuuming after lay-up, which has been found to reduce trapped air in the specimens. To reduce this type of microdamage individual laminae must be pressed together tightly when producing the laminate. Added pressure during the cure cycle of the composite should also be performed to extricate as many voids as possible.

High or low fibre content is seen when too little or too much pressure is applied when curing the composite. When there is high fibre content in the laminate, the fibres can cluster together with no polymer matrix between them. Stress concentrations arise and are likely sites for damage initiation in the specimen. On the other hand, areas of low fibre content have an abundance of polymer. In these regions, when a crack initiates, it can propagate very easily without hitting any restricting boundaries such as fibres. These are also sites for likely damage initiation in the specimen. Any void in the matrix is a potential site of stress concentration and could result in crack initiation.

The last type of microdamage is defects that arise during manufacture of the laminate. This can be in the form of interfibre cracking, debonds between the fibre and the matrix, and broken fibres. These develop due to residual stresses in the composite.

Residual stresses are the result of different expansion and contraction properties between the fibres and matrix. When the specimen is cured the matrix and fibres expand. After curing, when the specimen cools, the two different materials contract at different rates, leaving residual stresses that may initiate microdamage [7]. This microdamage, once initiated, is distributed throughout the specimen.

1.2.2 Matrix Cracking

The second type of damage consists of matrix cracking. Matrix cracking takes place in two forms. The first is a combination of fibre and matrix decohesion, and the second is interfibre matrix cracking. This damage is usually a growth from defects in the material, such as microdamage or from defects at the edges of cut composites, and is distinguished from microcracking by the formation of macroscopic cracks. These cracks typically run parallel to the fibre direction and through the thickness of the ply. Work performed by Reifsnider et al.[8,9] on transverse cracking (matrix cracking perpendicular to the loading direction) found that there was a point where the accumulation of matrix cracks saturated and new damage modes took place instead. He called this the Characteristic Damage State (CDS). This is simply a semi-uniformly distributed pattern of matrix cracks that form in a laminate for any cyclic loading condition. Figure 1.1 shows a typical matrix crack through a laminae ply of a composite specimen. The dark areas surrounding the individual fibres are resin, and the crack has propagated vertically down the middle of the image.

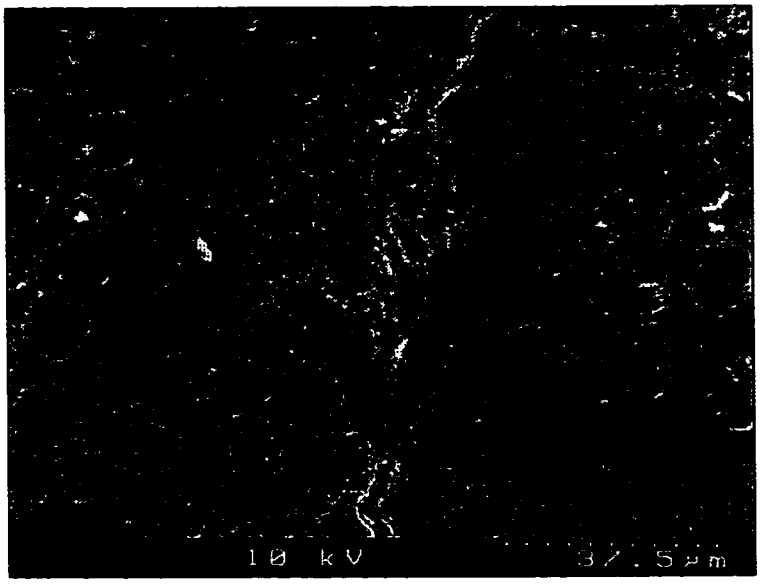

Figure 1.1. Typical matrix cracking in a glass fibre/epoxy resin laminae ply

1.2.3 Delamination

Delamination damage is separation of layers due to differences in properties between the plies. When the stiffness variance between differing ply orientations is large, and when there is a defect such as a transverse crack [10,11] or a geometric boundary such as a free edge [12,13], delaminations can initiate and propagate.

Delaminations usually follow matrix cracking in the tensile coupon testing of a specimen. During cyclic loading a matrix crack propagates until it reaches a constraining boundary, i.e. varying angle plies. When this happens, the crack takes the path of least resistance, which often can be propagation between the two plies. This crack then becomes a delamination. Figure 1.2 shows a matrix crack that has propagated until it reached a boundary and then proceeded into a delamination. The delamination can be

seen on the far right side of the figure and propagates in both directions from the matrix crack.

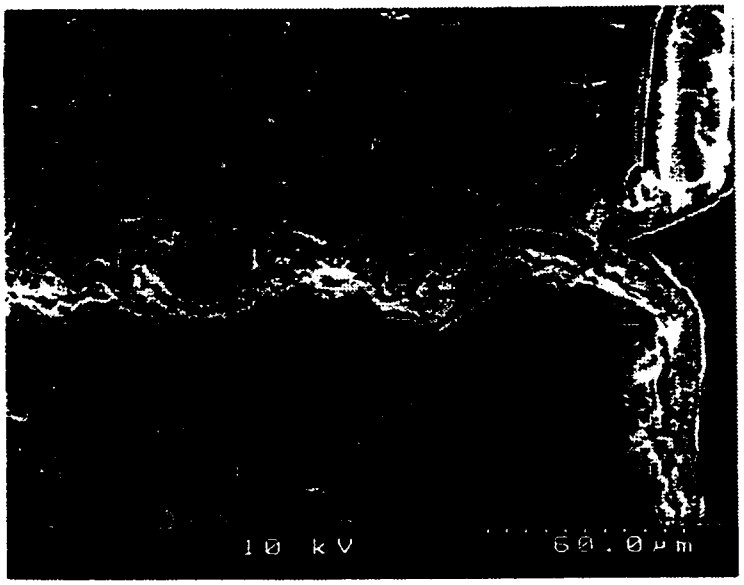

Figure 1.2: Delamination growth between 90° and 0° ply where transverse crack has propagated into a delamination

It has been noticed that varying types of delamination occur in different specimens. Whereas a cross-ply laminate will have delaminations that grow throughout the length of the 0° plies, a quasi-isotropic or angle-ply specimen will experience delamination in a concentrated cross-section. It is these delamination characteristics that determine the ultimate failure of the specimen. In the cross-ply laminates, the delaminations grow throughout the length of the specimen until a final brush failure results. (See Figure 1.3). In the angle ply and quasi-isotropic specimens the delamination growth occurs in a smaller cross-section which results in ultimate failure. (See Figure 1.4).

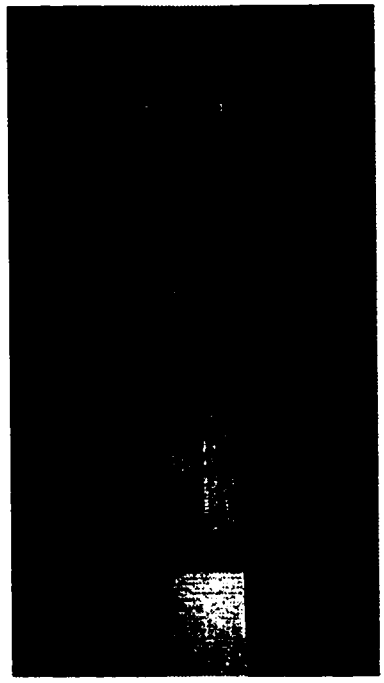

Figure 1.3. Brush failure due to lengthwise delamination growth in a $(0_2/90_3)_s$ laminate

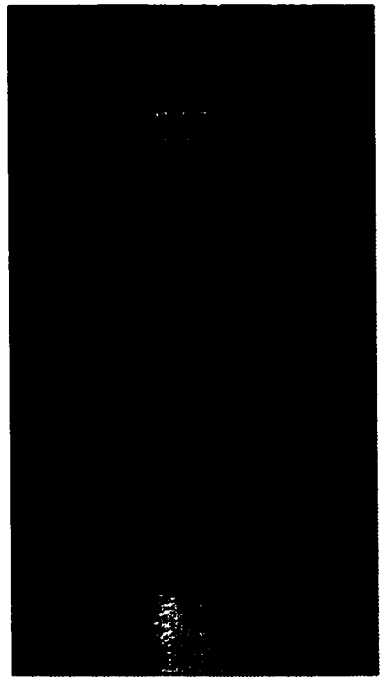

Figure 1.4. Failure due to widthwise delamination growth in a $(\pm 45/90_3)_s$ laminate

1.2.4 Fibre Failure

Fibre failure is the final mode of damage in a specimen. This mode is the result of the tensile strength of the fibres themselves being exceeded. This type of damage typically takes place when all other modes of damage have been exhausted, since the strongest part of the composite constituents is the fibres. This damage results in the ultimate failure of the laminate for fibre dominated loading.

Figure 1.5 shows a common fibre-failure in the constraining 0° plies of a cross-ply laminate. The fibres have fractured across the cross-section and there is considerable fibre pull-out, as shown by the long fibre strands.

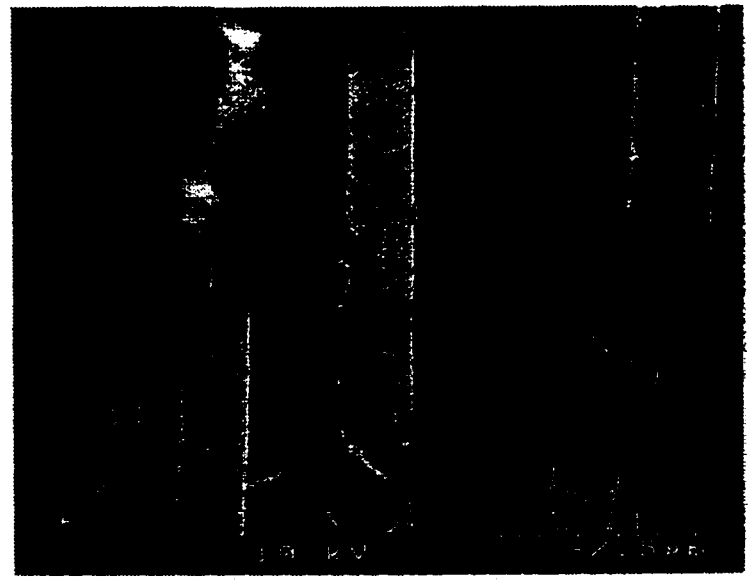

Figure 1.5. Fibre failure in constraining plies of a $(0_2/90_3)_s$ laminate (Courtesy of Rohrbacher [27])

Although most fatigue-life curves for composites are plotted with respect to the final fibre failure of the specimen, such a curve does not show all of these damage modes, and conveys nothing of the preceding damage that has taken place in the specimen.

1.3 Types of Composite Laminates

There are various geometries of laminates used in fibre/resin composite experimentation. The orientation of the fibres in a composite can be described by a standard set of symbols. The standard laminate description consists of the angle that the plies are oriented with respect to the loading direction, and are organized from the outside inwards. An example is $(0_2/90_3)_s$. This description implies that the outer plies are oriented 0° with respect to the direction of loading. The subscript '2' indicates that there are two plies in this direction. Next are the inner 90° plies. The subscript here shows there are three such plies. The 's' subscript outside of the brackets indicates that the laminate is symmetric with respect to the mid-plane. In total there are ten plies in this description in a configuration of (0/0/90/90/90/90/90/90/0/0). In some laminate descriptions the subscript 'S' is replaced with a 'T' representing the total lay-up.

The types of specimens examined can be split into four different categories, described on the following pages:

1.3.1 Cross-ply : $(0_m/90_n)_s$

Cross-ply specimens are made up of varying numbers of plies that are oriented in two directions. The plies are either in the direction of loading (0° plies), or in the direction perpendicular to loading (90° plies). These specimens are useful in examining the damage that occurs in the matrix of the specimen. A typical cross-ply specimen would be (0/90/0), $(0_2/90_3)_s$, or $(0_n/90_m)_s$.

1.3.2 Uni-directional : (θ_n)

Uni-directional specimens are made up of varying numbers of plies of specimens all oriented in the same direction. These specimens are useful in determining the material properties of a single orientation of the test material.

1.3.3 Multi-directional : $(\pm\theta/90_n)_s$

Multi-directional specimens refer to those specimens that have a wide variety of differing laminae geometries. These are sometimes prepared with the fibres in many directions to give quasi-isotropic material properties for the composite laminate.

1.3.4 Angle-ply : $(\pm\theta)_{ns}$

Angle-ply specimens refer to those specimens that have plies of varying angle of orientation with respect to the direction of loading. These specimens are important to examine due to the fact that for many practical applications of composite laminates, the

plies are oriented in directions different from that of the direction of the largest load. The reason for this can be either multidirectional loading, or uncertainty in the actual direction of loading of the laminate.

1.4 Characterization of Damage in Composite Coupon Specimens

In the last 20 years a large amount of research has been aimed at the examination of damage growth in composite materials. Of considerable note, much work has been done on the cross-ply laminates, namely any laminates with an orientation of $(0_n/90_m)_s$. These have been examined in large part due to the ease of seeing the damage growth in the matrix dominated 90° layers. These lay-ups are also one of the easiest to model, since damage in the form of matrix cracking occurs almost exclusively in the 90° layers, and because the viscoelastic effects of the matrix can be minimized.

As early as 1969, the cyclic properties of composite materials were being examined. Boller [14] aimed his research at unidirectional specimens and found that the anisotropic nature of composite laminates lead them to be more complicated to analyze than isotropic materials such as metals. He found that the fatigue strength of composites was dependent upon the proper fibre to epoxy ratio. He also found that there were many factors that could effect the final fatigue properties of the composite laminate. These included the stiffness properties of the composite laminates, environmental factors, fabrication factors, and service factors. This was then classified into effects such as temperature, moisture, notches, imperfections, surface conditions, specimen size, damping characteristics, adhesion, orientation of fibres, and the rate of loading.

A large amount of experimental work has been performed trying to model the damage growth during cyclic loading of composite laminates. Much of this work has focused on the stiffness reduction over the life of the composite. Work performed by Highsmith and Reifsnider [8,9] found that the stiffness reduction was linked to the transverse matrix cracking in a cross-ply laminate. This work found that for a given laminate ply orientation, a characteristic damage state (CDS) occurred, whereby the matrix cracking in the cross-ply grew until it reached an approximately uniform crack pattern. They found that as matrix cracking increased in a specimen, the stiffness decreased in a very similar pattern, indicating that the matrix cracking was the dominant cause of the reduction in stiffness. The matrix cracking grew at a rapid rate at first and then slowed until a characteristic damage state was reached. In a similar manner, the stiffness reduction grew rapidly early on and reached a steady level as the CDS was reached. Another interesting point was that the largest stiffness changes developed when the crack density was the largest. Experimental plots of the stiffness reduction and the crack density were found to correlate well with theoretical shear lag analyses. Similar results were found by Camponeschi and Stinchcomb [15], Talreja [16], and by Ogin, Smith, and Beaumont [17].

Work performed in recent years by Crocker et al. [18] has focused on mixed mode transverse crack growth in (0/θ/0) specimens. Crack initiation and propagation was investigated for (0/θ/0) specimens with holes drilled in the θ layers to various depths before performing the tests. It was found that the matrix cracking of the specimens was dependent on the angle θ, while the depth the holes were drilled into the specimen had no

effect on the propagation rate of matrix cracks. With regard to the angle θ, they found that a (0/90/0) laminate is notch insensitive, while laminates that had a θ value between 45° and 75° were notch sensitive. This meant that there was an increase in the incremental strain required to grow a crack as the value of θ decreased.

Work was also performed by Tong, et al. [19] in the area of quasi-static and cyclic loading of quasi-isotropic laminates. Investigations were undertaken to see how matrix cracking grew in $(0/90/-45/+45)_s$ laminates. They found that there were large differences in the damage states between quasi-static and cyclic loading. Higher saturation crack densities were observed in the 90° layers under quasi-static loading than under cyclic loading, while the cyclic loading produced a larger reduction in stiffness, mainly due to extra damage accumulation in the ±45° layers. They noted that trying to model fatigue loading using simply static results could lead to non-conservative estimates of damage.

Angle-ply laminates were studied in a similar manner by Tahiri, Henaff-Gardin, and Lafarie-Frenot [20]. They studied a $(+45_2/-45_2)_{2s}$ specimen under both quasi-static and cyclic loading. They found that under quasi-static loading for this type of laminate there were large axial stiffness and shear modulus decreases. These decreases were largely attributed to non-linear visco-plastic and visco-elastic phenomena occurring in the matrix of the laminate. Under cyclic loading they found that the axial stiffness and shear modulus reductions fell by only 9% before failure of the specimen. They reasoned that the non-linear visco-elastic and visco-plastic effects did not have time to manifest under the higher strain rates that the specimens underwent in cyclic loading.

Another study by Henaff-Gardin and Lafarie-Frenot consisted of examining the crack growth in two different carbon/epoxy cross-ply specimens under cyclic loading [21]. The two specimens examined were a $(0_3/90/0_4)_s$ specimen and a $(0_7/90)_s$ specimen. These specimens had equivalent numbers of 0° and 90° layers, with the only difference being the stacking sequence. The purpose of this study was to see what the effect of the total of the 90° plies thickness had on the transverse cracking in the specimen. They found that for similar cyclic tests, the $(0_7/90)_s$ specimen produced approximately half (2 cracks/mm) of the final number of transverse cracks that the $(0_3/90/0_4)_s$ specimen produced (4.4 cracks/mm). A crack onset delay was found to occur in both specimens. The crack onset delay for the $(0_3/90/0_4)_s$ specimens was 1000 times longer than for the $(0_7/90)_s$. This work suggested that for design purposes, thinner 90° plies are more favourable. Longer crack onset delays, lower cracked surface growth rates, and smaller cracked surface areas are the result of thinner transverse plies.

An examination of angle ply cracking in $(\pm\theta/-45_3/+45_3)_s$ glass-fibre/epoxy resin laminates undergoing monotonic loading was performed by J. Hoover [22]. He found that by adding constraining plies to a composite specimen the failure stress and strains increased. This effect increased as the θ angle decreased. It was also suggested that crack densities, and damage in plies was lower for specimens whose neighbouring plies were 'compatible plies'. Compatible plies are those plies that have angles of less than 30° between themselves. It was observed that no delamination grew between compatible plies. The only delamination growth was seen in 'incompatible plies' with larger stress and strain gradients. These tests were performed only under uniaxial monotonic loading.

The relevant angles between compatible plies may increase or decrease during cyclic loading. Further research is needed to determine if the above holds true for cyclic loading.

Hoover, Kujawski, and Ellyin [23] also looked into transverse cracking of symmetric and unsymmetric glass-fibre/epoxy-resin laminates under monotonic loading. Symmetric specimens with orientations of $(\pm\theta/90_3)_s$ with θ = 0°, 25°, and 45°, and unsymmetric specimens with orientations of $(\pm\theta/90_6/0_2)_T$ with θ = 25° and 45° were examined. In this work the effect that transverse cracking had on the stiffness reduction of the specimen was studied. The findings showed that during a quasi-static test, three distinct damage stages took place. The first stage was before any transverse cracking materialized and was in a range of 0 – 0.5% strain. The second stage was a linear range in which almost all of the transverse cracks emerged. The third and final stage had a large stiffness drop over a small range that was due to large scale delamination, fibre failure, and constrained ply cracking as well as some transverse cracking. It was in this third and final stage that the specimen failed.

Work performed by Kujawski [24] looked into the width effects of angle ply laminates under both monotonic and cyclic loading. He performed tests on six different $(\pm\theta_2)_s$ specimens with angles ranging from ±25° to ±75° and for five different widths. He found that as the angle decreases below 45°, the effects of the specimen width becomes more pronounced. For specimens with fibre angles below 45°, an increase in the specimen width led to an increase in both the tensile strength and fatigue life of the specimens. For specimens with fibre angles greater than 45° the width effects were less

pronounced. This study suggests that the edge effect may be similar between all specimens, although in relation to the overall cross-sectional area of a specimen it has less total effect on specimens with larger cross-sections.

A qualitative examination of the frequency-dependant behaviour of laminates under cyclic loading was also undertaken by Kujawski and Ellyin[25]. Through the examination of a matrix dominated specimen ($(\pm 45)_{5s}$) they found that an accumulated cyclic creep occurred which depended on the frequency and applied load. Specimens at low loads and higher frequencies failed later than specimens at low loads and low frequencies. Specimens at higher loads and higher frequencies failed earlier than specimens at higher loads and lower frequencies. They also found that specimens had larger cyclic creep at the beginning and end of the fatigue tests, while there was a lower, steady creep rate throughout the rest of the specimen life. By examining the hysteresis loops of the specimens throughout their life, they also saw that there was a significant decrease in the stiffness of the specimen throughout its life.

1.5 Description of the Current Study

Work performed in the current study has two aims. The first objective is to examine damage growth and propagation between cross-ply and multi-ply laminates. The second objective is to examine the fatigue properties of constrained angle-ply laminates that have practical significance.

For the first objective, monotonic and cyclic tests are performed to investigate how the composite material varies with different loading conditions. Two different lay-

ups, one $(0_2/90_3)_s$ and the other $(\pm45/90_3)_s$, were examined. These specimens were chosen because the $(0_2/90_3)_s$ specimens produce ultimate failure modes that are dominated by the 0° fibres, while the $(\pm45/90_3)_s$ specimens produce ultimate failure modes that are dominated by the matrix in the 45° constraining plies. As well the 90° layers in both provided distinct matrix crack patterns for qualitative damage analysis. The differences between monotonic and cyclic loading was determined by examining parameters such as crack density, stiffness reduction, the achievement of a characteristic damage state, visual inspection of damage propagation, as well as fatigue life curves for the different lay-ups. Differences in cyclic loading between the two types of specimens were examined. The damage characteristics were also compared between the different loading types (load control vs. strain control), to study the laminate response to the loading mode.

The purpose of the second objective was to examine the cyclic properties of constrained angle-ply laminates with lay-ups similar to those that might be used in a high-pressure composite pipeline application. For this objective three different laminates were examined. These consisted of $(0/\pm\theta_4/0)$ laminates where θ was 25, 45, and 75 degrees. By producing fatigue life curves for the initiation of cracking, the onset of delimitation, and the saturation of matrix cracking in the specimens, an idea of the variance in damage with respect to θ could be determined.

2 Test Methodology

This chapter contains all procedures implemented in the manufacture and testing of the composite specimens. Described below are the types of specimens examined, preparation of the specimens, aspects of the testing machine and testing parameters used, the testing procedure, and methods of examining and recording the damage growth in the composite specimens.

2.1 Test Specimens

Various test geometries were fabricated for this study. For the first objective (Chapter 3) cross-ply and multi-ply laminates with a configuration of $(0_2/90_3)_s$ and $(\pm 45/90_3)_s$ were examined. These specimens each had six 90° layers which produced highly visible through-width cracks when the specimen was loaded. The only variance between these two types of specimens was the constraining plies. In the $(0_2/90_3)_s$ specimen the 0° layers, which have the fibres in the direction of loading, produce a very strong and elastic constraint. This specimen is sometimes referred to as a fibre-dominated specimen. In the $(\pm 45/90_3)_s$ specimen the load in the 45° layers was carried by both the matrix and the fibres. Because the matrix is the weaker of the two materials, it fails first. For this reason these specimens are sometimes called matrix-dominated specimens.

In the second objective (Chapter 4) three constrained angle ply specimens were prepared. These consisted of laminates with a geometry of $(0/\pm25_4/0)_T$, $(0/\pm45_4/0)_T$, and $(0/\pm75_4/0)_T$.

The geometry of all of the specimens examined was approximately 2.0-2.5 mm thick (depending on the number of plies) by 22 mm wide by 200 mm long.

2.2 Specimen Preparation

A large part of the validity of experimental testing can be attributed to quality control during fabrication of the test specimens. Factors that go into the specimen fabrication must be kept constant to ensure that all specimens have similar properties. These factors include specimen cure time, curing pressure, type of material, method of laying up the laminae, the cutting method, end-tab application, and storage of the specimens. By keeping these parameters the same between different tests, the results are more repeatable and any comparisons made between them can be deemed valid.

2.2.1 Material Examined

The type of material used in all tests consisted of 3M type 1003 (Scotchply) E-glass-fibre/epoxy resin. Pre-impregnated uni-directional tape rolls 0.3m wide by 66m long were acquired and pieces were cut into individual laminae. Each individual laminae was 0.2 mm thick. The hand lay-up techniques were used to produce a laminate sheet.

A complete set of material properties have been compiled by Hoover [26] for the 3M type 1003 E-glass-fibre/epoxy resin material and are presented in Table 2.1. These

values were used in the classical laminate theory calculations to determine the initial stiffness of the specimens. Since these results were compiled for specimens manufactured with the same fabrication techniques used in this study, they are considered the most repeatable.

Engineering Constant	Value
Longitudinal Modulus, E_1	43.2 GPa
Transverse Modulus, E_2	10.0 GPa
In-plane Shear Modulus, G_{12}	4.49 GPa
Out-of-plane Shear Modulus, G_{23}	4.17 GPa
In-plane Poisson ratio, ν_{12}	0.31
Out-of-plane Poisson ratio, ν_{23}	0.44
Co-efficient of linear expansion, α_1	8.6×10^{-6} per °C
Co-efficient of linear expansion, α_2	22.1×10^{-6} per °C
Temperature drop from stress-free temperature, ΔT	-125 °C
Specific Fracture Energy, γ_f	201 J/m^2
Average Ply Thickness	0.210 mm
Fibre Volume Fraction (After cure), v_f	52%

Table 2.1: Material properties of 3M type 1003 E-glass-fibre/epoxy resin composite as manufactured at the University of Alberta (Courtesy of Hoover [26])

2.2.2 Laminate Manufacturing Method

Manufacture of the composite laminate was performed by first cutting individual laminae from a tape roll of Scotchply pre-preg. The pre-preg roll was stored below 0°C to ensure that no curing occurred in the epoxy before manufacturing the laminates. To ensure that no condensation formed on the pre-preg, it was stored in a plastic bag while it warmed up to room temperature. Laminae sheets approximately 200 mm by 153 mm were cut by hand at varying angles relative to the fibre, so as to produce the required lay-up. A sheet of release film was placed over the pre-preg, then a metal plate was placed

on the sheet to act as a cutting guide. A sharp utility knife was used to cut the sheets. The method for cutting these individual plies of different orientations is shown in figures 2.1 and 2,2.

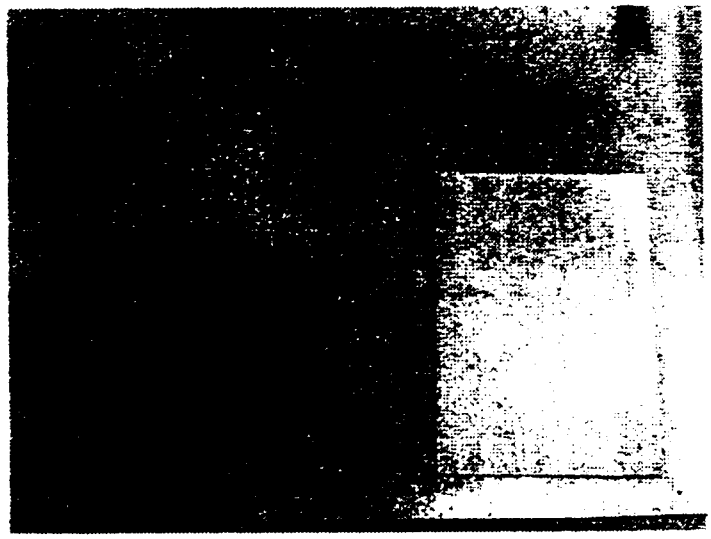

Figure 2.1: Cutting process for an individual 0° laminae ply

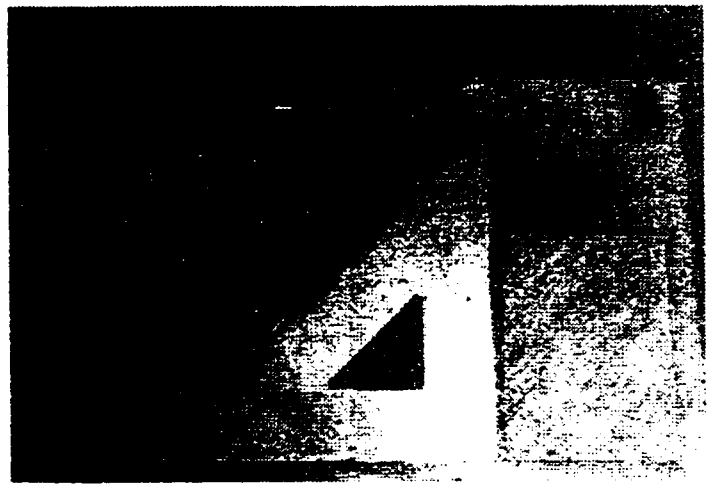

Figure 2.2: Cutting process for an individual 45° laminae ply

The individual laminae sheets were then pressed tightly together in a mold to get as many voids out as possible. Figure 2.3 shows the process of cutting the pre-preg in different orientations and constructing a laminate.

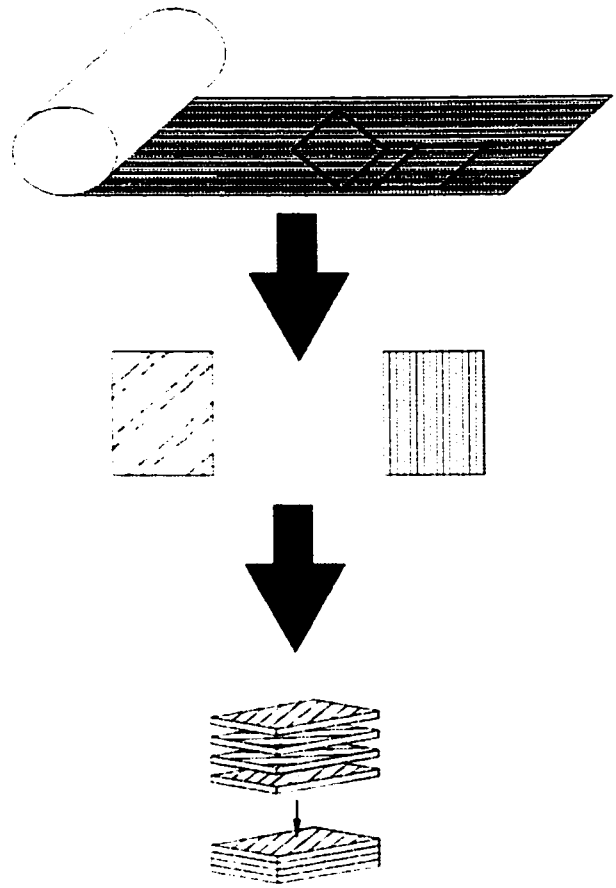

Figure 2.3: Manufacture of composite laminate sheet (Courtesy of Wolodko [29])

2.2.3 Vacuuming and Curing of the Laminate

After the laminae had been grouped into the laminate, the stack was placed in a vacuum chamber with a maximum pressure of 133 Pa for approximately 12 hours. This step was performed to reduce as much trapped air as possible from the specimen. Figure 2.4 shows a sketch of the specimen in the vacuum chamber apparatus.

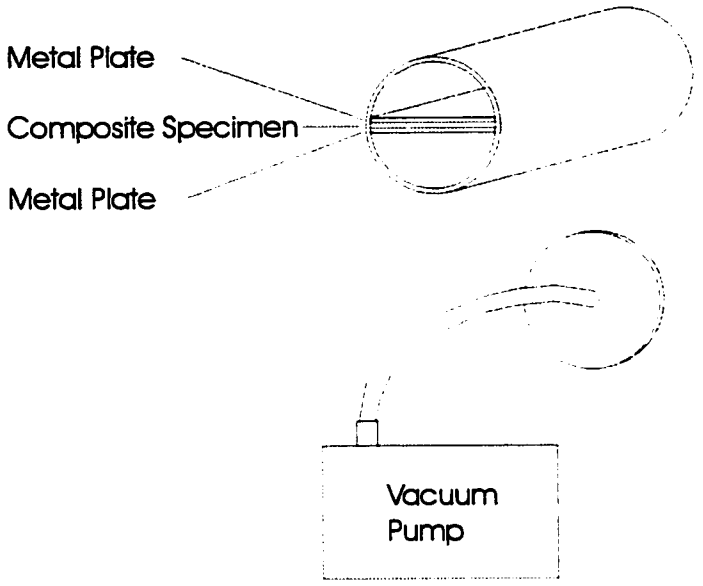

Figure 2.4: Vacuum chamber apparatus

After the laminate had been in the vacuum chamber, it was placed in a mold and cured in an oven at 150 °C under a bladder pressure of 25 psi for 12 hours. A schematic of the mold set-up is shown in Figure 2.5:

In the curing mold the metal plates are inserted to ensure that the specimen remains flat and uniform during curing. They also protect the specimen from pits and scratches that may be present on the mold.. The pressure bladder is used to push excess resin out of the composite laminate as it cures. The absorbent cloth is inserted to soak up resin that leaks from the mold during curing. Anti-cling film is placed on both sides of the specimen for ease of release after the curing process. Figure 2.6 shows the oven used in the curing process of the laminates. The pressure line was hooked up and run out through a hole in the oven wall.

This method produces a composite sheet of uniform thickness and fibre volume throughout the length and width of the specimen.

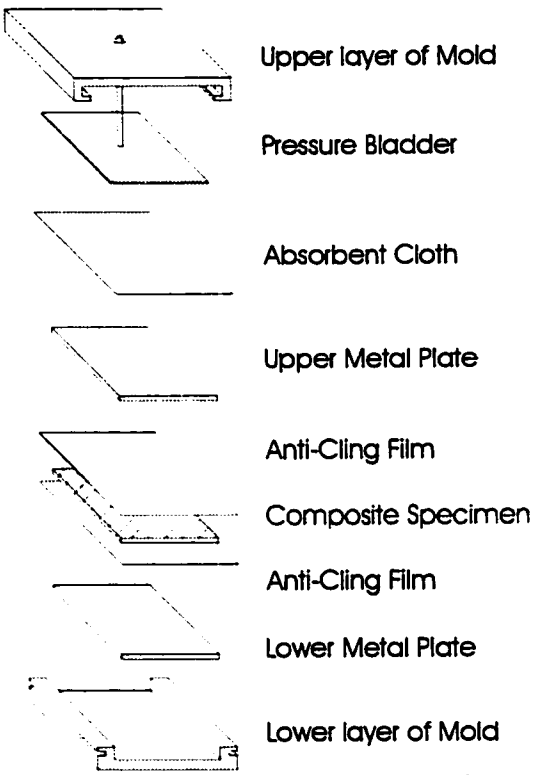

Figure 2.5: Schematic of composite curing mold

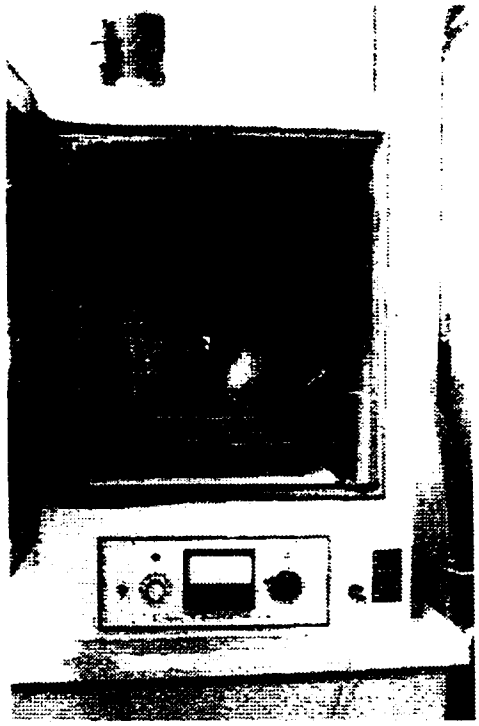

Figure 2.6: Specimen curing oven with pressure bladder attached to a mold

2.2.4 Cutting of Laminate into Individual Specimens

After the laminate is produced, it is cut into individual specimens. Six specimens can be cut from each composite sheet. A low RPM diamond blade saw fabricated at the University of Alberta is used to cut the specimens. This saw has been shown to reduce the number of edge defects when compared to conventional cutting techniques. Figures 2.7 and 2.8 show a typical specimen being cut using the diamond-blade saw.

Figure 2.7: Diamond blade saw apparatus

Figure 2.8: Specimen being cut using the diamond blade saw

2.2.5 Polishing of Specimens

To further ensure that edge effects are reduced, a systematic method of polishing each individual specimen was developed. Each specimen was sanded using a Handimet grinder in 240, 320, 400, and 600 grit sandpaper respectively. The specimens were sanded for 30 seconds per side, for each of the different sandpaper grits. Afterwards the polished surfaces were checked for abrasions and if any were found, the procedure was repeated. Figures 2.9 and 2.10 show two scanning electron microscope images of sections of the same specimen, the latter of which was polished using the above procedure. In the first figure large areas of pitting and scratching are present, mainly between the two plies of differing orientation. The second figure, under the same magnification shows a much smoother surface. These defect areas can act as nucleation

sites that can affect the crack density, stiffness, and ultimate failure strength of the specimens.

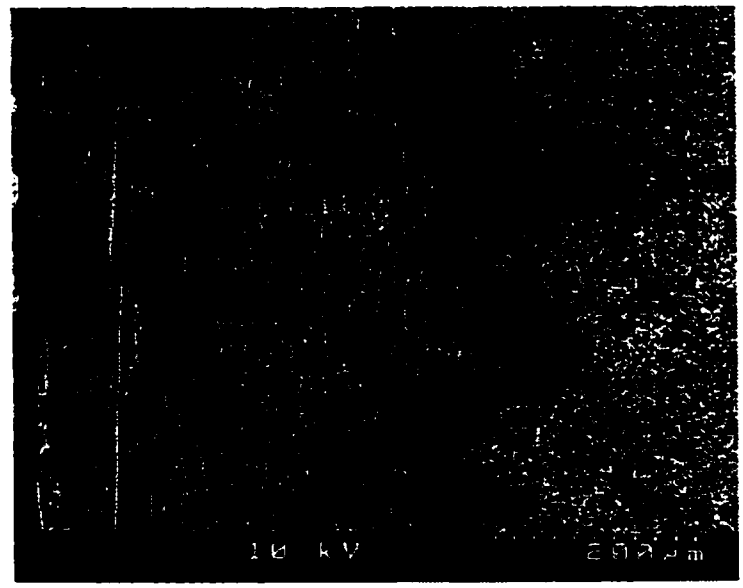

Figure 2.9: Unpolished section of cross-ply laminate showing pitted areas between plies

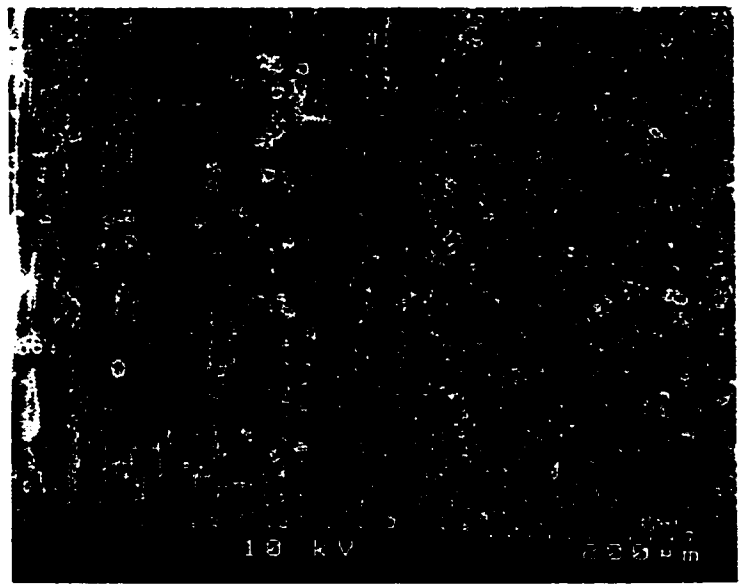

Figure 2.10: Similar specimen polished as specified, showing a cleaner surface

2.2.6 Measurement of Specimens

To determine the exact cross-sectional area of the specimens, measurements of the width and thickness were systematically taken and recorded. Measurements were taken at three different locations along the length of the specimen and an average of these three measurements was recorded. These values were used to calculate stress by dividing the load measured by the load cell by the cross-sectional area of the specimens.

2.2.7 Application of End Tabs

End tabs were applied to the specimens using 3M 12-hour epoxy adhesive. Earlier specimens had the end tabs applied with Loctite 380 but it was found that this didn't provide enough strength when the composite plies were oriented in the 0° direction. Failure in the tabs and slippage out of the tabs was observed in these specimens.

2.2.8 Marking Specimens for Image Processing

A marking system was used for each specimen so that the imaging system (Described in section 2.6.1) employed could track a constant area of the specimen between different images. This consisted of marking 'X's with permanent marker in the upper left and lower right hand corners of the specimens. As in-situ measurements were taken, the length between these markings increased, yet the final crack density could be calculated over the same initial area of the test.

2.2.9 Storage of Laminates and Completed Specimens

Previous work has shown that moisture can affect the material properties of a composite specimen [27]. Although the effects require a long time period and a significant amount of humidity on the surface, they could still affect the outcome of a test. To alleviate this problem, finished specimens were stored in a dessicator until they were taken for testing. The dessicator effectively removes any humidity from the environment of the specimens and leaves them in their original state.

2.3 Uniaxial Testing Machine

All specimen tests were performed on the same uniaxial testing machine. This consisted of a 100 kN MTS machine that was servo-controlled under a closed-loop. Coupled with the testing machine was a computer that controlled the loading conditions and also acquired data during the tests.

2.3.1 Data Acquisition System and Controlling Software

The Data acquisition system collected load and strain data throughout the life of the cyclic test. Measurements of stress were calculated using a 2000 lb load cell. These loads were converted into voltages for the data acquisition system where 1V was the equivalent to 2000 lbs. Measurements of strain were taken over a 75mm section of the specimen using an extensometer. Measurements of the strain were converted into voltages for the data acquisition system where 1V was the equivalent of an increase in strain of 1%.

Over the span of this investigation, three different data collection systems were employed.

The initial method consisted of simply hooking up a voltmeter to the testing machine and recording the output load and strain voltages over time. Any adjustments to achieve a set span and amplitude of the tests were done manually. It was impossible to obtain hysteresis loops of the specimens with this system. Another problem was that adjustments to achieve the required amplitude of load or strain had to be performed after the test had started. This resulted in it being very difficult to get accurate crack density measurements during the first 500 cycles of the test, when the amplitude of the test was being increased to that required. It was in this initial period that much of the damage took place in the highly stressed specimens.

The second method used a data acquisition card in conjunction with the testing machine. This was an older data acquisition system and all span and set point adjustments were still made manually. This again resulted in difficulty in data acquisition during the first 500 cycles, as well as the problem of keeping the set point and span at constant values. The system recorded data points so hysteresis loops could be examined throughout the life of the specimen. This data collection system was used when looking at the cross-ply and multi-ply specimens, specifically the $(0_2/90_3)_s$ and $(\pm 45/90_3)_s$ specimens.

The third and best method of control and data acquisition was achieved through using a data acquisition software program called MTM301 developed in-house at the University of Alberta by Wolodko [29]. This program consisted of controlling software

that would automatically ramp to the set point and span of the cyclic tests instantly. It was able to stop the test at regularly scheduled intervals so that damage detection methods could be implemented. Accurate stiffness reduction information and crack growth data could be found for the initial cycles of the test. This software was used mainly with the $(0/\pm25_4/0)$, $(0/\pm45_4/0)$, and $(0/\pm75_4/0)$ specimens.

2.4 Testing Parameters

2.4.1 Frequency and R-ratio

The tests were performed at a frequency of 3.0 Hz. A sinusoidal waveform was used for all tests. The R-ratio (R=Pmin/Pmax) throughout all tests was chosen to be 0.1.

2.4.2 Load Control

Load control tests were performed on the multi-ply $(\pm45/90_3)_s$ and cross-ply $(0_2/90_3)_s$ specimens. It was found that under load control the specimens failed at lower initial loading conditions than under strain control. This is because during cyclic loading damage initiates and propagates with increased number of cycles. To maintain the same maximum and minimum load amplitude, the strain amplitude and maximum strain must increase. This results in more damage, which then results in even larger strains. This process of a continuous increase in strain is called cyclic creep. Eventually the strains increase to the point of ultimate failure of the specimen. Figure 2.11 shows typical hysteresis loops for a load-controlled test.

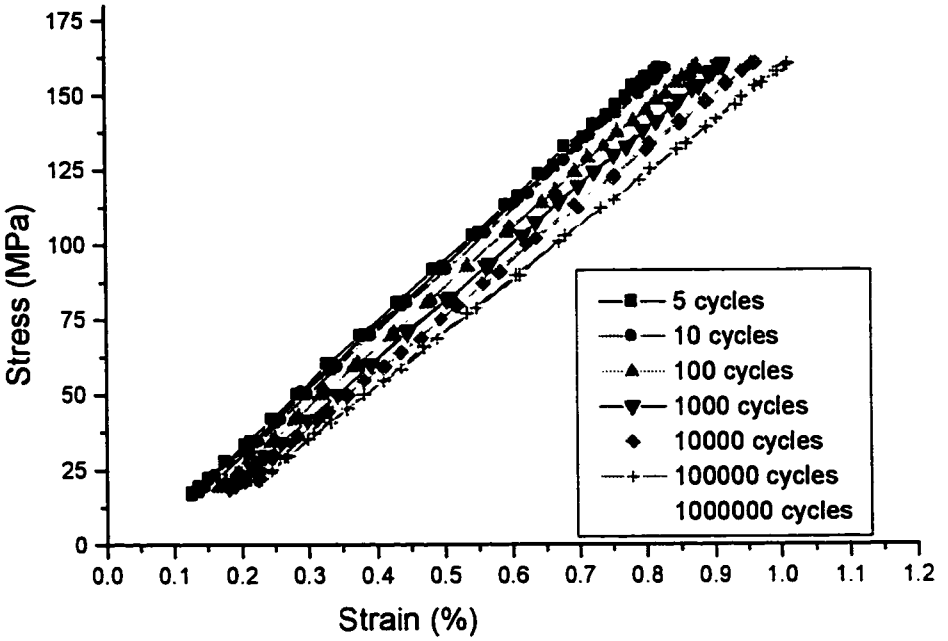

Figure 2.11: Hysteresis loops for a $(0_2/90_3)_s$ specimen tested under load control showing ratcheting effect

2.4.3 Strain Control

Strain control tests were performed on a set of $(\pm 45/90_3)_s$ multi-ply specimens as well as on the $(0/\pm 25_4/0)_T$, $(0/\pm 45_4/0)_T$, and $(0/\pm 75_4/0)_T$ constrained angle-ply specimens. Under strain control, a mean stress relaxation occurs. The reason for this is that as damage propagates in the specimen, lower loads are required to achieve the same level of strain. This then results in specimens taking a long time to fail. Figure 2.12 shows typical hysteresis loops for a strain controlled test.

Strain control was essential for examining crack initiation in the constrained angle ply composites. In strain controlled tests, the strain acting on each undamaged ply

remains the same. Since the strains in the undamaged plies remain the same, the load distribution must therefore vary. In a strain control test, the variance between the global and localized strains is very small. This constrasts with a load controlled test, where the variance between the local and global loads can be very high. For this reason a strain controlled test gives a better understanding of the conditions experienced by individual plies.

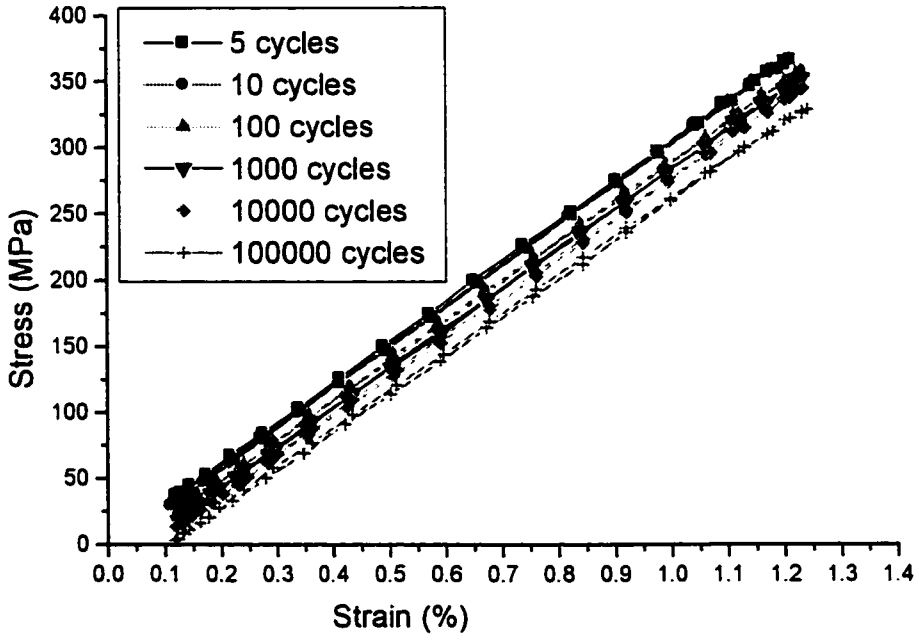

Figure 2.12: Hysteresis loops for $(0/\pm25_4/0)_T$ specimen tested under strain control showing stress relaxation

Some efforts were made to test $(0_2/90_3)_s$ specimens under strain control at strains high enough for failure. Unfortunately, as the specimens are cycled, it becomes hard for the extensometer to remain on the test specimen. Large longitudinal delaminations cause the extensometer to slip off in these specimens. When the extensometer slips off, the

controlling software sees a large decrease in strain, which is compensated for with a large load increase. This pulls the specimen apart instantaneously. This problem was best resolved by performing the tests on the $(0_2/90_3)_s$ specimens under load control.

2.5 Testing Procedure

To maintain repeatability of the tests, a specific set of procedures were adhered to for all different laminate geometries.

For tests of the $(0_2/90_3)_s$ and $(\pm45/90_3)_s$ specimens, damage examination consisted of analysis of the hysteresis loops, and visual recording of matrix crack growth. Recordings of the hysteresis loops were taken at regular intervals throughout all tests so as to develop stiffness reduction plots. The image processor was used to determine the crack density throughout the test life. For both the recording of the hysteresis loops and the imaging of the cracks, collection of data was recorded at exponentially decreasing intervals during the life of the specimen. This was done because most of the cracking and stiffness reduction occurs early on, when the primary mode of damage growth is matrix cracking. As damage growth slowed, there was less need for frequent recording of data. To examine the effect of control mode (load control vs. strain control) on the life of the specimen, some tests were performed in both load and strain control modes for the $(\pm45/90_3)_s$ specimens.

For the constrained angle-ply tests of the $(0/\pm25_4/0)_T$, $(0/\pm45_4/0)_T$, and $(0/\pm75_4/0)_T$ specimens, damage examination was more extensive. Two visual damage detection methods were used in conjunction with analysis of the hysteresis loops. Analysis of the

edge crack growth was done with the aid of visual penetrant and a binocular microscope. The image processor was used to record damage growth through the sides of the specimen. When examining these specimens, the test was momentarily stopped at 5,10,50,100,500,etc. up to $1x10^6$ cycles. At each stoppage, visual penetrant was applied, an edge crack count was performed, and a video image was captured. All of the constrained angle ply tests were performed under strain control for easier comparison.

2.6 Damage Examination Techniques

Included in this section is a complete listing and explanation of damage examination techniques that were used in this study. The examination techniques varied for different specimen configurations. Early tests of the $(\pm 45/90_3)_s$ and $(0_2/90_3)_s$ specimens utilized only the image processor system and stiffness reduction measurements. In the tests of the $(0/\pm 25_4/0)_T$, $(0/\pm 45_4/0)_T$, and $(0/\pm 75_4/0)_T$ specimens damage growth was not easily visible, therefore the microscopic examination method of crack growth, delamination, and crack saturation was used along with of the image processor and stiffness reduction techniques. In addition to the examination methods used herein and described below, a listing of other damage examination techniques is presented in Appendix 1.

2.6.1 Image Processor

Optical imaging consists of using a video camera to digitally capture images of the specimen as it sustains damage at various stages of its life. The method used here

was developed at the University of Alberta by Wolodko, Hoover, and Ellyin [28]. After the images for a test have been captured, they are analyzed by a computer program to determine the damage growth. Figure 2.13 illustrates the method by which images of the damaged coupon specimen are captured.

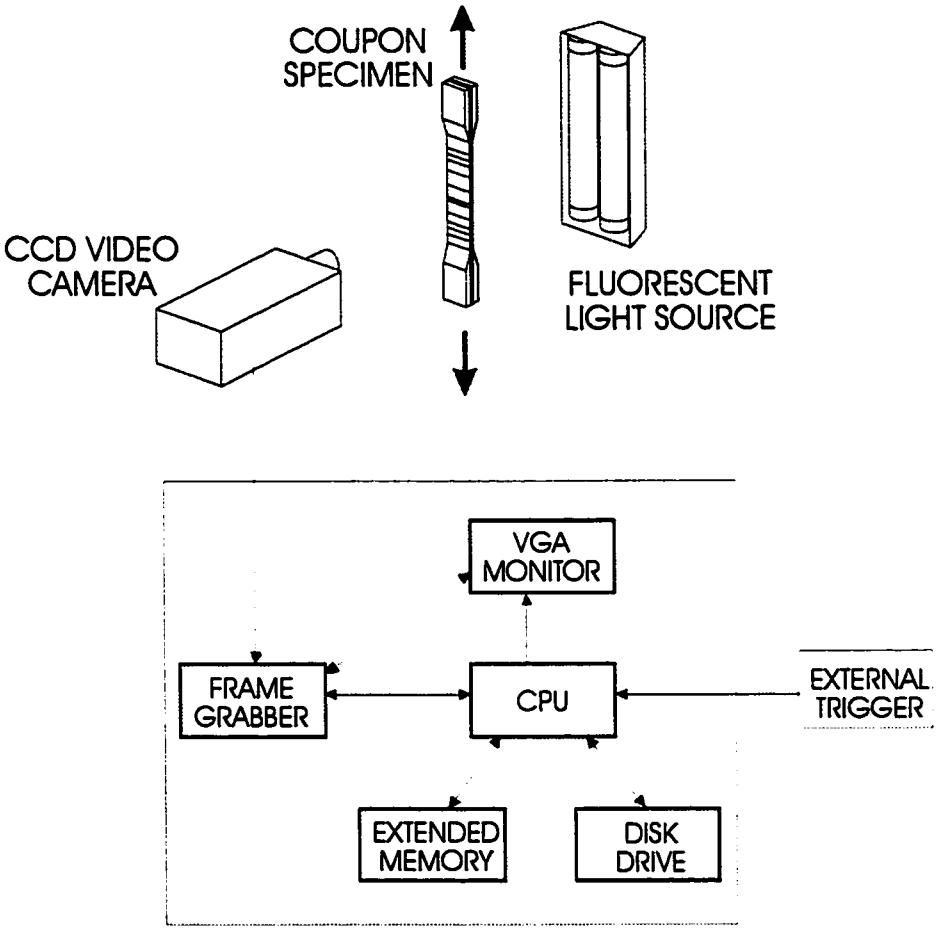

Figure 2.13: Schematic of crack detection apparatus (Courtesy of Wolodko [28])

The optical imaging system operates by first directing a strong light through the semi-transparent composite specimen, and then capturing an image on the opposite side of the specimen using a digital video camera. Any damage in the specimen can be seen as a darker region in the specimen where the damage has reduced the intensity of light that can travel through the composite.

For the $(0_2/90_3)_s$ and $(\pm 45/90_3)_s$ specimens, crack growth in the 90° plies is in the form of through-width cracks perpendicular to the direction of loading. Images are analyzed by the computer by summing the intensity of light in bands parallel to the direction of the matrix cracks. Large spikes in the intensity are determined by the program to be matrix cracks. Figure 2.14 illustrates the process that the software employs to determine the transverse crack damage information.

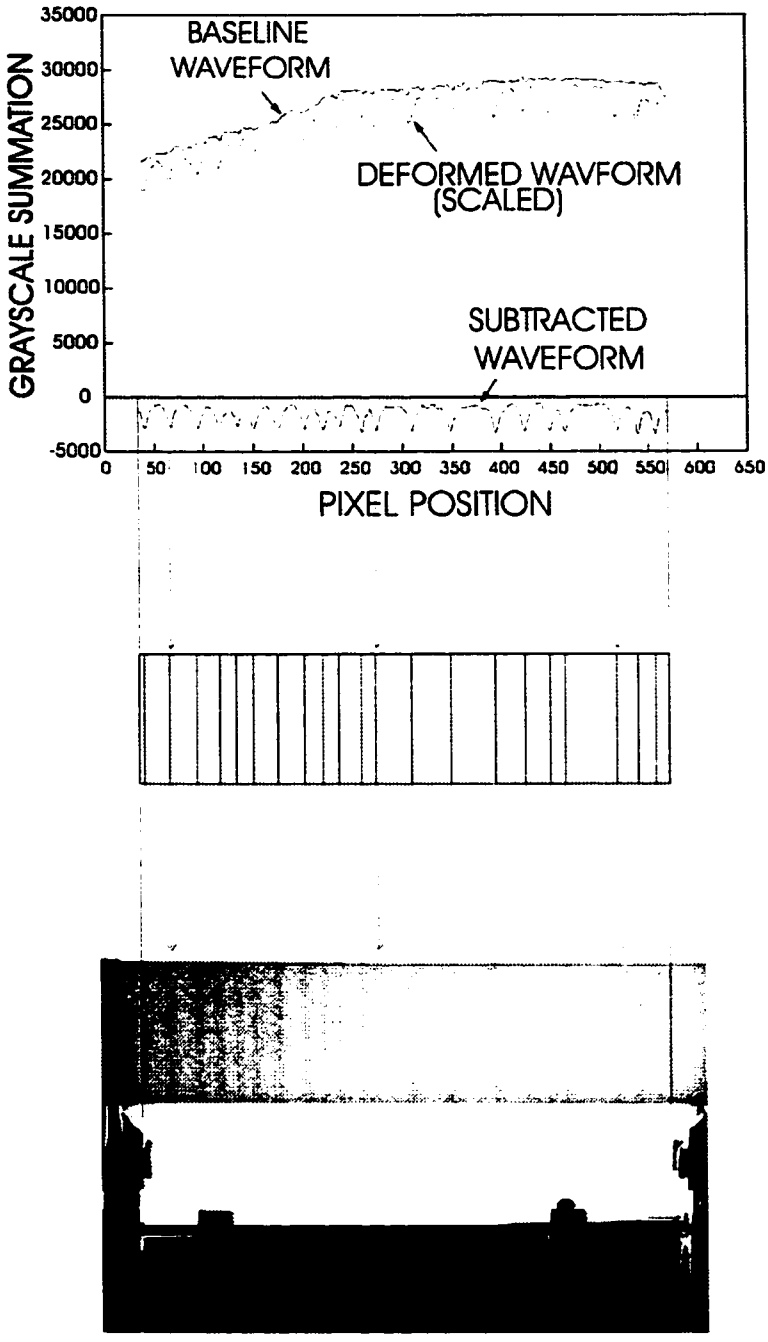

Figure 2.14: Light intensity summation technique for in-situ transverse crack information (Courtesy of Wolodko [28])

In later angle-ply specimens, such as the $(0/\pm75_4/0)_T$ specimens, the optical imaging system was used to find the saturation state of matrix cracking. Images were recorded throughout the test and then afterward viewed in reverse order until changes in the crack density could be noticed. The image that first showed the entire crack pattern was taken as the point of crack saturation.

2.6.2 Microscopic Edge Examination

The second method of visual damage detection used was an optical binocular microscope. This device proved very useful in determining the point of edge crack initiation, edge crack saturation, and the onset of delamination in the constrained angle ply specimens. Since almost all damage initiates through edge defects in the specimens, this method is very good at determining points of crack initiation. By applying visual dye penetrant to the edge surface of the specimen, contrast in the edge cracks can be enhanced for easier examination. This microscope also had a camera mount that proved useful in documenting damage along the edge of the specimens. Some of the images from this camera are shown later in Chapter 4. The microscope was kept on a set magnification so that the vertical length of the specimen being examined was always 7.5mm in length. This was useful in determining edge crack densities. A picture of the Optical microscope configuration is show below in figure 2.15.

Figure 2.15: Optical microscope used to examine edge crack growth in composite laminates

2.6.3 Stiffness Reduction

The measurement of the reduction in stiffness has proved to be a good damage parameter for cyclic testing of composite specimens [8]. The amount of stiffness reduction changes depending on the dominant damage mode in a composite. Stiffness reduction has also been found to correlate well with matrix crack damage growth. By recording the hysteresis loops for individual cycles, and fitting a linear slope to them, an accurate measurement of the specimen stiffness can be obtained. Analysis of individual hysteresis loops for all types of specimens examined showed that the inelastic effects were small in the specimens. This made it very easy to determine the stiffness, since the hysteresis loops were almost linear in shape.

3 Damage Growth During Cyclic Loading of Cross-ply and Multi-ply Coupon Specimens

This chapter has three objectives:

The first is to examine the differences between specimens tested under quasi-static and cyclic loading. By understanding the differences between these, it may be possible to reduce future cyclic testing and use the much simpler method of quasi-static, or even monotonic testing to gain the required information for composite design.

The second objective is to study how damage initiates and propagates in the $(0_2/90_3)_s$ and $(\pm45/90_3)_s$ laminates under cyclic loading. By examining the different damage modes of these specimens, comparisons are made to see how these damage modes differ between the two laminate geometries.

The third objective involves examining differences between tests performed under load control and deformation controlled modes. For this part of the study $(\pm45/90_3)_s$ laminates are tested under both control modes and comparisons are made.

3.1 Summary of Cyclic Tests Performed

Several cyclic tests were performed for the two laminate geometries. Tables 3.1, 3.2, and 3.3 show test data compiled for the various specimens. The tests were divided into groups based on their orientation as well as the control mode (strain or load control).

Table 3.1: $(\pm 45/90_3)_s$ specimens tested under strain control

SPECIMEN: $(\pm 45/90_3)_S$	Loading type : Strain Control
Specimen Number	Maximum Applied Strain
AF-4	0.67%
AF-5	0.30%
AF-6	0.55%
AF-7	0.60%
AF-22	0.33%
AF-24 (I)	0.90 %
AF-33 (I)	1.10 %
AF-34 (I)	1.25 %
AF-35 (I)	0.85 %
AF-41 (I)	0.80 %
AF-178 (I)*	0.80 %
AF-181 (I)*	0.40 %
AF-182 (I)*	0.30 %
* Performed with new software, (I) indicates image processor used.	

Table 3.2: $(\pm 45/90_3)_s$ specimens tested under load control

SPECIMEN: $(\pm 45/90_3)_S$	Loading type: Load Control
Specimen Number	Maximum Applied Load
AF-26 (I)	71.00 MPa
AF-36 (I)	60.00 MPa
AF-43	59.00 MPa
AF-44 (I)	61.00 MPa
AF-45 (I)	55.00 MPa
AF-46 (I)	50.00 MPa
AF-179 (I)*	40.00 MPa
AF-180 (I)*	45.00 MPa
* Performed with new software, (I) indicates image processor used.	

Table 3.3: $(0_2/90_3)_s$ specimens tested under load control.

SPECIMEN: $(0_2/90_3)_S$	Loading type: Load Control
Specimen Number	Maximum Applied Load
AF-12 (I)	300 MPa
AF-14 (I)	210 MPa
AF-15	237 MPa
AF-16	257 MPa
AF-19	275 MPa
AF-20 (I)	245 MPa
AF-117	230 MPa
AF-184 (I)*	290 MPa
AF-185 (I)*	240 MPa
AF-186 (I)*	160 MPa
AF-187 (I)*	80 MPa
AF-188 (I)*	90 MPa
AF-189 (I)*	70 MPa
AF-190 (I)*	60 MPa
AF-191 (I)*	50 MPa
* Performed with new software, (I) indicates image processor used.	

3.2 Quasi-Static Test Results

Quasi-static test data was obtained for comparison with cyclic tests. The sources of this data were: a) tests performed by the author, and b) those from a previous investigation at the University of Alberta by Hoover [30]. Stiffness and crack density data was obtained so that crack density vs. specimen stiffness plots could be produced.

Quasi-static tests by the author were performed under strain control on both $(\pm 45/90_3)_s$ and $(0_2/90_3)_s$ specimens. The test procedure consisted of the following:

Initially the specimen was loaded at a rate of $1 \times 10^{-4} s^{-1}$. Loading ramps started at 0% strain and increased by 0.2% strain for each successive ramp. After loading to the set

strain increment the load was ramped to zero at the same rate, and upon reaching zero an image was captured using the image processor. A five minute hold time was implemented with the strain at 0% before reloading to the next highest increment. This procedure was performed until failure of the specimen.

3.2.1 Damage Propagation and Failure of Specimens Under Quasi-Static Loading

For the two types of specimens examined under quasi-static loading ($(0_2/90_3)_s$ and $(\pm45/90_3)_s$), ultimate failure occurred in different ways. Both specimens experienced a similar initiation of through-width matrix cracking at 0.6% applied strain. In these quasi-static loading tests, neither specimen type developed a true saturation state of matrix cracks. Instead, due to the constantly increasing strain, new matrix cracking continued up until the ultimate failure of the specimen.

Delamination growth was different between the $(0_2/90_3)_s$ and $(\pm45/90_3)_s$ specimens. The $(\pm45/90_3)_s$ specimens first experienced small triangular delaminations at approximately 1.8% applied strain. These delaminations then continued to grow at a constant rate up until the failure of the specimen. No delaminations were observed for the $(0_2/90_3)_s$ specimen until very close to ultimate failure of the cross-ply laminate at a strain of approximately 2.1%. When these delaminations did occur, they were in long strips that were the result of fibre-breakage underneath the tabs of the specimen, and they propagated very quickly along the length of the specimen.

Ultimate failure of the $(\pm 45/90_3)_s$ specimens took place at an applied strain of 2.33%, whereby the delamination within the 45° plies grew across the width of the specimen

The $(0_2/90_3)_s$ laminate has a much different ultimate failure than the $(\pm 45/90_3)_s$ one. In this specimen, there was very little forewarning of failure. Since the outer constraining plies are oriented in the direction of loading, the fibres sustain most of the load. When some of the 0° fibres fracture, the cross sectional load is redistributed to the other fibres that fail instantaneously under the increased load. The end result is a very quick brush-like failure throughout the entire gauge length of the specimen. Ultimate failure of this specimen occurred at a strain of 2.2%, not long after the initial delaminations were observed.

3.2.2 Quasi-Static Stress-Strain Curves

Stress-strain curves were produced for the quasi-static tests performed and are shown in Figures 3.1 and 3.2. On these plots the light lines under the darkened bold line each represent consecutive loading ramps with increased strain of 0.2%. In both of these figures there is a definite change in the slope of the specimen at approximately 0.6% strain. This change in slope is at the same point of crack initiation in the specimen. This knee-point is indicative of load redistribution to the undamaged constraining plies. These outer plies then undergo larger strains due to the increased load. In both plots, the successive ramps fall into a compressive stress regime near 0% strain. This is due to the

strain control of the tests, whereby after damage has occurred in the specimen, compressive stresses are required to reach 0% strain.

Of interest when comparing the two specimens is the difference in strength of the specimens. The $(0_2/90_3)_s$ specimen has an ultimate failure strength of approximately 350 MPa, while the $(\pm 45/90_3)_s$ specimen has an ultimate failure strength of only 100 MPa. The difference between these two specimens again lies in the constraining plies. The 0° plies with the fibres oriented in the direction of loading produce the maximum strength and stiffness possible. On the other hand, in the $(\pm 45/90_3)_s$ specimens, the constraining plies are oriented at 45° to the direction of loading, and they rely heavily on the matrix component for the strength characteristics.

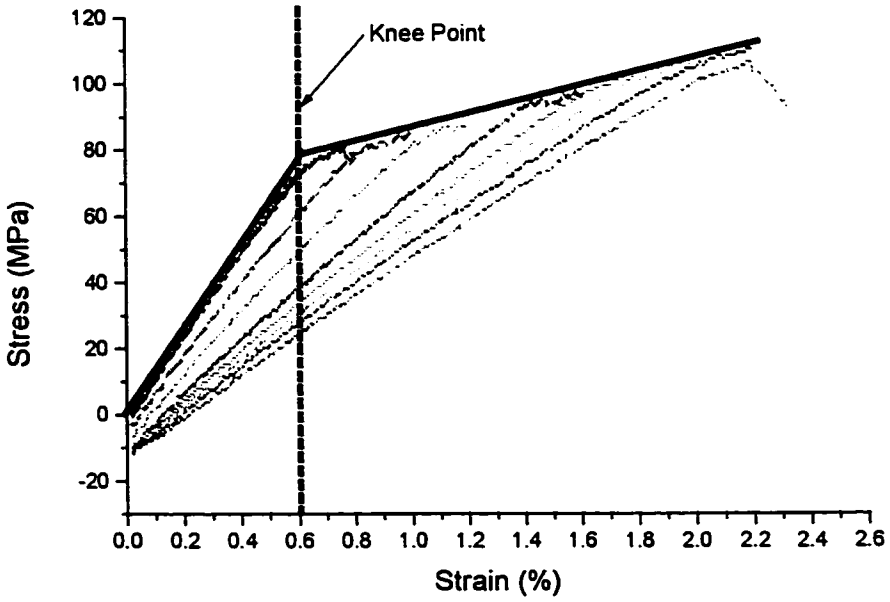

Figure 3.1: Stress-strain curve for $(\pm 45/90_3)_s$ specimen loaded quasi-statically under strain control (Each line represents a subsequent loading ramp)

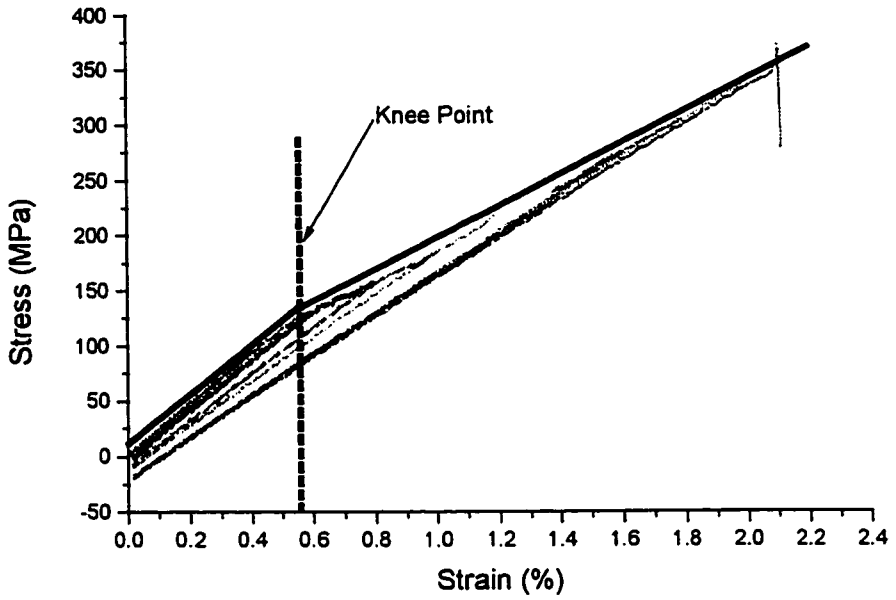

Figure 3.2: Stress-strain curve for $(0_2/90_3)_s$ specimen loaded quasi-statically under strain control (Each line represents a subsequent loading ramp)

3.2.3 Crack Density Curves

Crack density vs. strain curves were produced for both specimen types examined and are shown in Figure 3.3. Crack initiation for both orientations was at 0.6% strain, the same strain where large stiffness reductions were first seen. Both types of specimens followed similar crack density curves throughout their lives, although the $(0_2/90_3)_s$ specimen produced slightly more cracks as the strain increased. This is due to larger stress gradients between the 0° plies and the 90° plies than that seen between the 45° plies and the 90° plies, resulting in more load transfer and more matrix cracking.

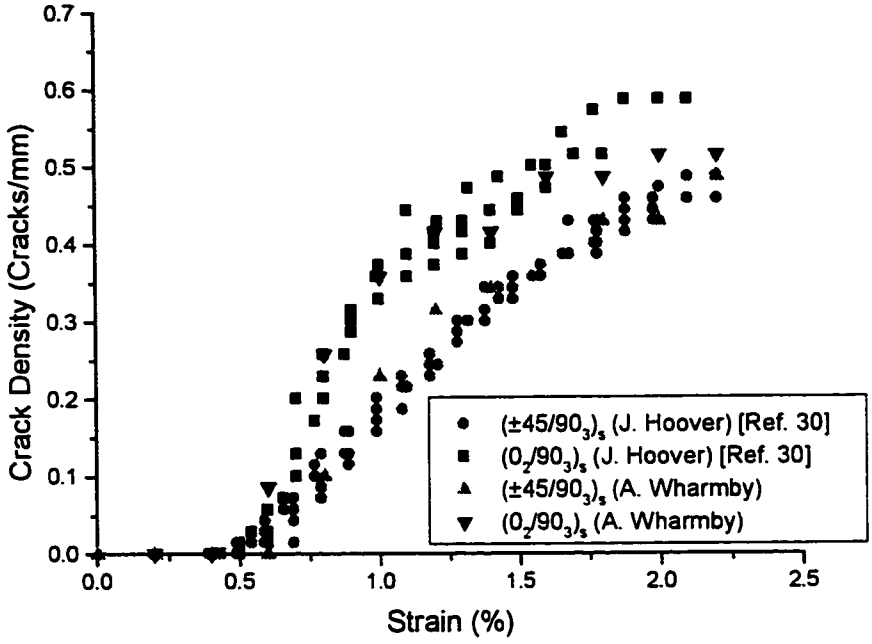

Figure 3.3: Crack density vs. strain for $(\pm 45/90_3)_s$ and $(0_2/90_3)_s$ specimens under quasi-static strain controlled loading (Courtesy of Hoover [30])

3.2.4 Crack Density vs. Stiffness Curves

Crack density vs. stiffness curves were produced for the quasi-static tests and are shown in Figure 3.4. By plotting both the $(\pm 45/90_3)_s$ and $(0_2/90_3)_s$ curves on the same figure, their slopes can be compared.

The slopes of both specimen geometries were found by fitting linear curves to the test data. For the $(0_2/90_3)_s$ specimens, the slope was –9.21 GPa/(crack/mm). For the $(\pm 45/90_3)_s$ specimens, the slope was –11.62 GPa/(crack/mm). These are quite close, although there is more change in slope for the matrix dominated specimen. This is due to two possible effects that occur in the $(\pm 45/90_3)_s$, but not in the $(0_2/90_3)_s$ specimens. The

first effect is increased stiffness reduction due to visco-elasticity in the constraining ply matrix in the $(\pm 45/90_3)_s$ specimens. The second reason for the larger stiffness drop could be that there is extra matrix cracking in the constraining plies of the $(\pm 45/90_3)_s$ specimens which is not accounted for in the crack density measurements.

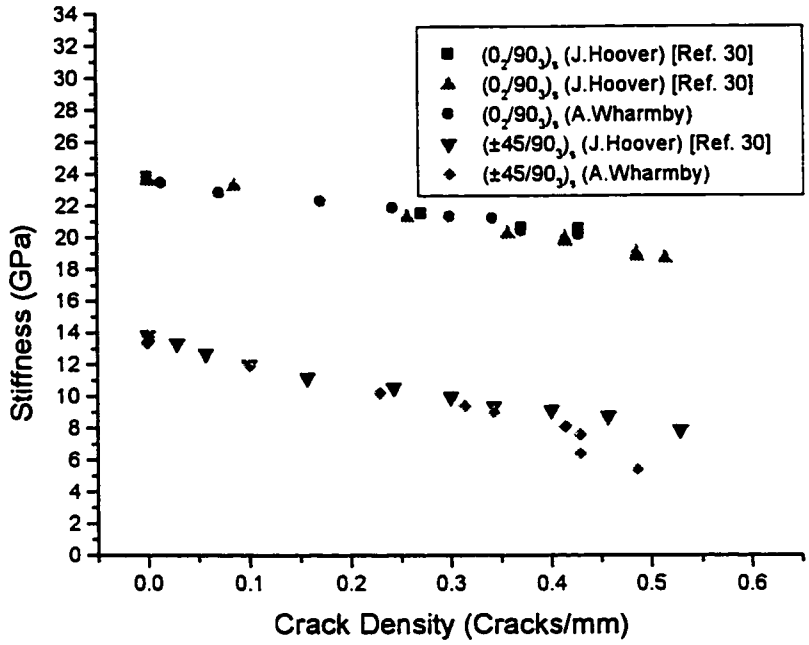

Figure 3.4: Stiffness reduction vs. crack density for $(0_2/90_3)_s$ and $(\pm 45/90_3)_s$ coupon specimens under quasi-static loading

3.3 Cyclic Test Results

3.3.1 Description of Damage Growth and Specimen Failure under Cyclic Loading

Failure of specimens under cyclic loading had some distinct differences from that of quasi-static loading. A number of extra factors are present in the cyclic tests including frequency, R-ratio, the number of cycles a specimen undergoes, as well as any effects of the cyclic waveform.

Presented in this section are consecutive images of typical specimens as damage initiates and propagates through them over their cyclic life. In these figures the life of the specimen was normalized with respect to the number of cycles at failure. When normalized in this manner, specimens of the same geometry have comparable damage growth at these points in the specimens life irrespective of the loading level, so these figures can be assumed to be general. The damage growth with respect to the normalized data will be discussed further in 3.3.3 and 3.3.4.

The systematic damage growth and failure of an $(0_2/90_3)_s$ specimen subjected to cyclic loading is outlined in the Figures 3.5 and 3.6. These show the damage growth in specimen AF-14, which underwent a maximum applied load of 210 MPa.

The first damage mode seen was matrix cracking which appear in the 90° layers as dark vertical bands. These matrix cracks occur very early in the overall life of the specimen (earlier than N/Nf = 0.0006). They immediately propagate through the width. Very little, if any, partial cracking can be seen with this type of specimen lay-up. Cracking continues until a saturation state of matrix cracks is achieved. Near the

saturation state a new damage mode begins. Matrix cracks propagate to the constraining plies where they grow perpendicular to the original crack direction, along the lengths of the 0° fibres. These are termed longitudinal matrix cracks, and are first seen at N/Nf = 0.006 in the form of dark horizontal lines. When damage growth in this form is nearly exhausted, the damage mode changes once again. From these longitudinal matrix cracks, and from the edges of the specimen, delaminations grow (First seen at N/Nf=0.012). These delaminations grow in long lengthwise strips. They slowly progress inwards until there is almost complete separation between the 0° and 90° plies. This damage mode comprises the largest portion of the specimen life. The damage mode doesn't change again until N/Nf=0.98, when fibre failure becomes the dominant damage mode. A quick and instantaneous failure of the specimen follows soon thereafter.

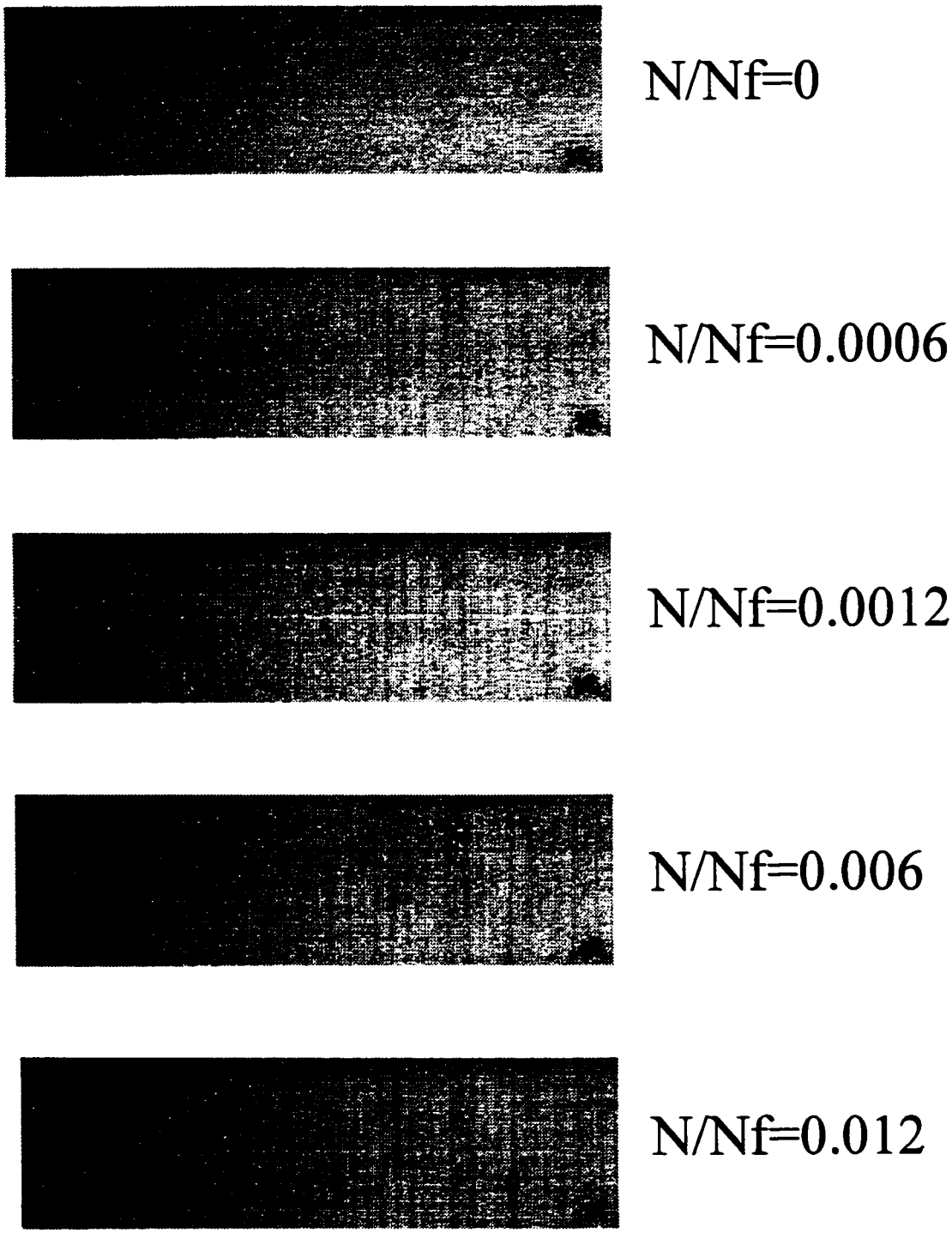

Figure 3.5: Damage progression of a typical $(0_2/90_3)_s$ composite laminate, cycles 0 through 10,000

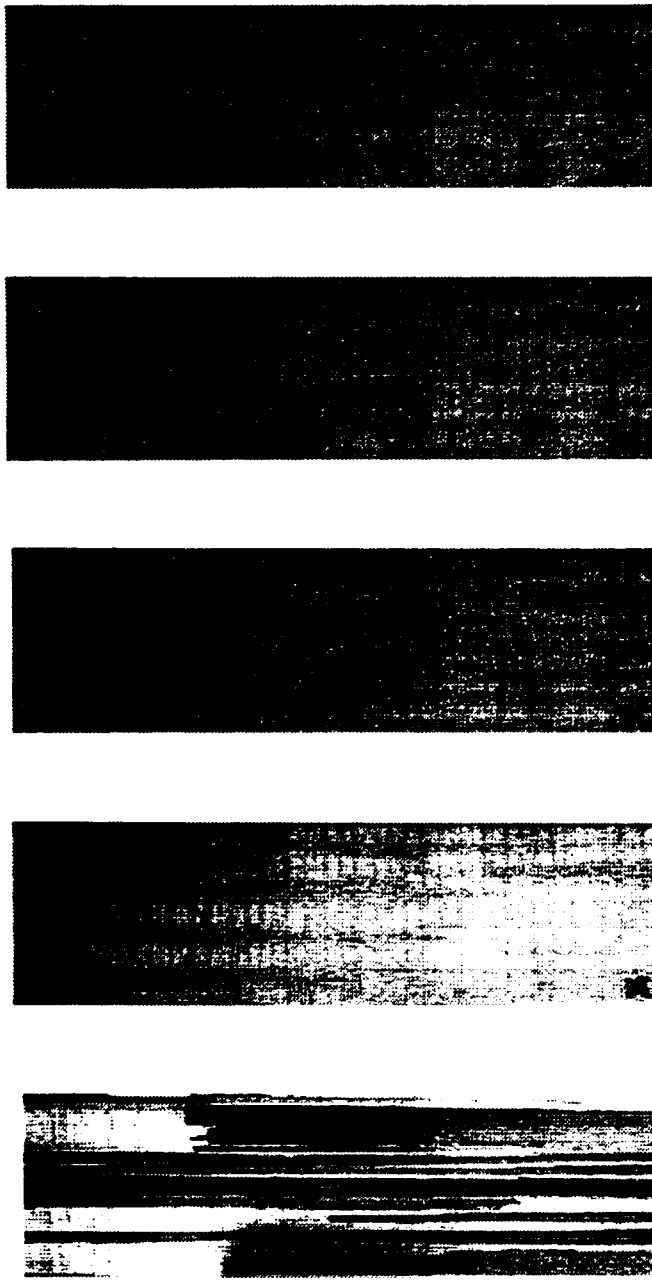

Figure 3.6: Damage progression of a typical $(0_2/90_3)_s$ composite laminate, cycles 100,000 through to failure at 865,000 cycles

A different damage growth is described below for the $(\pm 45/90_3)_s$ specimens.

Figured 3.7 and 3.8 show the damage progression throughout the fatigue life of a $(\pm 45/90_3)_s$ specimen. This is specimen AF-36, with a maximum applied load of 60 MPa. In the $(\pm 45/90_3)_s$ specimen the crack initiation is at N/Nf=0.012. Initially the matrix cracking in the $(\pm 45/90_3)_s$ specimen follows the same pattern as the $(0_2/90_3)_s$ specimen. Differences begin only when the damage propagates into the constraining plies of the specimen. In the $(\pm 45/90_3)_s$ specimens, matrix cracking is seen in the constraining plies at 45° angles from the direction of loading. This constraining ply matrix cracking is first seen at N/Nf = 0.06, and is mostly present where transverse cracks from the 90° layers have propagated into the constraining plies. These cracks begin as small partial cracks and propagate until they span the length of the 45° fibres.

Differences are apparent between the cracks in the 90° layers and those in the 45° layers. The 45° layer cracks start out as partial cracks, and appear to have a higher crack density. Previous work had found that when the thickness of the similarly oriented plies decreases, the crack density in that section increases, and more partial cracks appear [21]. In Figure 3.8, delaminations can be seen to propagate and grow near the point of matrix crack saturation. These small triangular delaminations begin at approximately N/Nf=0.29. They initiate in the 45° layers at the outer edges where the localized strain is the greatest. While delaminations propagate longitudinally in the $(0_2/90_3)_s$ specimens, in the $(\pm 45/90_3)_s$ specimens they grow at 45° angles from the edges. This delamination growth along the direction of the 45° layers continues until it is across the width of the

specimen. At N/Nf=0.98 the triangular delaminations have grown across half of the width of the specimen. The remaining delamination growth occurs in the last 2% of the specimens life. When the delamination has spread across the entire width, only the matrix in the 45° layers holds the specimen together, and this matrix fails under shear loading parallel to the fibres. Ultimate failure in this specimen is dominated by the strength of the matrix, as is seen when N/Nf = 1.0. There is no fibre failure present in this final failed state.

Visual differences in damage growth between the two specimens are most apparent in the constraining plies. It is here that the different fibre orientations produce the distinct delamination and ultimate failure patterns for each specimen.

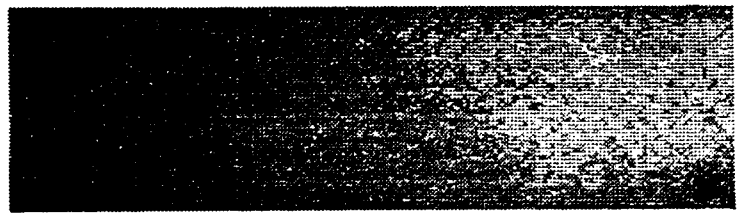

N/Nf=0

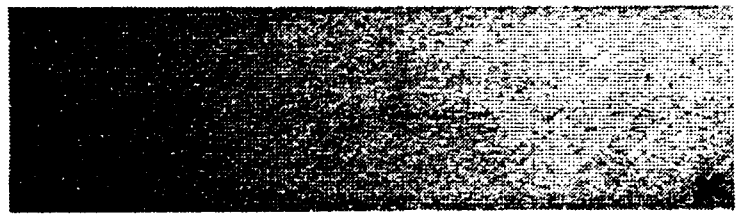

N/Nf=0.006

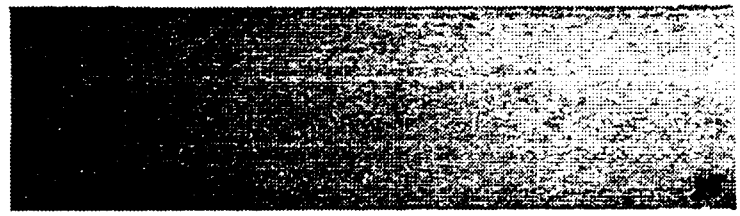

N/Nf=0.012

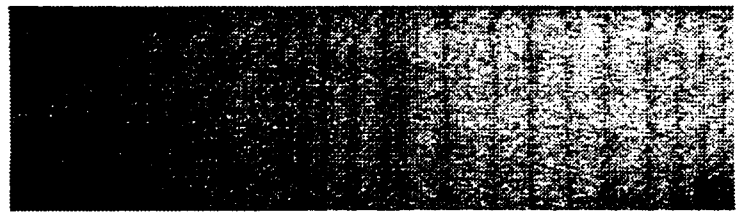

N/Nf=0.06

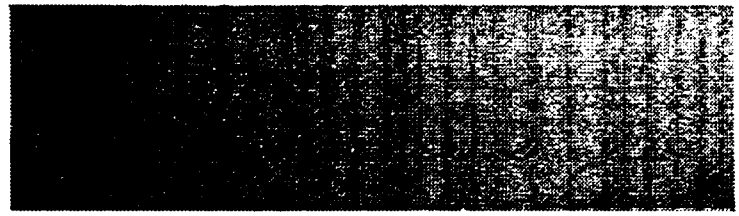

N/Nf=0.12

Figure 3.7: Damage progression of a typical $(\pm 45/90_3)_s$ composite laminate, cycles 0 through to 10,000 cycles

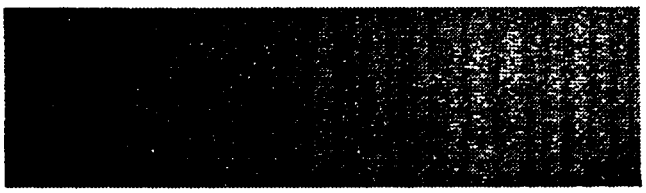

N/Nf=0.29

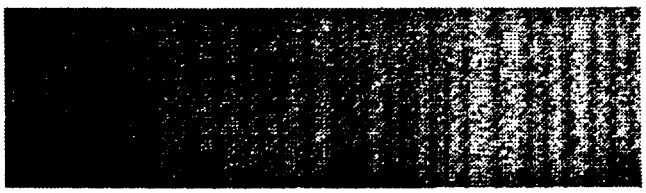

N/Nf=0.59

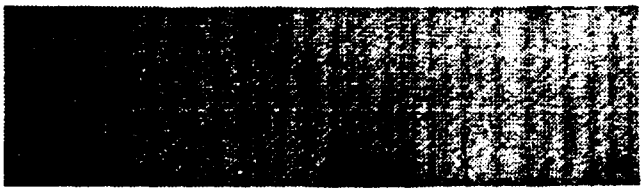

N/Nf=0.88

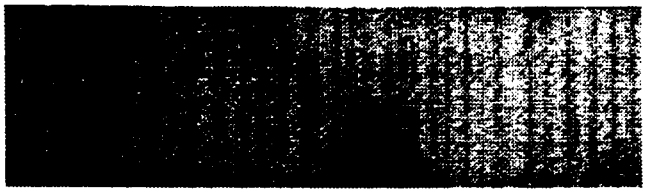

N/Nf=0.98

Failed Specimen at N/Nf=1.0

Figure 3.8: Damage progression of a typical $(\pm 45/90_3)_s$ composite laminate, cycles 25,000 through to failure at 84,900 cycles

3.3.2 Damage Mode Curves

Damage mode curves were produced for the $(\pm 45/90_3)_s$ specimens under strain control and for the $(\pm 45/90_3)_s$ and $(0_2/90_3)_s$ specimens under load control. ε-N curves for the $(\pm 45/90_3)_s$ specimens are shown in Figure 3.9. S-N curves for the $(\pm 45/90_3)_s$ and $(0_2/90_3)_s$ specimens are shown in Figures 3.10 and 3.11, respectively. In all cases, points for crack initiation, the onset of delamination, and ultimate failure of the specimen were recorded.

Figure 3.9 shows the damage mode curves for the $(\pm 45/90_3)_s$ specimens under strain control in which the maximum applied strain is plotted against the log of the number of cycles. All of the damage modes appear to follow fairly linear lines in the range of the applied strains.

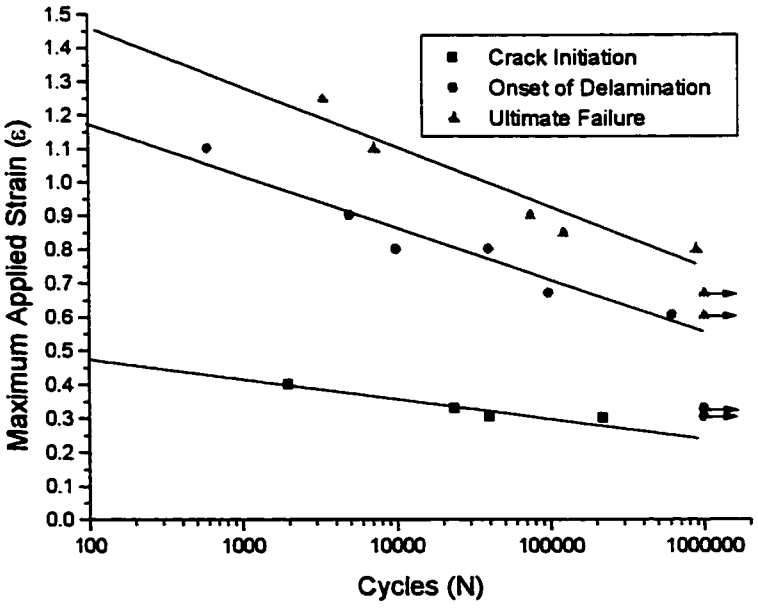

Figure 3.9: ε-N Curve for $(\pm 45/90_3)_s$ composite coupon specimens under strain control

Figure 3.10 shows the damage mode curves for the $(\pm 45/90_3)_s$ specimens tested under load control. The curves follow a similar trend as those under the strain control (Fig. 3.9). The $(\pm 45/90_3)_s$ specimens tested under load control had the shortest lives of all specimens examined. At a maximum applied stress of 40 MPa, crack initiation was not observed prior to $1x10^6$ cycles. This may indicate a possible crack initiation stress limit between 40 and 45 MPa. However, to verify this hypothesis, several long term tests need to be performed. This was beyond the scope of this study.

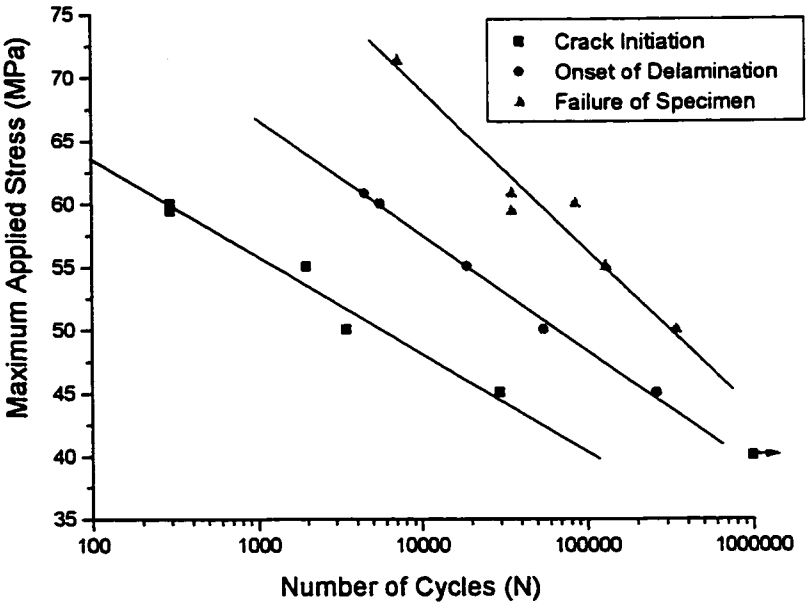

Figure 3.10: S-N fatigue curve for $(\pm 45/90_3)_s$ specimens under load control

The damage curves for the $(0_2/90_3)_s$ specimens under load control are displayed in Figures 3.11 and 3.12. In the case of the $(0_2/90_3)_s$ specimens, the range in life between the onset of cracking and ultimate failure of the specimen is very wide. This is because the matrix in the 90° layers is very weak in relation to the fibres in the 0° layers.

Specimens which developed crack initiation points, such as those shown in Figure 3.12, required much more than $1x10^6$ cycles to reach ultimate failure. For this reason two sets of specimens were tested, one set for the initiation of cracking in the 90° layers, and the other set to obtain points for the remaining damage modes. Compared with the applied loads to fail the $(\pm 45/90_3)_s$ specimens, the $(0_2/90_3)_s$ specimens loads were much higher. The loads required for cracks to initiate were also higher. This is because the 0° constraining plies contribute to a higher global stiffness, so that for a prescribed strain, a larger load would be required.

Of note in Figure 3.12 is a point that does not fall on the crack initiation curve. This is similar to that observed in Figure 3.10 and may be attributed to the existence of a crack initiation stress limit.

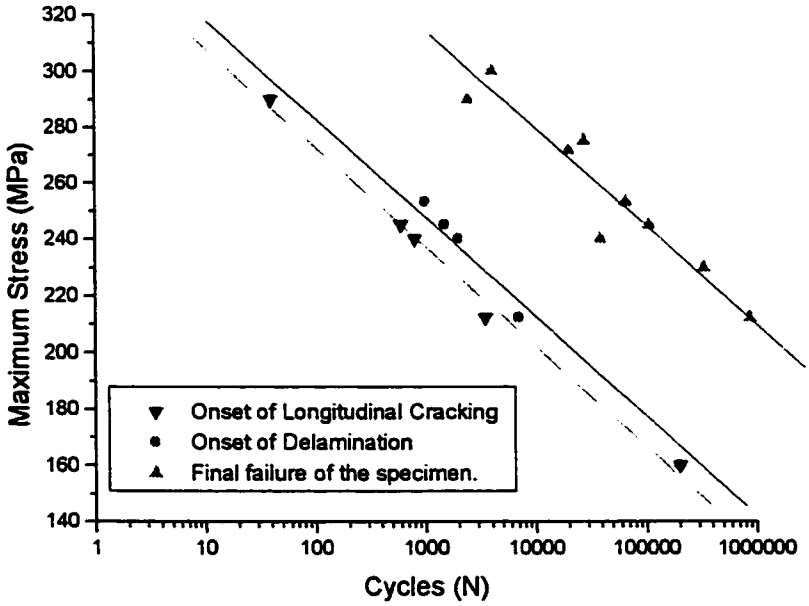

Figure 3.11: S-N fatigue curve for $(0_2/90_3)_s$ composite coupon specimens under load control

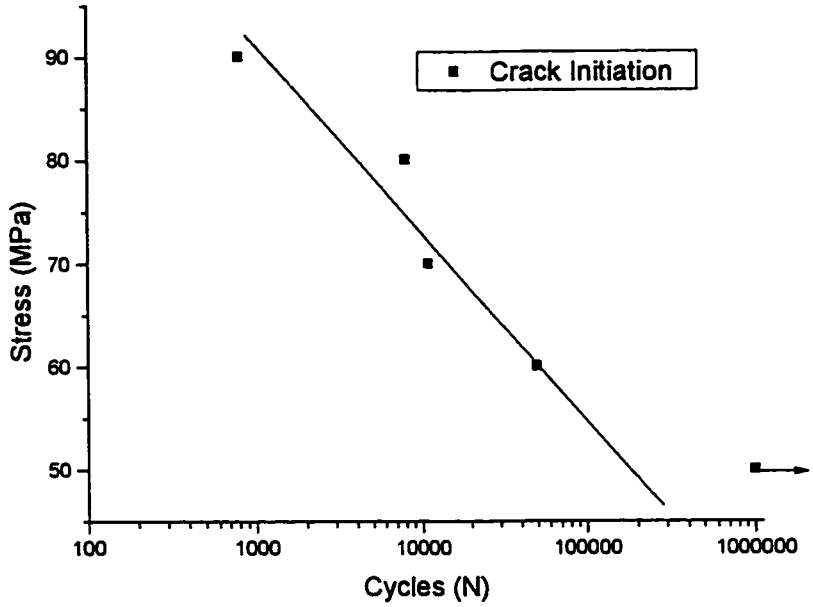

Figure 3.12: S-N fatigue curve for crack initiation in $(0_2/90_3)_s$ composite coupon specimens under load control

A check was performed to see how reliable were the crack initiation curves shown in Figures 3.9, 3.10 and 3.12. Since there is virtually no change in the global specimen stiffness prior to crack initiation, the strains at which cracking initiates should be similar irrespective of the imposed control mode (strain or load control). For tests performed under load control, the maximum strain at the crack initiation was determined by using a stiffness value found from the classical laminate theory calculations. A plot of the maximum strain vs. cycles for crack initiation is shown in Figure 3.13. There is a clear band of ±0.06% strain that all specimens fall within. This then confirms the accuracy of the crack initiation data plotted in Figures 3.9, 3.10, and 3.12.

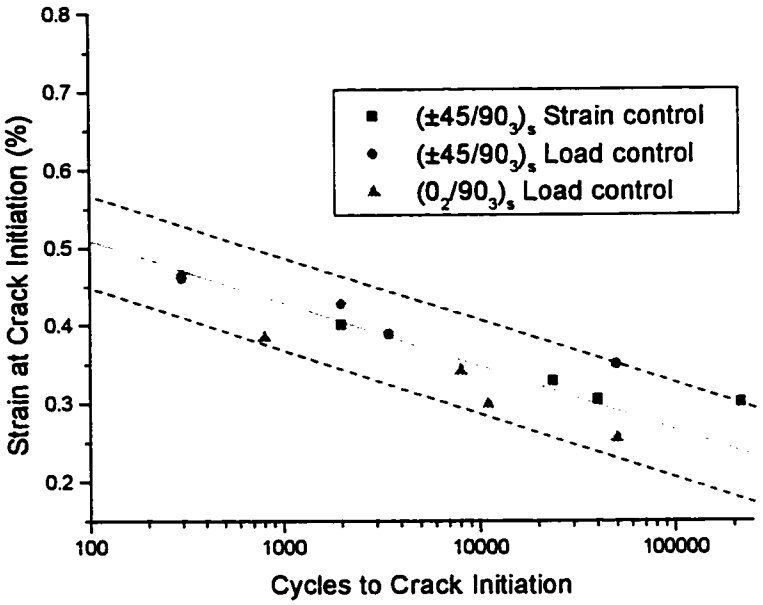

Figure 3.13: Strain vs. crack initiation for cross-ply and multi-ply specimens investigated

3.3.3 Damage Examination Technique I: Crack Density Curves

Crack density vs. life curves were produced for the three scenarios examined. Data was plotted in two forms: the first was crack density vs. cycles, and the second was crack density vs. the normalized cycles. In the second plot the cycles were normalized with the cycles to failure to examine how well all test data correlated. In some cases logarithmic plots were produced for easier investigation of damage growth near the start of the test. In all cases, the 90° matrix crack data was recorded using the image processor described in Chapter 2, section 2.6.1.

Crack density vs. life curves are presented in Figures 3.14-3.15, 3.16-3.18, and 3.19-3.20 for the $(\pm 45/90_3)_s$ specimens under strain control, $(\pm 45/90_3)_s$ specimens under load control, and the $(0_2/90_3)_s$ specimens under load control, respectively.

A table was developed outlining some of the interesting points from these figures, and are presented in Table 3.4:

Table 3.4: Details of crack density figures for the three scenarios examined

SPECIMEN	FINAL CRACK DENSITY (CRACKS/MM)	SATURATION STATE REACHED?	CRACK ONSET DELAY SEEN
$(\pm 45/90_3)_s$ Strain Control	0.45	YES	NO
$(\pm 45/90_3)_s$ Load Control	0.35-0.48	NO	YES (~1% of life)
$(0_2/90_3)_s$ Load Control	0.65	YES	NO

The final crack densities for all specimens were seen to vary with the laminate orientation. Higher crack densities were seen in the $(0_2/90_3)_s$ specimens due to higher interlaminar stresses present between the 0° plies and the 90° plies than is present between the 45° plies and 90° plies. A higher stress gradient in the $(0_2/90_3)_s$ specimens results in more load transfer. This then results in a higher crack density.

In these specimens a level of transverse crack saturation is seen in the $(\pm 45/90_3)_s$ specimens under strain control, and in the $(0_2/90_3)_s$ specimens under load control, similar to what was seen by other researchers [8]. In the $(\pm 45/90_3)_s$ specimens this is due to stress relaxation as the test progresses. As damage propagates, the same strain produces a smaller load , resulting in less new damage growth. Finally, at some point in the life of

the specimen the stress relaxes sufficiently so that no new damage growth takes place. In the $(0_2/90_3)_s$ specimens tested under load control, the strain required to reach the desired maximum loads in the constraining plies was fully elastic, so the overall strain that the specimen underwent throughout the test remained fairly constant, resulting in a saturation state of matrix cracks.

In the $(\pm45/90_3)_s$ specimens under load control the final crack density varied between 0.35 and 0.475 cracks/mm. No saturation state of cracking was observed. The strain in the constraining plies of these specimens constantly increases due to the ratcheting effect. This causes the crack density to increase up until the point of ultimate failure, resulting in no distinguishable saturation state.

A crack onset delay was seen in the $(\pm45/90_3)_s$ specimens under load control and are seen as the points before any crack growth in Figure 3.17. The crack onset delay for this specimen was approximately 1% of the specimen life. This onset delay is a result of the loading scenario, whereby the load control test constantly increases the strain as new damage grows. In this initial region, visco-plastic effects and microdamage may be leading to increases in strain, which eventually result in matrix crack growth. This crack onset delay is most likely present in the $(0_2/90_3)_s$ specimens tested under load control as well, although it is hard to detect. In these specimens the large differences in load capacity between the inner plies and constraining plies lead to matrix cracking occurring very early compared to the life of the constraining plies. This makes the crack onset delay a very small part of the overall specimen life, much less than 1%.

Other interesting findings from these figures was that for higher loads and strains, damage growth took fewer cycles. The initial slope of crack growth was steeper for specimens with larger loads and strains.

By normalizing the lives of the specimens, as shown in Figures 3.15, 3.17, 3.18, and 3.20, it could be seen that a correlation between crack densities at different loading levels occurred in the specimens which achieved a saturation state of matrix cracking. The data was more scattered for the $(\pm 45/90_3)_s$ specimens under load control, where no saturation state was reached.

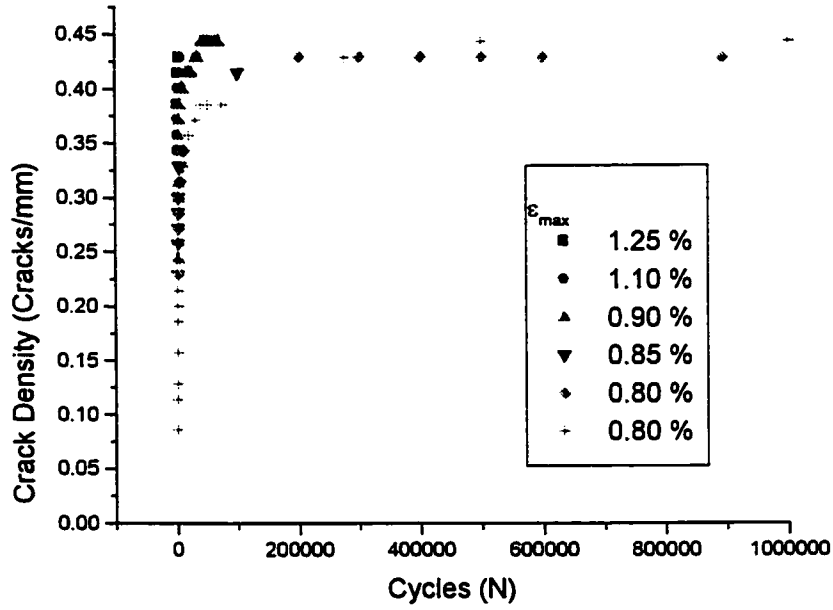

Figure 3.14: Crack density vs. cycles (linear scale) for $(\pm 45/90_3)_s$ specimens under strain control, showing a saturated state of matrix cracking

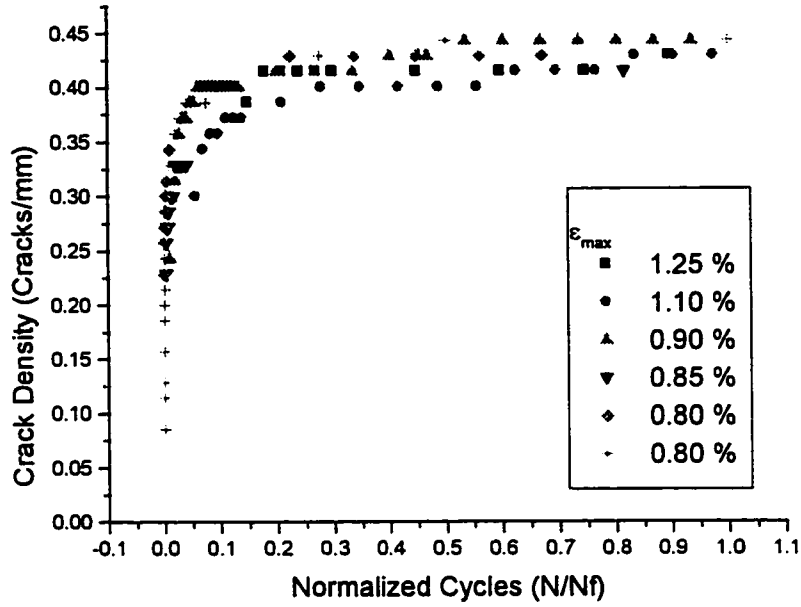

Figure 3.15: Crack density vs. normalized cycles (linear scale) for $(\pm 45/90_3)_s$ specimens under strain control

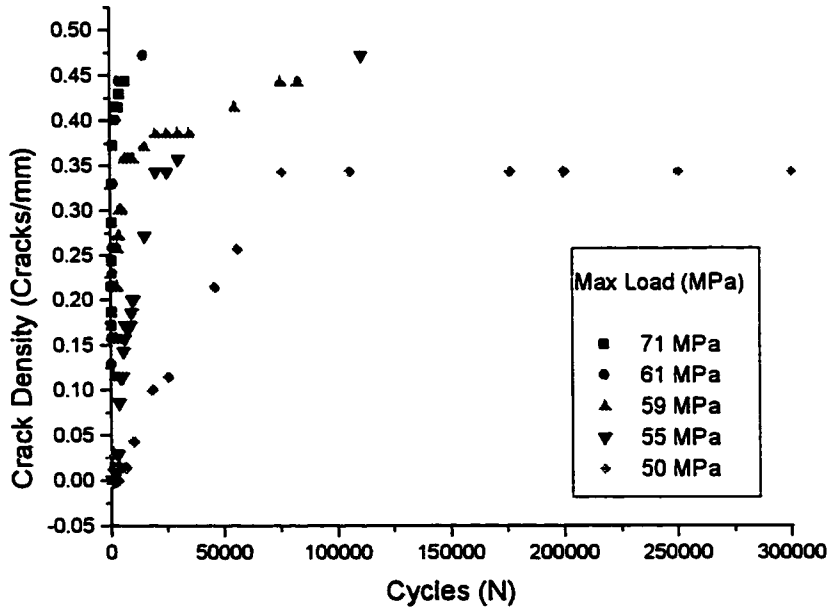

Figure 3.16: Crack density vs. cycles (linear scale) for $(\pm 45/90_3)_s$ specimens under load control

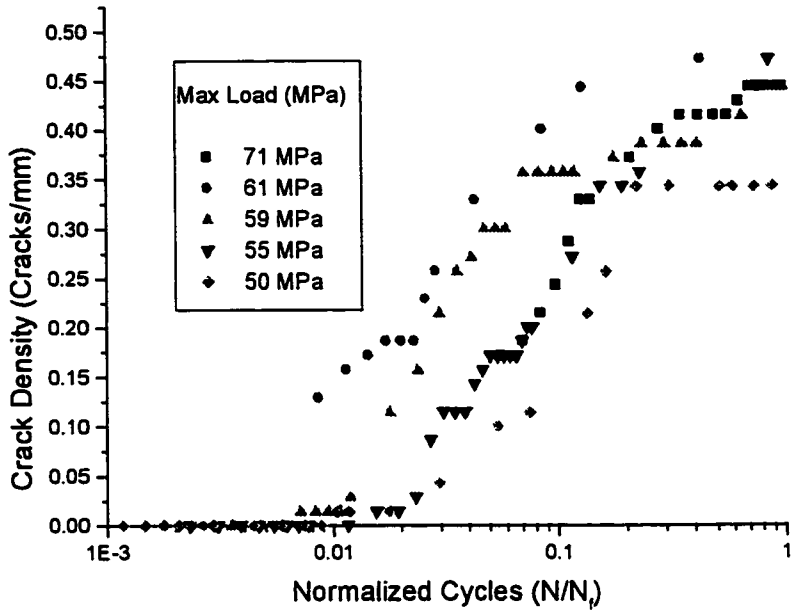

Figure 3.17: Crack density vs. normalized cycles (log scale) for $(\pm 45/90_3)_s$ specimens under load control

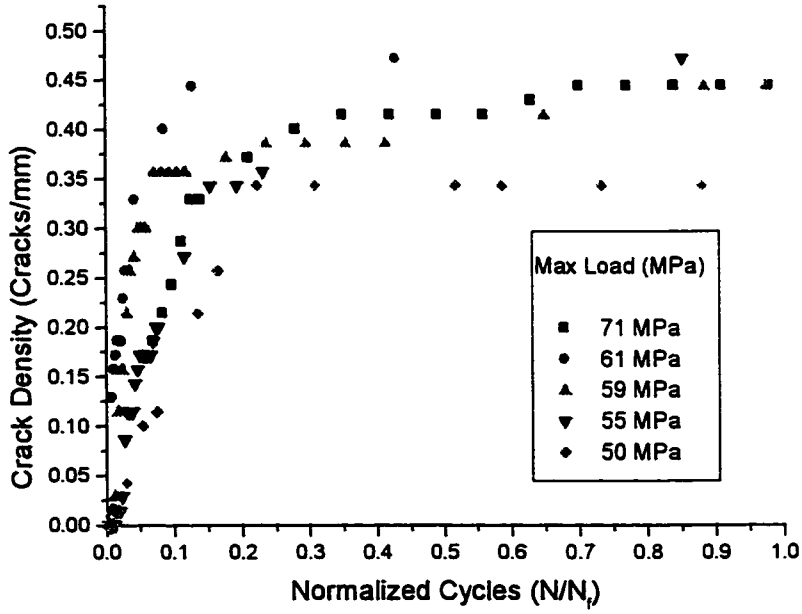

Figure 3.18: Crack density vs. normalized cycles (linear scale) for $(\pm 45/90_3)_s$ specimens under load control

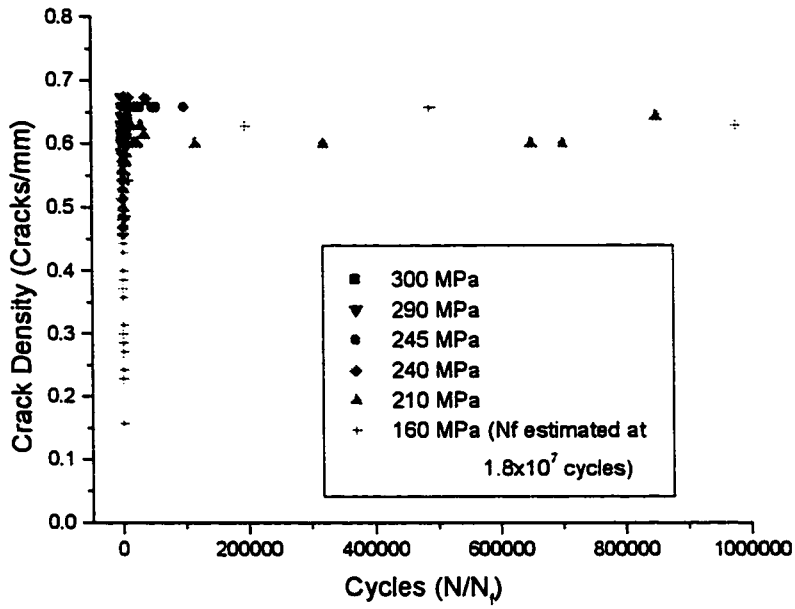

Figure 3.19: Crack density vs. number of cycles (linear scale) for $(0_2/90_3)_s$ specimens

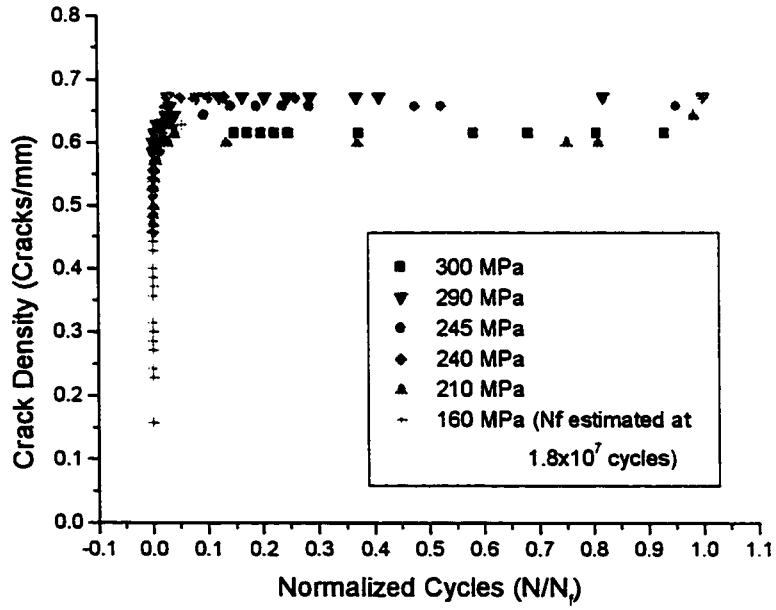

Figure 3.20: Crack density vs. normalized cycles (linear scale) for $(0_2/90_3)_s$ specimens

3.3.4 Damage Examination Technique II: Stiffness Reduction Curves

For all of the cyclic tests performed, stiffness measurements were determined from the stress-strain hysteresis loops of the specimens. These stiffness measurements were used to produce stiffness reduction curves of similar fashion to the crack density curves produced in the previous section. The stiffness reduction data is presented in two forms. In the first form, the data is plotted against the cycles on both linear and logarithmic plots. In the second form, plots are normalized with respect to the initial stiffness (E/Eo), and the failure cycles of the specimen (N/N_f). Figures 3.21-3.22, 3.23-3.25, and 3.26-3.27 show the stiffness reduction plots for the $(\pm 45/90_3)_s$ specimens under strain control, the $(\pm 45/90_3)_s$ specimens under load control, and the $(0_2/90_3)_s$ specimens under load control respectively.

Similar to the last section, a table was developed to outline the interesting differences between the specimens examined:

Table 3.5: Details of stiffness reduction figures for the three scenarios examined

	STIFFNESS REDUCTION			
SPECIMEN	TOTAL (GPA)	TOTAL (%)	DUE TO MATRIX CRACKING. (GPA)	DUE TO DELAMINATION (GPA)
$(\pm 45/90_3)_s$ (S.C)	8	58	6	2
$(\pm 45/90_3)_s$ (L.C)	7-10	50-65	5-8	2-3
$(0_2/90_3)_s$ (L.C)	6	20	6	Negligible

All of the plots show that there are two distinct sections of stiffness reduction. The first section is quite steep, and is the result of matrix cracking. The second section follows a flatter slope and is the result of stiffness reduction due to delamination. The

$(\pm 45/90_3)_s$ specimens experienced a much larger stiffness reduction from delamination due to the orientation of the constraining plies. As delamination grew through these 45° plies, less of the cross-section took up the load, resulting in increased strain and reduced stiffness. In the $(0_2/90_3)_s$ specimens there is negligible stiffness reduction due to delamination, although it is largely present as shown in Figures 3.5 and 3.6. In this laminate the 0° fibre angle prevents any increase in strain in the constraining plies over the life. This results in little stiffness reduction after the saturation state is reached, even though delamination occurs.

Stiffness reduction curves matched up well with crack density data examined in section 3.3.3. When the data was normalized with respect to the specimen life, all loading magnitudes followed similar curves for the $(\pm 45/90_3)_s$ specimens under strain control and the $(0_2/90_3)_s$ specimens under load control. More scatter in stiffness reduction was seen for the $(\pm 45/90_3)_s$ specimens under load control, which matched with findings in the crack density plots. The $(\pm 45/90_3)_s$ specimens under load control had a stiffness reduction onset delay of approximately 1% of the specimens life, as shown in Figure 3.25, similar to the crack onset delay seen earlier for the same specimen.

Although $(0_2/90_3)_s$ laminates undergo a stiffness reduction of similar magnitude to the $(\pm 45/90_3)_s$ specimens, the decrease relative to the total stiffness is only 20%. This is due to the much higher global stiffness of these specimens because of the fibres in the constraining plies being oriented in the loading direction.

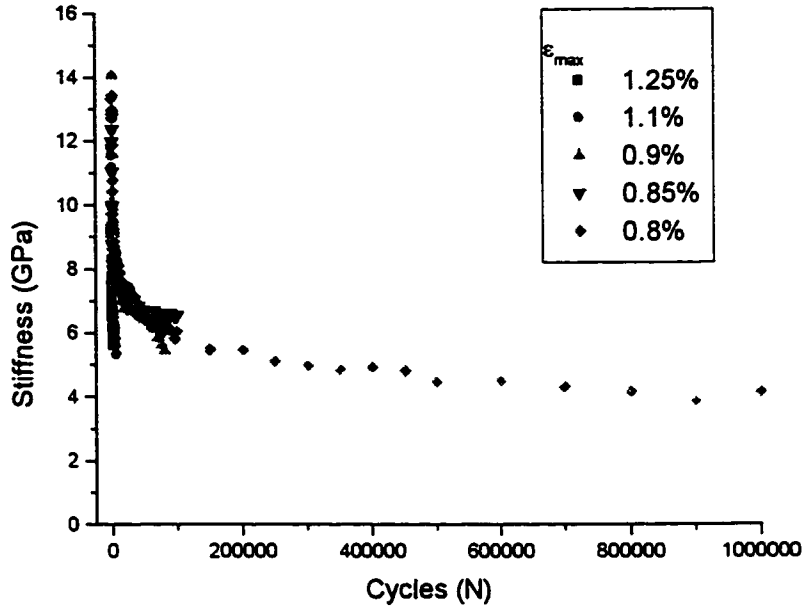

Figure 3.21: Stiffness vs. cycles (linear scale) for $(\pm 45/90_3)_s$ specimens under strain control loading

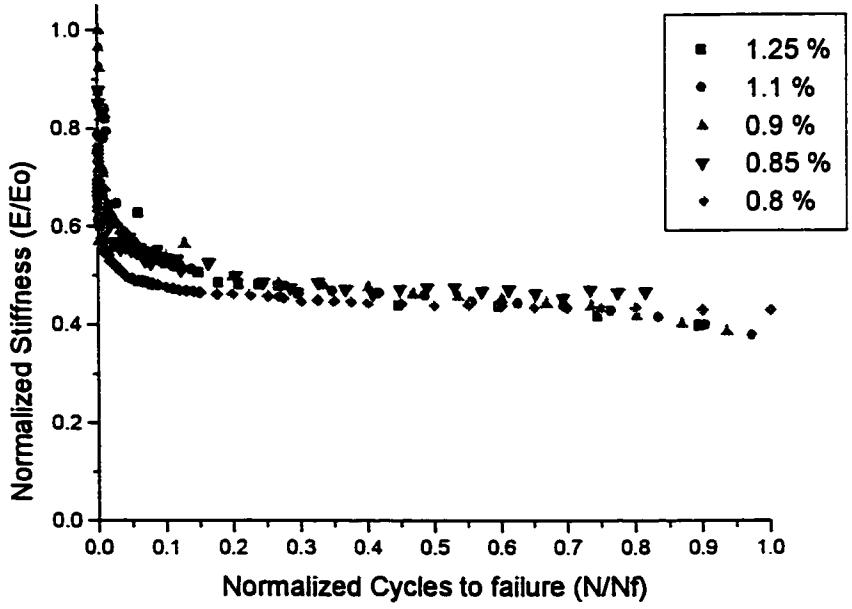

Figure 3.22: Normalized stiffness vs. normalized cycles (linear scale) for $(\pm 45/90_3)_s$ specimens under strain control loading

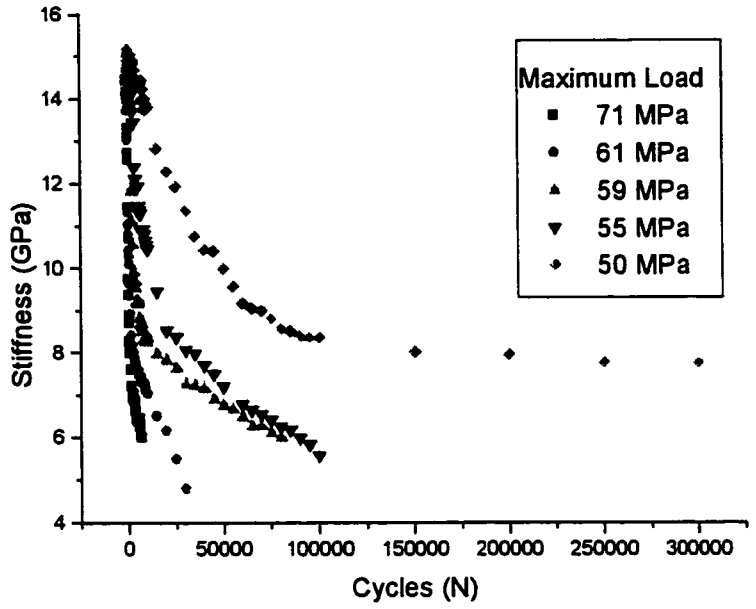

Figure 3.23: Stiffness vs cycles (linear scale) for $(\pm 45/90_3)_s$ coupon specimens under load control

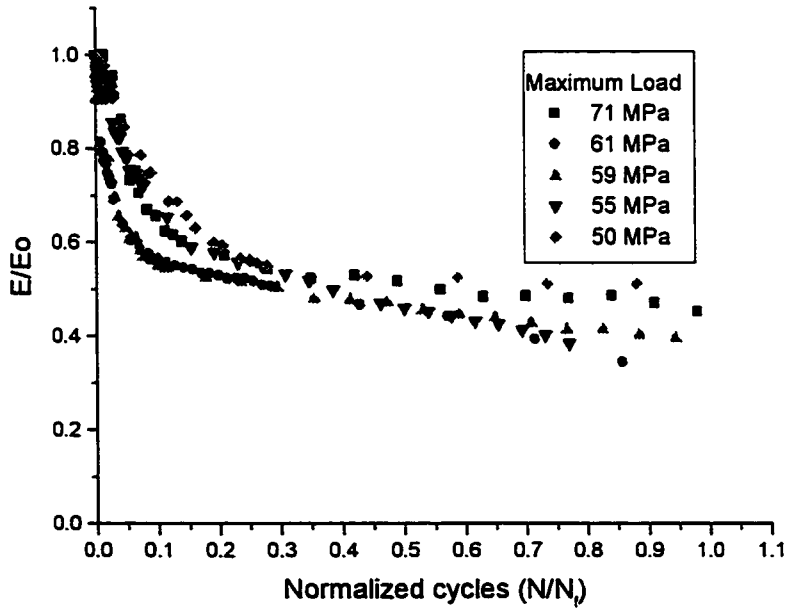

Figure 3.24: Normalized stiffness vs. normalized cycles (linear scale) for $(\pm 45/90_3)_s$ coupon specimens under load control

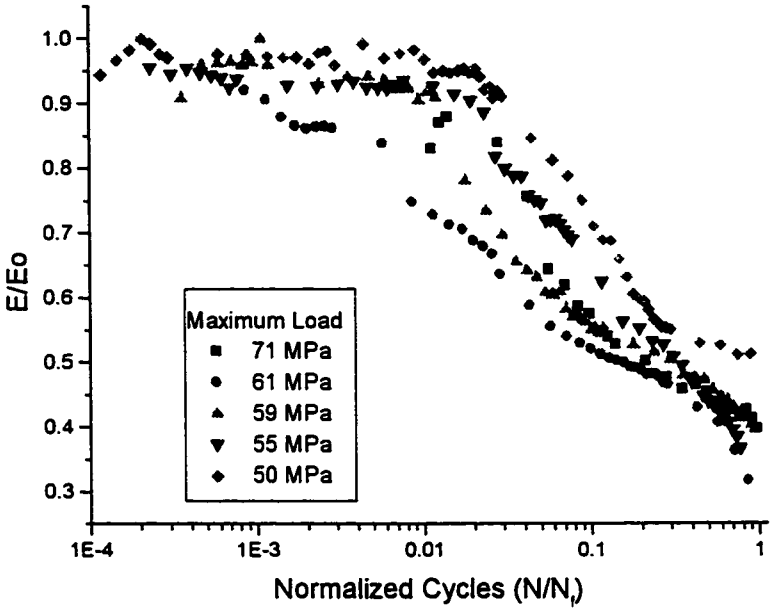

Figure 3.25: Normalized stiffness vs. normalized cycles (log scale) for $(\pm 45/90_3)_s$ specimens under load control where Eo is maximum stiffness found from all tests

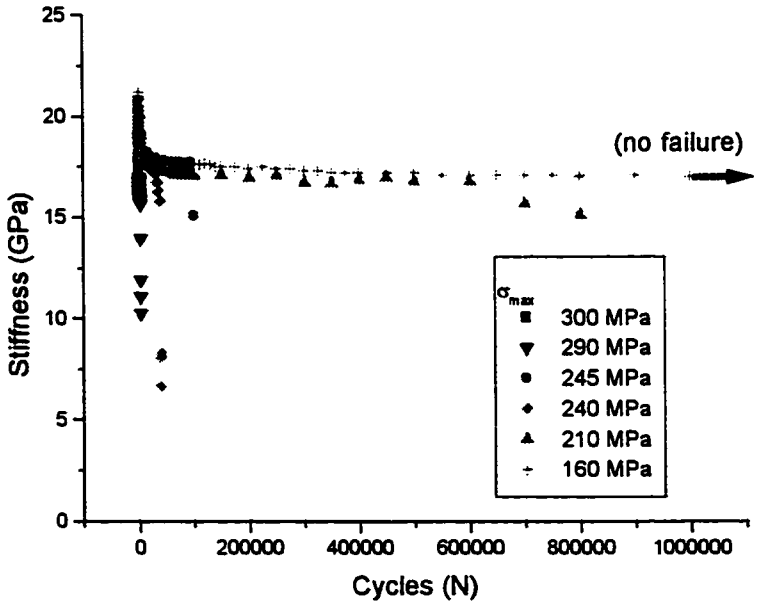

Figure 3.26: Stiffness vs. cycles (linear scale) for $(0_2/90_3)_s$ specimens

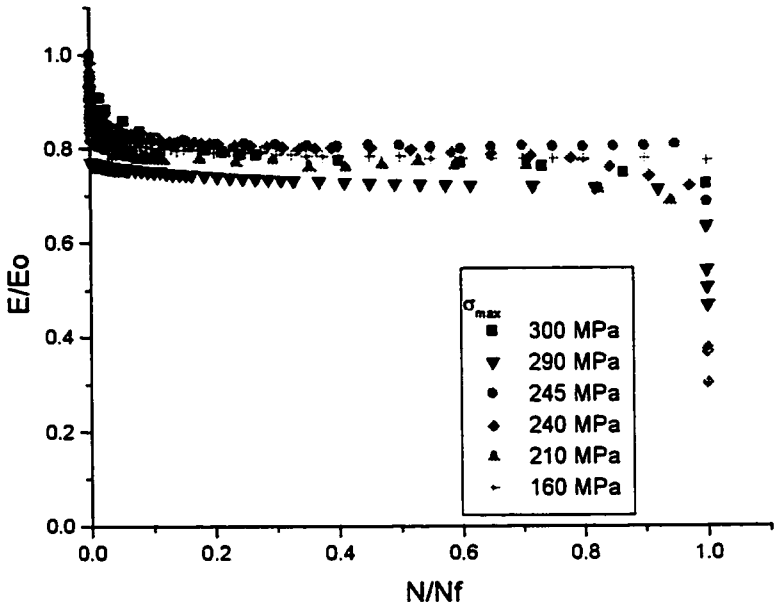

Figure 3.27: Normalized stiffness vs. normalized cycles (linear scale) for $(0_2/90_3)_s$ cross-ply specimens

3.4 Crack Density vs. Stiffness Reduction Curves

The graphs shown so far indicate that most of the stiffness loss in laminates can be attributed to transverse matrix cracking in the 90° plies of the tested specimens. To examine this further stiffness reductions were correlated with crack densities. Plots for the various specimens are shown in Figures 3.28-3.30. The slopes of these plots, as well as the quasi-static plots, were found using a linear fit and are displayed in Table 3.6.

Table 3.6: Slopes of crack density vs. stiffness curves for various laminates

	$(0_2/90_3)_s$	$(\pm45/90_3)_s$
Quasi-static tests	-9.2122 GPa/(crack/mm)	-11.623 GPa/(crack/mm)
Cyclic (load control)	-9.5101 GPa/(crack/mm)	-16.871 GPa/(crack/mm)
Cyclic (strain control)	No Data.	-14.696 GPa/(crack/mm)

Table 3.4 shows that there is a higher stiffness reduction per 90° matrix crack in the $(\pm 45/90_3)_s$ specimens when compared with the $(0_2/90_3)_s$ specimens. This may be attributed to matrix cracking in the constraining plies of the $(\pm 45/90_3)_s$ specimens that is unaccounted for in the crack density measurements. It may also be due to visco-plastic effects in the matrix of the 45° constraining plies which is not present in the 0° constraining plies. Also of interest is the steeper slope in the cyclic tests compared to the quasi-static ones. This is due to a higher rate of crack propagation in the constraining plies under cyclic loading. When the cracks are very small, as in the constraining plies, their propagation rate is also slower. In the quasi-static loading cases this results in a lower constraining ply crack density, and less stiffness reduction. Since the $(0_2/90_3)_s$ specimens do not have crack growth in the constraining plies which results in stiffness losses, these specimens do not have large differences between the quasi-static and cyclic tests.

In all of the crack density vs. stiffness curves the largest deviations from linearity occur near the start and the end of the curve. This is due to stiffness reduction from damage modes other than matrix cracking. At the start of the test the non-linearity may be due to microdamage, viscous effects, or some unknown effects which cause changes in stiffness. Near the end of the test the non-linearity is more likely from delamination growth which causes further stiffness reduction.

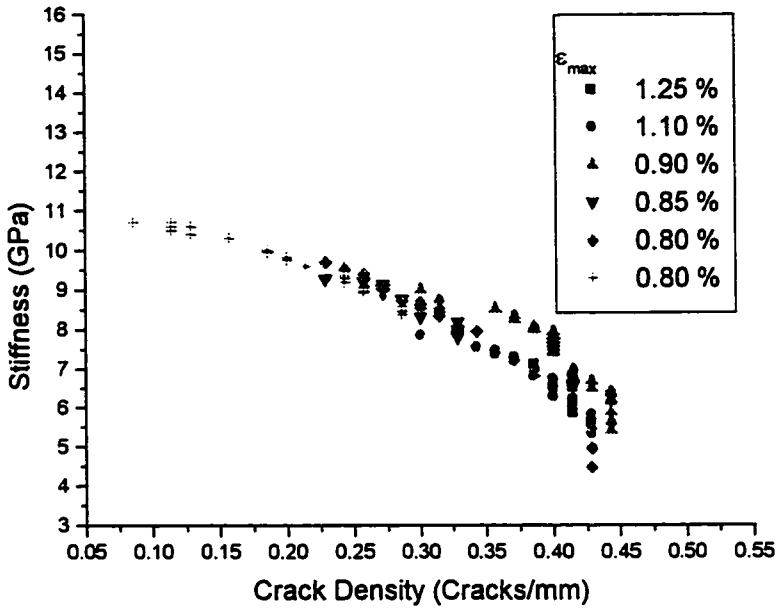

Figure 3.28: Stiffness vs. crack density for $(\pm 45/90_3)_s$ specimens under strain control

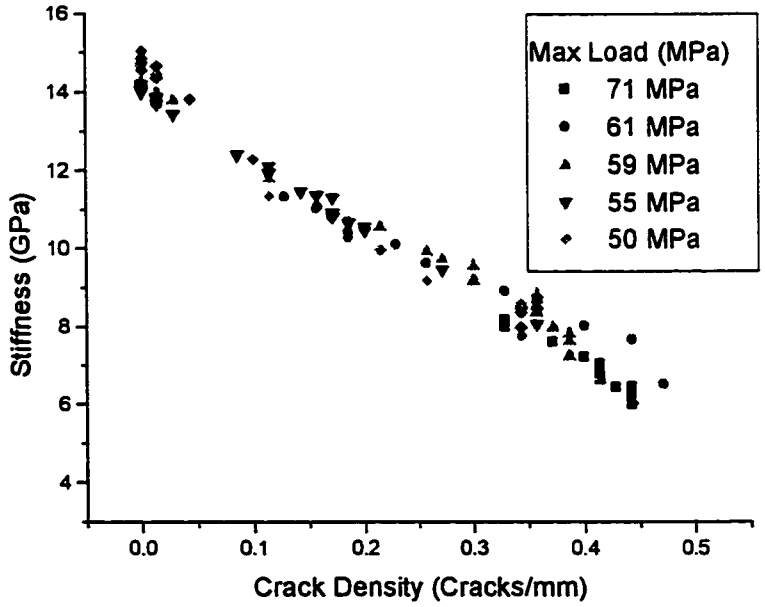

Figure 3.29: Stiffness vs. crack density for $(\pm 45/90_3)_s$ specimens under load control

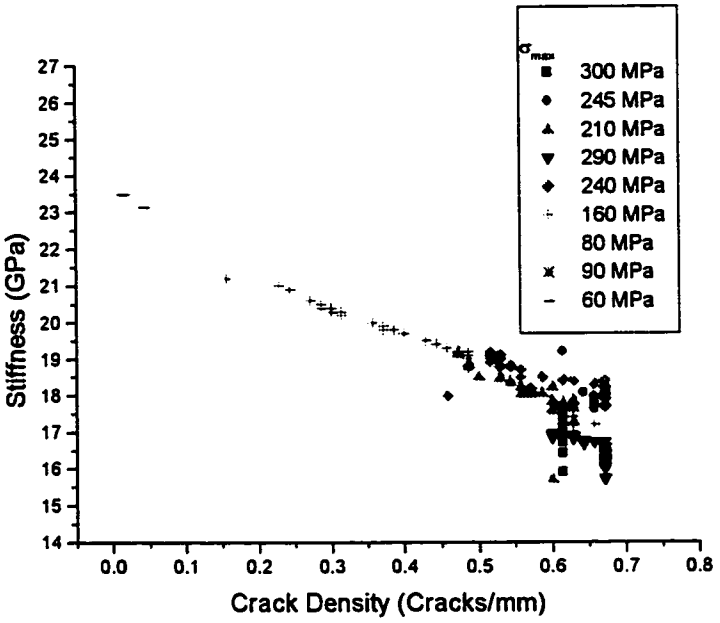

Figure 3.30: Stiffness vs. crack density for $(0_2/90_3)_s$ cross-ply laminates

3.5 Comparisons Between Quasi-Static And Cyclic Tests

Comparisons between cyclic and quasi-static tests of composites can be difficult. In this study, three variables were compared: the crack densities, the stiffness reductions, and the failure modes of the specimens.

To compare the crack growth between the quasi-static and cyclic loads, the common axis of maximum stress or strain and crack densities were plotted. The quasi-static results were plotted on the same figures as the cyclic results under the assumption that they were a cyclic test of one cycle in duration. By plotting this data against cyclic plots a good comparison could be made. The cyclic tests were stopped at 10, 100, 1000, etc. cycles and the crack density was counted. These values were then plotted against the

maximum applied load or strain. A variety of tests were performed over a range of stress values so that isocycle lines could be produced. These curved lines represent a constant number of cycles. These plots are shown in Figures 3.31,3.32,and 3.33 for the $(\pm 45/90_3)_s$ specimens under strain control, the $(\pm 45/90_3)_s$ specimens under load control, and the $(0_2/90_3)_s$ specimens under load control respectively.

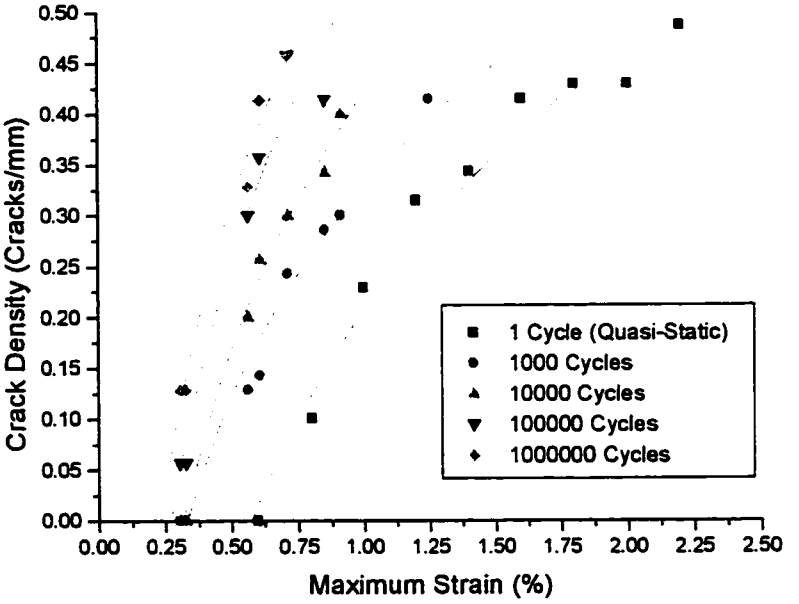

Figure 3.31: Relationship between maximum strain and crack density at N cycles for $(\pm 45/90_3)_s$ specimens under strain control

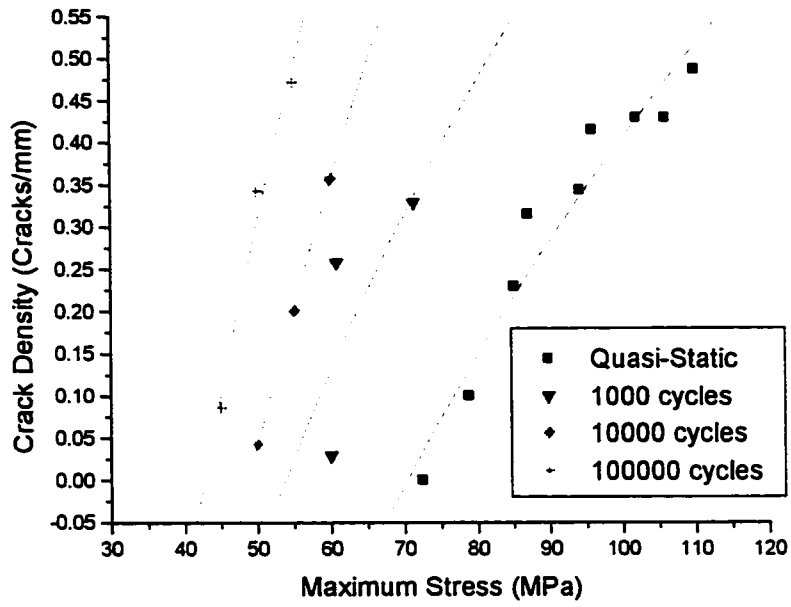

Figure 3.32: Relationship between maximum stress and crack density at N cycles for $(\pm 45/90_3)_s$ specimens under load control

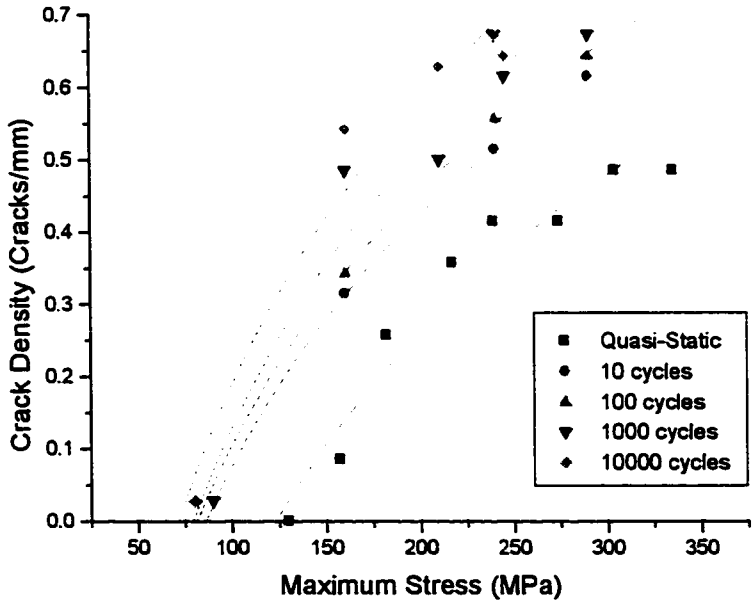

Figure 3.33: Relationship between maximum stress and crack density at N cycles for $(0_2/90_3)_s$ specimens under load control

In these figures the abscissa reflects the control mode: strain control tests have the x-axis as strain, while load control tests have the x-axis as stress. Several important findings come from these figures. In all of the plots, matrix cracks initiate at lower loads and strains under cyclic loading than under quasi-static loading. As well in all cases, for a given maximum stress or strain, a larger number of cracks occur under cyclic loading.

For the $(\pm 45/90_3)_s$ specimens under strain control cracking is seen to initiate at as low as 0.3% strain under the cyclic tests compared to an initiation point of 0.6% strain in the quasi-static tests. Both the quasi-static and cyclic loading reach a similar final crack density of 0.45 cracks/mm in this case.

The $(\pm 45/90_3)_s$ specimens under load control initiate cracks at applied maximum stresses as low as 50 MPa for the cyclic tests compared to about 70 MPa for the quasi-static tests. A final crack density of approximately 0.45 cracks/mm was seen in both the quasi-static and cyclic tests.

For the $(0_2/90_3)_s$ specimens under load control the cracks initiate at loads as low as 75 MPa compared with 125 MPa for the quasi-static tests. In the case of this specimen a higher final crack density is achieved under cyclic loading (0.65 cracks/mm) than is achieved under quasi-static loading (0.45 cracks/mm).

The isocycle curves appear to converge towards a single line for the $(\pm 45/90_3)_s$ specimens under strain control and the $(0_2/90_3)_s$ specimens under load control. These are the same specimens that reached saturation states of matrix cracks. Also of note is that in these two specimens, none of the curves fall lower than 0.25% strain for the $(\pm 45/90_3)_s$

laminates, or below 75 MPa for the $(0_2/90_3)_s$ laminates, suggesting that there is a level below which no cracks will initiate.

Another comparison between the quasi-static and cyclic loading is the stiffness drop per crack density, as outlined in section 3.4.5. Of particular note is the data from Table 3.6 which shows that there is a larger stiffness drop per 90° matrix crack under cyclic loading than that of quasi-static loading. This extra reduction in stiffness is due to increased crack growth in the constraining plies, which is not as prominent in the quasi-static test specimens. The constraining ply cracks have a slower propagation rate than the 90° cracks, which propagate through the width immediately under both quasi-static and cyclic loading. These constraining ply cracks are seen in the cyclic test specimens, but do not grow in the quasi-static specimens because of the short duration of loading. Consequently, a higher rate of stiffness reduction per 90° cracks is observed in cyclically loaded specimens.

There exist several differences between the failure modes of the specimens under the different test conditions. As mentioned, matrix cracking begins at lower loading rates in the cyclic specimens. Delamination growth also varies quite substantially between the two loading cases. In the $(\pm45/90_3)_s$ specimens under cyclic loading delaminations grow in many areas and one main delamination propagates to cause the ultimate failure of the specimen. The delamination growth differences are even more pronounced for the $(0_2/90_3)_s$ specimens. In the quasi-static tests the delamination growth is purely an effect of fibre failure just before the specimen failure. There is little redistribution of load to the outer plies, instead the load is increased until the outer constraining ply fibres break. In

the cyclic tests a substantial amount of the delamination growth is seen to propagate out of longitudinal matrix cracks and from the edges. When the delaminations have progressed to the point where the redistributed load is sufficient to cause fibre failure, an instantaneous failure results.

The ultimate failure modes for both quasi-static and cyclic loading are the same. In the $(\pm 45/90_3)_s$ specimens failure is due to shear failure of the matrix in the constraining plies. In the $(0_2/90_3)_s$ specimens ultimate failure is due to fibre failure in the constraining plies.

3.6 Comparisons of Matrix Dominated and Fibre Dominated Laminates Under Cyclic Loading

Comparisons between matrix dominated $(\pm 45/90_3)_s$ and fibre dominated $(0_2/90_3)_s$ specimens is useful in determining the effects of the fibres and the matrix on the overall composite laminates. It was found that although both of these types of specimens undergo the same modes of damage throughout their cyclic lives, there are some distinct differences in how the damage initiates and propagates throughout the specimens. Comparisons of the test cases under load control were performed.

Damage growth for the $(0_2/90_3)_s$ and $(\pm 45/90_3)_s$ specimens was described in section 3.3.1. Any differences between these two types of laminates began when damage propagated into the constraining plies. Here damage growth in the form of matrix cracking and delamination varied with respect to the fibre orientation. In the $(\pm 45/90_3)_s$ specimens matrix cracking was seen in the constraining plies at 45° angles from the

direction of loading. The $(0_2/90_3)_s$ specimens produced longitudinal matrix cracking at 0° angles with respect to the direction of loading.

Delamination growth resulted in different ultimate failure modes between the two laminates. In the $(\pm45/90_3)_s$ specimens triangular delaminations grew across the width of the specimen until only the matrix in the constraining plies remained to carry the load. When the specimen reached this stage, ultimate failure occurred due to shear failure of the matrix in the constraining plies. The $(0_2/90_3)_s$ specimens failed under cyclic loading when delaminations had grown throughout the length of the specimen. When sufficient load had been transferred to the constraining plies due to the delamination growth, fibre failure in the 0° plies began. An instantaneous failure was the result.

The fatigue-life curves, shown in Figures 3.9 and 3.10 for both of these specimens also were different. Damage growth initiated and propagated at lower global loads in the $(\pm45/90_3)_s$ specimens. This was due to the difference in stiffness of the constraining plies between the two specimens.

Stiffness reduction curves (Figures 3.23-3.25 and 3.26-3.27) showed that there was a much more significant reduction in stiffness for the $(\pm45/90_3)_s$ than that for the $(0_2/90_3)_s$ specimens. Another difference of note was that the reduction in stiffness in $(\pm45/90_3)_s$ specimens continued well after most of the matrix cracking in the 90° had been exhausted. This extra stiffness reduction was due to matrix cracking in the 45° constraining plies, delamination growth, and viscoplastic effects in the matrix. This type of response was not present in the 0° plies of the $(0_2/90_3)_s$ specimens since the elastic

fibres took the entire load, and matrix cracking in these plies resulted in only a slight decrease in stiffness.

Crack density plots also showed differences. The $(0_2/90_3)_s$ specimens were seen to reach a saturation state, whereas the $(\pm45/90_3)_s$ specimens did not. This was due to continuously increasing strain in the inner plies of the $(\pm45/90_3)_s$ specimens as the strain in the constraining plies increased (A combination of elastic and plastic strains). This allowed new cracks to form, hence no saturation state was achieved. In the $(0_2/90_3)_s$ specimens the strain in the constraining plies was fully elastic, so the overall strain that the specimen underwent throughout the test remained fairly constant, resulting in a saturation state of matrix cracks.

The crack density at failure for the $(0_2/90_3)_s$ specimens was ~0.65 cracks/mm, while the $(\pm45/90_3)_s$ produced a crack density of ~0.45 cracks/mm. This is due to higher stress gradients between the 0° and 90° fibres than between the 45° and 90° fibres.

The stiffness reduction vs. crack density plots for the two types of specimens (See Figures 3.29-3.30) showed a variance in stiffness reduction per crack. As outlined in Table 3.6, the stiffness reduction for a given crack density was much higher for the $(\pm45/90_3)_s$ specimens than it was for the $(0_2/90_3)_s$ specimens. The reason for such a large difference is that crack propagation in the 45° constraining plies results in a larger stiffness loss. This constrained ply cracking is unaccounted for as only the inner plies were considered in the stiffness reduction calculations. The result is a higher stiffness per inner ply crack density.

3.7 Comparisons Between $(\pm 45/90_3)_s$ Specimens Tested Under Load Control And Strain Control

Different control modes can have an effect on damage growth in composites. To determine the effect of the load control mode, the $(\pm 45/90_3)_s$ laminates were tested under both load control and strain control.

Visual damage examination found that specimens tested under load control had an accelerated rate of damage growth when compared to the strain control tests. In a load controlled test, the global load remains constant, while the local loads carried by individual plies varies. As matrix cracks propagate through the 90° plies, the load is largely redistributed to the outer plies. This results in an accelerated damage growth in the constraining plies, resulting in quicker ultimate failure of the specimen.

In the strain control tests the global strain remains the same. As damage grows in these specimens, a stress relaxation takes place. As a result of this relaxation, less damage initiates and propagates which leads to an increased life compared with the load controlled tests.

When comparing the stresses and strains for the initiation of cracking, both the load control and strain control tests had the initiation points fall on similar lines (See Figure 3.13). This is because it is the growth of damage that causes differences between the two control modes. To determine the point of initiation of damage in a composite specimen either control mode will give similar stress and strain results.

3.8 Summary

The analysis of the cross-ply and multi-ply specimens under cyclic loading produced some interesting results. Comparisons of the cyclic tests with quasi-static loading cases showed a number of differences. By testing the $(\pm 45/90_3)_s$ specimens under both load and strain control, differences in these loading conditions could be found.

By examining the visual damage growth, different damage modes were observed. In these laminates damage initiated in the form of matrix cracking in the 90° plies. It was followed by matrix cracking in the constraining plies, which then progressed to delamination between the inner plies and the constraining plies. Ultimate failure came in the form of shear failure of the matrix in the $(\pm 45/90_3)_s$ specimens, and brittle fibre failure in the $(0_2/90_3)_s$ specimens.

Damage curves developed for the specimens showed trends regarding how the damage modes initiated in the specimens. The trends showed that over the range of loads examined, all of the damage modes happened in a systematic and predictable way except at very low loads. On a logarithmic scale the damage curves all fell on straight lines, suggesting that the cycles between the different damage modes increased logarithmically. Figures 3.10 and 3.12 showed that at very low loads crack initiation points did not follow the damage curve. This could suggest that at low loads the crack initiation behaviour may change. Further testing at these low loads is required to substantiate this finding.

By examining the transverse crack growth the loading rate required for damage initiation, and trends of damage propagation could be seen. Transverse cracks grew

rapidly after initiation of cracking, and slowed as the stress in the inner plies relaxed. In the $(0_2/90_3)_s$ specimens under load control and the $(\pm45/90_3)_s$ specimens under strain control, a saturation state of matrix cracking was seen. In the $(0_2/90_3)_s$ specimens this was due to the high load carrying capacity of the 0° plies which allowed matrix cracking to fully propagate through the inner plies before any change in stiffness began in the constraining plies. In the $(\pm45/90_3)_s$ specimens under strain control the saturation state was achieved because the damage growth is related to the amount of strain applied. Since the strain was kept constant no new transverse cracking initiated after stress relaxation in the specimen. The crack growth curves showed that there was a crack onset delay of approximately 1% of the life of the specimen for the $(\pm45/90_3)_s$ specimens tested under load control.

Stiffness reduction plots showed a bi-linear curve for all of the specimens. This indicated that different damage modes were dominant throughout the life of the specimens. A similar drop in the magnitude of the stiffness was seen due to matrix cracking for both the $(\pm45/90_3)_s$ and $(0_2/90_3)_s$ specimens, although a much higher percentage of the total stiffness was reduced due to matrix cracking in the $(\pm45/90_3)_s$ specimens.

By comparing stiffness vs. crack density plots, a direct correlation between matrix cracking and stiffness losses was observed. The larger stiffness reduction in the $(\pm45/90_3)_s$ specimens was due to unaccounted matrix cracking in the constraining plies.

4 Constrained Angle-Ply Experiments

Angle-ply composites are among the most common lay-ups in service today. In many design cases forces act in a multiplicity of loading directions. This off-axis loading is best compensated for by using angle ply laminate designs.

The purpose of these tests was to produce damage curves for different damage modes (matrix crack initiation, matrix crack saturation, and delamination initiation) of angle ply laminates. In a high-pressure pipe, the functional failure of the pipe is in the form of weepage, where the liquid penetrates out of the composite pipe through minuscule matrix cracks. The onset of weepage is found to correlate with the point of crack saturation in the tubular specimens, well before ultimate failure of the pipe [29]. For this reason the design of the high pressure pipe to contain fluids should be at strain levels lower than that which produces a saturated crack state over the life of the design. In the tests performed here, the angle plies are surrounded on either end by 0° layers, hence the term "constrained angle-plies".

4.1 Summary of Cyclic Specimens Examined

Three angle-ply orientations were examined. The chosen lay-ups were $(0/\pm 25_4/0)_T$, $(0/\pm 45_4/0)_T$, and $(0/\pm 75_4/0)_T$. These were chosen to study the effect of different angles on the damage development states. Previous research at the University of Alberta found that the optimum fibre angle for a high pressure composite pipeline was approximately 65° relative to the axial direction of the pipe [31]. A composite pipe

oriented at 65° under hoop loading is comparable to the $(0/\pm25_4/0)_T$ coupon specimens under axial loading. As well, the $(0/\pm75_4/0)_T$ specimen under axial loading is similar to a 65° composite pipe under axial loading. This is a preliminary comparison, since tubular specimens do not have edge effects and the difference in geometry may effect the comparisons in damage growth. As well, biaxial loading conditions are not taken into account. Nevertheless, it is deemed useful to study the behaviour of angle-plies on coupon specimens to gain an insight into the damage development. An illustration of the comparable tests is shown in Figure 4.1.

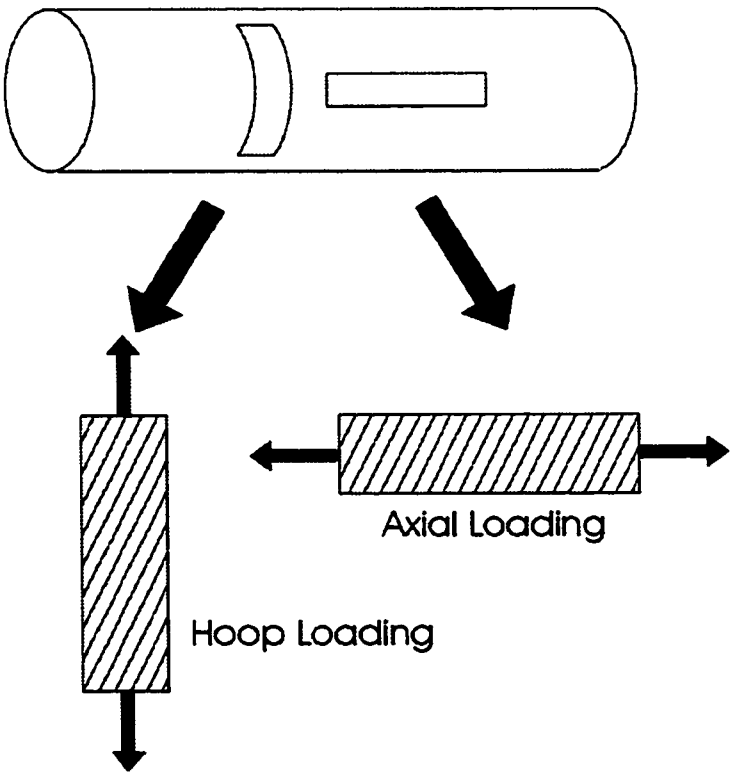

Figure 4.1: Application of coupon specimens to composite pipe design

The 0° layers were introduced to the specimens to act as outer constraining layers for the composite, as well as to prevent excessive creep in the matrix dominated angle-

ply specimens (45 and 75 degree specimens.) When matrix cracking begins in these specimens, the 0° layers also help to prevent immediate failure of the specimen.

A summary of the constrained angle-ply specimen tests performed was compiled and is shown below in Tables 4.1, 4.2, and 4.3.

Table 4.1: $(0/\pm25_4/0)_T$ specimens tested under strain control

SPECIMEN: $(0/\pm25_4/0)_T$	Loading type : Strain Control
Specimen Name	Maximum Applied Strain
AF-156	1.40%
AF-157	1.50%
AF-158	1.10%
AF-159	0.90%
AF-160	0.70%
AF-161	1.25%
AF-162	1.00%
AF-163	1.325%
AF-164	1.10%

Table 4.2: $(0/\pm45_4/0)_T$ specimens tested under strain control

SPECIMEN: $(0/\pm45_4/0)_T$	Loading type: Strain Control
Specimen Name	Maximum Applied Strain
AF-143	1.20%
AF-144	1.60%
AF-145	1.00%
AF-146	0.80%
AF-147	1.30%
AF-148	1.40%
AF-149	1.50%
AF-150	1.10%
AF-151	1.20%
AF-152	1.20%

Table 4.3: $(0/\pm75_4/0)_T$ specimens tested under strain control

SPECIMEN: $(0/\pm75_4/0)_T$	Loading type: Strain Control
Specimen Name	Maximum Applied Strain
AF-166	0.80%
AF-167	0.60%
AF-168	0.40%
AF-169	0.30%
AF-170	0.70%
AF-171	1.00%
AF-172	1.10%

4.2 Testing Procedure

The three different lay-ups were tested in similar fashions. First, monotonic tests were performed to determine the stress-strain characteristics of the specimen. Subsequently, cyclic tests were performed with the maximum strain amplitude being equal or less than the monotonic strain where the matrix cracking first occurred. This was done over a range of amplitudes to develop fatigue-life curves for the different damage modes.

For the monotonic tests, a strain rate of $10^{-4}s^{-1}$ was used in all cases. As the tests were being performed, images of the specimen, hence damage development, were taken at regular strain intervals. For cyclic tests the testing parameters outlined in chapter 2 section 2.5 were followed.

It is noted that to determine the initiation of matrix cracking required very low strains to be applied on the specimens. These loads proved to be too small to cause

ultimate failure of the specimens in a reasonable time period. To provide an upper bound, all tests were stopped after $1x10^6$ cycles.

4.2.1 Damage Detection Methods And Testing Software

Two separate apparati were used to visually examine damage growth in the angle-ply coupon specimens. These consisted of the image processor developed by Wolodko, Hoover, and Ellyin [28], and the optical microscope. Coupled with these visual methods were stiffness measurements that were recorded at regular intervals throughout the tests. These damage detection methods are outlined in chapter 2, section 2.6.

The testing software implemented in this series of tests was closed loop controlling software called MTM301 developed in house by Wolodko [29]. Further explanation of this controlling software is discussed in chapter 2, section 2.3.1.

4.3 Monotonic Test Results

Monotonic tests were performed on the three types of constrained angle ply specimens. In this examination only single-ramp monotonic tests were performed, differing from the quasi-static tests performed in the last chapter. Ultimate failure stresses and strains were found, and the onset of the various damage modes were recorded. These tests were used as a guide to determine the magnitude of strains to be applied in the cyclic tests.

4.3.1 Stress-Strain Curves

Monotonic stress-strain curves were produced for each of the different angle ply laminates and are shown in Figure 4.2.

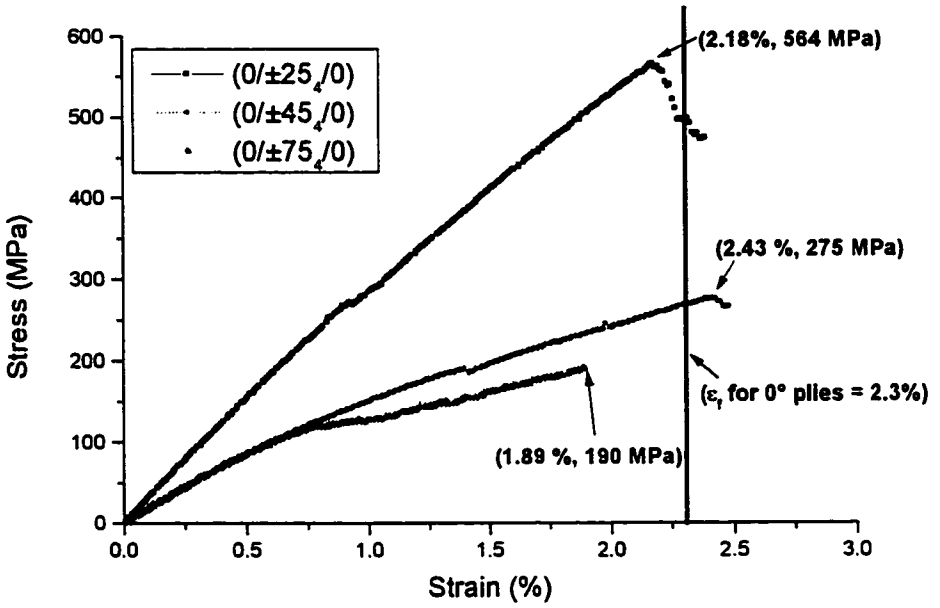

Figure 4.2: Monotonic stress-strain curves for $(0/\pm\theta/0)_T$ coupon specimens where θ =25,45, and 75 degrees

The stress-strain plot shows that the curves are very different for the various laminate configurations. The $(0/\pm75_4/0)_T$ specimen produced a bi-linear curve. At 0.75 % strain, matrix cracking began, and this caused a decrease in the load carrying capacity of the laminate. This matrix cracking continued until failure of the specimen at 1.89 % strain and a stress of 190 MPa. Matrix cracking could be seen visually in this specimen and produced a web-like crack pattern, cracking along the ±75° fibres, shown in Figure 4.3.

Figure 4.3: Characteristic crack pattern seen in $(0/\pm75_4/0)_T$ specimens

Both the $(0/\pm45_4/0)_T$ and $(0/\pm75_4/0)_T$ specimens followed similar initial curves. At 0.75% strain, the $(0/\pm75_4/0)_T$ specimen developed matrix cracks, while the $(0/\pm45_4/0)_T$ specimen did not. No visual matrix cracking was experienced in these specimens until the point of ultimate failure. The reason for this deviation is that less load is required to fracture the 75° laminae plies than is required to fracture the 45° plies. In the 75° layers, most of the cracking occurs in the form of Mode I fracture – most of the load enacted on these layers is in a direction normal to the fibres. For the 45° layers, a mixed mode fracture takes place. Equal shear and normal forces exist in the individual plies, so a higher total load is required to fracture the matrix. More of the load is directed to the fibres in the 45° plies than in the 75° plies. The result is the $(0/\pm45_4/0)_T$ specimens have a stronger load carrying capability of 275 MPa, and a higher failure strain of 2.43%.

The $(0/\pm25_4/0)_T$ specimen produced the steepest stress-strain curve of all with load carrying capabilities of 564 MPa, more than double that of the other laminates. The reason for this is the orientation of the 25° fibres is close to that of the direction of loading. The fibres retain most of the load in these specimens, as opposed to the other

specimens where the matrix retains a larger portion of the load. This specimen produced no matrix cracks or delamination until fibre failure began to appear at a strain of 2.18%. From here the specimen ruptured and failed almost immediately.

The $(0/\pm45_4/0)_T$ and $(0/\pm75_4/0)_T$ specimens followed similar initial stress-strain curves, while the $(0/\pm25_4/0)_T$ specimens followed a steeper slope. The reason for this difference is that in the $(0/\pm45_4/0)_T$ and $(0/\pm75_4/0)_T$ specimens the global stiffness is affected to a larger degree by the stiffness of the matrix in the θ plies, while in the $(0/\pm25_4/0)_T$ specimens the fibres are oriented in such a direction that they contribute to a higher stiffness in this specimen. Classical Laminate theory found stiffness values of 31.69 GPa, 19.79 GPa, and 16.69 GPa for the $(0/\pm25_4/0)_T$, $(0/\pm45_4/0)_T$, and $(0/\pm75_4/0)_T$ specimens respectively. This compares well with the slopes in Figure 4.2.

Another interesting note is the much lower failure strain of the $(0/\pm75_4/0)_T$ specimens. Since much more matrix cracking is present in these specimens, a higher percentage of the load is transferred to the outer 0° plies. This extra load transfer results in a much earlier failure strain than in the other two specimens. The other specimens do not develop through width matrix cracks, and thus do not redistribute as much load to the constraining plies.

Previous research by Wolodko [29] found that the failure strain for 0° plies alone was approximately 2.3%. This falls within the average of the failure strains for all of these specimens, as indicated by the solid line in Figure 4.2. This suggests that the ultimate failure of the specimen is dominated by the outer 0° plies. Since the purpose of

these tests was to determine how damage propagated in the inner angle plies, the ultimate failure of the specimens was not studied further.

4.3.2 Damage Propagation under Monotonic Loading

Damage propagation in each of the three specimens examined proved to vary with the changing angles.

It was very hard to determine any damage growth in the $(0/\pm25_4/0)_T$ and $(0/\pm45_4/0)_T$ specimens at the load levels listed in Tables 4.1 and 4.2. No visual crack growth or delamination was visible in either of these specimens until very close to the ultimate failure. Just before the ultimate failure, fibre failure in the 0° plies took place. Delaminations grew between the constraining plies and the angle plies from these failure sites. Matrix cracking also resulted at the same time in the angle plies. Fracture of the matrix in the inner angle plies was in the form of shear failure.

Damage growth in the $(0/\pm75_4/0)_T$ specimen took place in a much more systematic and steady manner. The first visible damage growth began at 0.75% strain, when matrix cracking became visible through the width of the specimen. This matrix cracking continued until the ultimate failure of the specimen. Since cracking continued until the ultimate failure, it was not possible to determine whether a saturation state of matrix cracks had formed. Visible delamination growth was not seen until very close to the failure of the specimen. Similar to the other laminates examined, the delamination growth occurred very close to the point of fibre failure.

Of the three angles examined, only the $(0/\pm75_4/0)_T$ produced any visual matrix cracking pattern on the image processor. In the $(0/\pm25_4/0)_T$ and $(0/\pm45_4/0)_T$ specimens the only hint of damage came in the form of acoustic emission as the strain increased. Since a microscope was not used to examine these specimens, the amount of edge crack growth for a monotonic test was not determined.

4.3.3 Ultimate Failure of Monotonic Specimens

The failure of the monotonic specimens varied between each specimen. Images of the three failed angle-ply laminates are shown in Figures 4,4, 4.5, and 4.6.

The failure of all specimens took place along the angle of the inner plies. For all of the $(0/\pm\theta_4/0)_T$ specimens the ultimate failure was along the fibre direction at an angle of $\theta°$. Of interest was the fact that although these specimens have an outer 0° layer, a large brush failure such as what was seen in earlier cross ply specimens was not experienced (See Chapter 3, Figure 3.6). Instead delamination and fibre failure in the constraining plies took place around the area where the inner plies had failed. This is likely due to lower stress gradients between the constraining plies and the inner plies than is experienced in the cross-ply specimens.

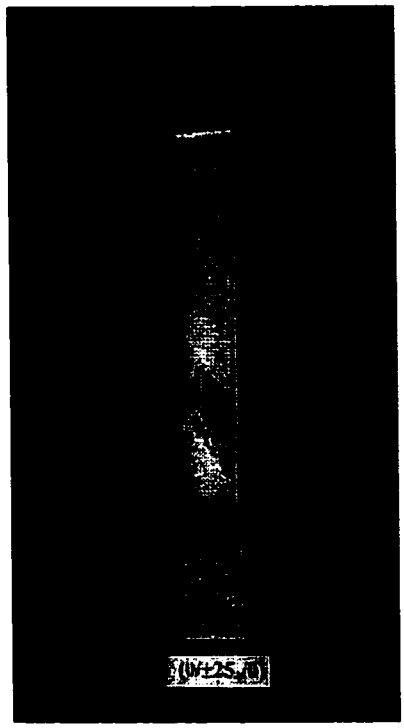

Figure 4.4: A failed $(0/\pm 25_4/0)_T$ coupon specimen under monotonic loading

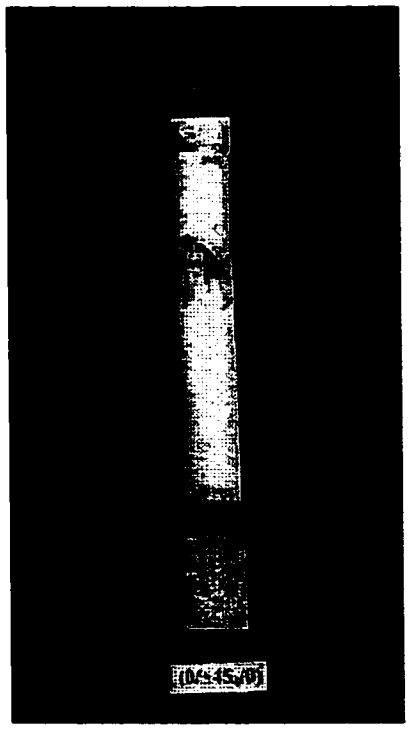

Figure 4.5: A failed $(0/\pm 45_4/0)_T$ coupon specimen under monotonic loading

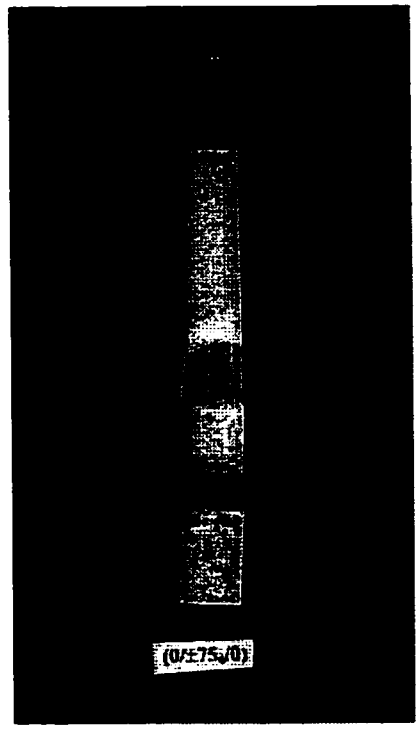

Figure 4.6: A failed $(0/\pm75_4/0)_T$ coupon specimen under monotonic loading

4.4 Cyclic Test Results

4.4.1 Description of Damage Growth During Cyclic Testing

Damage growth throughout all of the three geometries followed predictable patterns irrespective of the loading level. Damage growth in the constrained angle ply composites was much different from that of the cross-ply and multi-ply specimens examined in Chapter 3, testifying to the complexity of damage analysis in composites.

Similar to the monotonic test results, damage growth was very small in the $(0/\pm25_4/0)_T$ and $(0/\pm45_4/0)_T$ specimens. In these geometries damage propagation was only from the edges, with very little damage visible through the width of the specimen.

In contrast, the $(0/\pm75_4/0)_T$ geometries produced a matrix crack pattern throughout the width of the specimens, very similar in form to that seen during monotonic loading.

In all of the specimens, delaminations grew from the edges of the matrix cracks, linking matrix cracks in neighbouring plies. Delaminations also grew along the edges of the constraining plies, where there was a boundary preventing further matrix crack growth.

4.4.2 Damage Curves

Damage curves consisting of crack initiation, crack saturation, and delamination initiation were produced for the three constrained angle ply composites. These are shown in Figures 4.7, 4.8 and 4.9 for the $(0/\pm25_4/0)_T$, $(0/\pm45_4/0)_T$, and $(0/\pm75_4/0)_T$ specimens, respectively. The crack initiation and delamination initiation damage modes were found using the optical microscope. In the $(0/\pm25_4/0)_T$ specimens the onset of delamination was seen to begin at the same time as crack initiation. When the cracks initiated they quickly developed delaminations on either side. This is shown in Figure 4.7. Delamination growth was most difficult to determine in the $(0/\pm45_4/0)_T$ specimens. In these specimens, the delaminations grew from the edges of matrix cracks. It was difficult to determine when the edge of a matrix crack changed into a delamination site. This contributed to a larger scatter for this curve than for the other curves. This is seen in Figure 4.8.

Crack saturation curves were developed for all specimens. In the $(0/\pm25_4/0)_T$ and $(0/\pm45_4/0)_T$ specimens no visual cracking could be seen with the image processor, so edge crack counts were performed. When the rate of cracking levelled off this was taken

as the edge crack saturation state. For the $(0/\pm75_4/0)_T$, specimen, visual damage growth could be seen using the image processor. The saturation state for this specimen was determined by examining images obtained from the image processor.

In both Figures 4.7 and 4.8 saturation states of cracking could not be obtained at higher strain levels. This problem was not seen in the $(0/\pm75_4/0)_T$ specimens due to the lower strains required to produce a saturation state of matrix cracks.

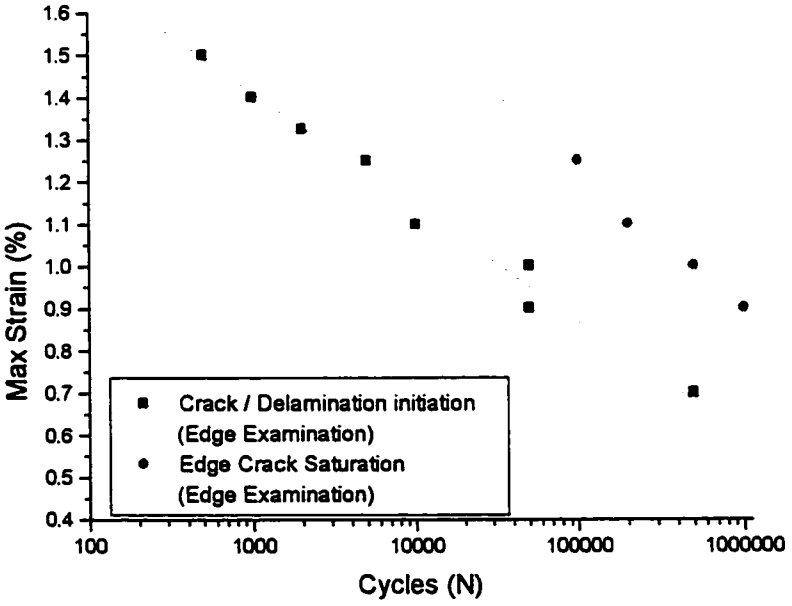

Figure 4.7: Damage curves for $(0/\pm25_4/0)_T$, specimens under strain control

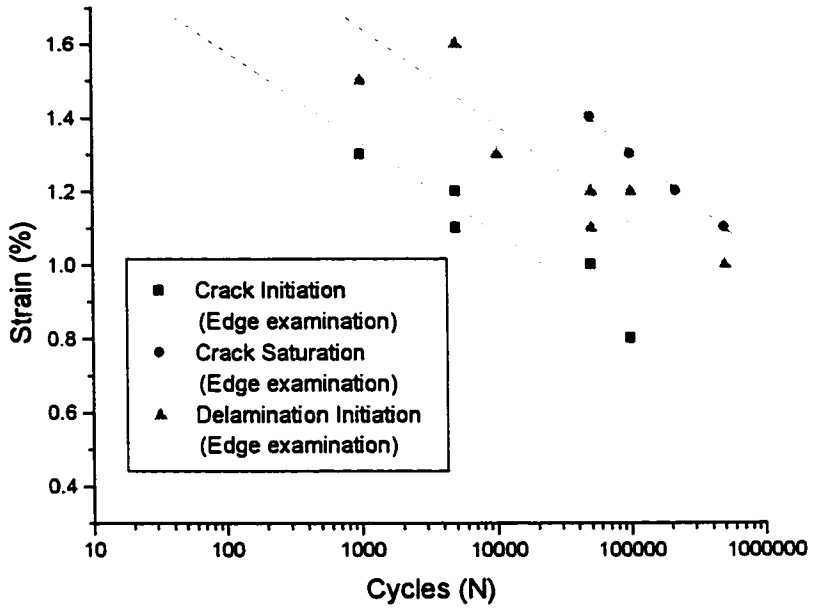

Figure 4.8: Damage curves for $(0/\pm 45_4/0)_T$, specimens under strain control

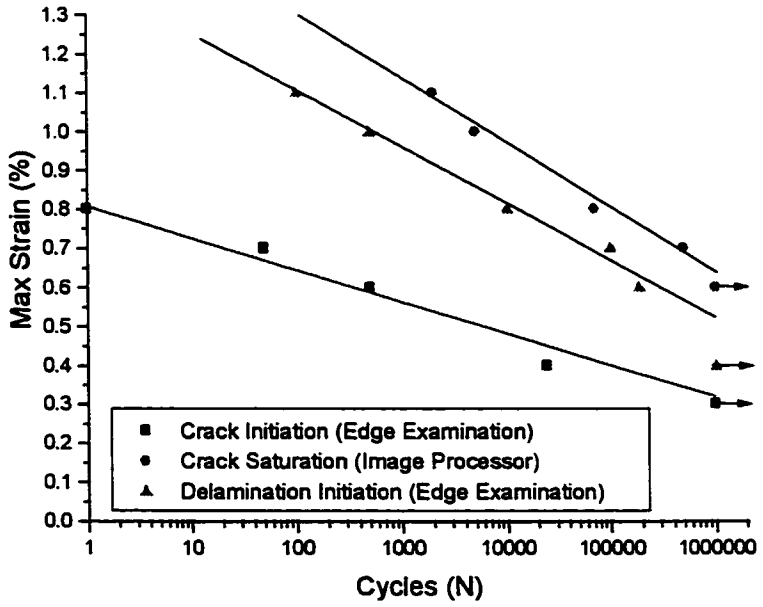

Figure 4.9: Damage curves for $(0/\pm 75_4/0)_T$, specimens under strain control

The three damage curves show a systematic method for damage initiation and propagation through the specimens. All of the specimens undergo initiation of matrix cracking, followed by delamination, followed by the achievement of a saturated state of matrix cracks. Interestingly, the matrix cracks reach a saturation state after delamination was initiated, showing that there is an interaction between the different damage modes. Further comparisons between the damage modes in the different specimens are reported in sections 4.4.4 - 4.4.6.

4.4.3 Edge Crack Initiation and Edge Crack Propagation

By using the optical microscope different edge crack states were seen to exist for each of the three different specimens. These are shown in Figures 4.10, 4.11, and 4.12 for the $(0/\pm25_4/0)_T$, $(0/\pm45_4/0)_T$, and $(0/\pm75_4/0)_T$ specimens, respectively. The left image of each figure shows the crack pattern, while the right image shows the same crack pattern enhanced to show the outline of the cracks. There is a definite wavy pattern that all three specimens follow. Delaminations grow between the ply cracks. This pattern of delamination decreases in height as the angle θ of the fibres increases.

It should be noted that the $(0/\pm25_4/0)_T$ and $(0/\pm45_4/0)_T$ specimens produced edge cracks that did not propagate through the width of the specimen. By examining the edge cracks an estimate of how far they penetrated into the specimen was determined. It was assumed that these cracks formed a triangular delamination, similar to that seen in earlier $(\pm45/90_3)_s$ specimens. From the images, measurements of the length of the vertical lines were measured as the height of the delaminations in the specimens, and from these an

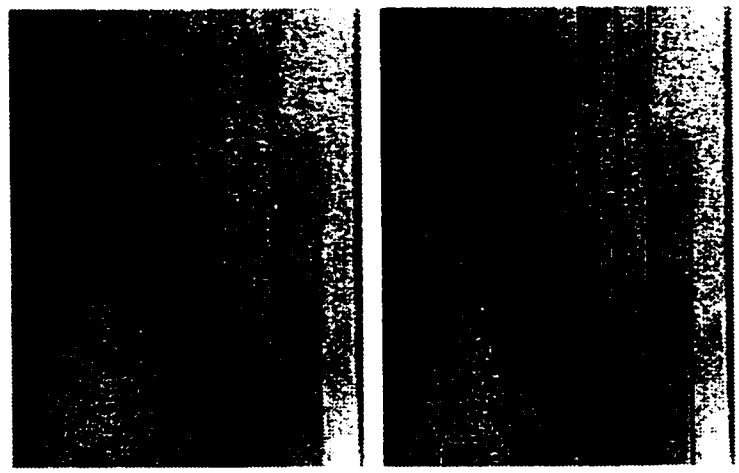

Figure 4.10: Edge crack state in $(0/\pm 25_4/0)_T$ specimen

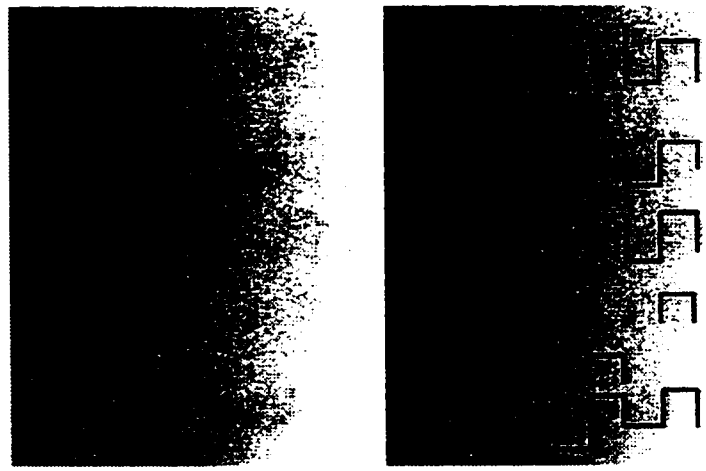

Figure 4.11: Edge crack state in $(0/\pm 45_4/0)_T$ specimen

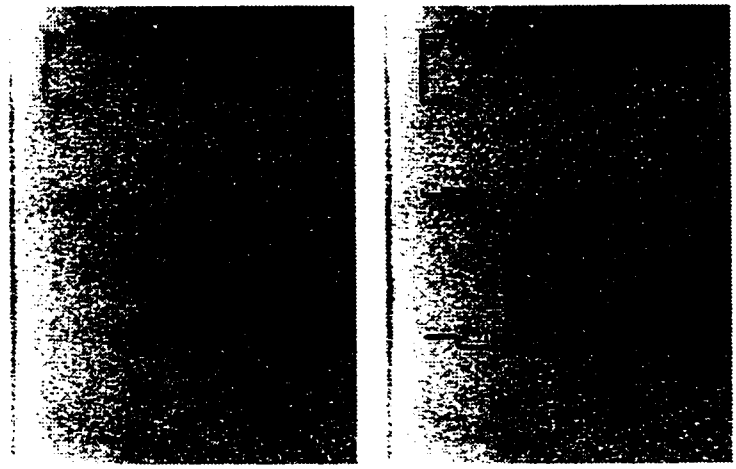

Figure 4.12: Edge crack state in $(0/\pm 75_4/0)_T$ specimen

average height was found. The depth of edge penetration could be found using the equation shown below:

$$\text{Tan}(\theta) = \frac{(2 \times \text{Edge Penetration})}{\text{Average Measured Height of Edge Delamination}}$$

The average height of the edge cracks was 0.634 mm for the $(0/\pm25_4/0)_T$ and 0.244 mm for the $(0/\pm45_4/0)_T$ specimens. This led to edge crack penetrations of 0.148 mm for the $(0/\pm25_4/0)_T$ and 0.122 mm for the $(0/\pm45_4/0)_T$ specimens. These values are fairly close to each other, suggesting that the penetration of the cracks into the interior of specimens is similar between angle plies when the fibre angle is less than 45°. A possible explanation for this is that the load required to fracture the matrix increase with the increasing distance from the edge. The fact that there is mixed mode fracture, mostly modes 1 and 2, suggests that very high loads are required for cracks to propagate. This is the same reason why little damage growth is seen before ultimate failure of the monotonic specimens. This suggests that when the θ angle is small, and no crack propagation exists after the initial edge cracking, the cracks can only propagate a certain distance into the specimens. Damage growth and propagation in these specimens can be largely attributed to edge effects.

The matrix cracks in the $(0/\pm75_4/0)_T$ specimens propagate through the width and thickness of the angle-plies very quickly, suggesting that the strains required for the propagation of cracks in fibres at this angle is very low and the mode 1 fracture is dominant. In these specimens the cracks grew until a saturation state throughout the specimen was reached, similar to that shown in Figure 4.3.

4.4.4 Crack Initiation Damage Curves

A plot of the crack initiation curves for all three geometries is shown in Figure 4.13. This plot shows that the strain to produce crack initiation for a given load is much lower for the $(0/\pm75_4/0)_T$ specimens. It is also interesting to note that for the $(0/\pm25_4/0)_T$ and $(0/\pm45_4/0)_T$ specimens the strains to produce crack initiation fall within a relatively narrow band.

The orientation of the plies in the $(0/\pm75_4/0)_T$ specimens results in dominant normal forces acting perpendicular to the fibres. In the $(0/\pm25_4/0)_T$ and $(0/\pm45_4/0)_T$ specimens the shear force component acting on the matrix parallel to the fibres becomes dominant. To fracture the matrix in the $(0/\pm25_4/0)_T$ and $(0/\pm45_4/0)_T$ specimens, a higher load is required.

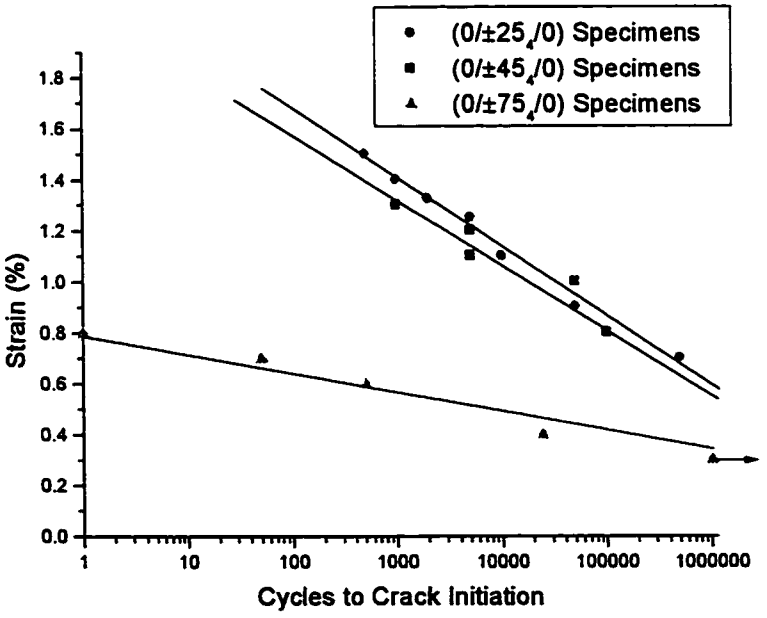

Figure 4.13: Crack initiation curves for the three types of specimens examined

4.4.5 Crack Saturation Damage Curves

Crack saturation curves were developed for all of the specimens. These are plotted in Figure 4.14.

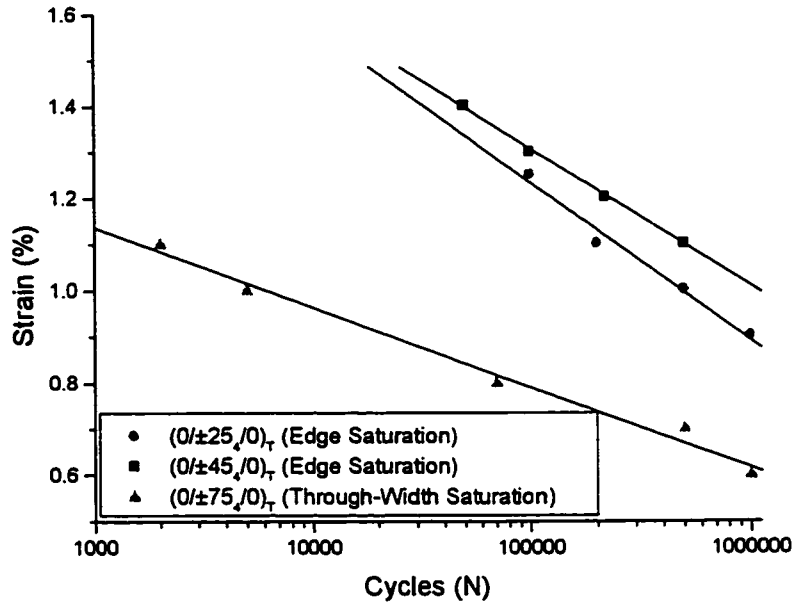

Figure 4.14: Crack saturation curves for $(0/\pm\theta_4/0)_T$ specimens

The saturation state requires a higher strain, as well as a longer life for the $(0/\pm25_4/0)_T$ and $(0/\pm45_4/0)_T$ specimens when compared with the $(0/\pm75_4/0)_T$ specimens. This trend is similar to the crack initiation curves shown in Figure 4.13.

For all three types of specimens a saturation state of edge cracks developed. Only the $(0/\pm75_4/0)_T$ specimen produced a visual state of cracking though the width of the specimen. Since it was known that the length of the specimen that could be viewed by the microscope was 7.5mm, a crack density value could be found by dividing the crack count by this length. Edge cracks were counted for each ply and then averaged to

determine the average crack density per ply vs. the number of cycles. Linear and logarithmic plots of this are shown in Figures 4.15 and 4.16 for the $(0/\pm25_4/0)_T$ specimens, in Figures 4.17 and 4.18 for the $(0/\pm45_4/0)_T$ specimens, and in Figures 4.19 and 4.20 for the $(0/\pm75_4/0)_T$ specimens, respectively.

It is important to remember when viewing these plots that these are only edge crack densities. The large differences in edge crack penetration aren't shown in these plots. There is much more damage growth and penetration in the $(0/\pm75_4/0)_T$ specimens than there is in the other two specimen geometries examined.

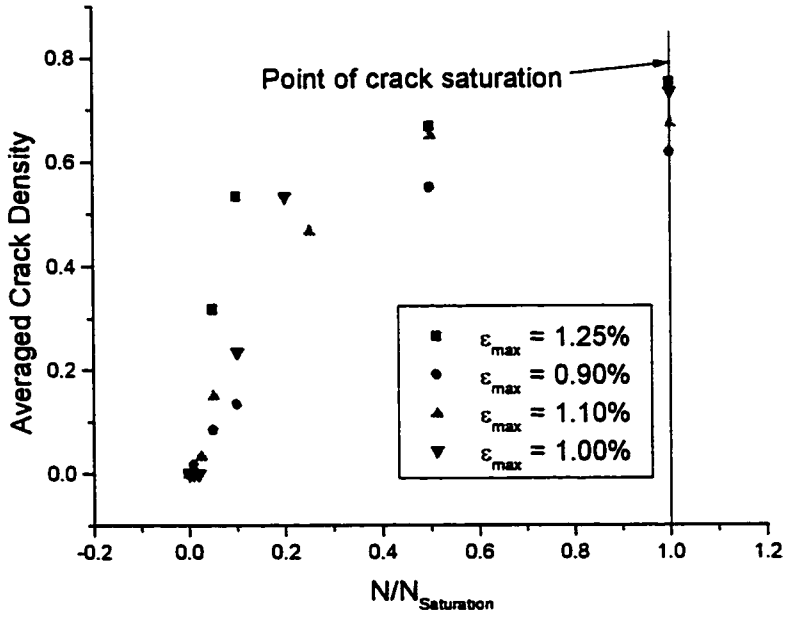

Figure 4.15: Linear plot of averaged edge crack density versus number of cycles normalized with respect to the saturation point for $(0/\pm25_4/0)_T$ specimens

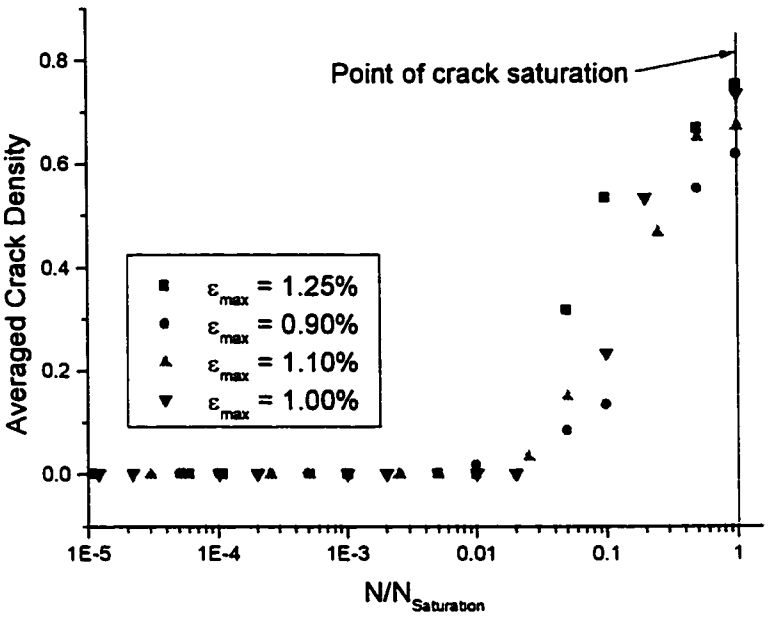

Figure 4.16: Averaged edge crack density versus log of number of cycles normalized with respect to the saturation point for $(0/\pm25_4/0)_T$ specimens

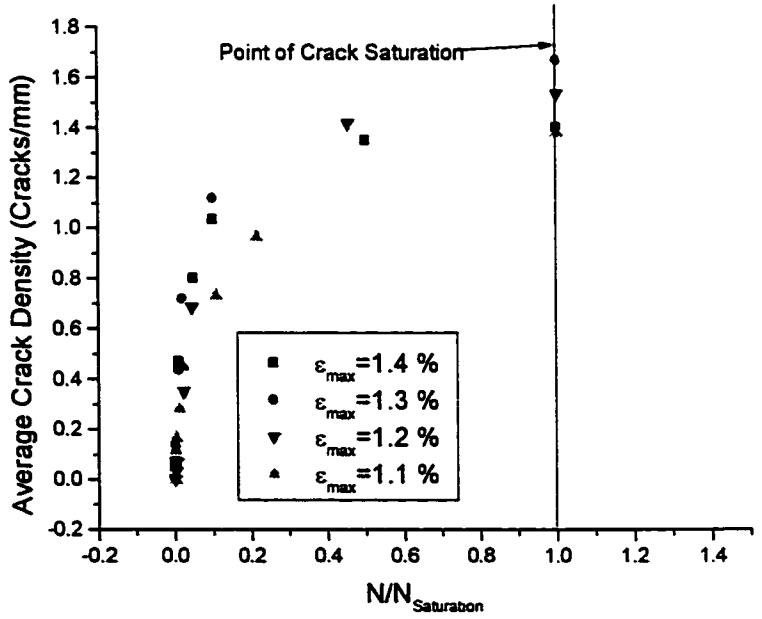

Figure 4.17: Linear plot of averaged edge crack density versus number of cycles normalized with respect to the saturation point for $(0/\pm45_4/0)_T$ specimens

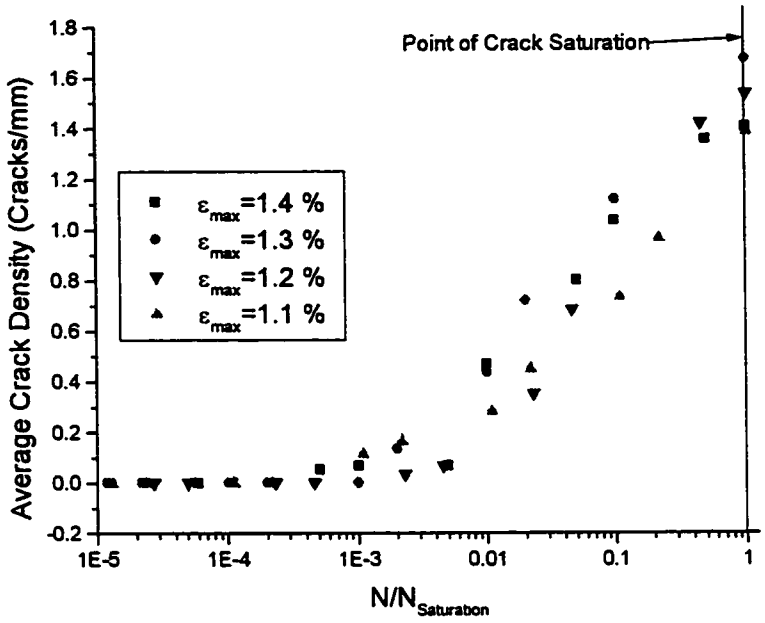

Figure 4.18: Averaged edge crack density versus log of number of cycles normalized with respect to the saturation point for $(0/\pm45_4/0)_T$ specimens

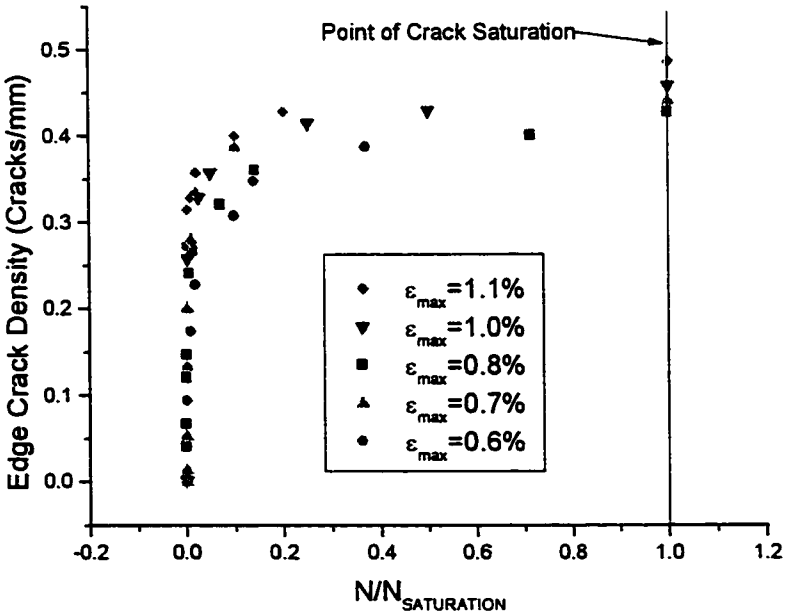

Figure 4.19: Linear plot of averaged edge crack density versus number of cycles normalized with respect to the saturation point for $(0/\pm75_4/0)_T$ specimens

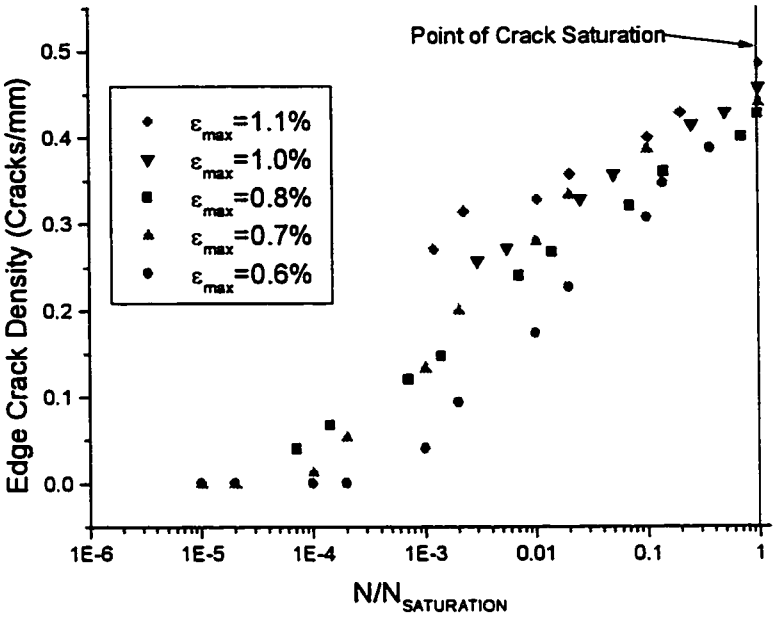

Figure 4.20: Averaged edge crack density versus log number of cycles normalized with respect to the saturation point for $(0/\pm75_4/0)_T$ specimens

All of the edge crack density plots, when plotted logarithmically, follow an S-shaped curve. In the first section there are no matrix cracks, a region before crack initiation. After this, a period of steep crack growth is observed, followed by levelling off and reaching a saturation state. When a specimen reaches its cracking saturation state, the predominant damage mode changes to delamination.

The edge crack density curves show a number of differences between the specimens. A comparison between the different angle plies and their respective crack densities are shown in Table 4.4. The variance in the fibre angles between neighbouring plies ($\Delta\theta$) is also included in the table to show what effect these have.

Table 4.4: Edge crack density comparison between different angle ply specimens

SPECIMEN TYPE	SATURATION EDGE CRACK DENSITY IN ANGLE PLIES. (CRACKS/MM)	$\Delta\theta$ PARALLEL TO DIRECTION OF LOADING. (DEGREES)
$(0/\pm25_4/0)_T$	0.72±0.10	50°
$(0/\pm45_4/0)_T$	1.52±0.15	90°
$(0/\pm75_4/0)_T$	0.46±0.04	150°

For the $(0/\pm25_4/0)_T$ and $(0/\pm45_4/0)_T$ specimens the crack densities were increasing when the $\Delta\theta$ values were also increasing. When the $\Delta\theta$ values are small in the direction relative to the loading direction, the interlaminar stresses are reduced. This results in lower crack densities. These findings are similar to previous work by Hoover [22] for monotonic loading which found that crack densities, and damage in plies was lower for specimens which had neighbouring plies with angles of less than 30° between themselves. Although the angles between the neighbouring plies are larger than 30° in this study, there is still a marked reduction in crack densities when the angle between two adjacent plies is lower.

This theory applies for the $(0/\pm25_4/0)_T$ and $(0/\pm45_4/0)_T$ specimens, but it can be seen that the crack density in the $(0/\pm75_4/0)_T$ specimens is much lower. In these specimens the cracks propagated immediately through the thickness of the specimens. In these specimens only the outer 0° constraining plies enact large shear forces on the inner angle plies, resulting in a lower stress gradient, and less matrix cracking. This is similar to what was seen in $(0_2/90_n)_s$ specimens tested by M.C. Lafarie-Frenot and C. Henaff-Gardin [21]. In these specimens when the 'n' value increased, the crack density

decreased. In effect the angle ply layers in the $(0/\pm75_4/0)_T$ specimens are oriented similar enough to one another so as to act as a thick ply which results in less matrix cracking.

4.4.6 Delamination Initiation Damage Curves

Delamination curves for all of the specimens are shown in Figure 4.21. All examinations of delamination initiation were performed using the optical microscope. The first indication of separation between two plies was taken as the initiation of delamination.

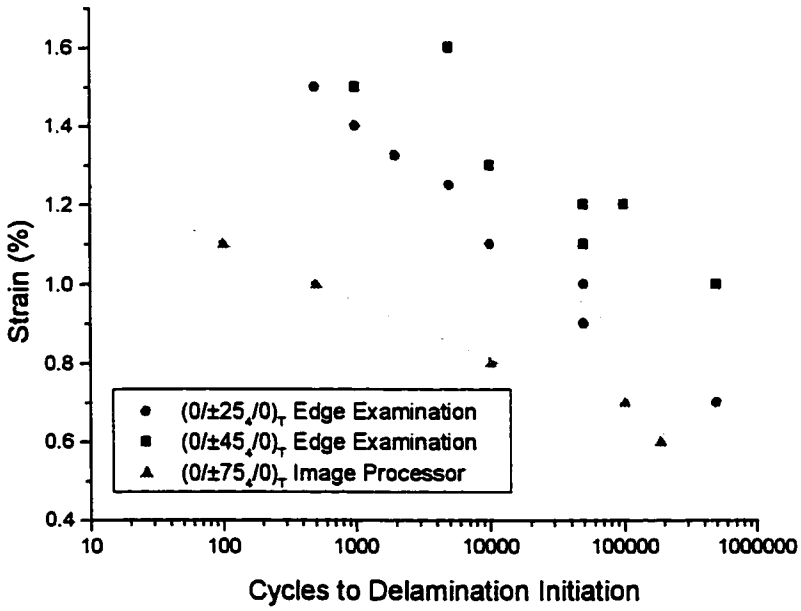

Figure 4.21: Delamination initiation curves for $(0/\pm\theta_4/0)_T$ specimens

Under cyclic loading there are many factors which contribute to delamination initiation and growth. In the tests performed, and in findings by others [11,36] it was found that delaminations initiated most easily along free edges and in the presence of

matrix cracks. The value of the interlaminar shear stress component plays a large role in the growth of the delaminations. There are many complicated factors that contribute to this stress gradient between plies. When the angle of neighbouring plies is similar, the stress gradient between them decreases. Another factor is residual stresses added during the cure cycle when manufacturing the specimen. The fibres and matrix in a composite have different thermal coefficients of expansion. When cooling from the melt temperature of the polymer residual stresses are introduced. The largest residual shear stresses are found between plies with large variance in fibre angles. As mentioned earlier, delamination is seen to initiate first in areas where there are matrix cracks. Once these cracks initiate, more of the load is transferred between plies through the shear stress. This is another factor that contributes to delamination initiation.

4.4.7 Stiffness Reduction Curves

Stiffness reduction curves were generated for all of the cyclic tests. By correlating the visual examination methods with the stiffness reduction curves a check could be used to make sure that the visual observations were consistent between tests.

Plots of the stiffness reduction curves for the $(0/\pm25_4/0)_T$, $(0/\pm45_4/0)_T$, and $(0/\pm75_4/0)_T$ specimens are shown in Figures 4.22, 4.24, and 4.26, respectively. The horizontal arrows indicate that ultimate failure of the specimens did not take place before $1x10^6$ cycles. The vertical arrows indicate the point at which the visual examination technique showed the initiation of matrix cracking.

To examine how closely these values correlate with one another the life of the specimens were normalized with respect to the crack initiation life, $N/N_{(Crack\ Initiation)}$. The resulting curves for the three cases are shown in Figures 4.23, 4.25, and 4.27, respectively. In these figures the stiffness was normalized with respect to the initial stiffness found from each test. There is a clear correlation between the onset of matrix cracking and the initiation of stiffness reduction for all three specimens.

The $(0/\pm25_4/0)_T$ specimens showed a slight decrease in stiffness of approximately 2.5-3.0 GPa after the point of crack initiation. This small decrease in stiffness coincides with a small amount of matrix cracking in the specimen. Note that no through width cracking was observed, all cracking was mainly along the edges of the specimen, and they did not penetrate far into the specimen. This small amount of cracking results in a small stiffness reduction.

Figure 4.23 shows the same plot, this time normalized with respect to the crack initiation life. For all but the two specimens that were subjected to the smallest strains, the specimens followed a similar drop in stiffness. Of interest was the fact that specimens with strains lower than 0.9% had crack initiation, yet they had very little stiffness reduction. This suggests that the strains were either too low for enough cracking to take place to show a stiffness reduction, or the test had not progressed long enough to see a visible reduction in stiffness.

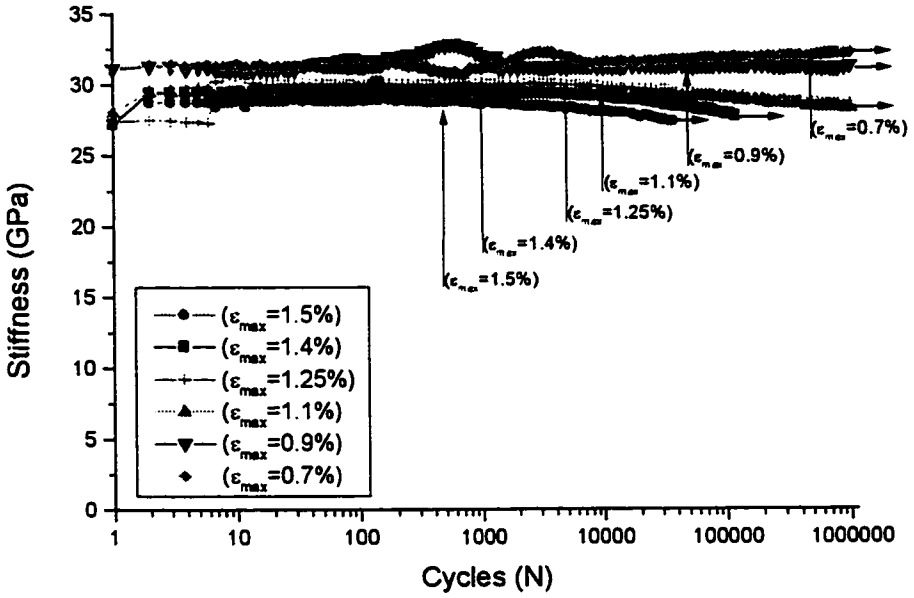

Figure 4.22: Stiffness reduction vs. cycles for $(0/\pm25_4/0)_T$ specimens under strain control

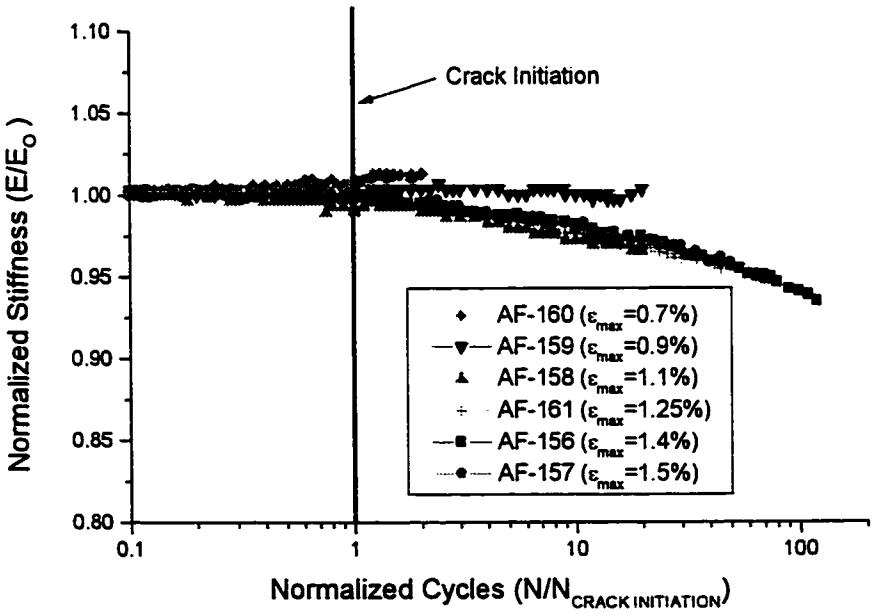

Figure 4.23: Normalized stiffness reduction vs. normalized cycles for $(0/\pm25_4/0)_T$ specimens under strain control

The stiffness reduction curves for the $(0/\pm45_4/0)_T$ specimens produced a larger reduction in stiffness relative to the initial stiffness than the $(0/\pm25_4/0)_T$ specimens. In these specimens the stiffness reduction is approximately 3.0 – 4.0 GPa. Although both geometries do not produce through-width matrix cracking, the larger reduction in stiffness is due to more matrix cracks along the edges of the specimens.

Figure 4.25 shows the normalized stiffness drop of the $(0/\pm45_4/0)_T$ specimens. There is a substantial stiffness drop of approximately 15% of the total stiffness. This drop correlates well between all of the applied strain levels.

Of note in the stiffness reduction plots for both the $(0/\pm25_4/0)_T$ and $(0/\pm45_4/0)_T$ specimens is that the stiffness reduction curves show no signs of levelling off. This suggests that the reduction may continue well after the imposed limit of $1x10^6$ cycles. The edge crack saturation state has been shown to exist before $1x10^6$ cycles suggesting that there is stiffness reduction due to either further crack propagation into the specimen, or due to delamination growth.

The stiffness reduction curves for the $(0/\pm75_4/0)_T$ specimens show a very significant reduction in stiffness soon after the initiation of matrix cracking. The decrease in stiffness is the largest for this geometry, approximately 6.0 - 7.0 GPa. This is 30-35% of the initial stiffness. This large stiffness reduction is the result of through width matrix cracking. Figure 4.26 shows that with these specimens there appears to be a point where saturation of matrix cracking takes place. The slopes have a distinct point where they level off, whereby there is no more stiffness reduction due to matrix cracking. Instead, a much slower reduction takes place due to delamination growth.

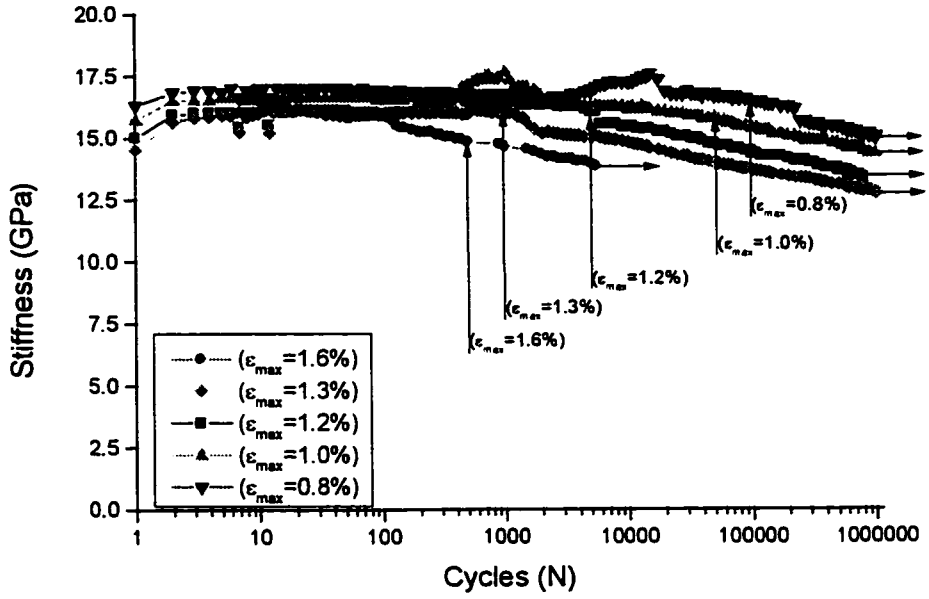

Figure 4.24: Stiffness reduction vs. cycles for $(0/\pm45_4/0)_T$ specimens under strain control

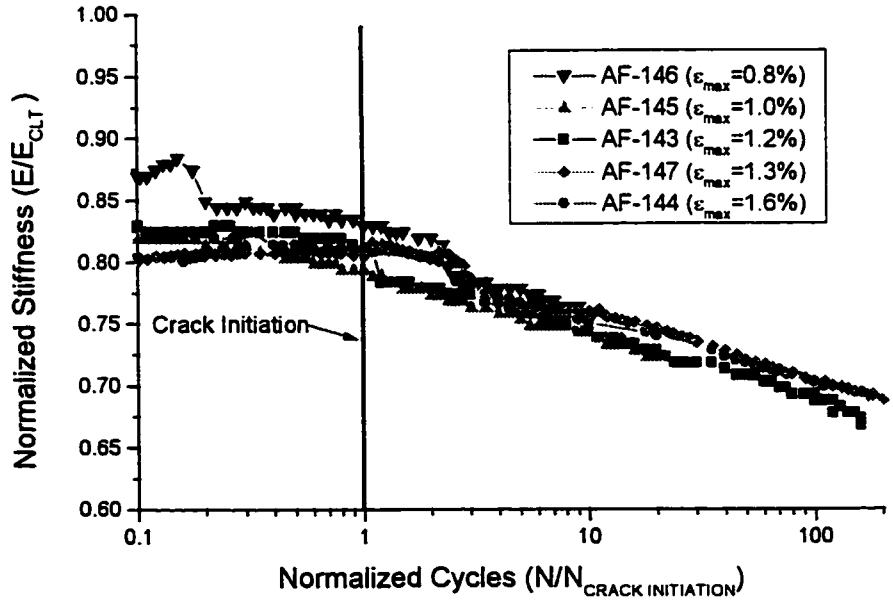

Figure 4.25: Normalized stiffness reduction vs. normalized cycles for $(0/\pm45_4/0)_T$ specimens under strain control

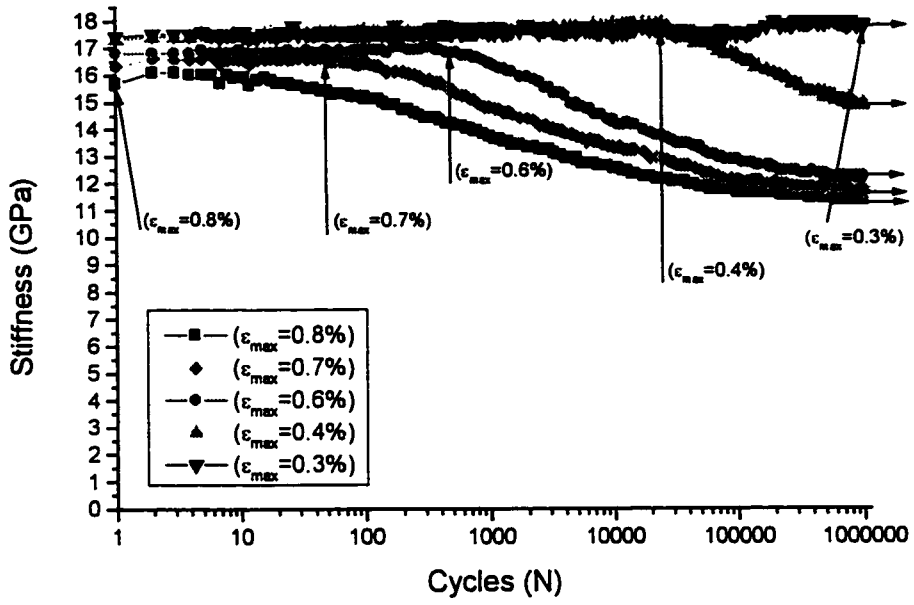

Figure 4.26: Stiffness reduction vs. cycles for $(0/\pm75_4/0)_T$ specimens under strain control

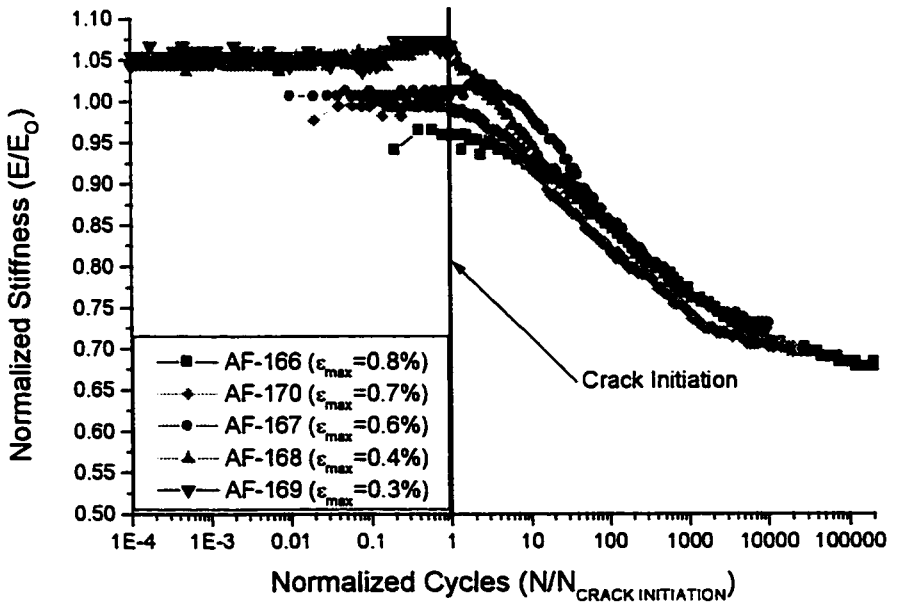

Figure 4.27: Normalized stiffness reduction vs. normalized cycles for $(0/\pm75_4/0)_T$ specimens under strain control

4.5 Summary

The study of constrained angle ply composites shows some very interesting results. By studying and documenting how the damage modes initiate and propagate a good idea of what factors affect damage growth was realized.

Visual damage examination during the life of the specimens found that the $(0/\pm25_4/0)_T$ and $(0/\pm45_4/0)_T$ specimens had damage growth only along the free edges. In contrast the $(0/\pm75_4/0)_T$ specimens produced a web-like crack pattern throughout the test section of the specimen. This was similar to what was seen in the monotonic tests.

Damage curves for crack initiation, crack saturation, and delamination initiation showed that the $(0/\pm75_4/0)_T$ specimens were the weakest orientation. The $(0/\pm25_4/0)_T$ and $(0/\pm45_4/0)_T$ specimens followed relatively similar curves for all of the damage modes investigated.

The overall strength of the specimens, when compared to the damage curves, matched up well with visual damage examination. Visual damage examination showed that only the $(0/\pm75_4/0)_T$ specimens produced any through-width matrix cracking, while the $(0/\pm25_4/0)_T$ and $(0/\pm45_4/0)_T$ specimens only produced visible damage growth along the edges of the specimens. In effect, the weaker specimen, the $(0/\pm75_4/0)_T$ laminate, did indicate larger amounts of damage propagation.

By examining the damage growth along the edges, a wavy pattern consisting of joined delaminations and matrix cracks was observed between the individual plies. The delamination joining the matrix cracks increased in height as the orientation of the angle plies decreased. Measurements of the height of these delaminations were taken for the

$(0/\pm25_4/0)_T$ and $(0/\pm45_4/0)_T$ specimens, and a simple calculation was done to determine the delamination penetration. It was found that the delaminations penetrated 0.148 mm for the $(0/\pm25_4/0)_T$ specimen and 0.122 mm for the $(0/\pm45_4/0)_T$ specimens. These were fairly similar distances suggesting that the crack growth in these specimens were mostly due to edge effects, that decreased as the distance into the specimen increased.

Comparisons of the crack initiation damage curves showed that the curves for the $(0/\pm25_4/0)_T$ and $(0/\pm45_4/0)_T$ specimens followed similar slopes, while the $(0/\pm75_4/0)_T$ specimen had a flatter slope with lower strains. This was due to the nature of the fracture in these specimens. Most of the load acting in the $(0/\pm75_4/0)_T$ specimens was normal to the fibres, resulting in matrix cracking under low loads. In the $(0/\pm25_4/0)_T$ and $(0/\pm45_4/0)_T$ specimens a larger total load was required to develop a similar load acting normal to the fibres.

Crack saturation curves were similar in slope to the crack initiation curves for the three specimens. The crack saturation life could be found by visually examining the edges of the specimens. Crack density plots showed that the final saturation state of cracking was the lowest in the $(0/\pm25_4/0)_T$ and $(0/\pm75_4/0)_T$ laminates. The $(0/\pm25_4/0)_T$ laminate had a low crack density due to 'compatible plies' which had relatively similar fibre orientations. These similarly oriented plies did not induce large variances in stress between neighbouring plies. The $(0/\pm75_4/0)_T$ specimens had a low crack density because the orientation of the 75° plies resulted in the crack immediately propagating through the thickness of the specimen. These plies acted as one very thick ply, where it has been shown that the thicker the ply, the more shear stress can be redistributed, and the lower

the crack density. The $(0/\pm45_4/0)_T$ specimens, which had 90° variances between plies had the largest crack densities.

The delamination initiation curves were amongst the hardest to determine. Delaminations were seen to always begin at free surfaces where matrix cracks had already developed. In the $(0/\pm25_4/0)_T$ specimens, delaminations were seen to initiate at the same time as crack initiation. For this to occur, the interlaminar stresses required to initiate delamination required would have to be of the same magnitude as in-ply stresses that initiated matrix cracks. The $(0/\pm45_4/0)_T$ specimens required the largest loads to initiate delamination, as shown in Figure 4.21. Earliest to initiate delamination were the $(0/\pm75_4/0)_T$ specimens. This is most likely due to high interlaminar stresses between the angle and constraining plies, as well as due to the high number of crack initiation sites where delaminations can grow from. Residual shear stresses during curing of the specimen are another factor that contributes to the growth of delamination in these specimens.

A strong correlation could be seen between visual damage mode examination and stiffness reduction. In all specimens the onset of cracking could be correlated with the initiation of stiffness reduction. Other damage modes such as delamination initiation and crack saturation proved difficult to correlate with changes in the rate of stiffness reduction in the $(0/\pm25_4/0)_T$ and $(0/\pm45_4/0)_T$ specimens. This was mainly due to the fact that the only visible damage growth in these specimens was along the edges, and the changing of damage modes along the edges had negligible effect on the rate of stiffness

reduction. In the $(0/\pm75_4/0)_T$ specimens a change in the dominant damage modes could be seen by a decrease in the slope of the stiffness reduction.

The magnitude of the stiffness drop in the specimens correlated with the amount of damage growth in the specimens. The $(0/\pm25_4/0)_T$ specimens with stiffness reductions of 2.5-3.0 GPa, had the lowest crack density of all three specimens, and didn't produce any visual through-width matrix cracks. The $(0/\pm45_4/0)_T$ specimens, with stiffness reductions of 3.0-4.0 GPa, had a large amount of edge cracks, yet no through width crack growth. Meanwhile the stiffness drop in the $(0/\pm75_4/0)_T$ specimens, which did have through width matrix cracking, produced a stiffness reduction of 6.0-7.0 GPa.

With respect to using angle ply composites in pressurized pipe design the coupon specimen tests performed here have limited use. For the $(0/\pm25_4/0)_T$ and $(0/\pm45_4/0)_T$ specimens the crack initiation and stiffness reduction results will have little applicability, mainly because the damage is largely related to the edge effect of the coupon. On the other hand, the results for the $(0/\pm75_4/0)_T$ specimens are applicable to a tubular specimen, since the initiation and propagation of damage was influenced very little by the edge effects.

5 Conclusions

The preceding chapters clearly show the complexity of damage initiation and propagation in composite laminates under cyclic loading. Damage growth occurs in four different damage modes: microdamage, matrix cracking, delamination, and fibre failure. These damage modes interact to form a complex failure pattern in the composite laminate.

The main purpose of this study was to determine stain/load vs. life curves for the different damage modes present in a composite laminate. By developing these damage curves for the differing geometries, and comparing with global parameters such as stiffness reduction data, a good appreciation was obtained with respect to how the damage spread through the specimens. Depending on the design conditions, certain modes of damage may be avoided, if an understanding of the damage initiation and growth is achieved.

5.1 Damage Initiation and Propagation in Multi-ply and Cross-ply Laminates

Damage growth under quasi-static and cyclic loading was examined for two different laminate geometries: $(0_2/90_3)_s$ and $(\pm 45/90_3)_s$ laminates. The salient results from this series of experiments are presented in point form below:

- The initial damage mode in all of these specimens consisted of matrix cracking perpendicular to the direction of loading in the 90° plies. This damage mode

propagated into delamination growth between the inner 90° plies and the outer constraining plies.

- The load required for the ultimate failure of the specimens was determined by the fibre orientations in the constraining plies. In the $(0_2/90_3)_s$ specimens ultimate failure was due to fibre failure in the constraining plies. In the $(\pm45/90_3)_s$ specimens ultimate failure was due to shear failure of the matrix in the constraining plies.
- Damage curve plots of the laminates indicated the relative life of each damage mode. All of the damage modes appeared to follow linear curves over the range of loads examined, except at very low loads. The $(0_2/90_3)_s$ specimens were found to require larger loads before damage initiated. This was due to the much higher stiffness associated with the outer constraining plies in this specimen. The 0° plies in the $(0_2/90_3)_s$ specimens contributed to a much higher global stiffness than the 45° plies in the $(\pm45/90_3)_s$ specimens. At very low loads the crack initiation points deviated from the curves and did not initiate cracks at the expected points. This suggests the presence of a crack initiation stress limit.
- A strain vs. cycles damage curve was plotted for the crack initiation points for all of the specimens geometries and loading modes examined. It was found that all of the points fell on a similar line, suggesting that the initial damage growth in all of these specimens occurred at the similar points irrespective of the constraining ply geometries or loading control mode (Stress or strain control).
- Examination of transverse crack growth showed that matrix cracks propagated rapidly throughout the specimens early on in the life. As the damage mode changed to

delamination, the matrix cracking rate decreased considerably. Any new damage was then seen as delamination.

- Saturation states of transverse matrix cracks were seen in the $(0_2/90_3)_s$ specimens under load control, and the $(\pm45/90_3)_s$ specimens under strain control. In the $(\pm45/90_3)_s$ specimens this was due to the control mode. As cracks grew in the plies, stress relaxation between cracks resulted in less new cracks forming, finally resulting in a saturation state of matrix cracks. In the $(0_2/90_3)_s$ specimens the strain that the outer 0° plies can withstand before failure is much higher than that of the 90° plies. The 90° plies produced a saturated state of matrix cracks before any significant damage started in the outer 0° plies. The only specimens not to produce a saturation state were the $(\pm45/90_3)_s$ specimens under load control. The continuous increase in strain throughout the constraining plies led to continued matrix cracking up until ultimate failure in these specimens, and no saturation state resulted.
- All specimens examined were seen to produce bi-linear stiffness reduction curves. In the initial steeper section of the curve, stiffness reduction was due largely to matrix cracking in the 90° plies. The slope became less steep when the matrix crack growth slowed and delamination between the 90° plies and the constraining plies became the dominant damage mode. Both the $(0_2/90_3)_s$ and $(\pm45/90_3)_s$ specimens experienced similar drops in the magnitude of the stiffness due to the matrix cracking. (5-7 GPa for the $(0_2/90_3)_s$ specimens and 8-9 GPa for the $(\pm45/90_3)_s$ specimens. However, in

terms of percentage with respect to the undamaged stiffness, the reduction for $(\pm 45/90_3)_s$ was 60% compared to 20% for $(0_2/90_3)_s$ laminates.

- Stiffness reduction vs. crack density plots showed a strong correlation between matrix cracking and any reduction in stiffness. Linear curves existed for all specimens. At either end of the curves the slopes deviated slightly from linearity. This was due to stiffness reductions due to the different damage modes of microdamage and delamination.
- Direct comparisons between the quasi-static and cyclic tests found some interesting differences. Cracks initiated at lower loads, and higher crack density was observed for a given maximum load under cyclic loading. More delamination growth was seen under cyclic loading than under quasi-static loading. For the latter loading, delamination damage growth was seen only at very high strains, very close to the ultimate failure of the specimens. In the cyclic tests the delamination damage mode comprised the largest proportion of the specimen life.
- By comparing the cyclic damage growth between the fibre dominated $(0_2/90_3)_s$ specimens and the matrix dominated $(\pm 45/90_3)_s$ specimens, the effect of the fibre angle variation could be found. The two types of specimens showed large differences related to damage growth in their constraining plies. Initial damage growth due to transverse matrix cracking was similar in both specimens. When delamination growth began between the 90° plies and the constraining plies, large differences in delamination growth were seen.

- Comparisons of the $(\pm 45/90_3)_s$ specimens under load and strain control found that larger lifespans were achieved under strain control loading, for a given initial stress/strain combination. The strain control tests exhibited stress relaxation as damage grew in the specimen, resulting in less damage growth as the life increased. The stress control tests exhibited ratcheting, resulting in increased strain, and hence increased damage over the life of the specimen.

5.2 Damage Initiation and Propagation in Constrained Angle-ply Laminates

Three constrained angle ply composites were examined. These had geometries of $(0/\pm 25_4/0)_T$, $(0/\pm 45_4/0)_T$, and $(0/\pm 75_4/0)_T$. By varying the inner angles of these similar lay-ups it was possible to determine how the damage growth varied over a range of angles. For each of these laminates damage curves were developed for matrix crack initiation, matrix crack saturation, and delamination initiation. The following are the main results:

- Visual damage inspection of the specimens found that the $(0/\pm 25_4/0)_T$ and $(0/\pm 45_4/0)_T$ specimens produced visible damage only along the edges of the specimens, suggesting that edge effects played a large role in all damage growth in these specimens. In contrast, a web-like pattern of cracks were seen throughout the width and thickness of the angle-plies in the $(0/\pm 75_4/0)_T$ specimens. These cracks were at 75° angles from the edges of the specimens and produced a highly visible saturated state of matrix cracking throughout the specimen.

- By producing damage curves for the specimens, it could be seen that the $(0/\pm75_4/0)_T$ specimens experience damage initiation under the lowest strains for all of the damage modes. This lay-up also required much lower loads for damage to propagate through the specimen.
- Crack initiation damage curves indicate that the $(0/\pm75_4/0)_T$ specimens produced matrix cracking at lower strains than the $(0/\pm25_4/0)_T$ and $(0/\pm45_4/0)_T$ specimens, which followed relatively similar curves. The reason for these differences was that the $(0/\pm75_4/0)_T$ specimens had orientations that exerted largely normal loads perpendicular to the matrix, whereas in the $(0/\pm25_4/0)_T$ and $(0/\pm45_4/0)_T$ specimens the load placed on the specimen was divided into normal and shear components. Therefore a larger total load was required to shear the matrix.
- Crack saturation damage curves produced similar slopes in relation to the crack initiation curves. Edge crack densities were determined at the saturation state. The edge crack densities were 0.72, 1.52, and 0.46 cracks/mm for the $(0/\pm25_4/0)_T$, $(0/\pm45_4/0)_T$, and $(0/\pm75_4/0)_T$ specimens, respectively. Crack densities were seen to be low in the $(0/\pm25_4/0)_T$ due to 'compatible plies' whereby the stress gradient between individual plies was low, resulting in a lower crack density. In the $(0/\pm75_4/0)_T$ specimens a low crack density occurred due to initial through thickness cracking. This resulted in lower stress gradients between individual plies, and a lower crack density.
- Delamination damage curves were developed for the three specimens. It was found in all cases that delaminations initiated at free edges, from the edges of matrix cracks.

The $(0/\pm45_4/0)_T$ specimens required the largest loads to initiate delamination, suggesting that this lay-up can withstand very large shear forces between the plies. In the $(0/\pm25_4/0)_T$ specimens the delamination damage initiated at the same point as crack initiation, suggesting that at these large angles the shear force required to initiate delamination, and the normal forces required to initiate matrix cracking are of similar magnitudes.

- Further damage examination showed that there was a wavy pattern of crack growth along the edges of all specimens, where through-ply matrix cracks met up with delaminations. This pattern produced delaminations of the longest length in the $(0/\pm25_4/0)_T$ specimens, smaller delaminations in the $(0/\pm45_4/0)_T$ specimens, and the smallest delaminations in the $(0/\pm75_4/0)_T$ specimens. By measuring the length of these delaminations and knowing the fibre angles, an estimate of how far the damage penetrated into the specimens could be determined. The values found were 0.148mm and 0.122mm for the $(0/\pm25_4/0)_T$ and $(0/\pm45_4/0)_T$ specimens respectively , suggesting that there is a definite edge effect that occurs in these specimens.
- Stiffness reduction measurements indicated that there was a strong correlation between the stiffness reduction and the observed visual damage. The $(0/\pm25_4/0)_T$ specimens which had stiffness drops of 2.5-3.0 GPa only experienced a low crack density of edge cracks. The $(0/\pm45_4/0)_T$ specimens, with a drop of 3.0-4.0 GPa produced similar edge cracks with a higher crack density. In contrast, the $(0/\pm75_4/0)_T$ specimens, which had the largest stiffness drop of 6.0-7.0 GPa developed through width cracking. A definite drop in stiffness could be correlated with the initiation of

matrix cracking. Correlating the onset of other damage modes with the stiffness reduction proved difficult, since new damage modes interacted with the prior damage modes. This interaction made it difficult to determine where one mode started and another ended.

5.3 Suggested Future Work

The following are a few suggested future directions of research:

An area of pursuit that may prove profitable is comparisons of tubular and coupon composite specimens. In the constrained angle ply experiments many of the results seemed to be largely dominated by edge effects. With no edge effect the propagation of damage in these specimens should be reduced, and designs can be further optimized.

This study used visual damage examination methods to examine damage growth through the width of the $(0_2/90_3)_s$ and $(\pm45/90_3)_s$ specimens, and along the edges of the $(0/\pm25_4/0)_T$, $(0/\pm45_4/0)_T$, and $(0/\pm75_4/0)_T$ specimens. This method of damage examination gives a good idea of the total damage occurring in the specimen, but it is very hard to quantify the total damage throughout the specimen. When the thickness of each separate geometry grows smaller, there is less damage growth, and it becomes much more difficult to detect the damage. Unfortunately these thin plies are also the most realistic in design, since they provide the strongest lay-ups. Previous researchers have used x-ray sources to develop images of the damage growth throughout the width and thickness of the specimens. By implementing this damage examination technique a

better idea of the damage growth inside the specimens can be determined. This method of damage examination can be used on both tubular and coupon test specimens. A description of this examination technique is discussed in Appendix A.

6 Bibliography

[1] H.T. Hahn and R.Y. Kim. Fatigue behaviour of composite laminate. Journal of Composite Materials, 10:156-180, 1976

[2] K.E. Jackson, S Kellas, and J. Morton. Scale effects in the response and failure of fiber reinforced composite laminates loaded in tension and in flexure. Journal of Composite Materials, 26:2674-2705, 1992.

[3] T.K. O'Brien and S. Salpekar. Scale effects on the transverse tensile strength of graphite/epoxy composites. In E.T. Camponeschi, Jr., editor, Composite Materials: Testing and Design (Eleventh Volume), ASTM STP 1206, American Society for Testing and Materials, Philadelphia, PA, pp 23-52, 1993.

[4] C.W. Dill, S.M. Tipton, E.H. Glaessgen, and K.D. Branscum. Fatigue strength reduction imposed by porosity in a fibreglass composite. In Damage Detection in Composite Materials, ASTM STP 1128, American Society for Testing and Materials, Philadelphia, PA., pp 152-162, 1992.

[5] J. Bai, P. Seeleuthner, and P. Bompard. Mechanical behaviour of ±55° filament-wound glass-fibre/epoxy-resin tubes: I. Microstructural analysis, mechanical behaviour and damage mechanisms of composite tubes under pure tensile loading, pure internal pressure, and combined loading. Composites Science and Technology, 57:141-153, 1997.

[6] B.D. Harper, G.H. Staab, and R.S. Chen. A note on the effects of voids upon the hygral and mechanical properties of as4/3502 graphite/epoxy. Journal of Composite Materials, 21:280-289, 1987.

[7] M.A. Stone, I.F. Schwartz, and H.D. Chandler. Residual stresses associated with post-curing shrinkage in GRP tubes. Composites Science and Technology, 57:47-54, 1997.

[8] A.L. Highsmith, K.L. Reifsnider. Stiffness-Reduction Mechanisms in Composite Laminates, Damage in Composite Materials, ASTM STP 775, American Society for Testing and Materials, Philadelphia, PA, pp 103-117, 1982.

[9] K.L. Reifsnider. The Mechanics of Fatigue in Composite Laminates, Proceedings of Japan-U.S. Composite Materials conference, K.Kawata and T.Akasaka, Ed.,pp131-144, 1981.

[10] J. Zhang, C. Soutis, and J. Fan. Strain energy release rate associated with local delamination in cracked composite laminates. Composites, 25:851-862, 1994.

[11] S.A.Salpekar, T.K. O'Brien, and K.N. Shivakumar. Analysis of local delamination caused by angle ply matrix cracks. Journal of Composite Materials, 30:418-440, 1996.

[12] C.T. Herakovich. Failure modes and damage accumulation in laminated composites with free edges. Composites Science and Technology, 36:105-119, 1989.

[13] W. Becker and G. Kress. Stiffness reduction in laminate coupons due to the free-edge effect. Composites Science and Technology, 52:109-115, 1994.

[14] K.H. Boller. Fatigue Fundamentals for Composite Materials. Composite Materials: Testing and Design, ASTM STP 460, American Society for Testing and Materials, Philadelphia, PA, pp 217-235, 1969

[15] E.T. Camponeschi, W.W. Stinchcomb. Stiffness Reduction as an indicator of Damage in Graphite/Epoxy Laminates, Composite Materials: Testing and Design (Sixth Conference), ASTM STP 787, American Society for Testing and Materials, Philadelphia, PA, pp 225-246, 1982.

[16] R. Talreja. Transverse Cracking and Stiffness Reduction in Composite Laminates. Journal of Composite Materials, 19: 355-375, 1985.

[17] S.L. Ogin, P.A. Smith, P.W.R Beaumont. Matrix Cracking and Stiffness Reduction during the Fatigue of a $(0/90)_s$ GFRP Laminate, Composites Science and Technology, 22: 23-31, 1985.

[18] L.E. Crocker, S.L. Ogin, P.A. Smith, and P.S. Hill. Intra-laminar fracture in angle-ply laminates. Composites Part A, 28A: 839-846, 1997

[19] J. Tong, P.A. Smith, S.L. Ogin, and F.J. Guild. A comparative study of matrix cracking under quasi-static and mechanical fatigue loading. Fatigue '96: Proceedings of the 6th international fatigue conference, G.Lutjering, H. Nowack (ed.), Pergamon press: pp.1573-1578, 1996

[20] V. L. Tahiri, C. Henaff-Gardin and M.C. Lafarie-Frenot. Damage and in-plane shear behaviour of a [±45°] carbon/epoxy laminate under quasi-static and fatigue tensile loadings. Fatigue '96: Proceedings of the 6th international fatigue conference, G.Lutjering, H. Nowack (ed.), Pergamon press: pp. 1561-1566, 1996

[21] M.C. Lafarie-Frenot, C. Henaff-Gardin. Formation and Growth of 90° Ply Fatigue Cracks in Carbon/Epoxy Laminates, Composites Science and Technology, 40: 307-324, 1991.

[22] J.Hoover. Angle Ply Cracking of $[\pm\theta/-45_3/+45_3]_s$ Glass Fibre/Epoxy Resin Laminates Subject to Monotonic Loading. University of Alberta Mechanical Engineering 409 Report: 1-24, 1996

[23] J.W. Hoover, D. Kujawski, F. Ellyin. Transverse cracking of symmetric and unsymmetric glass-fibre/epoxy-resin laminates. Composites Science and Technology, 57:1513-1526, 1997

[24] D. Kujawski. Width effects on the tensile strength and fatigue behaviour of angle-ply laminates. International Journal of Fatigue, 20:575-580, 1998

[25] D. Kujawski and F. Ellyin. Rate/Frequency-dependant behaviour of Fibreglass/epoxy laminates in tensile and cyclic loading, Composites, 26:719-723, 1995

[26] J.W. Hoover, J.D. Wolodko, F. Ellyin. Transverse Cracking of $[\pm\theta/90_3]_s$ Composite Laminates: Part I – Experimental Results 1999.(In preparation)

[27] C. Rorhbacher. Investigation of the effect of aqueous environment on glass-fibre reinforced epoxy resin. Department of Mechanical Engineering Report no. 102, University of Alberta, Edmonton, Alberta, 1998

[28] J.D. Wolodko, J.W. Hoover, F.Ellyin. Detection of Transverse Cracks in GFRP Composites using Digital Image Processing. Proceedings of ICM8 Conference, Volume II, F. Ellyin, J.W. Provan (ed.), Fleming printing ltd.:pp. 483-487, 1999

[29] J.D. Wolodko, Biaxial fatigue and leakage characteristics of fibre reinforced composite tubes. Ph.D. Thesis, University of Alberta, Edmonton, Alberta, 1999.

[30] J.W. Hoover, Transverse Cracking of $[\pm\theta/90_3]_s$ Composite Laminates. M.Sc. Thesis, University of Alberta, Edmonton, Alberta, 1999.

[31] D.J. Thornton, Finite Element Analysis of Fibre-Reinforced Composite Pipeline. M.Sc. Thesis, University of Alberta, Edmonton, Alberta, 1999.

[32] G.P. Sendeckyj, NDE Techniques for Composite Laminates. AGARD Conference Proceedings No. 355,London, United Kingdom, 2:1-22, 1983

[33] K.L Reifsnider and R. Jamison. Fracture of fatigue-loaded composite laminates. International Journal of Fatigue, 4: 187-197, 1982

[34] W.D. Rummel, T.L. Tedrow, H.D. Brinkerhoff. Enhanced X-Ray Stereoscopic NDE of Composite Materials. Air Force Wright Aeronautical Laboratories Technical Report, Wright Patterson Air Force Base, Ohio, pp 313-322, June 1980.

[35] C. Henaff-Gardin, M.C. Lafarie-Frenot, J.P. Amirault, D. Lang. Influence sur l'endommagement de stratifies carbone-epoxyde d'un radio-opacifiant a base d'iodure de zinc. Materiaux et Techniques, 82: 20-24, 1994

[36] C. Scarponi, R. Barboni, Delaminations onset and propagation for CFRP angle ply laminates under uniaxial fatigue loads. Journal of reinforced plastics and composites, 16:1181-1195, 1997

APPENDIX A

A variety of damage examination techniques were investigated, some of which performed well and were adopted herein, and some whose performance was not deemed satisfactory. This section includes those damage examination techniques which were not used, as well as some examination techniques that were not fully examined, yet may prove useful in future examination of damage initiation and propagation in composite structures.

1.0 X-Radiography of Specimens

A NDE technique that has become increasingly popular with composite materials testing is radiography. Radiography consists of bombarding a composite structure with X-rays, similar to medical examination of human bone structures. By taking x-rays successively throughout a cyclic test, or by just taking a single x-ray at some point in the test a good representation of crack growth in the specimen can be found.

A correctly exposed x-ray had two variables that can be adjusted: the voltage inputted to excite the x-rays, and the time the x-rays are subjected on the specimen. Research showed that by decreasing the voltage, and increasing the exposure time, the contrast between the crack and the composite material is increased. Typical x-ray parameters for composite specimens are around 10-20 KV, with exposure times between 30 and 60 seconds.

A problem with radiography of composites was that both the glass-fibres and the resin matrix absorb X-radiation only slightly differently than does air. To remedy this a

contrast enhancing material needed to be introduced. Studies found that the best method was the addition of a contrast enhancing penetrant into the crack voids [34].

Various X-ray penetrants have been used in the past:

- Tetrabromoethane – (TBE)
- 1,4 Diiodobutane – (DIB)
- Diiodomethane – (methylene iodide)
- Amipaque (Metrizamide)

Unfortunately all of these materials are halogenated organic compounds which are carcinogenic and dangerous to deal with.

A recipe for X-Ray Penetrant using Zinc Iodide was found to work well for Sendeckyj [32]. The Zinc Iodide penetrant solution is non-carcinogenic, has both polar and non-polar solvent properties that allow good penetration, and it also has high x-ray absorption characteristics. The mixture used in initial tests at the University of Alberta was as follows:

Zinc Iodide (ZnI_2)	- 60 grams
Water (H_2O)	- 10 mL
Isopropyl Alcohol	- 10 mL
Kodak "PhotoFlo 200"	- 1 mL

Results show that this penetrant was able to soak into most matrix cracks. Early x-ray pictures displayed penetrant that had entered through-width matrix cracks. This penetrant was thicker near the edges of the specimen than it was at the center. This suggests that there is a decreasing penetration rate, which could result in incomplete

damage characterization. Further research needed to be done on this subject to see the total effect of penetration.

The method has proved useful to other researchers when examining very thin ply thickness specimens. Optical image processing becomes increasingly difficult when the ply thickness is thinner, due to reduced contrast between the crack and the matrix. As well, in carbon-fibre composites, which aren't transparent, this is the only method of examining new crack growth.

Work using radiography to examine matrix cracking in composites has been done previously by Reifsnider and Jamison [33], Rummel, Tedrow, and Brinkerhoff [34], and Lafarie-Frenot, Henaff-Gardin et al [20,21,35]. Previous X-ray test parameters are presented in the following table:

RESEARCHERS: RUMMEL, TEDROW, BRINKERHOFF				
Penetrant: ZnI_2 mixture				
X-ray source: Balteau 5-50 kV, 20 Amp				
Film: Kodak Industrex R, double coated film w/ automatic processing.				
# of Plies	Killivolts	Milliamps	Exposure Time	Focal Distance
8	15	20	240 s	127 cm
16	15	20	480 s	127 cm
24	15	20	960 s	127 cm

RESEARCHERS: REIFSNIDER, JAMISON				
Penetrant: ZnI_2 mixture				
X-ray source: Hewlett Packard Faxitron				
Film: Kodak Industrex R, double coated film.				
# of Plies	Killivolts	Milliamps	Exposure Time	Focal Distance
8	25	25	30 s	?

RESEARCHERS: HENAFF-GARDIN, M.C. LAFARIE-FRENOT, ET AL.				
Penetrant: ZnI_2 mixture				
X-ray source: Pantak HF 100				
Film: Kodak Industrex R, double coated film.				
# of Plies	Killivolts	Milliamps	Exposure Time	Focal Distance
18	13	35	42 s	?

Because of limitations on the type of machine that was accessible, as well as types of films available, the following configuration was used in University of Alberta tests:

RESEARCHERS: WHARMBY, WOLODKO, ELLYIN				
Penetrant: ZnI_2 mixture				
X-ray source: Pantak HF 100				
Film: Kodak X-Omat AR-2 double coated film with automatic processing.				
# of Plies	Killivolts	Milliamps	Exposure Time	Focal Distance
8-10	50	10	3 s	94 cm

These parameters were found found to give poor contrast between the cracks and the composite material, especially as the thickness of the cracks grew smaller with decreasing number of similar plies.

2.0 Fluorescent Penetrant

Fluorescent penetrant had been examined as a method of examining crack initiation and growth in a specimen. By coating a specimen in the fluorescent penetrant and then placing the specimen under a dark-light. This method has proved useful in examining the damage growth in tubes undergoing pressure loading. The fluorescent penetrant is placed inside the specimens and as the fluid leaks out it shows where the damage is. In the coupon tests the fluorescent penetrant didn't prove to be any more

effective than the visual penetrant, while still requiring the darklight to view where it had penetrated the specimen.

3.0 Edge Replication of the Specimens

Edge replication of specimens is a method of recording crack initiation and growth along the edges of specimens. This is done by holding replicating tape over acetone fumes that soften the tape, then applying the tape to the side of the specimen and letting it harden. The hardened acetone records the crack pattern along the edge of the specimen. This method can be hard to perform, since the tape curls and is hard to place on the specimen.

4.0 Acoustic Emissions

Detection of damage by acoustic emissions consists of picking up noise emitted from the specimen due to microcracking as the specimen is damaged. Triangulation of individual microphones can be used to determine the location of damage growth, although when more than one crack emits noise at the same time the exact location of crack growth can become difficult to determine. This method is a good indicator of when significant damage happens (large acoustic emission), although it gives very little information about the nature of the damage growth.

5.0 Thermography

Damage detection by thermography is performed by examination of heat flow through the composite material. Temperature contours of a specimen can be detected and mapped out using either photochromatic coatings or infrared photography.

Two different approaches to this method exist. One of them examines damage growth due to hysteresis heating of the specimen, whereby internal heat generation causes the stress contours. The other approach is to induce a heat flow through the specimen. This idea relies on the fact that any defects and damage in the composite can restrict heat flow and these temperature contours can be seen. This method provides no information of the type of damage growth, and details of the damage magnitude are very poor.

6.0 Ultrasonic testing

Ultrasonic testing is a damage examination technique whereby a high frequency sound beam is directed through a composite, and the affected waveform is picked up on the other side of the specimen. Any changes in the waveform can be correlated with damage growth in the specimen. This method has proven most useful in delamination detection, since the delaminations affect a large in-plane section between two plies. Damage such as matrix cracking, which is thin in relation to the outer surface of the specimen, is very hard to detect unless the resolution of the ultrasonic testing is very fine. A problem with this detection method is that careful control of the acoustic parameters must be adhered to, since any variances can cause inaccuracy in damage predictions.

7.0 Sectioning

Damage examination by sectioning consists of soaking a specimen in visual penetrant and then cutting the specimen into sections for examination under the microscope. This has been shown to provide an accurate description of the matrix cracking and delamination damage in a cross-section of a specimen. It is a very difficult method to implement, mainly because new damage can be introduced when the sectioning operation is being performed. As well, it is a destructive damage examination technique that prevents further examination of the specimen.

8.0 Deplying

Deplying is a destructive damage examination technique. This method of specimen examination consists of soaking a specimen in a penetrant solution of gold chloride diethylether, then performing a burn-out test on the specimen. This removes the resin from the specimen, so that each of the individual plies can be removed. The residual gold penetrant remains showing where damage such as matrix cracking, delamination, and fibre failures had been. The benefits of this method are that it provides extremely accurate information on matrix cracking, and delamination in a specimen. The drawbacks are that because it is a destructive damage examination technique, it can't be used to document damage accumulation in a specimen.